26280.1-PH-CF

①

PROCEEDINGS

OF THE
INTERNATIONAL CONFERENCE
ON

LASERS '88

DTIC
ELECTE
JUL 3 1 1989
S
B D

89   31 036

REPORT DOCUMENTATION PAGE	READ INSTRUCTIONS BEFORE COMPLETING FORM

1. REPORT NUMBER	2. GOVT ACCESSION NO.	3. RECIPIENT'S CATALOG NUMBER
ARO 26280.1-PH-CF	N/A	N/A

4. TITLE (and Subtitle)	5. TYPE OF REPORT & PERIOD COVERED
Eleventh International Conference on Lasers & Applications	Final 9/1/88 – 8/31/89
	6. PERFORMING ORG. REPORT NUMBER N/A

7. AUTHOR(s)	8. CONTRACT OR GRANT NUMBER(s)
Frank J. Duarte (editor) R. C. Sze (editor)	DAAL03-88-G-0046

9. PERFORMING ORGANIZATION NAME AND ADDRESS	10. PROGRAM ELEMENT, PROJECT, TASK AREA & WORK UNIT NUMBERS
Society for Optical and Quantum Electronics McLean, VA 22101-0245	N/A

11. CONTROLLING OFFICE NAME AND ADDRESS	12. REPORT DATE
U. S. Army Research Office P. O. Box 12211 Research Triangle Park, NC 27709	1989
	13. NUMBER OF PAGES 794

14. MONITORING AGENCY NAME & ADDRESS(if different from Controlling Office)	15. SECURITY CLASS. (of this report)
	Unclassified
	15a. DECLASSIFICATION/DOWNGRADING SCHEDULE

16. DISTRIBUTION STATEMENT (of this Report)

Submitted for announcement only.

17. DISTRIBUTION STATEMENT (of the abstract entered in Block 20, if different from Report)

18. SUPPLEMENTARY NOTES

The view, opinions, and/or findings contained in this report are those of the author(s) and should not be construed as an official Department of the Army position, policy, or decision, unless so designated by other documentation.

19. KEY WORDS (Continue on reverse side if necessary and identify by block number)

Lasers, Laser Physics, Fiber Lasers, Optical Neural Networks, Dye Lasers, Laser Radar, Laser Lidar

20. ABSTRACT (Continue on reverse side if necessary and identify by block number) The conference began with a very much enlarged list of short courses on Sunday and provided an excellent opportunity for those interested in getting a more than cursory glance at topics of interest to them but not within their expertise. The conference strongly encourages individuals interested in giving courses to contact next year's program chairman and co-chairman. The conference program consisted of over 300 papers. The strength of the conference continued to be in the areas of laser physics and laser technology, and constituted 40% of the sessions. We continued to schedule a strong set of plenary papers that encompass topics in all areas of quantum electronics. Many technology oriented participants at the conference have especially expressed their appreciation in having the opportunity to listen to research in progress of a more fundamental nature. (cont'd)

DD FORM 1473 EDITION OF 1 NOV 65 IS OBSOLETE
, JAN 73

Efforts were made to organize sessions on emerging technologies that are potentially going to be very important in the future. These included topics on optical neural networks and fiber lasers. The panel discussions this year were on high power dye laser technology and the status of Laser Radar/Lidar. The dye lasers discussion comes at a time when commercial usage is increasing rapidly while a number of defense programs are terminating. The use of lasers for lidar is an important program at SDI but more significant is its increasing importance in pollution and effluence monitoring as federal standards are made more stringent.

PROCEEDINGS

**OF THE
INTERNATIONAL CONFERENCE
ON**
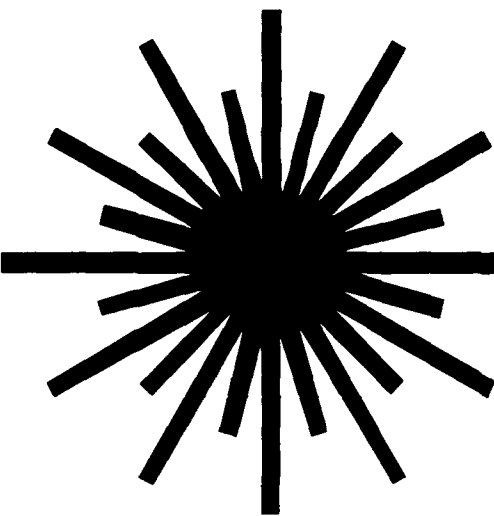
LASERS '88

PROCEEDINGS

**OF THE
INTERNATIONAL CONFERENCE
ON**

LASERS '88 ▬

LAKE TAHOE, NEVADA   **DECEMBER 4-9, 1988**

R.C. Sze
and
F.J. Duarte
Editors

CONFERENCE SPONSORED BY
THE SOCIETY FOR OPTICAL & QUANTUM ELECTRONICS

STS PRESS • McLEAN, VA • 1989

PRICE: $120.00
SOLD BY: SOCIETY FOR OPTICAL &
          QUANTUM ELECTRONICS
PER: MARGARET CONKLYN

CONTENTS

EXCIMER LASERS

FREE ELECTRON LASERS

CHEMICAL LASERS

NUCLEAR PUMPED LASERS

VII

DYE LASERS

SOLID STATE LASERS

SEMICONDUCTOR AND DIODE LASERS

NONLINEAR EFFECTS IN FIBERS AND FIBER LASERS

DYNAMIC GRATINGS AND WAVE MIXING

LASER RADARS, LIDARS, AND REMOTE SENSING

DIODE LASER APPLICATIONS

ADAPTIVE OPTICS AND PROPAGATION

ULTRAFAST PHENOMENA

LASER SPECTROSCOPY AND LASERS IN CHEMISTRY

X

LASERS IN INDUSTRY

LASERS IN EDUCATION

PANEL DISCUSSION

FOREWARD

For the second year in a row The International Conference on Lasers 1988 was held at Lake Tahoe, Nevada from December 4 - 9, 1988. It certainly is one of the most beautiful spots on earth and this year's snow was a quantum level better than the previous season so that the ski enthusiasts had an opportunity to test their skills. The conference began with a very much enlarged list of short courses on Sunday and provided an excellent opportunity for those interested in getting a more than cursory glance at topics of interest to them but not within their expertise. The conference strongly encourages individuals interested in giving courses to contact next year's program chairman and co-chairman. The conference program consisted of over 300 papers. The strength of the conference continued to be in the areas of laser physics and laser technology, and constituted 40 of the sessions. We continued to schedule a strong set of plenary papers that encompass topics in all areas of quantum electronics. Many technology oriented participants at the conference have especially expressed their appreciation in having the opportunity to listen to research in progress of a more fundamental nature. We were especially heartened by comments from many conference participants on the high quality of the papers presented. Frank Duarte and I would very much like to thank the program committee for their excellent effort in this regard. For in the last analysis this is the only important gauge to judge the success of a conference.

The theme of the conference in 1988 was on high power lasers and began on Monday with the keynote address by Dr. Charles Brau of Vanderbilt University titled The Development of Very High Power Lasers. Charlie played an important role in the development of the gas dynamic CO_2 laser, is the co-inventor of the rare-gas halide excimer system, and was the program manager of the Los Alamos National Laboratory's free electron laser effort. There were scheduled six plenary talks on various types and topics of high power laser technology. In addition to the usual strong sessions on laser physics and technology, this year Profs. Vladimir Danilychev and V. V. Apollonov graciously organized three sessions on high power lasers research in the Soviet Union.

Efforts were made to organize sessions on emerging technologies that are potentially going to be very important in the future. These included topics on optical neural networks and fiber lasers. The panel discussions this year were on high power dye laser technology and the status of Laser Radar/Lidar. The dye lasers discussion comes at a time when commercial usage is increasing rapidly while a number of defense programs are terminating. The use of lasers for lidar is an important program at SDI but more significant is its increasing importance in pollution and effluence monitoring as federal standards are made more stringent.

Prizes for the two best contributed papers this year were again sponsored by EG&G Princeton Applied Research with gold-plated plaques donated by Eastman Kodak. The nominating committee consisted of M. O. Scully, L. W. Hillman, F. J. Duarte and R. C. Sze. This year the prizes went to:

S. Benson and J. M. J. Madey of Stanford University for their paper titled "Demonstration of Harmonic Lasing in a Free-Electron Laser"

and to:

J. Gea-Banacloche of the University of New Mexico and L. M. Pedrotti of the University of Dayton for their paper titled "Laser Coupled to a Squeezed Loss-Reservoir".

The conference was also the place chosen for the initial presentation of the Einstein Prize for Laser Science which is cosponsored by industrial and university affiliates. This year Professor Marlin Scully of the University of New Mexico and the Max-Planck Institut fur Quantenoptik presented the prize. The prize was shared by

Prof. H. Walther of the Max-Planck Institut fur Quantenoptik and
Prof. S. Haroche of L'Ecole Normale Superiore, France and Yale University

for "Pioneering Contributions to Cavity Q.E.D. and the Development of the Micromaser.

Robert C. Sze
Los Alamos National Laboratory
Program Chairman

Conference Committee

The Program Committee dedicates these proceedings to the memory of Dr. David Korff.

THE DEVELOPMENT OF VERY HIGH POWER LASERS

C. A. Brau
Vanderbilt University
Nashville, TN 37235

Abstract

The development of high power lasers using excitation by electron beams and by transverse discharges of high pressure gases as in CO_2 and rare gas halides, and the use of high energy electrons in free-electron lasers are discussed.

This morning I am going to speak to you about garbage disposal. You probably didn't come here to listen to a lecture about garbage disposal, but this is the key concept in the development of very high power lasers.

The problem with operating lasers at very high power is getting rid of the waste heat. By high power, I mean high average power, rather than high peak power. For this reason, glass lasers, which produce enormous peak power in exquisitely short pulses, don't compete in the world of high average power. You simply cannot cool them very rapidly. The heat must diffuse to the surface of the glass, where it can be removed, and this is a slow process.

Gas lasers do somewhat better. Diffusion is faster in gases because they have a longer mean free path. But the real breakthrough was the garbage disposal principle, which was conceived at AVCO Everett Research Laboratory in the late 1960's. It works as shown in Fig. 1. In a conventional laser, the heat is removed in a time which I'll call the diffusion time. τ_{DIFF}. Since diffusion is a random-walk process, the time for heat to diffuse to the surface is just the square of the number of steps to reach the surface (of the order of D/λ times the time per step $(\lambda/\bar{c})$, where D is the diameter, λ is the mean free path, and $\bar{c}$ is the mean molecular velocity. The diffusion time is therefore

$$\tau_{DIFF} \sim (D/\lambda)(D/\bar{c})$$

The garbage-disposal concept uses gas flow (convection) to remove the waste heat. The cooling time, which I'll call τ_{CONV}, is just

$$\tau_{CONV} \sim D/v \sim D/\bar{c}$$

for a flow velocity v of the order of the speed of sound (which is of the order of the mean molecular speed $\bar{c}$). Clearly, the diffusion time is long compared with the convection time

$$\tau_{DIFF}/\tau_{CONV} \sim D/\lambda.$$

For a gas at one atmosphere pressure, $\lambda \sim 10^{-7}$ m. For a large device with a diameter of 1 m, the diffusion time is therefore of the order of 10^7 times longer! All things being equal--which they never are--the convective laser will have a power 10^7 times greater than the diffusive laser, under these conditions.

GARBAGE-DISPOSAL PRINCIPLE:
FLOWING MEDIUM REMOVES WASTE HEAT

Diffusion:
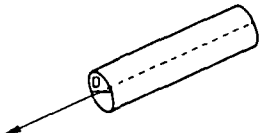
Convection:
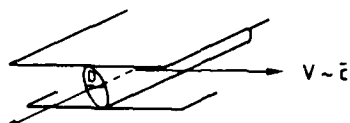
$$\tau_{DIFF} \sim \left(\frac{D}{\lambda}\right)^2 \frac{\lambda}{c} \sim \frac{D}{\lambda} \frac{D}{c} \qquad\qquad \tau_{CONV} \sim \frac{D}{V} \sim \frac{D}{c}$$

Fig. 1.

Back in the late 1960's, this factor of 10^7 seemed worth investigating. But what laser should the idea be tried on? An innovative proposal, called the gasdynamic laser, was put forward to use the flow itself to create the population inversion in a CO_2 laser. To see how this works, let's look first at the energy-level structure in CO_2, shown in Fig. 2. We see there that the upper laser level, the 001 level, is very close to the first vibrational level of N_2, and couples very strongly with it. To create the inversion, the gas is heated to a high temperature, as indicated in Fig. 3, and then expanded rapidly through a small, supersonic nozzle. At the initial high temperature, the nitrogen vibration becomes excited, albeit weakly. During the expansion the nitrogen vibration relaxes slowly and ends up at a high temperature, about that of the nozzle throat. The lower laser level is also excited at the initial high temperature, but during the expansion it couples to the 020 level which relaxes rapidly in the expansion and cools to a low temperature with a small population of the 100 level.

The very first experiment that was done at AVCO was a shock tube experiment. Instead of having an actual burner to create the hot gas, they used a shock wave to heat the gas. The shock wave reflected off of the end wall, where the nozzle was placed, and that left a stagnant region of hot gas, which expanded and gave an inversion, and everything worked splendedly. They used an old shock tube, for a quick and dirty experiment, and it worked like a charm. Well, flushed with success, they felt justified in doing a better experiment, so they got a new shock tube and a new nozzle and everything else and it didn't work, as you might have expected. As it turned out, the reason the first experiment worked was because the old shock tube was dirty and the pump oil decomposed and formed water and stuff like that, and that water is very useful for deactivating the lower laser level. So when they put water back in the mixture, the new experiment worked too. It worked out so well, in fact, that then they had to do a real experiment with a burner and all.

Eventually, some months later, they did an experiment that looked as shown in Fig. 4. At the right end is the actual burner where they burned cyanogen, which of course is nasty stuff, expanded through a bunch of nozzles between the burner and the window, and the supersonic flow then went downstream. They were able to lase at the point in the flow where the window is positioned. Now, to show you the importance of the garbage disposal principle, at the time this experiment was done, the second most powerful laser in the world, so far as we were aware, was a big non-flowing, diffusion-cooled CO_2 laser, quite a large device, and it had a power of about a kilowatt, whereas this device ran at 135 kilowatts. So flow makes a big difference. Now, those were exciting results, and in fact, eventually, a device somewhat similar to this was built by Pratt and Whitney,

2

CARBON DIOXIDE | NITROGEN
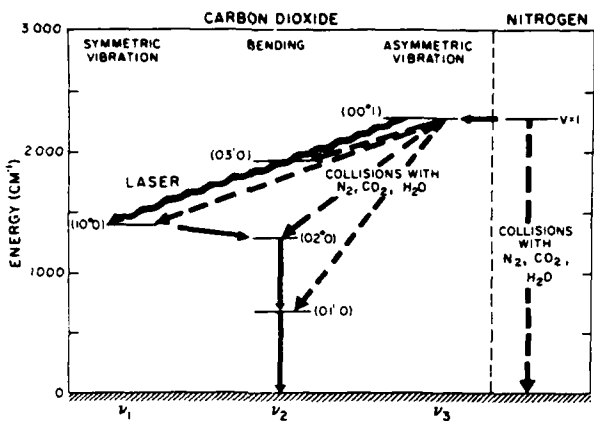
EXCHANGES BETWEEN ENERGY LEVELS

IN A CO_2 - N_2 LASER

Fig. 2.
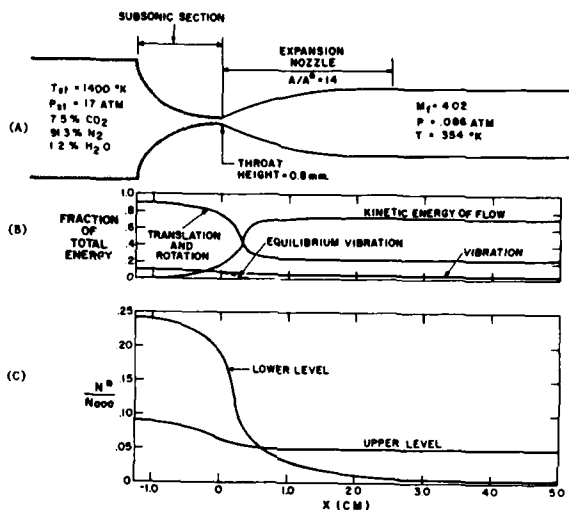
EXISTING CONDITIONS FOR A

SPECIFIC GAS DYNAMIC LASER

Fig. 3.

CO_2 GASDYNAMIC LASER
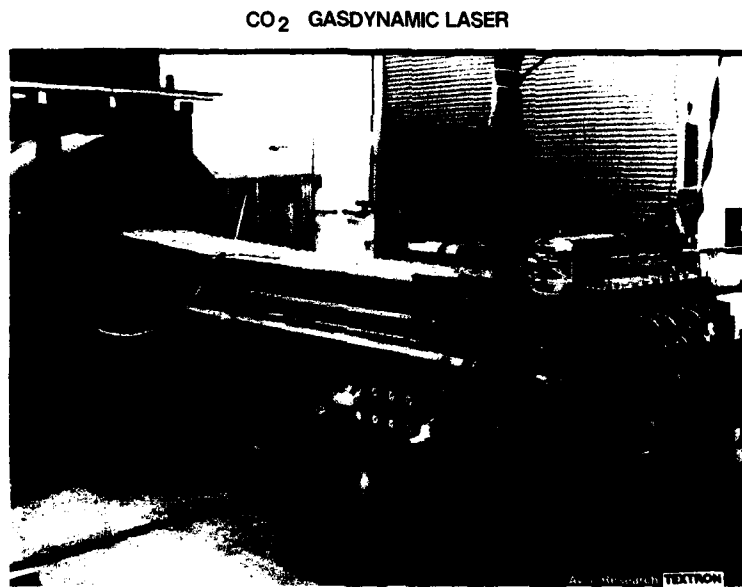
Fig. 4.

installed on a jet plane and used to shoot at air-to-air missiles that were fired at the plane. I'm told that the missiles had no warheads and didn't even have range enough to reach the plane, which shows you how much confidence they had. But nevertheless, those were important advances at that time.

On the other hand, as you may have noticed, the amount of energy that actually went into the upper laser level was very small. At 1400 K, the excitation of nitrogen vibration is not very great. So the efficiency of this device was rather small. It became interesting, then, to find a way to excite the nitrogen vibration directly without having to excite the whole gas. Well,

electron collisions excite nitrogen vibration very nicely. In fact, if you just put an electric field across the gas, and you have a few electrons around, the nitrogen gets excited very nicely--and the electric discharge goes out. But if you take a small electron beam and you create electrons in the gas, then you get a nice stable discharge. If you turn the electron beam off, the discharge goes out. If you turn the electron beam on, the discharge goes on again. And the whole thing is very stable because the rate of loss of electrons is quadratic in the number of electrons because of the collision processes that occur. In fact, the idea was simultaneously, within weeks as far as I can tell, independently discovered at both Los alamos and AVCO. But the principle of garbage disposal still applies. Here's an example of that. Figure 5 shows the so-called humdinger laser at AVCO. You can see that the electronic beam which is providing electrons for the discharge is on the right side of the flow, which goes up toward the ceiling. They were able to get greater than 500 J per pulse at greater than 100 Hz rep rate. So garbage disposal works very nicely.

REP-PULSED CO_2 LASER (HUMDINGER)

Fig. 5.

STRUCTURE OF RARE GAS MONOHALIDES

INTERNUCLEAR DISTANCE

Fig. 6.

4
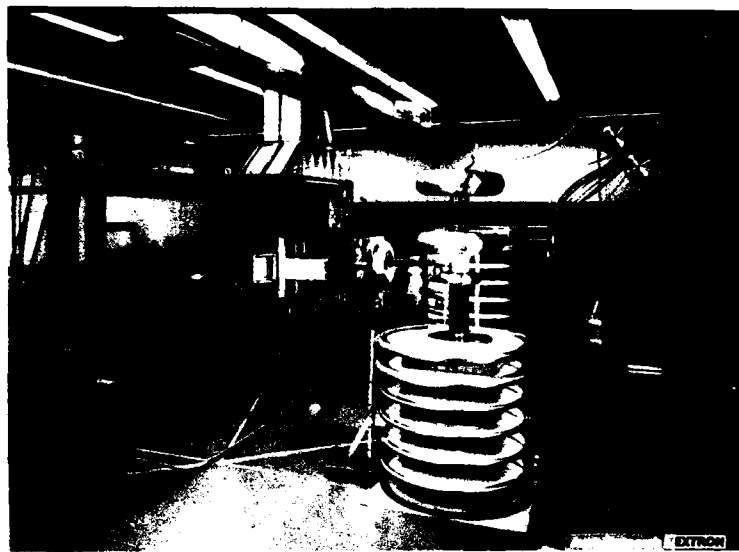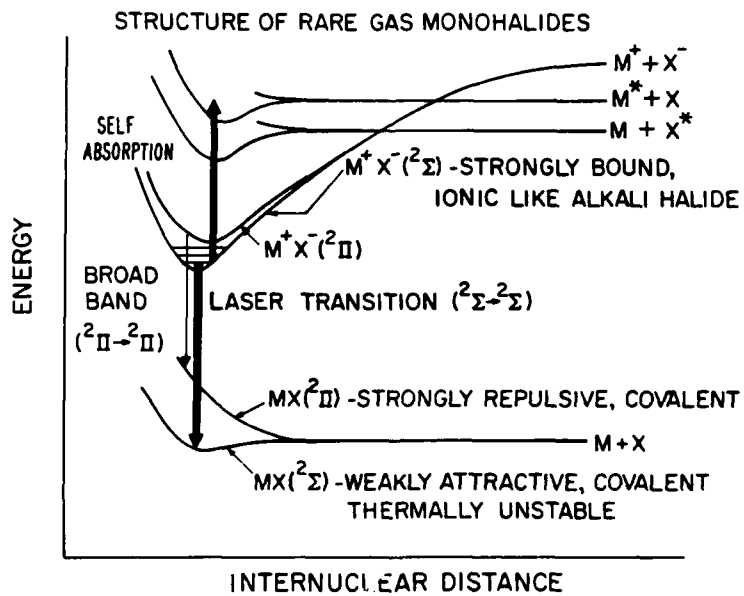
Well, the next thing that came along was the excimer laser. I'm going to skip over chemical lasers, in part, because there are a couple of talks coming up on chemical lasers that will tell you all about that, and in part because I don't know much about chemical lasers. But excimer lasers are interesting because one of the problems of CO_2 lasers is the wavelength. You can't focus 10 micron radiation at very large distances. So we looked around to find a short wavelength laser, and the one that came along was the so-called rare-gas-halide excimer laser. Now, the way these rare gas halide excimers look is shown in Fig. 6. This is a diagram which shows the energy of the molecule as a function of the distance between the two atoms, the atoms being the halogen and the rare gas atoms. Now, you all know that noble gases, rare gases, don't create molecules in the ground state. Well, that's almost true because you can actually create xenon difluoride, and that's a weakly stable gas. But most of the rare gas halides are so weakly bound that they thermally decompose at room temperature. Now in the upper level, what happens is you take a positive ion of the rare gas plus a negative ion of the halogen and those two attract one another with a Coulomb attraction, until finally they bump into one another and have a minimum in the potential curve, and this forms the upper laser level of the molecule. You can lase from the upper level to the lower laser level, which is thermally unstable and immediately comes apart. So you have a nice way of achieving an inversion in a transition at a wavelength in the near ultraviolet. Now, there are two ways to form these molecules. You can either begin with ions and let them attract one another and recombine along that Coulomb curve, or you can begin with an excited rare gas atom or an excited halogen atom. When an excited atom and a ground-state atom come together, they under go a transition to the ionic state, and then recombine as before. So you can create the upper laser level either by exciting the molecules or atoms or by forming the ions. Both those processes are extremely efficient and are easy to do in electrical discharges. Now in fact, in a discharge you preferentially form excited states, which is nice because they're lower energy. On the other hand, discharges in mixtures of rare gases and halogens are not stable because the recombination of the electrons takes place by a different mechanism than it did in the CO_2. So it's not possible to use discharges for high power lasers.

Fig. 7.

For low power lasers, you can avoid the fact that the discharge is unstable by having a very brief discharge, but this was discovered only later. The first experiments used just the electron beam, but we turned the electron beam up to hundreds of amps per square centimeter. Electron beams simply deposit their energy in the gas, the energy takes the form of both ions and excited states, and the upper laser level is formed with an overall efficiency approaching 50%, which is pretty good. The first experiment that we did is shown in Fig. 7. The flange shown there is the end of the electron beam gun, with the gas cell built

MASTER OSCILLATOR SPECIFICATIONS
AND SUBSYSTEMS CONFIGURATION
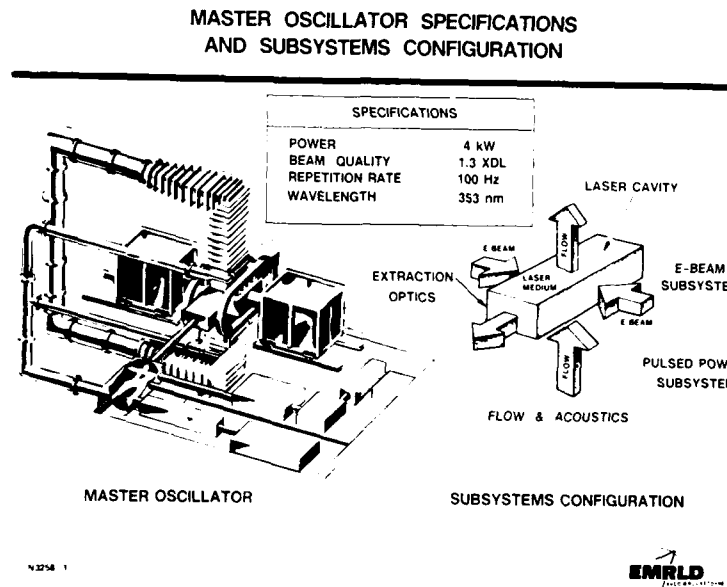
Fig. 8.

into it. In the space of a few weeks, we had actually observed lasing on xenon fluoride, krypton fluoride, xenon chloride and something that we didn't know. It later turned out to be iodine. Iodine wasn't the experiment we were trying to do, but the experiment lased on iodine instead of xenon iodide, which we had been looking for. Again, the garbage disposal principle still works. Figure 8 is a picture of the EMRLD laser built at AVCO, which operates at about 4 kilowatts. In this case, two electron beams excite the gas, one from either side. The gas flows around a loop so that it can be removed hot from the laser cavity, and then cooled before it's returned to the laser.

Well, that works very well. At 300 meters a second gas velocity, you can put a lot of gas through there and get a lot of power out. But you can do a lot better than that with electrons. Electrons travel the speed of light, which is 3×10^8 meters per second. That's a factor of a million faster than gases flow--and a factor of a million helps. So the next idea that came along that seemed really good was the free electron laser. The free electron laser, as I'm sure you all know, consists of an electron beam passing through a magnetic field, as shown in Fig. 9. As the electrons go through this magnetic field, which points alternately up and down and up and down, the electrons are deflected left and right and left and right. If you put yourself in a coordinate system moving along with the electrons, they simply appear to be moving back-and-forth, so they emit dipole radiation. In fact, they emit dipole radiation in every direction, but because they're traveling at almost the speed of light, when you transform back into the laboratory frame, the light appears to be going almost entirely in the forward direction. Therefore, an observer looking at this light sees the light Doppler shifted to a much higher frequency. The frequency conversion is such that if you have a two centimeter period for the magnetic field, and you have 100 MeV electrons, which is a modest energy for an RF accelerator, then you get light in the green part of the spectrum.

IN FREE-ELECTRON LASER, ELECTRONS VIBRATING
IN WIGGLER FIELD AMPLIFY OPTICAL BEAM
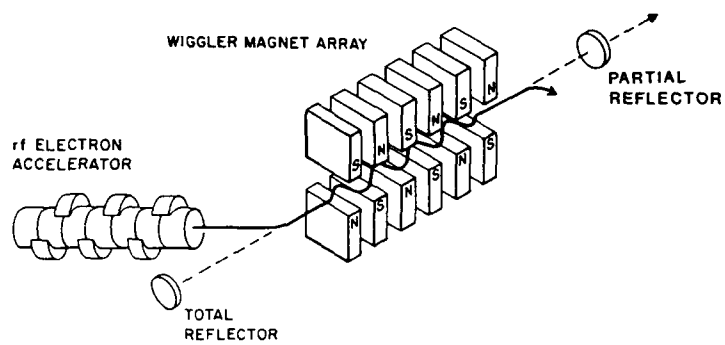
Fig. 9.

Clearly, by changing the electron energy, you can change the Doppler shift and change the wavelength of the light coming out. So the neatest thing about free electron lasers, at least the first and most obvious thing about free electron lasers, is the fact that you can tune them to all different wavelengths. That's already been done. Figure 10 shows the variety of different wavelengths that have been achieved with free electron lasers. In fact, at Livermore, Naval Research Laboratory and other places, they've made free electron lasers lase out to the centimeter region. There are two things you ought to notice. The first is that it has been possible to tune free electron lasers over a broad wavelength region in different experiments using electrons of different energy from different kinds of accelerators. The other thing is that even with one accelerator, one installation, it has been possible at Los Alamos to tune the electron energy over a factor of three or so, and get an order of magnitude tuning from about 4 microns to 40 microns. At Santa Barbara, they lased from 120 microns to 800 microns, and that's a factor of seven wavelength tuning. Those are already, so far as I'm aware, the broadest tuning range of any laser of any type. The shortest wavelength that's been achieved by straightforward lasing is in the near ultraviolet. That was achieved recently by a group at Novosibirsk. The people at LURE, near Paris, have gotten harmonics out of their free electron laser down to 0.1 micron. The harmonics were pretty weak by the time they got out to 0.1 micron.

Fig. 10.

7
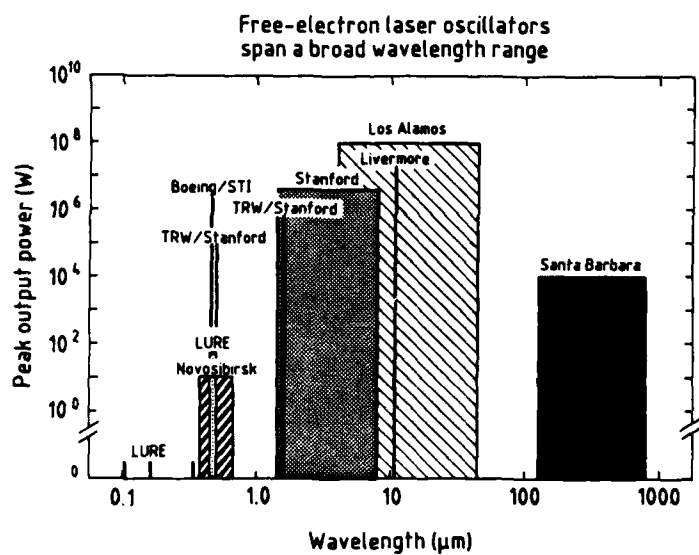
What are the advantages of free electron lasers? Certainly you can tune the wavelength by varying the electron energy. And in fact, you can tune it by small amounts by changing the magnetic field. More important for some applications, free-electron lasers can go to high power because you have very rapid heat rejection by the garbage disposal principle. In addition, it's also true that accelerator technology is very highly advanced. Of course, free-electron lasers demand things of electron accelerators that other applications don't need, so that development is required. Nevertheless, high power accelerators are well developed and quite reliable. At Stanford, for instance, the SLAC accelerator, which is two miles long, much bigger and more complicated than anything you would need for a free electron laser, runs 24 hours a day, seven days a week, month after month. The average electron beam power is 200 kilowatts, and the accelerator boasts 90% availability during scheduled operating time. For a laser, that reliability would be pretty good. I'll show you in a little while that good optical quality is another property of free electron lasers, and lately, we've been having some success at getting high efficiency. In fact, the overall efficiency can even be improved if the energy left over in the electron beam is recovered. We demonstrated that at Los Alamos.

APPROXIMATE ELECTRON ENERGY (MeV)
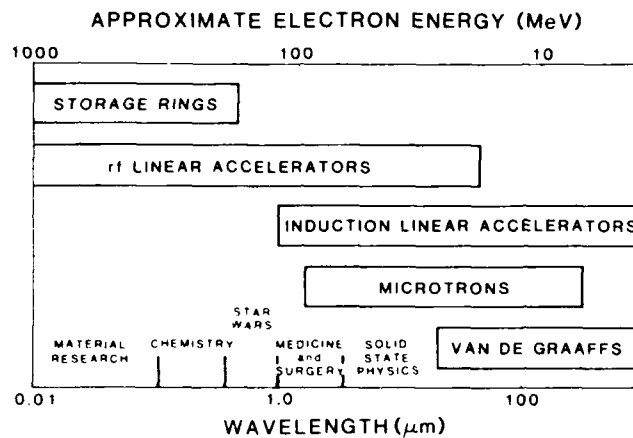
Fig. 11.

I showed you a lot of different wavelengths that had been achieved at different installations. Those wavelengths were achieved by using different electron energy from different types of accelerators. There's not a direct correlation between the electron energy and the wavelength because there is some latitude in the design of the magnetic field, but there's a rough correlation, as shown in Fig. 11. The wavelength is quadratic in the electron energy. To get different electron energies, you use different kinds of accelerators. At the low electron energy end, you can use Van de Graaff's. For a little higher electron energy, you can use microtrons. As you go up in electron energy, you can use induction accelerators, RF accelerators, and finally storage rings. As you go up in energy you go down in wavelength, of course, and as you go to different wavelengths, there are a variety of different applications, as indicated. The various applications overlap in the wavelengths they want, but you can do materials research and chemistry in the ultraviolet. Star Wars applications seem to require somewhere around a micron, and in the near infrared, medicine and surgery look like attractive applications. Finally, at long wavelengths, solid state physics is very interesting. We're going to talk today mostly about the high power applications epitomized by Star Wars.

I should point out that of the accelerator types that seem useful for getting to wavelengths around a micron, there are two that really lend themselves to high-power operation. The first is the induction linac and the other is the RF linac. Although storage rings can be used for near-infrared wavelengths, they don't operate well down at those wavelengths. The problem is that the electron beam is recirculated in the storage ring. When it goes through the wiggler magnet, the electron beam gets heated up. The next time it comes around to go through the free electron laser, it's not in a suitable form for lasing and you have to wait a while until the temperature cools down. So it's difficult to get storage rings to go to high average power. Thus, the two

8

MICROWAVE LINEAR ACCELERATOR

GUN

BUNCHER

KLYSTRON

ACCELERATOR CAVITIES
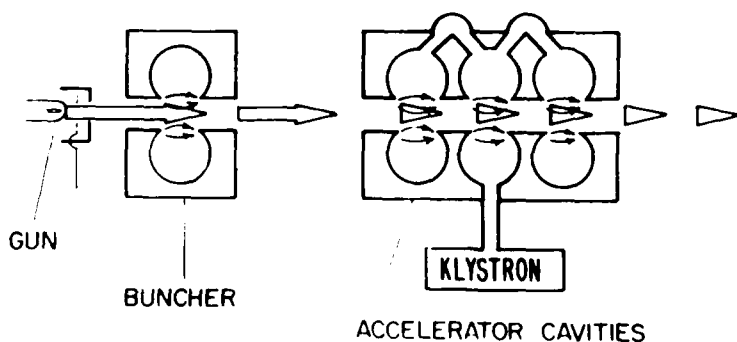
Fig. 12.

competing technologies for high power free electron lasers are RF linacs and induction linacs. I'll start off with RF linacs. An RF linac, or radiofrequency linac, works as shown in Fig. 12. You have a set of cylindrically symmetric resonant cavities, your basic pill box, and you have inside each cavity an electromagnetic field resonating at, typically, one to three gigahertz, so the cavities are of the order of 10 centimeters or so in diameter. Now, the fields that you can get oscillating in these resonant cavities have a much higher breakdown threshold than a D.C. field would have, and therefore, you can get, in a space of a few centimeters, voltages as high as a million volts or more per cell. So what you do is you stack a whole bunch of these cells

Fig. 13.

Fig. 14.

9
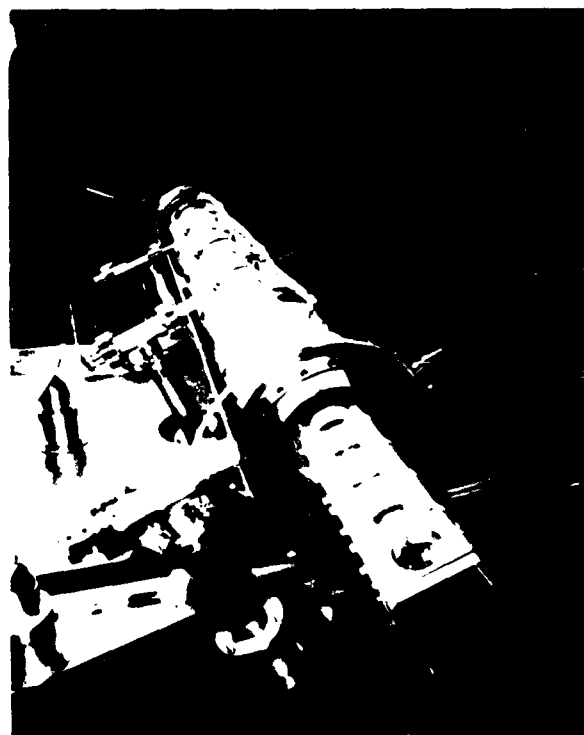
together--people have done it for up to two miles--and you can get very high electron energy. But because of the fact that you get a million volts per cell, you can get the kind of energies you're interested in for free electron lasers in a relatively small space. These cavities are fed by a klystron, which feeds one cavity from which the power is distributed to the other cavities by coupling cells. Because of the fact that these fields are oscillating, you can accelerate electrons only during the small part of the RF cycle when the field is a maximum. So you have to have your electron beam formed into bunches, and you do that in the following way. You start off with an electron gun. This emits electrons which you run through what's called the buncher. The buncher is just a small accelerator timed in such a way that the beginning of a pulse from the gun arrives during the decelerating phase, and the end of the pulse arrives at the accelerating phase. The back of the bunch gets speeded up, the front of the bunch gets slowed down, and by the time the bunch moves from the buncher to the accelerator, it has collapsed down from a bunch that's maybe a few feet long to one that's maybe a few millimeters long. If you time the bunches to arrive at the accelerator at the right phase, the bunches are accelerated very nicely and you can get very small energy spread, a percent or less. Figure 13 shows a picture of a typical RF accelerator, namely the one at Los Alamos. Each of the two accelerator sections has an acceleration of 10 million volts. Electrons come out of the accelerator, which is only a few meters long, at 20 MeV. The electrons are then directed into a wiggler, which looks as shown in Fig. 14. The period of this wiggler is about 2-1/2 centimeters. The overall length is one meter, so there are about 40 periods overall.

COMPONENT TECHNOLOGIES FOR A HIGH POWER
MASTER-OSCILLATOR POWER AMPLIFIER FEL
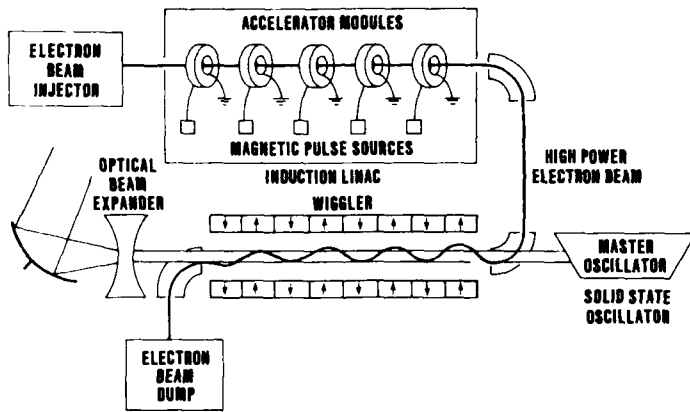
Fig. 15.

I mentioned earlier that one of the nice properties of free electron lasers is the diffraction-limited optical-beam quality. In an experiment that was done at Los Alamos we found that the Strehl ratio was about 0.92. In other words, the optical beam was 1.04 times diffraction limited. It's worth pointing out that the experimenters did everything they could to misalign the optical cavity and misalign the electron beam. By doing so, they could turn the laser off but they were never able to get an optical beam which was worse than 1.04 times diffraction limited. The reason for this is not that it's a free electron laser. It's not that magical. It's because of the fact that free electron lasers typically operate with an optical cavity which has a Fresnel number not much greater than one, and the optical cavity just doesn't support higher order modes.

The other competitor for the high power application is the induction linac, which is being promoted by Livermore. An induction linac works quite differently from an RF linac. An induction linac looks sort of like a one-to-one pulse transformer, as shown in Fig. 15. Each induction cell consists of a ferrite transformer core with a one-turn primary winding driven by a pulser. Clearly, if you have a secondary winding going around that transformer core, you induce a voltage on that secondary winding.

10

Now, if the secondary winding goes along the axis and then closes at infinity, you know that the only contribution to the voltage is along the axis, where the magnetic field is strong. If the secondary is the electron beam itself, the primary winding voltage shows up as an acceleration of the electrons by the same voltage. If you stack up a whole sequence of those transformer cores, you can accelerate electrons to whatever energy you like. The nice thing about induction linacs is that they have relatively long pulses, maybe 50 nanoseconds long, and they accelerate extremely high current. They're basically very low impedance accelerators. So you can accelerate something like 10 kiloamps through an induction accelerator.

Fig. 16.

You can achieve tremendous laser amplification because of the fact that you have such high electron beam current. On the other hand, with 15 nanoseconds there is not enough time to operate as an oscillator. There's no time for the oscillator to start up, so you run the free-electron laser as an amplifier, using something like a CO_2 laser or a YAG laser, or at very long wavelengths, a magnitron, as your master oscillator. The largest such device is being built at Livermore. Figure 16 is a photograph of the 50 MeV electron accelerator called ATA. It's quite a large device, as you can see. The wiggler is also quite large, in fact, as shown in Fig. 17. The wiggler at the stage shown is 15 meters long; it's going to be 25 meters long at the completion of the experiment. The master oscillator is a CO_2 laser. For the 15 meter experiments, the results are very encouraging. Prior to the 10-micron experiments at 50 MeV, they did some experiments at very long wavelength, around a centimeter, using a 3.5 MeV electron beam. In those experiments, they were able to get as much as a gigawatt peak power with an efficiency of 35%. By that, I mean a conversion of 35% of the electron energy into light, which is really remarkable. It's also remarkable that the theoretical predictions and the experimental results agreed so well. That's characteristic of free electron lasers, I should point out.

Both RF linacs and induction linacs have had their successes, as summarized in Fig. 18, RF linacs have gotten 4% extraction at 10 microns, much smaller extraction at a visible wavelength of half a micron. It's characteristic of free electron lasers that everything gets harder as you go to shorter wavelengths. Induction linacs have achieved 35% extraction at a wavelength of approximately a centimeter. They're just beginning experiments at 10 microns, and the best that has been achieved is about a tenth of a percent extraction efficiency. The objective of both the induction and RF linac experiments is much higher efficiency

11

than shown in Fig. 18, and those are experiments in progress.

How is one to decide between these two technologies? That's a very difficult issue. And at the risk of enormously oversimplifying things, I would summarize the most serious problems for each technology as shown in Fig. 18. For RF linacs, I think that the biggest problem is going to be that of optical damage to the resonator. As I explained, RF linacs operate with an oscillator configuration, and although they can use an amplifier following the oscillator, they don't have high enough gain to start
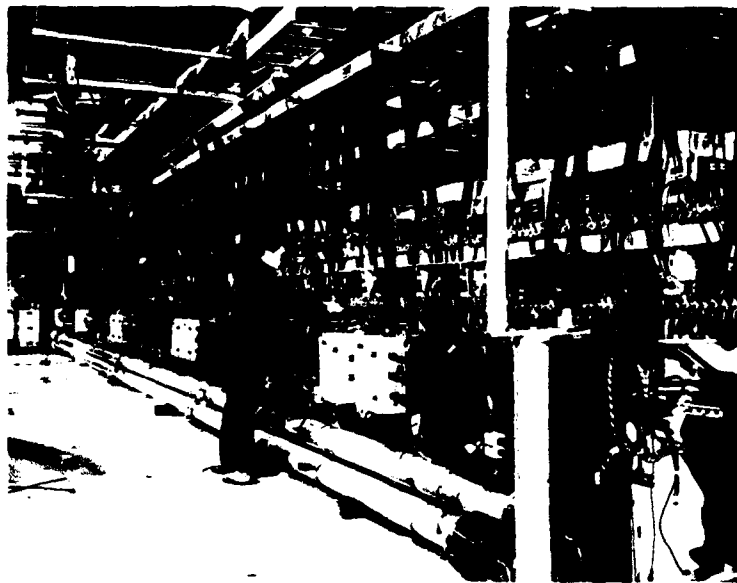
Fig. 17.

RF LINACS AND INDUCTION LINACS ARE
COMPETING FOR HIGH – POWER APPLICATIONS

RF linac	Induction linac
4% extraction @ 10μm	40% extraction @ 1cm
0.05% extraction @ 500nm	0.1% extraction @ 10μm
Problem: optical damage	Problem: e-- beam brightness

Fig. 18.

from a very small master oscillator and amplify up to a high power, so they have to have a powerful oscillator configuration in there somewhere. And because of the fact that the optical beam is highly columnated, you tend to blow away your optical components, and the resonators get extremely long, hundreds of meters long. And still, you have problems of optical damage. On the induction linac side, there is no high-power optical resonator for the free electron laser. That's the advantage of an amplifier configuration. So the problem of optical damage, while it's still around, is reduced because of the opportunities you have in running a free electron laser as an amplifier rather than an oscillator. I think the biggest problem for the induction linac is that of getting electron beam brightness adequate for operating at short wavelengths. It's been that problem as much as any

12

that's prevented Livermore from getting higher extraction efficiency than they've observed in the 10 micron experiments. At the present time, recent results show that they're about a factor of three low in electron beam brightness, and a factor of three or so low in electron beam current, compared with where they want to be for high-power applications.

Continuing this oversimplification then, you might look on the competing technologies as getting to high power and short wavelength in the following way. Induction linacs lend themselves to high power. In fact, in the first experiments they got, a gigawatt of peak power. This is not the same as a gigawatt of average power, but nevertheless, induction linacs represent a technology which can go to high power relatively easily. On the other hand, the electron beam problem and some others make it difficult for induction linacs to go to short wavelengths. So they're going to reach high power and short wavelengths by going to high power first. RF linacs, on the other hand, as I showed you, have run already down to half a micron, which is a shorter wavelength than you really need. Their problem is going to high average power, largely because of the damage to the optical components of the system. So RF linacs will go (have gone) first to short wavelength and then to high power.

It's even possible that the two approaches don't have to converge to the same point because there are ground based lasers and space based lasers. Space based lasers like to have shorter wavelengths because they can propagate the beam with smaller mirrors than longer wavelengths. Space based lasers must also be compact and light weight. Ground based lasers, on the other hand, don't mind being in the near infrared, but require higher power because of atmospheric and relay losses. So it's possible that RF linacs will lend themselves to space-based deployment, while induction linacs, because of their much larger size and longer wavelengths, will lend themselves to ground-based deployment. It's possible that RF linacs can reach the power required for ground-based deployment as well as the wavelength required for space-based deployment. It's also possible that neither technology will reach the power required for either application. Time will tell.

13

IS SPIN COHERENCE LIKE HUMPTY-DUMPTY? I. SIMPLIFIED TREATMENT

Berthold-Georg Englert[1,2], Julian Schwinger[1,3], and Marlan O. Scully[1,4]

[1] Center for Advanced Studies and Department of Physics and Astronomy
University of New Mexico, Albuquerque, New Mexico 87131
[2] Sektion Physik, Universität München, 8046 Garching, West Germany
[3] Dept. of Physics, Univ. of California, Los Angeles, California 90024
[4] Max-Planck Institut für Quantenoptik, 8046 Garching, West Germany

Abstract

When Humpty-Dumpty had his great fall nobody could put him together again. A vastly more moderate challenge is to reunite the two partial beams of a Stern-Gerl ... h apparatus with such precision that the original spin state is recovered. Nevertheless, as we demonstrate, a substantial loss of spin coherence always occurs, unless the experimenter is able to control the magnetic field's inhomogeneity with an accuracy of at least one part in 10^5.

Introduction

Contemporary research is dominated by observations on quantum systems. A thorough understanding of the role played by macroscopic devices in such measurements on microscopic objects is, therefore, mandatory for a complete, consistent interpretation of these observations. Unfortunately, some subtle features of such measurements are still controversial among theorists although one might think that the arguments among Bohr, Einstein, Heisenberg, and others, six decades ago, should have settled the issue. Most of the well-known "paradoxa" of quantum mechanics, which were the main topics of those historical debates, concern the loss of interference properties resulting from the measurement of one observable when some knowledge about a complimentary one was available before the measurement took place. For instance, if a Stern-Gerlach apparatus (SGA) is used for measuring the z-component of the magnetic moment of a spin-1/2 particle, the prior property of being polarized in, say, the x-direction is lost in the course of the measurement. There is no disagreement about the fact that microscopic coherence is destroyed during this observation (it can be confirmed experimentally), but the effect on spin coherence of the process of separating and then reuniting the two partial beams in the SGA certainly requires further study.

To address this problem we consider a SGA of the kind depicted in Fig. 1. In the first half of the apparatus the

Fig. 1. A schematic nonselective Stern-Gerlach apparatus of length $L = 4 \times L/4$.

beam of spin-1/2 particles is split *macroscopically* by the inhomogeneous magnetic field, thereby separating the particles with different z-components of their magnetic moments. Then, in the second half, the two partial beams are reunited, and a single beam emerges. By blocking one of the partial beams this apparatus can be used to select particles with a definite z-component. While the possibility of performing such a *selective measurement* is essential, no selection will actually be made. It is the objective of the present paper to find out whether, and to what degree, spin coherence can be maintained in such a *nonselective measurement*.

Prof. David Bohm, to whom we are pleased to dedicate this paper, offers, in his well-known textbook on Quantum Theory,[1] the following remark concerning this question: "If the (...) magnetic fields (...) are set up in exactly the right way, (...) the two wave packets can be brought together into a single coherent packet. Although the precision required to achieve this result would be fantastic, it is, in principle, attainable."[2] We shall establish quantitative statements about this "fantastic" accuracy by setting limits on the uncontrolled, irreproducible variations in the magnetic field that are tolerable. Only then can one decide whether a coherent spin-1/2 beam can be split and "put together again," or if it shares Humpty-Dumpty's fate.[3]

The present paper does not deal with the limits on the control of the fields in the SGA that are implied by fundamental quantum effects. That would require a calculation that takes into account the quantum properties of the *fields*. We intend to return to this problem on another occasion. Here we are only concerned with the other side of the coin: how well must the experimenter control the SGA to ensure that no substantial loss of spin coherence occurs as a result of the quantum properties of the *particles*?

Why should it be so difficult to maintain spin coherence? The essential features of the following qualitative argument are due to Heisenberg.[4] Consider the first stage of the measurement in which the SGA splits the beam macroscopically. This is achieved by applying a force F in the z-direction to those particles with one spin orientation, and a force $-F$ of equal magnitude but opposite direction to the particles with the opposite spin orientation. With these forces acting for a total time T, the momentum transferred to one of the particles is equal to FT in magnitude. In order
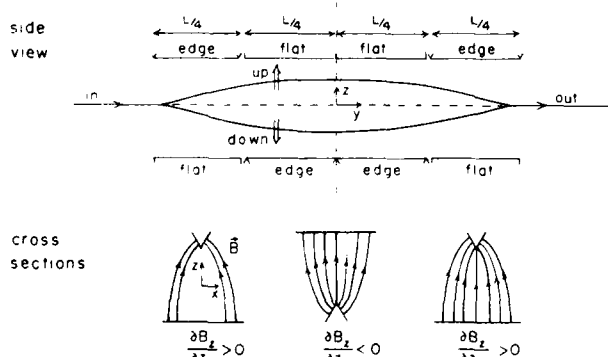
to split the beam this must be large compared to δp, the spread in momentum prior to entering the SGA:

$$FT \gg \delta p, \qquad (1)$$

where $\gg$ stands for a factor typically of order 10^3 in a practical experiment. The force F originates in a spatially dependent potential energy E, $F = -\partial E/\partial z$, which energy contributes to the phase of the wave function, the total change being $-ET/\hbar$. Since different parts of the wave function probe the potential energy at different points in space, this phase varies within the wave packet as a consequence of the spread δz in position. The phase has therefore an uncertainty given by

$$\delta(-ET/\hbar) \begin{cases} = -\delta ET/\hbar = -\frac{\partial E}{\partial z}\delta z T/\hbar \\ = FT\delta z/\hbar \gg \delta p \delta z/\hbar \geq \frac{1}{2}, \\ \gg 1, \end{cases} \qquad (2)$$

where the relation (1) and Heisenberg's uncertainty principle have been used. Note, in particular, that these large phase variations are an implication of the requirement (1) that the beam is split macroscopically. To avoid a possible misunderstanding, let us emphasize that (2) does not refer to the relative phases of the two partial beams but expresses the dispersion of phases within each individual beam. It is this phase dispersion that must be reversed during the focusing of the beam in the second stage of the nonselective measurement. The necessary extremely fine tuning of the SGA, beyond that required for spatial focusing, is what is so difficult.

Modeling the SGA

We associate Pauli matrices $\vec{\sigma} = (\sigma_x, \sigma_y, \sigma_z)$ with the $\frac{1}{2}$-spin of the beam particles so that

$$\vec{\mu} = \mu\vec{\sigma} \qquad (3)$$

is their magnetic moment. In the SGA of Fig. 1 the particles run along the y-axis, passing through (the center of) a magnetic field $\vec{B}$, directed along the z-axis, which has a strong z-inhomogeneity. The resulting force

$$\vec{F} = \vec{\nabla}(\vec{\mu} \cdot \vec{B}) \qquad (4)$$

splits the beam and then, it is hoped, focuses it, both spatially and in spin, before it leaves the SGA. The spatial dependence of $\vec{B}$ is somewhat complicated. In particular, there are the transition regions where the beam enters and leaves the various segments of the SGA which require an essential y-dependence of the magnetic field. Further, Maxwell's equation $\vec{\nabla} \cdot \vec{B} = 0$ implies that, in addition to a field gradient in z-direction, there must also be one in the x, y-plane. For the sake of simplicity we model the SGA by adopting (provisionally) these assumptions:[5] that the spin-1/2 particle maintains constant speed along y, permitting the y-dependence of the field to be replaced by a t-dependence; that the x- and y-components of the field are not significant; that the z-displacement is sufficiently small, relative to the center point $z = 0$, to justify the linear expansion of $B_z = B_z(y, z) \longrightarrow B(t, z)$:

$$B(t,z) \cong B(t) + z\frac{\partial B}{\partial z}(t). \qquad (5)$$

The interaction energy is then

$$-\vec{\mu} \cdot \vec{B} \longrightarrow -\mu\sigma_z B(t,z) = -\mathcal{E}(t)\sigma_z - F(t)z\sigma_z \qquad (6)$$

where the energy parameter $\mathcal{E}(t) \equiv \mu B(t)$ and the force parameter $F(t) \equiv \mu\partial B/\partial z$ are numerical functions of time t, which are nonzero only while the particle is inside the SGA, that is, say, for $0 < t < T$.

Our model Hamilton operator for the spin and the z-motion is then

$$H = \frac{1}{2m}p^2 - \mathcal{E}(t)\sigma_z - F(t)z\sigma_z, \qquad (7)$$

where, for notational simplicity, we write p for the z-component p_z of the momentum vector $\vec{p}$.

The Heisenberg equations of motion for $z(t)$ and $p(t)$ as well as $\sigma_z(t)$ and $\sigma_\pm(t) = \sigma_x(t) \pm i\sigma_y(t)$, implied by this Hamilton operator, are solved by

$$z(t) = z(0) + p(0)\frac{t}{m} + \sigma_z(0)\left[\frac{t}{m}\Delta p(t) + \Delta z(t)\right],$$
$$p(t) = p(0) + \sigma_z(0)\Delta p(t), \qquad (8)$$

and

$$\sigma_z(t) = \sigma_z(0),$$
$$\sigma_+(t) = \exp[-i(\Phi(t) + 2z(0)\Delta p(t)/\hbar$$
$$- 2p(0)\Delta z(t)/\hbar)]\sigma_+(0). \qquad (9)$$

The various numerical functions of t appearing here are

$$\Delta p(t) = \int_0^t dt' F(t'),$$
$$\Delta z(t) = -\int_0^t dt' t' F(t')/m,$$
$$\Phi(t) = \frac{2}{\hbar}\int_0^t dt' \mathcal{E}(t'). \qquad (10)$$

The latter is the accumulated Larmor precession angle for the field strength at $z = 0$ whereas Δp and $\Delta z + \frac{t}{m}\Delta p$ measure the displacements of the partial beams in momentum and position. Since the SGA should enable one to select one of these partial beams, the splitting must be macroscopic when the separation is maximal (and $\Delta p = 0$), which ideally happens at time $t = T/2$. In other words:

$$\Delta z(T/2) \gg \delta z(t = T/2) \cong \delta z, \qquad (11)$$

where $\delta z(t)$ is the spread in position of either of the partial beams at time t and δz is the initial spread. The latter statement of (11) reflects the requirement that in any practical experiment the natural spreading of a wave packet must not be too significant during the time T. Since the Hamilton operator (7) implies a spreading identical to that of a free particle, this requirement tells us that

$$T \cong m\delta z/\delta p \qquad (12)$$

15

is the order of magnitude of T. Here δp is the spread in momentum, which is time independent. In Eq. (11), as in (1), we write "$\gg$" to express the distinction between "macro" and "micro".

In Fig. 2, we sketch typical displacements in position and momentum, as a function of time. The corresponding force $F(t)$ is plotted in Fig. 3. The natural unit of this force
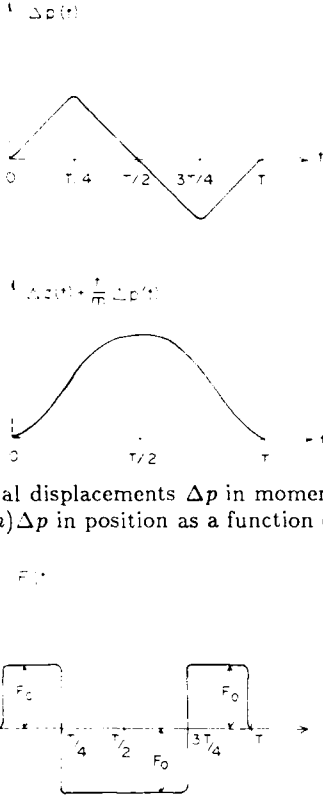
Fig. 2. Typical displacements Δp in momentum and $\Delta z + (t/m)\Delta p$ in position as a function of time.
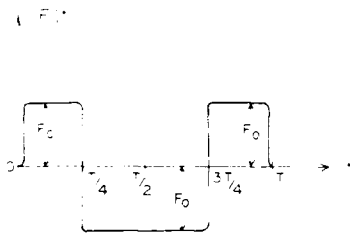
Fig. 3. Typical time dependence of the force $F(t)$.

is its maximal value F_0. It is related to the maximal spatial displacement by

$$\Delta z(T/2) = \alpha \frac{F_0 T^2}{m}, \qquad (13)$$

the number α depending on the particular time dependence of $F(t)$. It is of the order of $1/20$, as can be confirmed by considering the specific example

$$F(t) = \begin{cases} F_0, & \text{for } 0 < t < T/4, \\ -F_0, & \text{for } T/4 < t < 3T/4, \\ F_0, & \text{for } 3T/4 < t < T, \end{cases} \qquad (14)$$

for which $\alpha = 1/16$. Upon combining (13), (12), and (11), we find

$$\alpha F_0 T \gg \delta p, \qquad (15)$$

which, qualitatively, brings us back to Eq. (1).

Spin Coherence

Consider incoming particles selected in the eigenstate of σ_z with eigenvalue $\sigma_z' = 1$, so that

$$\langle \sigma_z(t=0)\rangle = 1, \qquad (16)$$

and

$$\langle \sigma_y(0)\rangle = 0, \langle \sigma_x(0)\rangle = 0, \qquad (17)$$

the latter implying that the beam will be equally split by the subsequent σ_z-measurement. The expectation value of $\sigma_x(t)$ is, according to (9), given by

$$\langle \sigma_x(t)\rangle = Re\langle \sigma_+(t)\rangle$$
$$= Re\left\{ e^{-i\Phi(t)} \langle \psi| \right.$$
$$\left. \times \exp\left[\frac{2i}{\hbar}(p(0)\Delta z(t) - z(0)\Delta p(t))\right] |\psi\rangle \right\}, \quad (18)$$

where $|\psi\rangle$ means the (normalized) *spatial* state of the incoming particle, which is specified by the probability amplitude referring to position or momentum measurements at time $t = 0$,

$$\langle z'|\psi\rangle = \psi(z'), \quad \langle p'|\psi\rangle = \psi(p') \qquad (19)$$

related to each other by the standard Fourier transformation.

Upon expressing the spatial expectation value of (18) alternatively as a z'- or a p'-integration,

$$\langle \psi| \exp\left[\frac{2i}{\hbar}(p(0)\Delta z(t) - z(0)\Delta p(t))\right]|\psi\rangle$$
$$= \int dz' \psi^*(z' - \Delta z(t))e^{-2iz'\Delta p(t)/\hbar}\psi(z' + \Delta z(t))$$
$$= \int dp' \psi^*(p' - \Delta p(t))e^{2ip'\Delta z(t)/\hbar}\psi(p' + \Delta p(t)), (20)$$

we observe, for instance, that the momentum displacement $\Delta p(t)$ produces a phase variation in the z'-description, which illustrates Heisenberg's argument.

The integrals (20) will tend to vanish, unless both $\Delta z(t)$ and $\Delta p(t)$ are small on the scale set by the initial spreads, δz and δp. To arrive at a more quantitative statement, we consider a minimum uncertainty state,

$$\psi(z') = (\delta z)^{-\frac{1}{2}}(2\pi)^{-\frac{1}{4}} \exp\left(-\left(\frac{z'}{2\delta z}\right)^2\right), \qquad (21)$$

which produces

$$\langle \sigma_x(t)\rangle = \cos(\Phi(t))e^{-\frac{1}{2}(\Delta z(t)/\delta z)^2}e^{-\frac{1}{2}(\Delta p(t)/\delta p)^2}, \quad (22)$$

where $\delta p = (\hbar/2)/\delta z$. Here we see that a macroscopic splitting, either in position or in momentum, produces $\langle \sigma_x\rangle = 0$, indicating a total loss of coherence.

The process of reuniting the two partial beams, as expressed by the spatial properties $\Delta z(T) \cong 0, \Delta p(T) \cong 0$, results in a spin state without substantial loss of coherence only if $\langle \sigma_x(T)\rangle$ does not differ significantly from its initial unit value. Ideally, one would need $\Delta z(T) = 0, \Delta p(T) = 0$ *and* an integer multiple of 2π for $\Phi(T)$. If one is willing to tolerate deviations (o = orbital is used in place of s = spatial to avoid confusion with s = spin),

$$|\delta\Phi(T)| \le \epsilon_*, \qquad \left|\frac{\Delta z(T)}{\delta z}\right| \le \frac{\epsilon_{\prime\prime}}{\sqrt{2}},$$

$$\left|\frac{\Delta p(T)}{\delta p}\right| \le \frac{\epsilon_{\prime\prime}}{\sqrt{2}}, \quad \epsilon_*, \epsilon_{\prime\prime} \ll 1, \tag{23}$$

from the ideal values, the ability of the SGA to conserve spin coherence is measured by

$$|1 - \langle\sigma_z(T)\rangle| \lesssim \frac{1}{2}|\delta\Phi(T)|^2 + \frac{1}{2}\left|\frac{\Delta z(T)}{\delta z}\right|^2 + \frac{1}{2}\left|\frac{\Delta p(T)}{\delta p}\right|^2$$

$$\le \frac{1}{2}\left(\epsilon_*^2 + \epsilon_{\prime\prime}^2\right) \equiv Q. \tag{24}$$

If, for instance, we are satisfied with maintaining 99% coherence, that is $Q = 1/100$, $\epsilon_* = \epsilon_{\prime\prime} = 1/10$ will do.

Accuracy Required in Controlling the Fields

Denoting the order of magnitude of the uncontrolled variations of the force $F(t)$ by δF, we may accumulate as much as

$$|\Delta z(T)| \cong \delta F T^2/m,$$

$$|\Delta p(T)| \cong \delta F T \tag{25}$$

during the measurement. Tolerable deviations, in the sense of (23), must not exceed the limits

$$\delta F \le \epsilon_{\prime\prime}\frac{m}{T^2}\delta z, \quad \delta F \le \epsilon_{\prime\prime}\frac{1}{T}\delta p, \tag{26}$$

which, in the light of (12), are equivalent. The comparison with (15) now establishes that

$$\frac{\delta F}{F_0} \ll \alpha\epsilon_{\prime\prime}. \tag{27}$$

Consider, for example, the situation where "$\ll$" $\sim 10^{-3}$ and $\alpha \sim 10^{-1}$. Then,

$$\frac{\delta F}{F_0} \cong 10^{-4}\epsilon_{\prime\prime} = 10^{-5}, \tag{28}$$

if we insert for $\epsilon_{\prime\prime}$ the number cited in the context of (24).[6]

Discussion

We found that a SGA can split a beam of spin-1/2 particles macroscopically without destroying the microscopic phase relations *provided* that the experimenter can reproduce the magnetic field gradient with a precision of 1 part in 10^5. This number reflects factors of 10^3 for the distinction between "macro" and "micro" and 99% coherence. [If, instead, "$\ll$" stands for 10^{-2} and one is content with 80% coherence, the respective precision is 1 part in 10^3.] In addition to that, we made a series of physical approximations along the way, which require attention. We are now going to argue that all of them are biased toward the success of the experiment, so that the required relative accuracies are *at least* 10^{-5}.

Let us repeat the assumptions we made in adopting the model: that the spin-$\frac{1}{2}$ particle maintains constant speed

along y, permitting the y-dependence of the field to be replaced by a t-dependence; that the x-and y-components of the field are not significant:

$$\vec{B}(x,y,z) \xrightarrow{1} \vec{B}(t,z) \xrightarrow{2} (0,0,B(t,z)) \xrightarrow{3} (0,0,B(t)$$

$$+ \frac{\partial B}{\partial z}(t)z), \tag{29}$$

which was followed by the linearization (5), here referred to as the third step. We shall now consider the three steps individually and argue that what is discarded in each step has a tendency to destroy spin coherence.

In *step one*, the change in velocity along y is ignored, which actual change originates in the y-dependence of the potential energy $-\vec{\mu}\cdot\vec{B}$. This velocity change is different for the two partial beams because one gains, and the other one looses, potential energy. As a consequence, the total time spent inside the SGA is slightly different for atoms with $\sigma_z' = 1$ and $\sigma_z' = -1$, so that there is a very small relative displacement along y preventing the experimenter from perfectly reuniting the beam. This presumably results in some loss of spin coherence. Another aspect of the spin dependence of the potential energy is the small, but different probability for reflection at the boundaries of the SGA, which again presumably reduces the spin coherence.

Step two disregards the time dependence of σ_z. In an arbitrary magnetic field we would have

$$\frac{d}{dt}\sigma_z = \frac{i}{\hbar}\mu(\sigma_+ B_- - \sigma_- B_+),$$

$$\frac{d}{dt}\sigma_+ = -2\frac{i}{\hbar}\mu(\sigma_+ B_z - \sigma_z B_+), \tag{30}$$

where $\sigma_\pm$ have the significance introduced in the context of Eqs. (8) and (9), and $B_\pm = B_x \pm iB_y$, analogously. A functioning SGA allows for selecting atoms with a specified value of σ_z; therefore $\sigma_z(t) \cong \sigma_z(0)$ must hold very well for all t. In Eq. (30) this requires rapid oscillations of σ_+ and σ_-, which condition is met if B_z dominates over B_x and B_y throughout the measurement. We now face the reality that σ_z is not a constant of the motion [B_x and B_y cannot both vanish everywhere, because $\vec{\nabla}\cdot\vec{B} = 0$ requires their presence if there is a nonzero force $\mu\partial B_z/\partial z$ in z-direction]. Likewise

$$m\frac{d^2}{dt^2}x = \mu\frac{\partial}{\partial x}(\sigma_z B_z + \frac{1}{2}\sigma_+ B_- + \frac{1}{2}\sigma_- B_+) \tag{31}$$

implies some deflection in the x-direction, which is negligible, provided that $\partial B_z/\partial x = 0$ and $\sigma_\pm$ oscillate rapidly. We conclude that the dynamical effects that are neglected in step two, are, indeed, small, but their presence may lead to a loss of spin coherence.

In *step three*, the z-dependence of the force is disregarded. If taken into account it results in paths of unequal lengths for the two partial beams. As a consequence, similar to the velocity effects in step one, perfect focusing of the beam is hampered, and some of the spin coherence presumably is lost.[7]

So much for the idealizations inherent in our physical model of a SGA. One additional idealization consists in the

use of the minimum uncertainty state (21). If no such special choice is made, Eq. (24) must be replaced by

$$|1 - \langle \sigma_z(T) \rangle| \lesssim \frac{1}{2} |\delta\Phi(T)|^2$$
$$+ \frac{1}{2}\left(\frac{\delta z \delta p}{\hbar/2}\right)^2 \left[\left|\frac{\Delta z(T)}{\delta z}\right| + \left|\frac{\Delta p(T)}{\delta p}\right|\right]^2 . \qquad (32)$$

As a consequence, one then needs

$$\left|\frac{\Delta z(T)}{\delta z}\right| \le \frac{\epsilon_o}{2}/D, \left|\frac{\Delta p(T)}{\delta p}\right| \le \frac{\epsilon_o}{2}/D,$$
$$D \equiv \delta z \delta p / \frac{\hbar}{2} \ge 1 \qquad (33)$$

to maintain $Q = (\epsilon_s^2 + \epsilon_o^2)/2$. For example, in a standard atomic beam experiment, with δz and δp implied by the geometry of the slits defining the particle beam, in conjunction with the velocity of the particles, the number D is typically of the order of 10^3. The relative accuracy has to be increased by this amount, that is: 10^{-8} for the gradient of the field.

In summary, we state that a perfect reconstruction of the initial beam, maintaining 100% spin coherence, is out of the question. In this sense spin coherence *is* like Humpty-Dumpty: once destroyed you cannot put it together again. In the real world it *may* be possible to recover, say, 99% coherence, provided the experimenter is able to control the SGA *at least* with the "fantastic"[2] precision of one part in 10^5 for $\partial B/\partial z$.

Acknowledgments

References

1. D. Bohm, *Quantum Theory*, (Prentice-Hall, Englewood Cliffs, 1951).
2. Ref. 1, pp. 604, 605.
3. *The Oxford Dictionary of Nursery Rhymes* (I. and P. Opie, *eds.*, Oxford, The Clarendon Press, 1951), p. 213.
4. W. Heisenberg, *Die physikalischen Prinzipien der Quantentheorie* (Hirzel, Leipzig, 1930), pp. 33,34.
5. Other models of SGAs have been considered by M. O. Scully, R. Shea, and J. M. McCullen, Phys. Rep. **43**, 487 (1978), as well as by M. O. Scully, W. E. Lamb, and A. Barut, Found. of Phys. **17**, 575 (1987).
6. The uncertainty $\delta\Phi$ of the accumulated Larmor precession angle must also be kept very small. This is more easily achieved for magnetic field configurations different from the one in Fig. 1. For details consult J. Schwinger, M. O. Scully, and B.-G. Englert, "Is Spin Coherence Like Humpty-Dumpty? II. General Theory," to appear in the Otto Stern Centennial Issue of Zeit. f. Phys. D. (1988).
7. Incidentally, in the original experiment by W. Gerlach and O. Stern, Zeit. f. Phys. **8**, 110 (1922), and **9**, 349 (1922), the deflection of the two partial beams showed a strong asymmetry.

LASER COUPLED TO A SQUEEZED LOSS-RESERVOIR

J. Gea-Banacloche and L.M. Pedrotti*

Instituto de Optica "Daza de Valdes"
C.S.I.C.
Serrano 121
28006-Madrid

and

*Department of Physics
University of Dayton
Dayton, Ohio 45469
(513) 229-2136

Abstract

In a recent paper the consequences of squeezing the external field leaking into a laser cavity on the laser's phase diffusion rate was calculated. In the present paper this work is extended to include the effect of such a squeezed loss-reservoir on the photon statistics of the laser field.

Specifically, the equations of motion for the reduced density matrix and, subsequently, for various moments of the operators describing the laser field can be obtained.

It is found that, in steady state, the average number of photons in the laser field does not differ appreciably from the case of coupling to ordinary vacuum. However, the variance in the average number of photons is significantly increased by the presence of the squeezed loss reservoir.

Introduction

The fundamental noise in a laser field can be thought of as resulting from the coupling of the field to the gain medium and the loss reservoir.[1] Each of these reservoirs feeds random noise into the laser field — the gain medium via spontaneous emission and the loss reservoir through the vacuum fluctuations leaking into the laser cavity. In this paper, preliminary results regarding the effect of squeezing[2] the loss reservoir on the photon statistics of the laser field are presented. This work is intended as a means to begin to understand the manner in which the statistical properties of a laser field might be tailored by restructuring the noise introduced by the coupling to the gain medium and the loss reservoir. Such a tailored light-field would have obvious applications in many areas including laser interferometry, spectroscopy and optical communications.

The Model

The model system studied in this paper is depicted in Fig. 1. Squeezed vacuum is injected through a partially transmitting mirror into a laser cavity containing a conventional gain medium. This system was originally studied by Gea-Banacloche[3] who showed that, under certain conditions, the phase diffusion rate of the laser field produced in such an arrangement could be a factor of two smaller than that in a laser coupled to ordinary vacuum. That only a factor of two could be achieved was attributed to the fact that only one of the two systems which feed noise into the laser field is squeezed in this system. That is, the noise introduced by the gain medium is phase insensitive and so gives rise to the residual phase diffusion. Further, this result is valid only in the transient regime, since as shown by Gea-Banacloche and later by Marte et.al.[4], the laser phase eventually locks to a value for which the phase diffusion rate is enhanced. That is, in steady state, the phase of the squeezed field θ is related to that of the laser field ϕ by the relation $\phi = \theta \pm /2$. Thus, the injection of the squeezed light has enhanced phase fluctuations (relative to the laser phase) and reduced amplitude fluctuations. For the sake of clarity it should be noted that, in the locked regime, free phase diffusion no longer occurs but rather the uncertainty in the laser's phase variable, as shown by Marte, et.al., reaches a steady state value somewhat larger than that for a coherent state field with the same average number of photons.

In this paper results pertaining to the photon statistics of the field produced by the model arrangement of Fig. 1 are presented. In particular, the rather surprising result that, while the average number of photons in the intra-cavity field is essentially unchanged by the injection of squeezed vacuum, the variance in the number of photons is dramatically increased. This dramatic increase is somewhat unexpected because, as noted above, in steady state the relative phase of the injected, squeezed vacuum is such that it has reduced amplitude (closely related to the number of photons) fluctuations. Still introduction of this squeezed vacuum results in enhanced number fluctuations. In the next section this result is formally established.

To complete the description of the model system, a short description of the squeezed vacuum injected into the laser cavity is given below. This squeezed vacuum is coupled into the laser cavity via the partially transmitting mirror (the only loss-source in the system) as depicted in Fig. 1. The injected field is assumed to be uniformly squeezed over a bandwidth larger than the cavity decay rate γ. Thus, the state of the injected field is given by

$$1/_s> = \prod_{\epsilon >0} \exp\left[-(r/2)e^{-2i\theta} b(\omega_0 + \epsilon)b(\omega_0-\epsilon) + (r/2)e^{2i\theta} b^\dagger(\omega_0+\epsilon)b^\dagger(\omega_0-\epsilon)\right] 10> \qquad (1)$$

Here, r is a real, positive squeezing parameter (for no squeezing, $r = 0$, for maximum squeezing $r \to \infty$), θ is the phase of the squeezed field, b ($b^\dagger$) is the annihilation (creation) operator for the squeezed field, and ω_0 is the nominal laser frequency.
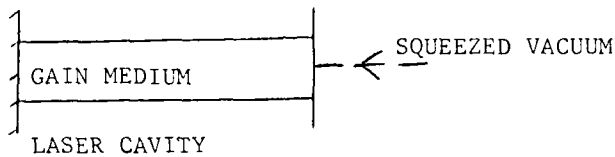
Fig. 1
Laser coupled to Squeezed Vacuum

Formalism

The equation of motion for the reduced (obtained by tracing over the operators associated with the gain medium and the squeezed loss-reservoir) density matrix describing the intracavity field can be shown to be of the form[5],

$$\frac{d\rho}{dt} = -\frac{C}{2}\left[a^\dagger a\rho - a\rho a^\dagger + adj.\right]$$

$$-\frac{A}{2}\left[aa^\dagger\rho - a^\dagger\rho a + adj.\right] \qquad (2)$$

$$+\frac{1}{8} B\left[\rho(aa^\dagger)^2 + 3aa^\dagger\rho aa^\dagger - 4a^\dagger\rho aa^\dagger a + adj.\right]$$

$$+\frac{S}{2}\left[e^{-2i\theta}(a^2\rho - 2 a\rho a + \rho a^2) + adj.\right]$$

Here, a (a^+) is the annihilation (creation) operator for the intracavity laser field and "adj." denotes the hermitian adjoint. Further, $C = \gamma\cosh^2 r$ and $A = A_0 + \gamma\sinh^2 r$ are, respectively, the linear loss and gain rates in the presence of the injected, squeezed

20

vacuum. As noted earlier, γ is the loss rate of the cavity into ordinary vacuum and A_o is the linear gain rate associated with the gain medium. Note that the difference between the loss and gain rates in the presence of the squeezed loss reservoir is the same as in its absence $(r = 0)$. That is, $A - C = A_o - \gamma$. Also, in Equation 2, B is the usual third order saturation parameter and $S = \gamma \sinh r \cosh r$. The first three terms in Equation 2 have the same form (with altered loss and gain rates) as the corresponding expression in the absence of the squeezing of the loss reservoir. The final term is due solely to the injection of the squeezed light and is primarily responsible for the new features of this system.

In order to calculate the average number of photons $\bar{n} = \langle a^\dagger a \rangle$ and the variance in this number $\sigma_n = \langle n^2 \rangle - \langle n \rangle^2$, one can construct equations of motion for $\bar{n}$ and σ_n via the prescription $\dfrac{d\langle O \rangle}{dt} = \mathrm{Tr}(\dot{\rho} O)$, where O represents a general operator and Tr denotes the tracing operation. Then one can attempt to solve these equations in steady state. In carrying out this procedure it is found, as in conventional laser theory, that these "moment" equations are coupled to higher moments of the number operator. In addition, the injection of the squeezed vacuum introduces a phase sensitive coupling to expectation values of operators involving a^2 and $a^{\dagger 2}$. The resulting hierarchy of coupled equations can be truncated by using the approximations,

$$\langle n^3 \rangle \sim \bar{n}^3 + 3\,\bar{n}\,\sigma_n, \tag{3a}$$

and

$$\langle n^2 v \rangle \sim \bar{n}^2 \bar{v} + 2\bar{n}\,\sigma + \bar{v}\sigma_n, \tag{3b}$$

where for simplicity the definition $v = a^2$ has been introduced and

$$\sigma = \langle nv \rangle - \bar{n}\bar{v}. \tag{4}$$

This approximation is motivated by a similar[6] procedure used in conventional laser theory and is based on the assumption that $\langle (n - \bar{n})^3 \rangle$ and $\langle (n - \bar{n})^2 (v - \bar{v}) \rangle$ are small compared to the terms retained in Equations (3) since they are essentially expectation values of odd powers of the difference between an operator and its average value.

Under this truncation scheme the following closed set of coupled equations can be derived:

$$\frac{d}{dt}\,\bar{n} = (A - C - B\bar{n})\bar{n} + A - B\sigma_n - 2B\bar{n} - B \tag{5a}$$

$$\frac{d}{dt}(\sigma_n) = (A + C - B\bar{n})\bar{n} + 2(A - C - 2B\bar{n})\sigma_n + 2S|v|\cos(2\phi - 2\theta) \tag{5b}$$

$$\frac{d}{dt}\,\bar{v} = (A - C - B\bar{n})\bar{v} - B\sigma - \frac{5}{2}B\bar{v} + Se^{2i\theta} \tag{5c}$$

and

$$\frac{d}{dt}(\sigma) = [2(A - C) - 3B\,\bar{n}]\,\sigma + (2A - 3B\bar{n})v - Bv\sigma_n + 2Sn\,e^{2i\theta} \tag{5d}$$

Here, $\bar{v} = |\bar{v}|e^{2i\phi}$ so that ϕ represents the phase of the lasing field. As noted above, Gea-Banaclocke has shown that, in steady state, $2\phi - 2\theta = \pi$. Under this locked condition, the set of equations can be solved in steady state subject to the usual third order conditions and so long as the average number of photons in the squeezed field $\bar{n}_s = \sinh^2 r$ is much less than that in the laser field). The results of performing this procedure are summarized in the next section.

21

Results

For simplicity, only the results appropriate in the strong-squeezing limit are presented here. That is, for the case when the average number of photons in the injected, squeezed field $\bar{n}_s = \sinh^2 r \gg 1$ (but still much less than $\bar{n}$), the pertinent results are,

$$\bar{n} \sim \bar{n}_o \left(1 + \sigma_{no}\bar{n}_s/2\bar{n}_o^2 \right) \simeq \bar{n}_o \qquad (6a)$$

$$\sigma_n \simeq \sigma_{no} \left(\bar{n}_s/2 \right), \qquad (6b)$$

and

$$|\bar{v}| \simeq \frac{1}{2} \bar{n} \qquad (6c)$$

Here, $\bar{n}_o = \dfrac{A_o - \gamma}{B} - 1$ and $\sigma_{no} = \gamma/B$ are, respectively, the average number of photons and the variance in the number of photons in the laser field in the absence of the squeezing of the loss reservoir. First, note that the average number of photons $\bar{n}$ is increased only by an additive term which is on the order of the number of photons in the squeezed field. That is $\bar{n}$ is changed by a negligible amount. However, the variance σ_n is dramatically enhanced. In fact, it is a multiplicative factor of $\bar{n}_s/2$ larger than in the absence of squeezing. A more detailed analysis shows that $\sigma_n \to \sigma_{no}$ in the weak squeezing limit and that $\sigma_n > \sigma_{no}$ for all values of the squeezing parameter r. This latter result is presented in a forthcoming paper. As noted earlier, such a dramatic increase is somewhat unexpected due to the fact that the laser phase locks such that the squeezed vacuum feeding into the laser cavity has reduced amplitude fluctuations. A possible resolution of this logical discrepancy emerges from noting that only one of the two sources of fluctuation in the laser field has been squeezed. The gain medium still contributes phase insensitive noise which, presumably, is responsible for the fact that $|\bar{v}| = |\langle a^2 \rangle| \simeq \bar{n}/2$, as shown in Equation (6c), rather than $\bar{n}$ as it would for a coherent state field. The phase of the laser field does jitter about its locked value. Thus, the phase of the injected, squeezed field is not always exactly aligned such that it is precisely the amplitude fluctuations of the injected field which are squeezed. A heuristic description of how this behavior can be understood to lead to the dramatic increase in σ_n displayed in Equation (6b) as well as other interesting features of this system will be explored in an upcoming publication.

Conclusions

In this paper the effect of injecting squeezed vacuum into a laser cavity on the photon statistics of the resulting laser field is explored. The surprising result that the variance in the number of photons in the intra-cavity field is dramatically increased in such a system, even though the laser phase locks so that it is the amplitude fluctuations in the injected squeezed vacuum that are squeezed, has been presented. This study is intended as background material for coming to a better understanding of the manner in which the statistical properties of a laser field might be tailored by an appropriate restructuring of the noise introduced by the gain medium and loss reservoir which are coupled to the field.

References

1. J. Dalibard, J. Dupont-Roc, and C. Cohen-Tannoudji, J. Phys. $\underline{43}$, 1617 (1982).

2. D.F. Walls, Nature $\underline{306}$, 141 (1983) and references therein.

3. J. Gea-Banacloche, Phys. Rev. Lett. $\underline{59}$, 543 (1987).

4. M.A.M. Marte, H. Ritsoh, and D.F. Walls, Phys. Rev. A. $\underline{38}$, 3577 (1988).

5. C.W. Gardiner and M.J. Collett, Phys. Rev. A. $\underline{31}$, 3761 (1985).

6. M. Sargent III, M.O. Scully, and W.E. Lamb, Jr., Laser Physics, (Addison-Wesley, Reading, MA, 1974) pp. 281-298.

TIME AVERAGE FORMALISM FOR LASER PUMPED LASERS

J.P. Stone and J.A. Goldstone
Advanced Programs/Rocketdyne Divsision
Rockwell International Corporation
6633 Canoga Ave. FA03
Canoga Park CA 91303

Abstract

We show that quantum time averages of the density matrix for a driven but undamped system lead to a physically transparent explanation of steady state population inversions that occur in certain systems with particular spontaneous emission damping rates. We review and show the relevance of a formalism which permits time-smoothed transient solutions to be generated *a priori*. We derive equations which extend this development to the case where there are time-dependent generated cavity fields. Theoretical results demonstrate lasing without inversion and we discuss this result in light of the time-average treatment. Finally we describe a symbolic manipulation computer code which allows us to start from limit operations on a certain matrix inverse to enumerate terms in explicit rational expressions for the time average operators, which give the averaged density matrix in terms of its initial values.

I. Introduction

We have recently pointed out the potential usefulness of certain types of laser-pumped multilevel atomic systems for frequency upconversion.[1] When these isolated atoms are subjected to coherent laser light at saturating intensities, large steady state population inversions are predicted. The pumped transitions in these systems share common levels and differ in this respect from certain recently proposed[2] and earlier[3] systems for upconversion. In addition, certain specific requirements are imposed on particular damping rates and detunings. Although the existence of inversions in systems with coherent pumping between multiple levels has been predicted in earlier calculations,[4,5] the large inversions in these particular systems have raised interesting questions concerning the physical mechanisms involved.

In addition to the inversions themselves, the predicted dynamical behavior when a resonant cavity is present at the frequency of the inverted transition also exhibits an unexpected degree of complexity. For low mirror reflectivities, a cavity field is generated and interacts with the inversion of the lasing medium in much the same way as in a standard laser as described by rate equations. At higher reflectivities, however, the medium in the presence of the (larger) cavity field displays behavior which is more like wave-mixing than standard lasing. Again the question of physical mechanism arises.

The basic theoretical description of pumping and energy-extraction in these systems utilizes Maxwell-Bloch equations to describe the coupled dynamics of the field and the density matrix of the atoms. Rate equations are commonly used to model laser dynamics in many types of systems, but these fail completely to give inversions such as these that are predicted by the full density matrix equations under saturating field conditions. A physical picture consisting of incoherent radiative transitions occurring between coupled levels is clearly not adequate in this case. We will show, nevertheless, that an equally simple physical picture does apply, but that it is quite different from the usual rate equations.

There are two essential features for inversion in the Frequency Adding MEdia (FAME systems) which we have described[1]: First, in a pumped three level system, the intermediate level should be detuned from resonance by an amount at least an order of magnitude over the Rabi frequency and the extreme level should satisfy the two photon resonance condition which allows Rabi cycling between the extreme levels as if they were a two level system with an effective Rabi frequency.[6] Second, specific incoherent transition rates from spontaneous emission or collisional damping, despite the saturating field conditions, exert an overriding influence on the steady state populations[5] and there are consequently conditions that these rates must satisfy if there are to be population inversions.

We begin in the following section by describing in greater detail the energy level structure of systems of interest and show why we should *expect* inversions to be created in these systems. We show that a previously developed reformulation[7] of the full density matrix equations in terms of time-average operators leads to an "intuitive" explanation of the population inversions in these systems. These time-average operators are linear operators[8] describing how the long time average behavior of the density matrix depends on its initial values. (Damping terms which would lead to an initial-value-independent steady state are explicitly excluded in determining this average behavior, although, as we shall see, they are included separately.)

Although the intuitive explanation for steady state inversions has been presented previously[1], we are discussing here for the first time its connection with the rigorous time-average formalism. We follow this with a discussion of some applications of the formalism to time dependent problems, including generalizations which allow treatment of systems where the fields themselves are time dependent. Finally we discuss the analytic form of the time-averaging operators

which form the basis for the formalism. These are rational functions of the field amplitude and detuning parameters[6]. While these are by no means as simple in general as the Lorentzian type expressions which appear in the standard rate equations, excellent approximations which are quite simple in analytic form apply in the two-photon resonance case. For more general applications, we describe a symbol-manipulation program which we have written, which will allow the time-average quantities to be determined for arbitrary detuning and (within practical limitations) for an arbitrary number of coupled levels.

II. Time Average Behavior and Steady State Inversions

The quantum levels for a typical FAME system and the evolution of their populations as a function of time (in the absence of any cavity which might support buildup of additional non-pump fields) are shown in Figs. 1 and 2 respectively.
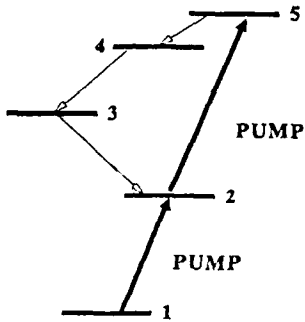
Fig.1 - Typical multilevel system which shows 4/1 population inversion with appropriate detunings and decay constants
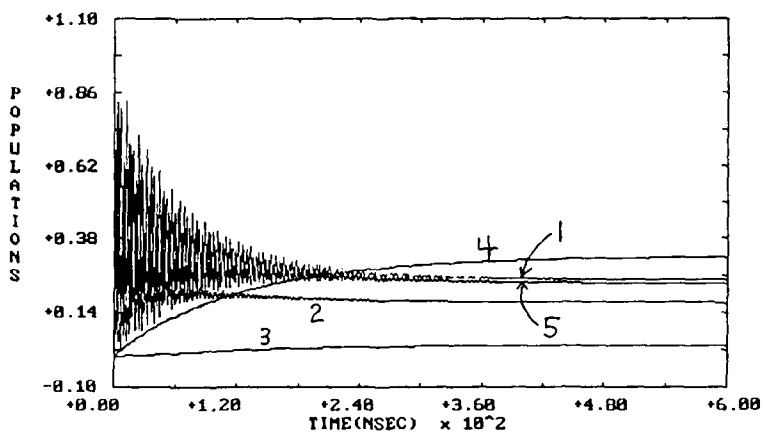
Fig.2 - Approach to steady state for system in Fig.1 with $\beta_1 = 5.$, $\beta_2 = 20.$, $\Delta_{12} = 50.$, $\Delta_{15} = 7.59$, $k_4 = .0049$, and $k_5 = .0068$ (nsec^{-1})

For the behavior predicted in Fig. 2, the essential parameters for the system depicted in Fig. 1 are that the resonance condition

$$\Delta_{15} = (\beta_1^2 - \beta_2^2)/\Delta_{12} \qquad (1)$$

be approximately satisfied and that the decay rate k_5 from level 5 to level 4 (from spontaneous emission, say) be large compared with the decay rate k_4 out of level 4. Here β_1 and β_2 are the respective Rabi frequencies for pumping between levels 1 and 2 and between levels 2 and 5. Under these conditions, the steady state population of level 4 is, as shown, inverted with respect to all the lower energy levels.

The above system, while having (as we shall see) certain desirable features with regard to ease of extracting energy from the inversion, is needlessly complicated from the point of view of illustrating the basic mechanism by which the inversion is created. A simpler system, which also shows the inversion, is shown in Fig. 3.

The ratio of level 2 to level 1 population for this system is shown in Fig. 4 as a function of both the detunings Δ_{12} and Δ_{13}. Note that the width of the "resonance" for this inversion process becomes much narrower in the Δ_{13} detuning as the Δ_{12} detuning becomes larger.

The systems illustrated here are characterized by the fact that oscillations due to Rabi frequencies or detunings take place on a faster time scale than the time scale of damping. (See Fig. 2, for example.) Physically, the behavior of such systems may be thought of as characterized most of the time by "free" Rabi cycling as if the system had no damping, punctuated at random intervals by collisions which result in transitions between levels and loss of phase. (This general picture applies even when the damping is provided by other than collisional mechanisms, since the statistics of spontaneous decay, for example, are similar to those of collision induced events.) Our "intuitive model"[1] for population inversion in FAME systems where Rabi cycling is simply assumed to "mix" certain levels and equalize their populations is based on this physical idea. However, this physical picture also leads[7] to a very general reformulation of the density matrix equations as a set of rate equations for the time-smoothed density matrix, which can, in effect, play a role similar to that played by ordinary rate equations in the strong damping regime. Here we review the physical arguments leading to the time-smoothed rate equations and show how the population inversions in the FAME system follow as a particularly simple consequence of the equations derived.

25
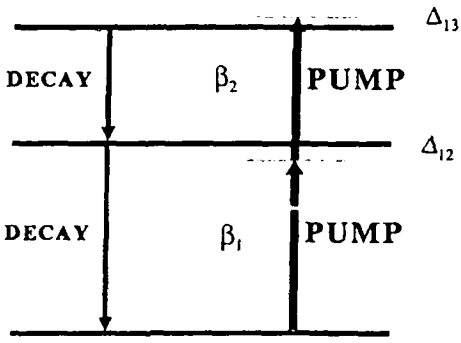
Fig.3 - Three level system which can show inversion for large intermediate level detuning.

Because of the time scales in these systems many Rabi oscillations occur *between* collisions and the phase of the oscillation at the *time* of a collision must itself be random. Therefore we can think of the collision event as involving the time-averaged density matrix. The linear dependence on the initial density matrix[8] (where in this context "initial" may mean after the *last* collision) can be described by a tetradic operator T where,
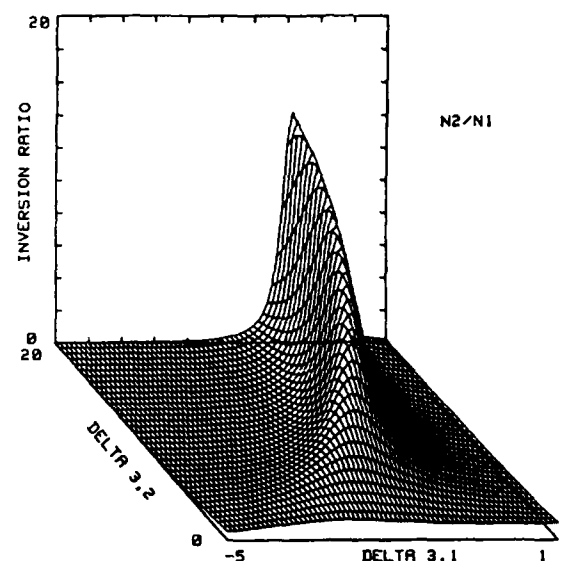
Fig.4 - Inversion of system in Fig. 3 as a function of the two detunings for $k_3 = .0016$, $k_2 = .0001$, $\beta_1 = 1.0$, $\beta_2 = 4.0$

$$\rho_{ij}^{(time\ average)} = \sum_{kl} T_{ij,kl}\rho_{kl}^{(initial)} \tag{2}$$

We can also describe the effects of damping by constructing a tetradic operator K which operates on the density matrix ρ before the random decay event to produce a new density matrix $K\rho$. For collisional damping, we assume[9]

$$K_{ij,kl} = \delta_{ij}\delta_{kl}P_{i \leftarrow k} \tag{3}$$

which means that phases are totally randomized at each collision and that atoms in state k undergo transitions to level i with probability $P_{i \leftarrow k}$.

Now we consider approximations to the density matrix solutions such as those shown in Fig. 2, where we smooth out the oscillations and obtain an average solution ρ_{av} as a function of time. We explicitly consider the ensemble average over collision histories which makes up the density matrix. Those atoms that have recently undergone a collision will have a time averaged density matrix of $TK\rho_{av}$, compared with ρ_{av} for those that have not. Since the probability of a collision in an interval Δt short compared with the collision time τ is $\Delta t/\tau$ and that of no collision is $1 - \Delta t/\tau$, the change in ρ_{av} in this time interval is given by

$$\Delta\rho_{av} = \frac{\Delta t}{\tau}TK\rho_{av} + \left(1 - \frac{\Delta t}{\tau}\right)\rho_{av} - \rho_{av} \tag{4}$$

and ρ_{av}, as a result, satisfies the differential equation

$$\frac{d\rho_{av}}{dt} = \frac{1}{\tau}(TK - 1)\rho_{av} \tag{5}$$

A derivation which is more mathematically rigorous and which allows the conditions for validity to be stated more precisely appears in Ref. 7. We note that since Eq (5) is an equation for a smoothed out ρ, we must use $T\rho^{init}$ rather than ρ^{init} itself as the initial condition.

Now we consider the application of Eq (5) to the system shown in Fig. 3, consisting, as previously noted, of an intermediate level far off resonance and extreme levels near two-photon resonance. Under these conditions systems starting out in either of the extreme levels have a very small time-averaged population in the intermediate level and vice versa, i.e.,

26

$$T_{11,22} = T_{22,11} \cong T_{33,22} = T_{22,33} \cong 0 \tag{6a}$$

which in turn implies

$$T_{22,22} \cong 1 \tag{6b}$$

The degree of transfer of population between the extreme levels depends on the exact two photon tuning condition,

$$T_{33,11} = T_{11,33} = r \tag{6c}$$

$$T_{11,11} \cong T_{33,33} \cong 1 - r$$

where[8],

$$r \cong \frac{2\beta_1^2\beta_2^2/\Delta_{12}^2}{4\beta_1^2\beta_2^2/\Delta_{12}^2 + \{\Delta_{13} - (\beta_1^2 - \beta_2^2)/\Delta_{12}\}^2} \tag{7}$$

The form of this population transfer expression is important because it enters directly into the steady state population inversions, which, for collisional relaxation, are solutions to the coupled equations

$$\sum_{k,j} T_{ii,kk} P_{k \leftarrow j} \rho_{jj} = \rho_{ii} \ , \quad i=1,3 \tag{8}$$

Including only those (spontaneous emission-like) terms in Eq(8) where $i < j$ in $P_{i \leftarrow j}$ and eliminating any terms where the T matrix elements are very small (see Eq(6)) leads to

$$P_{2 \leftarrow 2}\rho_{22} + P_{2 \leftarrow 3}\rho_{33} = \rho_{22} \tag{9}$$

Noting that $P_{2 \leftarrow 2} = 1 - P_{1 \leftarrow 2}$, we find that

$$P_{2 \leftarrow 3}\rho_{33} = P_{1 \leftarrow 2}\rho_{22} \tag{10}$$

Substituting this relationship in either the i=1 or i=3 equation then gives

$$r(\rho_{11} - \rho_{33}) + (2r - 1)P_{1 \leftarrow 2}\rho_{22} = 0 \tag{11}$$

We can now solve for the 2/1 population ratio,

$$\frac{\rho_{22}}{\rho_{11}} = \frac{rP_{2 \leftarrow 3}}{(1 - 2r)P_{2 \leftarrow 3} + rP_{1 \leftarrow 2}} \tag{12}$$

Now the expression in Eq(6) for r can be seen to vary between zero far from resonance and the value 1/2 exactly on resonance. The maximum population ratio in Eq(12) occurs at resonance and is just given by $P_{2 \leftarrow 3}/P_{1 \leftarrow 2}$, the same as predicted by the intuitive model by using a rate equation for level 2 (the same as Eq(10)) and forcing $\rho_{11} = \rho_{33}$ to account for strong "mixing" between the extreme levels. Off resonance the population transfer expression shows a width $2\beta_1\beta_2/\Delta_{12}$ proportional to the effective Rabi frequency[6] and this width, as well as the resonance condition, $\Delta_{13} = (\beta_1^2 - \beta_2^2)/\Delta_{12}$, are reflected in the location and width of the population ratio ridge shown in Fig.4.

It is interesting to note that if this basic two photon resonance situation is maintained, but one of the pump fields is increased in such a manner as to bring the population transfer between levels 2 and 3 up to a significant value s, level 3 can also become inverted with respect to the ground level. To illustrate this, we take

$$T_{23} = s \ ; \ T_{22} = 1 - s \ ; \ T_{12} = 0$$
$$T_{13} = r \ ; \ T_{11} = 1 - r \ ; \ T_{33} = 1 - r - s \tag{13}$$

(where we must, in every case have $T_{ij} = T_\chi$) and again solve Eqs(8), this time for the 3/1 population ratio. For two photon resonance (r=1/2),

$$\frac{\rho_{33}}{\rho_{11}} = \frac{P_{1 \leftarrow 2} + s - sP_{1 \leftarrow 2}}{P_{1 \leftarrow 2} + s - sP_{2 \leftarrow 3} - sP_{1 \leftarrow 2}P_{2 \leftarrow 3}} \tag{14}$$

and it is easy to see that for $P_{1 \leftarrow 2} < P_{2 \leftarrow 3}$ this population ratio can exceed unity by a considerable fraction. Three to one population inversions of this type have also been predicted from spontaneous emission damping models.

III. Time Dependent Solutions

We have applied the time-averaging formalism to obtaining steady state solutions in Sec. II. The physical arguments leading to Eq(5) (and the mathematical derivation in Ref.7), however, show that it should also correctly predict
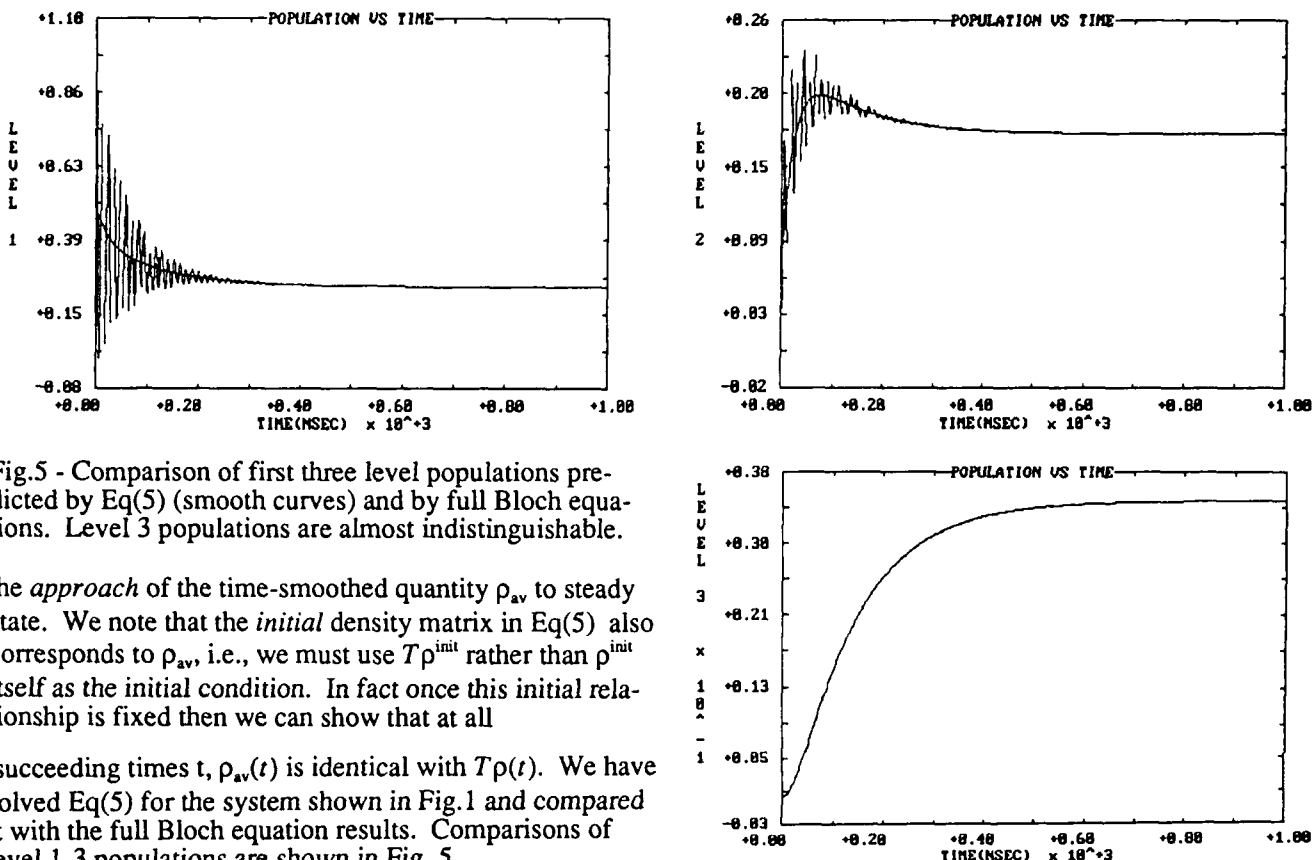
Fig.5 - Comparison of first three level populations predicted by Eq(5) (smooth curves) and by full Bloch equations. Level 3 populations are almost indistinguishable.

the *approach* of the time-smoothed quantity ρ_{av} to steady state. We note that the *initial* density matrix in Eq(5) also corresponds to ρ_{av}, i.e., we must use $T\rho^{init}$ rather than ρ^{init} itself as the initial condition. In fact once this initial relationship is fixed then we can show that at all

succeeding times t, $\rho_{av}(t)$ is identical with $T\rho(t)$. We have solved Eq(5) for the system shown in Fig.1 and compared it with the full Bloch equation results. Comparisons of level 1-3 populations are shown in Fig. 5.

The solutions of Eq(5) clearly represent a good approximation to the time-smoothed exact solutions.

The average behavior represented by the smoothed solutions may be all we care about for some purposes. In this case, the use of Eq(5) makes sense computationally since it is takes roughly an order of magnitude less calculation time. For applications of interest to us, the problem is modified by the existence of a resonant cavity which results not only in a different steady state with a cavity field present and feeding back to the system, but also in modified transient behavior in which there is a time-dependent build-up in the cavity field.

We can modify Eq(5) to cover the situation where there are time dependent fields. The most obvious change required arises from the fact that the Rabi cycling in the system depends on field amplitudes in such a way that the time-average operator T will be a function of the fields and will now depend on time because of the time dependence of these amplitudes. Therefore the T which appears in Eq(5) must take into account this time-dependence and must be redetermined at every step (or, in practice, at least periodically.)

There is a second, more subtle effect of making the fields time-dependent, which is most easily understood if we consider the case where the fields change in discrete steps at times t_i and are constant in the intervening subintervals. We define $T_i = T(\{f_i\})$ to be the time averaging operator which applies in the interval $t_i < t < t_{i+1}$. We know that, in order for the solution of Eq.(5) to smoothly approximate the exact solution in the *i*th subinterval, we must not only use T_i for T in Eq(5), but we must also choose the solution that starts out at $T_i\rho^{init}(t_i)$, where $\rho^{init}(t_i)$ is the value of the *exact* solution at the beginning of the subinterval. As we allow the time intervals $t_{i+1} - t_i$ to become small in order to approximate a continuous variation in the fields, we can consider the entire change in ρ_{av} in terms of the initial values in each interval, so that

$$\frac{d\rho_{av}}{dt} \cong \frac{T_{i+1}\rho(t_{i+1}) - T_i\rho(t_i)}{t_{i+1} - t_i} \tag{15}$$

Expanding T_{i+1} and $\rho(t_{i+1})$ to first order in the time interval leads to

$$\frac{d\rho_{av}}{dt} = \frac{\partial T}{\partial t}\rho(t_i) + T_i\frac{\partial\rho}{\partial t} \tag{16}$$

In the last term, we can consider T_i constant and bring it inside the time derivative. Since $T(t = t_i)\rho(t)$ represents ρ_{av} for the time independent field case, we can replace the last term using the right hand side of Eq(5) to obtain,

$$\frac{d\rho_{av}}{dt} = \frac{1}{\tau}(TK - 1)\rho_{av} + \frac{\partial T}{\partial t}\rho \tag{17}$$

This result will always allow ρ_{av} to be evaluated in a straightforward manner without the use of arbitrary "smoothing" schemes whenever ρ itself is being evaluated. As a generalization of Eq(5) for *numerical* calculations where we might want to avoid calculating ρ altogether, Eq (17) is somewhat disappointing. However, under certain conditions it may be a good approximation to replace ρ by ρ_{av}. For example, if the time dependence arises from the buildup of a cavity field, initially when ρ differs significantly from ρ_{av}, the derivative of T may itself be very small, while later ρ and ρ_{av} will be nearly equal anyway.

IV. Four-Level Considerations

Although the examples considered in this paper have involved only two pumping fields inducing transitions among three levels, once a cavity field has built up, it must be treated in much the same way as the pump fields. Referring again to the system in Fig. 1, we find, when we analyze Maxwell's equations with a polarization associated with the oscillating ρ_{14} term in the Bloch equations[1], that a cavity field near the 1-4 transition frequency is generated. This cavity field, shown in Fig. 6, builds up to a steady state value which increases in proportion to the cavity lifetime. The cavity fields and the corresponding steady state level populations are shown in Fig. 7 as the cavity lifetime is varied.
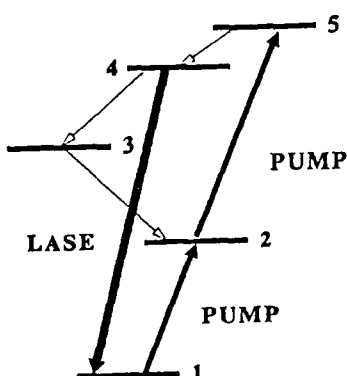
Fig.6 - Cavity lasing field which builds up for five level system discussed earlier (see Figs. 1 and 2)

We see that as conditions allow larger cavity fields to build up, at first the 4-1 inversion is gradually lost as one might expect from treating the dynamics of the energy extraction using ordinary rate equations. Later, however, for still larger cavity fields the inversion begins to increase again and then suddenly disappears altogether as the populations of level 1 and level 4 rather dramatically cross over each other and level 1 becomes the most populated again. Nevertheless, energy extraction continues as is evidenced by the continuing build-up of the cavity field.
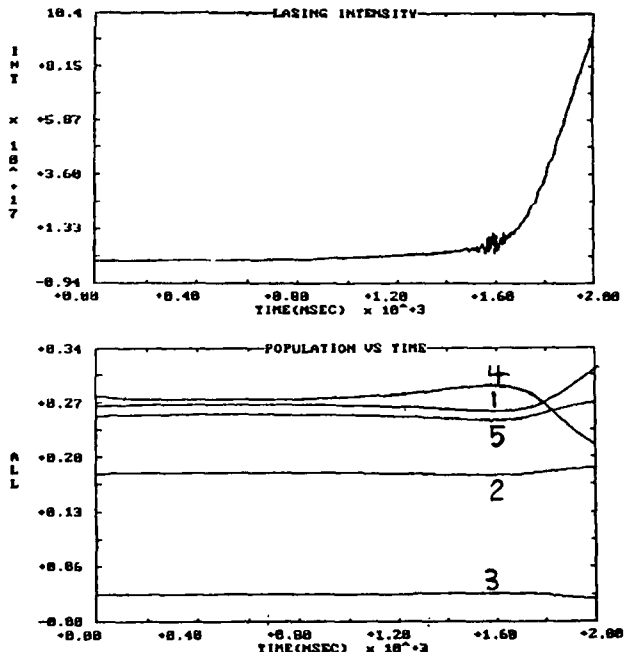
Fig. 7 - Cavity field and level populations for various cavity lifetimes, obtained by adiabatic (logarithmic) variation over indicated timescale from $\tau_C = 100ps$ (beginning of interval) to $\tau_C = 100ns$.

29

There are two things worth noting about this situation. First, *given the existence of the cavity field* there is nothing surprising about the disappearance of the inversion. With a strong cavity field, we must treat the Rabi cycling induced by *three* fields among the four levels (labeled 1, 2, 5, and 4 in Fig. 1), calculate the *new* time averaged dynamics (T operator in Eq. (5)) and reconsider the steady state problem in light of the substantially revised level mixing brought about by the added field. Second, *given the disappearance of the inversion* we are necessarily extracting energy by a process not *requiring* inversion. The resulting process is appropriately described as three wave mixing, although it should be emphasized that, like the standard lasing process that occurs at low cavity fields, it has no phase matching requirements.

The use of a fourth level to aid in energy extraction when population inversions can be created with just three levels (as discussed in Sec II) may seem like a needless complication. However, the use of the pumped levels for extracting energy leads to phase matching requirements which may be undesirable under many circumstances. With four levels even the advent of a "wave-mixing" type process poses no problems because there is still no requirement to match phases.

V. The Time Average Operator

The value of the above analysis is in part dependent on the existence of practical means for calculating the time-average quantities (T operator matrix elements) which appear as part of the equations. We present explicit expressions for a three level system and relate these to the analysis of Sec. II. These were derived using a symbol-manipulation program which is able to algebraically enumerate the (numerator and denominator) terms in rational expressions for the matrix elements. These evaluations are non-trivial because the rational expressions arise formally[8] as the $\tau = \infty$ limit of a matrix inverse.

We briefly review the steps leading to the actual expressions beginning with the observation that the T operator is just a projection operator onto the zero-eigenvalue eigenvectors of the Liouville operator L,

$$T = \sum_{\mu_i = 0} |\mu_i \rangle\langle \mu_i | \tag{18}$$

where $L\rho \equiv (i/h[\rho, H]$. These are the eigenvectors which provide eigensolutions of the differential equation $d\rho/dt = (i/h)[\rho, H]$ but can in turn[8] be expresssed using eigenvectors of the N-level time dependent Schroedinger equation. The projection can be carried out analytically using appropriate integrations to average over time. The following definition involving a Laplace transform integral,

$$\overline{\rho} = \lim_{\tau \to \infty} \rho(\tau) \equiv \lim_{\tau \to \infty} \frac{1}{\tau} \int_0^\infty e^{-t/\tau} \rho(t) dt \tag{19}$$

is useful because the connection with the Laplace transform formalism leads[8] immediately to the relationship

$$\left(L - \frac{1}{\tau}\right)\overline{\rho}(\tau) = -\frac{1}{\tau}\rho^{(initial)} \quad \Rightarrow \quad T = \lim_{\tau \to \infty}(1/\tau)(1/\tau - L)^{-1} \tag{20}$$

which implies the indicated expression for T when taken to the $\tau \to \infty$ limit. The enumeration of terms which result in this limit depends on recognizing that as an $N^2 x N^2$ matrix, L is singular, having N of its N^2 eigenvalues equal to zero. As a result, if the matrix elements of the inverse $(1/\tau - L)^{-1}$ are expressed as ratios of determinants, the lowest order terms in the denominator (the determinant of $(1/\tau - L)$) will be proportional to $(1/\tau)^N$, while the lowest order terms in the numerator (cofactors of $(1/\tau - L)$) will be proportional to $(1/\tau)^{N-1}$. We have written a computer code which enumerates (from all possible contributions to the determinants) and algebraically combines those terms with the requisite number of $1/\tau$ factors. (Any attempt to use the code to find a net contribution for terms involving *fewer* than the indicated number of factors verifies that these are indeed lowest order.) The results from a symbol processing run are numerator and denominator polynomials of order $N^2 - N$ for one or more T matrix elements, where $T_{ij} = X_{ij}/D$. Each term involves products of various detuning frequency and Rabi frequency factors up to the total order. Thus, for a three-level system, for example we have,

$$X_{13} = 2(\beta_2\beta_2^*)(\beta_1\beta_1^*)\{\Delta_{21}\Delta_{31} + \Delta_{32}^2 + 3(\beta_1\beta_1^*) + 3(\beta_2\beta_2^*)\} \tag{21}$$

$$X_{12} = 2(\beta_1\beta_1^*)\left\{\Delta_{31}^2\Delta_{32}^2 + (\beta_2\beta_2^*)[3\Delta_{31}^2 + \Delta_{31}\Delta_{32}] + 2(\beta_1\beta_1^*)\Delta_{13}\Delta_{32} + (\beta_1\beta_1^* + \beta_2\beta_2^*)^2\right\} \tag{22}$$

$$X_{32} = 2(\beta_2\beta_2^*)\left\{\Delta_{13}^2\Delta_{12}^2 + (\beta_1\beta_1^*)[3\Delta_{13}^2 + \Delta_{13}\Delta_{12}] + 2(\beta_2\beta_2^*)\Delta_{31}\Delta_{12} + (\beta_2\beta_2^* + \beta_1\beta_1^*)^2\right\} \tag{23}$$

30

and
$$D = \Delta_{21}^2\Delta_{23}^2\Delta_{13}^2 + (\beta_1\beta_1^*)(\beta_2\beta_2^*)(20\Delta_{32}^2 + 20\Delta_{12}^2 + 38\Delta_{21}\Delta_{32}) \tag{24}$$
$$+2(\beta_2\beta_2^*)\Delta_{12}\Delta_{31}(\Delta_{32}^2 + 2\Delta_{12}\Delta_{31}) + 2(\beta_1\beta_1^*)\Delta_{32}\Delta_{13}(\Delta_{12}^2 + 2\Delta_{32}\Delta_{13})$$
$$+(\beta_2\beta_2^*)^2(\Delta_{32}^2 + 8\Delta_{31}\Delta_{12}) + (\beta_1\beta_1^*)^2(\Delta_{12}^2 + 8\Delta_{13}\Delta_{32}) + 4(\beta_1\beta_1^* + \beta_2\beta_2^*)^3$$

We can simplify these expressions in the two-photon resonance case where $\Delta_{12} \cong \Delta_{32} \gg \beta_i$ and $\Delta_{13} \cong \beta_i^2/\Delta_{12}$ For example, X_{13} is totally dominated by the single term involving Δ_{32}^2. In the denominator expression, we notice that the combination of Δ's multiplying $(\beta_1\beta_1^*)(\beta_2\beta_2^*)$ in the first line can be expressed as $20(\Delta_{32} + \Delta_{21})^2 - 2\Delta_{21}\Delta_{32}$., with the first part being negligible since $\Delta_{32} + \Delta_{21} = \Delta_{31}$. In the remainder of the expression we proceed by retaining only those terms that are at least second order in Δ_{12} and dropping those terms in which the power of Δ_{13} exceeds that of Δ_{12}. The denominator expression in Eq(7) follows as a result. When similar criteria are applied to the X_{12} and X_{32} expressions, there are *no* surviving terms, confirming the fact that these expressions are quite small. Analysis of the small terms to estimate actual values is more tedious, but we simply note that because of the overall factor of $(\beta_2\beta_2^*)$ in X_{32}, a relatively large value of T_{32} such as we used in Sec.II while discussing the possibility of a 3 to 1 population inversion can be obtained by making the Rabi frequency for the upper transition disproportionately large.

VI. Conclusions

Time averages of the density matrix for driven systems form a natural basis for analyzing the steady state and transient behavior of the system for processes that are not dependent on the detailed oscillatory behavior. Analysis of the physics of systems which are damped but saturated by the fields shows that the damping actually enters in a way quite unlike its role in ordinary rate equations. Whereas in the rate equation formalism, damping appears in competition with pumping and would appear to be unable to compete under saturating field conditions, damping actually serves to periodically "re-initialize" the system and is effective in determining the behavior even with relatively infrequent collisions or spontaneous emissions because of the fact that the density matrix "remembers" its initial condition. This memory is expresssed in the dependence of the time-average density matrix on the re-initialized density matrix. Equations derived in the text quantify this memory effect and show that population inversions are a natural consequence of level mixing induced by strong pumping.

The time-averaging operator which expresses the dependence of a time averaged density matrix on its initial values can be determined either numerically through eigenvector expansions or analytically. Because the analytic form is that of a rational function we could also use eigenvector methods to determine values at a finite number of sets of detunings or Rabi frequencies and then use fitting methods to determine the values for other parameters. We note that time-averages can play a central role in the treatment of *equilibrium* problems in statistical mechanics[8] and that techniques for analyzing these quantites should also prove useful in that area.

Acknowledgment

VII. REFERENCES

1. J.A.Goldstone, J.Stone, and M.Johnson, Proc. SPIEE, Jan. 1988
2. A.J.Silversmith, W.Lenth, and R.M.Macfarlane, Appl.Phys.Lett. **51**, 1977 (1987)
3. L.F.Johnson and H.J.Guggenheim, Appl.Phys.Lett. **19**, 44 (1971)
4. N.Bloembergen, Nonlinear Optics, (Benjamin, 1965)
5. J.Stone, E.Thiele, and M.F.Goodman, J.Chem.Phys. **59**, 2909 (1973)
6. D.M.Larsen and N.Bloembergen, Opt.Commun. **17**, 254 (1976)
7. J.Stone, Phys.Rev.A**30**, 2517 (1984)
8. J.Stone, Phys.Rev.A**26**, 1157 (1982); J.Stone, E.Thiele, and M.F.Goodman,in Intramolecular Dynamics, ed.J.Jortner, B.Pullman (Reidel,1982)
9. M.F.Goodman and E.Thiele, Phys.Rev.A**5**, 1355 (1972)

STATISTICAL ANALYSIS OF LASER-SPECKLE FROM GLASS-CERAMICS

J. J. Chen, M. Kazmierczak, T. Keyes and A. Lempicki

Boston University, Department of Chemistry
590 Commonwealth Avenue; Boston, MA 02215

Abstract

The angularly-resolved and fixed-angle light scattering from glass-ceramics was investigated. Statistical analysis of specklelike spectra shows that single-scattering by microcrystallites is a primary process and weak double-scattering involving microcrystallites and defects is also present.

Introduction

Recently, there has been an increasing interest in the propagation and scattering of electromagnetic waves in disordered solid media.[1] Glasses, whose structure corresponds to frozen, disordered liquids, have been a subject of several experimental and theoretical studies.[2,3] In recent articles, we discussed angularly-resolved scattering in CVD silica glass and presented an improved estimate of the scatterer density by a new statistical method of data analysis.[4] We used the results from the CVD silica glass as a standard for studying the amorphous glass-ceramic solid.

In this paper we have investigated the angularly-resolved and fixed-angle elastic light scattering from mullite glass-ceramic samples represented by the same volume percent crystallinity but by different microcrystallites size due to the different heat-treatment conditions (temperature and time).

The angularly-resolved scattering spectra obtained were characterized by rapid intensity fluctuations. The average scattered intensity was found to be increasing with the microcrystallites' size. We interpreted the results by applying a structural model of mullite glass-ceramics in which microcrystallites and small defects are responsible for observed scattering patterns. The obtained spectrum results from single-scattering by microcrystallites (we believe that it is the dominating process) and defects in the glassy phase. In addition there is double-scattering involving microcrystallites and defects. Numerical calculation of speckle contrast (the ratio of standard deviation σ of intensity to mean intensity $<I>$) versus scattering angle θ reveals some interesting new results and more efforts are underway to explain it. Fixed-angle measurements were made for different regions in all samples and the contrast for each sample was calculated. The depolarization aspect of light scattering has also been investigated and interpreted in terms of optical properties of microcrystallites.

Experiment

Mullite glass-ceramic samples (obtained from Corning Glass Works) were prepared from a glass which has the composition by weight percentage of 48% SiO_2, 11% B_2O_3, 29% Al_2O_3, 10% ZnO, 2% K_2O, 0.4% As_2O_5. All light scattering measurements were made on mullite glass-ceramic samples which were prepared by three different kinds of heat-treatments: a constant nucleation hold of 750 °C for 4 hours was followed by a microcrystallites growth hold of 2 hours at either 800 °C, 850 °C, or 875 °C (denoted as 750-4/800-2, 750-4/850-2, 750-4/875-2 respectively). At 800 °C, according to

$300 \times 100 \times 100$ Å. The growth hold at 850 °C allows the mullite microcrystallite to grow to about $500 \times 150 \times 150$ Å. At 875 °C, they can grow to about $750 \times 200 \times 200$ Å with a more distinct shape of orthorhombic (pseudotetragonal) prisms.

The volume percent crystallinity of the glass-ceramic samples was determined by TEM to be about 34% by comparison of the crystalline area to that of the residual glass in a focal plane of less than 50 Å thickness.[5]

All mullite glass-ceramic samples were polished on all sides to the size of $10 \times 10 \times 10$ mm. A polarized He/Ne laser light of 632.8 nm with 500:1 minimum polarization ratio was used as the light source. The detail of experimental arrangement and optics of the scattering measurement were described in previous work.[4] Both the vertical (polarized) and horizontal (depolarized) component of the scattered light intensity were measured for all samples. The angularly-resolved light scattering was measured over the range from 10° to 160° at 0.15° increments with the 0.1 mm pinhole size. The measured scattered intensity data after background subtraction and $\sin\theta$ correction are shown in figures 1a, 1b, 2a, 2b, 3a and 3b. Similar measurement at 0.2° increment with pinhole size of 1 mm was repeated ten times at randomly selected regions of the same sample. The sum of ten spectra for all three samples were shown in figures 4a and 4b. The fixed-angle light scattering experiments were carried out by systematically changing the position of the sample in increments of 0.2 mm perpendicularly with respect to the scattering plane. Measurements were made at 90° angle with 0.1 mm pinhole size.

Discussion

Rapid intensity fluctuations are the common characteristic of all the polarized and depolarized, angularly resolved, light scattering spectra of mullite glass-ceramic samples with three different heat- treatments (shown in figures 1a, 1b, 2a, 2b, 3a and 3b). This kind of intensity fluctuation is due to the unaveraged light scattering from scatterers which are randomly distributed inside mullite glass-ceramic samples.

Both polarized and depolarized mean scattered intensity of mullite glass-ceramic samples increase with the higher temperature of the heat-treatment. We attribute this increased scattered intensity to the larger size of microcrystallites resulting from higher temperature heat-treatment since the volume percentage crystallinity (or the number of microcrystallites) in all samples is the same according to TEM. Also, the mean intensity is larger in the polarized component of scattered light than in the depolarized one in all three samples.

In the previous studies of CVD silica glass,[4] we observed very large scattered intensity with relative slow fluctuations at small angles and rapid fluctuations at large angles (figure 5a). The different scattered intensity pattern at small angle is caused by the nonrandom phase distribution. The onset angle of random to nonrandom phase distribution transition depends on the scatterer density. To some extent, the smaller the scatterer density, the smaller the angle associated with the transition.[3] In comparison, the scattered spectra from mullite glass-ceramic did not show this kind of transition within the smallest detection angle limit of the instrument. Estimation of crystallite density in mullite glass-ceramic samples by TEM shows it to be about two orders of magnitude less than scatterer density in CVD silica glass, as estimated previously by other measurements.[4,6] This might shift the transition beyond the instrument's detection angle limit and prevent us from observing the slow fluctuations and large scattered intensity at small angles as in the CVD silica glass. Further supporting evidence come from the studies of yttria ceramic samples which have higher scatterer density than mullite glass-ceramic. The same transition at small angles are observed from the yttria ceramic as in CVD silica glass.

In an attempt to gain more insight of scattering process of mullite glass-ceramic, the sequential numerical analysis[4] was applied to calculate the contrast from the scattered intensity data from figure 1a, 1b, 2a, 2b, 3a, and 3b. The results of calculated contrast

33

versus angle, as shown in figure 6a and 6b, are quite different compared to the CVD silica glass in figure 5b. This indicates that a different light scattering process is involved in mullite glass-ceramic than in CVD silica glass. Fixed-angle (90°) light scattering at three hundred different positions of each mullite glass-ceramic sample was also measured and the contrast for each sample was calculated. The results showed that the calculated contrast at 90° for the vertical component of the scattered light intensity is decreasing with higher temperature of heat-treatment. But, the opposite trend holds for the horizontal component. Compared with angularly-resolved cases in the figure 6a and 6b, the 90° fixed-angle contrast follows the same trend with respect to the heat-treatment temperature as the angularly-resolved contrast values at 90°. This confirms the results of the above mentioned numerical calculations and shows them as valid and not caused by random intensity fluctuation.

Depolarization ratio of scattering is defined as the horizontal to vertical component ratio of scattered intensity at 90°. The depolarization ratio for three mullite glass-ceramic samples was calculated from figures 4a and 4b. It is 0.74 for 750-4/800-2, 0.61 for 750-4/850-2 and 0.40 for 750-4/875-2. The dissymmetry factor of scattering was determined as the ratio of scattered intensity at 45° to 135° for both horizontal and vertical components. For the horizontal component, the dissymmetry factor is near unity for all mullite glass-ceramic samples. But for the vertical component, the dissymmetry factors are decreasing with higher temperature-treatment and the values ranges from 0.99 to 0.72.

Conclusion

There are two possible kinds of light scattering centers randomly distributed throughout mullite glass-ceramic; the scattering can be: from small glass defects, from relatively large microcrystallites, or due to a process which involves both defects and microcrystallites. In any case, the scattering involves three possible mechanisms: single, double, or multiple scattering. Since the percentage of microcrystallites in mullite glass-ceramic samples is relatively low (34%), the multiple scattering from this source is minimal because the long mean free path between microcrystallites will practically eliminate multiple scattering.

Statistical analysis of the intensity of the light scattered from the mullite glass-ceramic yields a probability distribution which closely matches the theoretical prediction based on the single scattering model. Yet a slight deviation from the theoretical prediction suggests a minor contribution of scattered intensity from weak double scattering.

In CVD silica glass, single scattering from defects has been shown to be the only light scattering process.[4] The low depolarization ratio (0.008) indicates that the defects are isotropic. The glass precursor of mullite glass-ceramic yields a scattered light intensity and depolarization ratio similar to the CVD silica glass. The scattered light intensity from mullite glass-ceramic is about one-hundred times stronger than CVD silica glass's and it increases with the increasing size of microcrystallites. The depolarization ratios of three mullite glass-ceramic samples range from 0.4 - 0.7.

These results indicate that scattering from mullite glass-ceramics is dominated by the single scattering from large, anisotropic microcrystallites. As the microcrystallite size increases (through temperature treatment) so does the scattering. This is confirmed by TEM results which show elongated prismatic shape of the microcrystallites, whose size again depends on temperature treatment. Double scattering played a weak secondary role in the scattering process.

The nature of the weak double scattering process in mullite glass-ceramics is speculated to be the result of scattering between glass defects and microcrystallites. Double scattering between defects in the glassy phase is unlikely based on previous results which indicate single scattering to be the only process which occurs in CVD silica glass. The double scattering process between microcrystallites should be insignificant

due to the relatively long mean free path between them. One can reasonably conclude that double scattering in the mullite glass-ceramic occurs between glass defects and microcrystallites.

Acknowledgement

References

[1] A. Ishimaru, Wave Propagation and Scattering in Random Media, (Academic Press, New York, 1978), vols I, II.

[2] R. Gillies, M. Kazmierczak, T. Keyes, A.J. Wojtowicz and A. Lempicki, Phys.Rev. B36 9413 (1987).

[3] M. Kazmierczak, T. Keyes and T. Ohtsuki, Phys.Rev. B 39 (1988) (in press).

[4] J. J. Chen, M. Kazmierczak, T. Keyes and A. Lempicki, Phy.Rev. B (in press).

[5] TEM data obtained at Corning Glass Works.

[6] S.R. Elliott, Physics of Amorphous Materials, (Longman, London, 1983), p. 270; M.A. Paesler, S.C. Agarwal, S.J. Hudgens and H. Fritzsche, in Proc. Int. Conf. on Tetrahedrally Bonded Amorphous Semiconductors, vol. 20, edited by M.H. Brodsky, S. Kirkpatrick and D. Weaire (Am. Inst. Phys., 1974), P. 37.
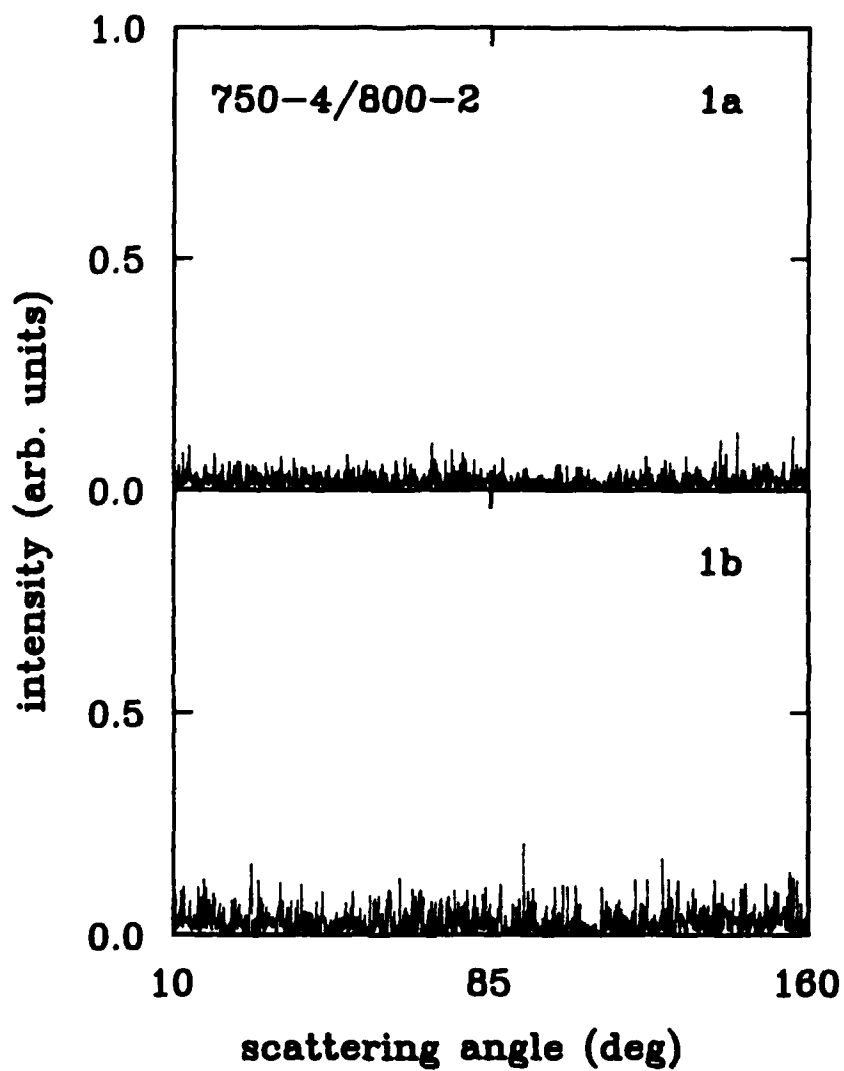
Fig. 1. Angular scattering spectra measured for mullite glass-ceramic sample (750-4/800-2) with 0.1 mm pinhole size: (1a) the horizontal component, (1b) the vertical component.
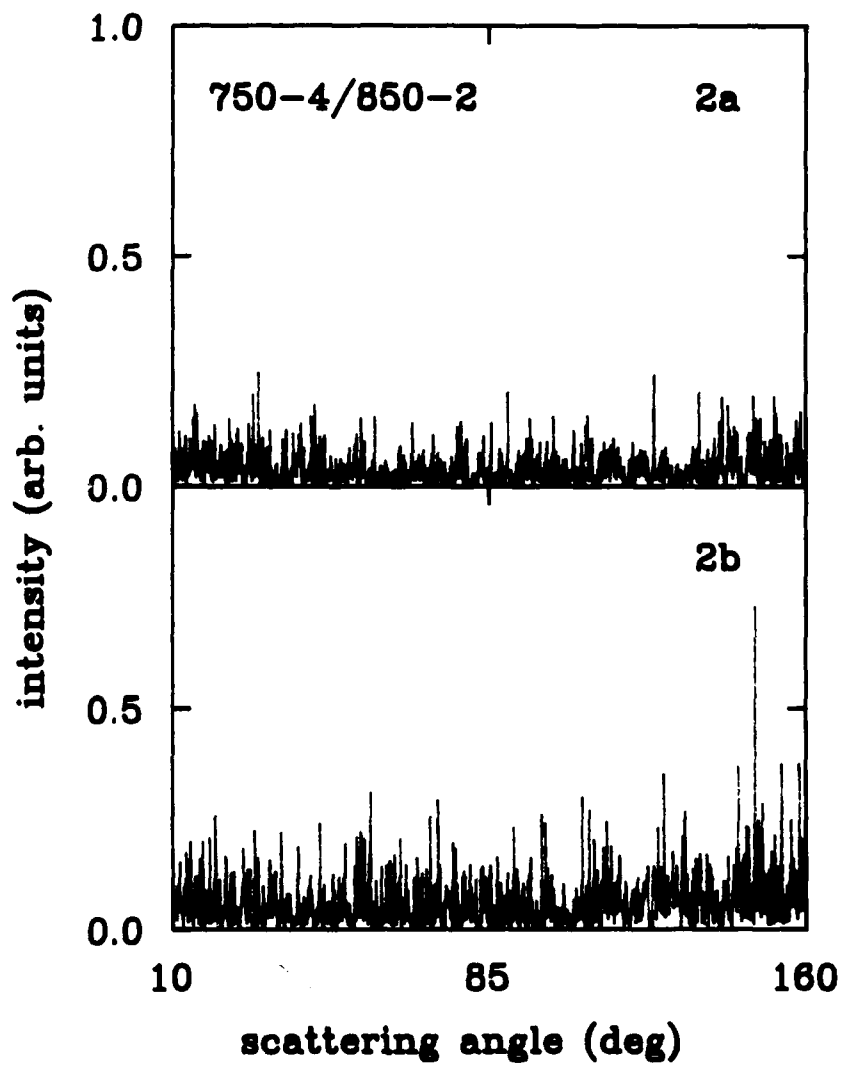
Fig. 2. The same as Fig. 1 except the spectra measured for mullite glass-ceramic (750-4/850-2).
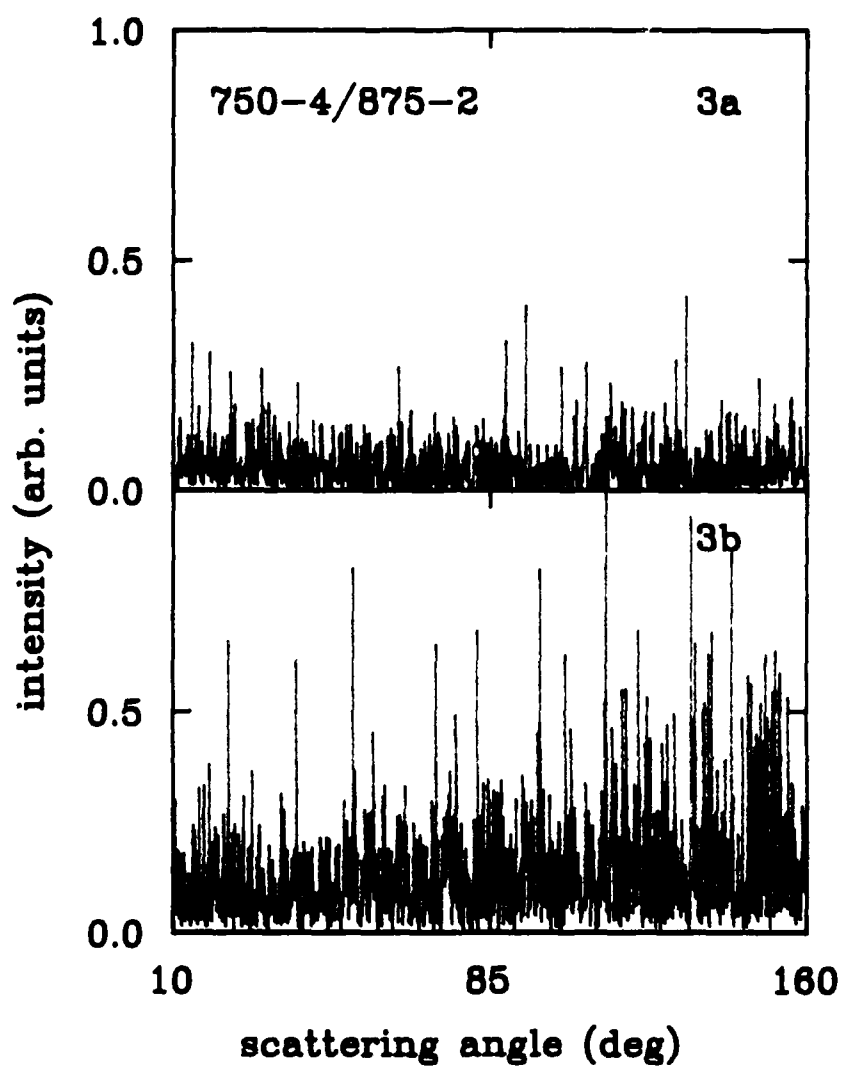
Fig. 3. The same as Fig. 1 except the spectra measured for mullite glass-ceramic (750-4/875-2).
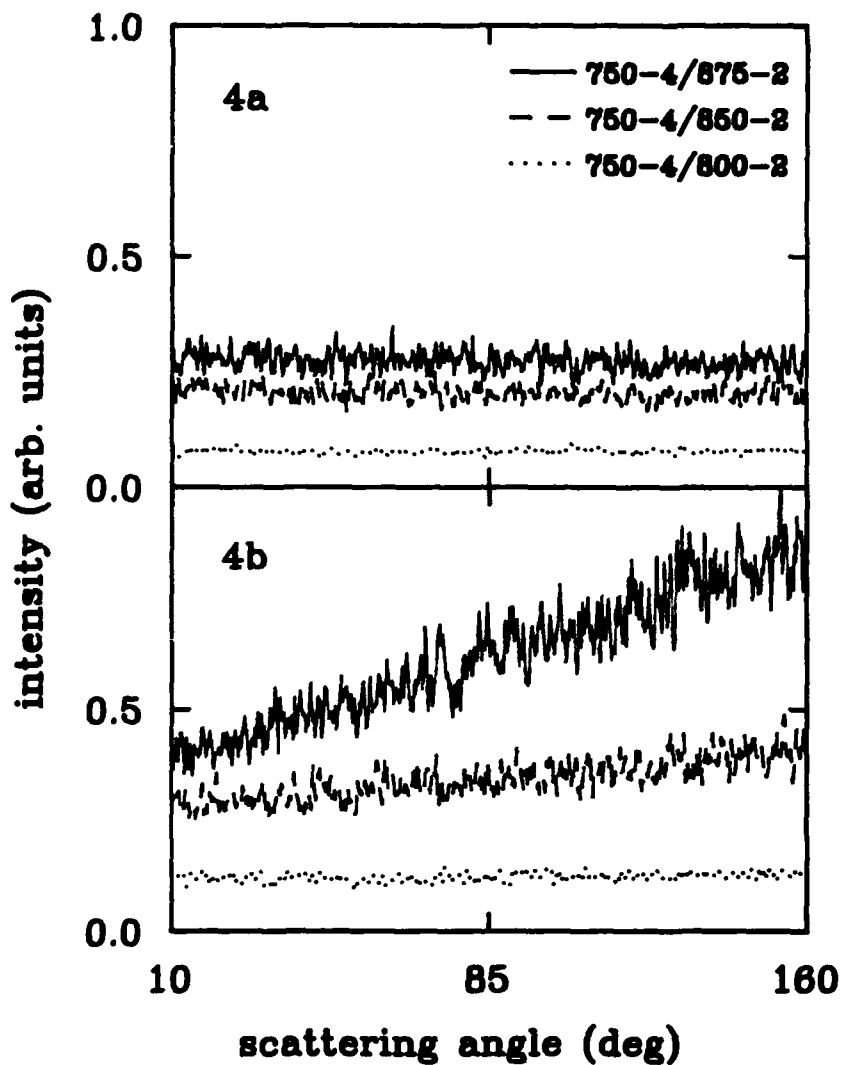
Fig. 4. Angular scattering spectra measured at ten randomly selected regions for three mullite glass-ceramic samples with 1 mm pinhole size. The spectra shown here are the sum of the ten spectra for each sample: (4a) the horizontal component, (4b) the vertical component.
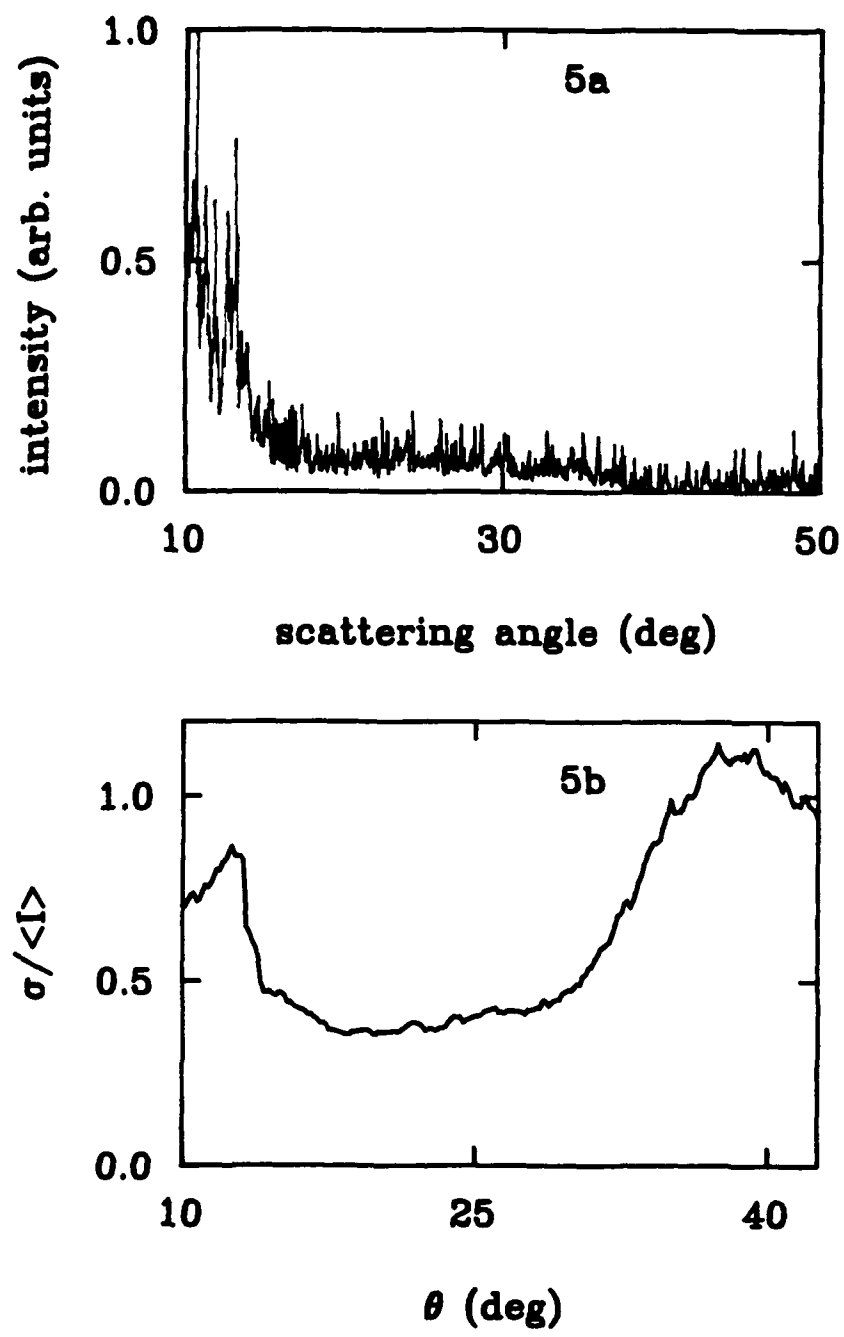
Fig. 5. (5a) Angular scattering spectra measured for CVD silica glass with 0.2 mm pinhole size. (5b) Angular spectrum of the ratio of intensity standard deviation and mean scattered intensity (speckle contrast) calculated for scattering spectrum on Fig. 5a.
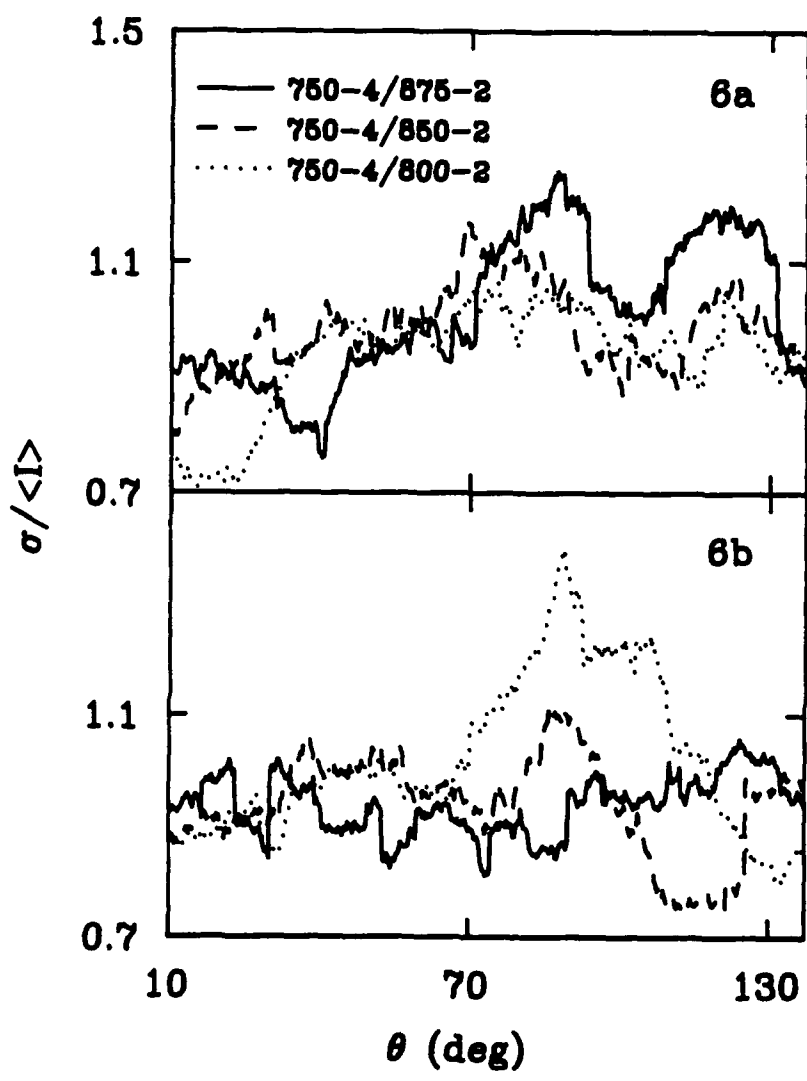
Fig. 6. Angular spectra of the ratio of intensity standard deviation and mean scattered intensity (speckle contrast) calculated for scattering spectra on Fig. 1, 2 and 3 for three mullite glass-ceramic samples: (6a) the horizontal component, (6b) the vertical component.

QUANTUM MECHANICAL DESCRIPTION OF N-SLIT INTERFERENCE PHENOMENA

F. J. Duarte and D. J. Paine
Photographic Research Laboratories – Photographic Products Group
Eastman Kodak Company, Rochester, NY   14650-1744

Abstract

Dirac's notation is utilized to establish a generalized interference equation which is then applied to calculate the resulting intensity pattern from transmission gratings made of N variable width slits.

Introduction

In this communication we describe the use of Dirac's notation in the description of interference resulting from the interaction of laser light diffracted at a one-dimensional array of N-slits. In this regard, the present approach was developed to analyze interference phenomena ranging from the classical double-slit interaction to generalized situations involving N number of slits of either fixed or variable width.

In the course of these experiments we have found that Dirac's notation is particularly suitable for incorporating the additional complexity found in transmission gratings of practical interest. The beauty of the approach is in the inherent elegance and compactness of the equations utilized. Indeed, All the complexity is incorporated via the wave functions, which in turn depend on the physical parameters associated with the slits.

Theory

Using Dirac's notation, a basic tool in quantum mechanics,[1] the probability amplitude for a photon to go from the source (s) to a screen (x), via an array of N slits (j), can be written as

$$\langle x|s \rangle = \sum_{j=1}^{N} \langle x|j \rangle \langle j|s \rangle \tag{1}$$

Following Feynman,[2] we use $\langle j|s \rangle = \Psi_{s,j} e^{-i\theta_j}$ and $\langle x|j \rangle = \Psi_{x,j} e^{-i\phi_j}$. In these probability amplitudes the quantities $\Psi_{s,j}$ and $\Psi_{x,j}$ may be assumed to take the form of a diffraction wave function or other appropriate distribution. Now, if we write $\Psi_j = \Psi_{s,j} \Psi_{x,j}$ and $\Omega_j = (\phi_j + \theta_j)$, then

$$\langle x|s \rangle = \sum_{j=1}^{N} \Psi_j \, e^{-i\Omega_j} \tag{2}$$

Hence, it can be shown that the probability that a photon from s will reach x is given by

$$|<x|s>|^2 = \sum_{j=1}^{N} \Psi_j^2 + 2 \sum_{j=1}^{N} \Psi_j \left(\sum_{m=j+1}^{N} \Psi_m \cos(\Omega_m - \Omega_j) \right) \qquad (3)$$

This is a generalized equation applicable to any one-dimensional N-slit interference problem. A detailed discussion of the theory and the wave function utilized will be given elsewhere.[3]

The angular relationships for the diffraction function and the interslit interaction were determined using exact geometrical expressions such as

$$\cos(\phi_m - \phi_j) = \cos \tilde{k}.\tilde{r} = \cos (2\pi/\lambda) |L_n - L_1| \qquad (4)$$

where $|L_n - L_1|$ represents the usual path difference term.

The degree of variability in the slit width of a particular grating was determined by measuring the average width and the corresponding standard deviation, that is, $\bar{w} \pm \delta w$. In the interferometric calculations related to gratings incorporating uncertainty in the slit dimensions, the slit widths (and interslit separations) were selected stochastically from a Gaussian distribution having this experimental mean and standard deviation.

Experimental

The light source utilized was a HeNe laser (λ = 632.8 nm) and the screen was a photodiode array composed of 1024 diodes, each 25 μm wide. The intensity profile of the multiple-slit interference incident on the photodiode array was recorded by a modified version of the EG&G Optical Multichannel Analyzer (1460-D OMA III, 1463 detector module, and modified 1420 detector). The detection semiconductor was not cooled.

A computer program in Fortran 77 language was written to calculate intensity distributions at x resulting from the interferometric interaction of 2 to N slits (up to 100).

The basic test of the theory was carried out utilizing a number of double slit sets. These double slit sets were composed of two precision slits separated by a distance equal to the individual width of the slits. For instance, a particular set included two slits 25 μm wide separated by 25 μm. Other sets included slits 50 μm, 75 μm, and 100 μm wide.

Following the basic double-slit test, the calculations were utilized to predict the interference pattern originated in N-slit transmission gratings of practical interest. These gratings were composed of slits 30 μm, 40 μm, 66.67 μm, and 100 μm wide. The distance between the slit array (j) and the detection screen (x) was typically in the 4 - 10 cm range.

Results

In Fig. (1) we include the measured interference pattern resulting from two high-precision 75-μm-wide slits for a slit-screen distance of 10 cm. Notice that the number of pixels from maximum to maximum is 15, and since each pixel is 25 μm wide, that represents

a total distance of 375 μm. The lack of detail near the base line of the measurement is due to photon noise limitations. The calculated interference pattern for those dimensions (shown in Fig. (2)) indicates that the maximum-to-maximum distance is also 375 μm. Thus, it is clear that there is good agreement between theory and measurement.
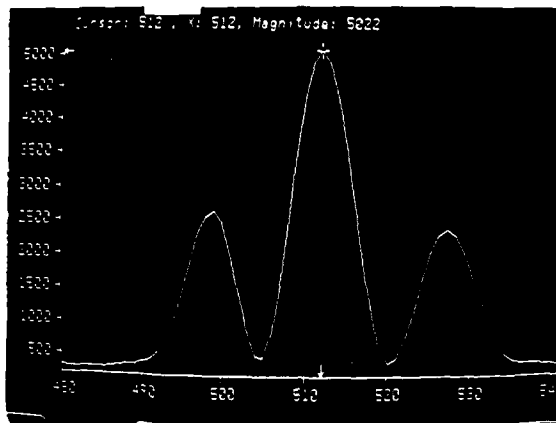
Fig. 1   Measured double-slit interference due to 75 μm slits. The distance from the slits to the screen is 10 cm. Each pixel, on the horizontal axis, represents a displacement of 25 μm.
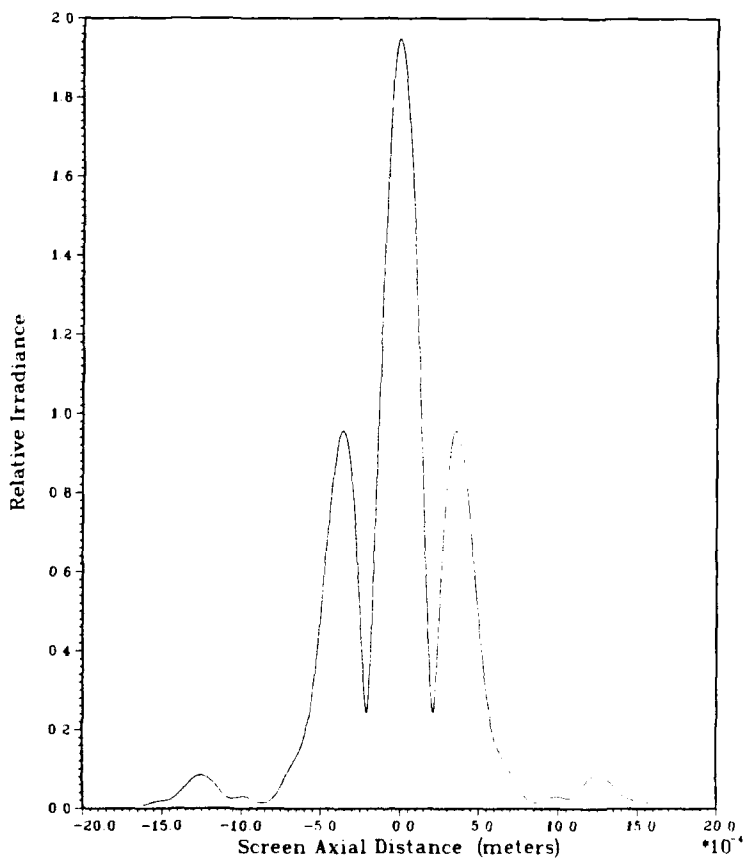
Fig. 2   Calculated interference for the double-slit case utilizing 75 μm slits.
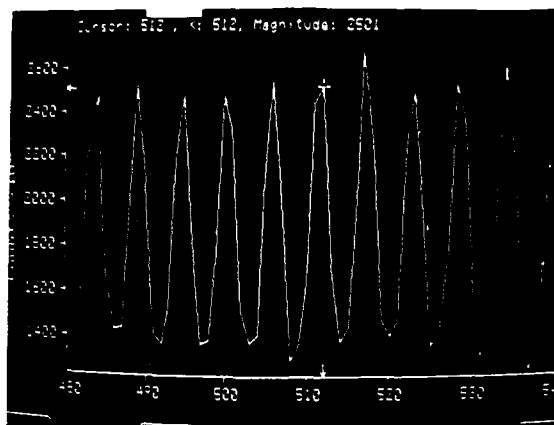
Fig. 3   Measured interference pattern resulting from the interaction of N-slits 66.67 μm wide; here, N = 30.
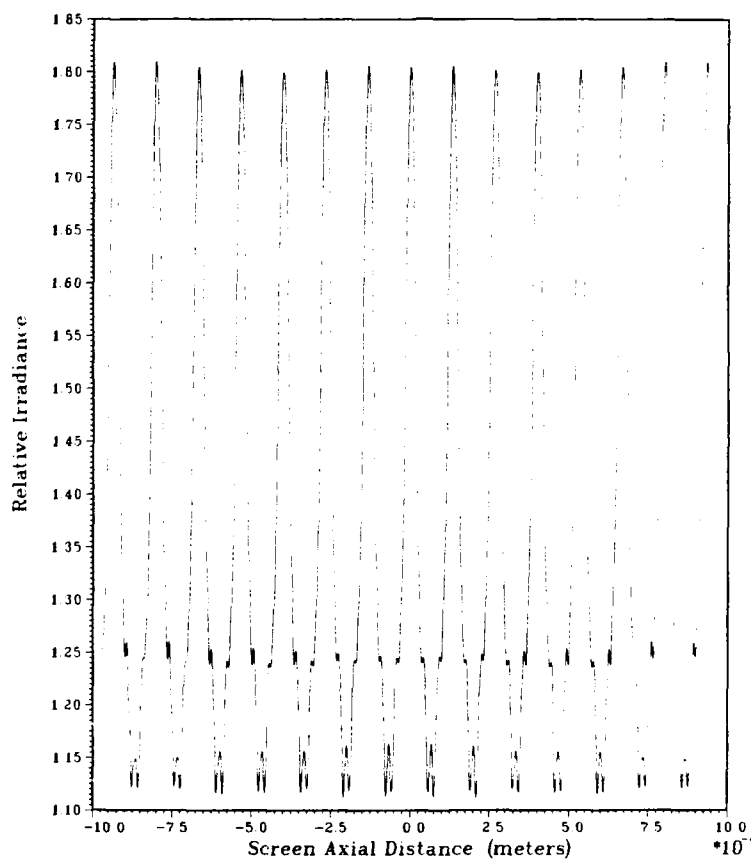
Fig. 4   Calculated interferogram for the N-slit case involving 66.67-μm-wide slits.

In Fig. (3) we show the interference pattern resulting from a grating incorporating 66.67 μm slits (for a 10 cm grating-screen distance). The measured peak-to-peak distance corresponds to 138 ± 13 μm. The calculated interference probability, shown in Fig. (4), indicates that the peak-to-peak distance is 135 μm. Certainly, the slight difference is due to the 25 μm resolution limit of the photodiode array, which also explains the absence of finer structure in the measurement.

The question of variability is illustrated in Fig. (5) where the calculated interference pattern for a 60-slit grating is included. In this case the slit width separation is 33.34 ± 1.21 μm. The main feature of this result is the irregularity of the interference pattern. Comparison with measurements shows that calculated interferograms of this type agree well with the measured signal in terms of average number of cycles per given unit distance at x.
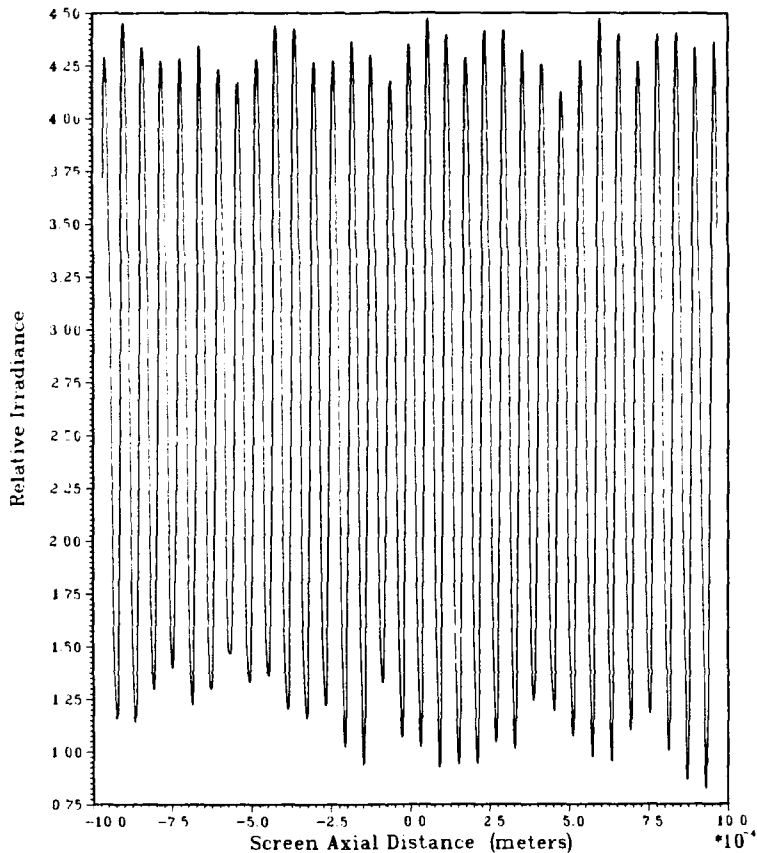
Fig. 5   Calculated interferogram resulting from the interaction of N slits
          33.34 ± 1.21 μm wide.

Discussion

Particular attention in these measurements is given to the intensity distribution, as a function of transverse distance, of the interferogram recorded at the screen (x). This is due to the fact that information from the interferogram coupled with knowledge about the source wavelength and grating-screen distance can be utilized to study the physical characteristics of the grating. In this regard, correlation of the theory with measurements of the interference profile is important. Applications in this area include fast on-site physical characterization of transmission gratings.

The aim of the double-slit experiments was to provide a basic test of Eq. (3) in conjunction with the respective wavefunctions and exact geometrical expressions. Results obtained with several double-slit sets, including those shown in Figs. (1) and (2), indicate that the theory and the numerical approach function well in this limit. In the case of regular N-slit gratings good overall results were observed with some minor deviations

due to the 25 μm resolution limit of the detector array.

A finding of particular interest was the realization that even minor variations in the physical dimensions of the slit width and interslit separation can lead to irregularities in the interference pattern. This observation holds true even for the case of uniform illumination.

Conclusion

In this communication we have demonstrated the use of basic quantum mechanical notation to describe interference phenomena related to N-slit gratings. The beauty of the approach provided here is that a simple equation of a generalized nature can be utilized to demonstrate the classic double-slit experiment and at the same time predict more complicated interferograms of practical interest.

References

1. P. A. M. Dirac, The Principles of Quantum Mechanics, Fourth Edition (Oxford University Press, London, 1978)
2. R. P. Feynman, R. B. Leighton, and M. Sands, The Feynman Lectures on Physics, Vol. III, (Addison Wesley, MA, 1971)
3. F. J. Duarte, in preparation

THE THEORY OF LIGHT AMPLIFICATION IN FAR ULTRAVIOLET LASERS

A.V.Borovskii, V.V.Korobkin, M.Yu.Romanovskii

ABSTRACT

The short wave radiation amplification is considered in thin expansed plasma filaments. There are the nonstacionarity of active medium and defocusing of short wave radiation analysis. Some perspective ways to create inverse populations are considered for dense gaseous mediums.

1. X-LASERS IN A LASER PLASMA.

Amplification of spontaneous radiation as a result of transitions in multiply charged ions in a laser plasma at wavelengths $\lambda < 50$ nm has been achieved experimentally [1-7]. The effect described in [1] occured as a result of the 3p-3s transitions in neon-like ions of Se (λ=20.6 and 20.9 nm), Y (λ=15.7 and 16.5 nm), and Mo (λ=13.1 and 13.9 nm). The amplification reported in [2-5] was due to the 3-2 transition in hydrogen-like carbon ions (λ=18.2 nm). Amplification due to the 5f-3d transition in lithium-like aluminum ions (λ=10.6 nm) was observed in [6]. This has greatly enhanced theoretical interest in schemes for amplification of spontaneous radiation as a result of transitions in multiply chagred ions in a plasma. It is difficult to maintain ionized plasme under steady-state conditions. One has to consider therefore amplification durihg plasma expansion, as observed in the experiments reported in [1-7]. The most convenient form of the amplifyihg medium is a plasma filament.

We shall investigate the characteristics of amplification of spontaneous radiation in an expanding plasma filament associated with transient nature of the active medium and with defocusing of the radiation. The main conclusions will be fairly general and will apply to any methods for creating a population inversion at short wavelengths. We shell consider a specific example of recombination pumping of H-like ions. We shell analyze this scheme because of the considerable interest it has recently attracted [9-12].

AMPLIFICATION CRITERIA. Amplification in an active medium is possible if the gain $\varkappa^+$ exceeds the attenuation coefficient $\varkappa^-$. Since the time dependence $\varkappa^+(t)$ is bell-shaped, it is natural to select the amplification condition in the form $\varkappa^m = \varkappa^+(t_m) \cdot \varkappa^-(t_m)$, where t_m is the moment corresponding to the maximum of $\varkappa^+(t)$. This condition is insufficient for effective amplification. In practice, we must ensure that $g_0 = \ln(I/I_{sp}) \geqslant 20$, where I is the final intensity and I_{sp} is the initial intensity of spontaneous radiation before amplification. The transient nature of the active medium is a factor wich reduces the final intensity I. In fact, if the condition $\varkappa^+ > \varkappa^-$ is obeyed in a time interval t_g, then the distance traveled in this time is $L_g = ct_g$. For $L_g < L_1$ ($L_1 = ct_g$ is the distance in which the intensity reaches saturation), the maximum intensity of a light puls is not achieved. The intensity which is obtained depends on $g^+ = c\int_0^{t_g} \varkappa^+(t)dt = \varkappa^m L_g$, which we shall call the gain coefficiet. As established below, we can achieve $g_0 \geqslant 20$ provided $g^+ \geqslant 30$. Assuming that the length of the active medium is $L \approx L_g \leqslant 30$ cm, we find that amplification requires that $\varkappa^m \geqslant 1$ cm^{-1}.

It therefore follows that amplification of spontaneous radiation can occur in a transient plasma filament in schemes characterized by $g^+ \geqslant 30$, $\varkappa^m \geqslant 1$ cm^{-1}, and $\varkappa^m >> \varkappa^-(t_m)$.

1.1. VALUES OF g^+ AND L_g IN THE CASE OF RECOMBINATION PUMPING OF HYDROGEN-LIKE IONS

Following [14] we shall consider only self-similar expansion of a plasma filament. We shall assume that initially a ring-shaped layer of matter is characterized by a nuclear charge Z, a density of heavy particles N_0, and an

electron temperature T_0 when the radius of the filament is R_0. For the sake of simplicity, we shall consider the behavior of the plasma parameters on the filament axis.

VALUES OF $x^+(t)$ AND g^+ [14,16]. In the simplest adiabatic case the thermal energy of electrons and nuclei is transformed into the kinetic energy of filament expansion. We then have

$$x^+(t)=q\left[\frac{1-\alpha x(t)}{1-\beta x(t)}\right]\exp\left[-p/x(t)^{9/4}\right]/x(t),\tag{1}$$

$$g^+=23.4B\gamma^{7/3}\frac{N_0^{7/9}R_0^{2/9}}{T_0^{10/9}Z^{20/9}}\left[\frac{1-\alpha(9/13p)^{4/9}}{1+\beta(9/13p)^{4/9}}\right]\exp(-\alpha^{9/4}p),\tag{2}$$

where

$$q=10^{-40}B\gamma^{10/3}N_0^{10/3}Z^{-4}T_0^{-5},\quad p\approx1.1*10^{-60}\gamma^{9/4}N_0^{17/4}R_0Z^{-25/4}T_0^{-49/8}$$

$$x(t)=x_0(t/t_0)^{4/3},\quad t_0=R_0/u,\quad u=1.7*10^6\sqrt{T_0},\quad x_0=\gamma N_0/10^{12}Z^5\sqrt{T_0}.\tag{3}$$

The constants B, α, β and γ are listed in Table.

	B	α	β	γ	$\mathcal{G}$	$\mathcal{H}$	$\mathcal{L}$	ξ_1	ξ_2	$\mathcal{G}_\nu$	$\mathcal{L}_\nu$
(3-2)	2.4-6	0.27	0.44	0.02	1.3+3	1.1	1.2+3	160	0.30	50	1.1+4
(4-3)	4.9-9	0.19	0.30	0.53	1.7+3	0.4	4.3+3	14	0.42	34	6.5+4

We can use Eq. (1-3) if $(9/13p)^{4/9}<\alpha^{-1}$.

VALUE OF g^+ AS A FUNCTION OF N_0 AND T_0. We shall assume that R_0 and Z are constants; we shall vary simaltaneously N_0 and T_0. The dependence of $g^+(N_0,T_0)$ on N_0 and T_0 resembles a wedge with a sharp edge (Fig.1). The asterisk is used for the values of the variables N_0 and T_0 on the edge of the wedge. The corresponding values of g^+, x^m and L_g are

$$g^+=\mathcal{G}N_0^{*1/147}R_0^{2/49}/Z^{86/49}\tag{4a}$$

$$x^m=\mathcal{H}Z^{56/49}/R_0^{40/49}N_0^{*20/147}\tag{4b}$$

$$L_g=\mathcal{L}N_0^{*1/7}R_0^{6/7}/Z^{20/7}\tag{4c}$$

The constants $\mathcal{G}$, $\mathcal{H}$, $\mathcal{L}$ are listed in table.

FIG.1. Gain coeffitient g_{32}^+ predicted for adiabatic expansion of a plasma filament in vacuum when the plasma contains carbon ions (Z=6) and the filament radius is $R_0=$ 10 μ.

DEPENDENCE OF g^+ ON Z. It is worth noting the rapid reduction in g^+ on increase in Z. This is due to the fact that in a freely expanding plasma the population lifetime decreases on increase in Z at a rate faster than the increase in the gain. In the case of the 3-2 transition and Z=6 when the initial parameters of the filament are optimal ($N_0=10^{20}$cm^{-3}, $R_0=10$ μ, $T_0=T_0^*$), we obtain $g^+=57$, $x^m=4$ cm^{-1}, and $L_g=14$ cm. For Z=13, the corresponding values are $g^+=15$, $x^m=9.6$cm^{-1}
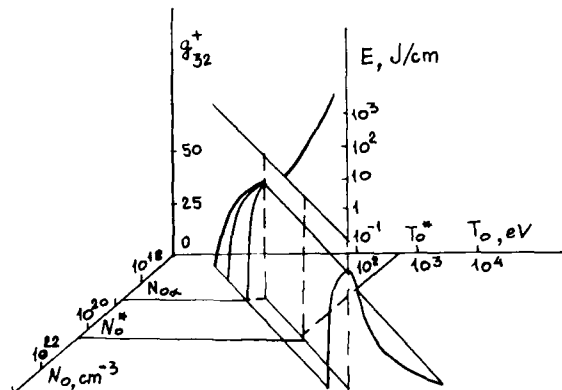
and L_g=1.5 cm. For the 4-3 transition under the same conditions and for Z=6 and 13, we obtain, respectively, g^+=74 and 19, $\varkappa^m$=1.5 and 3.5 cm^{-1}, and L_g= 49 and 5.4 cm.

Only media characterized by $g^+ \geqslant 30$ are of interest. In the case of adiabatic expansion the condition $g^+ \geqslant 30$ is obeyed if $Z \leqslant 8$ (3-2 transition) and $Z \leqslant 10$ (4-3 transition).

RESTRICTIONS ON Z DUE TO LOSSES CAUSED BY DEFOCUSING. Only the amplification has been considered so far. A recent investigation [8] makes it possible to use model of a planar Epstein layer to allow for the losses due to defocusing $\varkappa_d$ which, for the dimensions of a plasma filament under consideration, are due to refraction of radiation and ecxeed the losses due to diffraction, invers bremsstrahlung absorption, and photoionization of excited states of the ions [19-20]. In the case of a filament we have

$$\varkappa_d^- \approx 2\,(\omega_p/\omega R), \quad \omega_p = \sqrt{(4\pi e^2/m_e)ZN_+} \;, \tag{5}$$

where N_+ is a number of nuclei in 1 cm^3 .

Under optimal initial conditions at the moment of attainment of the maximum gain, we have

$$\varkappa_d^{-m} = \xi_1 Z^{513/98}/N_0^{47/98}R_0^{43/49}. \tag{6}$$

On increase in Z the value of $\varkappa_d^{-m}$ rises faster than $\varkappa^m$, so that at high Z the losses may exceed amplification. We shall now estimate Z at wich this occurs. It follows from $\varkappa_d^{-m} \leqslant \varkappa^m$ that

$$Z < Z_1 \equiv \xi_2 N_0^{101/1215}R_0^{2/135}. \tag{7}$$

The constants ξ_1 and ξ_2 are listed in Table. It should be noted that Z_1 is practically independent of the filament parameters. For N_0=10^{20}cm^{-3} and R_0=10μ we find that Z_1 =12 or 17 for the 3-2 or 4-3 transitions. In the case of 3-2 transition and these values of N_0 and R_0, we obtain $\varkappa_d^{-m}$=0.2 cm^{-1} if Z=6. The absorption due to the invers bremsstrahlung effect and photoionization of the excited states (in the case of the same parameters as before) is $\varkappa_{ph}^- < 1$ m^{-1}. The radiation due to the 3-2 transition in hydrogen-like carbon ions can be absorbed in the case of photoionization of the ground states of CIV, CIII..., but if $t \approx t_m$ ($\varkappa^+ \approx \varkappa^m$) there are practically no such ions [21].

As shown in [13,14,18], allowance for recombination heating lowers $\varkappa^+$ by 30-40% and reduces correspondingly g^+. For example, if N_0=10^{20}cm^{-3}, R_0=10μ, and Z=6, we obtain g^+=32 for the 3-2 transition. Allowance for reabsorption as a result of resonance transitions [18,22] reduces additionaly $\varkappa_{32}^+$ and g^+ by a factor of $\approx 2-3$.

1.2. INCREASE OF THE EFFECTIVE AMPLIFICATION TIME

In the case of recombination pumping we have $\varkappa^+(t) = \varkappa_0^+(t)\alpha_+(t)$, where $\varkappa_0^+(t)$ is found on the assumption that all the heavy particles are recombination centers (bare nuclei) and $\alpha_+(t)$ is the real fraction of the pair nuclei in the ion component of the plasma. A shortcoming of the scheme is that $\alpha_+(t)$ decreases with time. If a plasma is first irradiated with ionizing fluxes, we can maintain α_+=1 throughout the expansion stage. The largest ionization cross sections are known to be exhibited by photons.

EXPRESSIONS FOR g^+ AND L_g. The problem of expansion of a plasma filament in a field of external quasi-Planck radiation (ionizer) cut off below ionization potential was solved in [15,18] and the formulas for $\varkappa^+(t)$ were also obtained there. Calculations of g^+ and L_g were made in [16,17]. We shall give them without derivation for the case of the optimal temperature of an external radiation source:

$$g^+ = \mathcal{G}_\nu Z^{-1/57}(NR^2/u^2)^{7/57}, \qquad L_g = \mathcal{L}_\nu Z^{-61/19}(NR^2/u^2)^{9/19}, \qquad (8)$$

where u is the rate of inertial expansion of a filament. The values of $\mathcal{G}_\nu$ and $\mathcal{L}_\nu$ listed in table. If $Z=6$, $N_0=10^{20}$cm^{-3}, $R_0=10\mu$, and $u=200$ km/s, we find that, for example, in the case of the 3-2 transition we have $g^+=41$ and $L_g=19$ cm, whereas in the case of 4-3 transition the corresponding values are $g^+=28$ and $L_g=100$ cm. We can see that the use of an ionizer increases somewhat the value of g^+. We recall that in the case of filament expansion we obtain $g^+_{32}=32$.

2. SOME EXOTIC WAYS OF CREATING INVERSE POPULATION IN X-RAY REGION [23]

Much effort is currently concentrated on studying some major mechanisms for inverse population in the X-ray region. Among these are recombination, photopumping, recharging, collisions. But there are some interesting another ways.

2.1. IONIZATION OF INNER SHALLS BY OSCILLATED ELECTRONS IN INTENSE OPTICAL FIELD

To generate X-ray radiation, we consider interaction with the atoms of optical radiation with an intensity $I \approx 10^{17}$W/cm^2. If the amplitude E of the optcal field exceeds that of the field E_{at}, which acts on an external electron, the "electron-atomic remainder" system becomes loose, that the external electron is ionized. This electron acquires acceleration $a = e(E - \tilde{E}_{at})/m$, where $\tilde{E}_{at}$ is the collective field generated by all the rest particles in the electron location (it is less than E_{at}), e – is the charge, m – the electron mass. Let us set $E \gg E_{at}$. During the optical field halfwave the electron has enough time to acquire a velocity $v \approx eE/m\omega$ (ω – laser frequency). If the electron reaches a neighbouring atomic remainder, it may ionize the latter and, due to its high energy, even to kick out a lower lying electron, though this probability is by an order of magnitude longer than that for the higher lying electron shall. If in this case the upper electrons of the remainders keep to their locations, invers population energes a medium.

The act of ionization, even involving the lower lying electron ejection, runs rather rapidly, virtually for the time equal to the light field period. Most readily ionized in the sheme considered are alkali metals (in the vapoure state), most difficult – inert gases. In the X-ray wavelength region this is K-ionization for He and Na, L-ionization for Ar and K- and M-ionization for Rb and Kr. For estimates, let us consider these gases (and vapors) under atmospheric pressure ($N_0 \approx 3 \cdot 10^{19}$cm). $E_{Ne} \approx 2.5 \cdot 10^9$W/cm, $E_{Na} \approx 1.3 \cdot 10^9$ W/cm, $E \approx 10^{10}$W/cm (This corresponds to the laser radiation intensity of $I \approx 10^{17}$W/cm^2). An average distance between the atoms is $0.3 \cdot 10^{-6}$cm, the velocity acquired by an electron at this distance is $2.8 \cdot 10^9$cm/s, and energy $\varepsilon \approx 2000$ eV. At a laser puls duration, τ_ν, net ionization efficiency is determined by the value $\alpha\tau_\nu$,

recombination being neglected. At the $\sim_{ij} 10^{-13}$s, net efficiency of a single K shell ionization amounts to ~ 1 [24], i.e. almost all atomic remainders would lack one K electron. Minimal transition wavelength woud be ~ 10 A. A unit ionization efficiency for L shell in Ar and M shell in Kr can be expected at $\sim 10^{-14} 10^{-13}$ s.

2.2. INVERSION IN LASER SPARCS

Another approach is associated with the laser sparks effect in the regimes of electron and radiative heat conductivity of medium. The ionization wave velocity v in the high-power field may reach a value more than 10^7cm/s and appreciably exceed sonic velocity in a hot plasma. In this case the temperature of the plasma electron component $T_{\parallel}$ amounts to 1 keV. The laser radiation energy is absorbed by the electron component of the plasma. Under these conditions, during the ionization wave front travelling, the temperatures between the electron and ion components do not become lavelled, since the relaxation time $\sim_{ij}$ at these temperatures is less than that of the ionization wave front passing. Thus, the ions on the ionization wave front will be cold and recombination absent because this process has a haracteristic time of development comparable with $\sim_{ij}$.

The major transfer mechanizm for the ionization wave under these conditions is radiative heat conductivity. The plasma electron component spectral density is here well approximated by the black body radiational spectral density $\Box$. Let us consider the process of the ionization of cold neutral atoms located before the shock wave. The first way is successive ionization of the electrons starting from the upper one. In this case inverse population could occur as a result of recombination, but on the ionization wave front recombination has not enough time to occur. Since there are sufficiently hard quanta in the plasma radiative spectrum, the lower lying electrons may be ionized at once. In this case the value of the inverse population is determined by the probabilities of both ways of ionization. In the general form the process would be more complex. In particular, the appeared electron vacancy may "migrate" upward over the electron states of the ion. For neon (Z=10) the photoionization time for the K electron $\sim_{K} 1.1$ 10^{-11}s. The value $\sim 1.45\ 10^{-11}$s. Thus the rates of the development of both ways of the ionization are comparable. The value v 10^8cm/s and the time of the front passing over a separated section $\sim_{fr} (\sim v)^{-1} 10^{-11}$s ($\sim 10^3$cm^{-1} is the laser radiation absorption coefficient) correspond to the temperature $T_{\parallel} \sim 1$ keV. According to this estimates the processes of successive 8 multiple ionization of the ion and its K electron are equally probable. Since $\sim_{K} \sim_{fr}$ approximately half of the particles at the ionization wave front will be in an excited state. The main transition will be in a 7 multiple ionized neon without K electron. The wavelength of $\sim 2\pi c/(\omega_{K} - \omega_{?}) \sim 20$ Å corresponds to this transition. To generate radiation with a frequency of 10^{18}Hz, the ionization process can be considered instantaneous. In this case the atomic remainder transfers into an excited non stationary state, since ejection of part of electrons through ionization changes the energy of the atomic remainder and hence, its Hamiltonian, and the states of the rest electrons at an instance immediately after the ionization act keep the same as before it in the atom (ion). All the electronic sistem of the atomic remainder turns out to be in an

excited state; we'll consider only the electron located "immediately above the hole", i.e. which would be the first to transfer from the nonstationary state into the stationary one. The latter state may naturally be either fundamental or excited. The probability of these transition is known [25]. If Ψ^n_{old} is the wave function (WP) of a set of the corresponding quantum numbers of an unperturbed atom, Ψ^m_{new} is WP in state m of the atomic remainder, then the probability of transition from n into m is $W_{mn}=|q_{mn}|^2=|\int \Psi^{n*}_{old} \Psi^m_{new} dV|^2$. The rate of this transition , unlike that of transition between the stationarity states, is unknown, but it is this rate that virtually determines the lifetime of the "hole". If it is greater then the rate of the ionization considered the medium inverse population takes place, the portion of atomic remainders in the state of inverse population being determined by the way of ionization driving and may considerable (more than 10%).

III. ANALYTIC MODELS OF AMPLIFICATION OF SPONTANEOUS RADIATION

We shall now consider in greater detail the amplification of radiation in an active medium.

INSTABILITY OF BIDIRECTIONAL AMPLIFICATION IN LONG FILAMENTS [8]. At first sight it follows from symmetry considerations that amplification of spontaneous radiation in a long plasma filament of finite length L shoud establish a steady-state symmetric spatial distribution of the intensity. However, we can demonstrate that small fluctuations of the initial intensity of spontaneous radiation (which are always present) alter qualitatively the spatial distribution of the intensity so that it becomes asymmetric. This asymmetry is difficult to detect in the case of radiation emerging from the end. For example, the intensities at the right I_r and left I_l ends differ only by a few percent. This is due to the fact that the intensity I_l increases in the region where the radiation traveling to the right has not yet depleted the inversion.

AMPLIFICATION IN A SEMI-INFINITE FILAMENT. We shall consider unidirectional amplification of spontaneous radiation near the end of a long filament. In this case the intensity of the wave emerging from the filament depends on time. We can determine $I(t)$ by specifying the time dependenses of the gain and of the absorption coefficient. We shall assume that

$$\varkappa^+(t)=(0, t < 0; \; \varkappa^+, \; 0<t<t_p; \; 0, \; t > t_p), \quad \varkappa^-=Const, \tag{9}$$

i.e., in a constantly absorbing medium at a time $t=0$ the amplification acts for a time t_p. The equation governing the time dependence of the intensity is

$$\frac{dI}{cdt} = \varkappa^+(I,t)I-\varkappa^-I+q, \quad \varkappa^+(I,t)=\varkappa^+(t)/(1+I/I_s). \tag{10}$$

The assumed time dependens of the gain, subject to saturation, is typical of a homogeneously broadened line. In a transient medium the intensity I_s causing gain saturation is generally a function of time. We shall ignor this circumstance. We shall solve (10) subject to the initial condition $I(0)=I_{sp}=q/\varkappa^-$. Assuming that $\varkappa^+ \cdot \varkappa^-$ and $I_{sp}/I_s \ll 1$, we obtain

$$I(1-I/I_s)^{-\varkappa^+/\varkappa^-}=I_{sp}\exp[g^+(t)], \quad I_s=I_s\varkappa^+/\varkappa^-, \quad g^+(t)=c\varkappa^+t. \tag{11}$$

The time dependens of the intensity is shown in Fig.2.

The quantity $g^+(t)$ is limited to the value $g^+=c\varkappa^+t_g$. We shall determine the value g^+ necessary to reach an intensity $I=I_{sp}(1-\cdots)$ which is of practical interest only if $g_0 \ln(I/I_{sp}) > 20$. Substituting the expression for

I in (11), we obtain $g^+=g_0+\delta\mathfrak{x}^+/\mathfrak{x}^-\geqslant 20+\delta\mathfrak{x}^+/\mathfrak{x}^-$. Effective utilzation of the amplifying potential of the active mediumrequires that $\delta\geqslant 1$. Therefore if $\mathfrak{x}^+/\mathfrak{x}^->>1$, it follows that amplification can be achieved if $g^+>20$. For example if $\mathfrak{x}^+/\mathfrak{x}^-=10$, we should have $g^+\geqslant 30$.
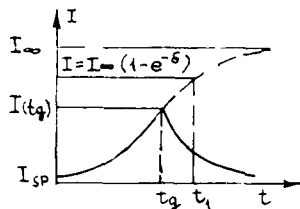
Fig.2. Time dependence of the intensity at the end of a semiinfinite transient filament when $t_g < t_1$.

We shall now determine the time taken by intensity to rise from I_{sp} to $I=I_\infty(1-e^{-\delta})$:

$$ct_1 \equiv L_1 = g_0/\mathfrak{x}^+ + \delta/\mathfrak{x}^- \qquad (12)$$

From now on we shall assume that $\delta=1$.

An increase in t_g in excess of t_1 has little effect on the output intensity. If $t>t_g$ the intensity decreases in accordance with the law

$$I(t)=[I(t_g)-I_{sp}]\exp[-c\mathfrak{x}^-(t-t_g)]+I_{sp}. \qquad (13)$$

If the time dependence of the gain coefficient is bell-shaped, then the integral $g^+=c\int\mathfrak{x}^+(t)dt$ should be used in (11). We shall find the time constant $t_g=g^+/c\mathfrak{x}^m$. As a rule, t_g is approximately equal to the half-width of $\mathfrak{x}^+(t)$ at midamplitude. A more detailed analysis of the amplification should be made using a secular time-dependent equation describing the transfer of the amplitude of a light wave.

RADIATION ENERGY. We shall estimate the energy which can, in principle, be obtained from a plasma filament as a result of recombination pumping. In the case of free expansion in vacuum we can obtain an upper limit to this energy on the assumpsion that each recombination center emits one photon:

$$E_{las}=\pi R_0^2 N_0 RyZ^2(1/a^2-1/b^2). \qquad (14)$$

If $N_0=10^{23}cm^{-3}$, $R_0=1\mu$, and $Z=6$, the energy obtained in the case of the 3-2 transition is $E_{las}=34$ mJ/cm. The energy E_{las} is reduced by the following circumstances: 1) for reasons associated with the gasdynamics of filament expansion, not all the particles have plasma parameters within the range favorable for amplification; 2) not all the ions recombine (ionization quenching); 3) not all the recombining electrons reach the upper laser active level and a part of the recombination flux bypasses the lasing transitions; 4) ot all the electrons reaching the upper laser-active level drop down on the energy scale because of stimulated emission and some of them drop down because of collisional deexcitation and spontaneous emission at an angle to the filament axis.

IV. CONCLUSIONS.

Our analysis deals with the problems associated with the influence of the transient nature of the active medium and of the distributed losses on the amplification of the spontaneous radiation at short wavelengths. An increase in the charge carried by each ion enhances the time dependence. The product of the gain and the distance wich light can travel during the gain lifetime tends to zero. This may limit the usefulness of some population inversion mechanisms as the wavelength is reduced. The majority of the proposed shortwavelength population inversion schemes are characterized by radiative depopulation of the lower active level, wich is effective only in very thin plasma bunches. Recombination pumping requiers rapid cooling and this again means that thin plasma bunches have to be used. The result is an increase in the role of distributed losses beacause of defocusing of the amplified radiation and

these losses exceed the losses usually allowed for (due to invers bremsstrahlung absorption and photoionization of exited levels of ions). An allowance for distributed losses can also limit the usefulness of some population inversion schemes at shorter wavelengths.

By way of illustration of these general ideas, a detailed analysis is made of recombination pumping of hydrogen-like ions in an expanding plasma filament. It is shown that in this case the variant of free expansion of the plasma filament in vacuum is unsuitable for higher values of Z. Limitations are imposed by a factors mentioned above such as the transient nature of the active medium and losses due to defocusing of radiation. The limiting values of Z at wich amplification can still be observed are 8 (for 3-2 transition) and 10 (for 4-3 transition). Forced ionization of an expanding plasma in the case of parameters optimal for the amplification of light in the free expansion variant improves somewhat the limiting value of Z (Z=12 for the 3-2 transition). The main limitations are then imposed by distributed losses due to refraction.

It is also shown, that high-power laser radiation $I > 10^{16}$W/cm^2 enables to produce an extended inversely populated active medium in light-atomic gases in order to generate coherent radiation in the soft X-ray region.

1. D.Matthews, M.Eckart, D.Eder, P.Hagelstein, A.Hazi, R.London, B.Macgowan, S.Maxon, D.Nilson, T.Phillips, M.Rosen, J.Scofield, G.Shimkaveg, R.Stewart, J.Trebes, D.Whelan, B.Whitten, J.Woodworth, S.Brown. Proc. Inter.Colloquium on X-ray Lasers, Aussois, France, 1986, in: J.Phis. (Paris)47, Colloq. 6, C6-1 (1986).
2. S.Suckewer, C.Skinner, D.Kim, E.Valeo, D.Voorhes, A.Wouters. *Ibid*,p.C6-23.
3. U.Feldman, J.Seely, C.Doschek. *Ibid*,p.C6-187.
4. M.Key, J.Boon, C.Brown, C.Chenais-Popovics, R.Corbett, A.Damerell, P.Gottfeldt, C.Hooker, G.Kiehn, C.Lewis, D.Pepler, G.Pert, C.Reagan, S.Rose, I.Ross, P.Rumsby, S.Sadaat, R.Smith, T.Tomie, O.Willi. *Ibid*, p.C6-71.
5. C.Skinner, C.Keane, H.Milchberg, S.Suckever. *Ibid*, p.C6-239.
6. P.Jaegle, G.Jamelot, A.Carrilon, A.Klisnick. *Ibid*, p.C6-31.
7. D.Jacoby, G.Pert, S.Ramsden, L.Shorrock, G.Tallents. Opt. Commun.37,193, (1981).
8. F.Bunkin, V.Bykov. Kvantovaya Electron. (Moscow) 13,869(1986).
9. F.Bunkin, V.Derzhiev, S.Yakovlenko. Kvantovaya Electron. (Moscow) 8,1621 (1981) [Sov.J.Quantum Electron, 11,981 (1981)].
10. V.Boiko, F.Bunkin, V.Derzhiev, S.Yakovlenko. Izv.Akad.Nauk SSSR ser.Fiz. 47,1880(1983); IEEE.J.Quantum Electron. QE-20,206(1984).
11. G.Pert. Philos.Trans.R.Soc.London, Ser A300,631(1981).
12. P.Hagelstein. Preprint LLNL, Livermore, Ca (1984).
13. A.Borovskii, V.Korobkin, Ch.K.Mukhtarov. Kvantovaya Electron. (Moskow) 12,289(1985) [Sov.J.Quantum. Electron. 15,185(1985)].
14. A.Borovskii, V.Korobkin, Ch.K.Mukhtarov. Kvantovaya Electron. (Moscow) 12,2456(1985) [Sov.J.Quantum Electron. 15,1623(1985)].
15. A.Borovskii, V.Korobkin, Ch.K.Mukhtarov. Preprint № 143 [in Russian], Institute of General Physics, Academy of Science of the USSR, Moscow (1985).
16. A.Borovskii, V.Korobkin, Ch.K.Muchtarov. Preprint № 17 [in Russian], Institute of General Physics, Academy of Science of the USSR, Moscow (1986).
17. A.Borovskii, F.Bunkin, V.Korobkin, Ch.K.Mukhtarov. Paper presented at Intern. Colloq. on X-ray Lasers, Aussois, France, 1986, [unpublished].
18. A.Borovskii, V.Korobkin, Ch.K.Mukhtarov. Izv.Akad.Nauk SSSR, Ser.Fiz., 50,1158(1986).
19. I.Sobelman, *Introduction to the Theory of Atomic Spectra. Pergamon Press. Oxford (1973)*.
20. A.Borovskii, V.Korobkin, L.Polonskii, L.Pyatnitskii, M.Uvaliev. Preprint № 5-186 [in Russian]. Institute of High Temperatures, Academy of Science of the USSR, Moscow (1986).
21. N.Bakhvalov, A.Borovskii, V.Korobkin, E.Chizhonkov, M.Eglit, A.Yakubenko. Preprint № 187 [in Russian]. Institute of General Physics, Academy of Science of the USSR, Moscow (1985).
22. A.Borovskii, V.Korobkin, Ch.K.Muchtarov. Preprint № 21 [in Russian]. Institute of General Physics, Academy of Science of the USSR, Moscow (1985).
23. V.Korobkin, M.Romanovskii, in Proc. Inter. Conf. of Coherent and Nonlinear Optics, USSR, Minsk, part 1, p.375 (1988) [in Russian].
24. J.Bretagne et all. J.Phys.D: Appl Phys., 19,761(1986).
25. A.Davydov. Kvantovaya Mekhanika [in Russian]. Fizmatgiz, Moscow (1963).

X-RAY LASER GAIN FROM BRAGG REFLECTION OF CHANNEL RADIATION

M. Strauss* and N. Rostoker
Department of Physics
University of California, Irvine, California 92717 USA

ABSTRACT

The effects of radiation losses and atomic motion on a distributed feedback induced by Bragg reflections in an electron-beam channeling X-ray laser is investigated. Standing wave-fields with nodes in the atomic sites are generated in this cavity mirror structure in single crystals which reduce the losses located close to the atomic sites. An explicit expression for the low threshold gain is derived which depends on the absorption, temperature, and on the order of Bragg reflection. It is noted that diffraction from several sets of atomic planes which satisfy the Bragg condition simultaneously may further reduce the threshold gain. These distributed feedback schemes have possible application in reducing beam high current requirements by many orders of magnitude. It is suggested that an electrostatic accelerator based on a field emission tip electron gun, as used in scanning electron microscopy, can generate the necessary brightness, but with a small current. A detailed discussion of electron beam and accelerator requirements is given and some accelerator ideas appropriate for a channeling X-ray laser are suggested.

I. INTRODUCTION

A relativistic electron beam propagating through planar or axial channels in a crystal free of imperfections may populate bound transverse energy eigenstates.[1] Spontaneous dipolar transitions between these discrete eigenstates have been shown experimentally to yield narrow-width, highly polarized, and intense X-ray radiation which is strongly forward-peaked.[2] One of the important issues in the possibility of using the channeling mechanism as a coherent X-ray source depends on future progress in creating sufficient gain from induced emission. This paper is related to the issue of identifying an efficient scheme for gain optimization in crystal channeling. Previous estimates suggest that in a one passage amplification scheme even modest gains may require currents above MA/cm^2 range for energies near 10 Mev.[3-5] The aim should be to suggest a mechanism to reduce this high current requirement by many orders of magnitude, thereby bringing the channeling X-ray laser closer to experimental reach.

An efficient scheme to significantly reduce the gain requirements for a channeling X-ray laser was proposed based on the concept of a distributed feedback laser (DFB) which is supplied by multiple Bragg reflections of the radiation.[6] This scheme was very useful for atomic emitters in the optical range[7] and was extended later on to the X-ray range.[8] The advantages of using DFB lasers includes the intrinsic compactness and high degree of spectral selectivity available without the need for cavity mirrors. The channeling DFB concept is favorable due to the possibility of radiation tunability. By adjusting the electron beam energy the Doppler up-shifted radiation can be tuned onto a line in the DFB mode spectrum near the Bragg reflection frequency.[6]

The present paper considers the channeling DFB scheme including the effects of absorption and atomic motion on the threshold gain condition and spectral selectivity. We find that the formation of a standing wave-field with nodes on atomic sites, where absorption takes place, reduces drastically the effect of absorption. This effect is related to the Borrmann anomalous transmission effect where standing wave generation makes X-ray losses small.[9-16] The atomic motion effect can be expressed in term of a Debye-Waller factor.[10,13,14] This effect limits the applicability of the DFB scheme to temperatures that are very low compared to the Debye temperature. We further consider the effect of the order of Bragg reflections on the threshold gain condition. In spite of the limitations introduced by the radiation losses the DFB mechanism does reduce drastically the high current requirements. However, the main threshold condition is dictated by the absorption.

To carry out a meaningful experiment of channeling X-ray laser an accelerator should be selected based on existing technology with a very low emittance and high current density. A possible concept can be to apply a field emission tip electron gun, as used in scanning electron microscopy, in an electrostatic accelerator. A low emittance beam can be obtained with very high current density (1 MA/cm^2), but very low current (10-100 nA). The transverse dimension of the beam can be in the range of 100 Å and radiation guiding is supported by Bragg reflections.[17]

* Visiting Scientist on leave from the Nuclear Research Center, Negev, P.O. Box 9001, Beer Sheva, Israel.

II. THE DFB X-RAY LASER MODEL

We characterize the set of channeling transverse eigenstates in the x direction as a two-level system with states $|1\rangle$ and $|2\rangle$, where W and $\hbar\omega_o = \epsilon_2 - \epsilon_1$ are the population and energy differences, respectively. The directions of beam channeling and Bragg reflections are taken in the z direction. The Doppler up-shifted electromagnetic wave frequency $\omega = \omega_o/(1-v/c) \approx 2\gamma^2\omega_o$ in the forward direction is chosen to closely match the n order Bragg frequency, $\omega \sim n\omega_B$, where v is the channeling electron speed, $\omega_B = \pi c/a$ and a is the periodic reflection plane spacing. Typically $\hbar\omega_o$ is a few electron volts in the laboratory frame so that for the relativistic factor γ on the order of 20, $\hbar\omega$ is on the order of several keV. Consequently, the channeling electron energy may be tuned to satisfy the Bragg reflection condition and induce distributed feedback in the channeling crystal (see Fig. 1).
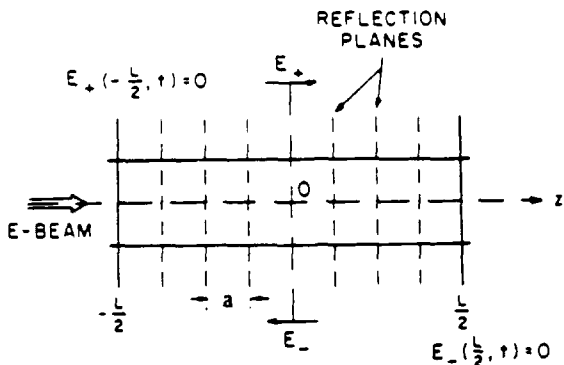
Figure 1

Channel radiation and Bragg reflection $\left(E(z,t) = E_+(z,t) + E_-(z,t)\right)$.

The behavior of the electric $\vec{E}$ field of the electromagnetic wave and the polarization $\vec{P}$ of the beam electrons are related by the Maxwell's wave equation:

$$\frac{\partial^2}{\partial z^2}\vec{E} - \frac{1}{c^2}\frac{\partial^2}{\partial t^2}\vec{E} = \frac{4\pi}{c^2}\frac{\partial}{\partial t}\left(\frac{\partial}{\partial t}\vec{P} + c\nabla \times \vec{M} + \vec{J}\right) \quad , \tag{1}$$

where $\vec{M} = \vec{P} \times \vec{v}/c$ is the magnetization due to the beam electrons and transverse field effects are not considered.[4] The induced current $\vec{J} = \vec{J}_{osc} + \vec{J}_{los}$, where $\vec{J}_{osc}$ is the oscillatory part and $\vec{J}_{los}$ is the dissipative current. The induced current $\vec{J}$ in r.h.s. of Eq. (1) can be represented as,[6,10]

$$\frac{\partial}{\partial t}\vec{J} = \frac{c}{2\pi}\left[\omega K \vec{E} + \mu \frac{\partial \vec{E}}{\partial t}\right] \quad , \tag{2}$$

where $K = 2\pi e^2 n_e/cm\omega$ is the reflection function, n_e is the spatially modulated atomic electron density, μ is the absorption function and an average is carried out over the transverse direction $\vec{\rho} = (x,y)$. In the present section the atomic motion is neglected so that K and μ are periodic functions in the z direction.

The electric $\vec{E}$ and polarization $\vec{P}$ fields are taken in the x direction and are defined in term of forward and backward traveling waves:

$$E(z,t) = \epsilon_+(z,t)e^{-i\omega(t-z)} + \epsilon_-(z,t)e^{-i\omega(t+z/c)} + c.c. \tag{3a}$$

$$P(z,t) = P_+(z,t)e^{-i\omega(t-z/c)} + P_-(z,t)e^{-i\omega(t+z/c)} + c.c. \quad , \tag{3b}$$

where $\epsilon_\pm$ and $P_\pm$ are slowly varying envelope fields.

Inserting Eqs. (3a, 3b, 2) in Eq. (1) we obtain

$$e^{ikz}[\frac{\partial \epsilon_+}{\partial z} + \frac{1}{c}\frac{\partial \epsilon_+}{\partial t} + (\mu + iK)\epsilon_+] + e^{-ikz}[-\frac{\partial \epsilon_-}{\partial z} + \frac{1}{c}\frac{\partial \epsilon_-}{\partial t} + (\mu + iK)\epsilon_-]$$

$$= \frac{2\pi i\omega}{c}[e^{ikz}(1 - v/c)P_+ + e^{-ikz}(1 + v/c)P_-] \quad , \tag{4}$$

where $k = \omega/c$ and second order derivatives are ignored because $\partial^2\epsilon/\partial t^2 \ll \omega\partial\epsilon/\partial t$ and $\partial^2\epsilon/\partial z^2 \ll k\partial\epsilon/\partial z$.

Equation (4) must be supplemented by the equation for $P_\pm$ and is readily determined from a density matrix approach obeying the Bloch equation:[6,18]

$$\frac{\partial}{\partial t}P_\pm + v\frac{\partial}{\partial z}P_\pm = i\Delta_\pm P_\pm - i(1 \mp v/c)d^2 n_b W\epsilon_\pm/\hbar - \Gamma P_\pm \quad , \tag{5}$$

where $d = e <1| x |2>$ is the electric dipole moment, n_b is the beam number density, Γ is a phenomenological damping constant related to the channeling coherence length v/Γ, $\Delta_\pm = \omega(1 \mp v/c) - \omega_0$ is a detuning frequency and v/c represents a magnetic dipole interaction correction. In the limit of short coherence v/Γ the l.h.s. of of Eq. (5) is small and Eq. (5) simplifies: $P_\pm = idn_b W(d\epsilon_\pm/\hbar)(1 \mp v/c)/(i\Delta_\pm - \Gamma)$. Near resonance $\omega \sim 2\gamma^2\omega_0$ and $\Delta_+/\Gamma \ll 1$ giving: $P_+ = -id^2 n_b W\epsilon_+(1 - v/c)/\hbar\Gamma$. In this limit $\Delta_- \sim \omega$, $\Delta_- \gg \Gamma$ and in the case of low gain P_- can be ignored in Eq. (4). We now define the scalar gain $g = 2\pi\omega d_1^2 n_b W/\hbar c\Gamma$, where $d_1 = d(1-v/c)$. Substituting $P_\pm$ in Eq. (4) we obtain

$$e^{ikz}[\frac{\partial}{\partial z}\epsilon_+ + \frac{1}{c}\frac{\partial}{\partial t}\epsilon_+ + (\mu + iK)\epsilon_+ - g_+\epsilon_+] +$$

$$+ e^{-ikz}[-\frac{\partial}{\partial z}\epsilon_- + \frac{1}{c}\frac{\partial}{\partial t}\epsilon_- + (\mu + iK)\epsilon_- - g_-\epsilon_-] = 0 \quad , \tag{6}$$

where the forward gain factor $g_+ = g$ and the backward gain factor $g_- = 0$.

In the following we obtain the equation of motion for DFB X-ray laser by using the resonance parts of Eq. (6). Notice that K and μ are periodic functions, i.e. $K(z) = K(z+a)$ and $\mu(z) = \mu(z+a)$. For a periodic function $f(z) = f(z+a)$ we can use the Fourier series expansion,

$$f(z) = \sum_{\ell=-\infty}^{\infty} f_\ell e^{2i\ell k_B z} \quad , \tag{7}$$

where $k_B = \omega_B/c = \pi/a$.

We insert the Fourier expansion Eq. (7) for K and μ in Eq. (6). For the case the radiation frequency is close to the n order Bragg reflection condition, $k \sim nk_B$, and ignoring highly oscillatory terms we obtain from Eq. (6),

$$\frac{\partial}{\partial z}\epsilon_+ + \frac{1}{c}\frac{\partial \epsilon_+}{\partial t} - (g_+ - i\delta - \mu_0 - iK_0)\epsilon_+ + e^{-W_n}(\mu_n + iK_n)\epsilon_- = 0 \tag{8}$$

$$-\frac{\partial}{\partial z}\epsilon_- + \frac{1}{c}\frac{\partial}{\partial t}\epsilon_- - (g_- - i\delta - \mu_0 - iK_0)\epsilon_- + e^{-W_n}(\mu_n^* + iK_n^*)\epsilon_+ = 0 \tag{9}$$

where we redefine $\epsilon_\pm$ as $\epsilon_\pm \exp[\mp i(k-nk_B)z]$ and include the atomic motion effect by replac-

ing K_n and μ_n by $K_n \exp(-W_n)$ and $\mu_n \exp(-W_n)$, respectively, with W_n as the Debye-Waller factor.[10,13,19] Here $\delta = nk_B - k$ is the detuning from the n order reflection and we note that K and μ are real functions, i.e. $K_{-m} = K_m^*$ and $\mu_{-m} = \mu_m^*$. Equations (8) and (9) are a coupled set of equations of motion for the DFB X-ray laser.

III. THRESHOLD AND SELECTIVITY CONDITIONS

We now find the effect of absorption and atomic motion on the threshold gain and selected resonance frequency. The system at threshold is presented by the solution of Eqs. (8, 9) at steady-state,

$$\frac{d}{dz}\,\varepsilon_+ - \left(g_+ - i\delta - \mu_o - iK_o\right)\varepsilon_+ + e^{-W_n}\left(\mu_n + iK_n\right)\varepsilon_- = 0 \tag{10}$$

$$-\frac{d}{dz}\,\varepsilon_- - \left(g_- - i\delta - \mu_o - iK_o\right)\varepsilon_- + e^{-W_n}\left(\mu_n^* + iK_n^*\right)\varepsilon_+ = 0 \ , \tag{11}$$

where g is identified as a threshold gain and δ as the selected frequency.

The coupled waves Eqs. (10) and (11) describe the spatial variation of transmitted and reflected wave amplitudes in a beam channeling DFB medium. For a slab of length L centered at z=0, the accompanying boundary conditions read: $\varepsilon_+(-L/2) = \varepsilon_-(L/2) = 0$ and no external radiation sources are assumed. The corresponding eigenvalue solutions to Eqs. (10) and (11) for the case that K_n and μ_n are real numbers are found directly:

$$\varepsilon_+(z) = e^{gz/2}\sinh\left[\lambda(z + L/2)\right] \tag{12}$$

$$\varepsilon_-(z) = \pm\, e^{gz/2}\sinh\left[\lambda(z - L/2)\right] \ , \tag{13}$$

where
$$\lambda = \left[\left(\frac{g}{2} - i\delta - iK_o - \mu_o\right)^2 + e^{-2W_n}\left(K_n - i\mu_n\right)^2\right]^{1/2} \tag{14}$$

and the dispersion relation is

$$\left(\lambda - \frac{g}{2} + i\delta + iK_o + \mu_o\right) + \left(\lambda - \frac{g}{2} - i\delta - iK_o - \mu_o\right)e^{-2\lambda L} = 0 \ . \tag{15}$$

A formal solution of allowed resonance frequencies δ and threshold values g can be obtained by inserting Eqs. (12, 13) in Eq. (8):

$$\lambda = \pm\left(iK_n + \mu_n\right)e^{-W_n}\sinh(\lambda L) \tag{16}$$

$$\frac{g}{2} - i\delta = \left(iK_o + \mu_o\right) \pm \left(iK_n + \mu_n\right)e^{-W_n}\cosh(\lambda L) \ . \tag{17}$$

Equation (16) determines λ. Substitution of λ into Eq. (17) and equating real and imaginary parts yields the allowed δ and g.

Approximate formulas can be obtained in the limit of strong reflections:
$\left(K_n L\right)^2 \gg (gL)^2 + 1$ and $|\lambda L| \ll 1$. Upon expanding Eq. (16) in this limit and using the expression for λ we find for the first resonance:

$$\delta = -K_o + |K_n|e^{-W_n} \tag{18}$$

and the threshold gain condition g_t for the typical case of $K_n^2 \gg \mu_o^2$,

$$g_t = \frac{6\,e^{2W_n}}{K_n^2 L^3} + 2\left(\mu_o - e^{-W_n}\mu_n\right) \quad .$$ (19)

The threshold gain in Eq. (19) includes two independent terms: the first term is due to reflection,[5] the second one is due to absorption. In a one passage amplification system (with no reflections) the absorption is with the average absorption coefficient μ_o which is large for X-rays, $\mu_o > 10$ cm^{-1}.[11] In the Bragg reflection coupling system standing waves are generated with nodes on the atomic sites and the absorption, located mainly close to the atomic sites, is strongly reduced. For this case at low temperature compare to the Debye temperature, where $\exp(-W_n) \sim 1$, μ_n is of the order of μ_o and g_t due to absorption is strongly reduced compared to μ_o. From numerical calculation of the anomalous absorption in a germanium single crystal the value of $1-\mu_n/\mu_o$ can be of the order of 10^{-3}.[14]

The threshold gain condition due to reflection can be evaluated using the reflection function $K(z)$ with a modulated atomic electron density: $n_e(z) = n_o\left(1 - \cos(2K_B z)\right)$.[6] Applying the Fourier expansion, Eq. (7), for $K(z)$ we obtain $K_o = 2\pi e^2 n_o/cm\omega_B$ and $K_1 = -K_o/2$. Typically K_o is on the order of 10^4 cm^{-1} in a number of crystalline samples used in channeling studies, e.g., silicon, diamond, where n_o is approximately the crystal bound electron density. For first order Bragg reflections $n = 1$ and $L = 0.1$ cm the value of g_t due to reflection is 2×10^{-4} cm^{-1}.[6] In crystals with low atomic numbers e.g., LiH, $\mu_o \sim 10$ cm^{-1} and for $1-\mu_1/\mu_o \sim 10^{-3}$ the value of g_t due to absorption is 10^{-2} cm^{-1}. Thus, the main contribution here to the threshold gain condition is absorption. But as L decreases below 200 μ the reflection contribution to g_t exceeds the absorption one.

It is shown in Refs. (15, 16) that by applying a diffraction scheme from several sets of atomic planes which satisfy the Bragg condition simultaneously, it is possible to reduce the absorption of the radiation. In this method, called the multi-beam Borrmann effect, standing waves are generated in several directions relative to the atomic site, generating larger nodal regions in radiation fields and the absorption for some of the radiation modes can be reduced by a factor of 10^{-4}.[16] For this case and $\mu_o \sim 10$ cm^{-1}, g_t due to absorption can be reduced to 10^{-3} cm^{-1}.

The inclusion of the atomic motion in Eq. (19) is through the Debye-Waller factor and is related to the average displacement U, where $U^2 = \langle (U_j^{(z)})^2 \rangle$ decreases with the increase in the Debye temperature T_D. For a crystal with a high Debye temperature W_n due to the zero point motion can be as low as $W_n \sim 10^{-3} n^2$.[14] Thus, for $n = 1$ and temperatures $T \ll T_D$ the zero point motion does not change g_t appreciatively. Furthermore, by applying the multi-beam Borrmann effect together with the DFB scheme the atomic motion effect and the threshold gain condition can be further reduced.

For the case the gain g is larger than the threshold gain g_t the radiation fields $\varepsilon_\pm$ increase with time as $\exp\left[(g-g_t)\,ct/2\right]$ in the linear range. Thus, an amplification factor $(g-g_t)ct/2 \sim 1$ is obtained for a beam pulse duration of 50 ns, $L = 0.1$ cm and $\mu_o \sim 10$ cm^{-1} for $g \sim 10^{-2}$ cm^{-1} in the DFB scheme and by including multi-beam Borrmann effect for $g \sim 2 \times 10^{-3}$ cm^{-1}. These results should be compared to the gain $(g - \mu_o)L \sim 1$ obtained in a one passage amplification, wherefore $L = 0.1$ cm and $\mu_o \sim 10$ cm^{-1}, $g \sim 20$ cm^{-1}. Thus, in spite of the limitations on g_t due to the absorption, in terms of beam current requirements the DFB mechanism in beam channeling has possible application in reducing current requirements by many orders of magnitude.

In the next section we show that it is useful to consider an accelerator concept based on a high current density (1 MA/cm^2) but with a low total current (1 μA). The minimum beam radius b depends on the mechanism to guide the radiation. In a one-passage amplification the guiding can be supported by spatial guiding base on Fresnel condition $4a^2/\lambda L > 1$ or by gain guiding condition $4a^2 g/\lambda > 1$. These forms of guiding require for $\lambda = 3$Å, $a = 100$Å that $g \gg 1$ and to a further increase in current density. In the DFB system guiding can be supported by Bragg reflections with the condition $4a^2 K_o/\lambda > 1$ and is independent of g.[17]

Thus, reflections can avoid the buildup of radiation diffraction for $\lambda = 3$Å, $a = 100$Å even with $g \ll 1$.

IV. ACCELERATOR REQUIREMENTS

In order to obtain significant gain from induced emission the current density of the electron beam must be of the order[3,6] of $10^7 - 10^8$ A/cm^2 for one-pass amplification. This requirement can be reduced to $10^4 - 10^5$ A/cm^2 by using the DFB scheme described in this paper.

The electron beam is characterized by the emittance $\varepsilon = R\langle\Delta\theta\rangle$ where R is the beam radius and $\langle\Delta\theta\rangle$ is the angular spread. The beam may alternately be characterized by the mean perpendicular energy

$$W_\perp = \frac{\gamma m}{2} \left[c\langle\Delta\theta\rangle \right]^2 \tag{20}$$

or the Brightness

$$B = I/(\pi\varepsilon)^2 \quad , \tag{21}$$

where I is the total current. The current density can always be increased by focusing. For example, for a magnetic lens in vacuum the envelope equation is

$$\frac{d^2 r}{dz^2} = \frac{\varepsilon^2}{r^3} + \frac{2\nu}{\gamma^3}\frac{1}{r} - \frac{\Omega_z^2}{2c^2} r \quad , \tag{22}$$

$\Omega_z = eB_z/\gamma mc$ where B_z is the axial magnetic field. The beam radius can thus be reduced to the limits of Eq. (22). However, the crystal channel eigenstates set a more restrictive limit. Since $\varepsilon = R\langle\Delta\theta\rangle$ is preserved as R decreases $\langle\Delta\theta\rangle$ increases as does $W_\perp$ given by Eq. (20). To have bound eigenstates $W_\perp \lesssim 10$ eV is required. Thus the minimum radius is $R_m = \varepsilon(\gamma mc^2/2W_\perp)^{1/2}$ and the maximum current density is

$$J_m = \pi B (2W_\perp/\gamma mc^2) \quad . \tag{23}$$

The accelerator that produces the maximum J_m is a field emission type employed in scanning electron microscopy.[20] For d.c. operation $\varepsilon \sim 3 \times 10^{-8}$, $\gamma = 1$ (5 keV) and $I = 10^{-8}$ A. Such beams are routinely focused to a current density of 10^6 A/cm^2. If the electron beam could be accelerated to 10 MeV without changing the normalized emittance $\varepsilon_N = \gamma\beta\varepsilon$, the resultant emittance would be $\varepsilon = 2 \times 10^{-10}$. The minimum radius for $W_\perp < 10$ eV would be 7.1 Å corresponding to a current density of 0.6×10^6 A/cm^2. A current density of 10^5 A/cm^2 would be obtained over a final focus radius of 18 Å or 10^4 A/cm^2 over 57 Å radius. For a channel of 100 Å radius the total current would need to be increased by a factor of about 30 to achieve a current density of 10^5 A/cm^2. Presumably with pulsed operation much larger currents could be obtained and larger final current density or larger minimum radius with the same current density would be possible.

The question that must be addressed is whether or not a low current beam can be accelerated from about 5 keV to 10 MeV without destroying the brightness due to some instability. For such a low current beam it is credible that this could be done with an electrostatic accelerator i.e., a Van de Graff. However, such an accelerator is expensive and requires a large facility which would limit the availability of the X-ray laser. For this reason we have also considered a particular type of Betatron that is a descendant of the Astron of LLNL. It is called the elongated[21] Betatron and has been developed to accelerate currents of the order of 100 A to a few MeV. It has also been employed to trap very low current beams which has not been possible with an ordinary Betatron.

In any case the electron beam requirements are not state of the art but appear to be achievable with some research on the source of electrons and the accelerator starting with field emission sources used in scanning electron microscopy.

Acknowledgements

V. REFERENCES

1. J. U. Andersen, E. Bonderup, and R. H. Pantell, Ann. Rev. Nucl. Part. Sci. 33, 453 (1983); V. V. Beloshitsky and F. F. Komarov, Phys. Rep. 93, 117 (1982); G. Kurizki and J. K. McIver, Phys. Rev. B 32, 4358 (1985).
2. R. K. Klein et al., Phys. Rev. B 31, 68 (1985); B. L. Berman, B. A. Dahling, S. Datz, J. O. Kephart, R. K. Klein, R. H. Pantell, and H. Park, Nucl. Instrum. Methods B 10/11, 611 (1985).
3. V. V. Beloshitsky and M. A. Kumakhov, Phys. Lect. A 69, 247 (1978).
4. G. Kurizki, M. Strauss, J. Oreg and N. Rostoker, Phys. Rev. A 35, 3424 (1987).
5. V. H. Ohtsuki, Nucl. Instrum. Methods B 2, 80 (1984).
6. M. Strauss, P. Amendt, N. Rostoker and A. Ron, Appl. Phys. Lett. 52, 866 (1988).
7. H. Kogelnik and C. V. Shank, Appl. Phys. Lett. 18, 152 (1971); J. Appl. Phys. 43, 2327 (1972).
8. A. Yariv, Appl. Phys. Lett. 25, 105 (1974).
9. V. G. Borrmann and W. Hartwig, Z. Kristallog, 121, 401 (1965).
10. B. W. Batterman, Rev. Mod. Phys. 36, 681 (1964).
11. L. V. Azaroff, Elements of X-Ray Crystallography (McGraw-Hill, New York, 1968).
12. J. P. Hannon and G. T. Trammell, Opt. Commun. 15, 330 (1975).
13. B. W. Batterman, Phys. Rev. 126, 1461 (1962); B. W. Batterman and D. R. Chipman, Phys. Rev. 127, 690 (1962); J. Appl. Phys. 34, 2716 (1963).
14. H. Wagenfeld, J. Appl. Phys. 33, 2907 (1962).
15. T. Joko and A. Fukuhara, J. Phys. Soc. Japan 22, 597 (1967); E. J. Seccocio and A. Zajac, Phys. Rev. 139, 225 (1965); J. T. Hutton, J. P. Hannon and G. T. Trammell, Phys. Rev. A 37, 4280 (1988).
16. T. C. Huang, M. H. Tillinger, and B. Post, Z. Naturforsch 28A, 600 (1973).
17. M. Strauss and N. Rostoker, in preparation for publication.
18. M. Strauss, P. Amendt, H. U. Rahman and N. Rostoker, Phys. Rev. Lett. 55, 406 (1985); M. Strauss, Phys. Rev. A 38, 1358 (1988).
19. N. W. Ashcroft and N. D. Mermin, Solid State Physics (Holt, Rinehart and Winston, 1976) p. 780-795.
20. J. F. Hainfield, Scanning Electron Microscopy, Vol. I, P. 591-604 (1977).
21. A. E. Blaugrund, A. Fisher, R. Prohaska, and N. Rostoker, J. Appl. Phys. 57(7), 2474 (1985).

PROSPECTS FOR PUMPING AN X-RAY LASER WITH SUPRATHERMAL ELECTRONS GENERATED IN LASER-PLASMA INTERACTIONS

J. P. Apruzese, P. G. Burkhalter, J. E. Rogerson, J. Davis, J. F. Seely, C. M. Brown, D. A. Newman*, and R. W. Clark

Naval Research Laboratory, Washington, D. C. 20375-5000

J. P. Knauer and D. K. Bradley**

Laboratory for Laser Energetics, University of Rochester
Rochester, New York, 14623

Abstract

Suprathermal electrons have been proposed in several contexts as a pump source for x-ray lasers. In a series of experiments performed at the University of Rochester, formvar-supported circular silver dot targets were simultaneously irradiated with 1.06μm and 0.35 μm laser light in the mid-10^{14} W cm^{-2} range. In some of the shots, only 0.35 μm light was used. Both high resolution and broadband spectral data reveal that higher states of excitation and ionization of neonlike and fluorinelike silver were achieved in the presence of the 1.06 μm beam. Evidence that this enhanced excitation and ionization is due to suprathermal electron pumping is provided by the broadband continuum data which show little or no increase in the thermal electron temperature, when the 1.06 μm light is superimposed. Analysis of the data indicates that, in a similarly structured linear target, the gain of the 3p-3s J=2 to 1 neonlike line at 99.6 Å would increase from 0.4 cm^{-1} to ~ 1 cm^{-1} when using both laser wavelengths. This conclusion is independent of the mechanism producing the increased excitation and ionization.

1. Background

The generation of suprathermal electrons in laser-plasma interaction has been the subject of intense experimental and theoretical investigation for more than 15 years[1-13]. The conversion of incident laser energy to suprathermal electrons has been found to be greatest for $I\lambda^2 \geq 10^{14}$ W cm^{-2} $μm^2$. The presence of such hot electrons is undesirable in laser fusion experiments, and they have been substantially eliminated through use of shorter laser wavelengths[10-13]. However, suprathermal electrons may be effective in pumping x-ray lasers[14-16].

The usefulness of suprathermal electrons in x-ray laser experiments has been investigated in detail[14-16] only for the achievement of population inversions in neonlike ions, although there is every indication[16] that the nickel-like sequence is equally promising. Stripping to the sodiumlike stage, or the ground state of the neonlike stage, requires a lower thermal electron temperature than that needed to both achieve and pump the neonlike stage. The excitation and ionization energies from the ground state of the closed shell neonlike configuration exceed the ionization potential of the sodiumlike stage. Therefore, a relatively cool plasma may contain substantial sodiumlike and/or neonlike ground state populations. Such a plasma, irradiated by the proper combination of laser wavelength and intensity, could then be "pumped" by the suprathermal electron population through ionization of the outer[14] or inner shell electrons[16], or direct collisional excitation of the upper lasing levels of the neonlike stage[15], all of which are energetically accessible to the suprathermals but not to the cooler thermal electrons. The term "pumping" is used to refer to all three possibilities mentioned above. In an attempt to provide experimental verification of this concept, a series of shots was undertaken using the 0.35 μm OMEGA facility at the University of Rochester, supplemented by the 1.06 μm GDL beam for suprathermal electron generation. In the succeeding sections, the experiments and diagnostics are described, the principal data obtained presented, and our interpretation is discussed. In the concluding section, the work is summarized and avenues for future investigation are suggested.

2. Description Of Experiments

It is now well established[12,13] that 0.35 μm laser light produces negligible numbers of suprathermal electrons when irradiating a plasma at intensities $I \leq 10^{15}$ W cm^{-2}. However, experiments using 1.06 μm light at I ~ 3×10^{14} W cm^{-2} have invariably revealed the presence of a suprathermal electron population which is generally believed to be produced by the

* Sachs-Freeman Associates, Inc. Bowie, Maryland 20715
** Lawrence Berkeley Laboratory, Berkeley, California 94720

resonance absorption mechanism.[4,6,8,9,12,13] Therefore, the state of ionization/excitation of the plasma without suprathermal electrons present may be established from target shots utilizing only the 0.35 μm beams. When the 1.06 μm beam is simultaneously present, it is expected that significant numbers of suprathermals will be created, allowing for the possibility of spectroscopic detection of their pumping effects.

The targets used consisted of a 3000 Å thick circular silver spot, 200 μm in diameter, deposited on a 1600 Å thick layer of formvar stretched over the 2.5 mm diameter hole of a nylon washer. The structure of the target – a potential lasing material deposited on formvar – is similar to that of the linear exploding foil targets successfully employed in neonlike x-ray lasers at Lawrence Livermore National Laboratory[17-19] and the Naval Research Laboratory[20]. The 3000 Å thickness of the silver layer (315 μg cm^{-2}) was chosen to produce an electron density of 2×10^{21} cm^{-3} at the peak of the 650 ps driving laser pulse using an intensity of 0.35 μm radiation of 3-5 × 10^{14} W cm^{-2}. This electron density permits resonance absorption with generation of suprathermal electrons by the superimposed 1.06 μm beam, for which the critical density is 1×10^{21} cm^{-3}. One-dimensional hydrodynamic calculations of these experiments using the model described in Ref. 21 and the scaling laws for exploding-foil hydrodynamics developed in Ref. 22 formed the basis for this choice of target thickness to obtain $N_e = 2 \times 10^{21}$ cm^{-3} at the laser pulse maximum. Useful data were obtained on seven silver target shots executed at the University of Rochester using 8 beams of the 0.35 μm frequency up-converted OMEGA Nd: phosphate-glass laser facility. On 3 of the 7 shots, the 1.06 μm GDL laser beam was superimposed on the 0.35 μm OMEGA beams with the peak of its 100 ps pulse coincident with that of the 650 ps OMEGA pulse. Irradiances and energies on target for both driving laser wavelengths for the 7 shots are given in Table 1. The 200 μm spot was overfilled with 300 μm beams to minimize formation of a cold boundary plasma.

Shot	I (0.35μm) (10^{14}W cm^{-2})	I (1.06μm) (10^{14}W cm^{-2})	E (0.35μm) (J)	E (1.06μm) (J)	Te(KeV)	F-like lines?
1	4.8	0	220	0	1.29	no
2	4.6	2.8	228	22	1.33	yes
3	4.4	0	201	0	1.50	no
4	4.5	0	228	0	1.38	no
5	3.6	3.0	181	24	1.36	yes
6	3.8	3.3	171	27	1.29	yes
7	3.2	0	167	0	---	no

Table 1. Irradiances and energies on target are given for the seven shots for both laser beams. T_e refers to the time-averaged thermal electron temperature derived from the broadband continuum data. The last column indicates whether transitions of fluorinelike silver were detected on the shot.

X-ray spectra were recorded with two time-integrating crystal spectrographs and one time resolving streaked elliptically curved crystal spectrograph. The latter device is part of the SPEAXS system[23]. Two crystal spectrographs[24] employed flat crystals to obtain high resolution spectra. A LiF (200) crystal covered the 3.62 - 3.72 Å region, and a Si (111) crystal produced data between 3.8 and 4.1 Å. A curved mica crystal spectrograph was used to record the entire silver L-series spectrum from 3.0 to 4.5 Å. The distinct neonlike Ag spectral lines are readily identifiable, and published wavelengths were used for the spectral calibration. For line identifications, ab initio atomic structure calculations were performed using scaled Slater parameters for 2p-3s and 2p-3d transitions in fluorinelike Ag XXXIX. XUV spectra in the 25 - 230 Å region were collected with a 3-m grazing incidence spectrograph[25]. Time-integrated broadband spectra of the recombination continuum in the 4-14 keV range were obtained on 6 of the 7 shots with an array of K-edge filtered detectors.[12]

1. Results Of Experiments

1.1 Line Radiation

X-ray and/or XUV lines of sodiumlike and neonlike silver were detected on all seven shots by one or more of the spectrographs deployed. However, an important feature of the data is that x-ray lines of fluorinelike silver were detected only when the 1.06 μm GDL beam was used (Table 1), on shots 2, 5, and 6. In shot 6, the $2s^2 2p^5 \,^2P_{3/2} - 2s 2p^6 \,^2S_{1/2}$ line of fluorinelike silver[26] at 28.5 Å was also weakly detected by the 3-m grazing

incidence spectrograph. No fluorinelike line could be uniquely identified, either in the x-ray or XUV region, on shots 1, 3, 4, and 7.

High resolution spectra obtained with and without the 1.06 μm GDL beam are presented in Figs. 1 and 2. Dual flat crystal x-ray spectrographs using LiF (200) and Si (111) diffraction crystals acquired these spectra. These spectrographs equipped with translation slits recorded juxtaposed spectral images on subsequent shots with OMEGA plus GDL and without GDL (OMEGA generated plasmas only).
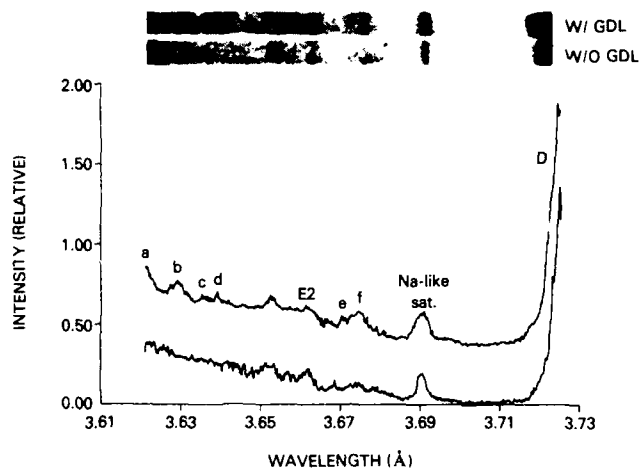
Fig. 1. Silver spectra obtained with the LiF crystal spectrograph both with (top spectrum, shot 2) and without (bottom spectrum, shot 1) the midpulse irradiation by the 1.06 μm GDL beam. Line D and electric quadrupole lines E2 arise from the neonlike stage; identifications of the fluorinelike lines a-d and e-f are given in Table 2.
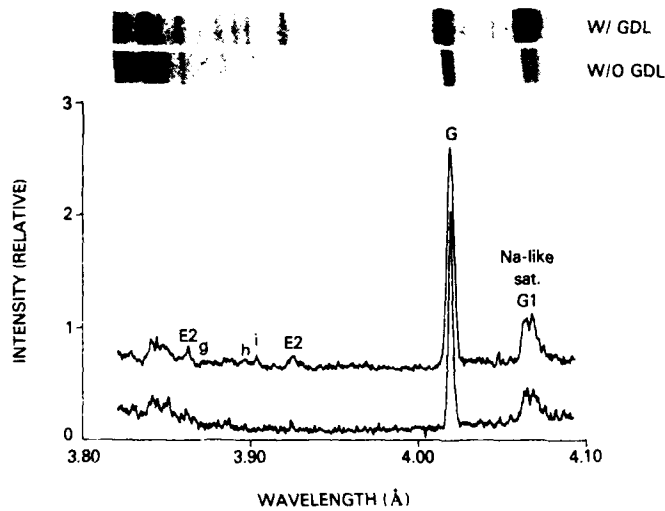
Fig. 2. Silver spectra obtained with the Si crystal spectrograph both with (top spectrum, shot 2) and without (bottom spectrum, shot 3) the midpulse irradiation by the 1.06 μm GDL beam. Line G and electric quadrupole lines E2 arise from the neonlike stage; identifications of the fluorinelike lines g-i are given in Table 2.

Photographs were taken from the ... resolution spectrographs were read with a digitizing ... and converted into intensities by computer processing. The conversion ... crystal diffraction and film response together with the detector window ... transmission factors. Spectral line intensities were determined ... contribution ... by total peak summation and by line fitting with Gaussian ... under the spectral regions were obtained by least squares fitting ... polynomial ... data points selected from regions of the spectrum free of ... identifications of the fluorinelike lines are given in Table 2. The ... between observed and calculated fluorinelike wavelengths was ±3mÅ except for the line ... shifted by ... mÅ as indicated in Table 2. In the presence of the 1.06 ... only ... the fluorinelike lines appear but the intensities of the neonlike ... lines are also enhanced. Specifically, the strong neonlike line $2p^6\ ^1S_0$ - ... Å (labelled 3 in Fig. 2) increases in intensity by a factor 1.6. ... quadrupole (E2) transitions $2p^6\ ^1S_0$ - $2p^5 3p\ (3/2, 3/2)_2$ at 3.863 Å and ... 3.924 Å have enhancements of at least a factor of 2.4, ... the plasma irradiated solely at 0.35 μm. The sum of the intensities of the 2p-... fluorinelike silver lines n=1 increases from an upper limit of 2% of the intensity of ... at 3... Å to 77 when the 1.06 μm beam is present, indicating ... of ... fluorinelike silver stage on the shots using both OMEGA and GDL.

Classification		gf		Upper Level*	
X J?	...	Value	J?	J'	j-j coupling
			$2p^5 - 2p^4 3d$		
		1.?	3/2	5/2	$0.55(^1S_0,\ 5/2)$
		1.5	1/?	1/2	$0.57(^1D_2,\ 5/2)$
		...	1/2	3/2	$0.38(^1D_2,\ 5/2)$
		...	3/2	3/2	$0.34(^1S_0,\ 3/2)$
		...	3/2	5/2	$0.65(^3P_2,\ 5/2)$
		...	3/2	3/2	$0.39(^3P_2,\ 5/2)$
		...	3/2	1/2	$0.61(^3P_2,\ 5/2)$
			$2p^5 - 2p^4 3s$		
		...	1/2	1/2	$0.59(^3P_0,\ 1/2)$
		...	3/2	3/2	$0.70(^1D_2,\ 1/2)$
		...	3/2	5/2	$0.73(^1D_2,\ 1/2)$
		...	1/2	3/2	$0.70(^1D_2,\ 1/2)$
		...	3/2	3/2	$0.71(^3P_2,\ 1/2)$
		...	1/2	1/2	$1.00(^3P_1,\ 1/2)$
		...	3/2	5/2	$0.73(^3P_2,\ 1/2)$

* ... $^3P_2,\ 1/2)$ in place of $(2p^4\ ^3P_0 3s_{1/2})$ in the j-j coupling scheme.

Table 2. Experimental and predicted wavelengths for F-like transitions in Ag XXXIX and ... ab initio atomic structure calculations.

Time-integrated broadband spectral data were obtained in five channels centered at energies of approximately 4.0, 6.0, 6.7, 8.0, and 13.6 keV. The spectral intensity is determined within an estimated overall uncertainty of 20%. Details of this instrument, which employs a K-edge filtered array of PIN diodes, are given in Ref. 12. Data from shots 4 (without GDL) and 5 (with GDL) are presented in Figs. 3 and 4, respectively. The ionization edge of neonlike silver is depicted by a line at 5.6 keV, lying between the first and second channels. An important feature of this data revealed in Figs. 3 and 4 is that the spectral intensity at 6 keV is larger relative to that at 4 keV when the 1.06 µm beam is present. This pattern persists for the other four shots not shown. This is attributable to the increase in the recombination edge discontinuity at 5.6 keV due to the presence of more fluorinelike silver. At energies above the 5.6 keV edge, the bulk of the continuum radiation arises from electron recombination onto the ground state of fluorinelike silver to form neonlike silver. Therefore, the more fluorinelike silver, the greater the intensity on the high energy side of the edge. Thus the continuum data provide direct corroboration of the high resolution x-ray spectra as to the increased abundance of fluorinelike silver in the presence of the 1.06 µm GDL beam.

The channels at 8.0 and 13.6 keV are free of overlap by lines or ionization edges. Therefore, the ratio of these intensities may be used to obtain an approximate time-integrated electron temperature T_e using an exponential fit to the intensity decrement. If $R = I(8)/I(13.6) = \exp(-8/T_e)/\exp(-13.6/T_e)$, then

$$T_e = 5.6/\ln R \qquad\qquad\qquad (1)$$

Assuming a 20% uncertainty in both $I(8)$ and $I(13.6)$, the uncertainty in their ratio R is $\sqrt{2}$ $\times$ 20% = 28%. However, according to Eq. (1), the temperature is logarithmically dependent on R; therefore the fractional uncertainty in T_e is obtained as (28%) (R/T_e) dT_e/dR = 28%/ln R = 7%, for T_e=1.4 keV, R=55, typical of these shots. In Table 1 the derived temperature is listed for each of the six shots. No correlation of T_e with use of the 1.06 µm beam is observed. Also, the standard deviation of the six temperatures is 0.07 keV, consistent with the expected 7% uncertainty derived above.

Time-resolved data were obtained with the SPEAXS streaked elliptically curved mica crystal spectrograph. This instrument spectrally integrated the radiation in a band from 3.1 to 3.4 keV. The intensity peak in this spectral band coincides in time with the peak of the driving 0.35 µm laser. Since the density in exploding-foil plasmas declines monotonically with time, the coincidence of these peaks strongly suggests that the temperature maximizes at or slightly after the driving laser pulse peak, confirming the model predictions of Ref. 22.

SHOT 4

E (0.35µm) = 228 J   E (1.06µm) = 0 J
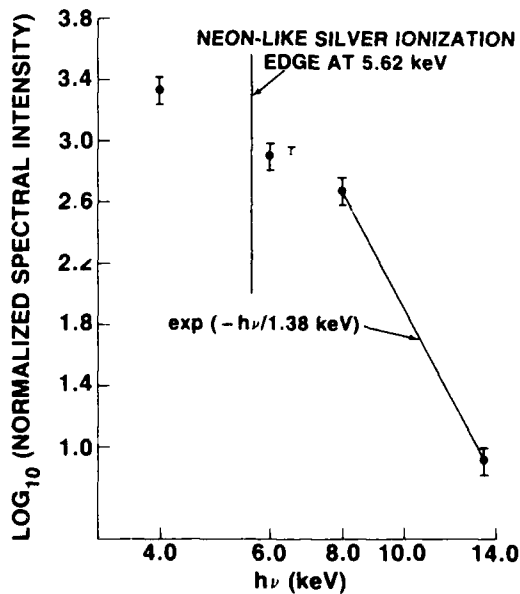
Fig. 3. Normalized, time integrated spectral intensity vs. energy for five broadband channels, as recorded for shot 4 which did not employ a supplementary 1.06 µm laser pulse.

SHOT 5

E (0.35μm) = 181 J   E (1.06μm) = 24 J
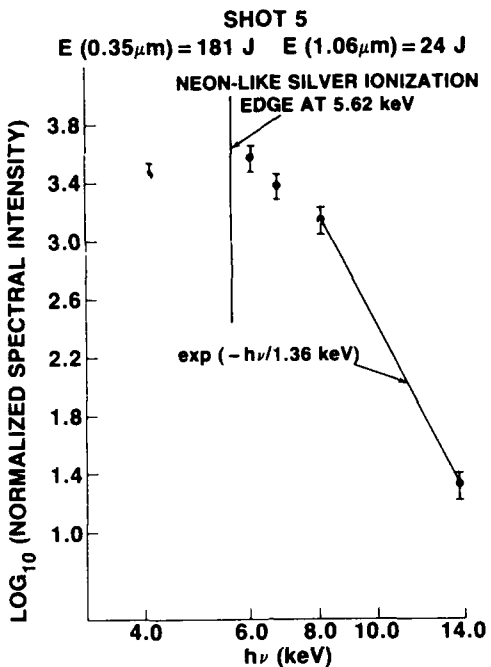
Fig. 4. Same as Fig. 3, except the data is for shot 5 which employed the 1.06 μm pulse as described in Table 1.

4.   Interpretation of the Experiments

As described above, for three of the seven target shots, lines from fluorinelike silver were identified.   These three shots differed from the other four only in that a supplementary 1.06 μm, 100 ps beam was superimposed on the principal driving 0.35 μm, 650 ps laser pulse. We now consider possible mechanisms which could produce this correlation.

In these exploding-foil plasmas, photoionization of neonlike silver is negligible, since no line radiation and comparatively little continuum radiation lies above the 5.6 keV threshold.   The ionization balance between the neonlike and fluorinelike stages is dominated by electron collisional ionization of the ground state of neonlike silver $(W_{CI}(T_e))$ and dielectronic recombination onto fluorinelike silver $(W_{DR}(T_e))$ to form the neonlike stage.   Chen[30] has tabulated dielectronic recombination rate coefficients for fluorinelike silver vs. electron temperature, showing that the total rate is fairly flat with temperature, declining from 3.0×10^{-11} cm^3 sec^{-1} at 1.5 keV to 2.6×10^{-11} cm^{-3} sec^{-1} at 2.0 keV, assuming statistical population of the $^2P_{1/2,3/2}$ fluorinelike ground sublevels. The characteristic equilibration time between the neonlike and fluorinelike stages is $(N_e W_{DR}(T_e))^{-1}$ = $(2 \times 10^{21}$ x $3.0 \times 10^{-11})^{-1}$ = 17 ps.   Therefore, a collisional-radiative equilibrium (CRE) model should provide a reasonable guide to the ionization balance as a function of temperature.

It is clear that use of the 1.06 μm beam produces more electrons with energies above neonlike ionization potential of 5.6 keV, resulting in a greater abundance of fluorinelike silver.   The principal question is whether the 1.06 μm laser has simply heated the electrons to a higher-temperature Maxwellian or are suprathermal electrons (at considerably higher energies) responsible for the observed effect. We first consider the possibility that purely thermal heating is responsible.   Since the dielectronic recombination rate varies slowly with temperature near $T_e = 1.4$ keV, the temperature dependence of the fluorinelike abundance is principally determined by the temperature dependence of collisional ionization of the neonlike stage.   The 2p-3d fluorinelike-to-neonlike line ratio increases by at least a factor of 3, therefore, a similar increase in the fluorinelike abundance is strongly suggested, since these lines arise from collisional excitation of their respective ground states.   Therefore a threefold increase in the thermal collisional ionization rate of neonlike silver would be required to produce this effect.   The factor of 3 necessitates a time-averaged temperature increase from 1.4 to 1.9 keV, as demonstrated, for example, by the Lotz ionization rate formula[31].   This expectation is confirmed by the CRE calculations presented in Fig. 6, showing that the observed line ratio for the GDL shots is reproduced at $T_e = 1.9$ keV. However, such a temperature increase from 1.4 keV appears to be ruled out by the broadband continuum data (Table 1) at 8.0 and 13.0 keV. As discussed in the previous section, the uncertainty of 28% in the spectral intensity ratio in these channels translates to only a 7% uncertainty in the temperature. Even doubling this estimated uncertainty to 15% allows a temperature increase to only 1.6 keV, which would produce just one-third of the observed extra ionization.

68

What if the required temperature increase is considered on a time-resolved basis, rather than time-averaged? Since the 100 ps CDL pulse peak coincided with the maximum of the OMEGA pulse, any thermal electron temperature increase caused by the 1.06 μm beam would exist only for the latter half of the OMEGA pulse. Therefore, the required extra ionization rate during this half of the plasma's existence would be approximately twice that needed if such ionization occurred throughout the lifetime of the plasma. This translates to a required thermal electron temperature of 2.2 keV during the half influenced by the 1.06 μm beam. The ratio of the intensity at 13.6 keV to that at 8.0 keV is a factor of two higher for an electron temperature of 2.2 keV than for 1.4 keV. The time-integrated ratio would increase by at least a factor two which is well above the ~28% uncertainty in the observed ratio.

In summary the observed constancy of the continuum slope in the 8.0-13.6 keV spectral region with and without the 1.06 μm supplementary beam, appears to rule out the possibility that an increase in the thermal electron temperature is responsible for most of the observed extra ionization. We now consider the plausibility of suprathermal electrons as the cause of this phenomenon.

The highest photon energy covered by the broadband data is 13.6 keV. Since the photons from recombination from fluorine-to-neonlike silver are responsible for most of this radiation, a photon of 13.6 keV is created by an 8 keV electron falling through the 5.6 keV ionization potential of neonlike silver. Therefore, suprathermal electrons with energies of 8 keV cannot be directly detected. However, the observed increased ionization along with the lack of increase of the thermal electron temperature can provide a strong indication for their presence, provided the required numbers and energy are in reasonable accord with previous investigations.

To create the observed threefold increase in fluorinelike silver, the collisional ionization rate from neonlike silver must also increase by a factor of three. For hot electron temperatures of 10 keV, the collisional ionization rate coefficient increases slowly with temperature, for example, from 1.6×10^{-11} cm^3 sec^{-1} at 10 keV to 2.2×10^{-11} cm^3 sec^{-1} at 20 keV. The 10 keV rate coefficient exceeds that at the diagnosed thermal temperature of 1.4 keV by a factor of 50. Therefore, a 4% population (by number) of 10 keV suprathermals will provide the required threefold increase in the ionization rate. This expectation is verified by the CRE calculation of Fig. 5, showing that a 10 keV suprathermal electron fraction of 4.8% coupled with a thermal electron temperature of 1.4 keV reproduces the observed time-integrated fluorine-to-neonlike line ratio. The total number of electrons in the silver plasma is calculable from the known mass of the target, and its degree of ionization. A 4.8% population of 10 keV suprathermals represents 2.3 J; if the suprathermal temperature is 20 keV, 3.3 J of fast electron energy would be required. Therefore, about 10-15% of the 22 J of 1.06 μm energy incident on the target is required to be converted to suprathermal electrons. This is consistent with previous investigations of suprathermal electron production[9,12,13] and supports the picture of ionization by suprathermal electrons.
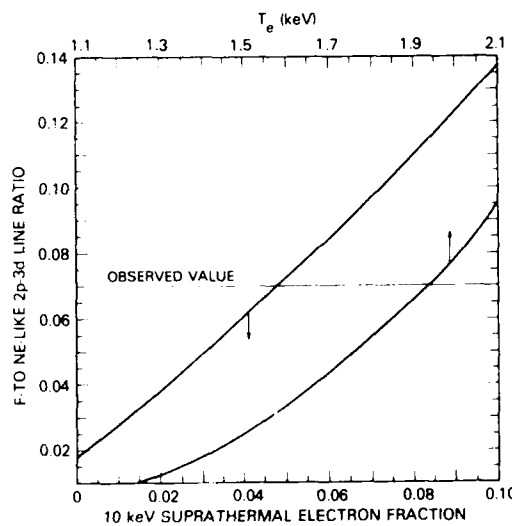
Fig. 4. The theoretical ratio of the fluorinelike-to-neonlike silver 2p-3d lines as described in the text is plotted vs. 10 keV suprathermal electron fraction (lower scale), with an assumed thermal electron temperature of 1.4 keV and density 2×10^{21} cm^{-3}. Also presented is the same ratio vs. temperature (upper scale) assuming no suprathermal electrons. Curves were generated assuming collisional-radiative equilibrium using an atomic model for silver analogous to that for iron described in Ref. 15.

Suprathermal electrons which are sufficiently energetic to ionize neonlike silver will also pump its 3p levels. The cross sections for electron collisional ionization and excitation[35] are comparable, about $1-3 \times 10^{-21}$ cm^2. Direct proof of the enhanced populations of the neonlike 3p levels is found in the x-ray spectra of Fig. 2. The 3p-2p electric quadrupole transitions labelled E2 are optically thin and their intensities therefore directly reflect the populations of the neonlike 3p levels. They have been previously observed elsewhere[27-29]. The intensity increase of the $2p^6$ $^1S_0$ - $2p^53p$ (3/2, 3/2)$_2$ line at 3.863 Å, shown in the top spectrum of Fig. 2, is at least a factor of 2.4 when the 1.06 μm beam is used. This 3p upper level is the analogue of the upper lasing level in neonlike selenium which successfully produced gain[17,18] at 206 Å. This enhancement of the quadrupole line intensity is strong evidence for the feasibility of gain enhancement using lasers of wavelength ≥ 1.06 μm. The CRE calculation[15] indicates that at the laser pulse peak, the gain in the 99.6 Å $2p^53p$ (3/2, 3/2)$_2$ - $2p^53s$ (3/2, 1/2)$_1$ line would be 0.4 cm^{-1} in the absence of the 1.06 μm GDL beam. With the beam present the predicted gain increases to ~1 cm^{-1}, in accord with the observed increase in the upper level population.

5. Conclusions and Future Prospects

We have presented evidence that suprathermal electrons produced in exploding foil targets with two-wavelength laser irradiation can pump neonlike silver. Enhancement of the $2p^53p$ (3/2, 3/2)$_2$ potential upper lasing level of neonlike silver by a factor of at least 2.4 has been observed only when 1.06 μm radiation is present. Ionization of neonlike silver to the fluorinelike stage has also been observed only when irradiation in the mid-10^{14} W cm^{-2} range at both 0.35 μm and 1.06 μm was used. Broadband continuum data indicated little or no increase in the thermal electron temperature in the presence of the 1.06 μm GDL beam. Spectroscopic analysis determined that conversion of 10-15% of the 1.06 μm beam energy to suprathermal electrons would produce the observed enhancements in excitation and ionization. Predicted gain in the J=2 to 1 3p to 3s neonlike silver transition at 99.6 Å is 0.4 cm^{-1} without the GDL beam and 1.0 cm^{-1} in the presence of the 1.06 μm radiation. These positive initial results suggest that line focus experiments using linear foil targets with the same thicknesses of silver (3000 Å) and formvar (1600 Å) would have a reasonable prospect of demonstrating gain, when both $3\omega_0$ and ω_0 beams are employed at similar irradiances. This approach would constitute the most straightforward and lowest risk follow-up to the present results. However, the exacting requirements of synchronization and superposition of line-focused beams of different wavelength may render such experiments unfeasible at many laboratories. We therefore consider alternative experimental approaches based on the same principle of hot electron pumping.

Long mean free paths are a well-known and critically important characteristic of suprathermal electrons in laser-produced plasmas. Their ability to penetrate to the core of laser-driven pellet targets led to the fuel preheat problem which necessitated their reduction for further progress in the laser fusion program. The mean free path d(μm) of an electron of energy E (in units of 10 keV), in a plasma of ion density N_I(cm^{-3}), charge Z, and electron-ion Coulomb logarithm λ_{ei} is

$$d(\mu m) = \frac{1.9 \times 10^{25} \ E^2}{Z^2 \ N_I \ \lambda_{ei}} \qquad (2)$$

In Eq. (2) the mean free path is defined as the distance travelled prior to an RMS deflection of 90° from the initial direction. Convenient approximations for the Coulomb logarithm have been given by Book.[33] For the plasmas created in the Rochester experiments, N_I = 5.4×10^{19} cm^{-3}, Z=36, λ_{ei} ~ 8.5, therefore, at the highest central foil densities d=70 μm for a 15 keV electron. Ref. 33 also provides useful expressions for calculating the energy loss rate of the suprathermals; this is dominated by electron-electron collisions whereas bending is dominated by electron-ion collisions and/or ambient fields. For conditions typical of the above-described experiments, it is found that suprathermals in the 10-20 keV range require ~ 20 ps for thermal equilibration at midpulse at the maximum electron density. A 15 keV electron travels 1.5×10^3 μm in 20 ps, enabling about ~ 20 reflexive traversals of the foil plasma before equilibration. The spatial density history of the suprathermals depends significantly on the presence and strength of ambient B-fields induced by return currents[34] which can be drawn by the charge separation as suprathermals leave their area of origin near the critical surface.

This lack of spatial localization of a suprathermal electron population could conceivably be exploited in experiments somewhat different from those described above. To obtain lasing always requires a line focused beam. However, the beam which produced the suprathermal electrons need not be line focused and need not be spatially coincident. A high-intensity spot focus adjacent to the linear focus could be used to efficiently create a suprathermal electron population which would spray into, and reflex through, the nearly linear, exploding-foil lasing plasma. Intensities well above 10^{15} W cm^{-2} can be achieved with spot focusing; at such intensities suprathermal electrons can be produced even at

wavelengths shorter than 1.06 μm. Mechanisms other than resonance absorption may also be effective at these high intensities; two such processes[35] are two-plasmon decay and stimulated Raman scattering. An advantage of the latter mechanism is that the observation of scattered photons[36] may provide direct confirmation of the presence of the plasma waves responsible for suprathermal electron generation.

6. Acknowledgments

7. References

1. J. P. Friedberg, R. W. Mitchell, R. L. Morse, and L. I. Rudsinski, Phys. Rev. Lett. 28, 795 (1972).
2. K. A. Brueckner, Phys. Rev. Lett. 36, 677 (1976); 37, 1247 (1976).
3. P. Kolodner and E. Yablonovitch, Phys. Rev. Lett. 37, 1754 (1976).
4. D. W. Forslund, J. M. Kindel, and K. Lee, Phys. Rev. Lett. 39, 284 (1977).
5. J. E. Balmer and T. P. Donaldson, Phys. Rev. Lett. 39, 1084 (1977).
6. K. R. Manes, H. G. Ahlstrom, R. A. Haas, and J. F. Holzrichter, J. Opt. Soc. Am. 67, 717 (1977).
7. K. Estabrook and W. L. Kruer, Phys. Rev. Lett. 40, 42 (1978).
8. M. D. Rosen et al., Phys Fluids 22, 2020 (1979).
9. D. C. Slater et al., Phys. Rev. Lett. 46, 1199 (1981).
10. W. C. Mead et al., Phys. Rev. Lett. 47, 1289 (1981).
11. W. Seka et al., Opt. Commun. 40, 437 (1982).
12. R. L. Keck, L. M. Goldman, M. C. Richardson, W. Seka, and K. Tanaka, Phys. Fluids 27, 2762 (1984).
13. M. C. Richardson et al., Phys. Rev. Lett. 54, 1656 (1985).
14. R. C. Carman and G. Chapline, in Proceedings of the International Conference on Lasers '81 (STS Press, McLean, VA, 1982), p. 173.
15. J. P. Apruzese and J. Davis, Phys. Rev. A 28, 3686 (1983).
16. W. H. Goldstein and R. S. Walling, Phys. Rev. A 36, 3482 (1987).
17. M. D. Rosen et al., Phys. Rev. Lett. 54, 106 (1985).
18. D. L. Matthews et al., Phys. Rev. Lett. 54, 110 (1985).
19. B. J. MacGowan et al., J. Appl. Phys. 61, 5243 (1987).
20. T. N. Lee, E. A. McLean, and R. C. Elton, Phys. Rev. Lett. 59, 1185 (1987).
21. D. Duston, R. W. Clark, J. Davis, and J. P. Apruzese, Phys. Rev. A 27, 1441 (1983).
22. R. A. London and M. D. Rosen, Phys. Fluids 29, 3813 (1986).
23. B. L. Henke and P. A. Jaanimagi, Rev. Sci. Instrum. 56, 1537 (1985).
24. P. G. Burkhalter et al., Rev. Sci. Instrum. 59, 1837 (1988).
25. W. E. Behring, R. J. Ugianski, and U. Feldman, Appl. Opt. 12, 528 (1973).
26. J. Reader et al., J. Opt. Soc. Am. B 3, 1609 (1986).
27. J. F. Wyart, C. Bauche-Arnoult, and J. Bauche, J. Phys. (Paris) Colloq. C6, Suppl. No. 10, 63 (1986).
28. P. Beiersdorfer et al., Phys. Rev. A 34, 1297 (1986).
29. J. C. Gauthier et al., J. Phys. B 19, L385 (1986).
30. M. H. Chen, Phys. Rev. A 38, 2332 (1988).
31. W. Lotz, Z. Phys. 216, 241 (1968).
32. P. L. Hagelstein and R. K. Jung, At. Data Nuc. Data Tables 37, 121 (1987).
33. D. L. Book, in Physics Vade Mecum, H. L. Anderson, Ed. (American Institute of Physics, New York, 1981), pp. 262-265.
34. A. Hauer and R. J. Mason, Phys. Rev. Lett. 51, 459 (1983).
35. C. E. Max, Lawrence Livermore National Laboratory Report No. UCRL-53107, 1981 (unpublished).
36. D. W. Phillion, E. M. Campbell, K. G. Estabrook, G. W. Phillips, and F. Ze, Phys. Rev. Lett. 49, 1405 (1982).

Modeling the Radiation Hydrodynamics of Pulsed Power Driven X-Ray Lasers

R. Clark, J. Davis, J. Apruzese, P. Kepple and T. Gallo*

Naval Research Laboratory
Plasma Radiation Branch
Washington, D.C. 20375-5000

ABSTRACT

Novel X-ray laser experiments involving hydrogenlike neon and lithiumlike aluminum were performed on the DNA/PITHON pulsed power generator, and the results were tantalizing, but difficult to interpret. In   order to understand the experiment, a series of computer simulations have been carried out with a detailed non-LTE radiation hydrodynamics model. A typical experiment involves the discharge of hundreds of kilojoules of electrical energy through a cylindrical neon gas puff, heating it and imploding it radially at speeds of about 3-5 x 10^7 cm/sec; the gas puff impinges and stagnates onto a thin aluminum coated capillary, converting the kinetic energy of implosion into thermal energy. Rapid plasma heating in the stagnation region results in ionization of the aluminum to the K-shell and partial stripping of the neon. In addition, K-shell radiation from both the aluminum and the neon can produce strong photopumping and enhanced ionization in adjacent plasma. The hot, dense plasma in the stagnation region can undergo rapid radiative cooling and recombination; sufficiently rapid three-body recombination into n=4 levels of Ne X and Al XI can result in population inversions for possible lasing in 4 to 3 transitions. In fact, anomalous brightness was initially reported in the 4f-3d and 4d-3p lines of Al XI and the 4-3 line of Ne X; however, opacity considerations made interpretation of the aluminum results difficult. In the numerical modeling of the experiment, emphasis was placed on understanding the dynamics of the target and on the role of optical pumping in producing conditions favorable for population inversion.

1. INTRODUCTION

There is considerable optimism that conditions favorable for X-ray lasing can be achieved in pulsed-power driven Z-pinch plasmas.   Advances in puff-gas technology, in the fabrication of structured targets, and in the theoretical understanding of pulsed power load dynamics have been reported by Physics International, Sandia National Laboratory and the Naval Research Laboratory (NRL)[1]. Although soft X-ray lasing has been demonstrated in laser-produced plasmas, the efficiencies which are attainable by this method are low. X-ray lasing in pulsed-power produced plasmas can be substantially more efficient; however, pulsed-power plasmas have a tendency to become unstable.   The "hot-spots" and other nonuniformities commonly observed in pulsed-power Z-pinches with single gas puffs or wire-arrays are incompatible with the stable, uniform gain medium required for an X-ray laser. Recent experiments with concentric gas puffs and with gas puffs imploding onto low density foam plasmas or solid density targets have shown that stable, uniform plasmas can be produced with the pulsed-power technology. In these experiments, the outer plasma, usually a gas puff, is imploded onto the inner plasma, producing a stagnation; the uniformity of the resulting plasma is a consequence of the uniformity of the inner target plasma.

Experiments at NRL have proceeded on the sodium/neon line coincidence photopumping configuration. Preliminary results[2] indicate that resonance fluorescence has been produced in the pumped transitions.   At Sandia, experiments have been carried out with inert-gas puffs imploding onto structured targets[3].   These targets are thin CH capillaries coated with a low-Z element (such as aluminum) on the outside and a high-Z lasant material on the inside.   Physics International has studied neonlike krypton lasers using double-puff krypton Z-pinches[4].   Computer simulations of the PI krypton experiment[5] suggest that substantial gains can be achieved for times of several nanoseconds over axial distances of about 2 cm.   However the radial extent of the calculated gain region is only of the order of 0.01 cm.

Physics International has also reported[6] on time-resolved measurements of XUV emissions from recombining neon and aluminum plasmas. Using the DNA/PITHON generator, neon gas puffs were imploded onto aluminum coated parylene capillaries (or onto equivalent mass solid aluminum targets).   The implosion heated the Al to form an axial plasma which was estimated to have an electron density of ~ 10^{20} cm^{-3} and a temperature of ~ 500 eV. Evidence was

* Berkeley Research Associates, Inc., Springfield, VA 22150

presented for anomalous brightness in the 4d-3p and 4f-3d lines of Al XI at 150.5 and 154.5 Å, and in the 4-3 line of Ne X at 187.3 Å. When compared with various n = 3-2 and n = 4-2 lines of Al XI and Ne X, the intensities in these lines suggested population inversion and gain possibly fed by recombination. Three-body recombination rates can be very high at low temperatures; if the plasma cools rapidly due to expansion or radiative loss, recombination into the n = 4 levels can set up inversions for possible lasing in 4 to 3 transitions.

Digitized spectra from 3 and 5 cm long, neon/aluminum Z-pinches were compared; the Al lines were confined to the innermost mm or so in radius, while the Ne emissions extended substantially further out. The 4f-3d and 4d-3p lines of Al XI were seen to be brighter than the 3d-2p line at 98.2 Å and the 4d-2p line at 39.2 Å, even though the latter line was favored by the grating, detector and film response. The intensities of the 4-3 lines relative to the 4d-2p line were significantly higher for the 5 cm pinch; however the continuum background and the nonlasing lines also appear brighter. An alternative explanation for these aluminum anomalies is opacity in the 4-2 transitions; this will be considered further below. In addition, the Ne X 4-3 line appeared to be anomalously bright compared with the 4-2 line at 48.55 Å. However, this latter line was not resolved from the Al XI 3p-2s resonance line at 48.3 Å. A possible contribution to the pumping of the n = 4 levels of lithiumlike aluminum is K-shell neon line radiation. The Lyman-alpha and He-alpha lines of Ne are capable of photoionizing Li-like Al; under the right conditions, this photoionization can substantially exceed collisional ionization and result in enhanced recombination to the n = 4 levels of Al XI. In a similar way, it is possible for aluminum radiation to photoionize H-like Ne.

2. MODEL DESCRIPTION

We studied these mechanisms with a radiation-hydrodynamics model that is described elsewhere[7,8]. The complexity of the atomic models for neon and aluminum can be adjusted, depending upon the requirements for detail in the calculation. The atomic models for neon which were used in this study ranged from 27 levels with 13 lines (reduced model) to over 100 levels with about 300 lines (detailed model); the aluminum models were comparable in scope. The rate coefficients that are used to calculate the level populations were obtained using atomic calculational methods summarized elsewhere[8].

Radiation emission from and absorption by a plasma are dependent on the local atomic level population densities. Except for optically thin plasmas, the level populations depend on the radiation field, since optical pumping via photoionization and photoexcitation can produce significant population redistribution. Thus, the ionization and radiation transport processes are strongly coupled and must be solved self-consistently. Both probabilistic and multifrequency multimaterial radiation transport algorithms were employed in this study. The probabilistic method forms local angle and frequency averaged escape probabilities for each emission line and for each bound-free process. It is a cost effective method and provides good overall energetics, but it cannot treat certain physical processes such as the photoionization or photoexcitation of one atomic species by another. The multifrequency model breaks each emission line and each bound-free edge into a number of discrete frequencies, and performs a radiation transport calculation at each frequency. The latter method is general and self-consistent, but relatively expensive. Both methods take into account Doppler and Voigt line profiles in the transport of bound-bound radiation.

Reduced atomic models for neon and aluminum were normally employed in the probabilistic simulations. Corresponding calculations with detailed models were performed in selected cases to verify accurate overall radiation energetics. In the cases studied, both the radiation dynamics and the hydrodynamic evolution of the plasmas were in good overall agreement. The models used in the multifrequency simulations were enhanced versions of the reduced models (with additional lines transported) or modified versions of the detailed models (with all of the atomic levels included, but with certain lines not transported).

3. RESULTS OF SIMULATIONS

3.1 Stagnation Calculations

A number of numerical simulations were performed with the radiation hydrodynamics model to determine the sensitivity of the results to the initial conditions of the aluminum target. It is possible[9] that some of the total current initially flows through the capillary. It is difficult to estimate the temporal behavior of this current or how important it is to the dynamics of the target. Even in its absence, there will be heating and ablation of the outer surface of the capillary due to incident radiation from the imploding gas puff. Two extreme assumptions with respect to the target can be made. One is that it remains cold and solid until the gas puff impacts upon it. In this case, neglecting radiation and thermal transport, the dynamics could be modeled analytically[10]: the target would stay cold, and the gas puff would become hot as the kinetic energy of

implosion was converted into thermal energy. A strong shock would propagate out from the target and mark the outer boundary of the stagnation region. In the other extreme, heated by some combination of driver current and radiation from the gas puff, the target rapidly expands; its density would be comparable to that of the gas puff when the stagnation commences. In this case, comparable volumes of gas puff and target plasmas become hot.

This series of simulations neglected the effects of the driving magnetic field, but instead assigned an initial radial velocity and temperature profile to the puff gas plasma. This allowed us to study the physics of the imploding plasmas in an idealized framework, without the complications of an external driver and coupled circuit. The simulations were performed with a neon gas puff having an initial Gaussian mass distribution with a total mass of 100 micrograms and an initial radial velocity of 4×10^7 cm/sec. Only the stagnation phase of the implosion was modeled in these simulations; thus, the gas puff was initially centered at 1.0 cm (when driven with a B-field, it takes several tens of nanoseconds to implode to this radius). The capillary was taken to be pure aluminum, and the initial density and temperature profiles were varied over a fairly wide range to model the effects of target preheat. The initial configuration for these simulations is shown schematically in Figure 1.

For the case where the target is initially at solid density, the neon puff gas stagnated and heated to several hundred eV, but the aluminum remained cool, substantially less than 100 eV (in the absence of thermal conduction and radiation transport, the analytic solution referenced above was closely approximated). When the aluminum was taken to be moderately preexpanded, but still substantially higher in density than the puff gas, radiation cooling maintained the aluminum at a relatively low temperature. Lower initial densities resulted in higher temperatures. When these cases were simulated without radiative cooling, the target temperatures were considerably higher (greater than 100 eV).

The initial (t=20 nsec) configuration that resulted in conditions approximating those reported by PI consisted of a Gaussian target with a peak ion density of $8 \times 10^{18} cm^{-3}$, centered at 0.08 cm, with an initial temperature of 30 eV. The time history of the aluminum/neon interface is given in Figure 2. The innermost 1.0 cm of plasma is represented along the horizontal axis, and time (20 to 50 nsec) runs along the vertical axis. Corresponding contours of electron density and temperature are given in Figures 3 and 4. The target electron density monotonically increases, reaching about $2 \times 10^{21} cm^{-3}$ at 50 nanoseconds; it also becomes quite hot (about 500 eV on axis) at about 45 nanoseconds, and then rapidly cools radiatively. These simulations could not directly model the experiment, since no self-consistent magnetic driver was included in the model. They serve as a test bed for the presence of processes possibly occurring in the experiment, including questions about optical pumping of one material by another.

One possibility is photoionization of Al XI to Al XII by the K-lines of neon, thereby increasing the recombination rate into the n = 4 levels of Al XI. At a few tens of eV, sufficient lithiumlike aluminum would be present, but the collisional ionization rate would be relatively small. Thus, the photoionization rate could exceed the collisional rate if the neon pump source were sufficiently large. The latter consideration requires that a substantial fraction of the neon be in the hydrogenlike or heliumlike ionization state. Conditions at 43 nsec looked promising. The temperature of the aluminum was about 36 eV and there was a substantial quantity of neon at about 500 eV. The hydro profiles at this time are shown in Figure 5. These profiles were post-processed with the multimaterial multifrequency code, described above. Radiation from the neon substantially altered the ionization state of the aluminum (there was considerably more heliumlike aluminum present when photopumping by the neon was allowed). In addition, some enhancement in the 4f and 4d levels of Al XI was observed. However, this enhancement was not suficient to cause population inversion. The emission spectrum as calculated by the multifrequency code at this time (43 nsec) is shown in Figure 6, and corresponding optical depths as a function of photon energy are shown in Figure 7. The 4f-3d and 4d-3p lines of Al XI are seen to be comparable to, but not more energetic than, the 4d-2p line. The corresponding optical depths for these lines can be estimated from Figure 7. Continuum opacity in the vicinity of the 4f-3d and 4d-3p lines is seen to be small (mostly free-free opacity), whereas it is substantially greater in the vicinity of the 4d-2p line (about equally divided between bound-free and inner shell opacity). Although the continuum optical depth is less than unity in the vicinity of the 4d-2p line, it will be a very sensitive function of the ionization state of the plasma. The inner-shell opacity (the dashed curve in Figure 7) "burns out" as the plasma ionizes[8]; at this time the 4d-2p line is situated near the threshold for inner-shell burnout. Relatively small changes in temperature can cause large changes in opacity in this neighborhood, and this line could be substantially reduced in intensity. Also, the optical depths shown in Figure 7 are for radial photon paths; the anomalous brightness measurements were taken along the z-axis. For these measurements the opacity effects can be considerably higher. This is one of the factors which complicates interpretation of the experimental spectra difficult.

3.2 Implosion Calculation

A fully self-consistent simulation was performed with the multimaterial probabilistic radiation hydrodynamics model. In this case, the implosion was driven by a magnetic field. The target was assumed to be solid density at about 0.5 eV initially, with a narrow density falloff, a consequence of the very small amount of current which was assumed to flow initially through the outer surface of the capillary. The neon gas puff was assumed to be a Gaussian centered at 2.0 cm, with a total mass of 100 micrograms. The current was assumed to rise linearly over about 70 nanoseconds to 3 megamperes, and then fall off as a Gaussian with a 40 nanosecond timescale. A time history of the aluminum/neon interface is shown in Figure 8, and contours of electron density and temperature are given in Figures 9 and 10. The innermost 1.0 cm of plasma is represented along the horizontal axis, and time (0 to 130 nsec) runs along the vertical axis. The aluminum is seen to expand until about 110 nsec; a low density blowoff develops, and stagnation with the bulk of the gas puff commences at about 120 nsec, producing aluminum and neon temperatures in excess of 500 eV. The total mass of the aluminum in the blowoff is low, and the blowoff density is correspondingly small, substantially less than for the case described above. However, the density is well matched to the density of the incoming puff gas in the sense that the temperatures of the aluminum blowoff and the puff gas should be comparable at the onset of stagnation, as is observed in the simulation. It should be noted that the simulations described in the previous section correspond to the stagnation phase (the final 20 or 30 nsec) of this calculation.

The potential for the photopumping of lithium-like aluminum by the K-lines of neon appears to be relatively small. From 90 to about 120 nsec, a region of cool (a few tens of eV) aluminum persists, but it is rarefied (the electron density is about 10^{18} to 10^{19} cm^{-3}). There is substantially less Al XI in this shell than in the case studied above, and there is less K-shell neon to do the pumping. Furthermore, there does not appear to be a sufficiently strong K-shell aluminum source to produce significant photopumping of the neon. One mechanism which may be important is recombination into the n = 4 levels of Al XI and Ne X following rapid cooling of the plasma in the post-stagnation phase. However cooling times must be sufficiently fast or the plasma will remain in collisional radiative equilibrium (CRE), and no population inversion will result. For example, 100 eV aluminum with an ion density of 7×10^{19} cm^{-3} would have to cool in less than about 0.3 nsec in order to drive it out of CRE. At higher temperatures (and lower densities) the characteristic time becomes greater. No attempt was made in the present study to address the question of recombination in the post-stagnation phase, and it cannot be ruled out that this mechanism is responsible for producing the enhanced brightness in the 4-3 transitions reported by PI[4].

4. ACKNOWLEDGEMENTS

5. REFERENCES

1. N.R. Pereira and J. Davis, J. Appl. Phys. 64, R1 (1988).
2. S.J. Stephanakis et al., IEEE Trans. Plasma Sci. 16, 472 (1988); F.C. Young et al., this conference.
3. T.W. Hussey, M.K. Matzen, E.J. McGuire and H.E. Dalhed, Sandia National Laboratory Report No. SAND88-0764, 1988, (unpublished), and submitted to J. Appl. Phys.
4. M. Krishnan, R. Nash, P. LePell and R. Rodenburg, Physics International Report No. PIT-87-02, 1987 (unpublished).
5. J. Davis, R.W. Clark, J. Apruzese and P. Kepple, IEEE Trans. Plasma Sci. 16, 482 (1988).
6. M. Krishnan, T. Nash, and P.D. LePell, IEEE Trans. Plasma Sci. 16, 491 (1988).
7. R.W. Clark, J. Davis and F.L. Cochran, Phys. Fluids 29, 1971 (1986).
8. D. Duston, R. Clark, J. Davis and J. Apruzese, Phys. Rev. A 27, 1441 (1983).
9. M. Krishnan (private communication), and T. Hussey (private communication).
10. H.W. Liepmann and A. Roshko, Elements of Gasdynamics (J. Wiley, NY, 1957), p. 62.

Neon–Aluminum Initial Configuration

Neon

4×10^7 cm/sec.

Aluminum

0.0   1.6 mm   20 mm
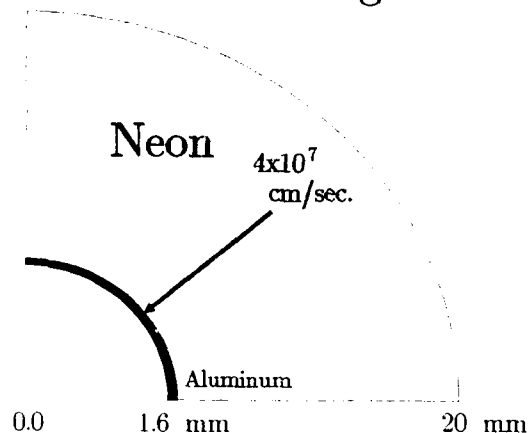
Fig. 1. Schematic of initial conditions for numerical simulations in the absence of a magnetic driver. The neon gas puff is given an initial radial velocity of 4×10^7 cm/sec.

ALUMINUM/NEON: interface

2.0E+00
1.8E+00
1.7E+00
1.5E+00
1.3E+00
1.1E+00
8.7E-01
7.0E-01
5.2E-01
3.5E-01
1.7E-01
0.0E+00
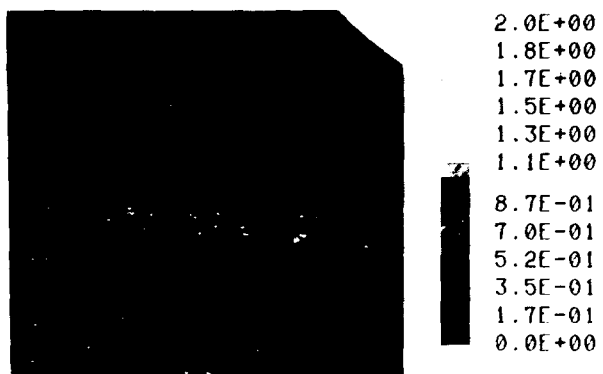
Fig. 2. Time history of the aluminum/neon interface. Radius from 0.0 to 1.0 cm. is represented horizontally, and time from 20.0 to 50.0 nanoseconds is represented vertically. The outer edge of the neon gas puff moves into view at about 45 nanoseconds.

ALUMINUM/NEON: electron density

1.0E+23
3.0E+22
9.0E+21
2.7E+21
8.2E+20
2.5E+20
4.1E+19
1.2E+19
3.7E+18
1.1E+18
3.3E+17
1.0E+17

Fig. 3. Electron density contours as a function of radius (0.0 to 1.0 cm) and time (20.0 to 50.0 nanoseconds). Peak density is reached on axis at about 46 nanoseconds.

ALUMINUM/NEON: temperature (eV)

1.0E+03
6.7E+02
4.5E+02
3.0E+02
2.0E+02
1.4E+02
7.4E+01
5.0E+01
3.3E+01
2.2E+01
1.5E+01
1.0E+01

Fig. 4. Temperature contours as a function of radius and time. Peak neon temperature occurs near the aluminum/neon interface. The aluminum reaches ~ 500 eV at about 45 nanoseconds, and then rapidly cools radiatively.

hydro profiles

total spectrum   43.13 nsec.
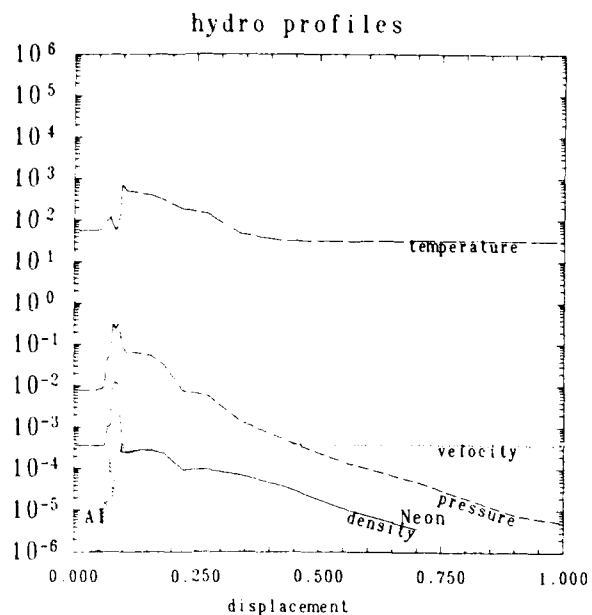
Fig. 5. Hydro profiles at 43.13 nano-
seconds. Radial displacement is given
in cm., $\log_{10}$density in g/cm^3,
$\log_{10}$temperature in eV, $\log_{10}$pressure
in 10^{12}ergs/cm^3, and $\log_{10}$velocity in
10^4 cm/nsec.
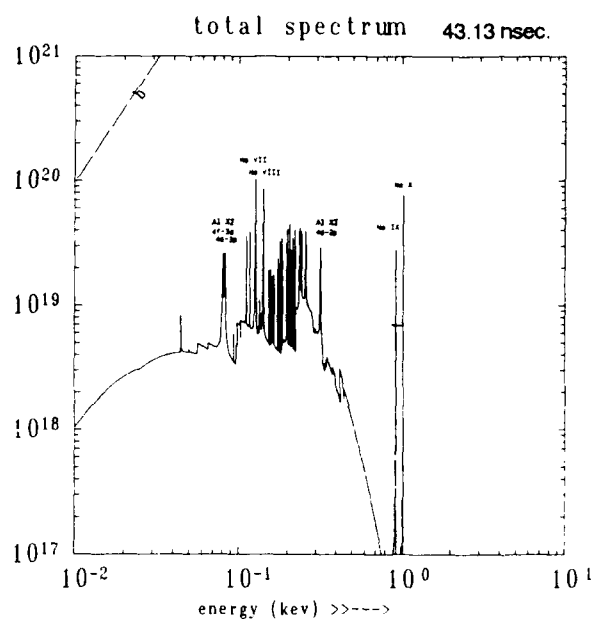
Fig. 6. Emission spectrum at 43.13 nano-
seconds. The instantaneous power (ergs/
sec-cm-keV) is given as a function of photon
energy (keV). Selected emission lines are
identified.

optical depths   43.13 nsec.

ALUMINUM/NEON: INTERFACE
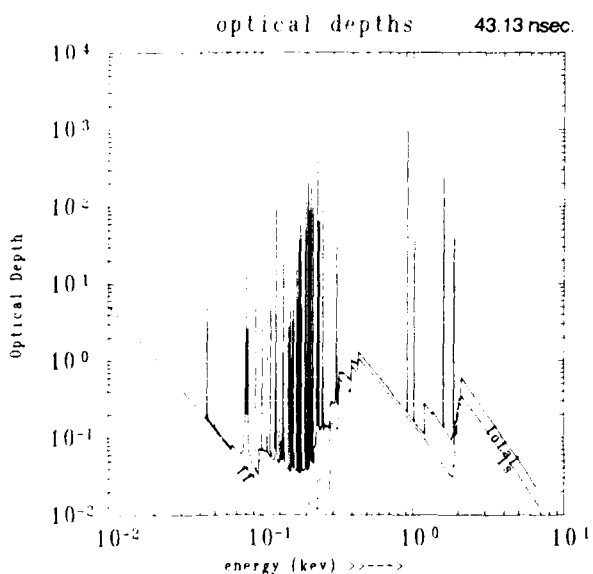
Fig. 7. Optical depths at 43.13 nano-
seconds as a function of photon energy
(keV). The contributions of free-free
opacity (ff) and inner-shell opacity (is)
are indicated. Total optical depth
includes contributions from free-bound
and bound-bound processes.
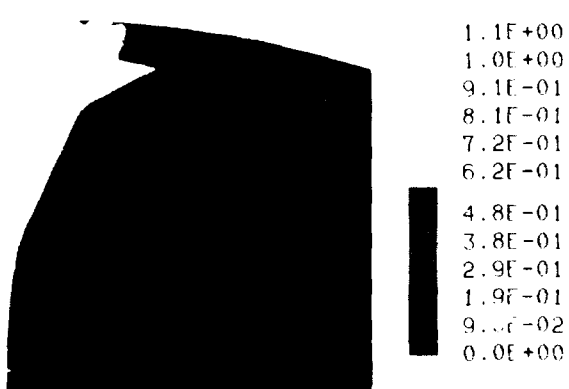
Fig. 8. Time history of the aluminum/neon
interface with B-field driver. Radius from
0.0 to 1.0 cm runs horizontally, and time
from 0.0 to 136.0 nanoseconds runs
vertically. The outer edge of the neon
gas puff moves into view at about 120 nano-
seconds.

ALUMINUM/NEON: ELECTRON DENSITY
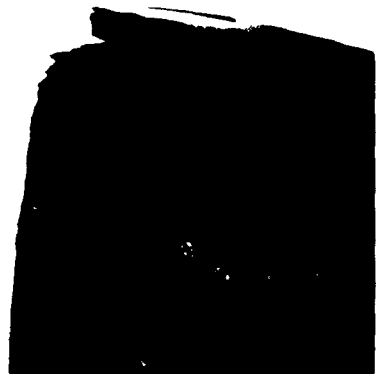
1.0E+23
2.0E+22
4.1E+21
8.2E+20
1.6E+20
3.3E+19

3.0E+18
6.1E+17
1.2E+17
2.5E+16
5.0E+15
1.0E+15

ALUMINUM/NEON: TEMPERATURE (eV)

1.0E+03
6.7E+02
4.5E+02
3.0E+02
2.0E+02
1.4E+02

7.4E+01
5.0E+01
3.3E+01
2.2E+01
1.5E+01
1.0E+01

Fig. 9. Electron density contours as a
function of radius (0.0 to 1.0 cm) and
time (0.0 to 136.0 nsec) with B-field
driver.

Fig. 10. Temperature contours as a function
of radius and time with B-field driver.

Multiphoton Double Ionization of Ba

T. F. Gallagher, R. R. Jones, Y. Zhu, U. Eichmann[+], and W. Sandner[+]
Department of Physics
University of Virginia
Charlottesville, VA 22901

Abstract

We have used wavelengths of 280 nm-710 nm to produce Ba^{++} from Ba by multiphoton ionization. All strong observed resonances in the Ba^{++} production are Ba^{+} multiphoton transitions, indicating that Ba^{++} is produced by sequential ionization of Ba via Ba^{+}.

In recent experiments high intensity lasers have been used to effect multiphoton multiple ionization in a variety of atomic systems.[1,2] Specifically, ions as highly charged as U^{10+} have been produced in this fashion[3]. Experiments in which high stages of ionization have been reached have been done at a few fixed wavelengths, 193 nm, 248 nm, 532 nm and 1.06 μm, corresponding to eximer laser wavelengths and the Nd:YAG laser fundamental and second harmonic wavelengths. Unfortunately, it is not exactly clear how multiple ionization occurs. The two extreme possibilities are that the electrons are removed simultaneously or sequentially. Let us consider for a moment the simplest case, double ionization, as an illustration. The two extreme possibilities are shown schematically in Fig. 1 for the specific case of Ba which we consider here. Which of these processes actually occurs is a rather fundamental question which has practical implications. For example, if the excitation is simultaneous, through virtual intermediate multiply excited states of the neutral atom, the probability of generating ions in excited states is likely to be higher, and this is clearly of interest for short wavelength laser development.

Figure 1 - Energy level diagram of Ba and Ba^{+} showing (1) direct ionization and (2) sequential ionization

The problem of multiphoton multiple ionization has been addressed theoretically by several groups.[4-6] Using an essentially hydrogenic model, Lambropoulos[4] has concluded that the existing experimental data can all be explained by sequential removal of the electrons from the atom. As the intensity of the laser pulse rises, successive stages of ionization are reached in which the remaining electrons are bound by increasingly strong fields, so that each successive multiphoton ionization process occurs in the perturbative regime. At the other extreme Boyer and Rhodes[5] have suggested that the ionization is produced via a collective oscillation of an entire shell of electrons which is driven by the intense field of the laser.

Experimentally, it is difficult to make measurements with fixed frequency lasers that unambiguously show whether multiple ionization occurs by a sequential or simultaneous process. The only variables are the laser intensity and the pulse length, and of these

the intensity is substantially easier to vary in a controlled way. As a result, a classic approach has been to measure n, the order of nonlinearity[7]. In the perturbation theory regime, a process requiring the absorption of n photons exhibits a dependence on laser intensity I of I^n. A direct multiple ionization process, requiring the absorption of ~100 photons, can be expected to exhibit a higher order of nonlinearity than sequentially removing the electrons, which is a sequence of lower order processes. In practice, there are two problems associated with measuring large orders of nonlinearity. First, a large dynamic range is required of the experiment, which must fall in the regime described by perturbation theory. Second, in such experiments the inherent spatial and temporal intensity variation of the strength of the focused laser field may distort any measurement of the order of nonlinearity. As an example of the difficulty, we note that the multiphoton ionization of Xe by CO_2 laser radiation, which requires the absorption of roughly 100 photons, does not exhibit an I^{100} dependence, but rather something closer to an I^{10} dependence [8]

A second approach to understanding multiphoton multiple ionization is to examine the ejected electrons. By analyzing the energies and angular distributions of the ejected electrons it is possible to gain some insight into how multiple ionization occurs. The primary focus has been on the energy spectra of the ejected electrons, which in principle gives unambiguous results. In practice the electron energy spectra are complex, due to the many available states of the resulting ions and the possibility of above threshold ionization (ATI).[9] Nonetheless, Johann et al[10] have examined the electrons ejected from rare gas atoms upon exposure to intense eximer laser radiation. By identifying sequences of ATI lines they have demonstrated that sequential removal of the electrons occurs.

As an alternative one can examine the wavelength dependence of multiple ionization, and such studies have been begun in several systems using tunable lasers.[11-15] We have been studying the wavelength dependence of double ionization of Ba, for two reasons. First, double ionization is, in principle, the simplest case of multiple ionization, and the wavelength dependence of the process, in particular resonances, should provide relatively unambiguous information as to how the double ionization occurs. Our second reason for choosing Ba, in which the second ionization limit lies only 15 eV above the Ba ground state, is that double ionization can be effected with the relatively low optical intensities of dye lasers. Here, we report the results of a study of the wavelength dependence of the double ionization of Ba to elucidate the double ionization process. In the following sections of the paper we describe the experimental approach and our results and the conclusions which may be drawn from them.

II. Experimental Approach

Our approach is multiphoton ionization of Ba atoms in a thermal beam by a pulsed laser coupled with time of flight discrimination between the Ba^{+}, Ba^{++}, and contaminant ions.[16] The experimental arrangement is shown in Fig. 2. The Ba atoms effuse from a resistively heated oven, are collimated, and pass midway between two parallel plates 1.2 cm apart where they are ionized by the laser. We estimate the density of Ba atoms at the interaction region to be 10^9 cm^{-3}. At the shortest wavelengths of less than 280 nm, two photon ionization of the background gas produces enormous signals, so a liquid nitrogen trap must be used to keep the background pressure below $<10^{-6}$ torr and contaminant signals at an acceptable level.

Figure 2 - Block diagram of the apparatus showing the lasers and the atomic beam apparatus

Approximately 100 ns after the laser pulse, a 50 V pulse is applied to the lower plate, driving the ions through an aperture in the upper plate. Thus, Ba^+ and Ba^{++} ions leave the interaction region with energies of 25 eV and 50 eV, respectively, and pass through a field-free region 10 cm long before being accelerated into a dual microchannel plate detector.

As shown by Figure 2 the dye lasers are pumped by a Q switched Nd:YAG laser. The intense pump dye laser receives most of the energy of the Nd:YAG laser and has pulse energies from 3-30 mJ depending upon the wavelength. The probe dye laser, which is only used occasionally to drive resonant transitions has typical pulse energies of 1 mJ. Both dye lasers have pulse lengths of 5 ns. The lasers beams are focused at their intersection with the atomic beam with a 10 cm focal length quartz lens. This leads to peak intensities of 10^{10}-10^{11} W/cm^2.

III. Results

We have observed many resonances in the production of Ba^{++} in the range 270-710 nm. The locations of the resonances are obtained from spectra such as the one shown in Fig. 3. In Fig. 3 there are three strong resonances at 18755, 18822, and 18922 cm^{-1} as well as what appears to be a Rydberg series. The three resonances correspond to the Ba^+ $5d_{3/2}$ - $7s_{1/2}$, $5d_{3/2}$ - $8p_{1/2}$, and $5d_{3/2}$ - $8p_{3/2}$ two and three photon resonances in the three and four photon ionization of the Ba^+ $5d_{3/2}$ state. The Rydberg series is the four photon excitation of the Ba^+ nd series from the Ba^+ $5d_{3/2}$ state. A fifth photon ionizes the Ba^+ Rydberg atoms. Spectra similar to the one shown in Fig. 3 have been recorded over the wavelength range 270-710nm, and seventy resonances have been found.[16] Just as for Fig. 3, all the strong resonances are easily matched to energy intervals in Ba^+[17] suggesting that irradiation by 5 ns laser pulses is most likely to produce double ionization by a sequential process. Since fewer ultraviolet than visible photons are required to produce Ba^{++}, a rather counter intuitive aspect of our results is the fact that light at 500 nm is much more effective in producing Ba^{++} than light at 280 nm. This apparent anomaly is explained when we examine the energy level diagrams of Ba and Ba^+. In both cases there are sequences of strong 500 nm transitions from low lying states to the ionization limits. However in neither case is there a similar sequence of strong 280 nm transitions.
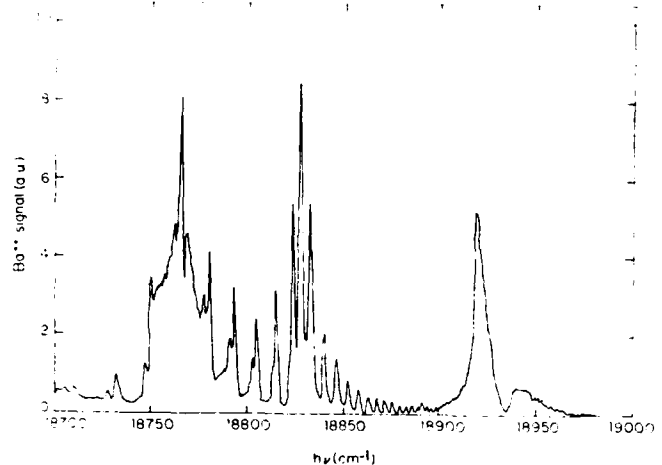
Figure 3 - Ba^{++} production for laser frequencies from 18700 to 19000 cm^{-1} There are three strong resonances, corresponding to the $5d_{3/2}$-$7s_{1/2}$, $5d_{3/2}$-$8p_{1/2}$, and $5d_{3/2}$-$8p_{3/2}$ Ba^+ transitions, and the Ba^+ $5d_{3/2}$ -nd four photon Rydberg series

As we have pointed out above, the strong resonances in the Ba^{++} production match the wavelengths of Ba^+ multiphoton transitions. We can check the assignments by using the probe laser to produce Ba^+ ions the specific low lying states assigned as the lower states of the Ba^+ multiphoton resonances. When sweeping the intense pump laser Ba^{++} resonances originating from the chosen Ba^+ state are enhanced and those originating from other levels are diminished. An example of this is shown in Figure. 4,[16] a scan of of the pump laser with and without the probe laser tuned to 413 nm to excite the Ba^+ $5d_j$ states, predominantly the $5d_{3/2}$ state. As shown, resonances originating from these Ba^+ states are enhanced when the probe laser is used, confirming our assignments.
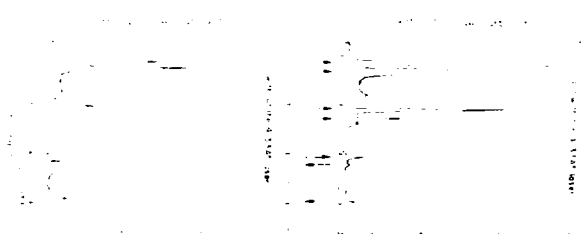
Figure 4 - Ba^{++} production vs pump laser wavelength with and without the probe laser at 4133Å to populate the Ba^+ $5d_j$ levels. Resonances originating from these Ba^+ levels are enhanced by the 4133Å laser

Just as the lower state may be checked so can the upper state.[15] At 17505 and 17584 cm^{-1} we observe five photon ionization of the Ba$^+$ 5d$_{3/2}$ state via three photon 5d$_{3/2}$-5f$_{5/2}$ and 5d$_{3/2}$ -5f$_{7/2}$ resonances. The intermediate 5f$_j$ states are ionized by the absorption of two 17,000 cm^{-1} photons. Alternatively they can be ionized by a single 23,000 cm^{-1} photon. If we set the pump laser to the resonances, attentuate it so as to populate the 5f$_j$ states but not ionize them, and scan the probe laser in the vicinity of 23,000 cm^{-1}, we observe the ionization thresholds from the 5f$_j$ states. An example is shown in Fig. 5, which is a scan of the probe laser with the pump laser set to the 5d$_{3/2}$ - 5f$_{5/2}$ resonance at 17505 cm^{-1}. The ionization threshold is manifested as an increase in the ionization signal, which occurrs at 23,250(8) cm^{-1}. This is lower than the expected limit of 23,296 cm^{-1} by 50 cm^{-1} due to field ionization of high lying states of Ba$^+$ by the electric field pulse used to collect the ions. We note that the observed ionization threshold for the 5f$_{7/2}$ state lies at 23,002(6)cm^{-1} cm^{-1}, below the expected limit of 23,055 cm^{-1} In addition the separation between the two observed limits, 248 cm^{-1}, matches the 5f$_{5/2}$ -5f$_{7/2}$ fine structure interval of 241 cm^{-1}. It seems clear that the 5f$_j$ states are indeed the upper states of the resonances at 17505 and 17584 cm^{-1}.
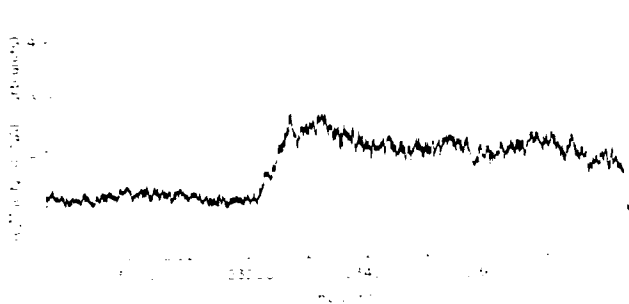
Figure 5 - Ba^{++} signal vs. probe laser wavelength when the Ba$^+$ 5f$_{5/2}$ level is excited by threee 17505 cm^{-1} photons. The increased signal at 23250 cm^{-1} corresponds to the ionization limit from the 5f$_{5/2}$ state, confirming that it is the upper state of the resonance

IV. Conclusion

In experiments show rather conclusively that using long, ns, pulses produces double ionization by sequential ionization. Furthermore it is clear that in any complex atom, which has transitions at many wavelengths, that multiphoton excitation will be most likely at the wavelength most closely matching the strongest atomic transitions, not necessarily at the shortest wavelengths. This is contrary to much of our intuition about multiphoton processes, perhaps because it is founded to a large extent on multiphoton ionization of the rare gases.[7]

While ns pulses clearly do not lead to direct double ionization, it is certainly possible that ps pulses will produce direct double ionization. There are two factors which favor shorter pulses. First, direct double ionization is a higher order process, which will be enhanced relative to lower order processes by the higher power and lower pulse duration of the ps laser. Second, direct multiphoton double ionization must proceed through autoionizing states of Ba. Such states are short lined, compared to ns laser pulses, but might not seem so short lived when compared to ps pulses. Work is currently in progress to explore this issue.

References

† present address: Department of Physics, University of Oregon, Eugene, OR 97403

+ permanent address: Fakultat fur Physik Universitat Freidburg D-7800 Freiburg, FRG

1. A. L'Huillier, L. A. Lompre, G. Mainfray and C. Manus, Phys. Rev. Lett. **48**, 1814 (1982).

2. T. S. Luk, H. Pummer, K. Boyer, M. Shahidi, H. Egger C. K. Rhodes, Phys. Rev. Lett. **51**, 110 (1983).

3. T. S. Luk, U. Johann, H. Egger, H. Pummer and C. K. Rhodes, Phys. Rev. A **32**, 214 (1985).

4. P. Lambropoulous, Phys. Rev. Lett. **55** 2141 (1985).

5. K. Boyer and C. K. Rhodes, Phys. Rev. Lett. **54** 1490 (1985).

6. X. D. Mu, T. Aberg, A. Blomberg and B. Crasemann, Phys. Rev. Lett. **56** 1909 (1986).

7. G. Mainfray, Journal de Physique **46** Cl-113 (1985).

8. S. L. Chin, F. Yergeau and P. Lavigne, J. Phys. B **18** L213 (1985).

9. P. Kruit, J. Kimman, H-G Muller and M. J. van der Wiel, Phys. Rev. A **28** 143 (1983).

10. U. Johann, T. S. Luk, H. Egger and C. K. Rhodes, Phys. Rev. A **34** 1084 (1985).

11. D. Feldman, H. J. Krautwald and K. Welge, J. Phys. B **15** L735 (1982).

12. P. Agostini and G. Petite, J. Phys. B **17** L811 (1984).

13. P. Agostini and G. Petite, Phys. Rev. A **32** 3800 (1985).

14. J. L. Dexter, S. M. Jaffe and T. F. Gallagher J. Phys. B **18** L735 (1985).

15. U. Eichmann, Y. Zhu and T. F. Gallagher J. Phys. B **20** 4461 (1987).

16. Y. Zhu, R. R. Jones, W. Sandner, T. F. Gallagher, P. Camus, P. Pillet, and J. Boulmer J. Phys. B, **22** xxx (1988).

17. C. E. Moore *Atomic Energy Levels. NBS Circular NO. 467* (USGPO Washington, DC 1947).

PULSED-POWER-DRIVEN, PHOTO-EXCITED X-RAY LASER RESEARCH AT PHYSICS INTERNATIONAL

T. Nash, C. Deeney, J. Levine & M. Krishnan

Physics International Company
2700 Merced St.
San Leandro CA 94577

Abstract.

The sodium-neon photopumped X-ray laser scheme is under investigation at Physics International, on the DNA/PITHON 3-TW facility. For the sodium-neon resonant photopumped scheme, DNA/PITHON is used to implode a sodium-bearing plasma, the pump, and a secondary capacitor bank will be used to drive a neon gas puff Z-pinch, the lasant. The characterization of the pinched sodium plasma is reported in this paper, as are pump power measurements, which showed 65 GW in the Na X $1s^2$–$1s2p$ [1]P line and a maximium total yield of 2.4 kJ in the best shot. The behavior of the yield with implosion conditions is discussed.

Introduction.

The energy levels for the sodium-neon photopumped[1] X-ray laser scheme are shown in Figure 1. The Na X $1s^2$-$1s2p$ [1]P line at 11.0027 Å pumps the Ne IX $1s^2$-$1s4p$ [1]P line at 11.0003 Å. This pumping could result in inversions in the 4-3, 4-2 and 3-2 lines. Apruzese and Davis[2] predict a gain on the 4-3 line, at 230 Å, of 1 cm^{-1} when the sodium and neon plasmas are 4 cm apart and the sodium plasma radiates 200 GW in the pump line. This gain estimate assumes a neon ion density of 10^{18} cm^{-3}.
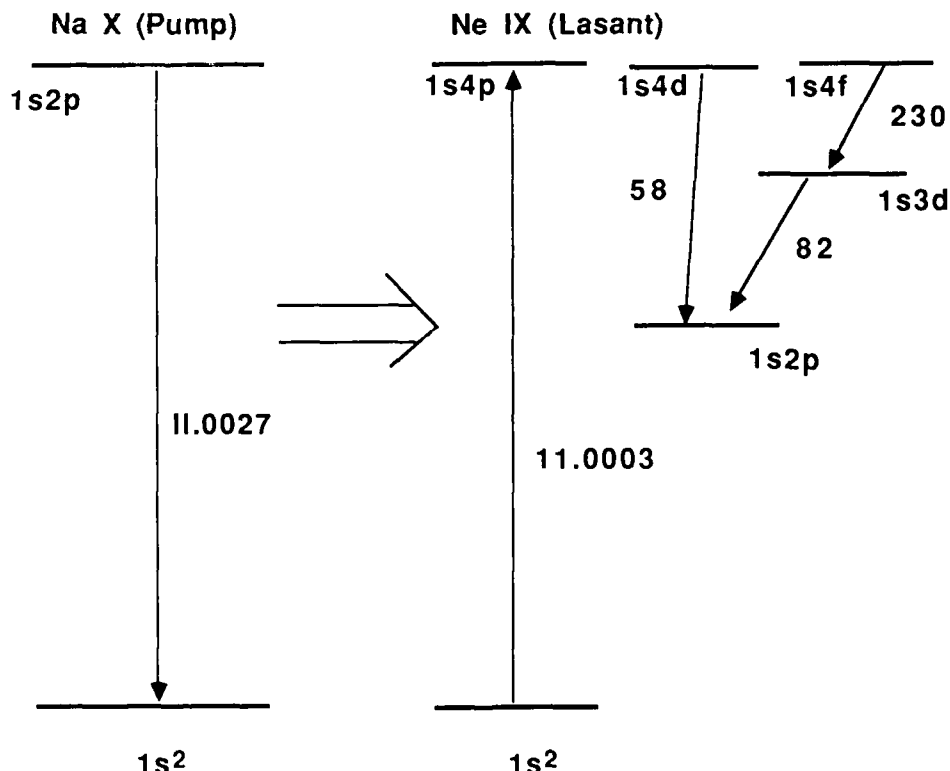
Figure 1. Energy Level Diagram for the Sodium-Neon Photopump X-ray Laser Scheme.

This photopump scheme has been investigated experimentally using laser-produced plasmas[3] and Z-pinches[4]. There has, to date, been no demonstration of gain. At Physics International, the sodium-neon scheme is investigated using pulsed-power-driven Z-pinches to produce both the lasant and pump plasmas. In a sodium Z-pinch, a large current, 3 MA, is passed through a sodium bearing vapor jet. The interaction of the current with its azimuthal self-magnetic field results in a Lorentz force which is directed radially inwards. This force compresses the plasma. When the sheath or imploding shell assembles on-axis, the directed radial kinetic energy is thermalized and a hot, dense plasma is formed, which is subsequently heated by the current as it continues to flow in the pinch.

Gas puff Z-pinches and imploding wire arrays are copious X-ray sources. When imploded with small, <10 kJ, slow, 1-μs risetime banks, 10% of the stored energy is radiated in the 100-1000 eV region over 500 ns or so and the plasmas formed typically have electron densities in the range of 10^{19} to 10^{20} cm^{-3} and electron temperatures less than 100 eV[5,6]. On large pulse-power-driven Z-pinches, which operate at the multi-TW level, greater than 1% of the stored energy is radiated at keV photon energies in 10-20 ns timescales,[9] and the plasmas have electron densities in the mid 10^{20} cm^{-3} and electron temperatures in the range of 400-1000 eV[7,8,9,10].
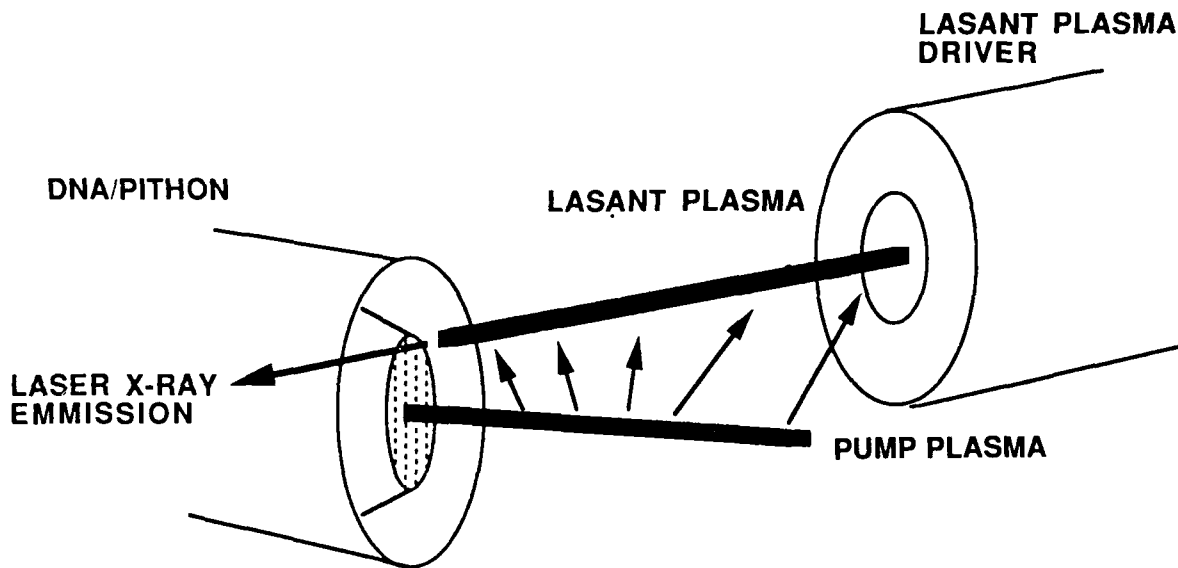
Figure 2. Physics International's Approach to Photopumped X-ray Laser Scheme.

Based on the performance of Z-pinches under different driver conditions, the approach shown in Figure 2 was adopted to perform sodium-neon photopump experiments. The DNA/PITHON generator, whose parameters are given in Table I, is used to implode a sodium-bearing plasma. This should provide the high pump power. The cooler, 50 eV, less dense, $n_e = 5 \times 10^{19}$ cm^{-3}, neon plasma will be formed using a 27-kJ, 9-μF capacitor bank, which generates 500 kA with a 2-μs quarter period. The geometry of these two Z-pinches is designed to allow them to be brought to within 4 cm of each other. The advantage of this approach is that the two plasmas can be independently controlled and optimized to the correct size, temperature, and densities. Also, length scaling can be examined without having to change the actual plasma length, which could otherwise alter the plasma parameters. The variation of intensity with length can be achieved by baffling the neon plasma so that different lengths of the lasant plasma are pumped by the sodium plasma.

Table I. PITHON parameters.

Machine Parameters:

Peak Current = 2 to 3 MA
Inductance = 20 to 30 nH
t_{rise} = 50 ns
E_{stored} = 3/4 MJ

Pinch Plasma Parameters:

$n_e \approx$ mid 10^{20} cm^{-3}
$T_e \approx$ 400 to 1000 eV
$1 \approx$ 3 cm
$d \approx$ 2 mm
Yield $\approx$ 10 kJ of 1 keV X-rays
$t \approx$ 10 to 20 ns

In this paper, preliminary efforts to produce the sodium plasma and the measurements of the Na He$_\alpha$ on DNA/PITHON are described. The development of the neon plasma is under way but is not described in this paper.

The Sodium Z-Pinch.

The chemical reactivity of pure sodium makes it difficult to use as a Z-pinch load, compared to ordinary metals which can be made into wires and imploded as arrays. Techniques do exist which allow sodium compounds to be vaporized and puffed, similar to a gas. An electrical discharge passed through a NaF capilliary[11] has been shown to produce a sodium containing jet, and this jet was used as a Z-pinch load on Gamble II to produce 35 GW in the Na X 1s^2-1s2p ^{1}P line[12,13]. Other work performed by Gazaix[14] has demonstrated highly collimated jets of aluminium, and this source may be developed to produce a pure sodium vapor jet.
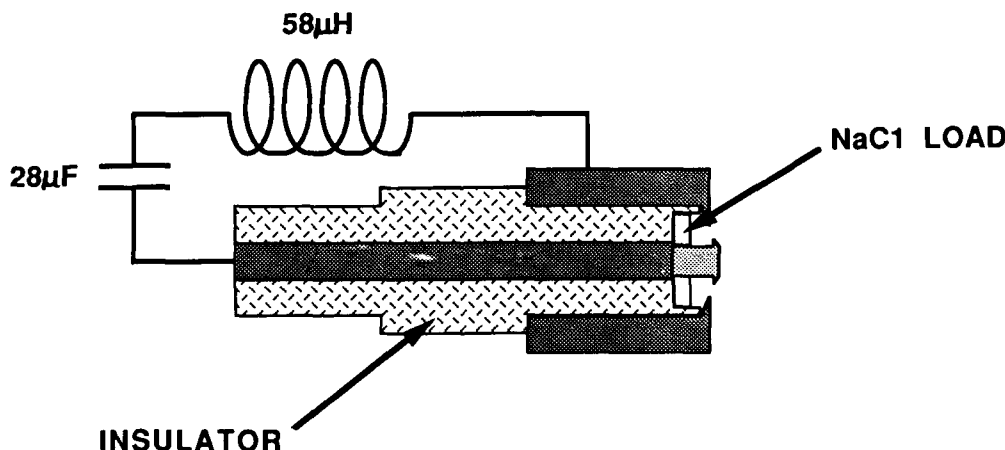
Figure 3. Sodium Source for PITHON.

The Physics International sodium source, shown schematically in Figure 3, had sodium chloride packed into a fixed annular volume,.which gave a mass loading of 100 ± 10 mg. The driver bank was a 28-µF capacitor, charged to 15 kV, which discharged through a 58-µH inductor into the sodium chloride load. The capacitor was crowbarred after 40 µs to allow the inductor-driven current to decay slowly in the sodium chloride plasma. Typically the main PITHON current would be fired between 30 and 50 µs after the current was initiated in the sodium chloride load. No detailed measurements were performed of the mass distribution of the sodium chloride vapor source prior to testing the source on PITHON. As the operating conditions of the source were varied during the pulsing session, there seemed to be no systematic dependence on the time to implode (which is a

measure of the mass of the Z-pinch load for a given current) with either the mass loading in the sodium chloride source or the delay between firing the source and triggering PITHON. Future experiments on the bench will endeavor to measure the mass flow from the source and the dependence of this with respect to mass loading and applied voltage.

The sodium source was mounted onto the DNA/PITHON generator, and sodium chloride vapor puffs were imploded. A range of X-ray diagnostics, as shown in Figure 4, was employed to measure the X-ray yield and the collapse dynamics. The pump line temporal behavior was measured using a germanium-filtered, copper cathode X-ray diode[14] (XRD) and a time-resolved (3 gated frames) crystal spectrometer. A 12-frame X-ray pinhole camera filtered with 8 μm of Kapton was used to study the spatial extent of the X-ray emitting regions in time. A time-integrated crystal spectrometer was used to measure the relative yield from one shot to another.
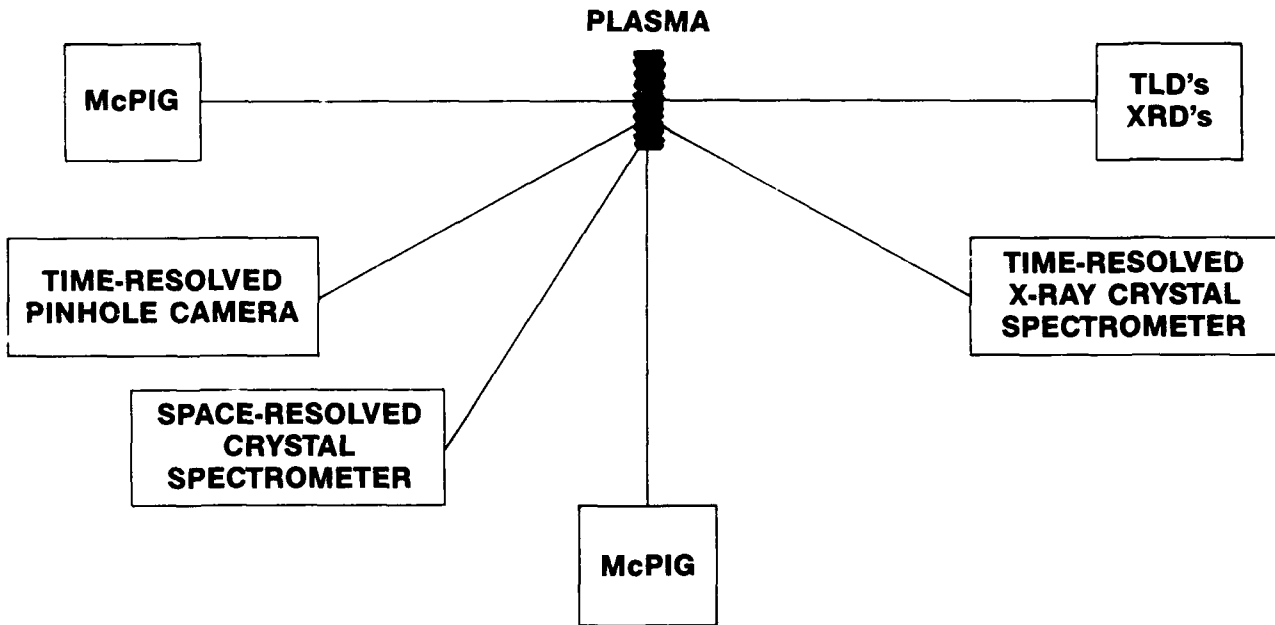
Figure 4. Diagnostic Layout.

The time-resolved pinhole camera shows that the sodium plasma Z-pinch is 3 mm in diameter and 2 cm long; however, it is not very homogeneous. This is acceptable, in this case, since there is sufficient separation of the pump and lasant plasma to compensate for non-uniformities in the sodium plasma. However, gross plasma instabilities in the sodium plasma should be avoided. The sodium plasma radiates typically for 40 ns with the most intense period being 15 ns in duration. The axial variation in time to pinch—the so-called *zipper effect* —is of the order of 10 ns. A typical time-integrated spectrum, shot No. 4706, is shown in Figure 5. The ratio of the Ly_α to the He_α lines of the sodium indicates a temperature of 600-800 eV, which is hotter than the optimal temperature estimated to maximize the He_α intensity. As can be seen from the spectrum, there is a significant fraction of radiation in aluminum impurity lines and some in zinc and copper lines. The source of these impurities are the puff nozzle, which is made from aluminum, and the current return cage, which is made from brass. Using a graphite nozzle, the aluminum radiation was eliminated but the pump line yield was not significantly increased.
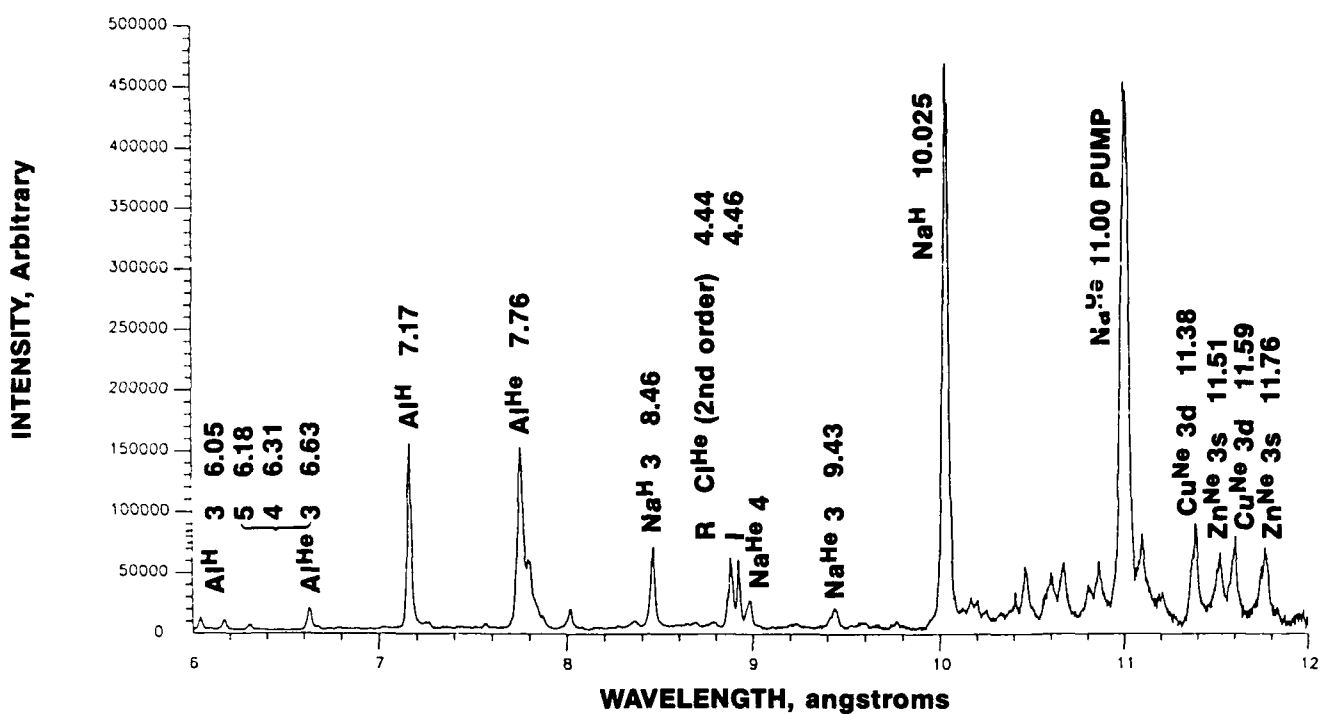
Figure 5. Time Integrated X-ray Crystal Spectra

In Figure 6, the germanium-filtered, copper cathode XRD signal is shown superimposed on the pinch current for shot No. 4706. The filtering on this diode rejects the Na Ly_α line and the aluminum radiation. From the published cathode sensitivities and known filter transmissions, the signal was analyzed to give the absolute power in the pump line. The peak power measured in the pump line was 65 GW with a 14 ns FWHM. The total yield in the He_α line was 2 kJ on this shot. The germanium filter does pass the copper and zinc impurites, which are seen
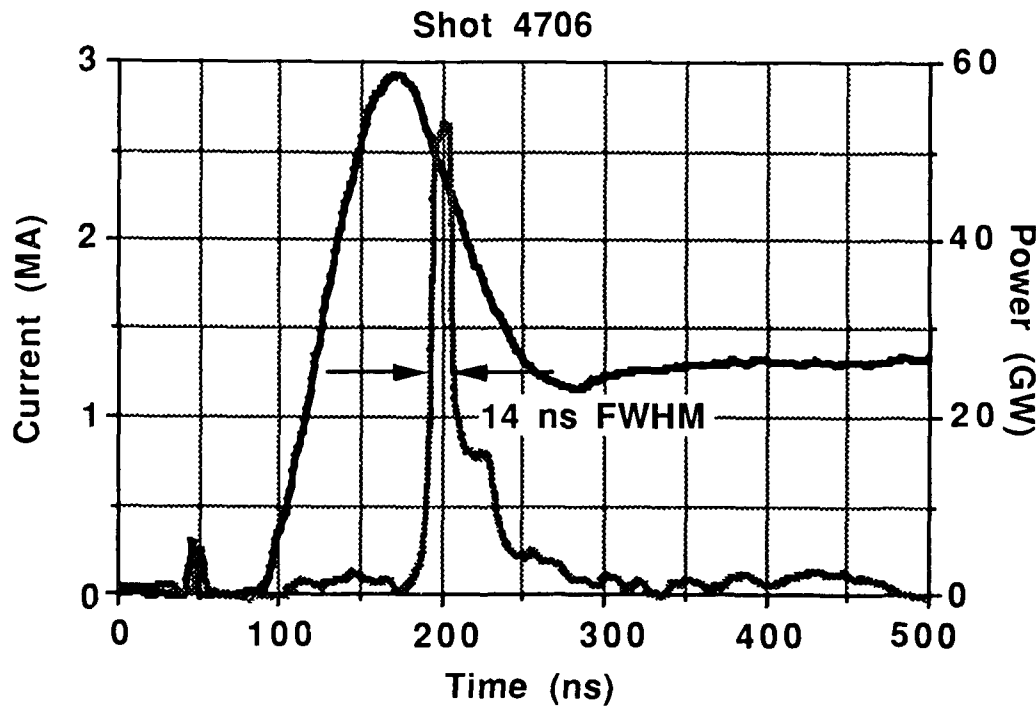
Figure 6. Germanium-filtered, Copper Cathode XRD: Signal and Pinch Current

86

on the spectra shown in Figure 6; however, their magnitudes are low. In shots where the pump line yield was low, the impurity emission was comparable to the pump line. This is demonstrated in the time-resolved spectra, shown in Figure 7. The 10-ns-long frames indicate an emission time of greater than 30 ns but a FWHM of 20 ns or so.
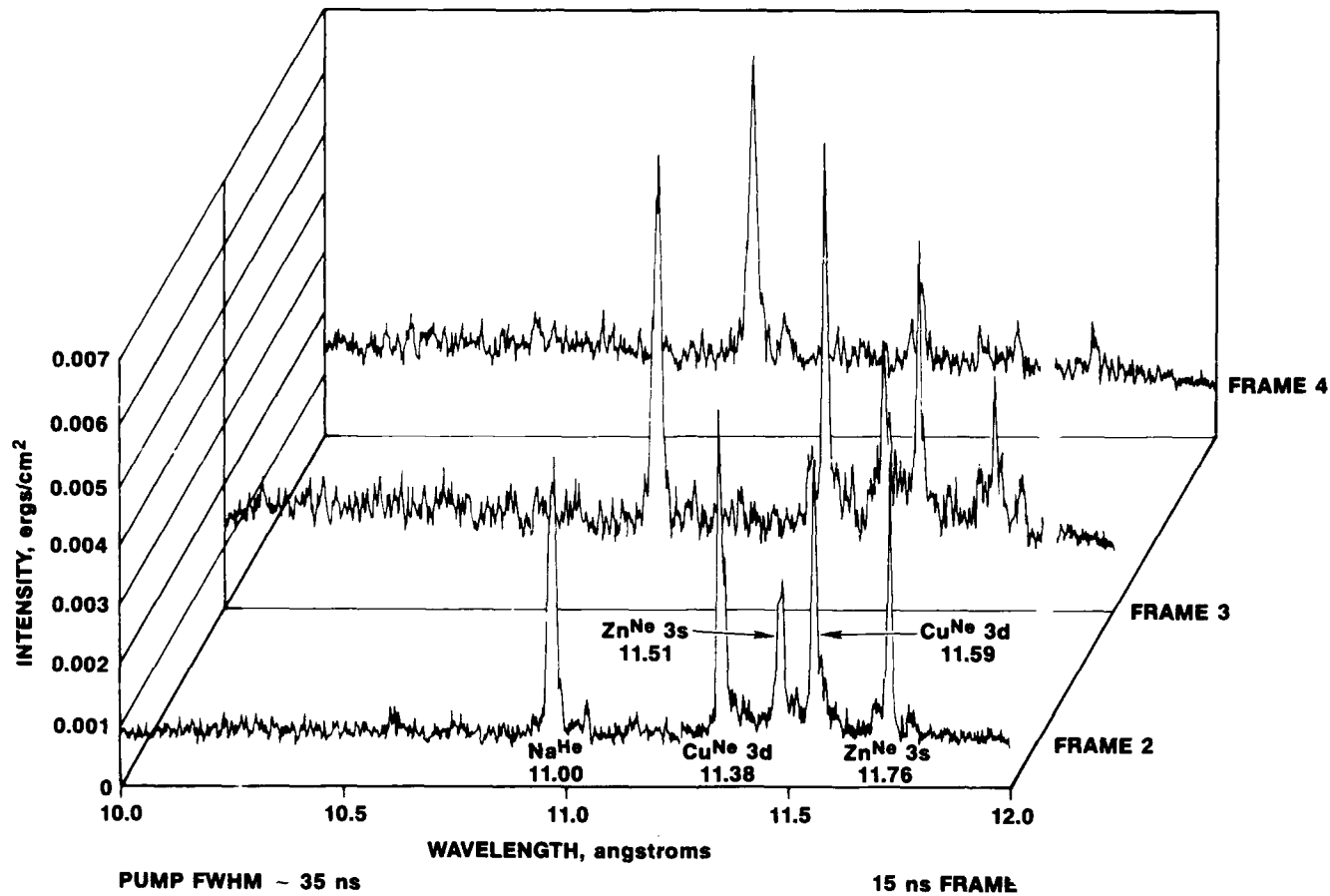
Figure 7. Time Resolved X-ray Crystal Spectra

Using shot No. 4706 as a calibration for the time-integrated crystal spectrometer, the total yield in the Na He_α pump line was measured from time-integrated spectra taken on different shots, and the yield in the pump line was studied as a function of the sodium source and PITHON parameters. In Figure 8, the yield in the pump line is plotted versus the peak current from PITHON and the current at the time of implosion. As the current increases, the yield increases. The large variation at a given current, up to a factor of two, does not allow an accurate current scaling to be determined but a scaling between I^2 and I^4 would fit the data. Prior to increasing the current to improve the yield, the sodium source must be refined so that the mass flow can be controlled in a systematic fashion, thus allowing the load mass to be optimized for a given current. The plot of the pump line yield versus implosion time, Figure 9, indicated that the yield was optimized when the implosion time was between 95 and 100 ns. This implosion time is some 15-20 ns after the peak of the current pulse

Conclusions and Future Work.

X-ray laser research on gas puff Z-pinches, focussing on the sodium-neon photopump scheme, is in progress. The results to date of this study are that sodium implosions using a 3-TW generator have resulted in 65 GW, 2 kJ on one shot and 2.4 kJ total yield on the best shot, being emitted in the Na X $1s^2$-$1s2p$ line. Future work will require the optimization of the sodium source so that the goal of 200-250 GW in the sodium He_α can be met. This can

87
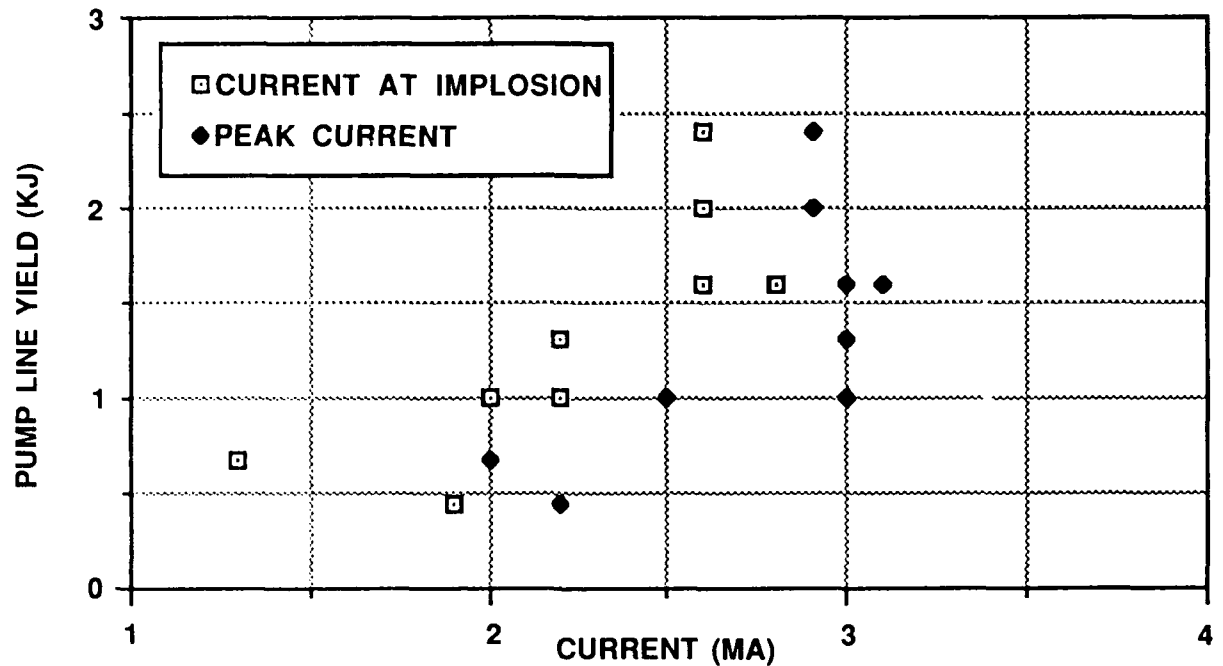
Figure 8.   Sodium He$_\alpha$ Line Yield vs. PITHON Current
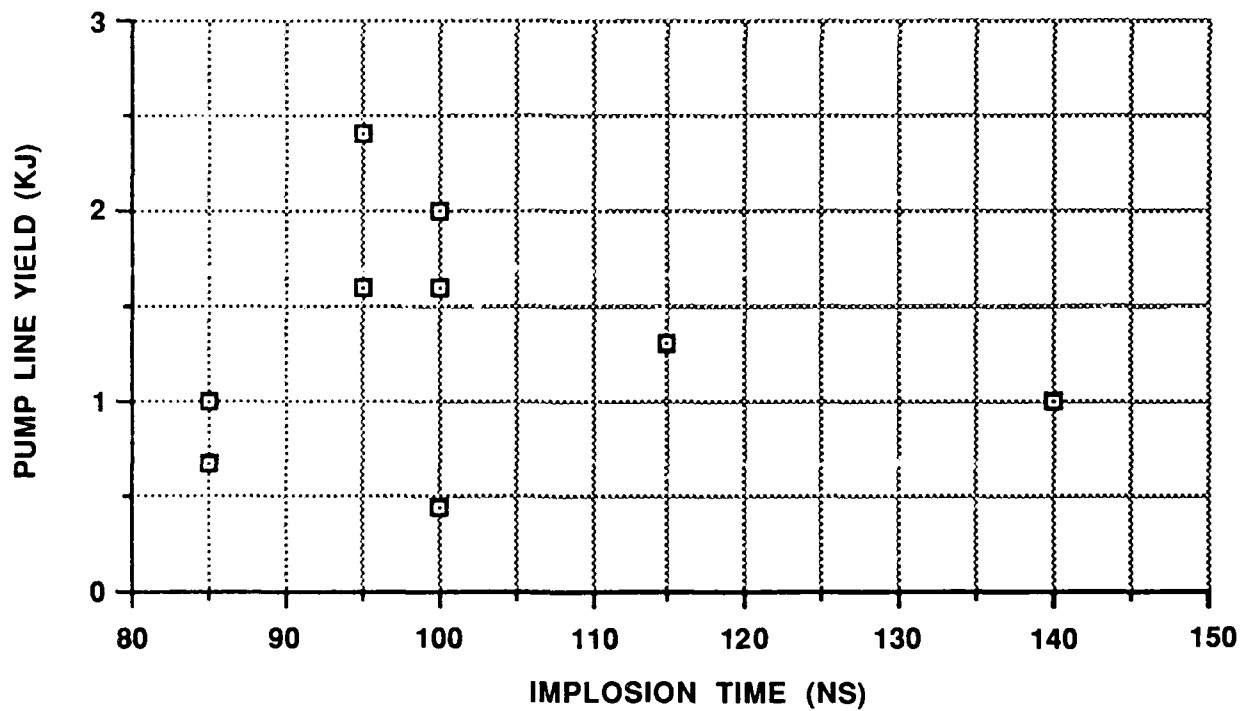
Figure 9.   Sodium He$_\alpha$ Line Yield vs. Implosion Time

88

certainly be achieved by increasing the current into an optimized load and may be possible by optimizing the load for the 3 MA that PITHON can generate at present. Since this design of sodium source does not appear to be easily controllable, other methods of implementing the sodium source, such as the NRL capilliary discharge or a metal vapor puff, may be tested. The neon plasma has to be characterized and the desired ionization stage achieved, before fluorescence and length scaling experiments are performed to look for gain in the He-like 4-3 line at 230 Å.

Acknowledgements.

References.

1. J.P. Apruzese, J. Davis & K.G. Whitney, J. Appl. Phys., 53(6), p4020, (1982).
2. J.P. Apruzese & J. Davis, Phys. Rev. A, 31(5), p2976, (1985).
3. J.G. Lunney et al, Optics Comm., 50(6), p369, (1984).
4. J.P. Apruzese et al, SPIE "Short and Ultrashort Wavelength Lasers" vol. 875, p2, (1988).
5. P.Choi, A.E. Dangor and C. Deeney, SPIE "Soft X-ray Optics and Technology" vol. 733, p53, (1986)
6. G. Nave, "Soft X-ray Spectroscopy of a Gas Puff Z-Pinch.", PhD Thesis, University of London, (1986).
7. C. Stallings et al, Appl. Phys. Lett., 35(7), p524, (1979).
8. W. Clark et al, J. Appl. Phys., 53(8), p5552, (1982).
9. R.B. Spielman et al, J. Appl. Phys., 57(3), p830, (1985).
10. P. Burkhalter et al, J. Appl. Phys., 50(2), p705, (1979).
11. F.C. Young et al, Record of IEEE Conf. on Plasma Sciences, Cat. No. 86CH2137-6, p87, (1986).
12. F.C. Young et al, Appl. Phys. Lett., 50(16), p1053, (1987).
13. J.P. Apruzese et al, Phys. Rev. A, 35(11), p4896, (1987).
14. M. Gazaix et al, J. Appl. Phys., 56(11), p3209, (1984).
15. F.C. Young, S.J. Stephanakis and V.E. Scherrer, Rev.Sci. Instrm., 57(8), p2174, (1986).

GAIN PREDICTIONS AND MEASUREMENTS IN NEON-LIKE IONS

Barbara L. Whitten[*], Mau H. Chen, Andrew U. Hazi,
Christopher J. Keane, Richard A. London, Brian J. MacGowan,
Dennis L. Matthews, Thomas W. Phillips,
Mordecai D. Rosen, James L. Trebes, and David A. Whelan[**]

Lawrence Livermore National Laboratory
University of California
Livermore, CA 94550

Abstract

The demonstration in 1984 of amplified spontaneous emission in neon-like selenium showed that it was possible to make a laser at soft x-ray wavelengths. When the results of the experiment disagreed with all previous predictions in that the predicted strongest line could not even be positively identified, the "J=0 anomaly" was introduced to the physics community. This large discrepancy implies a serious error in our understanding of soft x-ray laser plasmas and the problem has received a great deal of theoretical and experimental attention. In this paper we summarize the work that has been done to understand the anomaly, describe the present state of our knowledge, and propose further research.

I. Introduction

Neon-like ions have long been recognized [1] as potential candidates for producing soft x-ray lasers. The $2s^2 2p^5 3s$ excited states have a fast electric dipole radiative transition to the ground state, while the $2s^2 2p^5 3p$ states can radiate to the ground state only by much slower electric quadrupole transitions. A population inversion between the 3p and 3s excited states should be very natural and easy to create, provided the right plasma conditions can be obtained. This was confirmed in 1984 when amplified spontaneous emission was first demonstrated at Lawrence Livermore National Laboratory (LLNL) [2] in neon-like selenium by irradiating an exploding foil target [3] with the NOVETTE laser. The same experiment introduced the "J=0 Anomaly" to the physics community. The transition predicted to have the largest gain [3-5] was a 3p-3s (J=0-1) transition near 182 Å. This line was not significantly amplified in the experiment--it was not even unambiguously identified. Two other 3p-3s J=2-1 transitions did show strong amplification, in good agreement with prediction. But the absence of the strongest predicted line was very provocative, and has inspired a number of studies of neon-like ions. [6-10]

In later experiments using targets with longer gain lengths, the LLNL group has observed the anomalous J=0-1 transition at 182.43 A, and has measured a gain coefficient which is significantly below the predictions. In this paper we shall summarize the experimental results relevant to understanding the "J=0 anomaly," describe the theoretical efforts to resolve the discrepancy, and propose fruitful avenues for further research.

II. Summary of Experimental Results

Detailed gain measurements

We first discuss experiments in selenium and molybdenum, where gain has been measured for several lines, and detailed simulations are available for comparison. Table 1 summarizes experimental results and theoretical predictions for selenium. Gain has been measured for a total of five transitions, and it is clear that all are in good agreement with the predictions (within 50%), with the exception of the J=0-1 line at 182.43 A. Four years of work on the atomic physics, kinetics, and propagation physics of the simulation package, and on analysis of the data, has greatly improved the agreement between theory and experiment, but the predicted gain coefficient is still larger by a factor of more than four.

Table 2 shows detailed experimental [11] and theoretical [12] results for molybdenum. There is agreement to within a factor of two between theory and experiment for all observed transitions except the analogous J=0-1 transition at 141.6 A, where no gain at all is measured. Clearly, the anomaly scales to higher Z. Note that another J=0-1 transition at 106.4 A (analogous to the 168.67 A transition in selenium) shows significant gain.

Table 1. Comparison of measured and predicted gain coefficients (cm^{-1}) for neon-like selenium.

Transition		Wavelength (A)	Prediction	Measurement
2p3p-2p3s J=2-1	(7-3)	262.94	5.0	3.5
	(10-3)	206.38	5.7	4.0
	(14-5)	209.78	6.2	3.8
2p3p-2p3s J=1-1	(9-3)	220.28	2.8	2.2
	(12-5)	261.5 (theoretical)	1.3	--
2p3p-2p3s J=0-1	(15-5)	182.43	10.0	2.4
	(11-3)	168.67	1.2	--
	(15-3)	113.43	1.3	--
2s3d-2s3p J=2-1	(37-33)	181.95	2.4	--

Table 2. Comparison of measured and predicted gain coefficients (cm^{-1}) for neon-like molybdenum.

Transition	Wavelength (A)	Prediction	Measurement
2p3p-2p3s J=2-1	131.03	8.5	4.1
	132.70	8.4	4.2
2p3p-2p3s J=1-1	139.44	5.3	2.9
2p3p-2p3s J=0-1	141.62	5.3	--
	106.42	3.8	2.2

Z-scaling of gain

Gain measurements for the two strong J=2-1 transitions and the anomalous J=0-1 transition have been made for a number of other elements. A group at Naval Research (NRL) has measured gain in neon-like copper and germanium [13], and recently in zinc, arsenic, and selenium [14]. The LLNL group and French scientists at Centre d'Etudes de Limeil-Valenton [15] have measured gain for neon-like strontium. The results are similar to those for selenium and molybdenum; the two J=2-1 transitions show large gain, and the anomalous J=0-1 transition does not show measurable gain (although observations are complicated by a line coincidence with a sodium-like transition). Gain has also been observed at LLNL in yttrium [2], but the results are not useful because the J=0-1 line in that element is coincident with one of the J=2-1 transitions at 154.9 A. Significant gain is seen at this wavelength, but it is impossible to tell how much each transition is contributing.

These results are shown in Figure 1, along with available theoretical predictions. The two types of transitions clearly behave differently as a function of Z; the gain of the J=2-1 transitions rises at low Z, flattening out around Z=33, while the gain of the J=0-1 transition is large for low Z and falls as Z increases. The anomaly itself also appears to change with Z; comparison with a simulation of the copper plasma [16] shows rather good agreement for all three transitions, but the discrepancy is large for selenium and molybdenum.

This scaling with Z is very thought-provoking, but is not clear whether it is caused by differences in atomic or laser physics or by different experiment.' conditions. The lower Z experiments at NRL were performed in most cases on slab targets illuminated by 1.06 μm light in a long (1.2-2.5 ns) pulse. The higher Z experiments at LLNL and Limeil were done with exploding foil targets illuminated by 0.53 μm light in a short (0.5-1 ns) pulse. NRL measurements done on exploding foils of selenium [14] give results similar to the LLNL results, but preliminary analysis of Limeil experiments in germanium does not show strong amplification of the J=0-1 transition. A series of carefully analyzed experiments done in both laboratories on overlapping elements would clarify this very important issue.
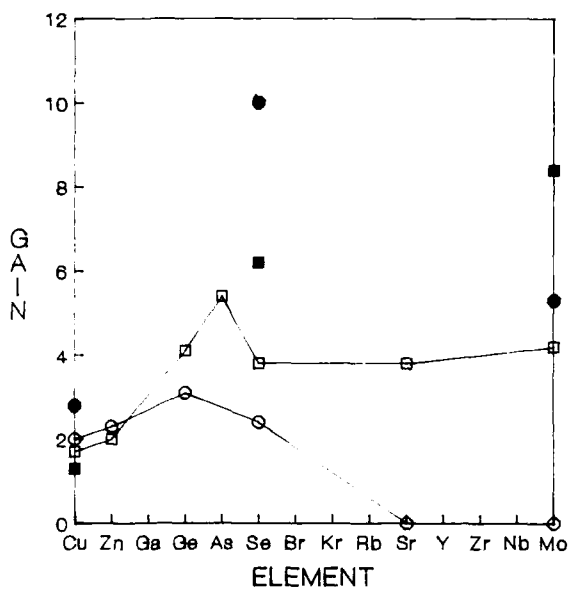
Figure 1. Gain measurements and predictions in several elements for one J=2-1 transition (squares) and the anomalous J=0-1 transition (circles). For each transition, open symbols represent measurements and filled symbols represent predictions.
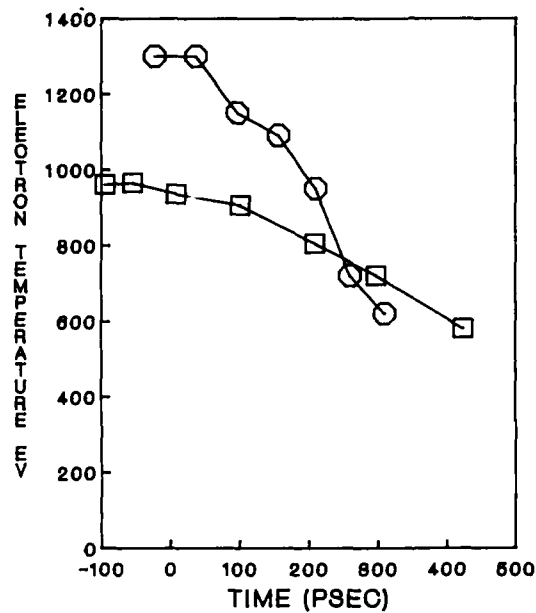
Figure 2. Electron temperature versus time (measured from the peak of the optical heating pulse). Squares represent measurements using stimulated Raman scattering and circles represent LASNEX predictions.

Plasma conditions

We next review what is known about the plasma conditions in the x-ray laser plasma. The parameter we best understand is the electron density. Laser interferometry experiments [17] have provided accurate density profiles of an exploding foil target at several times during the duration of the pulse. These profiles have been compared with LASNEX simulations for a wide range of pulse lengths, laser intensities, and foil thicknesses, and overall the agreement between theory and experiments is better than a factor of two. We therefore have some confidence in our modeling of the electron density, at least at the scale length (≈ 20 μm) sampled by this experiment.

The electron temperature is more problematic; experimental measurements are less straightforward and different techniques do not agree. The least model-dependent method is to observe of the slope of the bound-free recombination continuum; if the free electrons have a Maxwellian distribution, the continuum will be a straight line with slope proportional to electron temperature. Recently this technically difficult experiment has been performed for an aluminum dot on plastic [18]. Analysis of detailed time- and space-resolved x-ray spectra has revealed substantial qualitative and quantitative disagreement with LASNEX simulations.

This discrepancy is extremely disturbing, but it is difficult to assess its relevance to the selenium x-ray laser problem because the plasma conditions and target design are very different in the two experiments, and laser-plasma interactions are strongly Z-dependent. If it should turn out that the selenium x-ray laser plasma is much cooler than simulations predict, it will certainly require that we rethink our understanding of the modeling. But it will probably not completely resolve the J=0 anomaly. A LASNEX simulation with the temperature arbitrarily multiplied by 0 6 shows that the decrease in collisional excitation rates i duces the gain in all transitions. However, a shift in the ionization balance from mostly fluorine-like to mostly neon-like reduces the gain of the J=2-1 transitions as well as the J=0-1 transition.

An upper limit on the electron temperature in the x-ray laser plasma itself can be obtained from the spectral extent of the scattered Raman light by assuming that t e short wavelength cutoff is due to Landau damping [19], and that the density profile is Gaussian. Figure 2 compares the electron temperature estimated by this method with a LASNEX prediction.

It should be clear from this discussion that the electron temperature of the x-ray laser plasma is not well understood. It is essential that the discrepancy between LASNEX predictions and the continuum measurements be resolved, and, if possible, that the continuum measurement be made on a target designed to more closely resemble the x-ray laser target.

Another critical parameter is the ionization balance. This is even more problematic because it is very difficult to model, and there is no quantitative experimental information. Analysis of 4-2 and 5-2 radiation from different charge states in spectra taken by a time integrated x-ray spectrometer shows that variations in the laser and target parameters are reflected in the ionization balance. But it is difficult to extract useful quantative results which can be compared to simulations.

Clearly, our understanding in a primitive state. Moreover, because the population mechanisms of the J=2-1 and J=0-1 transitions vary significantly as a function of the ionization balance, it is critical to the kinetics of the neon-like laser scheme, and the J=0 anomaly. Experiments designed to directly measure ground state populations of the important charge states in the laser plasma would provide extremely useful information.

III. Possible Solutions to the J=0 Anomaly

The J=0 anomaly has been the subject of much interest, and many solutions have been proposed. We concentrate here on three major hypotheses which have received the bulk of theoretical and experimental attention.

Error in kinetic modeling

First, it is possible that our kinetic models do not contain all important atomic processes. Figure 3 shows the most important population mechanisms for the upper levels of the 182.43 A J=0-1 transition and the 209.78 A J=2-1 transition, respectively, as predicted by a steady state calculation of XRASER (These two transitions share the same lower state.) While the J=2 upper state (level 14 in selenium) is populated by several mechanisms, the J=0 upper state (level 15) is populated almost solely by collisional excitation from the neon-like ground state. This very large J=0-0 rate is something of an
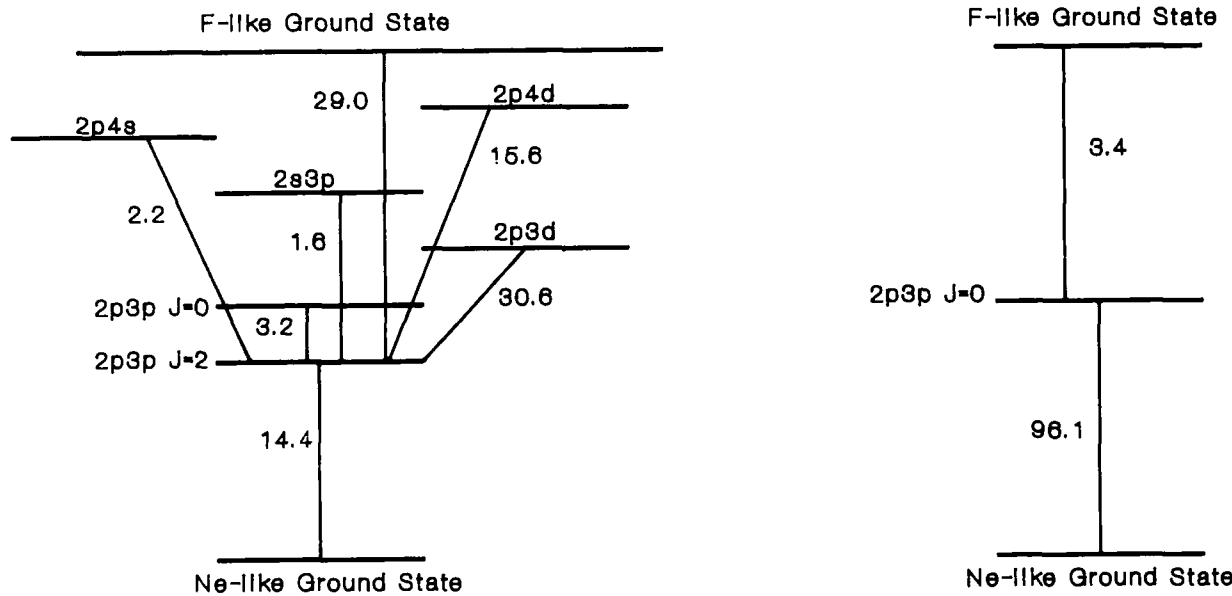
Figure 3. Population mechanisms for upper laser levels of neon-like selenium, as predicted by a steady state XRASER calculation for $n_e = 5 \times 10^{20}$ cm^{-3}, and $T_e = 1000$ eV. The ionization balance of the plasma is predicted to be $f_{Ne} = .16$, $f_F = .45$, $f_{Na} = .02$, and $f_O = .265$. The numbers shown on the diagram represent the percentage of the total (net) flux into that level.
    a.   Flux into level 14 (upper level of 209.78 A J=2-1 transition).
    b.   Flux into level 15 (upper level of 182.43 A J=0-1 transition).

anomaly--most atomic processes favor high multiplicity states. Therefore, improving the kinetic model by including some important process will most likely increase the relative gain of the J=2-1 transitions and reduce the J=0 anomaly.

This hypothesis has received much theoretical attention, and improvements in the kinetic model, most notably by the inclusion of detailed dielectronic recombination rates [7,9], have been largely responsible for the improvement in agreement between theory and experiment. However, no single process has been found that completely accounts for the J=0 anomaly and, even taken together, all the improvements do not completely eliminate it. Precisely because the kinetics hypothesis has been so thoroughly investigated, it is unlikely that further improvements which will have a major effect.

One potentially important effect which has not been examined in detail is resonant enhancement of the 3-3 collisional excitation cross sections. Generally speaking, resonant enhancement has a larger effect on more forbidden transitions, and transitions between level 15 and the other 3p levels tend to be strongly forbidden. Increasing these collision rates would shift population out of low multiplicity states, and so decrease the relative gain of the J=0-1 transition. The importance of this effect is presently being investigated by M.H. Chen, who finds that resonances of the form $2p^5 4\ell 4\ell'$ and $2p^5 4\ell 5\ell'$ can enhance the collision cross section by as much as a factor of two. Including the triply excited states $2p^4 3\ell^3$ will probably also have a significant effect, and is being investigated.

Error in collisional excitation rate

We saw in Figure 3 that level 15 is populated almost solely by a very large J=0-0 collisional excitation rate from the ground state. It is tempting therefore to suggest that the cause of the J=0 anomaly is an error in the calculation of this single rate. However, the best theoretical and experimental evidence available does not support this conclusion.

The original gain predictions [3] were based on models in which the ground-excited state collisional excitation cross sections were calculated in the distorted wave approximation, which should be excellent for highly charged ions. To test this assumption, a coupled channels calculation of the same set of cross sections has been performed for neon-like selenium [20]. This new calculation accounts for mixing among the various scattering states, and also for the effect of resonances. This calculation shows that, while resonance enhancement is important for low lying excited states, the excitation rate into level 15 is increased by less than 10%.

Until recently it was not possible to measure excitation cross sections for highly charged ions, so these calculations could not be checked experimentally. Recently, however, the Electron Beam Ion Trap [21] has make direct measurements possible. Results for neon-like barium indicate that measured and calculated collision cross sections near the excitation energy differ by no more than 4%.

We have noted the gain on the "other" J=0-1 line in molybdenum (see Table 2). The upper state of this transition is also populated mostly by collisional excitation from the ground state. This rate is large because the two J=0 states are mixed by spin-orbit coupling, which increases significantly for higher Z ions. It would be difficult to explain the observed gain for this transition if the excitation rate for the 2p-3p ($\Delta J=0$) transitions were small.

Error in propagation

Finally, it is possible that there are errors in our modeling of the propagation of the x-rays through the plasma. As we see in Figure 4, the simulated time history of the J=0-1 transition is quite different from that of the J=2-1 transitions (which show similar behavior). The J=0-1 transition peak early in time, when the density is high, the temperature is low, and the neon-like fraction is relatively large. The J=2-1 transition peaks later in time, when the plasma is hotter, less dense, and more fluorine-like. The predicted gain for the J=0-1 transition also shows a short time duration, while the J=2-1 gain is broader in time.

There is some evidence that these simulations are correct. In experiments [22] in which the time resolved output of the laser lines was compared with the
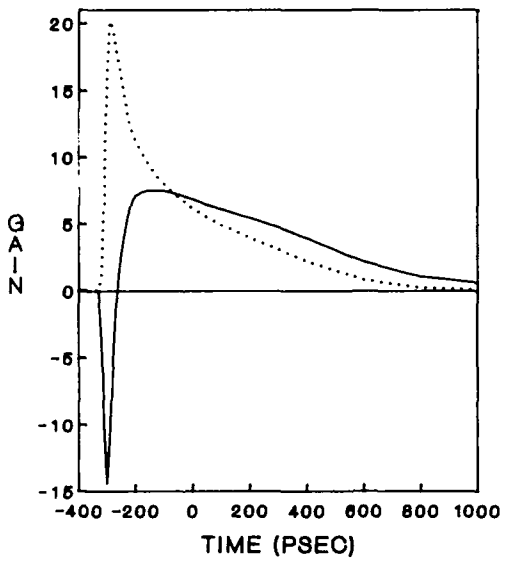
Figure 4. Predicted laser output power versus time (measured from the peak of the optical heating pulse) for the 209.78 A J=2-1 transition (solid line), and the 182.43 A J=0-1 transition (dotted line).

Figure 5. Intensity versus position in the plasma for the 209.78 A J=2-1 transition (solid line) and the 182.43 A J=0-1 transition (dotted line). The two curves have been offset for clarity.

timing of the optical heating pulse, the J=2-1 line peaked 30-50 ps. before the peak of the optical laser pulse, and lasted about 270 ps. (FWHM). The J=0-1 line peaked about 20 ps. earlier and was slightly shorter in time (250 ps.). The times are small compared to the error in measuring the time of the optical laser pulse, but the trends are consistent. The simulation accurately predicts the behavior of the J=2-1 lines, but the J=0-1 line lasts longer than predicted. This difference in timing, combined with the fact that refractive effects are larger early in time, indicates that it might be more difficult for the J=0-1 radiation to propagate down the plasma column.

Space-resolved data from the imaging MCPIGS spectrometer [23] shows that the J=0-1 line is amplified in a smaller region of the plasma. Figure 6 shows lineouts in the spatial direction of the 182.43 and 209.78 A lines. It is clear that the source size of the J=0-1 transition is significantly smaller than the J=2-1 line. This smaller region of strong amplification enhances any propagation difficulties.

These results led us to estimate the effect on the J=0-1 gain of propagation problems not included in the simulations, for example scattering off inhomogeneities in the plasma, diffraction, non-uniformity along the plasma column due to non-uniformity in the optical laser, or finite light travel times. We arbitrarily removed all signal prior to the peak of the optical heating pulse. We do not expect significant propagation problems after the peak of the pulse because density profiles are very smooth and because the gain and timing measurements of the J=2-1 lines are in good agreement with theory. This exclusion reduces the effective gain by about 40%, which implies that propagation difficulties by themselves are unlikely to fully explain the J=0 anomaly.

Other interesting solutions have been proposed. Apruzese et al. [6] suggested that the selenium laser was pumped primarily by radiative recombination after the peak of the optical pulse in a cool, primarily fluorine-like plasma. However, timing data [22] indicate that lasing occurs before or near the peak of the pulse. Apruzese [24] recently pointed out that the kinetics of the plasma may be different toward the ends of the plasma column, where the driver laser is less intense and the plasma is cooler. Recombination will be more important in these regions, and may boost the gain of the J=2-1 transitions. Greater refraction in the ends of the plasma may increase the difficulties of propagation discussed above [25].
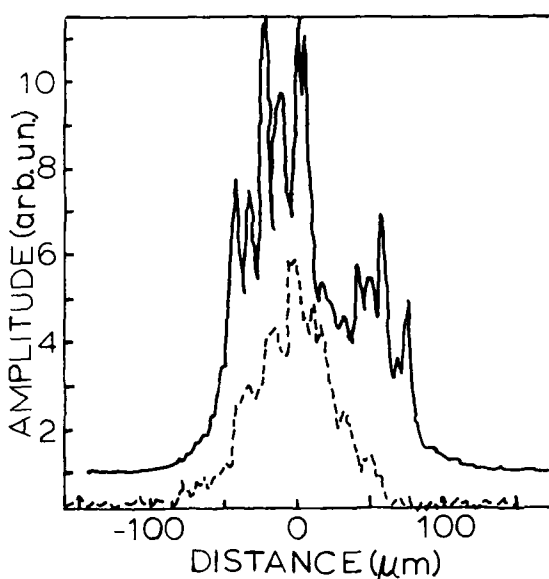
95

Griem [8] has proposed that plasma effects on the line shapes might differentially affect the J=0-1 transition. It would be interesting to further explore this hypothesis; very little work has been done on the shape of the laser lines. Finally, Peter Hagelstein [26] has suggested that the J=0-1 line is absorbed by a weak transition in a neighboring charge state. This hypothesis is difficult to test; there are many weak lines in the correct spectral range, and their positions are not known exactly. As the anomaly is observed in more elements, however, a series of accidental coincidences becomes less likely.

IV. Conclusions and Discussion

Based on careful simulation of the selenium x-ray laser plasma and detailed comparison with experimental results, some clear distinctions between the J=0-1 transition and the two strong J=2-1 transitions have emerged. The J=0-1 inversion is created almost entirely by the very large 2p-3p $\Delta J=0$ collisional excitation rate from the ground state. The highest gain for this transition occurs before the peak of the optical heating pulse when the plasma is cooler, denser and more neon-like. In contrast, the J=2-1 transitions are populated by dielectronic recombination from fluorine-like ions and cascade from higher excited states, as well as by collisional excitation. The high gain for these transitions occurs at or after the peak of the optical pulse, when the plasma is hotter, less dense, and more fluorine-like. This scenario is reasonably well supported by experimental evidence about the spatial and temporal behavior of the lasing lines, although questions remain about the temperature and ionization balance of the plasma.

We have tested three hypotheses which might explain the J=0 anomaly. The first, that we have neglected some important process which will increase the predicted gains of the J=2-1 lines, has been thoroughly investigated and no previously neglected process has proven to have an effect large enough to explain the J=0 anomaly. The second, that the calculated ground-excited state collisional excitation rate is too large, is contradicted by recent experimental and theoretical evidence. Finally, we estimated the effect of propagation problems neglected by the simulation and found an effect too small to explain the anomaly.

We can suggest several areas where further research may cast light on the J=0 anomaly. First, measurements of ground state populations of the important charge states in the plasma would test our modeling of the ionization balance and allow us to sort out the influence of competing population mechanisms. Experiments using absorption spectroscopy are currently being planned at LLNL. Further experiments to determine the electron temperature would allow us to explain the discrepancy between theory and experiment, and to determine the significance of these results for the selenium x-ray laser plasma.

Second, further investigation of the apparent scaling of the J=0 anomaly with Z would be most fruitful. We must decide whether the differences between low and high Z elements are due to different experimental conditions by doing a careful set of measurements on a set of overlapping elements. Then further theoretical work will be necessary to track down the source of any remaining variation with Z.

Finally, further investigation of propagation issues is necessary. More work on the temporal and spatial extent of the laser action would tell us whether our theoretical predictions are correct. Some investigation of the shape of the laser lines, and the possible effects of turbulence in the plasma would also be useful.

Acknowledgements

References

*   Present Address: Physics Department, Colorado College, Colorado Springs, CO 80903.

**   Present Address: Hughes Aircraft, P.O. Box 92426, Los Angeles, CA 90009.

1. A.N. Zherikhin, K.N. Koshelev, and V.S. Letokhov, Kvantovaya Elektron. (Moscow) 3, 152 (1976) [Sov. J. Quant. Electron. 6, 82 (1976)].
2. D.L. Matthews, et al., Phys. Rev. Letters, 54, 110 (1985).
3. M.D. Rosen, et al., Phys. Rev. Letters, 54, 106 (1985).
4. A.V. Vinogradov and V.N. Shlyaptsev, Sov. J. Quantum Elec. 10, 754 (1980); and references within.
5. U. Feldman, A.K. Bhatia, and S. Suckewer, J. Appl. Phys. 54, 2188 (1983); U. Feldman, J.F. Seely, and A.K. Bhatia, J. Appl. Phys. 56, 2475 (1984).
6. J.P. Apruzese, J. Davis, M. Blaha, P.C. Kepple, and V.L. Jacobs, Phys. Rev. Letters 55, 1877 (1985).
7. B.L. Whitten, A.U. Hazi, M.H. Chen, and P.L. Hagelstein, Phys. Rev. A 33, 2171 (1986).
8. H. Griem, Phys. Rev. A 33, 3580 (1986).
9. P.L. Hagelstein, M.D. Rosen, and V.L. Jacobs, Phys. Rev. A 34, 1931 (1986).
10. W.H. Goldstein, B.L. Whitten, A.U. Hazi, and M.H. Chen, Phys. Rev. A 36, 3607 (1987).
11. B.J. MacGowan, et al., J. Appl. Phys. 61, 5243 (1987).
12. M.D. Rosen, et al., in Atomic Processes in Plasmas, Santa Fe, NM, 1987, AIP Conference Proceedings #168, A. Hauer and A. Merts, Eds. (AIP, New York, 1988), p. 102. NOTE: The numbers quoted here supercede those published, due to a change in the calculation to reflect the thickness of the target actually used in gain measurements.
13. T.N. Lee, E.A. McLean, and R.C. Elton, Phys. Rev. Letters 59, 1185 (1987).
14. T.N. Lee, E.A. McLean, J.A. Stamper, H.R. Griem, and C.K. Manka, Bull. APS 33, 1920 (1988).
15. C.J. Keane, J.L. Bourgade, M. Louis-Jacquet, et al., manuscript in preparation.
16. A.L. Osterheld and C.Cerjan, Bull. APS 33, 1042 (1988).
17. G. Charatis, Gar. E. Busch, C.L. Shepard, and M.D. Rosen, in Laser Interaction and Related Plasma Phenomena, H. Hora and G.H. Miley, Eds. (Plenum Press, New York, 1986), p. 67.
18. B.K.F. Young, R.E. Stewart, and Gar. E. Busch, C.J. Cerjan, and G. Charatis, Phys. Rev. Letters 61, 2851 (1988).
19. R.E. Turner et al., Phys. Rev. Letters 54, 189 (1985); Whelan, et al., Bull. APS 31, 1553 (1987).
20. G.P. Gupta, A.E. Kingston, and K.A. Berrington, J. Phys. B 20, (1987).
21. R.E. Marrs, M.A. Levine, D.A. Knapp, and J.R. Henderson, Phys. Rev. Letters 60, 1715 (1988).
22. M.D. Rosen, et al., Phys. Rev. Letters 59, 2283 (1987).
23. D.A. Whelan, et al., Proc. SPIE 831, 275 (1988).
24. J.P. Apruzese, Naval Research Laboratory, private communication.
25. M.D. Rosen and P.L. Hagelstein, in Short Wavelength Coherent Radiation Generation and Applications, Monterey, CA, 1986, AIP Conference Proceedings #147, D.T. Attwood and J. Bokor, Eds. (AIP, New York, 1986), p. 110.
26. P.L. Hagelstein, Phys. Rev. A 34, 924 (1986).

EXPERIMENTS TO DEMONSTRATE SODIUM/NEON RESONANT PHOTOPUMPING

F.C. Young, V.E. Scherrer, and S.J. Stephanakis

Naval Research Laboratory
Washington, DC 20375-5000

D.D. Hinshelwood and P.J. Goodrich

JAYCOR
Vienna, Virginia 22180

G. Mehlman and D.A. Newman

Sachs-Freeman Associates, Inc.
Landover, Maryland 20785

B.L. Welch

University of Maryland
College Park, Maryland 20742

Abstract

Resonant photopumping of heliumlike neon by heliumlike sodium is being investigated in order to extend this pumping technique to the soft x-ray regime. More than 30 GW of sodium pump x-rays, concentrated in a resonance line at 11 Å, has been produced by imploding a sodium fluoride plasma with a peak current of 1 MA from a pulsed-power generator. A separate neon plasma, created 5 cm from the sodium pump, has been improved in uniformity recently by using a mini-nozzle to collimate the neon gas puff prior to implosion with a 150-kA current pulse. Fluorescence has been observed by comparing spectral measurements of K-shell x-rays from the neon with and without the sodium pump. Three different null tests, replacing the sodium with magnesium, replacing the neon with argon, and mistiming the sodium and neon implosions, all indicate that fluorescence is observed only if the sodium pump and the neon plasma are present and the implosions are coincident in time.

1. Introduction

Resonant photopumping is a promising approach to produce x-ray lasing in a plasma. Selective excitation with line radiation which is nearly coincident with the excitation energy of a specific level in an ionic species is used to create a population inversion. Lasing has been observed with this technique at wavelengths as short as 2163 Å.[1] A large number of line coincidences between pairs of ions have been proposed to extend this pumping technique to shorter wavelength. However, the Na X and Ne IX combination, identified in one of the earliest proposals for x-ray lasing,[2] is still most attractive because the exceedingly good Na-Ne line coincidence (2 parts in 10^4) leads to efficient coupling of the sodium pump radiation to the neon lasant. Also, the heliumlike ionic stages of sodium and neon persist over a reasonably wide temperature range. The plasma conditions required for this lasing scheme have been analyzed extensively.[3] The present experiments are directed at using pulsed power to achieve lasing with the Na-Ne system. This approach offers the potential of high efficiency ($\sim 10^{-3}$) with Joules of energy emitted in the lasing radiation.[4]

The theory of Na/Ne resonant photopumping with pulsed power was described at the LASERS '87 Conference.[5] Preliminary experimental results indicative of fluorescence have been reported,[6] but several important questions remained unanswered. Some of these questions are addressed in this report of new experimental results. First, the Na/Ne photopumping experiment on the Gamble II generator at the Naval Research Laboratory (NRL) is described briefly. Recent developments which have improved the sodium pump power are summarized. Measurements are presented which indicate that a more uniform neon plasma is created by using a supersonic mini-nozzle to collimate the neon gas puff. Finally, the results of experiments with these improvements are used to confirm that photopumping with x-rays from a sodium plasma has produced fluorescence of the neon plasma.

2. Experimental Conditions

Sodium and neon are used for this experiment because there is a natural line coincidence between the n=2 to n=1 transition in heliumlike sodium (Na X) and the n=4 to n=1 transition in heliumlike Ne (Ne IX). This 11-Å radiation from Na X can resonantly populate the n=4 level of Ne IX with the potential for lasing on the 4-3, 4-2, and 3-2 transitions at wavelengths of 230 Å, 58 Å, and 82 Å, respectively. In this experiment, we do not look at these potential lasing transitions, but at transitions in the range from 9 to 14 Å from the n=2, 3, 4,... levels of Ne IX to the ground state. Requirements on the properties of the sodium and neon plasmas have been described in Ref. 6. To maximize the pump-line power, a hot dense sodium plasma (~ 300 eV, $\sim 10^{20}$ ions/cm^3) is used. To keep the neon plasma primarily in the heliumlike ground state for photopumping, a cooler plasma (50-100 eV) is
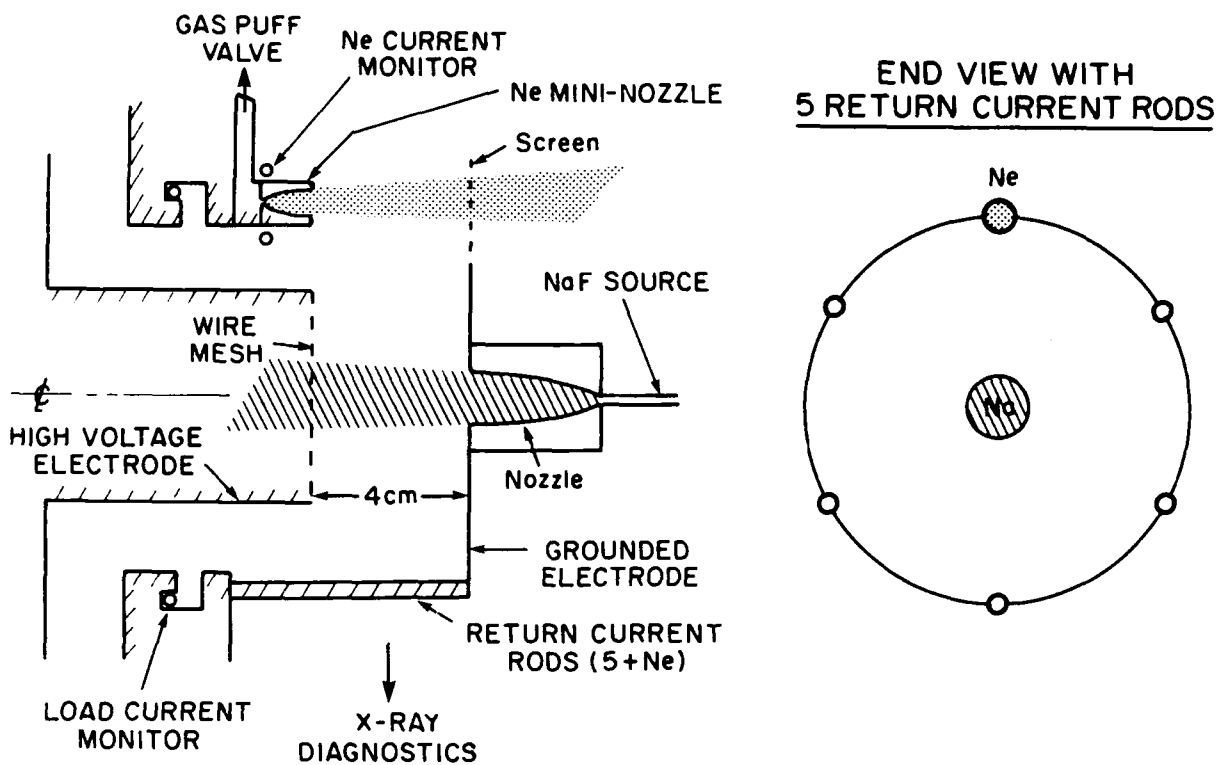
Figure 1. Arrangement of the NaF capillary-discharge source and the neon gas puff in the diode region of Gamble II. The diode geometry is cylindrical with the generator to the left. The NaF is on axis and the neon is in a return-current path.

required. The neon density must be large enough to provide detectable output, but small enough to avoid radiation trapping ($\sim 10^{18}$ ions/cm^3). These plasma conditions are so different that two separate plasmas are required.

These two plasmas are formed by Z-pinch implosions in the diode region of the Gamble II pulsed-power generator as shown in Figure 1. A sodium fluoride (NaF) plasma from a capillary discharge is injected across the 4-cm diode gap. A current of up to 1 MA is conducted from the high voltage electrode through this plasma and back to ground through six return-current paths. One of the return-current paths consists of a neon gas puff, and about 150 kA is conducted by the neon plasma. The NaF plasma is imploded to produce the 11-Å pump x-rays, and the neon is imploded weakly to produce a heliumlike neon plasma. X-rays from these two plasmas are recorded at 90 degrees to the axis of the generator; the NaF plasma is viewed through gaps in the return-current rods.

Three types of x-ray detectors are used to diagnose these two plasmas: time-integrated pinhole cameras, a time-integrated KAP curved crystal spectrograph, and filtered vacuum x-ray diodes (XRD's) for time resolution. For the sodium plasma, x-ray emissions from Na X and Na XI are recorded. Pinhole-camera images give the size of the plasma, and the crystal spectrum provides the ionization stage distribution and energy in the pump line. The density and temperature of the imploded sodium can be adjusted so that the n=2 to 1 pump line (He-α) is the most intense sodium line in the spectrum.[6] Two XRD's with different cathodes and filters are used to measure the total sodium K-shell emission and the He-α pump power.[6] For the neon plasma, both K-shell and L-shell x-ray pinhole-camera images are recorded, but only K-shell x-ray spectra. The neon x-ray emission is so weak that only the L-shell x-rays are time-resolved with an appropriately filtered XRD.[6]

3. Sodium Pump Improvements

The sodium pump radiation is produced by the implosion of a NaF plasma from a capillary discharge.[7] A peak power of up to 25 GW in the sodium He-α line has been reported previously for implosions driven by a peak current of 1.2 MA from the Gamble II generator.[8] In the initial photopumping experiment,[6] the pump power was no more than 10 to 15 GW probably because the current driving the implosion was only 1.0 MA. During the past year, this power has been more than doubled by making the following improvements. Both the initial radius and the linear mass density of the NaF plasma were adjusted to provide a better match to the Gamble-II driving current and to match the implosion time of the sodium to the implosion time of the neon. The initial radius was changed by adjusting the exit diameter of the capillary nozzle. The linear mass density was changed by adjusting the

99
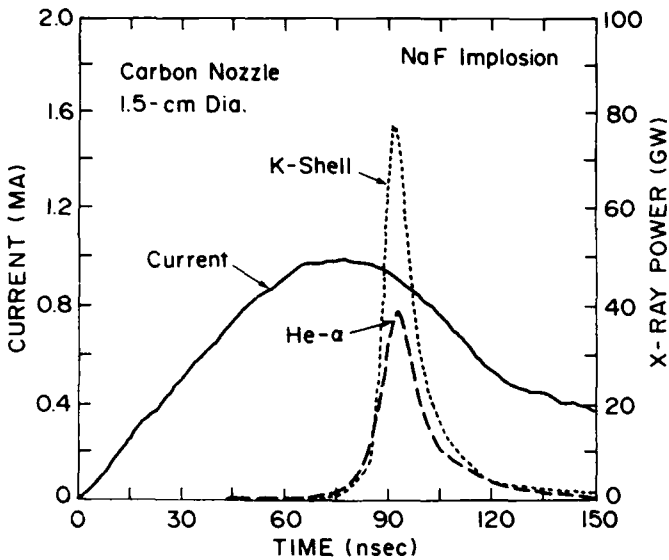
Figure 2. Driving-current and x-ray traces for a NaF implosion on Gamble II. The K-shell trace is the total sodium K-shell power, and the He-α trace is the power in the sodium He-α line.

Figure 4. Spectrum of neon K-shell x-ray emission from an implosion driven by a 150-kA peak-current pulse. Spectral lines from heliumlike and hydrogenlike neon are identified.

current through the capillary discharge. Finally, the nozzle was changed from brass to carbon to minimize higher-atomic-number impurities in the plasma. The results of our best shot with a 1-MA current pulse are shown in Figure 2. The peak power of 39 GW in the He-α line is about one-half of the total K-shell power. The total energy in this He-α trace is about 700 J. These results were achieved with a 1.5-cm exit-diameter carbon nozzle.

4. Neon Plasma Conditions

Now we turn our attention to the formation of the neon plasma. In the initial experiment,[6] the neon gas puff was coupled to a guide tube instead of a supersonic mini-nozzle. The flow of neon from the nozzle and from the guide tube was studied by using visible-light photography of neon excited with a glow discharge. Photographs taken for the same glow-discharge voltage and gas-puff pressure are compared in Figure 3a. Clearly, a less divergent mass distribution is produced with the nozzle. Neon L-shell x-ray pinhole-camera images from implosions of these two plasmas in the return-current geometry on Gamble II are compared in Figure 3b. With the guide tube, the imploded plasma does not fill the 4-cm diode gap, while emission across the entire gap occurs with the nozzle. The x-ray image with the nozzle in Figure 3b contains an over-exposed central core which includes neon K-shell emission. An image of only neon K-shell emission is presented in Figure 5a. This K-shell emission extends nearly across the entire 4-cm diode gap but is most intense near the nozzle. These neon pinhole-camera images were recorded with a short circuit on axis in place of the NaF plasma, as shown in Figure 5a. For this setup, the neon gas was preionized with a UV source before the generator was discharged.

The radial displacement of the imploded neon in Figure 3 is a consequence of forces on the neon due to magnetic fields produced primarily by the currents in the neon and sodium plasmas. The plasma should implode along the locus where the total magnetic field is zero. For the plasma from the guide tube, the neon self-magnetic field decreases rapidly as the plasma diverges from the tube. As this self-field decreases, the magnetic null occurs at larger radii from the axis of the generator. If the self field is too small to form a magnetic null, no implosion is observed. For the plasma from the nozzle, the neon self-field is more nearly constant along the plasma column so that a magnetic null exists along the entire 4-cm gap where the implosion occurs. This scenario is consistent with the x-ray images recorded for the guide tube and for the nozzle in Figure 3b.

K-shell x-ray spectra of the neon plasma (see Figure 4) indicate that there is very little Ne X emission and that the Ne IX emission is small. The spectrum in Figure 4 suggests that the neon has been heated to the Ne IX stage with a dominant Ne IX ground-state population as required for photopumping. The intensity scale for this spectrum is two orders-of-magnitude smaller than for similar spectra of the sodium pump plasma.[6] Fortunately, the spectrograph can be aligned on the neon source and shielded from the sodium source. For photopumping experiments, we focus on the relative intensity of the β- and γ-lines of Ne IX corresponding to the n=3 to 1 and n=4 to 1 transitions, respectively. The γ/β ratio is about 0.6 for the spectrum in Figure 4.
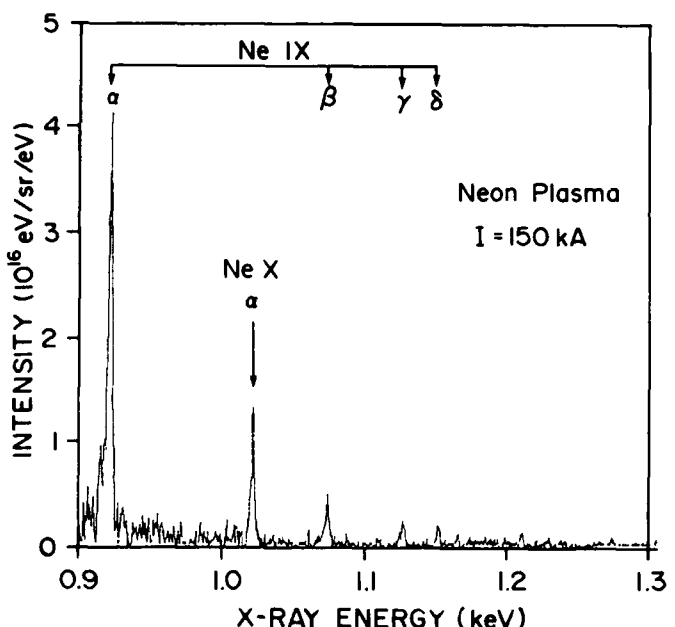
(a) VISIBLE LIGHT IMAGES
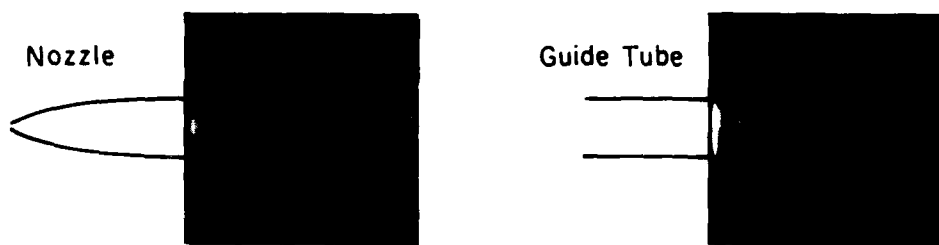
Nozzle

Guide Tube

(b) NEON L-SHELL X-RAY IMAGES

Nozzle

Guide Tube

Figure 3. Images of neon from the gas puff coupled to either a mini-nozzle or a guide tube. (a) Visible-light images before implosion. (b) L-shell x-ray images of imploded neon. A transmitting screen is located 4 cm from the nozzle or guide tube.
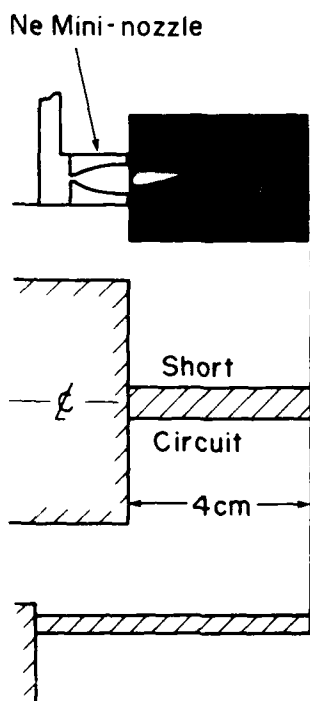
(a) Ne K-SHELL X-RAY IMAGE   (b) Na and Ne K-SHELL X-RAY IMAGES

Ne Mini-nozzle

Ne Mini-nozzle

Screen

Short

Circuit

Wire
Mesh

NaF Source

4cm

4cm

Nozzle

Grounded
Electrode
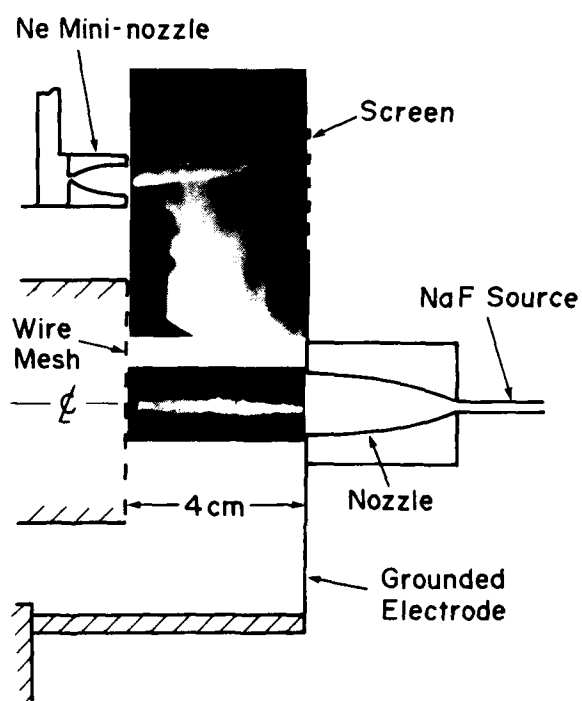
Figure 5. K-shell x-ray images of neon and NaF implosions superimposed across the diode gap of Gamble II. (a) Short circuit on axis and (b) NaF capillary plasma on axis.

5. Photopumping Studies

Now the sodium and neon plasmas are combined for photopumping experiments. K-shell pinhole-camera images of these two plasmas are presented in Figure 5b. X-rays from the sodium plasma are imaged through a 0.1-mm diameter pinhole, while the pinhole for the less intense radiation from the neon plasma has a 1-mm diameter. Comparison of the neon image in Figure 5b with that in Figure 5a suggests that emission from some sodium plasma which has expanded into the region of the neon plasma is superimposed on the neon image. These are time-integrated images. Time-resolved measurements with an XRD, designed to record x-rays from the neon plasma, indicate that some x-rays are emitted from the region of the neon plasma several hundred nanoseconds after the neon has imploded. This emission is attributed to sodium which has expanded into the region of the neon late in time.

The current and XRD traces for three shots with both sodium and neon implosions are presented in Figure 6. For the sodium implosions, the driving current and He-α pump power are presented. For the neon implosions, the driving current and the L-shell x-ray emission are presented. For shot 4238, the sodium pump precedes the neon implosion - as measured by the neon L-shell x-ray emission. The peak pump power is only 17 GW because the sodium implodes before peak current. For shot 4236, the pump power is 30 GW and coincides with the neon implosion. For shot 4237, the sodium pump peaks at 31 GW slightly after the peak of the neon emission. The duration of the neon x-ray emission in these shots is attributed partly to zippering as the neon implodes first at the nozzle exit and later in time farther from the nozzle.
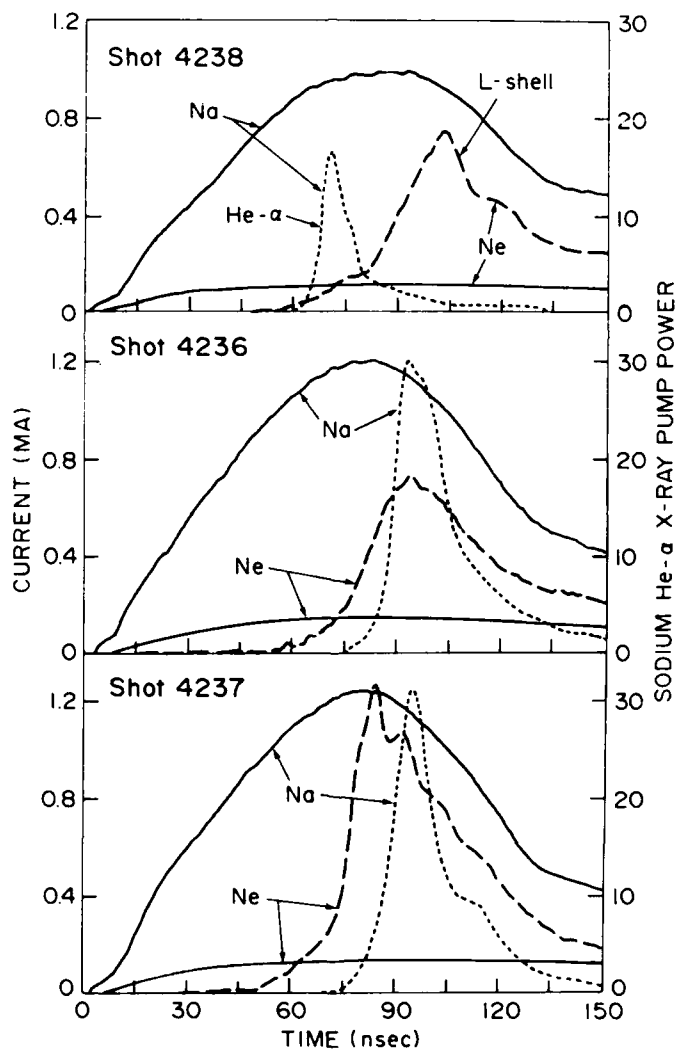
Figure 6. Current and x-ray traces for three shots with both sodium and neon implosions. The solid curves are current traces. The short-dash curves are the sodium He-α x-ray power. The long-dash curves are the neon L-shell x-ray emission.

102

Neon K-shell x-ray spectra were measured for these three shots, and the spectrum for shot 4236 is shown in Figure 7a. The sodium nozzle is located at the top of the spectrum and the neon mini-nozzle is at the bottom. There is an x-ray background probably due to scattered radiation from the intense sodium source, which increases from left-to-right on the film. Despite this background, the α-, β-, and γ-lines of Ne IX are clearly observed. Also, lines associated with Ne X are observed in these spectra. The spectrum for shot 4236 is compared in Figure 7b with the spectrum for a shot where the NaF was replaced with MgF_2. For this shot, the timing of the magnesium and neon implosions was similar to that for shot 4237 (see Figure 6). The γ-line appears weaker than the β-line in Figure 7b, while the γ-line is comparable to the β-line in Figure 7a. Above, but near the γ-line in Figure 7a, is an extended region of sodium x-rays emitted from sodium plasma which has expanded across the field-of-view of the spectrometer late in time. This extended source is imaged as a broad feature on the film. This extended region of x-rays is shifted to higher energy, as expected, when the sodium is replaced by magnesium.
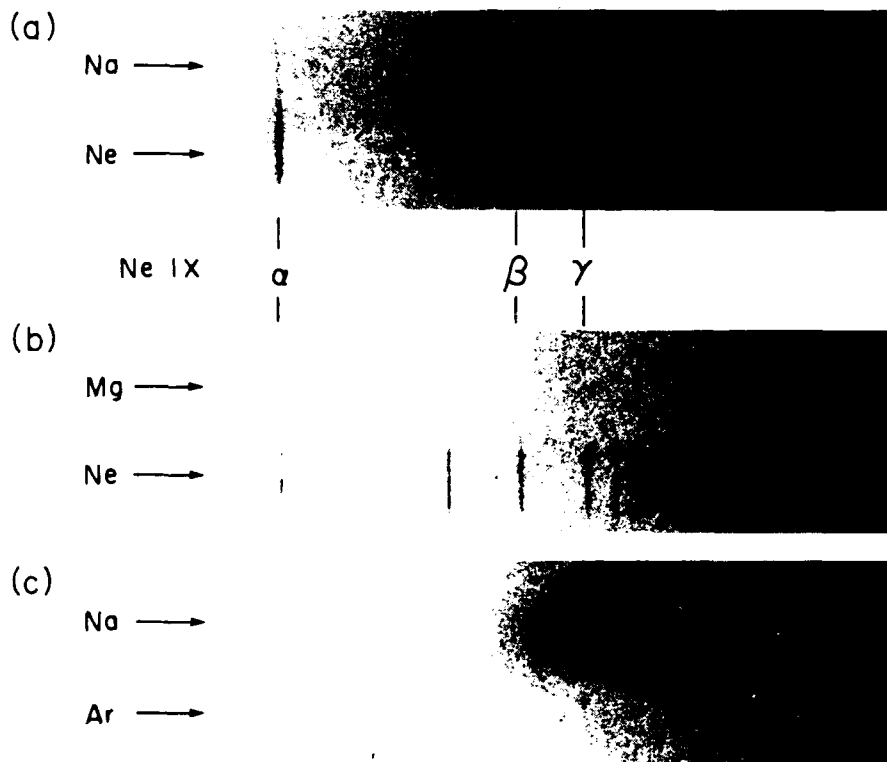
Figure 7. Film record of neon K-shell x-ray spectra (a) for shot 4236 in Figure 6, (b) for a shot with MgF_2 in place of NaF, and (3) for a shot with argon in place of neon. The locations of the α-, β-, and γ-lines of heliumlike neon are identified.

In a preliminary analysis of the neon spectra, the ratio of the intensities of the γ- and β-lines of Ne IX was determined for the three shots in Figure 6 and for the shot with MgF_2 in place of NaF. The results are plotted against the difference in the implosion times of the two plasmas in Figure 8. The vertical error bars are primarily due to uncertainties in background subtractions. The horizontal error bars are from uncertainties in the times of peak x-ray emission. The γ/β ratio is 50% larger when the sodium pump is coincident with the neon implosion. No enhancement is observed when the sodium is replaced by magnesium or when the sodium pump occurs before the neon has imploded. For comparison, the γ/β ratio is about 0.6 for the neon spectrum in Figure 4 where the NaF was replaced with a short circuit on axis.

A spectrum was measured with the neon replaced by argon to test for intermixing of the neon and sodium plasmas. This spectrum is shown in Figure 7c. None of the lines associated with neon are observed when argon is used. The extended region of sodium emission is observed, but there is no evidence for 11-Å Na X emission at the spectral location of the γ-line of Ne IX. Clearly, the enhancement of the γ-line is not due to sodium intermixing with the neon (or argon) before or during the implosion. The sodium (or magnesium) emission observed is a late-time occurrence in these time-integrated spectra.
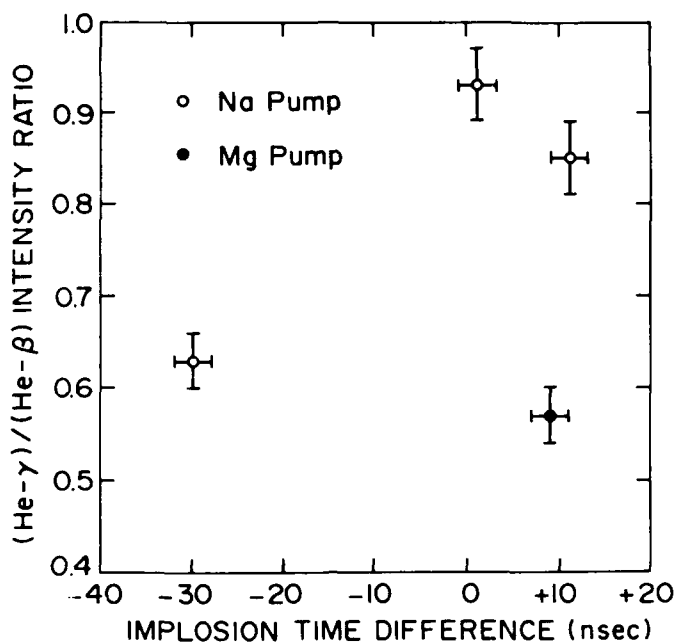
Figure 8. Ne IX line intensity ratios, γ/β, for the three shots in Figure 6 (open circles) and for the shot with MgF_2 in place of NaF (solid circle).

6. Summary

A sodium pump power of more than 30 GW has been produced by imploding a NaF plasma with a driving current of 1 MA. For lasing experiments, it is estimated that a pump power exceeding 200 GW is required for a sodium-neon separation of 5 cm.[6] To achieve this power, driving currents of 2 to 3 MA from a larger generator can be used. The x-ray yield increases rapidly with driving current; a fourth power scaling of K-shell yield with current has been reported for neon gas-puff implosions.[9] For this scaling, a NaF implosion driven by a peak current of only 1.7 MA should produce more than 200 GW. For a more conservative quadratic scaling (based on generator-to-load energy coupling), a peak current of 2.6 MA is required to produce more than 200 GW. Currents of either magnitude are available on existing pulsed-power generators. To match the implosion to the increased driving current, the mass per unit length of the NaF plasma from the capillary discharge must be increased. Measurements on Gamble II suggest that the mass can be increased by driving more current through the capillary source.

The neon plasma uniformity has been improved by using a mini-nozzle to collimate the gas puff before implosion. Ionization of the neon into the heliumlike stage is observed, but some detailed properties of the neon, such as the density and temperature, are not known. An extensive analysis of the neon spectra is planned in order to determine these properties and to quantify the absorption of the sodium pump radiation by the neon plasma. In addition, more work is needed to measure and optimize the conditions of the neon plasma for lasing experiments.

Fluorescence of the neon has been observed with a 30-GW pump source. Three different null tests; replacing the sodium with magnesium, replacing the neon with argon, and mis-timing the sodium and neon implosions, all indicate that fluorescence is observed only if the sodium pump and the neon plasma are present and the implosions are coincident in time.

7. Acknowledgements

8. References

1. N. Qi and M. Krishnan, Phys. Rev. Lett. 59, 2051 (1987).
2. A. V. Vinogradov, I. I. Sobelman, and E. A. Yukov, Sov. J. Quantum Electron. 5, 63 (1975).
3. J. P. Apruzese, J. Davis, and K. G. Whitney, J. Appl. Phys. 53, 4020 (1982); and J. P. Apruzese and J. Davis, Phys. Rev. A 31, 2976 (1985).
4. J. P. Apruzese, G. Mehlman, J. Davis, J. E. Rogerson, V. E. Scherrer, S. J. Stephanakis, P. F. Ottinger, and F. C. Young, Phys. Rev. A 35, 4896 (1987).
5. J. P. Apruzese, P. G. Burkhalter, G. Cooperstein, J. Davis, D. Mosher, P. F. Ottinger, J. E. Rogerson, S. J. Stephanakis, V. E. Scherrer, J. W. Thornhill, and F. C. Young, in Proceedings, International Conference on LASERS '87, F. J. Duarte, Ed. (STS Press, McLean, VA 1988), pp. 37-43.
6. S. J. Stephanakis, J. P. Apruzese, P. G. Burkhalter, G. Cooperstein, J. Davis, D. D. Hinshelwood, G. Mehlman, D. Mosher, P. F. Ottinger, V. E. Scherrer, J. W. Thornhill, B. L. Welch, and F. C. Young, IEEE Trans. Plasma Sci. 16, 472 (1988).
7. B. L. Welch, F. C. Young, R. J. Commisso, D. D. Hinshelwood, D. Mosher, and B. V. Weber (to be published in J. Appl. Phys., March, 1989).
8. F. C. Young, S. J. Stephanakis, V. E. Scherrer, B. L. Welch, G. Mehlman, P. G. Burkhalter, and J. P. Apruzese, Appl. Phys. Lett. 50, 1053 (1987).
9. S. J. Stephanakis, J. P. Apruzese, P. G. Burkhalter, J. Davis, R. A. Meger, S. W. McDonald, G. Mehlman, P. F. Ottinger, and F. C. Young, Appl. Phys. Lett. 48, 829 (1986).

A LASER PLASMA X-RAY SOURCE FOR MICROSCOPY STUDIES

N.H.Rizvi, R.J.Rosser
Rutherford Appleton Laboratory
Chilton, Didcot
Oxon. OX11 0QX
England

C.B.Hills
Department of Physics
King's College
University of London
England

A.D.Stead, T.W.Ford
Department of Botany
Royal Holloway and Bedford College
Egham, Surrey
England

Abstract

A new facility for generating laser plasma X-rays at the Rutherford Appleton Laboratory is described. Initial results are presented where the angular distribution of X-rays from an aluminium plasma is found to follow a cosine function. Contact images of diatoms obtained with a X-ray flux of $54mJ/cm^2$ at the specimen are presented.

Introduction

There has been interest for many years in using X-rays in the 2.2-4.4nm wavelength region - the so-called "water window" - for studying biological specimens. This has been due to the natural contrast offered by hydrated samples arising from the markedly different absorption coefficients of protein and water in this region, as shown in Fig.1.
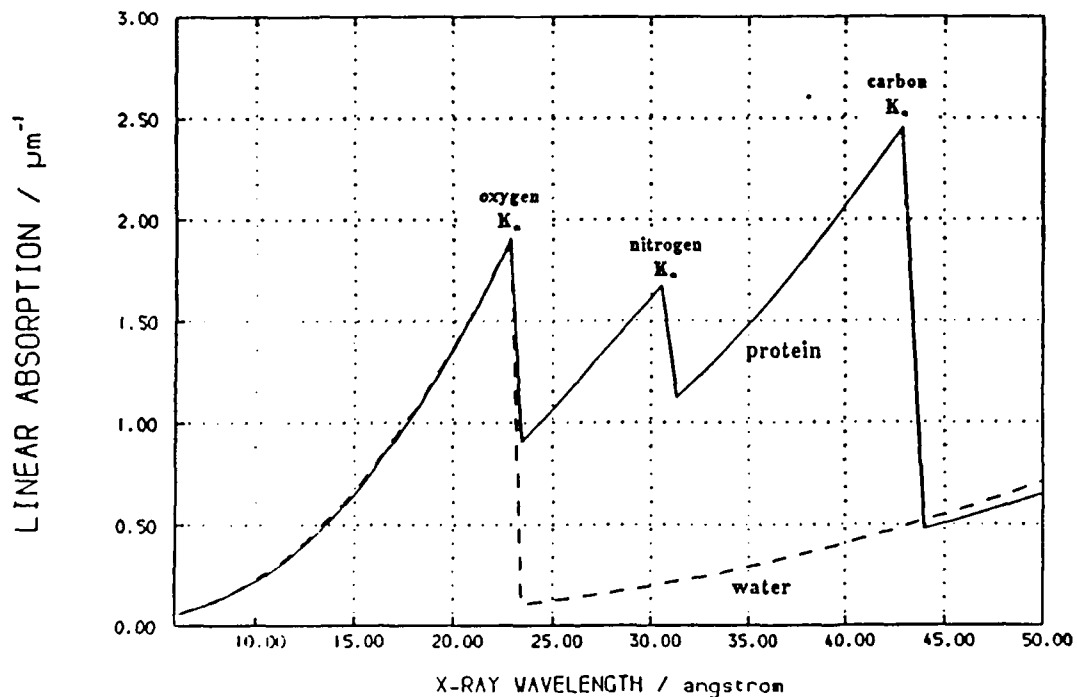
Fig.1   The Soft X-Ray "Water Window"

The first image of a living cell was recorded by Feder and co-workers[1] in 1984. Since then, X-ray microscopy work has continued using a variety of sources such as gas-puff z-pinches, synchrotrons and laser-produced plasmas. One of the main advantages of laser produced plasmas is that their single pulse peak X-ray brightness can exceed that of synchrotrons by many orders of magnitude[2]. This allows full exposures to be made with single shots on nanosecond timescales or less. This time is short enough for any damage to the specimen not to manifest itself even though the X-ray dose may ultimately prove fatal. Hence the image is recorded with the sample in its natural state.

X-ray microscopy studies have been performed for several years at the Rutherford Appleton Laboratory[3] using the high power VULCAN glass laser. These have been successful in obtaining good quality images aswell as exploring the techniques involved in contact microscopy.

VULCAN Glass Laser

VULCAN is a seven-beam glass laser system with two synchronised Nd:YLF oscillators operating at a wavelength of 1053nm. The amplifying chain consists of a series of phosphate glass rod and disk amplifiers. The parameters of VULCAN are listed below in Table 1.

Six Beams	1800J/1ns
	500J/100ps
Single Beam	300J/1ns
	80J/100ps
Pulse Lengths	70 - 500 ps
	and
	0.7 - 25 ns
Wavelengths	1053nm
	527nm (at 50% energy)
	315nm (at 50% energy)
Repetition Rate	20 minutes

Table 1   Laser Output Parameters

Full power laser shots may be fired every 20 minutes, this time being governed by the cooling requirements of the disk amplifiers. In previous work when full power shots were used for the microscopy studies, this long wait between shots and the unavoidable conflict for laser time from other users of the facility meant both a low duty cycle for exposures and an uncertainty in predicting when the next shot would occur. Hence there was a likelihood that a wet specimen might either dehydrate or change state in some fashion in the time between loading and making the exposure.

The new facility that has been commissioned avoids this problem. This target area (called TA4) does not use full power shots but is serviced by just the rod amplifiers. This allows a two minute shot cycle to be operated into the area yet still permitting about 20J of infra-red energy to be delivered in pulses of 1-10ns. Shorter pulses of 100ps duration may alternatively be used if desired. By using the laser in this way, minimum disruption is caused to the other users of VULCAN while maintaining a high repetition rate of exposures.

The Target Chamber

The TA4 target chamber was specifically designed for the area and incorporates some features to aid the microscopist. The 160litre vessel is pumped with an Edwards turbomolecular pump to obtain rapid pumping times and to maintain an oil-vapour-free environment inside the chamber. This avoids contaminating sensitive components like the silicon nitride windows which are used inside.

The target can be remotely moved in x, y or z from outside the chamber. This allows a fresh target to be chosen for each shot. There is also a vacuum feedthrough device which can insert specimens into the vessel without the need to let the chamber up to atmosphere. The source to specimen distance may also be varied using this device on each shot.

The specimen holders (shown in Fig.2) contain the X-ray-sensitive photoresist in contact with the sample with a 100nm thick silicon nitride entrant window for the X-rays. These windows have a transmission of about 70% in the X-ray region of study. These windows can withstand pressure differences of 1 atmosphere.
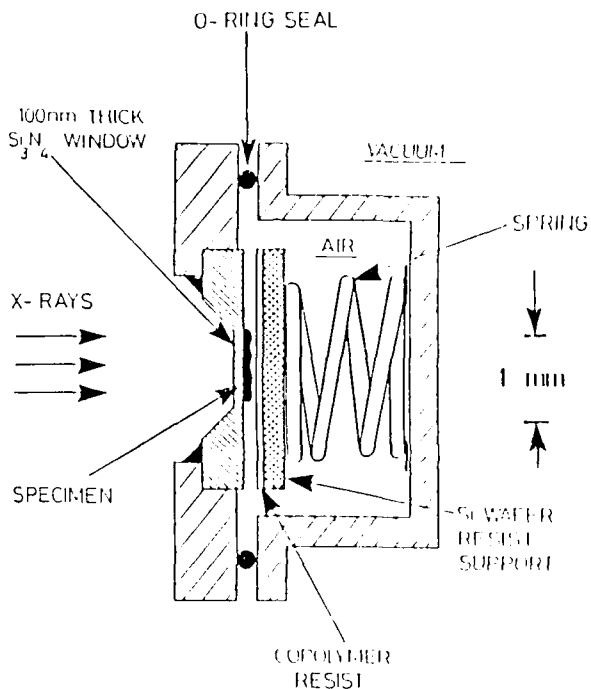
Fig. 2   Specimen Holder

There is also the facility for using a grazing-incidence, toroidal X-ray focussing optic (shown in Fig.3). This is useful as it collects a larger flux of X-rays, focusses them onto the specimen and eliminates the problem of target debris from damaging the silicon nitride window by allowing the specimen holder to be distant from the source. The grazing incidence use of the toroid also allows harder X-rays to be eliminated.
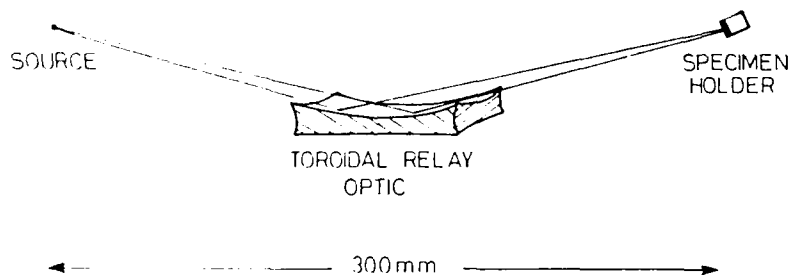
Fig.3   X-ray Focussing Element

The laser is focussed onto target using a 17cm focal length, f/4.25, BK-7 glass plano-convex lens. Typical focal spot sizes range from 70-100μm in diameter, thus allowing intensities of 10^{13} W/cm^2 or more on target. Laser light at the fundamental wavelength of 1053nm is currently used but there are plans to frequency double the light to 527nm, thus obtaining a better conversion efficiency into X-rays.

Angular Distribution of X-Rays

In the experiment to measure the source distribution, a solid aluminium target was positioned normal to the laser beam (see Fig.4). Two X-ray sensitive Si PIN diodes were used and these could be placed at different angles around the target.
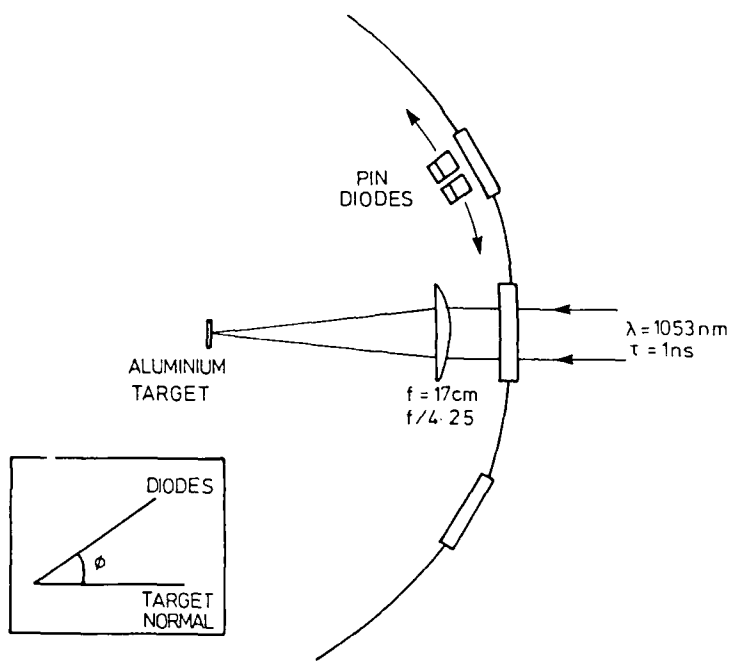
Fig.4   Experimental Arrangement for Source Distribution Measurement

One diode was filtered with 25um of berylium and the other with 0.5um of vanadium. Since 25μm Be transmits hard X-rays (λ<2nm) and 0.5μm V transmits hard X-rays plus a content in the region 2-8nm, comparison of the signals from the two diodes allows an estimate of the soft X-ray flux for that particular angle. These measurements were taken at angles above and below the target normal (±∅). A number of shots were taken for each angle and the results averaged. The results are plotted in Fig.5.
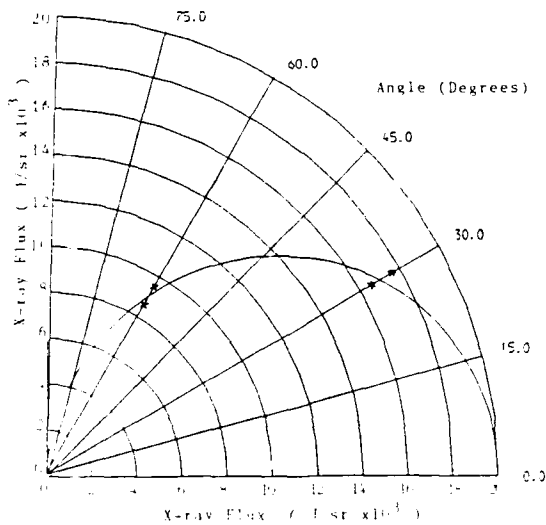
Fig.5   Angular Distribution from an Aluminium Plasma

Typical energies of one joule were used for these measurements (the energy was limited by experimental constraints on the laser). It was found that the flux was too small for the diode with the Be filter to give an adequate, reproducible signal and so only the readings for the V diode could be meaningfully analysed. Hence the distribution curve is for soft and hard X-rays.

A curve was fitted to the data points. It was assumed that the source was symmetric about the target normal and so $+\emptyset$ and $-\emptyset$ were treated as the same angle. The curve follows a $cosine^n$ function with $n=1.14\pm0.35$.

Imaging of Biological Specimens

To obtain images of some specimens, a gold foil target was placed normal to the laser beam. The specimen holder was positioned at $-30°$ from the target normal at a distance of 18mm. A PIN diode with a 0.5um V filter was placed at $+30°$.

Using 1J of infra-red energy in a 1ns pulse, with intensity on target of $2\times10^{13}W/cm^2$, exposures were made of diatomaceous earth. Diode measurements were taken at the same time which allowed an estimate of the X-ray flux incident on the specimen to be made.

Diatoms were used because they display a range of regular structures and have been previously studied.[4] Diatom images have also been obtained with full power shots from VULCAN so a qualitative comparison could be easily made.

The diatom imag , shown in Fig.6, were recorded without any filtering but with only a 100nm thick silicon nitride window in front of the specimen. It was calculated from the diode measurements that the X-ray flux incident on the specimen was $54mJ/cm^2$.
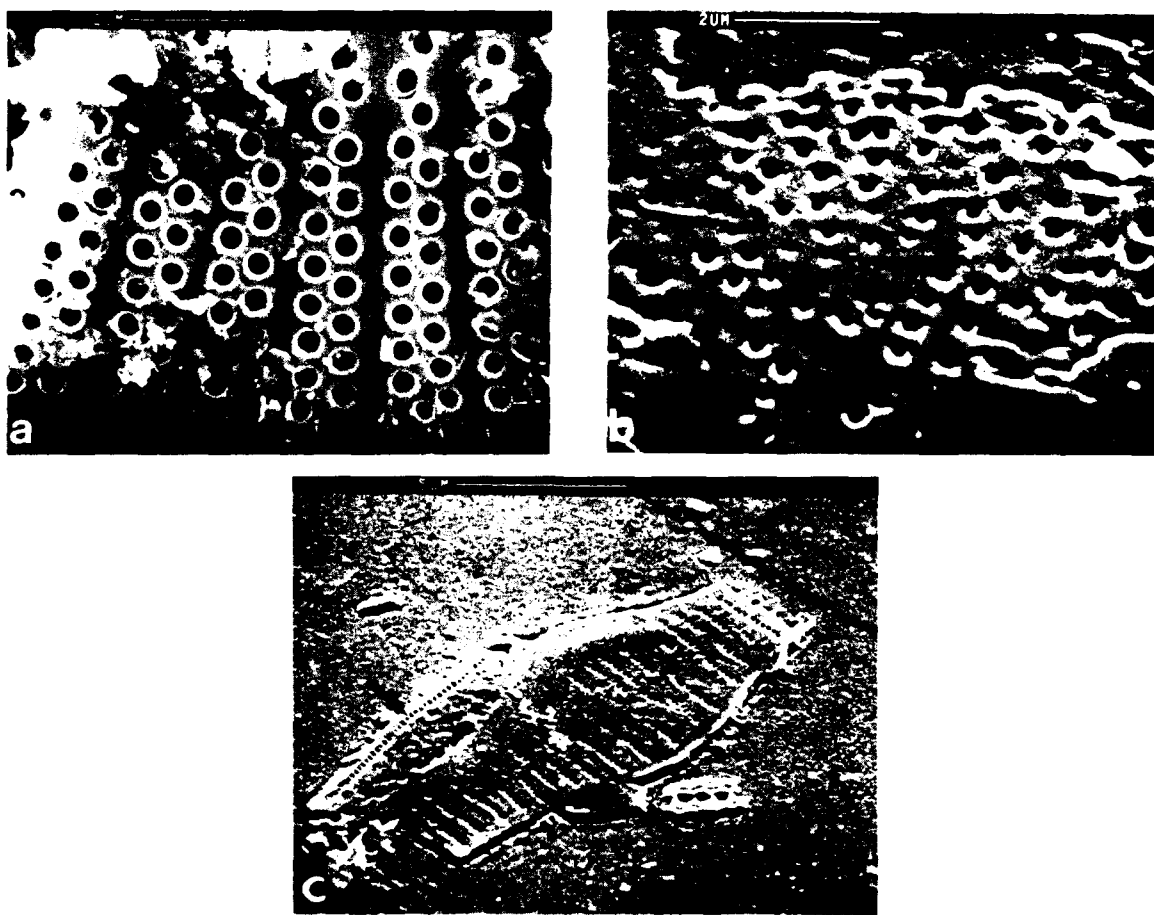
Fig.6   (a) Scanning electron micrograph of developed resist image of part of a
                centric diatom. Holes in frustule are approximately 200nm diameter.
        (b) Scanning electron micrograph of an actual diatom frustule.
        (c) Scanning electron micrograph of developed resist image of the major
                portion of the frustule of a pennate diatom. Also a fragment of
                another frustule (arrow) in which structures of 70nm can be resolved.

The resolution of the frustule in Fig.6(c) is amongst the best yet obtained at the Rutherford Appleton Laboratory.These images compare very well with previous work performed using full power VULCAN shots .

Additional Work

The versatility and ease of use of this target facility has allowed other work to also be performed there. A varied programme has developed which has included the testing and development of new spectrometers, testing of CCD arrays and the measurement of reflectivity of multilayer X-ray mirrors for use in the X-ray laser research program at RAL[5].

This has meant that the area now also plays an important role in supporting the other experimental programmes of the VULCAN laser as well as being available for microscopy research.

Summary

A new target area which has been commissioned for the specific purpose of X-ray microscopy studies has been described. The initial results presented show a cosine distribution of X-rays from an aluminium plasma. Contact images of diatoms have been shown which exhibit sub-100nm resolution and good contrast. These images, taken at 1J energy levels, compare favourably with similar exposures made using full power VULCAN shots. This area can now be routinely used for microscopy purposes with a shot rate of two minutes. Programmes are being instigated that will accurately measure the source distribution from a number of different z elements (Au, Al, C etc.). It is also envisaged that exposures in the future will be accompanied by a value for the X-ray flux aswell as spectral information concerning the source.

Higher energies than those reported here have since been used on target (10J or more) and so better contrast images and more detailed X-ray fluxes may now be recorded.

Acknowledgements

References

1. R.Feder, V.Banton, D.Sayre, J.Costa, M.Baldwin, B.Kim, Science 227, 63 (1984)

2. P.Rumsby, Journal of Microscopy, 138, 3, p245-265 (1985)

3. R.Rosser, K.Baldwin, R.Feder, D.Bassett, A.Cole, R.Eason,
        Journal of Microscopy, 138, 311 (1985)

4. RAL Annual Reprt to Laser Facility Committee 1985, Sec. A4.4

5. M.Grande, B.L.Evans, A.Al-Arab, N.H.Rizvi, Shi Xu, "Assessment of Multilayer Mirror for XUV Laser Use", presented at SPIE conference on X-ray Multilayer Mirrors at San Diego (1988)

Observation of an Ionic Excimer State in RbF

V. T. Gylys, D. G. Harris, T. T. Yang and J. A. Blauer

Rockwell International-Rocketdyne Division
Canoga Park, California 91304

Abstract

The results of an investigation of ionic RbF are presented. Based on analogy with the excimer KrF, calculations were made to estimate the emission wavelength of $Rb^{++}F^-$. Experiments were then carried out to measure the emission spectrum. A laser produced plasma was used to excite RbF. Fluorescence emission was observed at 130 nm and at 160 nm. There are tentatively assigned to the $(B \to X)$ and $(C \to A)$ transitions respectively.

Introduction

Most of the work in the development of lasers operating in the extreme ultraviolet (XUV) and vacuum ultraviolet (VUV) has dealt with core-excited atomic or excited ionic transitions. Recently another approach has been proposed, [1] using excited molecular species such as ionic alkali halide excimers. The ionic alkali halide excimers ($A^{2+}X^-$) are isoelectronic in structure to the well-known rare gas halide excimers (Rg^+X^-) and, are predicted to emit in the vacuum ultraviolet on the $A^{2+}X^- \to A^+X$ transitions. Sauerbrey et al, [1] and Basov [2] have derived theoretical estimates for the interacting potential curves of a number of ionic alkali halides, and from these the corresponding spectroscopic properties of these ionic alkali halide excimers were obtained. The estimated radiative lifetimes are typically near 1 nsec or about an order of magnitude shorter than the conventional rare gas halide systems. The cross sections for stimulated emission were estimated to be of the order of $1 \times 10^{-16} cm^2$. [1]

This paper reports the observation of fluorescence from the $Rb^{2+}F^-$ state at 131 nm using a laser-produced plasma as the excitation source. This emission has been recently reported using ion beam excitation. [3] In this work spectroscopic and time-resolved fluorescence intensity measurements were made. In addition, the dependence of the ionic excimer emission on RbF vapor pressure is reported. Using a Rittner potential[4] for the upper state and a Born-Mayer Potential[5] for the repulsive interation, the emitted wavelength was predicted to be between 115 to 130 nm for the $Rb^{++}F^-$ to Rb^+F transition. The potential curves for the RbF system are shown in Figure 1. Analogous to the rare-gas halide excimers, the emitted continua should also exhibit a fine structure. The strongest emission intensities are due to the $B \to A$ and $C \to A$ transitions.

Experimental Apparatus

In these experiments, a heatpipe cell operated between 850°C and 1050°C was used to produce RbF vapor pressures of several Torr in a buffer gas of He. The heatpipe cell was connected directly to a 1m VUV monochromator. The monochromator was flooded with helium and maintained at the same pressure as the heatpipe. The RbF vapor pressure was controlled by the He buffer gas pressure and the temperature of the heatpipe. [7]

The heatpipe cell used to produce the RbF vapor was built from inconel allowing safe operation of the cell up to 1100°C. It consisted of four arms arranged as shown in Figure 2, each about 28cm long. A fifth arm extended perpendicularly with respect to the plane defined by the four arms shown. Three of the arms are closed with Al_2O_3 windows. The window where the laser was injected was slightly tilted in order to avoid back-reflections into the laser cavity that might damage the output coupler of the amplifier. Visual inspection of the target was possible through both the vertical arm and the arm opposite the monochromator. A tantalum target was mounted on a hollow inconel tube containing an electric heater to prevent condensation. The target rod was rotated by an electric motor to provide a new target surface on successive shots.

The temperature distribution on the outside of the cell was monitored by 25 thermocouples (5 on each arm). The cell was heated by ceramic heaters encased in a block of thermal insulation. A photomultiplier with a sodium salicylate scintillator was used as a detector. The rise-time of this detector was about 5ns. Single-shot, temporally resolved observation of the fluorescence was possible using a 1GHz scope fitted with a digitizing camera system and connected to an IBM-PC.

A plasma was produced by focussing the output of a KrF laser on to a rotating tantalum target located inside the heatpipe cell. The KrF laser provided a 750mJ pulse with a 25ns pulse width at 248nm in a 1.5 x 3cm^2 rectangular mode. For most of the experiments, the laser was operated at a 1-5Hz pulse repetition frequency. The laser beam was focussed by a quartz lens with a focal length of 50cm at 248nm. The spot size in the focus was approximately square with sides less than 100 μm in length. The corresponding power density was approximately 10^{11}Wcm^{-2} in the focus. The soft x-ray radiation emitted from the laser produced plasma propagated into the surrounding RbF vapor, producing inner shell ionized Rb^{++}F$^-$ and hot electrons. The hot electrons may also produce Rb^{++}F$^-$ by direct impact ionization.

Results

The emission spectrum between 100nm and 200nm for an RbF vapor pressure of 2.8 Torr is shown in Figure 4a. The spectum was obtained using the experimental arrangement shown in Figure 3. The monochromator grating was scanned while the PMT signal was recorded on a chart recorder. A box-car integrator with a 50ns gate was employed to eliminate fluorescence due to plasma recombination. For comparison, a background spectrum obtained in a cold cell with 2.8 Torr of helium is shown in Figure 4b. Emission peaks at 121, 131, 157, 160 and 164 are observed. The 121 and 164nm emissions are due to well-known He II transitions. The fluorescence at 157nm is attributed to excited F$_2^*$ emission. The strong peak at 130.4nm is believed to correspond to the B$\rightarrow$X transition in RbF. The estimated wavelength range of 115nm - 130nm seen in Figure 1 is in good agreement with the experimentally observed value. The fluorescence wavelength is also identical within experimental uncertainty to that recently reported by Steigerwald and Langhoff[3] where ion-beam excitation was used.

Interpretation of the peak at 160nm is somewhat complicated because this emission is overlapped by the 157nm F$_2$ and 164nm He II emission peaks. However, it appears that the 160nm emission originates from RbF. With no known lines at this wavelength one can tentatively assign this broadband emission to the C$\rightarrow$A transition. Kr$^+$F$^-$, which is the analogous isoelectronic rare gas halide excimer molecule to RB^{++}F$^-$, has a B$\rightarrow$X transition wavelength of 248nm and a broadband C$\cdot$A transition centered around 285nm. The existence of B$\rightarrow$X and C$\cdot$A transitions in both RbF and KrF may imply that ionic RbF is not only isoelectronic to KrF, but also has a very similar molecular structure. The emission spectrum shown in Figure 4a was not corrected for grating efficiency. When the correction is included, the magnitude of B$\cdot$X is expected to be much higher than that of C$\rightarrow$A.

The time-resolved fluorescence intensity at 130.4nm is shown in Figure 5. The emission exhibits a temporal width of about 38ns. This is about the same observed by Kubodera et al[8] for the ionic C$_s^{++}$F$^-$ excimer transition.

The RbF pressure dependence of the 130.4nm B$\cdot$X and 160nm C$\rightarrow$A fluorescence was also investigated. Results obtained for RbF vapor pressures of 2, 4, and 6 Torr are shown in Figure 6. There was no reduction of the B$\rightarrow$X fluorescence intensity up to the 6 Torr of RbF vapor pressure studied. This suggests that the fluorescence is not significantly influenced by self-absorption of the RbF vapor or by electron quenching between 2 and 6 Torr.

Conclusion

The soft-x-ray apparatus has allowed a survey to be made of the spectroscopic properties of ionic RbF. It is believed that electron beam pumping will more easily demonstrate scalability of this system.

Acknowledgement

References

1. R. Sauerbrey and H. Langhoff, IEEE J. Quantum Electron QE-21, 179 (1985).
2. N. G. Basov, M. G. Voitik, V. S. Zuev, Soviet J. of Quantum Electron 15, 1455 (1985).
3. F. Steigerwald and H. Langhoff, J. Chem. Phys. 88, 7376 (1988).
4. E. S. Rittner, J. Chem. Phys. 19, 1030 (1953).
5. A. A. Abrahamson, Phys. Rev. 178, 76 (1969).
6. T. T. Yang and C. E. Turner, Jr., unpublished (1988).
7. C. R. Vidal and F. B. Haller, Rev. of Scientific Instr. 42, 2779 (1971).
8. S. Kubodera, L. Frey, P. J. Wisoff, and R. Sauerbrey, Opt. Lett. 13, 446 (1988).
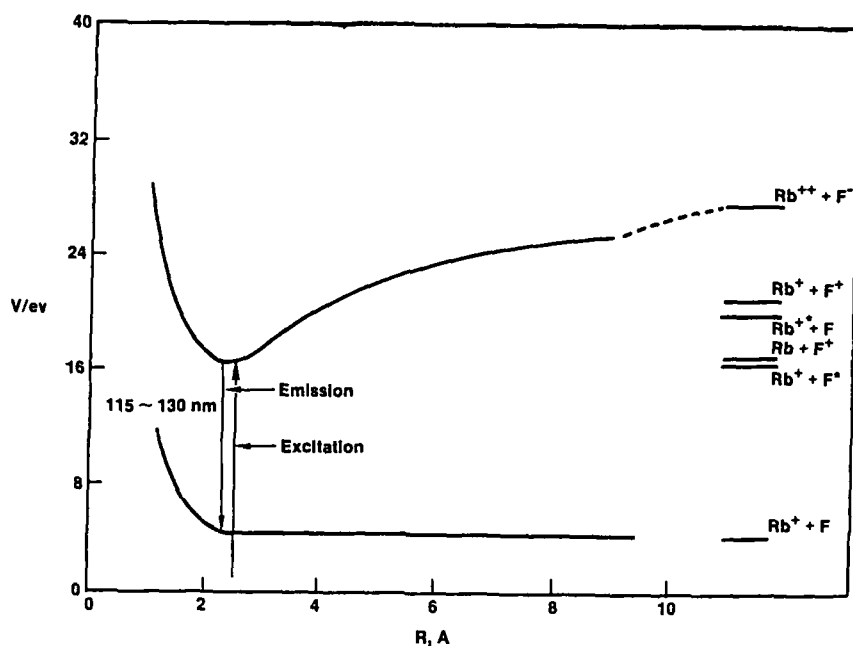
Figure 1. Energy diagram for the excitation and emission process
in Rb^{++}F$^-$. Using a Rittner potential for an upper state
and a Born-Mayer Potential for the repulsive interaction,
the emitted wavelength was predicted to be between 225nm
and 130nm for the Rb^{++}F$^-$ to Rb$^+$F transition.
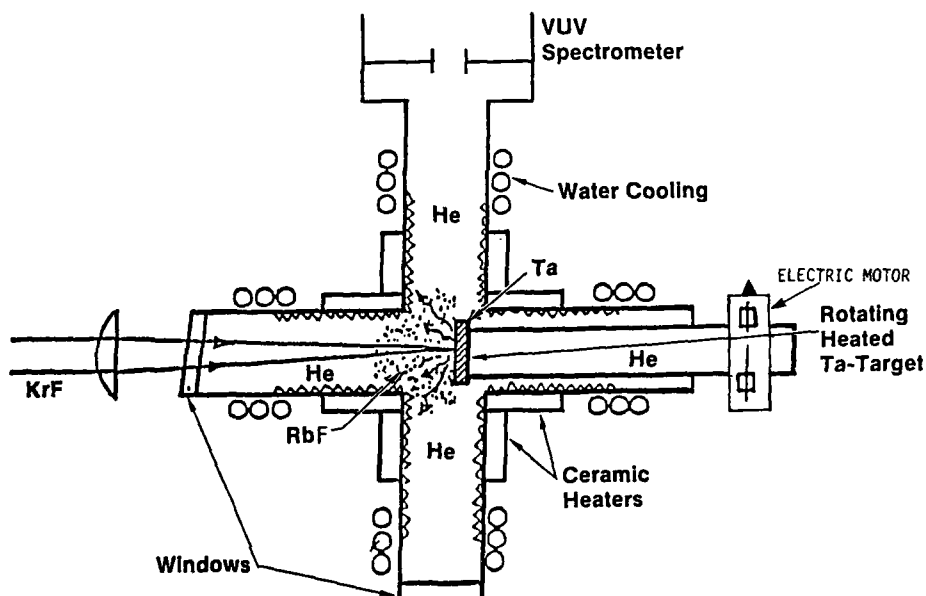
Figure 2. Schematic of the heatpipe cell. The heatpipe consists of five arms.
Four of the arms lie in the plane of the paper. A fifth arm is
perpendicular to the others and was used for viewing the target.

114
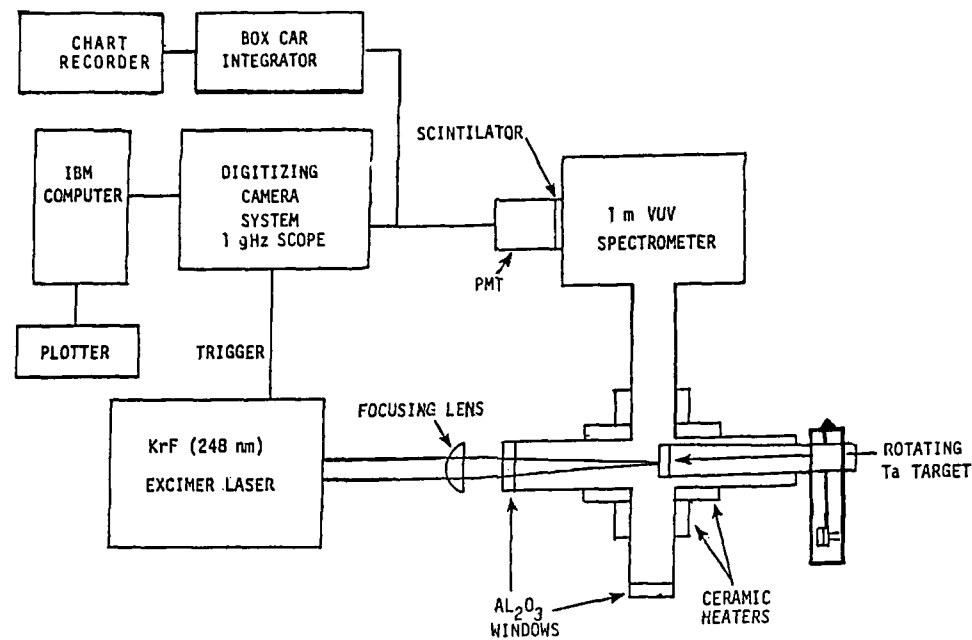
Figure 3. Experimental schematic. A plasma was generated by
focussing the output of a KrF excimer laser on to a
rotating tantalum target inside a heatpipe. The soft
x-rays emitted from the laser produced plasma propa-
gated into the surrounding RbF vapor causing photo-
ionization. The subsequent fluorescence in the VUV
is dispersed by a spectrometer and recorded.
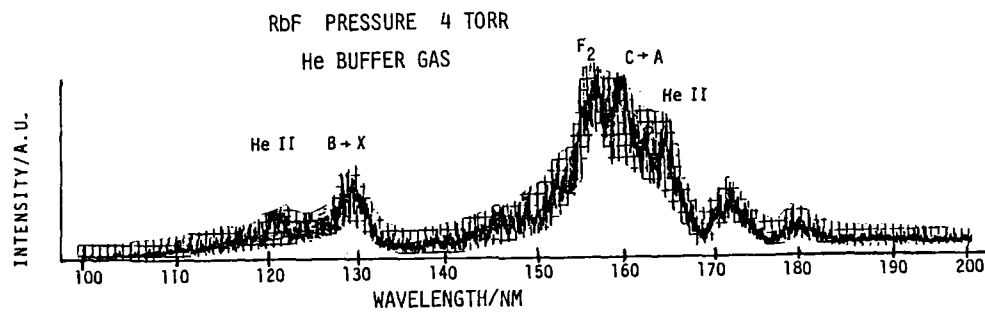
Figure 4a. Emission spectrum from laser-produced-plasma-excited RbF vapor
taken between 100 nm and 200 nm.
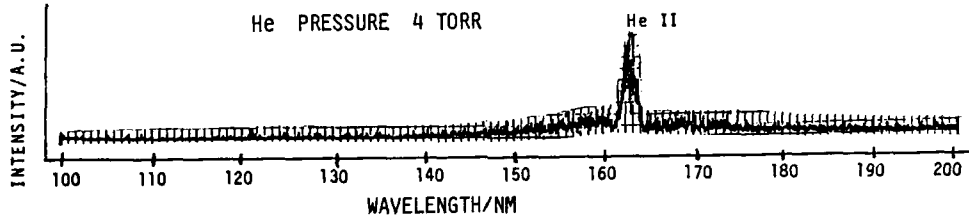
Figure 4b. Emission spectrum from laser-produced-plasma-excited He taken
between 100 nm and 200 nm.

115
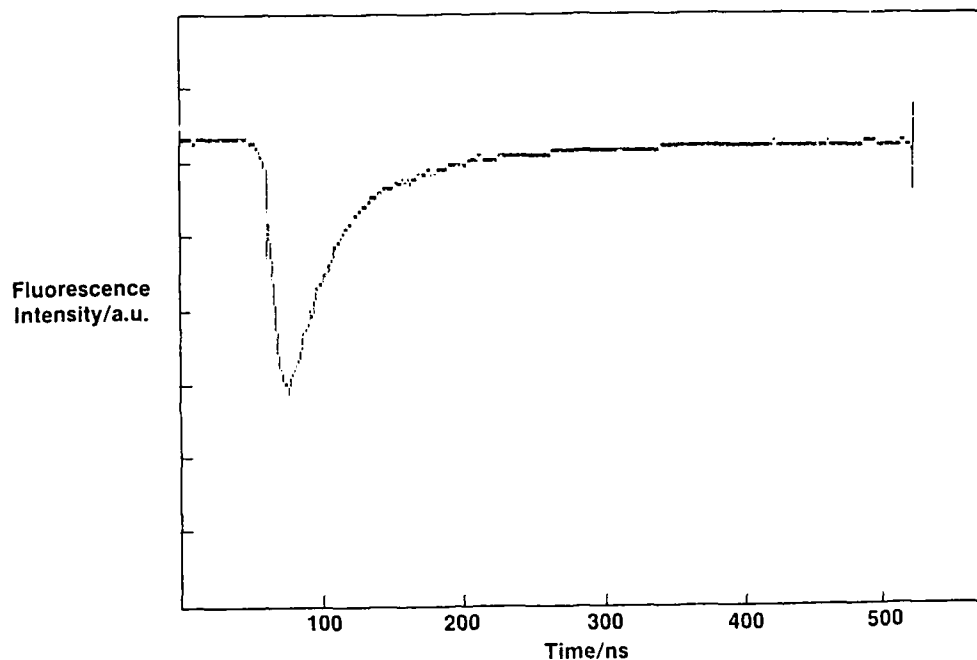
Figure 5. Temporally-resolved $Rb^{++}F^-$ $(B \rightarrow X)$ fluorescence signal at 130.4 nm. The temporal width is about 38 ns (FWHM).
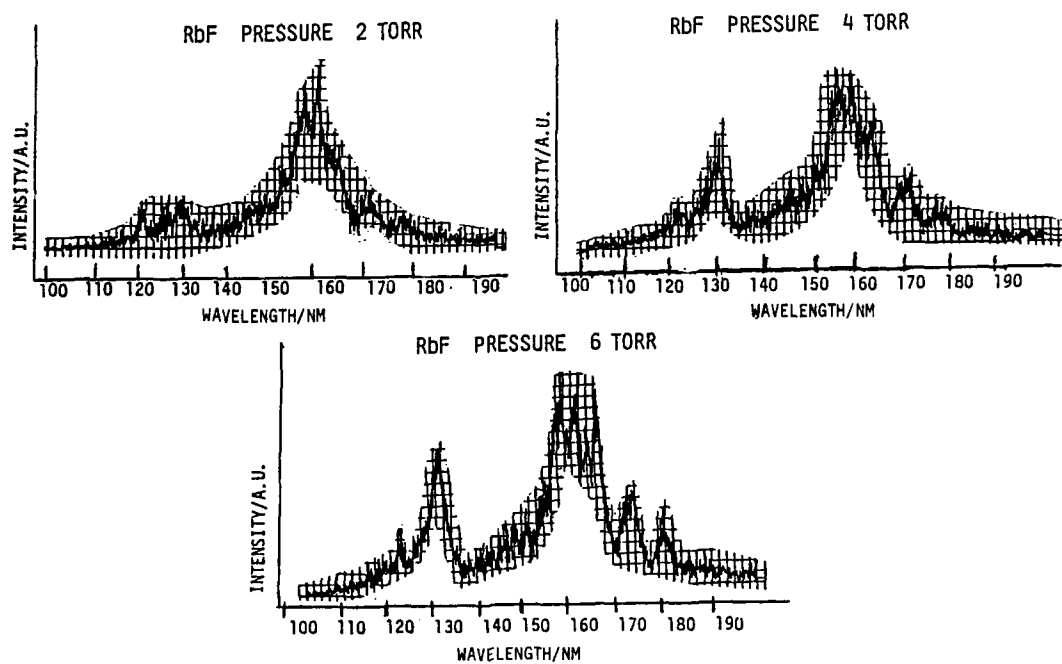
Figure 6. Pressure dependance of emission spectrum from laser produced-plasma-excited RbF vapor.

116

TIME RESOLVED FLUORESCENCE STUDIES OF THE XeF C-A TRANSITION IN AVALANCHE DISCHARGES

Robert C. Sze
Los Alamos National Laboratory
and
Tatsuhiko Sakai*
Rice University

Abstract

Time resolved fluorescence measurements have been obtained for the C-A and B-X transitions of XeF. We discuss the behavior of the fluorescence spectra in terms of relative concentrations of different components of the gas mix and compare the fluorescence intensities with preliminary gain measurements.

INTRODUCTION

Recent successes in electron beam pumped XeF C-A transition lasers in the blue-green spectrum in both short pulse[1] and long pulse[2] formats have stirred renewed interest in the possibility of obtaining similar performance in avalanche discharge devices. In a series of experiments in 1979[3,4] it was shown that while C-A lasing is possible in avalanche discharges, the lasing was very weak and continuous tuning could not be achieved due to various absorptions from atoms and molecules. Through the use of very complicated five component gas mixtures the Rice University and United Technologies effort was able to preferentially induce C-A state lasing over the B-X state. Further, under intense short pulse e-beam pumping absorption was observed during the time of energy deposition and gain only took place in the afterglow. The long pulse e-beam deposition format at AVCO showed that it is possible to sustain gain in the C-A transition for a long time under power deposition levels of 200 kw/cc. However, under these conditions it took over 300 ns to reach lasing threshold. The questions for successful discharge excitation are therefore quite involved. First, there is the consideration of whether reasonable discharges are sustainable in these complicated gas mixtures. Second, under what power deposition levels will we see absorption and for how long does this absorption last. Thirdly, what are the obtainable gain under different excitation power levels and for what period of time can this gain be sustained. We have used presently available discharge devices with minimal modifications to address these issues at different power loadings through the study of time resolved fluorescence data and gain-loss data. These studies serve to address exactly what type of device need to be built for it is not clear whether a short pulse high gain or a lower gain long pulse format is the best approach. This presentation will concentrate on the fluorescence data studies at power deposition levels in the region of 3MW/cc. Extensive gain-loss data have been obtained now in devices from 1MW/cc to 5MW/cc, however, we only compare data from the 3MW/cc power deposition level corresponding to the fluorescence studies presented here.

Fluorescence Measurements

Time resolved fluorescence measurements are obtained on the B-X and C-A frequency region of XeF as well as the B-X fluorescence region of KrF due to the presence of large amounts of krypton in the four component gas mixtures used in these studies. The fluorescence pulse widths and peak fluorescence of the C-A state represent the population behavior of the C state. However, these same parameters from the B-X fluorescence do not accurately represent B state population evolution as much of the gathered light is of a superfluorescent nature at low krypton partial pressures. This tends to greatly enhance the peak intensity and narrow the pulse width. Figure 1 gives a schematic of the experimental setup. Great care have been used to make sure the fluorescence were measured in the linear region of the detection system and the comparison of the different gas mixtures are believed to be good to within 5%. The detectivity of the optical system have been calibrated with a standard lamp and all data have be renormalized with respect to this calibration.
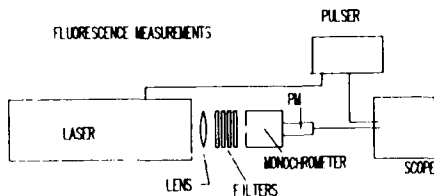
Figure 1. Experimental set-up of fluorescence experiment

Figure 2 plots the B-X and C-A peak intensities as a function of fluorine partial pressure for various buffer gases. Note that optimum C-A fluorescence peaks at different fluorine partial pressures with different buffers and do not necessarily peak at the same pressure as the B-X superfluorescence. In our studies of time resolved fluorescence under conditions of different krypton partial pressures we have chosen mixtures with 5 and 10 torrs of fluorine and 10 torrs of xenon. It is necessary to establish that we can sustain reasonable discharges with substantial amounts of krypton in the gas mix because in electron beam pumped systems krypton is believed to have many beneficial effects. These include quenching of absorbers in the blue-green, creation of absorbers in the ultraviolet, beneficial formation kinetics to the C state due to increased mixing of the upper laser levels and contribution to the net gain due to Kr_2F formation.
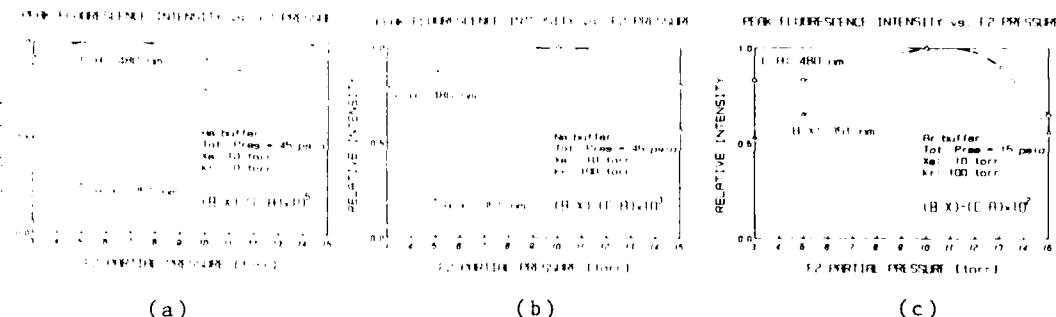
Figure 2. Plot of B-X and C-A peak intensities as a function of fluorine partial pressure for buffer gases (a)helium, (b)neon, and (c) argon

Figure 3 gives the peak fluorescence signals at KrF (B-X), XeF(B-X) and (C-A) wavelengths as a function of krypton partial pressure with 10 torrs Xe and 5 torrs F_2 in 45 psia of He and Ne buffer and in 15 psia of Ar buffer. Similar sets of data are obtained for 55 psia He and Ne buffer pressures and 20 psia Ar buffer pressure as well as at different charging voltage levels. The data shows that at the 3 MW/cc power deposition level and at power deposition times of 25ns very good avalanche discharges are possible up to 300 torrs of krypton. Absorber built up at the B-X transition wavelengths are seen to be very significant as the B-X superfluorescence signals dropped by more than four orders of magnitude as the krypton partial pressure was increased while the C-A fluorescence decreased minimally. We feel that this also tended to show that in a self sustained discharge the increased mixing between the C and B states due to krypton has little effect in increasing the population of the C state at the expense of the B state as the electron
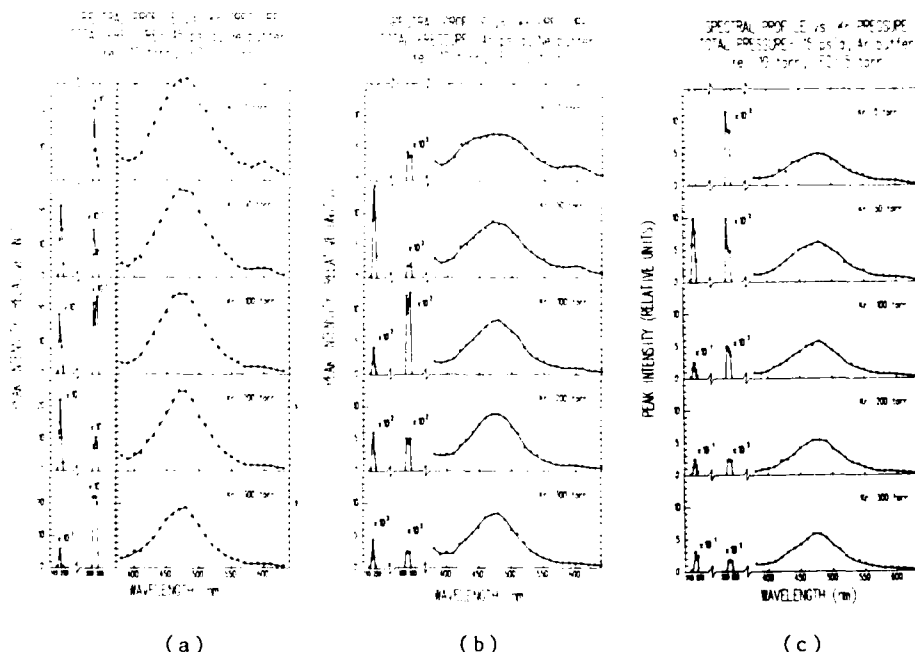
Figure 3. Peak fluorescence signals at KrF(B-X), XeF(B-X) and XeF (C-A) wavelengths as a function of krypton partial pressure with 10 torrs xenon and 5 torrs F_2 with (a) helium , (b) neon, (c) argon buffers.

118

temperatures are much hotter than the room temperatures assumed in the afterglow of the short pulse e-beam excitation situation.

In Fig.4 the data are plotted with all three buffers together at selected wavelengths. We see that the addition of krypton appears to contribute to a decrease in the population of the C state. The effect is most pronounced in He buffer and least in Ar. This is attributed to more significant changes in the electron temperature in the case of the very light helium buffer to much smaller change in Ar as Ar and Kr are closest in their atomic weights and in the energy separation of the metastable and resonance trapped lowest excited states. The change in electron temperature, therefore, translates to changes in the upper state formation rates. The anomalous rise in the fluorescence in Ne and Ar buffer at the peak of the C-A fluorescence at 480nm is attributed to increased vibrational relaxation due to collisions with krypton. This fact becomes evident when we plot the full width at half maximum intensity of the C-A fluorescence band in the different buffers in Fig. 5. Especially in the case of neon buffer we see that vibrational
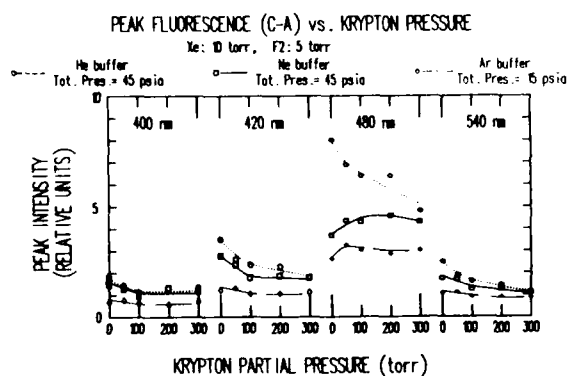
Figure 4. Peak fluorescence data plotted as a function of krypton pressure for different buffers, helium, neon and argon at four distinct wavelengths
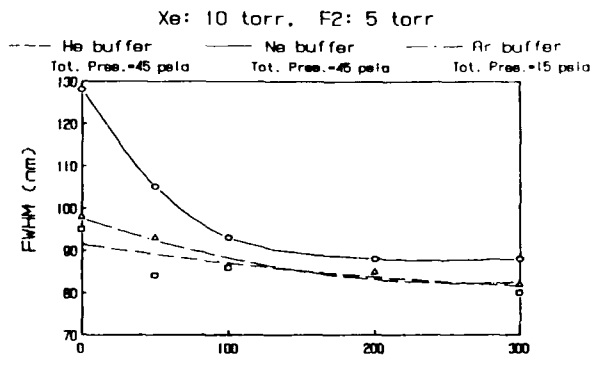
Figure 5. Fluorescence full spectrum bandwidth plotted as a function of krypton partial pressure for different buffers (He, Ne and Ar)

relaxation is very small in the absence of krypton. A close examination of Fig.3 shows that indeed the larger linewidth is due to higher emission in the shorter wavelength region of the C-A transition spectrum. The curves also indicate very little Kr_2F fluorescence in enhancing the gain in the shorter wavelength region of the C-A emission.

Comparison is made in Fig.6 for the case when the same total pressure of 15 psia is used for all buffers. There is a factor of two difference in the fluorescence intensity between He and Ar buffers. In Fig. 4 where the He pressure is three times that of Ar, there is a factor of four difference in the fluorescence intensities. It, thus, may be beneficial to operate with Ar buffer at three times the present pressure. This would also result in the need for much higher operational voltages which should also increase the power deposition giving an additional benefit. Such a discharge device may result in
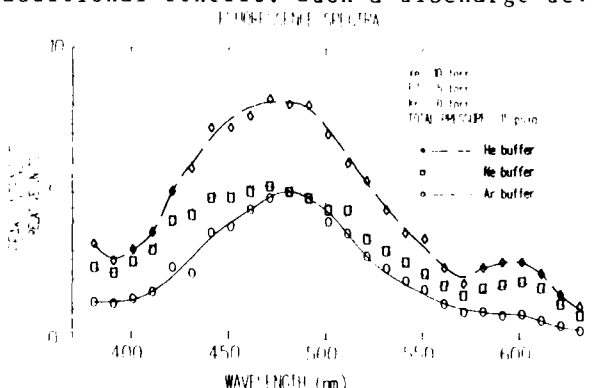
Figure 6. Peak fluorescence as a function of wavelength for helium, neon and argon buffers at 15 psia. Partial pressures are 10 torrs xenon, 5 torrs F_2 and 0 torr Krypton.

improved performance for the C-A laser as incorporation of large amounts of krypton showed very little degradation in the C-A fluorescence with argon buffer.

Comparison with gain measurements

Small signal gain measurements have been made with an argon ion laser and a flashlamp pumped dye laser on devices with power deposition levels of 1 MW/cc and 3 MW/cc. Figure 7 gives the curve for the single pass gain from a 1 MW/cc discharge of 93 cm gain length. Similar curves are seen for measurements at the 3MW/cc as well. There is an initial loss followed by a period of gain which starts in the middle of energy deposition and continues into the afterglow of the discharge. This gain generally lasts some 50ns. The measured gain for the 3MW/cc power deposition device is shown in Fig. 8 for the same mixture as that given for fluorescence in Fig. 4. The measured total gain is the round trip gain from a 40cm gain length device. The best gain is measured in helium buffer with zero krypton and translates to gains over 1%/cm. Note that the gain follows closely the peak fluorescence data of Fig.4.

— 5 mv/div C-A gain

— 50 mv/div B-X Fluor

— 0 level for C-A gain

20 ns/div
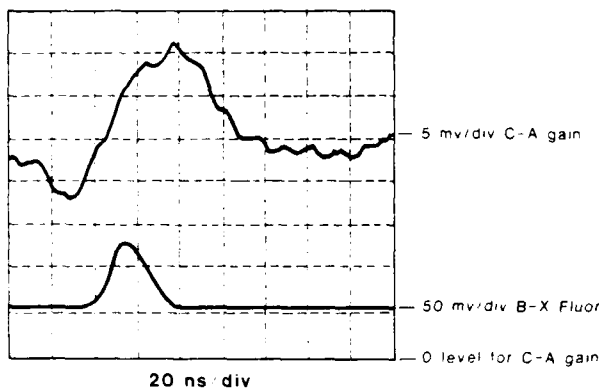
Figure 7. Typical time evolution of C-A gain 476.5 nm) and B-X fluorescence as a function of time in 1MW/cc power deposition device.
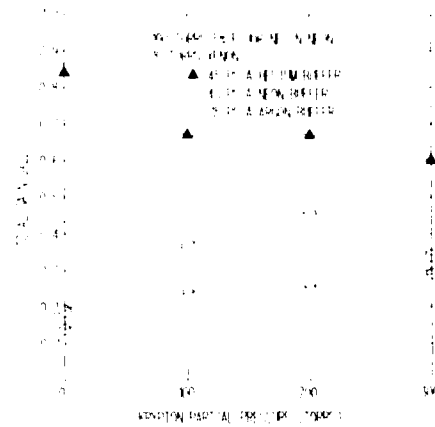
Figure 8. Total round trip gain as a function of krypton partial pressure for helium, neon and argon buffers.

Discussion

Detailed fluorescence and small signal gain measurements show that the best laser gas mix using F_2 alone as the halogen donor is in helium buffer without krypton. In neon as well as argon buffer the strongest fluorescence at the peak of the C-A fluorescence (480nm) is at 200 torrs of krypton. This is attributed to the increased vibrational relaxation of the C state in the presence of krypton. The measured gain in argon appears to continue to rise with respect to increasing krypton pressure although the fluorescence has began to drop after 200 torrs of krypton. This maybe attributed to the increasing quenching of argon based absorbers as in the case of electron beam pumped systems. At wavelengths away from the peak fluorescence, the highest intensities in neon and argon buffers are at zero torrs of krypton. However, the very strong quenching of the B-X superfluorescence may still favor discharges with krypton additive for best laser operation in the C-A state.

To achieve strong laser oscillation one in general need to reach e^{25} to e^{30} to reach saturation of the transition. This gives us a gauge as to the needed improvements with respect to present discharge systems. One would like to reach saturation in a time short compared to the total gain time. To reach e^{25} with 1% gain per cm one needs 83ns gain length and with 50ns gain length one needs 1.7% gain per cm. Thus, we are some factor of three to four away with these devices from really strong lasing outputs.

References

1. Y. Nachshon, F.K. Tittel, W.L. Wilson, Jr. and W.L. Nighan, J. Appl. Phys.,56, 36, (1984)

2. A. Mandl and L.N. Litzenberger, Appl. Phys. Letts., 53, 1387 (1988)

3. R. Burnham, Appl. Phys. Letts., 35, 48 (1979)

4. C. H. Fisher, R.E. Center, G. J. Mullaney and J.P. McDaniel, <u>Appl. Phys. Letts.</u>, <u>35</u>, 901 (1979)

*Present address Keio University, Japan

MEASUREMENT OF XeF GROUND STATE DISSOCIATION AND VIBRATIONAL RELAXATION

J. F. Bott, R. F. Heidner, J. S. Holloway, J. B. Koffend, and M. A. Kwok
Aerophysics Laboratory, The Aerospace Corporation, P. O. Box 92957, Los Angeles, CA 90009

Abstract

The photolysis of XeF_2 at 193 nm has been used as a source of ground electronic state XeF(X,v") for studies of vibrational relaxation and collisional dissociation of the lower level of the XeF(B → X) laser at $\lambda \simeq$ 350 nm. The time dependent concentrations of XeF(X,v") were monitored in absorption using a cw, frequency-doubled ring dye laser as a probe. The XeF(X) vibrational manifold was observed to undergo fast vibrational equilibration followed by slower collisional dissociation. For the first time, the actual lower vibrational levels of XeF(B → X) laser transitions were studied. In addition, the temperature dependence of the dissociation rate was measured between 293 and 368 K. Finally, various collision partners for XeF(X,v") were studied.

Introduction

The efficient operation of the XeF excimer laser depends critically on the rate of dissociation of the weakly bound XeF(X) ground electronic state. Unlike the KrF and ArF rare gas halide excimers whose ground state are essentially repulsive, XeF(X) has a significant (~ 1100 cm^{-1}) binding energy permitting approximately eight bound vibrational levels [Fig. 1]. Both vibrational relaxation (i.e., V → T) and collisional dissociation processes play a role in removing population from the lower laser levels. The rates of these processes must exceed the rate of lower state production by quenching, spontaneous and simulation emission in order to prevent premature termination of laser action. For these reasons, as well as others, the XeF(B → X) laser operates best at both elevated pressure (~ 3 atm) and elevated temperature (~ 425 K). The present study provides detailed measurements that isolate the effect of ground state removal on laser performance.

In a conceptually similar experiment, Fulghum et al.[1,2] measured XeF(X) kinetics for v" = 0, and 1 at room temperature and developed a model for the V → T and dissociation processes.[3] Since the typical lower vibrational levels in the laser device are v" = 2-4, extrapolations of this model were required both in vibrational quantum number and temperature. By contrast, the present study[4,5] has used detection methods which give improved data for the fast processes leading to vibrational equilibration. Although state-to-state rate coefficients are not measured, data were obtained on an extended set of vibrational levels (v" = 0-4) permitting us to better constrain any model that encompasses both the V → T and the collisional dissociation processes at the state-to-state level. The present study is compared with the model of Fulghum et al.[3] and with the results of Wilkins[6,7] who performed classical trajectory calculations of collisions between XeF(X,v") and He or Ne.
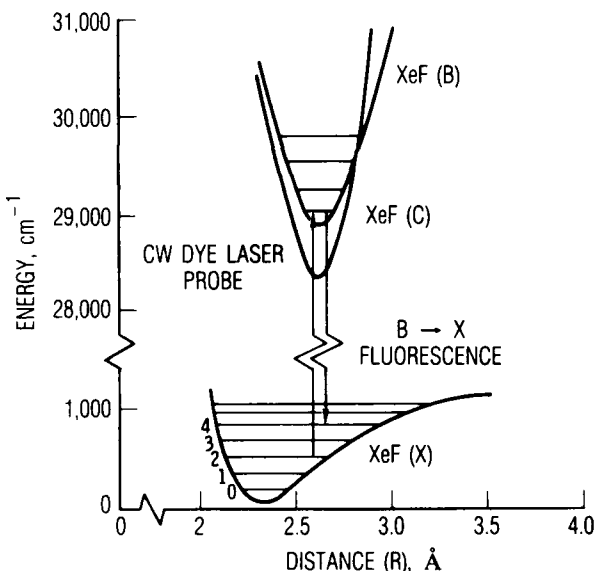
Figure 1. Partial Potential Energy Diagram of the XeF Molecule.

Experimental

The apparatus used to study the time-resolved kinetics of XeF(X,v") is shown in Fig. 2. The molecule XeF_2 is employed as a photolytic precursor for XeF(X). Although photolysis at λ = 248 nm provides insufficient energy to produce XeF(B) directly, Huestis and coworkers[8] have demonstrated that XeF(B) is produced by secondary pumping.

$$XeF_2 + h\nu \ (248 \ nm) \rightarrow XeF(X) + F \tag{1}$$

$$XeF(X) + h\nu \ (248 \ nm) \rightarrow XeF(D) \tag{2a}$$

$$XeF(D) + M \rightarrow XeF(B,C) + M \tag{2b}$$

Photolysis at $\lambda = 193$ nm can produce XeF(B) directly, although the quantum yield is thought to be small.[9]

$$XeF_2 + h\nu \ (193 \ nm) \rightarrow XeF(B,X) + F \tag{3a}$$

$$XeF(B) \rightarrow XeF(X,v") + h\nu \ (\sim 350 \ nm) \tag{3b}$$
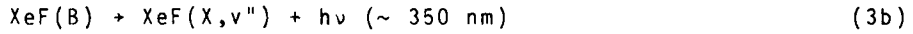
Under our experimental conditions, the quantum yield of observable XeF(X) appears to be small as well. Thus, the dominant channel appears to be

$$XeF_2 + h\nu \ (193 \ nm) \rightarrow [XeF]^{\ddagger} + F \rightarrow Xe + 2F \tag{4}$$

where $[XeF]^{\ddagger}$ is a very short lived species [perhaps including XeF(X,v" $\geq$ 5)]. Photolysis at either wavelength results in a great deal of background fluorescence (both discrete and continuous)[5] on the XeF(B $\rightarrow$ X) transition when XeF_2 is photolyzed by a conventional (Lamba Physik EMG 101) discharge-pumped excimer laser. This fluorescence precludes measurements by cw laser-induced fluorescence using the probe source described below. Thus, the experiments were done by time-resolved laser absorption.
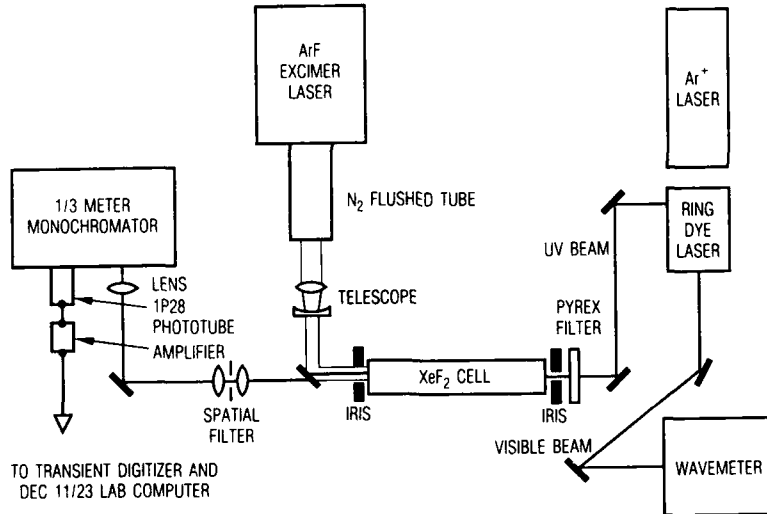
Figure 2. Schematic of the Apparatus for Time-Resolved Absorption Studies.

The probe laser was a frequency-doubled ring dye laser (Coherent CR 699-21) pumped by either an Ar^+ ion laser (Innova 100) or Kr^+ ion laser (CR 3000 K). The former source employed DCM Special dye and operated (after doubling) between 320 and 345 nm. The latter employed Rhodamine 700 and operated (after doubling) at $\lambda > 350$ nm. The wavelength of the dye prior to doubling was measured with a Burleigh Model WA-20 wavemeter with an equivalent accuracy near 350 nm of 0.0005 nm. The XeF Doppler width of each vibronic line is $\sim$ 0.00032 nm. The probe beam is counter propagated with respect to the ArF photolysis beam. As shown in Fig. 2, the probe beam is transmitted by the 193 nm turning mirror, spatially filtered to remove B $\rightarrow$ X fluorescence, and propagated approximately 2 m to a grating monochromator which provides further spectral isolation of the narrow linewidth cw probe. The beam is detected by a 1P28 phototube; the signal is amplified, digitized by a fast transient recorder and stored in a DEC 11/23 microcomputer for analysis. The overall response time of the system is comparable to the 15 nsec pulse width of the ArF photolysis laser.

Results and Discussion

In the photodissociation process described by Eq. (3), a "nascent" vibrational distribution is produced in the XeF(X) v" manifold by a combination of direct production and radiation from the B state. A simplified state diagram of the XeF molecule is shown in Fig. 1. That nascent vibrational distribution is modified by collisions with the parent XeF_2 or with the added collision partner.

$$XeF(X,v") + M \rightleftharpoons XeF(X,v" \pm 1) + M \qquad (5)$$

$$XeF(X,v") + M \rightarrow Xe + F + M \qquad (6)$$

Only single quantum vibrational transfer is represented in Eq. (5); however, trajectory calculations do show some contribution from multiquantum processes.

(a) XeF(v" = 0) in 0.25 Torr of XeF_2 and 4.47 Torr of He.

(b) XeF(v" = 3) in 0.25 Torr of XeF_2 and 7.2 Torr of N_2.
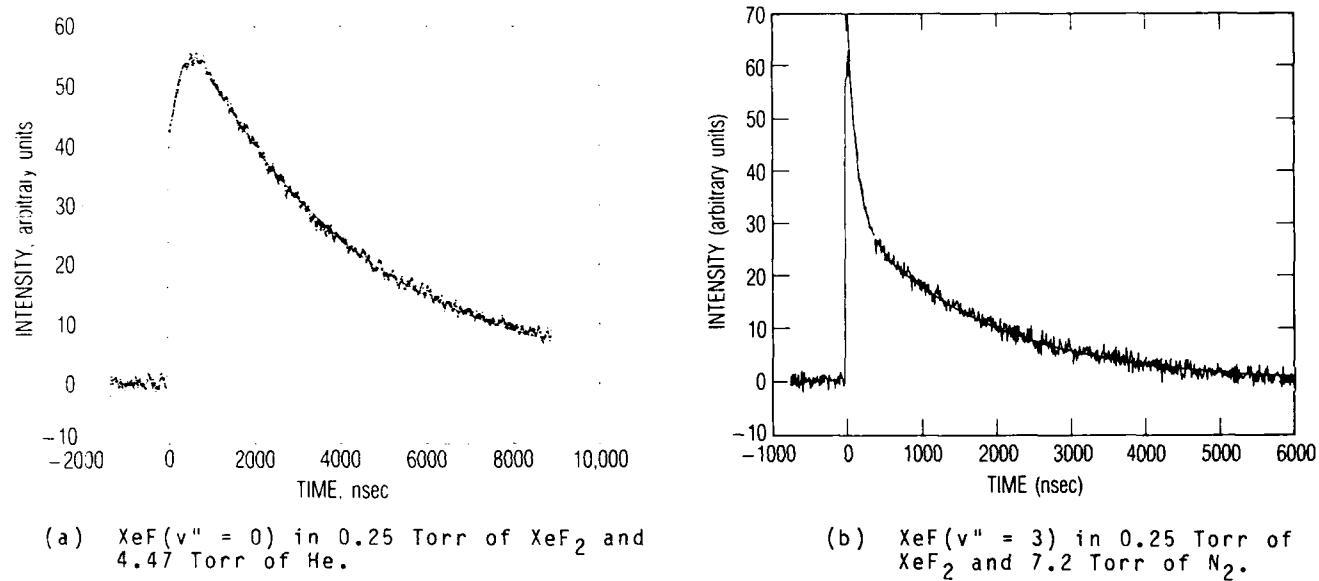
Figure 3. Time Histories of the XeF(X,v") Density.

These processes can be seen to operate in the data presented in Figs. 3(a) and 3(b). XeF(X,v" = 0) is produced promptly ($\tau \sim$ 50 nsec) by Processes (3a) and (3b). Vibrational levels v" = 0 and 1 are <u>underpopulated</u> with respect to a Boltzmann distribution; thus, at short times, collisions with the bath gas [He in Fig. 3(a)] cause the population to increase by cascading from high v" levels. Vibrational levels v" = 3 and 4 are <u>overpopulated</u> at short times [Fig. 3(b)] and collisions [with N_2 in Fig. 3(b)] produce a fast relaxation spike. At longer times, all vibrational levels observed in this study relax with a single exponential time constant. This decay rate represents a state-averaged collisional dissociation rate of XeF(X), i.e., Process (6). The short-time behavior is determined by vibrational equilibration processes represented by Process (5) and its reverse. Although Figs. 4(a) and 4(b) show that the vibrational equilibration rate and the collisional dissociation rate can be empirically described as single exponential functions, it must be stressed that state-to-state rate coefficients can be obtained only by modeling these data. Table I summarizes all the room temperature data as a function of vibrational level and collision partner. Both the vibrational equilibration rates and the collisional dissociation rates are extremely similar for all the rare gases. These rates are significantly larger for N_2, CO_2 and SF_6 and much larger for the parent XeF_2 as collision partners.

Because the XeF laser operates more efficiently at elevated temperature, the dependence of the collisional dissociation rate on temperature was measured for the collision partners He and Ne. Between 293 and 368 K, the data could be fit by a simple Arrhenius form (Fig. 5), $k = A T^{-0.5} \exp(-E/RT)$. A least squares fit to the data gives E = 1077 cm^{-1}, which can be compared to the spectroscopic value of the dissociation energy of 1062 cm^{-1}. Thus, it appears that the molecule undergoes a unimolecular dissociation with no significant barrier in the exit channel.

124
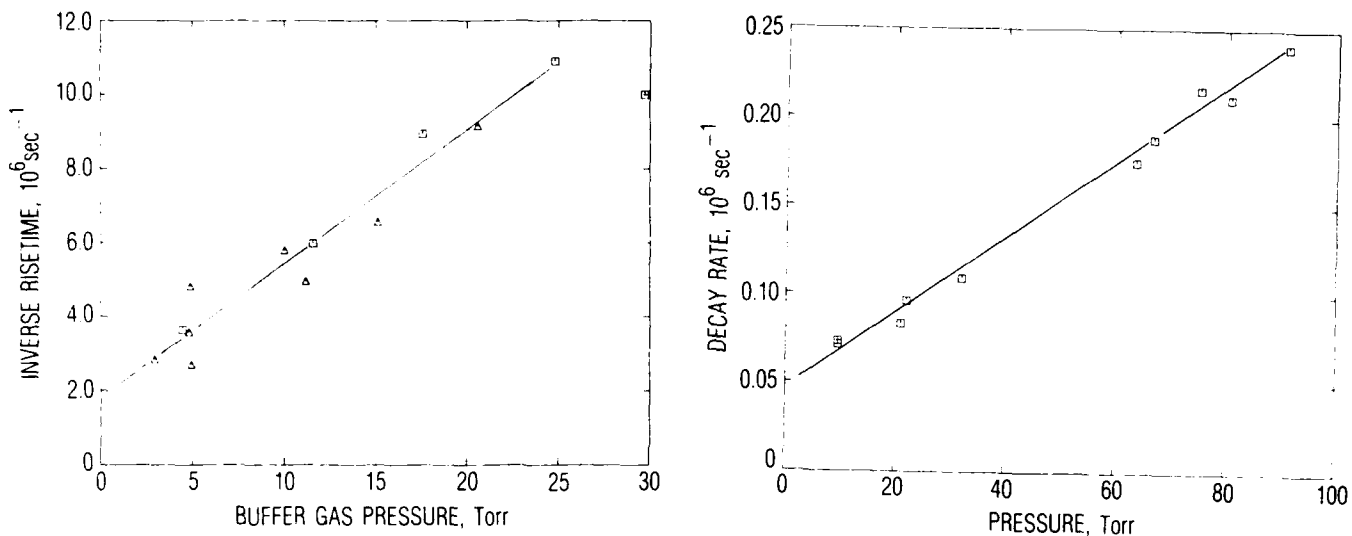
(a) XeF(X,v" = 0) vs He (squares) and Ne
(triangles) Pressure at T = 22°C.

(b) XeF(X,v" = 1) vs. Ne Pressure
at T = 26°C.

Figure 4. Rates of XeF(X,v") Vibrational Relaxation and Collisional Dissociation.

Table I. Rate Coefficients for the Various Collision Partners (T = 295 K).

Collision Partner	v	Dissociation Rate Coefficient 10^4 (sec-Torr)$^{-1}$	cm^3/molec.sec	Relaxation Rate Coefficient 10^5 (sec-Torr)$^{-1}$	cm^3/molec.sec
He	0-4	2.0 ± 0.2	6.3E - 13	3.0 ± 0.4	9.3E - 12
Ne	0-4	2.0 ± 0.2	6.2E - 13	3.0 ± 0.4	9.3E - 12
Ar	0,1	2.5 ± 0.2	7.7E - 13		
Kr	3	1.6 ± 0.2	4.9E - 13	2.8 ± 0.3	8.7E - 12
Xe	3	1.6 ± 0.3	4.9E - 13	2.8 ± 0.6	8.7E - 12
N_2	3	4.1 ± 0.5	1.3E - 12	8.8 ± 1.2	2.7E - 11
SF_6	0	6.1 ± 0.6	1.9E - 12		
CO_2	3	6.8 ± 1.0	2.1E - 12	19 ± 2	5.8E - 11
XeF_2	0-4	50 ± 7	1.5E - 11	70 ± 10	2.2E - 10

The results of this study can be compared with the semi-empirical model of Fulghum et al.[3] and with the recent trajectory studies of Wilkins.[6,7] The most significant departure from the Fulghum study surrounds the vibrational equilibration rates. Our data (Table I) for He and Ne give a rate approximately seven times larger than that of Fulghum et al. The faster rate seems plausible in that the spacing between v' = 0 and I is approximately kT [205 cm^{-1}) at room temperature. It is interesting to note that the vibrational dependence of the V → T rate coefficients and the collisional dissociation rate coefficients is quite similar between the modeling of Fulghum et al. and the Wilkins' calculation (Fig. 6); however, the absolute magnitudes, particularly for the V → T rates, are different. Our data for He and Ne are well described by a model which uses the Wilkins V → T rates and his collisional dissociation rates increased by a factor of 1.4.

Fig. 5. Arrhenius plot of collision dissociation rate coefficients in He and Ne vs $T^{-1} \times 10^3$.

Conclusions and Acknowledgments

Improved data for the kinetics of the ground electronic state of XeF have been obtained. The vibrational equilibration rates were shown to be significantly faster than previously measured. This has the effect of distributing XeF(X) population created by stimulated emission in a predictable fashion over the ground state vibrational manifold. Likewise, the increase in the overall dissociation rate with temperature is easily predictable from unimolecular rate theory. As additional data become available on excited state formation and quenching rates, and on the production and removal of intracavity absorbers, it will be possible to determine whether or not additional excursions in temperature, pressure, or gas composition can improve the efficiency of the XeF(B → X) laser.

Fig. 6. State-to-state rate coefficients for vibration equilibration and collisional dissociation versus v". Empirical model of Ref. (3) (---); trajectory calculation results of Refs. (6) and (7) (——).

References

1. S. F. Fulghum, M. S. Feld, and A. Javan, Appl. Phys. Lett. 33, 926 (1978).

2. S. F. Fulghum, M. S. Feld, and A. Javan, Appl. Phys. Lett. 35, 247 (1979).

3. S. F. Fulghum, M. S. Feld, and A. Javan, IEEE J. Quantum Electron. 16, 815 (1980).

4. J. F. Bott, R. F. Heidner, J. S. Holloway, J. B. Koffend, and M. A. Kwok, J. Chem. Phys. 89, 4154 (1988).

5. J. F. Bott, R. F. Heidner, J. S. Holloway, J. B. Koffend, and M. A. Kwok, "Photodissociaton of XeF$_2$ at 193 nm," submitted for publication (1989).

6. R. L. Wilkins, J. Chem. Phys. 89, 6267 (1988).

7. R. F. Wilkins, "Vibrational Relaxation and Collision-Induced Dissociation of Xenon Fluoride by Neon," submitted for publication (1989).

8. H. Helm, L. E. Jusinski, D. C. Lorents, and D. L. Huestis, J. Chem. Phys. 80, 1796 (1984).

9. D. L. Huestis, private communication (1988).

DIAGNOSTIC METHODS AND BEAM QUALITIES FOR THE DISCHARGE PUMPED EXCIMER LASER

T.Yagi, H.Saito, T.Fujioka

Industrial Research Institute, Laser Laboratory
1201, Takada, Kashiwa, Chiba 277, Japan

K. Ohta, M.Obara

Keio University, Faculty of Science and Technology,
Department of Electrical Engineering,
3-14-1 Hiyoshi, Kohoku-ku, Yokohama-shi, Kanagawa, Japan

Abstract

An imaging system with a two dimensional photo diode array is used for real time base pulse by pulse measurement of the far and the near field patterns, spatial distribution of the spectrum, and spatial coherence of a KrF excimer laser at high repetition rate. With these measurements the pointing stability and non-uniform spectral distribution of the band-narrowed KrF laser beam becomes clear. The streak camera measurement of the spectrum and coherence shows they can vary during the laser pulse.

Introduction

The krypton fluoride excimer laser has number of attractive features such as its uv wave length and high peak power. Although it has wide gain width, efficient extraction of the photon energy in a narrow spectral band has been obtained with the methods such as injection locking. However, As our previous work shows[1], the beam pattern of the injection locking system of the KrF laser reveals non-uniform intensity distribution and pointing stability which is very sensitive to mechanical vibration.

As an alternative, a phase conjugated laser system based on Stimulated Brillouin Scattering can produce high spectral brightness and be essentially free from any mechanical disturbances of the laser beam[2]. Since the performance of the phase conjugation depends strongly upon the characteristics of the injected beam, real time beam monitoring is indispensable.

In the present paper, we describe the method developed to monitor beam characterstics such as the far and near field patterns, spatial distribution of the narrow band spectrum, and spatial coherence for the KrF excimer laser, in pulse by pulse and time resolved manner. Some results regarding the narrow band oscillator, injecton locking system, and oscillator-amplifier system are also introduced.

Beam Pattern

Measurement System

The near field and the far field patterns of the KrF excimer laser are measured with the optical configuration shown in Fig.1, where the beam is divided to form a near field pattern by lens L_1 (f=0.27 m) and a far field pattern by lens L_2 (f=9.04 m) on the imaging sensor at the same time. The imager is a computer controlled two dimensional photo diode array featured with the sensitivity down to the uv wave length and small cross talk between the photo diode arrays, which enables high spatial resolution suitable for the beam diagnostics. The fast frame rate enables even consecutive measurement of both near and far field patterns simultaneously at 250 Hz repetition rate.

Field Patterns

The near and the far field patterns of the laser beam from the injection locking system operated at 250Hz are shown in Fig.2a, and the intensity profile scanned horizontally as indicated by the arrow in this figure is given in Fig.2b. Due to the high spatial resolution of the imager, the fine structures of the beam pattern characteristic to the unstable resonator is seen.

The pointing stability of the beam, which is important for machinning applicatons, is obtained by tracing the peak position of the far field spot. Fig3a shows how the far field spot moves around. The vertical and horizontal components of the far field spot positions are plotted against time in Fig.3b and Fig.3c respectively.

The periodic variation of the vertical component is due to the mechanical vibrations of the resonator cavity, while the horizontal motion is caused by the discharge instability. The vibrational origin of pointing instability is a intrinsic problem associated with the unstable resonater mounted on the gas flowing chamber, while our alternative method; phase conjugated laser system, is demonstrated to be free from the mechanical problem[2].

Narrow Band Spectrum

Method

The spatial distribution of the narrow band spectrum of the laser beam can be measured by taking advantage of the small free spectral range of the Fabry-Perot interferometer. Fig.4 shows the optical arrangement, where the incident beam is converted to a diverging beam by a concave lens L_1, and enters the Fabry-Perot etalon. The beamlet which satisfies constructive interference condition forms a bright fringe pattern on the imaging sensor S. If the divergence of the original beam is much smaller than that of the beam focussed by lens L_1, there is a one to one correspondence between the bright fringe on the sensor and the circular area in the beam at the Fabry-Perot etalon. Since the beam entering the circular area at the etalon passes through a similar circular area on the object plane A, we can estimate the spectral distribution in the beam cross section at A by measuring the position and width of the interference fringes.

The etalon, which has a free spectral range of 0.00489nm and finesse of 15, and the lens L_2 with f=27cm form about 10 fringes in our 2D photo diode array located at the image plane S. For absolute line position measurement a monochrometer with a optical fiber input (resolution is about 0.0031nm) is used simultaneously.

Spatial Distribution of the Spectrum

The spectral distribution of the KrF excimer laser beam operated in narrow band configuration, where the band narrowing is performed with a prism beam expander and a grating together with collimating apertures with diameter of 1mm, is measured. The beam diameter is about 2mm at a distance of 3m away from the laser. The laser cavity and grating are well aligned at a central wave length of the gain, producing a single spectrum with a band width of about 0.001nm.

One of the examples of the fringe pattern for the laser pulse at 100Hz rep. rate is given in Fig.5a, where about 10 fringes cover the cross section of the beam. Fig.6 presents the result of the analysis, showing that the wave number of the laser beam is not the same within the beam cross section. A more conspicuous example of the non-uniform spectral distribution is obtained by changing the tuning wave length of the laser. The fringe pattern shown in Fig.7a gives the example, where the left half and right half of the laser beam contain different wave lengths and each side has two fold spectral structure. The right-left asymmetry might be due to the combined effect of the finite size of the aperture and the grating which experience the incident beam at a sharp angle. The double structure of the fringe pattern probably originates in the gain structure of the KrF gas itself since our measurement of the ASE spectrum with the monochrometer shows number of sharp lines which resemble rotational-vibrational bands.

Long Term Drift of the Wave Length

Long term drift of the wave length of the band-narrowed KrF laser beam is performed with our measurement system. The tuning element is adjusted at the central wave length to form a single spectral line. When the measurement is not being performed, the cavity optics are blocked from the discharge to avoid the thermal effect on the optics. When in 40min. the laser is operated at 250Hz, the wave length shows red shift by about 0.00326nm.

Time Resolved Spectrum

Time resolved measurement of the narrow band spectrum is performed by forming the Fabry-Perot fringe pattern on the entrance slit of the streak camera. For convenience of measurement, 4% of the beam which forms the fringe pattern on the 2D photo diode array is sampled for the streak camera so that the time resolved and pulse by pulse measurements are obtained simultaneously. The entrance slit of the streak camera is placed horizontally as indicated by the arrow in Fig.5a, so that the right hand side of a few central fringes in this figure enters the streak camera. The time resolved spectra for the case of Fig.5a; perfect tuning to the single line, is presented in Fig.5b, where the horizontal axis is time with full span of 100ns

and the three central fringes have a duration of about 20ns with slight drift in wave length toward blue. This kind of "chirping" is more dramatic for the case of Fig.7a, when a two fold spectral structure appears. The time resolved measurement for this case is given in Fig.7b. The two different wave lengths are emitted at different times with a duration of about 10ns for each. Since the cavity length is about 1.2m, the duration of each wave length corresponds to almost one round trip within the cavity.

The importance of the time resolved measurement of the spectrum is shown in Fig.8a and Fig.8b, where the beam is produced from the injection locked unstable resonator system. We used the same optical configuration as in the previous experiment, and the central fringe of Fig.8a is located at the mid point between the central hole and right edge of the near field of Fig.2a. The injected beam enters the unstable resonator cavity just when the gain is onset, providing the locking efficiency to be >90%. Temporal variation of the spectra shown in Fig.8b is rather striking for the rapid variation at the period of about 10ns.

The variation of the spectrum within the laser pulse as shown in our measurements frequently happens in our laser system, and it may be a general problem associated with the narrow band operation of the KrF excimer laser. And it will result in erroneous measurement of the spectral band width and line position.

Coherence

Method

The measurement of the spatial coherence at high rep. rate is performed with a wave front shearing interferometer which uses the same principle as ref.(3), except that we use a Michelson type of the interferometer in place of the shearing cubic prism. Fig.9 presents the optical setup, where the laser with narrow spectral band width (coherence length > 1cm) is focussed with a lens of f=54cm, so that the focal point is located just before the beam splitter. The split beams are reflected by the mirrors, and one of them is slightly inclined to produce the shearing angle.
The 2D photo diode array is placed where two beams overlap to form interference pattern.

A thin lens converts the spatial coherence of the laser beam from the object plane to the image plane in such a way as (c.f. ref.(4))

$$| \mu(x_1,y_1;x_2,y_2) | = | \mu(\xi_1,\eta_1;\xi_2,\eta_2)| \qquad (1)$$

where μ is a complex coherence factor for the points x_1,y_1,x_2,y_2 on the image plane and for the points $\xi_1,\eta_1,\xi_2,\eta_2$ on the object plane. The coordinates are related as

$$\xi_1 = - \frac{b}{a} x_1$$

$$\eta_1 = - \frac{b}{a} y_1 \qquad (2)$$

in the same way for the coordinates of suffix 2, where a and b are the distances of the object plane and the image plane from the lens respectively with the additional relation,

$$\frac{1}{a} + \frac{1}{b} = \frac{1}{f} \qquad (3)$$

The modulus of the coherence factor is related to the visibility as

$$Visibility = \frac{I_{max} - I_{min}}{I_{max} + I_{min}} = \frac{2\sqrt{I_1 I_2}}{I_1 + I_2} | \mu | \qquad (4)$$

where I_1 and I_2 are the intensity of the two overlapping beams at the point where the fringe intensity is measured. By blocking one of the mirrors, we can measure the intensity distribution of the beam, then I_1 and I_2 are known, and the modulus of the coherence factor of the laser beam at the object plane is estimated from the measurement of the visibilty at the image plane of the lens L in Fig.9.

The visibility of the interference fringe pattern of the narrow band KrF laser beam with diameter of 2mm is observed with the optical configuration as explained

before. The focal length of the lens is 54cm, the distance from the lens to the imager is 120 cm, and the shear angle is about 4mrad. Observed visibility with the imager gives the coherence function for the points separated by about 2mm at about 98cm from the lens. Fringe pattern is given in Fig.10a and fringe profile scanned horizontally as indicated in Fig.10a is given in Fig.10b. For this measurement the modulus of the coherence function is estimated to be 0.5.

Time Resolved Measurement

It will be shown that, as in the case of the spectrum, the spatial coherence will vary within the duration of the laser pulse. It is measured by placing the entrance slit of the streak camera horizontally so that, as indicated by the arrow in Fig.10a, a part of the fringe profile enters the streak camera. The streaked fringe profile is given in Fig.11, where the sweep is from left to right with the time span of 100ns. This measurement shows the spatial coherence becomes poor in about 5ns from the arrival of the beam, however in about 12ns or so it becomes much improved. This feature is more clearly observed by passing the oscillator beam through an amplifier. Interference fringes are observed by changing the timing of the onset of the amplifier gain with respect to the oscillator beam. Fig.12a, Fig.12b, and Fig.12c shows the fringe profiles when the gain of the amplifier is onset at -3, 5, and 15ns respectively after the arrival of the oscillator beam at the amplifier.

As explained in relation with the streak camera measurement of the coherence, the oscillator beam amplified at the beginning shows good visibility, while in the intermediate stage the visibility becomes poor. However, after 12ns the coherence becomes much improved. Although the temporal variation of the spatial coherence as shown in these experiments may be characteristic to our laser system (cavity length is about 1.2m, gain length is 0.45m), the gross feature; improvement of the spatial coherence in the course of time will be a general tendency of excimer laser beams.

Conclusion

We have briefly described our method to measure the near and far field patterns, spectrum and coherence of the KrF excimer laser beam in band narrowed operation. The imaging spectroscopy and imaging interferometry based on the 2D photo diode array is demonstrated to be quite feasible for the monitoring the excimer laser beam. Pulse by pulse measurement of the spectrum shows that the spectrum is not uniform in the beam cross section and streak camera measurement shows that the spectrum varies during the pulse duration. The same imaging system is used to measure the coherence and it is found that it changes during the pulse duration as well.

Achnowledgment

Reference

1. T.Yagi, Y.Matsumi, K.Ohta, H.Saito, M.Obara, T.Fujioka, to be published in Proc. 7th International Symposium on Gas Flow & Chemical Lasers (Vienna, 1988)

2. T.Yagi, K.Ohta, H.Saito, T.Fujioka, to be presented at CLEO '89 (Bultimore, 1989)

3. D N.Grimes, Appl. Opt. 10, 1567 (1971)

4 J.W.Goodman, Statistical Optics (John Wiley & Sons, New York, 1985), pp 296-300
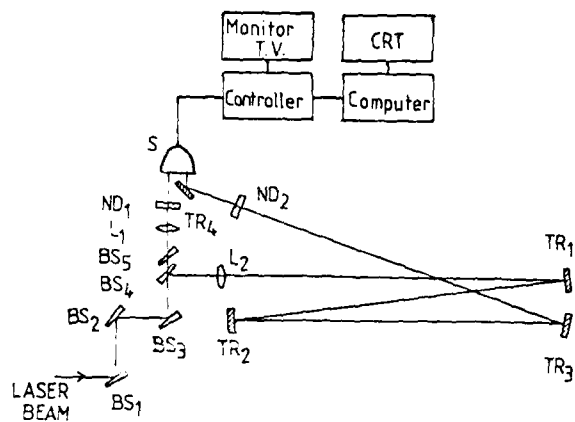
Fig.1 MEASUREMENT SYSTEM

Fig.2a Far (left) and
Near (right) Field Pattern

Fig.2b Intensity Profile
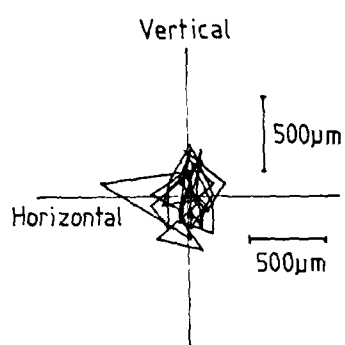
Fig.3a A trace of the peak position of
the far field spot at 250Hz pulse rate

Time Fig.3b Virtical Component

Time Fig.3c Horizontal Component
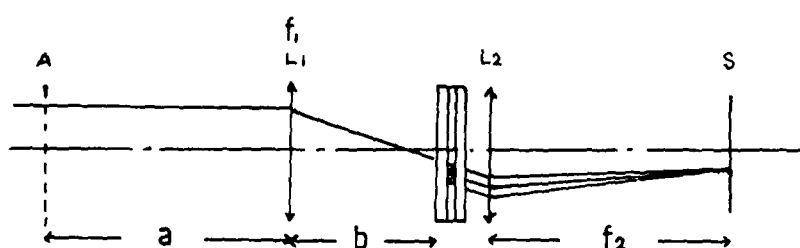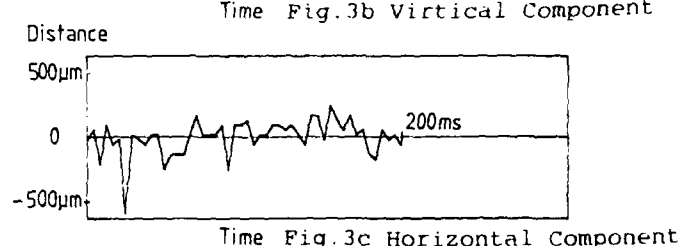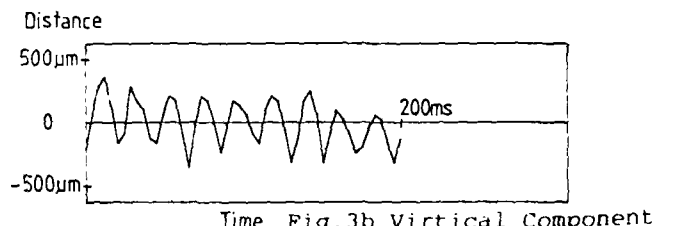
Fig.4 Measurement System for the Narrow Band System

Fig.5a Spectral Distribution of
Narrow Band Oscillator

Fig.5b Time Resolved Spectrum   time →
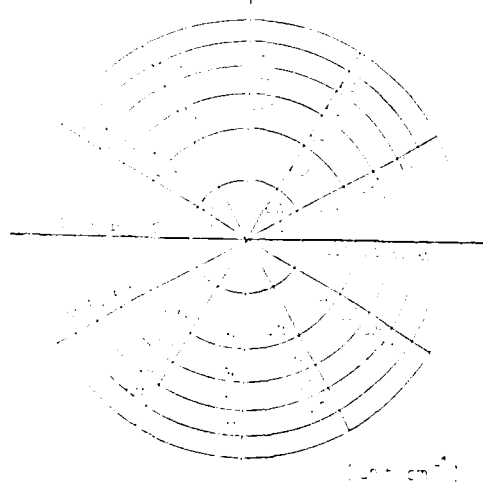
Fig.6 SPECTRUM DISTRIBUTION WITHIN THE BEAM CROSS-SECTION
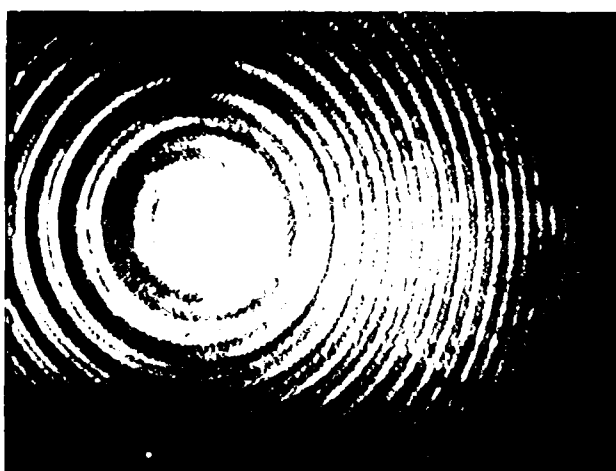
Fig.7a Spectral Distribution of
Narrow Band Oscillator
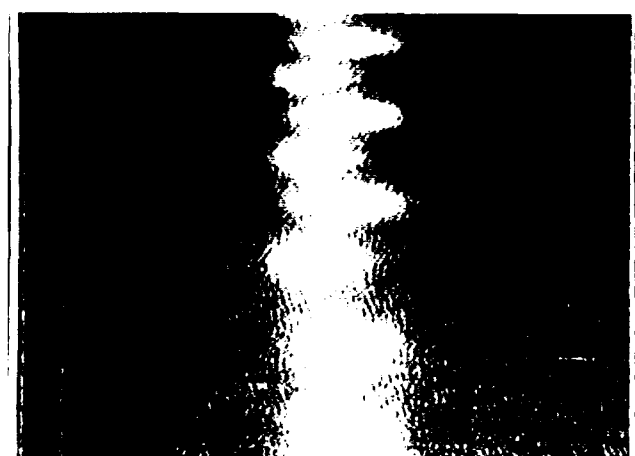
Fig.7b Time Resolved Spectrum   time →

132
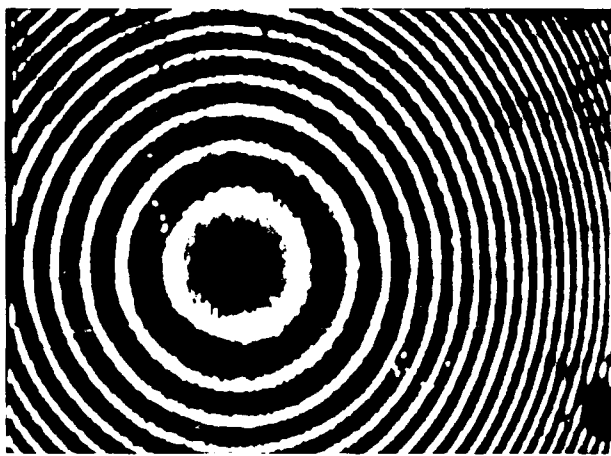
Fig.8a Spectral Distribution of Injection Locking System

Fig.8b Time Resolved Spectrum →time
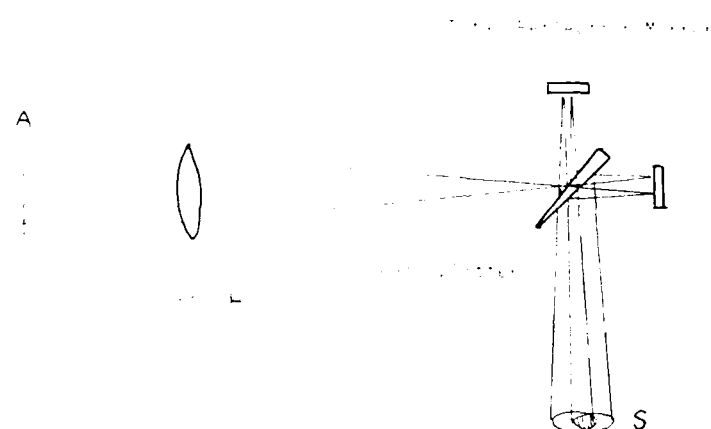
Fig.9 Optical Setup for the Coherence Measurement

Fig.10a Fringe Pattern of the Oscillator Beam

Fig.10b Fringe Profile
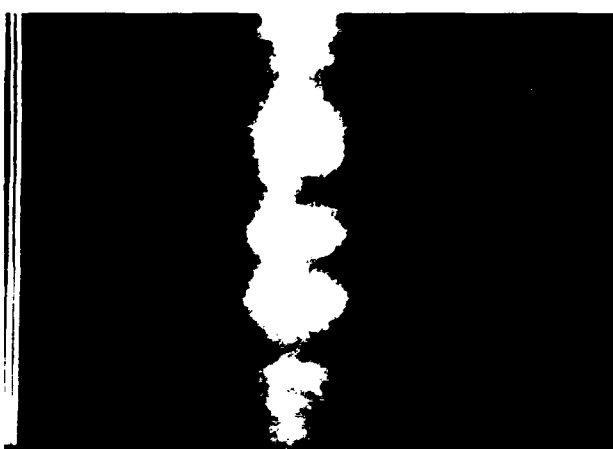
Fig.11 Time Resolved Measurement of the Coherence →time
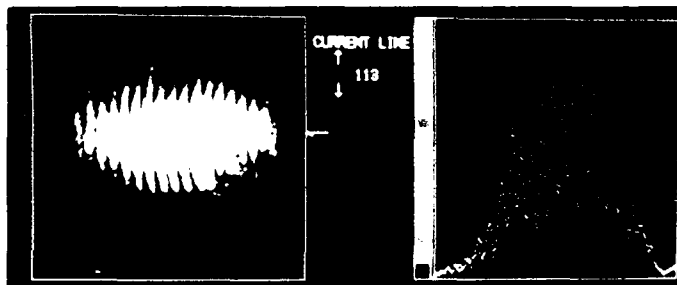
Fig.12a Fringe Pattern (right) and Profile (left) at 3ns of Delay

133
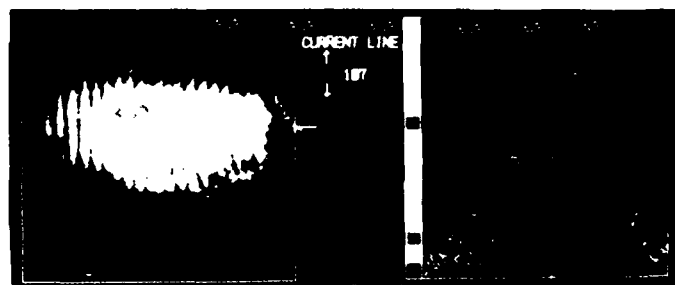
Fig.12b Fringe Pattern (right) and Profile (left) at 5ns of Delay
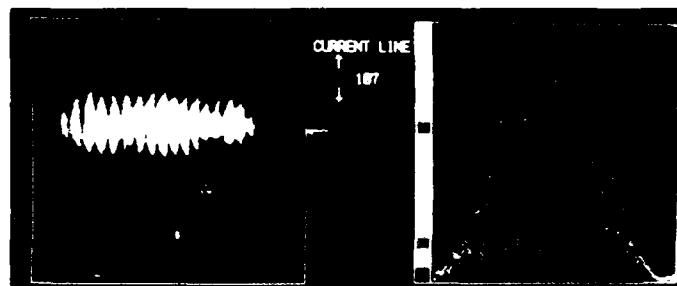
Fig.12c Fringe Pattern (right) and Profile (left) at 15ns of Delay

INTRINSIC EFFICIENCY OF THE DISCHARGE-PUMPED XeCl LASER AT VERY HIGH CURRENT-DENSITIES

Toshihiko Ishihara and Shao-Chi Lin

Department of Applied Mechanics and Engineering Sciences,
University of California, San Diego,
La Jolla, CA 92093

Abstract

Recent experiments show very high specific power output and high power-conversion-efficiency of the XeCl laser at high current-densities even thought the energy-conversion-efficiency is very low due to the duration of the discharge-current-pulse which is much longer than that of the laser pulse. Theoretical model which simulates the experiment with good agreement shows that such lasers can be operated at high energy-conversion-efficiencies while maintaining high specific power output.

Introduction

Interest in realizing the high power spaceborne lasers which can be used as communication devices[1] places severe constraints on the size, weight, efficiency, and durability of such laser systems due to the limitations imposed by the carriers of the laser systems, i.e., satellites and airplanes.

Recent experimental efforts on the x-ray preionized d.c. discharge XeCl laser have yielded promising results with respect to the availability of laser power and energy from a small discharge-volume device. Using a x-ray preionized d.c. discharge XeCl laser of ~ 3.8 cm^3 excitation volume at current-density $j \sim 10$ kA/cm^2, Xie et al.[2] at UC San Diego have recently observed peak laser power output of ~ 3 MW and output pulse energy of ~ 80 mJ, which implied specific power output ~ 800 MW/liter and specific energy output ~ 21 J/liter when such high-current-density discharge is scaled up to large excitation volumes.[2] The laser-pulse duration is only ~ 25 nsec FWHM (full width at half maximum intensity) which is much shorter than the ~ 400 nsec FWHM current-pulse employed. Consequently, the energy-conversion-efficiency is very low. However, by employing discharge-current-pulses of much shorter durations, preferably not much longer than the desired laser-pulse durations, it should be possible to increase the energy-conversion-efficiencies while maintaining high specific power output.

In this paper, the experimental results just described above are analyzed with the help of a theoretical model which uses experimentally measured discharge-current-pulse as one of the primary inputs. Also, some predictions are made on the performance of the discharge-pumped XeCl laser pumped by short (~ 50 nsec) discharge-current-pulses.

Theoretical Model

The model consists of a quasi-steady-state Boltzmann equation, a set of simultaneous chemical reactions, a laser-photon balance equation, and a time history of discharge-current-pulse. The Boltzmann equation is numerically solved by a self-consistent iteration scheme[3] in order to calculate the electron energy distribution function which in turn gives the electron kinetic rate coefficients as moments of the electron energy distribution function. All the important electron collision processes, i.e., the electron-impact electronic/vibrational excitation, electron-impact ionization, electron attachment, electron detachment, Penning ionization, Coulomb collision, and electron-electron collision, are included in the Boltzmann equation. A set of first order differential equations set up based on the simultaneous chemical reactions, including the electron collision processes, is numerically solved in

order to determine the temporal evolution of the chemical species existing in the laser plasma including the laser photons. A laser-photon balance equation which calculates the instantaneous laser output power is set up assuming that the number density of each chemical specie is uniformly distributed throughout the discharge-volume and that the photon number density is uniformly distributed inside the optical cavity. The detailed description of the Boltzmann equation, chemical equations and laser-photon balance equation can be found in Refs. 3, 4 and 5. In the previous models[4,5], E/n (electric field strength / total molecular number density) which is required by the Boltzmann code to calculate the electron energy distribution function is determined by solving the circuit equation which includes the laser plasma as a variable resistive element. In our alternative model, E/n is determined by using a given discharge current history as described below. The total discharge-current can be expressed as

$$I(t) = A e n_e(t) v_d(t) \tag{1}$$

where A is the discharge area, e is the electron charge, n_e is the number density of free electrons, and v_d is the electron drift velocity. The electron drift velocity under the influence of external field is a moment of the electron energy distribution function which poses strong dependence on E/n and weak dependence on the number densities of all the chemical species n_α participating in the electron collision processes. Thus , the electron drift velocity is also a function of E/n and n_a. Assuming that the drift velocity is a function of E/n only, that is, $v_d \equiv v_d(E/n)$, then the instantaneous value of E/n can be calculated using Eq.1 once proper initial conditions E/n(t=0) and n_α(t=0) are known.

This method of modeling becomes very convenient when the dependence of the laser performance on the discharge-current pulse is theoretically analyzed later in this paper.

Theoretical Analysis of the Experiment

Using the theoretical model just described above and the XeCl laser kinetic cross-sections and rate coefficients previously compiled in Refs. 4 and 5 with only minimum modifications and updating, a numerical simulation of the experiment done by Xie et al. is performed in order to check the validity of the new theoretical model and to help to analyze the experimental results.

In their experiment, Xie et al. successfully measured the laser pulse and discharge-current-pulse but failed to measure the discharge-voltage between two electrodes. As a consequence of difficulty in measuring the voltage drop through the excited plasma directly during the pulsed-avalanche discharge, it becomes necessary to calculate the discharge-voltage history V(t), which, along with the discharge-current history I(t), gives the instantaneous electric power input to the plasma $P_E(t) = V(t) I(t)$ in order to determine the efficiency of the laser.

The numerical simulation is done on a laser gas mixture of the mole fraction HCl:Xe:Ne = 2:40:5354 at total pressure of 7.1 atm. The optical cavity is formed by a total reflector and a output coupler of 40 % power reflectance. This setup when it is used in the experiment produces the 3 MW laser-pulse as described in the earlier section. The result of the simulation is shown in Fig. 1. The theoretically calculated peak laser power is ~ 2MW which is 30% lower than the experimentally measured peak power of 3 MW, and the laser-pulse duration is ~ 30 nsec which is 20 % longer than the
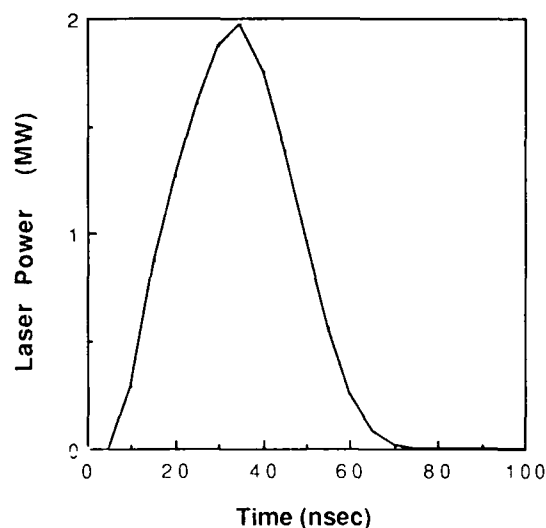
Fig.1 Calculated laser power output of the XeCl laser used by Xie, et al., in Refernece 1. The gas mixture used is HCl:Xe:Ne = 2:40:5354 at P = 7.1 atm.

experimentally measured pulse duration of ~ 25 nsec. Considering the uncertainties due to the experimental measurement of the discharge-current-pulse which is a primary input to this simulation and size of the discharge volume which must also be determined experimentally and some remaining uncertainties among the large number of the kinetic rates and cross-sections, the agreement between the experiment and theory is good.

Fig. 2 shows the power-conversion-efficiency $\eta_p(t) = P_L(t) / P_E(t)$ from the onset of the laser action, where P_L is the laser power output and P_E is the electric power input to the laser plasma. At $t = 5$ nsec in Fig. 2 where the laser power reaches its peak value of 3 MW, the electric input to the plasma is calculated to be only about 20 MW, thus, η_p is ~ 15 % at this point. However, the energy-conversion-efficiency $\eta_E(t) = \int P_L(t)dt / \int P_E(t)dt$ is very low due to the much long current-pulse, ~ 400 nsec FWHM, employed in the experiment.

Fig.2 Power-conversion-efficiency of the XeCl laser used by Xie, et al., in Reference 1.

The reason for very high specific laser power and energy can be explained by the effect of the high current-density on the formation of the XeCl laser upper state. The primary formation channel of the XeCl laser upper state is a 3-body ionic recombination process, i.e., $Xe^+ + Cl^- + M \rightarrow XeCl^* + M$, whereas the primary quenching channel of $XeCl^*$ at high current-densities is a collisional quenching process by the free electrons. The Xe^+ ions are produced by a direct electron-impact ionization of Xe atoms at their ground electronic state, or a two-step ionization of Xe atoms, i.e., the electron-impact excitation process $Xe + e \rightarrow Xe^* + e$, to be followed by the ionization process $Xe^* + e \rightarrow Xe^+ + 2e$. The Cl^- ions are produced by two successive electron-impact processes, i.e., the vibrational excitation process $e + HCl(v=0) \rightarrow e + HCl(v \geq 1)$, to be followed by the dissociative attachment process $e + HCl(v \geq 1) \rightarrow H + Cl^-$. Direct dissociative attachment of $HCl(v=0)$ also contributes to the production of Cl^- ions, but the rate coefficient is much smaller than those for $HCl(v \geq 1)$,[6] so that the two-step process is preferred. As the discharge-current-density increases, which may correspond to the increase in the electron number density in the laser plasma, the number densities of two important ionic species Xe^+ and Cl^- continue to increase via the electron-impact processes just described above, then the excimer formation rate is proportional to the 2nd power of the electron number density n_e while the quenching rate is proportional only to the 1st power of n_e. Thus, the saturation intensity of the XeCl laser under strong-pumping condition continues to increase with the discharge-current-density. This reasoning is supported by a series of the experiments done at UC San Diego[2,7] which clearly show that the specific laser output power and energy continue to increase as the discharge-current-density increases.

The reason for such a short laser-pulse duration in comparison with the discharge-current-pulse duration can be attributed to the depletion of halogen donor HCl molecules. The theoretical model predicts that the 99 % of HCl depletes in 68 nsec after the initial breakdown of the laser gas mixture. Once all the HCl molecules dissociate to H and Cl atoms through various kinetic paths, it may no longer be possible to produce enough Cl^- ions in order to form $XeCl^*$ via the 3-body ionic recombination process because the formation of HCl molecule is very slow process. The three-body recombination rate coefficient of the reaction $H + Cl + M \rightarrow HCl + M$ is, in deed, very low at 5.5×10^{-32} cm^6/sec,[8] and the recovery time for one half of the initial HCl molecular number density via this reaction is ~1.6 μsec.
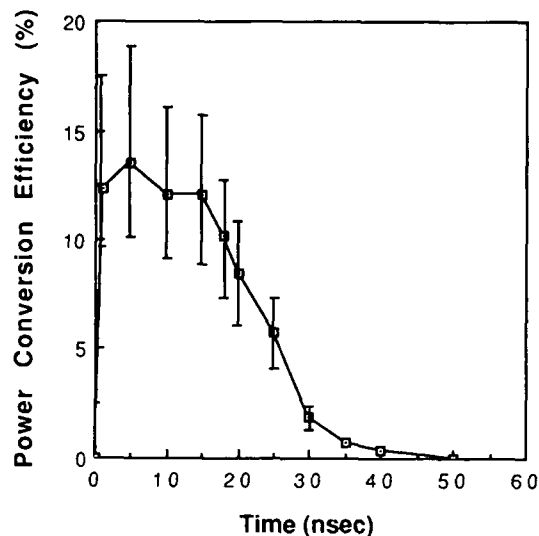
Therefore, much of the discharge-current-pulse employed by Xie *et al.* is wasted, and consequently the energy-conversion-efficiency is very low.

Highly Energy-Efficient Short Pulse Laser

The results just discussed in the preceding section strongly suggest the possibility of having a highly energy-efficient XeCl laser while maintaining high specific laser power output. One way to achieve such a goal is to employ short current-pulses which are not so much longer than the desired laser-pulse durations so that much of the current-pulse is utilized to pump the laser. In order to keep the high specific laser power output, the discharge-current-density must be kept high to keep the pumping rate high. Considering the requirements mentioned above and the fact that the laser-pulse duration observed by Xie *et al.* under very high discharge-current-density condition is only 25 nsec FWHM,[1] the theoretical analysis of the discharge-pumped XeCl laser pumped by hypothetical short discharge-current-pulses of 50 nsec is done. The dimension of excitation-volume, optics and gas mixture are chosen to be the same as those used by Xie *et al.* in their experiment. The shape of the discharge-current-pulse is chosen to be a sine curve with the half cycle of 50 nsec and is kept the same for all the calculations, but the peak value is changed from 5 kA to 30 kA, which corresponds to the peak current-density of from 1.2 kA/cm^2 to 7.1 kA/cm^2.

The results of the theoretical calculations are shown in Figs.3-6. Fig.3 shows the peak laser power and energy-conversion-efficiency as functions of the peak value of the discharge-current. The peak laser power continuously increases as the peak value of the discharge current increases. On the other hand, the energy-conversion-efficiency decreases as the peak value of the discharge-current increases. It should be noted that the energy-conversion-efficiency shown in Fig.3 is calculated by integrating P_L and P_E from t = 0 nsec to t = 50 nsec, but, in the real situation, the energy-conversion-efficiency is expected to be lower because the discharge-current would execute some kind of dumped oscillation and the current-pulse would last considerably longer than 50 nsec.

The continuous increase of the peak laser power can by explained by the same argument given in the preceding section with respect to the high current-density effect on the formation of XeCl*. The continuous decrease of the energy-conversion-efficiency is attributable to the premature

Fig.3 Calulated peak laser power output and energy-conversion-efficiency of the XeCl laser pumped by hypothetical discharge currents as functions of peak value of the discharge current. The gas mixture used is HCl:Xe:Ne = 2:40:5354 at p = 7.1 atm.

termination of the laser-pulses compared to the current-pulse duration at higher discharge-current. The comparison between Fig.4 and Fig.5 makes this point clear. Fig.4 shows the calculated laser output power and the employed discharge-current-pulse for the peak discharge-current of 10 kA, and Fig.5 shows those for the peak discharge-current of 30 kA. When the XeCl laser is pumped by the current pulse of 10 kA peak current, significant laser power output is seen almost till the end of the current-pulse, and most of the discharge-current is effectively used to pump the laser. Under the peak current of 30 kA, the laser pulse terminates at t ≈ 30 nsec as shown in Fig.5, and significant portion of the discharge-current is wasted. The premature termination of the laser-pulse under higher discharge-current is due to the depletion of the halogen donor HCl molecules prior to the termination of the

current-pulse. As shown in Fig.6, there is still left some HCl even at t = 45 nsec at the peak current of 10 kA. But, at the peak current of 30kA, the 99 % of HCl initially present disappears in 30 nsec which corresponds to the termination of the laser-pulse in Fig.5, and the rest of the discharge-current after t = 30 nsec is not used to pump the XeCl laser.
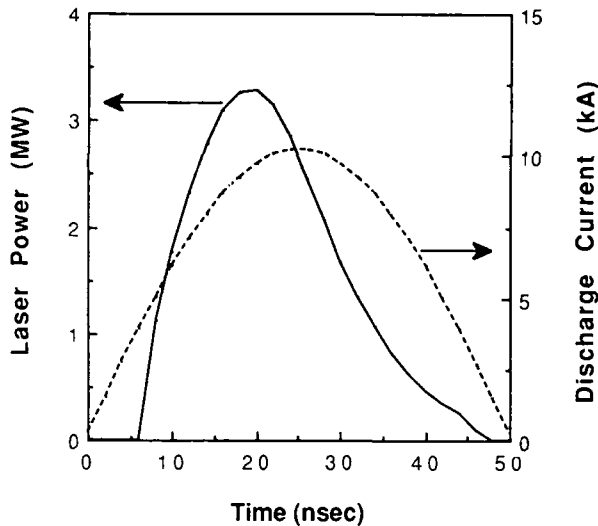
Fig.4 Discharge-current-pulse and calculated laser power output for the peak current of 10 kA.

Fig.5 Discharge-current-pulse and calculated laser power output for the peak current of 30 kA.

As we have seen from the theoretical calculations shown above, the termination of the XeCl laser-pulse under strong pumping condition is due to the depletion of the halogen donor HCl molecules, and therefore, by controlling the duration and peak value of the discharge-current-pulse one may be able to utilize the discharge-current-pulse effectively and to increase the energy-conversion-efficiency while maintaining high specific laser power output. Designing of the pulse forming networks which may produce such desired current-pulses is another matter of the engineering and ,therefore, is not discussed in this paper.
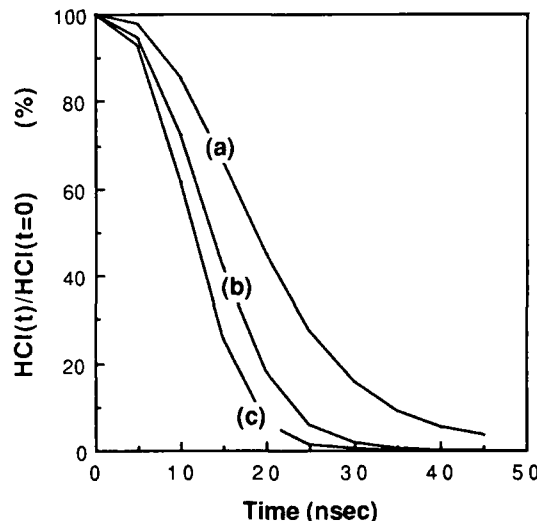
Fig.6 Depletion of HCl molecules for various peak values of the discharge-current.
(a): J_{peak} = 10 kA, (b): J_{peak} = 20 kA, (c): J_{peak} = 30 kA.

References

1. R. E. Chatham, presented at the Tenth International Conference on Lasers and Applications, Lake Tahoe, Nevade (1987), Invited Paper TH.1.
2. J. G. Xie, D. Lo and S. C. Lin, Paper in preparation for publication.
3. H. H. Luo, Ph.D. Dissertation, the University of California, San Diego (1978).
4. Y. S. Wang, Ph.D. Dissertation, the University of California, San Diego (1982).
5. S. B. Zhu, Ph.D. Dissertation, the University of California, San Diego (1984).
6. M. Allan and S. F. Wong, J. Chem. Phys. 74, 1687 (1981).
7. C. E. Zheng, D. Lo and S. C. Lin, Appl. Phys. B41, 31 (1986).
8. N. Cohen and J. F. Bott, Handbook of Chemical lasers, ed. by R. W. F. Gross and J. F. Bott (John Wiley & Sons, New York, 1976).

High Repetition Rate X-Ray Preionizer for Discharge Pumped Lasers

S. Bollanti, P. Di Lazzaro, F. Flora, G. Giordano, T. Letardi, C.E. Zheng*

ENEA, Dip. TIB, U.S., Fisica Applicata, C.R.E. Frascati,
C.P.   65 - 00044 Frascati, Rome (Italy)

Abstract

The construction characteristics and the performances of an X-ray generator working at 200 Hz are described. The possibility to scale this system up to 1 kHz for the preionization of high average power gas lasers is discussed.

The achievement of a homogeneous and small contamination preionization is a key problem in the development of high average power discharge laser systems. We present here a simple and inexpensive X-ray preionizer developed at the ENEA Center of Frascati in the frame of the european joint program EUREKA.[1]

A vertical section of the preionizer is shown in Fig. 1. The X-ray diode works in a reflection geometry configuration. This means that the cathode emitted electrons are accelerated toward the high atomic number anode target, producing brehmsstrahlung radiation in a direction much different from those of the incident electrons.

The system core is the surface plasma cathode,[2] depicted in Fig. 2. It consists of an insulator plate (e.g. fiberglass, Kapton), sandwiched between a Cu sheet connected with a trigger voltage and a sheet of grounded Cu on which there is a matrix of discs. Each disc is separated from the grounded Cu by an annular gap where the copper has been etched off. When the trigger is applied, a high electric field across the gap generates a vacuum breakdown, and neutral gas atoms are desorbed from the surface. This gas ionizes quickly, forming a plasma that expands away from the cathode.[3]

The geometrical arrangment of the Ta wrapped anode with respect to the cathode (see Fig. 1) has been choosen taking into account the results of a simulation work performed at the ENEA Center of Bologna.[4]

Figure 3 shows the equivalent circuit of the preionizer.

The measured voltage waveform at the transformer output is reported in Fig. 4, together with the typical shape of the current flowing in the diode measured by means of a Rogowsky coil.
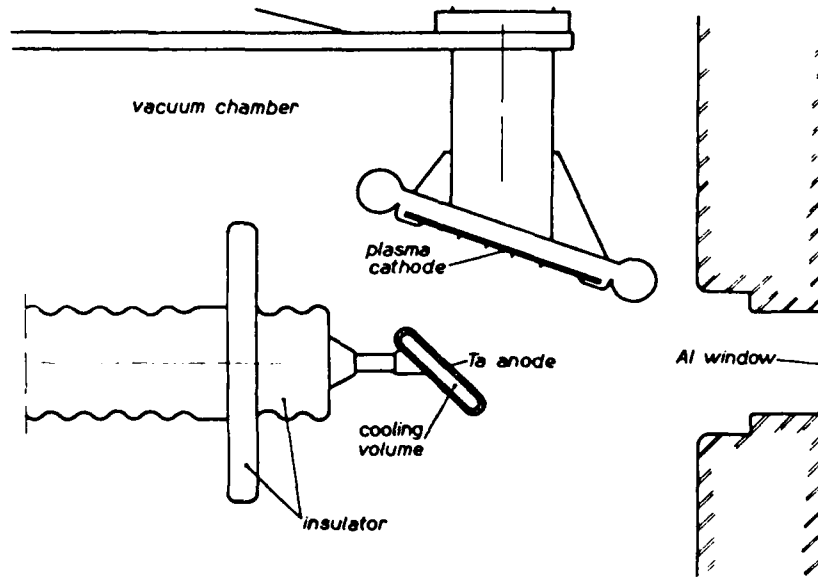
Fig. 1 - Vertical section of the X-ray diode

* ENEA Guest. On leave from Shangai Institute of Optics and Fine Mechanics
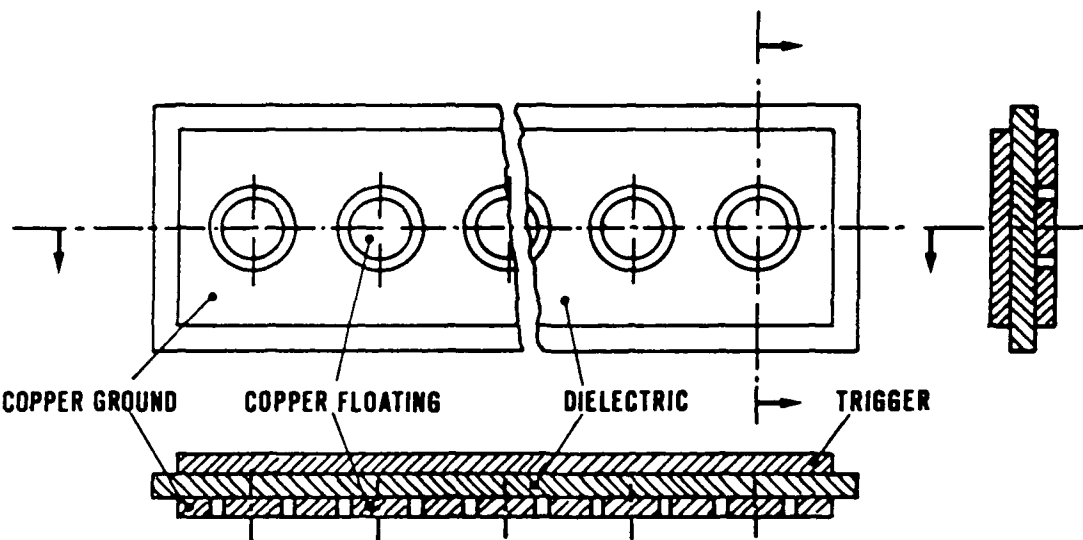
Fig. 2 - Scheme of the surface plasma cathode
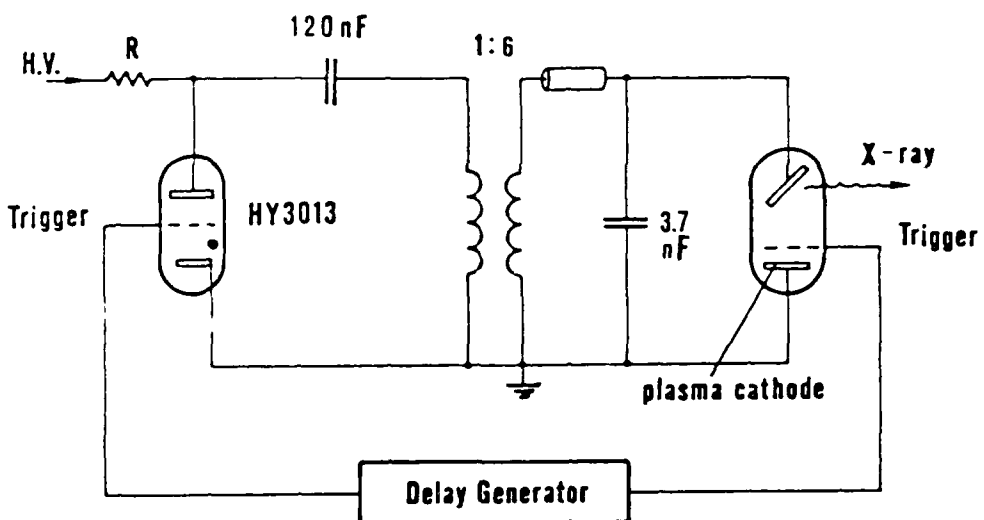
Fig. 3 - X-ray preionizer equivalent circuit

The 100 Hz repetition rate X-ray signal is shown in Fig. 5. This result has been obtained running the plasma cathode at 1 kHz, but firing the anode every 10 shots of the cathode. As a matter of fact, we have been limited so far by the power supply, as shown in Fig. 6. With the facility of a 20 kW power supply, measurements at higher repetition rate are now in progress.

The dosage decay (measured with dosimeters) along the X-ray beam direction is shown in Fig. 7. Starting from the laser discharge cathode, there is a 13% of the X-ray dosage decrease after crossing the 3 cm wide laser discharge gap.

The preionization electron number density has been measured by collecting the electric charge of the drift electrons in 1 atm of Ne. This method [5] allows a more easy solution of the EMI problem compared with the probe technology or the drift current measurement techniques. Moreover, as the original laser discharge electrode system can be used as the

142
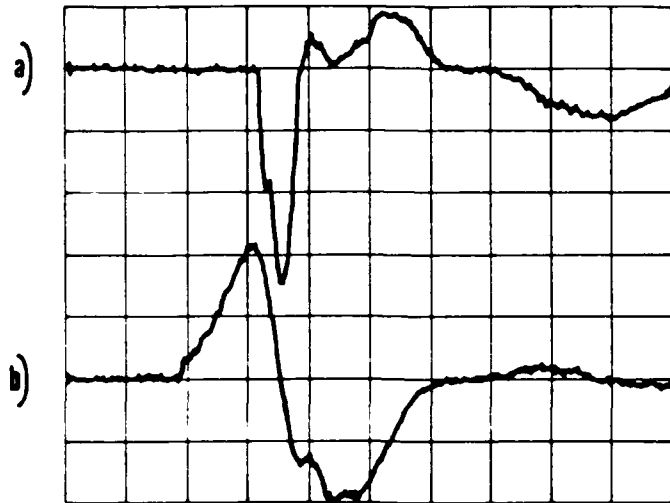
Fig. 4 – Current (a) flowing in the diode and voltage (b) measured at the transformer output of Fig. 3. Horizontal 1 µs/div. Vertical 240 A/div for the current, 30.8 kV/div for the voltage
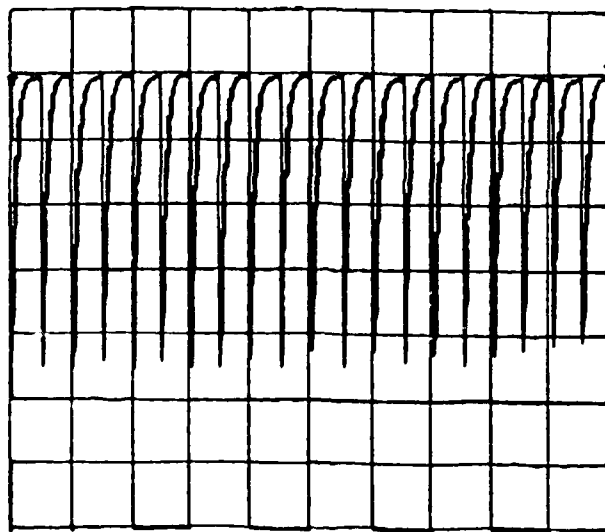
Fig. 5 – X-ray train pulses at 100 Hz, recorded by means of a plastic scintillator plus a photomultiplier and integrated with a time constant ~ 10 ms

electron charge collectors, no modifications of the discharge chamber are required for the sake of electromagnetic screen. The set-up is schematically drawn in Fig. 8. The experimental results obtained at two distinct cathode trigger voltage are reported in Fig. 9. The resulting maximum voltage drop ΔV on the capacitor $C = 2,8$ nF yields to the electron number density n through the relation $n = C \cdot \Delta V / e \cdot v$, where $e = 1,6 \cdot 10^{-19}$ C is the electron charge and $v = 0,45 \, \ell$ is the discharge volume.

A possible explanation of the results of Fig. 9 is that lowering the trigger voltage, the charge of the generated plasma on the cathode decreases, resulting in a lower diode current and a different X-ray spectrum, which is more efficient from the point of view of the electron-ion pair generation. We can therefore use the cathode trigger voltage as an additional degree of freedom to control the preionization electron density.

Finally, the X-ray dosage behaviour vs the repetition rate is reported in Fig. 10

143
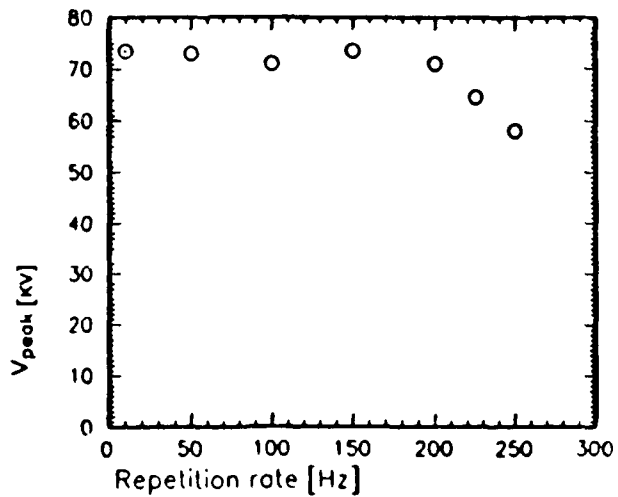
Fig. 6 - Charging voltage on the anode capacitors vs the repetition rate. Nominal power supply 5 kW
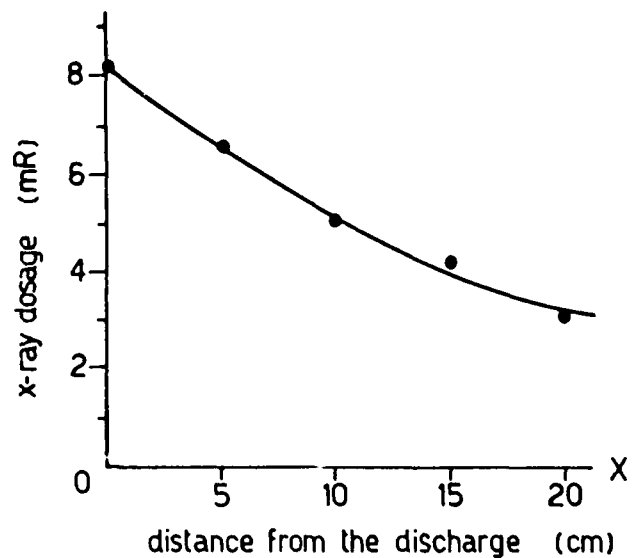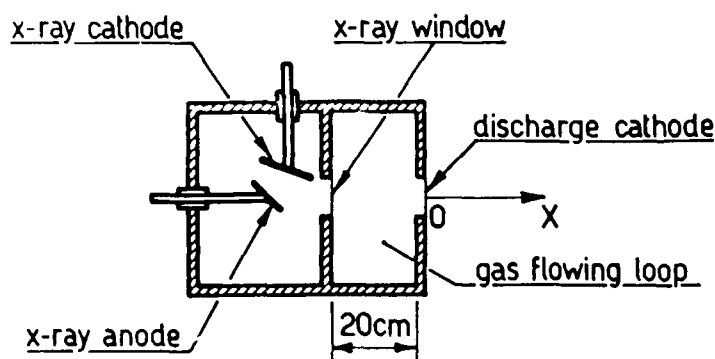
Fig. 7 - X-ray dosage distribution in air along the direction perpendicular to the laser discharge electrodes

together with the vacuum level of the X-ray diode chamber. Despite the pressure increment from 10^{-5} Torr at few Hz up to 10^{-3} Torr at 200 Hz, the X-ray dosage level remains almost constant in the range of repetition rate investigated here. This behaviour can be possibly attributed (according with Ref. 6) to the reliance of cathode surface on adsorbed material to be ablated. The material lost at each shot can be replaced by the residual pump oil and background vapor readsorbed on the cathode surface. Above a certain pressure level there is an equilibrium between adsorbed and ablated material, ensuring an effective cathode operation with a X-ray emission almost independent from the vacuum level, as shown in Fig. 10. On the other hand, the operating lifetime can be affected by the positive ion bombardment and the likelihood of low pressure arcs.

144
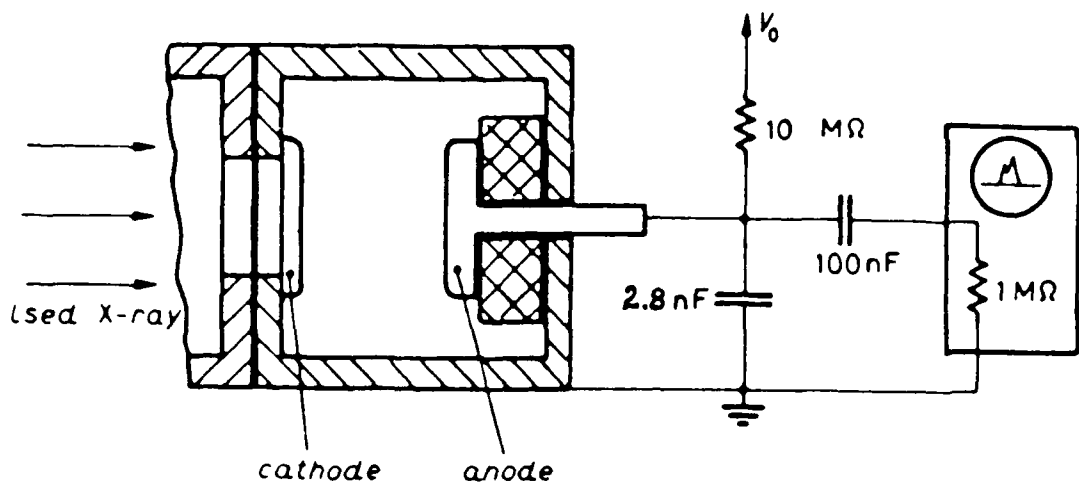
Fig. 8 - Experimental circuit and apparatus for the preionization electron number density measurement. The discharge region was filled with 1 atm Ne
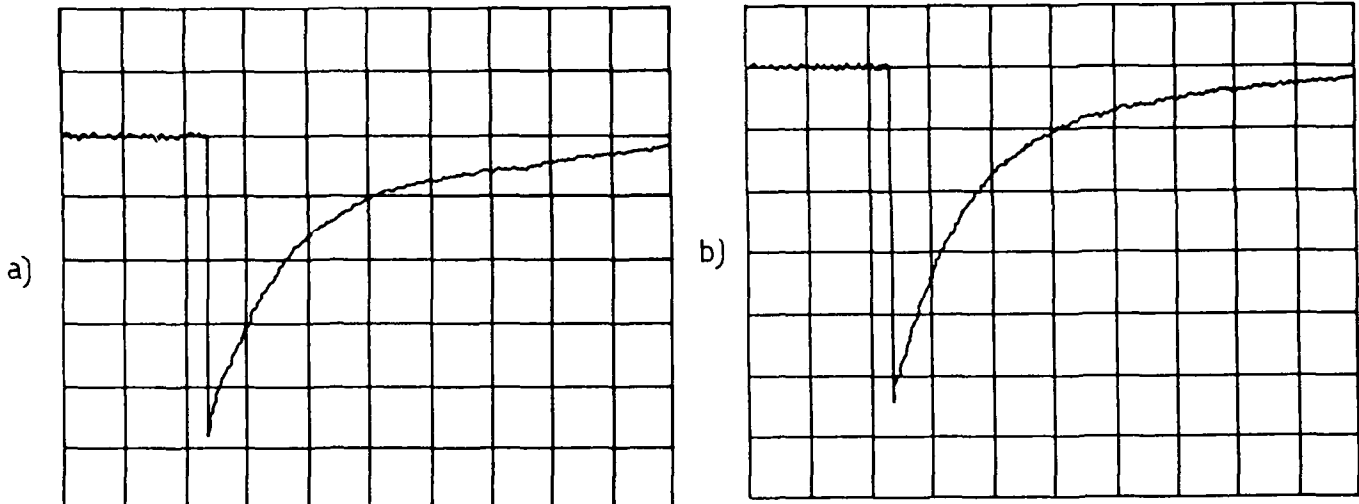
Fig. 9 - Measured voltage drop generated by the X-ray pulse in the circuit of Fig. 8. Vertical 200 mV/div, horizontal 2 ms/div; a) Plasma trigger voltage V=24 kV. Preionization electron number density $n=3.5 \cdot 10^7$ cm^{-3} b) V=16 kV, $n=4.2 \cdot 10^7$ cm^{-3}

Lifetime measurement have been performed continuously running the diode for extended periods at 100 Hz. Overheating of the cathode limited the performance to 10^5 shots, and work is in progress to overcome this problem.

In conclusion, a simple and inexpensive high repetition rate X-ray diode has been constructed and tested. The main experimental data are summarized in Table I. The possibility to run the surface plasma cathode at 1 kHz repetition rate has been proved, giving the experimental evidence that no problems in principle could prevent the efficient operation of the diode at least up to 1 kHz. A preionization electron number density greater than 10^7 cm^{-3} in 1 atm Ne with a good uniformity has been obtained. Preliminar results show that the outlined system is effective for the preionization of a (3×3×50) cm^3 active volume discharge XeCl laser: 700 mj/shot at 40 Hz have been achieved with an unoptimized spark-gap switched pumping discharge system at a dc charging voltage of 38 kV.
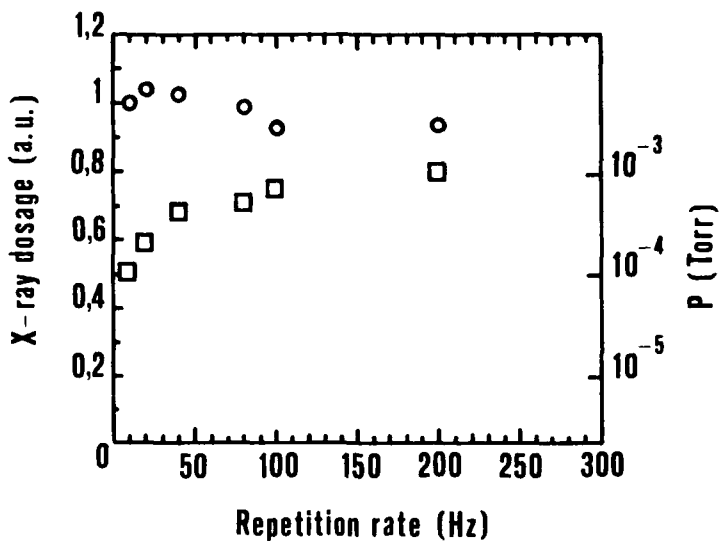
Fig. 10 - X-ray dosage (o) and vacuum level in the diode chamber (□) vs the repetition rate. The pressure values were measured after a few seconds of working, when the equilibrium condition was reached

TABLE I - Experimental summary

Diode operation mode	Pulsed, reflection geometry
Cathode type	Surface plasma
Input energy	10 J
Repetition rate	> 200 Hz
X-ray pulse duration	200 ns (FWHM)
Dosage in the laser cell	10 mR/shot
Dosage attenuation in air	(distance)-1
Dosage uniformity	> 70%
Preionization electron density	> 10^7 cm^{-3} in 1 atm Ne
Lifetime at 100 Hz	10^5 shots (continuous operation)

References

1. T. Letardi, P. Burlamacchi, M. Fantini, U. Perito and R. Salimbeni, in Proc. Int. Conf. on Laser 87, F.J. Duarte Ed. (STS Press, McLean, VA, 1988) pp. 73-85.
2. S. Humphries, J.J. Ramirez, and M.G. Wilde, IEEE Trans. PS-8, 517 (1980). D.G. Colombant, B.V. Weber, IEEE Trans PS-15, 741 (1987).
3. T. Letardi, P. Di Lazzaro, G. Giordano, and C.E. Zheng, "Large Area X-Ray Preionizer for Electric Discharge Lasers" to be published in Appl. Phys. B.
4. S. Pagnutti, "Spettri di emissione di brehmsstrahulung" (1988) unpublished.
5. G. Giordano, T. Letardi, and C.E. Zheng, Nuovo Cimento 101B, 569 (1988).
6. S.J. Scott, J. Appl. Phys. 64, 537 (1988).

LONGITUDINAL AND TRANSVERSAL WAVE BEHAVIOR IN A HIGH AVERAGE POWER EXCIMER LASER.

M.L. Sentis, P. Canarelli, Ph. Delaporte, B.M. Forestier, B.L. Fontaine.

Institut de Mécanique des Fluides, Aix-Marseille University, UM 34 CNRS, Marseille 13003
France.

ABSTRACT

To increase the pulse repetition frequency, the average power and efficiency of the XeCl laser system, numerous problems must be solved. One of the most important, which is related to wave propagating in the gaseous medium, is discussed. Excitation of active medium in a subsonic loop is achieved by means of a classical discharge, through transfer capacitors. The discharge stability is controlled by a wire ion plasma (W.I.P.) X-ray gun. The strong acoustic waves induced by the active medium excitation are analyzed by means of a Michelson interferometer and fast pressure transducers.

1. INTRODUCTION

Potential applications such as laser processing of semiconductors, laser machining, laser photo-chemistry and medical uses have stimulated studies and development of ultraviolet excimer lasers. These lasers operate generally at PRF to achieve high average output power. The general aim of these studies is to scale up excimer lasers to obtain higher average output power, longer pulse duration, higher efficiency and beam quality. Work is presently in progress in several laboratories[1-4]. However numerous problems are still to be solved ; the most important are : a) the electrical energy deposition at high PRF into gas mixture (stable discharge, homogeneity of the discharge ; b) to optimize the laser beam quality. Fluid mechanic studies may play a leading role to solve these problems.

Under the high pulse repetition rate and high energy per pulse conditions which are characteristic of future 1 KW (or more) average power excimer lasers, the fluid dynamic of the gas flow loop and laser head become a central issue. This problem, which is relatively well solved in the case of infrared CO_2 or chemical lasers, is much more severe here due to the short wavelength and regarding to the stability of the discharge in electronegative excimer active medium mixtures. Two main problems have to be solved : a) the heated gas has to be swept out of the laser cavity between two excitations (i.e. in much less than 1 ms for 1 kHz PRF) ; b) the density fluctuations induced by acoustic waves inside laser cavity have to be damped from $dr/r = 10^{-1}$ which is an average value of the density fluctuations immediately after an energy deposition of 100 to 150 J/1, to $10^{-4} - 10^{-3}$ in the same time scale. Attenuation of the aerodynamic disturbances without acoustic dampers is, at high PRF (> 200 Hz), too low to insure the uniformity of the density flow field required to obtain a stable discharge and a good optical beam quality at the time of the following energy deposition.

Three families of waves, at least, are present in a high PRF gas laser cavity : one family of longitudinal waves and two families of transversal waves. The longitudinal waves travel in the upstream and downstream directions of the flow and can be reflected by the previous hot gas column and also by any cross section shift or obstacle placed upstream or downstream the cavity. One family of transversal waves propagate between the electrodes, and the other one along the optical axis. They may play a leading role in the filamentation and loss of discharge stability at high PRF.

A program to investigate extensively the XeCl laser system (308 nm) for conditions of long pulse (50 to 100 ns), high PRF (1 kHz) and high average power (100 to 500 W) has been undertaken at I.M.F.M. A laser test bed called LUX for "Laser Ultraviolet preionisé par rayons X", has been developed. It permits to achieve in a laser head not yet designed to dampe the different acoustic waves, an average power of 200 W operating in burst mode (250 shots). The laser head has been recently modified to study detailed wave behavior in relation with Eureka program.

2. EXPERIMENT

2.1. Wind tunnel

[5-6] The 170 liter nickel plated stainless steel loop, already described in part elsewhere is designed for achieving a long "life time" operation in the working mixture. It has very low baseline flow turbulence level and flow pressure drop. Provisions have been made for fast damping of acoustic waves. A centrifugal compressor powered by a 4 kW continuous current motor allows an average flow velocity up to 65 m/s in the laser discharge head (2.5 x 30 cm cross section). The maximum working pressure is 2.5 atmospheres and is limited by the motor-compressor ferrofluidic seal capabilities. A turbo-molecular vacuum pump allows us to pump down to a residual pressure as low as 10^{-5} Torr to achieve good initial purity of gas mixtures.

2.2. Electrical excitation

The electrical excitation system consists essentially of a X-ray preionizer and a main discharge pulse.

2.2.1. The X-ray preionization generator

The X-ray are generated by means of a wire ion plasma (WIP) electron gun .The WIP electron gun was developed at O.R.A.[7]. This type of electron gun allows the control of the high voltage pulse by the low voltage (15 kV) control pulse on four thermionic wires. When a discharge pulse of 15 kV is applied to the anode, in the ionization cavity filled to 1.5 X 10^{-2} bars of helium, a plasma is created. The ions are accelerated to a ground extraction grid. Beyond this grid, ions are accelerated up to the constant negative high voltage cathode (-40 kV to -150 kV) where these generate secondary electrons by shock. Secondary electrons are accelerated to the grid and beyond up to the ground window. They produce Bremsstrahlung radiation mainly in the forward direction when they hit a 12.5 µm thick tantalum ($Z = 73$) foil placed directly behind the screen anode. Beyond the tantalum foil is a 0.5 mm thick aluminum foil which serves as a high pressure window for the X-ray.

2.2.2. The main discharge circuit

A classical thyratron switched C-L-C transfer circuit allows an average laser output power of 200 W at 1 kHz operating in burst mode. An electrical circuit diagram of the complete system, including the WIP gun, is shown in Fig. 1.
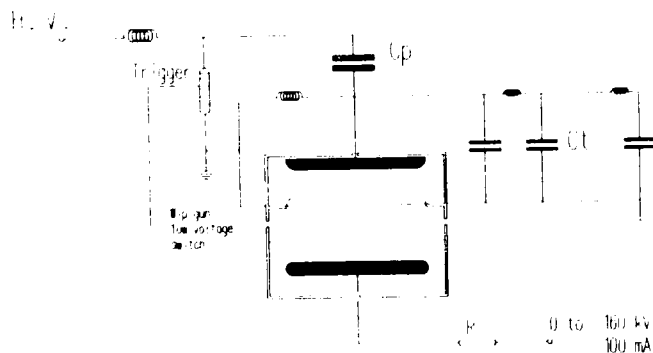
Figure 1 : Electrical circuit diagram.
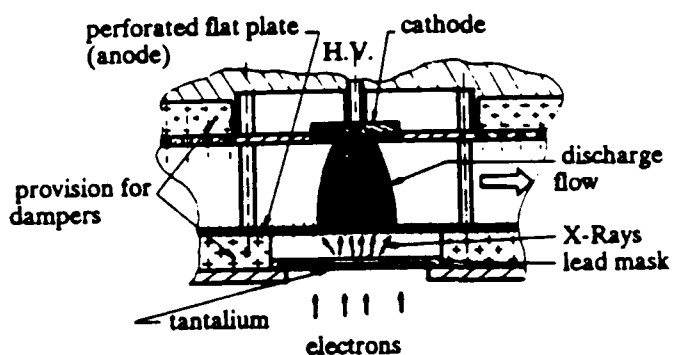
Figure 2 : New laser head diagram.

The charging voltage from the power supply, V_{max} = 15kV, is doubled through the resonance charging circuit to charge the main storage capacitors C_p. The thyratron (EEV CX 1572) is triggered by a synchronized pulse via a transformer connected to the (15 kV) input trigger pulse of the X-ray gun, which slowly charges the transfer capacitor bank (C_t) with a rise time of 150 ns. The time delay between the X-ray pulse and the laser discharge is controlled by a synchronization unit. The transfer capacitor array approximates a relatively fast transmission line with time constant fast compared with the 150 ns voltage rise time of the primary circuit. When the electrode voltage reaches the breakdown voltage the energy stored in the the transfer capacitor array is quickly deposited into the gas mixture.

The optical resonator is of the stable type, with long radius mirrors. The dielectric coated fused silica mirrors are set directly in the laser head side walls in contact with the working medium. The curvature radius of the mirrors are r = 2m. The reflection

coefficient at $\lambda = 308$ nm is $R_1 = 0.98$ for the rear mirror and $R_2 = 0.48$ for the extraction mirror.

A new laser head, which the volume has been strongly increased to manage the possibility to set acoustic dampers very close to the electrodes has been built. It is not yet fully optimized regarding aerodynamic and electric field distribution. At the present time, a shaped solid electrode is used as cathode and a flat foil as anode. With this configuration it is easy to dispose perforated foil or screen as anode and to investigate wave behavior in laser head with backing volume behind the anode. It will be possible to put in this backing volume absorbing materials or wave deflectors. A diagram of this laser head is shown on Fig. 2.

Specific diagnostics have been developed. They allow to study quantitatively the key parameters of LUX test bed. They include frame and streak laser interferometry, fast piezoelectric pressure transducers. Shot to shot variations in the beam energy profile in the near field are obtained using a specially designed home detector[3].

3. EXPERIMENTAL RESULTS

3.1. Interferferometric study of the flow field in the laser cavity

Interferometric study of the flow field have been undertaken with a classical Michelson streak interferometer. The optical source is a cw argon ion laser associated to an electro-mechanical shutter. The fringe pattern is recorded by means of a drum camera which permits to follow fringe shift as a function of time during 4 ms with a resolution on the film of 5.4 μs/mm. The observation zone is defined by a slit optically conjugated with the film and the laser head.

The results presented hereafter have been obtained with an horizontal or vertical slit. The analysis of interferograms leads to the evolution of flow density as a function of time along X or Y axis. The vertical slit use permits a much more precise study of the transversal waves propagating between the electrodes. The influence of these waves on laser characteristics have been already underlined in a previous paper [9]. The sensitivity of the interferometer is equal to (dr/r = 5.10^{-4}). This sensitivity is too low to check the goal of the required density fluctuation level for some excimer laser applications (dr/r = 10^{-4}). Classical method of fringe pattern analysis has been developed by means of digitizer and personal computer.

The interferogram of Fig. 3 shows up the fringe pattern recorded with a horizontal slit with two shots at 1 kHz PRF. It permits to follow the evolution of density fluctuations over the total width of the laser cavity for a time greater than 1.3 ms. The fringe pattern before the time of electrical excitation may be considered as a tare. In this interferogram two sets of induced shock waves flowing upstream and downstream are clearly visible. The columns of heated gas, swept out of excitation zone by the flow, are also visible as well as the effects of thermal diffusion between heated slugs and cold gas. The reflections of induced shock waves by the previous thermal slug and by the current returns (6 insulated rods (D = 8 mm) disposed orthogonally to the flow and at 4 cm to both sides of the electrodes) are relatively weak. The main disturbances yet visible 1ms after a shot seem to be due to the propagation of transversal acoustic waves in a orthogonal direction to the flow and laser beam axis.

Fig. 4 shows the comparison between the density profiles along X axis 0.1 ms after a first shot and a 125th shot. The energy deposition is strongly modified. We observe random modifications of discharge volume and discharge location which are theoretically controlled by the electrode shape or by the preionization. This modifications may explain the shot to shot laser energy decrease which has been recorded on Lux device. Fig. 5 is an extrapolated three dimensional plot of density field in the laser cavity from 14 X-profiles and one t-profile. The decreasing of aerodynamic perturbations is clearly visible with the disappearing of heated gas column which is slowed by thermal diffusion. These interferograms have been recorded on a simple laser cavity without sophisticated acoustic dampers.

Fig. 6 shows a first shot (Y,t) interferogram when the observation zone is located just upstream of the excitation zone (1mm). The straight fringes at the bottom correspond to the flow density field in the laser head just before the first energy deposition. The first

(X,t) INTERFEROGRAM

- W = 150 J/L
- Ne/Xe/HCl   1700/16/10
  P = 2.3 Bars
- PRF = 1000 Hz
- V = 43 m/s

t (ms)

1
(shot No2)

FLOW

0.5

0
(shot No1)
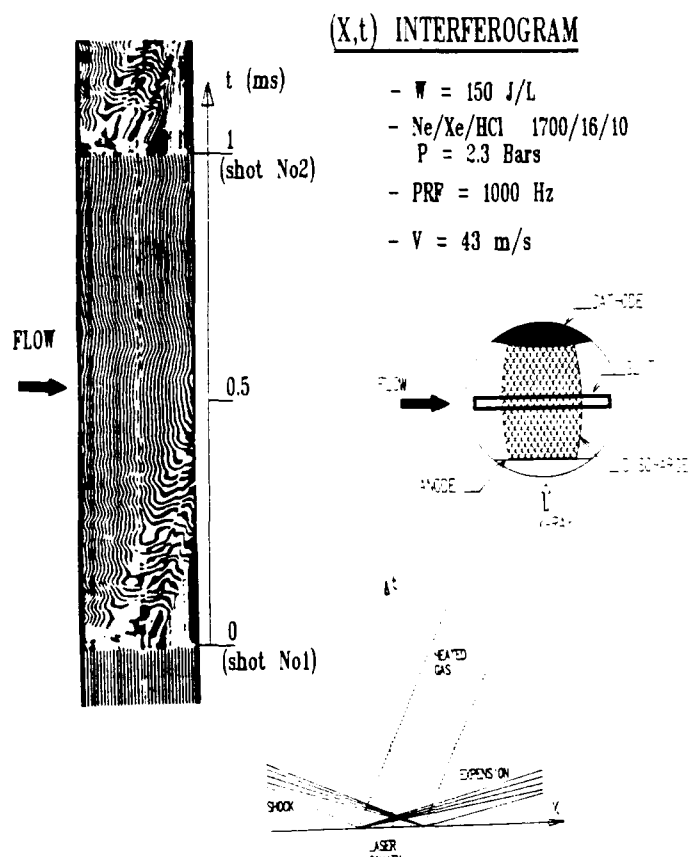
Figure 3 : (X,t) Interferogram of two energy deposition at 1 kHz PRF.
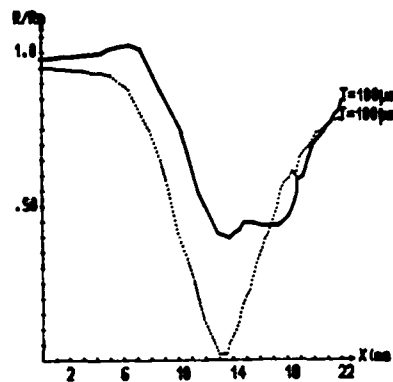
Figure 4 : Comparison between two profiles of density : 1st shot (——) and 125th shot (....).
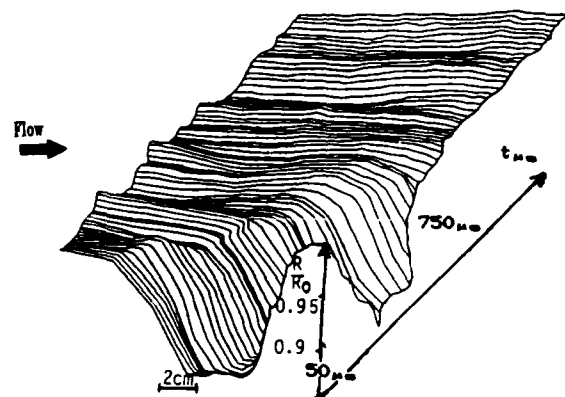
Figure 5 : Density evolution between two successive pulse.

fringe displacement (toward the left) is induced by the density increase due to the arrival of the compression wave in the observation zone. During a short time (dt = 3 µs), according to classical theory, the density field is relatively stationary before the passage of expansion waves which lead to a fringe shift toward the right. Following these three classical zones, the fringe shift permits to deduce the density flow field at the entrance of the laser head ; the reflections of transversal waves by the electrodes are clearly visible. These waves seem to carry most of density perturbations even 1 ms after the first energy deposit.

Fig. 7 shows an (Y,t) interferogram corresponding to a third energy deposition at 1 kHz PRF. Here the observation zone is inside the discharge volume. Theoretically the energy deposition must be uniform in all the volume of excitation zone and the fringe shift must be instantaneous and uniform on the total gap height. The interferogram shows up a distortion of discharge (3 mm). Part of these heterogeneities may be attributed to the density fluctuations clearly visible just before the third deposition of energy. This type of pattern is not stable and changes from shot to shot occur.

3.2. Pressure wave studies

The results given hereafter have been achieved with fast pressure transducers (PCB 112A22) whose rise time is equal to 2 μs and cut off frequency equal to 140 kHz. Two locations are used : mark A and B of Fig. 8.

Pressure time histories are dependant of channel geometry and energy deposition profiles. The results of Fig. 9a and 9b show pressure variations of a single shot experiment as a function of time, and without flow through the laser head already described and optimized[10] after years of studies. The same pressure waveform is shown with two different time scales (2 ms (9a), 50 μs (9b)). In Fig. 9a, the very short signal corresponds to an electromagnetic noise and indicates time and duration of energy deposition. The first jump shows up the increase of pressure due to the longitudinal shock wave induced by the discharge; the following decrease of pressure is related to the associated expansion wave. Taking into account the ratio between the heated gas volume (100 cm3) and the total volume of the loop (≃ 200 liters) the pressure will normally decrease to a near one level. The superimposed fluctuations are induced by reflections by channel walls. The period of pressure oscillations corresponds to the beating of the two waves between horizontal channel walls. The correlation with interferometric study (Fig. 6) is very clear and underlines again the importance of the transversal waves between the electrodes. The beating of waves between lateral walls is less visible and corresponds to modifications of wave pattern 0.2 ms after the passage of the initial shock wave.

The other results presented hereafter (9c to 9g) have been achieved with the new laser head (Fig. 2). In this new configuration, beating of transversal waves between electrodes is nearly masked by strong perturbations which seem to be due to spatial non uniformity of the energy deposition. Later structure and electrode disassembling has clearly shown different zones of enhanced sputtering on electrode material. These zones correspond to positions where electric arcs appears, probably at the end of the useful laser discharge. A larger energy density is locally and lately deposited ; these additions of wasted energy generate strong acoustic perturbations. The positions of these zones in the actual device, are related to the electrode configuration and discharge circuit characteristics and more particularly to the position of current return rods across the flow. A precise analysis of trace 9c shows that the jumps (x) (y) (z) are strongly related with the described sputtering zones here above and the increases of recorded pressure with the transducer at the location B (9d).

In order to underlines the effects of discharge quality on the pressure waveforms, various discharge conditions have been investigated. Fig. 9e and 9f represent the recorded signals when discharge stability is very poor (in this case the X-ray preionization has been switched off). The comparison of Fig. 9c and 9d on one hand and 9e and 9f on the other hand underlines clearly the strong modification of energy repartition. The default of preionization leads to a full filamentation of the discharge along electrode axis and to a multiplication of arcs (9f). The "useful" deposit of energy which could be considered, at first order, as proportional to the first jump of traces 9c and 9d is drastically lowered when preionization is switched off.

A first comparison of wave behavior when the anode is a solid or a perforated foil has been done nevertheless the poor quality of the spatio-temporal profiles of injected energy. It has however been possible to achieve, with this configuration, an average laser power above 150 W at 1 kHz PRF operating in burst mode. This output power value has to be compared with the one that has been achieved in the previous laser head (200 W) in quite similar experimental conditions. The pressure waveforms (9c and 9g) have been recorded with two different anode configurations : a thin (0.5mm) aluminum plain flat foil and a thin (0.5mm) perforated aluminum flat foil which the transparency is equal to 20 % (hole diameter 1mm). The comparison of first pressure jumps of traces 9c and 9g underlines the decreasing of initial shock wave induced by the useful energy deposition. This decreasing is caused by the expansion of the heated gas in the backing volume through the perforated anode foil. Unfortunately the ratio of useful energy (first jump) to wasted energy (other jumps) is lowered when perforated plate is used and that is confirmed by the pressure traces recorded with transducer B not reported here. The last jump, visible on the waveform 9g, appears at a time corresponding to the reflection of initial shock wave by the ends of

the backing volume which does not yet contain absorbing materials. The acoustic energy which has not been transported away of discharge zone is so redistributed later in the laser head.

4. CONCLUSIONS

Study of waves behavior in a high PRF excimer laser are in progress at IMFM. Specific diagnostics have allowed a quantitative analysis of pressure and density time histories in the LFX test bed laser head. Pressure transducers allow to readily verify the homogeneity of electrical energy deposit. The results show that energy is much less homogeneously deposited at high PRF. A new laser head designed to permit the study of damping devices in the immediate vicinity of discharge zone has been built. Pressure waveforms and density profiles as well as laser average power, achieved on this laser head, are much more dependent of the frequency than in previous one. These results underline : a) small changes in channel geometry and electric field distribution may play a leading role - b) interest to dispose of a test bed with powerful diagnostic tools to optimize the design of the future European excimer laser.

6. ACKNOWLEDGMENTS

5. REFERENCES

1. More than 20 European organizations or laboratories are implied in EUREKA Excimer Laser program.
2. Borisov and al. ; Sov. jour. quant. 17 (5) May 1987 p595
3. R.S. Taylor : Appl. Phys. B 41, (1986), pp 1-24.
4. W. Long : Laser 87,(Dec. 1987,Lake Tahoe USA.
5. M.L. Sentis : Revue Entropie No 115, (1984).
6. M.L. Sentis, B.L. Fontaine, B.M. Forestier : Proceedings of the fifth International Symposium on Gas Flow and Chemical Lasers, Series N 72, Adam Hilger Ltd Ed., (1985), pp 277-282.
7. D. Piguache, G. Fournier : J. of Vacuum Science and Techn., 12, 6, (1975).
8. Ph. Delaporte and al. : Proceedings of the 4th Int. Symp. on Optical and Optoelectronic applied Science and Engineering (High Power Lasers), SPIE Vol 801, (1987), p 86.
9. M.L. Sentis : thesis , U. Aix-Marseille II, Marseille (France) (may 1988).
10. M.L. Sentis and al. : Proceedings of the 6th International Symposium on Gas Flow and Chemical Lasers, Springer verlag Ed, (1988), p 125.

Figure 6 : (Y,t) INTERFEROGRAM

t (ms)

Fringe pattern after an energy deposit of 100 J/L

V = 43 m/s

0.25

0

(shot No1)
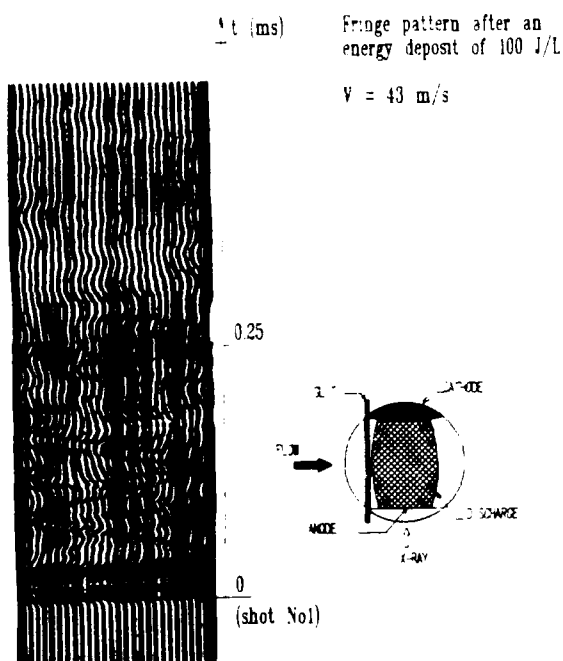
Figure 7 : (Y,t) INTERFEROGRAM

t (ms)

Fringe pattern after an energy deposit of 150 J/L

V = 43 m/s

0.25

0

(Shot No3)
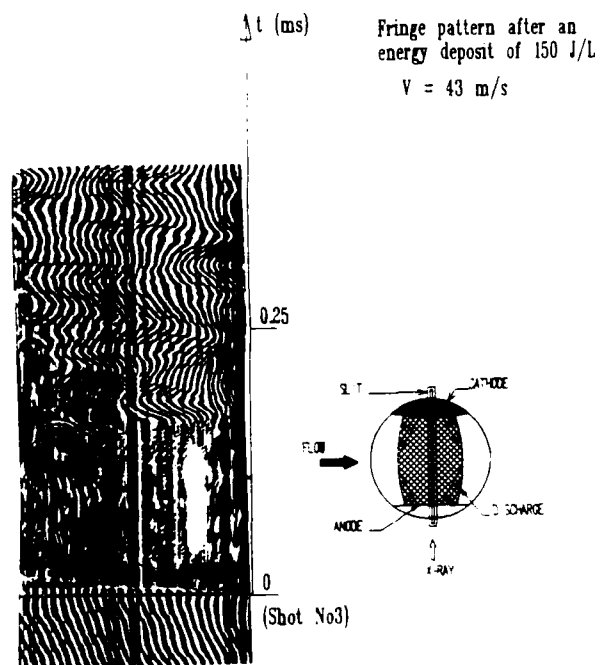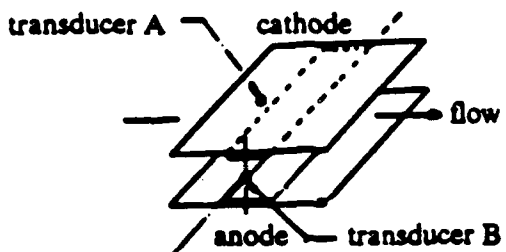
Figure 8.: Transducer position diagram.

0.13bars/div
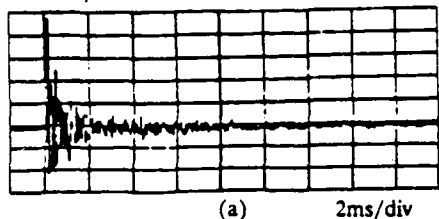
(a)   2ms/div

0.13bars/div
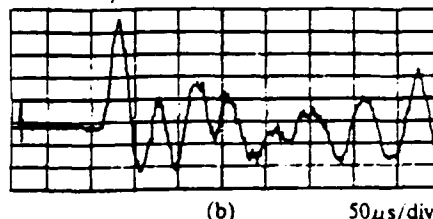
(b)   50μs/div

0.13bars/div
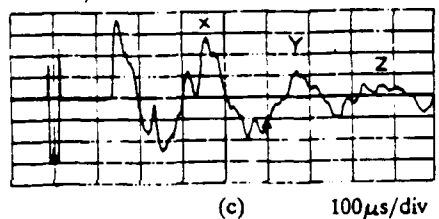
(c)   100μs/div

0.03bars/div
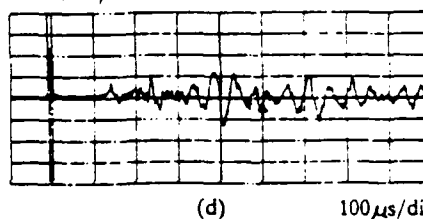
(d)   100μs/div

0.13bars/div
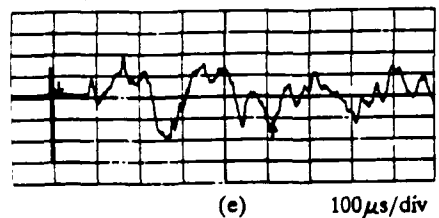
(e)   100μs/div

0.03bars/div
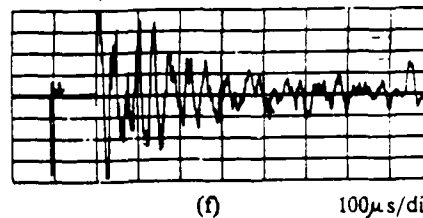
(f)   100μs/div

0.13bars/div
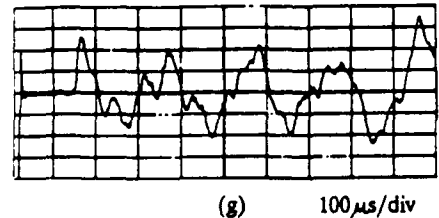
(g)   100μs/div

- electrode voltage : 24KV.
- Ne/Xe/HCl : 5300/50/10.
- Pressure : 2.3 Bars.
- previous laser head
  (a) , (b) transducer A : 2 different time scales
- new laser head
  (c) transducer A : plain flat plate
  (d) transducer B : plain flat plate
  (e) transducer A : plain flat plate without preionization
  (f) transducer B : plain flat plate without preionization
  (g) transducer A : perforated flat plate

Figure 9 : Pressure wave recordings.

153

PROGRESS TOWARD THE DELIVERY OF HIGH ENERGY PULSES WITH THE AURORA KRF ICF LASER SYSTEM

L.A.Rosocha, R.G. Anderson, S.J. Czuchlewski, J.A. Hanlon,
R.G. Jones, M. Kang. C.R. Mansfield, S.J. Thomas, R.G. Watt,
and J.F. Figueira

University of California, Los Alamos National Laboratory
P.O. Box 1663, MS-E548, Los Alamos, NM 87545
(505)667-6900

Abstract

Because of the attractiveness of short wavelength lasers for inertial confinement fusion (ICF), the Los Alamos National Laboratory is engaged in a program to investigate the feasibility of high power KrF lasers as future ICF drivers.

The main hardware element in this program is the Aurora KrF laser system, which is a prototype for demonstrating the applicability of optical angular multiplexing and serial amplification by large electron-beam-driven KrF laser amplifiers to potential large-scale fusion drivers. Multiplexing is a straightforward scheme for matching the energetic component (~5 ns) of the required target pulse to the longer pulse time (~500 ns) required for practical, efficient large-scale KrF laser amplifier operation.

Aurora uses a multiplexed 96-element train of 5-ns pulses, which is amplified and passed through a demultiplexer, where all pulses in the train are stacked in time by using suitable time-of-flight delays. Presently, the laser system is configured to deliver 48 stacked 5-ns pulses to the target at multikilojoule energy levels. In principal, it is possible to extract energy levels exceeding 10 kJ from the final Aurora amplifier. That device has produced over 10 kJ in the past when operated in a resonator configuration.

In this paper, we will report on the performance of the front end, amplifiers, and the optical train. Amplifier improvements, energy extraction experiments, and subsequent progress in the delivery of demultiplexed pulses to the target plane will also be discussed. As of this conference, we have tested the amplifier upgrade hardware, measured the gain on two modified amplifiers, installed optics on the main power amplifier, sized the beams to the target chamber, and begun firing the amplifier chain in a step-by-step process of integration from the front end lasers to the target plane. At the time of presentation, the second amplifier in the chain of four has exceeded the original design output of 50 J by more than 20%. Driven by this amplifier, the third amplifier yielded an extracted energy of 550 J. Experiments are in progress to energize the final amplifier and deliver pulses to the target chamber.

Introduction

The attractiveness of using short wavelength lasers such as KrF for inertial confinement fusion (ICF) have been well recognized for several years [1–3]. To translate the potential advantages of KrF lasers into practical ICF laser drivers, Los Alamos is constructing the Aurora prototype. Aurora is intended to demonstrate the applicability of KrF lasers to fusion and to serve as a test bed for particular technological aspects of larger KrF laser fusion systems (particularly angular multiplexing).

The Aurora system has been described in detail in several earlier publications [4–7]. An artist's conception of the system is shown in Figure 1. In this system, the front end laser output is replicated by means of aperture slicers, beamsplitters, and mirrors, to produce a train consisting of 96 individual 5-ns pulses. These time-encoded (multiplexed) pulses, which are spatially separated, are individually adjusted at the entrance pupil of an optical relay system. At this point, the beams are angle-encoded (multiplexed) in one-to-one correspondence to their time position in the beam train. The beam train is then relayed through two single-pass amplifiers (the Preamplifier and the Intermediate Amplifier), a double-pass amplifier (the Large Aperture Module), and then demultiplexed by the decoder before being delivered to the target chamber. Three automated alignment systems are employed to maintain optical alignment: these are located at the input pupil, the Large Aperture module (and its associated feed array), and at the final aiming mirrors.

To deliver short-pulse KrF laser energy to fusion targets, a decoder (demultiplexer) optical system is installed to compress the multiplexed beam train into a single 5-ns pulse at the target chamber. The decoder optics, the target system, and the target diagnostics for 48-beam energy delivery are presently installed and operational. We have chosen to use only 48 of the 96 beams to demonstrate the principle of Aurora at reduced system cost.

RECOLLIMATOR ARRAY — LAM FEED ARRAY — DECODER BEAM TUNNEL — INTERMEDIATE AMPLIFIER — LARGE APERTURE MODULE — 8-FOLD ENCODER — OPTICAL RELAY TRAIN — BEAMPLIFIER — DECODER OPTICS — TARGET CHAMBER — TARGET BUILDING — FRONT-END OSCILLATOR/AMPLIFIER — FRONT-END ROOM — 12-FOLD ENCODER — 96-CHANNEL MIRROR ARRAY — SAM AMPLIFIER
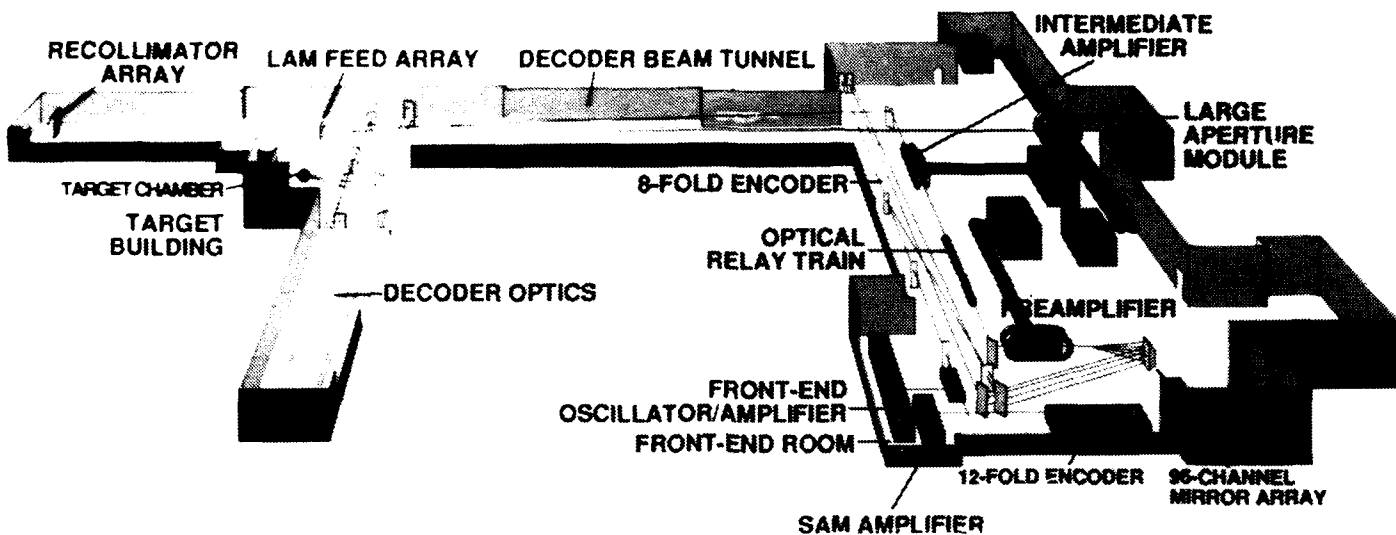
A schematic drawing of the Aurora laser system. The part of the building on the right contains the front end, the optical multi-plexer (encoder), most of the optical relay train, and the amplifiers. The structures on the left house the optical demultiplexer (decoder), the recollimator, and the target facility. To determine the scale, it should be noted that the distance from the Large Aperture Mod-ule to the target chamber is approximately 100 m, and the total flight path from front end to target approaches 1 km. The entire system is now constructed and in the process of high energy operation.

Aurora laser system components are now being integrated to amplify some 96 encoded pulses and to demultiplex 48 of these into a single 5 ns pulse at the target plane. We will report on progress toward that objective in this paper. As of the conference, we have amplified 96 multiple beams with the final 1 m x 1 m aperture ...

Front end

The Aurora front end system, which consists mainly of commer-cial laser hardware, provides the initial pulse that is replicated and amplified en route to the target. The front end, which is described in earlier publications [7, 8], employs a high pressure SF₆ cell to extract a 5 ns pulse from a longer 25 ns oscillator pulse by Stimulated Brillouin Scattering (SBS). A front end schematic diagram is presented in Figure 2. Typical output from the front end is approximately 100 mJ in two 5 ns pulses, which are subse-quently passed to the multiplexer.

Recent improvements in shortening the front end pulses have been performed by adjusting the pressure at which the SBS cell operates. Figure 3 shows pulses as short as 2 ns produced ... the ability to shape the front end pulses is important for a variety of laser matrix experiments on Aurora.
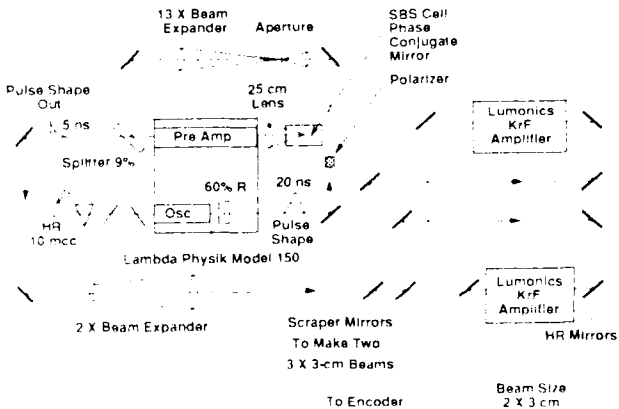
Fig. 2. Schematic diagram of the Aurora front end. Phase conjugation by Stimulated Brillouin Scattering (SBS) is em-ployed to shorten the KrF oscillator pulses.

Amplifiers

The gaseous gain medium in the Aurora amplifiers is excited by cold cathode electron guns, which have been extensively described elsewhere [9]. Figure 4 shows a cross section of a representative Aurora amplifier electron gun. In brief, our electron guns use planar cold cathode diodes employing graphite felt emitters rang-ing in emission area from 1,200 cm² to 20,000 cm². The diodes are

155
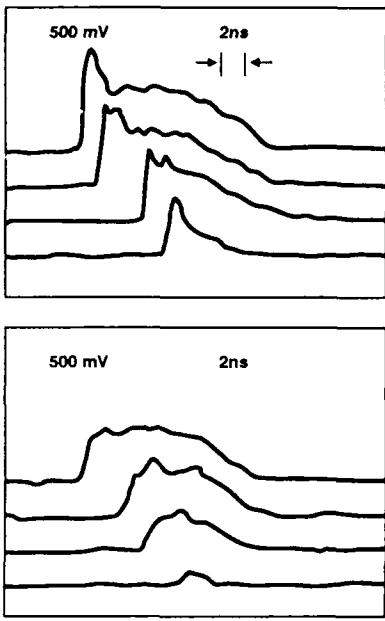
Fig. 3: The intensity at which the SBS cell reaches threshold is adjusted by changing the SF_6 pressure to produce variable pulse widths from the front end.
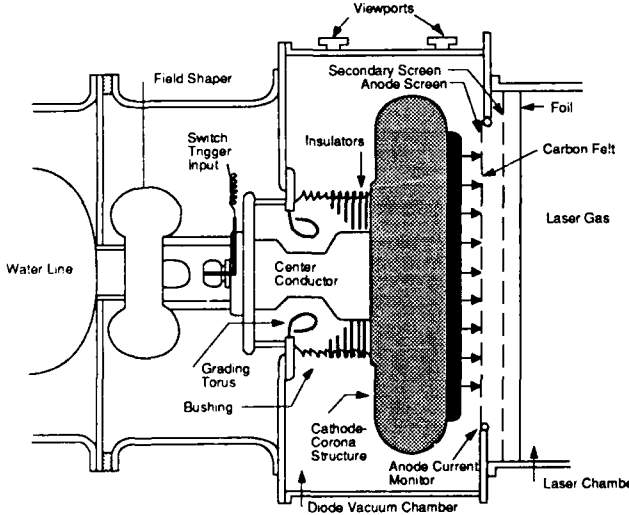
Fig. 4: Cross section for the Aurora LAM e-gun assembly. The LAM e-gun is representative of the major Aurora devices. It employs two parallel-connected PFLs for each of its e-guns in a double-sided excitation arrangement to achieve uniform pumping across its 1-m laser aperture. The laser axis is perpendicular to the plane of the figure. The e-beam emitter dimension is 200 cm along the laser axis and 100 cm transverse to the axis.

typically driven by Marx generator-charged pulse forming lines (PFLs) of low impedance (~2.7 Ω for most amplifiers). The usual electrical excitation pulse length is 650 ns, the diode voltage 500-700 kV, and the current density 25 A/cm² at the cathode. Electron current is transported into the laser gas through metal (Ti and Al) foils and a hibachi support structure. Beam transport is aided by externally applied magnetic guide fields of kGauss-level strengths.

Aurora contains four electron beam-driven KrF laser amplifiers ranging in optical aperture size from 10 cm x 12 cm to 100 cm x 100 cm. These devices are called the Small Aperture Module (SAM), the Preamplfier (PA), the Intermediate Amplifier (IA), and the Large Aperture Module (LAM). The nominal design characteristics of these four amplifiers are summarized in Table I.

Table I

Summary of Nominal Design Specifications for Original Aurora Amplifiers

Device	SAM	PA	IA	LAM
Pump pulse length (ns)	100	650	650	650
E-Gun voltage (kV)	300	675	675	675
E-Gun current in gas (A/cm²)	12	10	10	12
E-Gun Area (m²)	0.12	1.20	1.20	2.00
Input/output light energy (J)	0.25/5	1/50	50/2k	2k/20k
Stage gain	20	50	40	10
Laser Aperture (cm x cm)	10x12	20x20	40x40	100x100

Recently, we have completed upgrades on the SAM, PA, and LAM to increase their performance and reliability. Changes in the cathodes, hibachis, and PFLs have enabled us to increase the amount of electron beam energy deposited in the laser gas. Table II lists the new performance characteristics compared to previously achieved values.

The performance of Aurora amplifiers has also been characterized by measuring the gain of the excited laser media. Figure 5 illustrates gain calculations and measurements for the LAM including the effects of gain depletion by amplified spontaneous emission (ASE). In these measurements, the gain was measured with a probe

Table II

Electron Energy Deposition for Upgraded Amplifiers

Amplifier Device	Fraction of Max. Charge Voltage	Electron Beam Energy Deposited in Laser Gas		Hardware Changes
		Old	New	
SAM	93%	585 J	800 J	Cathode & Hibachi
PA	92%	10 kJ	20 kJ	Cathode & Hibachi
LAM	83%	125 kJ	>175 kJ	PFLs & Bushings
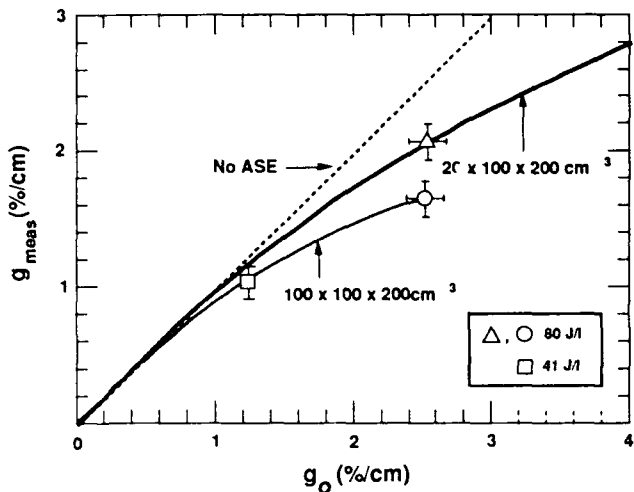
Fig. 5: Gain calculations and measurements for the LAM amplifier, considering the effects of ASE.

Fig. 6: Optical layout showing the beam paths and optics from the IA to the target focusing lenses. Previous system integration experiments used a set of surrogate LAM optics and a different coating on the turn mirror past the IA. A new higher reflection coating has now been applied to the IA turn mirror and different LAM optics are installed.

laser beam at two different e-beam pump rates. To test the effects of ASE, baffles were employed to reduce the LAM aperture size from 100 cm to 20 cm in the vertical direction. The performance of the staged amplifiers will be discussed in the section on system integration.

Optical System

The Aurora optical system serves to match the short target pulse requirement to the long pulse amplifier requirement. The system uses angle and time multiplexing to perform the match. Distance is used to provide the time delays needed to time-encode and decode a 96-beam pulse train of individual 5-ns pulses. The system has been described in detail elsewhere [4–7]. The main parts of the system are: (1) an optical encoder to generate the pulse train; (2) an angle-encoder to spatially separate beams and help direct them through the amplifier chain; (3) a centered optical system to relay beams through the amplifiers; (4) an optical decoder to provide the delay times necessary to stack the train of pulses into a single pulse at the target; (5) a set of final aiming mirrors, focusing lenses, and alignment systems to direct the beams on target and to keep the optical train aligned. The entire optical system has been assembled and beams have been sent to the target chamber at low power.

Most of the recent effort on the optical system has concentrated on the post-IA optical train, particularly the installation and integration of the LAM optics. The optical elements from the IA to the target are shown in Figure 6. The LAM mirror and window are shown in Figure 7. The mirror that we are presently using is downsized (about 20% of the full area) because we are still awaiting delivery of the full-sized (1 m x 1 m) mirror. The optical train shown in Figure 6 contains a new coating on the IA turn mirror, which will increase the overall transmission of the optical system by several percent.

Fig. 7: Photograph showing the downsized (20% area) LAM mirror and the monolithic 1 m x 1 m full-aperture window.

System Integration

Previously, we demonstrated a significant integration milestone by extracting amplified 96-beam energy through the Intermediate Amplifier [7]. Since then, we have improved the performance of three components (Front End, SAM, and PA), resulting in an increase in the chain performance through the IA from 250 J to 550 J. Figure 8 summarizes the Aurora system performance at the time of this conference. We are now in the process of directing the beam train through the LAM to amplify the total beam energy to the kilojoule level and of delivering high energy pulses to the target
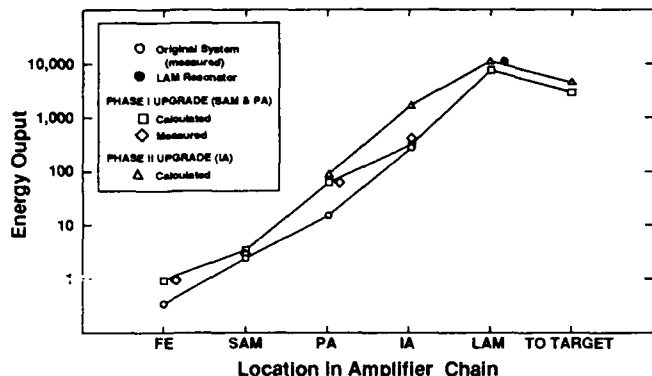
Fig. 8: The Aurora laser amplifiers are being staged to eventually produce 5 kJ in 48 beams at the target chamber. Calculated and measured energies are plotted as a function of position in the path from front end to target.

chamber. When the full-sized LAM mirror is installed, the LAM output energy is expected to increase to 3-7 kJ with the present IA performance.

Amplifier chain performance and energy transport to the target chamber will be characterized by measuring the laser energy and intensity at various points along the beam paths. Figure 9 illustrates the placement of the diagnostic instruments that will be used in these measurements. Figures 10, 11, and 12 are photographs of the diagnostics located at the LAM feed array, the recollimator array, and the target lens plate, respectively. Additional detectors, which are not shown in photos, will also be placed behind the decoder mirrors (which have been designed to pass about 1% of the incident beam energy for diagnostic purposes).

Future Upgrades and Anticipated Performance

Recently we have begun the design and construction of an upgrade to the existing Intermediate Amplifier. The objective is to increase the operational performance and reliability of the present device. Our motivation for the upgrade is that we cannot achieve the design value of stage gain (40x at 50 J input) with the present maximal e-beam pumping of about 35 J/l. The major change is to increase the electrical drive for the electron gun by adding a second pulse forming line, which in turn will increase the cathode voltage and the specific energy deposited in the laser gas. Table III compares the performance characteristics of the present IA and the upgraded amplifier. Figure 13 illustrates the expected LAM output when driven by the present IA and the upgraded IA. The IA upgrade should permit the Aurora system to operate very close to the design value of 5 kJ on target.
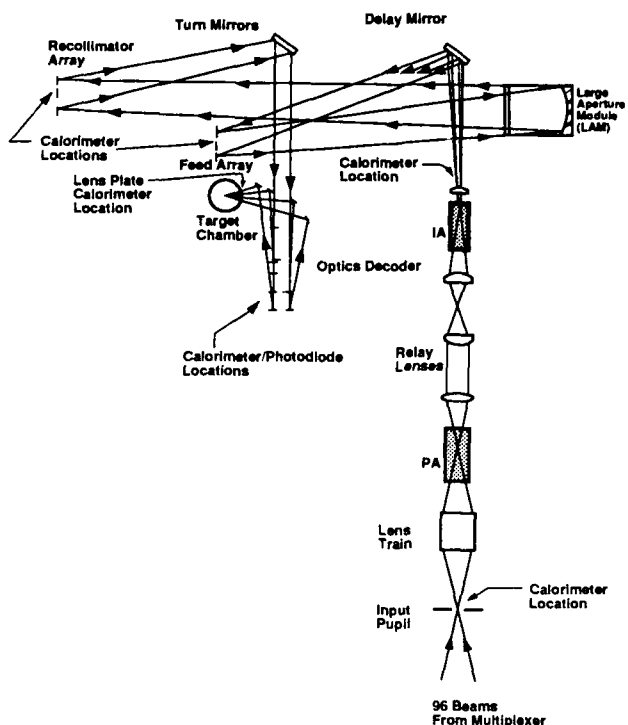
Fig. 9: Schematic diagram showing the placement of diagnostics that are being used to characterize the performance of the Aurora system.
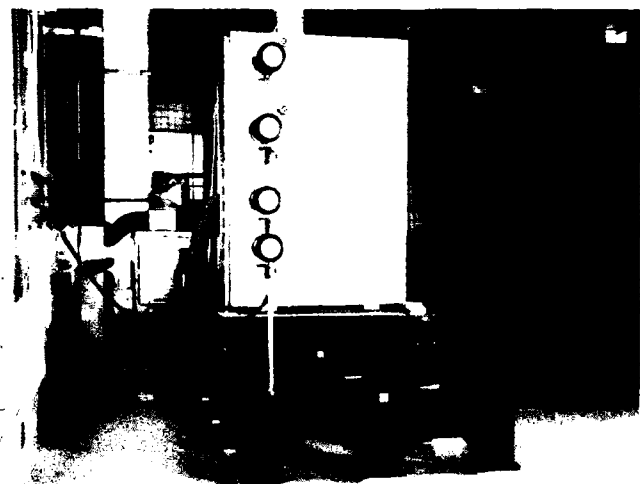
Fig. 10: Calorimeters are installed at the LAM feed array to measure the LAM input (or IA output) energy.

158
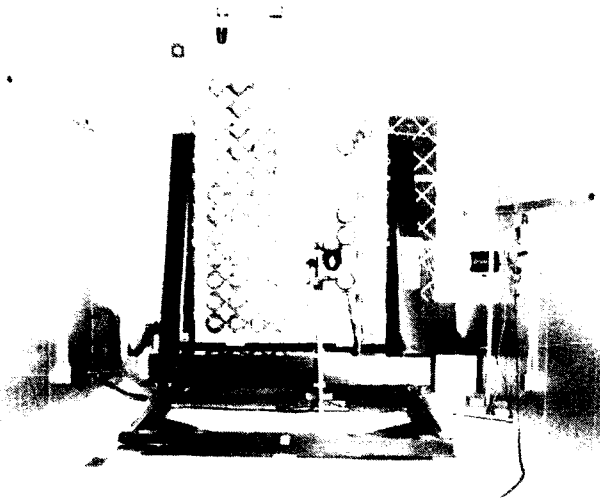
Fig. 11: Calorimeters and photodetectors are placed at the recollimator array to characterize the LAM output.

Fig. 13: Plot of LAM output energy vs IA driving energy for the present and upgraded Intermediate Amplifiers.

Fig. 12: Calorimeters and photodetectors are installed on the target lens plate to characterize the short pulses being sent to the target plane.

TABLE III

Design E-Beam Pumping Performance Characteristics
for Intermediate Amplifier (IA) Upgrade

	Pump Energy	Cathode Voltage	Maximal Pressure	Current Density* Diode	Gas
Present IA	35 J/L	550 kV†	1000 torr	17.6	7.0 A cm⁻²
Upgrade	97 J/L	770 kV	1400 torr	42.8	17.1 A cm⁻²

†machine limitation
*40% transmission assumed for hibachis

Some sensitivity analysis has also been done to examine the effects of changing the F_2 concentration and the IA gas pressure [10]. Figures 14 and 15 show the results of this theoretical analysis. This kind of analysis will be expanded in the future to provide practical guidance in optimizing the performance of the integrated Aurora amplifier chain. Additionally, we have carried out investigations concerning the effects of laser gas contaminants and gas mixing procedures on amplifier performance. It has been found that careful control over impurities and the mixing process must be exercised to ensure consistent performance. Impurities generated
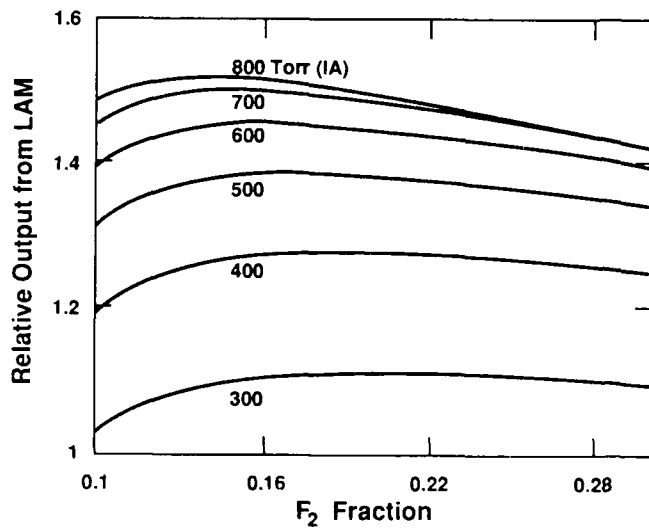
Fig. 14: Relative LAM output energy plotted vs changing F_2 concentration (mixture adjusted in all amplifiers). A family of curves are plotted with the IA pressure as a parameter.

159
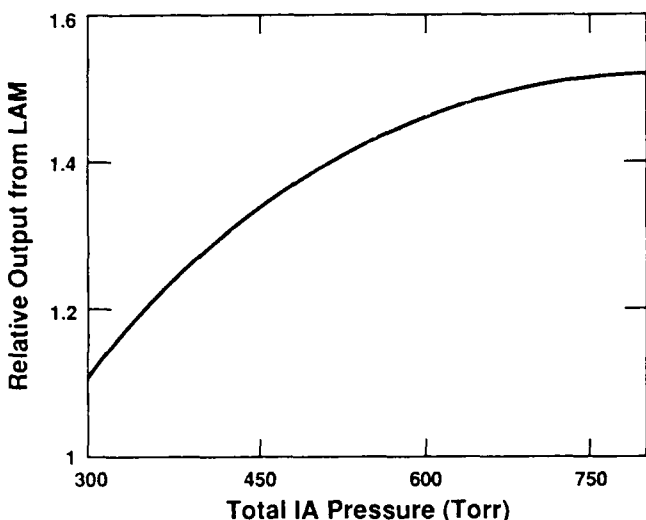
Fig. 15:   Relative LAM output energy plotted vs IA laser gas pressure. Little advantage is derived from increasing the pressure beyond 700 torr for the present IA.

by the interaction of the fluorine-bearing laser gas with the electron beam foil materials have also been studied. These results will be more completely discussed in a future conference [11].

Post-Conference Progress

Four days after the presentation of this paper, the entire integrated Aurora laser chain was fired for the first time. A 96-beam multiplexed pulse train containing approximately 2.5 kJ was extracted from the LAM and nearly a kilojoule of this energy (780 J) was delivered to the target chamber in 48 beams. For this first shot, a reduced size LAM mirror was used to extract energy from the central 20% of the full amplifier optical aperture. Work is now in progress to install a full-sized mirror in the LAM, which should allow energies in the range 4-7 kJ to be extracted from the complete 10,000 cm^2 LAM aperture.

Acknowledgments

The authors express their appreciation to the members of the Aurora project team for their dedicated effort toward the accomplishments reported in this paper. Additional thanks go to Ruth Holt for illustrations and layout and to Becky Johnson and Donna Duran for document preparation.

References

1. A.F. Gibson, "Lasers for Compression and Fusion," Contemp. Phys., 23, 285 (1982).

2. J.F. Holzrichter, D. Eimerl, E. V. George, J.B. Trenholme, W.W. Simmons, and J.T. Hunt, "High Power Pulsed Lasers," J. Fusion Energy, 2, 5 (1982).

3. R.J. Jensen, "KrF for Fusion: An overview of Laser Issues," Fusion Technology, 11, 481 (1987).

4. L.A. Rosocha, J.A. Hanlon, J. McLeod, M. Kang, B.L. Kortegaard, M.D. Burrows, and P.S. Bowling, "Aurora Multikilojoule KrF Laser System Prototype for Inertial Confinement Fusion," Fusion Technology, 11, 497 (1987).

5. J.A. Hanlon and J. McLeod, "The Aurora Laser Optical System," Fusion Technology, 11, 635 (1987).

6. J. McLeod, "Output Optics for Aurora: Beam Separation, Pulse Stacking, and Target Focusing," Fusion Technology, 11, 654 (1987).

7. L.A. Rosocha and L.S. Blair, "Recent Progress on the Los Alamos Aurora ICF Laser System," Proceeding of the Int. Conf. on Lasers '87, p. 164 (1988).

8. S.J. Thomas, K.W. Hosack, L.J. Lopez, I.J. Bigio, and N.A. Kurnit, "Improved Performance of the Aurora Front End with the Use of a Phase-Conjugate Mirror," Digest of Technical Papers, CLEO '88, p. 92 (1988).

9. L.A. Rosocha and K.B. Riepe, "Electron-Beam Sources for Pumping Large Aperture KrF Lasers," Fusion Technology, 11, 576 (1987).

10. B.J. Krohn, Los Alamos National Laboratory, unpublished results, Dec. 1988.

11. R. G. Anderson and R. A. Tennant, "Evaluation of E-Beam Foil Materials," to be presented at CLEO '89 Conference, Baltimore, MD.

HIGH-POWER, NARROW-BANDWIDTH KrF EXCIMER LASER

Hajime Nakatani, Hitoshi Wakata, Yoshibumi Minowa, and Haruhiko Nagai

Mitsubishi Electric Corporation, Itami Works and Central Research Laboratory
8-1-1, Tsukaguchi-honmachi, Amagasaki, Hyogo 661, Japan

Abstract

A narrow-bandwidth KrF excimer laser for use in microlithography has been developed. The output power and the bandwidth of the laser is 6.4 W at 250 Hz repetition rate and 3pm respectively. The laser is preionized by a surface corona discharge in order to prolong the gas life-time.

Introduction

Device design criteria of half micrometer linewidths have driven optical lithography to extend its imaging wavelength into the deep ultraviolet region. Excimer lasers are the only source which produce the high spectral brightness at these wavelengths. The required specifications of an excimer laser (KrF) presented at the Nikkei Micro-Devices Symposium held in 1987[1] are as follows ;
  (1)   Long life-time of laser gas.
  (2)   Low coherency of the output laser beam (to avoid speckle noise on the IC pattern).
  (3)   A spectral bandwidth narrower than 5pm. (1pm = 1×10^{-12}m)
  (4)   Output power higher than 15 W.
In this paper, we describe the newly-developed preionization system using a surface corona discharge, estimation of spectral bandwidth and efficiency, and experimental results.

Electrode configuration and gas life-time

The laser is pre-ionized by a newly-developed corona discharge on the surface of a dielectric as shown in Fig. 1. A perforated metal plate (anode) is attached to an alumina dielectric plate. On the opposite side of the alumina, an auxiliary electrode is placed and connected to the cathode. The electrode spacing between the anode and the cathode is 20mm. When the pulse voltage having a rise-time of 100ns and a crest voltage of 2^rkV is applied, corona discharge occurs automatically and uniformly on the surface of the alumina plate.

This configuration is effective for suppressing the reduction of output power due to gas deterioration. Fig. 2 shows the gas life-time. The laser is operated at a constant charging voltage and at a repetition frequency of 200 Hz under gas-sealed condition. The laser gas is recirculated through a cryogenic gas purifier system. No fluorine gas is injected into the laser during the test. This laser can operate for 8 hours without any power drop.

Construction of the resonator

It was made clear by Prof. Watanabe that, in order to get a low coherent beam, a stable resonator having a large beam diameter bigger than 10 mm has to be used[1]. Fig. 3 shows the construction of the resonator. More than one Fabry-Perot etalons are used inside the stable resonator in order to reduce the spectral bandwidth. The beam profile in the case of a spectral bandwidth of 3pm is shown in Fig. 3. The beam size is 6mm × 16mm (FWHM), which is large enough to reduce the beam coherence.

Spectral bandwidth and spectral narrowing efficiency

Curve A in Fig. 4 shows the free-running spectrum of the KrF excimer laser and curve B shows the spectral distribution of the transmitted laser beam through an etalon. The important parameters of the etalon are the spectral bandwidth (denoted by $\Delta\lambda$) and the peak transmission (denoted by T_p).

Spectral bandwidth

When the etalon is used inside the resonator, the laser bandwidth becomes narrower than the etalon bandwidth. The laser bandwidth depends on the number of times of the laser light passing through the etalon. In order to estimate the laser bandwidth the temporal

change in the laser light intensity has been calculated.

Fig. 5-(a) shows the measured waveforms of the fluorescence intensity and the laser light intensity. On the assumption that the gain coefficient g_0 is proportional to the fluorescence, the waveform of g is approximated by a triangular shape as indicated in Fig. 5-(b). g, the loss coefficient ι per unit length and saturation intensity I_s are found from measurements of the output power with a number of different mirror reflectances fitted to Rigrod's relation[2].

The laser light intensity is calculated against the number of times, P, that the laser light passes through the etalon, after the gain overcomes the loss. It is normalized by the spontaneous emission intensity and plotted in Fig. 5-(c). From this calculation it is found that the laser light passes through the etalon from 5 to 10 times in this case. The pulse duration time is 18 ns.

Fig. 6 shows the effective finesse of the etalon increases with increasing the number of times, P. When the number is from 5 to 10, the effective finesse becomes three times the initial value. Therefore, it is estimated from this model calculation that the laser bandwidth is reduced to one third of the etalon bandwidth. This result coincides well with the experimental result.

Efficiency of spectral narrowing

As the peak transmission of the etalon is lower than 100%, the etalon is considered to be equivalent to a loss plate having a transmission of T_p inside the resonator. The laser output as a function of peak transmission is calculated by adding the loss plate to Rigrod's model[2].

The dotted curves in Fig. 7 indicate the calculated results. In this diagram, the circles, triangles and squares show the experimental results. It was found that the calculated results coincide well with the experimental results, and that in order to achieve high efficiency of spectral narrowing, the peak transmission of etalon has to be raised as high as possible.

Data

Fig. 8 shows the laser output power as a function of repetition frequency. Curve A indicates the data without the etalon. The laser power is 24 W at 250 Hz. Curves B and C show the data when the etalons having different specifications are used. In every case, the output power increases almost linearly with increasing repetition frequency up to 250 Hz. The maximum power of 13 W has been obtained with a spectral bandwidth of 10pm. The power was decreased to 6.4 W when the bandwidth was narrowed down to 3pm.

The spectral distribution in the case of curve C was measured by an external etalon. Fig. 9-(a) shows the fringe pattern. The spectral bandwidth (FWHM) is narrower than 3pm as shown in Fig. 9-(b). Almost all the output energy is contained within the spectral range of 10pm.

Conclusions

(1) A KrF excimer laser pre-ionized by a corona discharge on the surface of alumina has been developed for use in microlithography. This laser can operate for 8 hours at a repetition frequency of 200 Hz without any power drop under gas-sealed condition and without F gas injection.

(2) A low coherent beam with a spectral bandwidth of 3pm is obtained by using etalons inside a stable resonator. The beam cross-section is 6mm × 16mm, large enough to reduce the beam coherence.

(3) In order to reduce the spectral bandwidth from 400pm to 3pm, the laser output decreases from 24 W to 6.4 W.

(4) The calculated results of the bandwidth and efficiency of spectral narrowing coincide well with the experimental results. The laser bandwidth is reduced to about one third of the etalon bandwidth.

References

1. E. Watanabe, in Proceedings, The First Nikkei Microdevice Symposium on Excimer Laser Lithography, (Nikkei BP Press, Tokyo, Jan. 1987), pp. 77-89
2. W. W. Rigrod, IEEE QE-14, No. 5, 377 (1978)
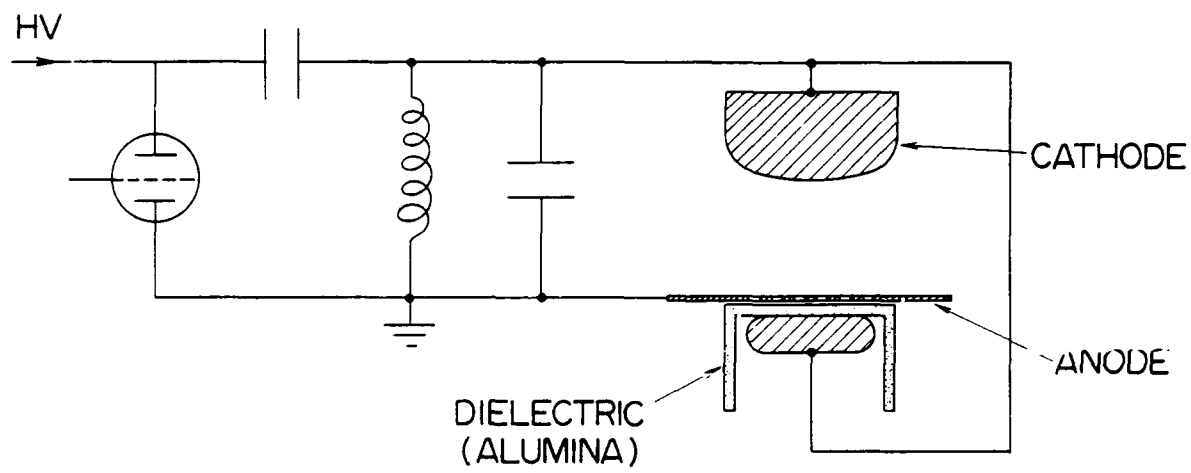
Fig. 1 Electrical Circuit and Discharge Electrodes.

KrF   Excimer Laser
Repetition Frequency = 200 Hz
Without Etalon
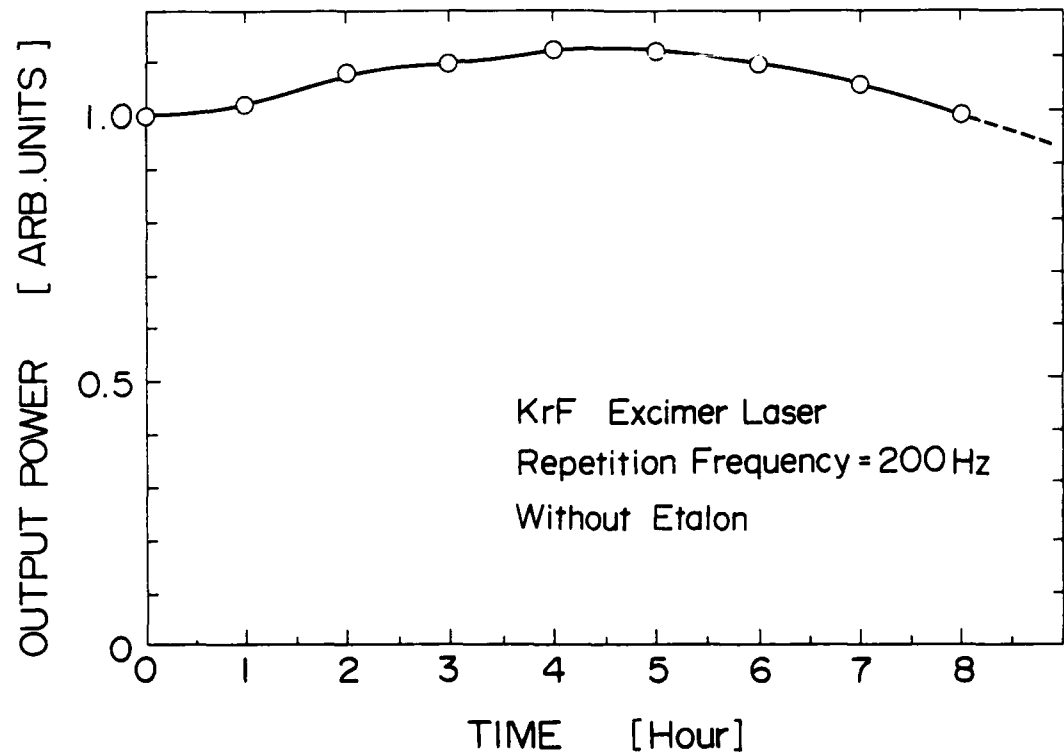
Fig. 2 Gas life-time under gas-sealed condition.
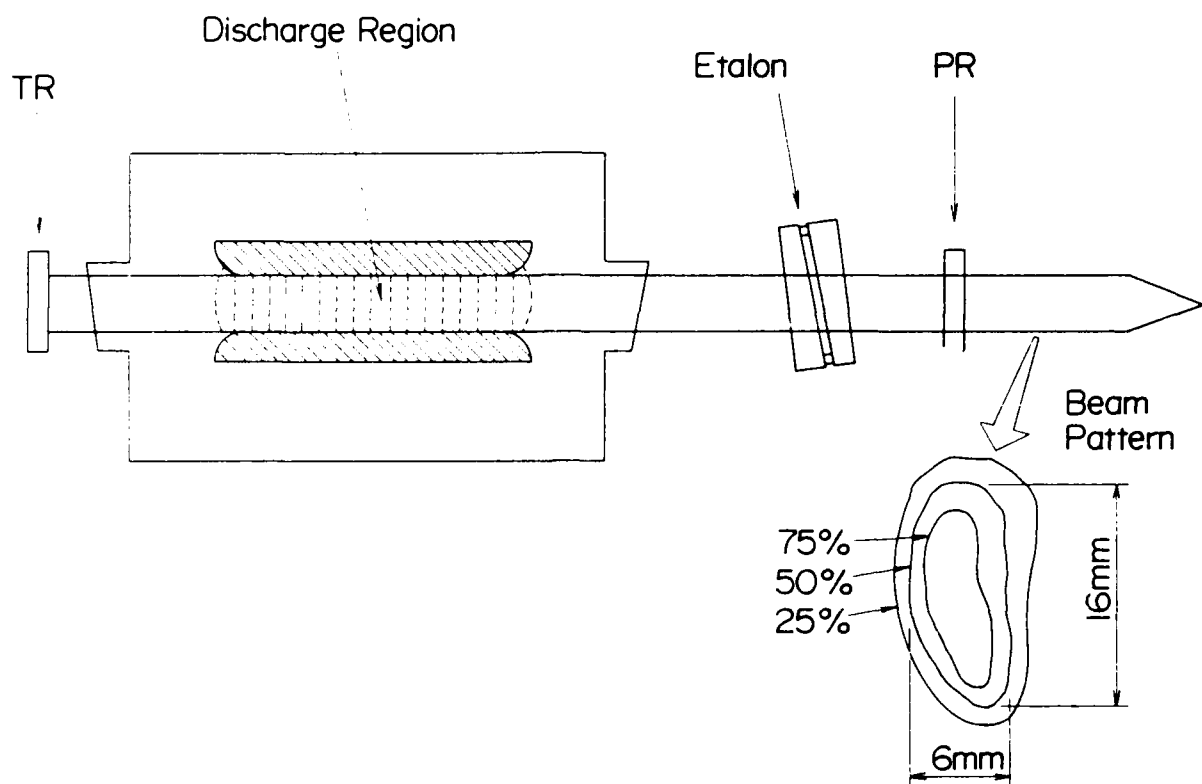
Fig. 3 Narow bandwidth KrF excimer laser.
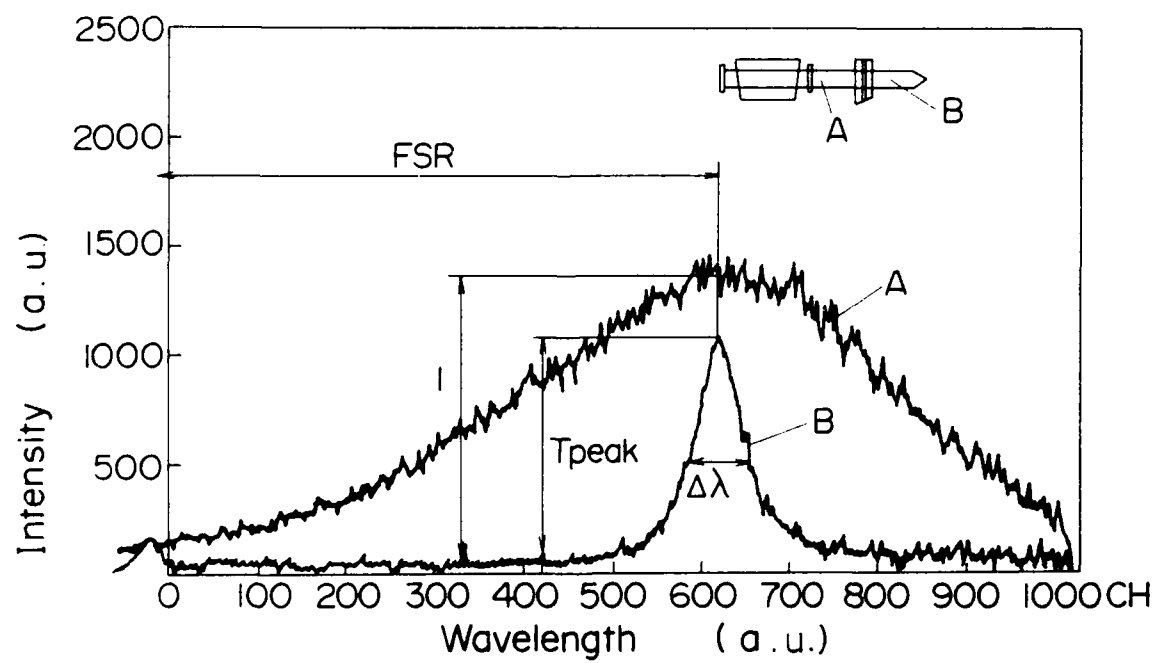
Fig. 4 Free-running spectrum of KrF excimer laser (Curve A) and the spectral distribution of the transmitted laser beam through an etalon (Curve B).

(a) Intensity (a. u.) — fluorescence, laser — 0, 50, 100 t(ns)

(b) Gain (%/cm) — gain, loss — 0, 10, 20, 30, 40, 50 t(ns)

(c) Normalized Laser Intensity Ip/Isp(×10³) — L = 1.3m, Is = 0.6, R 30% — 0, 10, 20, 30, 40, 50 t(ns) — Number of times P: 0, 2, 4, 6, 8, 10, 12
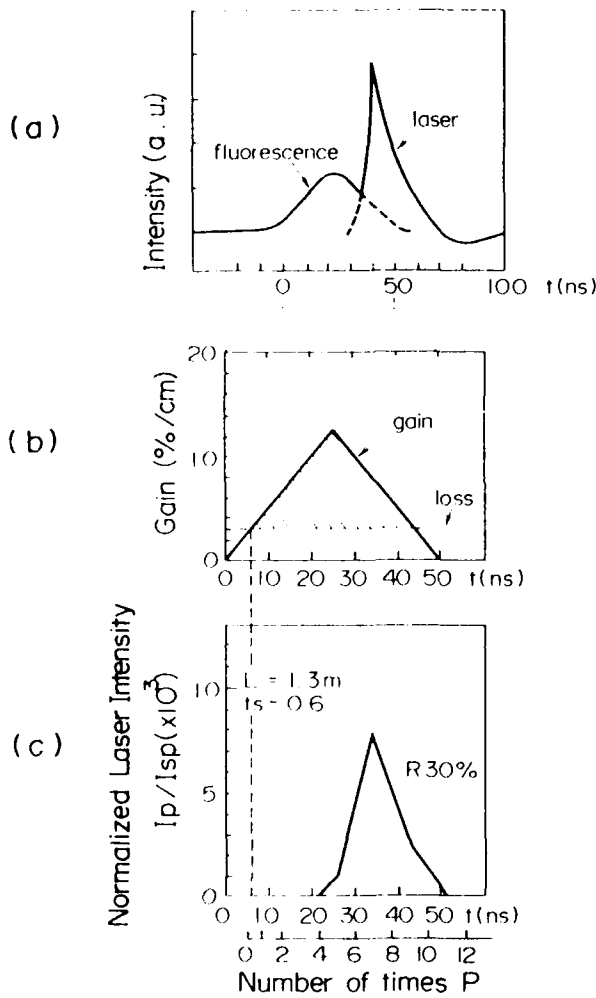
Fig. 5 Estimation of waveform of laser intensity.
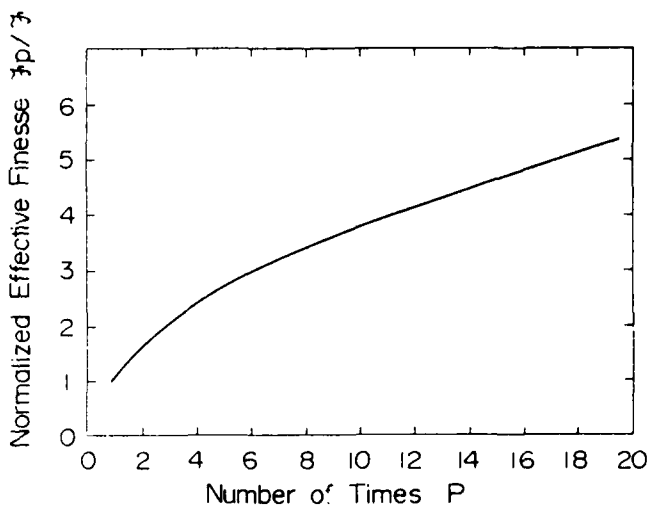
Fig. 6 Increase in effective finesse v.s. number of times passing through etalon.
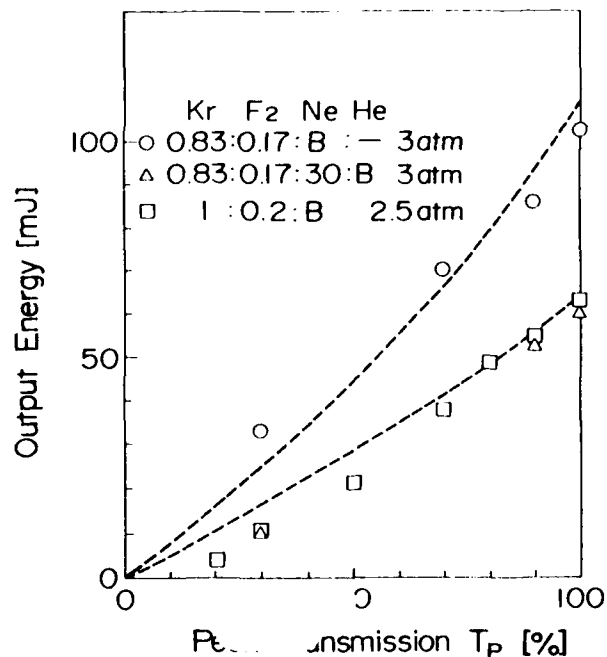
Fig. 7 Output energy v.s. peak transmission

$$
\begin{pmatrix}
\text{(}\Delta\text{)} & g \sim 12.5\%/cm \ \alpha \sim 3\%/cm \ Is \sim 1.7 MW/cm^2 \\
& \tau \sim 18nS \ l \sim 40cm \ A \sim 2cm^2 \ r \sim 30\% \\
\text{(}\bigcirc\text{)} & g \sim 10.7\%/cm \ \alpha \sim 12\%/cm \ Is \sim 1 MW/cm^2 \\
& \tau \sim 31nS \ l \sim 40cm \ A \sim 2cm^2 \ r \sim 30\%
\end{pmatrix}
$$
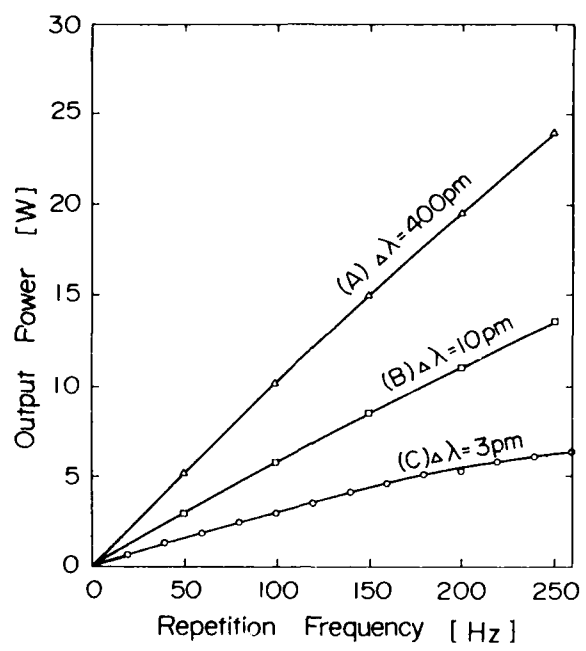
Fig. 8 Output power v.s. repetition frequency.

(a) Fringe pattern

25.6 pm

×5

10 pm

(b) Spectral distribution
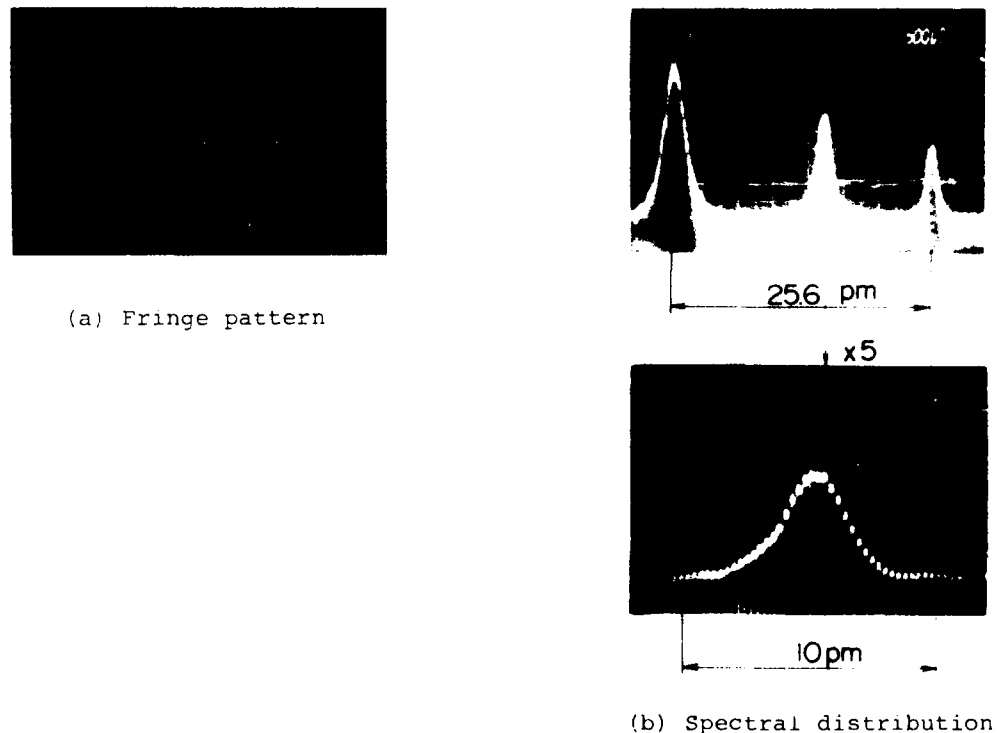
Fig. 9 Experimental results of spectral bandwidth.
(monitor etalon: FSR = 25.6pm, resolving power > 0.85pm)

INTRACAVITY FLUX DEPENDENT ABSORPTION IN E-BEAM PUMPED KRF

J.F. Seamans, W.D. Kimura
Spectra Technology, Inc.
2755 Northup Way
Bellevue, Washington 98004-1495

and

D.E. Hanson
Los Alamos National Laboratory
P.O. Box 1663, MS-J569
Los Alamos, New Mexico 87545

Abstract

Transient absorption measurements are performed on e-beam excited KrF under lasing and nonlasing conditions for 10% Kr (Ar diluent) and 99.6% Kr gas mixtures. The intracavity flux is varied by changing the output mirror reflectivity. The deposition rate for this experiment is $\approx$386 kW/cm^3. For the 10% Kr and Kr-rich mixtures, the small signal absorption at 248.4 nm is 0.76%/cm and 1.25%/cm, respectively; while the nonsaturable absorption is 0.62%/cm and 0.90%/cm, respectively. A flux loading of $\approx$1.5 MW/cm^2 is needed to achieve nearly complete saturation of the saturable absorption.

Background

In an ongoing effort to support the KrF laser modeling program at Los Alamos National Laboratory (LANL), Spectra Technology, Inc. (STI) has been conducting various experiments on its e-beam pumped laser facility (Tahoma). One of the goals of these experiments is to generate a complete set of data at a known operating condition in order to provide data to help validate the LANL model. The Tahoma laser facility has proved to be a device very suitable for such a task. The laser has been used extensively in many experiments. It is both a well characterized and reliable device. Some of the experiments included in the set of KrF characterization data are transient absorption and gain measurements under lasing (loaded) and nonlasing (unloaded) conditions, e-beam pumping characterization measurements, and intrinsic efficiency measurements. This paper discusses the transient absorption experiment results.

Description of Experiment

The laser is a Marx powered cold-cathode vacuum diode that delivers $\approx$375 keV electrons at the foil. A magnetic guide field of 2 kgauss confines the e-beam to a 6 cm x 70 cm area at an average current density of $\approx$32 A/cm^2. The pulse length is variable, but for this work it is $\approx$450 ns. The cylindrical active volume of 3.5 cm dia. x 70 cm is located 3.5 cm away from the e-beam foil.

Absorption in the laser active volume is obtained by measuring the input and output intensities of a tunable pulsed probe laser passing twice through the laser chamber. Measurements are made during lasing and nonlasing conditions in order to investigate the dependence of the absorption on the laser flux. A similar technique has been used by others[1,2] to measure the absorption characteristics in KrF. Figure 1 is a schematic of the measurement system.

A tunable dye laser is pumped by a pulsed Nd:YAG laser tripled to 355 nm. The dye output is then doubled utilizing a BBO crystal cut for 250 nm. Due to gain around 248 nm, the absorption characteristics of the medium must be measured by tuning the probe light sufficiently away from 248 nm to avoid detecting any off-line gain. It is found that the

probe wavelengths must be at least ≈8 nm on either side of line center to avoid any appreciable gain contributions. The wavelengths chosen for the off-line measurements are 240.0 nm and 257.3 nm. (The absorption on line center is calculated by performing a linear interpolation between the 240.0 nm and 257.3 nm data.)
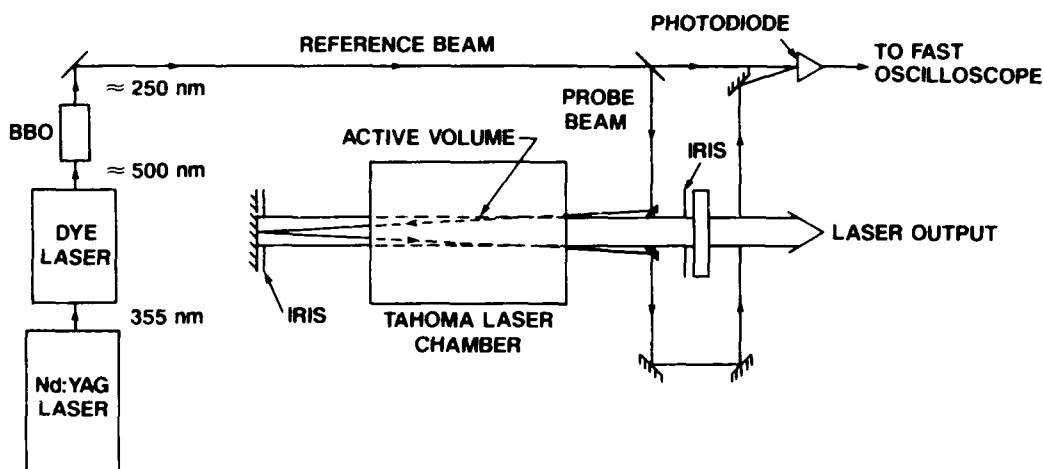
Fig. 1. Schematic of transient absorption measurement system.

A beam splitter divides the primary beam into two beams. The transmitted beam (reference) travels directly to a photodiode while the reflected beam (probe) is directed through an optical delay path that includes two passes through the laser chamber before detection by the same photodiode. Employing a single photodiode eliminates the need to calibrate multiple detectors. The optical delay is long enough to allow viewing both reference and probe signals without temporal overlap. The probe is inserted into and extracted from the oscillator cavity without interfering with the intracavity flux by using small turning prisms. Intracavity irises control the output laser beam diameter to prevent coupling any significant laser radiation into the prisms and the photodiode. Note that the rear high reflector mirror of the laser cavity also serves as the middle mirror for the double pass of the probe beam. Although a convenient method for enabling the double pass of the probe beam, this feature also tends to complicate the analysis of the absorption data because of amplified spontaneous emission (ASE) effects during nonlasing conditions. This will be discussed later. The intracavity flux is varied by simply changing the output couplers.

Additional diagnostics not shown in Figure 1 are two photodiodes and an laser energy meter. One photodiode measures the laser pulse profile by detecting the small amount of laser light that leaks through the high reflector, and the second photodiode detects the sidelight fluorescence at the center of the active volume. The energy meter measures the laser output fluence from which the intracavity flux can be calculated.

The KrF gas mixtures studied are an argon diluent mix (14.5% Kr) and an argon-free (99.6% Kr) mix at total pressures of 1004 and 665 torr, respectively. For both mixtures, the F_2 pressure is kept constant at 2.8 torr.

As mentioned earlier, the feedback from the high reflector during nonlasing conditions aggravates the ASE loading within the cavity. This potentially impacts the absorption measurements because during nonlasing there may still be an appreciable amount of intracavity flux present due to ASE. An ASE code developed at STI[3] predicts ≲20 kW/cm^2 of flux loading based on the gain measurements made by probing on-line center at 248.4 nm. As will be shown, the saturable loss component α_s requires >1 MW/cm^2 to saturate. Consequently, the ASE effects can be considered negligible and are therefore ignored throughout the analysis.

168

Figure 2 shows the measured absorption values versus the average intracavity flux. The average flux is calculated using the measured laser output fluences in the aforementioned ASE code. As part of its calculations, the code also calculates the flux conditions during lasing within the cavity. For this data, the pumping rate is $\approx$386 kW/cm^3.
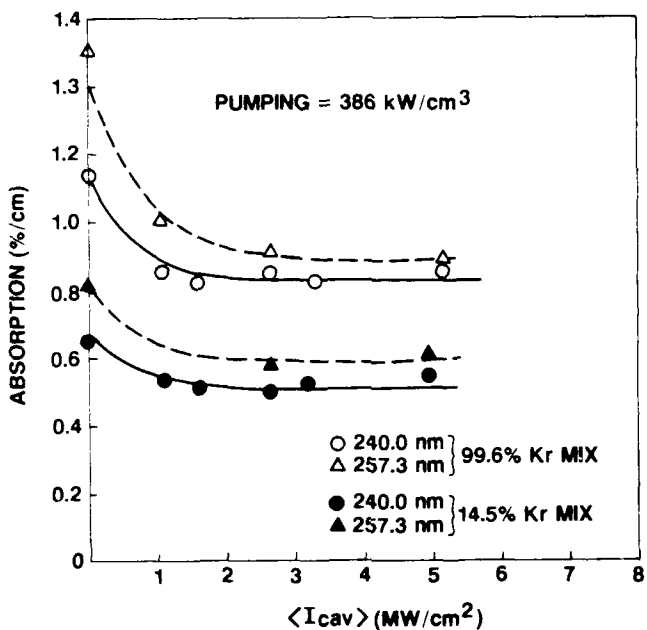
Fig. 2. Absorption data as a function of the average intracavity flux.

The absorption results for both Kr-rich (open symbols) and Ar-diluent mixtures (closed symbols) are presented. The graph shows that at both probe wavelengths, the absorption for the Ar-diluent mix is always smaller at a given flux loading than for the Kr-rich mix. Also, the absorption at 257.3 nm is always higher than at 240.0 nm. The higher absorption at the longer wavelengths has been observed by others and is probably due to absorbing species such as Kr_2F^*, Ar_2^+, and Kr_2^+.

With regard to the effects of the intracavity flux, for an average flux of ≥ 1.5 MW/cm^2, the absorption in all cases drops to a constant level which is interpreted as representing the nonsaturable loss. Performing the experiment at 15% to 20% higher deposition yields nearly identical results.

Discussion

The absorption at 248.4 nm, derived by linear interpolation of the 240.0 nm and 257.3 nm absorption data, are summarized as follows. For the Kr-rich mixture, the small signal absorption (saturable + nonsaturable) is 1.25%/cm, which is 64% larger than the absorption for the Ar-diluent mixture at 0.76%/cm. For the saturable absorption component, it is found that: α_s(Kr-rich) $\approx$ 2.5 α_s(Ar-diluent). While for the nonsaturable component the relationship is: α_n(Kr-rich) $\approx$ 1.5 α_n(Ar-diluent). Finally, the data indicates that saturation of α_s requires a flux of $\approx$1.5 MW/cm^2.

Comparison of the results obtained at STI with other results found in the literature,[2,4-5] show a general tendency for the absorption to increase with deposition rate. Figure 3 shows the measured small signal absorption versus deposition rate. Also plotted is the LANL model prediction of the small signal absorption for pumping rates

<500 kW/cm^3 (10% Kr mixture). The agreement with the data is fair.

Additional work is in progress to consolidate the absorption data with other measurements performed on the laser in order to complete the characterization package for the model validation.
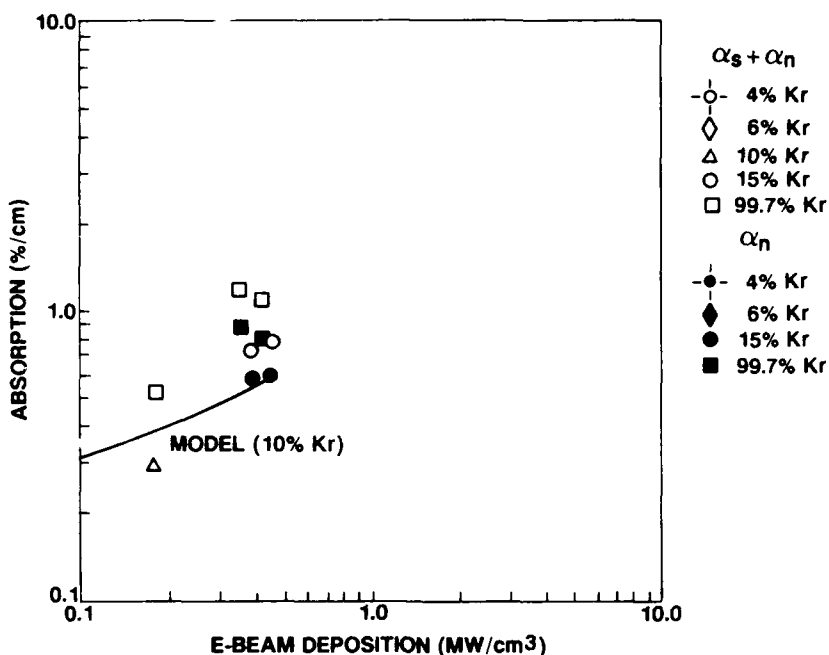
Fig. 3. Absorption data as a function of the e-beam deposition. The solid curve is the prediction from the LANL model for a 10% Kr mixture.

Acknowledgments

References

1. A.M. Hawryluk, J.A. Mangano, and J.H. Jacob, Appl. Phys. Lett. 31, 164 (1977).

2. D.C. Thompson, R. Fedosejevs, and A.A. Offenberger, Conference on Lasers and Electro-optics (CLEO), April 25-29, 1988, Anaheim, CA, Session TUB1.

3. D.D. Lowenthal, Spectra Technology, Inc. (private communication).

4. C.B. Edwards, F. O'Neill, and M.J. Shaw, Appl. Phys. Lett. 38, 843, (1981).

5. E.T. Salesky and W.D. Kimura, Appl. Phys. Lett. 46, 927, (1985).

VISIBLE WAVELENGTH FREE ELECTRON OSCILLATOR

D. R. Shoffstall
Boeing Aerospace Company
Seattle, Washington

Abstract (U)

(U) The overall goal of the visible oscillator program is to demonstrate that a large FEL interaction strength can be obtained at approximately 600-nm wavelength. The gain-extraction product increases with increasing wiggler length, and a 5-m length with hybrid $SmCo_5$ technology was identified at the program start[3] as providing satisfactory interaction strength, reasonable cost, and an acceptable extrapolation from previous wigglers. The 120-MeV LINAC comprises five accelerator sections, each powered by a 12-MW peak output RF klystron power station. The operating frequency is 1.3 GHz. The structure is a constant gradient traveling wave (TW), operating in the $3\pi/4$ mode. A TW design was chosen to accommodate the wide range of beam loading conditions required in the FEL experimental series. The radio frequency (RF) LINAC current format is a series of high-current micropulses spaced at the two way oscillator cavity transit time. The envelope of these pulses, the macropulse, is selected to be long enough to examine the laser startup and beam quality physics, nominally 100-200 μs.

1.0 Summary (U)

(U) The extension of free electron lasers (FEL) laboratory scale research dedicated to a deployed and fully operational weapon system requires significant advances in accelerator and laser technology. The power and, wavelength scaling to a weapon size system entails critical technology risks and related issues. The Boeing Aerospace Company (BAC) with Strategic Defense Initiative Office (SDIO) and United States Army Strategic Defense Command (USASDC) concurrence, has mapped an incremental approach. The successful execution of this experimental series will prove the scientific feasibility, provide the critical technology and support the USASDC readiness to proceed with a medium-power FEL device demonstration at White Sands Missile Range (WSMR).

(U) This paper reports on the progress and status of the first incremental step.

2.0 Experimental Design and Configuration (U)

(U) The overall goal of the visible oscillator program is to demonstrate that a large FEL interaction strength can be obtained at approximately 500-nm wavelength. This interaction strength is properly measured in terms of the gain-extraction product[1,2] and in this case, a design goal was chosen for 5% extraction with the available optical gain large enough for suitable oscillation startup and saturation within the macropulse length (100-200 μs nominal).

(U) The gain-extraction product increases with increasing wiggler length, and a 5-m length with hybrid $SmCo_5$ technology was identified at the program start[3] as providing satisfactory interaction strength, reasonable cost, and an acceptable extrapolation from previous wigglers. With the assumption of a wavelength and wiggler length, an optimization analysis assuming a perfect electron beam (no energy spread or emittance) shows that approximately 100-MeV energy and a 2-cm period are required. The incorporation of realistic emittance and energy spread values modify this result, and a detailed calculation of the available gain for various[4] electron beam qualities is shown in figure 2.1. Each curve is drawn under the assumption that the wiggler is optimized for the particular conditions at that point.

(U) The shift in optimum operating point with changing electron beam quality is seen in figures 2.2 and 2.3. In figure 2.2, the trend to larger e-beam energy with increasing emittance is observed. This shift results from the sensitivity to off-axis electrons being dependent on the wiggler wavelength. The design point of figure 2.2 is purposefully chosen to slightly higher than optimum energy for the expected 0.01-cm-rad emittance, to reduce the gain loss if slightly larger emittances are encountered. The importance of designing the system for the particular emittance expected is shown dramatically in figure 2.3. Here the gain fall off as a function of emittance is shown for three separate designs, each optimized for a different emittance. The performance at 0.01 cm-rad is quite poor for the zero emittance design, but for operation at 0.01 cm-rad with the 0.01-cm-rad design, the gain is substantially larger.

(U) The basic parameter set for the electron beam, wiggler, and optical cavity is shown along with the fundamental laser parameters in figure 2.4. The combination of 100-A peak current and the 5-m tapered undulator produce a small signal gain of 20% and a saturated gain of 10%. The extraction at saturation is 5%. Higher gains are available at reduced taper and extraction. The 55-m optical cavity length is determined directly by the required extraction and available gain. The mirrors are separated from the wiggler to the point at which the macropulse average incident intensity of 300 kW/cm^2. This operating point for the mirrors is estimated to be within the capability of the dielectric coatings, based on related measurements at Los Alamos National Laboratory (LANL)[5].

(U) The Physical Sciences Center at Boeing has been enlarged to accommodate the accelerator and laser. The experimental configuration is shown in figure 2.5. The facility size is roughly 12 m x 70 m.

3.0 RF LINAC (U)

(U) **Accelerator Design.** The 120-MeV LINAC

(U) comprises five accelerator sections, each powered by a 12-MW peak output RF klystron power station. The operating frequency is 1.3 GHz. The structure is a constant gradient traveling wave (TW), operating in the $3\pi/4$ mode. A TW design was chosen to accommodate the wide range of beam loading conditions required in the FEL experimental series. The radio frequency (RF) LINAC current format is a series of high-current micropulses spaced at the two way oscillator cavity transit time. The envelope of these pulses, the macropulse, is selected to be long enough to examine the laser startup and beam quality physics, nominally 100-200μs. As a consequence of this long macropulse requirement, the susceptibility of the accelerator waveguide to beam breakup becomes a major issue. To address this problem, the structure has innovative features to mitigate the influence of dipole cavity modes and transverse wakefields. Synchronous interaction of the beam with transverse electromagnetic modes is minimized in $3\pi/4$ mode structure since TM_{11}-like modes do not propagate at the velocity of light[6]. In addition, since the transverse modes have a negative group velocity, they can be removed from the structure at the upstream end of the waveguide. This is accomplished by routing the higher modes through the input RF coupler to a resistive, probe loaded coaxial pipe.

(U) Transverse wakefield effects which can degrade emittance of high-charge micropulses are strongly dependent on the disk aperture diameter. A large aperture structure with acceptably low group velocity is achieved with thick disks. Shunt impedance is enhanced by contouring the disk nosecones and coving the cavities. The resultant apertures range from 5-7 cm, roughly three times the size used in our S-band Stanford Linear Accelerator Center (SLAC)-like prototype accelerator.

(U) Measurements of beam induced cavity modes have been performed for candidate structure designs. These tests[7] show significant transverse mode reduction in the design structure.

(U) Figure 3.1 is a schematic drawing of the acceleration guide. The electrical characteristics are given in figure 3.2.

(U) The electric field strength at 12-MW input is 9.9 MV/m and the section no-load energy gain is 29.1 MeV. The full accelerator load line and FEL operating point are given in figure 3.3.

(U) Injector. A two stage subharmonic injector for the 120-MeV LINAC has been designed and tested with the existing S-band accelerator. Single microbunch output beam current of 120A with emittance of 0.008 cm-rad and energy width of 1% has been measured[8,9].

(U) The subharmonic injector, figure 3.4, consists of a high-current triode gun, two standing wave cavity prebunchers and a fundamental frequency tapered phase velocity buncher. A "pepper pot" emittance measurement and tuning diagnostics occupy the space between

(U) the prebuncher cavities. A full solenoidal magnetic field provides radial containment and focusing of the electron beam. A tapered collimator in the last drift section limits beam size and entry angle at the buncher.

(U) The electron source is similar to the SLAC-collider injector gun design. This gun provides a high brightness output and the relatively low grid drive voltage is advantageous for our requirement of high repetition, nanosecond pulse gating.

(U) RF Power Stations. Installation and testing of the 1.3-GHz RF power stations for the FEL oscillator experiment have been completed. Each of these stations was tested to the following specifications.

RF Power	15 MW	10 MW
RF Pulse Width	150μs	300μs
RF Average Power	50 kW	50 kW

(U) A drawing of the RF power station is shown in figure 3.5.

(U) The RF power supply circuit is divided into three subassembly cabinets:

a. (U) The high-voltage dc power supply is a 30-kV, 10 average, SCR-regulated supply with soft start voltage programming and an automatic load over-current trip with 6-ms response time to isolate the power supply from the mains.

b. (U) The regulator circuit includes the filter capacitors, a 2H air-core resonant charging choke, and a floating deck de-Q regulator. The circuit regulation is 1%. The air-core choke prevents high-current faults from load shorting.

c. (U) The modulator circuit includes the 52-coil, 52-capacitor, 300 μs, 10-ohm pulse-forming line; the output thyratron switch; and the line and load protection circuitry. The power supply control electronics are also located in this enclosure.

(U) The power supply average power is upgradable to 100 kW with a replacement thyratron, all other components are full 100 kW RF rated.

(U) The supplies are fully computer controlled, with fiber optic linkage to the main control room for electrical noise immunity.

(U) Thomson-CSF has developed a new long pulse L-band klystron designated as TH2104 for the FEL series. Six of these tubes have been procured. All tubes were delivered on time and all have fully met or exceeded our operating requirements. A configuration drawing and the performance specifications for the TH2104 klystron are shown in figure 3.6.

4.0 Beamline (U)

(U) The FEL electron beam transport system is composed of three sections, as shown in figure 4.1. The beam from the accelerator enters the

172

(U) first section, a quadrupole focus-drift-defocus-drift (FODO) array, which measures beam and transports the beam to the second section, a 180-deg bend, where beam energy and emittance are tailored. The third section focuses and steers the beam into the wiggler.

(U) The beamline contains several diagnostic and tuning aids, which include fluorescent screens, collimators, energy slits, and steering coils. A spectrograph is located after the wiggler for examining energy spectra during low-power tuning. In addition, 25 stripline detectors are located along the length of the beamline. Energy selection slits are located at two points in the center of the diagonal legs of the 180-deg bend where the energy dispersion is the highest. The principal electron beam diagnostic measurements for the FEL experiment are shown in figure 4.2.

(U) Collimator holes are incorporated at the beginning and the end of the first FODO array. A third collimator is located in the center of the 180-deg bend. Steering coils are located all along the beamline. These coils serve as a tuning diagnostic and a steering corrector. The beamline is now completely assembled and operational.

5.0 Wiggler (U)

(U) The FEL experiment wiggler is a 5-m variable taper permanent magnet device. The magnetic circuit uses samarium cobalt magnetic material and vanadium permendur pole pieces. The wiggler was designed and built by Spectra Technology, Inc (STI). STI has named the wiggler THUNDER (for tapered hybrid undulator).

(U) The THUNDER wiggler has been designed to provide the high interaction strength required for efficient laser operation at visible wavelengths. The 10 kG magnetic field, roughly three times higher than that of previous 10-μm experiments together with a 5-m overall length, provide 10% optical gain at 5% electron energy extraction. The high field is achieved with a hybrid design in which samarium cobalt permanent magnets drive vanadium permendur poles. This geometry allows higher field strengths for a given gap-to-wave- length ratio than possible with pure samarium cobalt designs. The hybrid design is also chosen because the steel pole pieces provide improved field uniformity and, therefore, better electron transport. The transport issue becomes increasingly critical at short wavelengths with the small optical beam size, and to further reduce field errors, the magnets and wiggler structure are dimensionally and positionally controlled to less than 0.001 inch. The system employs two- plane electron beam focussing by means of pole canting. This canting imposes a quadrupole field component which adds focussing in the plane of the wiggler while reducing the natural focussing in the orthogonal plane. Such two-plane focussing was unnecessary in earlier 10-μm experiments.

(U) The wiggler is built in ten 50-cm segments, which can be seen just prior to final assembly in figure 5.1. The magnetic gap is manually adjustable by choice of a precision

(U) ground spacer block. This allows variation of the energy taper from 0 to 12%.

(U) At either end of each 50-cm segment resides a compact diagnostic station (figure 5.2). A "pop-in" target, which is either a fluorescent screen or the Cherenkov cell, provides visual information on the profile and size of the electron beam with respect to the alignment laser beam that also is imaged on the screen. Additionally, stripline electrode beam position monitors are provided. These striplines are mounted on the tips of the poles of the steering elements to conserve space. The design resolution of the striplines is better than the requirement of 30 μm.

6.0 Optical Cavity (U)

(U) The optical cavity for the visible oscillator experiment placed unusually high demands on both fabrication and alignment of the spherical cavity mirrors. It was important to fabricate the mirrors so that the Rayleigh range and the mirror spacing were fixed to a value predetermined by the wiggler size and the micropulse interval. When reduced to figure requirements, the mirror radius had to match an absolute radius to within approximately $\lambda/50$.

(U) Damage limitations required a spot size of at least 1 cm on the end mirrors; to accommodate the 5-m long wiggler, a Rayleigh length of 2.4m was chosen. This dictated a cavity that is approximately 60m from end mirror to end mirror. The actual length chosen was 55.4m to provide a cavity round-trip time equal to the micropulse spacing.

(U) The mirrors themselves are 4 in. in diameter and 1.5 in. thick. The FEL beam illuminates the central portion only, and the remainder of the mirror is used for the stabilization system. Fused silica was chosen as the mirror material for several reasons: it can polished to a supersmooth surface; which is ..cessary for damage resistant coatings; it has a low coefficient of thermal expansion so that small changes in temperature throughout the structure of the mirror have little effect on the figure of the mirror; and it is transparent to the FEL light, which is important since we are outcoupling light through the cavity end mirrors.

(U) Once in place, 55.4m from each other, the mirror must be aligned and stabilized to better than 50 nanoradians. To accomplish this, a servo controlled stabilization system was designed and built. The heart of the system is the voice-coil driven, active optical mount shown in figure 6.1, and the analog electronics which command it. The system has been built, installed and tested. It provides active stabilization of each mirror to a few tens of nanoradians with a bandwidth of 200 Hz. Initial alignment of the system is done by injecting an on-axis laser light and maximizing the containment time for that light.

(U) All components of the optical system have been built, tested and installed. The system reached initial operational status in July 1986.

173
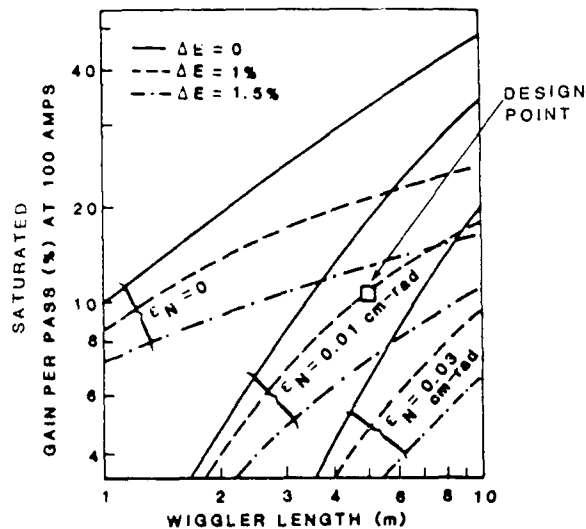
Figure 2.1 Calculated Optical Gain

LINAC		WIGGLER	
• E	= 120MeV	• LENGTH	= 5m
• I_{peak}	= 100A	• WAVELENGTH	= 2.18cm
• $\epsilon_N = \gamma\pi r\theta$	= 0.01cm-rad	• PEAK FIELD	= 10.2kG
• $\Delta\gamma/\gamma$	= 0.01FW	• TAPER (ENERGY)	= ADJUSTABLE TO 12%
OPTICAL CAVITY		LASER	
• LENGTH, 55m		• GAIN: SMALL SIGNAL 20% SATURATED (AT 6GW) 10%	
• SPOT SIZE W, 1cm AT MIRROR, 0.5mm AT CENTER			
		• EXTRACTION AT 6GW: 5% (12% TAPER)	
• MIRROR LOADING, 300kW/cm² AT MAXIMUM EXTRACTION		• MACRO POWER, 30kW	

Figure 2.4 System Design Parameters
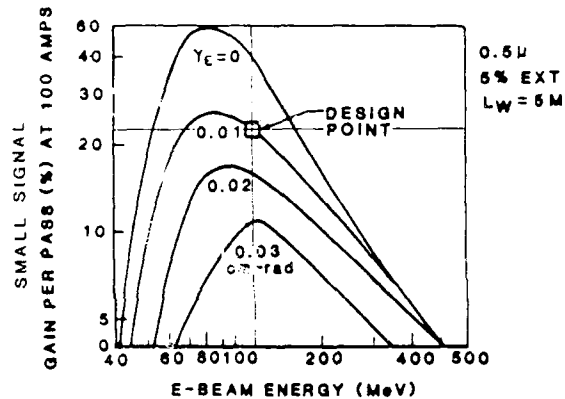
Figure 2.2 Calculated Optical Gain
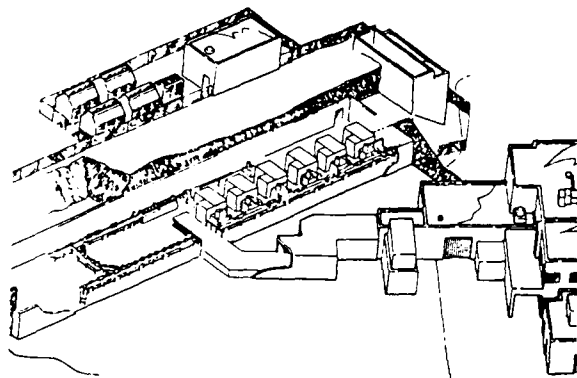
Figure 2.5 Visible FEL Experiment

Figure 2.3 Calculated Optical Gain
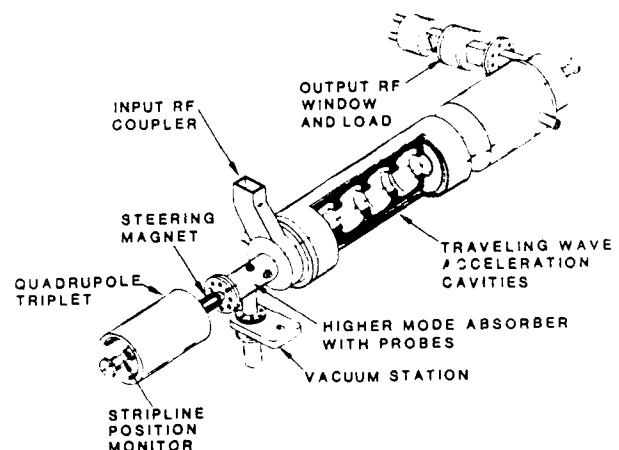
Figure 3.1 Accelerator Waveguide Section

174

NOMINAL OPERATING FREQUENCY f	= 1300 Mcs (v_p = C)
DESIGN INDEX (ATTENUATION) 2I_0L	= .8 NEPERS (4dB)
INITIAL ATTENUATION COEFFICIENT, I_0	= .102 NEPERS/m
WAVEGUIDE LENGTH, L	= 2.94m
SHUNT IMPEDANCE PER UNIT LENGTH, r	= 40 MEGOHMS/m
FIGURE OF MERIT, Q	= 20,200
INITIAL NORMALIZED GROUP VELOCITY, vg/C	= .0067

Figure 3.2   Accelerator Structure Design Parameters
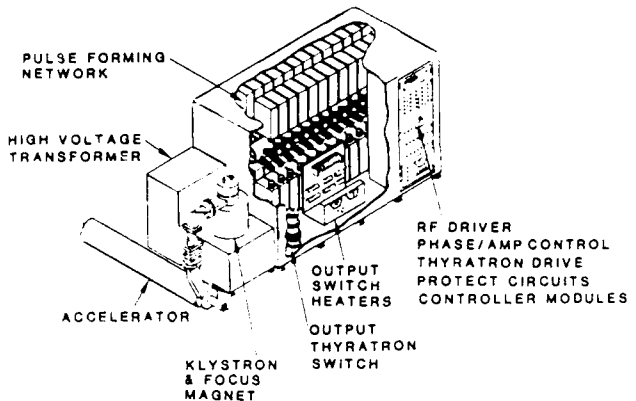
Figure 3.5   RF Power Station
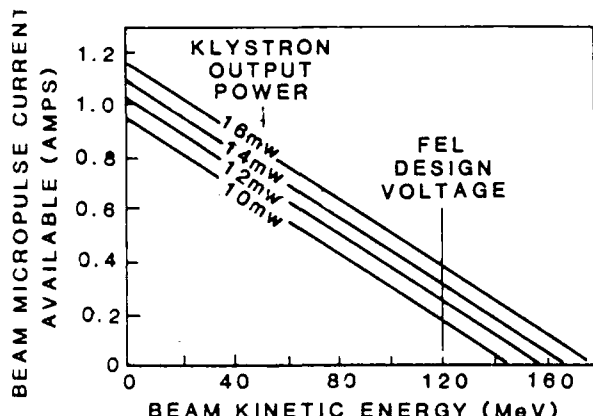
Figure 3.3   Accelerator Load Line

THOMPSON CSF TH2104
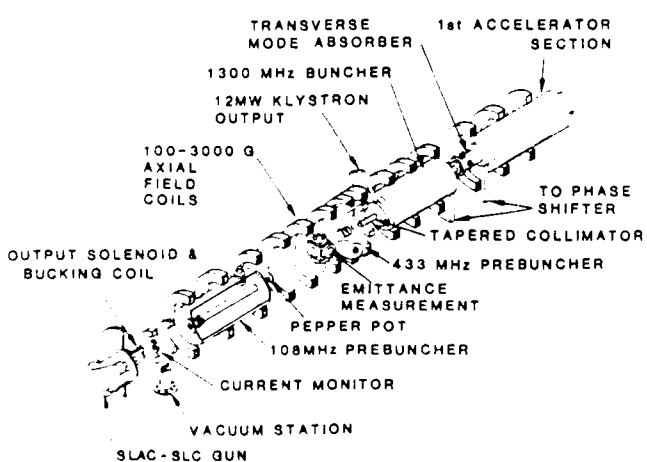
Figure 3.4   Two-Stage Subharmonic Injector
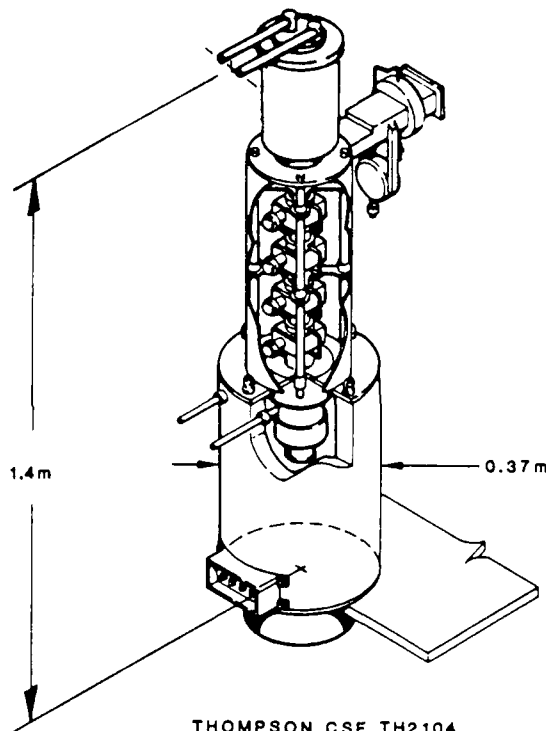
TH2104 KLYSTRON OPERATING SPECIFICATIONS	
● FREQUENCY, MHz	1300
● PEAK POWER, MW	10 – 15
● AVERAGE POWER, MW	0.1 – 0.05
● PULSE DURATION, ms	0.2 – 0.1
● CATHODE VOLTAGE, kV	185 – 215
● CATHODE CURRENT, A	160 – 200
● HEATER VOLTAGE, V	25
● HEATER CURRENT, A	25
● EFFICIENCY (MINIMUM), %	38
● GAIN AT SATURATION, dB	50
● INSTANTANEOUS BANDWIDTH, MHz	8
● LOAD VSWR (MAXIMUM),	1.5
● SOLENOID, kW	10

Figure 3.6   FEL Klystrons

175
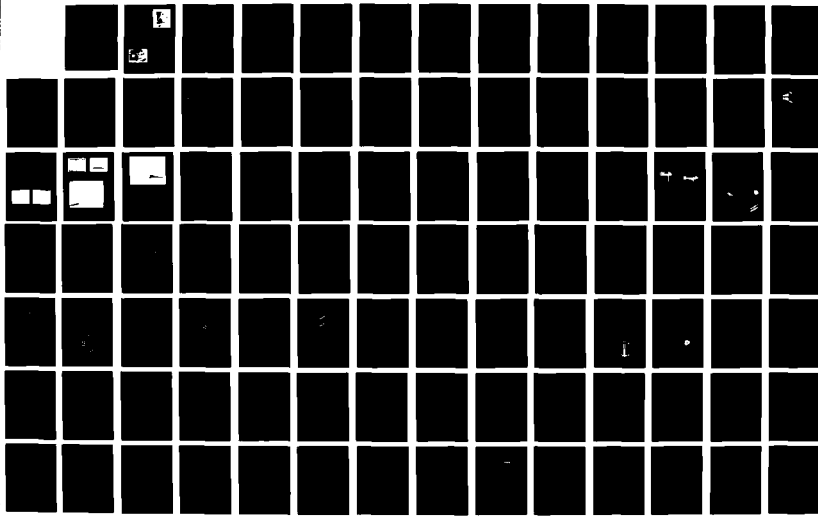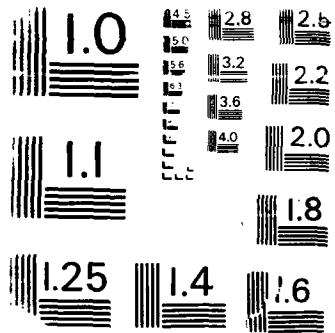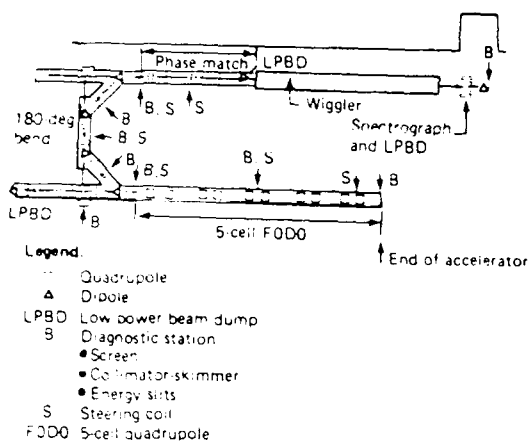
Figure 4.1   FEL Electron Beam Transport System

Legend.
- · · Quadrupole
- △ Dipole
- LPBD Low power beam dump
- B Diagnostic station
  - ● Screen
  - ● Collimator-skimmer
  - ● Energy slits
- S Steering coil
- FODO 5-cell quadrupole

Figure 4.2   FEL Experiment Electron Beam Diagnostic
Measurements
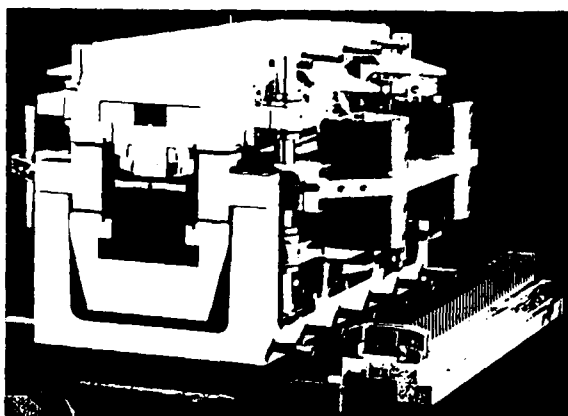
Figure 5.1   THUNDER Wiggler Section

Figure 6.1   Mirror and Voice-Coil Driven
Flexure Mount
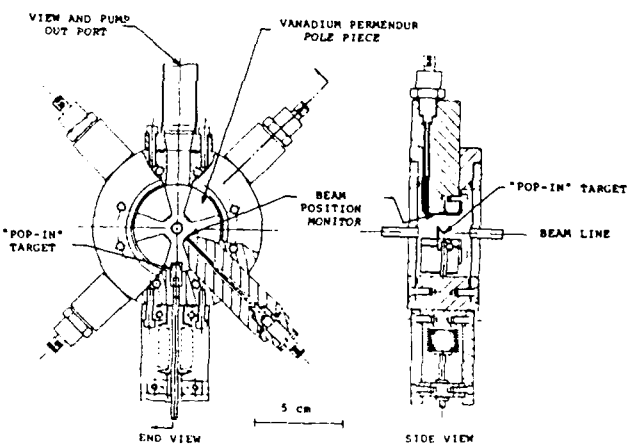
Figure 5.2   Wiggler Diagnostics

176

THE STANFORD/ROCKETDYNE FREE ELECTRON LASER MASTER OSCILLATOR/ POWER AMPLIFIER EXPERIMENT

Anup Bhowmik, Mark S. Curtin, and Wayne McMullin
Rockwell International/Rocketdyne Division
6633 Canoga Avenue, Canoga Park, CA 91303
and
Stephen V. Benson, John M. J. Madey, Bruce A. Richman, and Louis Vintro
Stanford Photon Research Laboratory
Stanford University, Stanford, CA 94305

Abstract

A near infrared free-electron laser master oscillator and power amplifier driven by a common electron beam is described. The Stanford Mark III free electron laser is the master oscillator and the Rocketdyne wiggler is the power amplifier. At 3 μm wavelength the optimum small signal gain spectrum of an untapered power amplifier was obtained. Up to 60% single pass, small signal gain was observed with an estimated peak current of 35 A. Follow-on experiments are also discussed.

Introduction and Objectives

In order to scale up radio-frequency linear accelerator (rf-Linac) driven free-electron lasers to very high average power levels, a concept that relieves the severe demands of the laser beam on resonator optics is essential. One such concept is the master oscillator driven power amplifier (MOPA) in which both the oscillator and amplifier are free-electron laser (FEL) devices.[1] In this proposed concept, the output from an FEL oscillator is injected into one or more rf-Linac driven FEL amplifier stages. By using this concept the advantages of high beam brightness and the pulse format of the rf-Linac are preserved while the outputs of several amplifiers are added coherently. One of the principal advantages of the FEL over other high power lasers, continuous tuneability over a wide range, is also preserved. Factors of ten or greater signal enhancement can be realized quite readily without placing additional stress on resonator optics.

In a joint research program between Rockwell International's Rocketdyne Division and the Stanford Photon Research Laboratory (SPRL) an experiment was undertaken to demonstrate an FEL-MOPA, wherein both the master oscillator (MO) and the power amplifier (PA) are FEL devices. A unique feature of this experiment is that the MO and the PA are both driven by sharing an electron beam from a single rf-Linac. The experiment was designed to address key technological and physics issues associated with the operation of an rf-FEL-MOPA. The scientific goals of the experiment are (1) to show theoretically predictable amplifier performance by characterizing its small signal gain (that is readily compared to analytic theory, or numerical simulations), (2) evaluate the effects of gain guiding (to address high gain phenomena), (3) quantify amplifier harmonics and sidebands, and (4) examine mode buildup in the MO and saturation in the PA. Although the experiment was operational and diagnostic instrumentation was available to conduct all of the above experiments, some of the tasks were precluded by schedule constraints. Following its initial successful operation, the experiment is being dismantled and moved to its new home, Duke University in North Carolina.

In this paper, results from operating the first FEL-MOPA driven by a single rf-Linac are presented. The Stanford Mark-III FEL served as the MO while the Rocketdyne FEL was used in a PA configuration. Two new transport lines were designed and constructed to provide a connection between the two wigglers - one for the e-beam, and the other for the laser beam. An e-beam from the Stanford Mark-III rf-Linac was transported through the two wigglers in succession, the MO first and then the PA. Laser output from the MO was transported to the PA with appropriate mode matching and delay optics, described below. Electrons in every rf-bucket were allowed to interact with laser pulses in the MO and the PA. As shown below, in the small signal regime the effect of energy spread on the e-beam was small and adequate e-beam quality was preserved through the transport system for subsequent amplification in the PA. With the MO operating at approximately 3 μm, the optimized small signal gain spectrum of the amplifier was obtained by tuning its gap. A maximum small signal gain of 60% per pass was measured (with an estimated peak current of 35 A).

Following the small signal gain experiments the optical resonator in the MO (the Mark-III FEL) was modified to accommodate an rf-electro optical cell, which, in conjunction with a polarizer serves as either (1) a cavity Q-modulator or (2) a

Q-switch. As a Q-modulator, the cell is used to spoil the cavity-Q periodically, so that selected electron pulses emerge from the MO with little, or no laser interaction and unaltered energy distribution. These unperturbed, or "unused" electron pulses are then available for signal amplification in the PA without the energy spread normally induced by the MO, as is the case in experiments described above. In the PA, these electron pulses can interact and amplify the laser output produced by the MO during the rf-cycle when its Q is high. By Q-switching, the entire cavity power may be dumped to the PA to explore its operation in the high power regime. The optical cavity modifications, and the eo-cell are described below.

In Section 2 we describe the experiment configuration. Section 3 describes the optical beam transport line to the Rocketdyne wiggler, and alignment of the optical components. Small signal gain results are discussed in Section 4. Future experiments and recent modifications of the Mark-III optical cavity are described in Section 5.

Experiment Configuration

Two independent gap tuneable wiggler magnets were available in-line on the SPRL 45 MeV, high brightness(> 10^{12} A/m^2/Ster), s-band, radio-frequency linear accelerator beamline. The first of these is the Stanford Mark III FEL.[2] It uses a constant parameter, permanent magnet hybrid wiggler whose period is 2.3 cm. It is 47 periods long, and has a peak field of 7 kG. The second in-line wiggler is the Rocketdyne magnetic field taperable, high quality, all permanent magnet device.[3] The Rocketdyne wiggler has a 2.5 cm period. Its length is 200 cm, and peak field is 3.7 kG. By installing two independent transport lines for electron and laser beam transport the two devices were used to perform an FEL-MOPA experiment. The Mark-III FEL was used as a high gain MO, while the Rocketdyne wiggler served as a high gain, high efficiency PA. The two wigglers were connected directly by taking electrons from the output end of the Mark-III wiggler and matching them into the Rocketdyne wiggler (with appropriate dipole and quadrupole magnets described below). The Mark-III laser output was transported (in air) through mode matching and delay optics, described in Sec. 3. In designing the transport systems a critical requirement was to assure that the very bright electron beam and the high power laser beam were transported over many meters with little, or no, degradation in their respective beam qualities. In addition, the two transport systems were required to have sufficient flexibility so that an optimum spatial and temporal match between the picosecond electron and laser pulses could be empirically found in the amplifier.

As mentioned earlier, the e-beam traverses the two wigglers in sequence, first through the MO and then the PA. Electrons in every rf-bucket participate in sustaining oscillations in the MO and also provide further amplification in the PA. The high electron beam quality required in the PA was assured by operating the MO in the small signal, unsaturated regime thereby minimizing the energy spread induced in the electron beam in its passage through the MO.

The physical layout of the SPRL FEL MOPA experiment is shown schematically in Fig. 1. The electron beam that drives both the Stanford Mark III FEL oscillator and the Rocketdyne FEL amplifier is provided by a 3-meter long section of the 1 GeV Stanford Mark III linear accelerator. The accelerator is capable of supplying a 45 MeV electron beam with a peak current of 45 A. The primary power to the accelerator and electron gun is supplied by an s-band ITT klystron which provides a microwave drive pulse up to 12 μsec long at 30 MW peak input power. The instantaneous micropulse energy spread is 0.5%, and the electron beam normalized horizontal and vertical emittances are estimated to be 10π mm-mrad and 2π mm-mrad respectively. At the input and exit ends of the Mark-III FEL the electron beam is bent around the resonator optics by four 11° permanent magnet dipole bending magnets. The electron beam is then matched into the Rocketdyne wiggler with a quadrupole triplet by bending around the injection optical element (a turning flat) with four 22° permanent magnet dipole magnets. At the Rocketdyne wiggler exit the electron beam is bent around the output optical element (another turning flat) with two 22° permanent magnet dipoles and sent to a below ground beam dump. The optical beam line contains a telescope to match the optical beam into the Rocketdyne wiggler, and provides a variable optical delay to facilitate temporal overlap between the optical and electron micropulses in the Rocketdyne wiggler. The optical beam transport line is discussed in more detail in Section 3. The optical output from the Rocketdyne amplifier is then transported to the optical diagnostics area where its properties are studied.

Optical Beam Transport Line and Alignment Requirements

The optical beam transport line leading from the Mark III FEL to the Rocketdyne wiggler is shown in Fig. 1. The optical beam transport line is located on top of the two wigglers. The mode matching telescope matches the optical beam into the Rocketdyne wiggler with a nominal waist of 1 mm at the wiggler center. The telescope is designed

to locate the waist anywhere along the length of the wiggler, so that effects of waist position on the amplifier performance can be studied. The telescope is also designed so that the waist size can be varied $\pm$ 10% about the nominal value of 1 mm. Also shown schematically in Fig. 1 is the optical delay line downstream of the mode matching telescope. The delay consists of two turning flats mounted on a translational stage that can be moved axially. The delay allows axial matching of the laser and electron pulses in the amplifier. The delay has a continuously adjustable range of 10.5 cm, corresponding to the distance between successive electron micropulses, and has a readout resolution of 30 microns.

In addition to proper transport and match of the laser and electron beams, they must be spatially and temporally superimposed in the PA for MOPA operation. This is accomplished by first aligning the electron beam with the aid of alignment screens in the MO and the PA. Once the MO is properly aligned and operational, the laser beam must then be superimposed on the electron beam in the PA. There are seven degrees of freedom in which accurate superposition must be maintained. These, and their alignment tolerances (for no more than 10% reduction in gain), established primarily from steady-state computer simulations using the Rocketdyne simulation code FELOPT[4], are summarized in Table I.

Table I.   Alignment tolerances in Rocketdyne wiggler.

Displacement between optical and electron pulses

Vertical	$\pm$ 50 μm
Horizontal	$\pm$ 50 μm
Axial	$\pm$ 75 μm

Angular displacement between optical and electron beams

x-z plane	$\pm$ 500 μrad
y-z plane	$\pm$ 500 μrad

Optical spot size variation	$\pm$ 10%

Displacement between optical and electron beam waists	$\pm$ 10 cm

---

Alignment is achieved in several steps. The electron beam is aligned by centering (with remote video cameras) the visible, fluorescent spot it produces on retractable alignment screens located along the length of the vacuum chambers in both the MO and the PA. Boresight alignment of the two wiggler axes and the optics in the intervening optical transport system is achieved with a He-Ne laser, retractable alignment targets and apertures, and a theodolite. The latter is also used to verify alignment on-line, by observing the visible harmonics of the MO. The components of the adjustable, mode-matching telescope, and the optical delay assemblies were prealigned on a breadboard. The assemblies were then installed in the optical beamline. The adjustable telescope alignment was checked over its entire range of travel during breadboard tests. Final alignment was accomplished with the free-electron laser on line. The MO output was first maximized by taking small, corrective steps; once signal enhancement was observed in the amplifier, its performance was optimized by fine adjustments of the injection optics.

For a successful MOPA demonstration it is essential that electro beam energy spread and brightness, as well as laser beam quality is not seriously degraded in transporting the two beams from the MO to the PA. The key components of the optical transport system, the mode matching telescope and the optical delay, were individually tested in separate breadboard setups. The optical components of each were precisely aligned, and their optical quality following assembly was verified with a Zygo interferometer. Wavefront distortion over the total aperture was, typically, less than λ/10 (at 0.6328 μm) over the entire range of travel of each sub-assembly. The electron beam quality was indirectly verified by simultaneously operating the Mark III oscillator in the small signal regime and the PA wiggler as an FEL oscillator. Resonator optics used in earlier tests were added to convert the amplifier into an oscillator. Rocketdyne laser performance similar to earlier tests[3] was obtained. These tests verified that e-beam brightness (and energy spread) was not seriously degraded in transporting it to the PA. Upon completion of these tests, resonator optics were replaced by injection and output optics (two turning flats) to convert back to an amplifier configuration.

Small Signal Gain Results

The first experiment has addressed measurement of the small signal gain spectrum in the untapered Rocketdyne amplifier for optimum temporal and spatial matching of the input optical beam and the electron beam. Details of the experiment can be found elsewhere.[5] The experiment was performed using the two mirror, near concentric Mark III FEL optical resonator with a Brewster plate outcoupler. An optical chopper with a fixed delay window provided a reference signal. The reference signal and amplified signal emerging from the PA were measured with a high speed Ge:Au detector whose output was ratioed to give a direct measure of amplification. Experimental parameters are summarized in Table II.

Table II.   FEL MOPA parameters.

Electron beam:

Peak current	35A
Normalized emittance	
Vertical	2π mm-mrad
Horizontal	10π mm-mrad
Waist	
Vertical	0.3 mm
Horizontal	0.7 mm
Energy	38 MeV
Energy spread	0.5%
Macropulse length	3 μs
Micropulse length	3 ps

Input optical beam at power amplifier:

Wavelength	3 μm
Wavelength spread	0.6%
Macropulse length	2 μs
Micropulse length	2 ps
Waist	1 mm
Average energy	3 mJ
Peak power at small signal	100 kW

Power amplifier wiggler:

Length	200 cm
Period	2.5 cm
Variable gap	0.76-2.0 cm
Peak magnetic field	3.7-0.8 kG

At optimum matching and overlap conditions, the gain spectrum was obtained by gap tuning the power amplifier wiggler over the range 3.7 - 3.5 kG. Gain as a function of the resonance parameter is shown in Fig. 2. The resonance parameter is $\nu = [(k+k_0)v-\omega]L$, where k_0 is the wiggler wave number, L the wiggler length, v the electron axial velocity, and k, ω are the optical wave number and frequency. The solid curve is a FELEX[6] simulation with Table II parameters, and assumes a square electron pulse shape and an initial Gaussian TEM_{00} optical mode. Excellent agreement between the simulation and data is seen in Fig. 2. The amplification peak of 60% occurs when the resonance parameter is 4.3, while the absorption peak of -35% occurs at -2.2. Theoretically for plane waves the low gain amplification and absorption peaks occur at the resonance parameter values $\pm$ 2.6, respectively. Also, for plane waves the FEL gain is proportional to the slope of the spontaneous emission spectrum. In the present experiment the spontaneous emission spectrum has been measured and its slope was found not to correspond[5] to the gain spectrum in Fig. 2.

As discussed in Ref. 7, the validity of the plane wave approximation depends on the dimensionless parameter $q = L/Z_R$, where L is the wiggler length and Z_R is the Rayleigh range. For q < 1 the plane wave approximation is valid, while for q $\geq$ 1 a Gaussian approximation for the optical radiation must be used. The present experiment has q = 1.9, so the effects of a diverging Gaussian optical beam are taking place. Ref. 7 points out that in the presence of a Gaussian mode the gain is no longer proportional to the slope of the spontaneous emission spectrum, which agrees with the present results. Also, the Gaussian mode introduces a phase shift relative to a plane wave, which produces a shift in the resonance parameter, with the consequence that the amplification and absorption peaks occur at larger values of the resonance parameter.

Modified Mark-III Resonator and Future Experiments

Although initial small signal gain experiments were performed with the two mirror Mark III FEL optical resonator, follow-on small signal gain and saturated regime experiments will be performed with an electro-optic switch in place, which will allow electron micropulses with undegraded emittance (and energy spread) into the Rocketdyne wiggler. The electro-optic switch will also allow dumping all of the circulating optical power in the Mark III FEL, so that the Rocketdyne amplifier can be operated in the saturated regime. Installation of an electro-optic switch in the existing Mark III FEL optical resonator configuration was not feasible, since the fluence on the device is enough to severely damage it. In order to alleviate this problem, the upstream end of the resonator was modified as shown schematically in Fig. 3.

The modified optical cavity is also a standing wave cavity. The existing downstream, translatable mirror which provides cavity length control remains in place. The length of the cavity was increased from 183.75 cm to 315 cm by placing a turning flat in front of the existing upstream mirror to divert the radiation up to a convex element. The convex element expands the beam a factor of three by the time it reaches the concave end mirror. The angle of incidence (and reflectance) at the expanding element is kept near normal (5 deg) to minimize aberrations. All the mirrors in the new resonator are made of diamond turned copper substrates with silver overcoating, while the outcoupling Brewster plate near the upstream concave end mirror is made of calcium fluoride. The mounts for the mirrors in the upstream end of the resonator provide remote tip-tilt actuation of the mirrors, although they do not provide any length control. It is also possible to withdraw the turning flat in front of the existing upstream end mirror to allow independent operation of the Mark III FEL with the present resonator configuration.

The electro-optic switch shown in Fig. 3 is located near the upstream concave end mirror, where the fluence in the beam is the lowest. The $1/e^2$ point, where the electro-optic switch is located, is approximately 0.42 cm which is a peak fluence of 0.4 GW/cm^2 per micropulse. The width of the electro-optic switch was chosen to be 1.5 cm, while its length is 1.5 cm. The switch is made of Cadmium Telluride. This material was chosen for its high electro-optic coefficient which requires less voltage to operate, and for its low absorption (0.14% per cm at 3 μm). Damage tests[8] on this material at 3.7 μm have been carried out using the Mark III FEL. Uncoated CdTe has been observed to break down at a fluence level of 5 GW/cm^2, while coated samples break down at approximately 2 GW/cm^2. The expected fluence on the switch, 0.4 GW/cm^2, is well below these levels. The electro-optic switch is located near the upstream end mirror, such that only one optical pulse will be in the device at any time to minimize its thermal load.

Follow on small signal gain measurements will be performed with the new Mark III FEL resonator and electro-optic switch in place, which will provide an electron beam with less energy spread to the Rocketdyne wiggler than in the present experiments. The measurements will concentrate on effects of input mode matching where temporal matching is varied through the optical delay in the optical beam transport line and spatial matching is varied by adjusting the optical beam line telescope to adjust the waist location and size in the Rocketdyne wiggler. In these experiments optical guiding effects and misalignment effects on the small signal gain and optical mode quality will also be explored. The measurements will be performed for both untapered and tapered regimes of operation of the Rocketdyne wiggler.

After completion of the small signal gain experiments, the Rocketdyne amplifier saturated regime of operation will be concentrated on. Assuming the approximate 100 MW of peak circulating optical power in the Mark III FEL cavity can be dumped into the Rocketdyne wiggler, simulations indicate that an energy conversion efficiency of up to 2% can be expected in the amplifier. The saturated lineshape will be measured for both an untapered and tapered wiggler. Effects of matching and location of the optical waist in the wiggler on energy conversion efficiency, as well as effects of misalignment on efficiency will be examined. Also, if sidebands are observed to develop effects of mismatch and misalignment on the development of the sideband content will be studied.

Acknowledgment

References

1. A. Bhowmik, J. M. J. Madey, and S. V. Benson, Nucl. Instrum. Methods Phys. Res., Sect. A $\underline{272}$, 183 (1988).

2. S. V. Benson, J. M. J . Madey, J. Schultz, M. Marc, W. Wadensweiler, G. A Westenskow, and M. Velghe, Nucl. Instrum. Methods Phys. Res., Sect. A $\underline{250}$, 39 (1986).

3. A. Bhowmik, M. S. Curtin , W. A. McMullin, S. V. Benson, J. M. J. Madey, B. A. Richman, and L. Vintro, Nucl. Instrum. Methods Phys. Res., Sect. A $\underline{272}$, 10 (1988).

4. A. Bhowmik, R. A. Cover, and R. H. Labbe, SPIE, $\underline{642}$, 10 (1986).

5. L. Vintro, Ph.D. dissertation, Stanford University, 1989 (unpublished).

6. B. D. McVey, Nucl. Instrum. Methods Phys. Res., Sect. A $\underline{250}$, 449 (1986).

7. W. B. Colson and P. Elleaume, Appl. Phys. B $\underline{29}$, 101 (1982).

8. E. L. Dottery, J. Schultz, and J. M. J. Madey, unpublished.
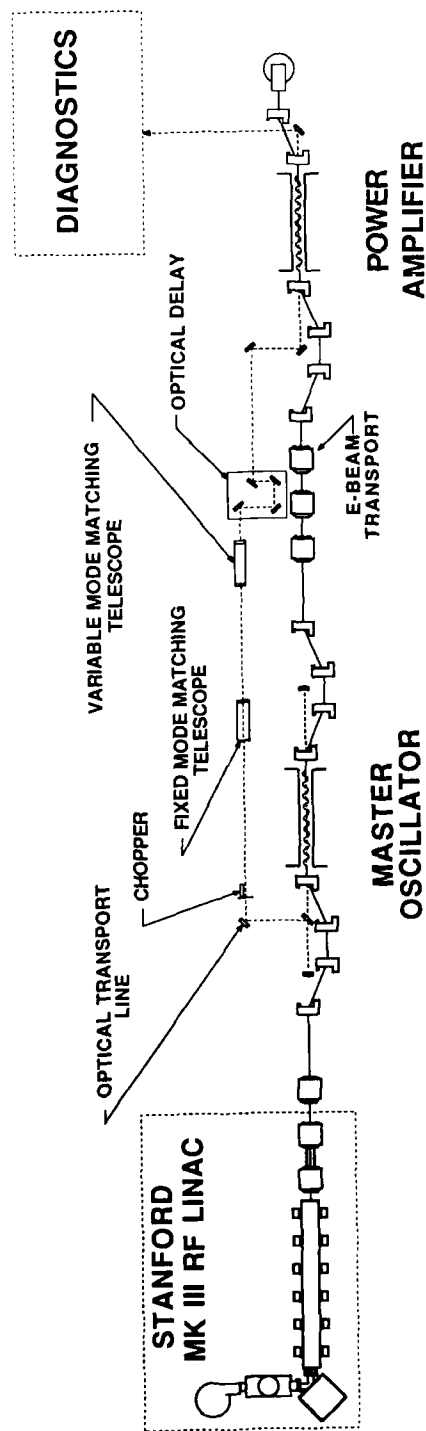
Figure 1. Schematic of the FEL MOPA experiment as configured in the Stanford Photon Research Laboratory
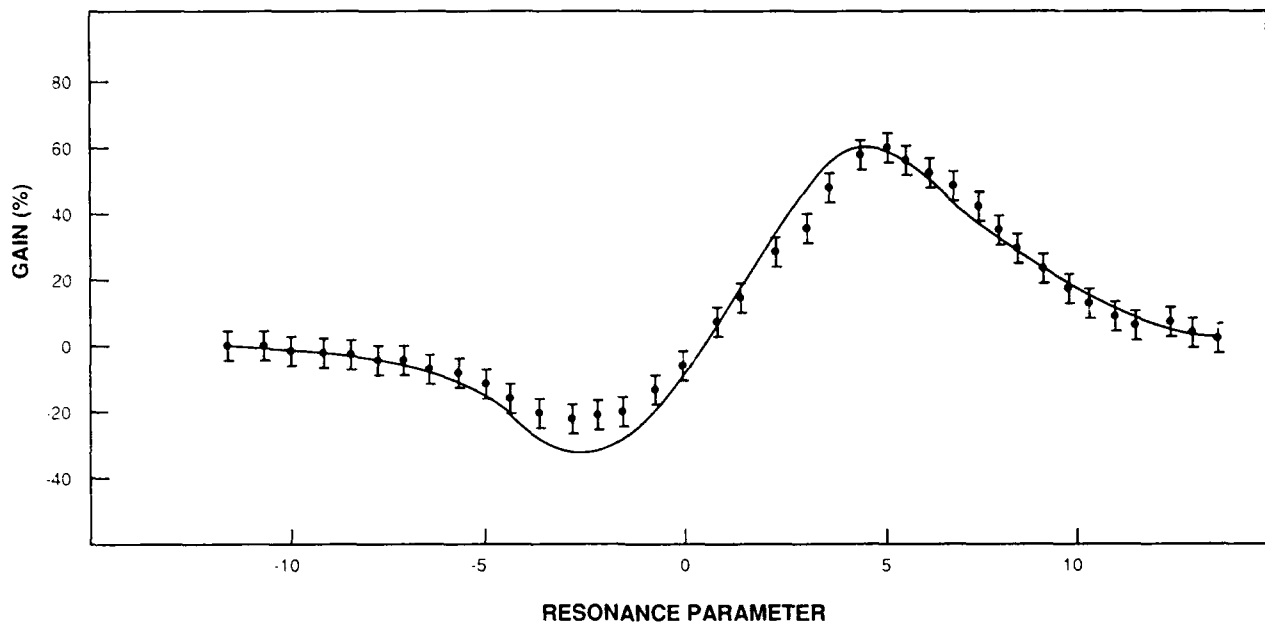
Figure 2. Power amplifier small signal gain as a function of the resonance parameter. The solid curve is a FELEX simulation.
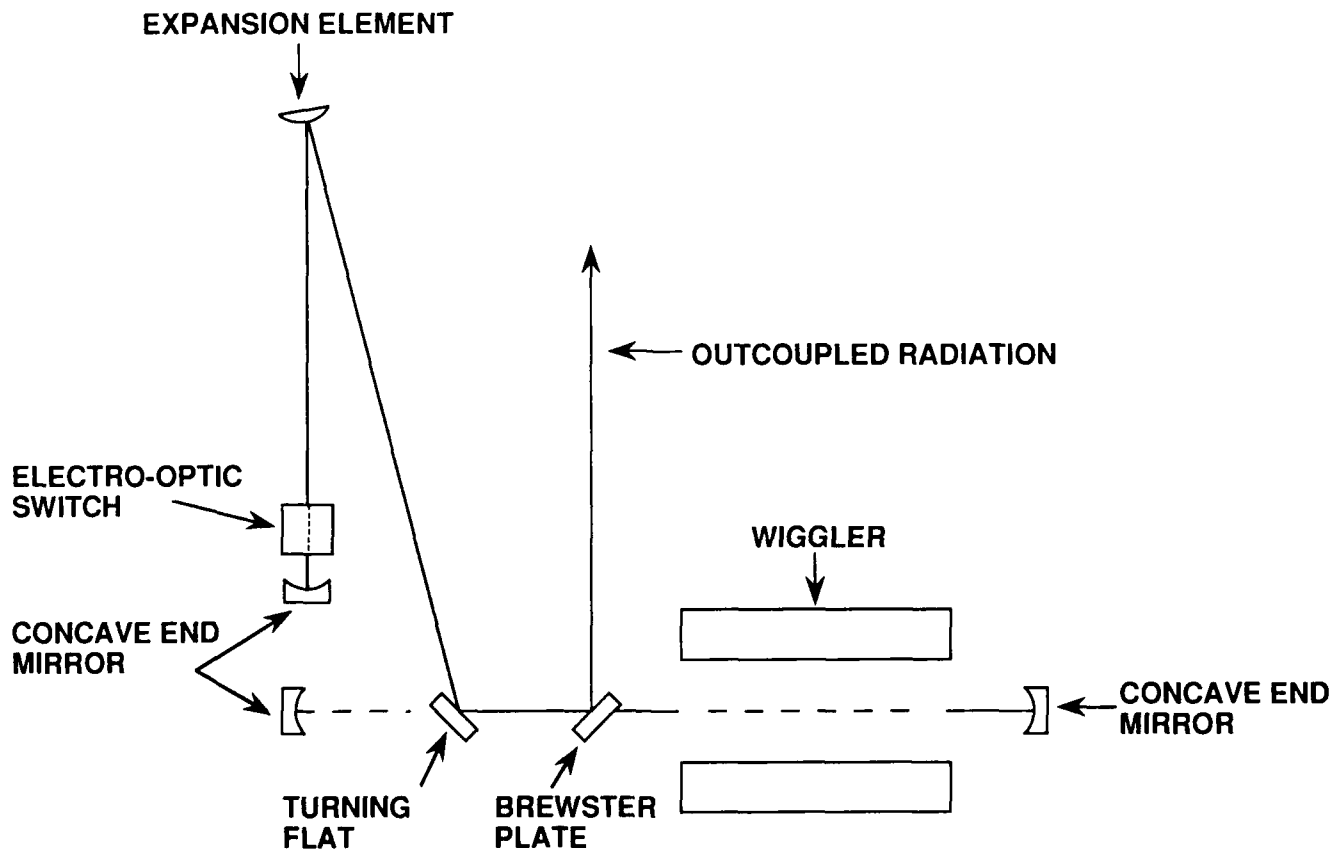
Figure 3. Schematic of the modified Mark III FEL optical cavity.

INTENSITY-INDUCED ABSORPTION IN ZnSe[*]

Jon E. Sollid, Donald W. Feldman,
Claude R. Phipps, Jr., and Roger W. Warren
Los Alamos National Laboratory
P. O. Box 1663, MS J579
Los Alamos, NM 87544
(505) 667-2767

Abstract

In a particular sample of ZnSe, working at 10 µm, a nonlinear absorption was observed that was generated by light intensities greater than 100 MW/cm^2. This absorption was subsequently bleached by light intensities over 600 MW/cm^2. This result was obtained using 10-ps pulses from the Los Alamos National Laboratory Free-Electron Laser.

Summary

In the course of experiments at the Los Alamos FEL, resonant cavities with losses ranging from 10% to 1% were used. At the higher losses, good agreement between the number of photons generated, as inferred from the electron spectrometer data, and the number actually measured optically was obtained. As the resonator cavity losses decreased, thus increasing the intracavity power, a discrepancy appeared. Less photons were measured than generated, as though photons were being absorbed by the resonator mirrors. We believe that at a certain fluence, free carriers are generated in the semiconducting material forming the mirrors which leads to increased absorption. At higher fluences yet the absorptive material appears to bleach, and once again the behavior can be fit within this free-carrier model. For a particular multilayer dielectric high reflectance coating (R>99.8%) the lowest threshold observed for saturation was about 100 MW/cm^2, and the threshold for bleaching appeared at around 600 MW/cm^2. However, the threshold varies from mirror to mirror, which implies that extrinsic properties are important.

Introduction

The Los Alamos FEL operates at wavelengths tunable from 3.7 to 44.7 µm. The wiggler and accelerator are optimized to produce light at 10 µm. Free-electron lasers are unique because of their unrivaled broad tunability, for their high extraction efficiency (4.4%),[2] and for the high output powers achievable (on the order of 50 MW peak).

Figure 1 is a schematic of an RF FEL showing the essential features: (1) an RF accelerator capable of producing a relativistic electron beam, (2) a wiggler with periodically alternating magnetic fields that force the electrons passing through it to oscillate, and therefore radiate (spontaneous emission), and (3) a resonator structure which supplies feedback and allows the electromagnetic field to interact coherently with the electron beam producing coherent emission, i.e. lasing.

Figure 2 shows the floor plan of the Los Alamos FEL. At a. is shown the electron beam injector (a thermionic Pierce-type electron gun). At b. is shown the two stages of rf linear accelerators that accelerate the electrons to 20 MeV. In the center of the figure at c. is shown the achromatic, nonisochronous 60° bend, which also can act as a magnetic buncher for the electrons. On the west end of the vault at d. are the resonator mirrors and the wiggler.

Statement of the Problem

In the course of conducting experiments on the fundamental properties governing the production of photons in an FEL, energy balance measurements were made. The amount of energy removed from the electrons during lasing could be determined from electron spectrometer data by comparing the electron energy distribution before and during lasing. Except for the cavity losses, this same amount of energy should show up as photons. This was often the case, but there were instances when only 3% of the expected energy could be found as light. In what follows we describe steps in analyzing this problem and eliminating it. We give evidence to indicate that the ZnSe mirrors in the resonator cavity exhibit nonlinear optical absorption due to the high intensity achievable in the Los Alamos FEL. We show by analogy with n-type germanium that a possible mechanism is impact ionization in the ZnSe, which is a zincblende structure semiconductor.
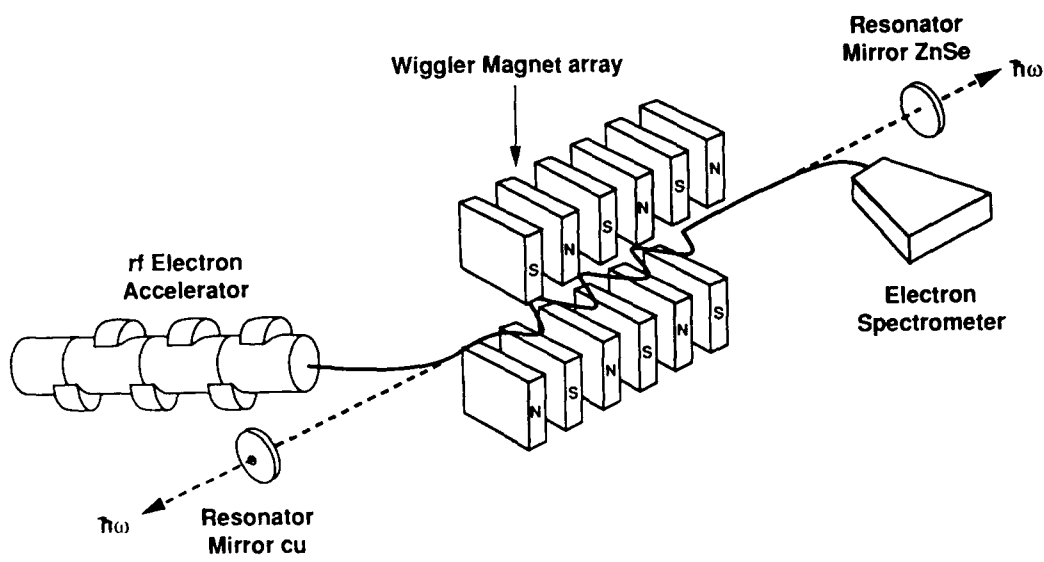
Figure 1. Schematic diagram of radio frequency linear accelerator driven free-electron laser.
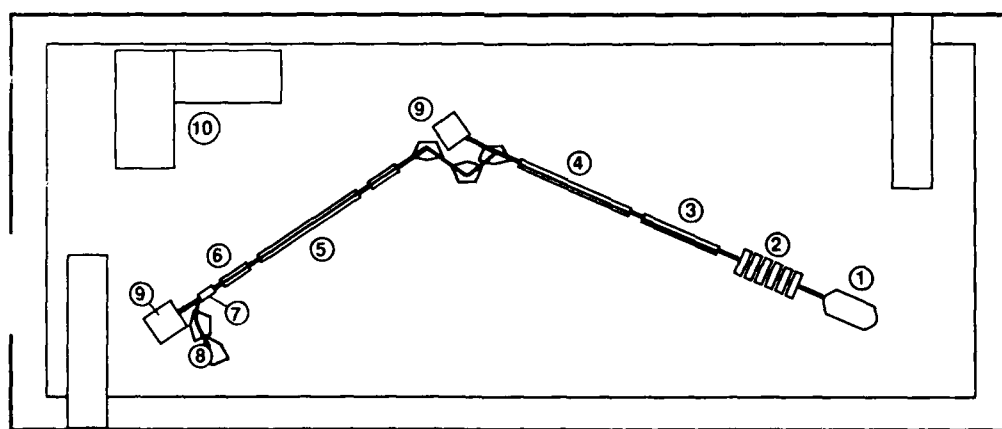
1. 80 keV Electron Gun	6. Slow Vertical Deflector
2. 108 MHz and 1300 MHz Bunchers	7. 1300 MHz Vertical Deflector
3. 10 MeV LINAC Tank	8. Electron Spectrometer
4. 11 MeV LINAC	9. Optical Resonator Mirrors
5. Wiggler	10. Optical Diagnostics

Figure 2. Experimental layout of LANL FEL.

Experimental Configuration and Observations

The unusually large discrepancies occurred only when very high reflectivity resonator mirrors were used. The mirror substrates were chemical vapor deposited (CVD) ZnSe. To achieve high reflectance a multilayer stack of quarterwave layers of ZnSe and ThF was deposited. For the particular set of mirrors under consideration the transmission was 0.0035.

Ionizing Radiation Considered

The accelerator produces a fairly high flux of ionizing radiation (about 10^7 rads/s) when the laser operates. It was possible to watch the downstream mirror from inside the resonant cavity using an intensified CID TV camera. Points of light were produced on the mirror surfaces during lasing. These might be due to ionizing radiation we reasoned. The downstream mirror received much more ionizing radiation than the upstream mirror due to its proximity to the electron spectrometer and the beam dump. A means was contrived to allow observation of the upstream mirror. As many or more points of light were seen on the upstream mirror than on the downstream mirror. Hence, at least the flashing was not caused primarily by the ionizing radiation flux. Transient absorption effects have been reported in ZnSe from ionizing radiation[3] but only at fluences of 10^9 rads/s, 100 times more than the Los Alamos FEL produced.

ZnSe vs Copper Resonator Elements

It seemed likely that the transient transmission change was due to the light itself. To test this, we left one of the high reflectance ZnSe elements in the downstream mirror, but replaced the upstream mirror with a copper mirror pierced with a small central hole to allow outcoupling, as shown in Figure 3. The energy from the downstream and upstream mirrors was measured as a function of e-beam current.
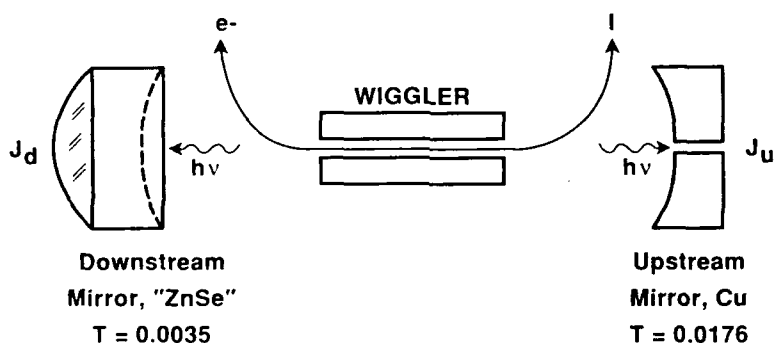
Figure 3. Schematic drawing of resonator configuration.

If the absorption by both mirrors was completely linear a constant ratio between the upstream and the downstream outcoupled energies would be maintained over the entire range of currents. The ratio would be sensitive to all the losses such as Fresnel reflection, absorption and scatter. The data are displayed as a graph of downstream outcoupled energy versus the upstream outcoupled energy in Fig. 4. Measurements were made when the spectral character of the light was both broadband and single line. However, there is no significant difference observable between the two cases. Note that the points do not lie on a straight line. The initial departure begins at very low energy, about 50 mJ corresponding to a fluence of 100 MW/cm^2. In this region we may be generating free carriers by an avalanche mechanism in the ZnSe, hence the transmission seems to flatten out. Between 210 and 250 mJ we note a dramatic increase in the transmission, as though the ZnSe were bleaching. The 230 mJ output corresponds to a peak fluence on the mirror inside of about 500 MW/cm^2. This is calculated as follows:

$$P = 2J_u \, d/\pi \, w^2 \, t_{mac} \, t_{mirror} \tag{1}$$

where P is the peak power inside the cavity, J_u is the energy measured exiting the upstream mirror, d is the duty cycle in the macropulse (we have 10-ps pulses spaced by 46 ns within the macropulse, hence the duty cycle is 4600), w is the laser waist size at the mirror (9.7 mm), t_{mac} is the macropulse length 80 μs, and t_{mirror} is the transmission through the hole in the copper mirror 0.0176. For the very highest powers better agreement was achieved between the electron spectrometer and the optical measurements. So for very low powers good agreement was obtained, and for very high powers agreement was seen, but for the intermediate values for fluences between 100 and 600 MW/cm^2 there were discrepancies of up to 30 times between the number of photons detected and the number implied by the electron spectrometer data.
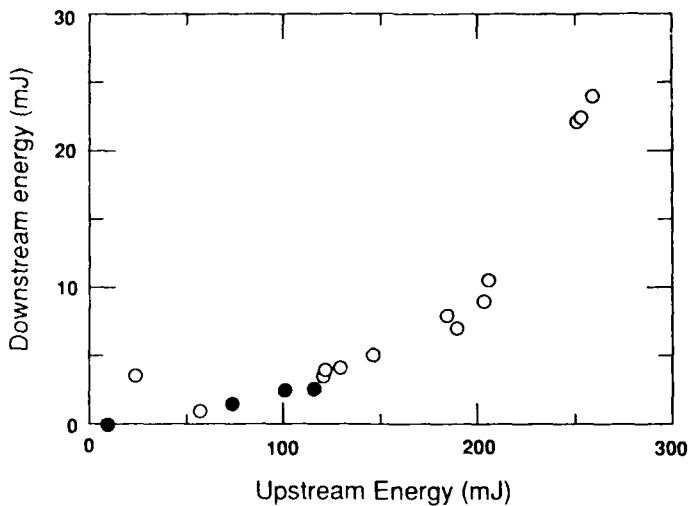
Figure 4. Experimental Data
The energy measured downstream, as shown in Fig. 4, is plotted vs the energy measured upstream. The open circle is for broadband (12%) spectral emission and the closed circle is for a narrow (0.3%) spectral line.

Interpretation of the Data

The behavior seen is similar to that for p-type germanium except that there is no bleaching in germanium. Germanium displays free carrier avalanche absorption at about 200 MW/cm^2.[4] Germanium has a band gap of 0.665 eV whereas the band gap in ZnSe is 2.67 eV. In germanium when the absorption starts it is very rapid, going as the intensity to the 5.5 power. The photon energy is about 0.125 eV. Once the process starts by avalanche it looks like a five or six photon process. This would imply that once an electron avalanche began in ZnSe it would go as intensity to the 21.5 power. Hence only a very thin layer would participate in the absorption. If the material were rich in electrons, say if there were free zinc because of a nonstoichiometric deposition process during the coating, it would be much easier to start the avalanche. The behavior of n-type germanium is similar to that of the p-type except that in p-type the absorption actually decreases slightly with increased intensity until the strong absorption turns on.[5] What we have observed is probably not characteristic of intrinsic zinc selenide, but a property of the first layer of the antireflection coating.

Conclusion

To be safe, we avoid the use of ZnSe or other semiconductor components in high intensity applications.

References

1. "Proposed Extended Tuning Range for the Los Alamos Mid-Infrared Adjustable Coherent Light Experiment (MIRACLE) Facility." A. H. Lumpkin, D. W. Feldman, J. E. Sollid, R. W. Warren, W. E. Stein, B. E. Newnam, J. C. Goldstein, W. J. Johnson, and J. M. Watson; Abstract 13.18, 10th International Free-Electron Laser Conference, Jerusalem, Israel, August 29-September 2, 1988.

2. "High-Extraction Efficiency Experiments with the Los Alamos Free-Electron Laser," Donald W. Feldman, Harunori Takeda, Roger W. Warren, Jon E. Sollid, William E. Stein, and W. Joel Johnson; Abstract 13.7, 10th International Free Electron Laser Conference, Jerusalem, Israel, August 29-September 2, 1988.

3. "Transient Absorption of Light Induc⋯ by Radiation," R. Godwin, F. B. Harrison, A. Larson; NBS Special Publication 746, ASTM STP 1015, "Laser In⋯⋯ ⋯amage in Optical Materials: 1985, p. 480ff.

4. "Subnanosecond Extinction of CO_2 Laser Signals Via Bulk Photoionization in Germanium," C. R. Phipps, Jr., S. J. Thomas, and D. E. Watkins, CLEA 19⋯⋯ ⋯d LA-UR 78-3348.

5. "Theory of Nonlinear Optical Absorption Associated with Free Carriers in Semiconductdors," Ralph B. James and Darryl L. Smith, IEEE Journal of Quantum Electronics, Vol. QE-18 No. 11, 1841 (1982). See in particular Fig. 19, page 1861.

Demonstration of Harmonic Lasing in a Free-electron laser

Stephen Benson and John M. J. Madey
Department of Physics,
Duke University, Durham NC 27706

Abstract

Using an intracavity element to separate fundamental and harmonic lasing, we have demonstrated saturated third harmonic lasing at 1.4—1.8 μm using the Stanford Mark III free-electron laser. Gain at the third harmonic agrees with theory to within experimental limits. The wavelength shift between the fundamental and third harmonic does not agree with one dimensional theory. The excess frequency shift suggests that frequency pulling predicted in previous two dimensional modelling efforts are present.

Free-electron lasers, unlike atomic and molecular lasers, are not limited to any one wavelength. The lasing wavelength is given approximately by the relation

$$\lambda_s = \frac{\lambda_w}{2\gamma^2}(1+K^2) \tag{1}$$

where λ_s is the laser wavelength, λ_w is the undulator wavelength, γ is the energy of the electron divided by its rest mass and K is the undulator parameter which is equal to the RMS bending angle of the undulator times γ. The wavelength is then a continuously variable parameter limited only by the energy of the electrons and the wavelength and strength of the undulator. As an example, the Mark III free-electron laser, used in the experiments reported in this paper, has a maximum energy of 43 MeV, an undulator period of 2.3 cm, and an undulator parameter K of up to unity. The gain is approximately proportional to K^2 for small K so one cannot reduce the undulator parameter arbitrarily in order to reduce the wavelength. The Mark III has operated with a K^2 as low as 0.15. This yields a minimum wavelength of 1.9 μm. With this weak an interaction the gain is just barely sufficient for the laser to turn on before the accelerator turns off. In order to reduce the wavelength further, the undulator period would have to be reduced, or the electron beam energy would have to be increased. Both options are expensive and reduce the laser gain.

Because of the non-linear nature of the laser interaction in a FEL, gain also exists at harmonics of the wavelength given in equation (1). This was first noted by Madey and Taber[1]. The magnitude of the gain can be calculated from the gain-spread theorem[2]. As the electrons traverse the undulator, they emit a $1/\gamma$ cone of radiation which sweeps past an on-axis observer producing a series of bursts of radiation with a repetition rate given by the optical frequency determined from equation (1). As the undulator parameter is increased, the harmonic content of the on-axis radiation increases. The result is a radiation spectrum consisting of a series of $(\sin x/x)^2$ curves at each of the odd harmonics of the fundamental. The width of each curve is the same and the height, proportional to the strength of the modulation, is given by

$$A_f \propto [J_{\frac{f-1}{2}}(f\xi) - J_{\frac{f+1}{2}}(f\xi)]^2 \tag{2}$$

where f is the harmonic number and $\xi = K^2/(2(1+K^2))$. The gain spread theorem states that the gain is proportional to the slope of these curves with respect to the change in electron beam energy. Since the harmonic curves shift faster with energy than the fundamental by a factor of f, the gain ratio should be f times the ratio of the harmonic amplitudes. Since the optical mode size also varies inversely with f, the gain ratio in an actual device for a perfect electron beam will be

$$\frac{G_f}{G_1} = \frac{f^2[J_{(f-1)/2}(f\xi) - J_{(f+1)/2}(f\xi)]^2}{[J_0(\xi) - J_1(\xi)]^2} \tag{3}$$

This is plotted vs. K in figure 1a for the case of the third harmonic.

It would seem that the gain at the third harmonic can be greater than that of the fundamental for sufficiently high field strength. In fact, this is rarely the case since the electron beam is rarely ideal enough to reach the curve shown in figure 1a. The ratio of the actual gain to the ideal gain vs. the effective electron beam energy spread is shown in

figure 1b. The energy spread is given by $2N\delta\gamma/\gamma$ where $\delta\gamma$ is the full width at $1/e$ of the energy distribution. Since one usually designs the undulator for the fundamental, a typical value is around unity or larger. The gain at the third harmonic is thus quite small compared to the fundamental. For the laser used in these experiments, the effective energy spread was approximately 0.3, so one expects a third harmonic gain about half that of the fundamental at $K^2=1$. The quality of the undulator may also degrade the third harmonic gain. For these experiments the third harmonic gain should have been reduced by 13% by wiggler imperfections.
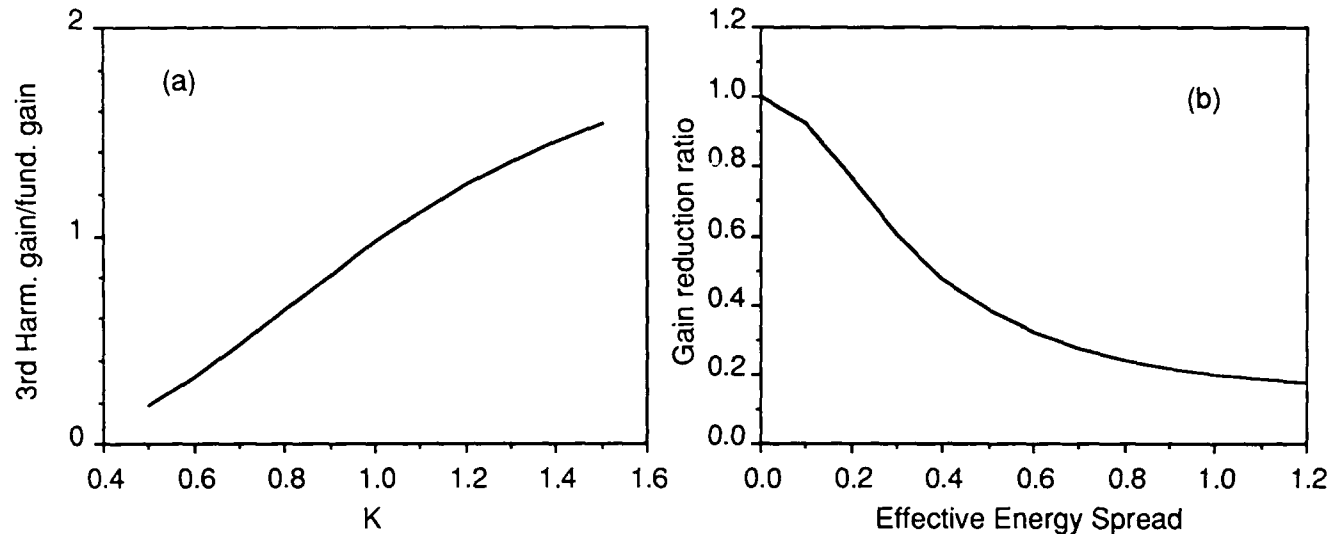
Figure 1. (a) Ratio of the third harmonic gain to the fundamental gain for an ideal electron beam and undulator. (b) Reduction in the gain ratio caused by the electron beam effective energy spread $2N\delta\gamma/\gamma$.

In 1982 researchers at Frascati lab using the ADONE storage ring measured the gain curves for the third harmonic and suggested that lasing on a storage ring was preferable at the third harmonic due to the better emittance at the lower energy[3]. Unfortunately the gain was still to low to lase. In 1983, a Stanford TRW collaboration found evidence of enhanced third harmonic output in a 1.6 μm FEL oscillator[4]. The evidence for lasing was not conclusive however and the third harmonic power level never exceeded one thousandth that of the fundamental. In the TRW system the fundamental and third harmonic could in principle lase simultaneously. Such a system is very difficult to study. In general one gets very strong coherent emission at the third harmonic from FEL oscillators even with gain well below threshold due to the overbunching of electrons by the laser interaction at the fundamental[5]. It is difficult to separate the lasing signal from this coherent spontaneous signal in such a device[6].

The optical cavity in the Mark III FEL consists of two opaque metal mirrors(uncoated amorphous silver) at each end of the laser undulator. Output coupling is accomplished by means of a calcium fluoride plate mounted a few degrees away from Brewster's angle as shown in figure 2. The plane of incidence is parallel to the plane of electron oscillations in the wiggler. Since the laser output is strongly polarized in this plane, the reflection off the plate is fairly weak. For the experiments reported here we used a 64.8° plate which yields 5.9% total output coupling at 4.8 μm and 5.65% output coupling at 1.6 μm. The cavity itself has losses of the order of 2% between 1 and 8 μm. The intracavity CaF_2 plate is dispersive and leads to a wavelength-dependent round-trip cavity time. Since the laser is driven by a radio frequency linear accelerator, the laser gain and power are very sensitive to the cavity length. The laser can only operate within a few microns of the *synchronous length*, defined as the length at which the round-trip path length is equal to the arrival time between electron pulses. Due to laser lethargy[7] the laser power peaks near the synchronous length, falling off very steeply for longer cavity length and somewhat less steeply for shorter lengths.

The synchronous cavity length difference between the fundamental and third harmonic plotted vs. the third harmonic wavelength is shown in figure 3. At the 4.8 μm wavelength used in these experiments, the third harmonic radiation at 1.6 μm should be synchronous for a cavity length 60 μm longer than that of the fundamental. Since the power falls off very quickly on the long side of the cavity length detuning curve, there is no chance of any significant amount of coherent spontaneous radiation at 1.6 μm. This is essential for turn-on since the initial length enhancement seen is usually smaller than the spontaneous radiation level.
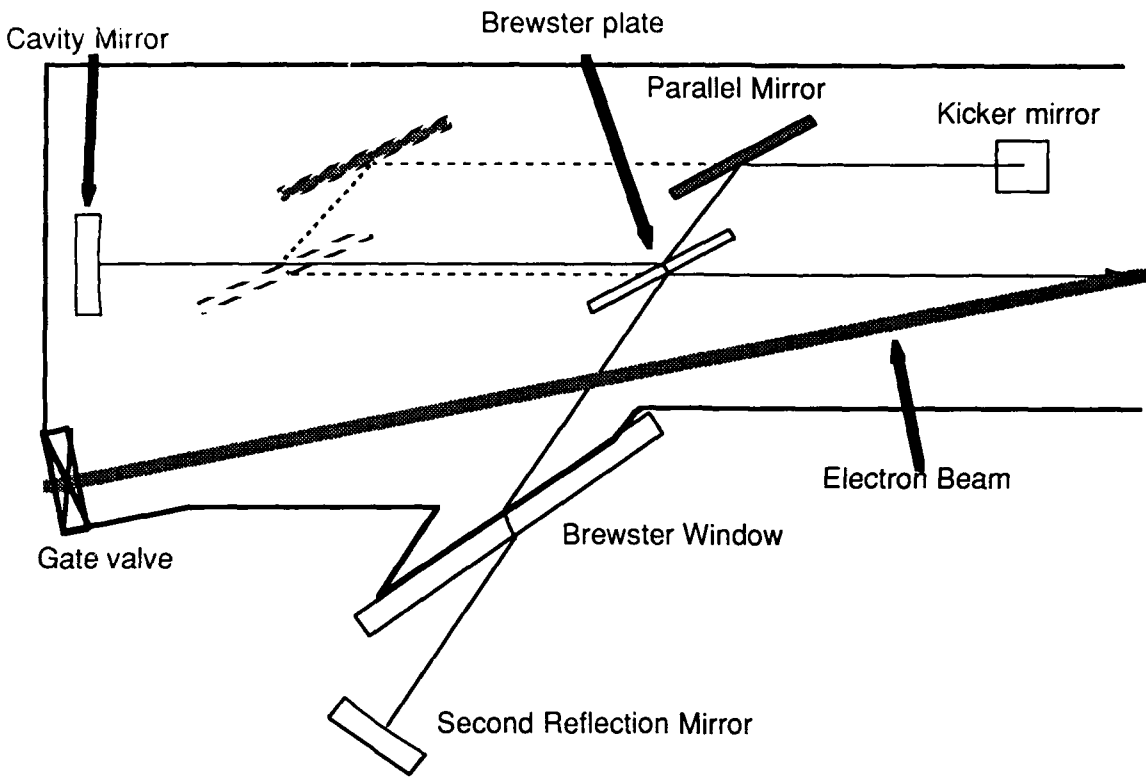
Figure 2. Schematic layout of the Mark III optical cavity. The undulator and moveable cavity mirror are to the right. Dashed lines indicate removeable output coupler. The second reflection mirror was not used in these experiments.
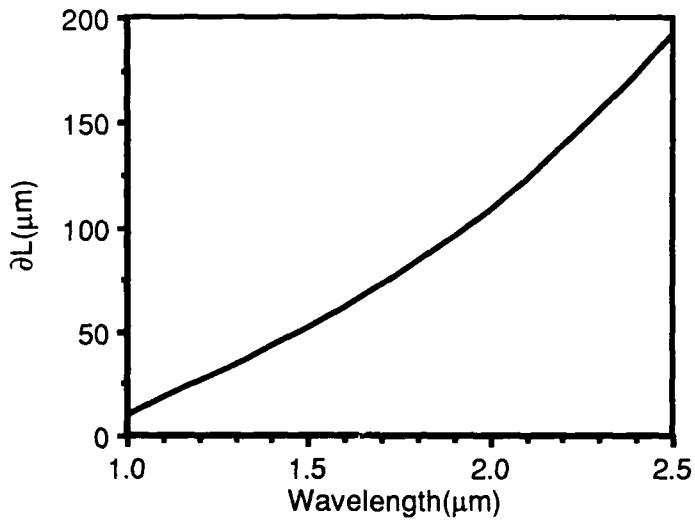
Figure 3. Difference in the synchronous cavity length for the fundamental and third harmonic wavelengths vs. the third harmonic wavelength.

Harmonic lasing was achieved as follows: The laser was started at the fundamental wavelength and tuned up for maximum power and gain. The cavity length was then changed to search for the peak in the 1.6 μm output expected due to the third harmonic gain. A fast Ge(Au) detector was used to measure both the fundamental and the third harmonic. This detector is very sensitive at 1.6 μm due to its intrinsic germanium response, so most data were taken for harmonic lasing at this wavelength. A 1.6 μm notch filter was used to filter out all radiation except the third

harmonic. The cavity length was set at the peak of the length enhancement and the mirrors and electron beam were then tuned until saturation was achieved. At wavelengths other than 1.6 μm we used a Pellin-Broca prism to separate out the third harmonic. The rest of the procedure was the same. Saturated pulse energies were measured using a broadband pyroelectric detector.

Once saturated harmonic lasing was achieved, the laser could be switched from the third harmonic to the fundamental by changing the cavity length alone. A scan of the peak laser power vs. cavity length is shown in figure 4. Note the asymmetric nature of both the laser curves. Different filters were used for each wavelength, so the ratio of the power in these curves is not indicative of the actual power ratio. The distance between the peaks in the curves is 58 μm, close to the expected value of 60 μm.
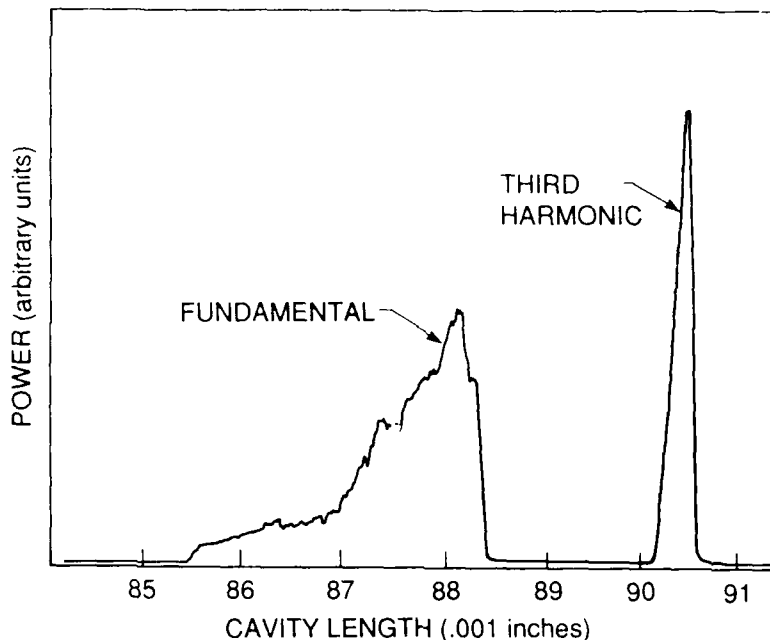
Figure 4. Laser power vs. oscillator cavity length in thousandths of an inch. A larger value for the length indicates a longer cavity. The power is not to scale. Different filters were used for the third harmonic power and fundamental power. The actual maximum powers are listed in table II.

As noted above, the effective energy spread should reduce the third harmonic gain to about half that of the fundamental. The exact value of the energy spread is close to the resolution of the electron spectrometer so the gain reduction factor cannot be known to better than 20%. The measured gain, cavity losses, power, and wavelength at the fundamental and third harmonic are listed in table 2. The experimental gain ratio was, in fact, close to one half.

Table 1: Mark III laser/accelerator parameters during harmonic lasing

Parameter	Value
Electron beam energy	35 MeV
macropulse length	3.2 μsec
micropulse length	2.5±0.5 psec
beam current(peak)	20±5 amps
Energy spread	0.4±0.1% FWHM
Transverse emittance($\beta\gamma\epsilon$)	15±5π mm-mrad
Wiggler wavelength	2.3 cm
Wiggler parameter K	1.39
Number of periods in wiggler	47
Optical cavity length	183.6 cm
Rayleigh range	73 cm

The ratio of the power extracted from the electron beam for the two wavelengths should be 0.28. The measured ratio, calculated from the known coupling efficiency and transport mirror losses, is 0.12. One might think that this is because of incomplete saturation, but the spectra showed evidence of sidebands both at the fundamental and the third harmonic. These should only be present at saturation. In addition, the coherent spontaneous radiation at 530 nm for harmonic lasing was quite bright, indicating full saturation. Scattering losses in the optical transport system may account for part of the discrepancy since scattering is strongly dependent on wavelength. Full simulations should be run to confirm the expected power ratio however.

Table 2: Relative performance of fundamental and third harmonic lasing.

	Fundamental	Third Harmonic
Net Gain	47±2%	19±1%
Total cavity losses	7.2±0.2%	8.8±0.2%
Output coupling	5.9%	5.65%
Ideal transport losses	14%	24%
Macropulse power	30 kW	2.4 kW
Peak wavelength	4.85 μm	1.59 μm

In order to determine whether the laser was operating in the lowest order transverse cavity mode, we placed an aperture in the laser far field and reduced its size until the transmitted power was reduce by half. The aperture size indicated that the laser was lasing in the TEM_{00} mode. A higher order mode would have required a significantly larger aperture.

One interesting feature of harmonic lasing is that the wavelength of the third harmonic is not exactly one third of the fundamental wavelength. This is due to the asymmetry of the FEL gain curve and the distortion of the gain curve at saturation. Both of these effects are inversely proportional to the effective number of wiggler periods. In addition, the fundamental is more strongly saturated due to its higher gain and lower cavity losses. When one takes all these factors into account in laser simulations one finds a difference of 1.3% in the lasing wavelength. The experimental curves are shown in figure 5. The third harmonic curve was taken at the third order in order to eliminate doubts about the calibration of the monochromator sine drive. The measured shift is 1.6%. This large of a shift or larger was measured in every run in which the laser was run at the harmonic.
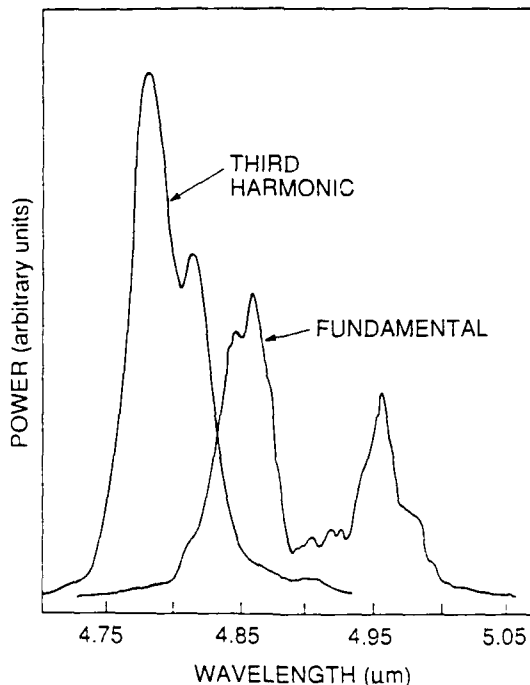
Figure 5. Optical spectra for the fundamental and third harmonic in third order. Both spectra were taken at the peak in the cavity length detuning curves. The signal was gated to look at the same part of the electron beam pulse. Secondary peaks in each curve are sidebands.

This discrepancy may be due to 3D guiding effects which can pull the frequency to longer wavelengths for a small electron beam[8]. The phenomenon arises due to the differing phase shifts for the higher order cavity modes as they traverse the length of the interaction region. In order to form the smaller optical mode caused by optical guiding effects, it is necessary to include some of the higher order cold cavity modes. The gain curves for the first three Gauss-Laguerre modes in the original Stanford 3 μm laser are shown in figure 6. Large ν corresponds to longer wavelengths. It is clear from this figure that the mean wavelength will be pulled to longer wavelengths with the inclusion of higher order modes.
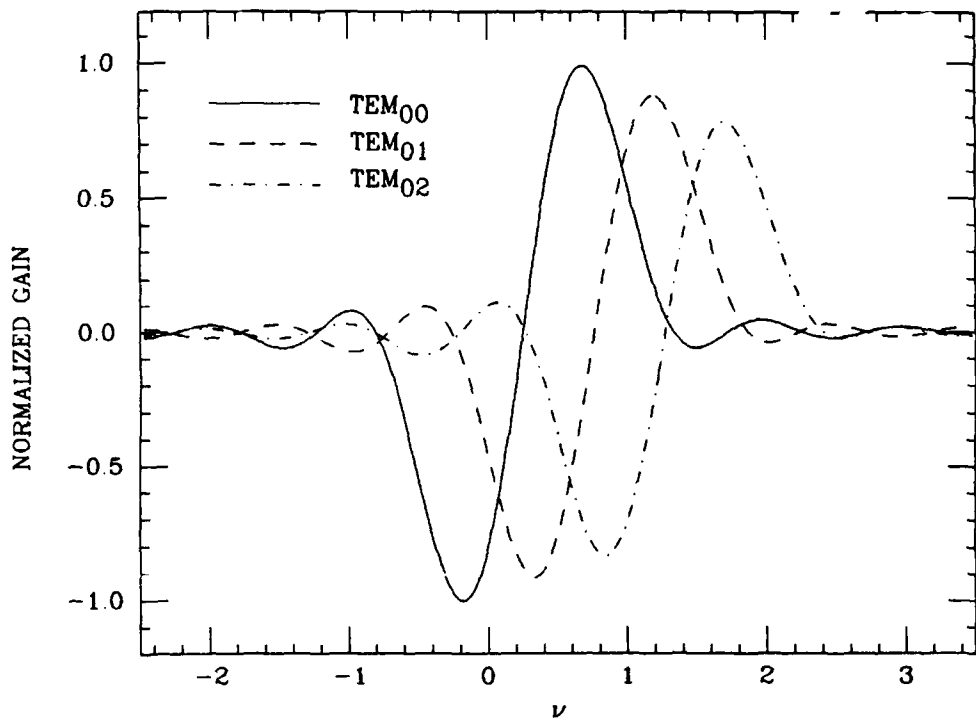
Figure 6. Laser gain normalized to the TEM_{00} mode for the first three Gauss-Laguerre modes of a FEL with cylindrical symmetry. The parameter ν is the frequency or energy detuning. Larger values of ν correspond to longer wavelengths.

We note that there are several phenomena which might reduce the difference in the fundamental and third harmonic wavelengths. We can only account for two phenomena which might increase the difference. The first is the saturation effect noted above. This is limited by the appearance of the sideband. The mean frequency of the pulse does move off to longer wavelengths as one saturates harder, but the first peak is stationary. The change in the mean is produced by the production of more and stronger sidebands. The second phenomenon is the guiding effect. This effect would only be strong for the fundamental due to the relatively large size of the optical mode. This effect is not limited like the saturation effect. It could easily account for the extra frequency shift seen in these experiments.

In conclusion we note that several free-electron laser designs rely on the option of harmonic lasing to extend the wavelength range of the laser to wavelengths not possible with the energy delivered by the accelerator system. It may also be possible to extend the range of a laser by enlarging the optical bore size to allow longer wavelength operation without giving up short wavelength operation. Finally, one can reach wavelengths not available through extra-cavity harmonic generation. This now seems feasible given adequate beam quality. We should also note that harmonic lasing has already been used to generate light in the range of 1.4 to 1.8 μm for studies in materials sciences[9].

[1] J. M. J. Madey and R. C. Taber, in Physics of Quantum Electronics Vol. 7 (Addison-Wesley, Reading, MA, 1980) p. 741

[2] J. M. J. Madey, Il Nouvo Cimento 50B 64 (1979)

[3] R. Barbini et. al. J. de Physique 44, C1-1 (1983)

[4] J. Edighoffer, presented at the Ninth international FEL conference, Sept. 1987, Williamsburg, VA

[5] S. V. Benson et. al., J. de Phys. 44, C1-1 (1983)

[6] Recently, a group at Los Alamos has reported lasing to saturation at the third harmonic using apertures to prevent the fundamental lasing.

[7] F. A. Hopf, P. Meystre, M. O. Scully and J. F. Seely, Phys. Rev. Lett. 35, 511 (1975)

[8] S. V. Benson and J. M. J. Madey, Optics Commun. 56, 212 (1985)

[9] W.S. Fann et. al. submitted to Phys. Rev. Lett.

FIRST DEMONSTRATION OF A FREE-ELECTRON LASER DRIVEN BY ELECTRONS FROM A LASER IRRADIATED PHOTOCATHODE

Mark Curtin, Glenn Bennett and Robert Burke
Rockwell International/Rocketdyne Division
6633 Canoga Avenue, Canoga Park, CA 91303, USA
and
Stephen Benson and J. M. J. Madey
Stanford Photon Research Laboratory
Stanford University, Stanford, CA 94305, USA

Abstract

We report the results from the first operation of a free-electron laser (FEL) driven by an electron beam from a laser irradiated photocathode. The Rocketdyne/Stanford FEL achieved sustained oscillations, lasting in excess of three hours, driven by photoelectrons accelerated by the Stanford Mark III radio-frequency linac. A LaB_6 cathode, irradiated by a tripled Nd:Yag mode-locked drive laser was the source of photoelectrons. The drive laser operating at 95.2 MHz, was phase-locked to the 30th subharmonic of the S-band linac. Peak currents in excess of 125 A were observed and delivered to the Rocketdyne two meter undulator which was operated as a stand-alone oscillator. The electron beam had an energy spread of 0.8% (FWHM) at 38.5 MeV and an emittance, at the undulator, comparable to that observed for thermionic operation of the electron source. Small signal gain in excess of 150% was observed. The turn-on time of the FEL macropulse relative to the start of the electron macropulse suggested 100% small signal gain could be sustained over two hour time periods. Preliminary estimates of the electron beam brightness deliverable to the undulator range from 3.5 x 10^{11} (A/m^2) to 5.0 x 10^{11} (A/m^2).

Introduction

Rf-linac driven free-electron lasers require electron beams possessing high peak brightness and low energy spread. The advancement of FEL technology toward operating regimes characterized by shorter wavelength and higher power hinges on finding suitable electron beam sources that can produce high-brightness, high current beams. Conventional electron sources consist of a thermionic cathode positioned within a dc or rf electron gun followed by either a subharmonic or magnetic bunching element , used primarily to increase peak current, and matching optics to preserve beam brightness into the accelerator. Recently, laser illuminated photoemitters have emerged as an alternative to conventional thermionic sources.[1,2] Photocathodes have three significant advantages over thermionic cathodes

1) photocathodes produce intrinsically brighter electron beams[3]
2) photocathode gun systems offer controlled time gating of the charge emitted from the cathode
3) photocathode gun systems provide a means of controlling the charge density profile at the cathode so as to maximize beam brightness at the undulator

For rf-linac driven FELs, a train of low emittance, high peak current pulses are converted to high fluence optical pulses possessing similar temporal characteristics via the interaction of the electron beam pulses and undulator magnetic field. Typical pulse formats associated with rf-linacs are micropulse lengths between 1-100 psec separated by .35 - 250 nsec over macropulse lengths of 5-100 msec. Pulse formats characteristic of rf linacs are easily replicated by lasers used to drive photocathodes and thus, allow a range of experiments which can shape initial electron beam phase space to exploit any correlations which may prove beneficial to FEL performance.

The Rocketdyne Photoinjector Program

In 1987 the Rocketdyne division of Rockwell International committed internal research and development funds to study the feasibility of converting the thermionically operated LaB_6 cathode in the Mark III electron gun into a photocathode gun system. Measurements were made to determine the quantum efficiency of LaB_6 in a testbed established at Rocketdyne.[4] These measurements resulted in a measured quantum efficiency of approximately 10^{-4}. The favorable quantum efficiency data resulted in the allocation of internal research and development funds to purchase a tripled Nd:Yag mode-locked laser to be installed at the Stanford Photon Research Laboratory (SPRL) so that photocathode experiments could commence on the Rocketdyne/Stanford FEL system.

Delivery cf the laser occurred in August 1988 with final installation being completed in late October. Initial experiments began in early November with a successful measurement of 125 A peak current for the fully accelerated electron beam. Lasing in the Rocketdyne 2 meter oscillator using electrons from a laser irradiated photocathode was demonstrated in mid November, representing a significant milestone in FEL technology development. Final experiments to quantitatively measure electron beam brightness and energy spread characteristics were conducted at the end of November. Continuation of the photocathode experiments will resume in mid summer 1989 once the Mark III has been commissioned at Duke University.

System Description

The FEL facility at the Stanford Photon Research Laboratory consists of a microwave gun[5] feeding the Mark III rf-linac[6] which is capable of accelerating electrons to approximately 40 MeV. Electrons are emitted by a 3 mm diameter LaB_6 cathode which is typically operated at 1800 K as a thermionic electron source. In the experiment reported here we irradiated the LaB_6 with 40 µJ, 100 psec laser pulses at 355 nm. The drive laser was a tripled Nd:Yag operating at 95.2 MHz which was phase-locked to the 30th subharmonic of the Mark III linac.[4] The drive laser system sat directly above the microwave gun on the shielding blocks which formed the roof of the accelerator vault. This minimized the length of the optical transport system needed to deliver the light pulses to the cathode and allowed access to the drive laser during operation of the accelerator. A layout of the drive laser system is shown in Figure 1. The laser light was delivered to the cathode via an optical transport system which consisted of a matching telescope, delay line and a remotely controllable steering mirror which directed the laser pulses through a sapphire vacuum window and onto a stationary final pointing mirror (see Figure 2). The final pointing mirror, located inside the vacuum enclosure of the microwave gun assembly, directed the laser pulses onto the LaB_6 cathode at an incidence angle of 50 degrees. Electrons emitted from the LaB_6 are accelerated by the rf gun cavity to approximately 1 MeV and then transported through the alpha magnet and into the Mk III linac (see Figure 3). The action of the alpha magnet is twofold first, it acts as a momentum filter eliminating the wings of the energy distribution and secondly, it acts to compress the electron pulse from 100 psec at the cathode to approximately 2 psec at the entrance to the linac. Located approximately 8 meters downstream of the accelerator is the Mark III hybrid undulator[7] and approximately 5 meters further downstream is the Rocketdyne permanent magnet undulator.[8] The undulators are positioned so that they lie along the common axis of the accelerator which simplifies electron beam transport and offers extended possibilities for experiments using multiple FEL systems (see Figure 4). This unique placement of two separate undulators driven by the same rf-linac provides an extremely flexible FEL testbed. Each undulator has its own resonator allowing oscillator experiments to be performed on each undulator individually. In addition, an optical transport line linking the two undulators allows the system to operate in a master oscillator power amplifier (MOPA) configuration.[9,10]

Electron Beam Energy Spread and Brightness

Electron beam energy and energy spread are determined using a magnetic spectrometer located downstream of the Mark III linac. An energy spread of 0.8% FWHM was measured for a nominal electron beam energy of 38.5 MeV. Total charge contained within the macropulse is estimated from the average macropulse current supplied by the linac toroid (see Figure 5). A typical micropulse charge of 170 pCoul was observed during the energy analysis described above. For the fully accelerated electron beam, a maximum micropulse charge of 250 pCoul was observed. Utilizing the alpha magnet calibration, as established from previous MOPA experiments, we can estimate micropulse lengths of 2 psec at the two meter undulator. If this calibration remains valid for these higher values of total micropulse charge then peak currents of 125 A should be obtainable at the two meter undulator. The electron beam emittance associated with photocathode operation was studied using two different methods. The first method employs a quadrupole focusing element which is varied while the resulting spot size on a downstream screen is measured. Spot size data at the downstream screen location as a function of quadrupole focusing strength allows both the horizontal and vertical emittance at the entrance to the quadrupole to be determined. This technique for determining electron beam emittance has proven unreliable in previous experiments due to screen saturation effects thus, the results can only be assessed in a qualitative manner. One apparent observation was that the electron beam from the photocathode did not appear to have a halo characteristic of thermionic operation. The second method employed for emittance determination was to use the spontaneous light emitted from the Rocketdyne 2 meter undulator while in an amplifier configuration. Measurement of the size of the light source at differing locations within the undulator may be linked to the electron beam size within the

undulator. This then provides an estimate of the electron beam emittance deliverable to the undulator. Preliminary analysis suggest normalized horizontal and vertical emittances of

$$(\gamma\beta\epsilon_x)_{photocathode} = 0.8 \quad (\gamma\beta\epsilon_x)_{thermionic} = 8\pi \text{ mm-mrad}$$
$$(\gamma\beta\epsilon_y)_{photocathode} = 1.0 \quad (\gamma\beta\epsilon_y)_{thermionic} = 4\pi \text{ mm-mrad}$$

These measurements were taken for linac toroid readings corresponding to 170 pCoul per micropulse. Analysis of the emittance data is continuing and will be published at a later date.[11]

FEL Performance

The ability to operate the LaB_6 as both a thermionic and photoelectric emitter provided us with a simple and reliable procedure for achieving laser oscillation with electrons generated from the laser irradiated LaB_6. The initial step was to achieve an optimized match through the two meter undulator by maximizing FEL performance during thermionic operation. Beam positions on the screens along the transport line were recorded allowing us to re-establish this trajectory with electrons from the laser irradiated photocathode. The transition between thermionic and photocathode operation was achieved by reducing the cathode temperature and irradiating the LaB_6 with 355 nm light from the Nd:Yag drive laser. Adjustment of the gun matching optics provided sufficient degrees of freedom to preserve the recorded beam positions on the screens along the transport line. Once the electron beam trajectory was re-established through the undulator, the system lased. FEL performance was further improved by fine adjustments of the quadrupole triplet upstream of the two meter undulator. Oscillations were sustained over a three hour time period. We observed deterioration of the laser signal toward the end of the experiment which was later attributed to mirror damage in the Nd:Yag laser transport system. Lasing, during a majority of the experiment, was accomplished using 170 pCoul micropulses. Macropulse energies as high as 0.5 mJ were measured with a pyroelectric detector in the optics shack. During the experiment, typical and sustainable macropulse energy measurements yielded approximately 0.35 mJ (see Figure 6). Electron beam macropulses of 4 msec resulted in 3 msec optical macropulse lengths. The measured turn-on time of the laser suggested sustainable small signal gain of 100% per pass. Amplitude fluctuations within the FEL macropulse were observed to be correlated with small fluctuations within the drive laser intensity profile. The effect produced a macropulse saturation intensity that took on the appearance of the neighboring Sierra mountains and thus is currently referred to as the "Sierra Mountain Effect" (see Figure 7). The micropulses were easily resolvable because of the 10.5 nsec spacing produced by the drive laser pulse train as illustrated in Figure 8. Turn on of the FEL oscillator was extremely fast as evidenced in Figure 9. Table 1 provides a summary of the parameters established by this set of experiments.

Parameter	Thermionic Operation	Photocathode Operation	
	Typical	Typical	Maximum
Small signal gain (per pass)	60%	100%	150%
Micropulse charge (pCoul)	70	170	250
Micropulse current (A)	35	60	85
Normalized emittance (mm-mrad)			
$\gamma\beta\epsilon_x$	10π	8π	
$\gamma\beta\epsilon_x$	4π	4π	
Peak brightness (A/m^2)	1.8×10^{11}	3.8×10^{11}	5.4×10^{11}

Table 1. Comparison of Electron Beam Parameters Observed During Thermionic Operation and Photocathode Operation

Conclusions

The Rocketdyne/Stanford photocathode experiment represents the first achievement of FEL oscillations using electrons from a laser irradiated photocathode. The experiment was performed using the Mark III rf-linac and the Rocketdyne 2 meter undulator. We observed peak currents in excess of 125 A with energy spread corresponding to 0.8% FWHM and an improved emittance relative to thermionic operation. Small signal gains in excess of 150% per pass were observed. We demonstrated sustained oscillations over a

three hour time period with 100% per pass small signal gain at 3.1 μm. The quantum efficiency of LaB_6 was measured to be 10^{-4} for electron current densities of 100 amp/cm^2. We have not witnessed any deterioration of the LaB_6 cathode after approximately 100 hours of photocathode operation. We estimate electron beam brightness at the undulator to be approximately 4×10^{11} (A/m^2) and do not foresee any intrinsic system limitations which would prevent us from obtaining peak brightness approaching 1×10^{12} A/m^2.

Acknowledgements

References

1. R. L. Sheffield, E. R. Gray and J. S. Fraser, Nuclear Instruments and Methods A272 (1988) 222
2. C. H. Lee, P. E. Oettinger, E. R. Pugh, R. Klinkowstein, J. H. Jacob, J. S. Fraser and R. L. Sheffield, IEEE Trans. Nucl. Sci NS-32 (5) (1985) 3045
3. P. Oettinger, I. Bursuc, R. Shefer and E. Pugh, Proc. 1987 Particle Accelerator Conf., Washington, DC, IEEE catalog no. 87CH23A7-9, Vol. 1 (1987) 286
4. G. Bennett et. al., these proceedings
5. S. V. Benson, J. Schultz, B. Hooper, R. Crane and J. M. J. Madey, Nucl. Instr. and Methods A272 (1988) 22
6. S. Benson, J. M. J. Madey, J. Schultz, M. Marc, W. Wadensweiler, G. Westenskow and M. Velghe, Nucl. Instr. and Methods A250 (1986) 39
7. G. Stolovy, W. Wadensweiler, J. M. J. Madey, S. Benson and M. Velghe, Proc. SPIE, Vol. 582 (1985) 163
8. M. S. Curtin, A. Bhowmik, W. McMullin, S. Benson, J. Madey, B. Richman and L. Vintro, Nucl. Instr. and Methods A272 (1988) 187
9. L. Vintro, Thesis at Stanford University
10. A. Bhowmik, M. S. Curtin, W. A. McMullin, S. Benson, J. M. J. Madey, B. Richman and L. Vintro, these proceedings
11. S. Benson, M. S. Curtin, J. M. J. Madey, B. Richman and E. Szarmes, To be published.
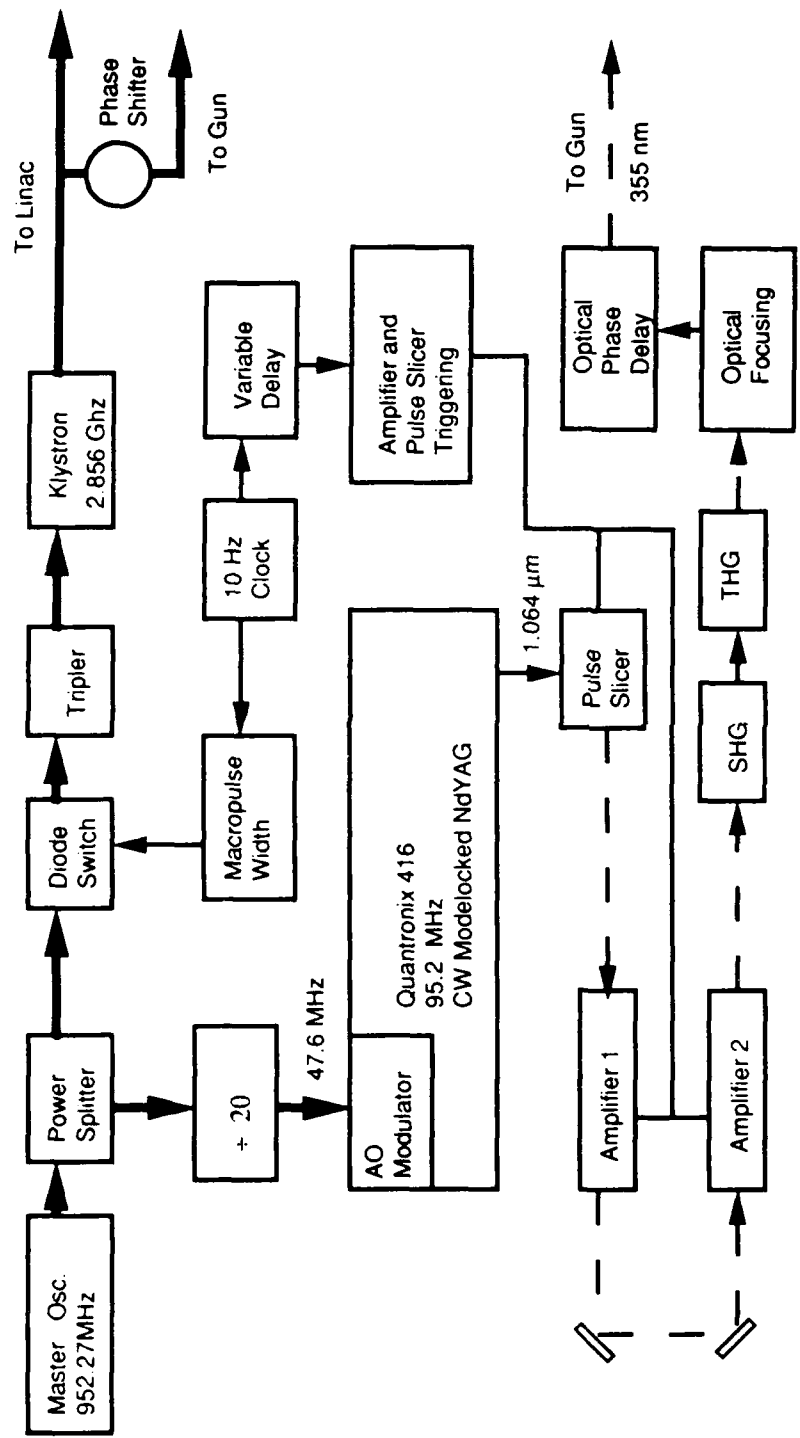
Figure #1   Schematic layout of the Nd:Yag drive laser system
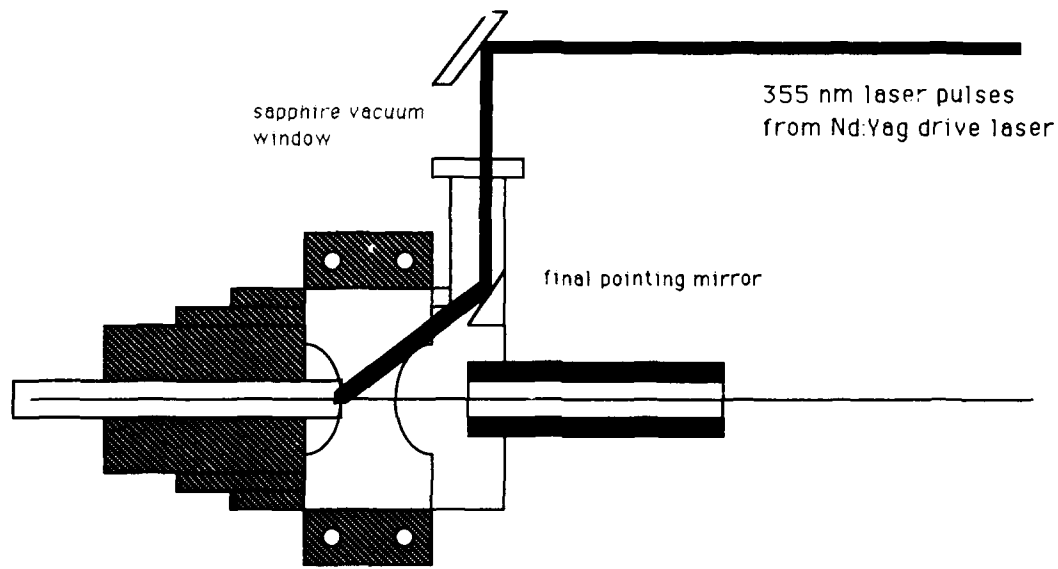
Figure #2   Illustration of the final pointing mirror and the microwave gun
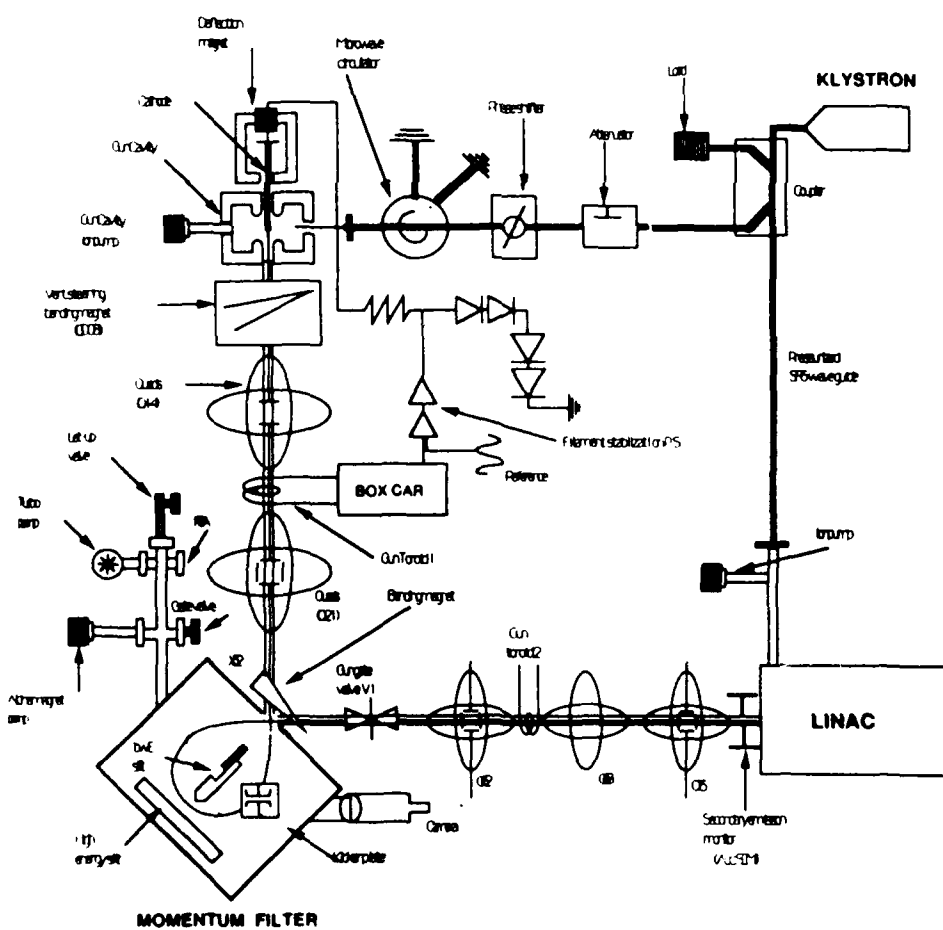
Figure #3   Schematic layout of the Mark III microwave gun and linac
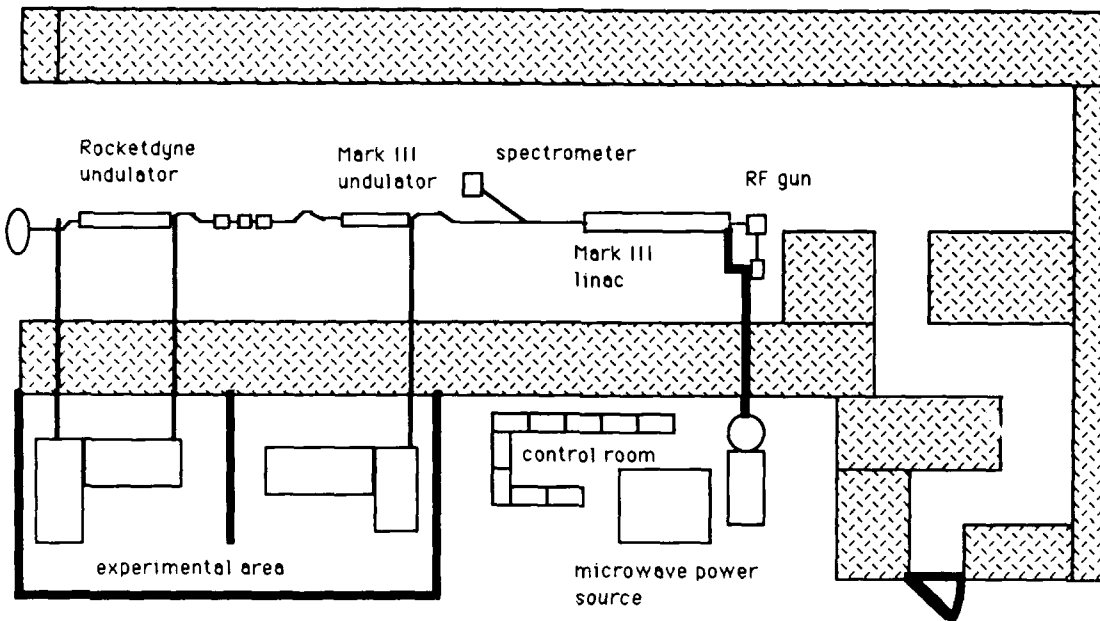
Figure #4   Layout of the SPRL FEL facility.
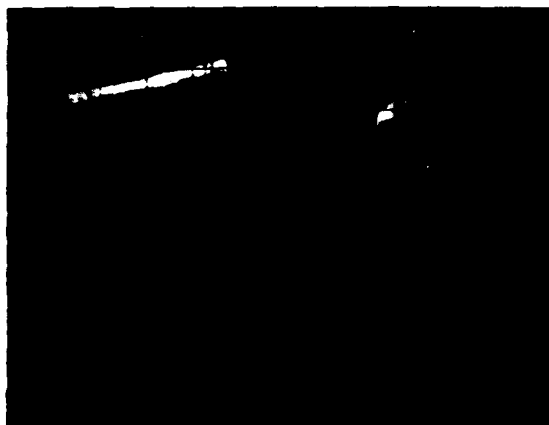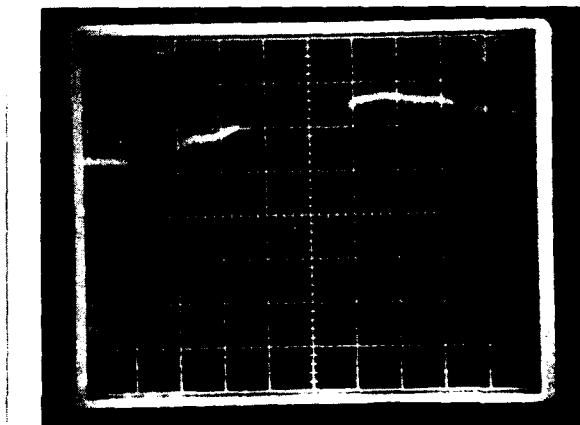
(A)   (B)

Figure #5   The gun toroid signal (A) suggested   micropulse charge of 250
pCoul. off the cathode. The linac toroid signal (B) indicated that only 125
pCoul. was transmitted through the alpha magnet.
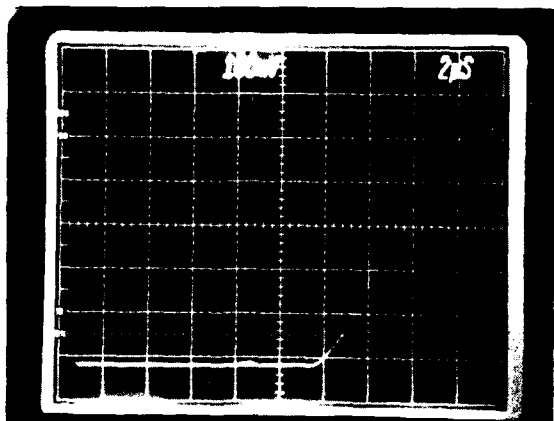
Figure #6   Typical optical macropulse energies of 0.35 mJ were measured in the optics shack during the photocathode experiment.
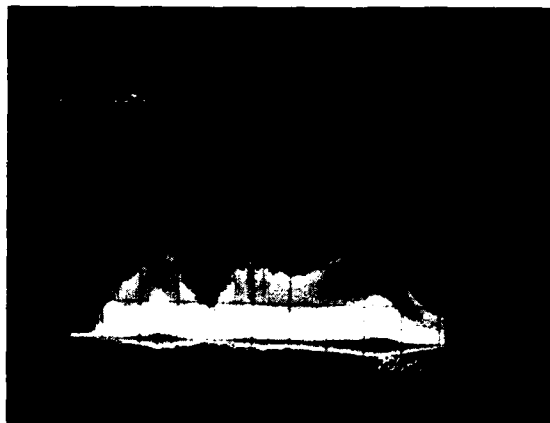
Figure #7   Small fluctuations within the Nd:Yag drive laser produced large amplitude fluctuations in the FEL macropulse.
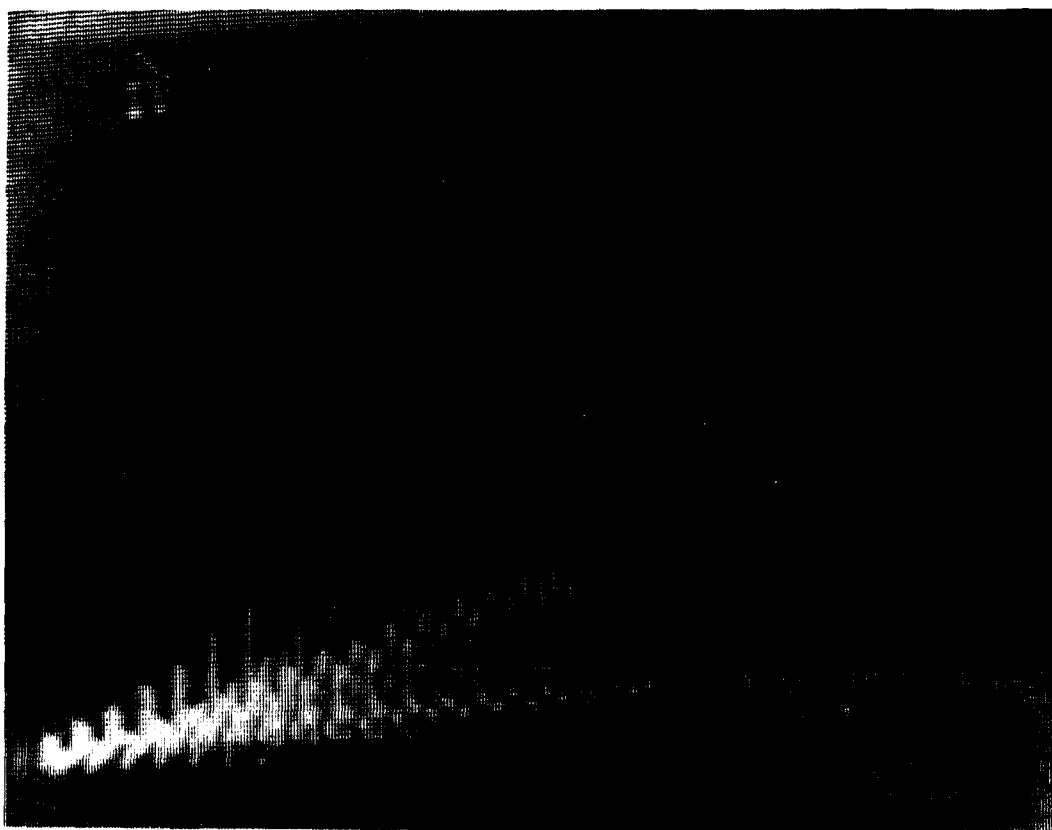
Figure #8   The FEL micropulse structure associated with the 95.2 MHz operating frequency of the drive laser was clearly evident .
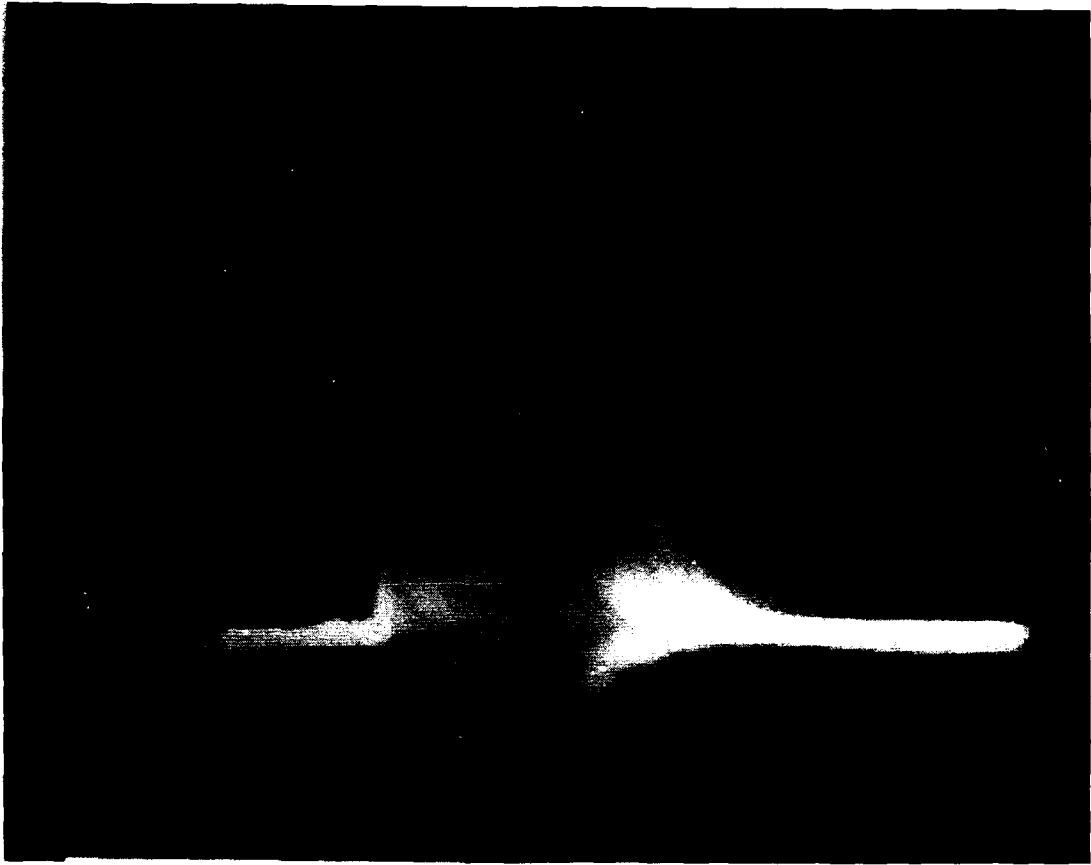
Figure #9   A typical FEL macropulse captured from video tape during the 3 hour photocathode experiment.

STATUS OF SHORT-WAVELENGTH CHEMICAL LASER RESEARCH

R. F. Heidner III

Aerophysics Laboratory, The Aerospace Corporation, P. O. Box 92957, Los Angeles, CA 90009

Abstract

A brief review of the factors determining the success of short-wavelength chemically pumped electronic transition lasers is presented. Those principles are applied to the chemical oxygen iodine laser (COIL) and to a leading candidate laser system, NF^* pumped BiF, which would operate at significantly shorter wavelength ($\lambda \simeq 450$ nm). Recent additions to the kinetic and spectroscopic database for NF^* - BiF are discussed.

Introduction

Work on chemically-pumped electronic transition lasers intensified after the discovery of chemically-pumped vibrational lasers in the infrared.[1] Although photodissociation electronic transition lasers have been demonstrated, the chemically-pumped oxygen-iodine laser (COIL)[2] is the only current example of a chemically-pumped electronic transition laser; no clear cut demonstration of chemically-pumped lasing in the visible has been forthcoming. This is despite a good deal of work on a number of apparently promising systems.[3,4]

The object of the present status report is not to provide a comprehensive review of the work in this area. It will evaluate the underlying chemical physics constraints that control the viability of such a short-wavelength chemical laser (SWCL) system, test those constraints against the prototype COIL system and, finally, examine current data on both the efficient production and storage of $NF(a^1\Delta)$ (isoelectronic to $O_2(^1\Delta)$ in the COIL system) and the conversion of that energy into electronically-excited $Bi(^2D_{3/2})$ and $BiF(A0^+)$. The latter molecule will be discussed as a candidate for laser action at $\lambda \simeq 450$ nm.

Background

Following a simplified formalism used by Cool,[4] two complementary requirements for producing a population inversion by chemical reaction can be developed for the generic process

$$A + BC \rightarrow AB^* + C \qquad (1a)$$

$$\rightarrow AB + C \qquad (1b)$$

Both of these requirements will be developed for the most favorable case of a premixed chemical system exhibiting no population build-up in the lower laser level, a Doppler broadened transition, and no electronic quenching of the upper laser level. Any "real" laser system will be more difficult to demonstrate. The gain coefficient can be written

$$\gamma(\nu) = (1/I)dI/dx = (\lambda^2/8\pi)\Delta Ng(\lambda-\lambda_0)/\tau_s \qquad (2)$$

where $\Delta N = N_u - N_1(g_u/g_1)$, g_u and g_1 are the upper and lower state degeneracies, $g(\lambda - \lambda_0)$ is the lineshape function, and τ_s is the spontaneous emission lifetime. If the loss from the cavity results solely from the outcoupling of laser radiation, the photon loss can be written

$$dI/dt = c^{-1} dI/dx = -1/\tau_p \qquad (3)$$

where τ_p is the cavity photon lifetime, $\tau_p = L/c\alpha$, and α is the fractional outcoupling per pass. Assuming a Doppler broadened linewidth and setting gain equal to loss, the first device requirement, the <u>critical inversion density</u>, can be written

$$\Delta N_c = (4\pi^2/\lambda^3)[8kT/\pi m]^{1/2}/c](\tau_s/\tau_p) = (4\pi^2/\lambda^3)(8kT/\pi m)^{1/2}(\alpha/L)\tau_s \qquad (4)$$

From Eq. (4), it can be seen that the critical inversion density for lasing increases as λ^{-3}. This is one of the key factors that has slowed development of SWCL devices. A more complete and accurate derivation of the gain equation for diatomic molecules is given by Sutton and Suchard,[5] however, the basic arguments presented here are valid.

The second requirement related to chemical lasers is the <u>critical pumping rate</u> which has to exceed, at a minimum, the loss rate represented by $\Delta N_c/\tau_s$ (i.e., loss of the upper laser level by spontaneous emission). In Fig. 1, the evolution of a chemical inversion density is traced. In order to invert a given vibronic transition in a diatomic product molecule (AB^* in Fig. 1),

$$d[AB^*(v',J')]/dt = k_t[A][BC] \times f(E',v',J') \geq \Delta N_c/\tau_s \tag{5}$$

where k_t is the overall reaction rate coefficient and $f(E',v',J') = f(E') \times f(v') \times f(J')$ is the fraction of molecules residing in a given vibration-rotation state of AB^*. Assuming that the rotational levels are thermalized to the bath gas temperature, $f(J'_{max}) = (2Bhc/kT)^{1/2} \exp(-0.5) = 0.01-0.05$. The fractional population in the optical vibrational level, $f(v')$, is expected to be large, i.e., 10-90%. No chemical laser system that exhibits less than 10% branching ratio to AB^* $(f(E'))$ is expected to be interesting because the system will be energetically inefficient. Note that while the critical inversion density is a function of τ_s, the critical pumping rate in a premixed system is not. If the lasing species is atomic rather than diatomic, the dilution of population among vibrational and rotational levels is eliminated (critical pumping rate reduced by approximately 10^2 - 10^3).
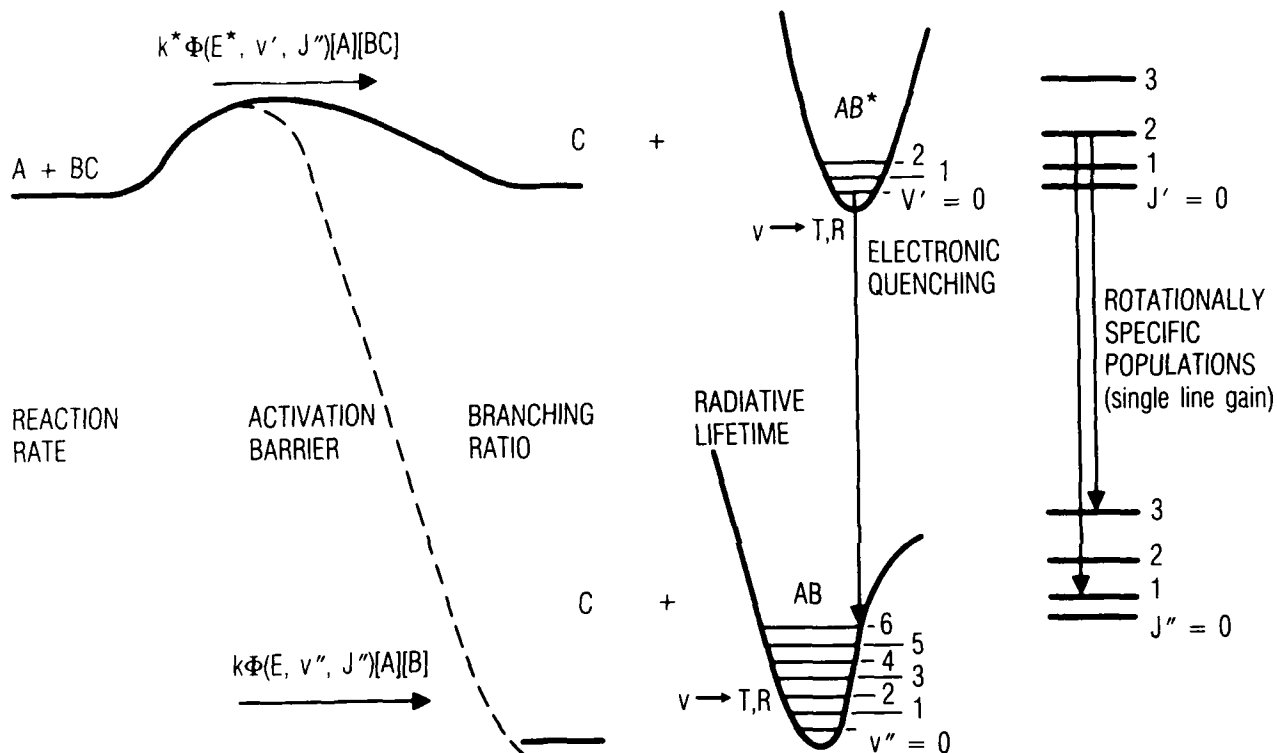
Fig. 1. Schematic Requirements for a Chemically-Pumped Electronic Transition Laser.

A useful comparison can be made between two SWCL systems. The COIL system is based on electronic energy transfer between $O_2(^1\Delta)$ and ground state I atoms:

$$O_2(^1\Delta) + I(^2P_{3/2}) \neq O_2(^3\Sigma) + I(^2P_{1/2}) \tag{6}$$

$$I(^2P_{1/2}) \rightarrow I(^2P_{3/2}) + h\nu \ (\lambda = 1.315 \ \mu m) \tag{7}$$
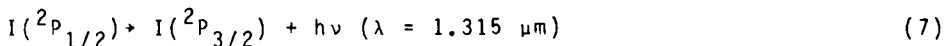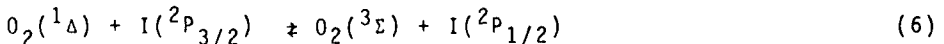
The second system is a candidate SWCL device based on energy storage in $NF(^1\Delta)$, mixing with Bi, and lasing on either Bi or BiF.[6-9] Although the mechanism is not fully verified, we will discuss the most likely pathway:

$$NF(^1\Delta) + Bi(^4S) \neq NF(^3\Sigma) + Bi(^3D_{3/2}) \tag{8}$$

$$NF(^1\Delta) + Bi(^2D_{3/2}) \rightarrow BiF(A0^+) + N(^4S) \tag{9}$$

$$Bi(^2D_{3/2}) \rightarrow Bi(^4S) + h\nu \ (876 \ nm) \tag{10}$$

$$BiF(A0^+) \rightarrow BiF(X0^+) + h\nu \ (450 \ nm) \tag{11}$$
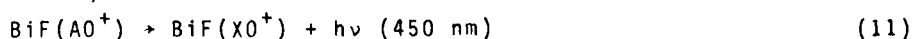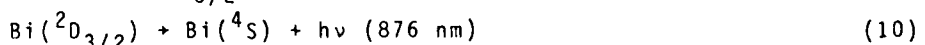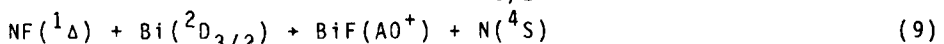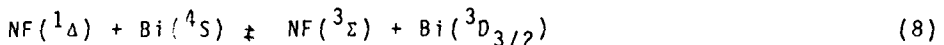
The COIL system has a number of advantages that have led to its demonstration as the first cw electronic transition laser (Fig. 2).

POOLING   TRANSFER

1. $O_2(^1\Delta)$ can be made in large densities ($>10^{16}/cm^3$) by a highly efficient chemical reaction (E > 90%).

2. $O_2(^1\Delta)$ is not easily quenched.

3. $O_2(^1\Delta)$ transfers energy rapidly ($k_6 = 7.8 \times 10^{-11}$ cm^3/sec) and efficiently (E ~ 100%) to I.

4. $O_2(^1\Delta)$ does not pool energy rapidly or react chemically with itself or with I^*.

5. The I atom can be inverted when $O_2(^1\Delta)$, $O_2(^3\Sigma)$, I^* and I are in an electronic equilibrium.

6. An atom is being lased. Thus, there is no vibrational or rotational dilution of the upper level.

Fig. 2. Kinetic Processes in the Chemically-Pumped Oxygen-Iodine Laser (COIL).

The NF^*-Bi and NF^*-BiF systems have a number of attributes that contribute to the difficulty of a laser demonstration (Fig. 3), although there are many positive features:

POOLING   TRANSFER   CHEMISTRY
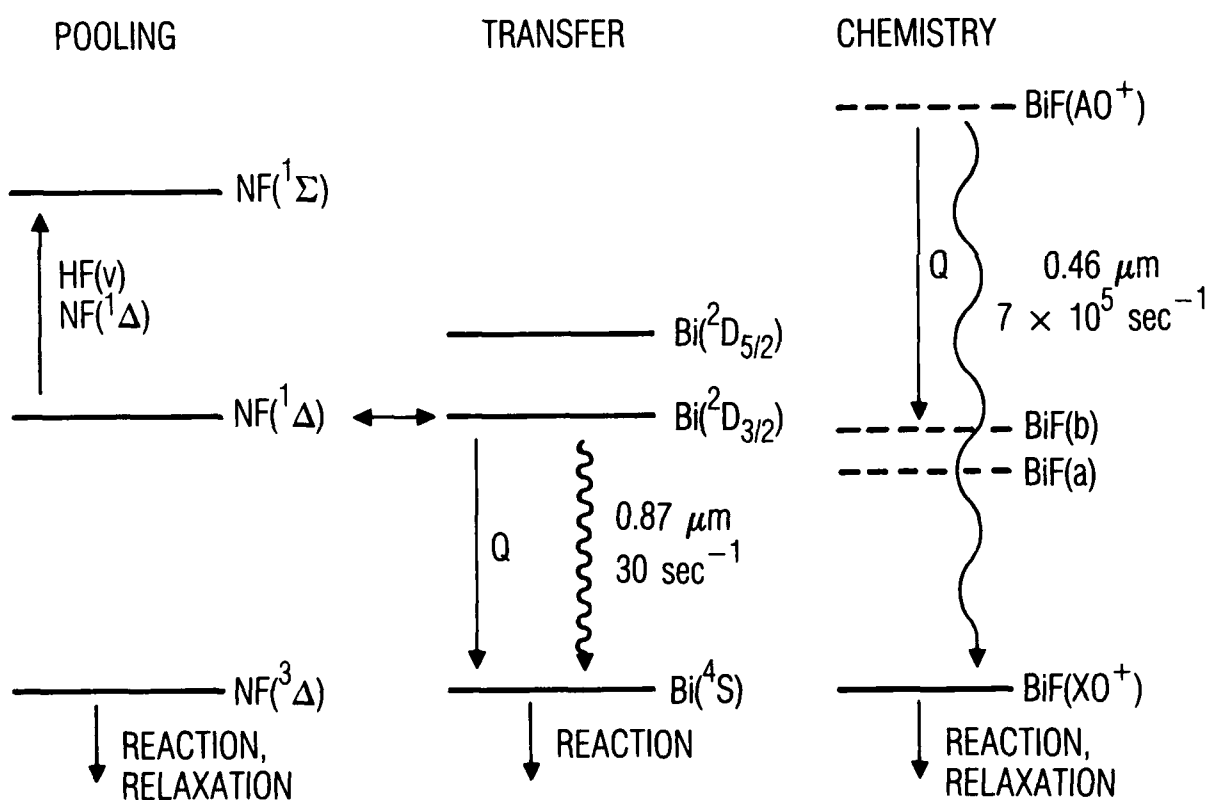
Fig. 3. Kinetic Processes in the NF^*-Pumped Bi^*, BiF^* Laser Candidate System.

1. $NF(^1\Delta)$ can be created with large densities (~ $10^{16}/cm^3$) and with high efficiency (E ≈ 90%).

2. $NF(^1\Delta)$ is not easily quenched.

3. Although $NF(^1\Delta)$ transfers energy rapidly to $Bi(^4S)$ ($2 \times 10^{-10}cm^3/sec$), the rate and efficiency of Process (9) are less certain.

4. NF($^1\Delta$) has the potential to react with both Bi and BiF$_x$ species, thus vastly compli-
cating the system chemistry.

5. Ground state BiF($X0^+$) removal is a serious constraint on a laser demonstration.

6. A diatomic molecule is being lased. Significant vibrational and rotational dilution
will take place.

These factors are presented in Table I within the context of Eqs. (4) and (5). It can
be seen that the chemical pumping rate of the atomic systems would be trivial to obtain if
spontaneous emission rather than electronic quenching dominated the upper state loss.
Since this is not the case, the principal problems are associated with minimizing upper
state quenching in order to achieve the required ΔN_c. For the BiF($A0^+$) case, the short
radiative lifetime mitigates against quenching, but now puts serious strain on the
required chemical pumping rate.

Table I. Critical Inversion Densities and Chemical Pumping Rates for I*, Bi* and BiF*

Lasing Species	$\lambda(\mu m)$	$(4\pi^2/\lambda^3)^\dagger$	M	$(8kT/\pi m)^{1/2}$	τ_s	d/L	ΔN_c	$\Delta N_c/\tau_s$
I($^2P_{1/2}$)	1.315	1.7×10^{13}	127	2.2×10^4	0.13	10^{-3}	4.8×10^{13}	3.7×10^{14}
							$(8.2 \times 10^{13})^{\dagger\dagger}$	(6.3×10^{14})
Bi($^2D_{3/2}$)	0.876	5.9×10^{13}	209	1.7×10^4	0.031	10^{-3}	3.1×10^{13}	1.0×10^{15}
							(1.2×10^{14})	(4.0×10^{15})
BiF($A0^+$)	0.447	4.4×10^{14}	228	1.7×10^4	1.44×10^{-6}	10^{-3}	1.1×10^{10}	7.6×10^{15}
							$(\sim2 \times 10^{12})$	(1.5×10^{18})

†All unlabeled units are cgs.

††Values for the entire upper electron state are in parentheses.

Recent Progress on NF*-Pumped BiF

The production of NF($a^1\Delta$) from the reaction

$$H + NF_2 \rightarrow NF(a^1\Delta) + HF \tag{12a}$$

$$\rightarrow NF(X^3\Sigma) + HF \tag{12b}$$

has been studied for nearly two decades.[10-12] Recent work in this Laboratory[13] has con-
firmed that the branching ratio (k_{12a}/k_{12}) is $\geq$ 90%. Earlier work reached the same con-
clusion; however, in those studies, the NF(X) ground state was not measured. Other re-
actions have also provided large yields of NF($^1\Delta$) such as

$$F(^2P) + N_3(^2\pi) \rightarrow NF(a^1\Delta) + N_2(X^1\Sigma_g) \tag{13}$$
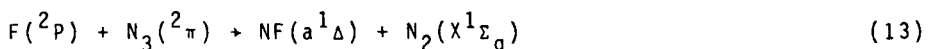
All of these reactions constitute part of a larger class, which conserve the basic struc-
ture of N(^2D) as it passes from one chemical environment to another. Additional examples
are provided by O + CN and H + NF($^1\Delta$) [N(^2D) product] and by N + N$_3$ and N(^2D) + NF($^1\Delta$)
[N$_2$(B$^3\pi$) product].
If Reaction (12) is coupled to the well known laser reaction

$$F + H_2 \rightarrow HF + H \tag{14}$$

one can see that an NF$_2$/H$_2$ mixture can be run on a chain reaction if NF(a,X) can be made
to regenerate F atoms to propagate the chain. If NF($a^1\Delta$) is deactivated to NF($X^3\Sigma$) [for
example, by Process (8)], NF(X) can regenerate F atoms by

$$NF(X) + NF(X) \rightarrow N_2 + 2F \tag{15}$$

or

$$NF(X) + NF_2 \rightarrow N_2F_2 + F \tag{16}$$
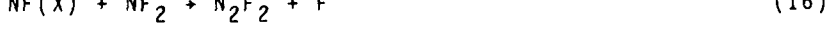
Recent work[13] has measured the rate of Process (16), but has obtained no evidence of the disporportionation Reaction (15). Finally, the chain terminates by the three-body recombination process

$$F + NF_2 + M \rightarrow NF_3 + M \qquad (17)$$

This analysis has been previously reported.[14]

When Bi atoms are introduced into a stream of $NF(a^1\Delta)$, the near resonant energy transfer Process (8) rapidly converts a major fraction of the Bi from the ^4S to the $^2D_{3/2}$ state.[6] At higher densities of $NF(a^1\Delta)$, spectra such as the one shown in Fig. 4 appear with considerable intensity.[7-9] As shown in Fig. 3, neither $NF(a^1\Delta)$ nor $NF(b^1\Sigma)$ has sufficient energy to directly populate $BiF(A0^+)$. Either the mechanism suggested by Processes (8) and (9), or a sequential pumping mechanism.

$$NF(a^1\Delta) + BiF(X0^+) \rightarrow NF(X^3\Sigma) + BiF(b0^+) \qquad (18)$$

$$NF(a^1\Delta) + BiF(b0^+) \rightarrow NF(X^3\Sigma) + BiF(A0^+) \qquad (19)$$
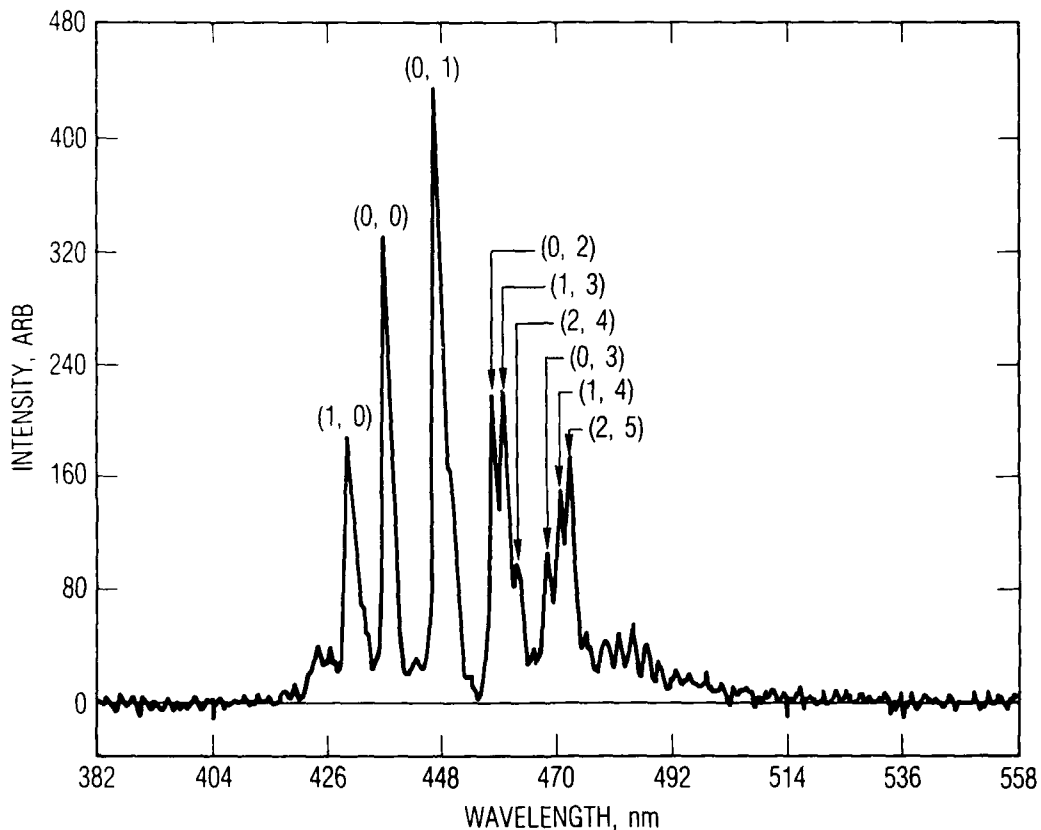
Fig. 4. Chemically-pumped $BiF(A \rightarrow X)$ Emission. KrF Laser Photoinitiation of NF_2(0.44 Torr), H_2 (0.23 Torr), $Bi(CH_3)_3$ (0.007 Torr), Ar (10.9 Torr).

appears to be the most likely candidate. Both mechanisms could contribute. In addition to work on the mechanism of the NF_2/H_2 system, several studies on Bi and BiF have been recently completed. The radiative lifetime, electronic quenching rate coefficients, and V → T transfer rate coefficients of $BiF(A0^+)$ have been measured in the presence of Ar, He, and SF_6.[15,16] These data were obtained using pulsed laser-induced fluorescence on BiF molecules formed by reacting Bi and F_2 in a Broida oven apparatus. The results are summarized in Table II. The ratio of the radiative lifetime to the electronic quenching of $BiF(A0^+)$ is favorable for efficient lasing, however, the radiative lifetime (τ_s = 1.4 µs) is quite short if the reagents must be mixed. Under most experimental conditions, a Boltzmann distribution in vibration is observed, characterized by a vibrational temperature of T_{VIB} ~ 1000 K. If the $BiF(A0^+)$ formation mechanism of Reaction (9) is dominant, the behavior of $Bi(^2D)$ is critical to the overall efficiency of the device, since Reaction (9) must compete against $Bi(^2D)$ quenching by the other medium constituents. Table III summarizes a number of recently measured rate coefficients for $Bi(^2D_{3/2})$.[17] The only significant quenching reactions involve the widely used Bi precursor, $Bi(CH_3)_3$, its CH_3 fragments, and the molecule NF_2.

209

Table II. Radiative Lifetimes, V → T Relaxation Rates, and Electronic Quenching Rates for BiF(AO$^+$).

LEVEL	τ_{RAD} (μsec)	BiF (AO$^+$, v → AO$^+$, v − 1) (cm^3/molecule·sec)			BiF (AO$^+$, v → X, b, a$_2$) (cm^3/molecule·sec)		
		Ar	He	SF$_6$	Ar	He	SF$_6$
v = 0	1.44				3.8E-13	3.5E-13	9.5E-14
v = 1	1.30	1.5E-12	6.1E-12	5.2E-12	4.3E-13	3.8E-13	1.1E-13
v = 2	1.44	5.7E-12	1.8E-11	1.1E-11	5.0E-13	4.3E-13	1.3E-13
v = 3	1.47	1.1E-11	3.5E-11	2.6E-10	8.1E-13	5.0E-13	1.5E-13

Table III. Rate Coefficients for Removal of Bi($^2D_{3/2}$) by Gas Phase Collisions.

COLLISION PARTNER	RATE COEFFICIENT (cm^3/molecule·sec); T = 295K		
	HOLLOWAY ET AL (Aerospace)	TRAINOR (AVCO)	BEVAN & HUSAIN (Cambridge)
Ar	$<2 \times 10^{-17}$	$<1 \times 10^{-16}$	—
SF$_6$	$<9 \times 10^{-17}$	$<6 \times 10^{-16}$	—
CO$_2$	$<8 \times 10^{-17}$	$<1 \times 10^{-15}$	$<4 \times 10^{-15}$
H$_2$	$(4.1 \pm 0.2) \times 10^{-15}$	$(7.2 \pm 0.3) \times 10^{-15}$	$(7.9 \pm 0.8) \times 10^{-14}$
D$_2$	$<(1.4 \pm 0.1) \times 10^{-16}$	$<(2.5 \pm 1.6) \times 10^{-16}$	$(1.1 \pm 0.3) \times 10^{-14}$
HF	$(2.3 \pm 0.2) \times 10^{-14}$	—	—
DF	$<(5.8 \pm 0.5) \times 10^{-16}$	—	—
HBr	—	—	—
N$_2$F$_4$	$>(1.1 \pm 0.4) \times 10^{-12}$	—	—
NF$_2$	$<(1.2 \pm 0.3) \times 10^{-11}$ (T = 170C)	—	—
Bi(CH$_3$)$_3$	$(7.7 \pm 1.4) \times 10^{-11}$	$(1.2 \pm 0.1) \times 10^{-10}$	—
CH$_3$	$\geq(2.6 \pm 0.6) \times 10^{-10}$	—	—
NF(a$^1\Delta$)	$\sim 2 \times 10^{-10}$	—	—

The remaining work on the system is clearly focussed on the mechanism of BiF(AO$^+$) production and on the removal of ground state BiF(XO$^+$). Scaling of BiF(AO$^+$) to the critical inversion density calculated in Table I, requires a better understanding of the chemical physics of the medium, as well as sound engineering of any demonstration.

Summary and Conclusions

This review has stressed the requirements for constructing SWCL devices. The primary issues are the λ^{-3} dependence of the chemical pumping rate and the dilution of population by vibration and rotation in diatomic lasing species. Both of these phenomena mandate larger reagent densities, which in turn increase the problems associated with unwanted side reactions and electronic quenching. The recent progess on energy storage in NF(a$^1\Delta$) and excitation of BiF(AO$^+$) has been reviewed.

References

1. Handbook of Chemical Lasers, R. W. F. Gross and J. F. Bott, eds., John Wiley and Sons, New York (1976).

2. W. E. McDermott, N. R. Pchelkin, D. J. Benard, and R. R. Bousek, Appl. Phys. Lett. 32, 469 (1978); Appl. Phys. Lett. 34, 40 (1979).

3. Electronic Transition Lasers, J. I. Steinfeld, ed., MIT Press, Cambridge, Massachusetts (1976).

4. T. A. Cool, Physical Chemistry of Fast Reactions, I. W. M. Smith, ed., Plenum Press, New York (1980), p. 241-272.

5. D. G. Sutton and S. N. Suchard, Appl. Opt. 14, 1898 (1975).

6. G. A. Capelle, D. G.Sutton, and J. I. Steinfeld, J. Chem. Phys. 69, 5140 (1978).

7. J M. Herbelin and R. A. Klingberg, Int. J. Chem. Kin. 16, 849 (1984).

8. J. M. Herbelin, "Efficient Production of Electronically Excited BiF(AO$^+$) via Collisions with NF(a). II," Proceedings, International Conference on Lasers '86, Orlando, Florida (1986).

9. J. M. Herbelin, Chem. Phys. Lett. 133, 331 (1987).

10. M. A. A. Clyne and I. F. White, Chem. Phys. Lett. 6, 465 (1970).

11. J. M. Herbelin and N. Cohen, Chem. Phys. Lett. 20, 605 (1973).

12. R. J. Malins and D. W. Setser, J. Phys. Chem. 85, 1342 (1981).

13. R. F. Heidner III, H. Helvajian, J. S. Holloway, and J. B. Koffend, "Direct Observation of NF(X) Using Laser Induced Fluorescence: Kinetics of the NF($^3\Sigma^-$) Ground State," J. Chem. Phys, (submitted for publication) (1988); "Direct Observation of NF(X) Using Laser Induced Fluorescence: The Branching Ratio for H + NF$_2$ → NF(a,X) + HF," (submitted for publication) (1988).

14. J. B. Koffend, C. E. Gardner, and R. F. Heidner III, J. Chem. Phys. 83, 2904 (1985).

15. J. B. Koffend, H. Helvajian, and J. S. Holloway, J. Chem. Phys. 84, 2137 (1986).

16. H. Helvajian, J. S. Holloway, and J. B. Koffend, J. Chem. Phys. 89, 4450 (1988).

17. J. S. Holloway, J. B. Koffend, and R. F. Heidner III, "Spin-Orbit Relaxation Rates for Bi(6p^3, $^2D_{3/2}$) following Photolysis of Bi(CH$_3$)$_3$ at λ = 193 nm," J. Phys. Chem. (submitted for publication (1989).

Hydrogen Fluoride Overtone Chemical Laser Technology

William A. Duncan, Barbara J. Rogers, and Miles E. Holloman
U.S. Army Missile Command
Redstone Arsenal, AL 35898

William Q. Jeffers
Helios, Inc.
Longmont, CO 80501

Jeffery L. Sollee
TRW Space and Technology Group
Redondo Beach, CA 90278

Gary F. Morr, Phillip Goede and William Hansen
W.J. Schafer Associates, Inc.
Woodland Hills, CA

Dennis Kitchens
Deposition Sciences
Santa Rosa, CA

Abstract

The Hydrogen Fluoride Overtone Chemical Laser Technology Program has exploited the technology base developed over the last two decades for hydrogen fluoride lasers and successfully demonstrated a short wavelength chemical laser. This technology development centers on overtone lasing of the hydrogen fluoride molecule to produce laser radiation at 1.33 micrometers rather than the conventional fundamental lasing at 2.8 micrometers. The overtone wavelength can lead to significant improvements in brightness potential as well as atmospheric propagation properties. The concept has matured from initial demonstrations at the ten watt scale to the currently demonstrated multi-kilowatt level. In the course of these test programs it was necessary to develop new highly reflective coatings that permitted short wavelength lasing while completely suppressing lasing on the fundamental. This paper briefly reviews the performance of both discharge driven and combustion driven chemical laser devices, and the optical configurations employed in the scalability steps. Appropriate diagnostics are discussed, including power, efficiency, and spectra.

I. Introduction

FUNDAMENTAL OVERTONE
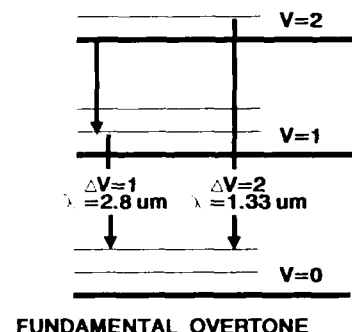
Figure 1. Overtone Concept

High power hydrogen fluoride (HF) chemical lasers have been the subject of research in the United States of America for approximately two decades. The basic principal of operation for continuous wave chemical lasers has been presented in several places . During this period the technology advanced from the laboratory scale to major demonstration systems including Baseline Demonstration Laser (BDL), Navy-ARPA Chemical Laser (NACL), Mid-IR Advanced Chemical Laser (MIRACL) and ALPHA. Cylindrical as well as linear concepts have been investigated. Reference 4 presents a review of the High Power Laser Programs. Emphasis during this period was placed on improvements in efficiency, scalability of concepts and improvements in beam quality. For space-based applications size and weight considerations are critical. Planned growth to include addressing responsive strategic threats requires substantial increases in power as well as efficiency. An alternate approach to increasing the power requirements on the laser is to shorten the wavelength, thereby increasing brightness. Several efforts are ongoing to address this issue , however success in the area is limited. Among the potential candidates for a shorter wavelength laser is the overtone chemical laser that builds directly on the hydrogen fluoride technology base. The overtone chemical laser uses the same chemical reaction and produces the same excited populations as does the conventional hydrogen fluoride laser. It differs in that the optics employed suppress lasing at 2.8 micrometers and allow lasing at 1.33 micrometers, Figure 1.

II. Subsonic Experiments

Prior to this development under the Overtone Chemical Laser Program, overtone lasing had been observed at very low levels using techniques not scalable to the power levels necessary for the envisioned applications . Overtone lasing has been observed at low levels in other laboratories but no attempts were made to improve the modest performance . In 1984 a Helios CL-I chemical laser, Figure 2, demonstrated approximately 10 watts of laser energy at approximately 1.33 micrometers. Significantly, this level represented approximately 12 of

212

the corresponding lasing power on the fundamental transition. Only the optics were changed to allow the overtone lasing. Transmissive optics designed for Nd-YAG applications were used in the demonstration test. The device illustrated in Figure 2 measures 15 centimeters in gain length. Improvements were made in the optics, eventually allowing the demonstration of 21 of the fundamental power at the shorter wavelength. Limited scalability of the concept was achieved by increasing the gain length to 30, 45, and finally 75 centimeters by combining individual 15 centimeter modules, Figure 3. The performance of these devices is summarized in Figure 4. The data illustrated in Figure 4 suggests an upper performance limit of approximately 30 of the fundamental. Suppression of the fundamental lasing in the longer gain length devices tended to be a problem. Techniques of multiple mirror resonator designs prevented the fundamental wavelength from achieving lasing threshold by multiple reflections. Figure 5 illustrates the four mirror design used in the 75 centimeter device experiments. Representative spectra for these lasing tests are illustrated in Figure 6.
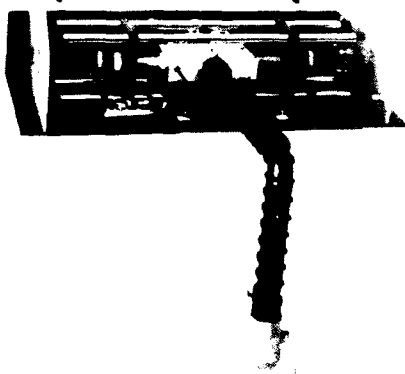
Figure 2. CL-I Laser
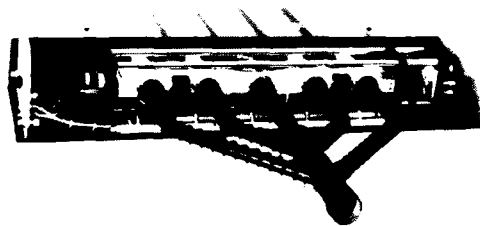
Figure 3. CL-IV Laser
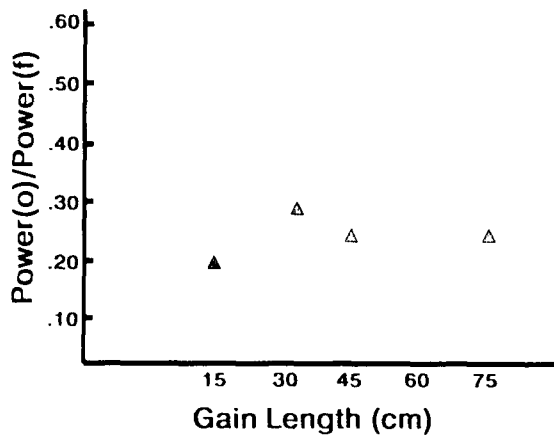
Figure 4. Subsonic Device
Performance Summary

Figure 5. Four Mirror
Configuration

The multiple optical surfaces required to suppress the fundamental introduced an additional source of loss in the cavity design, which to the low gain overtone laser was significant. Subsonic performance was improved by the introduction of a new nozzle design of greater flow height, optics/optical coatings specifically designed to suppress the fundamental and support overtone lasing, and hemispherical calorimeters designed to measure any radiation scattered from the highly reflective mirror surfaces. This improved design called the ZEB laser has demonstrated 55 of the fundamental performance at overtone power levels of approximately 200 watts or approximately an order of magnitude power scalability with a doubling of the efficiency.

213
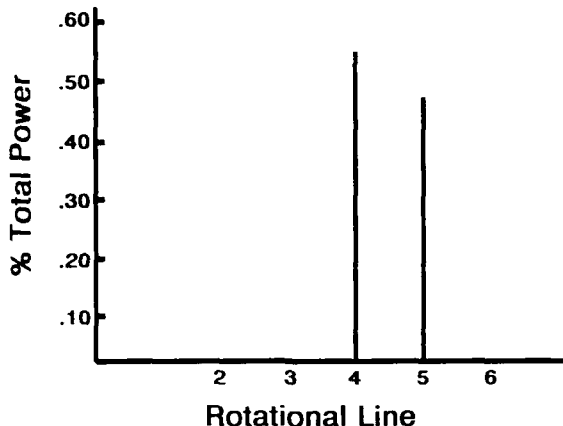
Figure 6. CL-I Spectrum

III. Supersonic Experiments

The subsonic designs do not lend themselves to being scalable to truly high power levels analogous to BDL, NACL, MIRACL, etc. The Overtone Chemical Laser Development Program transitioned into scalable supersonic chemical laser hardware in 1986. Tests performed at TRW demonstrated overtone performance at 24-35% of the fundamental using two chemical laser hardware configurations, the Hypersonic Wedge Nozzle (HWYN) and the Hypersonic Low Temperature (HYLTE) Nozzle conceptually illustrated in Figures 7 and 8. A companion paper describes these laser concepts in more detail[8]. The reactants used were nominally deuterium, fluorine, hydrogen and helium as a diluent. Mode lengths were found to be somewhat shorter than for the fundamental and the lasing spectra were as expected from the Helios experiments, Figure 9. The resonator configuration consisted of transmissive Nd-YAG mirrors as in the initial Helios subsonic tests.
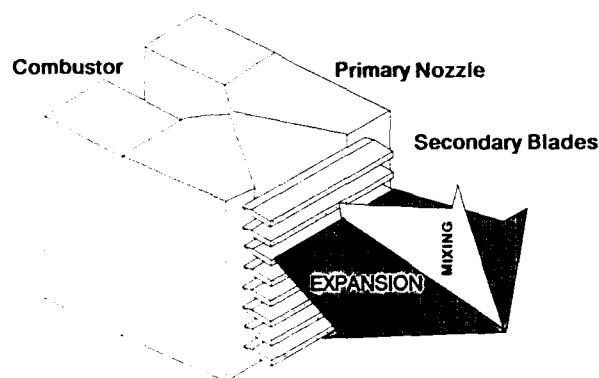
Figure 7. HYWN Nozzle
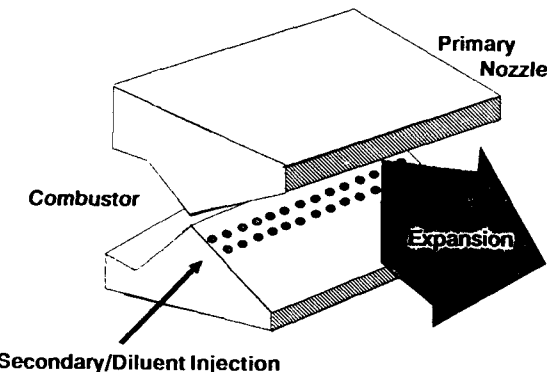
Figure 8. HYLTE Nozzle
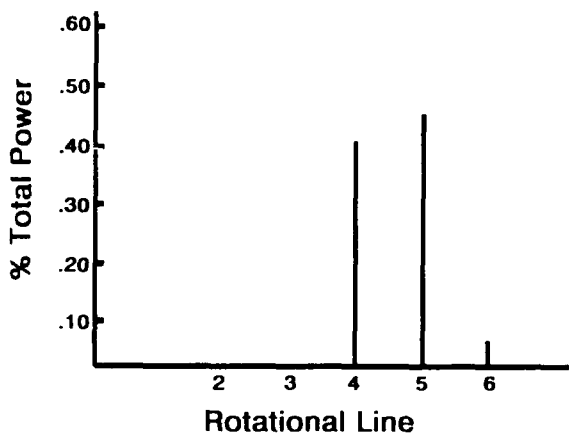
Figure 9. HYLTE Spectrum
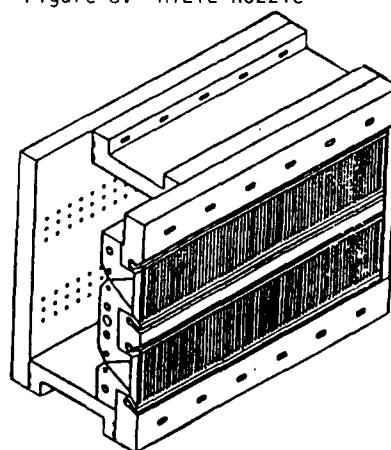
Figure 10. ZEBRA Nozzle

214

The success of these first supersonic experiments was somewhat misleading as to the true understanding of the overtone chemical laser concept. This fact was dramatically illustrated in the failure to demonstrate the scalability to higher power levels using larger nozzle hardware, ALPHA Verification Module (VM). To scale to higher power levels the more conventional closed cavity reflective optics were used. The gain length of the VM was such that the reflectivity suppression of the first generation optical coatings was inadequate to prevent fundamental lasing. The initial tests failed due to inadequate optical discrimination at the low fundamental rotational transitions. Improvements were made in coating design that achieved complete suppression of the fundamental transitions and allowed the demonstration of overtone performance at 25% of the fundamental at a total power level of approximately 4 kilowatts. However, these results were limited by repeated optical coating failure at flux levels greater than 30 kw/cm^2. The following section will discuss the optical coating development in more detail. These VM tests did provide a much better understanding of the difficulties in the design of optical coatings highly reflective at one wavelength, totally absorbing in another, and having a characteristic damage threshold sufficiently high to support high power lasing.

Differences in mode lengths between the overtone and fundamental lasing indicated that the optimum overtone nozzle design would not necessarily be identical to that for the fundamental laser. All supersonic lasing tests to this point had been run using existing hardware residual from previous chemical laser technology development programs that addressed fundamental lasing. The ZEBRA nozzle, Figure 10, was designed, fabricated and tested to better understand the geometric influences of the HYWN nozzle on overtone lasing. This hardware, along with redesigned optics and resonator configuration demonstrated overtone lasing at 56% of the fundamental at a total power level in excess of 4 kilowatts. The overtone lasing spectrum is again simple as compared to the transition rich fundamental. Figure 11 provides a chronological summary of the overtone performance to date.
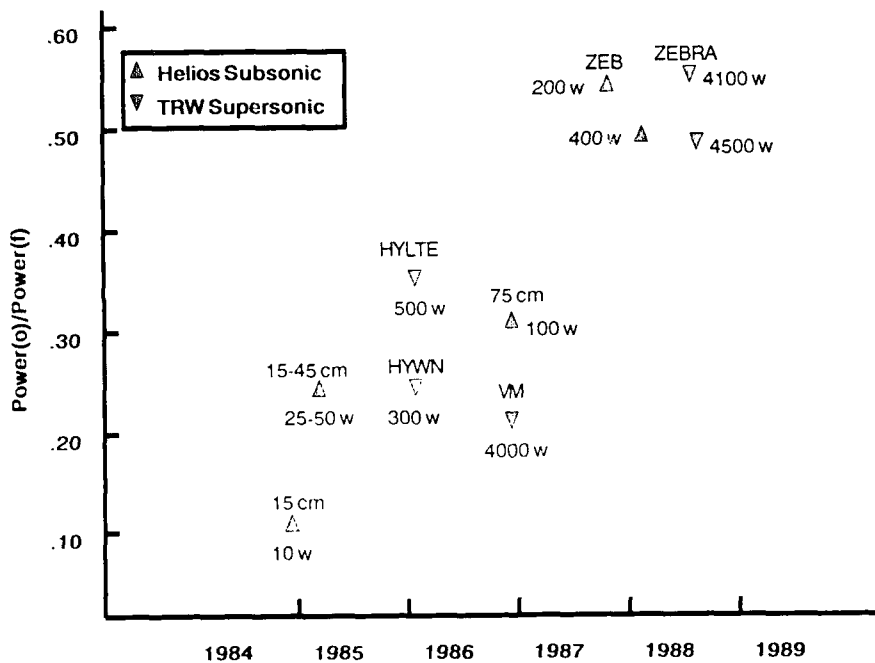
Figure 11. Overtone Lasing Performance Summary

IV. Optics/Optical Coating Development

The development of unique optical coatings has proven to be critical to the current success of the overtone chemical laser development and will likely continue to be a critical component. Initially the role of the optical coating was not totally appreciated or understood. Several iterations in the development of successful coatings have been necessary to support overtone lasing at the current levels. It was understood that coatings must be developed that were highly reflective to the overtone transition and nearly totally absorbing to the fundamental. These coatings had to be such that the absorbed energy was transmitted efficiently to the cooled mirror substrate and also withstand relatively high power fluxes. What was not initially appreciated was the wavelength band over which the fundamental lasing had to be suppressed. An error was made in the specification of the coating characteristics for the early Verification Module tests. Fundamental lasing typically occurred at wavelengths from 2.7 to 2.9 micrometers in this hardware. The coatings developed adequately suppressed lasing in this band. However, this suppression caused the lasing process to occur at shorter wavelengths, approximately 2.6 micrometers, on lasing transitions not normally observed. The optical coating developed and used in these early tests had sufficient reflectively in this

215

region to allow inefficient fundamental lasing to occur. Subsequent developments in the optical coatings for the overtone chemical laser progressed to the point of approximately 0.3% reflectivity over the entire fundamental lasing band and highly reflective in the overtone lasing band. Figure 12 summarizes the development in optical coatings and illustrates performance of current designs. Typical designs are multi-layer stacks of approximately twenty-five layers. Typical stack materials are ZnS, ThF_4, and SiO.
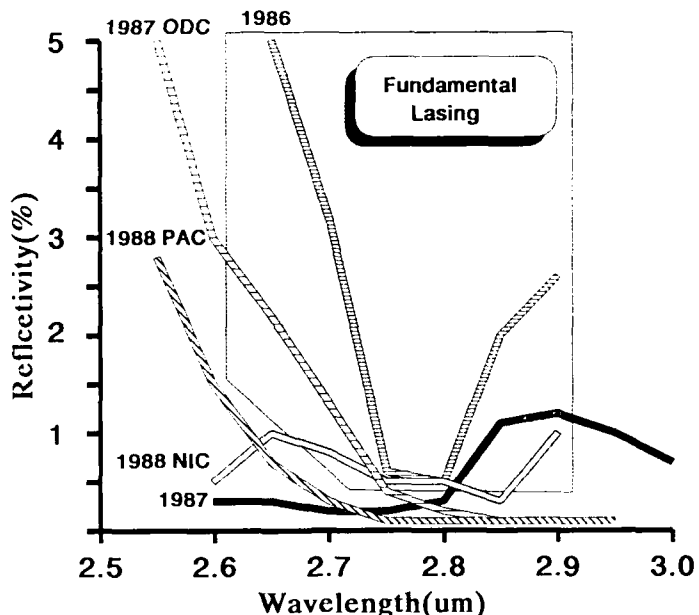
Figure 12. Overtone Lasing Optics Summary

V. Conclusions

The successful high performance short-wavelength chemical laser has proven to be quite elusive. To date only two candidates stand out in their demonstrated laser performance, both lasing at approximately 1.3 micrometers. The successful chemical oxygen-iodine laser (COIL) has characteristics undesirable for certain applications, making the overtone chemical laser more preferred though not without reservation.

The overtone chemical laser development has demonstrated rapid improvement over the past four years. Much of the technology development to date has concentrated on optics development to support the concept. Even though the currently demonstrated performance is promising, the overall performance levels must continue this improvement, both in efficiency of performance as well as scalability for the concept to be a viable alternative to other more mature technologies.

References

1. K. L. Kompa, Chemical Lasers, 37 (Springer-Verlag, New York, 1973).

2. R. W. F. Gross and J. F. Bott, Handbook of Chemical Lasers (John Wiley & Sons, Inc., New York, 1976)

3. W. R. Warren, Jr., Astronautics & Aeronautics, 13, 4, 36, (1975).

4. J. Miller, Proceedings of the International Conference on Lasers, 1987.

5. C. R. Jones, Proceedings of the International Conference on Lasers, 1987.

6. S. N. Suchard and G. C. Pimentel, Applied Phys. Lett. 18, 530 (1971).

7. R. Meinzer, private communication.

8. J. M. Walters, these proceedings.

XeCl-LASER-PUMPED IODINE LASER OSCILLATOR WITH t-C$_4$F$_9$I

In Heon Hwang* and Ja H. Lee
NASA Langley Research Center, Hampton, VA 23665-5225
(804) 864-1473

Abstract

An iodine laser oscillator with t-C$_4$F$_9$I as the active material was pumped by a XeCl laser at an improved efficiency (3.75 percent). The oscillator is suitable for the highly repetitive master oscillator of a MOPA system.

I. Introduction

Since the atomic iodine photodissociation laser was discovered by Kasper and Pimentel in 1964 [1], numerous research efforts have concentrated on this laser to increase the power level needed for laser fusion [2, 3]. The fusion-experiment-oriented iodine laser is constructed in a master-oscillator power-amplifier (MOPA) architecture [4]. The amplifiers and the oscillator of the iodine laser are usually pumped by short pulse flashlamps.

The iodine laser is also being considered as a direct solar-pumped laser for space applications, such as the space power transmission and the laser propulsion for an orbital transfer vehicle. The first solar-simulator-pumped iodine laser was reported in 1981 by Lee, et al. [5]. This laser was operated in quasi-continuous-wave mode. After this report, various iodine compounds were tested and evaluated as candidates for direct solar-pumped laser materials. [6, 7, 8].

Although many space applications are best served by a continuous wave (CW) laser, a continuously pulsed, high-peak power laser also has good applicability in space, especially for laser propulsion. Since the solar radiation, even concentrated, is relatively weak, the solar-pumped laser system must be in a MOPA

system for obtaining high peak power and the beam profile control. Especially, the long upper-state lifetime (~ 150 ms) of an iodine atoms makes the MOPA system to be well suitable. In previous research, the feasibility of the oscillator-amplifier scheme was favorably evaluated for the solar-pumped iodine laser [7, 9].

The iodine laser oscillator must generate temporally smooth and short pulses in order to be incorporated in the MOPA system. In the fusion-oriented iodine laser experiment, the short pulse is provided by mode-locking of the flashlamp-pumped oscillator. However, the repetition rate of the flashlamp-pumped oscillator is usually very low (<5Hz), and the mode-locking devices are generally complicated.

An excimer laser-pumped iodine laser oscillator was demonstrated by Fill et al. [10]. In their experiment, a 500-mJ excimer laser was used for pumping an iodine laser, and a temporally smooth laser pulse with duration from 2.6 ns to 12 ns was obtained by using i-C$_3$F$_7$I as the laser material. However, the efficiency of the system was very low, and no report of its application to a MOPA system has been found to date.

In this report, a XeCl-laser-pumped iodine laser oscillator using t-C$_4$F$_9$I is described. This laser oscillator has a much higher efficiency and a lower threshold pump power than the system using i-C$_3$F$_7$I. The laser output energy dependence on the gas-fill pressures and on the reflectances of the output mirrors are measured for both longitudinal and transverse pumping. A preliminary result of its application to a solar-pumped MOPA system is also presented.

II. XeCl Excimer Laser

A laboratory-built XeCl laser was used for the pumping of the iodine laser in this experiment. The electrical circuit of the XeCl laser is shown in Fig. 1. The main discharge was energized by a two-stage Marx generator. The capacitance of each stage is 40 nF. A pyrex tube with an I.D. of 10 cm and a length of 66 cm was used as the laser chamber. The two brass electrodes were rounded in order to prevent development of arc discharges in the chamber. The width of the electrodes was 2 cm, and the length was about 45 cm.

The separation between the two electrodes was 2 cm. Seventeen pairs of spark arrays were located beside the electrodes so that the discharge volume could be uv-preionized uniformly.

The optimized gas composition was HCl: Xe: Ar: He = 0.2: 5.9: 19.5: 74.4% at a total pressure of 2 atm. The addition of Ar improved the discharge uniformity at the higher operating voltage. The XeCl laser was operated in a sealed-off mode. No significant reduction of the laser output energy was shown for a few hundred discharges.

Fig. 1. Electrical circuit diagram of the XeCl laser.

The optical resonator of the XeCl laser was composed of a full reflector with a radius of curvature of 5 m and a flat partial mirror with a reflectance of 30%. All the mirrors were coated outside so that the mirror surfaces could not be damaged by the volatile discharge products. The two laser mirrors were separated about 75 cm. A spatially uniform laser output in a cross section of 0.7 x 2 cm^2 was obtained with the optical resonator.

The XeCl laser was operated with the charging voltage of 25 kV, and the output energy of 80-mJ per pulse was measured. When the charging voltage was increased further, the laser output was also increased, but an arc discharge was developed between the electrodes. Thus, operation above 25 kV was not pursued.

The output energy was measured with a calorimeter. The output pulse shape of the laser output was monitored with a Si

PIN photodiode with the glass window removed. The removal of the glass window improved the near UV response of the diode. A typical laser pulse is shown in Fig. 2. The half width (FWHM) of the XeCl laser pulse was about 25 nsec, and no significant variation of the laser pulse shape was found for prolonged operation.
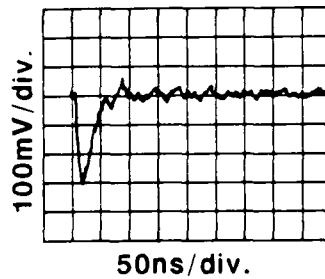
Fig. 2. A typical pulse shape of the XeCl laser output.

218

III. Iodine Laser Oscillator

The iodide used on the laser medium was perfluoro-tertiary-butyl iodide (t-C_4F_9I). This chemical was chosen mainly due to the high absorption cross section at the wavelength of XeCl laser light (308 nm). The published data show that the absorption cross section of t-C_4F_9I at 308 nm is about 3.6 x 10^{-19} cm^2 [7]. Also, t-C_4F_9I has shown good chemical reversibility in a flashlamp-pumped system [6, 7], and thus the iodine molecule buildup in the laser cell is minimized. The main disadvantage of this iodide is the low vapor pressure (~ 85 torr) at room temperature. The other chemical kinetic properties are nearly the same or better than the other commonly used perfluoroalkyl iodide in flashlamp-pumped experiment [7]. The quantum yield of excited atomic iodine in the UV photodissociation is nearly unity [11].

A quartz cuvette with a square cross section of 1 cm^2 and a length of 5 cm was used as the iodine laser cell. The windows of the laser cell were nearly perpendicular to the optic axis of the laser cell. Both longitudinal and transverse pumping of the iodine laser were employed.

For the longitudinal pumping, a dichroic mirror was used to introduce the XeCl laser light into the iodine laser cell. The dichroic mirror transmitted about 80% of the XeCl laser light and fully reflected the iodine laser light. The XeCl laser light was directed through the dichroic mirror and was focussed into the center of the laser cell by a quartz circular lens with a focal length of 20 cm. The output pattern of the iodine laser was monitored on a carbon-paraffin paper. A typical laser output pattern was an ellipse with minor diameter 1 mm and major diameter 4 mm when the gas pressure in the cell was 80 torr and the reflectance of the output mirror was 85%.

For the transverse pumping, a quartz cylindrical lens with a focal length of 30 cm was used to focus the XeCl laser light into the iodine laser cell. Because of the long focal length of the focussing lens, the laser output pattern was a long rectangle with an area of 1 x 10 mm^2.

The TEM mode pattern was not analyzed in either experiment, and no attempt was made to operate the iodine laser in the TEM_{00} mode. The output energy dependences on the gas fill pressure at different output mirror reflectances are shown in Figs. 3 and 4.
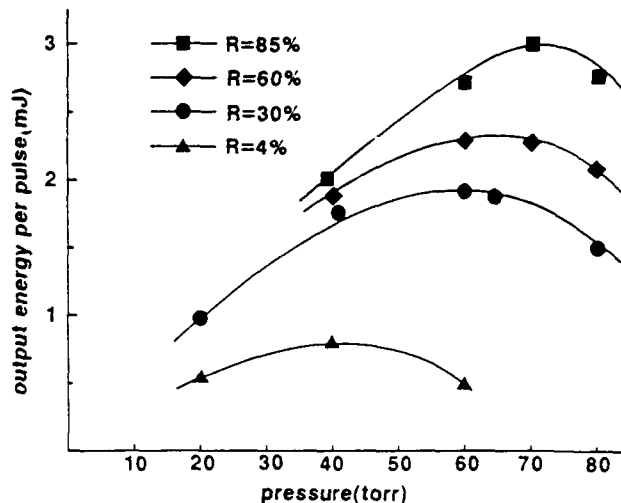
Fig. 3. Iodine laser output dependence on the gas fill pressure in the laser cell at each output mirror reflectance when the iodine laser was pumped longitudinally.
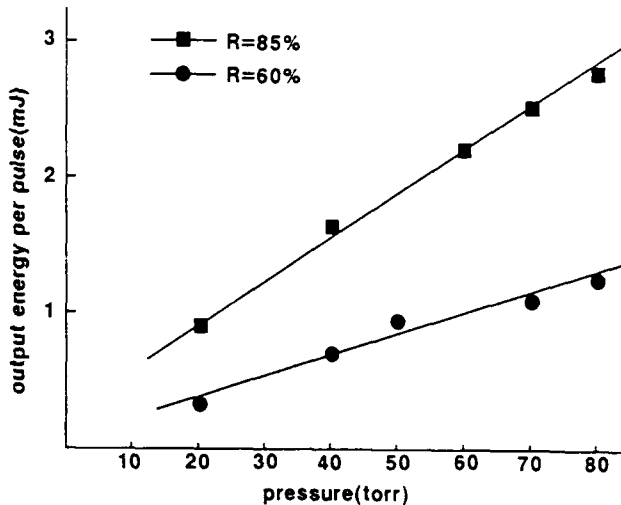
Fig. 4. Iodine laser output energy dependence on the gas fill pressure when the iodine laser was pumped transversely.

As shown in Fig. 3, there is an optimum iodide pressure for each output mirror reflectance for the longitudinal pumping. However, for the transverse pumping, the laser output energy increases monotonically with the t-C_4F_9I pressure as

219

shown in Fig. 4. The results in Figs. 3 and 4 were taken when the laser was operated at 2-Hz repetition rate. When the pulse repetition rate was increased to 5 Hz, the laser output energy per pulse was reduced slightly (~ 10%) due to the reduction of the XeCl laser pump energy.

A typical pulse shape of the iodine laser monitored by a pyroelectric detector is shown in Fig. 5. The half width (FWHM) of the pulse is about 25 nsec. The iodine laser onset is delayed from the XeCl pump laser and occurs at the end of the pump pulse. This pulse shape is nearly the same for both pumping geometries.
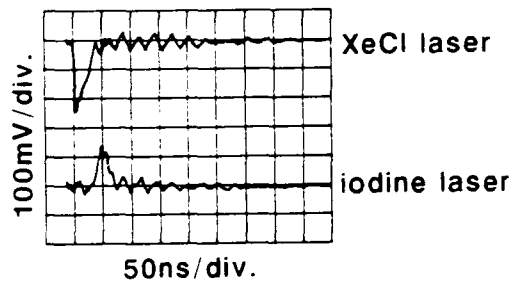
Fig. 5. A typical iodine laser output pulse shape compared with the XeCl pumping laser pulse.

IV. Discussion

In this experiment, a XeCl-laser pumped iodine laser was developed and tested by using t-C_4F_9I as the laser material. This lasant t-C_4F_9I has larger absorption cross section at the XeCl laser line compared with other iodides used in the laser experiment, such as i-C_3F_7I.

The large absorption cross section allows the high utilization of pumping energy in short gain length and low pressure operation of the iodine laser. The low-pressure operation of the iodine laser is suitable for single longitudinal mode output because of the reduced pressure broadening of the gain profile. The single-longitudinal mode operation of the laser oscillator is necessary to obtain a temporally smooth pulse.

The iodine laser described in this report was operated up to 5 Hz, which was limited by the power supply of the XeCl laser. Further increases of the repetition

rate can be made by scaling up the pump laser system (laser systems operable at 100 Hz are commercially available). The iodine laser was operated in a sealed-off mode with no significant reduction of the laser output energy for a few hundred pumpings. There was also no noticeable color change in the t-C_4F_9I gas after a few hundred pumpings and no deposits on the wall of the laser cell (in strong contrast to the report of Ref. 10 where i-C_3F_7I was used). This may be attributable to the superior chemical reversibility of the iodide used.

V. Application to a Solar-Pumped MOPA System

The amplification experiment of a solar simulator-pumped iodine laser amplifier is under way by using the XeCl-laser pumped oscillator as shown in Fig. 6. The Suprasil quartz amplifier tube is water cooled by flowing the deionized water through the Suprasil water jacket. The amplifier tube and the arc lamp of the solar simulator is housed in a elliptic reflector, such that the optical radiation from the arc lamp can be focussed into the amplifier tube. The amplifier tube has a length of 15 cm and the diameter 2 cm.

The measured spectral irradiance on the inner surface of the amplifier tube is about 1700-solar constants of air mass zero solar irradiance for 300-A arc current. The iodide used in the amplifier is n-C_3F_7I which provides high vapor pressure at room temperature. The fast gas flow through the amplifier tube is obtained by adopting evaporation and condensation method. The flow velocity of the iodide gas could be reached up to 20 m/sec with this method. The amplifier system was operated previously as an oscillator and reported in Ref. 12. For the present experiment, the system is operated similarly after removing the cavity mirrors.

The preliminary results of single-path amplication indicate that an amplication factor of > 1.5 is obtainable for the 15-cm gain length at a high repetition rate.
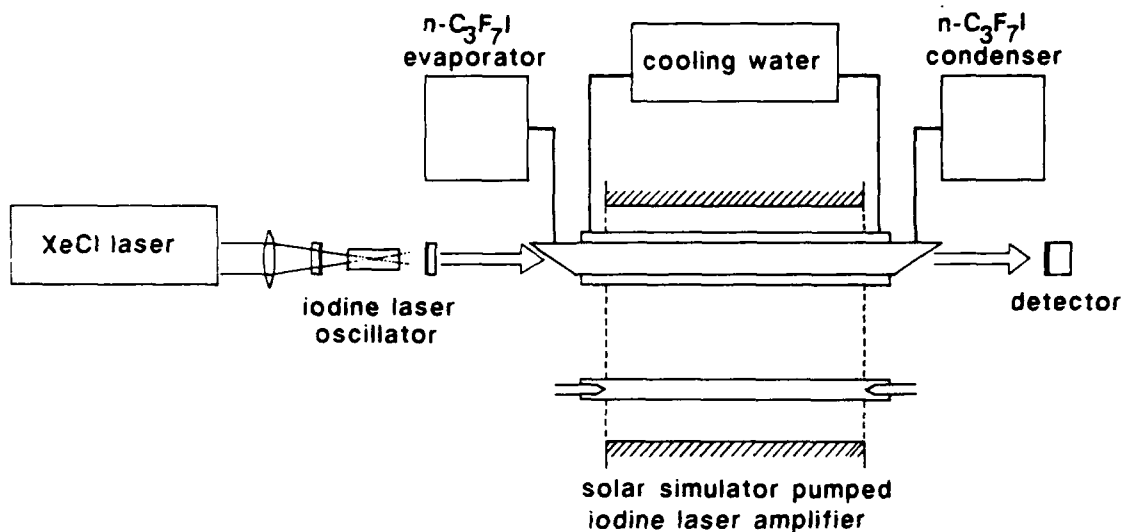
Fig. 6. Solar simulator pumped iodine laser MOPA system with the XeCl laser pumped iodine laser oscillator.

VI. Conclusion

A XeCl laser that pumped an iodine laser oscillator was developed using t-C_4F_9I as the laser material, and a 3-mJ laser output energy was obtained with only 80-mJ pump laser energy. Compared with previously reported results by others, the pumping energy was significantly reduced in this experiment. The pumping efficiency (i.e., the ratio of the iodine laser energy to the XeCl laser energy) was 3.75%. This experiment also demonstrated a repetitive operation of the iodine laser oscillator with a stable output. Since the threshold pumping energy (20 mJ) is low for t-C_4F_9I, a moderate size XeCl laser may suffice for pumping the high-repetition-rate iodine-laser oscillator required for high power, solar-pumped MOPA systems.

*Department of Physics, Hampton University, Hampton, VA 23668

References

1. J. V. V. Kasper and G. C. Pimentel, Appl. Phys. Lett. 5, 231 (1964).
2. G. Brederlow, E. Fill and K. J. Witte, "The High-Power Iodine Laser," Springer-Verlag, New York, (1983).
3. S. B. Kormer, Izvestiya Akademii Nauk SSSR. Seriya Fizicheskaya 44, 2002 (1980).
4. K. J. Witte, Czech. J. Phys. B34, 790 (1984).
5. J. H. Lee and W. R. Weaver, Appl. Phys. Lett. 39, 137 (1981).
6. J. H. Lee, J. W. Wilson, T. Enderson, D. H. Humes, W. R. Weaver and B. M. Tabibi, Optics Comm. 53, 367 (1985).
7. B. M. Tabibi, M. H. Lee, J. H. Lee and W. R. Weaver, Proceedings of the International Conference on Lasers '86, pp. 144-149 (1986).
8. R. J. De Young, IEEE. J. Quant. Electron. QE-22, 1019 (1986).
9. I. H. Hwang, J. H. Lee and M. H. Lee, Optics Comm. 58, 47 (1986).
10. E. Fill, W. Skrlac and K. J. Witte, Optics Comm. 37, 123 (1981).
11. A. B. Alekseev, A. M. Pravilov, I. I. Sidorov and V. A. Skorokhodov, Sov. J. Quantum Electron. 17, 1539 (1987).
12. J. H. Lee, M. H. Lee and W. R. Weaver, Proceedings of the International Conference on Lasers '86, pp. 150-156 (1986).

NUCLEAR-REACTOR-PUMPED LASER RESEARCH AT SANDIA NATIONAL LABORATORIES

G. N. Hays, W. J. Alford, D. A. McArthur, D. R. Neal and D. E. Bodette
Sandia National Laboratories
Albuquerque, New Mexico 87185-5800

Abstract

Sandia National Laboratories has been investigating reactor-pumped gas laser systems for a number of years. Because of the relatively long excitation time scales involved, as compared to more conventional pulsed lasers, reactor-pumped systems offer a unique opportunity to study lasers in a quasi-CW environment. At Sandia, we have examined both rare-gas halogen systems (e.g., XeF) and rare-gas atomic systems (e.g., Xe). Our data indicate that the XeF system, promising fairly high efficiency in the UV, requires pump levels difficult to achieve with current reactors (5-10 kW/cc deposited power). Conversely, the atomic xenon laser appears to peak in its efficiency at much lower pump levels ($<$ 100 W/cc). We have studied the xenon laser with both of Sandia's pulsed reactor facilities (SPR-III and ACRR), resulting in a very wide range of pulse widths (0.2-22 msec) and pumping rates from a few watts/cc to $>$ 300 W/cc. We have found that depending on the specific gas mixture chosen (He/Ar/Xe or Ar/Xe) and the detailed cavity losses, one can obtain lasing on either the 2.03-μm line of xenon, or the 1.73-μm line, and sometimes on both simultaneously. Energy efficiencies appear to be in the 2-3% range, with instantaneous (power) efficiencies approaching 6%. Detailed kinetic mechanisms for the xenon-rare gas system are not well understood, and studies of the various emitting lines under extremes of energy and power loading are expected to clarify some of the issues. For some cases, we have performed a Rigrod-type analysis of the xenon laser, and will report on values for gain, distributed loss and saturation flux.[1] Additionally, we have performed some measurements on the spatial profile of the laser, and will summarize those results, which indicate multi-mode behavior as well as some impact of the refractive index variation on the laser.

Acknowledgments

References

1.   W. J. Alford and G. N. Hays, submitted to J. App. Phys.

THE ADVANTAGES AND DISADVANTAGES OF USING THE TREAT REACTOR
FOR NUCLEAR LASER EXPERIMENTS

P. W. Dickson and A. M. Snyder
Idaho National Engineering Laboratory
EG&G Idaho, Inc.
P.O. Box 1625
Idaho Falls, Idaho 83415-3123

G. R. Imel and R. J. McConnell,
Argonne National Laboratory
Idaho Site
P.O. Box 2528
Idaho Falls, Idaho 83403-2528

Abstract

TREAT (Transient Reactor Test Facility) is a large, air-cooled test facility located at the Idaho National Engineering Laboratory (INEL). This facility was originally designed to evaluate reactor fuels and structural materials under conditions simulating various types of nuclear excursions and transient undercooling situations. However, for several reasons, it lends itself well to supporting a variety of nuclear laser experiments. Two of the major design features of TREAT -- its large size and its being an air-cooled reactor -- provide the clues to both its advantages and disadvantages for supporting nuclear laser experiments. Its large size, which is dictated by the dilute uranium/graphite fuel, permits accommodation of geometrically large experiments. However, TREAT's large size also results in relatively long transients so that the energy deposited in an experiment is large relative to the peak power available from the reactor. TREAT's air-cooling mode of operation allows its configuration to be changed fairly readily. Not only can individual fuel elements be removed to admit a large test article but, perhaps more importantly, special slotted elements can be installed in line with removable shield plugs to provide line-of-sight access through the reactor. For the same reason -- air cooling -- the reactor cools down slowly, permitting only one full power transient a day which can be a disadvantage in some experimental programs. In addition, the reactor is capable of both steady-state or transient operation.

Introduction

A major concern in most nuclear powered laser programs is the threshold power required to drive the system. A second, no less important, concern is the scalability of the data from the experimental program to the typically larger scale of the deployed laser system. The first concern requires that any nuclear powered laser experiment be performed in a facility large enough to adequately drive the laser system. The second concern makes it extremely advantageous for any nuclear powered laser experiment to be performed in an experimental environment which lends itself to addressing the scalability issues as extensively as practical. At the INEL, this has led to the use of an extremely unique facility for performing nuclear powered laser experiments. This facility, the Transient Reactor Test Facility (TREAT), is a large air-cooled, thermal test facility located at the Argonne National Laboratory-West (ANL-West) site within the INEL. This facility was originally designed to evaluate reactor fuels and structural materials under conditions simulating various types of nuclear excursions and transient undercooling situations. The TREAT reactor is capable of both steady-state operation to 120 kW or transient operation with integrated powers up to 2100 MJ and peak powers as high as 16,000 MW. For the past three and one-half years, the TREAT facility has also been used to support various Strategic Defense Initiative (SDI)-related activities. Three major nuclear powered laser test programs have been successfully conducted in the TREAT reactor during these last three years. A fourth is planned for next calendar year.

Two of the major design features of TREAT -- its large size and its being an air-cooled reactor -- provide the clues to both its advantages and disadvantages for supporting nuclear laser experiments. Its large size permits accommodation of geometrically large experiments. But its size also results in a large amount of energy being deposited in an experiment relative to the peak power available from the reactor. Another advantage to a nuclear laser program is TREAT's air-cooling mode of operation, which allows its configuration to be changed fairly readily. Not only can individual fuel elements be removed to admit a large test article but, perhaps more importantly, special slotted elements can be installed in line with removable shield plugs to provide line-of-sight access through the reactor. For the same reason -- air cooling -- the reactor cools down slowly, permitting only one full power transient a day. This slow repetition rate may be a disadvantage in

some experimental programs. Figure 1 shows a cutaway view of the TREAT reactor with a typical nuclear laser experiment installed in the core.

Description of the TREAT Facility

The INEL is in southeastern Idaho as shown on Figure 2. TREAT is located approximately 17.7 km from the INEL eastern boundary and 6.4 km north of U.S. Highway 20 (see Figure 3). The TREAT complex is comprised of reactor and control buildings located approximately 762 m apart. The topography of the region permits an unobstructed view between the two buildings.

The Reactor Building is an aluminum-sided, steel-frame structure which features two high-bay sections and two low-bay sections. The south high-bay section contains the reactor, an instrument room, and various assembly and storage areas for both the reactor and experimental hardware. The north high bay contains reactor fuel storage and some experiment storage holes underground, where radioactive spent experiments can be stored for cooldown. Two bridge cranes provide coverage of the reactor top, work areas north and south of the reactor, and the reactor fuel and experiment storage areas. The west low bay area contains a health physics laboratory, washrooms, an instrument and control room, an instrument shop, an experimenter's room, and the suspect waste tank room. The east low-bay areas include equipment storage areas, the hodoscope instrument room, a mechanical shop, an electrical equipment room, and a diesel generator room. The Reactor Building also includes two mezzanine areas: the lower mezzanine which is at the same elevation as the top of the reactor biological shield and the upper mezzanine which is somewhat higher.

The TREAT reactor is operated from the Control Building. The Control Building is a prefabricated, modular building containing a control console and various support areas. Neutron detector signals are amplified in the Reactor Building and transmitted, via underground cables, to the Control Building. Control signals from the control console are returned via underground cables.

The major design features and operating characteristics of TREAT are summarized in Table 1. The standard TREAT fuel assembly consists of an upper and lower graphite reflector section, and a central uranium oxide-bearing graphite fuel section. The 1.22-m long fuel section contains six fuel blocks canned in Zircaloy-3. The upper and lower reflector sections are contained in aluminum cans which are riveted to the ends of the fuel section. A gripping fixture and a support and alignment pin complete the fuel assembly. The complete fuel assembly is slightly under 2.74 m long. It has a nominal cross section of 10.06 x 10.06 cm with 1.59-cm chamfered corners. The chamfered corners permit passage of the air coolant. The total assembly weighs 43 kg.

In addition to the standard TREAT fuel assemblies, there are numerous modified assemblies used for special applications. These special assemblies include dummy fuel assemblies (containing pure graphite), slotted fuel assemblies (with the center 0.61 m of fuel removed), and control-rod fuel assemblies (with the center machined to accommodate the control rod).

The control rods themselves are carbon steel tubes packed with compacted boron carbide (B_4C) powder. There are currently sixteen control rods used in the TREAT core; twelve are shutdown rods and four are transient rods. The control-rod drives are located below the reactor. Two types of drives are utilized. The shutdown control-rod drives consist of a pneumatically-driven fast scram cylinder and a motor-driven lead screw mechanism for relatching and intermediate positioning. The transient rod drives are hydraulically driven.

The individual fuel assemblies which make up the TREAT core are aligned and supported from the bottom by a carbon steel grid plate. The grid plate is aligned by the control-rod guide thimbles and supported by a concrete ledge. The grid plate also contains a square opening centered on a 20.3-cm-diameter hole in a bottom concrete shield. An adapter plate which will interface with a variety of experimental configurations can be located in the center of this grid plate. The lower coolant plenum chamber of the reactor is formed by the grid plate, concrete ledge, and the bottom concrete shield.

A permanent radial reflector is made up of graphite blocks stacked along the four inside walls of the shield cavity. Large movable blocks of graphite are installed in regions which face viewing slots in the core.

The reactor is shielded radially with high-density concrete encased in steel plate. The bottom concrete shielding forms the ceiling of the subpile room. The shielding above the reactor is comprised of removable heavy concrete blocks and a rotating shield plug consisting of three 10.16-cm thick layers of steel. The top and bottom surfaces of the

TABLE 1. DESIGN and OPERATING PARAMETERS for TREAT REACTOR

Core

Nominal size (210 fuel assemblies)	1.68 m dia pseudocylinder x 1.22 m high
Maximum size (361 fuel assemblies)	1.93 m square x 1.22 m high
U-235 loading (nominal core)	7.45 kg

Fuel Assemblies
Overall dimensions	10.058 cm square x 2.72 m long, with 1.59-cm chamfered corners

Fuel Section
Configuration	6 graphite-urania blocks clad with 0.0653-cm-thick Zircaloy 3
UO_2 content	0.248 wt-%
U-235 enrichment	93.24%

Graphite Reflectors (Top and Bottom Sections)
Length	0.61 m

Permanent reflector	Graphite (ʋ.61 m thick, minimum)

Coolant	Air at atmospheric pressure (0.09 MPa) and ambient temperature (293-311 K)

Control Rod Drives (in typical core with 2 control rods per drive)	Six pneumatic operated drives Two hydraulic operated drives

Maximum Operating Conditions

Transient -- type	Unshaped	Shaped
Integrated power	2100 MJ	2060 MJ
Peak power	16,000 MW	3850 MW
Thermal neutron flux level	0.5 to 1.3 x 10^{21} n/m^2-s	
Fuel temperature	873 K	873 K

Steady State
Power level	120 kW

Flux data in central void
Neutron	5.6 x 10^6 fissions/g U-235-W-s
	5.0 x 10^6 nvt/W-s (cross section = 440 barns)
Gamma	22 r/hr/W
	6.0 x 10^3 r/MJ

steel slabs are coated with 0.64-cm thick layers of boral for thermal-neutron attenuation. The top layer of boral is covered with steel safety plate which serves as a working floor. The shielding is adequate to allow continuous personnel access at most locations around the reactor during operations at 120 kW and above the reactor after two hours of reactor cool-down from 100 hours of continuous operation at 120 kW. Shielding of personnel during tran-sient operations poses no problem, since these operations are conducted by remote control. Controlled access to the TREAT reactor building is generally permitted within an hour after a full power transient. Access to certain higher dose areas (including the sub-pile room, reactor top directly over an opening in the shielding, etc.) during steady-state operation and following transients is administratively controlled because of the potential for higher radiation exposures to personnel.

Three horizontal access slots which converge on the core center are provided in the radial concrete shield, permanent reflector, and core. The north and west openings in the concrete shield are convertible; they are designed to provide either a 10.16-cm x 10.16-cm rectangular access slot or a 60.96-cm square access slot. The south opening in the con-crete shield provides a rectangular slot aligned with the north slot, thereby allowing straight through access to the reactor center.

Requirements for a Nuclear Laser Experiment

Nuclear powered lasers (NPLs) derive their power directly from the reactor (instead of electricity). The power to drive them is thus directly related to the neutron flux in the reactor. The neutron flux level within the test bed must therefore be sufficient to "pump" the laser system with enough power to reach laser action threshold as a minimum. For excimer lasers that value is quite high -- greater than a few hundred kilowatts per cubic centimeter. To maximize the "pumping" power the laser must be located directly in the region of highest flux.

Therefore, the first requirement for a NPL is that the reactor must have sufficient peak flux.

Because the laser must operate within the harsh environment of a reactor, a second requirement is for optical access for the laser diagnostics. In some configurations, this results in the beam being propagated some distance from the laser cavity.

In a nuclear powered experiment the safety issue associated with neutron and gamma radiation emanating from the reactor core must be evaluated. The radiation must be considered not only from the standpoint of personnel exposure but also for its impact on hardware design and lifetime.

Although a relatively small active volume may be adequate for some NPL experiments, the availability of a large laser region permits certain scaling factors to be addressed more directly than possible in a small scale experiment. Thus a large active volume is desirable although not strictly a requirement.

Advantages of Using the TREAT Reactor for Nuclear Laser Experiments

There are several advantages to utilizing the TREAT facility for nuclear laser experiments. These include: (a) its large size which allows the testing of large experimental components, (b) its flexibility of configuration which allows a large variety of experimental configurations to be tested, (c) its long transients, and (d) its adequately high peak flux.

As previously noted, the TREAT reactor core consists of up to 361 fuel assemblies, each 10.1-cm square and 2.72-m long. All TREAT experiments require a central void to allow insertion of the experiment and sixteen control rod assemblies for transient control. A typical TREAT experiment may require the removal of one to three TREAT fuel assemblies. The remainder of the fuel assembly positions are filled with either standard fuel assemblies, slotted fuel assemblies, or dummy graphite-filled fuel assemblies. In some cases, the central void will itself be surrounded by dummy graphite elements to act as a thermal insulator and to enhance the thermal neutron flux at the central void location. As shown in Figure 4, a nuclear laser experiment previously performed in TREAT required that three fuel assemblies be removed to insert the experiment and twelve more assemblies be replaced by dummy graphite elements. This brought the total number of removed fuel assemblies to fifteen. Additional core configurations will be discussed in the "Enhancements to the TREAT Reactor" section of this paper. Numerous core physics calculations and calibration transients are performed for each specific core configuration to verify that a sufficient excess reactivity (k_{ex}) is present to achieve the desired peak flux, that adequate reactor control is available to safely operate the reactor, and that the desired operating characteristics of the transient are obtained.

Figure 5 shows an experiment previously performed at TREAT in which the experimental test gas entered the top of the in-reactor test assembly (hereafter termed the test vehicle), flowed downward, turned and flowed horizontally for a short distance at the reactor core centerline, turned again and flowed upward, and finally exited the test vehicle. The laser diagnostics in this configuration were physically located on top of the reactor at 90° to the vertical centerline of the test vehicle. They were installed on a multi-port diagnostic "tree" which allowed multiple diagnostics for any single transient. The diagnostics "viewed" the active region of the test vehicle through suitable windows which constituted the test vehicle pressure boundary. The diagnostics were interchangeable, port-to-port, and did not constitute part of the test vehicle pressure boundary. In this configuration, the diagnostic "viewing" was generally along the same path as the gas flow except at the core centerline where the flow was horizontal. The total "diagnostic viewing" path length was on the order of 6.8 m with approximately 4.6 m being in the flowing gas region and 2.2 m in evacuated viewing tubes.

Figure 6 shows an experiment to be performed at TREAT in which the experimental test gas enters the top of the test vehicle, flows downward through the test vehicle, and then exits from the bottom of the test vehicle. In this configuration, the test gas flows vertically

past the active region of the test vehicle. The laser diagnostics in this configuration are physically located on the main floor of the Reactor Building just outside of the reactor's biological shielding. This configuration uses the north and south openings in the concrete shield, thereby allowing straight through access of the reactor so that the diagnostics can "view" the active region of the test vehicle horizontally through pressure boundary windows. As a result, the diagnostic "viewing" is truly perpendicular to the gas flow path. The path length for this horizontal "diagnostic viewing" configuration is on the order of 7.9 m. Although this is a slightly longer path length than with the other configuration, all but the central 0.5 m is in evacuated viewing tubes. This results in potentially less distortion and/or signal attenuation than present in the other configuration. As can be seen from Figures 5 and 6, the interfaces to various experimental sup t systems, including systems supplying experimental gases and laser diagnostic equipment, differ significantly for different experiments. These support systems can be located either on the reactor top or on the main floor of the Reactor Building depending on the configuration of the experiment.

Two major types of transients are of primary interest in any nuclear powered laser program to be performed at TREAT: (a) exponential or peaked bursts and (b) shaped power bursts. Figure 7 shows the reactor power and energy release for a typical exponential burst transient. The thermal neutron flux at the core center during an exponential burst transient is typically about 5×10^{20} neutrons-m^{-2}-s^{-1}. This flux level and the width of the burst [typically 100 milliseconds full width at half maximum (FWHM)] are what makes this facility so unique and valuable to a laser test program. The reactor core for the exponential-burst transient shown in Figure 7 contains 223 standard fuel assemblies, sixteen control-rod assemblies, and a dummy experimental capsule in the central fuel-assembly location. Other core configurations have been used which contained as many as 266 standard fuel assemblies, sixteen control-rod assemblies, and an experiment void area in the center of the reactor which displaced fifteen fuel assemblies. In a true exponential burst transient, shut-down is effected by the increase in leakage of the reactor as a result of its increased temperature. Because the energy in the tail of an exponential transient is generally not useful, the natural burst transients are frequently clipped by rapid insertion of the control rods during the power rise. Of particular value to a nuclear powered laser program is the FWHM pulse width of 100 ms for the exponential burst-type transient which, compared with most other testing facilities, is an extremely long pulse. Therefore, scalability to steady-state conditions (> seconds) is a more easily attained goal for a nuclear powered laser experiment performed in TREAT than in most other facilities.

The shaped power bursts (as shown in Figure 8) are produced by the step insertion of reactivity (similar to the exponential bursts), followed by reactivity insertion or removal at rates required to produce the desired burst shape. A shaped power burst of this type, providing a 1000-MW flattop pulse for approximately 2 s, was utilized for a nuclear powered laser experiment at TREAT. The thermal neutron flux at the experiment during this shaped power burst was approximately 5×10^{19} neutrons-m^{-2}-s^{-1}.

Disadvantages of Using the TREAT Reactor for Nuclear Laser Experiments

Along with the advantages of using TREAT to support nuclear laser experiments there are, unfortunately, certain disadvantages associated with the facility. These include: (a) its large energy deposition relative to its peak power, and (b) its low duty cycle.

TREAT's large size and its dilute uranium oxide-graphite matrix results in a large amount of energy being deposited in the reactor core and in an experiment relative to the peak power available from the reactor primarily because the neutron lifetime is greater in this fuel mix compared to most other pulse reactors. This large energy deposition can influence the design of an experiment placed in the TREAT reactor in many ways. For instance, the experiment may require a flowing gas system to minimize any temperature effects in the test gas. The structural design and analyses, materials, and construction techniques applied to the experimental hardware may have to specifically address elevated temperature effects. Energy deposition from the fission process can increase gas temperatures in a non-flowing system to as high as several thousand K. The thermodynamic and laser kinetic stability of the test gas can be significantly affected at these high temperatures. On the other hand, the gas temperature rise in a flowing system may only be several hundred K. The addition of a flowing gas delivery system significantly adds to the complexity of the experiment and, therefore, to its cost. However, many of the final applications of the NPL concept will require a flowing gas delivery system anyway. Therefore, the necessity of such a system in an experimental program at TREAT can be an advantage with respect to future applications and scalability.

During a typical full power TREAT transient, direct nuclear heating from the reactor can increase the test vehicle's temperature by as much as 25 K, if it is made of aluminum, and

by as much as 40 K, if it is made of stainless steel. This increase alone is not excessive. A greater concern for thermal effects on experimental hardware is the slow overall rate of heat removal from the core by the air cooling. As a result of this slow heat removal, the temperature of the reactor core equilibrates at approximately 700 K before it begins to cool. Since the test vehicle resides in this large heat source, it too will increase in temperature after the reactor pulse is completed unless it is adequately cooled and insulated from the reactor heat source. All heat transfer paths must be well analyzed to make certain that the experimental hardware does not exceed its temperature limitations during this posttest period.

This slow heat removal also limits the number of full power transients to only one a day. This low duty cycle can be a disadvantage in some experimental programs although in complex systems, similar to those previously tested at TREAT, the reactor's duty cycle is generally not the critical path item in the experiment's schedule.

Enhancements to the TREAT Reactor

For the upcoming TREAT NPL experiment (see Figure 6), enhancing the reactor performance beyond its baseline operating conditions was highly desirable in order to improve the experiment's chances of success. As noted, it is the peak power and not integrated power that is of interest to most NPL experiments. Ultimately, it is the power deposited into the experiment that is important; this is related to the total reactor power by the power coupling factor (pcf), defined as test fission power per gram U-235 per MW of TREAT reactor power. Thus, there are two ways to enhance the power to a given test: (1) increase the TREAT reactor power and (2) increase the pcf.

The obvious way to enhance the power to a given test is to increase the TREAT reactor power. The initiating reactivity for a natural burst transient is the parameter that governs the peak power. In most cases in TREAT, the initiating reactivity must be held below the available reactivity, thus limiting the peak power, in order to assure that the final reactor fuel temperature does not exceed specified safety limits. The peak power scales with the square of the initiating reactivity while the final reactor fuel temperature is linear with the initiating reactivity. This opens the possibility of obtaining significantly higher peak powers in TREAT by modest increases of the allowable reactor fuel temperature. At the present time, transients are limited such that a final temperature of 723 to 773 K is obtained with a transient of 16,000 MW, while the actual safety limit is 1093 K (a high degree of conservatism). For example, a recent full power transient had a final temperature of 733 K. The power could be doubled if the final temperature were allowed to be increased to 1023 K, which is still below the safety limit. Enhancing the peak power of the reactor and thus increasing the power to the experiment by approaching the temperature safety limit is technically feasible, but it may not be practical in today's reactor operations environment. At a minimum, it would require a great deal of safety analyses and administrative approvals.

The power to an experiment can be increased without increasing the reactor power by increasing the pcf. The pcf is influenced by both the material and geometrical composition of the experiment. For a typical TREAT experiment involving fuel pins or large loops, the pcf will be much lower than the baseline value (as determined in a voided fuel element location in the center of the core) because significant amounts of structural materials (typically stainless steel) are necessary to provide containment of the fuel. However, the same level of containment is not needed for NPL experiments because of the small amounts of fissile material involved. Thus, aluminum or Zircaloy become viable as containment materials and pcf values approaching the void value are easily attained.

The TREAT neutron spectrum is not well thermalized. Thus, introducing a neutron moderator to an experiment can produce fairly significant increases in the pcf. For example, if stainless steel is needed as an experiment containment (thereby severely depressing the pcf), an increase in the pcf of over 200% is possible by surrounding the test hardware with a 3.6-cm layer of polyethylene (inside the containment). With an aluminum containment, the increase is only 70%. A disadvantage of using a hydrogenous material is that hydrogen is a reactivity poison in TREAT. For tests in which excess reactivity is marginal, graphite can be used instead of hydrogen as a moderator.

An example of the enhancement of the pcf is provided in the design change which was made for the upcoming (FY-1989) TREAT NPL experiment. Originally, the configuration for the FY-1989 TREAT NPL experiment was as shown in Figure 9. This original rectangular configuration was developed to minimize the amount of fuel removed from the center of the reactor in order to maintain an acceptable amount of excess reactivity for reactor operations. As shown on the left side of Figure 10, this configuration required the removal of seven fuel assemblies for the test vehicle and the replacement of twelve full fuel assemblies with slotted fuel assemblies for viewing access. In addition, fourteen fuel assemblies were replaced with dummy graphite-filled fuel assemblies to act as a thermal buffer. This rectan-

gular configuration required thick, flat plate walls which were not only difficult to fabricate and assemble to strict tolerances but also significantly lowered the pcf.

Detailed nuclear analyses of this configuration revealed two things. The excess reactivity available was significantly greater than the allowable pulse initiating reactivity. Furthermore, the replacement of fuel assemblies with dummy graphite-filled fuel assemblies enhanced the power to the experiment by increasing the pcf. This led us to explore whether adequate excess reactivity could be maintained while moving fuel from a higher reactivity value region to a lower reactivity value region. It would be possible to insert a cylindrical test vehicle, partially filled with graphite, into the TREAT reactor if a 5 x 5 array of fuel assemblies at the core center was removed. In addition, by slightly reducing the diameter of the test vehicle, four fuel assemblies could be placed in the corners of the array and four graphite-filled moderator blocks could be attached to the outside of the test vehicle. This cylindrical vehicle (shown previously in Figure 6 and in cross-section on the right hand side of Figure 10) would permit more moderator around and in the experiment, would be much less expensive since the walls could be thinner, would be much simpler to fabricate, and, in fact, requires only slightly more fuel be removed from the core than for the rectangular configuration.

Detailed nuclear analyses of this cylindrical configuration revealed that, although there was a decrease in excess reactivity as compared with the rectangular geometry, there should still be sufficient excess reactivity for a full power burst. More significantly, the pcf was increased by both the increased amount of graphite and thinner vessel walls to result in greater power to the experiment. The comparison is a pcf of 143 watts/g-U-235/Mw TREAT power for the rectangular geometry versus a calculated pcf of 190 watts/g-U-235/Mw of TREAT power for the cylindrical geometry.

A bonus with this change was the cost of the experiment. Although the graphite replacement elements outside and inside the test vehicle are not readily available standard dummy graphite-filled fuel assemblies and have to be especially fabricated, the overall cost of the experimental hardware was significantly reduced.

Conclusions

The TREAT reactor is a large, air-cooled test facility originally designed to evaluate reactor fuels and structural materials under conditions simulating various types of nuclear excursions and transient undercooling situations. It is, as stated, also extremely well suited to support certain types of nuclear laser experiments. Two of the major design features of TREAT -- its large size and its being an air-cooled reactor -- provide the clues to most of its advantages and disadvantages for supporting nuclear laser experiments. Its large size permits accommodation of geometrically large experiments, but also results in relatively long transients so that the energy deposited in an experiment is large relative to the peak power. The fact that TREAT is air cooled allows its configuration to be changed fairly readily. Not only can individual fuel elements be removed to admit a large test article but, perhaps more importantly, special slotted elements can be installed in line with removable shield plugs to provide line-of-sight access through the reactor. For the same reason -- air cooling -- the reactor cools down slowly, permitting only one full power transient a day which can be a disadvantage in some experimental programs. Also because of its slow air cooled mode of operation, experiments performed at, or near, full power in TREAT may require a flowing gas system to minimize any temperature effects in the test gas. Energy deposition from the fission process can increase gas temperatures in a non-flowing system to as high as several thousand K. The thermodynamic and laser kinetic stability of the test gas can be significantly affected at these high temperatures. On the other hand, the gas temperature rise in a flowing system may only be several hundred K. The addition of a flowing gas delivery system significantly adds to the complexity of the experiment and, therefore, to its cost.

In addition to those more significant advantages and disadvantages, the reactor is capable of either steady-state or transient operation. This operating flexibility can be extremely useful in many experimental programs.

In summary, TREAT is a facility which permits a large experiment size and offers flexibility of configuration, access, and operating characteristics, but it has a large energy-to-power ratio and a low duty cycle. This large energy-to-power ratio may require that a costly and complex gas delivery system be included in the NPL experimental program to be performed at TREAT. However, it is generally believed many of the final applications of the nuclear powered laser will themselves require a flowing gas delivery system. Therefore, the necessity of such a system in an experimental program at TREAT can be deemed an advantage with respect to future applications and scalability.
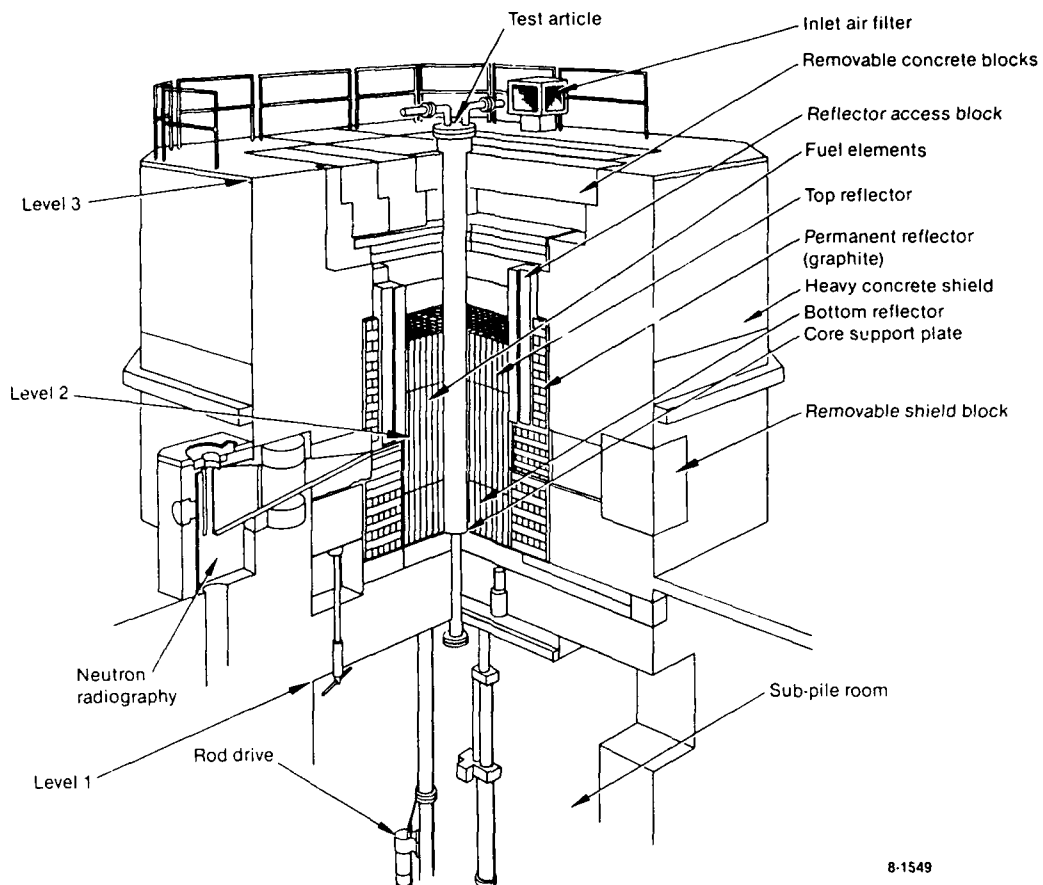
Figure 1. Cutaway view of the TREAT reactor.

Figure 2. Map of Idaho showing the location of the INEL.
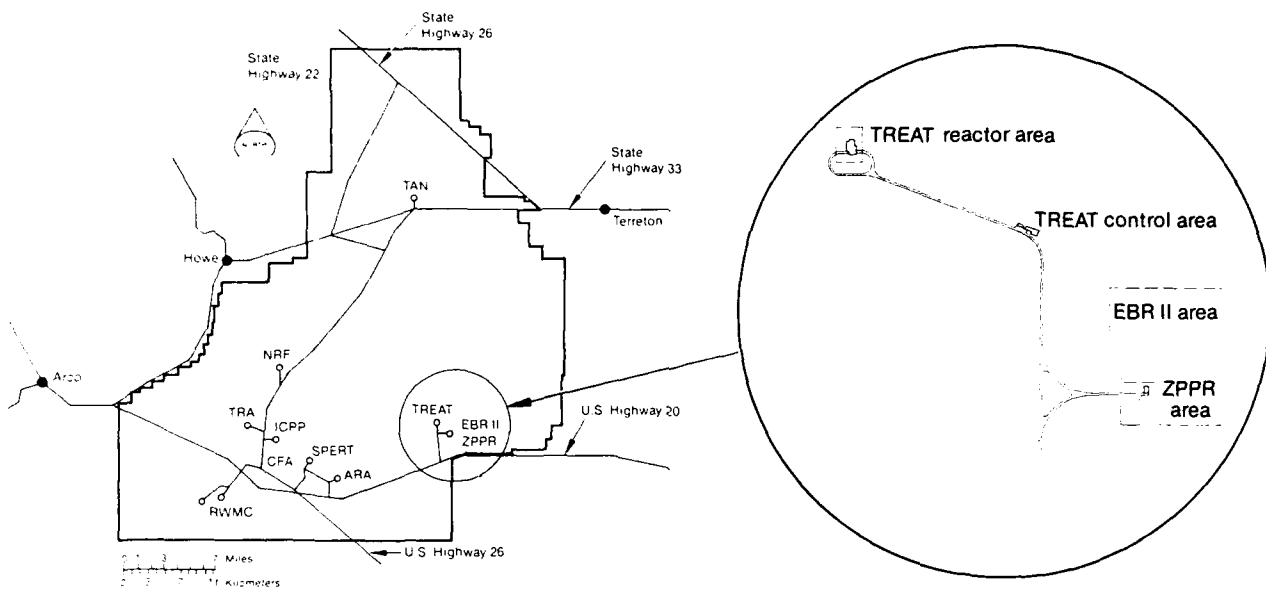
Figure 3. INEL site map showing location of the TREAT reactor.
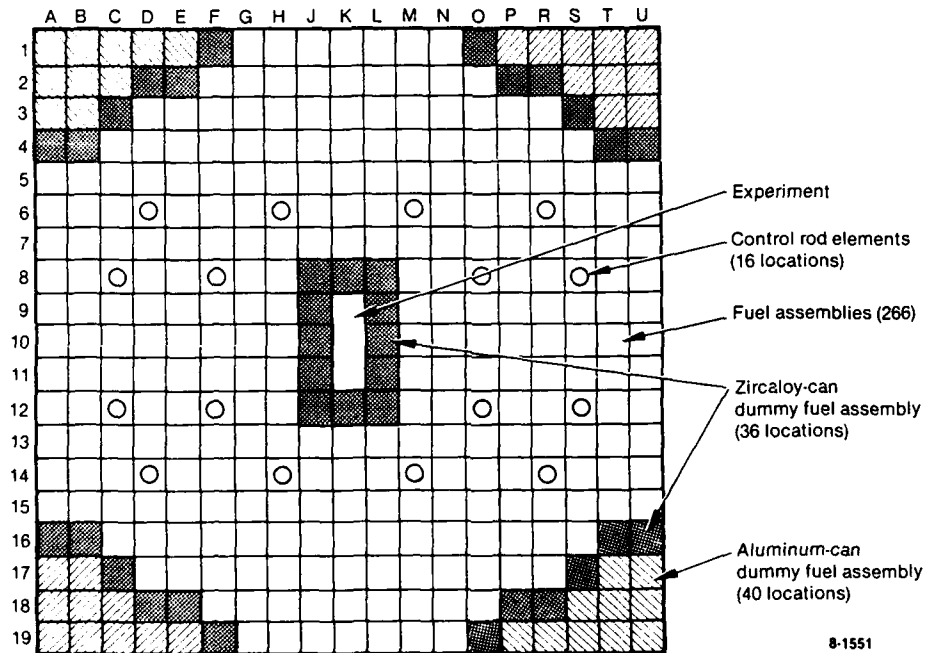
Figure 4. TREAT core configuration for an early NPL experiment.
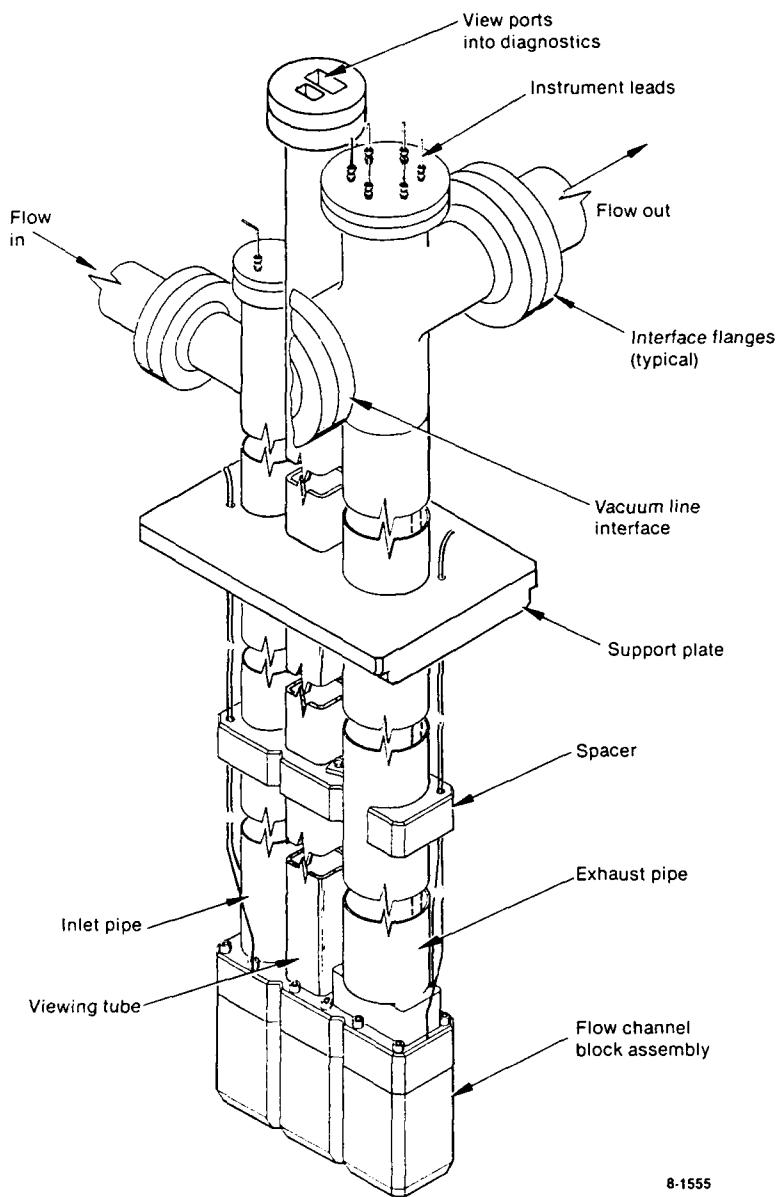
Figure 5.   Isometric view of an early NPL experiment performed in TREAT.
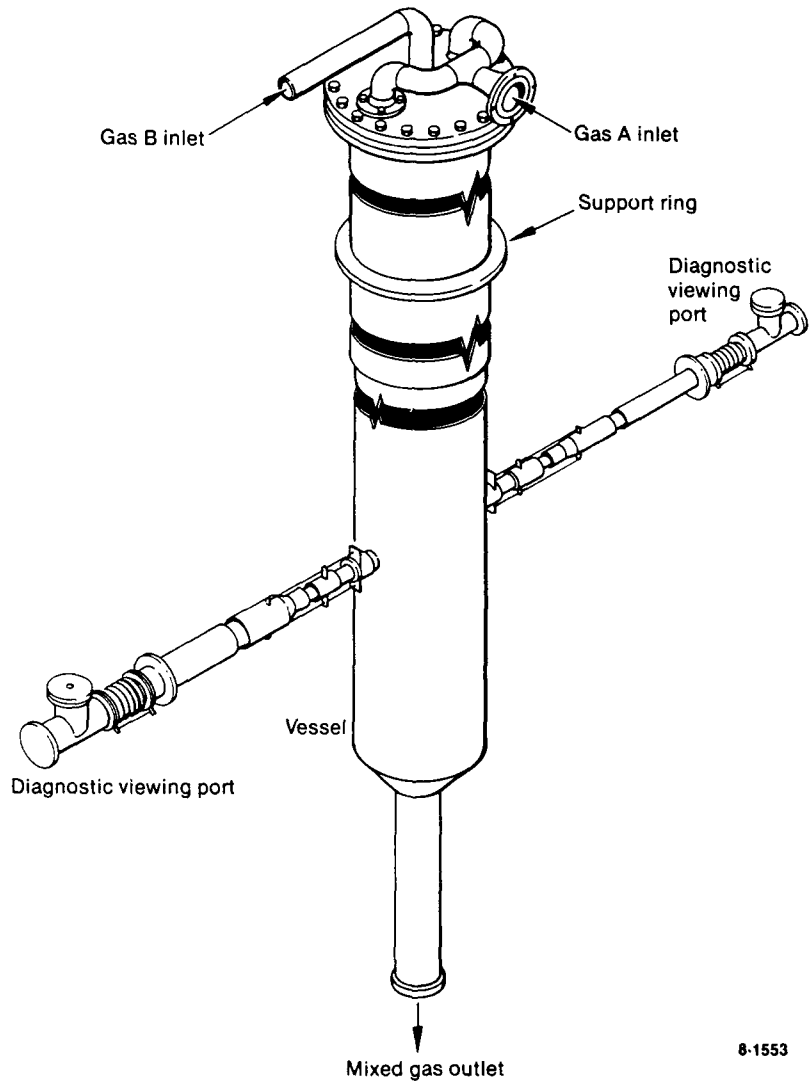
Figure 6. Isometric view of a future NPL experiment to be
performed in TREAT.

233
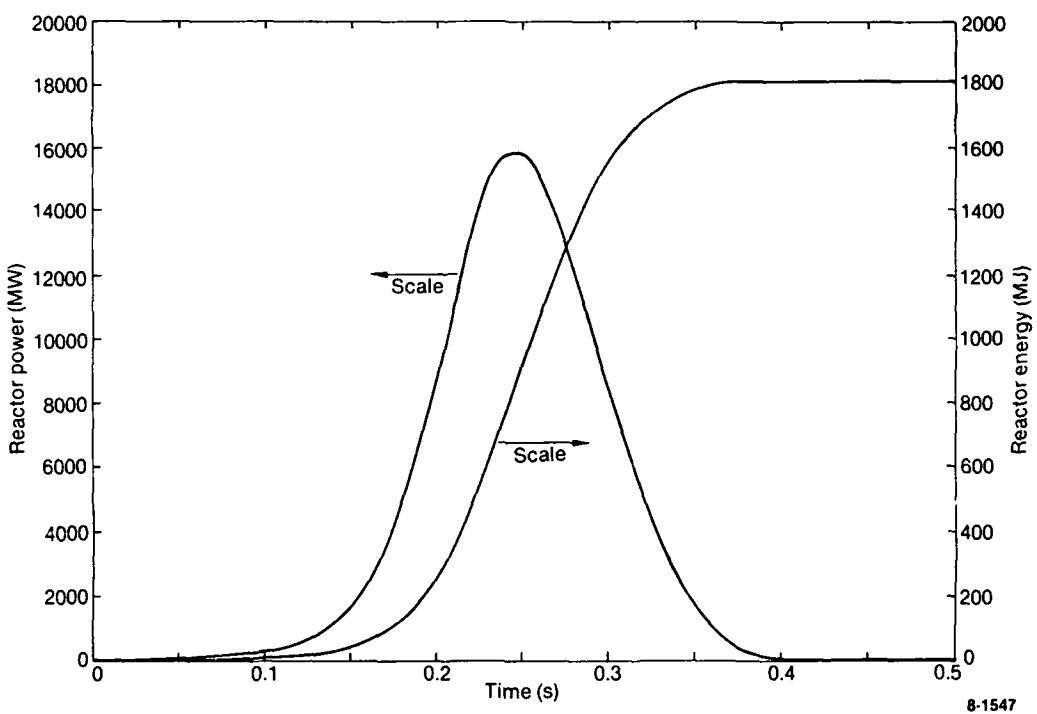
Figure 7. Reactor power and energy for a typical TREAT exponential burst transient.
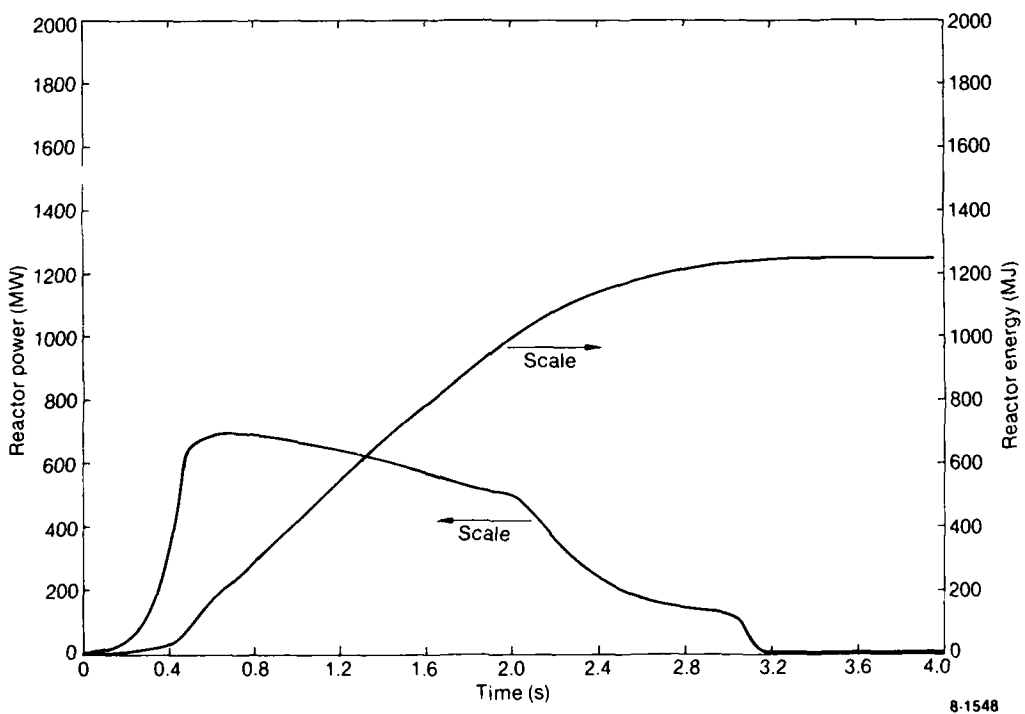
Figure 8. Reactor power and energy for a typical TREAT shaped transient.
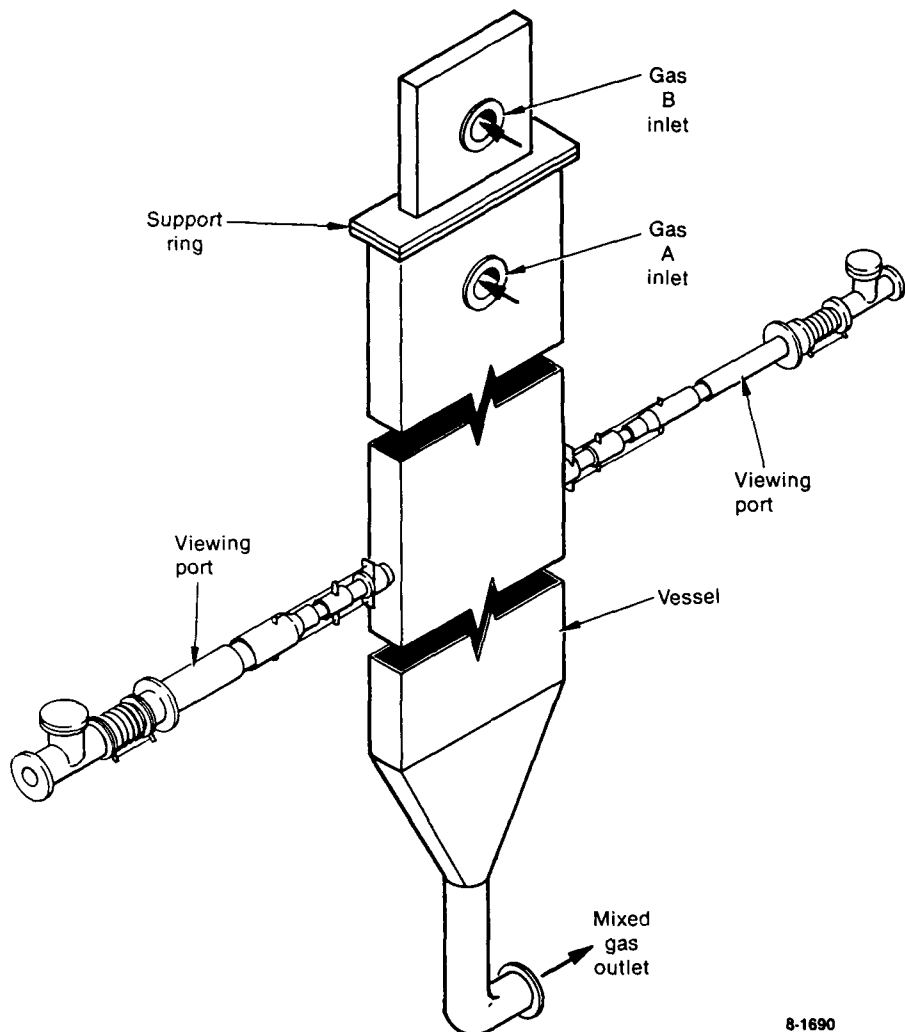
Figure 9. Original configuration of future NPL experiment.
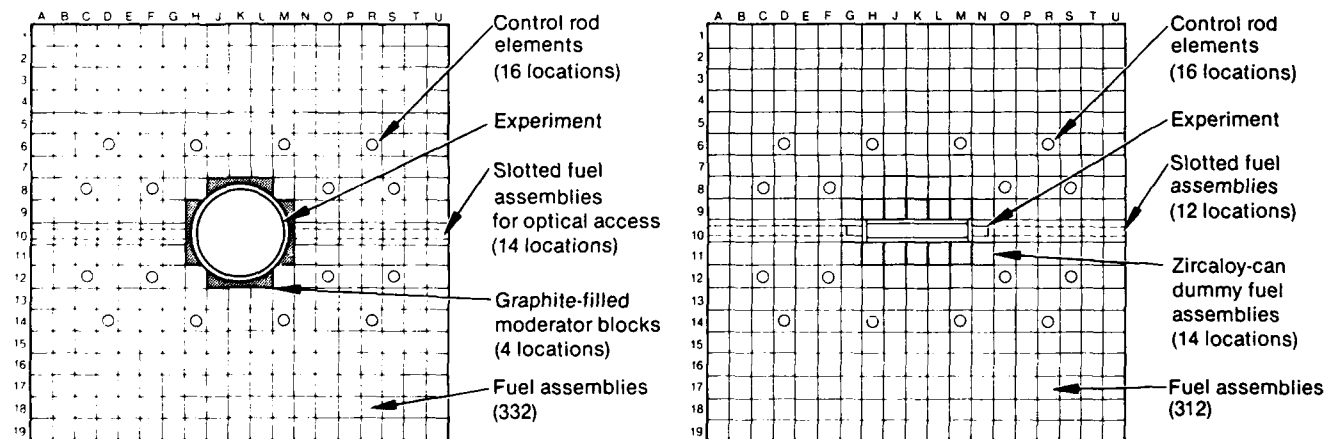
Figure 10. TREAT core configuration for original version
of future NPL experiment.

NUCLEAR-PUMPED LASERS FOR LARGE-SCALE APPLICATIONS

R.E. Anderson, E.M. Leonard, R.F. Shea, and R.R. Berggren
Los Alamos National Laboratory
Los Alamos, New Mexico 87545 USA

ABSTRACT

Efficient initiation of large-volume chemical lasers may be achieved by neutron induced reactions which produce charged particles in the final state. When a burst mode nuclear reactor is used as the neutron source, both a sufficiently intense neutron flux and a sufficiently short initiation pulse may be possible. Proof-of-principle experiments are planned to demonstrate lasing in a direct nuclear-pumped large-volume system; to study the effects of various neutron absorbing materials on laser performance; to study the effects of long initiation pulse lengths; to demonstrate the performance of large-scale optics and the beam quality that may be obtained; and to assess the performance of alternative designs of burst systems that increase the neutron output and burst repetition rate.

Introduction

There has been considerable interest, both in the past[1] and more recently[2,3] in the issue of nuclear pumping of gas laser media. Two characteristics of a nuclear reactor that have fueled this interest are the high-energy output that is coupled with a relatively small, self-contained system. These features provide mechanisms for overcoming the restrictions imposed by volume, weight, or maintenance-limited systems. The long mean-free paths associated with uncharged particles such as the neutron also provide a convenient mechanism for pumping large-volume gas systems.

We have been interested in the possibility of using neutrons to initiate a DF-CO_2 transfer laser. This type of chemical laser has an inherent advantage over excimer lasers, because the output energy arises as a result of chemical reactions among the constituents of the laser medium rather than as a result of the energy supplied by an external pumping device. In the DF-CO_2 laser, the neutron pump only provides sufficient energy to initiate the chemical reaction chain. The laser may then produce an output energy approximately ten times larger than that supplied by the pump, compared to a conventional system which might produce an output energy equal to a few percent of the pump energy.

In the reactor pumping concept, neutrons produced by the reactor are absorbed by a nucleus within the lasing medium. The nucleus then undergoes a reaction that produces highly energetic charged particles, which deposit energy in the laser gas. This is similar to the process in an electron-beam-pumped laser.

To accomplish this process most efficiently, the nuclei that dope the laser must have a large absorption cross section for low-energy neutrons, a large positive q-value for the nuclear reaction, and must not substantially perturb the operation of the laser. It would also be advantageous if the species of interest were to exist in a gaseous form. Several candidates that have received considerable attention in the literature[1-3] are ^{3}He, ^{6}Li, ^{10}B, and ^{235}U. The relevant properties of these isotopes are listed in Table I. The quantities of these nuclei that must be present vary considerably, depending on the energy release per absorption event, as discussed in Sec. V. For example, uranium hexafluoride needs to be present only in very small quantities. The addition of any of these species raises complex questions regarding its effect on the laser kinetics. For some species (such as ^{3}He), we have enough information to predict DF-CO_2 laser operation if a quantity of ^{3}He were added to the gas mixture.

TABLE I. PROPERTIES OF LASER ADDITIVES			
Isotope	Thermal Cross Section	Energy Release	Availability
^{3}He	5300 b	0.76 MeV	gas
^{6}Li	950 b	4.8 MeV	---
^{10}B	3800 b	2.3 MeV	gas
^{235}U	580 b	170. MeV	gas

Effect of Helium on Laser Kinetics

Detailed studies have been performed on photolytically initiated and, more recently, on e-beam initiated DF-CO_2 transfer lasers. Recent unpublished experiments on these systems have shown that weakly initiated systems can provide reasonable energy extraction (~30 J/l) with lasing pulses (on-time to off-time) longer than 50 μsec.[4] We will use the parameter space investigated by these experiments as a point

of departure. Therefore we will fix the total operating pressure at 1 atm and the gas composition as shown in Table II. For neutron initiation we will replace 10% - 50% of the argon buffer gas with ^{3}He.

| TABLE II. GAS COMPOSITION FOR DF-CO$_2$ LASER ||
Components	Pressure (torr)
Buffer (argon)	664
F$_2$	45
D$_2$	15
CO$_2$	35
O$_2$	1
Total pressure	760

The basic kinetics of the system are straightforward. The laser is initiated by producing free F-atoms that set off the D$_2$,F$_2$ chain:

$$F + D_2 \rightarrow DF(v) + D$$
$$D + F_2 \rightarrow DF(v) + F$$
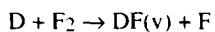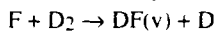
The vibrational energy in DF may then be transferred to CO$_2$,

$$DF(v) + CO_2(000) \rightarrow DF(v-1) + CO_2(001) \ ,$$

which lases at 10.6 μ:

$$CO_2(001) \rightarrow CO_2(100) + h\nu(10.6\ \mu)$$
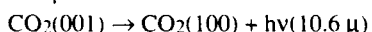
The production of free F-atoms in these devices is most conveniently provided by photolysis of F$_2$:

$$F_2 + h\nu(280\ \mu) \rightarrow F + F$$
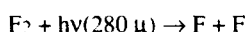
An e-beam may also be used to provide free F-atoms in the Ar, F$_2$ mixture. Since neutron absorption and subsequent fission of ^{3}He produces energetic charged particles, the neutron initiated system acts very much like e-beam initiation.

The system is clearly unstable: any inadvertent production of F-atoms (such as that due to fluorescent lamps) could cause the laser to fire. Pre-ignition is prevented by the addition of a "chain breaker" that acts to remove free F and D atoms. The chain breaker also sets the threshold, which the pump must exceed to fire the laser. The laboratory experiments mentioned above have used 1-2 torr of O$_2$ for this purpose.

In the transfer system there are only a few reactions where the buffer gas plays a major role. These processes are listed below.

$CO_2(001) + M \rightarrow CO_2(030) + M$	(1)
$CO_2(010) + M \rightarrow CO_2(000) + M$	(2)
$DF(v) + M \rightarrow DF(v-1) + M$	(3)
$D + O_2 + M \rightarrow DO_2 + M$	(4)
$F + O_2 + M \rightarrow FO_2 + M$	(5)

In Table III we give rate constants for the first three of these processes at representative temperatures and with M as either argon or helium. We have used the CO$_2$ rate constants recommended by Feber and Sullivan[5] and the DF rates recommended by Cohen and Bott.[6]

Reaction 4 has the same rate[7] with either M = Ar or M = He. No data exist on Reaction 5 with helium as a third body, and we have assumed the same rate for both helium and argon.

Because of the rapid deactivation rate of the CO$_2$ bending mode by helium (Reaction 2), most CO$_2$ lasers use it as a buffer gas. All three reports of e-beam-initiated DF-CO$_2$ lasers in the literature used helium[8-10]. Our system, however, operates with much longer lasing pulses (>50 μs), making deactivation of the bending mode less critical. Performance limitations on the long pulse DF-CO$_2$ laser are more dependent upon quenching of the upper laser level, where argon and helium have comparable rates.

To arrive at a quantitative comparison, we have used a computer model to calculate laser performance with argon and helium as buffers. Our model contains approximately 200 reactions and over 40 different species or vibrational states. The kinetics of F-atom production are treated phenomenologically: we input a source term that describes the energy deposited per cubic centimeter per second into the gas, and we assume that one F-atom was produced for every 5 eV deposited in the gas, regardless of whether the buffer was helium or argon (Sec. IV explores this issue). Our results showed that with the use of helium, the laser specific energy increased by 17% and pulse length shortened by about 0.7%.

A reactor-driven laser, however, will use ^{3}He and not ^{4}He, as discussed above. Because both species have nearly identical electronic structures, the isotopic substitution should have little effect on the cross sections for kinetic processes. In fact, measured cross sections for

deactivating $CO_2(001)$ by ^{3}He and ^{4}He do exist and are identical.[11] Bimolecular kinetic rates, however, depend on a cross section and a collision frequency. The latter varies inversely with the square root of the reduced mass. For ^{3}He interacting with CO_2 or DF, there is a net increase in the rate by 13% or 14%, respectively. The scaling of three body rates is somewhat ambiguous and depends on the model chosen. A simple-minded approach leads to increases in the rates for Reactions (4) and (5) of only 7%.

TABLE III. COMPARISON OF KINETIC RATES INVOLVING ARGON AND HELIUM				
Reaction	M	k(300)	k(600)	K(800)
$CO_2(001) + M$	Ar	1.56×10^{-15}	1.72×10^{-14}	5.11×10^{-14}
	He	2.30×10^{-15}	1.86×10^{-14}	5.69×10^{-14}
$CO_2(010) + M$	Ar	9.33×10^{-16}	1.63×10^{-14}	4.46×10^{-14}
	He	1.17×10^{-13}	8.29×10^{-13}	1.65×10^{-12}
$DF(1) + M$	Ar*	3.73×10^{-18}	8.43×10^{-17}	3.08×10^{-16}
	He*	5.82×10^{-18}	1.32×10^{-16}	4.81×10^{-16}

* Rates for higher DF-levels scale as $V^{1.9}$ for both helium and argon.

Incorporating the above changes in kinetic rates to account for ^{3}He, we repeated our previous calculation. The increases in the rate constants decreased specific power by 2.5% and shortened pulse length by 0.5%. The net effect is that the DF-CO_2 laser using ^{3}He should out-perform an argon-based system.

By-products of the nuclear reaction may have another effect on the kinetics. The reaction: $n + {}^3He \rightarrow {}^1H^+ + {}^3He^+ + 2e$ yields a proton and a triton at energies of 0.57 MeV and 0.19 MeV, respectively. Assuming both these species eventually pick up an electron, we have the possibility of reactions with F_2 to produce HF and TF in various vibrational states. Both HF-CO_2 and TF-CO_2 have lased but have not performed as well as DF-CO_2 lasers.[12,13] If we assume that the nuclear reaction deposits a total of 3 mJ/cm^3 in the gas, we can readily calculate from the numbers given above that the densities of TF and HF will be on the order of 10^{10}/cm^3. Because this is significantly below the level of DF densities encountered, both species will have little effect on laser performance.

Effect of Reactor Pulse Shape on Laser Performance

Historically, DF-CO_2 lasers have been initiated with flashlamps or an e-beam operating for, at most, a few microseconds. This is much shorter than the neutron pulse from the Los Alamos burst reactors: GODIVA (FWHM of 30 µs) and SKUA (FWHM of up to 400 µs). If the energy deposited (i.e., the total number of F-atoms produced) is kept constant but the initiation pulse is lengthened, fewer F-atoms are present at any one time to drive the chemistry. In this section we will examine the effect of initiation pulse length on laser performance.

We have estimated the total neutron fluence with the Los Alamos Monte Carlo code MCNP[14], based on a total of 5 x 10^{16} fissions for GODIVA and 3 x 10^{17} fissions for SKUA. Some aspects of the design were adjusted to attempt to make the energy deposition uniform throughout the laser. With 61 torr of ^{3}He in the laser, the neutrons can deposit about 3 mJ/cm^3 in the gas. As before, we assumed that one F-atom was produced for every 5 eV deposited in the gas. The gas mixture is given in Table I.

Our results are summarized in Figs. 1 and 2. Specific energy has been normalized for simplicity. We note that short initiation pulses (30 µs FWHM) yield higher specific energies and shorter lasing pulses. As the initiation pulse broadens, the laser energy drops, and its pulse length becomes very long. (Laser pulse length as described in this document is measured from the onset of lasing to termination. Generally it is much longer than the FWHM of the lasing pulse.) A close examination of the shape of the laser output flux reveals a long gradual tail followed by a dramatic rise and abrupt termination. With very long initiation pulses, the lasing terminates at about the time that the neutron flux peaks.

Increasing the concentration of ^{3}He in these calculations has the effect of increasing energy deposition and more strongly initiating the laser. We have repeated our calculations for the 400-µs initiation pulse with 332 torr of ^{3}He instead of the 61 torr considered previously. Though this raises the total energy deposition by a factor of 5.4, it yields only a 28% increase in specific energy and a 56% decrease in pulse length. This effect is much less pronounced than might be expected. Despite the large total energy deposition, the pulse length is so long that few F-atoms are available at any one time to drive the chemistry.

Effect of Helium on F-atom Production

Dissociation of F_2 to produce free fluorine atoms and to initiate the chemistry of the transfer system can be accomplished either by UV-photolysis or an e-beam. The photolysis processes are straightforward: F_2 absorbs a photon and is excited to a repulsive state. The e-beam initiation is considerably more complex: high-energy electrons deposit their energy in the rare gas and produce metastable atoms, ions, and free electrons. A series of reactions of these species with F_2 generates the free F-atoms. The efficiency of this process is measured by the number of electron volts that must be deposited in the medium to create an F-atom. In previous sections of this report we have

assumed a nominal value of 5 eV/F-atom. If this number is significantly higher for the reactor-based system, higher neutron fluxes will be required to generate the same level of initiation.
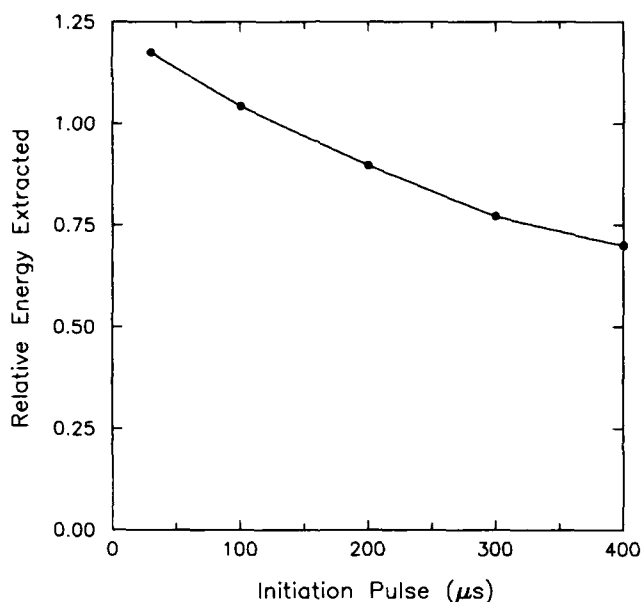
Fig. 1. Efficiency of energy extraction as a function of initiation pulse length. Total energy deposited was the same for all calculations.
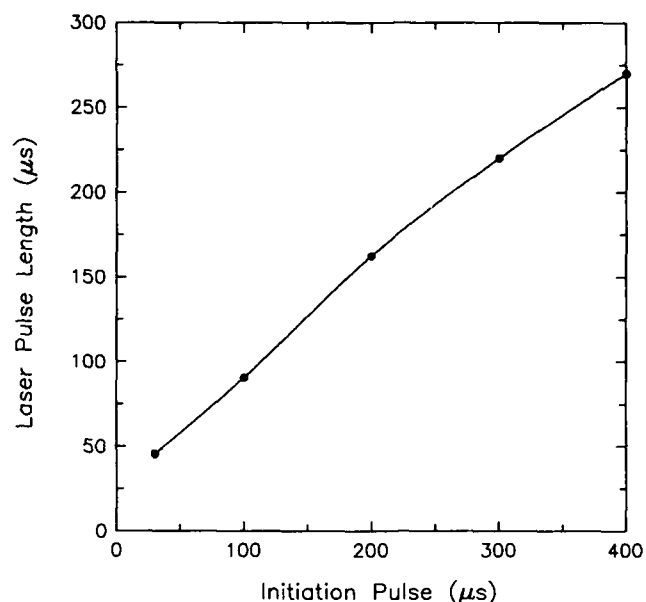
Fig. 2. Laser pulse length as a function of initiation pulse length.

The basic difference between the e-beam and reactor-pumped lasers is the replacement of argon by ^{3}He. To better understand how this affects F-atom production, we need to discuss e-beam initiation in more detail. In the following we will consider a laser volume containing mainly the rare gas and small amounts of F_2.

As mentioned above, the high-energy electrons create argon ions, argon metastables, and secondary electrons. Low-energy electrons can very rapidly attach themselves to F_2 and produce a free F and a free F^-. Argon ions attach themselves to the F^- to produce ArF*. This excimer is also produced by the reaction of F_2 with argon metastables. The ArF* will eventually react with F_2 and produce three free F-atoms. Approximately 80% of the free F produced in the Ar-F_2 mixture comes from the reaction of ArF* and F_2. In a He-F_2 mixture things are very different: the excimer HeF* is not bound, and this major channel in producing F-atoms will be cut off.

In He-F_2 mixtures the major channel to F-atom production comes through F_2^+. This species can be created either by charge exchange with helium ions or by Penning ionization with helium metastables. The F_2^+ then combines with F^- to produce three F-atoms. In mixtures containing He, F_2, and Ar, all the processes described above take place with charge exchange between helium ions and argon, as well as Penning ionization of argon by helium metastables.

We have used the model of Wilson and Shapiro[15] to make quantitative comparisons of F-atom production in He, Ar, and F_2 mixtures. This model incorporates a total of 18 species and 45 reactions. By making the major assumption that all electrons are instantly thermalized, we eliminate the need to include a Boltzmann analysis. Source terms that drive the kinetics come from the reaction of neutrons with ^{3}He.

For the reactor-initiated laser, we want to compare F-atom production in various He, Ar, and F_2 mixtures, with F-atom production in the e-beam-initiated Ar and F_2 mixture. By slightly modifying the Wilson and Shapiro model to treat an e-beam-driven Ar and F_2 mixture, we can calculate a base-line number for F-atom production in argon. This analysis yields a value of 5.2 eV/F-atom, which is slightly higher than the approximate value of 5 eV/F-atom used earlier. Losses of ArF* through radiation and collisional dissociation with argon account for much of the difference.

We used the 5.2-eV/F-atom value to normalize our results for argon and helium mixes. Figure 3 reports the relative initiation strength needed for the same F-atom density in various mixtures. The total buffer gas pressure (He + Ar) was fixed at 715 torr for these calculations. Though more energy deposition is required in pure helium than in pure argon, a few hundred torr of argon makes the F-atom production close to what it would be if only argon were present. Our calculations ignore a number of small contributions, and we have dropped the F-atom recombination process[15] that artificially inflates the eV/F-atom number. In an actual laser, the F-atoms will be removed by reaction with D_2 much more quickly than they can recombine.

Burrows[16] has pointed out the additional processes that can occur when D_2 and CO_2 are included in Ar-F_2 mixtures. The presence of helium metastables and ions further complicates the kinetics. Of major importance is the very rapid (k~10^{-9}) reaction between helium ions and CO_2 to produce O^+, CO, CO^+, and O.[16] The reaction between helium ions and D_2 is slow and can be ignored[17] Reaction rates for helium metastables with CO_2 and D_2 have been measured.[18] In the case of D_2, the products are also known (mainly D_2^+).[19] Because both

239

helium ions and metastables are very effective in producing F_2^+, these additional processes lower the production of F_2^+ and create instead D_2^+, CO_2^+, O^+, and CO^+. The most likely fate of these ions is reaction with the excess F^- that will be present. Unfortunately, there are no measured rates for processes such as these.

Fig. 3. Relative amounts of energy needed to produce one F-atom as a function of argon concentration. The total pressure is 715 torr, and the gas is composed of helium and argon. The results are normalized to one (~5 eV/F-atom) for a pure argon system.
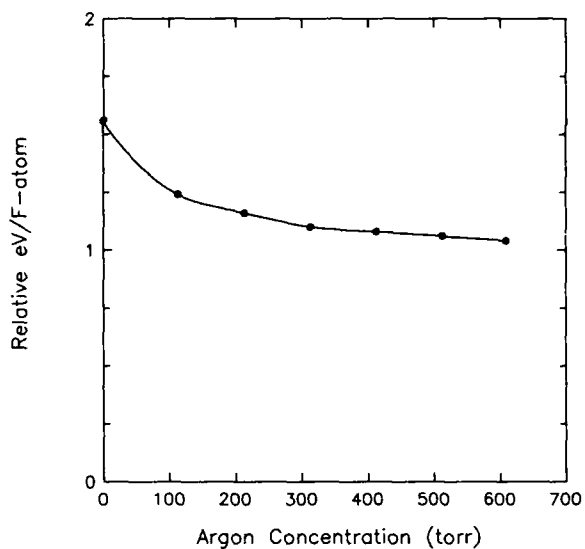
In view of the uncertainties, we can make no prediction for the efficiency of F-atom production in actual laser mixtures (Ar, He, F_2, D_2, and CO_2). Our earlier analysis (Figs. 1 and 2) was based on 61 Torr of ^{3}He in the gas, an energy deposition of 3.0 mJ/cm^3, and an assumed value of one F-atom produced for every 5 eV deposited in the gas. If, however, it were to take 10 eV to produce one F-atom, we need only increase the ^{3}He concentration to achieve the same level of initiation from the same reactor flux. This indicates that we have some leeway in achieving a specific level of laser performance, even if we do not know the level of initiation. Because laser performance is very sensitive to the level of initiation (among other things), the impact will be in our ability to make a reliable prediction.

Burst Reactor Operation

Initiation pulses for the DF-CO_2 laser are provided by one of two Los Alamos burst reactor facilities: GODIVA[20] or SKUA[21].

Figure 4 shows the GODIVA assembly and controls. The fuel is a 1.5-wt % molybdenum-uranium alloy with ~93.5% enriched uranium. The fuel components are all aluminum-ion-plated and have a total mass of about 66 kg. Three external C-shaped clamps (3/4 in. thick by 1 and 3/4 in. in cross section), fabricated from high-strength maraging steel, fasten the stack of six stationary fuel rings.

Fig. 4. GODIVA assembly and controls.
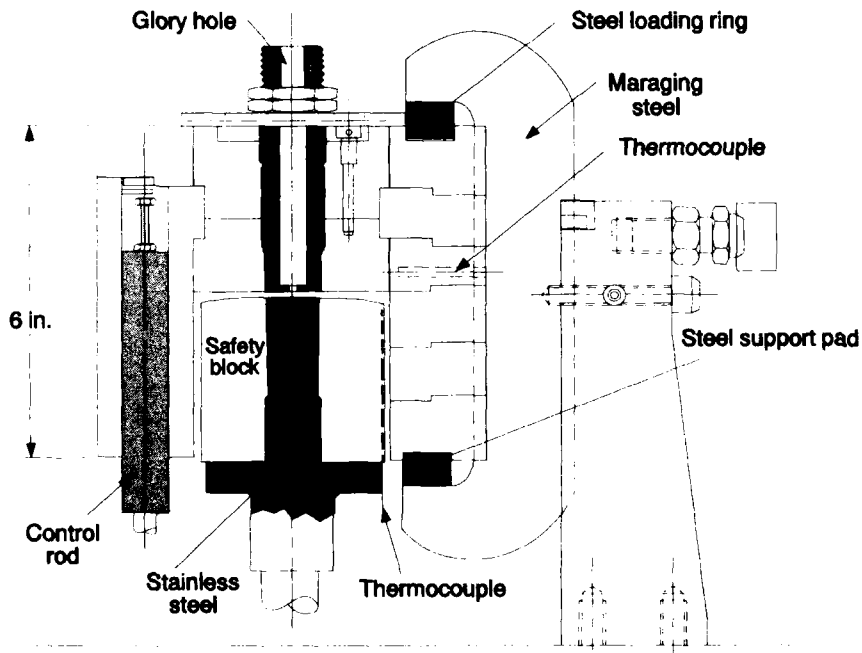
The burst assembly is supported on a three-legged structure that houses actuators for reactivity control elements, which enter the core from below. The safety block is threaded onto a stainless steel mandrel at the lower end, so that thermal expansion exerts a downward thrust on the support shaft, opening a magnetic clutch to provide shock-induced scramming. Total burst yield and burst width are plotted against reactor period in Fig. 5. Yield data and leakage flux per core fission have been obtained via foil activation and from aluminum (n,α) detectors.
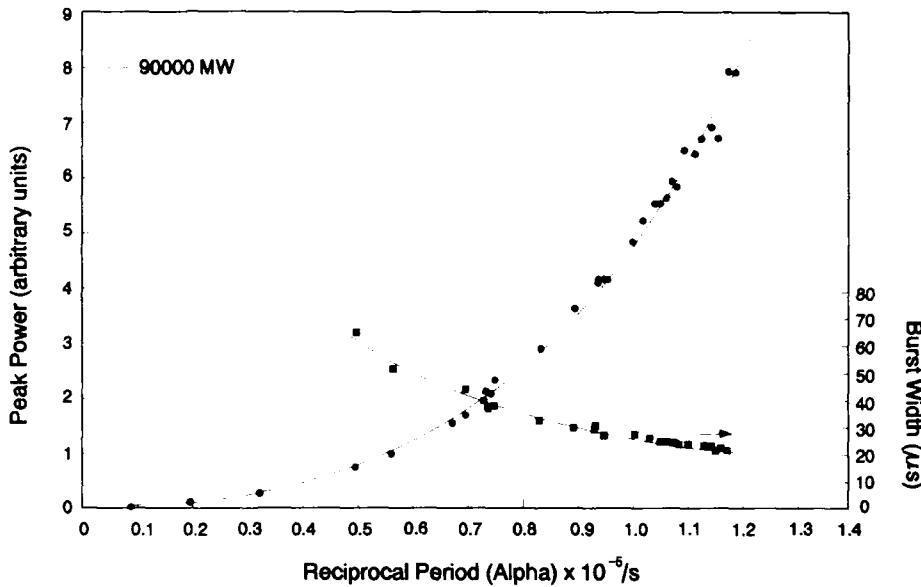
Fig. 5. Burst width and peak power of the GODIVA assembly plotted as a function of the reciprocal period. The dashed line is simply a guide for the eye. The solid curve has the functional form $P = (\alpha^2/2b\alpha_r)(1 + \alpha^2\tau^2)$, where b is the thermal quench rate of the device (about -0.2 c/°C), α_r is the Rossi alpha (about 0.86×10^6 sec^{-1}), and τ has been adjusted for best fit to a value of 8.9 µs.

Figure 6 shows a top view of the SKUA assembly. This 18-in.-diam cylindrical annulus, consisting of 170 kg of 93.5% enriched uranium, is controlled by six external copper reflector elements. A 9.5-in.-diam glory hole is available for experimental use. When a lower average-energy neutron spectrum is desired, a 3-in. annular flux trap with a 3-in. glory hole may be inserted. Though the SKUA assembly has not yet operated in the prompt critical regime, initial delayed critical operations have confirmed the SKUA design.
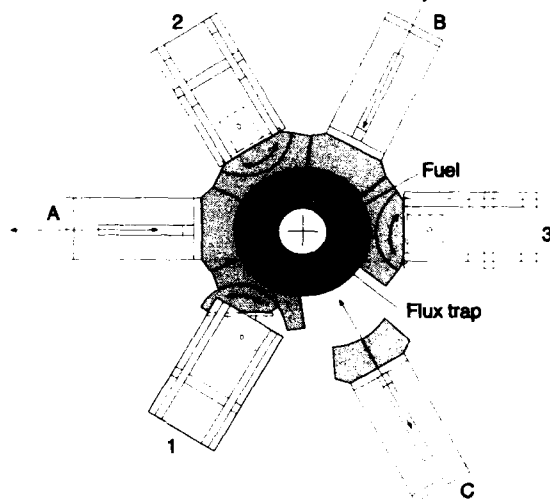
Fig. 6. Top view of the SKUA burst assembly.

No special cooling following bursts is envisioned for either assembly, even though temperatures as high as 300°C (for GODIVA) or 500°C (for SKUA) may be achieved. The cool-down time for these devices defines the burst repetition rates that can be achieved.

A wide variation in irradiation pulse characteristics is possible using these facilities. Fission yields of between 1×10^{16} and 3×10^{17}, with burst widths between 30 and 400 µs, are possible. Some of the burst properties of these two assemblies are summarized in Table IV; a typical short-burst pulse from the GODIVA assembly is shown in Fig. 7.

Because these assemblies produce primarily fast neutrons, a moderator is necessary to thermalize the neutrons that enter the laser volume. The assemblies are relatively small, and the laser can be placed quite close to the source, which increases the efficiency of the system. On the other hand, a large laser volume will not be uniformly pumped under these circumstances. Some regularization of the

241

neutron flux profile may be achieved by proper shaping of the moderator; however, this procedure produces some elongation of the initiation pulse length.

Energy deposition within the laser volume was estimated using the Los Alamos Monte Carlo code MCNP[14]. Estimates were made for both the GODIVA and SKUA assemblies for several different laser volumes. Continuous-energy cross-section sets were used in the calculations, and the results were collapsed into 16 to 50 groups for analysis. A typical geometric model used in the calculations is shown in Fig. 8. Average energy depositions for several replacements of the argon buffer gas are shown in Table V. According to these results, minimum requirements for the ignition energy were met, with considerable room left for variation of the exact fill gas composition. However, we still must show that any degradation of the laser kinetics remains at an acceptable level. Degradation could occur from the alteration of the fill-gas composition, nonuniformities in the pumping profile, or longer initiation pulses provided by the burst assembly.

Fig. 7. A typical fast initiation pulse from the GODIVA assembly.

Power (arbitrary)

► ◄ 35 μs FWHM

Time (20 μs/div)
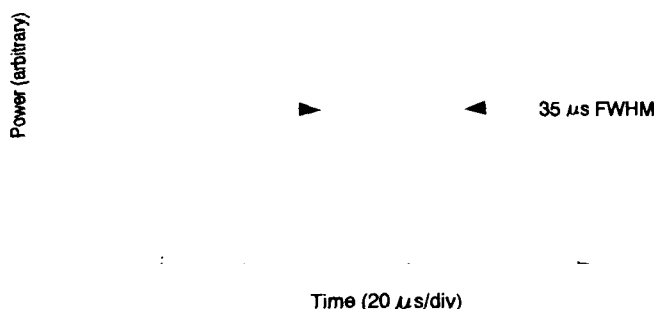
TABLE IV. COMPARISON OF BURST CHARACTERISTICS			
	Godiva IV	SKUA (est.)	LBR (est.)
Burst width (μs)	30	100-400	500-5000
Joules/burst	1.8×10^6	5.4×10^6	8.9×10^7
Leakage neutrons	8.9×10^{16}	2.7×10^{17}	3.0×10^{18}
Flux at 1 m (n/cm²-s)	2.4×10^{16}	5.3×10^{15}	4.8×10^{15}
Central fluence (n/cm²)	3.3×10^{14}	3.3×10^{14}	---
Average central flux (n/cm2-s) average	1.1×10^{19}	8.0×10^{17}	---
Peak	2.0×10^{19}	1.5×10^{18}	---

One of the objectives of the experimental program will be to study the characteristics of alternative types of burst systems that may be more suitable for use with a large-scale laser. Among the characteristics of such a system would be increased neutron output, increased burst repetition rate, and greater uniformity in the energy deposition within the laser volume. The size of the GODIVA and SKUA pulses is fundamentally limited by the mechanical stresses produced by thermal expansion of the fuel during the burst and, to a lesser extent, by the temperature rise in the fuel produced by the fission fragments. The pulse length is determined fundamentally by the physical size of the assembly.

Fig. 8. Geometric model for determining the energy deposition within the laser during a typical burst from SKUA. The laser has been segmented to study the space and time profiles of the initiation pulse.

Moderator

Laser

SKUA
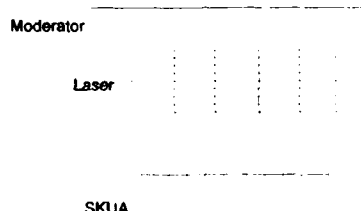
TABLE V. ENERGY DEPOSITIONS ACHIEVABLE IN A LARGE-SCALE DF-CO_2 LASER	
Additive	Energy Deposition
none	0.1 mJ/cm^3
0.5-atm ^{3}He	4.5 mJ/cm^3
0.1-atm ^{3}He	1.5 mJ/cm^3
0.1-atm ^{10}B	4.5 mJ/cm^3
0.1-atm ^{6}Li	3.5 mJ/cm^3
0.1-atm ^{235}U	50.0 mJ/cm^3

A new liquid burst facility, the SHEBA assembly, is presently being constructed to study the dynamics of nuclear excursions in a liquid system. Compared to a metal system, the SHEBA assembly might ultimately produce an increase by a factor of 10 to 100 in the neutron output and a substantially higher burst repetition rate at the cost of a somewhat longer pulse length. In its final form, this liquid burst facility would have a substantial volume, and its shape would be tailored to the requirements of the laser system. A critical mass of liquid material would be pumped into a shape of interest, then allowed to burst and vaporize. The material would then be cooled, reconstituted, and pumped back into the critical configuration for another burst. A comparison of the characteristics of such a liquid burst reactor (LBR) with GODIVA and SKUA has been included in Table IV.

Proposed Experiments

A large-volume laser experiment is currently being planned to examine the issues of laser and burst assembly operation raised here. We propose to do proof-of-principle experiments whose objectives are

1. to demonstrate lasing in a neutron-initiated DF-CO_2 laser;

2. to examine the kinetics of the laser when various fractions of the buffer gas are replaced by ^{3}He and other gases;

3. to examine the feasibility of long pulse initiation (30- to 500-μs range);

4. to produce a laser large enough to demonstrate optics performance and beam quality; and

5. to study the characteristics of solution burst assemblies.

We envision the use of two laser volumes. The smaller of the two will be approximately 40 cm in diam by 2 m long. Using ~20-cm-diam optics, we will measure gain, total output energy, and pulse shape to verify and adjust performance predictions. Full-size, 40-cm-diam optics would then be used to show pumping uniformity and extraction over the full volume of ~280 l.

A second laser would have a larger volume (~2 m^3) with a folded optical path; an unstable resonator would extract the full volume. Preliminary calculations indicate that this volume will be large enough to give an equivalent Fresnel number well above the critical Fresnel number for mode separation, allowing the laser to produce a single plane wave.

Conclusions

In this report, we have examined some of the issues that arise in attempting to initiate a large-volume, DF-CO_2 transfer laser with a burst reactor. While several issues remain to be settled in both the operation of the burst reactor and in the laser kinetics, analysis of a system in which ^{3}He is used to replace some fraction of the buffer gas indicates that excellent performance of the system may be expected.

References

1. J. A. DeShong, "Optimum Design of High-Pressure, Large-Diameter, Direct Nuclear-Pumped Gas Lasers," Argonne National Laboratory report ANL-7030 (June 1965).

2. N. W. Jalufka, "Direct Nuclear-Pumped Lasers," NASA Technical Paper 2091 (January 1983).

3. M. A. Prelas, et al., "Nuclear Driven Flashlamps," *Lasers and Particle Beams*, 6, Part 1, pp. 25-62 (1988).

4. G. York, Los Alamos National Laboratory, private communication, (August 1988).

5. R. C. Feber and J. H. Sullivan, Los Alamos National Laboratory report LA-11049-MS, (August 1987).

6. N. Cohen and J. F. Bott, Aerospace Corporation report SD-TR-82-86, The Aerospace Corporation, El Segundo, California, October 1982.

7. G. K. Vasil'ev, E. F. Makarov, and Yu. A. Chernyshev, *Kin. i Kat.* 16, 272 (1975).

8. A. S. Bashkin, A. N. Oreavskii, V. N. Tomashov, and N. N. Yuryshev, *Sov. J. Quantum Electron.* 10, 781 (1980).

9. S. T. Amimoto, J. S. Whittier, G. Harper, R. Hofland, J. M. Wlaters, T. A. Barr, R. L. Kerber, and W. K. Jaul, Aerospace Corporation report SD-TR-83-05, The Aerospace Corporation, El Segundo, California.

10. H. Inagaki, K. Kumamoto, A. Suda, M. Obara, and T. Fujioka, Inst. Phys. Conf. Ser. No. 72, presented at 5th GCL Symp., Oxford (1984).

11. J. F. Stephenson, R. E. Wood, and C. B. Moore, *J. Chem. Phys.* 54, 3097 (1971).

12. V. Y. Argoskin, G. K. Vasil'ev, V. I. Kir'yanov, and V. L. Tal'roze, *Sov. J. Quantum Electron.* 8, 1366 (1978).

13. A. I. Nikitin and A. N. Oreavskii, *Sov. J. Quantum Electron.*, 6, 1280 (1976).

14. "MCNP - A General Monte Carlo Code for Neutron and Photon Transport," ed. by J. Briesmeister, Los Alamos National Laboratory report LA-7396-MS, Rev. 2, (September 1986).

15. J. W. Wilson and A. Shapiro, *J. Appl. Phys.* 51, 2387 (1980).

16. M. D. Burrows, Los Alamos National Laboratory, private communication (December 1987).

17. F. C. Fehsenfeld, A. L. Schmeltekopf, P. D. Goldan, H. I. Schiff, and E. E. Ferguson, *J. Chem. Phys.* 44, 4087 (1966).

18. A. L. Schmeltekopf and F. C. Fehsenfeld, *J. Chem. Phys.* 53, 3173 (1970).

19. L. T. Specht, K. D. Foster, and E. E. Muschlitz, *J. Chem. Phys.* 63, 1582 (1975).

20. T. F. Wimett, "Fast Pulse Reactor Kinetics: Theory and Experiment," Proceedings of the US/Japan Seminar on Fast Pulse Reactors, Jan. 1976.

21. J. D. Orndoff, H. C. Paxton, and T. F. Wimett, "Safety Analysis of the Los Alamos Critical Experiments Facility: Burst Operation of SKUA," Los Alamos Scientific report LA-6206, Vol. II, Addendum (Dec. 1980).

Resonator Stability Effects in "Quadratic-Duct" Nuclear-Reactor-Pumped Lasers

D. R. Neal, J. R. Torczynski, and W. C. Sweatt
Sandia National Laboratories
Albuquerque, NM 87185

Abstract

In some experiments involving reactor pumping of atomic xenon, lasing intensity has been observed to change abruptly well before the peak of the pumping pulse. Recent advances in gasdynamic modeling and laser resonator stability theory have shown that resonator stability transitions caused by gasdynamically induced refractive index gradients are responsible for some of these observed intensity fluctuations.

1. Introduction

A number of experiments involving reactor pumping of atomic xenon have been conducted on research reactors at Sandia National Laboratories. Lasing has been observed at 1.73 μm and at 2.03 μm for a variety of pump rates and gas mixtures [1-4]. In some of these experiments, abrupt variations in lasing intensity were seen during the pumping pulse, including termination and subsequent reinitiation of lasing [4]. Many different effects could conceivably produce these variations, including laser kinetics, energy/power loading, line competition, radiation-induced absorption, and cavity alignment. In this paper the possibility is considered that gasdynamically induced refractive index gradients can attain amplitudes sufficient to change resonator stability.

In the experiments considered here, the pumping is from the walls, and therefore spatially nonuniform (largest near the walls and smallest near the axis). The pulse length is comparatively long (1-12 ms), so gas motion can affect the laser resonator modes by producing significant density gradients (and hence refractive index gradients) normal to the optical axis (see Fig. 1). This causes the laser medium to act approximately like a positive cylindrical lens (more precisely, like a quadratic duct) [2], and for large enough index gradients an initially stable resonator can become unstable [3-4]. A theory is developed based on the paraxial approximation which describes the stability of a resonator containing a quadratic-duct region. A gasdynamics model is then used to determine the strength of the refractive index gradients during the pumping pulse. Use of these two calculations in concert allows calculation of the times or energy depositions at which gasdynamically induced laser resonator stability transitions are expected. These predictions are then compared with the experimentally observed intensity fluctuations.

2. Laser Resonator Stability Theory

In the paraxial approximation, propagation of a ray is described by the ray matrix ABCD [5]. The complex radius of curvature $\tilde{q}$ for a Gaussian beam is defined to be

$$\frac{1}{\tilde{q}} = \frac{1}{R} - \frac{j\lambda}{\pi w^2} , \qquad (2.1)$$

where λ is the wavelength, R the beam radius of curvature, and w the Gaussian beam spot radius. A new complex curvature can be calculated after propagation through any system described by the ray matrix $ABCD$ using the relation $\tilde{q}_1 = (A\tilde{q}_0 + B)/(C\tilde{q}_0 + D)$. For a resonator where $ABCD$ is the round-trip ray matrix, the complex curvature must be the same after one round trip:

$$\frac{1}{\tilde{q}} = \frac{C + D/\tilde{q}}{A + B/\tilde{q}} , \quad \text{or} \quad \frac{1}{\tilde{q}} = \frac{D - A}{2B} + \frac{1}{B}\sqrt{\left(\frac{A+D}{2}\right)^2 - 1} , \qquad (2.2ab)$$

where use has been made of the ray-matrix property that $AD - BC = 1$. Combining (2.1) with (2.2b) yields the geometrical radius of curvature R and the Gaussian beam radius w:

$$\frac{R}{L} = \frac{R}{L} = \frac{2B}{D - A} , \quad w^{*2} = \frac{w^2}{L\lambda} = \frac{|B|/L}{\pi\sqrt{1 - \left(\frac{A+D}{2}\right)^2}} = \frac{|B^*|}{\pi\sqrt{1 - m^2}} , \qquad (2.3ab)$$

where L is a normalizing length scale usually taken to be the gain region length, $B^* = B/L$ is the normalized cavity length parameter, and $m = (A + D)/2$ is the *resonator stability parameter*. The resonator stability is entirely determined by the radical in (2.3b): the resonator is stable for $m < 1$ and unstable elsewhere. Thus, in plots of m vs. time or energy deposition during the laser pulse, resonator stability transitions are the points at which m crosses ± 1.

For a parabolic transverse index gradient, it is useful to adopt the notation of Siegman [5], $n(r) = n_0 - \frac{1}{2}n_2 r^2$, for the quadratic term, where r is measured from the centerplane (see Fig. 1). measurements of the index of refraction profile for

reactor-pumped lasers indicate that the medium is well characterized as a quadratic duct during most of the pumping pulse 2). A nondimensional variable γ^*, termed the *index gradient strength parameter*, which characterizes the transverse refractive index gradients, can be defined for a medium of gain length L_g: $\gamma^* = L_g\sqrt{n_2/n_0}$. Following the approach of Siegman [5], the round-trip ray matrix for a two-mirror linear resonator (Fig. 1) is evaluated expanding about mirror 1 (the output coupler):

$$
\begin{bmatrix} A & B \\ C & D \end{bmatrix} = \begin{bmatrix} 1 & 0 \\ -2/R_1 & 1 \end{bmatrix} \begin{bmatrix} 1 & \frac{L_1}{n_A} \\ 0 & 1 \end{bmatrix} \begin{bmatrix} \cos\gamma^* & \frac{L_y}{n_0\gamma^*}\sin\gamma^* \\ -\frac{n_0\gamma^*}{L_y}\sin\gamma^* & \cos\gamma^* \end{bmatrix} \begin{bmatrix} 1 & \frac{L_2}{n_A} \\ 0 & 1 \end{bmatrix} \times
$$

$$
\begin{bmatrix} 1 & 0 \\ -2/R_2 & 1 \end{bmatrix} \begin{bmatrix} 1 & \frac{L_2}{n_A} \\ 0 & 1 \end{bmatrix} \begin{bmatrix} \cos\gamma^* & -\frac{L_y}{n_0\gamma^*}\sin\gamma^* \\ \frac{n_0\gamma^*}{L_y}\sin\gamma^* & \cos\gamma^* \end{bmatrix} \begin{bmatrix} 1 & \frac{L_1}{n_A} \\ 0 & 1 \end{bmatrix} .
$$

(2.4)

Here, n_A is the index of the ambient medium outside the gain region, with a numerical value typically close to unity. The matrix equation (2.4) can be solved to determine an explicit expression for m, given below:

$$
m = \left(1 - \frac{2L_1}{n_A R_1}\right)\left(1 - \frac{2L_2}{n_A R_2}\right)\cos 2\gamma^* - \left\{\left(1 - \frac{L_1}{n_A R_1}\right)\frac{L_1}{n_A R_2} + \left(1 - \frac{L_2}{n_A R_2}\right)\frac{L_2}{n_A R_1}\right\}\left(\cos 2\gamma^* + 1\right)
$$

$$
- \left\{\frac{n_0^2 L_1 L_2}{n_A^2 L_g^2}\left(1 - \frac{L_1}{n_A R_1}\right)\left(1 - \frac{L_2}{n_A R_2}\right)\gamma^{*2} + \frac{L_g^2}{n_0^2 R_1 R_2}\gamma^{*-2}\right\}\left(\cos 2\gamma^* - 1\right)
$$

$$
- \left\{\frac{n_0 L_1}{n_A L_g}\left(1 - \frac{L_1}{n_A R_1}\right)\left(1 - \frac{2L_2}{n_A R_2}\right) + \frac{n_0 L_2}{n_A L_g}\left(1 - \frac{L_2}{n_A R_2}\right)\left(1 - \frac{2L_1}{n_A R_1}\right)\right\}\gamma^*\sin 2\gamma^*
$$

$$
- \left\{\left(1 - \frac{2L_1}{n_A R_1}\right)\frac{L_y}{n_0 R_2} + \left(1 - \frac{2L_2}{n_A R_2}\right)\frac{L_y}{n_0 R_1}\right\}\gamma^{*-1}\sin 2\gamma^* .
$$

(2.5)

Since m is a function of the resonator geometry parameters and γ^*, the stability for any given resonator configuration can be explicitly determined. For a given fixed resonator geometry, the resonator stability parameter will vary periodically with increasing γ^* because of the sinusoidal terms in (2.5). Points where m crosses ± 1 are the stability transition points for the resonator, and the corresponding γ^* values are the critical values for the index gradient strength parameter.

As an example, the function $m(\gamma^*)$ is presented in Fig. 2 for several different cavity geometries. The cavity geometry parameters have been normalized by the gain length $L_g = 60$ cm. Since the index gradient strength parameter γ^* increases monotonically with time during a reactor pulse, for a particular resonator geometry stability transitions will occur where m crosses 1. For example, for the geometry of the curve labeled $L_1^* = 0.28$, the resonator is unstable for $1.15 < \gamma^* < 1.50$. The curves in Fig. 2 are almost independent of gas fill pressure and composition, varying only in the values of n_0 and n_A, which are very close to unity for gas lasers. Thus, for a given geometry, the stability transition points do not change significantly for different gas conditions. What does change is the possibility of the medium reaching the specified critical values of γ^*.

The location of the first stability transition can be determined as a function of resonator geometry factors in order to study a wider variety of cases. Figure 3 presents the index gradient strength parameter at the first stability transition (refered to as the *critical* index gradient strength parameter) as a function of free end space for an asymmetric resonator. This critical index gradient strength parameter is a function *only* of resonator geometry factors, with the sole assumption being that the gain region is a "quadratic duct." Since the resonator geometry can be varied in a straightforward fashion, experiments can be conducted to infer the index gradient strength from stability transition points by changing the cavity geometry. Further parameter studies for different resonator geometries may be found in Reference 3.

For an initially stable low-gain laser, lasing would occur only while the resonator remained stable and would be expected to terminate as the resonator became unstable. Similarly, an initially unstable low-gain resonator would begin lasing only when the resonator crossed the stability boundary to the stable region. Thus, stability transitions might be observed experimentally as terminations or initiations of lasing. For a high-gain laser, abrupt decreases in lasing intensity would be expected for a stable-to-unstable transition although lasing might continue even after the stability boundary was crossed.

Since resonator stability transitions take place only at the critical γ^* values for a particular resonator geometry, the times or energy depositions at which intensity fluctuations are experimentally observed can be compared with gasdynamic computations of the times or energy depositions at which γ^* reaches the critical values. In addition, since the stability transition points are a function only of resonator geometry, the geometry can be varied to produce stability transitions at different values of γ^*. For pulsed reactor-laser experiments, different γ^* values correspond to different amounts of energy added to the laser gas, and thus comparisons can be made between gasdynamic and experimental results.

3. Gasdynamic Theory and Modeling

In the reactor-pumped-laser experiments discussed above, the fission fragments used to pump the gas enter the gas from

246

foils, thin coatings of fissionable material, located on the side walls of the chamber. The fission-fragment power density is smallest at the center of the chamber and largest near the side walls. This spatial nonhomogeneity acts to drive gas toward the centerplane of the device, producing a focusing optical duct. Spatial variation in the neutron flux used to induce the fissions can also produce some gas motion along the laser axis. However, the gas motion normal to the side walls and hence to the laser axis is of principal importance for determining the effect of gas motion on laser resonator stability.

The acoustically filtered equations of motion [4,6-9] provide an accurate description of the gas motion induced by fission-fragment heating. In the acoustic filtering approach, the Mach numbers of the induced flow are assumed to be small, so the pressure is taken to be composed of a large mean pressure, which is a function of time alone, and a small (with respect to the mean) temporally and spatially varying pressure perturbation. This is a good approximation for the above experiments, which generally have energy-deposition time scales that are much longer than the acoustic time scales for the laser chamber. If gas motion along the laser axis is neglected, the acoustically filtered equations of motion for the gas take the following forms in a rectangular geometry [4,7-9]:

$$\frac{d\bar{p}}{dt} = (\gamma - 1)\bar{Q} \ , \quad \frac{\partial u}{\partial x} = (\gamma - 1)\hat{Q}/\gamma\bar{p} \ , \quad \frac{\partial \rho}{\partial t} + \frac{\partial}{\partial x}(\rho u) = 0 \ . \tag{3.1abc}$$

Here, x is the perpendicular distance from the centerplane (see Fig. 1), $\rho(x,t)$ the density of the gas, $u(x,t)$ the velocity of the gas (normal to the foils), γ the ratio of specific heats for the gas, $\bar{p}(t)$ the volume-averaged pressure in the gas, $Q(t)$ the volume-averaged power density, and $\hat{Q}(x,t) = Q(x,t) - \bar{Q}(t)$ the amount by which the local value of the power density differs from the mean. The power density Q uses the fission-fragment energy deposition model of Miley and coworkers [9,10].

The form of Q allows the above system of equations to be solved analytically [4,6-9], and the calculations discussed in the remainder of this section were performed using a computer code which evaluates this analytical solution. It is found that the normalized pressure rise $(\bar{p} - p_0)/p_0$ is the only dynamic variable on which the density field depends: the time rate of change of $\bar{p}$ does not enter into the solution [8,9]. This rate-independent nature of the gas motion allows generic curves to be computed describing experiments which have the same initial conditions but quite different power-density histories. In Fig. 4, curves relating the variation of γ^* to the normalized pressure rise $(\bar{p} - p_0)/p_0$ are presented for several gas mixes used in a recent series of experiments. Note that by the ideal gas law the normalized pressure rise is equal to the normalized energy deposition (the ratio of the deposited energy ΔE to the initial thermal energy E_0 in the gas), $(\bar{p} - p_0)/p_0 = \Delta E/E_0$. The gas mixtures and initial temperatures for the analyzed cases are shown in Table 1. Curves like those discussed in this section are useful for separating gasdynamic effects from other potential causes of intensity fluctuations. They are also useful in delineating the parameter space in which a cavity remains stable. For a specified chamber geometry, gas mix, and energy deposition, the maximum value of γ^* that will be produced during the pumping pulse can be determined, regardless of the specifics of the power-density history. Mirror locations and radii of curvature can then be selected so as to place the critical value of γ^* for resonator instability above the maximum value that will be encountered in the experiment. Also, if cavities of other lengths are considered, the new γ^* values for the cases listed in Table 1 can be determined directly from Fig. 4 since γ^* is proportional to the chamber length. Of course, the laser resonator stability theory would have to be used to determine new critical values for γ^*.

Table 1. Specifications for Generic Simulations.

Case	T (K)	$p_{^4He}$ (kPa)	p_{Ar} (kPa)	p_{Xe} (kPa)	Gap Width (cm)	Gain Length (cm)
A3539	295	105.0	105.5	1.081	1.5	60.0
A	300	68.9	68.9	0.240	1.0	60.0
B	300	51.7	51.7	0.147	1.0	60.0
C	300	172.3	34.5	0.173	1.0	60.0
D	300	258.5	17.2	0.173	1.0	60.0

4. Comparison of Theoretical and Experimental Results

Two series of experiments have been conducted using reactor-pumped lasers to investigate stability transition effects. In the first, a cell with a given, fixed geometry was filled with a ^{4}He/Ar/Xe mixture to 30 psi and pumped with significant energy (see Fig. 5 for a schematic diagram of the experimental setup). In this experiment (designated A3539), multiple stability transitions were observed. Since this experimental configuration did not lend itself well to changing the resonator geometry, a second experiment series was conducted based around a more flexible experimental apparatus. In this series, the cavity length was varied from experiment to experiment by selecting different values for the free-end spacing L_1 (see Fig. 1). Times at which intensity fluctuations occurred were recorded for each individual experiment.

In experiment A3539, two intensity fluctuations were observed [4]: lasing first terminated and soon thereafter reinitiated early in the pumping pulse (see Fig. 6). Time-resolved pressure-rise and neutron-flux measurements for this experiment thus

247

allow calculation of the times and energy depositions at which the intensity fluctuations occurred. Experiment A3539 involved a mixture of ^{3}He, Ar, and Xe (see Table 1). The gas was contained in a 1.5 cm × 60 cm rectangular enclosure and pumped using 1-μm UO$_2$ foils mounted on the side walls. The energy deposition pulse is reasonably described by a Gaussian function, $\exp\{-(t - t_1)^2/t_o^2\}$, where $t_1 = 14.7$ ms and $t_o = 4.25$ ms. An amplitude of 0.2579 kW/cm^3 used as input to the gasdynamic model yields the experimentally observed pressure rise of 1103 kPa (160 psi). Figure 7 shows the gasdynamic computation of the time variation of γ^*. The experimental points on this figure correspond to measurements from Fig. 6 of the times at which the lasing terminates and reinitiates. If the experimentally observed intensity fluctuations result from gasdynamically induced laser resonator stability transitions, then these times should correspond to γ^* values of 1.15 and 1.50, the first two critical values for resonator stability transitions for this geometry (the dashed curve on Fig. 3 represents this experimental geometry). The good agreement seen in Fig. 7 between the experimental data and the theoretical predictions thus suggests that gasdynamically induced laser resonator stability transitions are responsible for the intensity fluctuations observed in experiment A3539.

In the second series of experiments, corresponding to Cases A–D, data were obtained for four different gas mixes, with several different L_1 values for each mixture. Stability transitions were observed as sharp changes in the laser intensity. Since this reactor-laser configuration produced considerably higher gain than in the previous experiment, the laser was observed to continue lasing at a reduced level after the stability transition occurred. With this configuration, the total energy deposition into the laser gas (0.2–0.3 J cm^3) was not sufficient to induce multiple stability transitions, so only one transition was expected during each experiment. A typical laser signal is presented in Fig. 8, which also includes curves describing the pumping pulse and the pressure history measured with a transducer located at the end of the cell (the intensity fluctuation is the sudden sharp drop in the laser signal seen at 2.13 ms).

Results from many experiments such as the one shown in Fig. 8 can be condensed into a form which can be compared to the theoretical results of Fig. 6. The amount of energy added to the laser gas up to the stability-transition time can be calculated by comparing the integral of the pumping pulse up to the stability-transition time to the total integral of the pumping pulse. Since the measured total pressure rise is proportional to the total energy added to the gas (which in turn is proportional to the total integral of the pumping pulse), the energy deposited in the gas at transition can be calculated. When normalized by the thermal energy initially present in the gas occupying the pumped region prior to pumping, this normalized energy deposition is equivalent to the normalized pressure rise of the gasdynamics model, as discussed in the previous section. In the experimental apparatus, there is some unpumped volume into which gas can flow. This necessitates scaling the measured pressure rise by the ratio of the total internal volume to the pumped volume, here 1.289, to determine the equivalent pressure rise that would have been measured in the absence of unpumped regions. If a gasdynamically induced resonator stability transition is responsible for an experimentally observed intensity fluctuation, then the index gradient strength parameter must have reached the critical value calculated from the stability theory for the given resonator. Since the critical index gradient strength parameter is a function of resonator geometry alone, Fig. 3 can be used to infer the index gradient strength at transition for each value L_1 (the chain-dotted curve on Fig. 3 represents the experimental geometry used for this series). To test this hypothesis, the normalized energy deposition, as determined by the gasdynamic model, was plotted against the index gradient strength parameter for Cases A–D (see Figs. 9–12), and the normalized energy depositions at experimentally observed intensity fluctuations were plotted on the same graph assuming they occurred at the calculated critical values of the index gradient strength parameter. The close agreement seen in these figures provides strong evidence that gasdynamically induced resonator stability transitions are indeed responsible for some of the observed intensity fluctuations. It should be noted that the converse is also true — intensity fluctuations of the sort shown in Fig. 8 were not observed in experiments for which the combination of gasdynamic modeling and resonator stability theory predicted that gasdynamically induced stability transitions would be absent.

5. Conclusions

In some reactor-pumped atomic-xenon laser experiments, fluctuations in lasing intensity during the pumping pulse have been observed. While laser kinetics, line competition, radiation induced loss, and cavity misalignment are possible causes of such fluctuations, it has been shown that gasdynamic effects on resonator stability are responsible for some of the observed fluctuations.

A methodology has been developed that allows prediction of gasdynamically induced resonator stability transitions. This theory predicts resonator stability as a function of a single parameter γ^*, which characterizes the strength of the index gradients in the medium. For a given laser cavity geometry, the resonator will exhibit cyclic stability transitions for increasing values of γ^*. Gasdynamic calculations allow the determination of the time variation of γ^* for specific experiments. The gasdynamic computations of γ^* can thus be used to find the γ^* values for the times at which stability transitions were observed. Good agreement is found between these γ^* values and the critical γ^* values determined by the resonator stability theory, indicating that gasdynamically induced laser resonator stability transitions account for some of the experimentally observed intensity fluctuations.

For a given gas mixture and resonator geometry, it is possible to predict the index gradient strength based only on the normalized energy deposition into the laser gas (independent of the pumping *rate*), so experiments pumped at entirely different

248

rates can easily be compared, provided pump times are long enough to allow significant gas motion. This allows immediate determination of the experiments in which gasdynamically induced stability transitions play a role. The combination of gasdynamic modeling and resonator stability analysis is thus capable of discriminating gasdynamically induced resonator stability transitions from other effects as causes of experimentally observed intensity fluctuations.

Acknowledgments

References

1. D. A. McArthur, G. N. Hays, W. J. Alford, D. R. Neal, D. E. Bodette, and J. K Rice, in *Laser Interaction and Related Plasma Phenomena* **8**, G. H. Miley and H. Hora, Eds., (Plenum, New York, 1988).

2. D. R. Neal, W. C. Sweatt, D. A. McArthur, W. J. Alford, and G. N. Hays, in *High Speed Photography, Videography and Photonics V*, H. C. Johnson, Ed., *Proc. SPIE* **832**, 52 56 (1988).

3. D. R. Neal, W. C. Sweatt, and J. R. Torczynski, in *Current Developments in Optical Engineering III*, R. E. Fischer and W. J. Smith, Eds., *Proc. SPIE* **965**, in press (1988).

4. J. R. Torczynski and D. R. Neal, *Effect of Gasdynamics on Resonator Stability in Reactor-Pumped Lasers*, Sandia Report SAND88 1318, Sandia National Laboratories (1988).

5. A. E. Siegman, *Lasers*, (University Science Books, Mill Valley, CA, 1986), Chap. 16.

6. S. Paolucci, *On the Filtering of Sound from the Navier-Stokes Equations*, Sandia Report SAND82-8257, Sandia National Laboratories (1982).

7. J. R. Torczynski and R. J. Gross, in *Proc. of the Int. Conf. on Lasers '87*, F. J. Duarte, Ed. (STS Press, McLean, VA, 1988), pp. 241 248.

8. J. R. Torczynski and R. J. Gross, *J. Appl. Phys.* **64** (9), 4323-4328 (1988).

9. J. R. Torczynski, *J. Fluid Mech.*, in press (1989).

10. G. H. Miley and P. E. Thiess, *Nucl. Appl.* **6**, 434 451 (1969).

11. J. C. Guyot, G. H. Miley, and J. T. Verdeyen, *Nucl. Sci. Eng.* **48**, 373 386 (1972).
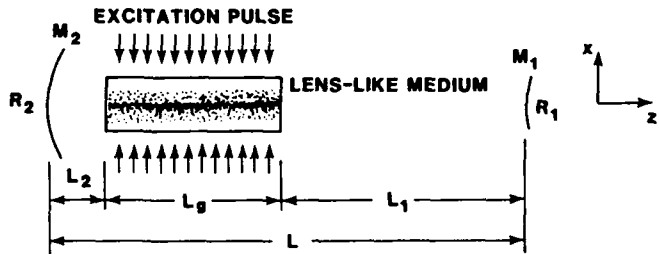
Figure 1. Linear, two-mirror resonator geometry. The spatially nonuniform pumping causes gas to move toward the axis.
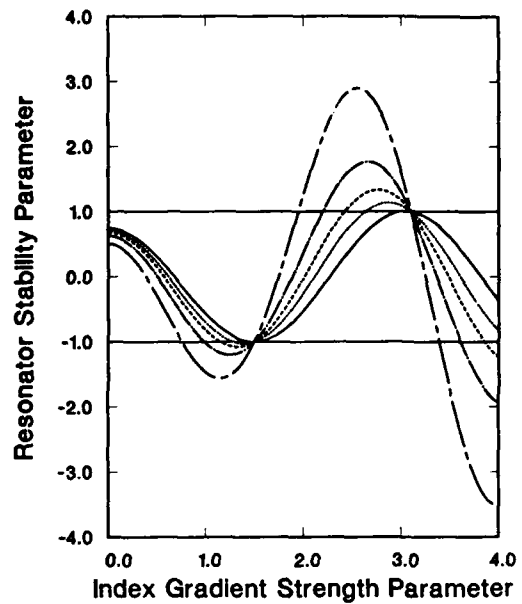
Figure 2. The resonator stability parameter $m = (A + D)/2$ as a function of the index gradient strength parameter γ^*, for $L_1^* \equiv L_1/L_g = 0.0$ (solid curve), 0.15 (dotted curve), 0.28 (dashed curve, corresponding to experiment A3539), 0.5 (chain-dotted curve), and 1.0 (chain-dashed curve), $L_2^* \equiv L_2/L_g$ 0.05, $R_1^* \equiv R_1/L_g = \infty$, $R_2^* \equiv R_2/L_g - 8.33$, and x_{wall}^* $x_{wall}/L_g \doteq 0.012$. The resonator is stable if and only if $|m \cdot 1$.
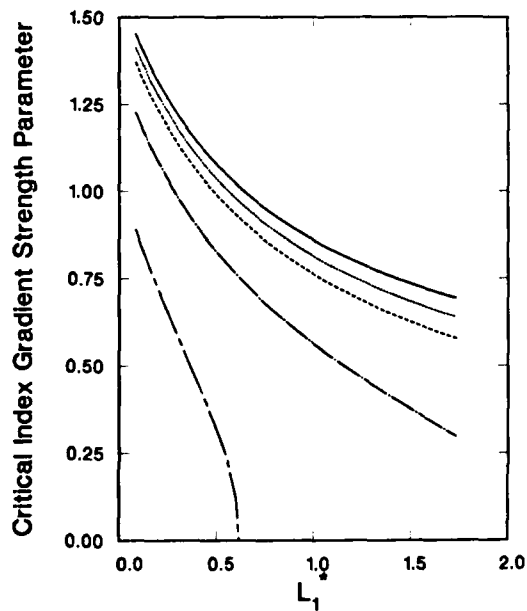
Figure 3. Critical value of γ^* as a function of L_1^* for an asymmetric resonator with L_2^* 0.05, $R_1^* = \infty$, and R_2^* ∞ (solid curve), 16.67 (dotted curve), 8.33 (dashed curve, A3539), 3.33 (chain-dotted curve, Cases A D), and 1.67 (chain-dashed curve).
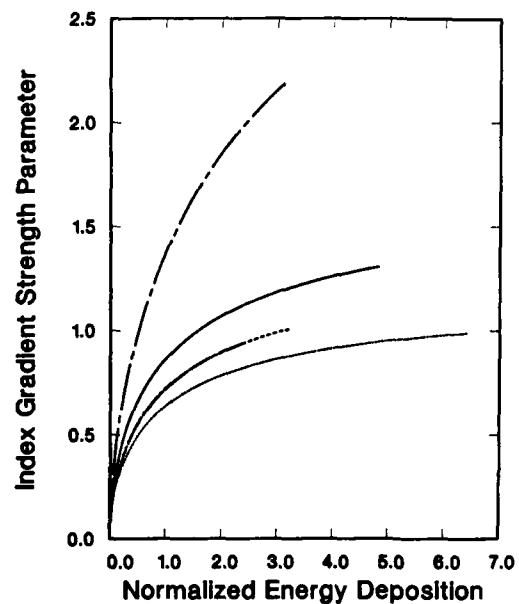
Figure 4. Variation of γ^* with normalized energy deposition (normalized pressure rise) for the cases in Table 1. Case A (solid), Case B (dotted), Case C (dashed), Case D (chain-dotted), Case A3539 (chain-dashed). The rightmost point on each curve corresponds to an energy addition of 1.0 J/cm^3.

250
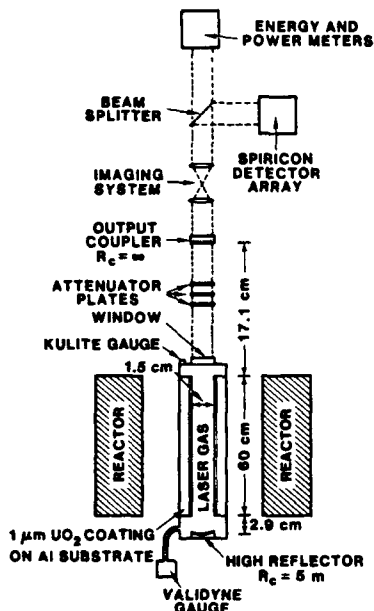
Figure 5. Schematic diagram of the experimental apparatus used in experiment A3539.
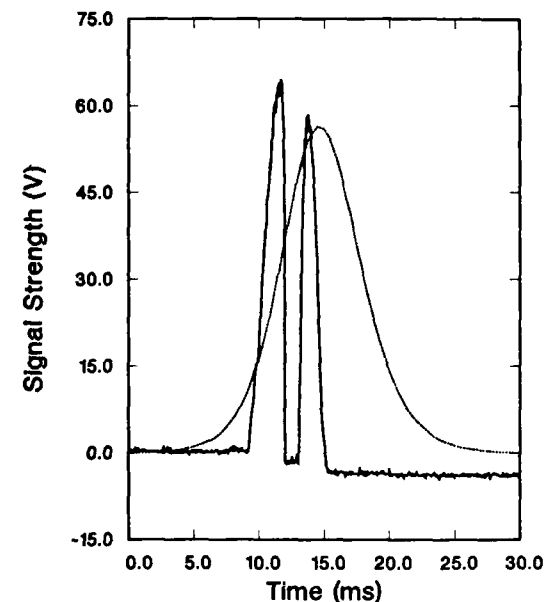
Figure 6. The time variations of the observed lasing intensity (solid curve) and the pumping pulse (dotted curve) for A3539. The total energy deposition in this case was 1.6 J/cm^3.
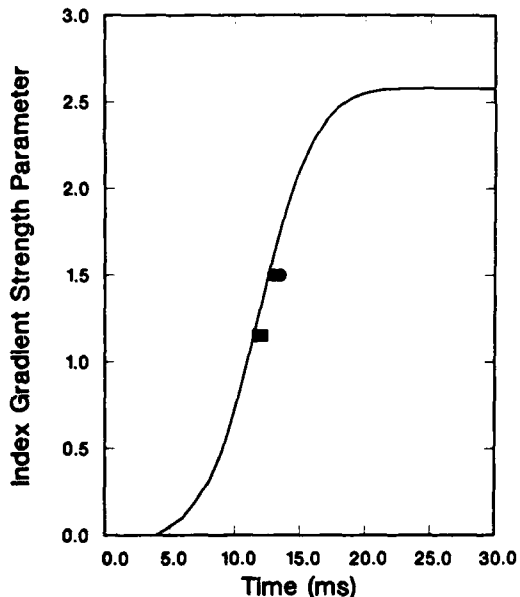
Figure 7. The time variation of γ^*, as determined by gasdynamic calculations, is shown for A3539. The solid squares correspond to the measured time at which lasing was observed to terminate ($\gamma^* = 1.15$), and the solid circles correspond to the measured time at which lasing was observed to reinitiate ($\gamma^* = 1.50$). The slight spread results from the experimental uncertainty in fixing exact termination and reinitiation times. The close agreement indicates that gasdynamically induced resonator stability transitions are responsible for the observed intensity fluctuations in this experiment.
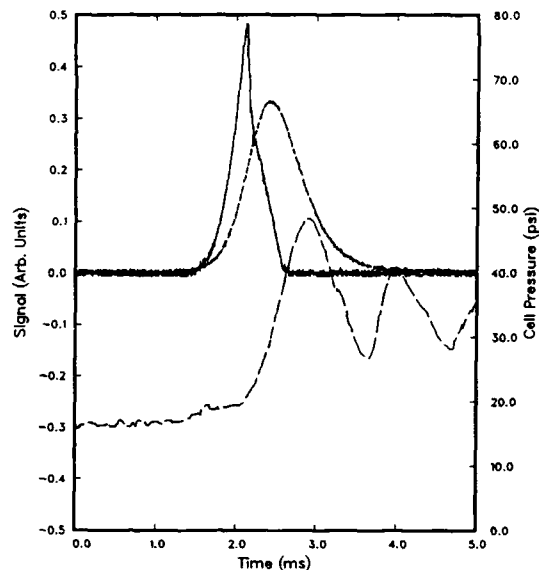
Figure 8. Time variations of the laser intensity (solid curve), the pumping pulse (dashed curve), and the pressure (long-dashed curve) for experiment S6302.

251
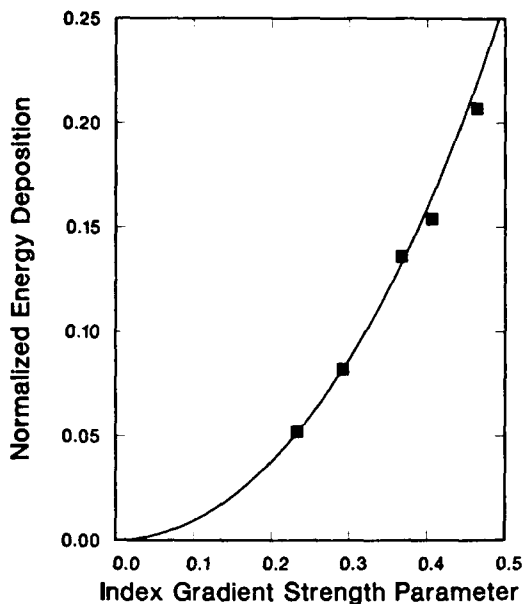
Figure 9. Normalized energy deposition (normalized pressure rise) is plotted against γ^* for Case A. The solid points are experimental measurements, and the line is the gasdynamic calculation. One experiment corresponds to one value of L_1.
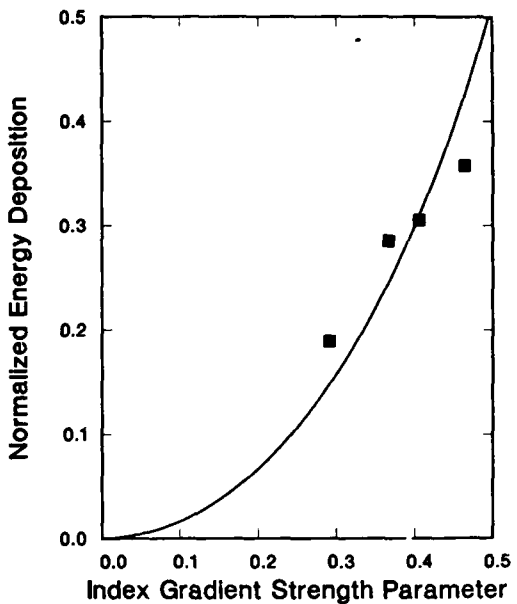
Figure 10. Normalized energy deposition (normalized pressure rise) is plotted against γ^* for Case B. The solid points are experimental measurements, and the line is the gasdynamic calculation. One experiment corresponds to one value of L_1. Note that the ordinate scale differs from Figs. 9, 11, and 12.
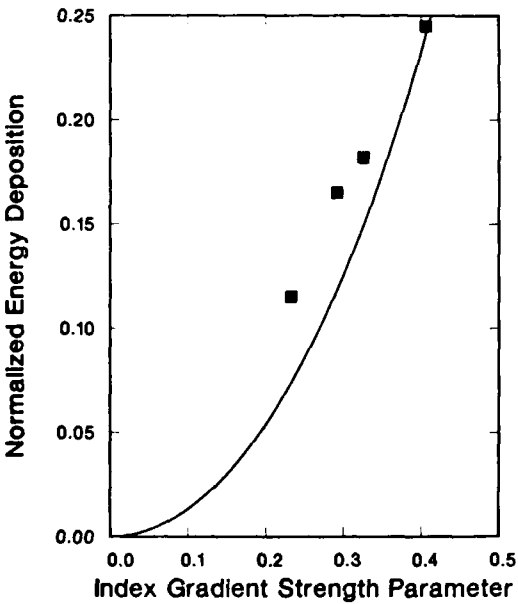
Figure 11. Normalized energy deposition (normalized pressure rise) is plotted against γ^* for Case C. The solid points are experimental measurements, and the line is the gasdynamic calculation. One experiment corresponds to one value of L_1.
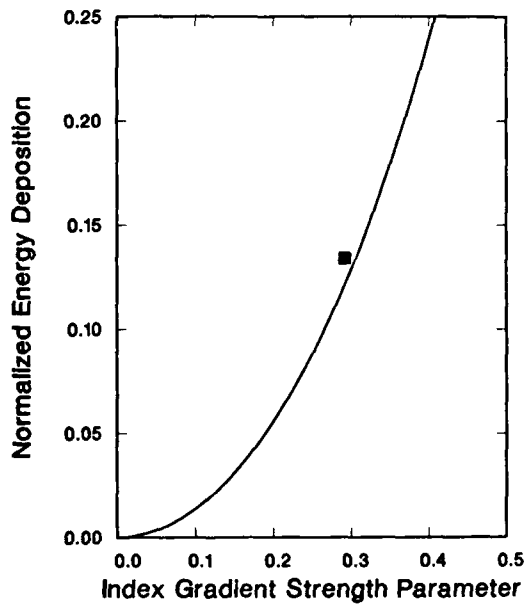
Figure 12. Normalized energy deposition (normalized pressure rise) is plotted against γ^* for Case D. The solid points are experimental measurements, and the line is the gasdynamic calculation. One experiment corresponds to one value of L_1.

252

ELECTRON-BEAM PUMPED LIQUID EXCIMER LASERS

Thomas R. Loree, Robert R. Showalter, and Tamara Johnson
Los Alamos National Laboratory
Los Alamos, New Mexico 87545

Brian S. Birmingham
U.S. Air Force, Space Command
Los Angeles, California 90009

William M. Hughes
Mission Research Corporation
Los Alamos, New Mexico 87544

Abstract

We have investigated the excimers formed in liquid argon when various cryogenic gas mixes were excited by 1-MeV electrons. Fluorescence was detected from many excimers at their new red-shifted wavelengths, and XeO, Xe_2, and Kr_2 were lased.

Introduction

The efficacy of excimer and exciplex molecules in gas lasers has been well established; the commercial availability of exciplex uv lasers has created a host of new applications in both science and industry.[1] Excimers (and exciplexes) in a liquid state are of interest for several reasons. The physical factors and high gain implied high excited-state densities could engender compact, high-energy designs rather like cryogenic dye lasers. In addit.. e changing red-shifts of the emission wavelengths in various liquid hosts[2] (usually tens of nanometers) will create an extensive set of new laser wavelengths.

Although it is not common knowledge, the first excimer lasers were liquid-state excimers. In early 1970 Shank et al. published a series of experiments demonstrating gain and lasing from optically pumped large polyatomic exciplexes based on dye molecules.[3-5] More pertinent to the subsequent mainstream of research, lasing of a dimer excimer was first accomplished in late 1970 by Basov et al.,[6] who formed and lased Xe_2 in e-beam-pumped liquid xenon. Aside from some isolated efforts such as the nuclear pumping of liquids[7] theory and experiment then mostly turned to gas-phase excimers, although Shahidi et al.[8] recently lased optically pumped XeF at 404 nm in liquid argon.

We have investigated liquid-argon-based excimers under e-beam excitation from a 1-MeV, 40-ns source. This pumping method lacks the selectivity of optical pumping, but was quite effective in some cases; XeO, Xe_2, and Kr_2 all lased. In some sense the e-beam excitation represents the final step of any "nuclear" pumping technique, and thus has importance beyond the scope of this study.

Apparatus

A schematic of the cryogenic laser cell is shown in Fig. 1. The vacuum-isolated cell was cooled by pulses of liquid nitrogen vapor regulated by a thermocouple-driven temperature controller which maintained cryogenic temperatures to better than ±1 K. The 1-MeV, 40-ns e-beam pump pulse entered the side of the cell through a 50-μm nickel foil. The e-beam energy deposited in the lasing medium was 0.3 J, measured calorimetrically. The penetration depth of the electrons in liquid argon limited the active volume to about a 2-mm depth; the height was 2 mm and the length 19 mm; thus, the pump power density was on the order of 100 MW/cm^3. Both mirrors were mounted directly on the ends of the cell and sealed with spring-loaded calcium-lead alloy gaskets to the diamond-turned faces of the OFHC copper body. This sealing system survived many pressure and thermal cycles from room temperature down to nominal operating conditions (104 K and 2.8 atm) and back. The high-reflector was usually an overcoated aluminum film on a concave 10-cm radius substrate and the output coupler was flat, varying from a bare magnesium fluoride window to another HR as required.

Early in these investigations we found that if the argon host were contaminated by oxygen at tens of parts per billion, the only emission that would appear would be the fluorescence of ArO in the green, no matter what the ostensible mix was. This acute sensitivity to impurity oxygen was not found by Rhodes' group in optically pumped mixes,[9] but has been noted in studies of solid rare gases.[10] In our case it proved sufficient to purify the research-grade argon gas by flowing it through a Hydrox Ti-gettered purifier. As most of our mixes contained less than 1% of the lasing species, mixing was usually carried out in two steps. A primary mix was made with several percent of the lasant (all mix values are room temperature pressure ratios), which was further diluted with argon to the desired concentration. When the final mix was well homogenized, it was directly condensed in the cold optical cell. We tried to maintain the accuracy of the mix by

always starting runs at the lowest concentrations and moving monotonically to richer mixes. This procedure minimized the influence of residual gases in the system on the concentrations.

The reproducibility of the lasing results was greatly improved when we added the pump shown in the cell schematic of Fig. 1. The stirring afforded by the centrifugal pump both prevented thermal striations and kept the additives from forming large ice crystals (most had limited solubility in argon at the operating temperature of the laser). The efficacy of the circulation could be appreciated by aligning a He-Ne laser beam through the cell when it was equipped with a pair of windows. When the pump was turned off, the He-Ne beam broke up in a matter of seconds as thermal layering took place. The 10-mm diameter pump was run at 1500 rpm by a magnetically coupled external motor.

The temporal measurements of the lasing and the sidelight fluorescence were made with appropriate photodiodes. Energies were also inferred from the photodiode signals after calibration (in the exact geometries used) with known laser beams. Vacuum uv spectral measurements were made with a vacuum spectrometer; the output was viewed by a Tracor Northern intensified diode array through a magnesium fluoride input window. This setup successfully detected Ar_2 fluorescence at 130 nm, demonstrating more than adequate short-wavelength sensitivity.

Fluorescence Results

Rare Gas Dimers

In Fig. 2 we show the emission spectra of the three rare-gas dimers, Ar_2, Kr_2, and Xe_2. For the spectra shown, the krypton and xenon were at concentrations of 10% and 0.01%, respectively. The low xenon level was chosen to show an accompanying atomic xenon peak, which quenched out at higher concentrations. The maximum photodiode signals observed from these three species (with constant conditions and nearly constant photodiode response over these wavelengths) were 60 mV for the Ar_2, 2.8 V for the Kr_2, and 6.0 V for the Xe_2. The peaks were red-shifted by 2-3 nm from their gaseous wavelengths, depending on the concentration of the donor. Subsequently, Kr_2 and Xe_2 lased, which will be discussed in a later section.

Argon/Donor Binary Mixtures

The rare-gas oxides are interesting excimers that lase on thinly disguised singlet oxygen transitions.[11] The ArO transition and that of KrO are almost identical to the oxygen green auroral transition itself, and all occur at 558 nm. (XeO, however, will be seen to be more strongly bound.) ArO,[12] KrO,[13] and XeO[13-15] have all been lased in high-pressure gases on the auroral transition (^1S-^1D or the molecular $2^1\Sigma^+$ - $1^1\Sigma^+$) near the 557.7 nm of the unpertured oxygen line. Figure 3 shows the ArO peak generated by 100 ppb of N_2O in Ar (the N_2O donor was more effective than O_2, and became our standard oxygen donor). This peak could still be detected with less than 10 ppb of oxygen donor in the system. The ArO peak was quite bright and, curiously, increased strongly when the liquid mixture was solidified.

The formation of trimers is expected to occur in high concentrations of the noble gas component. Thus, donors of F and Cl in pure liquid Ar produced trimer excimers in addition to Ar_2. Figures 4 and 5 show the resultant Ar_2F and Ar_2Cl (we preferred NF_3 over F_2, as NF_3 was as effective a fluorine donor, but much easier to handle). These broad peaks were both red-shifted from their gaseous central wavelengths of 285 and 245 nm by 20 nm. Note that upon solidification the red shift increased.

Krypton Plus Donor in Argon

This family of mixes was the least successful of our excimer-producing liquids, forming strong Kr_2 but only weak emissions from KrF, KrCl, Kr_2F, and KrO.

Xenon Plus Donor in Argon

All three donors produced bright fluorescence, once the proper relative concentrations were found. The data shown were taken with xenon/donor ratios of 1/1. XeO lased and will be discussed later.

The donors NF_3 and Freon-11 produced complete sequences of XeF and XeCl, as shown in Fig. 6. It is obvious that the e-beam pumping excited all the transitions of the molecules, and we were not able to force it to be more specific in its excitation. Large red shifts are evident in the (B-X) transitions, which are the normal lasing transitions. In gas lasers these occur at 308 nm (XeCl) and 352 nm (XeF), but in liquid Ar we saw these (B-X) transitions shifted to 352 and 405 nm. The concentrations were 10 ppm for the NF_3/Xe run and 100 ppm for the FR-11/Xe data.

Lasing XeO

Of the rare gases, xenon has the most profound effect on excited oxygen. The ^1D state (the molecular $1^1\Sigma^+$ state) of XeO is bound enough to support vibrational levels, which are seen in the fluorescence spectra of gaseous, liquid, and solid[16] forms. Thus, the XeO lasing transition terminates on a lightly bound valence state, unlike most excimer transitions to repulsive ground states. However, curve crossings insure the rapid deactivation of the ^1D state by collisions with rare-gas elements.[17]

We used N_2O for the oxygen donor because we anticipated photolytic production of singlet oxygen; Ar_2 radiation of 130 nm is extremely effective at producing singlet oxygen from this molecule.[18] We then disproved our own hypothesis by trying CO_2 for the oxygen donor and finding that the XeO still lased, even though there was no source of the 110-nm photons required to dissociate CO_2. This suggests that the photolytic production of singlet oxygen does not control the formation of XeO*, as concluded by Kligler et al.[19] Even at liquid densities the formation of XeO* is probably diffusion-controlled, since the gaseous deactivation rate of $O(^1S)$ in argon gas[20] is only 5×10^{-18} cm^3 sec^{-1}.

Spectral narrowing upon lasing is shown in Fig. 7, a plot that contrasts the broad XeO sidelight fluorescent spectrum with the endlight from the HR-HR cavity. The lasing line was a single 0.9-nm-wide line centered at 547 nm. This wavelength corresponds to the 0-6 vibrational transition (red-shifted from 544 nm in gas),[21] and is easily spectrally located by the obvious side-scattered lasing peak superimposed on the fluorescence spectrum. The 0-5 peak is stronger, both in gaseous or liquid-state fluorescence and in the lasing obtained in high-pressure gases, but despite our broad-band mirrors we did not observe lasing on the 540-nm 0-5 vibrational transition. We fortuitously had an output coupler with a reflectance edge that fell off through the wavelength of the 0-6 transition. With that output coupler in the cavity, we saw simultaneous lasing on the 0-5, 0-4, and 0-3 transitions. The numbering of the vibrational transitions is a subject of some controversy, and is quite different in the solid-phase spectra reported by Goodman et al.[16] Bearing in mind that solid-phase wavelengths are red-shifted somewhat beyond those of the liquid,[22] we lased on what they identified as the 0-10 line, which again is the second strongest in fluorescence.

The time histories of the sidelight and endlight are illustrated in Fig. 8, and demonstrate depletion of the upper state in the fluorescence; without lasing, the trailing edge of the fluorescence was a smooth function of time. The initial fluorescence spike at 20 ns was a consistent feature contributed by the argon host in all mixes and in pure argon alone. Lasing did not start until well after the e-beam was gone, as was also seen in high-pressure gases.[13] The multiple lasing pulses exhibited a pattern normally associated with gain-switched spiking. The width (FWHM) of the first pulse was 3 ns.

We roughly mapped out the field of xenon and N_2O combinations that produced lasing with the HR-HR optical cavity, and these data are shown in Fig. 9. Changes in the cavity or pumping parameters will modify this lasing field, but the data generally suggest a preference for N_2O-rich mixes and considerable tolerance in concentrations. While lasing at the edges of the field was clearly degraded, no patently superior mix was observed within the main body of the lasing ratios.

The spectral lasing signals (integrated over time) were calibrated against the spectral areas and measured energies of 532-nm pulses from a doubled, q-switched Nd:YAG laser. This procedure led to the conclusion that with the HR-HR cavity, the XeO laser output energy was on the order of 0.1 μJ. A flat output coupler with 88% transmission at 547 nm was then tried in combination with the curved HR, and the laser produced 0.1 mJ. To overcome the mirror losses, the gain (γ_0) was at least 23% per centimeter. We can estimate a minimum inversion density (ΔN) from the relationship:

$$\Delta N = \gamma_0/\sigma_{se} \quad .$$

(1)

In the spirit of making a rough estimate, we will use the gaseous stimulated emission cross section (σ_{se}) value[23] of 10^{-17} cm^2, and conclude that the inversion density was at least 2×10^{16} cm^{-3}. A mix containing 30 ppm of Xe and N_2O contains 6×10^{17} of each, which is thus the maximum possible density of XeO. Our estimated inversion density is a reasonable fraction of that.

Lasing Xe_2 and Kr_2

The lasing line of Xe_2 centered on the fluorescence peak at 175 nm and narrowed to 1.0 nm wide at half-maximum (the fluorescence was 9.0 nm wide). Note that in the gas phase lasing occurs at 172 nm; the red shift in the liquid is small because Xe_2 (and Kr_2) molecules are homopolar.[24] In contrast, the red shift of the lasing line for the polar molecule XeF in liquid argon was 53 nm (Fig. 6).

Figure 10 illustrates the temporal characteristics of the sidelight and lasing. The fluorescence reflects the 40-ns pump pulse shape with a depletion notch at the moment of lasing; the lasing pulse was about 4 ns wide. While these data suggest more straightforward kinetics than the XeO data, the lasing pulse is not without interest, as it is not symmetric to the fluorescence peak. Both of these Xe_2 figures are data from a 0.1% mix, which was near optimum for energy and reproducibility, although mixes from 0.05 to 15% Xe lased. In Fig. 11 we show the increasing red shift in the lasing wavelength as the xenon concentration was increased, caused by the increasing average molecular weight of the local environment surrounding each lasing molecule.

The best Xe/Ar mixes would lase with a bare magnesium fluoride window as the output coupler. The output from this setup was attenuated by several 90-degree reflections (from bare magnesium fluoride windows) and detected by a previously calibrated (at 193 nm) photodiode. This measurement yielded a reproducible energy output of 10 mJ. To

cross-check this number, we put a piece of burn paper on the output window; when compared to burns taken at 193 nm, this rough energy measurement indicated a value greater than 5 mJ. A less quantitative but more dramatic measure of the lasing energy was the clean hole blown in the Al coating of the high reflector after some tens of shots. At 10 mJ, the tiny lasing volume produced better than 100 J/L, a beam with 10 MW/cm^2, and a gain of at least 35%/cm. The output was 3% of the deposited e-beam energy, a number that is close to the efficiency found in large high-pressure e-beam-pumped Xe_2 lasers.[25]

The mixes of Kr/Ar clearly had less output than the Xe_2, and required a pair of high reflectors to induce lasing; at 147 nm the "HRs" were down to 80% reflectivity and leaked enough of the beam to be useful for diagnostics. Figure 12 shows the temporal narrowing of the lasing compared to the fluorescence. The time behavior was much like that of Xe_2. The lasing wavelength occurred at the peak of the fluorescence, and was narrowed from 8.0 nm to 1.0 nm at half-maximum. The range of concentrations that lased was about 0.3-20% krypton. In both Kr_2 and Xe_2 the high concentration cutoff was caused by the formation of slush (seen both by the slowing of the pump and a lack of He-Ne beam transmission through the cell). The red shift with increasing concentration was not measured for krypton. The lasing was rather erratic, but comparisons of the leakage signal through a common aluminum-coated HR showed the energy to be down an order of magnitude from the Xe_2 output. This would imply an energy density in the medium of some tens of joules per liter.

Conclusions

We have investigated a new class of e-beam-excited excimer lasers based on commonly employed excimeric species dissolved in a cryogenic liquid argon host. We observed the fluorescence of noble-gas fluorides, oxides, dimers, and noble-gas trimers, all excited with 1-MeV electrons. Laser action was observed from XeO, Kr_2 and Xe_2. The Xe_2 dimer was found to lase with 3% efficiency, producing 10 mJ when pumped with 300 mJ of deposited e-beam energy.

This new class of lasers has potentially important applications. Because of the red-shifting of the emission wavelengths, every excimer studied offered new laser wavelengths in the visible-to-vuv range. These outputs may be additionally solvent tuned, but the range of such tuning was not explicitly investigated in this study. As compact versions of the commonly employed gaseous excimers, these lasers offer new deployment opportunities and applications. In the sense that electron-beam pumping represents the final stage of any particle excitation technique, this is also a new class of nuclear laser candidates.

References

1. W. O. N. Guimaraes, C.-T. Lin, and A. Mooradian, eds., Lasers and Applications, (Springer-Verlag, Berlin, 1980).
2. H. Jara, H. Pummer, H. Egger, and C. K. Rhodes, Phys. Rev. B, 30, 1 (1984).
3. C. V. Shank, A. Dienes, A. M. Trozzolo, and J. A. Meyer, Appl. Phys. Lett. 16, 405 (1970).
4. A. Dienes, C. V. Shank, and A. M. Trozzolo, Appl. Phys. Lett. 17, 189 (1970).
5. C. V. Shank, A. Dienes, and W. T. Silfvast, Appl. Phys. Lett. 17, 307 (1970).
6. N. G. Basov, V. A. Danilychev, Yu. M. Popov, and D. D. Khodkevich, JETP Lett. 12, 473 (1970).
7. W. M. Hughes, J. F. Davis, W. B. Maier, R. F. Holland, and W. L. Talbert, Jr., Digest of the Nuclear-Pumped Laser Workshop (NASA Langley Research Center, July 1979) p. 95.
8. M. Shahidi, H. Jara, H. Pummer, H. Egger, and C. K. Rhodes, Opt. Lett. 10, 448 (1985).
9. H. Pummer, private communication.
10. E. E. Huber, Jr., D. A. Emmons, and R. M. Lerner, Opt. Comm. 11, 155 (1974).
11. T. H. Dunning and P. J. Hay, J. Chem. Phys. 66, 3767 (1977).
12. W. M. Hughes, N. T. Olson, and R. Hunter, Appl. Phys. Lett. 28, 81 (1976).
13. H. T. Powell, J. R. Murray, and C. K. Rhodes, Appl. Phys. Lett. 25, 730 (1974).
14. N. G. Basov, Yu. A. Babeiko, V. S. Zuev, L. D. Mikheev, V. K. Orlov, I. V. Pogorelskii, D. B. Stavrovskii, A. V. Startsev, and V. I. Yalovoi, Sov. J. Quant. Electron. 6, 505 (1976).
15. I. S. Datskevich, V. S. Zuev, L. D. Mikheev, and I. V. Pogorelskii, Sov. J. Quant. Electron. 8, 831 (1978).
16. J. Goodman, J. C. Tully, V. E. Bondybey, and L. E. Brus, J. Chem. Phys. 66, 4802 (1977).
17. G. C. Tisone and J. M. Hoffman, Sandia Laboratories Report, SAND 74-0425 (1974).
18. G. Black, R. L. Sharpless, and D. C. Lorents, J. Chem. Phys. 72, 484 (1980).
19. D. Kligler, D. Pritchard, W. K. Bischel, and C. K. Rhodes, J. Appl. Phys. 49, 2219 (1978).
20. J. R. Murray and C. K. Rhodes, J. Appl. Phys. 47, 5041 (1976).
21. C. D. Cooper, G. C. Cobb, and E. L. Tolnas, J. Mol. Spec. 7, 223 (1961).
22. T. R. Loree, R. R. Showalter, T. M. Johnson, J. M. Telle, R. A. Fisher, and W. M. Hughes, Proceedings of the Southwest Conference on Optics (SPIE Vol. 540, 1985) p. 279.
23. I. S. Lakoba and S. I. Yakovlenko, Sov. J. Quant. Electron. 10, 389 (1980).
24. H. Jara, Thesis, "Ultraviolet Excitation of Rare Gas-Halogen (F_2, Cl_2) and Rare Gas-Oxygen Cryogenic Solutions," University of Illinois at Chicago, 1985.
25. W. M. Hughes, unpublished work.
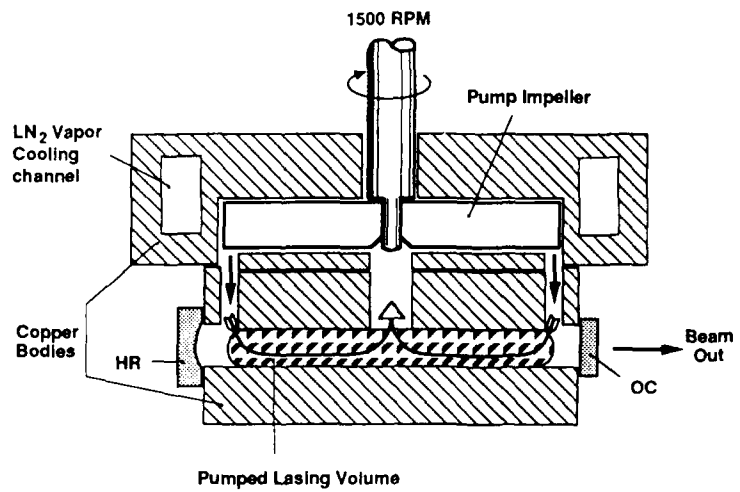
Figure 1. A schematic of the laser cell, which was 2 cm long. The entire
assembly was enclosed in an evacuated chamber for thermal
isolation. The normal operating conditions were 104 K and
2.8 atm. In this view the e-beam entered from the back; the foil
is shown as the checked area behind the lasing volume.
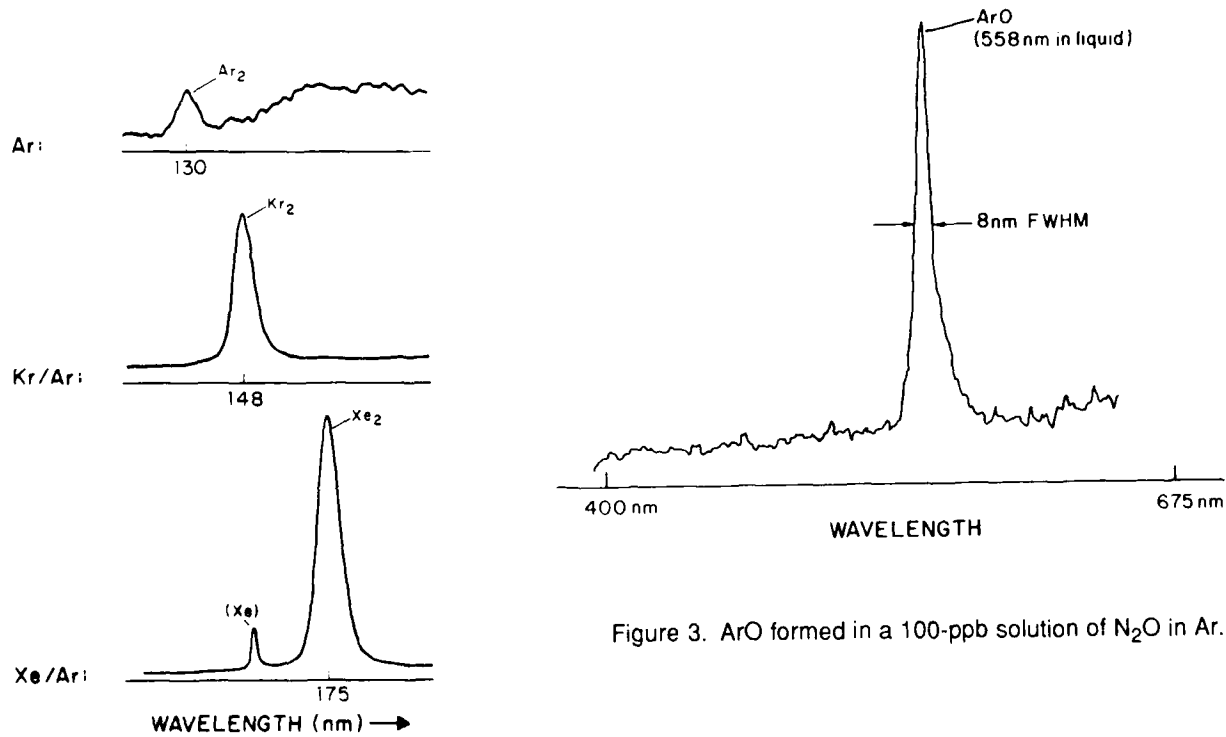
Figure 2. The noble gas dimer fluorescence spectra as seen in
pure Ar, 10% Kr/Ar, and 0.01% Xe/Ar.

Figure 3. ArO formed in a 100-ppb solution of N_2O in Ar.

257
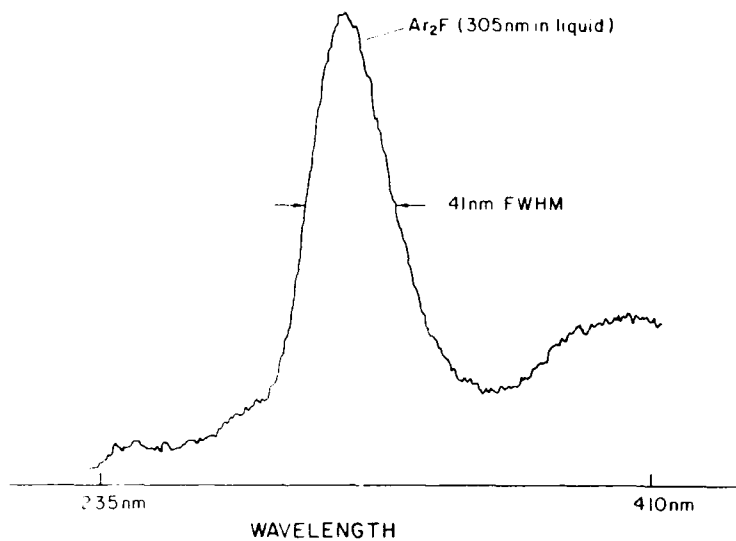
Figure 4. The halogen donors in Ar alone resulted in trimer excimers, as the Ar$_2$F seen here produced by 50 ppm of F$_2$.
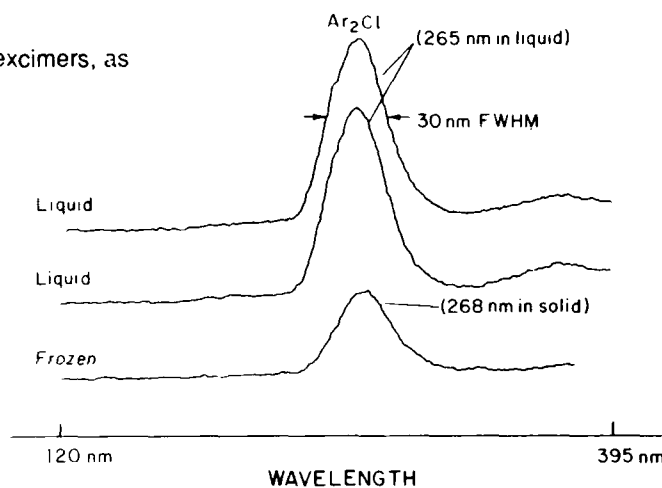
Figure 5. The Cl-donating Freon-11 at 1 ppm in Ar produced Ar$_2$Cl. The additional red shift in a solid matrix is also shown.
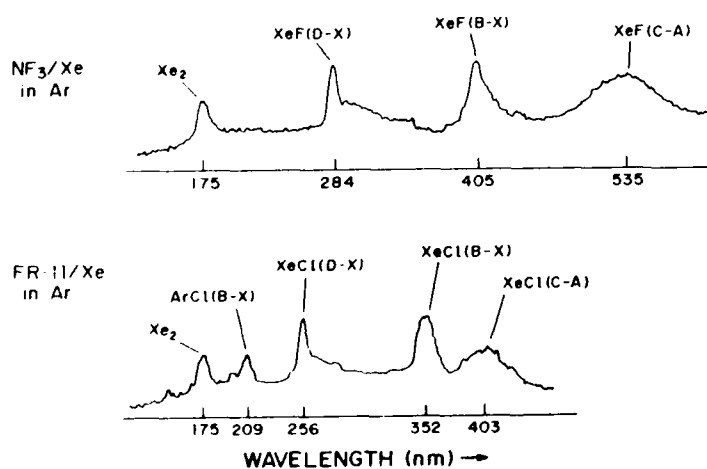
Figure 6. In ternary mixtures of (1:1) Donor:Xe in Ar with NF$_3$ (10 ppm) and Freon-11 (100 ppm) donors we observed these complete series of XeF and XeCl transitions. The (B-X) are the normal lasing transitions. The (C-A) are quite broad because of the curvature of the repulsive A states.

258
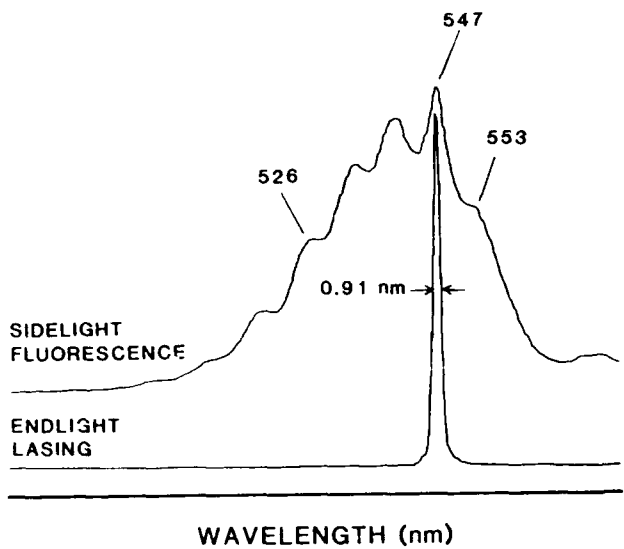
Figure 7. A comparison of the sidelight and lasing spectra of XeO, showing the vibrational structure on the fluorescence and the narrowing of the lasing line. The lasing wavelength is also seen as a small superimposed peak in the sidelight; the 547-nm 0-5 feature is not the highest peak in the unperturbed fluorescence.
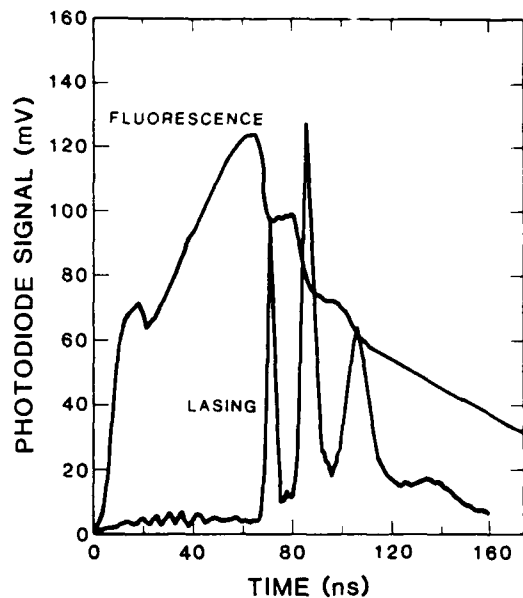
Figure 8. The temporal histories of the sidelight (upper curve) and lasing output (lower curve) of XeO, showing the multiple lasing pulses from the HR-HR cavity and the corresponding fluorescence depletions for each pulse. The mix was 30 ppm of both Xe and N_2O in liquid argon.
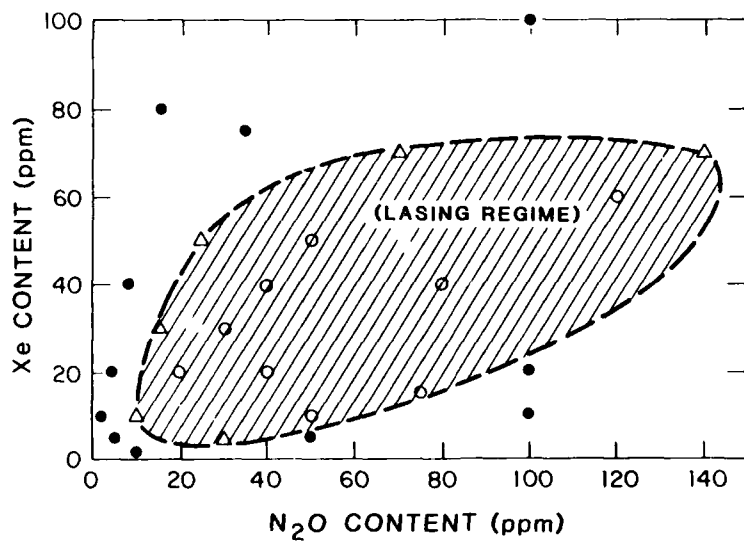
Figure 9. A plot of the XeO mixes tried in the HR-HR optical cavity. The solid dots represent nonlasing mixes, the triangles were marginal mixes, and the open circles lased well.
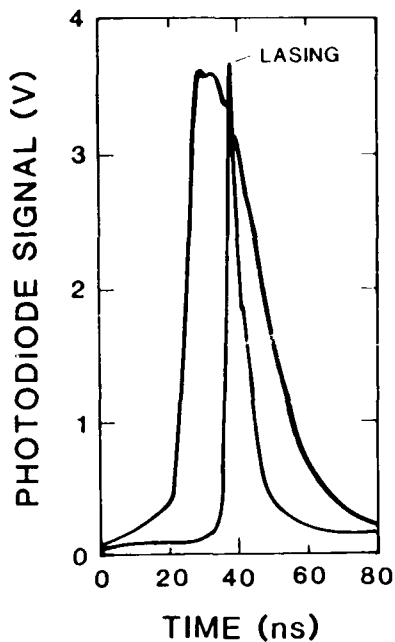
Figure 10. The Xe$_2$ time histories for sidelight fluorescence and lasing. At the moment of lasing a small depletion notch was seen in the sidelight.
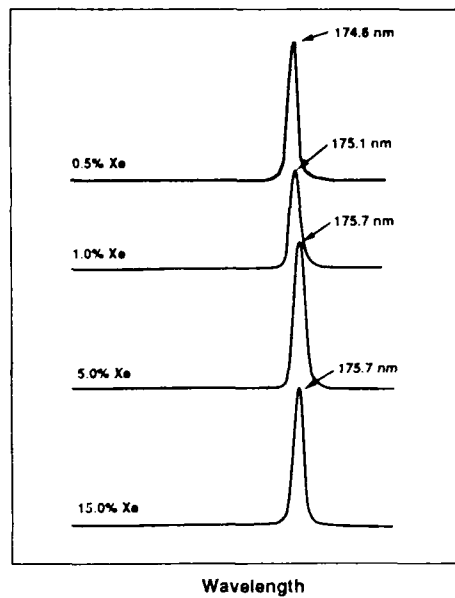
Figure 11. The red shift of the lasing wavelength of Xe$_2$ as a function of the xenon concentration in the argon host.
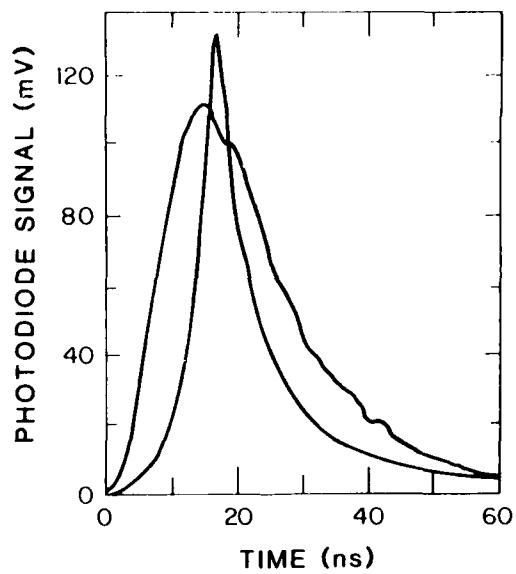
Figure 12. The Kr$_2$ fluorescence and lasing time signals for the same shot.

260

EXCITATION OF LASING MEDIA
USING ANTIPROTON-ANNIHILATION PRODUCTS

Steven D. Howe and Michael V. Hynes
Los Alamos National Laboratory
Los Alamos, New Mexico 87545

Abstract

Lasing has been achieved in many different media using a wide variety of excitation mechanisms including low-energy electron or proton beams and recoiling fission products. In all cases, the power density produced in the medium has been the critical parameter. Recent calculations indicate that a region of high-power density can be achieved in high-density lasing media by allowing antiprotons to annihilate in the material with an intense magnetic field present. Because of the long range of the energetic annihilation products, the media can be gaseous, liquid, or solid. The thermalization time is the critical parameter for this excitation mechanism which for liquid-density media, such as Ar-Xe mixtures, is about 2.1 ns. Based on these calculations power densities of about 100 MW/cm^2 can be achieved using a level of antiprotons that is currently available today. Development of an antiproton pumping source may allow fundamental reaction kinetics in a wide variety of lasing systems to be performed in a university environment. The results of the calculations in a liquid medium and at different magnetic field strengths will be presented. In addition, the design of an ongoing experiment using an 800 MeV proton beam to pump a liquid density excimer cavity will be discussed. These preliminary experiments intend to focus on fundamental kinetics and on the effects of a strong magnetic field on reactions.

1 INTRODUCTION

Antiprotons are produced at a variety of accelerator facilities around the world for basic research in nuclear and particle physics. The advent of the new cooling technology [1] which has opened many new areas for high-energy physics, also can open new research opportunities in other areas that can use a source of very low-energy antiprotons. The Low Energy Antiproton Ring (LEAR) at CERN can provide beams of antiprotons (10^6/sec) at energies down to 2 MeV [2] which have been used for a wide variety of measurements in low-energy antiproton physics.

Recently there have been a number of experiments at LEAR that propose to capture and store significant numbers of these particles for the measurement of fundamental properties [3]. All of these proposals rely on the well established ion-trap technology that is in common use in atomic physics [4]. Briefly, ion traps achieve storage of charged particles using a combination of electric and magnetic fields. Although this technology will never be able to store enough antiprotons to be of interest in a prime power application, (there will always be more energy in the magnetic field than in the rest mass energy [5]), it does offer unique opportunities to investigate specialized applications that can take advantage of the unique way in which antiprotons convert their rest mass into energy. One such application is to use the annihilation products to excite a large-volume, liquid-excimer lasing medium.

During the last fifteen years many researchers have used energetic particle beams to excite lasing media [6]. In general, these beams have been composed of either electrons with kinetic energies of up to 1-2 MeV, or of protons with energies up to 450 keV. These particles will produce a very high specific ionization due to their relatively short range in most lasing media. Power densities of about 100 MW/cm^3 can easily be achieved. However, these low-energy particles can excite only very small volumes. Moreover, again because of their short range, the volume that they can excite in a typical experiment is never coaxial with the cavity.

Until very recently, the use of much higher energy charged particle beams for laser excit   s not been very attractive because of the low peak-current available at most high-energy accelerator facilities. Even the highest current proton accelerator in the world, LAMPF at Los Alamos, could not produce sufficient power density in a medium to lase. However, the addition of the Proton Storage Ring (PSR) at LAMPF allows for the time compression of a beam burst and the resulting increase in instantaneous current. Thus, it is now possible to obtain a burst of 2×10^{13} protons in 270 ns at 800 MeV with spot sizes of about 0.5 cm. This is more than enough power and energy density to achieve lasing in liquid or high density media. Although the majority of recent work on excimer lasers has been based on gaseous phase media, the first excimer laser work was with liquid phase systems [7, 8]. The most recent work in liquid phase excimers is from a Los Alamos group who have investigated a wide variety of such systems [9, 10]. This work has focused on rare gas dimers and rare gas halogen mixtures in a liquid argon host.
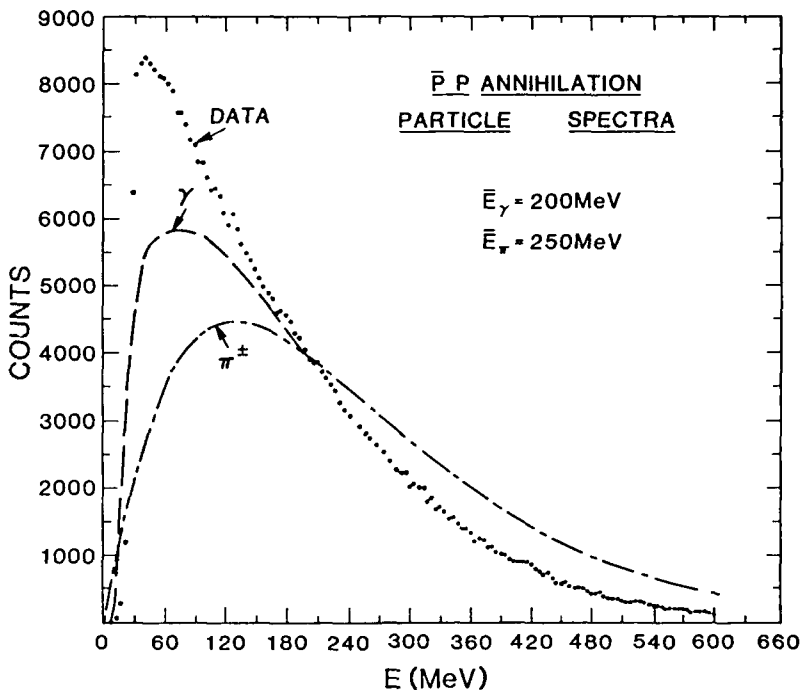
Figure 1: Calculated kinetic-energy spectra of charged pions and gamma rays resulting from antiproton-proton annihilation at rest. All final states not involving kaons are included. Data for gamma production is also shown (see text). These spectra result from 93,000 events which produced and average of 3.12 pions/event and 3.08 gamma/event.

Antiproton annihilation leads to the production of very high-energy charged particles. However, there is a central physics question that needs to be resolved: Do these high-energy particles lead to the same excitation modes of the medium that result in lasing action? The proton beam available at the PSR can simulate the specific energy loss of these annihilation particles (on the average). Thus, this question can be resolved without using antiprotons.

We have designed and built a cavity that could be installed in a PSR beam line. Of the possible liquid excimer systems that our pumping method and cavity could test, we hope to study the XeO system in our initial runs. Our design can easily change optics for investigating other systems.

The eventual use of antiprotons to pump laser media has the advantage that relatively compact devices can be built for exploring a wide variety of samples on a university laboratory scale.

2   THE ANTIPROTON-PUMPED LASER CONCEPT

Currently, efforts are underway at the Los Alamos National Laboratory to develop a modified Penning trap which can contain up to 10^{10} antiprotons at relatively low energies (a few keV) for long periods of time. The trap design allows for the accumulation of antiprotons produced at the modest rate of about $10^6 - 10^7$ per second. Once accumulated the antiprotons can be extracted all at once, or in short bunches a few 10's of ns long.

The spectra of the reaction products from a proton-antiproton annihilation event at rest are shown in Fig. 1. Over half of the annihilation energy is produced in the form of charged pions with an average energy of 250 MeV. Because the range of such particles is several many g/cm^2 the annihilation can occur in a solid medium with most of the energy deposition well removed from the reaction point. Consequently, the pion's energy can be used to excite a lasing medium even if the material is external to the annihilation point.

The problem with the very long range of the particles produced in the antiproton-annihilation reaction and with the deposition of their energy over a dilute region can be solved in part by allowing the annihilation to take place in a strong magnetic field. Such a field would be present anyway due to the storage of the antiprotons in an ion-trap configuration. Thus, the idea for the laser is simply to have a suitable laser cavity with an annihilation targe´ at its center located in the same solenoid that provides the magnetic field for storing the antiprotons. The resulting annihilation particles will be bent into overlaping orbits, thus confining the region over which the energy is deposited.

262
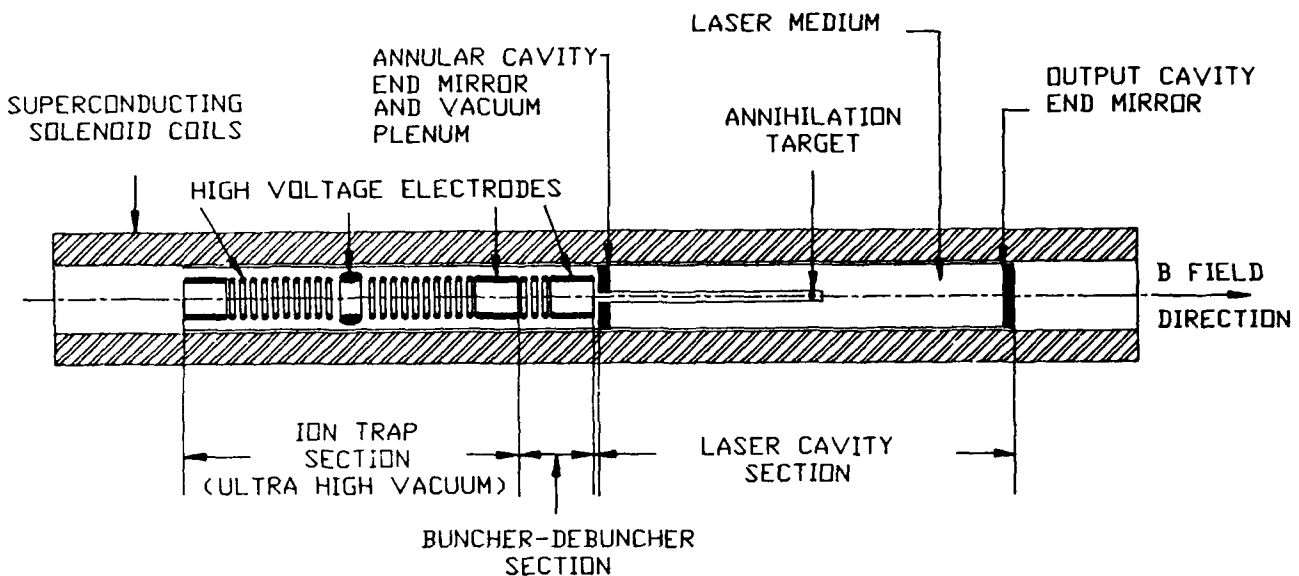
Figure 2: Schematic cross-sectional view of the antiproton pumped laser concept.

A schematic cross-sectional view of our proposed concept is shown in Fig. 2. In the figure the overall solenoid providing both the storage field for the antiprotons and the guiding field for the annihilation products is shown on the outside of the azimuthally symmetric device. On the left, inside the solenoid is the multiring ion trap that is used to store the particles. By adjusting the potentials on the electrodes the shape of the charge cloud can be adjusted prior to ejection to the right into the laser cavity. Between the trap and the cavity is located a series of electrodes that are used as a buncher section for the antiproton cloud as it approaches the annihilation target located in the center of the laser cavity. Everything up to the annihilation target is at very high vacuum (10^{-13}-Torr). The resonant cavity itself is annular in configuration with a fully reflective mirror on the ion-trap side and a partially transmitting mirror on the output side. The interior annulus is filled with a cryogenic lasing media in liquid form. The liquid form is preferred in our application due to the much higher density over gas. This higher density leads to more rapid energy loss and thermalization of the annihilation products and thus to higher peak-power density. An added advantage of the cryogenic operation is that higher vacuums are possible in such systems.

Preliminary calculations show that the antiprotons stored in the trap can be ejected and subsequently bunched at the target so that all the particles annihilate in about 50 ns. The emerging annihilation products would spread into 4π if the magnetic field were not present. With this field present the charged particles go into orbits whose radii are determined by the magnitude of the field and the momentum of the particles. Because the particles loose energy as they transit the lasing media the particle momentum is continuously being degraded. Thus, the resulting orbits are spirals. For the gamma rays the magnetic field has no effect until they shower into electron-positron pairs. These charged particles will also be bent in the field into orbits. However, the electrons and positrons will generate further gamma rays in the classic shower process that these light particles generate in matter. Thus, some of the gamma ray energy will simply escape the lasing media and not lead to excitation. We are at present modeling this effect. For the purpose of this design concept, we assume that the gamma ray energy which amounts to about half of the annihilation energy is simply lost to lasing action. As the charged pions decelerate in the lasing media they will finally decay into a muon and a neutrino. The muon will continue to orbit in the magnetic field losing energy and finally decay into an electron and two neutrinos. The energy contained in the neutrinos is lost to the excitation of the lasing media whereas the muons and electrons will deposit their kinetic energy just as the charged pions did before decay. The energy lost in the neutrinos is about 80 - 100 MeV on the average and is thus only about 5% of the total energy available.

We have simulated the orbits of these particles in a typical cryogenic lasing media, liquid argon with trace amounts of xenon. Particles with the spectrum of energies shown in Fig.1 are released at the center of a semi-infinite solenoidal field in the horizontal direction as shown in Fig. 2. Particles that emerge from the annihilation target exactly vertical in the figure will simply spiral around in the central plane of the figure as they loose energy. Particles that have a component of momentum parallel to the magnetic field direction will naturally propagate in this direction as well as spiraling. There
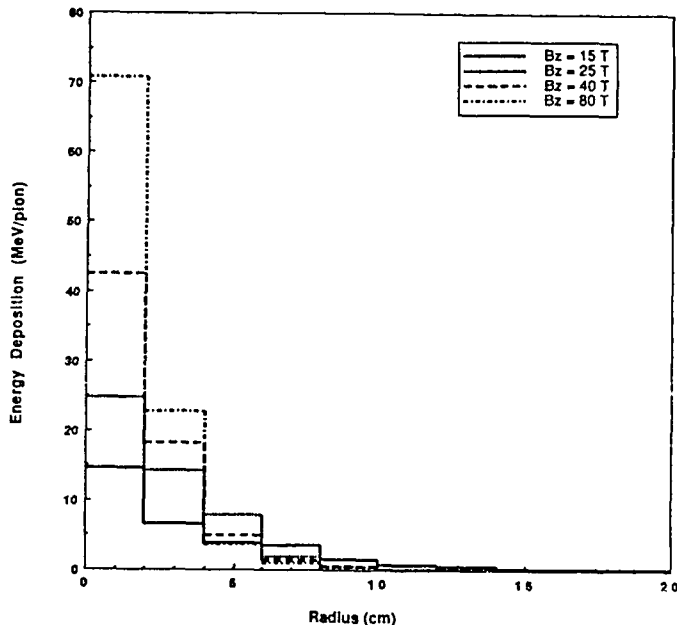
Figure 3: Azimuthally averaged energy deposition plotted as a function of radial distance from the laser axis.

will be some particles that have no momentum transverse to the magnetic field or such a small component that they propagate outside the cavity leaving little or no energy. From these simulations we have determined that the energy lost due to particles lost out the ends of the cavity could be as high as 40% for a 15 Tesla field. By increasing the field strength to 40 Tesla or by adding azimuthal field components using Jaffe coils, the losses may be reduced to 25% - 30%. Naturally this figure depends strongly on the specific configuration of the cavity and some steps can be taken to prevent this occurrence by further tailoring the fields near the ends of the cavity. Nevertheless, we will assume that 30% of the annihilation energy is lost due to end effects. The average time for the particles to thermalize is calculated to be about 2.1 ns. Thus, the annihilation energy is deposited in about 52 ns total. Finally, we have determined how large a volume of lasing media can be fully excited by the particles. This depends on the size of the magnetic field. For 15 Tesla this volume is about 200 cm^3. With 10^{13} stored antiprotons we release about 3000 joules of energy. The annihilation and thermalization time being about 52 ns total means that 5×10^{10} watts of power have been released. The azimuthally averaged spatial distribution of the energy deposition is shown in Fig. 3 for a variety of magnetic field strengths. The peak energy and power densities involved are 1.5 J/cm^3 and 28 MW/cm^3, respectively, for the 15 Tesla example, but are 6 J/cm^3 and 115 MW/cm^3 for the 25 Tesla case. These densities are very near those required for achieving lasing action in liquid eximer systems.

Previous work [9]-[11] has shown that either low-energy protons or relativistic electrons can excite excimer systems above the lasing threshold. Because of the short range of these particles however, very small volumes of liquid- or low-density gas targets have been used. Consequently, the power density thresholds, reaction rates, and large-scale collective effects have not been fully characterized. By utilizing the results of these experiments as a measure of the efficiency of conversion together with the calculated deposition from the antiproton model an estimate for the energy conversion to laser output can be made. Thus, we estimate that around 10^{12} – 10^{13} antiprotons would be required to produce about a 300 J laser pulse. This quantity of antiprotons is within current production levels and will soon be within ion-trap storage capabilities as well. Thus, an experiment using antiprotons could be executed within the next few years.

However, there are two outstanding physics questions that remain: Do high-energy ionizing particles excite the lasing media in modes that are similar to those achieved by more conventional charged particle excitations? Does the presence of a large magnetic field disrupt the lasing kinetics? Both these questions can be answered using high-energy protons and a specially designed cavity.
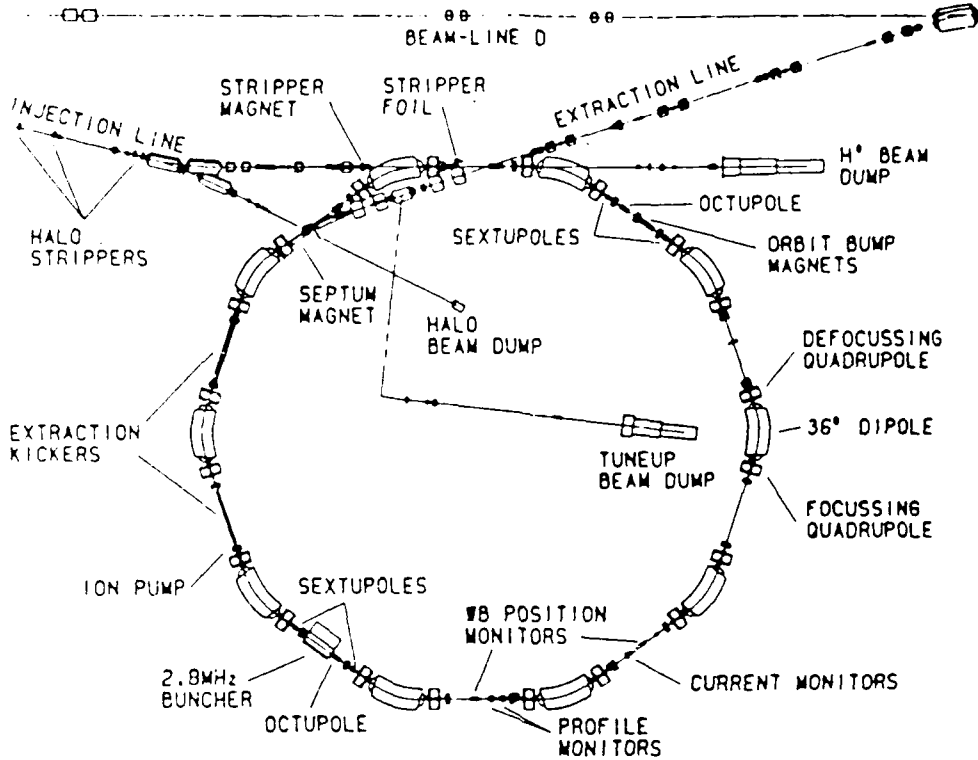
Figure 4: Shematic overview of the PSR facility at LAMPF.

3 THE PROTON-PUMPED LASER EXPERIMENT

Liquid excimer systems have achieved lasing using about 100 MW/cm³ power densities with about 4 J/cm³ total energy density. To achieve these quantities with a high-energy proton beam, the PSR facility at LAMPF is an ideal candidate. Beam bursts at 800 MeV with ~ 2 × 10¹³ particles in 270 ns can be delivered in spot sizes of a few millimeters. The 800 MeV protons (1463 Mev/c) will loose energy in a material at nearly the same rate as pions of about 250 MeV. Thus, the beam energy is ideal for our simulation of the antiproton-annihilation product excitation. Additionally, with an energy loss of 1.7 MeV g/cm² in liquid argon (ρ = 1.4 g/cm³) and a spot size of 0.5-cm a single beam burst will deposit about 38 J/cm³ at a power density of 140 MW/cm³. These numbers are above those required for achieving lasing action using conventional pumping methods.

3.1 The PSR Facility at LAMPF

The Proton Storage Ring (PSR) at LAMPF delivers very intense beams of protons for a wide variety of basic research experiments [2]. An overview of this facility is shown in Fig. 4. The LAMPF accelerator delivers a single macropulse, 800 microseconds long, at 800 MeV, to the PSR on demand. The PSR is designed to compact this macropulse, or any subset of it, in time to achieve a much higher peak current (40 A, designed) in a correspondingly shorter time. After many circulations the compacted burst is ejected from the ring structure for experiments. At present the burst can only be delivered at full intensity to the neutron production target. The difficulty for our experiment is to find a suitable location at the facility that does not interfere with conventional beam operations and that can accommodate the equipment needed for our experiment. The 7° beam dump line in the main ring area is the only location that meets these requirements. This beam line exits the main ring at a 7° downward slope and proceeds through a 48-inch-wide trench to a beam stop somewhat removed from the ring area (see figure). Spot sizes in this beam line are about 1 cm. However, additional optics in the beam line preceeding our experiment can bring the focus of the beam to about 0.5-cm over about a 10-cm-long region. These criteria drive many of the design choices that we made in our experiment.

265
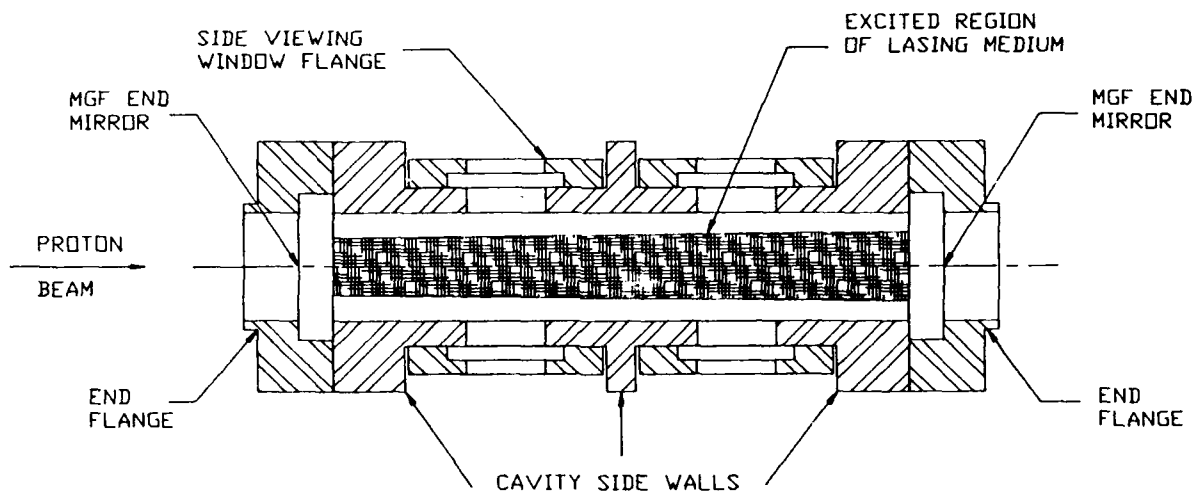
Figure 5: Schematic view of the lasing cavity with the region excited by the beam burst indicated.

3.2   Experimental Design

The Cavity. Because of the eventual focus that can be achieved in the beam line the natural length for the cavity is 10 cm. In principle, the cavity could be much longer due to extremely long range for 800 MeV protons in liquid argon ($\sim$ 70 cm). This points to one of the advantages for using the PSR beam to pump a lasing medium: very large volumes can be excited. However, only relatively dense materials such as liquids or solids can be considered due to the dependence of the dE/dx on material density. Naturally, if a given gaseous system has a particularly low lasing threshold, it too can be considered. Fluorescence measurements are possible on any system.

For the cavity diameter, the design is driven by activation considerations. The beam spot without the additional optics will be about 1-cm across. Because every beam burst has a low intensity halo of larger diameter surrounding it, and because the collision of this halo with the casing material of the cavity itself will lead to induced radioactivity, this casing should be well outside of the beam halo area. Based on estimates of this halo, the diameter of the cavity was chosen to be about 2 cm (0.750 in.). A schematic cross-sectional view of the cavity volume is shown in Fig. 5. Also shown in the figure is the volume of the medium excited by the beam burst. Because of multiple scattering in the medium, the beam spot will spread as it transits the material which we assume to be liquid argon. Thus, the cross section of the excited volume is shown as slightly conical. For a 10-cm-long cavity the multiple scattering angle is about 9.6 mrad. With an intial spot size of 1-cm and taking 95% of the beam this increases the excited volume over a simple cylindrical shape by about 17%. This increase of the spot size due to multiple scattering is within the design sizing for the diameter of the cavity.

We considered at the outset designing the cavity for other excitation geometries. In more conventional excitation experiments the excitation is done from the side of the cavity and not down its length as we have planned. However, exciting the cavity from the side puts the excited region of the medium off the center of the cavity. The only sections of the medium that are going to resonate are those that fall within the gaussian envelope of the resonance set up by the mirrors at the cavity ends. By exciting the medium directly along its central axis all the excited medium is exactly where it is supposed to be. This is the reason for the axial excitation in our design. It could be that we will measure even lower lasing thresholds for a given power input due to the more efficient coupling that our design has over other systems.

The cavity design also includes four side-viewing windows that will be used to measure the size of the beam envelope in the lasing medium both on entrance, center, and exit from the cavity, and to measure side fluorescence in the same configuration. Measuring the beam spot size in the cavity during the experiment is important for the normalization of the results in terms of volume. Measuring the side-light fluorescence will be one of the diagnostics that we will use to determine if lasing action has occurred. The additional window allows for another detector arrangement and could be easily accommodated in the design.
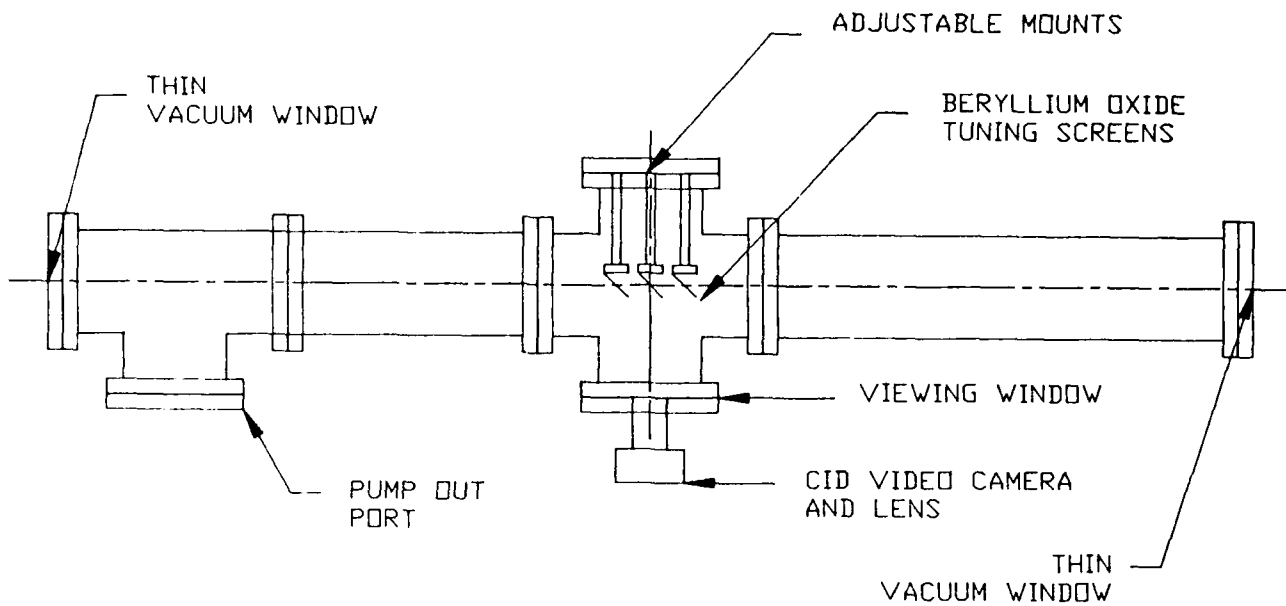
Figure 6: Schematic view of the tuning beam line.

The cavity and feed lines will be operating at cryogenic temperatures near liquid argon ($B.P. = 87.25\ K$). Because of the sensitivity of the index of refraction of the cryogenic media to temperature gradients, special consideration to thermal isolation had to be incorporated in the design. Our first line of defense in the design against the thermal problems was to simply make the thermal mass of the cavity itself as large as possible. This was consistent with the mechanical requirements of mounting the side-viewing window flanges. The limitation in the thickness of the sidewall of the cavity comes from fitting it inside the bore of the superconducting solenoid. The next design step was to isolate the cavity from its surroundings in a vacuum. With a vacuum of 10^{-6}-Torr convection is eliminated leaving only radiational heat flow as the only loss mechanism remaining [13]. To defeat this process we gold coated (0.0001 in thick) all parts of the cavity as associated feed lines in the vacuum including the inside of the vacuum pipe. The emissivity of gold is the key operating feature in this approach. Because the feed lines themselves will penetrate the vacuum wall at some point we used thin wall stainless tubing, taking advantage of the poor thermal conductivity of stainless steel and the reduced cross-sectional area to minimize the thermal conductive path to the vacuum wall.

The Tuning Beam Line. At any accelerator facility some hours with beam on target are used to tune the beam for the experimental requirements. For our laser experiment this means that the laser cavity would be subject to substantial heating due to the beam tuning. Consequently we have incorporated in our system design a beam line mounted below the laser cavity beam line expressly for the purpose of tuning the beam. A schematic view of this beam line is shown in Fig. 6. In the figure the tuning beam line is shown to be the same length as the cavity beam line with tuning screens located in the same position along its length as the entrance and exit of the cavity. These screens are made of beryllium-oxide ceramic and glow in the area where the beam strikes them. The image is viewed from the side as shown using a conventional video camera. The screens are tilted at $45°$ with respect to the viewing camera so that a true image of the beam spot size can be read. Each screen is ruled in 0.5-cm marks along both axes. These targets will allow the machine operator to tune the beam for the optimum focus and spot size in the region of the cavity. The thickness of the screens was chosen to simulate the multiple scattering in the lasing material and end mirrors of the cavity. This will allow us to get a measure of the spot size before the cavity is put in place for checking against the fast video camera image of the excited lasing media as the beam passes through.

The tuning beam line is not connected to the vacuum of the laser cavity beam line. Because at only 10^{-3}-Torr the multiple scattering from air is extremely small this beam line is connected to the roughing pump. The entrance and exit windows of this beam line are the same as for the cavity beam line.

System Mounting Structure. The cavity and tuning beam lines will be moved in and out of the beam with some regularity during a given run. Each beam line must be repositioned with respect to the beam itself to within about 0.020 in. The cavity beam line and all its associated optical equipment has to move as a unit with the tuning beam line

267
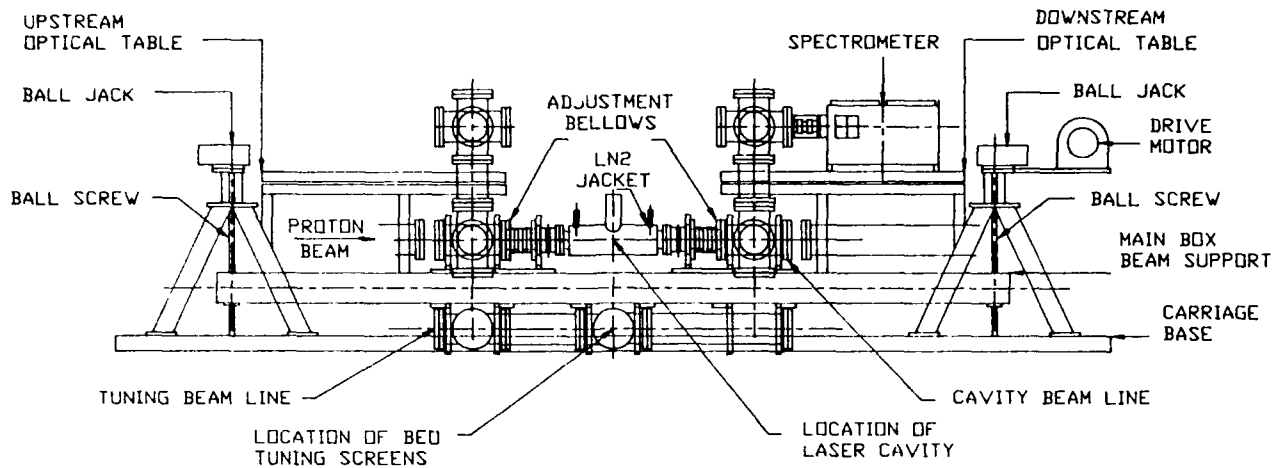
Figure 7: Schematic view of the overall mounting system for both the cavity and tuning beam lines.

slung beneath. When the cryostat becomes available the same support structure and motion assembly should be able to support and move this device as well. In addition, the entire structure must fit inside the 4-foot-wide trench that is available at the PSR. To meet all these requirements, we have designed a four-point lifting system using ball jacks. The overall mounting system is shown in Fig. 7. The cavity beam line without the solenoid and cryostat in place is shown in the center of the figure with the tuning beam line slung beneath from the aluminum box-beams that provide the structural support for the mounting platform. The proton beam enters from the left. The mounting system is shown in the position with the cavity in the proton beam. At each end of the box beams is located a precision ball screw with a gear box on top. Through these gear boxes and two 90° miter gear boxes, torque is transmitted to the ball screws through hardened steel shafts so that all screws turn at the same time and rate. The torque for the system is provided from a 1/2 hp DC motor that can be computer controlled.

Moving the cavity beam line requires that all the associated optical equipment has to be moved as well. In the figure the optical tables left and right are mounted on the box beams. Inside the vacuum a mirror relay system directs the beams from the side-viewing windows and the laser output beam up to the top of the optical tables. In our design we take two windows each upstream and downstream with the laser output being readout downstream. The spectrometer shown on the downstream optical table has a movable grating allowing for the input to be read either from the side or the front. The laser output and one of the side windows is directed into these ports on this device. The other window downstream is directed into a video imaging camera for excitation volume measurements. Upstream one of the windows is also directed into a video-imaging system whereas the other is directed to a photodiode for normalization purposes.

The vacuum required for the deep ultraviolet measurements we envision is about 10^{-3}-Torr. Because of this and that probably frequent entries into the optical table vacuum system will facilitate the setup and alignment we have provided for a set of MgF windows in an intermediate flange (see Fig. 7) to isolate the high vacuum in the cavity beam line. The optical table vacuum is provided by its own roughing pump.

4 SUMMARY

We have designed, fabricated and tested a laser cavity that is suitable for insertion at the PSR facility at LAMPF. Using the high-energy proton beam from this facility, large volumes of liquid or other high-density lasing media can be excited at levels of energy and power density that are beyond those currently known to result in lasing action. This cavity and beam line system was originally designed to answer the physics questions that need to be resolved before a proof-of-concept demonstration of pumping lasing-media using antiprotons. Because of the growing interest in nuclear and reactor pumped laser systems and the difficulty in testing the lasing media, our system can serve as a test bench

for these investigations. In addition, because of the long range of high-energy protons lasing media that could not be pumped using conventional techniques can now be studied.

5 ACKNOWLEDGEMENTS

The authors wish to acknowledge the contributions of Tom Loree (CLS-6) for his valuable recommendations and consulting in regard to standard practice in laser physics, Dave Clark and Jim Hurd (MP-6) for their expertise in PSR and WNR operations, Tamara Johnson for enabling the successful operation of the instrumentation, and Joe King for the construction of tolerant mechanisms and beam line operations.

References

[1] *Design Study pp Facility* CERN report, CERN/PS/AA 78-3.

[2] D. Mohl, *Proceedings of the 1987 IEEE Particle Accelerator Conference*, March 16-19, 1987, Washington, D. C., E. R. Lindstrom and L. S. Taylor, eds.

[3] N. Beverini, et al., Los Alamos Document No. LAUR- 86-260, CERN Document No. CERN-PS-200 (1986); G. Gabrielse, W. Kelis, et al., *Phys. Rev. Letts.* **57**, 2504 (1987).

[4] H. G. Dehmelt, *Advan. At. Mol. Phys.* **5**, 109(1969).

[5] L. Brillouin, *Phys. Rev.* **67**, 260 (1945).

[6] I. S. Lakoba, S. I. Yakovlenko, *Sov. J. Quant. Elec.* **10**, 389 (1980).

[7] C. V. Shank, A. Dienes, and W. T. Silvast, *Appl. Phys. Letts.* **17**, 307 (1970).

[8] N. G. Basov, V. A. Danilychev, Yu. M. Popov, and D. D. Khodkevich, *JETP Letts.* **12**, 473 (1970).

[9] T. R. Loree, R. K. Showalter, T. M. Johnson, J. M. Telle, R. R. Fisher, and W. M. Hughes, *Proc. Soc. Photo-Opt. Instr. Eng.* **540**, 279 (1985).

[10] T. R. Loree, R. K. Showalter, T. M. Johnson, B. S. Birmingham, and W. M. Hughes, *Opt. Letts.* **11**, 510 (1986).

[11] J. G. Eden, et al., *Appl. Phys. Letts.* **35** 2 (1979).

[12] G. P. Lawrence, *Proceedings of the 1987 IEEE Particle Accelerator Conference*, March 16-19, 1987, Washington, D. C., E. R. Lindstrom and L. S. Taylor, eds.

[13] R. H. Kropschot, *Cryogenics* **1**, 171 (1961).

Advances in Directed Energy Technology for Strategic Defense

Richard L. Gullickson

Strategic Defense Initiative Organization, Washington, DC

Advances in lasers, optics, beam control, and particle beam technology have enhanced the prospects for directed energy applications in strategic defense. This paper will focus upon such advances since last year's conference, using our SDI related papers from last year as a starting point."

Summary

Chemical Lasers: In 1988, the Alpha megawatt class chemical laser has been assembled and the combustor operated. The feasibility of efficient overtone lasing of an HF chemical laser at 1.3 microns has been demonstrated. The use of stimulated Brillouin scattering (SBS) for phase conjugation of CW chemical lasers has advanced through the demonstrations of long pulse operation and of a flowing SBS cell with an aero window.

Optics and Beam Control: The Large Active Mirror Program (LAMP) mirror has demonstrated fine figure control under both quiescent and active conditions for all of the seven segments. A process to spin cast large glass mirrors with near final shape has been developed and tested by Schott. The MIRACL DF chemical laser at the White Sands Missile Range (WSMR) has been operated with the SKYLITE beam director to demonstrate the ability to track and engage target drones at tactical ranges and slew rates.

Free Electron Lasers (FEL): Gain guiding and high gain with a linear a wiggler up to 25 m long on an induction linac FEL have been demonstrated at LLNL at 10.6 microns. Boeing has operated an RF linac FEL with a 5 m wiggler at 120 MeV to produce kilowatts of average power at 0.62 microns over an 80 microsecond macropulse. Rocketdyne and Stanford have demonstrated that an RF FEL can operate in a Master Oscillator - Power Amplifier (MOPA) configuration using a single accelerator. Los Alamos has improved the efficiency of operation of its 20 MeV RF FEL to 4% (at 10.6 microns) by improving injector brightness and beam transport.

Excimer Lasers: The Excimer Moderate Power Raman Shifted Laser Device (EMRLD) at WSMR has operated at 100 Hz for three pulses of more than 20 J at a wavelength of 0.35 μm. The ability to operate a high energy excimer laser amplifier in the "Raman look-through" configuration was demonstrated by MIT Lincoln Lab at AVCO using the "Scale-up" device.

Ground-Based Laser Uplink Propagation: The ability to compensate for thermal blooming for moderately high distortion numbers has been demonstrated by MIT Lincoln Lab in the laboratory using a several watt argon laser and a liquid absorption cell to simulate the atmosphere.

Laser Applications in Particle Beam Technology: Laser systems have been developed for diagnosing, neutralizing, and sensing the position of a neutral particle beam. Two different short wavelength laser systems (130 and 226 nm) have been developed and demonstrated for the Delphi laser guided electron beam concept.

TABLE 1. Status of Directed Energy Laser Programs.

Name	Type	Wavelength	Average Power	Status
Alpha	HF Chemical	2.7	MW	Combustor tested
MIRACL	DF Chemical	3.8	MW	Operating with beam director
ZEBRA	HF Overtone	1.35	kW	> 50% relative efficiency demonstrated
ATA/Paladin	Induction FEL	10.6	W	Operating with 25m wiggler
Boeing	RF FEL	0.62	W	Operating with 5 m wiggler
LANL	RF FEL	10.6	W	Operating with 1 m tapered wiggler
Stan./Rock	RF FEL	3	W	Single accelerator MOPA demonstrated
GBFELTIE	FEL	1	MW	Mid 90's
EMRLD	XeF Excimer	.35	kW	3 pulse operation at 100 Hz
Delphi 1	4 Wave Mix	.13	mW	6% optical efficiency, 1.1 mj, mercury vapor
Delphi 2	KrF Anti-Stokes	.23	mW	10% optical efficiency to anti-Stokes

Chemical Lasers

The Alpha HF Chemical Laser is shown in Figure 1. Alpha features a cylindrical design for ease in packaging for space and to facilitate scaling to higher powers. Lasing occurs in an annular gain region a few cm thick in vibrationally excited HF formed in a two step combustion process. The fuel flows radially outward at supersonic velocities to form the mixing region. The gain generator is made from 27 extruded aluminum rings 1.1 m in diameter. The cooled resonator optics are made of copper cladded molybdenum. Alpha is described in more detail in references 1-3 and in the companion paper by Neil Griff at this conference.

Figure 2. The Alpha chemical laser operates with multiple lines between 2.7 and 3.0 μm using vibrational transitions between the 2-1 and 1-0 states (the "fundamental" transitions). Zenith Blue is a program to examine lasing on the 2-0 and or 3-1 vibrational transition. Although the efficiency for "overtone" lasing is lower than for the fundamental, an overall brightness improvement can be realized if the efficiency of overtone lasing is at least 25% as great as for the fundamental.
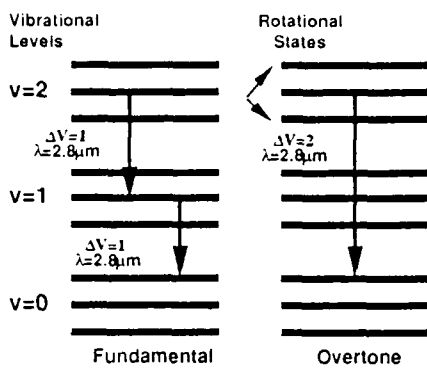
Figure 2.
Short Wavelength Chemical Laser Operation

The Zenith Blue Research Array ("ZEBRA") uses Alpha nozzle technology to examine the efficiency of overtone lasing. Using absorbing coatings (at 2.7-3.0 microns) to suppress lasing on the fundamental, 2.5 kw of power was obtained at 1.3 μm. This represents 55% of the power obtainable with this device from the fundamental transitions between 2.7 and 3.0 μm, with similar flow conditions.

Figure 3. APACHE is a program to examine the utility of nonlinear phase conjugation (by stimulated Brillouin scattering) for beam control of HF chemical lasers. The APACHE program has already demonstrated techniques for reducing the threshold power requirements through multiple SBS cells, the feasibility of CW operation, and beam combining.[1-3]

TRW has demonstrated that SBS can be used with a flowing xenon medium to avoid thermal blooming induced distortions. They used an aerodynamic window consisting of flowing helium gas to separate the high pressure SBS medium from the vacuum region simulating space. The beam quality of the phase conjugated beam is the same with and without flow in the SBS cell.

TRW also recently showed that SBS can be used to phase together the segments in a 19 element mirror. A probe laser is used to record piston, tilt, and figure aberrations. After the probe beam is phase conjugated using SBS, the segmented primary mirror is re-illuminated. The resulting output beam has all of the segment errors removed and provides the performance of a beam from a single large aperture monolithic primary mirror.

Figure 4 shows a Zerodur (glass) mirror cast as a single parabolic blank by Schott. By using a rotating table for the casting, the parabolic shape was obtained to a surface precision of 1 mm, substantially reducing the time required for grinding.

Figure 5. MIRACL is a high power DF chemical laser operating at 3.8 microns. It supports both space and ground-based laser technology development activities. It is integrated with the SKYLITE beam director which has the capability to track targets and illuminate them at the high slew rates associated with tactical applications.

A local loop beam control system using a 69 channel cooled deformable mirror has already demonstrated improved beam quality. Recently the MIRACL system demonstrated the ability to track and engage target drones at tactical ranges.

Free Electron Lasers

The Ground-Based Free Electron Laser Technology Integration Experiment will demonstrate the major land based elements of a ground based laser system. These elements include the laser device, beam control system, and atmospheric propagation capability.

Several parallel approaches are being pursued for the ground-based FEL program. The radio-frequency linac approach offers a pulse format of closely spaced micropulses (Figure 6). This pulse format may offer atmospheric propagation advantages with lower losses to stimulated Raman scattering from rotational levels in nitrogen molecules. High electrical efficiency is possible because the unused portion of the electron beam can be converted back into RF power using energy recovery cells. Both oscillator and master oscillator power amplifier configurations should be possible.

In two separate experiments at Stanford, with TRW; and at Boeing, RF FELs have lased at 0.5 microns. The light weight accelerator cavities of the RF FEL also make this device promising as a space-based laser. The use of superconducting cavities offers the promise of very compact accelerators with high current capability for MOPA configurations in space. Cooling to liquid hydrogen temperatures may be relatively simple using platform cryogenic fuel and may offer most of the advantages (e.g. high gradient and low losses) associated with superconducting operation.
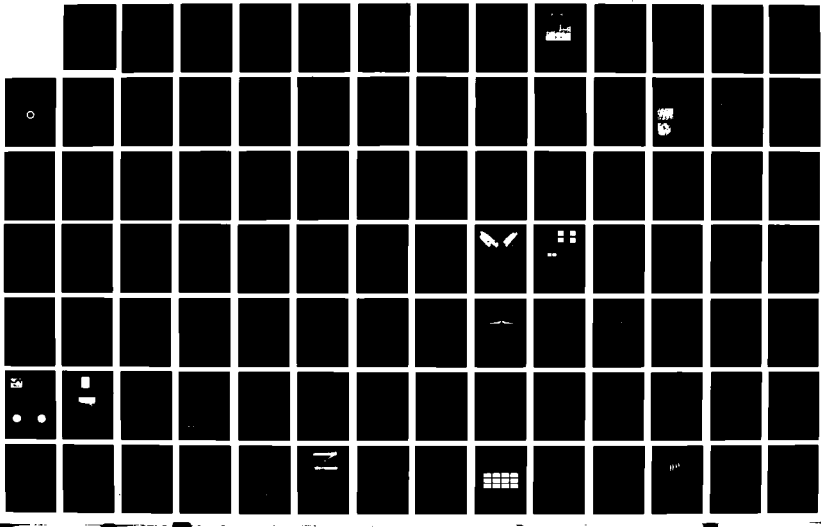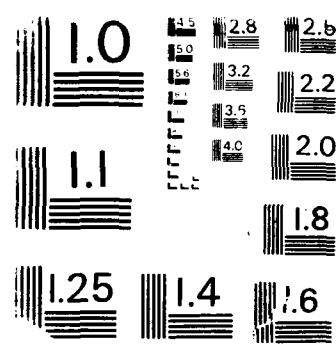
Radio-frequency Linac FEL
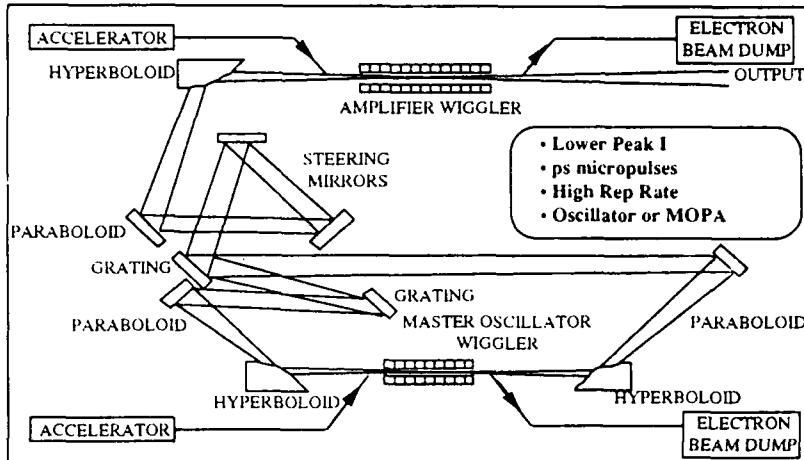
Figure 6.

In more recent results, Boeing has upgraded their power conditioning system to provide flat top macropulses more than 100 microseconds long. The peak micropulse current is more than 300 A and the SpectraTechnology permanent magnet wiggler has a maximum field error of less than 0.5%. The system was recently modified to lase at 0.62 microns.

In initial experiments conducted with a confocal resonator (the next phase will employ a new ring resonator), 0.1% of the energy in the 120 MeV electron beam was converted into red light. This represents 2 kW of average power over the 80 microsecond macropulse and a peak cavity power of 40 MW (4 MW outcoupled) with a 4 MHz rep rate.

The Los Alamos National Laboratory has recently improved the efficiency of operation of their RF FEL oscillator operating at 10.6 μm using a tapered wiggler. By prebunching the electron beam, improving the injector brightness, and improving the electron beam transport through the accelerator by eliminating discontinuities, the efficiency for converting electron beam energy to light at 10.6 μm was improved from the old value of 1% to the new result of more than 4 %.

Figure 7 shows that the maximum efficiency is obtained when a 30% taper is used on the wiggler resulting in more electrons being captured in the RF "buckets." The modelling of efficiency as a function of electron beam emittance suggests emittance values in good agreement with measurements. The LANL 4.4% oscillator efficiency at 10.6 microns is similar to the value obtained by Boeing several years ago in an amplifier experiment.

Figure 8 is a streak camera picture illustrating how the energy distribution of the electron beam broadens as energy is extracted from the beam. Approximately 30% of the electrons were trapped in the RF buckets and were reduced in energy by 7%.

These results show that prebunching does improving efficiency for tapered wigglers (by a factor of about 2), that a large fraction of the electrons in the beam are trapped and their energy converted into light, and that existing FEL models do an excellent job in predicting experimental results.

Figures 9. Stanford and Rocketdyne recently showed that the MOPA configuration is feasible for the RF FEL. Using the Mark III accelerator operating at 35-40 MeV with a peak current of 10-40 amps, the team examined the wavelength dependence of gain and found good agreement with theory. Typical gains of 50% per pass were measured using a novel configuration where a single accelerator provided the electron beam for both the master oscillator and the tapered wiggler power amplifier. The gain peaked at 3.1 micron with a maximum value of 65% { at this conference they reported increasing the maximum gain to 150% and the successful operation of a laser illuminated LaB_6 photocathode to produce a peak current of more than 100 A }. These results are important for establishing the promise of the RF FEL for both space and ground applications.

The other approach to the Ground Based Free Electron Laser is the high current induction linac (Figure 10). This produces longer pulses with a lower repetition rate. The high current (several kiloamperes) possible with this approach lends itself to MOPA configurations. Induction linacs have produced extremely high efficiencies at mm wavelengths and have demonstrated high gain at wavelengths ranging from 9 mm to 10.6 μm. The 50 MeV Advanced Test Accelerator (ATA) at LLNL is used with currents of up to 1.2 kA for FEL experiments.
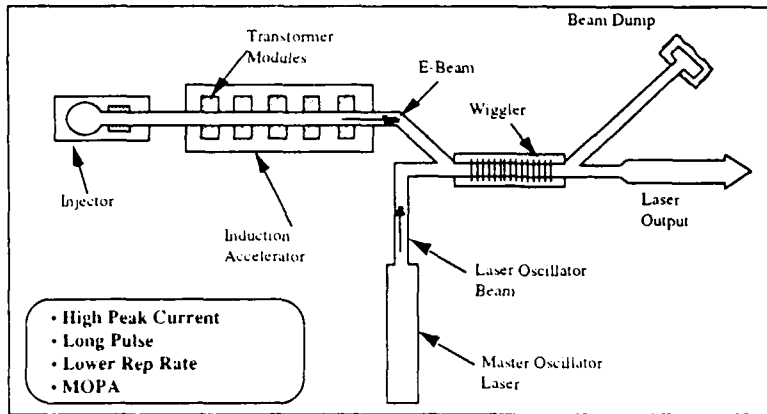
Figure 10.

Figure 11. "Paladin" is the current FEL experiment on ATA and uses wiggler lengths of up to 25 m. Its goal is to extend high efficiency operation to the 10.6 micron wavelength and to demonstrate that refractive and gain guiding effects in intense electron beams can guide the amplified electromagnetic wave to reduce diffractive spreading in long wigglers and produce high quality optical output.

The PALADIN wiggler (Figure 12) is a hybrid. It is a dc iron-core electromagnet with coils surrounding steel poles. The permanent magnets reduce the flux density in the iron poles, permitting a higher wiggler field to be attained before saturation. The use of an electromagnet also allows easily varying the magnetic field as a function of axial position (the "taper"). The PALADIN wiggler with its 8 cm period is more than 300 periods long at 25 m and has a maximum field error of 0.15%

Figure 13. Preliminary results at LLNL suggest that gain guiding does occur in high gain induction linac amplifier FELs. Gain guiding was demonstrated earlier in low gain oscillators at Stanford (with a low current RF device) and at Columbia (using a low voltage diode machine) 4.

LLNL is now operating with the full 25 m wiggler. They have been able to transport up to 1200 amps of current through the wiggler with no appreciable losses at an electron energy of 42 MeV. In initial experiments with an untapered wiggler operating ATA at 44 MeV and 1000A, the maximum gain was 31db. An 18 kw carbon dioxide laser was amplified to produce a saturated output peak power of 23 MW.

Technology advances have brought induction and RF linac operating characteristics closer together. The development of magnetic modulator technology to replace gas blown spark gap switches has allowed operation at high repetition rates. LANL has developed a technology for FEL injectors which allows RF linacs to operate with higher current and brightness [6]. A doubled Nd:YAG laser caused photoemission of

a high current electron pulse from a cathode. This bunch is accelerated to megavolt potential in a single step, reducing emittance growth. With this approach, not every RF wave bucket is filled with electrons. This results in higher peak currents allowing high gain and operation in a MOPA configuration.

Excimer Laser Technology

Figure 14. The Excimer Moderate Power Raman Shifted Laser Device (EMRLD) is now operating at the White Sands Missile Range. The EMRLD master oscillator is designed to produce 40 j per pulse at 100 Hz with XeF at .35 μm and has demonstrated a total of 59 J for a three pulse train. When the flow loop is completed, full CW operation will be possible.

The EMRLD design also includes both Raman and power amplifiers for increased power and the ability to perform Raman "lookthrough" for atmospheric compensation.

Northlight typifies the state-of-the-art in transportable discharge excimer laser technology. Discharge excimers use lower voltage pulsed power technology to excite the lasant through current flow by a preionized medium. Northlight operates at 10 Hz in 1 sec bursts and produces more than 40 j per pulse. With the installation of the flow loop, more than 50 j per pulse at 50 Hz should be achievable.

Ground-Based Laser Propagation

Figure 15 is a diagram of the thermal blooming experiment at the MIT Lincoln Laboratory. Absorption in an iodine doped organic liquid (carbon tetrachloride) simulates thermal blooming in the atmosphere while phase screens produce turbulence like effects. A several watt CW argon laser is corrected for these effects using two 69-channel deformable mirrors.

Lincoln Lab has shown that even when a periodic phase ripple is placed in the beam to stimulate the growth of the thermal blooming instability that the beam can be stably compensated for distortion numbers up to 150.

273
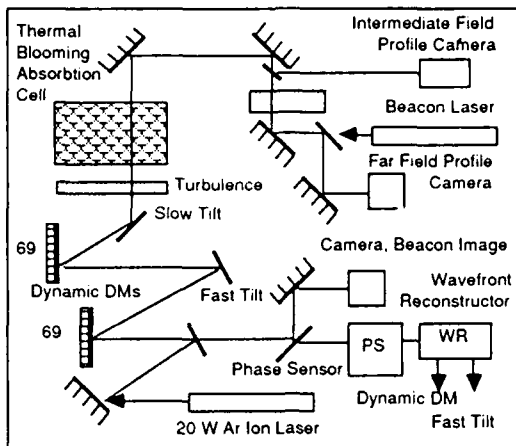
Figure 15. Thermal Blooming Experiment
at MIT Lincoln Laboratory

By picking an appropriate wavelength such that atmospheric absorption of laser light is minized, thermal blooming can be reduced. Science Research Laboratory has developed an interferometric absorption spectrometer with high sensitivity. They have found windows near 1:06 μ with an absorption at or below 10^{-9} cm for 14^{-1} torr water vapor in nitrogen at one atmosphere. In these windows, molecular absorption by water vapor is actually less than losses by Rayleigh scattering. Jaycor

Particle beam Technology

SDIO particle beam technology programs have also advanced laser technology. Figure 16 illustrates the applications of laser technology to the neutral particle beam system. Such a system accelerates negative hydrogen ions to high energy, magnetically expands the beam and points it at the target, strips the beam to form neutralized atoms which will propagate ballistically, undeflected by the earth's magnetic field, and senses the beam direction as it leaves the platform to allow "boresighting" with the acquisition, tracking, and pointing system.

LASER APPLICATIONS IN THE
NEUTRAL PARTICLE BEAM SYSTEM
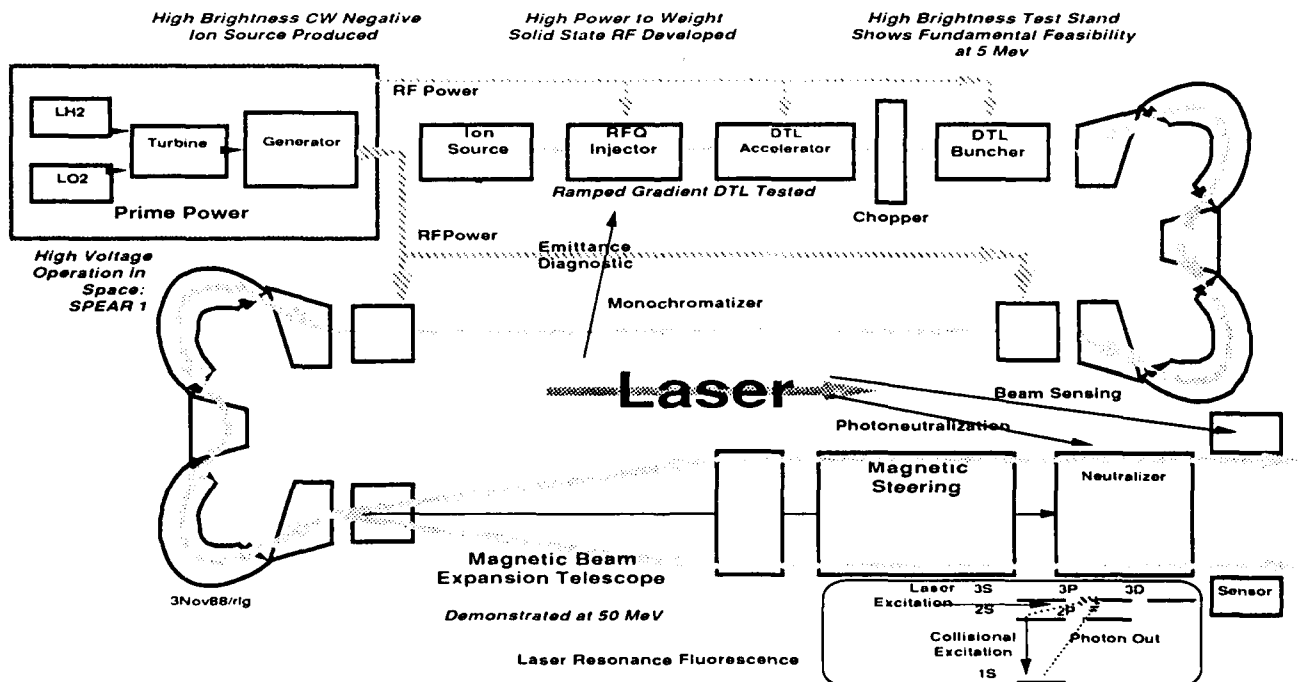
Figure 16.

Lasers are a leading candidate for both high brightness beam neutralization and sensing. A photon of about 1 ev (~ 1 μm) can strip the extra electron from the hydrogen ion to produce the neutral beam. Higher photon energies produce an increased probability of stripping at the expense of imparting more transverse momentum (and divergence) to the beam.

Currently this photoneutralization process is used by Los Alamos National Laboratory as a diagnostic technique. Picosecond pulses from a mode-locked frequency-doubled Nd:YAG laser are used to sample the emittance of a small portion of the beam in the Accelerator Test Stand.

Laser resonance fluorescence is a beam sensing technique. Hydrogen atoms in the 2P excited state are produced in the stripping process. These atoms can be resonantly excited to the 3P state by a properly tuned laser. The excitation cross section depends upon the angle between the laser and the outgoing beam. By observing and maximizing the fluorescence from the 3P-2S transition, the beam can be properly boresighted with respect to the accelerator platform.

LANL recently demonstrated this technique at the 50 MeV beam line at Argonne National Lab. They used a flash lamped pumped dye laser producing up to 80 mJ at 623 nm operating at 0.5 Hz. Frequency doubled Nd:YAG laser systems have also been used to provide greater intensity for higher particle energy beams (on LAMPF). Because system applications require CW operation, the next phase of the experiments will employ a CW ring dye laser.

The Delphi concept is under investigation at Sandia National Laboratory. A laser produces an ionization channel in the upper atmosphere. A high current relativistic electron beam follows the positive ion column produced by the laser ionization in a straight path to the target. Electrostatic forces keep the electron beam following the channel undeflected by the earth's magnetic field.

Figure 17. There are a variety of different methods to ionize atomic oxygen. We are currently investigating two. The first (1+3) uses 130 nm UV radiation to produce an excited state in atomic oxygen. An auto-ionizing state is produced by three additional non resonant IR photons. Because of the large cross section for each of these two steps, the energy required is small.

In the second approach (2+2), two photon excitation occurs using high intensity 226 nm UV light. Two additional IR photons produce the auto-ionizing state.

Atomic-Oxygen Photoionization Schemes
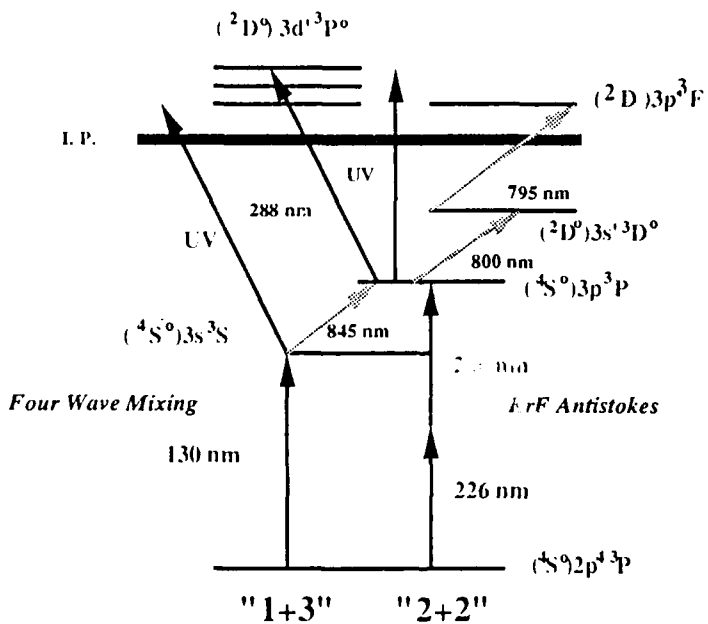
Figure 17.

Figure 18 shows the four wave mixing method used to produce the 130 nm UV photons for excitation at Spectra Technology Inc. A frequency-doubled Nd:YAG laser drives dye and Ti:Sapphire amplifiers for the CW dye laser oscillators. Each laser operates at a slightly different wavelength between 0.7 and 0.9 nm. The 765 nm beam from one Ti:SAP amplifier is frequency tripled to 255 nm. The 810 nm from another is frequency doubled to 405 nm and a third 777 nm beam is used directly. The 405 and 255 nm photons added are resonant with the Hg 7^{1}S state.

275
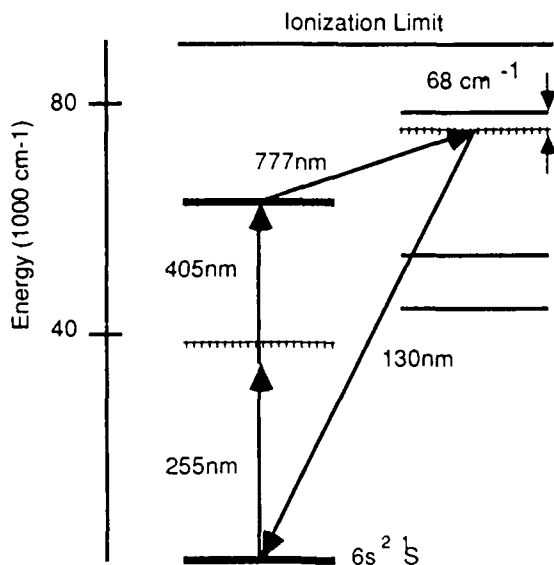
Figure 18.
Generation of 130 nm Radiation by Four-Wave
Mixing in Mercury Vapor

These are combined to produce 130 nm UV light in a 1 m long Hg vapor cell operated at 200° C. Each pulse of the input lasers produces 1 mJ at 130 nm with a 2 ns pulse length. The optical efficiency of this sum-frequency-mixing process is 5%.

Figure 19 illustrates the excimer laser research facility. The key to obtaining high efficiency from an excimer is to make the input pulse length short compared to the storage lifetimes of these lasers which are typically a few ns. Sandia uses a train of sub ns pulses separated by a few ns to allow the gain medium to recover between pulses. They use a Littman oscillator (which employs a diffraction grating as a frequency selective element to insure single mode operation) as the master oscillator of the dye laser to produce the the 1 μj, 0.3 ns pulses used to drive the excimer system.

Sandia has obtained 80% relative extraction efficiency using this technique with an electron beam-pumped amplifier driven by a discharge-pumped preamplifier using 2 nsec interpulse spacing. They demonstrated 10% conversion (10j in; 1 j out) into the 226 nm Anti-Stokes line in an energy scalable geometry. The key factor in obtaining high efficiency was the co-injection in the H filled Raman cell of a phase matched Stokes beam with about 5% of the energy of the 248 nm pump.

Excimer Laser and Raman
Conversion Research Facility
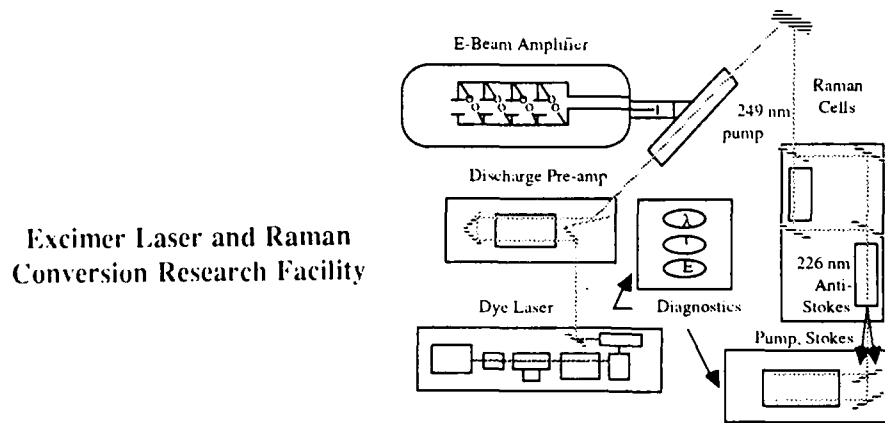
Figure 19.

The Delphi program has also pioneered the development of photoconductive semiconductor switches (PCSS). In such switches, light from a laser creates charge carriers in an (almost) intrinsic semiconductor. Such switches operate in both an open and closing mode because when the light is removed, the number of charge carriers decays exponentially with the characteristic recombination time (1-100 ns for typical opening switch materials) and the resistance increases. Opening times comparable to the recombination time (20 ns e fold time with Au:Si) have been demonstrated at 1 kA and 57 kV.

Sandia National Labs has demonstrated PCSSs which can open and close in 1-10 ns and can switch high power RF circuits at rates above 10 MHz (driven by a 2X YAG with 300 mj per pulse in a regenerative amplifier configuration). They plan to use this high frequency waveform to drive induction linac cavities.

Summary

Many advances in directed energy technology have changed the perspective on applications for strategic defense. The many breakthroughs in nonlinear optics and the development of efficient overtone lasing have revitalized the chemical laser program.

The emergence of the free electron laser with the demonstration of high efficiency operation, high brightness electron beam technology, short wavelength operation, and gain guiding have made this the leading candidate for ground based applications and a promising device for space.

Both neutral and charged particle beam programs have advanced laser technology with the noteworthy developments by Sandia Laboratories and Spectra Technology of several efficient short wavelength laser systems.

Cleared for Open Publication, 6 Dec 88, OASD-PA 885188.

Appendix A. Figures used in presentation. Because of space limitations, not all of the figures used in the presentation are reproduced here. Many are included in other papers in these conference proceedings as indicated below.

T1	Status of DE Laser Programs	Table 1	F11	Paladin Objectives	Ref 10
F1	The Alpha Chemical Laser	Ref 5	F12	Paladin Wiggler	Ref 10
F2	SWCL Laser Operation	Fig 2	F13	Gain Guiding Results	Ref 10
F3	The Apache Program	Ref 6	F14	EMRLD	Ref 11
F4	Large Zerodur Mirror	—	F15	Lab Thermal Blooming Exp	Fig 5
F5	The MIRACL System	Ref 5	F16	Laser Applications for NPB	Fig 6
F6	Radio-frequency Linac FEL	Fig 3	F17	Atomic Oxygen Photoionization	Fig 7
F7	LANL Tapered Wiggler Results	Ref 8	F18	Generation of 130 nm Radiation	Fig 8
F8	LANL RF FEL Electron Spectrum	Ref 8	F19	Excimer Laser Facility	Fig 9
F9	Stanford-Rocketdyne RF MOPA	Ref 9			
F10	Induction Linac FEL	Fig 4			

"High Power Hydrogen fluoride Chemical Lasers: Power Scaling and Beam Quality," ibid.

T. W. Meyer, R. L. Gullickson, B. J. Pierce, D. R. Ponikvar, "The Ground-Based Free Electron Laser: Challenges and Solutions," (and other papers at this conference) Proceedings of "FEL 88," Jerusalem, Israel, 29 Aug - 2 Sep 88.

Neil Griff and Douglas Kline, "High Power Chemical Laser Research Status," proc. of this conference.

C. G. Koop, "Stimulated Brillouin Scattering at 2.9 μm," this conference.

D. R. Shoffstall and D. Yeremian, "FELs Driven by LINACs," this conf.

R. W. Warren, "Lasing in Practice Versus Theory," this conf.

A. Bhowmik, M. Curtin, W. McMullin, S. Benson, J. Madey, B. Richman, and L. Vintro, "Observation of Gain in a Single Accelerator Driven FEL MOPA," this conference (see also the other two Rocketdyne FEL papers in these proceedings).

T. J. Orzechowski, et al., "Paladin, A 10.6 u FEL Amplifier Driven by a Linear Induction Accelerator," this conf.

M. J. Boness, "EMRLD Master Oscillator: A Progress Report," this conference.

S. F. Fulghum and M. Milleman," Interferometric Absorption Spectroscopy of Water Vapor Near 1.06 m," this conference (FC7).

G. Sutton, Session FC, this conference.

R. Sander, C. R. Quick, R. Reeder, D. J. Taylor, "Recent Results in Laser Resonance Fluorescence Beam Sensing," NPB Annual Program Review, October, 1988.

A. V. Smith and W. J. Alford, "Practical Guide for 7S resonant frequency mixing in mercury; generation of light in the 230-185- and 140-120-nm ranges," Journal of the Optical Society of America B, Vol.4, 1765, November 1987. A. V. Smith, W. J. Alford, and G. R. Hadley, "Optimization of two-photon-resonant four-wave mixing: application to 130.2 nm generation in mercury vapor," JOSA B, Vol. 5, page 1503, July 1988. C. H. Muller, D. D. Lowenthal, M. A. DeFaccio, A. V. Smith, "High efficiency, energy-scalable, coherent 130-nm source by four-wave mixing in Hg vapor," Optics Letters, Vol.13, page 651, August 1988.

T. D. Raymond, C. Reiser, R. G. Adams, R. B. Michie, and C. Woods, "Pulse-train Amplification of Subnanosecond Near-transform-limited KrF Laser Pulses," SPIE Vol. 912 Pulsed Single Frequency Lasers: Technology and Applications (1988).

F. J. Zutavern, G. M. Loubriel, and M. W. O'Malley, Proc. of 6th IEEE Pulsed Power Conf., Arlington. VA, 1987, 577.

F. J. Zutavern, et al., "Multiple Pulse Photoconductive Semiconductor Switching," Proc. of the 18th Power Modulator Symposium, Hilton Head Island, SC, 1988.

PROSPECTS OF XUV RECOMBINATION LASERS IN CAPILLARY DISCHARGES

J.J. Rocca, M.C. Marconi, D. Beethe and M. Villagran Muniz

Colorado State University

Electrical Engineering Department

Fort Collins, CO 80523

ABSTRACT

The possibility of using capillary discharge excitation to create extreme ultra-violet recombination lasers is discussed. In the proposed scheme a highly ionized capillary plasma is created by a short current pulse; subsequently electron heat conduction to the ca pillary walls and radiation losses are expected to rapidly cool the plasma resulting in a large recombination rate which under optimized plasma conditions should lead to population inversions. Time resolved spectra of capillary plasmas are reported. Spectra from a 500 um lithium hydride capillary discharge show the simultaneous emission from lines corresponding to highly ionized species (LiIII, OVI) and single ionized species (OII), indicating the co-existence of a hot highly ionized plasma region at the center of the capillary surrounded by a significantly cooler plasma. Diffusion of totally stripped ions from the core plasma into the cooler plasma at the end of the current pulse might give origin to an annular gain region.

The use of collisional electron-ion recombination as a laser population inversion mechanism was first suggested by Gudzenko and Shepelin [1]. Since then, lasers [2-5], discharges [6-10] and electron beams [11] have been successfully used to generate plasmas which adequately evolve to recombine and produce laser action. The majority of the experiments have concentrated in demonstrating lasers at infra-red and visible wavelengths [1-3, 6-11]. The possibility of extending this type of lasers to shorter wavelengths was analyzed by Bohm [12], and recombination of laser produced plasmas have been among the first experiments in demonstrating large amplification at soft X-ray wavelengths [4-5]. To obtain similar gains with discharge excitation, the plasma created by this method need to be more highly ionized and more dense that those successfully used to excite visible recombination lasers. In addition to these requirements the discharge geometry has to allow for rapid cooling of the plasma, to be able to obtain large recombination rates and population inversions at wavelengths at which mirror reflectivities are low. Also the plasma has to be optically thin to radiation originated from the lower laser level to allow for a rapid rate of depopulation of this level.

We recently suggested the use of plasmas created by capillary discharges with a large length-to-diameter ratio to obtain amplification at short wavelengths following three body electron-ion recombination [13]. Herein we present time resolved visible and extreme ultraviolet spectra of the emission from capillary plasmas created by fast (50 ns FWHM) discharges, and discuss observations that relate to the possible use of these plasmas as extreme ultraviolet laser media.

The discharge device used in the experiments is schematically represented in figure 1, and illustrated in the photograph of figure 2. A 6.6 nF ring of ceramic capacitors, which could be charged to a voltage up to 100 kV is placed co-axially with the capillary channel in a low inductance configuration. No additional current switch other that the capillary itself is included in the circuit. The capacitors are charged to a voltage below the capillary flashover value, and initiation of the discharge at the desired time is obtained by firing a smaller trigger discharge between a third electrode and the cathode, which is kept at ground potential. A solenoid coil capable to generate an axial magnetic field of up to 100 kG with a half cycle of 170 us surrounds the capillary to provide additional control over the plasma evolution. The high voltage components are enclosed in the grounded stainless steel container visible in figure 2 and immersed in transformer oil to avoid corona and the possibility of undesirable external flashover. The discharge volume is evacuated to a pressure below 1 10^{-5} Torr using a turbomolecular pump. The optical and electrical diagnostics equipment are placed inside a Faraday enclosure. The current pulse is monitored with a Rogowski coil, digitized by a 200 MHz waveform digitizer and stored for every shot of the discharge. The radiation emitted by the plasma in the axial direction was analyzed with a visible 0.3 m spectrograph and with a normal incidence vacuum spectrograph of 1 m focal length.
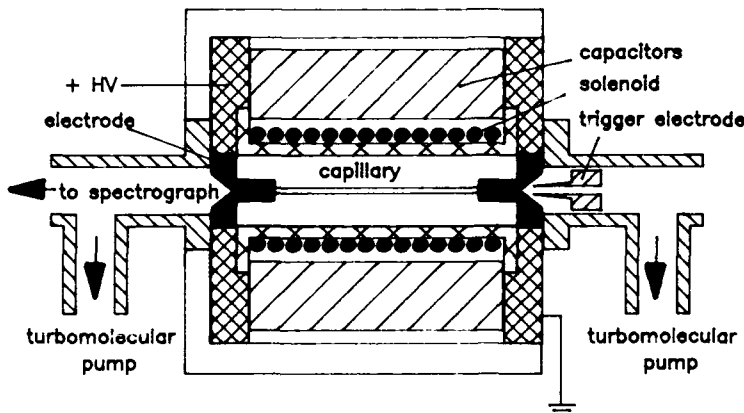
Figure 1- Schematic diagram of the capillary discahrge
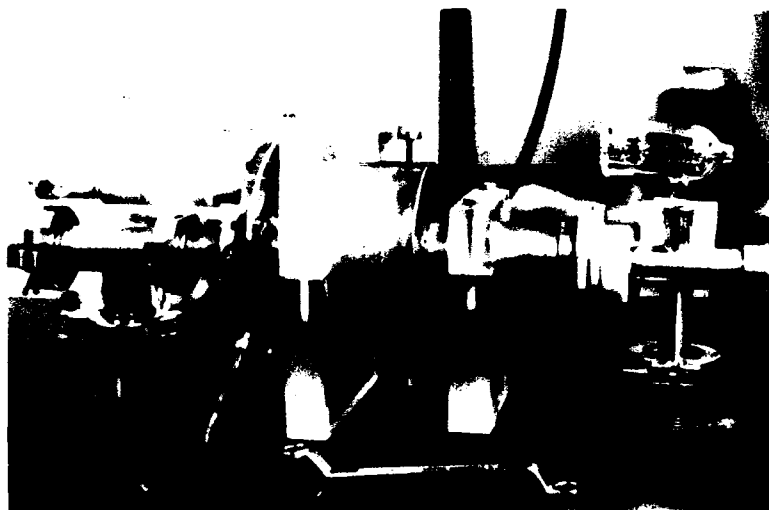
Figure 2- Photograph of the capillary discharge devise.

The 3-2 transition of hydrogenic ions having the wavelengths ranging from 72.9 nm for LiIII to 18.2 nm for CVI are good candidates for amplification by electron-ion recom bination and require excitation energies that can be obtained from relatively compact dis-charge devices. To obtain inversion in these transitions an initially nearly totally ionized plasma is required. Our initial study of the plasma evolution in a capillary discharge was made using a polyethylene capillary 500 um in diameter and 5 cm in length. While the dis-charge set-up described above was not designed to have the power required to completely ionize carbon [13-15], polyethylene was chosen for the initial test of the discharge becau-se a carbon plasma with a relatively low degree of ionization is of interest in relation with the possibility of amplification in the 116.9 nm transition of CIV [16]. Also in this material elongated capillaries are relatively easy to construct.

The current pulse corresponding to the discharge obtained charging the capacitor to 40 kV is shown in figure 3 having a FWHM of 50 ns and a peak of 5 kA. The radiation emit ted by one of the ends of the capillary was focused with a quartz lens into the slit of a 0.3 m visible spectrograph and was detected with a gated multichannel-plate array detector. Time resolved spectra obtained with an optical window of less than 18 ns are shown in figu-re 4 for a 15 kV excitation pulse. The spectra correspond to the 217 nm to 290 nm region and illustrate the evolution of the plasma emission from 10 ns to 230 ns after the peak of the discharge current pulse. Emission from the CIV 253.0 nm line, which populates the upper level of the 116.9 nm line, is intense 10 ns after the peak of the excitation. The CIII 229.7 nm, and the 283.7 nm and 283.8 nm lines of CII are also visible. The CII 251.2 nm line is also observed but it is not completely resolved from the CIV 253.0 nm emission du-ring the current pulse. As the discharge current decays, the intensity of the emission from the CIV lines rapidly decreases; and a large increase is observed in the intensity of the CIi lines. The temporal variation of the intensities of the lines associated with the dif-ferent stages of ionization is more easily observed in figure 5. For 15 kV excitation, cor-responding to a discharge energy of only 0.75 J, CIV is the dominant specie at the peak of
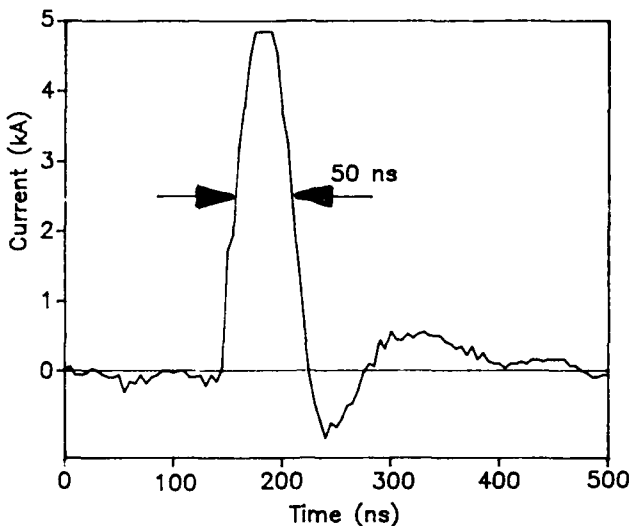
Figure 3- Current pulse measured through a 5 cm long,
500 um diameter polyethylene capillary excited by a
40 kV pulse from a 6.6 nF capacitor.

the current pulse. For the ionization time from CIII to CIV to be of the order of the cur-
rent pulse rise time the electron temperature has to be about 16 eV.Assuming this temperatu-
re and pressure equilibrium of the plasma, the electron density can be estimated to reach 6
10^{16} cm^{-3}. The intensity of the 253.0 nm CIV emission is observed to rapidly decrease as the
current drops, and the maximum intensity for the CII lines occurs 110ns after the peak of
the current pulse, indicating excitation by three-body electron-ion recombination as the pla
sma cools.The effects of applying a 55 kG magnetic field to the 15 kV discharge is illus-
trated in figure 6. The magnetic confinement is observed to increase the degree of ioniza-
tion of the plasma as indicated by an increase in the emission of the CIV line and a simul-
taneous decrease in the CII emission. The increased plasma confinement by the applied mag-
netic field is evidenced by the slower decay of the CIV 253.0 nm line in figure 6 as compa-
red with figure 4. The magnetic field also affects electron heat transport to the capillary
walls and thereby affects the recombination rate into ions of lower charge. In the presence
of a strong axial magnetic field the transport coefficients are substantially reduced and
plasma cooling has to rely in radiation losses, which could be enhanced by adding higher Z
impurities to the plasma [16].

   An increase in the degree of ionization of the plasma, can be achieved by increa
sing the excitation energy. As the discharge voltage was increased line emission in the
spectral region of figure 4 was observed to degenerate into broadband emission as the plas-
ma becomes more dense and optically thicker. In this case more information on the plasma
evolution could be obtained by observing the radiation emitted at shorter wavelengths. The
time resoved carbon plasma spectra presented herein illustrate that multiple ionized ions
created by a short pulse in a capillary discharge recombine at the end of the excitation to
excite transitions in ions of lower charge. Since collisional recombination preferentially
excites highly excited levels, it might be possible to optimize the discharge parameters to
obtain inversions in selected ions. For optical gains to be significant it will be necessa-
ry to adjust the plasma conditions to avoid excessive collisional de-excitation of the up-
per laser level and trapping of lower level radiation.

   To gain information on the possibility of inverting the 72.9 nm LiIII line we
introduced a 500 um diameter, 4 cm long lithium hydride capillary in the set-up of figure 1.
The axial emission of the discharge in the extreme ultraviolet was analyzed with a vacuum
spectrograph with 600 and 2400 lines per millimeter gratings. Time resolved spectra were
obtained gating a windowless multichannel-plate intensified array detector. Each spectra
was obtained with an optical window of approximately 5 ns.

   Figure 7 is a time resolved spectrum covering the 68-110 nm region, at the time
corresponding to 3 ns after the peak of the discharge current for a 35 kV discharge. Inten-
se emission from the OVI 103.1 nm and 103.7 nm is observed at the right side of the spec-
trum. Also visible is the emission from the LiIII 3-2 transition at 72.9 nm and oxygen im-
purity lines corresponding to all degrees of ionization from OVI down to OII. The higher
resolution spectrum also shown in figure 7 allows to assign the emission in the 83 nm re-
gion to OII and OIII transitions. The simultaneous emission from species with such diffe-
rent degrees of ionization as OVI and OII cannot occur in a plasma of uniform temperature.
To make possible the existence of a large concentrations of OVI at the time of the current
peak the time constant for ionization from OV to OVI has to be of the order of the risetime
of the current pulse, which requires an electron temperature of ab^   27 eV. Also signifi-

280
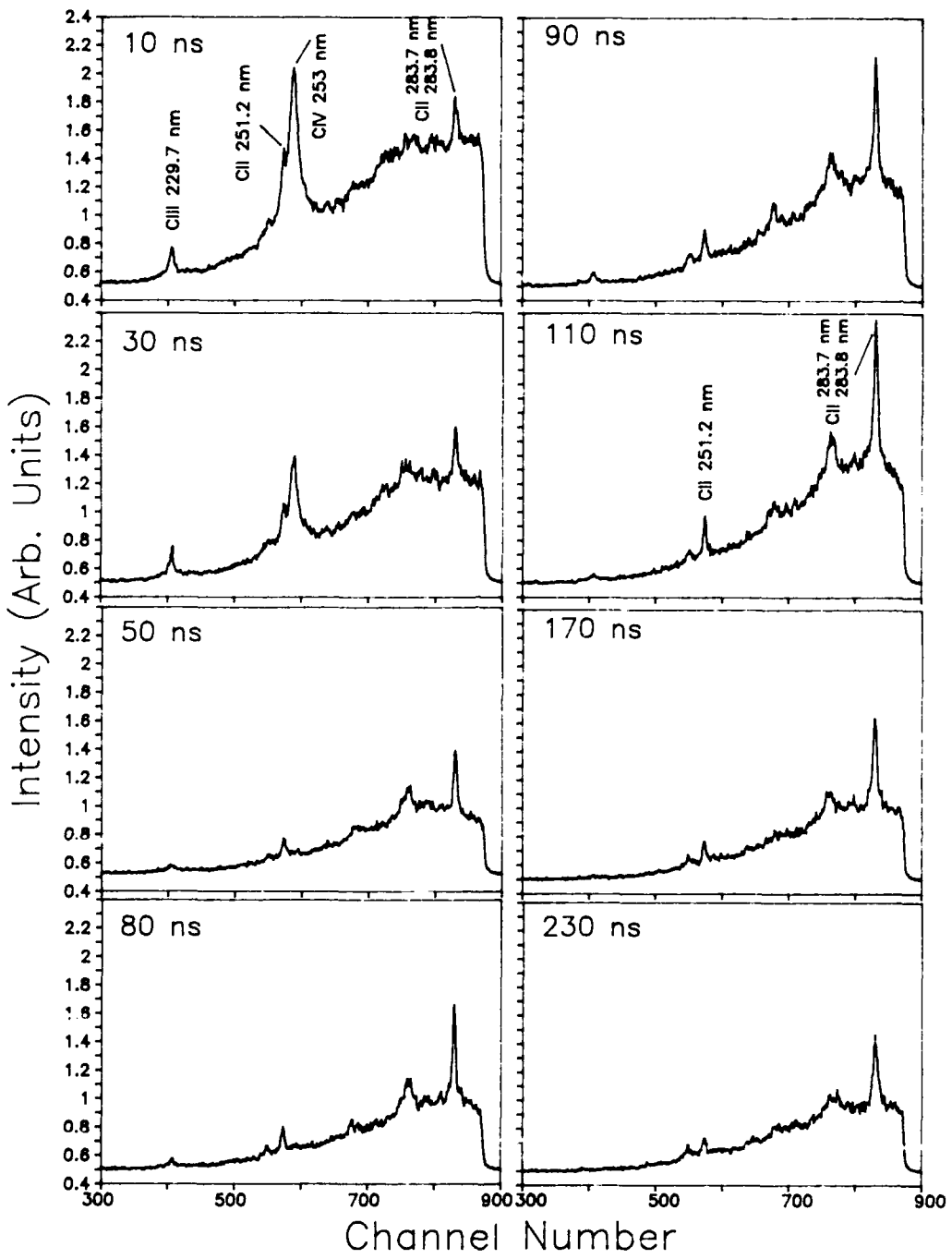
Figure 4- Time resolved UV spectra of the axial emission
from a 500 um diameter, 5 cm long polyethylene capillary
emitted by a 15 kV pulse. The external magnetic field ap-
plied is B=0. The time delay respect to the peak of the
current pulse is indicated for each spectrum.

cant emission from the OII will only occur at temperatures below 6 eV. These observations
suggests the existence of a hot (>25 eV) highly ionized plasma core surrounded by a much
cooler plasma near the walls of the capillary as illustrated in figure 8. This situation is
consistent with the model developed by McCorkle [15], in which ablation of the wall mater-
ial is assumed to form a high density plasma layer surrounding a less dense and significan-
tlyhotter plasma core. It is possible to envisage that at the end of the current pulse,
when the confinement produced by the self-induced magnetic field decreases, diffusion of
totally stripped ions from the plasma core might form a high recombination region of an-
nular shape where inversion might take place under optimized plasma conditions [16]. The
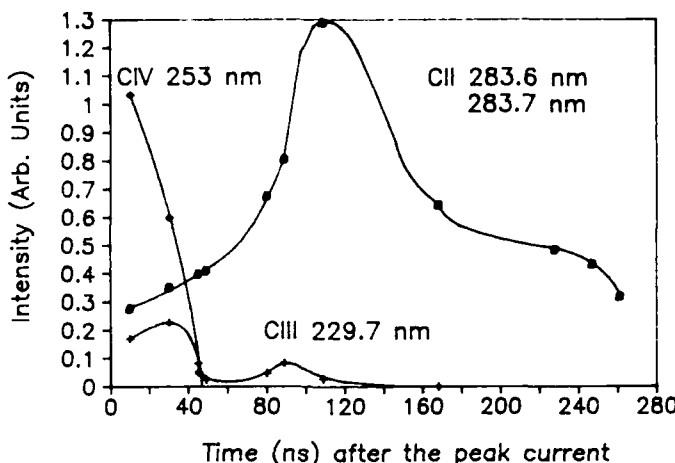
Figure 5- Evolution of the intensity of the emission from lines corresponding to different degrees of ionization of carbon in a polyethylene capillary discharge for 15 kV excitation in the absence of an externally applied magnetic field. The time is measured respect to the peak of the current pulse.

scenario of highly stripped ions diffusing into a cooler plasma of higher density has similarities to conditions that recently lead laser action in an annular region at 18.2 nm in Al in a plasma created with a high energy CO_2 laser [17].

Time resolved spectra of the emission from a 40 kV discharge show a significant increase in the emission from the 72.9 nm line as the discharge current decreases, as can be expected from the excitation of the n=3 level of LiIII following electron-ion recombination [18]. Assuming pressure equilibrium in the plasma core, the electron density of this plasma is estimated to reach about $1 \cdot 10^{18}$ cm^{-3}. For amplification in the LiIII 3-2 line the discharge conditions will need to be optimized limiting the electron density to be less than $1 \cdot 10^{17}$ cm^{-3} at the time of the peak recombination to avoid excessive de-excitation of the upper level by electron collisions of the second kind.
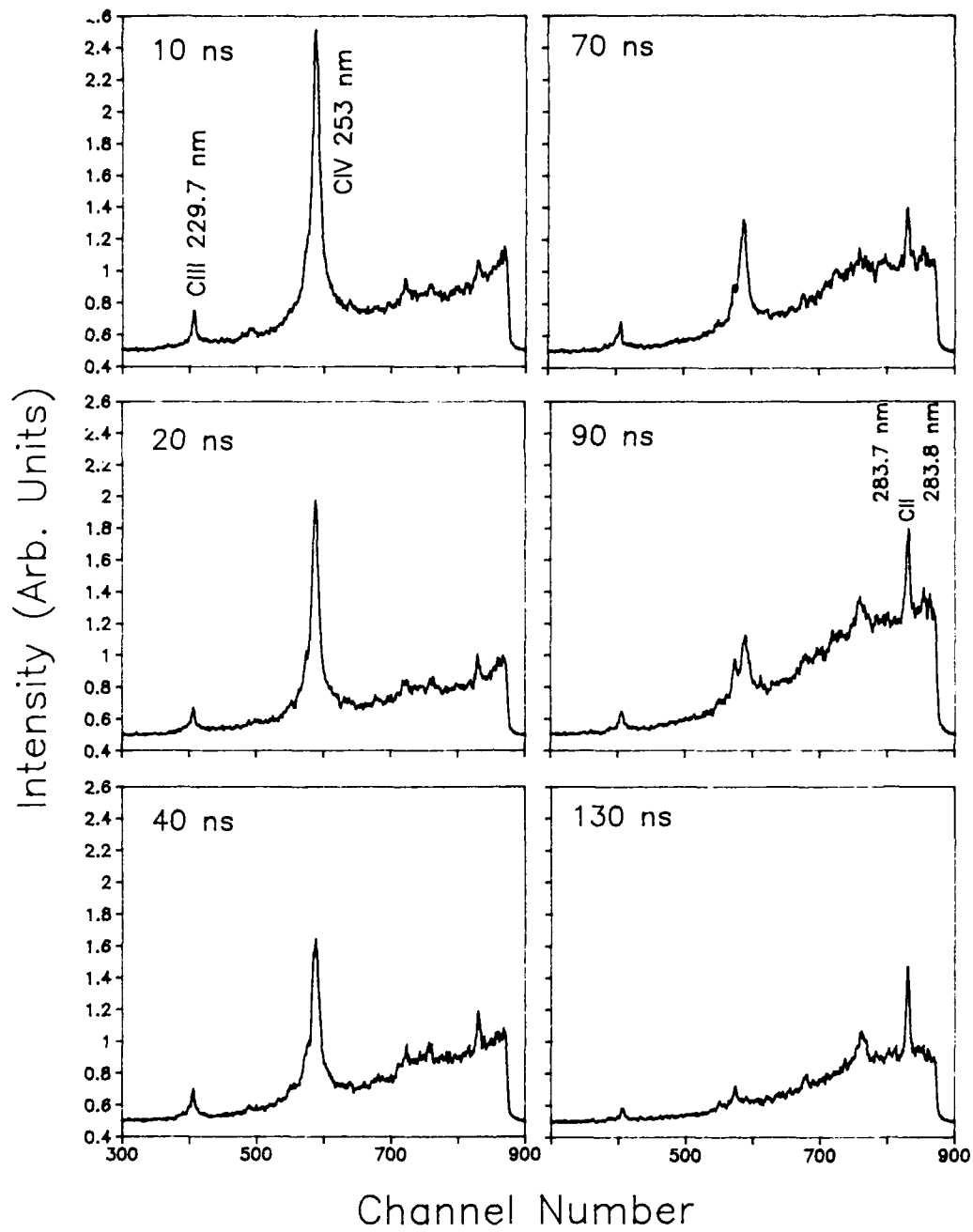
Figure 6- Time resolved UV spectra of the axial emission
from a 500 um diameter, 5 cm long polyethylene capillary
emitted by a 15 kV pulse. The external magnetic field ap-
plied is B=55 kG. The time delay respect to the peak of
the current pulse is indicated for each spectrum.
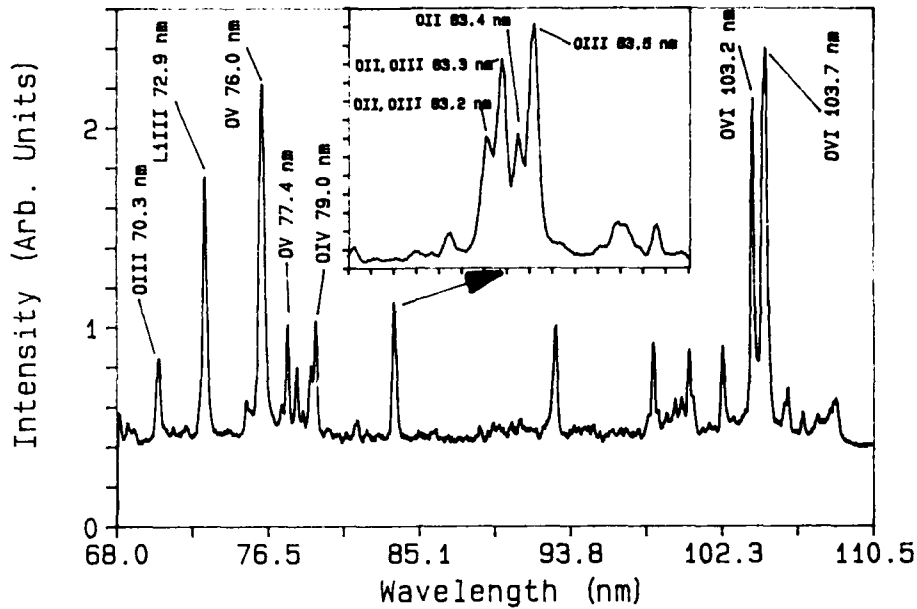
Figure 7- Time resolved XUV spectrum from the axial emission from a 35 kV discharge in a 500 um diameter, 4 cm long lithium hydride capillary. The spectrum was taken 3 ns after the peak of the discharge current pulse.
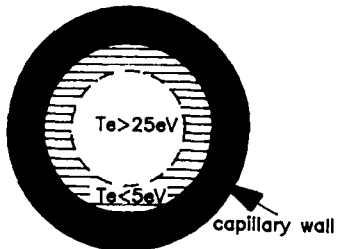
Figure 8- Diagram of the radial characteristic of the capillary discharge plasma illustrating the existence of a highly ionized plasma core surrounded by a cooler and more dense plasma.

REFERENCES

1- L.I. Gudzenko and I.A. Shepelin, Zh. Eksp. Teor. Fiz. 45, 1445 (1963). [Sov. Phys. JETP. 18, 998 (1984)].

2- W.T. Silfvast, L.A. Szeto and O. Wood II, Appl. Phys. Lett. 31, 334 (1977); Appl. Phys. Lett. 34, 213 (1979); Opt. Lett. 4, 271 (1979).

3- V.A. Boiko, B.A. Brynetkin, F.V. Bunkin, V.I. Derzliev, B.N. Duvanov, V.M. Dyakin, V.D. Lisov, I.Yu. Skobolev, V.S. Sulakvelidze, A.Ya. Faenov, A.I. Fedorimov and S.I. Yakovlenko, Sov. J. Quantum Electron. 10, 901 (1983).

4- D. Jacoby, G.J. Pert, L.D. Shorrock and G.J. Tallents, J. Phys. B: Atom. Mol. Phys. 15, 3357 (1982).

5- S. Suckewer, C.H. Skinner, H. Milchberg and D. Vorhees, Phys. Rev. Lett. 55, 1973 (1985).

6- W.T. Silfva , L. Szeto and O. Wood II, Appl. Phys. Lett. 36, 615 (1980). W.T. Silfvast, O. Wood I J. Macklin, Appl. Phys. Lett. 42, 347 (1983).

7- V. Zhukov, E. Latush, V. Mikhalewskii and S. Sem, Sov. J. Quantum Electron 7, 407 (1977).

8- J.J. Rocca, Appl. Phys. Lett. 47, 1145 (1985).

9- M.S. Butler an J.A. Piper, Appl. Phys. Lett. 42, 1008 (1983); Appl. Phys. Lett. 43, 823 (1983).

10- E.M. Campbell, R.G. Jahn, W.F. Von Jaskowsky and K.E. Clarck. Appl. Phys. Lett. 30, 575 (1977); J. Appl. Phys. 51, 109 (1980).

11- J.J. Rocca, H. Mancini and B. Wernsman. IEEE J. Quantum Electron. QE-22, 509 (1986).

12- W.L. Bohn, Appl. Phys. Lett. 24, 151 (1974).

13- J.J. Rocca, D.C. Beethe and M.C. Marconi. Opt. Lett. 13, 565 (1988).

14- R.U. Datla, J.R. Roberts, W.T. Silfvast and O.R. Wood II, Opt. Lett. 12, 675 (1987).

15- R.A. MacCorkle, Appl. Phys. A 26, 261 (1981).

16- H. Milchberg, C.H. Skinner, S. Suckewer and D. Voorhees, Appl. Phys. Lett. 47, 1151 (1985).

17- S. Suckewer, C.H. Skinner, D. Kim, E. Valco, D. Voorhees and A. Wouters, Journal de Phy. Colloque C6, 23 (1986).

18- J.J. Rocca, M.C. Marconi, D. Beethe and M. Villagran Miniz, presented at the Short Wavelength Coherent Radiation: Generation and Applications, North Falmouth, Cape Code (1988), paper TuC13.

CO2 LASER PERFORMANCE WITH A DISTRIBUTED GOLD CATALYST

John A. Macken, President; Dr. Suresh K. Yagnik, Research Scientist; Dr. Michael A. Samis, Research Scientist
Lasercraft, Inc.
3300 Coffey Lane
Santa Rosa, California 95403

Abstract

The performance of a CO_2 laser has been improved by coating the inside wall of the discharge tube with a discontinuous gold film. In the presence of the discharge, the gold acts as an ambient temperature catalyst to reform decomposed CO_2. The gold coated laser delivered 122 W/m for both sealed-off and flowing operation. CO_2 decomposition levels are presented as a function of input power, gas pressure and temperature. Atomic oxygen, generated by the discharge, appears to be required for gold to exhibit any detectable catalytic activity.

Introduction

A persistent problem with CO_2 lasers has been the decomposition of CO_2 molecules in the discharge [1,2,3] The pertinent decomposition reactions by electron (e) impact are as follows:

$$CO_2 + e \longrightarrow CO + O + e \tag{1}$$
$$CO_2 + e \longrightarrow CO + O^- \tag{2}$$
$$N_2 + e \longrightarrow 2N + e \tag{3}$$

This produces a host of dissociation products such as CO, O, O_2, O_3, NO and N_2O, as well as various ions In a sealed-off CO_2 laser, the dissociation of CO_2 proceeds until an equilibrium is reached. Typically, about 60 to 80% of the CO_2 is dissociated at equilibrium. Our research has centered on catalytically reforming the CO_2 inside the discharge tube.

Internal Catalyst

An internal catalyst must operate at the relatively low temperature of the cooled wall. However, this constraint is offset by the benefit that atomic oxygen (having an energy of 2.6 eV relative to $1/2$ O_2) is available for CO oxidation.

Atomic oxygen produced by reaction (1) has a lifetime which depends on tube diameter, gas pressure and wall material [4]. A typical lifetime for atomic oxygen is about 80 ms for a 2.2 cm diameter laser tube. Stable molecular oxygen (O_2) is formed on the wall (w) as follows:

$$O + O + w \longrightarrow O_2 + w \tag{4}$$

A successful catalyst must promote reaction (5) below while minimizing the primary competing reaction which is the formation of O_2 by reaction (4):

$$CO + O + w \longrightarrow CO_2 + w \tag{5}$$

Experimental Methods

Catalyst Selection Tests

Preliminary tests were conducted to find the most desirable internal catalyst. These tests are described in U. S. patents [5,6]. Materials which exhibited catalytic activity on the wall of the discharge tube were gold, oxides of silver, and under special conditions, platinum, palladium and rhodium. The oxides of silver were found to operate best at temperatures in excess of 45C. The platinum group metals required the presence of a small amount of hydrogen (water vapor) to maintain the high catalytic activity needed to produce the color change. Furthermore, the platinum group metals were more susceptible to poisoning compared to gold. All the catalyst materials required an activation step which will be discussed later. Clean gold showed catalytic activity in all deposition methods tested. Maximizing the coverage of the wall surface area was found to be beneficial, but it was not necessary to use finely divided gold particles.   Sputtered gold films exhibited the highest activity and were chosen for further testing in a laser.

Laser Apparatus

The performance of the gold catalyst was evaluated by using two CO_2 lasers which differed only in the fact that one laser (Laser A) had a gold catalyst coating on the entire inside length of the discharge tube. The second laser (Laser B) had an uncoated pyrex glass tube.

Each laser had an internal tube diameter of 1.64 cm and a positive column discharge length of 258 cm (Figure 1). Both tubes were water cooled to a temperature of approximately 23C.   Each laser was equipped with a 99.4% reflectivity enhanced silver rear reflector and ZnSe output coupler with 65% reflectivity. The mirrors were separated by 320 cm. Both the mirrors were concave with a radius of curvature of 10 m. This produced a stable TEM01* (donut shaped) beam. This mode was chosen because it produced the highest output power. Under the flowing conditions, the percentage of CO and CO_2 was measured at the vacuum pump exhaust using a Horiba model MEXA-311GE infrared gas analyzer (resolution 0.01%).
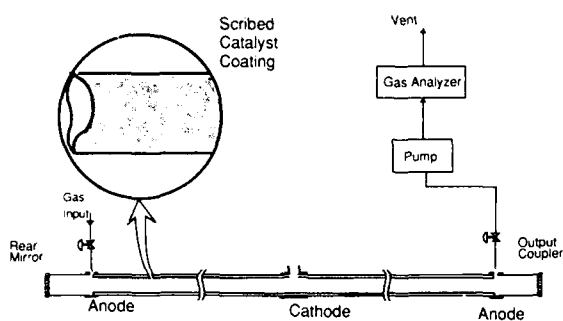
Figure 1: Schematic of the CO2 laser used for experiments. Details of the scribed gold catalyst coating are shown in inset.
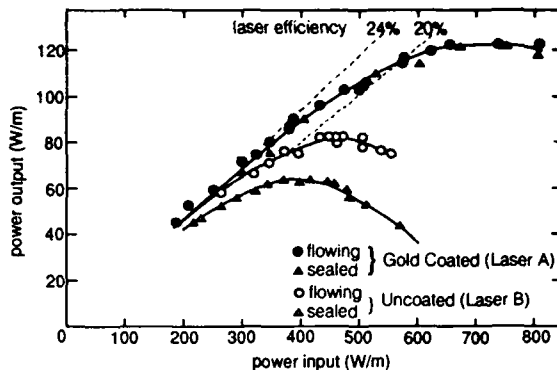
Figure 2: Output laser power as a function of power input to the discharge for flowing and sealed conditions for Laser A and Laser B. In each case, the gas mixture was optimized for maximum power output.

Sputtering Methods

Gold was sputtered on the inside of the discharge tube using a device fabricated by wrapping gold foil on a pyrex tube forming a 1 cm diameter and 20 cm long cylindrical gold cathode. A copper anode wire lay adjacent to the gold cathode cyclinder. The entire device could be inserted and centered in the 1.64 cm diameter discharge tube. The sputtering was performed in a flowing gas consisting of 5% CO2 and 95% helium at a pressure of about 5 to 8 torr (0.7 to 1.0 kPa). After sputtering, approximately 4 torr of carbon monoxide was added to the flowing gas mixture. The sputtered film exhibited a dramatic darkening within about 30 seconds of exposure to the CO.

The sputtered film was then scribed by springy steel wires mounted radially on an aluminum rod. By simultaneously rotating and traversing the rod through the laser tube, the scribes created multiple, electrically isolated islands in the gold film (see Figure 1). These islands were about 6 mm in size. This size insures that the voltage gradient across the conducting island is much less than the 400 volt cathode drop.

Besides the non-reflecting gold black film described above, another series of tests were conducted with the gold coating tube was washed with a 2% dilute nitric acid solution and followed by a thorough water rinse. This treatment eliminated the black appearance and only a specularly reflecting metallic gold film with the scribes retained. This coating will be referred to as the "specular gold" coating.

Catalyst Activation

As will be discussed later, the gold catalyst was poisoned by exposure to either the air or to a discharge containing oxygen in excess of the stoichiometric CO/O2 ratio for CO2 formation. Therefore, following exposure to air, the catalyst coating was activated. Two different activation methods were used. Both of these activation methods started with a discharge in the gold coated tube in a gas mixture of 5% CO2, 15% N2 and 80% He, at 20 torr total pressure and 40 mA current. One activation method referred to as the "hydrogen discharge activation" involved adding 1% H2 to the flowing gas mixture and running the discharge for a period of 30 seconds. The second activation method referred to as the "carbon monoxide discharge" involved adding 8% CO to the gas mixture and maintaining the discharge for 30 seconds. The gold black film responded best to the carbon monoxide discharge activation while the specular gold film responded best to the hydrogen activation. The presence of the discharge was essential for activation.

Results

Laser Power Measurements

Figure 2 compares the performance of coated Laser A and uncoated Laser B under flowing and sealed-off conditions. Both the laser output power and the input power are normalized into units of W/m. The gas flow rate was 1 liter per minute at STP for the flowing case. The gas mixture was optimized in each case to achieve the highest output power.

Within the scatter of experimental measurements, the coated Laser A gives approximately the same power output for flowing and sealed-off conditions. For low input power, all the curves are merged together with approximately equal slopes. The initial slope is equivalent to about 24% laser efficiency. As the power input is increased, the curves break-off, each reaching a different peak output power at a lower efficiency. The uncoated Laser B shows a maximum power of 63 W/m for the sealed-off case and 83 W/m for the flowing case. These values compare well with those obtained by others. The catalyst coated Laser A showed a more gradual decline in efficiency with increasing input power. The highest output attained was 122 W/m (315 W total power). This is believed to be the highest reported output power per meter from a diffusion cooled CO2 laser.

287

Figure 3: Measured CO2 decomposition at the laser exit as a function of input power for Laser A and Laser B in slow flow condition. A line, calculated from a and the CO2 flow rate, is also shown for comparison.

Figure 4: % CO2 decomposition as a function of inlet CO2 partial pressure for gold coated Laser A. The partial pressures of CO and CO2 at the exit are also plotted.

Figure 5: The oxygen poisoning of gold catalyst coating is shown by a hysteresis effect with O2 addition. The lower curve starts with an activated catalyst (note arrows). Decreasing the O2 pressure produces the upper curve.

Figure 6: Effect of cooling water temperature on the measured CO2 decomposition in Laser A. The catalytic effect decreases with increasing temperature.

Equilibrium Decomposition Tests

Figure 3 shows the CO2 decomposition present in the exhaust gases as a function of input power. The CO2 decomposition is defined as the ratio of CO/(CO2 + CO) in the exhaust gas. The dashed line, in Figure 3, is the calculated decomposition rate (2.5 x 10^{16} decomposition/joule) if there was no CO2 reformed. The measured graph in uncoated Laser B, shows a departure from the dashed line at high decomposition of CO2. Gold coated Laser A maintains low CO2 decomposition which demonstrates reformation of CO2 by the catalyst. At 1 liter per minute (STP) flow rate, the decomposition is virtually at equilibrium for the gold coated tube and, therefore, equals the sealed-off decomposition.

Figure 4 shows the influence of changing the input partial pressure of CO2 in the gold coated tube. The results are plotted both as decomposition percentage and as partial pressure of CO and CO2. It can be seen that there is only a slight increase in CO pressure with increasing CO2 pressure.

Figure 5 shows the effect of adding O2 to the flowing gas mixture in the gold coated tube. The partial pressure of CO2 was 1 torr. The other conditions were the same as for Figure 4. Starting off with an activated gold surface, the initial decomposition was 17%. Adding O2 to the gas mixture produced a decrease in CO2 decomposition. However, there is a hysteresis effect as indicated by the arrows in Figure 5. Decreasing the O2 pressure created a new set of data points which ended with 41% decomposition when returning to the starting gas mixture. If oxygen is added for a second time without reactivation, then the solid line portion of the upper graph is retraced. The hydrogen activation step must be performed to return to the initial activity. From this and many other tests, oxygen appears to have a poisoning effect on the gold surface when the O2 partial pressure exceeds more than half the CO pressure (the stoichiometric ratio for CO2). However, it should be noted that the gold is not fully poisoned after oxygen exposure. If there was no catalytic effect, the gas would be 73% decomposed under these conditions. The addition of O2 always decreases the laser output power.

Figure 6 shows the effect of temperature on CO2 decomposition in the gold coated tube. The cooling water temperature was changed to obtain this data. From Figure 7, it can be seen that increasing the water temperature from 23C to 50C increased the decomposition from 12% to 14%. This effect is opposite to thermally driven catalysts which exhibit increased reaction rates with increased temperature. This graph showed no hysteresis effect.

288

Several experiments were conducted in different diameter discharge tubes. There is a trend which indicates that the catalyst must work harder as the diameter decreases. In other words, the number of CO_2 molecules reformed/cm^2 must increase as the diameter decreases. The gold catalyst had sufficient activity to give good laser performance in the 16 mm diameter Laser A without the need of any special gas additives. However, a 9 mnm diameter tube required the addition of 0.04% H_2 and 0.2% CO to a CO_2, N_2, He gas mixture at 20 torr in order to maintain the higher activity level required by the small tube. The hydrogen maintains the activation level when the discharge is on, while the CO maintains the activation level when the discharge is off. This concentration of H_2 is about 25 times less thant he amount typically used to obtain a homogeneous catalytic effect [4,5].

Conclusion

It has been shown that gold, coated on the inside walls of a discharge tube, can act as a catalyst for the formation of CO_2 in a laser discharge. The gold coating shows no detectable catalytic activity in absence of the discharge. A CO_2 laser with the gold catalyst achieved 122 W/m output power both flowing and sealed-off. Compared to an identical laser without the gold catalyst, this was a 47% increase in output power for the flowing case, and 93% increase in the sealed-off power. The gold only exhibits detectable catalytic action in the presence of a discharge. Also the catalytic activity decreases at elevated temperature. Therefore, energetic species generated in the discharge must be driving the catalytic reaction.

References

1. E.N. Lotkova, V.N. Ochkin, and N.N. Sobolev, "Dissociation of carbon dioxide and inversion in CO laser," IEEE I. Quantum Electron., vol. QE-7, pp. 396-402, 1971

2. P.D. Tannen, P. Bletzinger, and A. Garscadden, "Species composition in CO_2 discharge laser," IEEE J. Quantum Electron., vol. QE-10, pp. 6-11, 1974

3. K.J. Siemsen, "Axial gain distribution in a cw CO_2 laser," Appl. Opt., vol. 19, 818-821, 1980

4. A.L.S. Smith and J.M. Austin, "Atomic oxygen recombination in carbon dioxide laser gases," J. Phys. B. Atom. Molec. Phys., vol. 7, pp. 191-194, 1974

5. J.A. Macken, "Discharge driven gold catalyst with application to a CO_2 laser," U.S. Patent 4,756,000, July 1988

6. J.A. Macken, "Discharge driven silver oxide catalyst with application to CO_2 lasers," U.S. Patent 4,757,512, July 1988

7. W.J. Witteman, "High output powers and long lifetimes of sealed-off CO_2 lasers," Appl. Phys. Lett., vol. 11, pp. 337-338, 1967

8. F.H.R. Almer, M. Koedam, and W.M. ter Kuile, "Influence of hydrogen and oxygen on the gas composition of sealed-off CO_2 laser systems," Z. Angew. Phys., vol. 25, pp. 166-167, 1968

PROMISING REALIZATION OF STABLE HEAT TRANSFER BY MEANS OF EVAPORATION-CONDENSATION

V.V.Apollonov, S.A.Chetkin, V.A.Khmara,V.I.Mankeev, V.N.Motorin, A.M.Prokhorov.

General Physics Institute, Academy of Sciences of the USSR
117942 Moscow, Vavilov street, 38, USSR

Abstract.

The widespread application of lasers in physical research has put forward an urgent necessity of developing coherent radiation-resistant optical elements. The report presents the ways of producing high-intensity laser optics using compact heat exchangers based on penetrable materials, such as regular macrorelief structures and highporosity cellular materials providing the conditions for forced convective and evaporation-condensation heat-mass transfer.

Introduction.

The development of the elements of forced optics based on microdispersion powder porous structures has permitted to satisfy unambiguously a set of requirements imposed on metal-coated laser mirrors [1] and to realize the state-of-the-art level of the reflecting surface optical capacity threshold [2,3]. We have achieved high-quality mirror surfaces in the forced optics elements of this type enabling to separate radiation and heat carriers in a compact layer of 100-200 mcm thickness and to realize in the heat exchanger an intensive intraporous convective filtering heat-mass transfer which removes thermal fluxes of some kW/cm from the mirror surface under small overheating. Intensification of heat transfer from the surface is attained through the development of a heat-exchange surface in a porous material and through increasing the local coefficient of the heat transfer to a liquid used as heat carrier due to its "quasiturbulization" in the microcnannels of a porous material [4].

A somewhat different approach to the development of high-stability reflecting surfaces currently enjoying widespread application, suggests dynamic evaporation-condensation cooling [5]. Intensification of heat transfer is reached under mixed boiling, i.e. at the presence of bubble and sheet forms of vapor generation when local overheating is continuously redistributed and, consequently, the densities of the removed thermal fluxes on the nonizothermal cooling ribs of the cooled reflecting plate are also redistributed. Since the boiling temperature depends upon pressure, one may attain the conditions under which heat is emitted at the temperatures close to that of optical finishing of the mirror surface. This way of intensification of heat transfer is advantageous, since it involves the mechanism of phase transition into the general balance of heat exchange. The potentialities of this mechanism greatly exceed those of intraporous convective heat imission [4].

The achievement of high levels of heat removal at virtually room temperature might currently be possible when realizing dynamic evaporation-condensation cooling in finely porous dispersion structures. The major requirements on the structure are its high penetrability for vapor bubbles which emerge at forced intraporous mass transfer with underheating of the main stream of the liquid heat carrier and, as a matter of fact, its penetrability for a vapor-liquid mixture. The results of [6] illustrate the prospects of this approach for solving the problem of forced low-temperature heat-mass transfer.

An advance in getting high-penetrable dispersed composite structures enables to use them in the compact heat exchangers possessing both hydraulic and heat characteristics comparable with powder materials but more adoptable to streamlined production. A manufacturing process enables to vary widely such parameters as porosity, penetrability, thermal conductivity so that to intensify heat transfer.

This work is devoted to studing the capability of producing two sorts of structures. The first one has a regular macrorelief consisting of fins, pyramids, grooves, cells produced from a compact blank by cutting with secondary plastic shaping (Fig.1) [7]. The second structure is made from a high-porous cellular metal (HPCM) [8,9] by metallization of foamed polyurethane (Fig.2). Both structures quite satisfy all these requirements for the heat exchanger material where reinforced heat-mass transfer is realized as:

1. The structure must provide considerable development of the heat exchange surface up to the value $10\text{-}10^3$ cm^2/cm^3 in order to reduce the temperature drop.

2. The structure must be integrated with the branched system of heat exchanger in order to achieve a certain level of hydraulic characteristics.

3. The structure of the heat exchanger material must allow the application of high-quality and well preserved from external effects mirror surface on the heat absorbed layer of 0.1-0.5 mm thickness.

Structures of Regular Macrorelief (SRMR) Obtained by Secondary Plastic Shaping.

This sort of structures obtained on the surfaces of rotation and planar surfaces by using standart metal-working equipment. The idea of the secondary plastic shaping method is in combining the processes of cutting and shaping of the worked metal layer. The cutting tool must have one cutting edge due to the fact that the blank material is only cut but not separated from the blank as a chip. A solid mechanic bond of the cut layer with the blank allows to spell the structure from the cut layer by the same tool. The depth of the ribs, their geometric form and mutual position depend on the geometry of the cutting tool. Under this working the ribs gain a rough surface (Fig.1) and, therefore, both the heat exchanger surface development and the extra turbulizasion of the heat carrier are achieved. So, the use of such a structure enables to intensify heat transfer and regular position of ribs to provide high hydraulic penetrability. A scheme of the structures worked by this technology is presented in Fig.3 A-C. Generally, the porosity of SRMR can be estimated as:

$$\Pi = [1 - (1 + h/(2a))^{-1}(1 + h/(2b))^{-1}] \qquad (1)$$

where $h_{1,2}$ is the groove width in crossed directions; a, b correspond to those directions ribs width. Being worked according to this technology, SRMR get porosity of 50-70%, groove depth up to 8 mm, ribs width not less than 0.1 mm, groove width not less than 0.08 mm.

Tne grooves can be directed actually in any mutually crossing directions, and what is more, their depth in these directions can be a difference to provide an optimal structure of heat carrier flux along the ribs.

A thin heat absorbed layer on SRMR can be produced by either expanding the ribs, or using a compact SRMR base. We have realized a 0.5-1 mm thickness of the compact layer. Figure 4 A-C illustrates hydraulic characteristics of SRMR when using water as a heat carrier.

SRMR possess high penetrability and realize the flow rate up to 10 gramm/(sm s) under insignificant hydraulic pressure(P=0.5 atm). So, SRMR enable to intensify the convective mass transfer, that is necessary for the reinforced convective heat removal. SRMR can be considered as a porous structure if to use the corresponding characteristics from the percolation theory[10]. For example, SRMR penetrability can be estimated according to a linear law of percolation - Darcy law:

$$K = \frac{\mu \, Q}{2\pi \Delta P \, \rho \, H} \ln\frac{R}{r} \qquad (2)$$

where μ is dynamic viscosity of water, H is the thickness of the heat exchanger, ΔP is the pressure difference, R and r are the external and internal heat exchanger radia. For the corresponding geometry of flow (Fig.4B) this quantity was $1.9 \cdot 10^{-7} m^2$,what is much more than that for powder and fibrous structures, which are used for cooling elements of optics (for powder and fibrous structures the value of penetrability is $10^{-9} -10^{-12} m^2$) [8,9]. The hydraulic diameter of the investigated SRMR is estimated as

$$d_{hyd} = \sqrt{K} \qquad (3)$$

to be 0.44 mm, that is in a good order-of-magnitude agreement with d_{hyd} calculated from the SRMR geometric characteristics:

$$d_{hyd} = 4(S_1 S_2 / P_1 P_2)^{1/2} \qquad (4)$$

here $S_{1,2}$ are the channel cross-section squares; $P_{1,2}$ are its perimeters around the corresponding directions. For the SRMR studied:

$$d_{hyd} = 2\sqrt{\frac{h_1 h_2 H_1 H_2}{(h_1 + H_1)(h_2 + H_2)}} \qquad (4')$$

Disagreement of those data, i.e. reducing of the d_{hyd} value estimated in (3) may be accounted for by the ribs roughness resistance to the flow.

To estimate the magnitude of the developed SRMR surface S we may use the Karman-Kozeny formula having set the adjust parameter at =2.11:

$$S = \sqrt{\frac{\varsigma \, \Pi^3}{K}} \qquad (5)$$

where Π is porosity equal to 84.8%. The estimation shows that S equals 26.1 cm^2/cm^3.

High -Porous Cellular Material (HPCM).

The HPCM is produced by doubling the polymer matrix by means of metallization of foamed polyurethane framework with the following organics removal and sintering to the end [11]. Porosity of this material may vary from 72% to 97% and controlled size of pores - from 0.4 to 5 mm.

HPCM usually consists of a 3-dimensional lattice-cellular structure with a relatively high degree of order. The structure is an assembly of polyhedron cells united in rather a firm framework (Fig.2).The cell next to the regular 14-hedron with a cavity (Fig.5) having the form of a streched spheroid provides their close packing in space. The matrix metall is formed as jampers, points and membranes. The cell faces can be 4- or 5- gons.The jumpers are the void-body rods of variable cross-section with increased thickness to points and have some curvature. The porosity decrease evokes an increase in the share of the matrix material in the cell points, growth of the number of membranes on the faces and decreasing length-to-width ratio of the jumpers, but the polyhedron form of the cells remains the same.

The channel porosity is a distinguishing peculiarity of HPCM (Fig.7). All of the jumpers are crossed with delta-shaped sections. The channel pore volume share does not depend on the HPCM integral porosity and equals the foamed polyurethane volume share (1.6-2.1%). The channel pore size is determined by the technology to amount to 10-100 mkm. Besides cellura and channel cavities HPCM has microporosity whose magnitude is 15-30% of the volume, and and the micropore mean size equals 0.5-10 mkm. Although the snare of microporosity is insignificant, they essentially affect the HPCM properties and, first of all, its strength.

As we have found from the experiments, the fluid flow is well described by Dupue-Reynolds-Forchheimer equation

$$- \nabla P = \alpha \mu \vec{U} + \beta \varrho |\vec{U}|\vec{U} \tag{6}$$

where P is pressure, μ is dynamuc viscosity, ϱ is the fluid density, $\vec{U}$ is the filtration velocity, α and β are the correcting coefficients, so that penetrability $K = (\alpha / \beta)^2$, the usual hydraulic size $d_{nyd} = \beta/\alpha$ and Reynolds criterion $Re = \varrho|\vec{U}|\beta/(\mu\alpha)$. The executed investigations under hydraulics of HPCM with the porosity Π =72-94%, withing a specific consumption (ratio) range $46 \leqslant |\varrho \vec{U}| \leqslant 3600$ for the Reynolds range $0.1 \leqslant Re \leqslant 25$ are presented on Fig.6A,B demonstrating that α and β can be generalised by the following terms:

$$\alpha = 6.3 \ 10^7 \ \Pi^{-9.35}$$

$$\beta = 4.78 \ 10^2 \ \Pi^{-9.25} \tag{7}$$

The estimate of the mean hydraulic pore diameter d_{hyd} based on a simultaneous solution of Durcy and Haagen-Puizale equations

$$d_{hyd} = \left(\frac{32|\vec{U}| \mu}{\Pi |\nabla P|} \right)^{1/2} \tag{8}$$

using the experimental data, has shown that for the studied structures d_{nyd} reduces with increasing heat carrier consumption. It is obviously caused by the flow turbulization in large pores.

Heat Conduction in SRMR and HPCM.

It is difficult to estimate whether any material can be utilized in overheating constructions without taking into account its thermal conductivity. If any penetrable material is used in a compact heat exchanger, conduction becomes a fact of importance among other types of transfer.

Thermal conductivity of SRMR can be found from a priory suggestion about its regularity. Indeed,in the SRMR production process one type of structure is built on another so that all of them lie parallel to the heat absorbed surface. Therefore, in the direction perpendicular to the layers, SRMR represents a branching connected grid of jumpers, membranes, etc, having a corresponding thickness h_i and porosity Π_i at each layer. The value of the effective square through which the heat flux is transfered is (1-Π_i) times less than the corresponding continuous elementary squares. The thermal conductivity of SRMR in this direction is found from the expression

$$\lambda_{ef} = \frac{\sum h_i}{\sum \{h_i / (1 - \Pi_i)\}} \tag{9}$$

The thermal conductivity in the direction parallel to the heat absorbed surface can be equal either to 0, if the elements are not connected, or to $\lambda_i / (1 - \Pi_i)$, where Π_i is effec-

tive porosity in this direction. So, SRMR possesses an adjustable anisotropy of heat properties, what is very important for practical application.

The HPCM structures do not feature such anisotropy. The HPCM know-how analysis shows it impossible to express thermal conductivity analitically due to a complex microdispersed structure. Thermal conductivity can be approximated by means of Odolevsky equation and similar ones [8,9]. Exact values of thermal conductivity are determined from the values of intergranule contact resistance. Therefore, to find them it is necessary to use either direct experimental methods or similarity between electric and heat conduction.

We have discovered in direct experiments that within a porosity range 83%-94% thermal conductivity of the copper HPCM is described with 9% accuracy by an empirical equation (Fig.7):

$$\lambda = -16 + 16.2 \, \rho \tag{10}$$

where ρ is density [gramm/cm^3], and λ has the dimensions W/m·K°.

Following the interparticle contact theory [12] the HPCM thermal conductivity can be described by a linear function of electric conductivity σ

$$\lambda = A_1 \sigma + A_2 \tag{11}$$

where $A_{1,2}$ involve all the electric and mechanical properties.

In many cases this way is more simple and effective from the experimental point of view because it does not require taking into account free convective heat transfer within the atmospheric gas structure.

In the case of HPCM the analogy of heat and electric conduction characteristics can be effectively used when analyzing the mechanical and strength properties [8,9,13]. For example, the HPCM strength and elasticity can also be described with high accuracy by the universal ratio

$$\sigma_{mech} = A_3 \sigma_{el}^n + A_4 \tag{12}$$

So, the conducted analysis demonstrates that these structures can ensure efficient conductive heat removal and high hydraulic penetrability.

Convective and Evaporation-Condensation Heat-Transfer Conditions in HPCM and SRMR.

HPCM and SRMR have large values of porosity and penetrability,therefore, besides convective heat rejection, one can realize the stable reinforced evaporation-condensation heat rejection so that one regime would transfer to the other under continuous heat load increase.

The peculiarities of the convective heat exchange have been explored on an installation illustrated in Fig.8, in which a heat flux was modelled by a heater. When the heat flux value was up to 20-30 W/cm^2 , we did not manage to achieve an essential heat transfer because of the lack of a well-developed surface. Conventional heat-transfer coefficient dependences for these structures on the flow rate and heat flux magnitude are presented in Figs.9,10. As it is seen, the heat transfer processes are similar and depend on the filtrate rate.

When the heat flux intensity achieves a value of 1500-2000 W/cm^2 in the surface layer of such heat exchangers, bubble evaporating begins with the heat mass transfer intensification. These processes have been studied on the installation presented in Fig.11. The heat exchanger mock-up of a copper HPCM with 81% porosity, average cell diameter 0.67 mm and framework thermal conductivity 0.3 W/cm·°K was soldered into the case having a two-layer heat absorbed surface of 1 mm thickness. The heat absorbed layer was cooled by a jet and, besides, there was a thermocouple soldered in. A heat flux was modelled by a 2 kW electron beam. Its density was varied by the electron beam focusing. The heat transfer coefficient was determined by the steady heat flux method.

A certain audible signal is known to accompany the boiling and its registration enables to control both the beginning of the process and the burn-out [6]. For this aim a piezo-electric hydrophone was fixed in the heat exchanger system, so that the signal could be registered by the spectrum analyzer.

The burn-out due to bubble-to-sheet transition of evaporation is accompanied with a change in the audible signal power. Figure 12 illustrates the dependence of the normalized audible signal power due to boiling on the heat flux density when the flow rate is fixed. The quantity q^* corresponding to the signal power maximum was believed to be a critical value of heat flux. A stable regime of heat transfer into boiling water corresponded to the region where the flux value was less than q^*,while the mixed sheet-bubble boiling corresponded to the flux regime $q > q^*$ [6].

A quantitative measure of the heat removal intensity is the heat transfer coefficient defined as $\alpha_s = q/(T_w - T_s)$, where q is the applied heat flux, Tw is the wall temperature and Ts is the heat carrier (water) temperature. We have connected by a relationship the heat transfer coefficient with the rate of flow (Fig.13) and heat flux density (Fig.14).

The only convective regime was observed in the heat flux region about 2 kW/cm^2, meanwhile depending on flow rate varied within 15-25 W/cm·K°. As heat flux increased, bubble evaporation through intensifying heat-mass transfer in the boundary layer on the back evoked the λ_s growth up to 30 W/cm K, so it ensured a stable regime of heat removal under 6 kW/cm^2 (while flow rate was not far from 1.1 m/s).

The α_s-dependence on the filtrate flow rate u is linear for u > 0.5 m/s. When u ≳ 2 m/s the magnitude of λ_s achieves 46 W/cm·°K (Fig.13).

It should be noted that α_s (u) dependences for the convective regime and boiling one are similar. Therefore, we may state that in our experiments the heat carrier boiling in HPCM was not the main type of heat utilization, because the heat transfer regime was only convective and stream phase was a means of effective mixing of heat carrier, i.e. the phase intensified the convective heat-mass transfer in HPCM. In this case the heat transfer intensity is one-two orders of magnitude greater than that of rough-surfaces under reinforced flow regime. It enabled us to provide stable regime of heat removal up to 7 kW/cm^2 under a negligible overheating of HPCM about 130°C and moderate consumption of heat carrier (u ≃ 2m/s, Q ≃ 200 gramm/s).

So, investigation of a stable evaporation-condensation heat transfer in HPCM and SRMR has shown that in-porous boiling occurs in the following way [15]: the steam bubbles fill the whole section of a pore. As a pore is filled the steam rushes into largest connected porous channels and streams as separated microjets. The steam microjets either are intercepted by liquid thrombs or fill the terminated pores. With heating up, the number of evaporating centers and microjets increases, as a result of that the steam phase fills microdispersed porous cells. A natural result of the process is heat crisis, i.e. the occurrance of a steam space which separates the filtrate flow field from the heat absorbed one in the HPCM. The reinforced heat carrier flow in a porous structure only directs the steam phase penetration and somehow shifts the srisis to a more intensive heating region.

Analysis of the acoustic emission signal spectrum enables not only to determine the crisis starting, but to study more closely the convective heat transfer intensification in case of boiling.

The characteristic spectra of the heat exchanger mock-up with and without a penetrable structure are presented in Fig.14.

When heat flux is absent we can observe a certain equidistance spectrum of the signal obviously associated with the heat carrier cavitation. The low-frequency modes of the spectrum are enhanced by the heating load causing the surface layer boiling. A further growth of the heat flux density leads to the equidistance spectrum degeneration into the main current, so that its frequency reduces to 1 kHz. Such spectrum transformation may be attributed to an increase in the average diameter of a bubble in the structure and decrease in their account. We may also assert that when the boiling starts the evaporation in different places is incorrelated, therefore, the bubbles have a variety of diameters and generation-collapse frequencies, while in the precrisis regime a certain feedback occurs which makes the bubbles to achieve some value of diameter and then collapse. Evidently, an acoustic standing wave of rather a large amplitude (1 atm) occurs in the heat exchanger. At the moment of discharge in the crests of the wave the evaporating conditions are lightened, while at the periods of compression the condensation conditions are lightened and it is due to the controlling acoustic wave that the steam sheet srisis (burn-out) does not occur. The existance of this phenomenon is illustrated by the oscillogram of an acoustic emission signal in case of impulse-periodic heating (Fig.15). Between the heat impulses there are observed acoustic oscillations multiple of heat impulses frequency. The multiplicity is defined by heat carrier consumption. On maximum and minimum of differential pressure, noise signal has its source in bubbles generation and collapse.

So, these experimental results of evaporation-condensation heat transfer in the structures like HPCM and SRMR have shown that their utilization enables to realize the magnitude of heat removal about 7.0 kW/cm^2.

Conclusion.

SRMR and HPCM are the structures of new types used as heat exchangers of laser mirrors. They possess an unique combination of structural, thermal and hydraulic properties. Their use will enable realizing the record level of heat removal in the regime of subcooled reinforced in-porous boiling of heat carriers.

References.

1. Tsesnek, L.S., Sorokin, O.V., Zolotukhin, A.A., Metal-coated mirrors. Moscow: "Mashinostroenie", 231p., 1983.
2. Apollonov,V.V, Barchukov, A.I.,et al. "Optical damage threshold increasing for metallic mirror surfaces under their cooling through the structures with open porosity." Soviet JTP Letters, 4, ser.19, 1193, 1978.
3. Apollonov,V.V, Bystrov, P.I., et al, "Prospects of application of porous structures for

cooling reinforced optics elements", Kvantovaya Electronika, <u>6</u>, No12, 2533-2545, 1979.

4. Apollonov, V.V., Borodin V.I., et al. "Static and adaptive elements of reinforced optics". Izvestiya AN SSSR, ser.phys., <u>48</u>, No8, 1639-1643, 1984.
5. Apollonov, V.V., Prokhorov, A.M., et al "On possibility of using vaportron cooling in reinforced optics", Soviet JTP Letters, <u>4</u>, ser.8, 433-436, 1978.
6. Apollonov, V.V., Gamarinsky, V.P., et al. "On opportunity of attaining stable evaporation-condensation heat transfer in high-porous cellular structures". Soviet JTP Letters, <u>14</u>, ser.3, 1988.
7. Preparation technology for surface structures with deep regular microrelief by cutting with secondary plastic shaping (Proceedings of Moscow College of High Technical Education), Moscow, MCHTE, 2p, 1988.
8. Apollonov, V.V.,et al. High-porosity materials in laser optics. Problems and prospects. Physical and mechanical properties of high-porosity materials. Preprint IOFAN SSSR, No65 65p., 1988.
9. Antsiferov, V.N., et al, High-porosity materials in laser optics. Problems and prospects Structures of high-porosity materials and their hydraulic and thermal characteristics. Preprint IOFAN SSSR, No66, 66p., 1988.
10. Zhukovsky, N.E., Selected works, v.1, GIITL, Moscow-Leningrad, 1948.
11. Antsiferov, V.N., Khramtsov, V.D., et al. "Porous metal production technique", Author certificate No577095, published in Bl No6, 1977.
12. Holm R., Electric Contacts Theory and Application. - Berlin: Springer-Verlag, p.482, 1967.
13. Antsiferov, V.N.,et al. "Properties of high-porosity metals". Poroshkovaya Metallurgia, No12, 20-24, 1980.
14. Nesis, E.I., Liquid Boiling, Moscow, "Nauka", 1973.
15. Maiorov, V., Vasil'ev, L.," An evaporating flow structure inside a heated porous metal" <u>41</u>, No6, 965-969, 1981.

FIG. 1 A CHARACTERISTIC VIEW OF A COPPER SRMR AT 100 ENLARGEMENT.
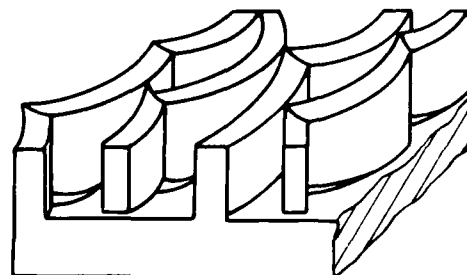
FIG. 3A CELL TYPE SRMR.

FIG. 2 A CHARACTERISTIC VIEW OF A COPPER SRMR POROSITY 42% MEAN CELL DIAMETER 1 mm.

FIG. 3B PIN TYPE SRMR

FIG.1: GROOVE HEAT PIPE (SPMB)
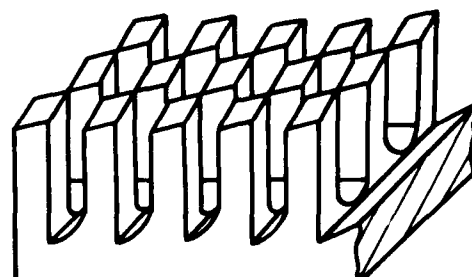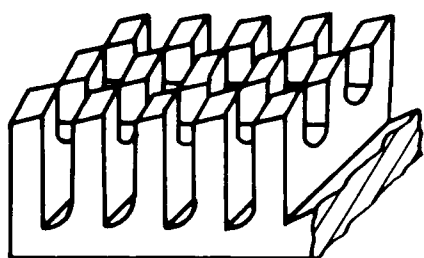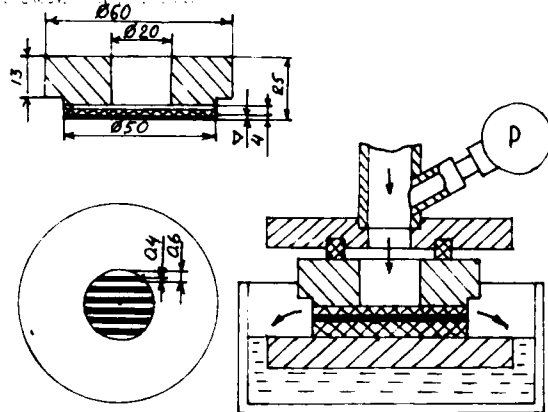
FIG. 2: DIAGRAM OF AN EXPERIMENTAL SETUP FOR STUDY OF DEFORMING THE SPMB WITH A GIVEN PROPERTIES
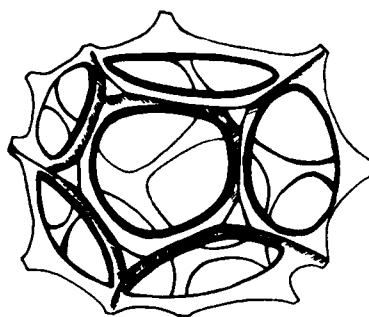
FIG. 3: AN ELEMENTARY CELL OF THE HPCM STRUCTURE

λ, W/m.°K

FIG. 7: COPPER HPCM HEAT CONDUCTIVITY COEFFICIENT VS POROSITY: 1 EXPERIMENT, 2 ODELEVSKY RELATION

FIG. 4: SKETCH OF AN EXPERIMENTAL SETUP FOR HPCM MAKING: 1 CAPACITANCE 2 PUMP 3 BYPASS 4 FILTER 5 VALVE 6 FLOW METER 7 ACTIVE SECTION 8 PRESSURE TAKE OFF CONNECTION 9 THERMAL MODULE 10 FEED CIRCUIT REFRIGERATOR 11 HEAT INSULATION

$Nu \cdot 10^{-2}$

$Re \cdot 10^{-3}$
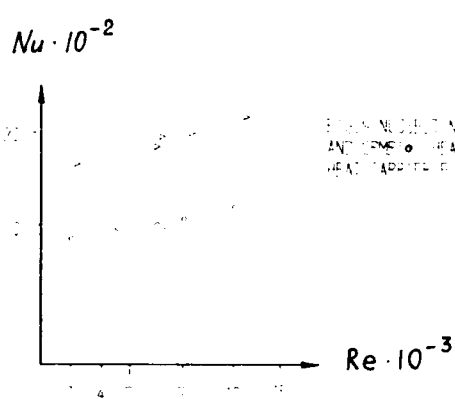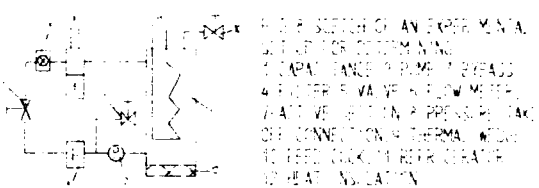
FIG. 8: NUSSELT NUMBER FOR HPCM AND HPMB HEAT EXCHANGER VS HEAT CARRIER FLOW REYNOLDS NUMBER

$\alpha \, [m^{-2}]$ $\beta \, [m^{-1}]$

FIG. 6A   FIG. 6B

FIG. 6A,B: VISCOSITY (A) AND INERTIA (B) COEFFICIENTS OF THE DUPUIT REYNOLDS FORCHHEIMER EQUATION VS POROSITY FOR COPPER HPCM

α_S, W/sm².°K

q, W/sm²
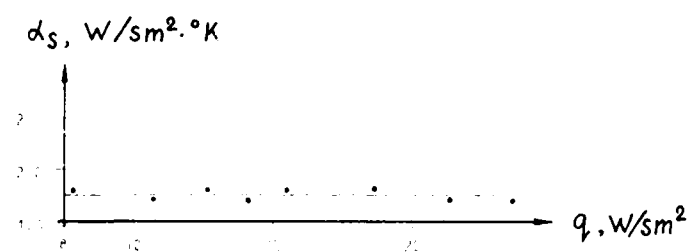
FIG. 10: SURFACE HEAT TRANSFER COEFFICIENT FOR HPCM AND HPMB VS HEAT LOADED DENSITY IN FORCED CONVECTIVE HEAT TRANSFER REGIME
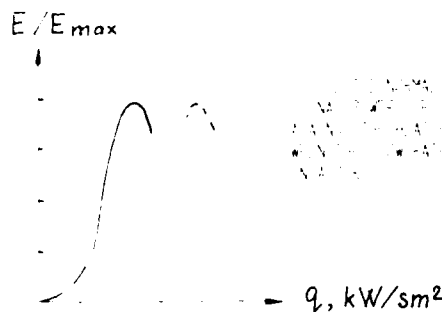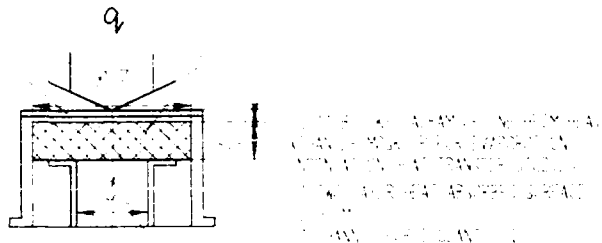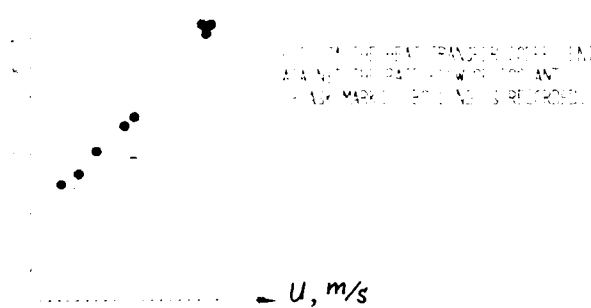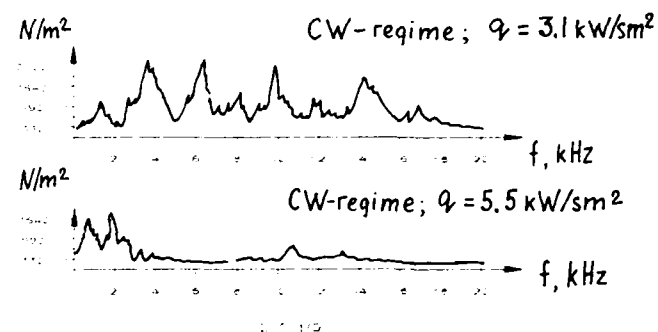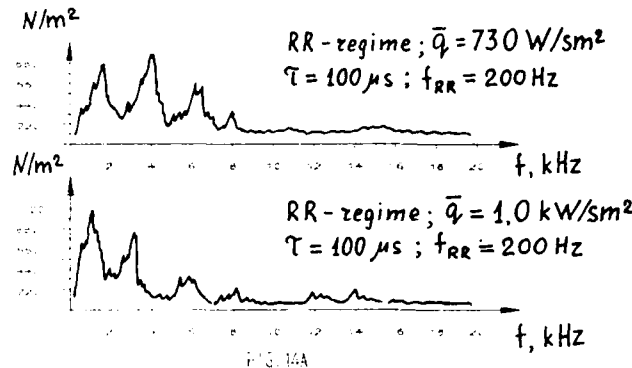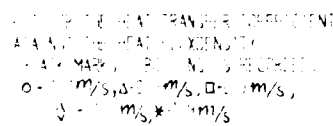
296

q

E/E_{max}

$q, kW/sm^2$

$\alpha_s, W/sm^2 \cdot °K$

$U, m/s$

$\alpha_s, W/sm^2 \cdot °K$

N/m^2

RR - regime; $\bar{q} = 730\ W/sm^2$
$\tau = 100\ \mu s$; $f_{RR} = 200\ Hz$

f, kHz

N/m^2

RR - regime; $\bar{q} = 1.0\ kW/sm^2$
$\tau = 100\ \mu s$; $f_{RR} = 200\ Hz$

f, kHz

FIG.14A

N/m^2

CW - regime; $q = 3.1\ kW/sm^2$

f, kHz

N/m^2

CW - regime; $q = 5.5\ kW/sm^2$

f, kHz

4 MS
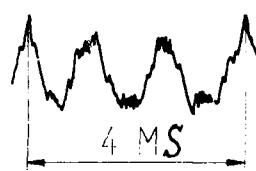
FORMATION OF A PREGIVEN REFLECTING SURFACE TOPOGRAPHY
BY ELASTIC DEFORMATION OF THE MIRROR SUBSTRATE.

V.V. Apollonov, S.A. Chetkin, E.A. Ivanova, A.M. Prokhorov.

General Physics Institute, Academy of Sciences of the USSR
117942 Moscow, Vavilov street, 38, USSR

Abstract.

Method of precise formation of a pregiven reflecting surface topography is suggested and investigated. Accurate experimental verification of this method is conducted.

Introduction.

Synthesis of the reflecting surface, conjugated to wave front aberrations with the use of control elastic substrate deformation makes it possible to correct phase distortions of the coherent radiation flows.

This method is rather simple in realization and widely used while constructing the adaptive optical systems for lasers and astronomical telescopes. At the present time there constructed a few mirror-type phase correctors (adaptive mirrors (AM)) having aperture diameter from several cm [1] to a meter [8] and a number of control channels (i.e. amount of actuators) from several units [3,7] to several hundreds [9]. Study of the AM in adaptive optical system showed that this method of forming of aberrationless coherent radiation flows in the media with nonstationary sources of phase distortions is universal and highly-efficient. However, the application limits of this approach and, in the first place, the problem on the accuracy of formation of the AM reflecting surface conjugated with different wave front aberrations has no practical solution [2,4-6].

Any phase-conjugated AM surface can be represented as a superposition of its influence functions. Therefore, for a solving this problem, physically grounded model notions on the formation of influence function to the action of one actuator should be stated which adequately reflect the specific features of deformation of AM substrate by a striction actuator and assume accurate analytic interpretation.

The present work reports the theory of formation of the surface conjugated to the wave front aberration by AM made as a thin plate fixed on boundary and supported at the finite number of points upon elastic supports - actuators. The main experimental results validated the fundamental positions of the theory are also reported.

For experimental investigation we have chosen a model of adaptive mirror with 5 piezo-electric ceramic actuators. Dimensions and position of the mirror elements are represented in Fig.1 A,B. Interferometric study of the formation of the reflecting surface relief in static and dynamic regimes has been carried out in a stroboscopic Fizeau interferometer (Fig.2, [10]). The method used for interferogram processing garanties a λ/20 accuracy (λ =0.6328 μm) for a definition of the mirror surface relief in chosen cross-section.

Experimental Results.

a.Static regime.

Study of the formation of the AM influence functions at the drive voltage -600 $\div$ +600 V, applied on one actuator has demonstrated that the influence functions defined in the cross-section via a central and two adjacent actuators have a bell-like form. Maximum of the mirror surface response takes place at the actuator disposition. The relief is concave or convex versus a sign of drive voltage. Figure 3A illustrates the influence functions of central (1) and peripherial (2) actuators for +600 V drive voltage. The AM influence functions profiles are spacially similar for different values of drive voltage. The deflection of mirror surface can be represented as:

$$W(r)=Wmax \cdot f(r) \qquad (1)$$

where f(r) is the mirror influence function normalized to a maximum deflection, this function is independent of drive voltage; Wmax is the maximum deflection of reflecting surface with the given voltage applied to actuator. The reflecting surface profiles, forming under drive voltage -600 $\div$ +600 V are spacially similar with 2% accuracy. That lies within the error of interferogram processing. Maximum deflection dependences of the AM surface on applied voltage for central and peripherial actuators are represented in Fig.3B. In the voltage range studied the dependences are linear. Hence, the AM reflecting surface profile, forming under the drive voltage U is the following:

$$W(r)=K \cdot U \cdot f(r) \qquad (2)$$

The influence function $f(r)$ determines the shape of the surface relief, factor K characterizes maximum deflection dependence of the AM surface on drive voltage. The value of K and the form of $f(r)$ are independent of drive voltage, but they are defined by the actuators arrangement, their mechanical and piezoelectric properties and substrate stiffness.

The formation of mirror surface relief under the action of several actuators was investigated in the case when the same drive voltage which varied in the -600 ÷ +600 V range was applied to central and two adjacent actuators. The data show that the actuator influence on AM substrate is additive. Hence, the AM surface profile formed when voltage is applied to all the actuators is the following:

$$W(r)= \sum_{i=1}^{5} W_i(r) \qquad (3)$$

where $W_i(r)$ is the surface profile formed under the action of the i-th actuator defined by eq.(2).

The experiments have demonstrated that experimental definition of the maximum deflection dependence on drive voltage and mirror influence functions for the all actuators completely defines a form of the AM reflecting surface profile in the static regime.

b.Dynamic regime.

For continuous elastic substrate mirrors with discrete actuators in a static regime the shape of the influence function is determined only by elastic forces. In this case the determinated features of the formation of AM influence function are universal, i.e. they are valid for all the AM considered.

In the case of actuator excitation by a time variable drive voltage, elastic forces are added with inertial terms limiting by the substrate and actuator mass; partial contribution of these forces being determined by the time constant of control signal. While forming AM surface of the given shape, determination of the time interval in which the stationarity conditions remain valid and the boundary condition beginning from which resonance effects become sufficient is important.

The AM surface profiles which are formed with the sinusoidal 400 V amplitude and 0 ÷ 3 kHz friequency voltage applied to the peripherial actuator are studied in the dynamic regime. The AM surface profiles corresponding to maximum of sinusoidal drive voltage and different frequencies are represented in Fiq.4. The influence function depends on control signal frequency which is higher than ~100 Hz and critically changes with frequency increase.

At the frequency range up to 2.4 kHz with maximum excitation voltage the reflecting surface is concave, a maximum deflection being decreased with frequency growth, surface becomes more sloping with respect to a shape. With the frequency 600 Hz maximum deflection of reflecting surface is by 13% differed from the corresponding one in a static, with frequency 2 kHz this difference is 63%.

Increasing of the exciting signal frequency from 2.4 to 3 kHz a shape of the reflecting surface is rapidly changed, causing the excitation of resonance vibration of AM substrate.

Thus, the results of experimental study showed that in a static the interaction between one actuator and AM substrate is reversible linear (i.e. elastic). When AM substrate is subjected by several actuators at the same time, the forming surface is a superposition of AM influence functions to the action of each actuator separately. These features show that for description of the influence function the elastisity and piezo-effect linear theories should be used.

Model of the Adaptive Mirror.

The AM with a continuous reflecting surface and discrete actuators typically satisfies the following conditions: the thickness of mirror substrate is small in comparison with its radius, mirror surface deflections are small in comparison with substrate thickness. If these conditions are satisfied, the process of elastic deformation of the mirror substrate by a system of actuators can be considered using the thery of thin plate.

Within this theory the substrate deflection can be solved by the following equation:

$$\Delta \Delta W(r,\varphi)=p/D \qquad (4)$$

where p is the load per unit area; $D=Eh^3/12(1-\mu^2)$ (E is the Young modulus, μ is the Poisson coefficient, h is the substrate thickness).If the plate edge is clamped the following conditions are satisfied :

$$W=0; \partial W/\partial n=0 \qquad (5)$$

If the substrate is loaded by transverse pointwise force F at the point (r,φ), the solution

299

of eq.(4) with the edge conditions (5) has the form [11] :

$$W(r,\varphi)=(R^2/16\pi D)\cdot F\cdot a(r,\varphi,\rho,\theta) \tag{6}$$

$a(r,\varphi,\rho,\theta)=(1-r^2)(1-\rho^2)+(r^2+\rho^2-2r\rho\cos(\varphi-\theta))\ln[(r^2+\rho^2-2r\rho\cos(\varphi-\theta))/(1+r^2\rho^2-2r\rho\cos(\varphi-\theta))]$,
R is the substrate radius.

Let us consider the problem of deformation of the substrate, fixed on a boundary and supported in N points under the action of a pointwise force F applied to one of the supports. As the force is applied, the substrate is deformed, causing the reaction forces at the points of location of the other supports. Hence, forming relief can be represented in the form of a superposition of a thin plate influence functions on the action of force F and reaction forces $R_{i(j)}$(force F is applied to the j-th support):

$$W(r,\varphi)=\sum_{i=1}^{N} P_i\, a_i(r,\varphi), \tag{7}$$

where $P_j = (R^2/16\pi D)F$, $P_i = (R^2/16\pi D)R_{i(j)}$ ($i\neq j$); $a_i(r,\varphi) = a(r,\varphi,\rho_i,\theta_i)$; (ρ_i,θ_i)- i-th support coordinates.

Substrate deflection at the point of support can be written as $W(\rho_i,\theta_i)=k_i^{-1}R_{i(j)}$,where k_i is the actuator stiffness. Then, reaction forces are defined from the following system:

$$(-a_{ij} + 16\pi D/R^2\cdot 1/k_i\cdot\delta_{ij})R_{i(\mu)}=F_{(\mu)}a_{\mu j} \tag{8}$$

where $a_{ij} = a_i(\rho_j,\theta_j)$, $R_{i(\mu)}$is the reaction force taking place in the i-th support when force $F_{(\mu)}$ is applied to the μ-th support. Thus, there is a linear relation between the reaction and applied pointwise force:

$$R_{i(\mu)}=G_{\mu i}F_{(\mu)} \tag{9}$$

where $G_{\mu i}$ is defined from the matrix equation:

$$G_{\mu i}=(-a_{ij}+16\pi D/R^2\cdot 1/k_i\cdot\delta_{ij})^{-1}a_{\mu j} \tag{10}$$

Hence, the plate surface relief, forming under the action of pointwise load $F_{(\mu)}$ is the following:

$$W(r,\varphi)=(R^2/16\pi D)F_{(\mu)}(\sum_{\substack{i=1\\i\neq\mu}}^{N}G_{\mu i}a_i+a_\mu)=F_{(\mu)}f_\mu(r,\varphi) \tag{11}$$

where $f_\mu(r,\varphi)$ is substrate influence function for the action of unit force, applied to the the μ-th support which is defined by arrangement of elastic supports, substrate and supports stiffness. Load $F_{(\mu)}$definds the amplitude of substrate deflection. When drive voltage is applied to all the actuators, forming profile, because the equations of the theory of thin plate are linear, has the form :

$$W(r,\varphi)=\sum_{i=1}^{N} F_i\, f_i(r,\varphi) \tag{12}$$

The longitudinal deformation of piezoelectric ceramic actuator is caused by a transversal or longitudinal piezoeffect.The relationship between electric and mechanical variables in the case of transversal piezoeffect is given by the form [12]:

$$\begin{aligned}S_1 &= s_{11}\, T_1 + d_{31}\, E_3\\ D_3 &= d_{31}\, T_1 + \varepsilon_{33}\, E_3\end{aligned} \tag{13}$$

where $S_1$is the longitudinal deformation of actuator , T_1 is the mechanical stress in transverse actuator cross-section, E_3 is the intensity of transverse electric field applied to actuator; s_{11} is the elasticity, d_{31} is the piezoelectric constant,ε_{33} is free electric constant of the actuator material.

The actuator elongation is $S_1 l$, where l is the actuator length. As actuator is rigidly connected with the mirror substrate, this elongation is equal to deflection of the mirror surface W_0. The force applied to the elastic substrate can be written in the form $F=-T_1 G$,where G is the area of transvers actuator cross-section. $E_3=U/d$,where U is the voltage applied to actuator, d is its transverse dimension. Then, $F=G/s_{11}[-W_0/l+d_{31}U/d]$. The substrate deflection upon actuator is related to influence function by the equation $W_0= F\, f_i(\rho_i,\theta_i)$,where i is the actuator number ,(ρ_i,θ_i) are its coordinates. Elasticity is $s_{11}=G/(lk_i)$,where $k_i$is the actuator stiffness. Hence, the force produced by actuator is related to voltage by linear equation:

$$F_i =d_{31}\, U_i/((f_i(\rho_i,\theta_i)l^{-1}+G^{-1}S_{11})d) \tag{14}$$

Piezoelectric and mechanical properties of actuators may be different. In this case for a definition of the influence function and the proportional coefficient between force and applied voltage we must use individual stiffness and piezoelectric constants for each actuator. Thus, the presented method of the description of the AM surface shape allows to take into account the differences in actuators' properties.

The model of thin plate makes it possible to explain the main mechanisms of the formation of experimentally studied AM surfaces: spatial similarity of profiles forming with different voltage applied to one actuator; linear dependence of the amplitude of AM surface deflection on the control voltage applied to actuator, additivity of the actuator influence on substrate. Let us consider the accuracy of the description of AM surface profile within a theory of the thin plate.

As a result of experimental research of the 5-element AM we have recieved influence functions for central and peripherial actuators (Fig.3A). Within a theory of the thin plate these functions can be represented in the form (7):

$$W(r,\varphi=0)=\sum_{i=1}^{5}a_i(r,\varphi=0)P_i \qquad (15)$$

where $\varphi=0$, because experimental data are obtained for a cross-section via central and two adjacent actuators. A comparison of the model and real AM profiles enables one to estimate the accuracy of profile description within a theory of the thin plate. While determining the parameters P_i according the represented equations, a substantial problem is that the constants of actuators and substrate stiffness ,piezoelectric constant of actuator material are not pregiven. Therefore, parameters P_i have been proceeded from experimental data by r.m.s. approximation. Model profiles obtained for approximation of the AM influence functions of central and peripherial actuators are presented in Fig.3A. In the former case, r.m.s error of approximation is 2.7% , in the latter one - 3.4% of maximum deflection of the mirror surface: for drive voltage +600 V, it is 0.06 and $0.1\mu m$, respectivly. Thus, the AM surface profile, forming in chosen cross-section is approximated by thin plate influence functions with the accuracy 3%.

The estimation obtained proves that application of the method based on the theory of thin plate for description of the formation of AM reflecting surface relief and estimation of the quality of correction of phase distortions is expedient.

Numerical Simulation of the Correction of Aberrations by Adaptive mirror.

For the correction of aberrations, the AM control system must provide a coincidence of control voltage on actuators in order to form reflecting surface of the given shape.

A reflecting surface profile, forming by the action of actuators is (7):

$$W(r,\varphi)=\sum_{i=1}^{N}a_i(r,\varphi)P_i \qquad (16)$$

where $a_i(r,\varphi)$ depends on actuator position relatively to the point (r,φ), P_i defines the actuator contribution to the formation of reflecting surface. The equation for approximated surface in the uniform form is:

$$Wa(r,\varphi)=Wmax\,\emptyset(r,\varphi) \qquad (17)$$

The problem of formation of reflecting surface profile of the given shape is solved by a determination of P_i which provide best approximation $W(r,\varphi)$ to the profile of forming surface $Wa(r,\varphi)$. The approximation degree can be characterized by the r.m.s. error:

$$S=(1/\pi A^2)\int_0^{2\pi}\int_0^A(W(r,\varphi)-Wa(r,\varphi))^2 rdrd\varphi \qquad (18)$$

where A is the aperture radius on which the surfaces are conjugated. The minimum S condition in view of equation (16) has the following form:

$$\int_0^{2\pi}\int_0^A(\sum_{i=1}^N a_i(r,\varphi)P_i-Wmax\,\emptyset(r,\varphi))a_K(r,\varphi)rdrd\varphi=0 \qquad (k=1,N) \qquad (19)$$

or matrix form:

$$b_{ij}P_i=g_j \qquad (20)$$

where $b_{ij}=\int_0^{2\pi}\int_0^A a_i(r,\varphi)a_j(r,\varphi)rdrd\varphi$, $g_j=Wmax\int_0^{2\pi}\int_0^A\emptyset(r,\varphi)a_j(r,\varphi)rdrd\varphi$

By solving a set of simultaneous equations (19) we find P_i, providing minimum r.m.s. deviation of mirror reflecting surface forming under the action of actuators from the surface of a required shape. Coefficients $a_i(r,\varphi)$ depend only on mutual actuators' location and do not depend on the other mirror parameters. Hence, parameters P_i characterizing the actuators contributions to the formation of profile are determined by mutual actuators' location and the shape of approximated surface.

301

To characterize the accuracy of approximation we introduce the dimensionless error, i.e. r.m.s. deviation within the active aperture:

$$\mathcal{E} = \sqrt{s}/W_{max} \qquad (21)$$

The presented method of the definition of best approximation of surface of a pregiven shape by AM is universal because parameters P_i and dimensionless error $\mathcal{E}$ are the same for all the mirrors with identical actuators' number and arrangement, and are independent of the mirror size, material parameters.

The distortion shape has been represented in the form : $\emptyset(r,\Psi)=C-\Psi(r,\Psi)$, where $\Psi(r,\Psi)$ is one of the Zydel aberrations:

$$r^2 \quad - \text{ defocus}$$
$$r^4 \quad - \text{ spherical aberration}$$
$$r\cos(\Psi) \quad - \text{ distortion}$$
$$r^3\cos(\Psi) \quad - \text{ coma}$$
$$r^2\cos^2(\Psi) - \text{ astigmatism}$$

C is the constant providing minimum conjugation error of the mirror surface with one of the Zydel aberrations. A choice of the 5 primary aberrations for a simulation is due to the fact that in practice these aberrations greatly contribute to light intensity distribution quality. We have considered round thin plate AM with a clamped edge. This is standart small size AM construction used in laser systems. The edge fixation permits to render the construction stiffness and stability requied for preparing high optical quality reflecting surface. However, this feature limits the opportunities of the control of the mirror surface shape because edge deflection and slope are determined. By limiting the active aperture, on which the surfaces are conjugated, it is possible to decrease the influence of edge conditions on the accuracy of correction. The residual compensation error of pregiven distortion by the AM is defined by the type of distortion, the number of actuators, their mutual location and the diameter of active aperture.

The hexagonal actuator arrangement is typical for AM. This configuration is defined by a number of points N and distance between the points - b. We have chosen the following set of configurations: N=7,19,37,61; distance b was varied from the value, corresponding to actuator filling of the half of aperture, up to the value, corresponding practically to a full mirror aperture filling (with regard to the actuator finite size). Aperture radius was varied from Rm to 0.6Rm (Rm is the mirror radius). Figure 5 illustrates the results of optimization of a distance between actuators for the compensation of primary aberrations by the mirror with N=37 and three values of aperture radius. For all types of aberrations considered, the actuator arrangement on maximum distance from each other is optimum. The study of configuration with N=61 has demonstrated that in this case maximum distance between the actuators is optimum too. The dependences are similar to those in Fig.5. In the case of N=19 the dependence of r.m.s. error on the distance between actuators for three types of aberrations (which are coma, astigmatism and distortion) are similar to N>19, but for defocus and spherical aberration for some values of aperture radius minimal error corresponds to values b which are not equal to maximum distance between the actuators (Fig.6). However, the actuators displacement at maximum distance from each other insignificantly decreases the accuracy of correction in comparison with best value which can be achieved. Hence, this arrangement, apparently, is optimum. For N=7 (Fig.7) the minimum of $\mathcal{E}$(b) essentially depends on aperture radius and the type of aberration. The universal configuration for the correction of primary aberrations does not exist in this case. Figure 8 illustrates the dependence of the accuracy of correction on a number of actuators for the aperture A=0.8Rm and the optimum actuators arrangement in each case. The dependences are symbolic because for hexagonal arrangement the number of actuators take on discrete values. The smoother is aberration the less is influence of variation of the number of actuators on compensation r.m.s. error. The general tendency is the more quiet dependence with increase of N, that proves that the substantial increase of the number of actuators is not expedient for the compensatian of rather smooth distortions.

The study of hexagonal arrangement has demonstrated that the residual error is rather sensitive to actuators arrangement when their number is constant. Let us consider the case of 19 actuators arranged as is demonstrated in Fig.9. The data for three types of aberrations and optimum arrangement of actuators in each configuration are represented in tab.1.

The form of optimum arrangement depends on the type of corrected distortion. For correction of defocus an arrangement of all the actuators on one ring is preferable. For astigmatism correction the best is two rings configuration; for coma correction the best is hexagonal arrangement.

The important problem of the correction of pregiven wave front distortions by the AM is the dependence of the accuracy of correction on the accuracy of adjustment of the system which involves tne AM. We have considered the defocus approximation by the AM with hexagonal arrangement of 19 actuators, when the axis of light incident on the mirror is shifted relatively to the mirror center at the value ranging from 0.01Rm to 0.3Rm. The distance betwcen actuators is b=0.3Rm. The research has shown that small shift of the beam axis relatively to the mirror center causes the critical error increase (Fig.10). The 0.01Rm shift

causes the error increase in 4 times, the 0.1Rm shift causes the error increase in 30 times.

In all the cases considered we have assumed that optical system is adjusted for normal radiation incidence on mirror surface. However, in practice AM may be used at unnormal incidence. Figure 11 illustrates the dependence of accuracy of the correction of defocus and astigmatism by the mirror with hexagonal arrangement of 19 actuators on an angle between the normal to the mirror surface and the axis of incident light. The distance between actuators is b=0.48Rm, the aperture is A=0.6Rm. The dependences demonstrate that the maximum accuracy of conjugation corresponds to the case of normal incidence of radiation.

The results of simulation of the correction of 5 aberrations by the elastic AM with substrate in the form of thin plate showed that:

1. No configuration of arrangement of the given number of actuators in AM exists, providing highest accuracy of the correction of a given set of aberrations: each type of aberration has optimum number and a configuration, providing the given accuracy of correction at the given subaperture.

2. The accuracy of AM correction of the wave front aberrations can not be enhanced by unlimited increasing of the actuator number.

3. As an optical element, the AM in optical system acts as a lense and must be adjusted with high accuracy.

4. The accuracy of AM correction of phase distortions sufficiently depends on the angle of incidence of laser radiation on reflecting surface. Maximum accuracy of the correction reaches at normal radiation incidence.

5. Due to a principle fixation of the AM substrate perimeter maximum accuracy of the correction of aberrations such as distortion, coma, astigmatism and more high orders is not principally achievable at the whole AM aperture.

In conclusion the authors are grateful to V.I. Andryushin, G.A. Jhitomersky and V.V. Ostanin.

References.

1. J.E. Pearson, S. Hansen. JOSA, 67, 325-333, 1977.
2. R. Hudgin. JOSA, 67, 393-395, 1977.
3. J.W. Hardy, J.E. Lefebure, C.L. Koliopoulos. JOSA, 67, 360-369, 1977.
4. D. Bushnell. AIAA Journal, 17, No1, 71-77, 1979.
5. D. Bushnell. AIAA Journal, 17, No1, 78-84, 1979.
6. D. Bushnell, J. Skogh. AIAA Journal, 17, No3, 288-295, 1979.
7. R. Grane. Appl. Optics, 8, No3, 538-542, 1969.
8. W.D. Henderson, S.V. Gun. Proc. SPIE, 179, 51-60, 1979.
9. H.R. Garcia, L.D. Brooks. Proc. SPIE, 141, 74-81, 1978.
10. V.V. Apollonov, S.N. Temnov, S.A. Chetkin. Investigation of adaptive deformable mirror with piezoelectric actuators. Preprint IOFAN SSSR, No231, 26p., 1987.
11. A.P. Lurie. Journal of Applied Mathematics and Mechanics, 7, No1, 93-101, 1940.
12. Physical Acoustics, edited by W.P. Mason, v.1, part A. Moscow: Mir, 592p., 1966.
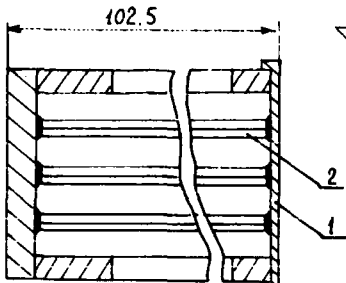
Fig.1A
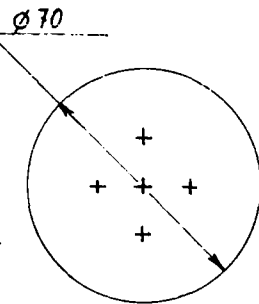
Fig.1B

Fig.1A Adaptive mirror schematic.
  1 - reflecting surface;
  2 - piezoelectric ceramic actuator.
Fig.1B Arrangement of adaptive mirror
actuators.
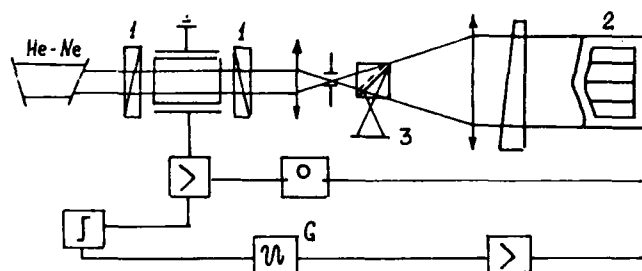
Fig.2 Block diagram of the stroboscopic
interferometer
  1 - electrooptical modulator
  2 - adaptive mirror
  3 - interferometer patten recorder
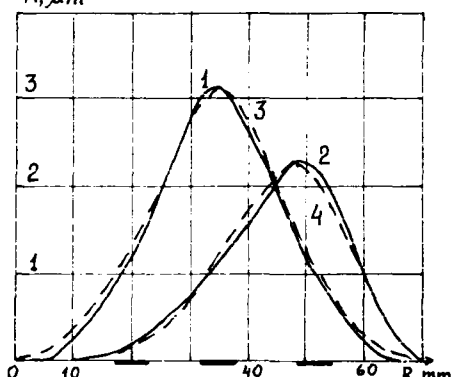
Fig.3A Adaptive mirror influ-
ence function profiles obtai-
ned experimentally (1,2) and
from the theory of thin plate
(3,4).
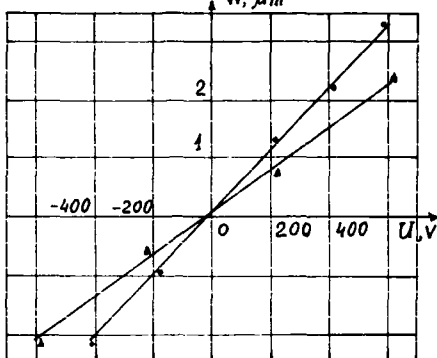
Fig.3B Maximum deflection of
adaptive mirror surface vs
drive voltage on central (•)
and peripherial (▲) actuator.
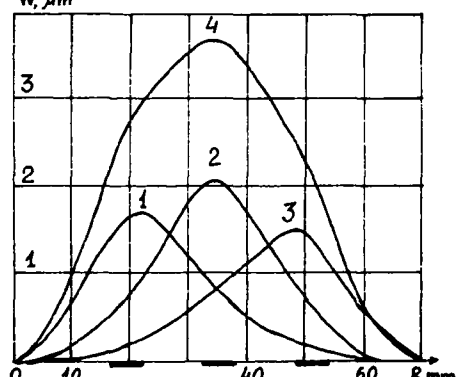
Fig.3C Profiles of adaptive
mirror surface at +400 V dri-
ve voltage applied on 1 - left
actuator, 2 - central actua-
tor, 3 - right actuator, 4 -
three actuators semiltaneously
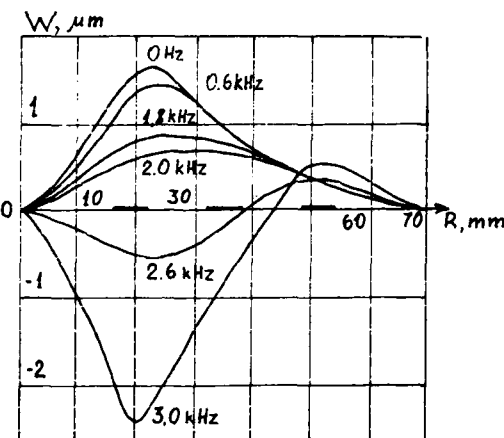
Fig.4 Profiles of vibrating adaptive mirror
surface with sinusoidal drive voltage 400 V
on peripherial actuator.

Fig.5A

304
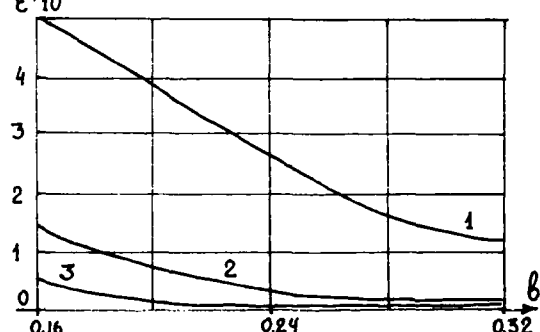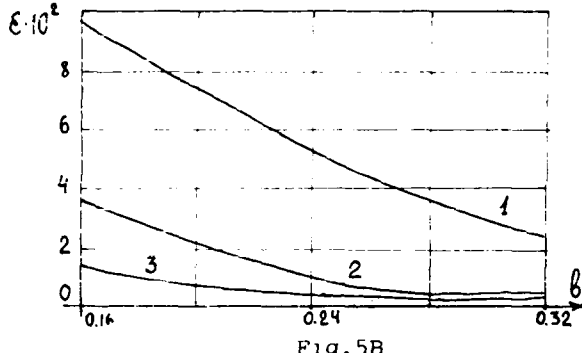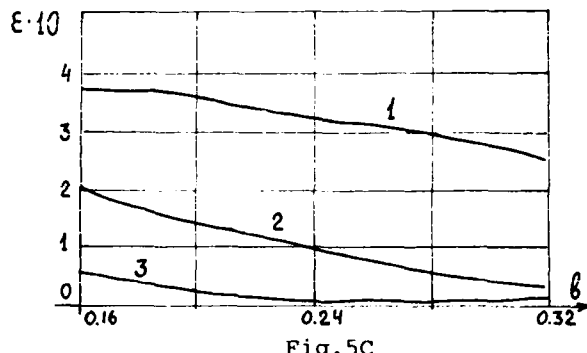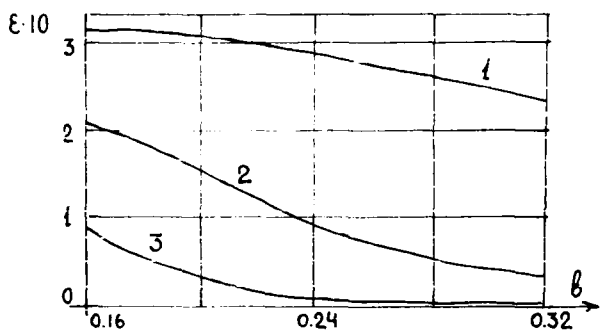
Fig.5 R.m.s. error of correction of aberrations by the adaptive mirror with 37
actuators vs the distance between actuators: 1 - A=Rm; 2 - A=0.8Rm; 3 - A=0.6Rm
A - defocus, B - spherical aberration, C - distortion, D - coma, E- astigmatism.
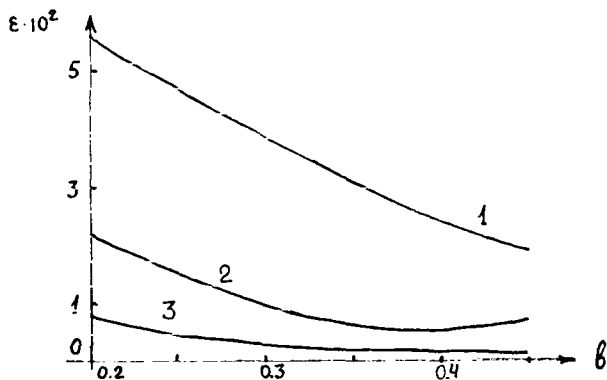
Fig.6 R.m.s. error of defocus (A) and spherical aberration (B) correction by the adaptive
mirror with 19 actuators vs the distance between actuators: 1-A=Rm; 2-A=0.8Rm; 3-A=0.6Rm
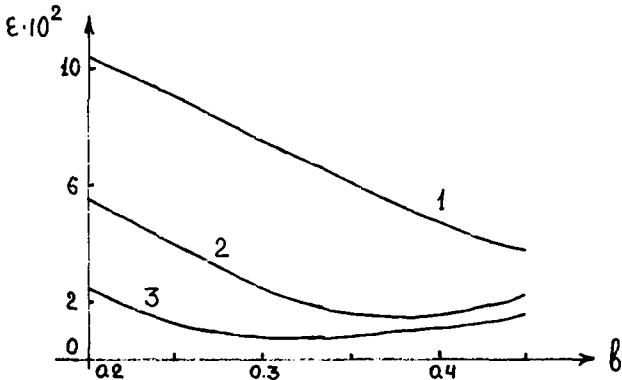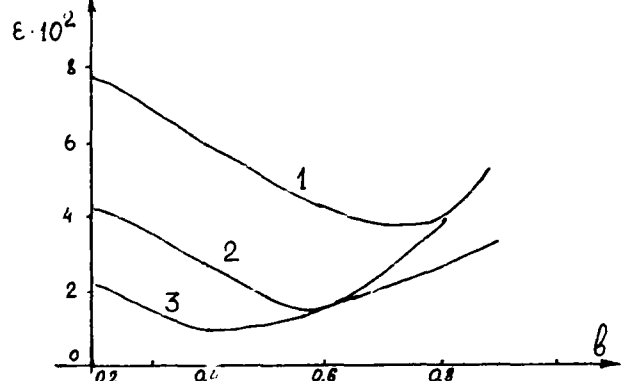
Fig.7 R.m.s. error of defocus (A) and astigmatism (B) correction by the adaptive mirror
with 7 actuators vs the distance between actuators: 1 - A=Rm, 2 - A=0.8Rm, 3 - A=0.6Rm.

305
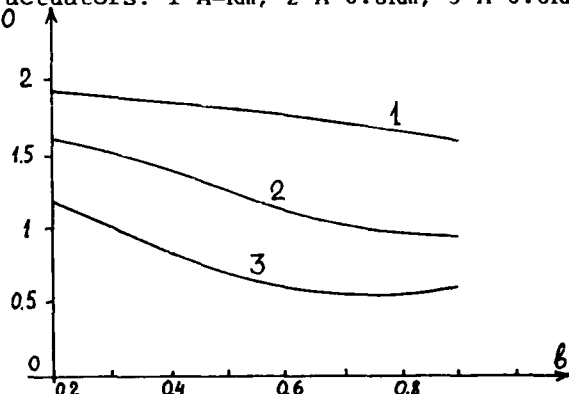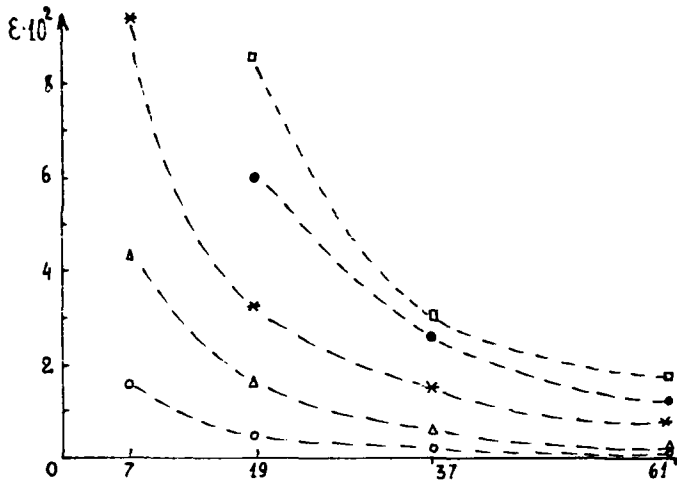
Fig.8 R.m.s. error of correction of
aberrations by the adaptive mirror with
hexagonal arrangement of actuators vs
the number of actuators: o - defocus ,
Δ - spherical aberration, □ - distortion,
● - coma, * - astigmatism.

Fig.9 Adaptive mirror actuator arrangement

Type of aberration	Arrangement		
	1	2	3
Defocus	0.001	0.009	0.005
Astigmatism	0.050	0.030	0.035
Coma	0.080	0.060	0.043

Tab.1 R.m.s. error of correction of aber-
rations by the adaptive mirror for
three types of actuator arrangement.

Fig.10 R.m.s error defocus correction
by the adaptive mirror with 19 actuators
vs the shift between the center of the
mirror and the center of the incident
beam.
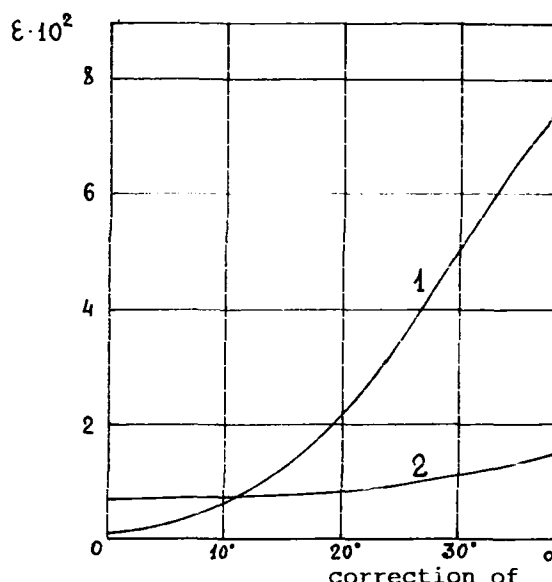
Fig.11 R.m.s. error of defocus (1) and
astigmatism (2) by the adaptive mirror
with 19 actuators vs the angle between
the normal to the mirror surface and the
axis of the incident beam.

THE ROLE OF PLASMOCHEMICAL REACTIONS IN THE FORMATION OF SPER-LASER ACTIVE MEDIUM

V.V.Apollonov, A.A.Sirotkin

General Physics Institute of the USSR Academy of Sciences, Vavilov str. 39,
117942 Moscow, USSR

Abstract

Investigation of the mechanisms of active medium formation in lasers with segmented plasma sources of metal vapors is presented. It is shown that plasmochemical reactions are the main mechanism in the processes of active medium formation in lasers.

The attempts to realize a recombination pump scheme [1] have resulted in the creation of a SPER-laser (segmented-plasma-excitation-recombination)[2-5]. It is a new type of lasers operating on metal vapour and using excitation by the pulsed electrical discharge. The generation at a great number of atom and ion transitions was realized in the IR, visible, and UV wavelength regions. The authors[2-5] suppose that the inversion at the atom and ion transitions in this type of lasers is formed as a result of the ion recombination of higher ratio at the metal vapour plasma scattering into the buffer gas. From the other point of view in papers[6-8] the possibility is considered of the CdII ion levels population at the recharge with He^+ ions at the segmented excitation. Besides that, the bulk preionization of the buffer gas was observed in /8/, and it was shown that the metal vapour plasma scattered not into the cold, but into the preliminary excited buffer gas.

Thus, the mechanisms of the buffer gas excitation and the role of the plasmochemical reactions in the process of the SPER-laser active media formation are not clear yet. These problems are considered in this paper on the example of a SPER-laser operating at the Cd, Zn, In atom and ion transitions.

The experimental set-up is presented in Figure 1. A number of metal (Cd, Zn, In) electrodes with the sizes of 12x2x1 mm^3 were used as active elements (AE). They were positioned in a line on a dielectric plate with a 1+1.5 mm gap between the neighbouring electrodes. The pumping is realized by rectangular current pulses (I_n 20+100 A, voltage U_n= 10+20 kV, pump duration $\tau_n \sim 3$ us). He or Ne with the pressure P= 3+50 torr was used as the buffer gas. The density of the excited atoms and ions of the buffer gas and metal vapour was measured by the method of intracavity laser spectroscopy (ICLS). The ICL-spectrometer consisted of a dye laser with the lamp pumping into the cavity of which the active element of SPER-laser under investigation was placed and a diffraction spectrograph DFS-452. The spectrum was recorded on a photofilm or by a multichannel optical analyzer (MDA) with the following output of the absorption contours on a recording oscillograph.

Figure 2 shows the dependences of the excited He (2^3P) buffer gas atoms on the pressure P_{He}. The excited He atoms were registered at a distance of 18 mm from the electrodes, and the maximum density of the excited atoms was observed at the leading edge of the pulse. It is clear from the figure that the reduction of the buffer gas pressure resulted in the sharp increase of He (2^3P) excited atoms density from $3.10^9 cm^{-3}$ to $5.10^{11} cm^{-3}$ at the variation of P_{He} from 30 to 5 torr. At $P_{He} < 5$ torr firstly we observed the breakdown by the gas between the neighbouring electrodes and then - between the extreme ones, i.e. the glow discharge by the buffer gas formed. On the other hand, at P_{He} increasing a monotonous growth of the metal density N_{CdI} was observed (Figure 3). The density dependence of the excited two-fold ions had another character. Firstly, the sharp growth of CdII ions concentration was observed, at $P_{He} \sim 12$ it achieved its maximum, and after that we observed its slow decrease (Figure 3).

Let us consider the way in which the buffer gas atoms are produced under segmented excitation. It is well known that the glow discharge in the low-pressure gas develops at the voltage exceeding the static breakdown one U_{st}, which is determined for the gas under consideration from the Pashen curve by the parameter Pd (there d is the distance between the electrodes).

Figure 4 shows the oscillograms of the current and voltage pulses operating on the active element of SPER-laser. It is clear that firstly the total charge voltage is applied to the ends of AE U = 15 kV which significantly exceeds the static one ($U_{st} \sim 3$ kV at d = 50 cm, P_{He}= 5+ 10 torr). Thus, between the extreme electrodes of AE the glow discharge begins to develop. Simultaneously, a spark channel starts its formation in the gaps between the neighbour electrodes. Note that in this case the UV radiation from the spark channel plasma as well as the field disturbance caused by the electrodes make easier the development of the glow discharge.

The conditions for the development of the brek-down in the gas and spark channel between the electrodes depend on the pressure P, type of the buffer gas, overvoltage E=U/d, the size of a gap between the electrodes, and the material of the electrodes.

Three regions can be separated by the pressure of the buffer gas.

At low pressures P < 3+5 torr the glow discharge in the gas develops earlier than the spark channel between the electrodes. In this case the current runs by the ionized gas,

and to this case the maximum density of the buffer gas excited atoms is corresponded (see Figure 2) at the minimum value of the metal vapour.

At P > 30 torr we observe quite the reverse case - the discharge in the gas is not formed yet, and the development of the spark channel is already finished. For the most part , the current runs through the plasma in the gaps between the electrodes.

There is a third intermediate region 3÷5 < P< 20÷ 30 torr where the excitation of the buffer gas atoms at the development of the glow discharge is observed together with the formation of a spark channel. In this region we can observe the generation on the atom and ion transitions in SPER-laser [2-5]. Thus, there is a relation between the conditions for the formation of SPER-laser AM and the presence of the excited buffer gas. On account of this fact we can come to a conclusion that the energy is transferred from the buffer gas by the metal ions and atoms. And this can account for the behaviour ofdensity of the excited metal ions (Fig.3) at the variation of Pb , assuming that the metal ions are formed as a result of plasmochemical reactions of the buffer gas with the metal vapour atoms.

Let us consider if such plasmochemical reactions as recharge on the buffer gas ions, Penning ionization, reactions of the type metastable-metastable as well as two-stage reactions, can occur under the condition of segmented excitation of the metal vapour.

1. Figure 5 presents the oscillograms of the current I_n pulses and radiation pulses of the lines Zn II $6d^2D5/2$ (λ = 384 nm), Zn II $4f^2F$ 5/2 ($^n\lambda$ =491.1 nm) and Zn II $4d^2D$ 5/2 (λ = 210 nm) with the buffer gas He (Fig.4a,b,c) and Ne (Fig.4 d,e,f), respectively. It is clear that the character of the line glow depends on the position of Zn II and buffer gas levels. For the levels Zn II $6d^2D$ 5/2 (Zn II $4f^2F$ 7/2) which are situated higher than He^+(Ne) and are populated only due to the electron shock and recombination, the quick decrease of the glow observed after the extinction of the pump current is quite characteristic. For the lines Zn II $4f^2F$ 5/2 (Zn II $4d^2D$ 5/2), which can be populated due to the recharge with He^+(Ne) ions He^+ + Zn He +Zn^{+*}($4f^2F$ 5/2), Ne^+ +Zn Ne + Zn^{+*}($4d^2D$ 5/2), we have observed durable afterglow (Fig.5b,f) similar to the glow of the spectral lines in the direct-current discharge [10]. It is also clear from the figure that the change in the radiation intensity is observed both during the action of the pump current and and during afterglow. Fig.5 presents the dependence Na(He)/Na(Ne) (where Na(He) and Na(Ne) are the populations of the levels with helium and neon buffer gas, respectively) for different distances r from the electrodes after the end of the pump pulse. The Na(He)/Na(Ne) ratio was determined by measuring the radiation intensities of the spectral lines Zn II $4f^2F_{5/2}$ and Zn II $4d^2D_{5/2}$. It is seen from the figure that at small r, where mixing of the metal vapor and buffer gas is negligible, the processes of recharging and recombination are comparable. At large r, mixing is more efficient and recharging makes the major contribution to the level population . It is in that spatial region where lasing is observed.

These experiments show that the process of Zn ion formation (a similar picture was observed for Cd also) is by an order of magnitude more efficient that the electron shock or recombination due to the recharge reaction.

At the change of the buffer gas from He to Ne the redistribution of the population on the lower levels occurs. It should be pointed out that at such a change the intensity of the SPER-laser radiation at the atom transitions varies insignificantly, i.e. to a first approximation we assume the number of the recombining one-time-charged ions to remain constant.

2. It is well known that neon and argon break the metastable states He (2^1S_0) and He (2^3S_1). In our experiments at the addition of Ne into He buffer gas we observed the reduction of the intensity and duration of the line glow Cd II $4d^9$ ^2D 5/2, 3/2) and Zn II ($3d^9$ ^2D 5/2, 3/2). These lines can be populated at the Penning reaction with the He metastables [11]:

$$He(2^3S_1) + Cd \rightarrow He + Cd^{+*}(4d^9\ ^2D_{5/2,\ 3/2}) + e$$

$$He(2^3S_1) + Zn \rightarrow He + Zn^{+*}(3d^9\ ^2D_{5/2,\ 3/2}) + e$$
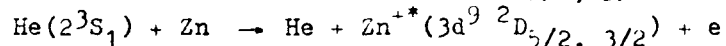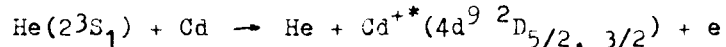
Thus, at the analysis of the formation mechanisms of SPER-laser active media it is necessary to take into account the Penning reaction as well.

3. In /6/ the possibility of Cd II $4f^2F^0$ levels population at the Penning reaction of He metastables with Cd metastables (He(2^3S_1) + Cd(5^3P_2)→He + Cd^{+*}+ e) was considered for the explanation of the second burst of afterglow.

This effect was observed in our experiments with Cd and Zn as well (see Figures 5b, 5f), but we failed to explain it for this reaction since the process does not pass by energy. To our mind, the radiation intensity in the far afterglow is associated with the recharge of the metal atoms on He^+ ions, which are formed at the interaction of He metastables [12].

4. In /3-4/ the generation was realized in the visible and UV wavelength regions on In III and Bi III transitions as a continuation of Cd II and Pb II electron row, respectively. Let us consider the possibility of the population of In III and Bi III upper laser levels by means of plasmochemical reactions.

Figure 7 shows the partial diagrams of energetic levels for In and Bi. It is clear that they have a similar structure. The main states $In^{++}$and Bi^{+} are in the vicinity of the the resonance with He^+, which makes possible the reaction of recharge accompanied by the Penning ionization.

$$He^+ + In \rightarrow He + In^{+} + e \qquad\qquad He^+ + Bi \rightarrow He + Bi^{+} + e$$

In /13/ they pointed out that great cross-sections ($6 \sim 10^{-15} cm^2$) correspond to such reactions at which the summary energy of the electron coatings is kept constant.

Besides, it is clear from the diagram (Figure 7) that for such elements a unique situation is realized, since the energetic gaps between the main states In^{++}, Bi^{+} and the upper laser levels $4f^2F_{5/2}$In III and $6f^2F_{5/2}$BiIII are 20.08 eV and 20.114 eV, respectively, which is near the resonance with He metastable state ($2's_0$).

Due to this fact the excitation transfer should be effectively realized according to the following scheme:

$$He(2'S_0) + In^{+-} \rightarrow He + In^{++*}$$

$$He(2'S_0) + Bi^{+} \rightarrow He + Bi^{++*}$$
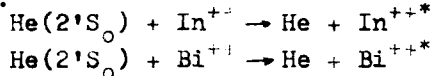
Such a two-stage recharge process with Penning ionization by He^+ ion and the excitation transfer from He metastable can result in the selective population ofthe upper laser levels in In III and Bi III.

For the experimental test of such a supposition some quantity of neon and argon was added into He buffer gas of SPER laser operating on In vapour, which causes the destruction of He ($2'S_0$) and Ne (2^3S_1) metastables. The reduction in the glow intensity of In III spectral lines ($4f^2F_{5/2, 7/2}$) was obtained with the increase of the additive concentration. At the total change of He for Ne these lines were not registered.

Taking into account all the mentioned above we can explain the fact that the authors of /4/ did not obtain generation on Bi III transitions ($5f^2F_0 - 6p^2P$) with λ = 2074 A. It can be explained by the great difference in the energetic levels between Bi^{++} (17.04eV) and He metastable, and consequently by the low efficiency of the excitation transfer.

Thus, it is shown in this paper that plasmochemical reactions are the main mechanism for the formation of the laser active media with a segmented plasma source of the metal vapour. The population of Cd II and Zn II ion levels occurs at the recharge with He^+ ions In III - at the recharge with ionization and the following excitation. These processes are more efficient than recombination or electron shock.

The pump recombination mechanism is realized on the atom transitions, in this case the one-time-charged ions are formed in the process of plasmochemical reactions. The recombination pump, o our mind, can also be observed for the one-time-charged ions of the elements (Ca,Sn,Pb,Sr, etc) the two-times-charged ions of which can be obtained using the recharge with ionization.

References

1. L.I.Gudzenko, L.A.Shelepin, Doklady AN SSSR, 160, p.1296 (1965).
2. W.T.Silfvast et al. Appl.Phys.Lett., v.36, p.615(1980).
3. W.T.Silfvast et al. Appl.Phys.Lett., v.39, p.212(1981).
4. W.T.Silfvast et al. Opt.Lett., v.7, p.34(1982).
5. J.J.Machlin et al. IEEE J.Quantum Electronics, v.QE-18 (1982).
6. A.A.Babin, I.I.Muravjev, L.D.Shatova, A.M.Yangarina, Izvestija VUZ and MV and SSO SSSR Fizika No.7 (1986).
7. M.Vilargan, M.Gallardo, and J.O.Tocho, J.Appl.Phys., v.61, No9, p.4447(1987).
8. V.V.Apollonov, S.I.Derzhavin, A.M.Prokhorov, A.A.Sirotkin. Pis'ma Zh.Tekh.Fiz., v.14, No11, p.983(1988).
9. V.V.Apollonov, S.I.Derzhavin, A.A.Sirotkin. The All-Union Meeting "Inverse population on transitions in atoms and molecules", Tomsk, p.3.(1986).
10. V.L.Latush, V.S.Mikhalevskii, M.F.Sem, Optika i Spektroskopia, v.34, No2, p.214(1973).
11. G.J.Collins, J.Appl.Phys., v.44, p.4633(1973).
12. Col. Spectroscopy of gas-discharge Plasma, L. LGU, 1976.
13. L.I.Gudzenko, S.I.Yakovlenko. Plasma Lasers. M.Atomizdat, 1978.
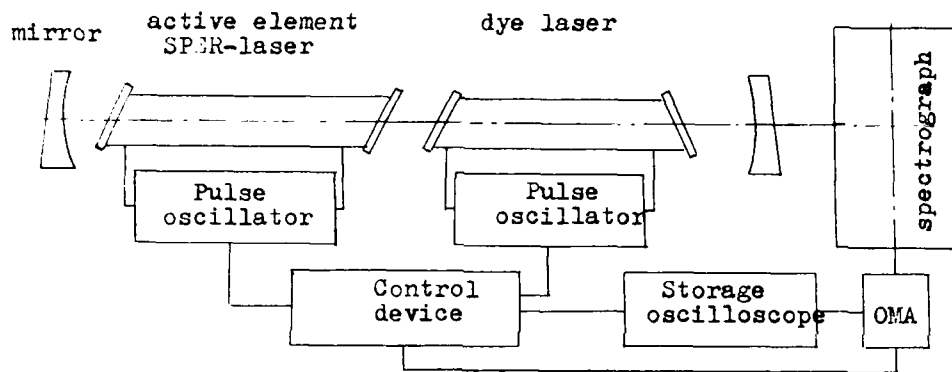
Fig.1. Schematic diagram of intracavity absorption spectrometer
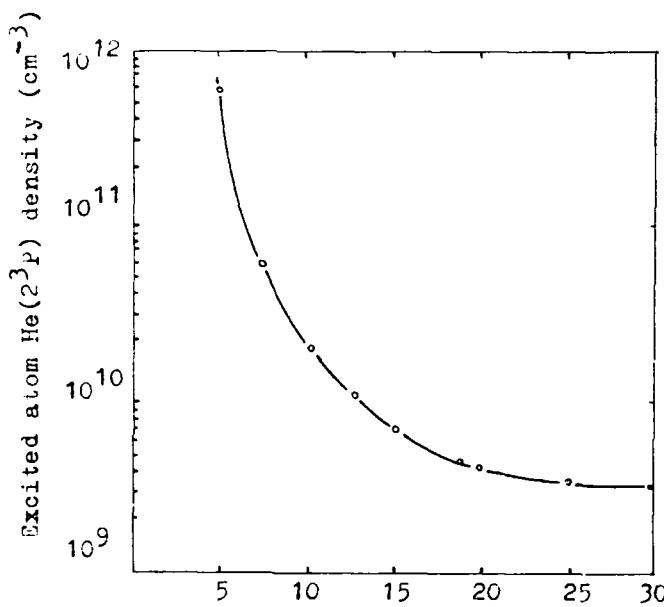
Fig.2. Excited atom He(2^3P) as a function of pressure buffer
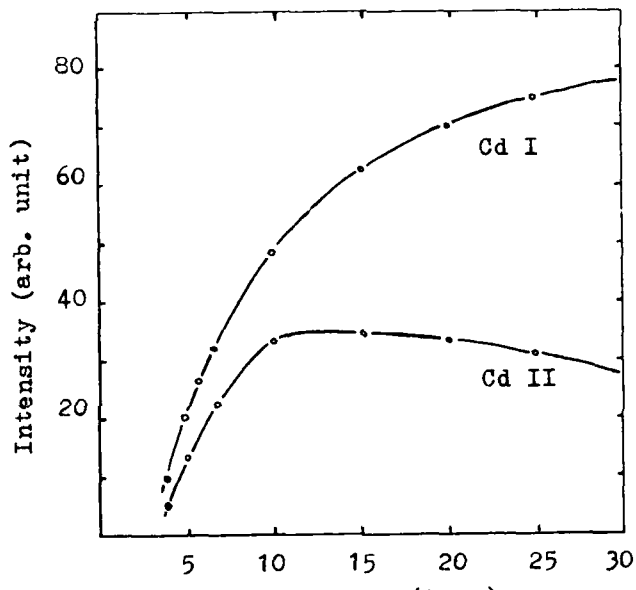
Fig.3. Spectrum line CdI6s^{3}S (λ =467.8nm) and CdII4f^{2}F^o (λ =587.3 nm) intensity as a function of pressure buffer gas.
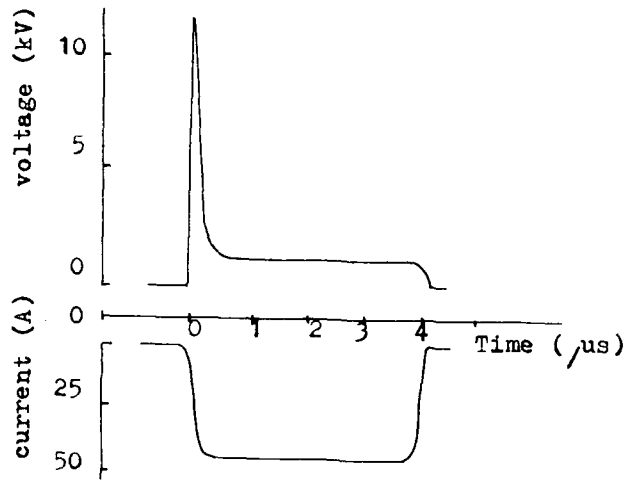
Fig. 4. Oscilloscope trace voltage and current pulse.
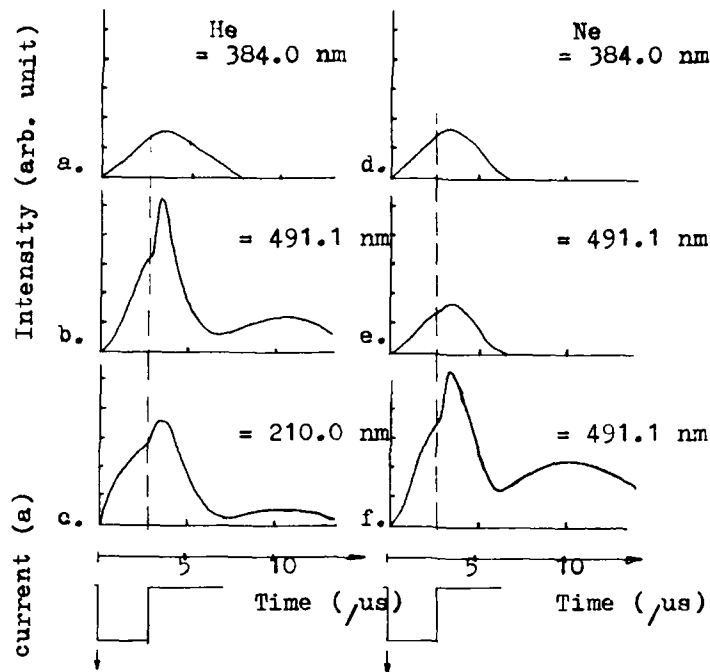
Fig.5. Oscilloscope trace of current pulse I and spectrum line $ZnII6d^2D_{5/2}$(λ=384 nm), $ZnII4f^2_{5/2}$(λ= 491.1 nm), $ZnII4d^2D_{5/2}$(λ=210.0 nm) intensity with He (a,b,c) and Ne (d,e,f) buffer gas.
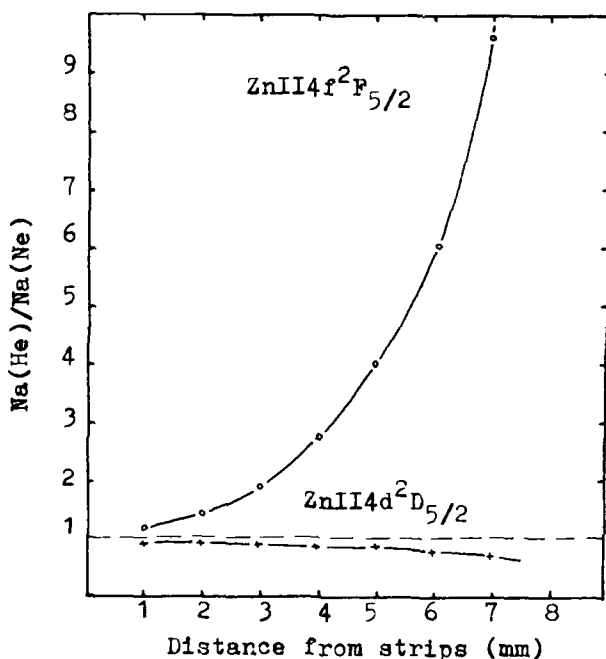
Fig. 6. Ratio of population of the levels $ZnII4f^2F_{5/2}$ and $ZnII4d^2D_{5/2}$ with He and Ne bufeer gas as a function of distance from strips.
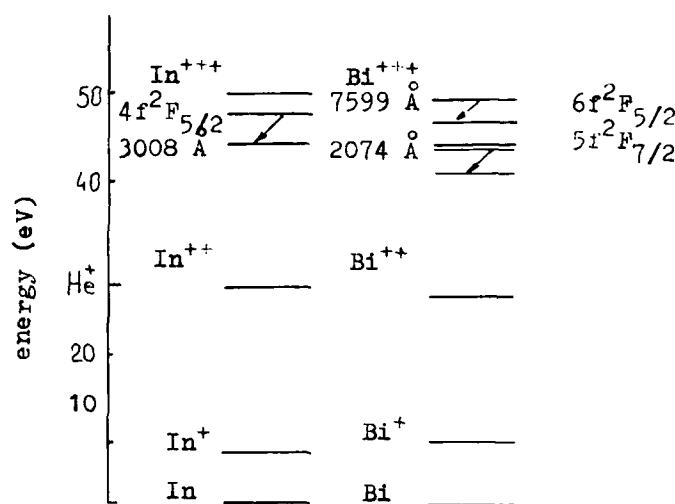
Fig.7. Partial energy levels diagrams in In and Bi

RECENT ADVANCES IN FAR-INFRARED LASERS

F.K. Kneubühl, D.P. Scherrer and J.P.G. Arnesson

Infrared Physics Laboratory
Institute of Quantum Electronics
ETH (Swiss Federal Institute of Technology)
CH-8093 Zurich, Switzerland

ABSTRACT

We present a review on the actual significance of far-infrared gas lasers in basic laser physics. The main aspects are deterministic chaos and linear as well as nonlinear distributed feedback.

INTRODUCTION

In recent years far-infrared gas lasers evolved as valuable tools for the experimental study of two different basic concepts in laser science, i.e. distributed and helical feedback on one hand as well as deterministic chaos on the other hand.

In 1975 Haken proved that the theoretical model of deterministic chaos postulated by Lorenz in 1963 can also be applied to the nonlinear dynamics of lasers under specific conditions. In the meanwhile it was realized that specifically designed optically pumped far-infrared gas lasers exhibit the phenomena characteristic for deterministic chaos. These include the transition from the stationary oscillation as well as the intermittant route of Manneville-Pomeau. Therefore, the current research concentrates on the quantitative interpretation of instabilities and chaos in far-infrared gas lasers in view of the theory on deterministic chaos.

With respect to the experimental investigation of the mode properties of distributed and helical feedback laser systems and the comparison of the results with the theoretical predictions the optically pumped far-infrared lasers have proven to be superior to semiconductor and dye lasers mainly due to their narrow gain profile. Thus, it was possible to test the coupled-wave theory relevant to distributed feedback (DFB) with weak periodic modulation of the index of refraction or waveguide cross-section, to investigate the in-gap modes occurring in distributed feedback with phase matching achieved by gaps in the periodic laser structure, to realize helical feedback (HFB) with waveguide structures of the symmetries of the helix and the double helix, and finally, to verify quantitatively nonlinear gain saturation and pulse formation in distributed and helical feedback lasers.

DETERMINISTIC CHAOS

Instabilities in laser emission notably in the form of coherent pulsations have been observed almost since the first demonstration of laser action. The first laser operated in 1960 by Maiman [1] generated noisy spiked output even under condition of quasi steady excitation. Subsequent theoretical effort towards an understanding of these phenomena remained on a modest level until Haken [2] demonstrated that the Lorenz model [3,4] of deterministic chaos can also be applied to the nonlinear dynamics of lasers. In the meanwhile, a large variety of experiments on pulsating instabilities and chaos in lasers has been performed [5-8]. Optically pumped far-infrared lasers have proven to be predestinated for this kind of

experiments. This was first recognized by Weiss et al. [8-11]. For this purpose they applied 81.5 μm NH_3 [8-10] and 117 μm CH_2F_2 [11] lasers. Laser-pumped gas lasers are usually not properly described by the three Lorenz equations of a two-level laser derived by Haken [2]. The coherent coupling of the three levels of a laser-pumped gas laser includes nine equations. The conditions for the reduction of these nine equations to the three Lorenz equations have been formulated by Dupertuis et al. [12]. This reduction is possible with some restrictions for optically pumped far-infrared lasers.

Consequently, optically pumped far-infrared lasers are especially suited for the study of pulsating instabilities and chaos in lasers. In this context it should be mentioned that they permit to demonstrated the sequence of subharmonic instabilities to chaos in detail [10]. Other phenomena of deterministic chaos are under investigation.

DISTRIBUTED AND HELICAL FEEDBACK LASERS

In lasers the optical feedback is usually provided by the reflections on the two mirrors of the conventional laser resonators. The main handicap of these resonators with the optical feedback localized at the mirrors is the similarity of the losses of their fundamental longitudinal modes which are separated by c/2R in frequency. R indicates the length of the resonator and c the speed of light. This handicap impedes the single-mode operation of lasers with a broad-band gain of the active medium, i.e. of dye, semiconductor and high-pressure gas lasers. This can be avoided by replacing the conventional optical resonators by axially periodic or helical laser structures. In these laser structures the optical feedback is provided by backward Bragg scattering from periodic or helical modulations of the waveguide, the refractive index and/or the gain of the laser medium. In this arrangement the optical feedback is distributed along the entire laser structure. Therefore, it is called distributed feedback (DFB) for axially periodic and helical feedback (HFB) for helical laser structures. The relevant feature of DFB and HFB is the high spectral selectivity inherent in the Bragg effect which permits easy selection among the fundamental longitudinal laser modes even for laser-active media with broadband gain.

Distributed feedback (DFB) was accomplished first in a dye laser [13], later in a semiconductor laser [14] and in a gas laser [15-17]. The DFB gas laser is an optically pumped far-infrared 496 μm CH_3F laser [18-20] with a periodic waveguide acting as optical feedback system.

The majority of calculations on DFB lasers are based on perturbation theory. It can be applied to lasers with weak axially periodic modulations of waveguide cross-section, refractive index or/and gain of the laser medium. The coupled-wave theory [21-23] is relevant for the far-infrared DFB gas lasers. Therefore, these have been applied to test this theory [16,17,24-28]. On the other hand, they are not suited for a study of DFB with strong axially periodic modulations [28-29].

DFB lasers with low gain and pure index modulation, e.g. DFB far-infrared gas lasers exhibit frequency gaps without modes. They correspond to the energy gaps of solids. It is possible, however, to generate modes within these frequency gaps by, e.g. phase matching with the aid of a spatial gap in the continuous periodic laser structure. Also this phenomenon can be demonstrated theoretically by coupled-wave theory [22,23,27] and experimentally with far-infrared gas lasers [27]. The in-gap modes are of special interest in the design of semiconductor DFB lasers.

The concept of helical feedback (HFB) which is based on group theory [25,30] was first verified on an optically pumped far-infrared gas laser equipped with a helical waveguide for optical feedback [25,30,31]. In the meanwhile it was noticed that HFB is also present in dye lasers with cholesteric liquid crystals serving as optical feedback [22,23,28,32].

Recently, it was discovered that the power distributions of the modes near the frequency gaps of far-infrared DFB gas lasers manifest nonlinear gain saturation [33-35]. This effect is illustrated in Fig. 1 which shows the output power of consecutive longitudinal (TM_{22}/TM_{-22})-modes $\bar{q}$ of an optically pumped 496 μm CH_3F-DFB laser with a periodic hollow metal waveguide with period $L = 248.0$ μm, corrugation depth $a_1 = 89.1$ μm and inner radius $a = 2370$ μm. The frequency tuning is performed by thermal expansion. Therefore, the waveguide temperature T represents the tuning parameter. The modes $\bar{q} = -1,-2,-3...$ are adjacent to the stopband characteristic for DFB laser with periodic refractive index or waveguide-cross-section modulation. According to linear DFB theory [21-23,28] the output power is expected to increase with decreasing modulus $|\bar{q}|$ of the mode number $\bar{q}$. Consequently, the mode $\bar{q} = -1$ adjacent to the stopband should exhibit the highest output power. This is contradicted by the experimental result shown in Fig. 1, where the maximum output power occurs for the mode $\bar{q} = -7$. This shift is explained by the theory of nonlinear gain saturation in DFB lasers [33-35].

Finally, we should mention the first observation [36] of the dependence of the pulse duration on the DFB mode $\bar{q}$ of a DFB laser with periodic modulation of the waveguide cross section or the refractive index. This effect was demonstrated with an optically pumped 496 μm CH_3F-DFB laser equipped with a periodic hollow metal waveguide characterized by $L = 252.0$ μm, $a_1 = 92.3$ μm and $a = 2369$ μm. The relative output power of its (TE_{11}/TE_{-13})-modes $\bar{q} = -1$ to -3 are shown in Fig. 2, whilst the DFB pulse shapes for $\bar{q} = -1$ and -2 are plotted in Fig. 3 together with the pump pulse of the 9.55 μm CO_2-TEA laser. The pulse durations of these DFB modes differ considerably, i.e. 50 ns for $\bar{q} = -1$ and 90 ns for $\bar{q} = -2$.
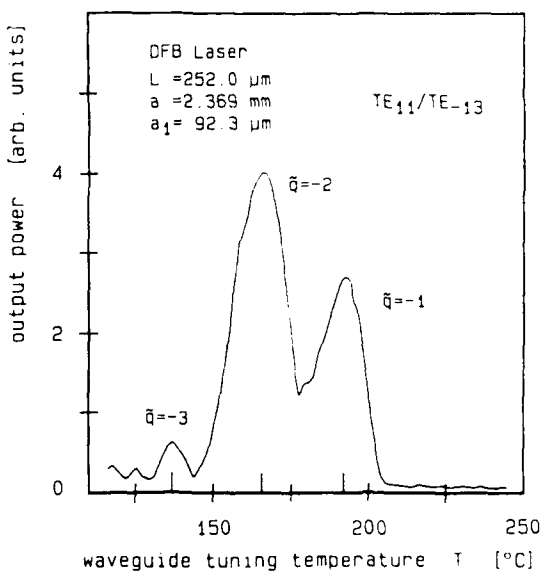
Fig. 2: (TE_{11}/TE_{-13})-modes of 496 μm CH_3F-DFB laser with a periodic hollow metal waveguide. For parameters see text.

Fig. 3 suggests that the pulse durations and the threshold gains of DFB modes are related. Hitherto, the dependence of pulse shapes and durations on the DFB modes has been known only for DFB lasers with periodic gain modulation, i.e. DFB dye lasers [e.g. 37,38]. According to linear DFB theory [21-23,28] the mode $\bar{q} = -1$ has the lowest threshold gain and consequently the longer pulse duration than the mode $\bar{q} = -2$, which contradicts the experimental facts illustrated in Fig. 3. Reliable theories on this phenomenon are still missing, yet it must be explained by threshold gains influenced by DFB nonlinearities.

Fig. 1: Experimental demonstration of nonlinear gain saturation in an optically pumped 496 μm CH_3F-DFB laser [33-35]

9.55 μm TEA-CO₂ LASER

496 μm DFB-CH₃F LASER

L=252.0 μm

TE_{11} / TE_{-13} MODE

50 ns

$\tilde{q}=-1$

90 ns

$\tilde{q}=-2$
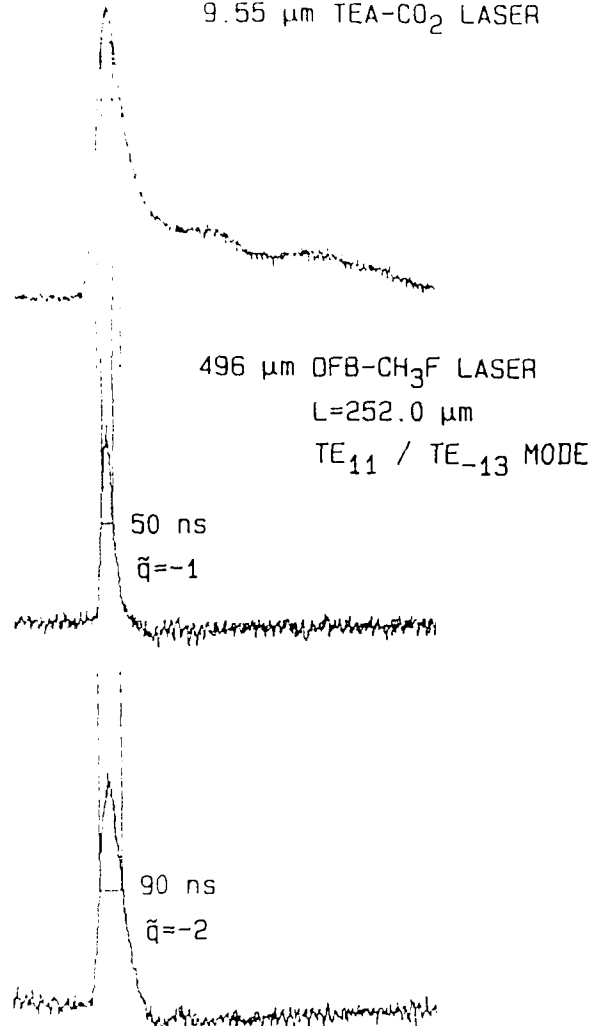
Fig. 3: Pulse shapes of the (TE_{11}/TE_{-13})-modes $\tilde{q}$ = -1,-2 of a 496 μm CH₃F-DFB laser and of the 9.55 μm CO₂ pump pulse.

CONCLUSION

Actually, the optically pumped far-infrared gas lasers developed in the seventies prove to be the predestinated tool for the study of two basic aspects of laser physics, i.e. deterministic chaos and distributed feedback. Consequently, these lasers permit to relate theories with rather complicated observed phenomena.

ACKNOWLEDGEMENTS

REFERENCES

[1] T.H. Maiman:
      Nature 187, 493 (1960)

[2] H. Haken:
      Phys. Lett. 53A, 77 (1975)

[3] E.N. Lorenz:
      J. Atmos. Sci. 20, 130 (1963)

[4] C.T. Sparrow:
      The Lorenz Equations: Bifurcations, Chaos and Strange Attractors", Springer, Berlin (1982)

[5] R.G. Harrison, D.J. Biswas:
      Progress in Quantum Electronics 10, 147 (1985)

[6] R.G. Harrison, D.J. Biswas:
      Nature 321, 394 (1986)

[7] D.J. Biswas, R.G. Harrison, C.O. Weiss, W. Klische, D. Dangoisse, P. Glorieux, N. Lawandy:
      in "Instability and Chaos in Quantum Optics", ed. R.G. Harrison, F.T. Arecchi, Vol. 34, 109 (1987)

[8] C.O. Weiss:
      Proc. 4th Int. Conference on Infrared Physics (CIRP 4), Zurich, August 1988, 208

[9] C.O. Weiss, W. Klische:
      Opt. Comm. 51, 47 (1984)

[10] C.O. Weiss, W. Klische, P.S. Ering, M. Cooper:
      Opt. Comm. 52, 405 (1985)

[11] C.O. Weiss, W. Klische:
      Opt. Comm. 50, 413 (1984)

[12] M.A. Dupertuis, R.R.E. Salomaa, M.R. Sigrist:
      Opt. Comm. 57, 410 (1986)

[13] H. Kogelnik, C.V. Shank:
      Appl. Phys. Lett. 18, 152 (1971)

[14] N. Nakamura, A. Yariv, H.W. Yen:
      Appl. Phys. Lett. 22, 515 (1973)

[15] E. Affolter, F.K. Kneubühl:
      Phys. Lett. 74A, 407 (1979)

[16] E. Affolter, F.K. Kneubühl:
      IEEE J. of Quantum Electron., QE-17, 1115 (1981)

[17] F.K. Kneubühl, E. Affolter:
      in "Infrared and Millimeter Waves", K.J. Button, ed., Academic Press, N.Y., Vol. 5, Ch. 6, 305 (1982)

[18] T.Y. Chang, T.J. Bridges:
      Opt. Comm. 1, 423 (1970)

[19] T.A. De Temple:
      in "Infrared and Millimeter Waves", K.J. Button, ed.,
      Academic Press, N.Y., Vol. 1, Ch. 3, 129 (1979)

[20] T.A. De Temple and E.J. Danielewicz:
      in "Infrared and Millimeter Waves", K.J. Button, ed.,
      Academic Press, N.Y., Vol. 7, Ch. 1, 1 (1983)

[21] H. Kogelnik, C.V. Shank:
      J. Appl. Phys. 43, 2327 (1972)

[22] F.K. Kneubühl:
      Revue Roumaine de Physique 33, 691 (1988)

[23] F.K. Kneubühl, Cui Dafu: (in Chinese)
      Chinese J. of Infrared Research 7A, 241 (1988)

[24] X. Zheng, S. Gnepf, H.P. Preiswerk, D. Wildmann, F.K.
      Kneubühl: (in Chinese)
      Chinese J. of Infrared Research 3, 81 (1984)

[25] H.P. Preiswerk, M. Lubanski, F.K. Kneubühl:
      Appl. Phys. B33, 115 (1984)

[26] F.K. Kneubühl:
      Optica Acta, special issue in commemoration of the 25th
      anniversary of the first laser, 32, 1055 (1985)

[27] D. Wildmann, S. Gnepf, F.K. Kneubühl:
      Appl. Phys., B42, 129 (1987)

[28] F.K. Kneubühl, M.W. Sigrist:
      "Laser" (in German), Teubner, Stuttgart, 1st ed. (1988),
      2nd ed. (1989)

[29] S. Gnepf, F.K. Kneubühl:
      in "Infrared and Millimeter Waves", K.J. Button, ed.,
      Academic Press, N.Y., Vol. 16, Ch. 2, 35 (1986)

[30] H.P. Preiswerk, M. Lubanski, S. Gnepf, F.K. Kneubühl:
      IEEE J. of Quantum Electron., QE-19, 1452 (1983)

[31] H.P. Preiswerk, G. Küttel, F.K. Kneubühl:
      Physics Lett. 93A, 15 (1982)

[32] F.K. Kneubühl:
      Infrared Physics, 23, 115 (1983)

[33] J. Arnesson, Cui Dafu, S. Gnepf and F.K. Kneubühl:
      Proc. 4th Int. Conf. on Infrared Physics (CIRP 4), Zurich,
      August 1988, 358

[34] J. Arnesson, Cui Dafu, S. Gnepf and F.K. Kneubühl:
      Opt. Comm. (1989)

[35] J. Arnesson, Cui Dafu, S. Gnepf and F.K. Kneubühl:
      Appl. Phys. (1989)

[36] D. Scherrer:
      Report Infrared Physics Laboratory ETH (1988)

[37] Z. Bor:
      IEEE J. Quantum Electron., QE-16, 517 (1980)

[38] G. Szabo, Z. Bor:
      Appl. Phys. B31, 1 (1983)

SEALED ALL-METAL CO$_2$ LASER TUBE TECHNOLOGY

Stanley Byron and Peter Laakmann
Synrad, Inc.
11816 North Creek Pkwy N., Suite 103, Bothell, WA 98011

ABSTRACT

A newly developed RF plasma configuration for CO$_2$ lasers is described that offers high performance at low cost using an all-metal, sealed-off laser tube design. The plasma bore of 5mm square cross-section supports a free-space TEM$_{00}$ optical mode and a laser power density 1/3 that of CO$_2$ waveguide lasers, allowing fabrication of compact sealed-off CO$_2$ lasers from 10 to 100 watts with good optical and mechanical integrity. Design and manufacturing factors are discussed that affect gas life, beam quality, modulation, optical stability, and cost.

INTRODUCTION

The work reported here was started in 1984 and was aimed at developing a new approach in sealed-off RF excited CO$_2$ laser technology that would provide much lower cost devices, expanding established markets and opening new market applications. The initial goals were met in 1988, with over 150 lasers delivered during the first year of manufacturing at Synrad, Inc.

To achieve low cost as well as high performance, the problems of previously developed RF-excited CO$_2$ waveguide lasers had to be solved. The earlier lasers[1] used metal ceramic "composite" construction techniques that required tight tolerances, extensive machining, and lengthy processing time to remove laser gas contaminants. The small bore (2 to 3mm) of the waveguide has the advantage of high optical gain and high power from short devices, but it has the disadvantage of high optical power density on the laser mirrors, approaching the damage threshold limit of commercially available optics. The waveguide approach also suffers from intracavity losses at the walls, and high sensitivity to mirror orientation which causes mode instability problems.

These difficulties are resolved by the approach described here, which retains the advantages of RF excitation (low voltage, electronically controllable, stable discharge), but eliminates the waveguide and its problems by opening the bore to 5mm and using a TEM$_{00}$ mode optical cavity configuration. A unique feature of RF discharges was discovered that allows all of the walls of the bore to be metal, which can be extruded in the proper shape at very low cost. This laser tube construction technique is the basis for a Synrad patent[2]. The assembled laser tube can be processed much more rapidly than CO$_2$ waveguide tubes, by using higher temperatures and because there are no tightly fitting surfaces that require a long time for outgassing.

Another key factor in cost reduction and product reliability is the use of the laser tube as the resonator in a self-oscillating RF circuit, the subject of a second Synrad patent[3]. Previous RF excited CO$_2$ lasers have used an external RF oscillator and amplifier chain coupled to the laser by an impedance matching coaxial cable. Synrad has developed a much simpler and lower cost approach that uses a single transister power oscillator driven by feedback from an LC resonator built into the electrode structure of the laser tube.

These factors as well as careful attention to thermal and mechanical design of the single integrated chassis have resulted in very low cost, high performance, sealed-off CO$_2$ lasers in the power range from 10 to 25 watts.

LASER DESCRIPTION

Each of the two lasers, shown in Fig. 1, is a completely integrated unit, requiring only input power and cooling, as determined by the application and mode of operation. Two input power options are available, either 28 volts dc or 110 volts ac. The chassis is provided with air cooling fins for fan cooled operation up to 50% duty cycle, and with four grooves where water cooling tubes can be inserted for high duty cycle or full power operation. The chassis of each laser is only 3 inches wide by 4 inches high. The length of the 10 watt laser is 17 inches and that of the 25 watt laser is 32 inches.

The all aluminum chassis is carefully integrated to contain the laser tube, the power supply, and all of the electronic circuits, as shown in Fig. 2. The laser tube is a 2 inch square aluminum extrusion with the ends welded in place. A gas fill valve and RF electrical feedthrough post is located on one side of the laser tube. The laser mirrors are held against o-rings on each end by simple mounts that are adjusted and locked into place at the factory. The laser tube fits closely into the chassis to assure good thermal contact. Heat from both the laser tube and the electronic circuits is carried by the aluminum chassis to the side walls where it is removed by forced air or water cooling. The basic operating parameters for the lasers are listed in Table 1.

Laser Tube Structure

A cross-section of the internal structure of the aluminum laser tube is shown in Fig. 3. The four extruded aluminum parts slide in through the ends of the tube and lock into place. After internal assembly is completed the aluminum ends are welded on to the tube, making a leak free structure that can be vacuum baked at high temperature for rapid removal of impurities.

The two extruded aluminum side pieces (ground spacers) serve three functions. They restrict the RF discharge at the sides of the central 5mm square plasma region, they conduct heat from the laser gas to the outer perimeter of the laser tube, and they provide the support structure for the two RF electrodes. The RF

discharge electrodes at the top and bottom of the laser tube are also extruded aluminum and are anodized everywhere except where electrical contact surfaces are required. The anodized layer helps to maintain discharge uniformity. The electrodes are locked firmly against the ground spacers with 1/8" diameter ceramic ball insulators sandwiched between the parts.

The upper electrode is connected to the external RF circuit through the feedthrough post. A 0.5mm gap between the electrode and the tube wall forms a capacitance to ground that becomes a component in the RF oscillator circuit. The upper electrode is connected to the lower electrode (and its capacitance) through an inductor. The RF drive on the lower electrode is shifted in phase by 180 degrees from the upper electrode, making the peak voltage between the 2 electrodes twice that between one electrode and the grounded laser tube. RF breakdown in the gas occurs only in the central 5mm square bore of the laser tube. Plasma current flows between the 2 RF electrodes, not to the ground electrodes.

RF Breakdown

As noted above, the laser tube is constructed almost entirely of metal parts, yet the RF plasma forms only in the central bore of the tube. This all-metal construction method is based on the unique electrical breakdown characteristics of low pressure RF discharges. MacDonald[4] has shown that experimental data for RF breakdown voltage can be correlated by plotting $E \Lambda$ versus $p\Lambda$, where Λ is a characteristic scale length for electron diffusion losses. This correlation is applicable for RF frequencies that are high enough that the electron drift distance in a half period is much less than the electron diffusion loss distance. Under these conditions there is no requirement for secondary electron emission from the electrodes, and the RF breakdown voltage can be considerably lower than the DC breakdown voltage. At reduced pressure and high frequencies the electron drift distance may become less than the electron-molecule mean free path. At pressures below this value the RF breakdown voltage rises, exhibiting a minimum in the curve of breakdown voltage versus pressure. The location of this minimum depends on the RF frequency. For pressures above this minimum, and for RF frequencies well above the electron momentum transfer collision frequency, the RF breakdown voltage does not depend on frequency, and is simply a characteristic of the gas.

For the high pressure (frequency independent) part of the breakdown curve, the voltage is determined by requiring that the net ionization rate coefficient, ν_i, in the gas equals the loss rate coefficient by diffusion,

$$\nu_i = D/\Lambda^2 \tag{1}$$

where D is the free electron diffusion coefficient, given by

$$D = v^2/3\nu_m \tag{2}$$

Here v is the electron speed ($v^2 = 3kT_e/m$) and ν_m is the electron momentum transfer collision frequency. These parameters can be calculated as a function of E/N by solving the Boltzmann equation for the electron distribution function. The characteristic length for electron diffusion loss is d/π for a circular tube of diameter d, and only slightly larger for a square tube with wall separation equal to d. The voltage is then E/N times pd, the product of the pressure (density) times the electrode gap spacing.

We carried out this calculation for the CO_2 gas mixture used in Synrad lasers and the result is shown as the lower right hand part of the curve in Fig. 4. The minimum occurs at the RF oscillation amplitude limit, which is the point where the characteristic loss distance equals the electron drift distance,

$$V_D/\omega_{RF} = d/\pi \tag{3}$$

where v_D is the electron drift velocity and ω_{RF} is 2π times the RF frequency. For the lower pressures or dimensions, the voltage must be higher in order to provide secondary electron emission at the cathode to make up for electron losses at the anode. As pressure is reduced further, the breakdown voltage curve increases to merge with the DC voltage curve.

The DC breakdown part of the curve was calculated by using the empirical curve fit expressions given by Cobine[5] for the minimum sparking potential, V_{sm}, and pd_{min}, the value of pd where it occurs.

$$V_{sm} = 2.718 \ (B/A) \ \ln \ (1/\gamma) \tag{4}$$
$$pd_{min} = (2.718/A) \ \ln \ (1/\gamma) \tag{5}$$

The parameters A, B, and γ were estimated for the CO_2 laser gas to have values of 8, 180, and 0.07, respectively.

Also shown in Fig. 4 are the voltage, pressure and gap spacing parameters for the Synrad laser tube electrodes relative to each other and relative to ground. The voltage of the electrodes relative to each other is twice that relative to ground because the inductance coupling between the two electrodes makes them 180 degrees out of phase. This breakdown curve shows how the use of small gap spacing and lower voltage between the individual RF electrodes and ground prevents breakdown there, while breakdown occurs readily between the two RF electrodes with their larger gap spacing and higher voltage.

RF Circuit

The RF self-oscillating circuit is shown in Fig. 5. A single power transistor amplifier with a gain of about 10 is used as the active element in the oscillator. The RF frequency is set by the resonance of the inductance and capacitance of the electrode structure inside the laser tube. With this approach the oscillator automatically adjusts for the small shift in frequency between the initial laser gas breakdown conditions and the steady plasma excitation conditions.

About 10 percent feedback from the laser tube to the input to the transistor is provided by a 50 ohm, 1/4

wavelength impedance matching cable. The output of the transistor is matched to the input impedance of the laser tube by a tunable impedance matching network. Approximate values for the circuit parameters are given in Fig. 5.

Heat Removal

The laser gas is surrounded by the aluminum electrodes and ground spacers, which conduct heat rapidly to the perimeter of the laser tube. The heat transfer is symmetrical, maintaining the dimensional integrity of the laser tube, which is necessary to retain the optical alignment of the mirrors on the ends of the laser tube. The power transferred out each electrode is about 0.8 watts per cm of length, producing a temperature drop of only about 2 degrees C (see Fig. 6). The heat is then transferred to the aluminum tube walls across the laser gas gap of 0.5mm, requiring a temperature drop of about 20 degrees C for the ° RF electrodes. The ground spacers have a smaller gap (0.2mm) and a correspondingly smaller temperature drop. The laser tube fits closely into the chassis with air gaps of about 0.1mm, which introduce an additional drop of about 4 degrees C. Thus the internal walls adjacent to the laser gas have a surface temperature of 10 to 25 degrees C above the chassis temperature. This value is roughly the same as the inside wall temperature of a cooled glass tube of the same diameter. Since the internal laser gas temperature at the center of the tube is 200 to 300 degrees C, this wall temperature rise has a relatively small effect on output power.

Optical Resonator

The laser cavity for both lasers uses a 3 meter radius of curvature silicon total reflector and a flat zinc selenide output coupler. The optical parameters for the cavity resonator of the laser tubes are listed in Table 2. These parameters were found to provide a good combination of high power extraction efficiency and good mode quality and stability. The internal losses in the cavity are quite low, allowing high reflectivity output couplers to be used. The resulting high cavity intensity saturates the laser gas very well, yielding high optical extraction efficiency. High cavity intensity also was found to help in the suppression of higher order transverse modes and parasitics due to spurious wall reflections.

The calculated Gaussian free space $1/e^2$ mode diameter at the two ends of each cavity is seen to be comparable with the bore size. The bore then serves to discriminate against higher order transverse modes. Since the Fresnel number of the 10 watt laser tube is somewhat larger than 1, additional discrimination against the TEM_{01} mode is provided by a small tilt of the optical axis in the vertical plane containing the two RF electrodes.

The optical cavity mode spacing of the zero order transverse modes is seen to be comparable with the pressure broadened width of the CO_2 spectral lines (Table 2). When the laser tube temperature changes, the mirror spacing changes and the cavity modes shift across the optical gain profiles of the lasing lines. The laser output then shifts in a regular pattern from one line to another as one of the cavity modes moves through the central high gain part of each line. During the transition from one line to another, two lines may operate simultaneously. The 10 watt laser with its larger mode spacing scans through 6 or 7 lines in the P branch of the 10.4um band, whereas the 25 watt laser scans through only 3 or 4 lines. The laser tube moves through this thermal cycle with a change in temperature of 0.5 degrees C for the 10 watt laser and 0.25 degrees C for the 25 watt laser. After a 10 to 20 minute warm up period the thermal drift is slow enough to maintain output on one spectral line for several minutes.

The output power also fluctuates somewhat due to thermal drift. The short term (10 minute) power stability of the 10 watt laser is typically +5 percent, whereas it has been seen to be less than +2 percent for the 25 watt laser.

<center>LASER PERFORMANCE</center>

Laser Power and Efficiency

Since the RF input power to the laser tubes can be turned on and off rapidly, it is convenient to vary the laser output power by varying the duty cycle of a high frequency control signal applied to the RF power source. Fig. 7 shows the dependence of output power and laser tube efficiency on duty cycle using 5 Khz modulation. There is a minimum input power required to achieve stable output, which limits the low end of the power curves to 0.5 to 2 watts. As the duty cycle increases, the laser tube efficiency rises sharply to a level of 15 to 20 percent. At 50 percent duty cycle the output power is about 70 percent of the CW output power. Maximum output occurs at about 90 percent duty cycle. This enhancement in efficiency and output power caused by modulation of the input power is thought to arise from the motion of the laser gas through the electrode gaps and within the discharge region, increasing the cooling rate and reducing the average temperature of the gas.

Modulation Characteristics

The laser output response to modulated input power is shown in Fig. 8 for a 10 watt tube. Under normal operating conditions the CO_2 in the laser gas is about 50 percent dissociated. The time constant for the rise and fall of the laser output is then about 100 μsec. For 2 Khz modulation at 50% duty cycle the laser output falls to zero on each cycle, producing 100% modulation of the output power. At 5 Khz the laser power is only 70% modulated.

By adding a small amount of water vapor to the gas, the steady state dissociation of CO_2 is reduced, shortening the time constant to about 40 μsec and producing 100% modulation at 5 Khz. However, the added

<center>318</center>

water vapor also reduces laser efficiency.

The laser tube also can be superpulsed by increasing the RF input power. For example, a factor of 2.5 increase in input and output power using 1 Khz modulation at 25 percent duty cycle is shown in Fig. 8.

Laser Gas Fill Operating Lifetime

The lifetime of sealed off laser tubes is limited by various factors such as the buildup of impurities in the gas, depletion of the CO_2 content during operation, and optical mirror degradation or damage. The Synrad lasers are vacuum baked at high temperature which effectively removes the internal sources of gas contamination. However, water vapor from the atmosphere diffuses slowly inward through the o-ring seals at the RF feedthrough and the optical mirrors. To achieve long life the water vapor is adsorbed by zeolite pellets placed inside the tube. The resulting shelf life of the laser tube is measured in years, and testing is still underway to obtain quantitative results.

The integrity of the optical mirrors has been maintained satisfactorily on all lasers placed in service as far as we know. This is due in part to the high quality optical components supplied to us and in part to the moderate optical intensity in the laser cavity.

The principal limitation in operating lifetime observed for these lasers as well as earlier CO_2 waveguide lasers is a gradual reduction in the amount of CO_2 present in the gas. The discharge dissociates CO_2 to form CO and O_2 as well as small amounts of O and O_3. The oxidizing nature of these gas constituents leads to a gradual loss of oxygen to various metal surfaces in the laser. This effect is seen in Fig. 9 where the output power of 2 lasers is traced over a period of steady operation for 1000 hours. At the end of this period the addition of a small amount of O_2 restores the laser to its original output power and its original modulation waveform.

The oxygen depletion time constant can be increased considerably by processing the laser tube with a high oxygen content discharge for a longer period of time. The lifetime also can be increased by further study to determine which materials in the laser tube become oxidized and changing to more inert materials. Using some of these methods we have one laser on test that has reached 1800 hours lifetime with only 15% drop in power. It appears likely that low cost, sealed-off CO_2 lasers with 5,000 to 10,000 hour operating lifetime soon will be available commercially.

References

1. Katherine D. Laakmann, "Waveguide Gas Laser with High Frequency Transverse Discharge Excitation," U.S. Patent Number 4,169,251.
2. Peter Laakmann, "An RF Excited All Metal Gas Laser," U.S. patent granted, 1988.
3. Peter Laakmann "Electrically Self-Oscillating RF Excited Gas Laser," U.S. patent granted, 1988.
4. A.D. MacDonald, Microwave Breakdown in Gases, John Wiley & Sons, Inc., New York (1966).
5. J.D. Cobine, Gaseous Conductors, Dover Publications, New York (1958).

Table 1 CO_2 LASER OPERATING PARAMETERS

OUTPUT POWER	10W	25W
Power Source	28 VDC or 110 VAC	
Input Power	300 W (AC)	600 W (AC)
Overall Efficiency	3 to 6%	4 to 8%
RF Drive Voltage	less than 150 V	
RF Frequency	45 MHz	
Modulation Range	up to 5 kHz	
Gas Mixture	6 Xe, 8 CO_2, 8N_2, 36 He	
Gas Pressure	58 torr	
Gas Fill Operating Life	1000 hrs	
Wavelength	10.55 to 10.67 μm	10.57 to 10.63 μm
Mode	TEM_{oo}	
Polarization	Linear	

Table 2   OPTICAL RESONATOR PARAMETERS

LASER POWER	10 WATTS	25 WATTS
Bore Size, mm	4.8 square	4.8 square
Discharge Length, cm	37	74
Mirror Spacing, cm	40	78
Output Coupler Refl.,%	95	92
Fresnel Number	1.4	0.7
TEM_{oo} Mode Dia., mm	4.2 and 3.7	4.9 and 4.2
Cavity Intensity, I/I_{sat}	6	10
Mode Spacing, MHz	375	190
Line Width, MHz	260	260
Spectral Lines	P(16) to P(28)	P(18) to P(24)
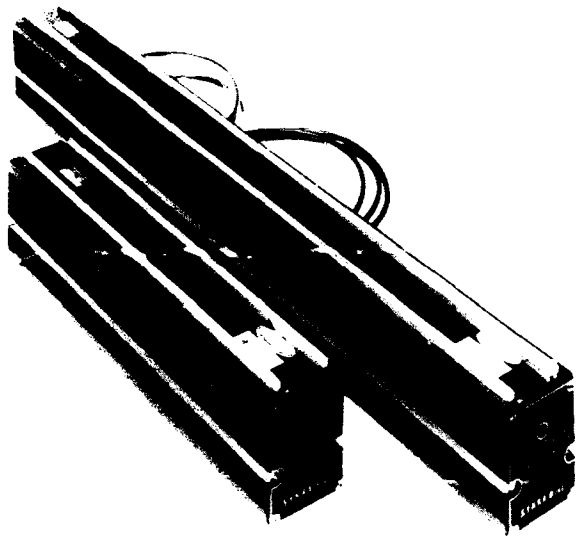
Figure 1. Photograph of 10 Watt and 25 Watt CO_2 Lasers.
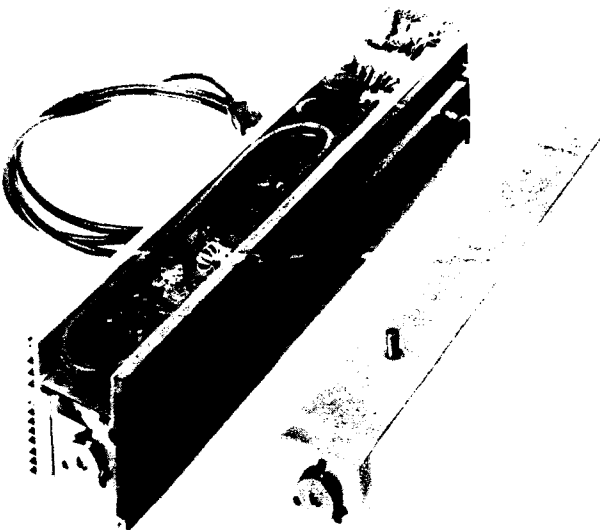
Figure 2. Photograph of 10 Watt CO_2 Laser with Cover Plates Removed. Also Shown is a Laser Tube Removed from its Chassis.
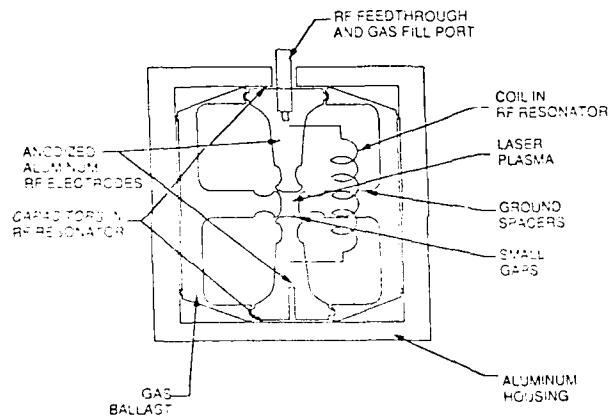
Figure 3. Cross-Section of the Internal Structure of the All Metal CO_2 Laser Tubes.

GAS: 37 He, 8 N_2, 8 CO_2, 5 Xe

pd, torr-cm
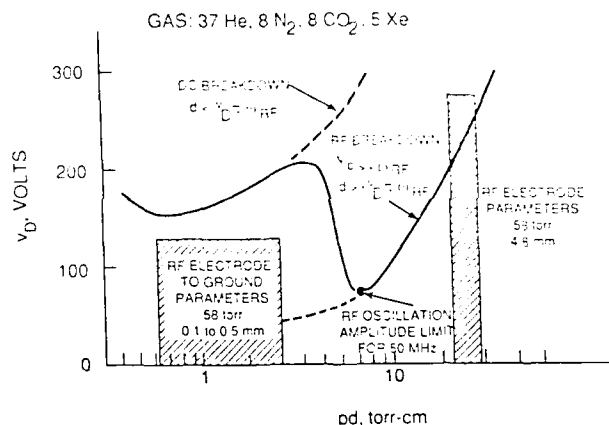
Figure 4. RF Electrical Breakdown Curve for the Operating Conditions of the CO_2 Laser Tube.
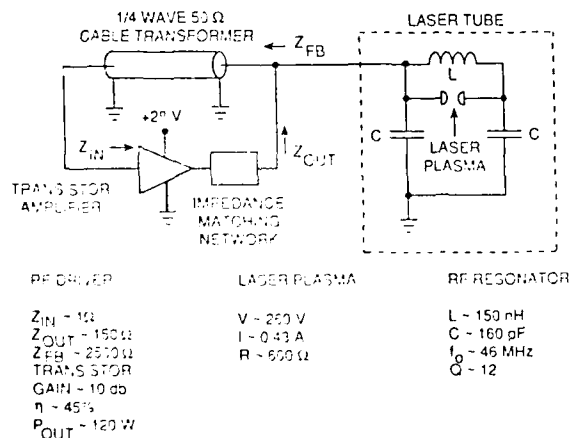
Figure 5. RF Self-Oscillating Electrical Circuit used to Excite the CO_2 Laser Tubes.
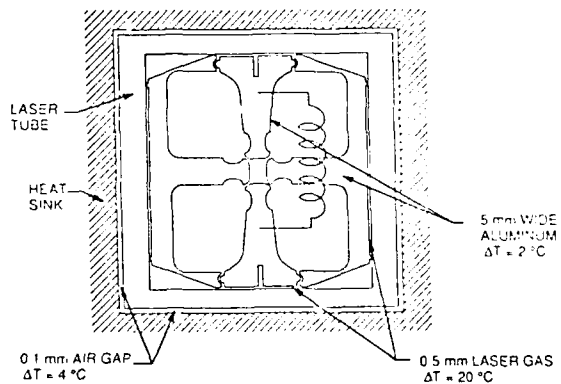
Figure 6. Heat Removal Paths and Temperature Drops in the CO_2 Laser Tubes.

320
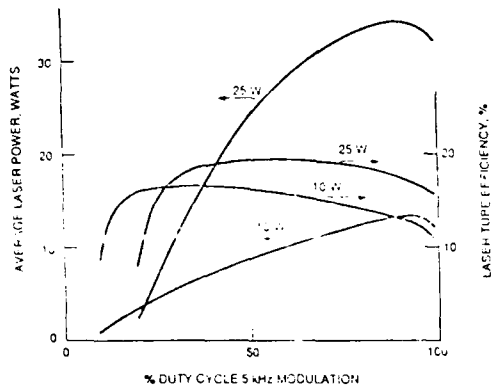
Figure 7. Laser Output Power and Laser Tube Efficiency as a Function of Duty Cycle Modulation at 5kHz.
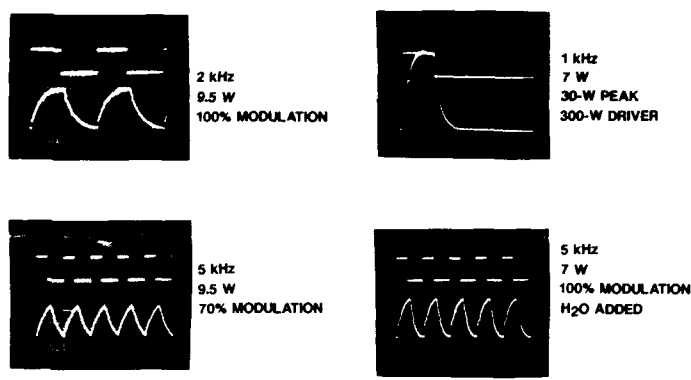
Figure 8. Modulation Characteristics of the 10 Watt CO_2 Laser. Sweep Speed is 100 usec/cm.
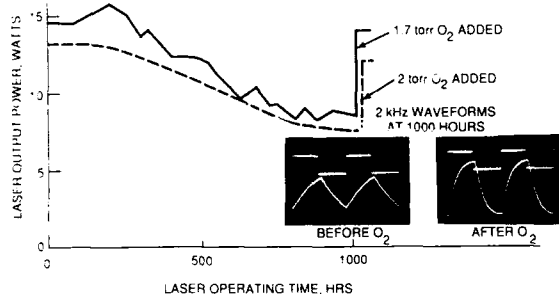
Figure 9. Laser Gas Fill Operating Lifetime. Also Shown is the Change in Modulation Waveform Caused by Adding Oxygen after 1000 Hours of Operation.

Noise Levels in a Tunable CO_2 Laser Source

A. L. Kachelmyer and R. S. Eng
Massachusetts Institute of Technology
Lincoln Laboratory
244 Wood Street
Lexington, Massachusetts 02173

ABSTRACT

This paper considers the measurement of amplitude modulation (AM) and phase modulation (PM) noise in a tunable CO_2 laser source. Theoretical and experimental heterodyned output spectrums compare the tunable source to a 'clean' reference laser.

1. Introduction

A broadband tunable CO_2 local oscillator (LO) laser has application for target velocity tracking with a heterodyne detection system such as a wideband imaging laser radar. By frequency shifting the LO in proportion to the target induced Doppler shift, the heterodyned detector passband of interest can be kept relatively narrow. The tunable LO is created by the modulation of a stable CO_2 laser with a tunable RF source. However, because the modulation process usually requires a high power RF drive signal, the noise quality of the tunable LO may be substantially worst than that of the stable CO_2 laser.

For a wideband imaging laser radar system, the detector passband can be kept at a minimum, approximately equal to the desired imaging signal bandwidth, provided that the tunable LO tracks out the target Doppler shift. For satellite and ballistic missile targets the Doppler shift can be as large as ± 1.3 GHz for a $10.6\,\mu m$ wavelength. The spectral purity of such a Doppler tracking tunable LO must necessarily be such that the degradation of the heterodyned signal spectrum is minimal.

An analytical model is presented which relates AM and PM noise in the local oscillator signal to a resultant heterodyne signal plus noise model. Heterodyned detected output power spectrums are described both analytically and pictorially. Theoretical output power spectrums are shown for both the AM and PM noise cases assuming a monochromatic laser input signal. The direct detected output power spectrum of the tunable LO is also described analytically.

Measured output power spectrums are presented for the heterodyne detection of a very stable rare isotope CO_2 reference laser (return signal) with a tunable CO_2 local oscillator source. The tunable LO source is created by modulating a regular isotope CO_2 laser with an acousto-optic (AO) modulator which is driven by a tunable RF source. Effective AM and PM noise power levels are determined from the measurement data using a direct spectral comparison technique.

The experimental results confirmed the general functional dependence predicted for AM and FM noises. An unexpected AM suppression by the acousto-optic modulator will be shown. In comparison with a 'clean' fixed frequency CO_2 laser, the acousto-optic modulated CO_2 laser showed a slightly higher noise level.

2.   SIGNAL AND NOISE MODELS

Let the input signal field and the ideal reference local oscillator field complex envelopes be described in the plane of the circular receiver aperture of diameter d as

$$e_s(\rho, t) = \sqrt{\frac{4P_s}{\pi d^2}} s(t) e^{jkz} \quad \text{for } |\rho| \leq d/2, \tag{1}$$

and

$$e_{LO}(\rho, t) = \sqrt{\frac{4P_{LO}}{\pi d^2}} n(t) e^{j\omega_{IF}t} e^{jkz} \quad \text{for } |\rho| \leq d/2, \tag{2}$$

where $s(t)$ and $n(t)$ are the signal (including background noise) and local oscillator noise complex envelopes, respectively. The position in the receiver aperture plane is given by the vector $\rho = x\, i_x + y\, i_y$ where i_x and i_y are the x and y unit coordinate vectors. Of course, P_{LO} and P_s are the local oscillator and return signal powers, respectively. The radian difference frequency between the return and the local oscillator signals is represented by ω_{IF}.

The receiver input signal complex envelope is composed of the desired return signal and a background noise signal as follows:

$$s(t) = \sqrt{P_r} r(t) + \sqrt{P_b} b(t), \tag{3}$$

where $r(t)$ and $b(t)$ are the normalized (unity) complex envelopes of the return and the background noise signals, respectively. The signal power is

$$P_s = P_r + P_b \tag{4}$$

where P_r and P_b are the return signal and background noise powers, respectively.

Let us define the local oscillator complex noise envelopes for the cases of PM or FM noise modulation as

$$n(t) = e^{j\Phi(t)}, \tag{5}$$

and for AM noise modulation as

$$n(t) = 1 + a(t), \tag{6}$$

where $\Phi(t)$ represents the complex phase noise process and where $a(t)$ represents the complex amplitude noise process.

3.   POWER SPECTRUMS

3.1.   HETERODYNE DETECTION

The count intensity function for the total field incident upon the detector is

$$\begin{aligned}
N(t) &= \alpha \int_{A_r} |e_s(\rho, t) + e_{LO}(\rho, t)|^2 d\rho \\
&= \alpha [P_{LO}|n(t)|^2 + P_s|s(t)|^2 + 2\sqrt{P_{LO}P_s}\,\text{Re}\{s(t)n^*(t)e^{-j\omega_{IF}t}\}] \,.
\end{aligned} \tag{7}$$

323

The constant α is defined as

$$\alpha = \frac{\eta}{h\nu} ,$$

where ν is the optical carrier frequency of the return signal, η is the detector quantum efficiency, and h is Planck's constant.

Let the photomixer output current be represented by the Poisson shot noise (PSN) process $x(t)$. From [1], the detected shot noise process has the time averaged power spectral density

$$S_x(\omega) = |H(\omega)|^2[E_t\{N(t)\} + S_N(\omega)] \tag{8}$$

where $H(\omega)$ is the transform of the electron current impulse response function, $S_N(\omega)$ is the power spectrum of the count intensity function, and $E_t\{N(t)\}$ is the time averaged expected value of the count intensity. At $\omega = 0$, the transfer function is

$$H(0) = q ,$$

where q is the electron charge.

The power spectral density of the count intensity function is the Fourier transform of its autocorrelation function, i.e.,

$$S_N(\omega) = \mathbf{F}\{R_N(\tau)\} , \tag{9}$$

where

$$R_N(\tau) = E_t\{N(t)N(t+\tau)\} , \tag{10}$$

is the time averaged autocorrelation function. In the strong local oscillator condition, the count intensity simplifies to

$$N(t) \cong \alpha[P_{LO}|n(t)|^2 + 2\sqrt{P_{LO}P_s}Re\{s(t)n^*(t)e^{-j\omega_{IF}t}\}] . \tag{11}$$

Using this simplification, the time averaged autocorrelation function becomes

$$R_N(\tau) = \alpha^2 P_{LO}\{P_{LO}R_{|n|^2}(\tau) + P_s R_s(\tau)R_n^*(\tau)e^{-j\omega_{IF}\tau} + P_s R_s^*(\tau)R_n(\tau)e^{j\omega_{IF}\tau}\} , \tag{12}$$

where

$$R_{|n|^2}(\tau) = E\{|n(t)|^2|n(t+\tau)|^2\} ,$$
$$R_s(\tau) = E\{s(t)s^*(t+\tau)\} , \tag{13}$$
$$R_n(\tau) = E\{n(t)n^*(t+\tau)\} .$$

Note that the time averaging assumption removes an autocorrelation term of the form

$$Re\{R_{ss}(\tau)R_{n^*n^*}(\tau)e^{j\omega_{IF}(2t+\tau)}\}$$

where

$$R_{xy}(\tau) = E\{x(t)y(t+\tau).\}$$

Assuming that the background noise is a zero mean stochastic process that is statistically independent of the return signal process, the signal autocorrelation function is

$$R_s(\tau) = P_r R_r(\tau) + P_b R_b(\tau). \tag{14}$$

Using (8), the power spectral density of the shot noise process $x(t)$ becomes

$$
\begin{aligned}
S_x(\omega) \quad &= |H(\omega)|^2 \, [\, E_t\{N(t)\} \;+\; \alpha^2 P_{LO}^2 \, S_{|n|^2}(\omega) \\
&+ \alpha^2 P_{LO} P_s \, S_s(\omega) \otimes S_n(-\omega - \omega_{IF}) \;+\; \alpha^2 P_{LO} P_s \, S_s(-\omega) \otimes S_n(\omega \quad \omega_{IF})\,] ,
\end{aligned}
\tag{15}
$$

where from (14)

$$S_s(\omega) = P_r S_r(\omega) + P_b S_b(\omega). \tag{16}$$

Note that $\otimes$ denotes the convolution operator.

To be completely explicit, using (16) the power spectral density becomes

$$
\begin{aligned}
S_x(\omega) \quad &= |H(\omega)|^2 \, [\, \alpha P_{LO} E_t\{|n(t)|^2\} \;+\; \alpha^2 P_{LO}^2 \, S_{|n|^2}(\omega) \\
&+ \alpha^2 P_{LO} P_r \, S_r(\omega) \otimes S_n(-\omega - \omega_{IF}) \;+\; \alpha^2 P_{LO} P_b \, S_b(\omega) \otimes S_n(-\omega - \omega_{IF}) \\
&+ \alpha^2 P_{LO} P_r \, S_r(-\omega) \otimes S_n(\omega - \omega_{IF}) \;+\; \alpha^2 P_{LO} P_b \, S_b(-\omega) \otimes S_n(\omega - \omega_{IF})\,] .
\end{aligned}
\tag{17}
$$

Hence, the IF passband signal spectrum of interest is convolved with the corrupting LO noise spectrum $S_n(\omega)$. Notice that any background light (noise) in the passband is also convolved with the LO noise spectrum. The LO noise intensity spectrum $S_{|n|^2}(\omega)$ is also present and will not disturb the IF passband unless the intensity noise is very broadband. Finally, the normal shot noise level is increased by the factor $E|n(t)|^2$ in the presence of AM noise.

A sketch of the power spectrum of the detector output current $x(t)$ is shown in Figure 1. Arbitrary spectral shapes were assumed for illustration purposes. Also, note that the resultant power spectrum is the sum of the individual spectra shown in the figure.

3.2. DIRECT DETECTION

The local oscillator quality can be measured directly with a direct detection measurement scheme. If the direct detection signal incident upon the detector consists of just the local oscillator signal (the background light noise is assumed to be negligible), then the power spectral density of the detected shot noise process is

$$S_x(\omega) = |H(\omega)|^2 \, [\, \alpha P_{LO} E_t\{|n(t)|^2\} \;+\; \alpha^2 P_{LO}^2 \, S_{|n|^2}(\omega)\,] \tag{18}$$

Notice that the direct detected local oscillator power spectrum need only be measured over the frequency band of interest, i.e., about the IF carrier frequency ω_{IF}. Notice that there is no degradation of the power spectrum in the case of PM noise modulation.

INTENSITY SPECTRUM OF LO SIGNAL ENVELOPE
$\alpha P_{LO}^2 S_{n^2}(\omega)$

CONVOLUTION OF SIGNAL AND LO NOISE POWER SPECTRUMS
$\alpha^2 P_{LO} P_r S_r(-\omega) \otimes S_n(\omega - \omega_{IF})$

POWER SPECTRAL DENSITY
$S_x(\omega)$

DETECTOR TRANSFER FUNCTION
$H(\omega)^2$

CONVOLUTION OF BACKGROUND THERMAL NOISE AND LO NOISE POWER SPECTRUMS
$\alpha^2 P_{LO} P_b S_b(-\omega) \otimes S_n(\omega - \omega_{IF})$

LO SHOT NOISE
$\alpha P_{LO} E_t\{|n(t)|^2\}$

RADIAN FREQUENCY (ω)
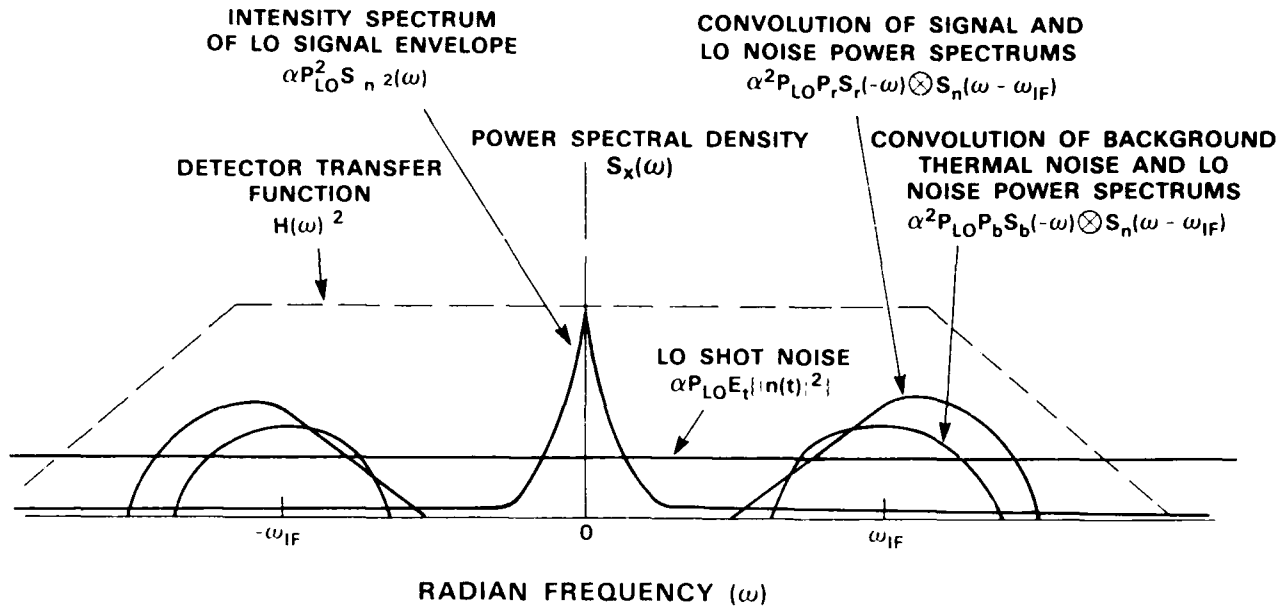
Figure 1: Heterodyned detector output power spectrum for a noise modulated local oscillator signal.

4. NOISE POWER SPECTRUMS

4.1. Systematic Noise Modulation

Consider first the case where the noise is modeled to be deterministic as in the case of systematic errors. Frequency modulation (FM) can be thought of as a special case of phase modulation (PM) when the phase function is of the form

$$\Phi(t) = \theta_0 \sin 2\pi f_m t . \tag{19}$$

θ_0 is the peak phase excursion and f_m is the modulating frequency. In the FM context, θ_0 can be thought of as the modulation index with

$$\theta_0 = \Delta f / f_m ,$$

where Δf is the maximum frequency excursion. In any case, when θ_0 is small the FM or PM complex envelope from (5) becomes

$$n(t) \cong 1 + j\theta_0 \sin 2\pi f_m t . \tag{20}$$

Similarly, for simple sinusoidal AM modulation, we have from (6)

$$\begin{aligned} n(t) &= 1 + a(t) \\ &= 1 + a_0 \sin \omega_m t , \end{aligned} \tag{21}$$

where a_0 is the modulation depth and $\omega_m = 2\pi f_m$ is the radian modulation frequency.

The power spectrum of $n(t)$ (for all three forms of modulation) becomes

$$S_n(\omega) = \delta(\omega) + \frac{\theta_0^2}{4}\{\delta(\omega - \omega_m) + \delta(\omega + \omega_m)\}.\tag{22}$$

Note that this is just the familiar double sideband spectrum which occurs for simple sinusoidal PM or FM with $\theta_0 = \Delta f / f_m$ or AM with $\theta_0 = a_0$. Note that the restriction that θ_0 be small for the approximations to be valid for PM or FM does not apply to AM. That is, the value of the modulation depth a_0 may be as large as one. The resulting sideband power can therefore be quite large for systematic AM noise. Although large FM and PM phase excursions may occur, it will be generally assumed that they are small, say, $\theta_0 < 0.1$.

The time averaged mean count intensity for simple sinusoidal AM, PM, and FM is

$$E_t\{|n(t)|^2\} = 1.\tag{23}$$

The intensity spectrum of $n(t)$ is

$$S_{|n|^2}(\omega) = \begin{cases} \delta(\omega) & \text{for FM, PM} \\[2mm] (1 + a_0^2/2)^2\delta(\omega) + a_0^2\delta(\omega - \omega_m) + a_0^2\delta(\omega + \omega_m) & \\[1mm] + \frac{a_0^4}{16}\delta(\omega - 2\omega_m)) + \frac{a_0^4}{16}\delta(\omega + 2\omega_m) & \text{for AM} \end{cases}\tag{24}$$

The heterodyned detector output spectrum for sinusoidal AM, PM and FM modulation is depicted in Figure 2. The return signal is assumed to be a simple sinusoid with normalized real envelope $r(t) = 1$ and the background light noise is assumed to be white with normalized power spectral density $S_b(\omega) = 1$.
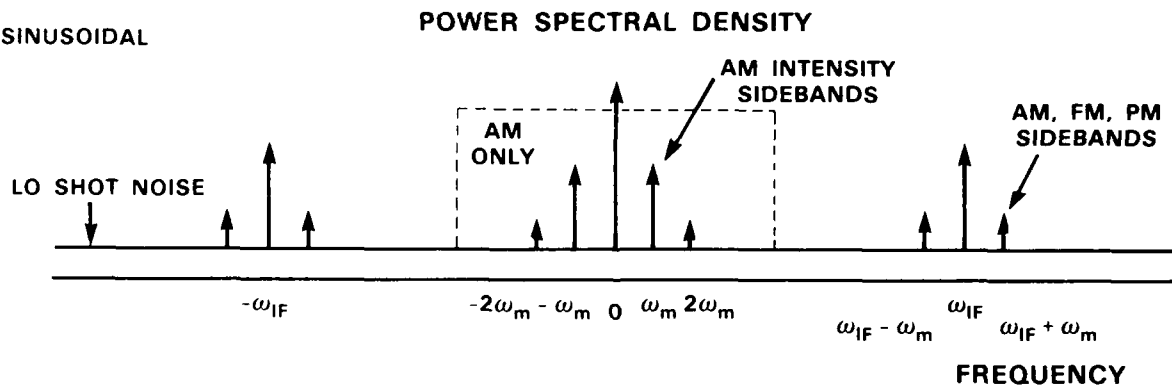
Figure 2: Heterodyned detector output power spectrum for small phase deviation sinusoidal PM or FM and for sinusoidal AM.

4.2. Random Noise Modulation

Let us assume that the phase of the PM or FM noise process is uniformly distributed. That is,

$$p_\Phi(\theta) = \begin{cases} 1/2\theta_0 & \text{for } -\theta_0 \le \theta \le \theta_0 \\[1mm] 0 & \text{otherwise} \end{cases}\tag{25}$$

Note that $\theta_0 = \Delta f / f_m$ for the FM noise process.

If we assume that the phase functions $\Phi(t)$ and $\Phi(t + \tau)$ are independent (uncorrelated) and identically distributed random variables except for $\tau = 0$, we get

$$
\begin{aligned}
R_n(\tau) &= E\{n(t)n^*(t + \tau)\} \\
&= (\tfrac{\sin\theta_0}{\theta_0})^2 + (1 - (\tfrac{\sin\theta_0}{\theta_0})^2)\delta(\tau) \\
&\cong 1 + \tfrac{\theta_0^2}{3}\delta(\tau) \quad \text{for } \theta_0 \text{ small.}
\end{aligned}
\tag{26}
$$

Again, if θ_0 is small, then the spectral densities which characterize the output shot noise spectrum in the PM or FM case are as follows:

$$
\begin{aligned}
S_n(\omega) &= \delta(\omega) + \theta_0^2/3 , \\
S_{|n|^2}(\omega) &= \delta(\omega) , \\
E_t\{|n(t)|^2\} &= 1 .
\end{aligned}
\tag{27}
$$

The form of the heterodyned detector output power spectral density is shown in Figure 3, where the return signal is assumed to be a simple tone, and the background noise is assumed to be negligible or else white.
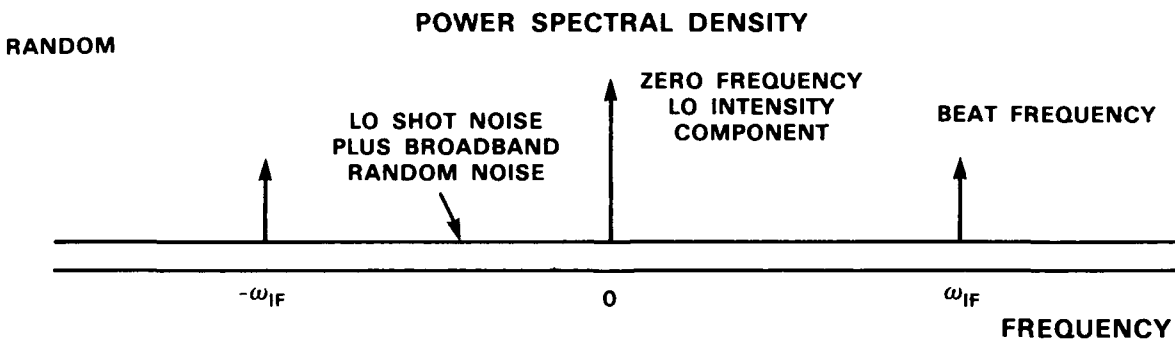
Figure 3: Heterodyned detector output power spectrum with random PM or or AM of the LO. The reference or received signal is assumed to be a monochromatic laser or tone signal at radian frequency ω_{IF} from the optical carrier frequency.

Let us assume that the complex AM noise envelope $a(t)$ is a complex circular Gaussian noise process. Let the real and imaginary parts of $a(t)$ be independent zero mean Gaussian processes with $E\{(Re\,a)^2\} = E\{(Im\,a)^2\} = \sigma_a^2/2$.

The corresponding power spectral densities for the complex process $n(t) = 1 + a(t)$ are as follows:

$$
S_n(\omega) = \delta(\omega) + \sigma_a^2 ,
\tag{28}
$$

328

$$S_{|n|^2}(\omega) = (1 + \sigma_a^2)^2 \delta(\omega) + 2\sigma_a^2, \tag{29}$$

$$E_t\{|n(t)|^2\} = 1 + \sigma_a^2. \tag{30}$$

The form of the heterodyned detector output power spectral density for complex Gaussian AM noise is shown in Figure 3, where again the return signal is assumed to be a simple tone and the background noise is assumed to be negligible or else white. Notice that the only significant difference between the random PM and AM cases is that the AM noise level is slightly higher because the AM noise is not a constant envelope process.

5. EXPERIMENTAL SETUP
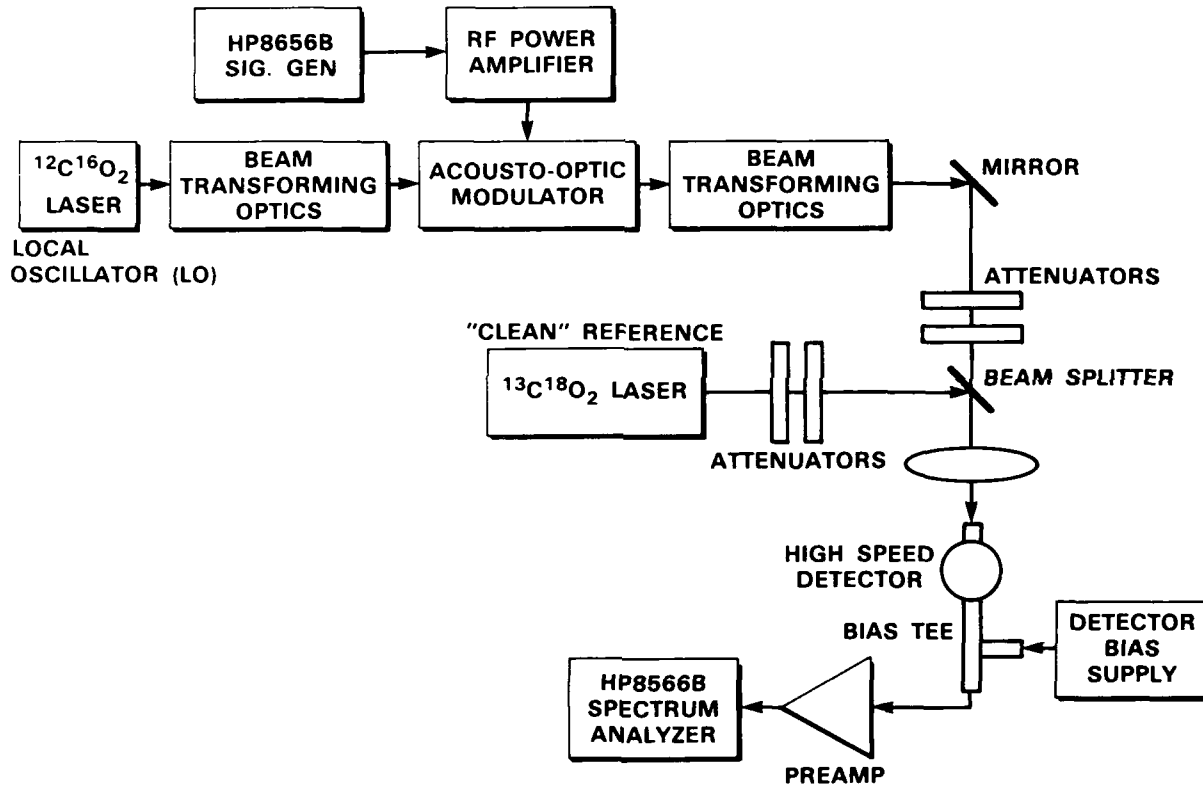
Figure 4: Experimental noise measurement setup.

Figure 4 shows a schematic diagram of the experimental setup. The I-P(12) output beam of a 1.5 m long grating-tuned $^{12}C^{16}O_2$ laser is transformed to a 3 mm $1/e^2$ beam spot on the acousto-optic (AO) modulator. The AO modulator is driven by an RF MOPA chain consisting of a 40 MHz CW sinusoidal signal from a frequency synthesizer (Hewlett Packard model HP8656B), and an RF amplifier (ENI Inc. model 325LA), which has a noise figure of about 10 dB and an output power of about 25 W when driven by a -6 dBmW sinusoidal input signal. The $+1$ order diffracted output beam from the AO modulator is transformed (by a 2 m radius of curvature mirror) to a $1/e^2$ beam waist diameter of 4.5 mm, which is the same as that at the zero-order grating output of the 1.5 m $^{13}C^{18}O_2$ laser. This frequency shifted beam is

next combined with the I-R(38) output beam of the $^{13}C^{18}O_2$ laser at the beam splitter. A final lens is used to focus the combined beam on the detector for heterodyned detection. The $^{13}C^{18}O_2$ laser beam waist, with a waist diameter of 4.5 mm, is positioned purposely the same distance from the beam splitter as that of the transformed 4.5 mm beam waist of the frequency shifted beam for optimum heterodyne efficiency.

The detector is a high speed HgCdTe detector, SAT Inc. model Class 5c, ser. no. 648 P, optimally biased for high effective quantum efficiency operation. The preamplifier block of Figure 4 consists of a first stage preamplifier, which has a small signal gain of about 30 dB and a noise figure of about 1.5 dB, and a second stage preamplifier, which has a small signal gain of about 30 dB and a noise figure of about 4 dB. The preamplifier stages are used to improve the sensitivity of the spectrum analyzer, Hewlett Packard model HP8566B. A 20 dB microwave attenuator is used between the preamplifiers to prevent saturation of the second amplifier, which is rated at +9 dBm at the 1 dB compression point.

The lasers are the Freed type [4] and are known to have high spectral purity with low phase and amplitude noises.

6. MEASUREMENT RESULTS

6.1. HETERODYNE SPECTRUM WITH AND WITHOUT AO MODULATION

In this first experiment, we measured the heterodyne signal between the $^{13}C^{18}O_2$ I-R(38) (rare isotope) laser line and the $^{12}C^{16}O_2$ I-P(12) (regular isotope) laser line passing through but unmodulated by the AO modulator. The frequency difference between these laser transitions is about 665 MHz. The input power from the regular isotope laser to the detector was sufficiently high with the shot noise level above the thermal noise level. The regular isotope laser then acts as the local oscillator. The beat signal near 665 MHz is shown as the top trace in Figure 5. The other traces in Figure 5 are the shot noise due mainly to the $^{12}C^{16}O_2$ I-P(12) laser line which serves as the laser local oscillator, the thermal noise at the input to the first amplifier amplified by the preamplifiers, and the noise level at the spectrum analyzer input with the preamplifiers off.

For comparison, when the +1 order output of the AO modulator (obtained with a 40 MHz RF drive signal) was heterodyned with the isotope laser line, we obtained the heterodyne signal shown in Figure 6. The frequency difference between these laser beams is about 625 MHz. The combined noise spectrum of the frequency synthesizer and the RF power amplifier, are impressed through the AO modulator onto to the regular isotope laser output. The result is that the heterodyne signal can be expected to contain a higher noise level in comparison with that in the 'clean' or unmodulated LO measurement shown in Figure 5. A detailed examination of Figure 6 reveals that this is indeed the case. Thus, we conclude that the noise in the +1 order output is higher than in the unmodulated output of the $^{12}C^{16}O_2$ I-P(12) laser line. In obtaining the above measurement results, great care was taken to prevent any signal saturation and spurious noise pickup in any part of the detection electronics.

For reference purposes, the 40 MHz RF drive spectrum at the input to the AO modulator and the heterodyned signal spectrum from 575 MHz to 675 MHz are shown in Figures 7 and 8. We want to point out in particular that the zero order signal from the AO modulator is as low as -72 dB below the first order signal, a number far lower than -40 dB generally reported. It may be due to the special construction of the AO modulator, IntraAction model AGM406B, which is made for high conversion efficiency at a moderate RF drive power.

6.2. SINUSOIDAL FM AND AM MODULATION OF THE RF DRIVE SIGNAL

In the this second experiment, the 40 MHz signal from the frequency synthesizer was frequency modulated using an external 350 kHz sinusoidal source. The modulation index was about 0.005. The drive spectrum at the input to the AO modulator, after proper attenuation, is shown in Figure 9, showing that the first sidebands are about 52 dB below the carrier. When this local oscillator signal containing FM
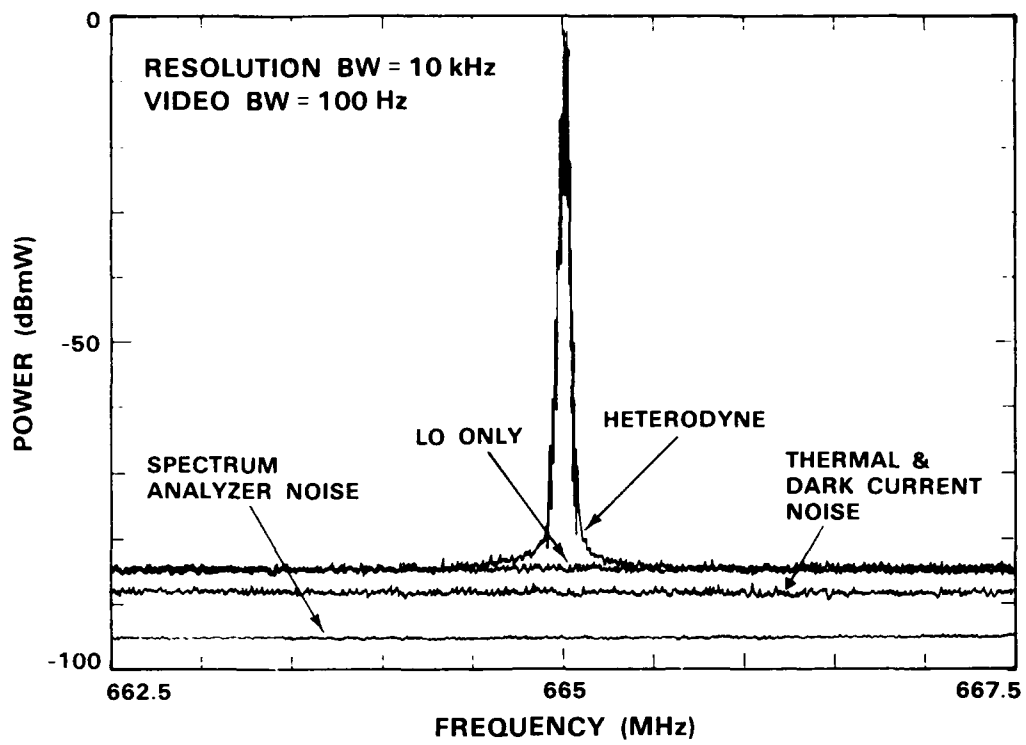
Figure 5: Heterodyne spectrum with an unmodulated LO laser.
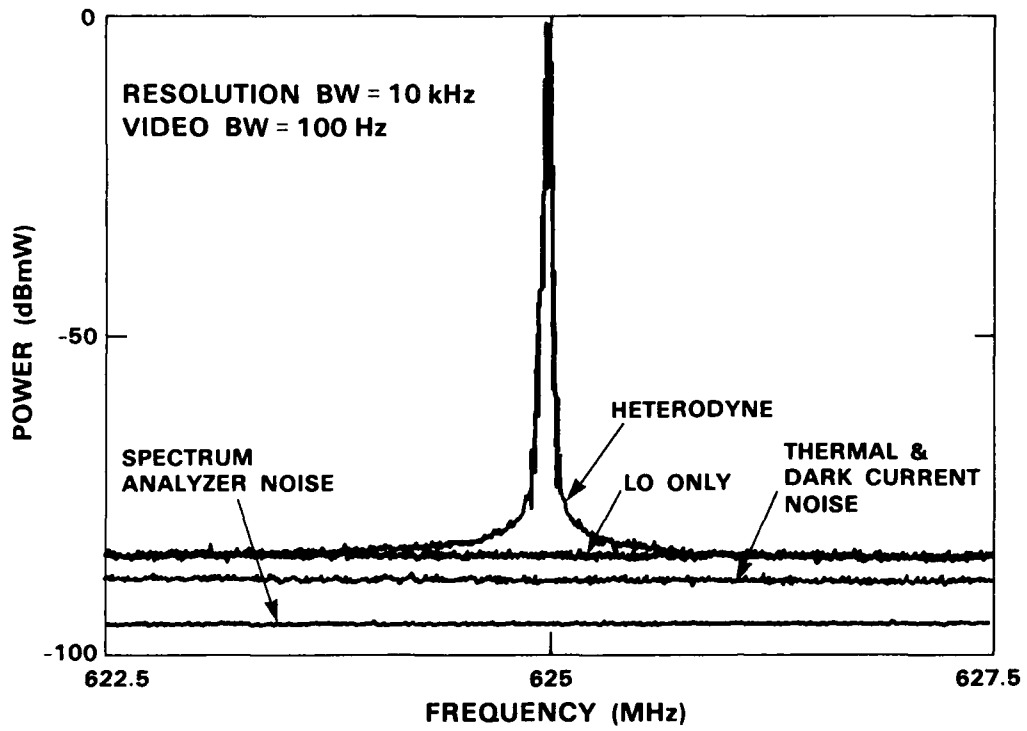
Figure 6: Spectrum of the reference laser heterodyned with an LO laser which is AO modulated by a 40 MHz sinusoidal RF drive signal.

331

sidebands was heterodyned with the laser beam from the rare isotope laser, we obtained the heterodyned signal shown in Figure 10, after amplification by the two preamplifiers. The rare isotope laser power was about 1/10 that of the laser local oscillator power. We note that the first sidebands are 52 dB below the carrier level, just as the sidebands of the 40 MHz RF drive signal. In addition, as the rare isotope laser signal was attenuated, the relative carrier-to-sideband ratio stays constant. This linearity in power is expressed by (17), which shows that both the carrier and the sidebands are proportional to the return signal or rare isotope laser power P_r.

On the other hand, when we applied an external amplitude modulation to the local oscillator signal, unexpected results were obtained in that the heterodyne sideband amplitudes were lower than those in the RF drive. Results are shown in Figures 11 and 12 for two levels of AM modulations, 0.2 % and 1.0 %, respectively. The corresponding 40 MHz AM modulated RF drive spectrum was measured and superimposed upon the measured heterodyne spectrum in each figure for comparison. For 0.2 % AM modulation, the amplitudes of the sidebands relative to the carrier in the 40 MHz RF drive signal are seen to be about 15 dB higher than those in the heterodyned case (see Figure 11). For 1.0 % AM modulation, we see that there are a number of sidebands; the amplitudes of the sidebands relative to the carrier in the 40 MHz RF drive signal vary from about 15 dB higher to about 5 dB higher than those in the heterodyned case (see Figure 12) as the order of the sideband increases. Repeated measurements produced essentially the same results.

The authors have no explanation for these unexpected results for AM modulation. Between the AM and FM measurements, there was no change in measurement setup other than the change in the frequency synthesizer modulation input. A likely explanation for the AM amplitude suppression could be in the nature of the acousto-optic modulation mechanism. For example, the moving acoustic grating generated on the AO interacting medium has a uniform grating spacing in the case of amplitude modulation and a non-uniform spacing in the case of frequency modulation. Perhaps a detailed analysis along this line can reveal the real reason for the difference in the sideband suppressions.

6.3. WIDEBAND NOISE CORRUPTION OF THE RF DRIVE SIGNAL

A third set of measurements was performed for an experiment wherein a high level broadband thermal noise was added to the frequency synthesizer output before amplification by the RF power amplifier. The broadband thermal noise was generated by amplifying noise, from the 50 ohm terminated input of the first preamplifier, through two stages of preamplifiers totaling about 60 dB of small signal gain . The combined signal and broadband thermal noise RF drive spectrum output from the power amplifier is shown in Figure 13, along with the original RF drive power spectrum. As can be seen, the amplified noise level is about 30 dB above that of the original noise level.

The noise level is purposely raised because the spectrum analyzer sensitivity is not high enough to detect the phase noise presence in the sinusoidal signal output of the frequency synthesizer. With the added thermal noise, we had no trouble in observing the noise levels as shown in Figures 14 and 15 for the wideband and narrowband heterodyned spectra around the 625 MHz sinusoidal beat frequency, respectively. In Figure 14, the bandwidth of the broadband noise is narrowed to about 8 MHz after heterodyned detection. This narrowing of the amplified broadband noise spectrum occurs because the higher difference frequencies are spatially filtered (attenuated) due to their misalignment with the optical train (the direction of the diffracted beam is a function of frequency) and because the AO modulator's conversion efficiency drops off at the higher frequencies (above 40 MHz).

Taking into account the difference in the resolution and video bandwidths between Figure 15 and Figure 13, the heterodyned carrier to noise power level is about 2 dB higher than that of the noisy RF drive signal. This noise level reduction seems to confirm that the thermal noise contains both AM and FM components, as expected.

Far away from the carrier, the noise level in Figure 14 drops down to the normal shot noise level because the broadband noise in the local oscillator is spatially filtered out due to the AO modulator diffraction and to wavefront mismatching.

Figure 15 shows a close-up view of the noise spectrum near the carrier. Spectrum analyzer traces are shown for the cases where the received signal or rare isotope laser power level is attenuated by 9 and 25 dB. Consistent with the theory of (17), we see that the noise level of the heterodyne spectrum is linearly proportional to the power of the received signal P_r, provided that the AM and/or PM noise level is above the LO shot noise level.

7. DISCUSSION

We have used a direct spectrum comparison technique for measuring the phase noise in a corrupted laser LO with respect to a clean laser LO. The measurement accuracy can be improved greatly by phase locking both lasers and the frequency synthesizer and then demodulating the laser beat frequency to baseband. The phase measurement could then be performed using a commercially available microwave phase noise measurement instrument like the HP 3048A system. Such a setup would involve relocating the lasers to a very quiet environment and building phase locking loops.

8. CONCLUSIONS

A heterodyne detection experiment was devised to measure the effects of frequency shifting the local oscillator laser with an acousto-optic modulator. The RF drive signal spectrum was shown experimentally to be translated to the heterodyne spectrum. This drive spectrum will set the ultimate performance limit of a heterodyne detection system when the heterodyne carrier-to-shot noise level is greater than the RF drive carrier-to-noise level. A generalized theoretical heterodyned detector power spectrum representation was used to relate the experimental measurements to the theory.

Theoretical and experimental results were shown to be in agreement, but the AO modulator produced an unexpected reduction in the AM sideband levels of the RF drive signal. It was found that the AO modulator reduced the sinusoidal AM sidebands of the RF drive signal by more than 10 dB. Also, the zero-order diffracted output of the AO modulator was about -70 dBc, compared to the typically reported -40 dBc level.

9. ACKNOWLEDGMENT

10. REFERENCES

1.   Gagliardi, R. M., and Karp, S., "Optical Communications," Wiley & Sons, 1976.

2.   Robins, W. P., "Phase Noise in Signal Sources," Peter Peregrinus Ltd., London, UK, 1982.

3.   Ku, R. T. and Spears, D. L., "High-sensitivity infrared radiometer using a tunable-diode-laser local oscillator," Optics Letters, Vol. 1, No. 3, September 1977.

4.   C. Freed, "Ultrastable Carbon Dioxide (CO_2) Lasers, " SPIE Proceedings on Laser Research and Development in Northeast, SPIE 709, pp. 36-45 (1986).

5.   Shapiro, H. J., Private communication.

ABSOLUTE PEAK = 34 dBmW
RESOLUTION BW = 10 kHz
VIDEO BW = 100 Hz, 3 kHz
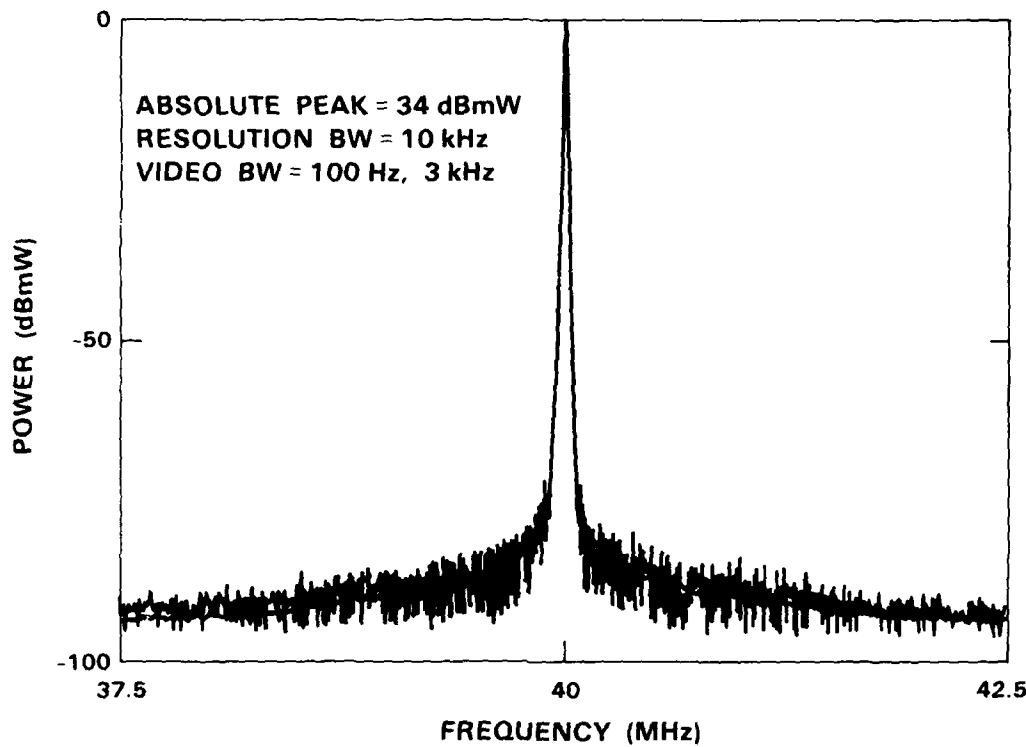
Figure 7: 40 MHz RF drive spectrum.

FREQUENCY
SHIFTED
FIRST ORDER
MODE BEAT
NOTE

RESOLUTION BW = 100 kHz
VIDEO BW = 1 kHz

ZERO ORDER
MODE (-72 dBc)
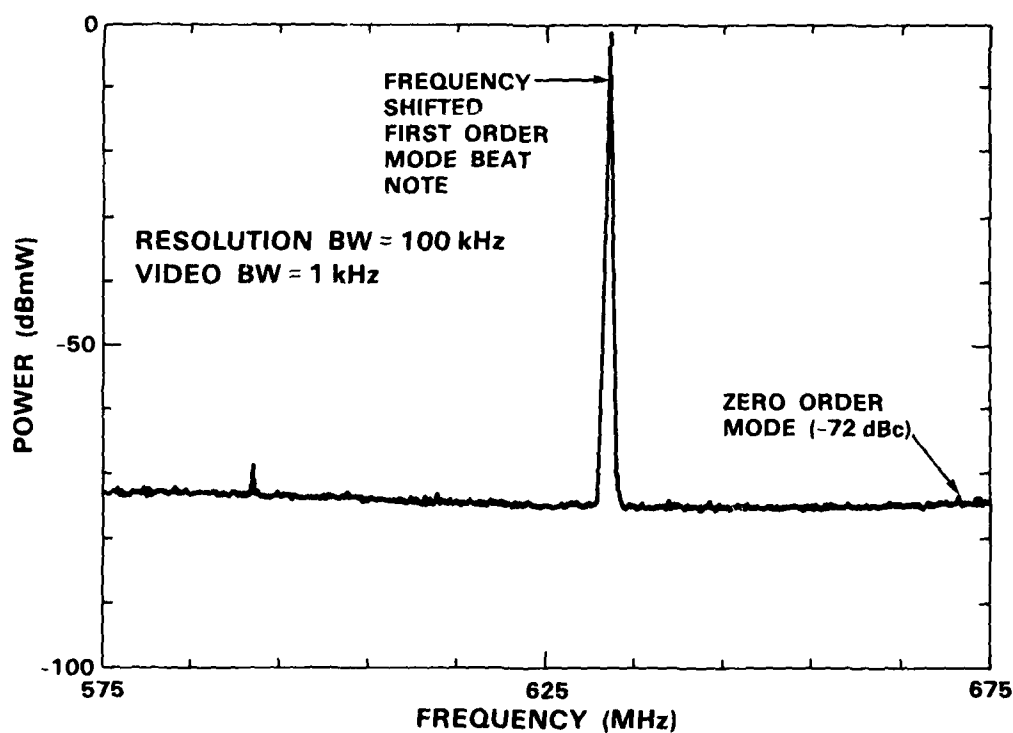
Figure 8: Broadband view of the spectrum of the reference laser heterodyned with an LO laser which is AO modulated by the 40 MHz sinusoidal RF drive signal.
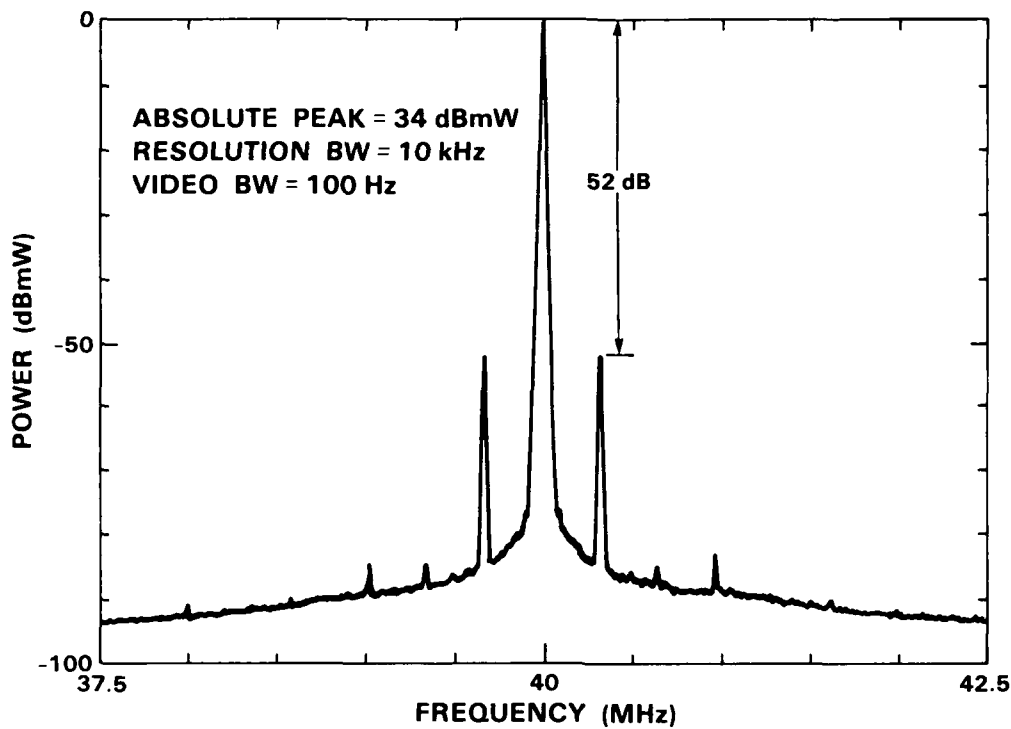
Figure 9: FM modulated 40 MHz RF drive spectrum.
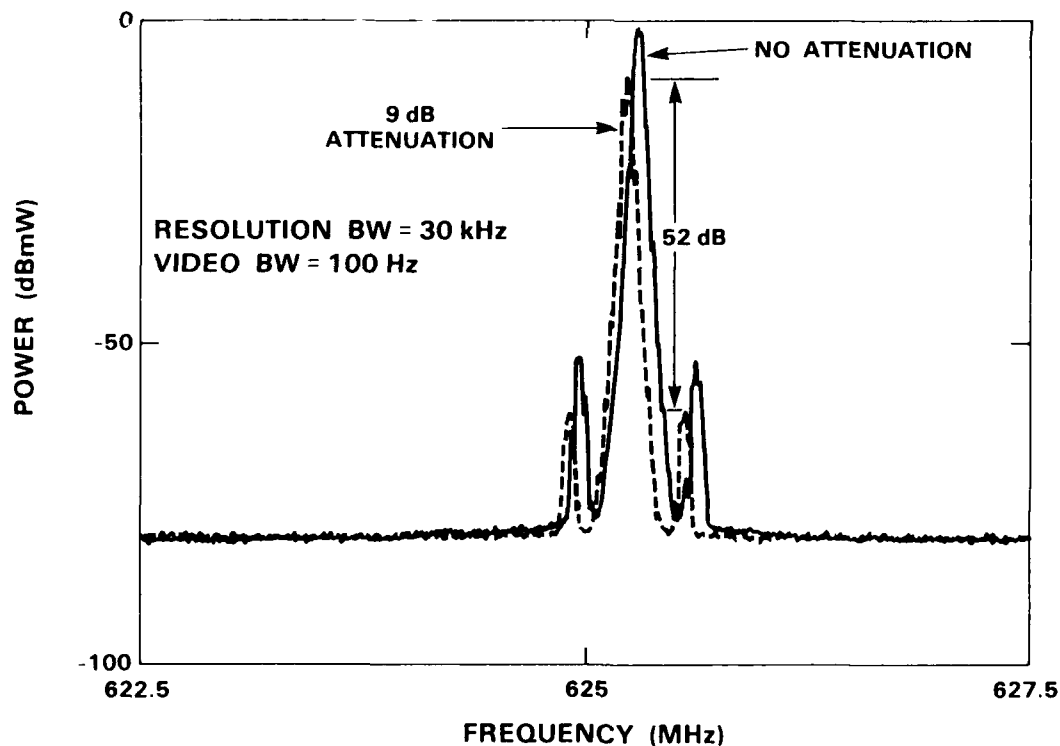
Figure 10: Heterodyne spectrum with FM modulation of the 40 MHz RF drive signal and attenuation of the isotope reference laser.

335
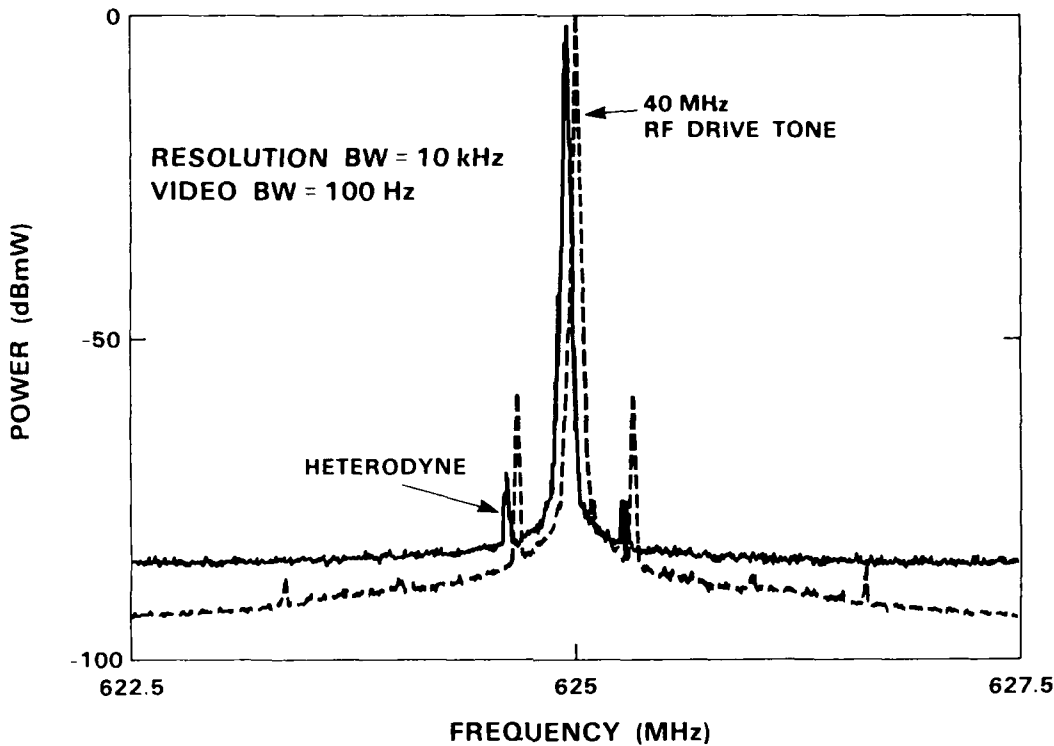
Figure 11: Heterodyne spectrum with 0.2% AM modulation of the 40 MHz RF drive signal.
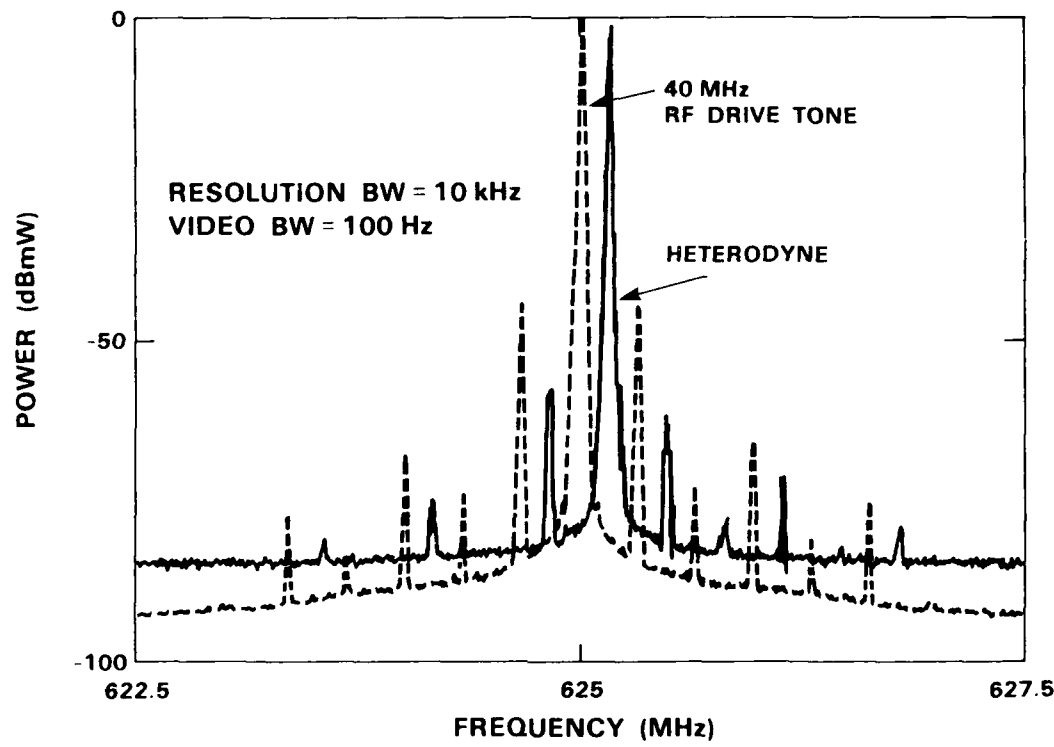
Figure 12: Heterodyne spectrum with 1.0% AM modulation of the 40 MHz RF drive signal.
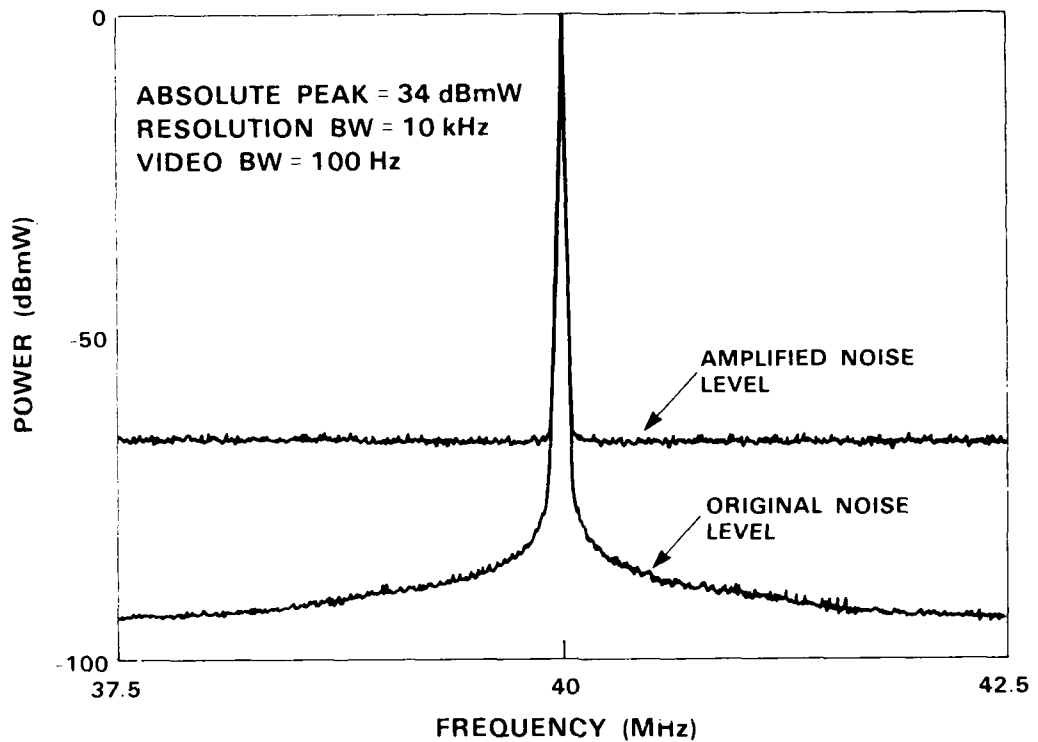
Figure 13: Very noisy 40 MHz RF drive signal.
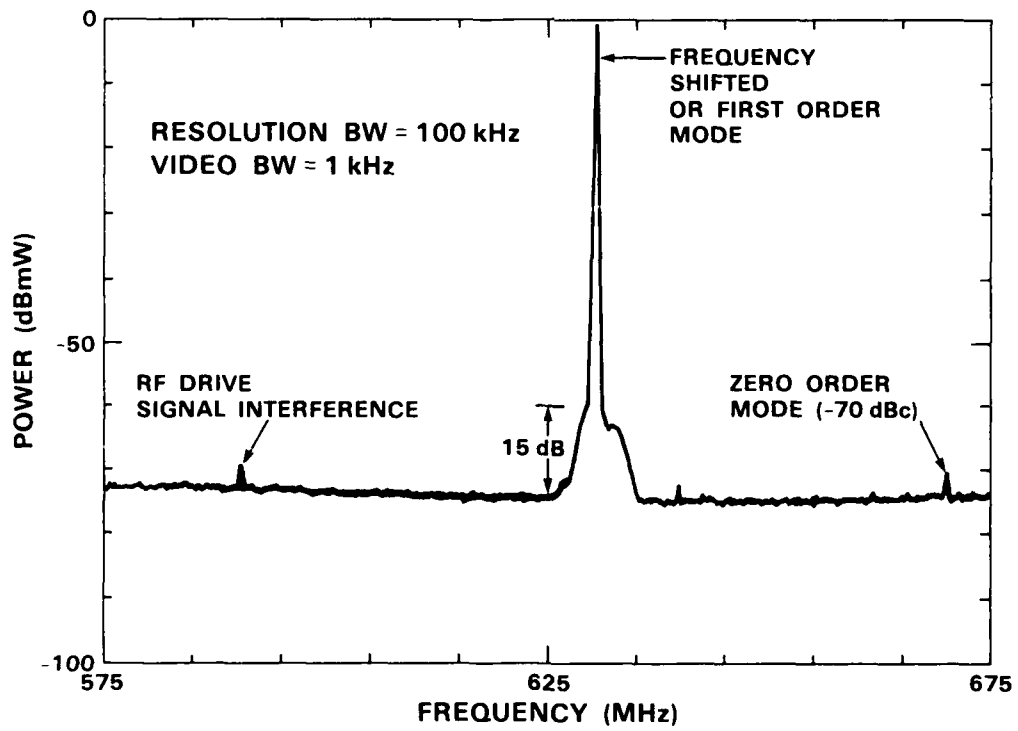
Figure 14: Wideband view of the heterodyne spectrum with a very noisy RF drive signal.

337
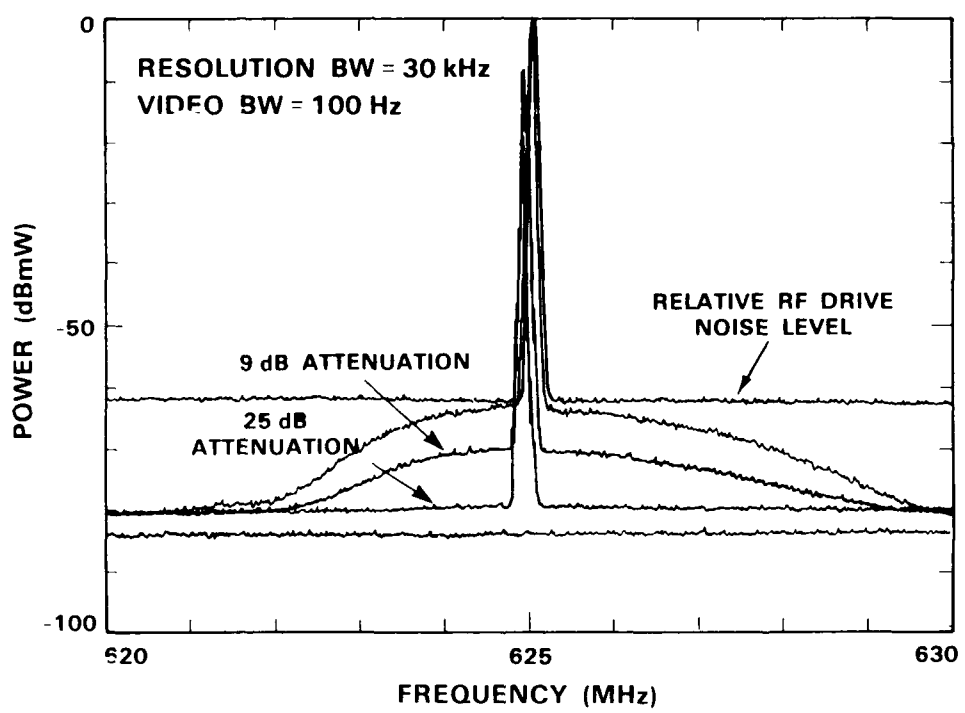
Figure 15: Narrowband view of the heterodyne spectrum with a very noisy RF drive signal.

PROPERTIES OF A LASER BEAM GENERATED FROM AN AXICON RESONATOR

V.M. Weerasinghe, J. Gabzdyl and R.D. Hibberd
Centre for Robotics and Automated Systems
Imperial College of Science, Technology and Medicine,
Exhibition Road, London, SW7 2BX, England

Abstract

A high power cw CO_2 laser beam is generated from a resonator configuration having an axicon mirror as its end reflector. The properties of this beam is evaluated in terms of its polarisation, focussing capability and temporal stability and the resulting effects on processing materials are presented. A comparison is made with a folded and a straight resonator having a spherical focussing mirror as its end reflector.

Introduction

Laser materials processing encompasses diverse applications such as welding, cutting, scribing, drilling and a multitude of surface modification processes. In each application, optimum results are obtained from a combination of specific properties of the beam. For example, of particular relevance to cutting, welding and scribing are the mode quality and the state of polarization of the beam (1,2). For surface modification processes, a multimode beam is preferred (3). Further, for multidirectional processing, the radial symmetry of the spatial intensity distribution is important. Therefore, it is necessary to 'engineer' the beam to suit the particular application.

The aim of this paper is to present experimental observations of some properties of a laser beam generated from an axicon resonator, from the viewpoint of materials processing. Development of a theoretical basis for the observed properties is at hand and will be the subject of a future paper.

Treacy (4), describes an open axicon resonator made of two concave conical mirrors, with inclusive angles of 146 degrees. Based on the original work by Fox and Li (5), optimum parameters for open resonators with full and truncated conical mirrors are derived by Voytovich (6). The resonator configuration investigated consisted of two identical conical mirrors with large inclusive angles. It is shown that for small Fresnel numbers, the loss in the conical resonator is similar to a confocal resonator and less than a plane parallel resonator.

Experimental

The conical resonator configuration investigated in the present study is illustrated in figure 1(a). It was constructed from one half of a folded cavity used in a 2Kw cw CO_2 machine manufactured by Control Laser. The inclusive angle of the concave conical reflector was 90 degrees, nominal value. The output aperture and the reflector aperture were 33mm in diameter and the cavity length was 4m (Fresnel No.3). Properties of the conical resonator was compared with the straight spherical resonator, figure 1 (b) and the folded resonator, figure 1 (c).

A rotating wire instrument (7) was used to study focussed spot sizes and power stability.
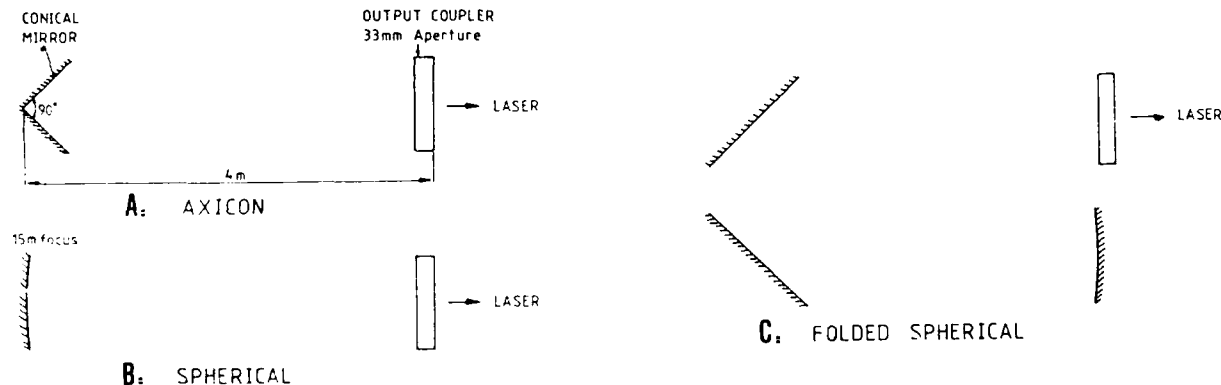
Figure 1: Resonator configurations which were investigated.

Figure 2 shows the conical mirror used. The mirror shown was diamond machined from copper and gold coated. A small 3mm diameter hole was required at the apex, to clear the diamond tool.
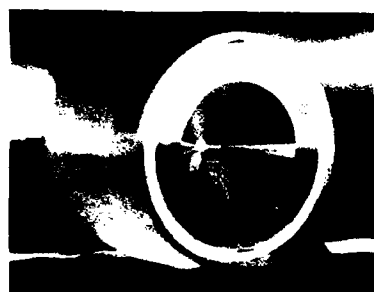
Figure 2: The conical mirror.

Results and Discussion

From geometrical optics, it can be shown that the deviation of a ray after two reflections from two mirrors inclined to each other at an angle 'a' is independent of the angle of incidence and is given by $2(\pi - a)$ if the plane of incidence is perpendicular to the line of intersection of the two mirrors. This is also valid for the conical mirror because it is the surface of revolution of two inclined line reflectors. Therefore, the conical resonator will be less sensitive to mirror misalignment because the mode axis is not displaced. The laser power was observed to be less sensitive to manual misalignments of the mirrors for the conical resonator, compared to other resonator configurations shown in figure 1 (b,c). The power variation from start-up and during warm-up of the laser was observed to be 10% for the straight spherical resonator and 2% for the conical resonator. For operating conditions of 35 torr and 110 mAmp, 1.0Kw was obtained from the conical resonator. For the same conditions, about 10% more power was obtained from the straight spherical resonator.

A laser cavity with large angled folded mirrors, linearly polarize the beam due to the enhanced 'S' reflection. The state of polarization of the straight spherical resonator will be random. A speculative theory is that the beam from the conical resonator will be equally polarized in all directions at a given instant. This is also based on observations of burn prints made by the conical beam which was reflected off a KCL flat held at an angle.

The effect of the polarization on laser cutting is well known. In drilling, a linearly polarized beam distorts the desired circular hole shape in the 'P' direction. Figure 3 shows the distortion of the hole shape produced by the linearly polarized beam from the folded resonator, compared to a good circular shape produced by the beam from the conical resonator.

a   b

Figure 3: Drilled hole shapes. (a) Linearly polarized beam from the folded resonator. (b) Conical resonator.

In the conical resonator, the mode volume will occupy a higher proportion of the gain medium compared to the other resonator configurations. Futher, due to ray reversal, the mode quality will be less susceptible to degradation by optical and gain inhomogenieties of the medium.

Figure 4 shows in a qualitative manner, the intensity distribution of the beam from the conical resonator, taken about 1.5 metres away from the output aperture. The two distinct

features are its symmetry or circularity and the 'doughnut' structure.
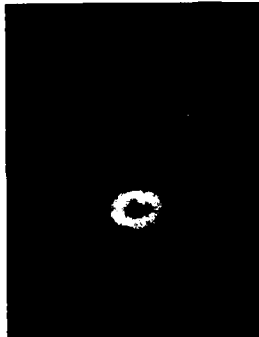
Figure 4: The 'doughnut' structure of the intensity distribution of the beam produced by the conical resonator.

The 'doughnut' structure is particularly useful in surface modification processes because of its less centralised intensity. For example, in hardening, it is desirable to obtain a high width/depth aspect ratio of the hardened zone without melting. Figure 5 shows a cross section of a hardened track produced by the conical beam. The width/depth aspect ratio of this particular track is 10 which is comparatively higher than 4 to 6 usually obtained from gaussian or multimode beams.

Figure 5: A cross section of a laser hardened track produced by the conical resonator. Width depth aspect ratio 10.

Figure 6 shows a summary of cutting results. A more detailed report, including a comparison with the folded resonator, can be found in (8). As shown in the results, a higher cutting speed was obtained for the beam from the conical resonator compared to the straight sperical resonator beam. Furthermore, the cut quality from the conical resonator beam was observed to be non-directional.

	CONICAL	SPHERICAL	RATIO
V max. Ar – 40 psi	16 mm/sec.	13 mm/sec.	1·23
V max. O₂ – 30 psi	90 mm/sec.	77 mm/sec.	1·17

Figure 6: Comparative cutting results. Material - 0.8mm thick car body steel. Lens focal length - 100mm. Kerf widths from conical resonator beam - 0.35 to 0.50mm. Laser power 1.0Kw.

The focussed spot sizes which were measured in a qualitative manner, using the rotating wire instrument (LBA), indicated the conical beam spot size to be approximately 15% larger than the straight spherical beam. Therefore, the higher cutting speeds obtained from the conical beam could be the result of a 'trade off' between the doughnut intensity structure which generates a higher mean temperature and the focussed spot size.

Conclusions

Specific characteristics of the conical resonator beam which are of interest are:
a) Less sensitivity to cavity mirror misallignments.
b) The state of polarization. This could elliminate the need for an external circular polarizer.
c) The 'doughnut' intensity structure.
Results obtained from this preliminary investigation clearly justifies a further detailed study of conical resonators and their application to materials processing.

References

1. I.A. Menzies, J. Powell, and K. Schenzinger, Laser beam cutting - the state of the art presented at ECLAT '88, Dusseldorf, West Germany, (October 1988).

2. M. Welch, Concepts of polarization physics, Lasers and Applications, (January 1986).

3. V.M. Weerasinghe, Laser cladding of flat plates, PhD thesis, University of London, (March 1985).

4. E.B. Treacy, Non-degenerate modes in a two cone resonator, Phy. Lett., Vol 15, No 1 (March 1965).

5. A.G. Fox, and T. Li, Bell Systems Tech. J., 40, (1961).

6. N.N. Voytovich, Open resonators and lines with correctors in the shape of cones and truncated cones, Radiotekhnica 1 Elecktronica, 11, (1966).

7. G.C. Lim, and W.M. Steen, Measurement of the temporal and spatial power distribution of a high power CO_2 laser beam, Optics and Laser Technology, (June 1982).

8. J. Gabzydl, PhD thesis, University of London, to be published.

COMPACT CO_2 LASERS OPERATING IN THE PULSED-REPETITIVE MODE

Prof. G.A. Mesyats, Dr. V.V. Osipov, Dr. V.M. Orlovsky
USSR Academy of Sciences Ural Division
Institute of Electrophysics, 620219 Sverdlovsk

The paper reports the results of a series of experimental and theoretical works aimed at the creation of compact sealed-off e-beam-sustained and TEA CO_2 lasers. It is shown that high-pressure e-beam-sustained lasers, in which a space discharge is initiated by an electron beam of duration 10^{-9} s may be made compact and capable of operating in the seal-off mode at a frequency of tens of hertz. These laser systems have the following features: (1) low W_e/W_d ratios where W_e is the electron beam energy, W_d is the energy delivered to the gas; (2) division of the space discharge, 10^{-5} s after its initiation , into two operating zones; (3) contraction of the space discharge after ~10^3 shots at the electric field exceeding a certain critical value; (4) existence of minimum values of both the delivered and the produced energy in the initial period of operation (~ 10^3 shots). An explanation of these features is given. Several laser designs operating at frequencies of 4 to 50 Hz and producing 1 to 10 j of radiation energy are described. The results of a study aimed at the improvement of energetic and resource characteristics of compact TEA CO_2 lasers by raising the intensity of preliminary ionization, shortening the period of pumping and using electrodes with good emissive properties are reported. For 1-1000 Hz, 0.05-0.3J lasers, pumping schemes and performance are given.

The compact CO_2 lasers operating in the pulse-repetitive mode are of a significant interest in view of using them for range-finding[1], location[2], atmospheric probing[3], in nonlinear optics[4], technology[5], etc. The works aimed at diminishing of the size of these devices focus on the study of sealed-off CO_2 lasers. At the same time, these lasers having high efficiency, good energetic characteristics[6,7] and ability of operation at a high pressure of the active medium[8] are promising there where it is necessary to re-tune continuously the radiation frequency or/and produce high-power radiation pulses of short duration ($\leq 10^{-8}$ s)[9]. In the recent years we made an attempt to investigate if it is possible to create pulse-repetitive sustainers and to improve the performance of sealed-off TEA CO_2 lasers.

Experiments were carried out on set-ups typical diagrams and laser parameters of which are shown in Fig.1 and Table 1, respectively.

Table 1

Characteristics e-beam lasers	MIG-4	MIG-5	Characteristics TEA lasers	LIAN-2	LIAN-3
active volume (cm³)	0.7x1.5x10	3x3x72	active volume (cm³)	0.5x0.4x20	0.5x0.5x35
C_1, nF	50 10^{-3}		C_1 n	33	13.6
C_2 nF	20	190	C_2 n		3.3
electron beam density(A/cm²)	0.6-90	70	C_3 n	0.6	0.76
duration electron beam(ns)	2.5	4.2	L_1 u		80
			L_2 u		20
			U_0 kV	till 11	till 25
frequency(Hz)	4	till 50	frequency(Hz)	till 100	till 1000
efficiency(%)	8	22	efficiency(%)	5.6	12
maximum multimode output energy	1	30	maximum multimode output energy	0.1	0.65
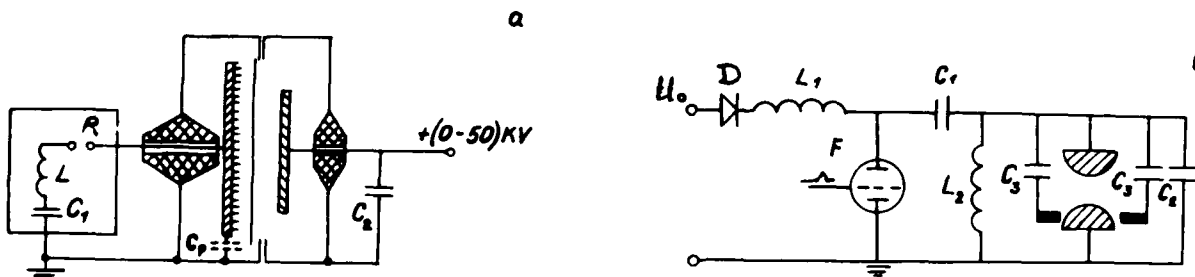
Fig. 1 Circuit schematic for electron beam sustainer (a) and TEA (b) CO_2-lasers

In the sealed-off e-beam-sustained lasers we used electron beams of nanosecond duration. This was caused by our desire to diminish the gas mixture dissociation and the laser dimensions. The laser dimensions can be reduced in this case because the insulator gaps may be made essentially shorter and electron beams are generated by sealed-off vacuum diodes, i.e. without application of any extra pumping equipment.
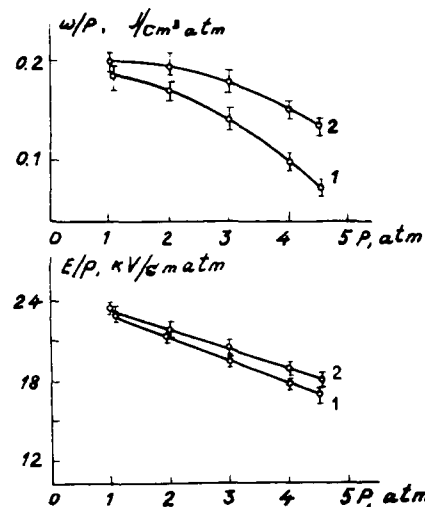
Fig.2
Maximum input energies W/p deposited into the gas and their corresponding values of E/p as a function of the pressure for aluminium (1) and lead (2) anodes. Active volume-1x1.5x10 cm; Gas mixture - $CO_2 : N_2 = 1 : 1$.
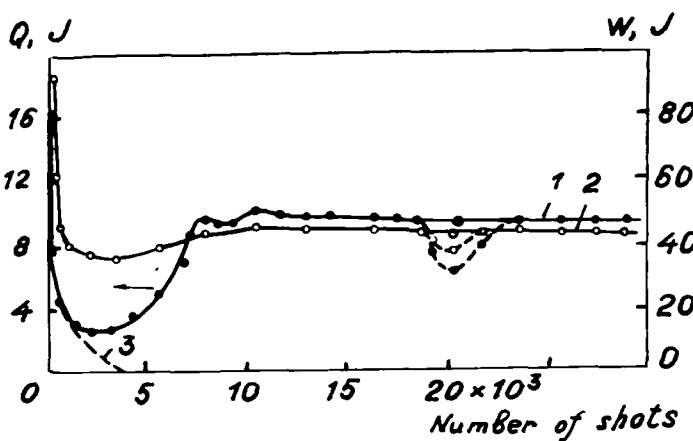
Fig. 3
Input W (1) and output Q (2) energies as a fuction of a number of shots. Gas mixture - $CO_2 : N_2 = 1 : 1$ p = 1 atm.

Figure 2 shows maximum input energies deposited into the gas and the corresponding values of E/p (E is the electric field strength, p-the pressure of the working gas mixture) as a function of pressure for aluminium and lead anodes. A considerable reduction of the electron beam duration and high input energies resulted in the improved ratio between the energy input into the gas by the electron beam and the energy deposited by the discharge process. For a pressure of 4.5 atm. This ratio is 10^{-2}. This suggests that it is possible to create compact e-beam-sustained lasers with overall dimensions not above those of TEA lasers.

The data presented in Fig.3 demonstrate that e-beam-sustained lasers can operate in the sealed-off mode with an efficiency of more than 20% and an output energy of 20 J/l. In this mode a certain transient effect takes place which is caused in our opinion by the following reactions[10]:

$$CO_2 \rightarrow CO + O \tag{1}$$
$$O + O + M \rightarrow O_2 + M \tag{2}$$
$$N_2 + O_2 \rightarrow NO + N \tag{3}$$
$$NO + O \rightarrow N_2O \tag{4}$$
$$N_2 + O \rightarrow N_2O \tag{5}$$

$$O_2 + e \rightarrow O + O^- \tag{6}$$
$$NO + e \rightarrow N + O^- \tag{7}$$
$$N_2O + e \rightarrow NO + O^- \tag{8}$$
$$NO_2 + e + M \rightarrow NO_2^- + M \tag{9}$$

$$CO + O_2 \rightarrow CO_2 \tag{10}$$
$$NO \rightarrow O_2 + N_2 \tag{11}$$
$$NO + CO \rightarrow N_2 + CO_2 \tag{12}$$
$$N_2O + CO \rightarrow N_2 + CO_2 \tag{13}$$
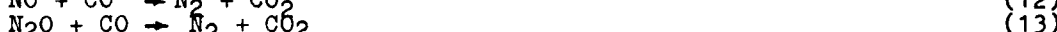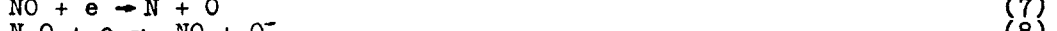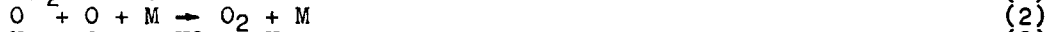
During the first cycle of reactions (1-5) there occurs a growth in the amount of electronegative nitrogen oxides. They reduce the discharge current (2nd cycle of reactions (6--9)) and, consequently, the radiation energy. The oxides decompose in the plasmochemical reactions with excited CO. As the CO concentration grows, the formation rate of nitrogen oxides at a certain time becomes lower than the rate of decomposition. The process is stabilised at a quasi-steady-state concentrations of CO and O_2 (reactions (10-13)).

In Fig. 3 the position of the minima of the curves depends on the parameters of the

electron beam and the space discharge, and the volume of the laser chamber.For instance, if an electron beam affects the working medium and a discharge is initiated in every 500 shots to make measurements, the generation stops after about (2.5-3) 10^3 shots (dash curves) the same effect can be attained with the same manipulations during the quasi - steady-state period.

It has been also noticed that the discharge operated for an unusually long time. For nitrogen, in particular, its operation time was longer than 10^{-3} s. The solutions of the continuity equation and the Poisson equation have shown that for our experimental conditions (d = 3 cm, U_0 = 37 kV, the gas was nitrogen at atmospheric pressure) the cathode voltage drop was comparable with the applied voltage and the cathode drop length - with the electrode separation at a current density of 35 mA/cm^2. That current density occurred at the 15th microsecond after the beginning of the discharge, and one could expect that the electronic conductance would change to the ionic one. However, no abrupt current change was observed in the waveforms. We connected this observation with the discharge division.

Figure 4 presents a character of a discharge glow in nitrogen during the first microsecond and 20 microseconds after the discharge ignition. Similar results were obtained for mixtures of CO_2 and N_2. As can be seen from these figures the discharge divides during the final stage of operation.

We were unable to elucidate clearly the form of the glow and the place of its operation. These observations, however, enable, us to state that the current in the laser active zone stops as the cathode drop disappears.

We have also revealed if the initial electric field exceeds a certain critical value then a non-sustained glow discharge contracts after a few thousands of shots both in pure CO_2 and in CO_2-containing mixtures.

When experimenting with the contraction of the glow discharge during the first shot by adding O_2 and CO to CO_2 we have found the following: for the ratios CO_2: O_2 = 1 : 1 and CO_2: CO= 1 : 1 no channel formed during the first shot. Mixing these gases in the proportion CO_2 : CO : O_2 = 99.5 : 0.25 : 025 resulted in the discharge contraction 180 to 450 μs after the ignition of the glow discharge for the beam current density range of 0.6 to 60 A/cm^2, the charging voltage of 12.8 kV, and the gap spacing of 0.7 cm.
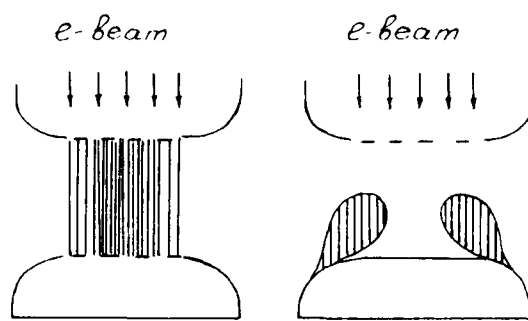
Fig.4 Pattern of a discharge glow in atmospheric pressure nitrogen at 1st and 20th microsecond j = 70 A/cm^2, τ = 45 ns.
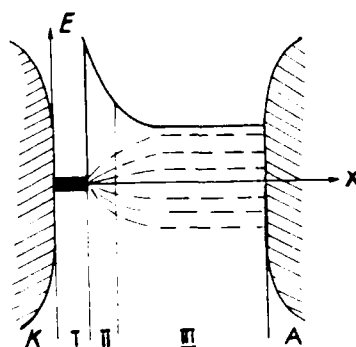
Fig.5 Model geometry

We failed to explain such a behavior of the discharge with the help of known mechanisms of discharge instability. Therefore, we have suggested an instability mechanism which involves associative ionization typical for carbon oxidation. A simplified chain of plasmochemical reaction is as
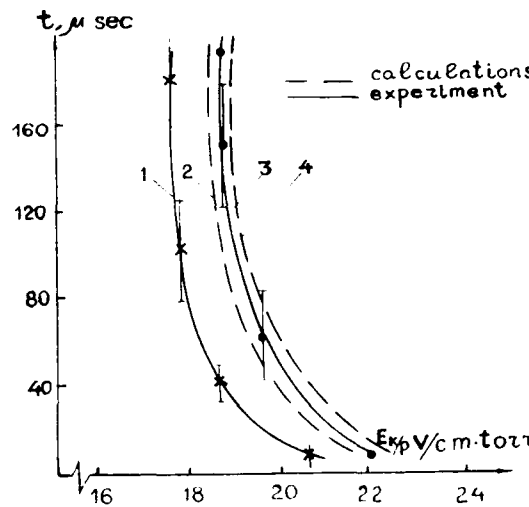
Fig.6 Time formation of the channel as a fuction of a quasi-stationary value of E_k/p at the beam current density 6 A/cm^2 τ = 2.5 ns and p = 1 atm.

345

follows[11]:

$$CO_2 + e \rightarrow CO + O + e \tag{14}$$
$$CO_2^* \rightarrow CO + O \tag{15}$$
$$CO (V_1) + CO (V_2) \rightarrow C + CO_2 \tag{16}$$
$$O + e \rightarrow O (1S) + e \tag{17}$$
$$O_2 + e \rightarrow O_2 (A^3 \Sigma_u^+) + e \tag{18}$$
$$C + O (1S_3) \rightarrow CO^+ + e \tag{19}$$
$$C + O_2 (A^3 \Sigma_u^+) \rightarrow CO_2^+ + e \tag{20}$$
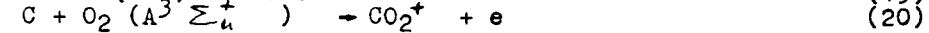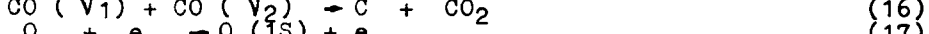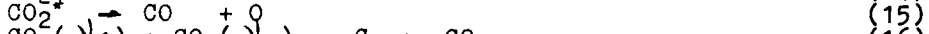
The suggested mechanism will be most prononced in the region of an enhanced electric field e.g., in the vicinity of the point or the cathode spot (Fig.5). The rate of the channel growth was calculated from the following set of equations:

$$\sigma_1 E_1 S_1 = \sigma_2 E_2 S_2 = \sigma_3 E_3 S_3 \tag{21}$$
$$E_2 = {}^1(E_3 - {}^2E_1{}^2)\beta^* + E_1 \tag{22}$$
$$N_i = eN_i \cdot V_i / E_i \tag{23}$$
$$dN_i/dt = \sum_j \alpha_{ij} - \sum_\kappa \beta_{i\kappa} \qquad i=1-27 \quad \alpha = K_\alpha /A/ /B/ \tag{24}$$
$$\qquad\qquad\qquad\qquad\qquad\qquad\qquad \beta = K_\beta /A/ /B/$$
$$V_{th} = d\kappa/\tau \tag{25}$$

Here Eqs. (21-23) are similar to those used in[12]. σ_1, σ_2, σ_3, E_1, E_2, E_3; and S_1, S_2, S_3 are the conductivities, the electric fields, and the cross-section of zone I and zoneII; and zone III, respectively. β^* is the field enhancement factor for the channel tip in zone I V_{ch}- the velocity of channel growth; τ- the period for which the electric field in zone II decreases from E_2 to E_1; e-the electric charge; N_i-the concentration of the i-type particles; V_i-the drift velocity of the i-type particles; $\sum \alpha_{ij}$-the rate of production of the i-type particles; and $\sum \beta_{ik}$-the rate of disappearance of the i-type par-ticles. As the conductivity σ_2 in zone II increases as a result of plasmochemical re-actions, the electric field E_2 decreases. As σ_2 becomes equal to σ_1, the channel ins-tantly travels to a distance d_k. The calculation procedure covered 27 equations including 115 plasmochemical reactions. The electron-involved reaction constants were determined from the calculated electron velocity distribution by the numerical integration of the steady-state Boltzmann equation. Other constants were taken from [13-17].

Figure 6 shows the calculated and the experimental time of channel formation as a fun-ction of E/p. (1,2,4 - CO_2 : CO : O_2 = 99 : 0.5 : 0.5; 3 - CO_2 : O_2 : CO = 99 : 5 : 5; 2-Ka = 10^{-10} $cm^3/$ sec; 4 - Ka = 10^{-11} $cm^3/$sec. Ka is the constant of the associative ioni-zation) The curves demonstrate good qualitative and satisfactory quantitative agreement.

We tried to improve energy and resource characteristics of the pulse-repetitive sealed-off TEA CO_2 lasers, first of all, by increasing the glow discharge stability. This was achieved by increasing the intensity of preliminary ionization, decreasing the pumping du-ration and the input energy in the near-electrode regions, and by using electrodes with good emissive properties. To improve the preliminary ionization we have suggested a sys-tem based on a sectionalized diffusion-channel discharge[18]. That discharge was initiated between the main electrode and a sectionalized auxilliary electrode. One section of the auxilliary electrode consists of two layers: a thin metal foil and a thicker dielectric substrate. The metal foil in each of 35 section is connected to an individual capacitor. 35 capacitors constitute the capacitor C_3 (Fig. 1b). By using shadow photography and a cut off discharge method it has been found that from 4 to 8 diffusion filaments appear per 5 mm section length, which absorb 60% of the energy spent for preionization. 40 ns later, a high-conductivity channel with the electron density of 3 10^{16} cm^{-3} develops along one of the filaments.

With this system of preionization, stainless-steel electrodes and a glow discharge of duration 250 ns we measured the ultimate number of shots as a function of the energy intro-duced into the mixture CO_2 : N_2 : He = 1: 1 : 8 at atmospheric pressure. It can be seen that the reduction of the input energy by a factor of 1.5 results in an increase an the number of shots by three orders of magnitude.

We account for this relation by the growth of the amount of electronegative oxides, such as NO, N_2O and others which diminish the electron density during the period of pre-liminary ionization. In this system, long operation is realized at comparatively low in-put energies of 80 to 90 J/l. When the discherge duration was shortened to 20 ns we were able to increase the input energy to 250 J/l in long operation,(10^6 shots) which we acc-ount for by a more stable glow discharge.

The specific input energy and, consequently, the radiation energy could be further in-creased, to our opinion, by decreasing the energy dissipated in the near-electrode regi-ons where the channel is known to origin. One of the approaches to solve this problem is the use of electrodes with good emissive properties.

The energy dissipated in the cathode layer can be found by solving the continuity eq-uation and the Poisson equation taking into account the emissive properties of the elect-rode[19]. The calculation has shown that the dissipated energy for lanthanum-strontium co-baltite(work function 2.5, secondary electron emission coefficient 0.2, surface average field enhancement factor β = 24) is lower by a factor of 10 or more than for typical

electrode materials based on iron or nickel.
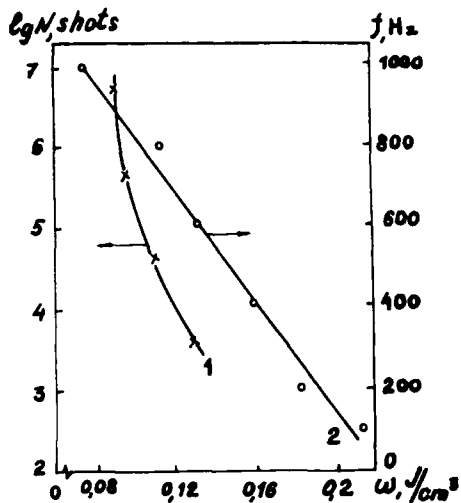
Fig.7 The maximum number of shots N (1) and maximum excitation pulse repetition frequency f (2) as a function input energy. Gas mixture $-CO_2$: N_2 : He = 1 : 1 : 8. Gas pressure - 1 atm. Discharge pulse duration - 250 ns; f = 400 Hz

Fig.8 Output laser energy as a function of the input energy for metal (1) and perovskite (2,3) electrodes. Active volume - 0.5 x 0.5 x 35 cm; gas mixture CO_2 : N_2 : H_2 = 5 : 5: 1; pressure - 1 atm; (1,2) U_0 = 20 kV; (3) U_0 = 23 kV; U_0 is the charged voltage; the perovskite-$La_{1-x}Sr_xCoO_3$.

The effect of the electrode material on the energetic characteristics was investigated in a e-beam-sustained laser having an active volume of 0.5 x 0.5 x 35 cm^3. The resonator was formed of a copper mirror with a curvature radius of 4 m and a ZnSe plane mirror with a reflection coefficient of 65%. The velocity of pumping of the gas medium through the active volume was 20 m/s.

Figure 8 shows the radiation energy as a function of the energy introduced into the gas obtained by measuring the store capacitance C_1, for two charging voltages. It can be seen that under the same conditions the ultimate energy introduced into the gas with $La_{0.3}$ $Sr_{0.7}$ CoO_3 electrodes is about twice as many as that with stainless-steel electrodes (curves 1 and 2). This corroborate the supposition that the space discharge becomes more stable with decreasing the energy dissipated in the near-electrode regions.

It was also investigated how the chemical composition of the gas mixture varies during the period of laser operation. It was found that the use of perovskite electrodes, without complement heating them, fails to in increase essentially the rate of decomposition of CO_2. With the specific input energy of o.3 J/cm, the CO_2 content in the working gas mixture becomes as stabilized after ~5 10^5 shots on the level of 60% to 70% of its initial value.

Thus, the above-described study has shown that the pulse-repetitive e-beam-sustained CO_2 laser is capable of operating in the sealed-off mode. This operation has some specific features which are also discussed. A model of the channel growth is developed and a chemical ionization mechanism of instability of a space discharge is suggested. The conditions under which the energy or resource characteristics of TEA CO_2 lasers can be improved are demonstrated.

References

1. H. Rudko, IEEE J. Quantum Electron QE - 13, 39 (1977)
2. T. Courtenay, F. Boulter, H. Henshall, Inf. Phys. 16, 95 (1976)
3. V.E. Zuev, The Laser as a Meteorologist (Gidroenergoizdat, Moscow, 1975), pp. 28-32
4. C.R. Jones, Laser Focus, August, 68 (1978)
5. D.C. Hamilton, J. Phys., D: Appl. Phys. 9, 43 (1976)
6. Yu.I. Bychkov, S.P. Bugaev, E.K. Karlova, N.V. Karlov, B.M. Kovalchuk, Yu.A. Kurbatov, G.A. Mesyats, V.M. Orlovsky, and A.M. Prokhorov, Pisma Zh. Tekh. Fiz. 1, 492 (1975)
7. N.G. Basov, E.M. Belenov, V.A. Danilychev, and Yu. F. Suchkov, Usp. Fiz. Nauk 114, 213 (1974)
8. N.G. Basov, V.A. Danilovychev, O.M. Kerimov, and A.S. Podsosensky, Pisma Zh. Tekh. Fiz. 17, 147 (1973)
9. Yu.I. Bychkov, Yu.D. Korolev, G.A. Mesyats, V.V. Osipov, V.V. Ryzhov, and V.F. Tarasenko, Injection Electronics (Nauka, Novosibirsk, 1985) pp. 141-171
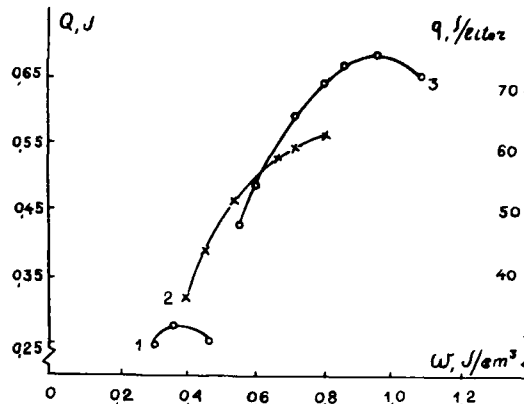
10. B.M. Karpov, Yu.G. Konev, V.M. Orlovsky, V.V. Osipov, and V.B. Ponomarev, Quant. Electr. 15, 465 (1988)
11. V.M. Orlovsky, V.V. Osipov, A.G. Poteryaev, and A.I. Suslov, in Proceedings, All-Union Workshop on Inverse Population and Lasing on Metal Atom and Molecule Vapors, Tomsk (1986) pp. 166-167
12. A.V. Kozyrev and Yu D. Korolev, Zh. Tekh. Fiz. 8, 569 (1982)
13. K. Smith, R.M. Thomson, Computer Modeling of Gas Lasers (Plenum Press, New York and London, 1978), pp. 269-277
14. F.E. Nilles, J. Chemical Physics 52, 1, 408 (1969)
15. R. Kummler, C. Leffert, K. Im, R. Piccirelli, L. Kevan and C. Willis J. Phys. Chemistry 81, 25, 2451 (1977)
16. H. Hokazono and H. Fujimoto, J. Appl. Phys. 62, 1586 (1987)
17. W.L. Nighau, and W.J. Wiegand, Phys. Rew. 10, 922 (1974)
18. V.A. Vizir, V.V. Osipov, V.A. Telnov, and G.M. Khamidulin, Quant. Electr. 18, 1256 (1988)
19. A.V. Kozyrev, Yu.D. Korolev, and G.A. Mesyats, Zh, Tekh. Fiz. 57, 1, 58 (1987)

SOURCES AND TECHNIQUES FOR ULTRAFAST PEEKING

J.-C. Diels
Department of Physics and Astronomy
The University of New Mexico
Albuquerque, New Mexico 87131

1. Introduction

By "Ultrafast Peeking", we mean having a quick look at some events, "quick" meaning here with picosecond or femtosecond resolution. A logical approach, as in photography, would be to use a shutter. There are many approaches to an ultrafast light switch. Some examples of mechanisms used are the optical Kerr effect [1], sum frequency generation type II in urea [2], and nonlinear interfaces [3]. The first of these is broadband, but requires high optical powers, and is limited in speed by the reorientation time of the molecules used. Sum frequency generation type II has been used as an optical gate for time domain reflectometry [4], time resolved fluorescence [2], and three dimensional imaging [5]. It combines all the essential characteristics of a good optical gate, namely:
  a) high contrast,
  b) linearity,
  c) low noise.
The first and last of these quality factors (a) and (c) are directly related to the quality of the nonlinear crystal, the rejection factor of polarizer used, and the quality of the pulses (absence of laser signal outside the "gate window". The transmission of the "open" window is linear in signal amplitude, but with a sensitivity proportional to the gating pulse intensity. Clearly, any "ultrafast shutter" will have to be a light activated switch. We will therefore review here recent progress in femtosecond pulse technology.

2. Progress in Short Pulse Generation

2.1. Introduction

There is little difference in the structure of the linear cavity of Dienes et al [6], where a pulse duration of 0.6 ps was reported, and that of the linear cavity of Fork et al [7], reporting a pulse duration of 32 fs. The main progress in the last decade has been in understanding and exploiting the mechanism of short pulse generation. However, despite claims to the contrary [8], we are still far from a global understanding of the operation of the mode-locked dye laser. A very simple theory of the dye laser is presented, which includes only saturation of gain and absorber, yet can explain oscillatory behavior in the pulse train. On the other hand, a similar oscillatory behavior of the pulse train can be explained by taking only dispersive effects into account, and neglecting saturation. A short review comparing some of the theories and the approximations involved in presented.

2.2. A Simple Model Based on Saturation

The pulse that evolves through the laser cavity is shorter than the energy relaxation time T_1 of the dyes, and longer than the phase relaxation time T_2. Therefore, using a simple two-level system description, the time evolution of the population difference ΔN during irradiation by a pulse of intensity I_1 is simply given by:

$$\frac{d\Delta N}{dt} = - \frac{I}{\mathcal{T}_s T_1} \Delta N \tag{1}$$

where $\mathcal{T}_s$ is the saturation energy density of the dye. This equation can be complemented by a conservation relation stating that the sum of the electromagnetic energy density W/S (S being the cross-section of the beam) and the energy stored by the medium is conserved:

$$\frac{d(W/S)}{dz} = (\Delta N - \Delta N_o) \frac{h\omega}{2} \tag{2}$$

Combining equations (1) and (2) leads to a simple differential equation for the evolution of the pulse energy. This equation can be integrated to yield a simple relation between the pulse energy W_1 entering the medium of thickness d, and the energy W_2 of the transmitted pulse:

$$1 - e^{\frac{W(d)}{S \mathcal{T}_s}} = e^{\alpha_o d} \left[1 - e^{\frac{W(0)}{S \mathcal{T}_s}} \right] \tag{3}$$

349

In Eq. (3), $A = \alpha_{oa}d$ is the (unsaturated) optical thickness of the *absorbing medium*. This latter equation applied to the absorbing and amplifying media can be used to find the evolution of the pulse energy over a round-trip [9]:

$$\{ 1 - e^A + e^{(A+sy)} \} = \{ 1 - e^G + e^{(G+rx)} \}^s \qquad (4)$$

or

$$F_A(y) = F_G(x) \qquad (5)$$

In Eq. (4), r is the fraction of the pulse energy coupled back into the cavity after each round-trip, G $(= \alpha_{oG}d)$ is the (unsaturated) optical thickness of the gain medium, and

$$s = k \frac{s_g}{s_a} \frac{\mathcal{T}_g}{\mathcal{T}_a} \qquad (6)$$

is a geometrical and physical parameter describing the ratio of the saturation energies in the absorbing and gain media. the number k ranges between 1 and 3, the larger values corresponding to standing wave interaction in the absorbing medium. x and y are the initial and final energies at each round-trip, normalized to the saturation energy density in the gain medium. Equation (4) can be solved graphically or numerically. For any value of the energy x_i, the energy at the next round-trip is y_i satisfying $F_A(x_i) = F_G(y_i)$. That value y_i is the initial energy x_{i+1} at the next round trip. This procedure leads in a stepwise manner to a stable operation point, for which $F_A(x_o) = F_G(x_o)$. The ratio of the derivatives $\eta = [F'_A]_x /[F'_G]_x$ is a measure of the stability of the operation point. It is worth noting that the approach presented here does not make the usual approximation that the changes of energy per element and per round trip is negligibly small (compared with the pulse energy). The output pulse energy $x_o/(1-r)$ as well as the stability factor η can be computed for various conditions of operation (linear gain, absorption, reflection coefficient r, "s factor") [9].

An interesting refinement of this model is to include losses that are proportional to the energy at the **previous** round trip. Such losses occur because the energy stored in the upper levels of the absorbing transition can relax in a few ns to another group of levels, which can absorb energy from the pulse at the **next** round trip. This effect can be incorporated in the model by introducing a reduced cavity feedback $r = r_0(1 - asx_1)$ where x_1 is the energy at the previous round trip, and a a proportionality factor. It is seen that, under high gain conditions, the inclusion of such losses leads to a periodic oscillation of the pulse energy, rather than a steady state condition. Figure 1a and Fig. 1b show typical oscillations, either with a single periodicity (Fig. 1a) of a multiple periodicity (Fig. 1b) for the pulse energy versus cavity round-trip index. More complex periodicities than those in Fig. 1b evolve when, for instance, the reflection coefficient is set to 0.95, and the gain is decreased to 1.15 (from 1.2). This model offers one explanation for the oscillations in the pulse train that have been observed since more than a decade [10] in mode-locked lasers.
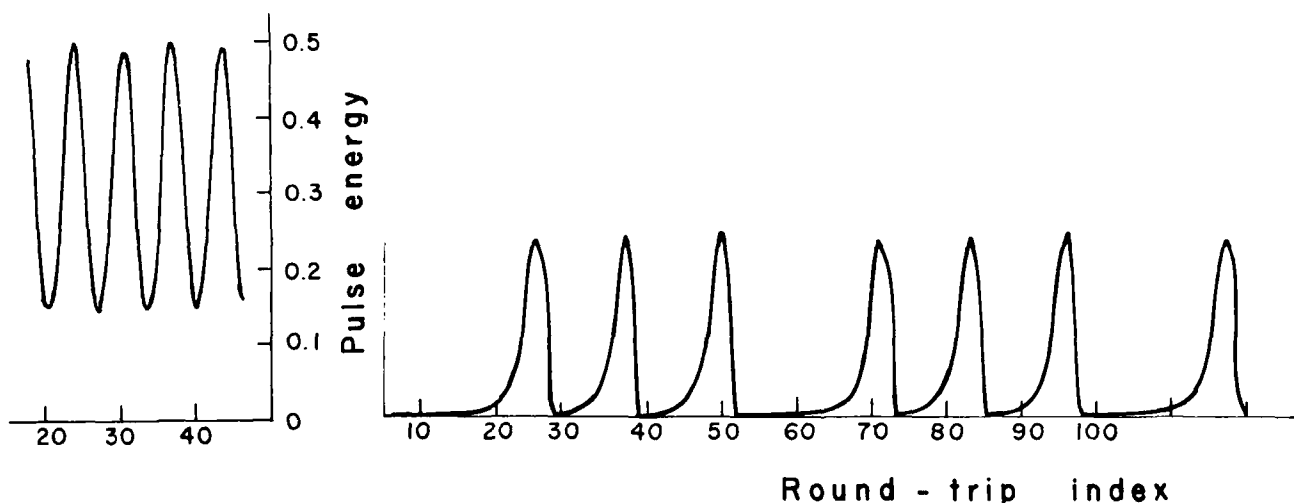
Figure 1 Pulse energy versus round-trip index. The reflection coefficient is r = 0.9, and the optical thickness of the absorber A = 0.8. The other parameters are: G = 1.1, s = 15, a = 0.1 (Fig 1a, left); and G = 1.2, s = 20 and a = 0.2 (Fig. 1b, right).

The global approach offers a description, rather than an understanding of the operation of the laser. In view of the the large number of parameters involved, it is very difficult to assign a particular function to any of them.

There are still physical phenomena and modes of operation excluded from the aforementioned theories. For instance, if a very large s parameter is used (very small focal spot in the absorber), it is possible to have a pulse corresponding to a full Rabi oscillation in the absorber, and linear gain in the amplifier. A quantum mechanical description of the absorber (with counterpropagating wave interaction) combined with a **linear** gain for the amplifier, leads to off-resonance steady state solutions [9]. The solutions are hyperbolic secant shaped (for the electric field amplitude) with an hyperbolic secant downchirp above resonance, or an upchirp below resonance. Similar coherent solutions have been predicted in computer simulations by Rudolph et al, in the case of smaller s parameters. This type of operation of the laser is particularly interesting, since it corresponds to a maximum energy extraction from the gain medium, as well as minimum losses from the absorber. A theoretical effort should be undertaken to determine all the parameters needed to synthesize a laser operating under these restricted, but particularly stable and efficient, conditions. However, a question that comes immediately to mind is whether one has sufficient control over the experimental parameters, as for instance the s factor defined in Eq. (6).

2.5. Controlling the "s parameter"

The effect of astigmatism on the stability range of a cavity is more drastic than is generally realized. Let us consider the idealized simple ring cavity sketched in Fig. 2.
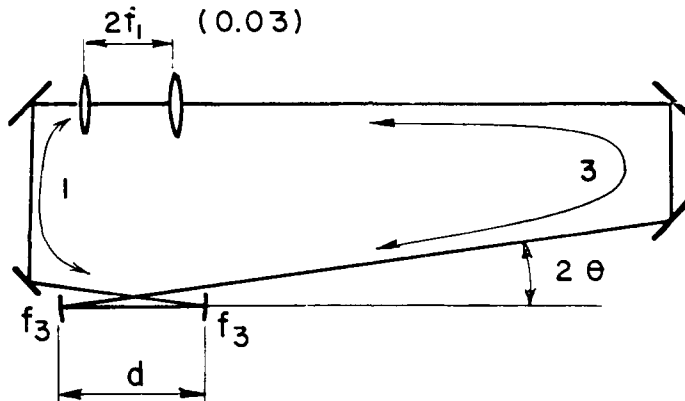
Figure 2: An elementary ring cavity

An ABCD matrix calculation on this cavity shows, in the ideal case of $\theta = 0°$, a stable region for $24 < d < 25.25$ mm. As the angle θ is increased however, the overlap of the stability regions in the sagittal and tangential planes decreases, vanishing even for $\theta > 6°$. Astigmatism being cumulative, one would expect even less overlap between stability regions in the sagittal and tangential planes, once the astigmatism at the absorber section is included. Detailed calculations [9, 19] show however that common intuition fails to assess correctly this complex situation. The astigmatism of one part of a cavity can be made to compensate that of other focusing elements, resulting in large stability regions and large variations of focal spot sizes - hence s factors - even at angles exceeding 15 or $20°$. For instance, with a focal spot of 4μm radius in the absorber section and 20μm in the amplifier, the antiresonant ring laser [19], with angles of $32°$ and $16°$ (at the gain and absorber sections, respectively) has an s parameter of 75. Changes in cavity parameters can enhance this value by an order of magnitude. Similarly, in the ring laser, complete analytical and numerical calculations carried out through the algebraic manipulation language MACSYMA show a range of variation of the s parameter of three orders of magnitude. The range of variation of the focal spot sizes in the absorber and amplifier jets can be extended by introducing an additional curved mirror in the ring cavity (typical radius of curvature: 1 m) [9]. The ratio of focal spots in the absorber and amplifying media is at most unity when this additional mirror is located close (0.3 to 0.5 m) to the absorber section. This same ratio can exceed 1000, with focal spots in the absorber jet of the order of $10 \mu m^2$, when this additional mirror is located in the proximity of the gain section [9].

2.3. The Dispersive Model

The previous approach neglected phase modulation and dispersive effects, which become important for pulse durations shorter than 500 fs. It is possible to construct a model for the mode-locked laser, based solely on phase modulation and dispersion, neglecting even saturation.

As a light pulse of electric field E traverses a transparent medium of time dependent index of refraction $n(t)$, its amplitude $\mathcal{E}$ remains unchanged, but its phase is incremented by $\omega n(t) d/c$, where ω is the light frequency, d is the thickness of medium traversed, and c is the speed of light. The electric field of the transmitted pulse becomes thus:

$$E(d, t) = E_0(0, t) \exp\{-i \frac{\omega}{c} n(t) d\} \tag{7}$$

An intensity dependent index of refraction results from saturating a dye off-resonance. If the radiation is sent below resonance through an absorbing dye jet, the resulting phase modulation has the temporal dependence $\exp\{-\int Idt/\mathcal{T}_g\}$, resulting in a downchirp during the major portion of the pulse. Such a type of frequency modulation dominates in lasers with a high concentration of saturable absorber (several mM) and a relatively small "s factor" (typically 4). The advantage of this type of operation is that the downchirped pulse can be compressed by the normal (positive) group velocity dispersion of a single prism of glass. It is possible to adjust the laser for either a bandwidth limited, of a linearly downchirped output [11]. For low concentrations of saturable absorber and a large "s parameter" however, phase modulation due to the Kerr effect dominates, resulting in an upchirp during most of the pulse. Such an upchirped pulse can be very efficiently compressed by negative dispersion, which can be obtained with a 4 prism sequence [12]. The phase modulation due to saturation below resonance of the dye still remains, and adds to that of the Kerr effect. This complex modulation results in an asymmetric spectrum of the pulse. However, larger compression factors, hence shorter pulses, can be obtained in this mode of operation.

Dispersion can be modeled as the frequency space analogue of phase modulation. The phase factor of the Fourier transform of the optical electric field is modified upon propagation through a transparent medium of thickness ℓ and index $n(\Omega)$ in a similar way as in (6):

$$E(\ell, \Omega) = E_0(0, \Omega) \exp\{-i \frac{\Omega}{c} n(\Omega) \ell\} \tag{8}$$

A model for mode-locking can be constructed on the base of Eqs (7) and (8) only. The approximations made are:
    a) thin medium, in order to expand the exponentials to first order;
    b) small change per step (hence per cavity round trip);
    c) Kerr effect nonlinearity in (7), $n(t) = n_0 + n_2 \mathcal{E}^2$;
    d) quadratic dispersion, obtained by expanding $n(\Omega)$ to second order in Ω.
Combination of Eqs. (7) and (8) results in the nonlinear Schrödinger equation [9, 13], which was solved by Zakharov and Shabat [14]. The solutions are either purely stationary (solitons of first order), or periodic (solitons of order n). Salin et al [13] have made the association between the higher order soliton solutions, and the modulation of the pulse train envelope observed often in mode-locked lasers [10]. It is rather intriguing that the two diametrically different approaches of sections 2.2 and 2.3 lead to similar conclusions.

2.4. Global Approach

It is clear that the drastic approximations that made the approaches taken in sections 2.2 and 2.3 mathematically elegant, at the same time made the model unrealistic. More rigorous approaches, incorporating both dispersion and saturation, have been made prior to the ones described above. Some of these calculations, and general features of the results, are summarized in table 1 below.

TABLE 1

Ref.	Approximations	Approach	Particular features	Comments
15 16	Small changes/cavity roundtrip Perturbation to second order to include coherent effects	Parametric fitting of sech shaped sol.	Coherent effects Dispersion Saturation	Correct lasing frequency (no filter included
17	" "	Numerical	Frequency filter	Periodic oscillations in pulse frequency and energy
18		Numerical	Noise source large changes / cavity round trip	Good fit for the laser under study

3. Single Shot Signal Characterization

The main purpose of developing sources of ultrashort laser pulses is to be able to time resolve fast events in physics, chemistry or biology. In a typical pump-probe experiment, an intense "pump" signal is used to excite the sample under investigation, which is subsequently probed by a weak pulse following after some delay. The probe pulse will determine for instance the complex susceptibility of the excited medium, by measuring the amplitude and phase of the transmitted and reflected signal. Since the probe can only sample the excited material after the pump pulse has decayed to negligible intensities (compared to the probe), such a technique is not able to investigate events that occur in the early (i.e. within the pump pulse duration) stages of the excitation. A more powerful method to determine the transient susceptibility of a sample is to directly measure, in amplitude and phase, the temporal modification of the excitation pulse in reflection and transmission. Such a technique has recently been proposed and implemented to determine the shape and chirp of the output of an antiresonant ring dye laser [19, 20]. The basic principle is to stretch out the signal to be measured by an operation involving a known transfer function. The original signal is determined by applying the reverse transformation to the temporally extended signal, the latter being measured through cross-correlation measurements with the original (shorter) pulse.

The simplest "stretching" operation is propagation through glass, which causes generally the pulse to be broadened by normal dispersion. The broader pulse is cross-correlated with the shorter one. The intensity cross-correlation yields information on the amplitude shape of the signal, while its phase can be extracted from the interferometric cross-correlation. The basic experimental set-up is a standard interferometric autocorrelator [9], in the arm of which a block of glass (typically 5 to 10 cm of BK7 or SF5 glass) has been inserted.

The accuracy of transient transmission measurements will be affected by statistical fluctuations as well in the source than in the sample. In particular, if laser damage is induced by each laser pulse, the measurement will be an average over many samples. There is in addition a significant pulse to pulse fluctuation in most high power amplifiers. Therefore, there is a need for a diagnostic method capable of capturing the amplitude and phase information of a fs signal in a single shot. Gyuzalian et al [21] have used the spatial distribution of the second harmonic in a non-colinear arrangement to determine the pulse duration. Salin et al [22] applied this method to the measurement of femtosecond pulses. Unfortunately, this method provides only an intensity autocorrelation, rather than a complete pulse characterization. We have recently proposed a single shot extension of the complete characterization method previously mentioned, in which the delay parameter is transferred to the transverse dimension of the beam [23]. In the sketch of Fig. 3, such a "transverse delay" is represented by a stepped mirror. Another possibility is to use group velocity dispersion in a prism, as used in the autocorrelator of Szabo et al [24], or a combination of both. The interferometric aspect of the crosscorrelation is obtained by slightly tilting one of the mirrors of the interferometer. The spatial recording of the second harmonic is a cross-correlation of the pulse broadened by glass with a reference pulse. The reconstruction procedure is identical to the one used for the cross-correlator using a mechanical delay line.
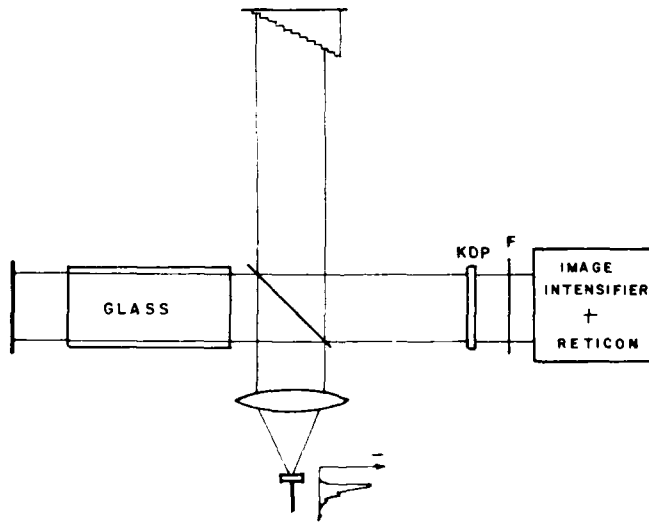
Figure 3

Acknowledgments

References

1. M. A. Duguay and J. W. Hansen, Appl. Phys. Lett. **15**, 192 (1972).

2. W. Rudolph and J.-C. Diels, "Femtosecond resolved fluorescence", Ultrafast Phenomena V, Springer Series in Chemical Physics **46**, 71, Springer Verlag (1986).

3. M. Mohebi, B. Jean-Jean and J.-C. Diels, "Reflection switching of Picosecond Pulses at Saturable Nonlinear Interfaces" Laser's 88 (this volume, 1988).

4. J.-C. Diels and C. Y. Wang, SPIE Meeting on Picosecond Lasers and Applications, SPIE **322**, 166-170 (1982).

5. J.-C. Diels, J. J. Fontaine, and W. Rudolph, Revue Phys. Appl. **22**, 1605-1611 (1987).

6. E. P. Ippen, C. V. Shank, and A. Dienes, Appl. Phys. Lett. **21**, 384 (1972).

7. J. A. Valdmanis, R. L. Fork, and J. P. Gordon, Optics Lett. **10**, 131 (1985).

8. R. L. Fork, Laser's 88.

9. J.-C. Diels, chapter on "Femtosecond Dye Lasers", in "Dye Lasers, principles and applications", Edited by F. J. Duarte and L. W. Hillman, to be published by Academic Press (1989).

10. J.-C. Diels, E. W. Van Stryland, and D. Gold, Picosecond Phenomena I, Springer Series in Chemical Physics **4**, Springer Verlag 117 (1978).

11. J.-C. Diels, J. J. Fontaine, I. C. McMichael, and F. Simoni, Applied Optics **24**, 1270 (1985).

12. R. L. Fork, O. E. Martinez, and J. P. Jordan, Opt. Lett. **9**, 150 (1984).

13. F. Salin, P. Grangier, G. Roger and A. Brun, Phys. Rev. Lett. **56**, 1132 (1986).

14. V. E. Zakharov and A. B. Shabat, Sov. Phys. JETP **34**, 62 (1971).

15. J.-C. Diels, J. J. Fontaine, I. C. McMichael, and B. Wilhelmi, Sov. J. of Quantum Electron. **13**, 1562 (1983).

16. J.-C. Diels, W. Dietel, J. J. Fontaine, W. Rudolph, and B. Wilhelmi, Journal of the Opt. Society B **2**, 680 (1985).

17. V. Petrov, W. Rudolph, U. Stamm, and B. Wilhelmi, to be published in Phys. Rev. **A**.

18. H. Avramopoulos, P. M. W. French, J. A. R. Williams, G. H. C. New, and J. R. Taylor, IEEE J. of Quantum Electron. **24**, 1984 (1988).

19. N. Jamasbi, J.-C. Diels and L. Sarger, J. Modern Opt. **35**, 1891 (1988).

20. J.-C. Diels, J. J. Fontaine, N. Jamasbi, Ming Lai and J. Mackey, "The Femtonitpicker", CLEO'87.

21. P. M. Gyuzalian, S. B. Sogomonian, and Z. Gy. Horvath, Optics Comm. **29**, 239-242 (1979).

22. F. Salin, P. Georges, G. Roger and A. Brun, Applied Optics **26**, 4528-4531 (1987).

23. J.-C. Diels, N. Jamasbi, C. Yan and M. Lai, SPIE conference on Advances in Semi-conductors and Superconductors, Newport Beach, CA. SPIE **942**, 190 (March 1988).

24. G. Szabo, Z. Bor and A. Müller, Opt. Lett. **13**, 746 (1988).

INTRACAVITY FREQUENCY DOUBLING IN PASSIVELY MODE-LOCKED LASERS

M. C. Downer, Glenn Focht, Paul Williams, and T. R. Zhang

Physics Department, University of Texas at Austin, Austin, TX 78712

ABSTRACT: We constructed a quantitative theoretical model of an intracavity frequency doubled and passively mode-locked laser and efficiently extracted an ultraviolet femtosecond pulse train of milliwatt average power and 100 MHz repetition rate from a colliding pulse mode-locked dye laser by intracavity frequency doubling in KDP.The ultraviolet and visible outputs, which are comparable in power and pulse duration, are perfectly synchronized with each other. The major findings are that for second harmonic conversion efficiencies consistent with continuing laser operation 1) a stable mode-locking regime always exists, although it narrows somewhat with increasing conversion efficiency; 2) the duration of the fundamental pulses can always be preserved, even in the femtosecond time domain, by re-adjusting saturable gain and saturable loss parameters; 3) the energy of the fundamental pulses can also be preserved under the same conditions.

Despite extensive developments of new femtosecond dye lasers operating from the green to the near infrared,[1] femtosecond source lasers in the blue and ultraviolet have been lacking. We recently demonstrated experimentally[2] that the simple non-perturbative technique of intracavity frequency doubling a visible wavelength, passively mode-locked, femtosecond dye laser could produce perfectly synchronized femtosecond ultraviolet and visible pulse trains, each at 100 MHz repetition rate and milliwatt average power. Our theoretical model[3] shows that saturable loss and gain media can compensate the destabilizing and pulse broadening influence of an intracavity frequency doubling crystal. Furthermore, our model defines quantitatively the regimes of saturable loss, saturable gain, and second harmonic conversion efficiency in which stable mode-locked operation is possible, as well as the effect of the frequency doubler on pulse duration and pulse energy within the stable regime. Our results suggest that stable intracavity frequency doubled operation, with synchronized ultraviolet and visible outputs of comparable power and pulse duration, should be generally achievable in all passively mode-locked lasers which employ saturable gain and loss media.

Fig. 1(a) depicts the essential mechanisms by which saturable loss and gain media, having relaxation times longer than the pulse duration, can compensate the destabilizing and pulse broadening effect of an intracavity frequency doubling. The intracavity fundamental pulse suffers temporal broadening in the doubling crystal because power dependent loss of second harmonic generation selectively attenuates the peak of the pulse. Passage through a saturable absorber, on the other hand, selectively attenuates and, therefore, sharpens the leading edge of the pulse. Analogously, saturation of the gain then sharpens the trailing edge. Appropriate adjustment of absorber and gain saturation levels can, therefore, precisely compensate for the pulse broadening effect caused by the second harmonic generation in the doubling crystal. The linear dispersion introduced by the crystal can be compensated by the now common intracavity prism configuration for negative dispersion. Also, the second harmonic pulses are broadened because of group velocity walk-off between the fundamental and second harmonic pulses, necessitating a thin doubling crystal to generate short ultraviolet pulses. However, the duration of the fundamental pulse, our chief concern, is unaffected by this walk-off, and therefore, was not considered in our analysis.

We augmented Haus' model[4] of a passively mode-locked laser with a slow saturable absorber by adding a frequency doubling element retaining the basic assumption that the intracavity pulse is perturbed only modestly upon passing through each intracavity element. Fig. 1(b) graphically illustrates the results of our model for the stable operating region as a function of saturable loss, q, saturable gain, g(i), and the dimensionless parameter for second harmonic conversion efficiency, γ. It can be seen from this figure that stable operation of the laser can always be recovered by adjusting the gain or loss, i.e. adjusting the pump power or intracavity focus into the saturable absorber. Figure 2 shows the pulse duration and energy as a function of saturable loss, and saturable gain for three different values of the second harmonic conversion efficiency. The points labeled A, B, and C all correspond to the same points on the figures 1(b), 2(a), and 2(b) and represent stable operating conditions at 0%, 1.2%, and 2.4% conversion efficiency with a pulse duration of 70 fs. These plots show that the original pulse width and energy can also always be recovered by a suitable readjustment of the saturable gain and loss parameters.This was confirmed by the observation of the laser at various operating conditions within the regime of stability.

We obtained efficient ultraviolet generation t y utilizing the high intracavity power of the fundamental red beam appropriately focused into a KDP doubling crystal. Figure 3 is a schematic of the subresonator where the doubling crystal was inserted into the laser cavity. The crystal was cut so that it would be at Brewster's angle when tuned to the type one phase matching angle for efficient second harmonic generation and would be thin enough (1 mm) to minimize broadening of the second harmonic pulses caused by group velocity walk-off and phase-matching bandwidth limitation. The ultraviolet second harmonic is extracted from the resonant cavity by a dichroic mirror coated for 99% reflectivity at 620 nm and 65 % transmission at 310 nm. The power of the extracted ultraviolet beam (~1mW) is sufficient to be easily measured with a calibrated power meter, and is brightly visible on a surface such as an ordinary business card which fluoresces in response to ultraviolet illumination. This ease of observation and measurement greatly facilitates experimental alignment of the extracted ultraviolet beam.

Figure 4 shows, (a), the autocorrelation traces and, (b), the spectral profile of the fundamental red pulse with (solid lines) and without (dashed lines) the doubling crystal inside the laser's resonant cavity. With a second harmonic conversion efficiency of approximately 0.3 %, the fundamental's pulse width was completely unmolested, remaining at 70 fs, and the slight difference in the spectral profile is due to the minor readjustment of the cavity required when the nonlinear crystal is inserted. Our calculation shows that a conversion efficiencies of up to 2% should be achievable while still maintaining stable operating conditions.

References

1. P.M.W. French and J.R. Taylor, **Ultrafast Phenomena V**, eds. G.R. Fleming and A.E. Siegman, (Springer-Verlag, Berlin, 1986), p. 11-13.
2. G. Focht and M.C. Downer, IEEE J. Quantum Electron., **24** (2), 431-434, (1988).
3. T. R. Zhang, G. Focht, P. E. Williams, and M. C. Downer, IEEE J. Quantum Electron., **24** (9), pp. 1877-1883, (1988).
4. Hermann A. Haus, IEEE J. Quantum Electron., vol. QE-11, pp. 736-746, Sept. 1975.
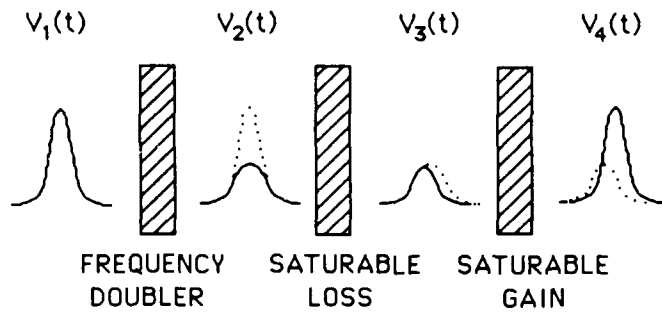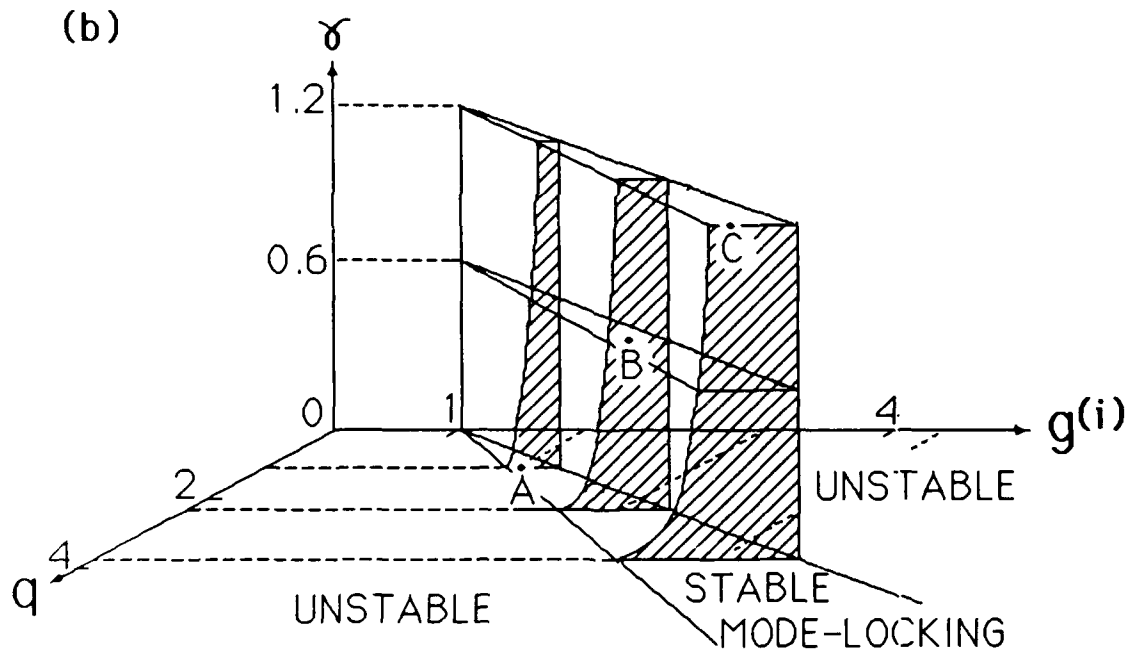
Fig. 1. (a)Changes in the intracavity pulse envelope upon the passage through the major components of a passively mode-locked laser with an intracavity frequency doubling crystal.(b)The stable operating regime as a function of saturable loss, q, saturable gain, g(i), and the dimensionless parameter for second harmonic conversion efficiency, γ.

(a) PULSE DURATION (fsec.)

$\gamma = 1.2$
$\gamma = 0.6$
$\gamma = 0$

(b) PULSE ENERGY(nJ)

$\gamma = 0$
$\gamma = 0.6$
$\gamma = 1.2$
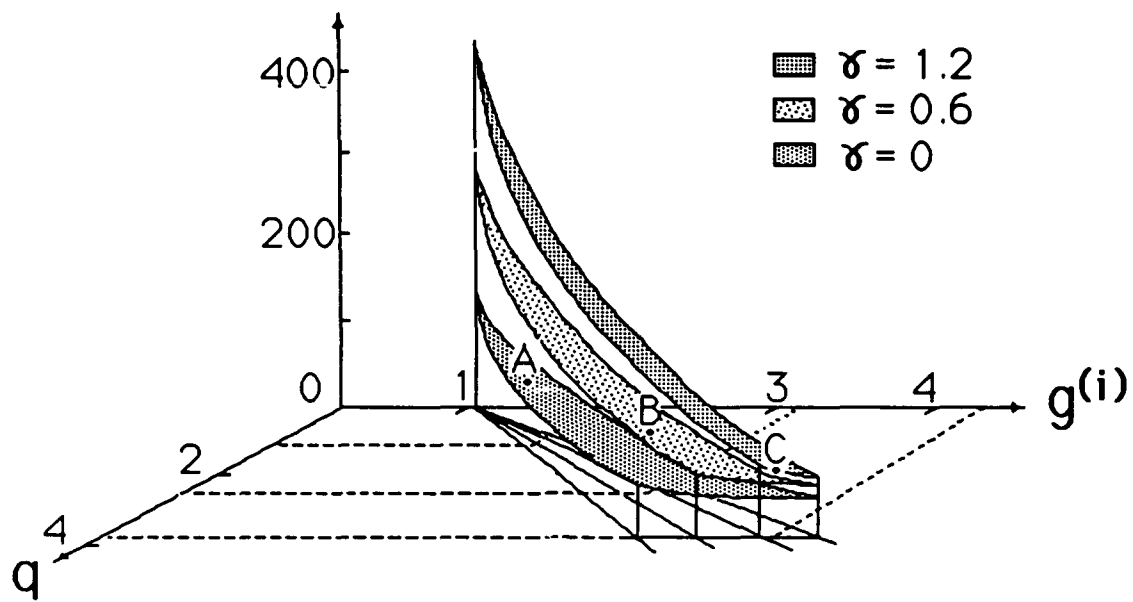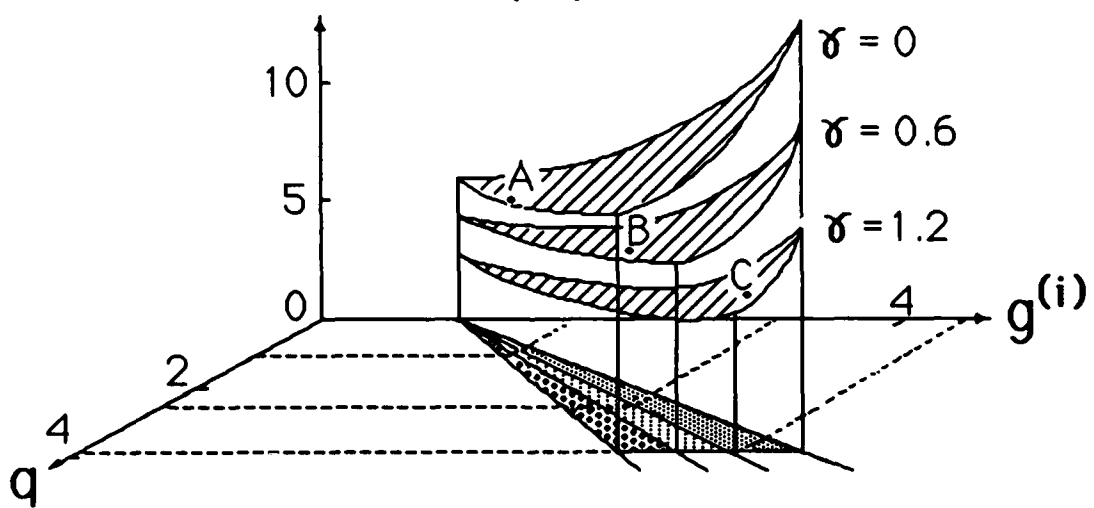
Fig. 2 Fundamental pulse, (a),duration and,(b), energy as a function of
saturable loss, q, saturable gain, g(i), and the dimensionless parameter for
second harmonic conversion efficiency, γ.

358

R = 10 cm

620nm INTRACAVITY
PULSE TRAIN

PHASE-MATCHED
BREWSTER ANGLE
KDP CRYSTAL

UV FEMTOSECOND
PULSE OUTPUT

DICHROIC
MIRROR
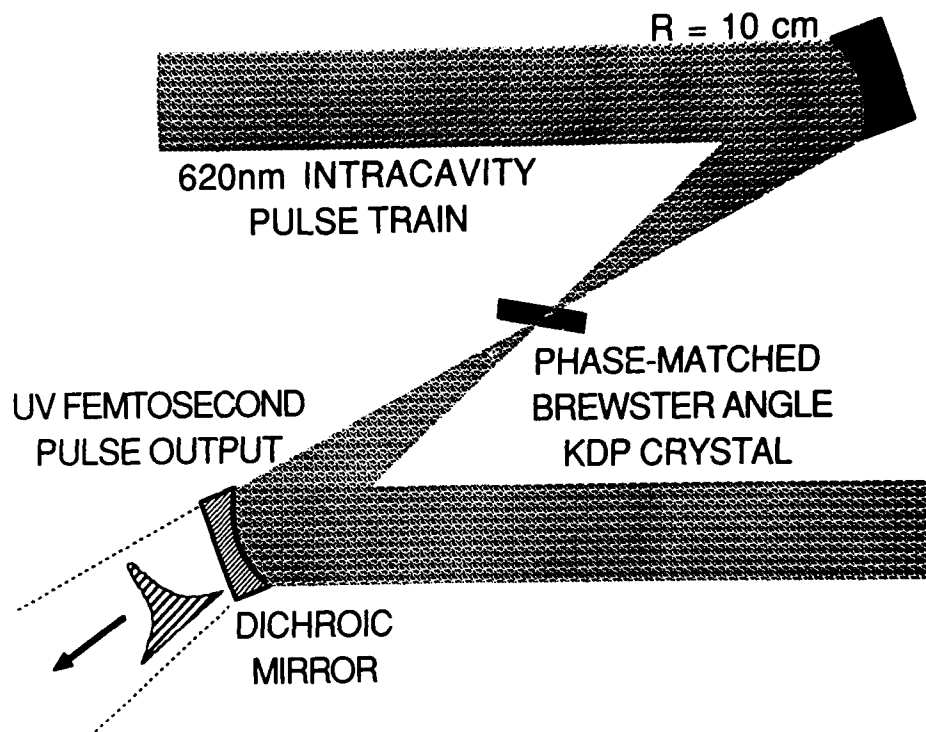
Fig. 3 Intracavity frequency doubling subresonator schematic.

(a)

SHG AUTOCORRELLATION
INTENSITY

70 fs

70 fs

(b)

RED SPECTRAL
INTENSITY

600   620   640
NANOMETERS
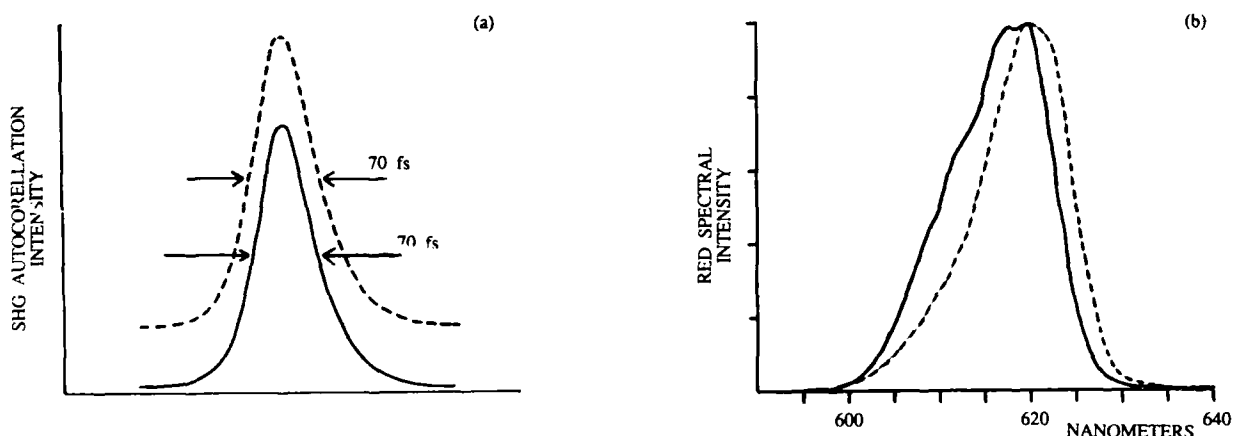
Fig.4. (a) Autocorrelation trace and, (b), spectral profile, with (solid lines)
and without (dashed lines) the intracavity frequency doubling crystal.

359

FEMTOSECOND PULSE GENERATION FROM THE ULTRAVIOLET TO THE NEAR INFRA RED

P.M.W. French, M.M. Opalinska, J.A.R. Williams and J.R. Taylor
Femtosecond Optics Group
H. Avramopoulos and G.H.C. New
Laser Theory Group
Physics Department, Imperial College, London SW7 2BZ

Abstract

Passively mode locked c.w. dye lasers now represent an important source of femtosecond optical pulses tunable through the visible and near infra red spectrum. Pulses as short as 70fs have been obtained from dispersion-optimised CPM cavity configurations using active/passive dyes other than the standard combination of Rhodamine 6G and DODCI. Complex pulse evolutions have been studied both experimentally and using a numerical simulation.

Passive mode locking is firmly established as a powerful and reliable technique for the generation of femtosecond optical pulses. As well as being proven capable of generating pulses of less than 30fs duration [1] in dispersion optimised cavities, it has the advantages of high (>100MHz) and/or variable repetition rate, low interpulse jitter (<1ps) and non-critical adjustment of cavity length. In addition, since it does not require a mode locked pump laser, it is cheaper, easier and potentially more tunable than its synchronously pumped counterparts.

Figure 1 shows the currently reported tuning ranges of passively mode locked c.w. dye lasers. Apart from the original Rhodamine 6G/DODCI system, all these active/passive dye combinations have been developed at Imperial College [2-9]. It should be noted that the Rhodamine 700/HITCI and DOTCI systems were pumped using a krypton ion laser while all the others were argon ion pumped - notably the Rhodamine 6G/sulphorhodamine 101, the DCM/Rhodamine 700 and the Pyriden 1/Rhodamine 800 energy transfer lasers. This technique of using an argon pumped "donor" dye whose fluorescence band overlaps the absorption band of an "acceptor" results in a highly efficient dye laser [eg. 10] and thus extends the tuning range of argon ion pumped systems into the infra red. It is interesting to note that the results obtained from the passive mode locking of the DCM/Rhodamine 700 energy transfer dye laser [9] were superior, in terms of minimum achieved pulse duration and amplitude stability, compared to the directly krypton-pumped Rhodamine 700 laser of reference 2. The Coumarin 102 laser [8] was pumped by the all lines u.v. output of a Spectra Physics model 171 u.v. enhanced argon ion laser and the Coumarin 6 laser was pumped by the 488nm line. The other argon ion pumped systems employed the all-lines visible output of a Spectra Physics model 2020 laser.
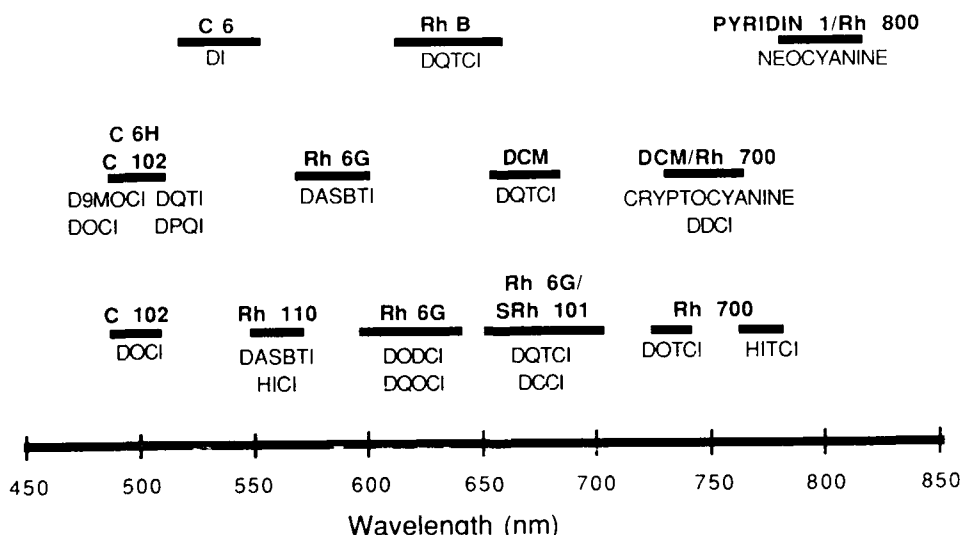
Figure 1. Currently available tuning ranges of passively mode locked c.w. dye lasers.

Initially, all the new argon ion pumped active/passive dye combinations reported here were demonstrated in a simple linear cavity in which no attempt was made to optimise the intracavity group velocity dispersion. Pulse durations typically around 250fs were obtained

across the range 490-615nm, depending on the particular values of the pump power and saturable absorber concentration.

With all these systems the pulses were not generally transform limited but exhibited sufficient bandwidth to support pulses of 120fs duration. Typical average output powers for these systems varied between 20mW and 140mW depending on the dye combinations and level of pump power. All of these systems exhibited good amplitude stability, as monitored via a photodiode (BPW28) and oscilloscope, which is characteristic of passively mode locked systems.

In order to demonstrate that the new active/passive dye combinations compare favourably with the standard of Rhodamine 6G with DODCI - thus showing that passive mode locking is an attractive source of femtosecond pulses over the visible and near infra red spectrum (perhaps the most attractive) - some of the new combinations were demonstrated in dispersion-optimised cavities.
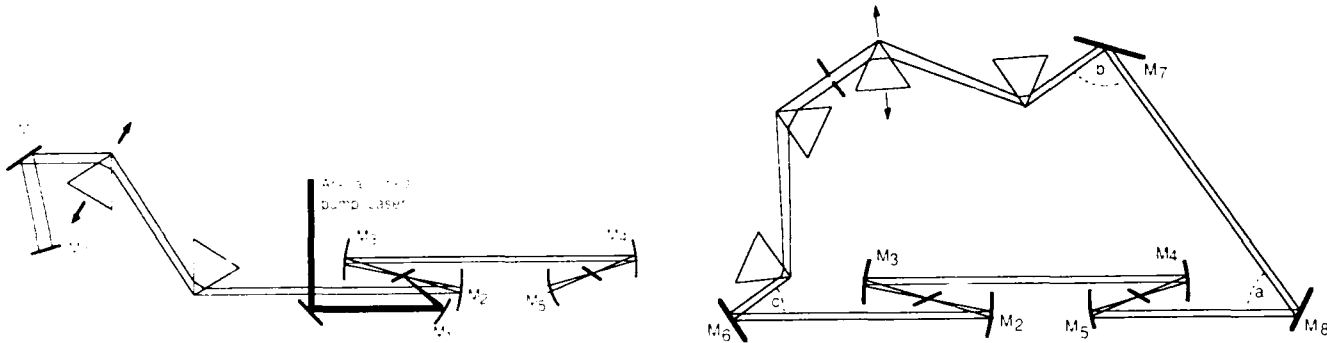
Figure 2.   Dispersion-optimised cavities: a) linear configuration; b) CPM ring configuration.
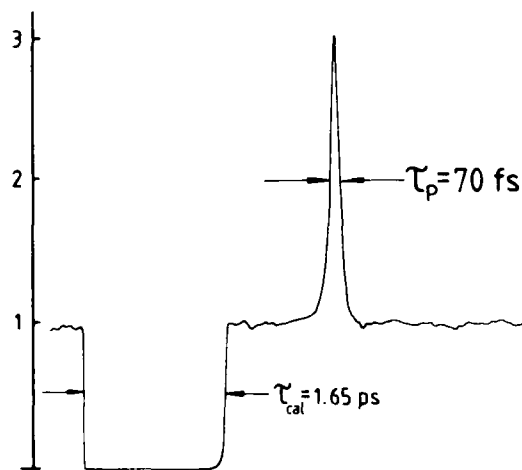
Figure 3.   Autocorrelation trace of pulses of 70fs duration obtained at 573nm.

Rhodamine 110, mode locked with HICI and DASBTI, was examined in both linear and CPM ring configurations [12] which incorporated narrow band single-stack dielectric mirror coatings, prism pairs and no standard bandwidth-limiting tuning elements. Optimisation of the intracavity group velocity dispersion was facilitated by the prism pairs (after Fork et al [13]) and by adjusting the angle of incidence to the narrow band dielectric mirrors (see eg. 14, 15). This latter adjustment also permitted some control of the laser wavelength since the mirrors acted as "long wavelength cut-off filters". Figure 2 shows two of the cavity configurations used.

From the linear cavity of figure 2(a), transform-limited pulses of 120fs duration were obtained for an angle a of 76° and an HICI concentration of 10^{-3}M. In this instance it was only mirror M_6 which restricted the laser wavelength or contributed to the intracavity dispersion – the other mirrors all being used near normal incidence. It was found that, unless there was some spectral control, the laser wavelength steadily increased with increasing absorber concentration and pulses of duration below 300fs could not be generated.

The shortest pulses were obtained from the configuration shown in figure 2(b). Here the mirror M_6, M_7 and M_8 contributed to both wavelength restriction and intracavity dispersion. Transform limited pulses of 70fs duration were obtained at 573nm with up to 60mW total average output power for 6.5W pump power with a 9ns cavity round trip time and angles a, b, c = 70°, 90°, 27° respective. Figure 3 shows an autocorrelation trace of these pulses and figure 4 shows how the autocorrelation trace varied as the intracavity glass path was decreased (a to l) via the translation of one of the prisms. Figure 5 shows the variation of the FWHM of the autocorrelation profile with intracavity glasspath.
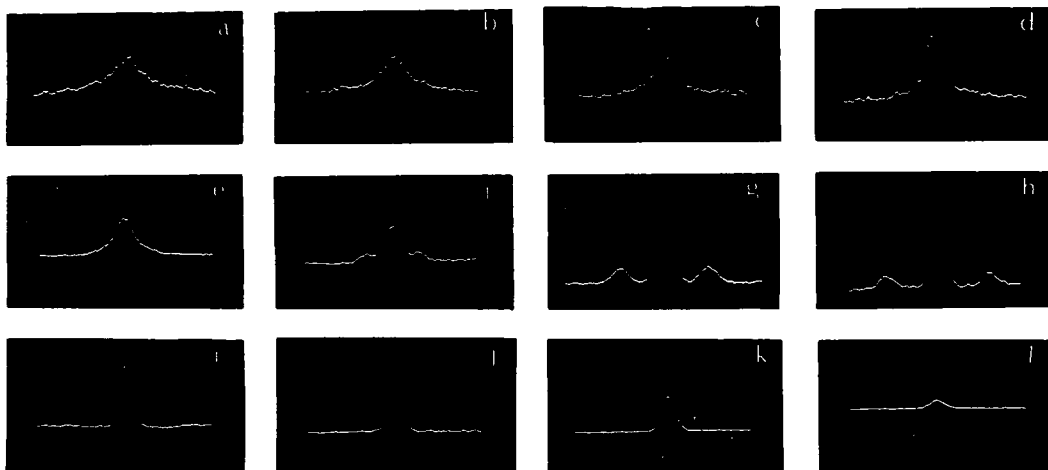
Figure 4. Evolution of autocorrelation trace as intracavity glass path is decreased (a-l).
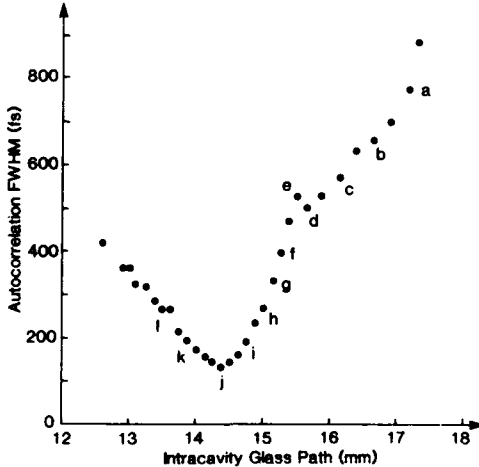
Figure 5. Variation of autocorrelation FWHM with intracavity glass path.

The lack of a strong asymmetry in the latter figure is in contrast to the results of Valdmanis et al [1] as is the observation that the shortest pulses appear to be obtained with the absorber at the focus of the passive folded section. It appears that the strong 'soliton shaping' of Martinez et al [16] is not dominant in this laser. With more intra-cavity glass path than that which yields the shortest pulses, a triple peaked autocorrela-tion trace appears, as seen in fig.4, which is reminiscent of the observations of 'high order soliton evolution' by Salin et al [17]. Recent theoretical work demonstrates that these observations can be simulated by a numerical model incorporating saturable absorption and gain, group velocity dispersion, the optical Kerr effect and the chirp arising from time dependant saturation of the absorber. A detailed account of the experiment and theoretical results is given in [18]. Figure 6 shows the theoretical evolution of the autocorrelation profile (averaged over 360 transits to simulate the integration of the real autocorrelation) as the intracavity GVD is decreased a to 1 and figure 7 shows the variation of the FWHM of the theoretical autocorrelation trace with intracavity GVD. The qualitative agreement between the experimental data and the numerical simulation is excellent (see ref [18] for further comparison) and it suggests the following points:

1. In this laser there are no higher order solitons present - the pulse evolution is not governed by the Nonlinear Schrödinger equation (NLS).

2. The shortest pulses obtained are transform-limited with $sech^2$ profiles. (This is only generally true for the optimum value of intracavity GVD).

3. The glass path corresponding to zero intracavity GVD can be determined for the experimental laser by comparing figures 4 and 6.

4. The relative strengths of the frequency chirping processes can be estimated from the parameter adjustment required to fit figures 4 and 5 with figures 6 and 7.
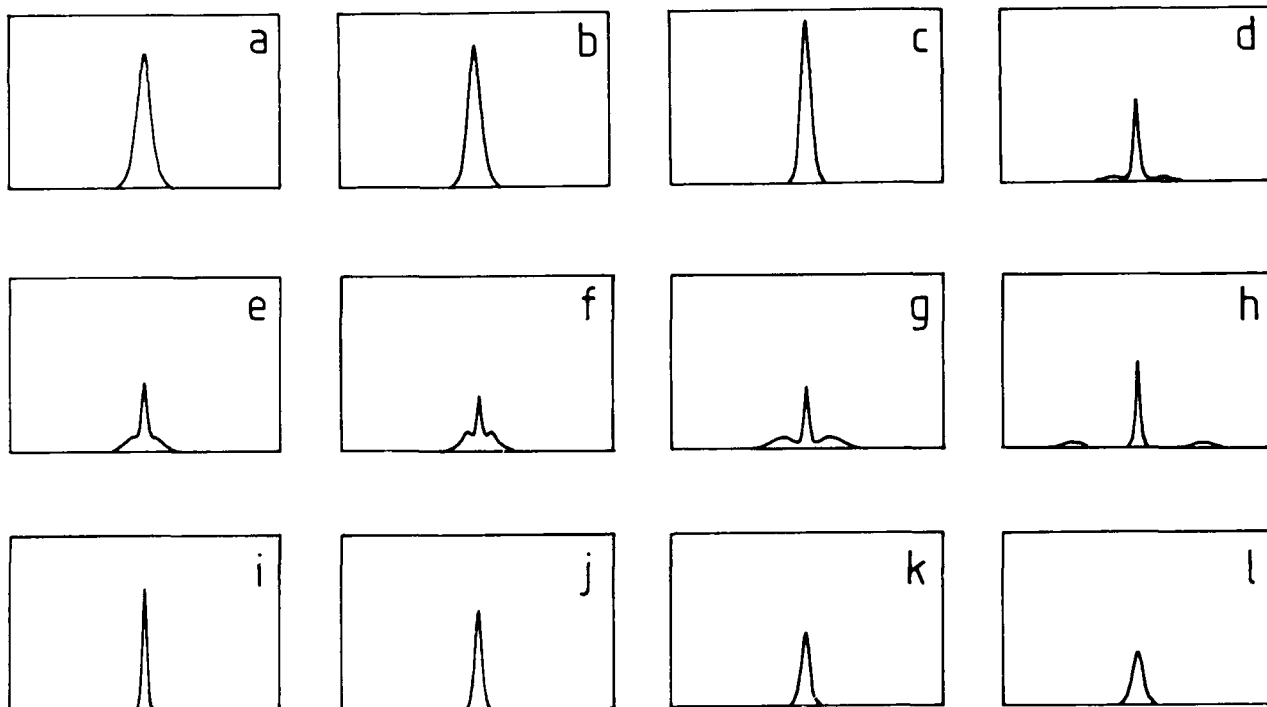
Figure 6.   Theoretical evolution of autocorrelation trace with intracavity GVD.
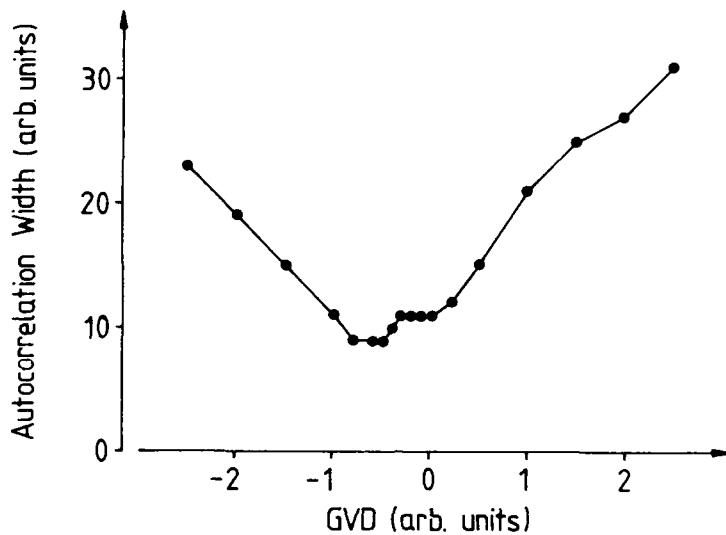
Figure 7.   Theoretical variation of autocorrelation FWHM with intracavity GVD.

Figure 8 shows the theoretical pulse evolution corresponding to trace 6 of figure 6 (i.e. zero intracavity GVD). Though periodic, it is clearly not governed by the NLS. Instead, a combination of frequency chirp and spectral filtering can be used to explain this behaviour. The resultant effect of the self phase modulation due to the optical Kerr effect and due to the time-dependent saturation of the absorption results in an increase in the mean carrier frequency of the pulse on each round trip. This means that the pulse frequency spectrum gradually 'walks' out of the gain profile of the laser and the energy is correspondingly reduced. Consequently, the amplifier is progressively less fully saturated and the undepleted gain then amplifies a second pulse which grows from noise and is, in turn, diminished through the spectral walk-off.

Carefully adjusting the parameters of the numerical model, it is possible to see high-order soliton-like pulse evolutions such as shown in figure 9. This regime, however, is achieved by reducing the strength of the passive mode locking and, consequently, the pulses are significantly longer than those represented by trace (i) of figure 7.

Using the same active/passive dyes, pulses of 80fs duration were obtained from a similar cavity in which the prism sequence was omitted – thus only the dielectric mirrors were used to optimise the intracavity dispersion. With the DCM/Rhodamine 700 energy transfer mode locked using DDCI, a CPM ring cavity was constructed which yielded transform limited pulses as short as 110fs duration from 742nm to 745nm [9]. Again the prism sequence was omitted and so both the laser wavelength and intracavity dispersion were determined by the angles of incidence at the cavity mirrors.

In the blue-green spectral region, the low efficiencies of the Coumarin dyes preclude the use of "off-resonance" dielectric mirrors to tune the cavity because of the high linear loss entailed in such a scheme. Instead, a CPM cavity based on the design by Valdmanis et al [1] was adopted where an aperture, located at the midpoint of the prism sequence, was used to control the laser wavelength. This is shown in figure 10. In this manner, pulses as short as 93fs were generated. At ^197nm, assuming the standard compression factor of~$\sqrt{2}$ in the frequency doubling, pulses of 65fs duration should be attainable at248.5nm with a transform-limited bandwidth of the order of the gain linewidth of KrF laser amplifiers. The spectral region from 200nm to 400nm should, in principle, be readily accessible through extracavity or intracavity frequency doubling and this will be of importance for molecular spectroscopy.

In conclusion, passive mode locking has been demonstrated as an effective technique for generating femtosecond pulses over the visible and near infra red spectrum. It has been shown that pulses of 100fs duration are obtainable from these new active/passive dye combinations when used in lasers with appropriate optimisation of the intracavity group velocity dispersion. Most, if not all, of these new dye combinations should yield such short pulses and it is highly likely that the preliminary results presented here will be considerably improved upon. All of these dyes will also work in synchronously pumped,

hybridly mode locked lasers. Various differences have been noted in comparison with reports of lasers using the standard combination of Rhodamine 6G and DODCI. In particular, the CPM configuration appears to yield shorter pulses than the dispersion-optimised linear cavities and the lasers need to be constrained to work at the wavelengths which give the shortest pulses. Further investigations of new active/passive dye lasers should afford greater insight into the mechanisms of passively mode locked lasers generally.
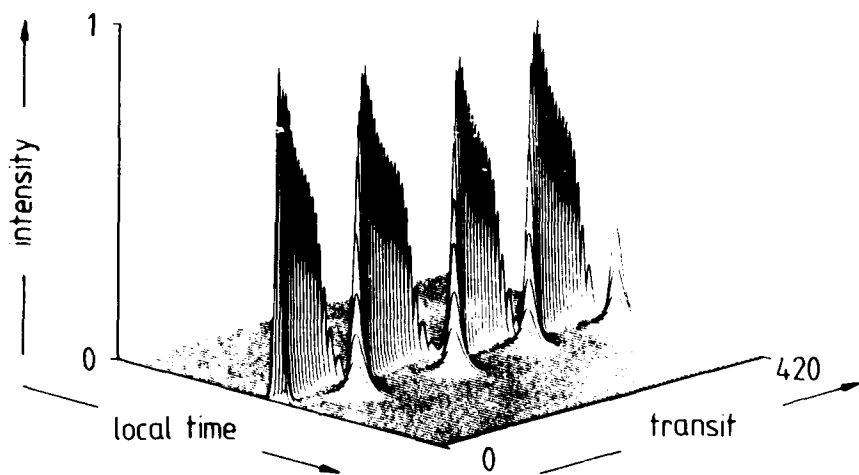
Figure 8. Theoretical pulse evolution for zero intracavity GVD.
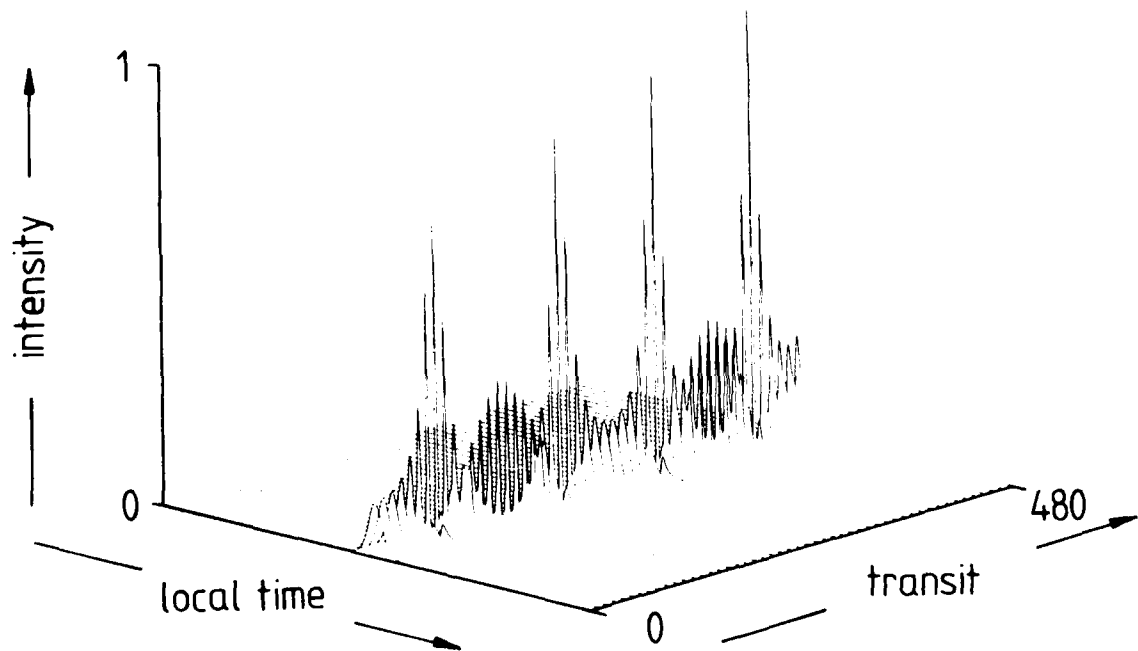
Figure 9. Theoretical pulse evolution similar to that of an N=3 soliton.
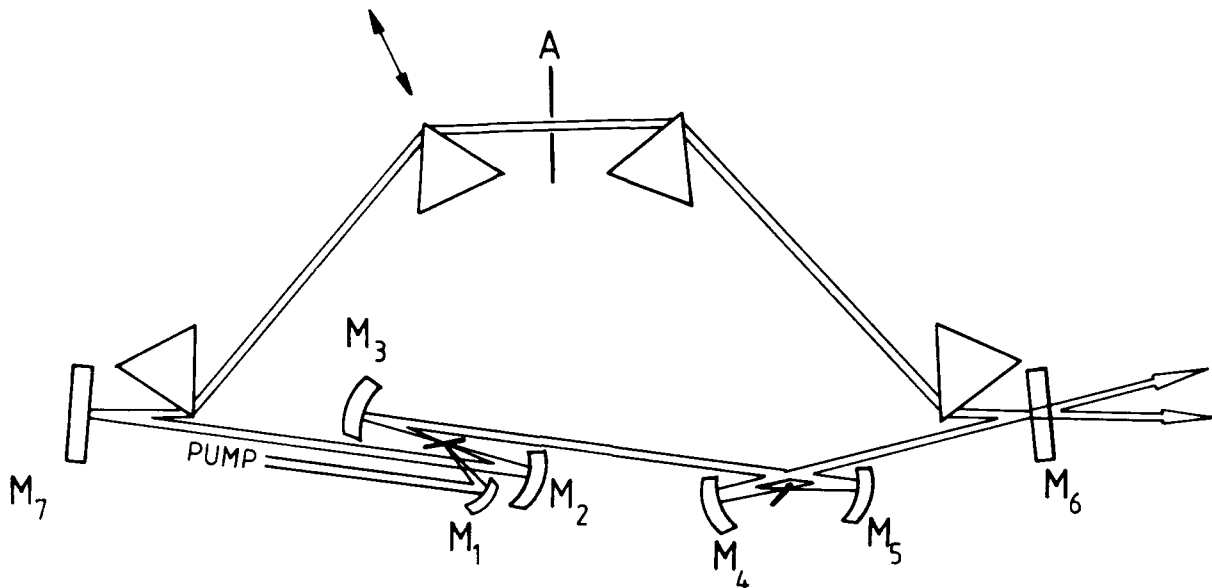
Figure 10. CPM ring cavity used for Coumarin femtosecond dye lasers.

References

1.   J.A. Valdmanis, R.L. Fork and J.P. Gordon, Optics Lett 10 131 (1985).
2.   K. Smith, N. Langford, W. Sibbett and J.R. Taylor, Optics Lett 10 559 (1985).
3.   P.M.W. French, M.D. Dawson and J.R. Taylor, Optics Commun 50 430 (1986).
4.   P.M.W. French and J.R. Taylor, Optics Lett 11 297 (1986).
5.   P.M.W. French and J.R. Taylor, Optics Commun 58 53 (1986).
6.   P.M.W. French and J.R. Taylor, IEEE J. Quantum electron QE-22 1162 (1986).
7.   P.M.W. French and J.R. Taylor, Appl Phys B 41 53 (1986).
8.   P.M.W. French and J.R. Taylor, Optics Lett 13 470 (1988).
9.   P.M.W. French, J.A.R. Williams and J.R. Taylor, Optics Lett 12 684 (1987), and
      P.M.W. French, J.A.R. Williams, J.R. Taylor and H. Goldsmith, Optics Lett 13 811 (1988).
10.   E.G. Macason, Optics Commun 40 212 (1982).
11.   G.H.C. New, IEEE J. Quantum electron QE-10 115 (1974).
12.   P.M.W. French and J.R. Taylor, Optics Commun 63 224 (1987).
13.   R.L. Fork, O.E. Martinez and J.P. Gordon, Optics Lett 9 156 (1984).
14.   S. De Silvestri, P. Laporta and O. Svelto, Optics Lett 9 335 (1984).
15.   W. Dietel, E. Dopel, K. Hehl, W. Rudolph and E. Schmidt, Optics Commun 50 179 (1984).
16.   O.E. Martinez, J.P. Gordon and R.L. Fork, Ultrafast Phenomena IV, Springer Verlag,
      Series in Chemical Physics, vol.38 (Springer, Berlin, Heidelberg, New York, Tokyo,
      1984) p7.
17.   F. Salin, P. Grangier, G. Roger and A. Brun, Phys Rev Lett 56 1132 (1986).
18.   H. Avramopoulos, P.M.W. French, J.A.R. Williams, G.H.C. New and J.R. Taylor, IEEE J.
      Quantum Electron QE-24 1884 (1988).

ATTOSECOND MODULATION IN SODIUM VAPOR

D. DeBeer, E. Usadi, and S. R. Hartmann
Columbia Radiation Laboratory, Department of Physics, Columbia University
538 W. 120 St., Box 41, New York, NY 10027
(212) 854-3273

ABSTRACT

Two transient time-delayed four-wave mixing experiments have been performed on the Na D doublet and modulations of 1.9 picoseconds and 980 attoseconds have been observed. These periods correspond to the difference and sum frequencies of the two Na D lines. Both experiments were performed using 7 ns pulses of light with frequency components at each of the D-line transitions. The effects of superposition-state modulations are observed in the integrated TDFWM signal as a function of the time delay. As the time delay is varied, the lowest diffraction order mixing signal is modulated. Higher diffraction order mixing signals contain modulation components at integral multiples of the beat frequency. In the case of the difference frequency beats this modulation exists even for delays greater than the excitation pulse width. This work thus extends photon-echo modulation spectroscopy into a new regime to study coherences between states that are widely separated in frequency compared with the bandwidth of the exciting laser pulses.

1. INTRODUCTION

Time-Delayed Four-Wave Mixing (TDFWM) experiments can yield spectroscopic and relaxation information about certain physical systems. In this paper we present the results of several such experiments performed in sodium vapor using pulsed laser excitation sources. The experiments we have done have in common the property that the excitation pulses interact with more than one transition in the sample resulting in interferences manifesting themselves as modulations in the TDFWM signal. Much of this work has been published.[1,2,3] In this introduction I will try to give a simple overview of what was done and what the results were. A brief historical survey will introduce this overview and a simple physical picture for interpreting the phenomena will follow. In Section 2 a more rigorous theoretical treatment will be given. Several predictions from this treatment have been verified experimentally and these results will be presented in Section 3. Section 4 will discuss the photon echo regime. Photon echoes can be thought of as four-wave mixing signals produced when the excitation pulses do not overlap in time. Section 5 will discuss possible applications of the techniques we have developed. The concluding section will try to indicate why this work is of interest to the burgeoning fields of broadband- and ultrashort- pulse spectroscopy even though our excitation pulses were neither broadband nor ultrashort.

OVERVIEW AND HISTORICAL SURVEY

Four-wave mixing is a process that involves the interaction of four light fields. It is nonlinear in that it depends on the third-order susceptibility $\chi^{(3)}$. There are several beam geometries in common usage. One that is closely related to our setup is shown in Figure 1.1. Consider the beams with wavevectors k_1 and k_2 to be incident on a nonlinear sample. The probe beam k_p then scatters off the sample producing four-wave mixing signals with wavevectors $k_s = k_p \pm (k_1 - k_2)$ providing the geometry allows for phase matching, that is, that the resulting wavevector, k_s, satisfies $|k_s| = \omega_s/c$. In the geometry illustrated the probe field has been made coincident with one of the pump fields. If we let the field with wavevector k_2 act as the probe field ($k_p = k_2$) this results in the signal fields being emitted in the k_1 and $2k_2 - k_1$ directions. The field emitted into the k_1 direction coincides with one of the pump fields making it difficult to observe whereas the field emitted into the $2k_2 - k_1$ direction is easily distinguished from the pump fields and is thus the signal of interest in practical experiments. In general there are three

$$k_p, \omega_p$$
$$k_2, \omega_2$$
$$k_1, \omega_1$$

$$k_s = k_p - (k_2 - k_1)$$
$$\omega_s = \omega_p - (\omega_2 - \omega_1)$$

$$k_s = k_p + (k_2 - k_1)$$
$$\omega_s = \omega_p + (\omega_2 - \omega_1)$$
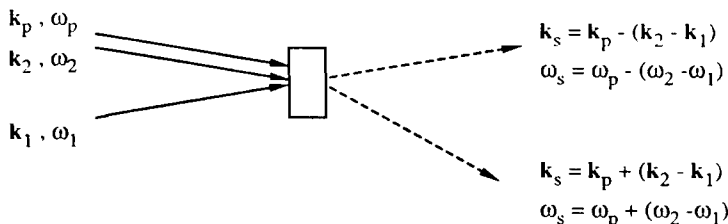
Figure 1.1 Schematic showing a general four-wave mixing scheme.

input fields and one emitted signal field comprising the four fields. In this geometry there are really only two input fields and from the symmetry of this geometry there are two emitted fields of interest, those in the $2k_2 - k_1$ and $2k_1 - k_2$ directions. We note that phase matching is not perfect in this geometry, but that the phase mismatch is small if the angle between k_1 and k_2 is small. Four-wave mixing is called degenerate when all four beams have the same frequency. We will be considering only the degenerate case throughout this paper.

The first observation of four-wave mixing is widely attributed to Maker and Terhune.[4] It is interesting to note that the photon echo, a type four-wave mixing signal for which not all input beams are coincident in time, was observed independently by Hartmann and co-workers[5,6] at about the same time.
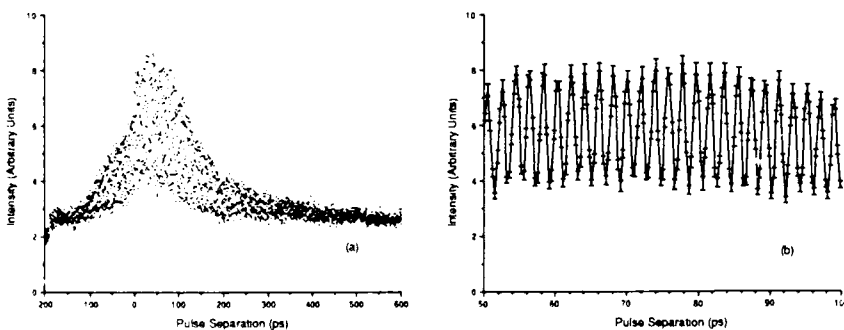
Figure 1.2 (a) Experimentally measured signal intensity vs excitation pulse separation in a 10-cm-long Na cell at 445 K. (b) A portion of the same data, for pulse separations of 50-100 ps, with error bars and lines connecting the data. The 1.9 ps modulation is due to the Na 3P fine-structure beating.
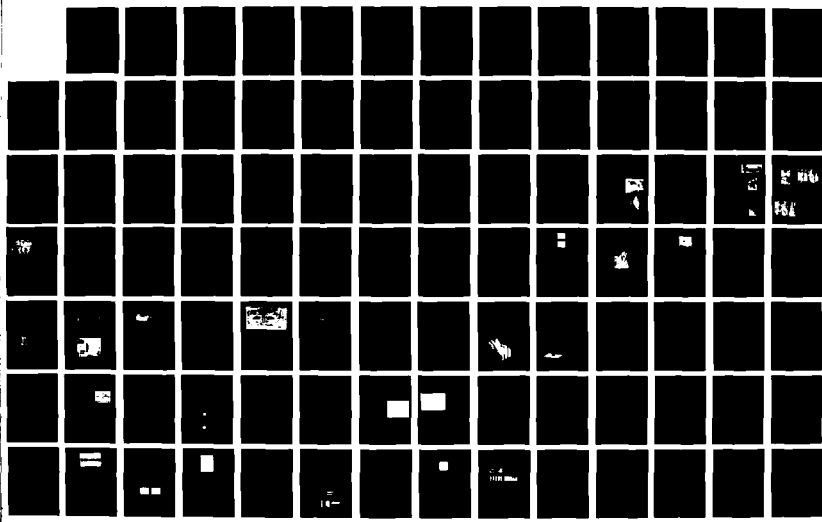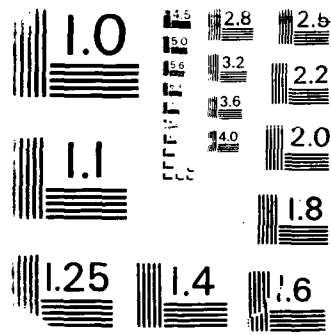
Four-wave mixing is called time-delayed when the signal is monitored as a function of a time delay, τ, introduced between the input pulses (k_1 and k_2 in Figure 1.1). This is sometimes done in order to investigate relaxation processes in the sample. In 1985 we did an experiment of this type[1] in which we observed relaxation induced by the incident light fields as well as from Doppler dephasing in a gaseous sample. Some of the data from that experiment are shown in Figure 1.2. From the data in Figure 1.2a the Doppler dephasing time T_2^* and the light-induced relaxation at large τ can be inferred.[1] The light used in that experiment had a bandwidth of about 12Å which explains how such short relaxation times could be measured using 7 ns excitation pulses. A "side-effect" of using such broadband light was that it interacted with both of the D-line transitions in the sodium sample resulting in interferences that were observable in the signal. Figure 1.2b shows a blowup of the same data in Figure 1.2a for time delays in the 50 to 100 ps range. The interference between the two transitions is clear. The period of 1.9 ps corresponds to the difference frequency of the D-lines.

The experiments described in this paper took their starting point with the data shown in Figure 1.2b. That is, we explore here this "side-effect" modulation of the TDFWM signal. The first experiment we did was to replace the broadband source with a source that had frequency components just at the two D-line frequencies. This resulted in a modulated TDFWM signal as before. These could perhaps be thought of as eight-wave mixing experiments, but I think they are better thought of as two four-wave mixing experiments being performed simultaneously on different transitions. It is interesting to note that at essentially the same time that we did these experiments, two other groups also observed beating at the difference frequency between the D-lines in sodium.[7,8]

Faster beats can be obtained by performing this experiment on two transitions with a larger difference frequency in order to obtain a faster beat. Mossberg and co-workers did a similar experiment with broadband light on the D-lines in rubidium resulting in a beat with a period of 139 fs.[9] To produce still faster beats becomes difficult due the large frequency differences necessary. However, by changing the geometry of the excitation beams a modulation at the sum-frequency of the two transitions can be generated. We again worked on the D-lines in sodium and this time obtained a beat with a period of 980 as (attoseconds).

The phenomena described above can be understood in terms of a simple picture involving gratings.

GRATING ANALYSIS

Four-wave mixing can be thought of as a scattering process in which two incident fields form a population grating in a sample and a third field is scattered off this grating. In our experiments the third field is self-same with one of the two incident fields. To understand the origin of the grating one merely has to calculate the intensity of the incident fields in the sample. The input fields can be written:

$$E = E_0\left[\cos\left(\omega t - k_1 \cdot r\right) + \cos\left(\omega(t - \tau) - k_2 \cdot r\right)\right]$$
$$= 2E_0\cos\left[\omega\left(t - \frac{\tau}{2}\right) - \frac{k_1 + k_2}{2} \cdot r\right]\cos\left[\frac{k_2 - k_1}{2} \cdot r - \frac{\omega\tau}{2}\right]$$

(1.1)

where τ is the amount by which the k_2 beam has been delayed with respect to the k_1 beam. The resulting intensity distribution (averaged over an optical period) in the sample is:

$$I = E_0^2\left[1 + \cos\left(\left(k_2 - k_1\right) \cdot r - \omega\tau\right)\right]$$

(1.2)
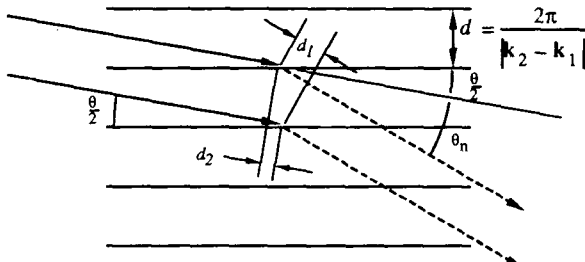
$$d = \frac{2\pi}{|k_2 - k_1|}$$

Figure 1.3 Diagram showing showing scattering from a grating.

Thus an intensity grating is formed in the sample. This produces a population grating with spacing $d=2\pi/|k_2 - k_1|$. Defining the angle between k_1 and k_2 as θ this grating scatters the beam with wavevector k_2 by an angle $n\theta$ (for scattering order n). This is easily seen from a simple diffraction grating analysis; we refer to Figure 1.3. Constructive interference of light scattered from adjacent planes requires $d_1 - d_2 = n\lambda$. If the angles are small, as they are in our experiments, this reduces to $d\left(\left(\frac{\theta}{2} + \theta_n\right) - \frac{\theta}{2}\right) = n\lambda$. Since $d = \frac{\lambda}{\theta}$ we have $\theta_n = n\theta$ as stated above.

When four-wave mixing is done on two transitions simultaneously two gratings are formed. If one imposes the geometry $(k_2 - k_1) = \pm(k'_2 - k'_1)$ then the gratings formed have the same spacing but are offset with respect to each other by a distance, s, obtained from $\Delta\omega\tau/2\pi = s/d$ where $\Delta\omega$ is the difference or sum of the two transition frequencies depending on whether $k_2 - k_1$ is chosen to be plus or minus $k'_2 - k'_1$. It is now easy to visualize what is happening in the two geometries. When k_2 is delayed with respect to k_1 the grating formed by those two beams simply scans in the $k_2 - k_1$ direction. In both geometries when $\tau = 0$ the gratings overlap and light scatters from both gratings in phase leading to constructive interference. However, as τ is increased the two gratings move and become displaced from each other. When one grating is displaced a distance s =d/2 with respect to the other there is total destructive interference of the scattered waves. Thus as τ is varied there is a modulation of the scattered light. The frequency of modulation depends on the geometry. In the $(k_2 - k_1) = (k'_2 - k'_1)$ geometry as τ is varied both gratings move in the same direction but at slightly different rates. This leads to a vernier type effect resulting in modulation at the difference-frequency of the transitions. In the $(k_2 - k_1) = -(k'_2 - k'_1)$ geometry the gratings move in opposite directions as τ is varied leading to a sum-frequency modulation. To be slightly more rigorous consider a wave scattering off adjacent gratings displaced by s. The two scattered waves have a relative phase shift of $\Delta\Phi = 2\pi s\theta_n/\lambda$. Using the relations from the previous paragraph we have $\Delta\Phi = n\Delta\omega\tau$. As a result, modulations are expected in the interfering four-wave mixing signals as a function of τ. This simplified analysis is correct only for n=1 where it includes all scattering pathways. The correct expression for the modulation behavior for all n is obtained by directly calculating the induced polarization from a step function excitation field of the form of Eq. 1.1. This will be done in Section 2.

2. THEORY OF TIME-DELAYED FOUR-WAVE MIXING

The grating analysis presented in Section 1 provides a visual picture that allows an intuitive grasp of the modulation phenomenon. We turn now to a rigorous calculation of the field emitted by the sample when it is excited by prompt and delayed input fields. We model the sample as a three-level system with dipole transitions at Ω and Ω' as shown in Figure 2.1. Assume that all the fields, prompt and delayed, are "turned on" at time t=0. Consider input fields with wavevectors k_1 and k_2 at frequency Ω and fields with wavevectors k'_1 and k'_2 at frequency Ω'. Each wavevector can contain both prompt and delayed fields. Assuming the excitation fields are single mode and exactly on resonance with the atomic transitions, and neglecting relaxation effects within the sample the Hamiltonian for this system is:

368

$$H = \frac{h}{2\pi}\begin{pmatrix} 0 & A & A' \\ A^* & \Omega & 0 \\ A'^* & 0 & \Omega' \end{pmatrix},$$ (2.1)

$$A = -\Omega_R\Big\{ e_{1p}\cos[\Omega t - \mathbf{k}_1\cdot\mathbf{r} + \phi_1] + e_{1d}\cos[\Omega(t-\tau) - \mathbf{k}_1\cdot\mathbf{r} + \phi_1]$$
$$+ e_{2p}\cos[\Omega t - \mathbf{k}_2\cdot\mathbf{r} + \phi_2] + e_{2d}\cos[\Omega(t-\tau) - \mathbf{k}_2\cdot\mathbf{r} + \phi_2] \Big\}$$

where $\Omega_R \equiv pE$ is the Rabi frequency of the dipole interaction coupling of the 1 and 2 levels, $\mathbf{k}_1$ and $\mathbf{k}_2$ are wavevectors at frequency Ω ($k = \Omega/c = 2\pi/\lambda$), and ϕ_1 and ϕ_2 are arbitrary phase factors. The quantities $e_{1p}, e_{1d}, e_{2p},$ and e_{2d} are either 0 or 1 depending on whether that field is present in a particular experiment. The corresponding quantities relating to the 1-3 transition are primed. The Schrödinger equation:

Fig. 2.1 Simple 3-level system

$$\psi = -\frac{2\pi i}{h} H\psi, \qquad \psi = \begin{pmatrix} \psi_1 \\ \psi_2 \\ \psi_3 \end{pmatrix}$$ (2.2)

can be solved in the rotating wave approximation. One finds

$$\psi(t) = \frac{1}{\lambda}\begin{pmatrix} \lambda\cos\lambda t \\ -ia^* e^{-i\Omega t}\sin\lambda t \\ -ia'^* e^{-i\Omega' t}\sin\lambda t \end{pmatrix}$$ (2.3)

$$\lambda = \sqrt{|a|^2 + |a'|^2}$$

$$a = -\frac{\Omega_R}{2}\Big[e_{1p}e^{-i(\mathbf{k}_1\cdot\mathbf{r}-\phi_1)} + e_{1d}e^{-i(\Omega\tau+\mathbf{k}_1\cdot\mathbf{r}-\phi_1)} + e_{2p}e^{-i(\mathbf{k}_2\cdot\mathbf{r}-\phi_2)} + e_{2d}e^{-i(\Omega\tau+\mathbf{k}_2\cdot\mathbf{r}-\phi_2)} \Big],$$

and a' has the same form as a except with all relevant quantities are primed. The polarization of the sample is:

$$\mathcal{P}(t) = \langle\psi(t)|\begin{pmatrix} 0 & p & p' \\ p^* & 0 & 0 \\ p'^* & 0 & 0 \end{pmatrix}|\psi(t)\rangle$$
$$= \psi_1^*\big(p\psi_2 + p'\psi_3 \big) + c.\,c.$$ (2.4)

Thus the polarization of the sample is obtained in closed form, exact in the rotating wave approximation:

$$\mathcal{P}(t) = \Big\{ p\Omega_R\big(e_{1p}\sin[\Omega t - \mathbf{k}_1\cdot\mathbf{r} + \phi_1] + e_{1d}\sin[\Omega(t-\tau) - \mathbf{k}_1\cdot\mathbf{r} + \phi_1]$$
$$+ e_{2p}\sin[\Omega t - \mathbf{k}_2\cdot\mathbf{r} + \phi_2] + e_{2d}\sin[\Omega(t-\tau) - \mathbf{k}_2\cdot\mathbf{r} + \phi_2]\big)$$
$$+ p'\Omega'_R\big(e'_{1p}\sin[\Omega' t - \mathbf{k}'_1\cdot\mathbf{r} + \phi'_1] + e'_{1d}\sin[\Omega'(t-\tau) - \mathbf{k}'_1\cdot\mathbf{r} + \phi'_1]$$
$$+ e'_{2p}\sin[\Omega' t - \mathbf{k}'_2\cdot\mathbf{r} + \phi'_2] + e'_{2d}\sin[\Omega'(t-\tau) - \mathbf{k}'_2\cdot\mathbf{r} + \phi'_2]\big) \Big\}$$
$$\times \frac{\sin 2\lambda t}{2\lambda}$$ (2.5)

where

$$|a|^2 = \frac{\Omega_R^2}{4}\Big\{ e_{1p}^2 + e_{1d}^2 + e_{2p}^2 + e_{2d}^2 + 2\big(e_{1p}e_{1d} + e_{2p}e_{2d}\big)\cos\Omega\tau + 2\big(e_{1p}e_{2p} + e_{1d}e_{2d}\big)\cos(\mathbf{k}_{21}\cdot\mathbf{r} - \phi_{21})$$
$$+ 2\big(e_{1p}e_{2d} + e_{1d}e_{2p}\big)\cos(\Omega\tau)\cos(\mathbf{k}_{21}\cdot\mathbf{r} - \phi_{21}) + 2\big(e_{1p}e_{2d} - e_{1d}e_{2p}\big)\sin(\Omega\tau)\sin(\mathbf{k}_{21}\cdot\mathbf{r} - \phi_{21}) \Big\}$$

$$\mathbf{k}_{21} \equiv \mathbf{k}_2 - \mathbf{k}_1$$

where again $|a'|^2$ has the same form except with all relevant quantities primed. Eq. 2.5 is the general result for the macroscopic polarization of the sample given the excitation implicit in Eq. 2.1.

We next consider the explicit geometries that give the sum- and difference-frequency modulation, followed by the scheme in which only beams of one frequency are used.

369

SUM- AND DIFFERENCE-FREQUENCY GEOMETRIES

To obtain the sum- and difference-frequency geometries described in Section 1 we set:

$$e_{1p} = e_{2d} = e'_{1p} = e'_{2d} = 1,$$
$$e_{1d} = e_{2p} = e'_{1d} = e'_{2p} = 0 \qquad (2.6)$$

Note that this makes for the useful mnemonic that the wavevectors subscripted 1 are prompt and those subscripted 2 are delayed. Also, let $k'_{21} = \pm k_{21}$. As we will see the "+" will yield difference-frequency modulation and the "-" sum-frequency modulation. Possible ways to impose the geometries $k'_{21} = \pm k_{21}$ are shown in Figure 2.2. For these parameters the polarization of Eq. 2.5 gives:

(a)   (b)
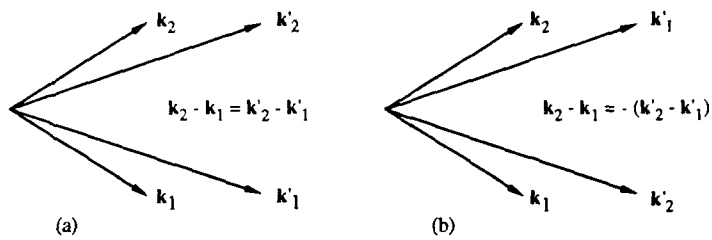
Figure 2.2 Possible ways to impose the geometries $k'_{21} = \pm k_{21}$. Note that the angles between the wavevectors are typically chosen to be a few milliradians and have been exaggerated here for the sake of clarity.

$$\mathcal{P}(t) = \left\{ p\Omega_R \sin\left[\Omega t - k_1 \cdot r + \phi_1\right] + \sin\left[\Omega(t - \tau) - k_2 \cdot r + \phi_2\right] \right.$$
$$\left. + p'\Omega'_R \sin\left[\Omega' t - k'_1 \cdot r + \phi'_1\right] + \sin\left[\Omega'(t - \tau) - k'_2 \cdot r + \phi'_2\right] \right\} \times \frac{\sin 2\lambda t}{2\lambda} \qquad (2.7)$$

where

$$(2\lambda)^2 = \frac{\Omega_R^2}{2}\left[1 + \cos\left(\Omega\tau + k_{21} \cdot r - \phi_{21}\right)\right] + \frac{\Omega'^2_R}{2}\left[1 + \cos\left(\Omega'\tau + k'_{21} \cdot r - \phi'_{21}\right)\right]$$

$$= 4\Omega_R^2\left\{1 + \beta\cos\left[\frac{\Omega' \pm \Omega}{2}\tau \pm k_{21} \cdot r - \left(\phi'_{21} \pm \phi_{21}\right)\right]\right\} + 2\left(\Omega'^2_R - \Omega_R^2\right)\left[1 + \cos\left(\Omega'\tau \pm k_{21} \cdot r - \phi'_{21}\right)\right]$$

$$\beta = \cos\left[\frac{\Omega' \mp \Omega}{2}\tau - \frac{\left(\phi'_{21} \mp \phi_{21}\right)}{2}\right]$$

We are interested in the four-wave mixing signals at Ω and Ω' that are emitted in the directions $k_2 + nk_{21}$ and $k'_2 + nk'_{21}$, respectively, where n (n > 0) indicates the diffraction order of the emitted signals. Our goal is to extract those components of $\mathcal{P}(t)$ as given in Eq. 2.7. For simplicity (and because our results do not deviate significantly from these predictions) we begin by restricting ourselves to the small pulse area limit $\Omega_R t_p \ll 1$, where t_p is the duration of the pulses. We will later consider arbitrary pulse areas and explore the limit of large pulse areas.

Small Pulse Area Limit In the small pulse area limit the term $\sin(2\lambda t)$ in Eq. 2.7 can be expanded and the series truncated after the lowest contributing term. We make the simplifying assumption that the pulse intensities have been adjusted to make $\Omega_R = \Omega'_R$. This yields the maximum modulation depth and makes the calculation much simpler. One finds that to lowest perturbation order the polarization of the sample phased to radiate at Ω in the $k_2 + nk_{21}$ direction is:

$$\mathcal{P}_n(t) = \frac{p}{2}\sin\left[\Omega(t - \tau) - \left(k_2 + k_{21}\right) \cdot r + \phi_2 \mp n\frac{\Omega \pm \Omega}{2}\tau \pm n\left(\phi'_{21} \pm \phi_{21}\right)\right] \times (-1)^n \frac{\left(2\Omega_R t\right)^{2n+1}}{(2n+1)!}\left(\frac{\beta_{\mp}}{2}\right)^n \qquad (2.8)$$

A similar result can be obtained for the polarization phased to radiate at Ω' in the $k'_2 + nk'_{21}$ direction. From this polarization of the sample the average intensity emitted into the four-wave mixing signal can be calculated. We assume that $\Omega \gg \Omega_R$ and thus the average over the optical frequency is trivial.

$$I_n \propto \frac{1}{t_p}\int_0^{t_p} \mathcal{P}_n^2(t)dt = \frac{1}{2}\left\{p\frac{\left(\Omega_R t_p\right)^{2n+1}}{(2n+2)!}\left(2\beta_{\mp}\right)^n\right\}^2 \qquad (2.9)$$

Of particular interest is the dependence on τ which is:

$$I_n \propto \beta_{\pm}^{2n} = \left\{\frac{1}{2}\left[1 + \cos\left((\Omega \mp \Omega)\tau - \left(\phi_{21} \mp \phi_{21}\right)\right)\right]\right\}^n \qquad (2.10)$$

Thus we see that the dependence on τ is a simple harmonic for the first diffraction order. For higher orders the modulation pattern narrows.

General Case. To obtain the polarization phased to radiate at Ω in the $k_2 + nk_{21}$ direction for arbitrary pulse area, $\Omega_R t_p$, we again expand the $\sin(2\lambda t)$ of Equation 2.7 but now we retain all terms in the expansion. This is somewhat tricky but we find that the polarization phased to radiate at Ω in the $k_2 + nk_{21}$ ($n>0$) directions is:

$$\mathcal{P}(t) = \frac{p}{2}\left\{ \sin\left[\Omega t - \left(k_2 + nk_{21}\right)\cdot r + \phi_1 \mp (n+1)\frac{\Omega \pm \Omega}{2}\tau \pm (n+1)\left(\phi'_{21} \pm \phi_{21}\right)\right]\{\cdots\}_{n+1}\right.$$

$$\left. + \sin\left[\Omega(t-\tau) - \left(k_2 + nk_{21}\right)\cdot r + \phi_2 \mp n\frac{\Omega \pm \Omega}{2}\tau \pm n\left(\phi'_{21} \pm \phi_{21}\right)\right]\{\cdots\}_n\right\}$$

(2.11)

where we have defined

$$\{\cdots\}_n \equiv \left\langle \cos(|n|\phi)\frac{\sin\left(2\Omega_R t\sqrt{1 + \beta_{\mp}\cos\phi}\right)}{\sqrt{1 + \beta_{\mp}\cos\phi}}\right\rangle .$$

We note that the first term of Eq. 2.11 was inadvertently omitted in Ref. 3. Finally, we calculate the average intensity assuming $\Omega \gg \Omega_R$:

$$I_n \propto \frac{1}{t_p}\int_0^{t_p} \mathcal{P}_n^2(t)dt = \left(\frac{p}{2}\right)^2\frac{1}{2t_p}\int_0^{t_p}\{\cdots\}_{n+1}^2 + 2\cos\left[\frac{\Omega \pm \Omega}{2}\tau - \phi'_{21}\right]\{\cdots\}_{n+1}\{\cdots\}_n + \{\cdots\}_n^2 .$$

(2.12)

In the small pulse area limit $\langle\cdots\rangle_{n+1} \ll \langle\cdots\rangle_n$ and it is easy to verify that this result simplifies to Equation 2.9. The integral can be approximated in the large pulse area limit by a J_0 Bessel function as we shall see below. However, in general the integral is intractable except to numerical (computer) analysis.

SINGLE TRANSITION TDFWM

We investigate now the sum-frequency geometry described above in the case where $\Omega' \to \Omega$. One might think that modulation would be obtained at 2Ω. This, however, is not the case; the modulation is at just Ω. The polarization of the sample for this geometry is governed by Equation 2.5 without the primed components. This yields:

$$\mathcal{P}(t) = p\Omega_R\left(\sin\left[\Omega t - k_1\cdot r + \phi_1\right] + \sin\left[\Omega(t-\tau) - k_1\cdot r + \phi_1\right]\right.$$

$$\left. + \sin\left[\Omega t - k_2\cdot r + \phi_2\right] + \sin\left[\Omega(t-\tau) - k_2\cdot r + \phi_2\right]\right) \times \frac{\sin 2\lambda t}{2\lambda}$$

(2.13)

with

$$(2\lambda)^2 = (2\Omega_R)^2(1 + \cos\Omega\tau)\left(1 + \cos\left(k_{21}\cdot r - \phi_{21}\right)\right)$$

Working as before, the polarization phased to radiate in the $k_2 + nk_{21}$ directions can be calculated in the perturbation limit :

$$\mathcal{P}_n(t) = p\sin\left[\Omega\left(t - \frac{\tau}{2}\right) - \left(k_2 + k_{21}\right)\cdot r + \phi_2 + n\phi_{21}\right] \times (-1)^n\frac{(2\Omega_R t)^{2n+1}}{(2n+1)!}\left(\frac{1 + \cos\Omega\tau}{2}\right)^n .$$

(2.14)

Thus the dependence on τ of the intensity emitted into the $k_2 + nk_{21}$ direction can be calculated to be:

$$I_n \propto \frac{1}{t_p}\int_0^{t_p}\mathcal{P}_n^2(t)dt = \frac{1}{2}\left[p\frac{(2\Omega_R t_p)^{2n+1}}{(2n+2)!}\right]^2\left(\frac{1 + \cos\Omega\tau}{2}\right)^{2n+1}$$

(2.15)

This shows that the modulation is at Ω, not at 2Ω as might at first be thought, and that the beats narrow quickly as one proceeds to higher diffraction order.

3. EXPERIMENTS

APPARATUS

All the experiments we will describe were performed in Na vapor. Sodium was chosen solely for convenience; it has two strong transitions in the yellow region of the spectrum at 589.0 and 589.6 nm. This is very near the peak output of a dye laser using Rhodamine 6G dye which is one of the easiest dyes with which to work.

The fact that the transitions are relatively close – they differ by one part in a thousand – implies another simplification in the experiment. Recall that for the difference- and sum-frequency experiments we want to impose the geometries $k_{21} = \pm k'_{21}$. These conditions can be satisfied to within the beam divergence by setting $k_1 \parallel k'_1$ and $k_2 \parallel k'_2$ or vice versa. This can be seen by observing that the minimum angular separation of the primed and unprimed wavevectors imposed solely by the condition $k_{21} = \pm k'_{21}$ is $\Delta\theta = (\lambda - \lambda')\theta/\lambda$ which

371

for our experiment, where $\theta \approx 1$ mrad, is $\Delta\theta \approx 10^{-6}$. Since this is much smaller than the 3×10^{-5} beam divergence in the interaction region the error introduced by our making the primed and unprimed wavevectors parallel is negligible. As a consequence of the geometry $k_1 \parallel k'_1$ and $k_2 \parallel k'_2$ or vice versa, the diffracted light at Ω is emitted in the same directions as that at Ω'. Thus one can consider the possibility of interference between diffracted light at the two optical frequencies. However, as can be seen from Equation 2.5 the light at Ω and Ω' is modulated the same way so that it doesn't make a difference in our experiments whether we detect the four-wave mixing signal at Ω, Ω', or both together.

The experimental apparatus is shown in Figure 3.1. The dye lasers were home-built and of the Littman design. They were pumped by the second harmonic of a Q-switched Nd:YAG laser and produced pulses 7 ns in duration at 589.6 and 589.0 nm, the wavelengths of the sodium $3S_{1/2} - 3P_{1/2}$ and $3S_{1/2} - 3P_{3/2}$ transitions, respectively. Each laser operated in 4 to 5 longitudinal modes yielding an overall laser bandwidth of about 5 GHz. Although not shown in the schematics of the apparatus the outputs of the dye lasers were spatially filtered and amplified to produce spatially clean beams. The amplification process also helped to reduce shot to shot amplitude fluctuations in the outputs as their gain was driven into saturation.

The sodium was contained in a heat pipe which was operated simply as an oven. The pipe was evacuated to <5 mtorr and the temperature adjusted to vary the vapor pressure. The cell had an actual length of 750 mm but an effective length of approximately 100 mm since only the center of the pipe was heated.

The angle between the excitation pulses in the two directions, k_1 and k_2, was typically set to be 1 mrad and was always in the range of .3 to 2 mrad. The four-wave mixing signals were separated from the excitation pulses by spatial filtering. A pinhole in the focal plane of a lens, with a focal length of either 300 or 450 mm, passed the TDFWM signal in the phase matched $k_2 + nk_{21}$ direction while blocking the excitation pulses. The signal was detected with either an EG&G FND-100 photodiode or an RCA C31034

(a)

(b)

Figure 3.1(a) Schematic diagram of the experimental apparatus used to generate difference-frequency TDFWM (for n=1). Mirror M1 is mounted on a precision translation stage which provides variable relative delays of up to 1 ns in increments of <100 fs. Mirror M2 can be repositioned to obtain large offset delays. (b) Schematic diagram of the apparatus used to generate sum-frequency beats in TDFWM. Mirror M1 is mounted on a precision translation stage which provides for variable relative delays of up to 30 fs in increments of <100 as. The delay was calibrated with a HeNe interferometer. M2 is a corner cube which displaces each beam so that it combines at the beam splitter with the beam of the other frequency.

photomultiplier tube. In all cases the signal was integrated over its full 7 nsec duration using a gated integrator with a gate width of 30 ns. The integrated signal was digitized and fed into a computer which averaged the data for each setting of τ. The entire experiment was automated with the computer generating the delays and taking data as a function of the delay with the results being plotted in real time on a video display terminal.

DIFFERENCE FREQUENCY EXPERIMENTS

Figure 3.1a shows the set up for the difference-frequency experiment. Here the dye laser outputs were combined to produce a double-frequency pulse which was split and then recombined with a variable relative delay to provide two double-frequency pulses directed along k_1 and k_2. In a typical run the TDFWM signal was monitored as the relative delay was varied by stepping the position of mirror M1. The result of such a run is shown in Fig. 3.2. In this particular run a spectrometer was used to look at just the 589.0 nm component of the signal. Similar results were obtained when we looked at just the 589.6 nm component or when no spectrometer was used and both transitions were viewed simultaneously. This is in agreement with the results of Section 2. The depth of modulation is less than would be expected from theory due to the imperfect spatial overlap of the excitation pulses in the sample and the difficulty in setting $\Omega_R = \Omega'_R$ precisely. We have taken data in the range of delays from minus a few hundred psec to +30 nsec. The data taken with delays near 30 ns will be discussed further in Section 4. All traces are essentially the same in that they exhibit 1.9 psec modulation.

Figure 3.2 TDFWM signal intensity vs pulse delay at 589.0 nm.

Figure 3.3 Data taken in the difference-frequency geometry showing the narrowing of the modulation in a high diffraction order (n=4).

We also experimentally observed the narrowing of the modulation pattern predicted in Equation 2.10. Figure 3.3 shows data taken when all the light emitted into the $k_2 + 4k_{21}$ direction was detected. Superimposed on the data is the theoretical prediction of Equation 2.10 modified by the addition of a background intensity.

SUM FREQUENCY EXPERIMENTS

Figure 3.1b shows the sum-frequency apparatus which is the same as the difference-frequency setup except for the beam splitting and recombination elements. Here the dye-laser outputs were split and recombined to provide two double-frequency pulses in such a way that the 589.0 nm component was delayed by τ in one beam and the other frequency component delayed by the same amount in the other beam. Note that in this geometry the vibrational stability of the optical elements is far more critical than in the difference-frequency case. Since the delays introduced in the two beams must be stable relative to the period of the modulation, the relative positions of the beamsplitter, cornercube, and translating mirror shown in Fig. 3.1b had to be stable to much better than an optical wavelength; this portion of the apparatus had also to be enclosed to prevent the effect of air currents from changing the effective delay.

Figure 3.4 Typical set of data for the sum-frequency geometry showing signal intensity vs relative pulse delay. The x-axis has an arbitrary offset with respect to absolute zero relative delay. The sodium vapor was held at a temperature of 470 K.

The first diffraction order sum-frequency signal presented in Figure 3.4 as a function of τ is a simple sinusoid as would be predicted in the low pulse area limit of Eq. 2.10. We found agreement even though the excitation pulses were not in the small pulse area limit. We have not observed any of the predicted narrowing of the modulation signal that is expected with the multiple π excitations with which we worked. Nor have we seen the narrowing of the peaks and flattening of the valleys expected from Eq. 2.10 when the sum-frequency signals are scattered into higher orders (n>1). We believe that both these experiments are sensitive to vibrational instabilities in our apparatus which average out the higher harmonic frequencies.

The observation of modulation narrowing at high scattering order in the difference-frequency geometry supports our suspicion that vibrational instabilities prevented the observation of such narrowing in the sum frequency mode. Our continued inability to observe modulation narrowing with large excitation pulse areas remains unresolved. One possible explanation may lie in the fact that our experiments have all been done with optically thick samples whose optical densities were in the range of 10 to 100. All our analysis assumes optically thin samples. The optically thick regime is complicated and we worked there in order obtain signals which we could differentiate from the noise.

SINGLE-TRANSITION EXPERIMENTS

Sum frequency beat observation depends on the simultaneous excitation of two distinct transitions sharing a common ground state. The analysis of Section 2 respects this restriction and does not allow the limit $\Omega' \rightarrow \Omega$, with both lasers tuned to the same transition. The expected result in this degenerate case is that the modulation in the TDFWM signal would have the period of the optical frequency Ω, as in interferometry, and not 2Ω. This is most easily understood via the simple induced grating analysis by including the (previously) moving grating component due to the product of the fields at Ω and Ω'. We looked carefully for the sum frequency beat using a single laser whose output was split to serve as a double source. Working this way we saw only the resonant beats and not the sum frequency beats. We did however observe the narrowing predicted by Eq. 2.15. We did not look at the higher diffraction order signals which we calculate should

narrow according to $I_n \propto \left[\frac{1}{2} + \frac{1}{2} \cos(\Omega \tau) \right]^{2n+1}$ similar to the case of the sum frequency beats.

4. PHOTON ECHO MODULATION

We now consider the photon echo regime in which the excitation pulses are well separated. We believe that echoes are observable with both the sum- and difference-frequency geometries. However, in order to see sum-frequency modulation in an echo signal the pulse durations must be short compared to the inhomogeneous dephasing time T_2^*. This is because the modulation occurs as a result of an interference between a photon echo process and a free decay process. In sodium, in the temperature range in which we worked T_2^* is about 100 ps. Thus, since our excitation pulses were 7 ns in duration, we have only observed difference-frequency modulation.

To understand the origin of the modulation in echo signals we can use the billiard ball model of coherent transients in gasses. This will be presented in the next section. We defer to Section 5 a discussion of the Doppler-free nature of the beats in the difference-frequency modulation of echoes and how this could be used as a high-resolution spectroscopic technique.

THEORY - BILLIARD BALL MODEL

The billiard ball model was developed to provide a simple way to analyze photon echo type phenomena. It has been discussed in some detail in a number of papers.[10,11,12] We use it here to analyze the modulation of echoes in both the difference- and sum-frequency geometries.

The billiard ball diagram for the difference-frequency geometry is shown in Figure 4.1. One begins with an atom at rest in its ground state. At t=0, the prompt excitation pulses at Ω and Ω' interact with the atom giving the atom some probability of being found in either of the two excited states. If the atom is excited, then it will have absorbed a photon and thus its momentum and will recoil with a velocity $hk/2\pi m$. Such absorption of the two frequencies is indicated on the diagram by the dashed and dot-dashed lines. Their slopes differ by one part in a thousand for the D-lines in sodium. The difference in slope is exaggerated here for the sake of clarity in the figure. Thus, each of the three lines propagating from t=0 represents the amplitude of the atom being in a particular state. The state of the atom is then the sum of those amplitudes. The billiard ball model gives rules for calculating populations and coherences from such a diagram but they are not of concern here. The relevant thing here is that the two excited state amplitudes have time-developments associated with them. The effect of
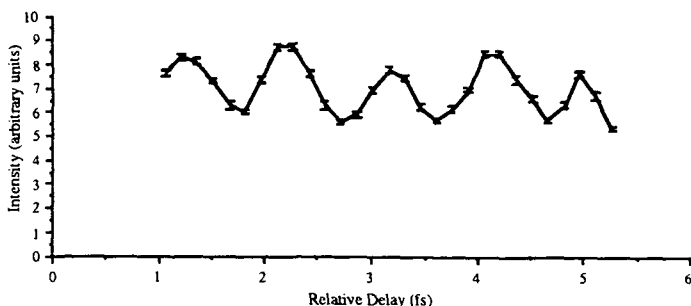
the second pulse is to generate two more recoiling excited state amplitudes from the ground state, and to generate a ground state amplitude from each of the recoiling excited states. This results in four crossings of the amplitudes near t = 2τ. Each of these crossings represents an echo being emitted. The two echoes produced by the dashed line crossing the two displaced ground states are emitted at Ω'. The echo is modulated because the population in the two displaced ground states is in fact modulated. Considering the two displaced ground states as one, the associated amplitude is gotten by adding the amplitudes of the two ground states:

$$e^{-i\Omega\tau} + e^{-i\Omega'\tau} = e^{-i\frac{\Omega+\Omega}{2}\tau}\cos\left(\frac{\Omega'-\Omega}{2}\tau\right)$$
(4.1)

The population in this displaced ground state is then just:

$$\left[\cos\left(\frac{\Omega'-\Omega}{2}\tau\right)\right]^2 = \frac{1}{2}[1 + \cos(\Omega - \Omega)\tau]$$
(4.2)

Figure 4.1 Billiard Ball diagram for difference-frequency geometry.

This is the same modulation as was obtained in Section 2.

In the case of the sum-frequency geometry the situation is not quite so simple and we will not discuss the billiard ball analysis here. Suffice it to say that the same dependence on τ is obtained as was found in Section 2 for four-wave mixing signals where all the pulses overlap in time.

EXPERIMENT

As mentioned above we have performed echo experiments only in the difference frequency geometry. With a pulse separation of approximately 20 ns, obtained by displacing the mirror labelled M2 in Figure 3.1a, the integrated echo intensity was measured as a function of delay. The data is essentially the same as shown in Fig. 3.2 except that the modulation depth has decreased by a factor of three or four from the data taken in the four-wave mixing regime. This degradation is not inherent in the technique but rather is caused by jitter in τ due to mechanical vibrations of the optics. We note that the beating lasts much longer than the few hundred picosecond coherence time of the lasers.

5. POSSIBLE APPLICATIONS

An obvious application of the modulation phenomena described in this dissertation is in spectroscopy, that is in studying transition frequencies. With the use of a calibrated delay the sum and difference frequencies of two transitions can be measured and from these the absolute transition frequencies can be determined. For this technique to be of practical use it must provide frequency information which is sub-Doppler. For this to be the case the modulation frequency must depend only on the transition frequencies and not on the velocity of the atoms in the sample. As has been shown[2] this is the case for the difference-frequency beats which can be observed well into the photon echo regime. Echoes can be observed many lifetimes after the initial excitation and thus the energy level splitting should be measurable to very high precision. In the sum-frequency case the maximum pulse separation is determined by the Doppler-dephasing time which severely limits spectroscopic applications.

Sum-frequency beat TDFWM could find application in a position transducer. Using the first order signal, a device similar to a laser interferometer distance encoder could be constructed with the advantage that roughly twice the number of fringes would be observed for a given translation. Presumably such a device would use CW lasers allowing a long coherence length and thus the ability to measure correspondingly long distances. The spikes in a higher order signal would lend themselves to positioning devices which step in precise equally spaced increments.

6. CONCLUSION

In summary, the new phenomena of sum- and difference-frequency beats in four-wave mixing experiments has been documented and their origin explained. By extension, the presence of beats in the TDFWM signal has been shown to depend critically on the excitation beam geometry and to provide spectroscopic information of a varied but well defined character. As faster processes are studied broader bandwidth excitations will be used which will in turn couple multiple transitions, resulting in complex signal modulations. Sum and difference frequency geometries may be separately employed to untangle confusing spectroscopic details. Lastly we note that the existence of sum frequency beats and their narrowing with scattering order and excitation intensity may allow development of more accurate position transducers.

REFERENCES

1. Beach, R., D. DeBeer, and S. R. Hartmann, Phys. Rev. A **32**, 3467 (1985)
2. DeBeer D., L. G. Van Wagenen, R. Beach, and S. R. Hartmann, Phys. Rev. Lett. **56**, 1128 (1986)
3. DeBeer D., E. Usadi, and S. R. Hartmann, Phys. Rev. Lett. **60**, 1262 (1988)
4. Maker, P. D., and R. W. Terhune, Phys. Rev. **137**, A801 (1965)
5. Kumit, N. A., I. D. Abella, and S. R. Hartmann, Phys. Rev. Lett. **13**, 567 (1964)
6. Abella, I. D., N. A. Kumit, and S. R. Hartmann, Phys. Rev. **141**, 391 (1966)
7. Rothenberg, J. E., and D. Grischkowsky, Opt. Lett. **10**, 22 (1985)
8. Burggraf, H., M. Kuckartz, and H. Harde, in *Methods of Laser Spectroscopy*, Y. Prior, A. Ben-Reuven, and M. Rosenbluh, Ed. (Plenum, New York, 1986), p. 105
9. Golub, J. E., and T. W. Mossberg, Opt. Lett. **11**, 431 (1986)
10. Beach, R., S. R. Hartmann, and R. Friedberg, Phys. Rev. A **25**, 2658 (1982)
11. Beach, R., B. Brody, and S. R. Hartmann, Phys. Rev. A **27**, 2537 (1983)
12. Beach, R., B. Brody, and S. R. Hartmann, J. Opt. Soc. Amer. B **1**, 189 (1984)
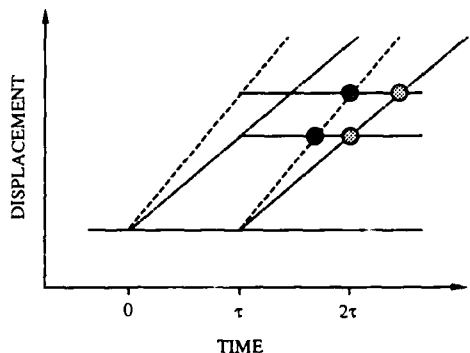
NEAR DIFFRACTION LIMITED FOCUSING AND BLUE SHIFTING OF MILLIJOULE FEMTOSECOND PULSES IN GAS BREAKDOWN AND SOLID STATE PLASMAS

Wm. M. Wood, Glenn Focht, D.H. Reitze, T.R. Zhang, M.C. Downer

Physics Department, University of Texas at Austin, Austin, TX 78712

Abstract: We present a femtosecond dye amplifier system with a novel final amplification stage which allows us to achieve extremely tight focusing of the output beam, and therefore reach intensities unattainable previously in the femtosecond regime. We use these pulses to generate gas and solid state breakdown plasmas, and observe the associated blue shift in the pulse bandwidth, consistent with the Drude model.

Amplification of femtosecond pulses to millijoule and higher energies has opened up the study of the interaction of matter with radiation fields of unprecedented intensity. The output of high power femtosecond amplifiers, however, often suffers from poor transverse beam quality and limited focusability caused by severe phase front distortion during the amplification process. We have constructed a high power dye amplifier pumped by a Q-switched Nd: YAG laser which achieves near diffraction-limited focusing of 100 fs millijoule pulses without any spatial filtering.[1] The peak intensity at our tightest focus (~2 μm radius) exceeds 10^{16} W/cm^2, where breakdown of air and other gases at pressures of 1-10 atm is easily observed.

Critical to achieving this result was a final stage gain cell of conical axicon geometry,[2] as shown in Fig. 1. The first three stages (not shown) use standard transversely pumped gain cells to pre-amplify femtosecond pulses from a CPM to ~ 0.1 mJ at a 10 Hz repetition rate. These pulses are then expanded to 1 cm diameter and injected into the gain region of the axicon, an 8 cm long cylindrical flow tube containing Rh640 centered on the axis of a solid glass cone. Incident to the base of the cone and expanded to match its 8 cm radius, counter-propagating 220 mJ, 532 nm pump pulses internally reflect from the sides and enter the gain medium at radial incidence, thereby maximizing pump absorption efficiency, Gaussian beam quality, and focusability.[1,2] Figure 2 shows measurements of transmission of the beam focused at f/2 through a 3 μm pinhole translated in 1 μm steps across the beam waist, and demonstrates the extremely tight focusability of millijoule femtosecond pulses amplified in such a cell. While a slight degradation in focusability occurs in the pre-amplification stages, the axicon cell preserves focusability perfectly.

We have shown that millijoule femtosecond pulses can be focused to spot radii as small as 2 microns when amplified in a "conical axicon" cell, thus creating peak intensities of 10 petawatts (PW)/cm^2.[3] We now use this source to generate dense gas breakdown plasmas in the strong field,[4] collisionless limit while using the plasma response on the light field in the form of blue shifts and defocusing as diagnostics to characterize the femtosecond ionization process.[5] Such diagnostics are compatible with a wide range of gas pressures.

Figure 3 shows how the blue shift of 90 fs pulses increases with light intensity after focusing at f/2 through a breakdown spark in 1 atm. neon. Numerous observations support the dominance of plasma generation, and the weakness of $\chi^{(3)}$ effects, in producing this shift: the similarity of the blue shifts in different gases (neon, air,[3] helium, argon at 1 atm.) having third order hyperpolarizabilities which vary by more than a factor of 20;[6] correlation of these blue shifts with appearance of a breakdown spark; correlation with beam defocusing caused by the plasma's lower refractive index; the consistent absence of any red-shifted spectral components (in contrast to spectral *broadening* observed by others[7,8] in the absence of gas breakdown); the absence of supercontinuum generation from intense femtosecond excitation of neon up to 40 atm in previous studies;[8] the absence of self-focusing or filamentation under breakdown conditions. The blue shift is caused by the ultrafast negative refractive index change when a plasma is created during the pulse. The temporal asymmetry of the index change is strong with femtosecond pulses, since electrons neither recombine nor escape from the focal region during the pulse, thus eliminating a compensating red shift, seen with longer pulses, when the index recovers.[5] According to a Drude model the blue shift can be approximated as:[5]

$$\Delta\lambda = (\lambda^3 e^2 / 2\pi m c^3)\, d/dt \int^L N(x)\, dx \qquad (1)$$

where N(x) is the plasma density along the propagation direction x, and the interaction length L is approximately the confocal beam parameter. The blue shift in neon increases steadily up to our highest intensity (10 PW/cm^2), rather than saturating because of complete single ionization within the focal volume at 2 PW/cm^2, as observed in air.[3] This difference may result from the lower ionization potential of nitrogen and oxygen compared to neon. Figure 4 shows a blue shift caused by 1 μJ 90 fs pulses generating a dense (~10^{20} cm^{-3}) electron-hole plasma in sapphire by three-photon absorption when focused at f/10 into a 1 mm. sample. In contrast to the gases, there is an accompanying red-shifted feature. Nevertheless the resulting spectra are accurately fit by combining plasma effects described by Eq. 1 with self-phase modulation resulting from the third order hyperpolarizability, as shown by the dots in Fig. 4.

Figures 5 and 6 show other characteristics of the blue-shifted pulses. Figure 5 shows the defocusing which accompanies blue shifting, manifested as an increased beam divergence angle. This effect is strongest in sapphire because of the high plasma density and long interaction length used. In other solids this effect has been used for optical limiting.[9] In gases at 1 atm with f/2 focus, plasma defocusing causes a 30% increase in divergence angle which can be correlated quantitatively with the blue shift. The blue shifted beam thus maintains sufficiently good beam quality to be useful spectroscopically. The autocorrelation traces in Fig. 6 demonstrate that the glass f/2 focusing optics cause 10% temporal broadening of low intensity pulses (no plasma formed), and that at high intensity the ionization process causes no further measurable broadening. As gas pressure increases above 1 atm we observe only a slight further increase in blue shift, as shown by the blue shifted neon spectra in Fig. 7. The saturation of the blue shift at 2 to 3 atm probably results

from increased defocusing caused by the higher plasma density in the interaction region. Consequently focal spot size is increased and peak intensity reduced.

The behavior of argon at 5 atm. contrasts strongly with other gases we have studied. Just above threshold the blue shift behaves as in other gases, and is well explained by Eq. 1. At an intensity near 10 PW/cm^2, however, we observe a sudden spectral broadening, with components blue shifted well beyond those observed in other gases, as shown in Fig. 8. The transmitted light contains yellow, green, and even blue components visible to the naked eye, although still no components which are red-shifted from the original pulse spectrum. Onset of double ionization, for which the threshold is lower in the heavy rare gases, may cause an increase in the rate of change of plasma density dN/dt, and may thus be partly explain the sudden spectral change. However, the absence of increased defocusing (see data for 5 atm. argon in Fig. 6), as expected from increased plasma density, together with the pressure dependence of the effect, suggest the role of self phase modulation in the argon plasma.

Highly focusable femtosecond pulses from an axicon amplifier provide a powerful new tool in ultrahigh intensity spectroscopy. The blue shifts observed here may be related to red shifted photoelectron energies observed in recent above threshold ionization (ATI) experiments.[10] Dynamic collisionless absorption in plasmas, important when electron acceleration in strong light fields becomes relativistic, may be observable with such pulses.[11] Finally, this source should be useful in generating picosecond soft X-ray pulses at noble metal surfaces.[12]

1. W. M. Wood, Glenn Focht, and M.C. Downer, Opt. Lett., in press (1988).
2. F.P. Schafer, Appl. Phys. B **39**, 1 (1986); G. Kuhnle, G. Marowsky, G.A. Reider, Appl. Opt., in press.
3. M.C. Downer et al., "New Developments in Ultraviolet and High Intensity Femtosecond Sources" in this volume; Wm. M. Wood, Glenn Focht, and M.C. Downer, Opt. Lett., in press (1988).
4. L.V. Keldysh, Sov. Phys. JETP **20**, 1307 (1965).
5. E. Yablonovitch, Phys. Rev. Lett. **32**, 1101 (1974); Phys. Rev. A **10**, 1888 (1974); Phys. Rev. Lett. **60**, 795 (1988); P.B. Corkum NATO ASI Series-Physics B **171**, 157 (1988).
6. H.J. Lehmeier, W. Leupacher and A. Penzkofer, Opt. Commun, **56**, 67 (1985).
7. D. Kuhlke, U. Herpers, and D.von der Linde, Opt. Commun. **63**, 275 (1987); J.H. Glownia, J. Misewich, and P.P. Sorokin, J.Opt. Soc. Am. B **3**, 1573 (1986).
8. P.B. Corkum, C. Rolland, and T. Srinivasan-Rao, Phys. Rev. Lett. **57**, 2268 (1986).
9. T.F. Boggess, Jr., A.L.Smirl, S.C. Moss, I.W. Boyd, and E. W. van Stryland, IEEE J. Quant. El. **21**, 488 (1985); S. Guha, E.W. Van Stryland, and M.J.Soileau. Opt. Lett. **10**, 285 (1985).
10. E. Yablonovitch, Phys. Rev. Lett. **60**, 795 (1988); R.R. Freeman, P.H. Bucksbaum, H. Milchberg, S. Darack, D. Schumacher, and M.E. Geusic, Phys. Rev. Lett. **59**, 1092 (1987).
11. R. Dragila and H. Hora, Phys. Fluids **25**, 1057 (1982).
12. O.R. Wood II, W.T. Silfvast, H.W.K. Tom, W.H. Knox, R.L. Fork, C.H. Brito-Cruz, M.C. Downer and P.J. Maloney, Appl. Phys. Lett., to be published.
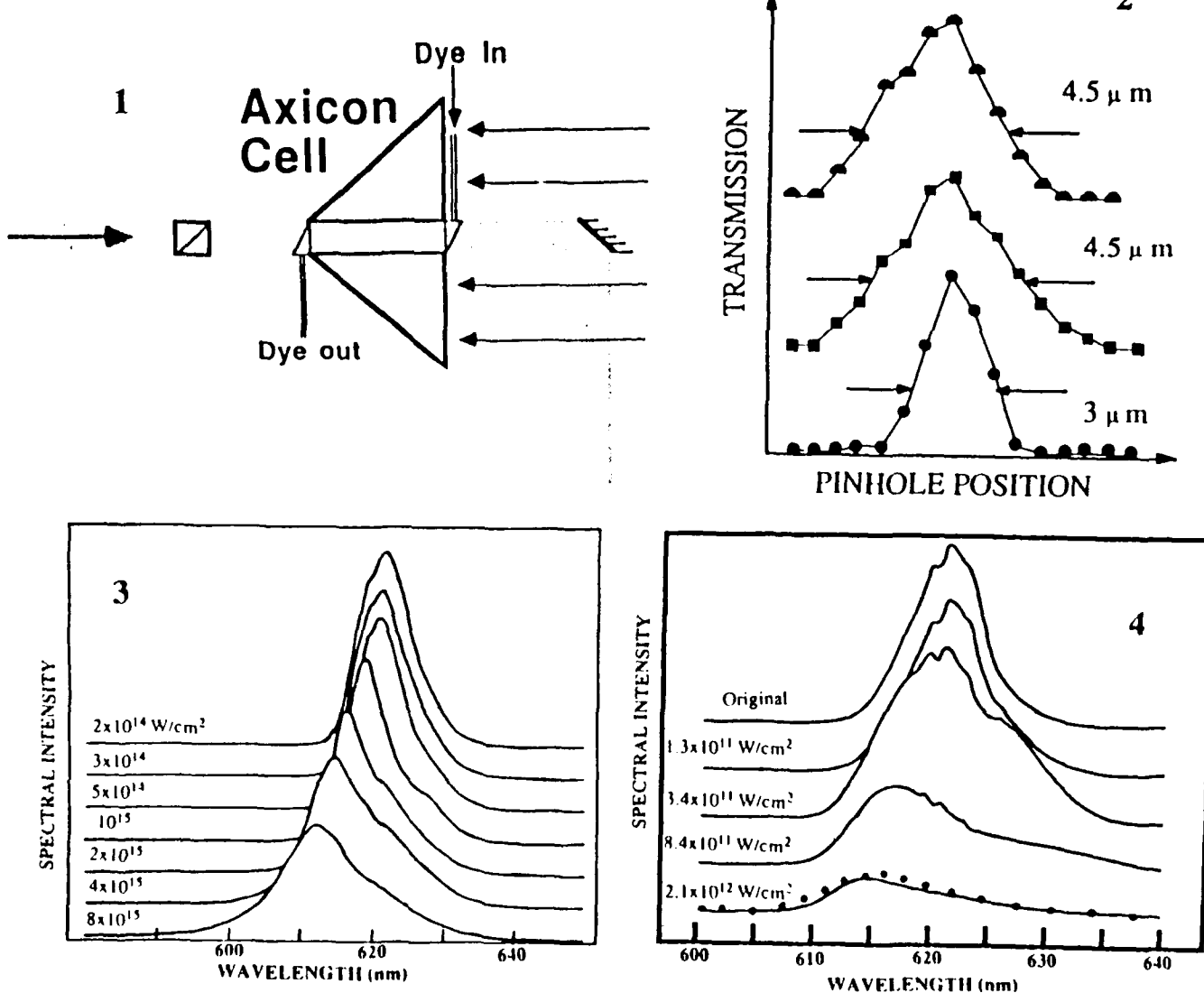
Fig. 1 Final stage geometry for the femtosecond axicon dye cell amplifier.

Fig. 2 Beam waist profile of unamplified CPM output (bottom curve), pre-amplified output prior to axicon cell (middle curve), and fully amplified output from axicon cell, all at focus of a 7x microscope objective.

Fig.3 Spectra of 90 fs. pulses transmitted through neon breakdown spark, with focal intensity increasing toward the front in increments of 0.2 optical density. Successive curves have been displaced from each other in an exact vertical direction to emphasize blue shift as intensity increases.

Fig. 4 Spectra of 90 fs. pulses after generating a dense electron-hole plasma in sapphire by a three-photon absorption process. Note blue shift accompanied by a weaker red-shifted feature. Dots represent a theoretical fit .

377
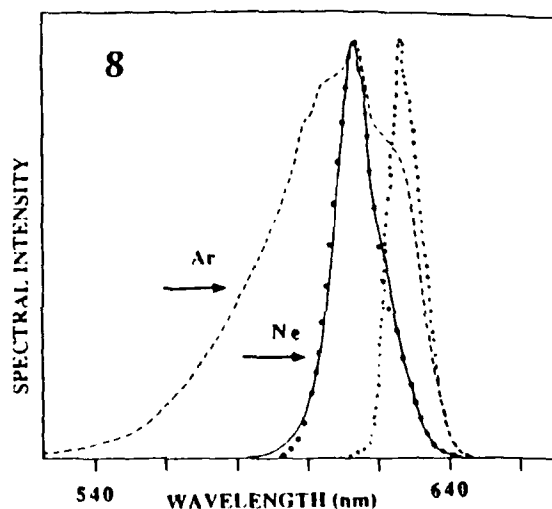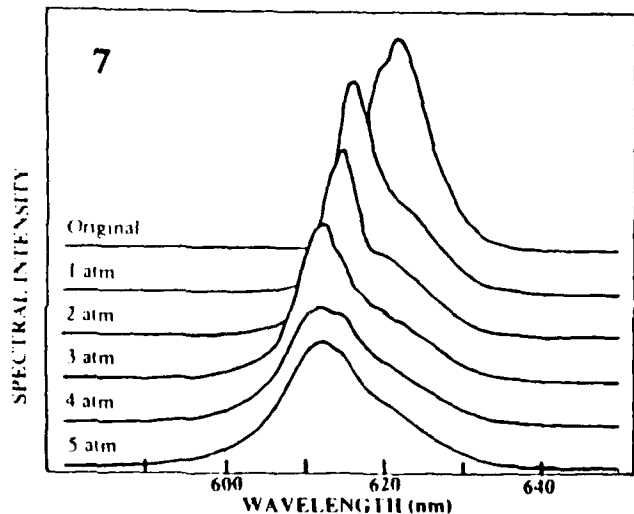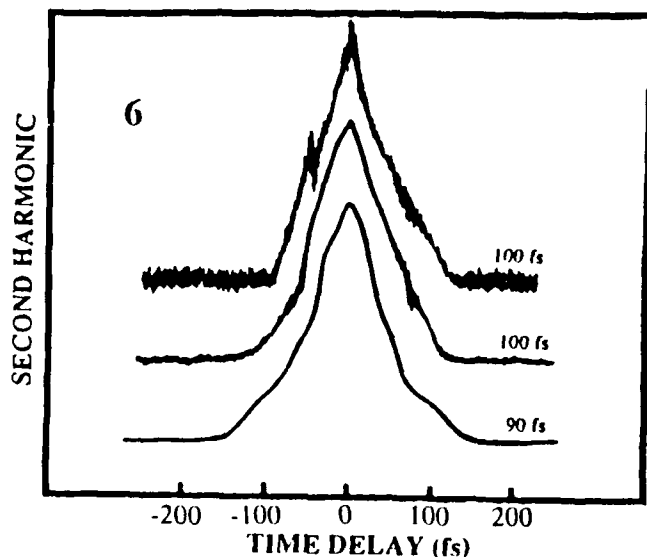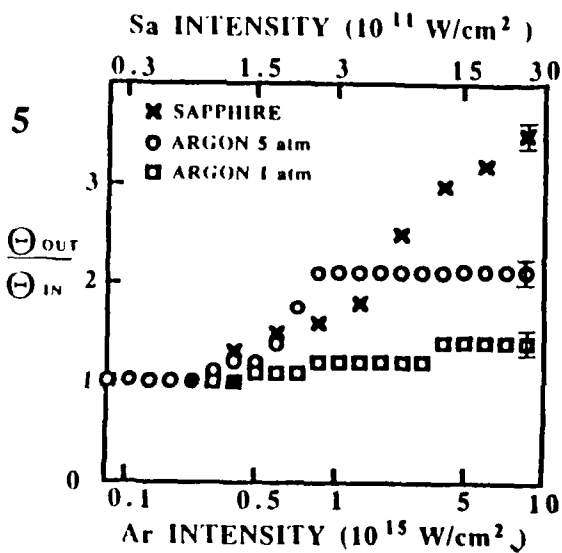
Fig. 5 Defocusing vs. peak focal intensity for sapphire, 1 atm. argon, and 5 atm. argon. The filled square and circle denote the first appearance of a breakdown spark

Fig. 6 Autocorrelation traces of unfocused millijoule pulses (lower trace), pulses after focusing at f/2 in air by 7x microscope objective and recollimation, but attenuated to avoid breakdown spark (middle trace), and full intensity pulses after focusing at f/2 through intense breakdown spark and recollimation (upper trace). Cited pulse durations assume sech² pulse shape

Fig. 7 Blue shifted spectra at 10 PW/cm² focal intensity for 5 pressures of neon, compared to original pulse spectrum.

Fig. 8 Original pulse spectrum (dotted curve) and blue shifted spectra following transmission through plasmas generated in 5 atm. neon (solid curve) and argon (dashed curve). Large dots are a theoretical fit based on Drude model (see Eq. 1 of text)

378

REFLECTION SWITCHING OF PICOSECOND PULSES AT SATURABLE NONLINEAR INTERFACES

M. Moheb, B. JeanJean and J.-C. Diels
Department of Physics and Astronomy
The University of New Mexico, Albuquerque, New Mexico 87131

Abstract

The nonlinear reflection of μJ pulses incident near the critical angle on glass-dye interface has been measured. A model including saturation through the evanescent wave, and the resulting change in resonant dispersion, accurately describes the self switching characteristics of this interface.

Introduction

The interesting phenomena -- such as switching, bistability, trapping -- that can occur at interfaces between an ordinary dielectric and a nonlinear material has been pointed out by several authors in the last decade. Most of these studies have focused on the optical Kerr effect as the nonlinear process [1-4]. The optical Kerr effect is generally a non-resonant nonlinearity requiring large optical powers densities. Switching capability at much lower power levels can be obtained with resonant nonlinearities, as demonstrated here. We present the first experimental study of the interface of a linear material and a saturable absorber.

The interest in such an interface is justified by its potential application in ultrafast switching, energy limiting, internal or external cavity pulse compressors, and mode locking of dye lasers. Nonlinear optical properties of materials with large absorption can also be studied by measuring the reflection from the interface.

Experimental Arrangement

The boundaries of the nonlinear interface were fused silica (as the linear dielectric) and a solution of 3,3'-Diethylthiadicarbocyanine iodide (DTDCI) in Ethylene glycol as the saturable absorber. A concentration of 5 mM/l of DTDCI is needed in order to have absorption lengths comparable to the penetration depth, which is of the order of the wavelength. Silylation of the quartz surface [5], as well as high flow velocities, were used to prevent the attachment of dye molecules to the quartz surface and their subsequent dissociation.

The peak absorption of the dye is at 660 nm. The reflection coefficient of the interface as a function of incident energy density is measured at and above resonance. Switching pulses of approximately 10 μJ energy are provided by an oscillator-amplifier combination. The oscillator consists in a tunable, synchronously pumped mode locked dye laser generating 6 psec pulses. The latter are sent through a three stage dye amplifier pumped by a frequency doubled Nd:YAG amplifier [6]. The beam is focused to a 100 μm spot at the interface with a 100 cm focal length lens. With this geometry, the radiation incident on the interface can be approximated by a plane wave.

Linear Properties of the Interface

The reflectivity is plotted versus internal angle of incidence on Fig. 1, using the (unamplified) beam from the laser oscillator alone as a source. The data points are for the pure solvent (a), 5 mM/l of DTDCI in ethylene glycol, with the laser tuned to 637 nm (b), and the same concentration of dye with the laser tuned to 660 nm (c). A straightforward application of the Fresnel formula completely describes the (linear) reflection at the interface (solid line). Because of the absorption of the dye through the evanescent wave, the reflectivity drops to a smaller value above the critical angle, and the sharp edge in the curve disappears. The effect of variations in the index of refraction on the reflectivity is also apparent, resulting for instance in an increase of reflectivity below critical angle in curve (b). Because of the negative contribution to the refractive index below resonance, one expects indeed the critical angle to decrease below resonance.

The calculated (solid lines) curves of Fig. 1 include two contributions of the dye solution to the index of refraction: a resonant (saturable) and a non-resonant (non saturable) part. The resonant contribution to the index of refraction was calculated by fitting the absorption spectrum of the dye to a Lorentzian shape. This results in a negative contribution above resonance (637 nm) and a zero contribution at resonance (660 nm). There is also a background index contributed by the dye which is nonsaturable, at least with the optical energy densities used in our measurements. The value of the latter

contribution was obtained by fitting the calculations to the data. The fitted index is indeed a nonsaturable contribution to the index of refraction from the dye molecules, since its value increases linearly with concentration. The average slope of the concentration dependence of the background index of refraction is 0.63×10^{-3} 1/mM. The same positive background index was found for the two dyes that we tested (DTDCI and 1,1´,3,3,3´,3´-Hexamethylindodicarbocyanine iodide or HIDCI) at the three wavelengths that we measured (637, 660, 663 nm).
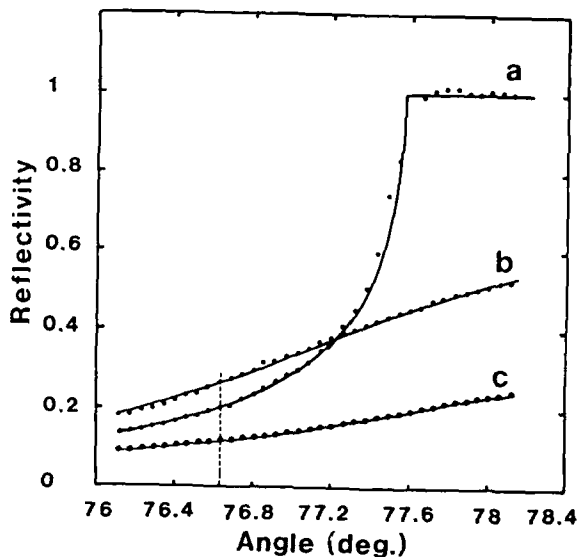
Figure 1

The Nonlinear Interface

The first nonlinear measurement is performed at half width of the absorption line above resonance at 637 nm. The incident angle is set to 76.637 degrees. At low intensities the reflection coefficient of the interface can be seen from Fig. 1 to be 0.27. With incident energies above the saturation energy density of the dye, the resonant index of refraction will saturate simultaneously with the absorption of the dye. The non-saturable part of the index, however, will remain. In this case the non-resonant contribution equals 0.003. Including the latter value as a correction to the "linear" index in the
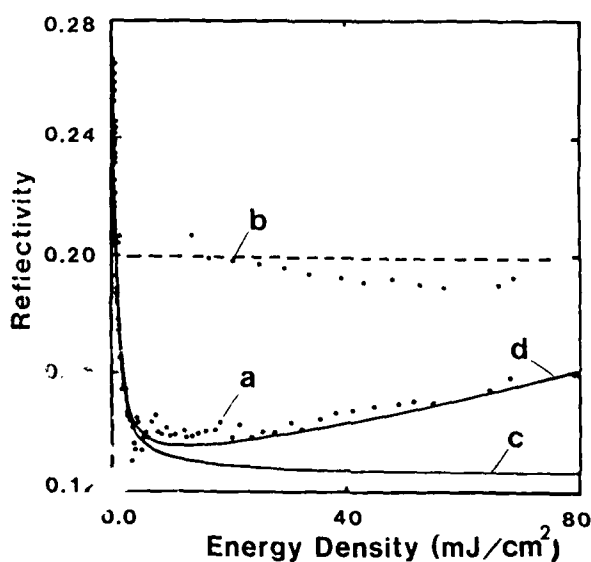
Figure 2

liquid phase leads to a reflection coefficient of approximately 0.14 at energy densities much higher than the saturation energy density of DTDCI. The measured reflectivity (in energy) is plotted as a function of the pulse energy in Fig. 2. Data points (a) are obtained with 5 mM lit of dye. The solid curve (c) is the result of the numerical model. The departure of the data from the model after complete saturation of the dye is to be attributed to other nonlinear processes becoming dominant at the highest intensities. The increase of reflectivity observed in the data at energy densities above 5 mJ/cm² can be explained by including Kerr effect with $n_2 = -6 \times 10^{-13}$ cm²/W as seen in the solid curve (d). The presence of Kerr effect in the quartz or the solvent is ruled out as is apparent from the data points (c) obtained with the pure solvent. The change in reflectivity due to the thermal decrease of the refractive index was also included in the model, and was seen to be qualitatively different from the observed reflectivity dependence, and quantitatively much smaller. The saturation energy density of 0.35 mJ/cm² used in the calculations was determined from saturated transmission measurements through a 300 μm thick dye cell.

Measurements of reflection versus pulse energy, at a laser wavelength of 660 nm at resonance with the absorption peak of the dye DTDCI, are shown in Fig. 3. The solid curves are the result of the numerical calculation, with a (negative) Kerr coefficient as a fitting parameter. The same value is found for the Kerr effect coefficient as for the case of Fig. 2. The curves (a) and (b) correspond to an internal angle of incidence of 78.06° and 78.40°. The data (c) showing the reflection coefficient at zero concentration (above critical angle) as a function of incident pulse energy, clearly indicate that the Kerr nonlinearity of the solvent and of the glass can be neglected in the range of pulse energies needed to saturate the dye. Because of the nonsaturable contribution of the dye to the index of refraction of the liquid phase, the asymptotic value of the reflectivity at high energies is less than unity. Indeed, incrementing the index of refraction of the solvent (1.4244) by the nonsaturable contribution of 0.0049 for a 4 mM l solution of DTDCI, leads to a critical angle arcsin(1.4293/1.4584) = 78.53° - in excess of the largest angle of incidence of data (b).
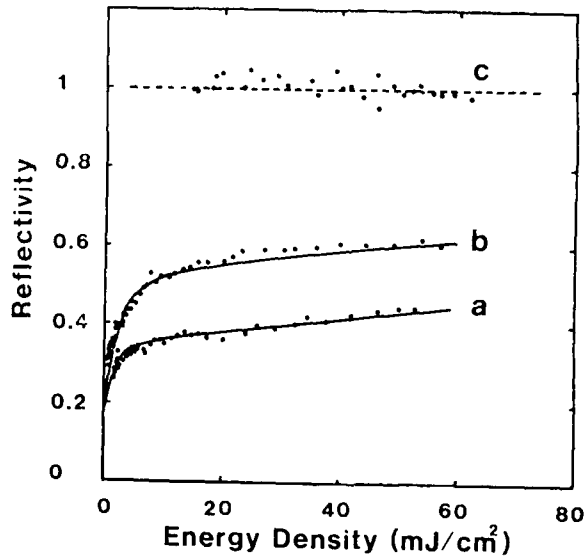
Figure 3

Conclusion

We have demonstrated the switching properties of the saturable absorber at an interface. A numerical model was developed which agrees very well with the experiments. A large negative Kerr effect had to be included in the model to explain the increase of reflectivity at high energy densities. This Kerr effect is associated with the dye molecule and can be eliminated by using a different dye, such as HIDCI. When the frequency of the switching radiation is tuned above resonance, the nonlinear interface can be used as an energy limiter. For the latter application, the index of refraction of the solvent incremented by the nonsaturable (nonresonant) contribution of the dye, has to match the index of the prism.

References

1. A. E. Kaplan, Sov. Phys. JETP 45, 896 (1978).
2. W. J. Tomlinson, J. P. Gordon, P. W. Smith, and A. E. Kaplan, Appl. Opt. 21, 2041 (1982).
3. P. W. Smith, W. J. Tomlinson, and P. J. Maloney, A. E. Kaplan
    Optics Lett. 7, 57 (1982).
4. P. W. Smith, W. J. Tomlinson, IEEE Journal of Quantum Electr. QE-20, 30 (1984).
5. F. Deyhimi and J. A. Coles, Helvetica Chimica Acta 65, 1752 (1982).
6. H. Vanherzeele, H. J. Mackey, and J.-C. Diels, Appl. Optics 23, 2056 (1984).

SUBTLE ANGULAR EFFECTS IN PRISMATIC PULSE COMPRESSION

F. J. Duarte

Photographic Research Laboratories – Photographic Products Group
Eastman Kodak Company, Rochester, NY   14650-1744

Abstract

Numerical techniques are employed to illustrate the subtle differences between two approaches used to augment dispersion in prismatic arrays. The numerical method provides a clear perspective on characteristics difficult to perceive from the mathematical theory.

Introduction

Here we provide an introduction to the main steps involved in these pulse compression calculations. This work utilizes the second derivative of the optical path length provided by Fork et al.[1]

$$\frac{d^2P}{d\lambda^2} = \left[\frac{d^2n}{d\lambda^2}\frac{d\theta}{dn} + \left(\frac{dn}{d\lambda}\right)^2\frac{d^2\theta}{dn^2}\right]\frac{dP}{d\theta} + \left(\frac{dn}{d\lambda}\right)^2\left(\frac{d\theta}{dn}\right)^2\frac{d^2P}{d\theta^2} \tag{1}$$

where $P = 2\ell\cos\theta$.

In this equation $(d\theta/dn)$ and $(d^2\theta/dn^2)$ are related to the prismatic dispersion and its derivative. For a generalized prism chain the single-pass dispersion is given by Duarte and Piper[2,3]

$$\frac{d\phi_{2,m}}{dn} = \frac{\sin\psi_{2,m}}{\cos\phi_{2,m}} + \frac{\cos\psi_{2,m}}{\cos\phi_{2,m}}\frac{\cos\phi_{1,m}}{\cos\psi_{1,m}}\left[\frac{\sin\psi_{1,m}}{\cos\phi_{1,m}} \pm \frac{d\phi_{2,(m-1)}}{dn}\right] \tag{2}$$

where $\phi_{1,m}$ is the angle of incidence and $\psi_{1,m}$ is the corresponding angle of refraction so that $\sin\phi_{1,m} = n(\lambda)\sin\psi_{1,m}$ (see Ref. 3 for a detailed definition of terms). The derivative of the generalized single-pass dispersion is given by[4]

$$\frac{d^2\phi_{2,m}}{dn^2} = \tan\phi_{2,m}\left(\frac{d\phi_{2,m}}{dn}\right)^2 + \frac{\cos\psi_{2,m}}{\cos\phi_{2,m}}\left(\frac{d\psi_{1,m}}{dn} + \frac{d\psi_{2,m}}{dn}\right) + \frac{\cos\psi_{2,m}}{\cos\phi_{2,m}}\tan\psi_{1,m}\tan\phi_{1,m}\frac{d\phi_{1,m}}{dn}$$

$$\pm \frac{\cos\psi_{2,m}}{\cos\phi_{2,m}}\frac{\cos\phi_{1,m}}{\cos\psi_{1,m}}\frac{d^2\phi_{2,(m-1)}}{dn^2} + \left(\frac{\sin\psi_{1,m}}{\cos\phi_{1,m}} \pm \frac{d\phi_{2,(m-1)}}{dn}\right)$$

$$\times\left(\frac{\cos\psi_{2,m}}{\cos\phi_{2,m}}\frac{\cos\phi_{1,m}}{\cos\psi_{1,m}}\tan\psi_{1,m}\frac{d\psi_{1,m}}{dn} - \frac{\cos\psi_{2,m}}{\cos\phi_{2,m}}\frac{\sin\phi_{1,m}}{\cos\psi_{1,m}}\frac{d\phi_{1,m}}{dn} - \frac{\sin\psi_{2,m}}{\cos\phi_{2,m}}\frac{\cos\phi_{1,m}}{\cos\psi_{1,m}}\frac{d\psi_{2,m}}{dn}\right)$$

$$\tag{3}$$

For a single isosceles prism these equations reduce to

$$\frac{d\phi_{2,1}}{dn} = \frac{\sin\psi_{2,1}}{\cos\phi_{2,1}} + \frac{\cos\psi_{2,1}}{\cos\phi_{2,1}} \tan\psi_{1,1} \tag{4}$$

and

$$\frac{d^2\phi_{2,1}}{dn^2} = \tan\phi_{2,1} \left(\frac{d\phi_{2,1}}{dn}\right)^2 - \frac{\tan^2\psi_{1,1}}{n} \frac{d\phi_{2,1}}{dn} \tag{5}$$

For incidence at the Brewster angle these equations reduce to the results introduced by Fork et al.,[1] namely, $(d\phi_{2,1}/dn) = 2$ and $(d^2\phi_{2,1}/dn^2) = [4n - (2/n^3)]$.

The emphasis here is in calculating $(d\phi_{2,1}/dn)$ and $(d^2\phi_{2,1}/dn^2)$ for two different configurational alternatives and consequently determining, via Eq. (1), the necessary prism separation to achieve negative dispersion.

Configuration Alternatives

In this section we consider two different geometrical approaches to increase the dispersion and its derivative. The first approach is due to Kafka and Baer[5] and consists in decreasing the angle of incidence in isosceles or equilateral prisms while the apex angle (α) is maintained constant. It should be noted that, at a constant α, decreasing the angle of incidence causes the angle of emergence to increase, thus producing a consequent increment in $(d\phi_{2,1}/dn)$ and $(d^2\phi_{2,1}/dn^2)$. The second approach considered is from Duarte[4] and consists in increasing the angle of incidence while the apex angle of the prism is adjusted to ensure that $\alpha = 2\,\psi_{1,1}$, is maintained as the angle of incidence $(\phi_{1,m})$ is varied. This latter approach also has the effect of increasing $(d\phi_{2,1}/dn)$ and $(d^2\phi_{2,1}/dn^2)$. In this regard, the net effect of these two alternatives is quite similar, and the main issue to be considered now is to elucidate the mechanics of the two methods and to highlight the differences.

Results

Numerical results from the two approaches are presented in Tables I and II. It should be emphasized that determination of the minimum prism separation (ℓ) to achieve negative dispersion is carried out using Eq. (1) and the beam parameters utilized by Fork et al.[1] This is done in order to provide a meaningful comparison with existing data. Certainly, the reader should be aware that changes in wavelength, material and/or beam dimensions will lead to different values for ℓ.

The results of Table I apply to an apex angle (α) of $45°$. For an apex angle of $60°$ the fixed apex angle approach yields $\ell \geq 49.04$ mm at $\phi_{1,1} = 25°$. The minimum value for ℓ utilizing the variable angle approach $(\alpha = 2\,\psi_{1,1})$ is 39.66 mm at $\phi_{1,1} = 84°$ (see Ref. 4). For incidence at the Brewster angle we need $\ell \geq 304.16$ mm, 201.78 mm, and 138.4 mm for $\alpha = 45°$, $\alpha = 60°$, and $\alpha = 2\,\psi_{1,1}$ $(\simeq 68.93°)$, respectively.

Table I

Fixed Apex Angle ($\alpha = 45°$) Approach in Quartz at 620 nm

$\phi_{1,1}$	$d\phi_{2,1}/dn$	$d^2\phi_{2,1}/dn^2$	$\ell(mm) \geq$
5°	2.76	28.73	105.58
10°	1.63	5.48	169.94
20°	1.11	1.41	244.47
30°	0.95	0.61	285.30
40°	0.89	0.27	304.07
50°	0.88	0.04	307.09
60°	0.90	-0.15	300.28
70°	0.93	-0.34	289.61
80°	0.96	-0.49	280.55

Table II

Variable Apex Angle ($\alpha = 2\psi_{1,1}$) Approach in Quartz at 620 nm

$\phi_{1,1}$	$d\phi_{2,1}/dn$	$d^2\phi_{2,1}/dn^2$	$\ell(mm) \geq$
10°	0.24	0.0079	1118.83
20°	0.49	0.07	542.45
30°	0.79	0.29	342.54
40°	1.15	0.92	236.44
50°	1.63	2.76	167.56
60°	2.37	8.90	117.02
70°	3.77	37.25	77.02
80°	7.78	339.35	45.97

Discussion

From Tables I and II it is clear that both the fixed and the variable apex angle approaches produce an increase in $(d\phi_{2,1}/dn)$ and $(d^2\phi_{2,1}/dn^2)$. In the fixed apex angle approach this effect is achieved by decreasing the angle of incidence, while in the variable apex angle method the effect occurs by augmenting the angle of incidence.

A comparison of the results in Tables I and II indicates that a greater affect is achieved via the variable apex approach. However, the use of $\alpha = 60°$ in the fixed apex angle method yields closer results so that the two methods appear to be comparable.

It is not the aim of this communication to advocate the superiority of either method. The aim here is simply to indicate the alternatives. However, it is clear that from a practical perspective the fixed apex angle approach is more attractive since it does not require different sets of prisms. Also, the fixed angle approach is more attractive from the view point of transmission characteristics.

The usefulness of the comparison provided here is the realization that two different and apparently conflicting approaches produce similar results. In addition, it should be stated that the variable apex angle approach provides a conceptual advantage that yields further improvements when combined with the appropriate material. Explicitly, the use of materials with higher refractive index allows the augmentation of the Brewster angle and subsequently an increase in $(d\phi_{2,1}/dn)$ and $(d^2\phi_{2,1}/dn^2)$, which ultimately results in a decrease in the required value of ℓ necessary to obtain a negative value for $(d^2P/d\lambda^2)$. Specific examples of this effect are given by Duarte[4] and include the materials of LaSF9 and ZnSe for which the corresponding Brewster angles are 61.56° and 68.86°, respectively. For incidence at the Brewster configuration the values for minimum ℓ are 49.3 mm for LaSF9 and 11.23 mm for ZnSe.

A further issue of interest concerns the fact of internal beam expansion as the angle of incidence is incremented. In this regard, it is straightforward to show that higher angles of incidence lead to larger internal beam expansion factors. It is also well known, to those familiar with multiple-prism beam expanders,[2,6,7] that higher beam expansion factors lead to higher dispersions.

An additional comment of interest is related to the use of Eq. (1) and the simplified dispersion expressions, Eqs. (4) and (5). This approach is valid as long as the prism pairs are perfectly balanced. Deviations from this idealized configuration will cause a complicated overall dispersion distribution that would necessitate the use of the generalized dispersion formulae.

Conclusions

The principal objective of this communication is to illustrate the fact that two apparently conflicting approaches lead to similar results in terms of the required prism separation to achieve the negative value for $(d^2P/d\lambda^2)$ necessary for pulse compression. The discussion provided solves the apparent paradox of reducing the minimum required ℓ by decreasing and increasing the angle of incidence. The solution to this conceptual difficulty is provided by stipulating the differing methodologies utilized in each case. That is, a reduction in the requirement for ℓ is attained by either decreasing the angle of incidence in the fixed apex angle approach or by increasing the angle of incidence in the variable apex angle approach ($\alpha = 2 \psi_{1,1}$).

On a practical perspective it should be indicated that the best way to achieve negative dispersion at reduced inter-prism separation is to employ materials with higher refractive indices at the Brewster angle of incidence. This approach inherently demands higher angles of incidence and correspondingly higher coefficients of internal beam expansion.

References

1. R. L. Fork, O. E. Martinez, and J. P. Gordon, Opt. Lett. 9, 150 (1984)
2. F. J. Duarte and J. A. Piper, Opt. Commun. 43, 303 (1982)
3. F. J. Duarte and J. A. Piper, Am. J. Phys. 51, 1132 (1983)
4. F. J. Duarte, Opt. Quantum Electron. 19, 223 (1987)
5. J. D. Kafka and T. Baer, Opt. Lett. 12, 401 (1987)
6. F. J. Duarte, Opt. Commun. 53, 259 (1985)
7. R. Trebino, Appl. Opt. 24, 1130 (1985)

INTENSE ULTRASHORT PULSE GENERATION IN TWO-PHOTON PUMPED DYE LASER GENERATORS AND AMPLIFIERS

A. Penzkofer and P. Qiu [*]

Naturwissenschaftliche Fakultät II - Physik,
Universität Regensburg, D-8400 Regensburg, Fed.Rep.Germany

[*] Shanghai Institute of Optics and Fine Mechanics,
Academia Sinica, Shanghai, P.R. China

The dyes rhodamine B, rhodamine 6G and PYC are excited by two-photon absorption of light pulses of a passively mode-locked Nd-glass laser. Ultrashort light pulses in the spectral range between 565 and 630 nm are generated by two-photon induced amplified spontaneous emission (TPI-ASE) and two-photon induced seeding pulse amplification (TPI-SPA) of picosecond light continua. The generated signals are amplified in a two-photon pumped dye laser amplifier (TPI-AMP).

1. Introduction

The single-photon pumped amplified spontaneous emission (SPI-ASE) in organic dyes allows the generation of frequency tunable ultrashort light pulses at the Stokes-side of fixed-frequency pump lasers. Longitudinal[1,2], transversal[3], and travelling-wave transverse[4-6] pumping techniques are applied. The selective spectral amplification of ultrashort light continua in single-photon pumped organic dye solutions (single-photon induced seeding pulse amplification SPI-SPA) is applied in frequency tunable picosecond[1,2] and femtosecond pulse generation[7,8].

The two-photon pumped amplified spontaneous emission (TPI-ASE)[9-11] and the two-photon pumped seeding pulse amplification (TPI-SPA)[11] of ultrashort light continua in organic dye solutions allow the generation of frequency tunable ultrashort light pulses in the wavelength region between the fundamental and second harmonic frequency. The generated signals may be amplified in two-photon pumped dye laser amplifiers (TPI-AMP)[11].

In this paper first the two-photon pumped amplified spontaneous emission and seeding pulse amplification are compared with single photon pumping. In the experiments a passively mode-locked Nd-glass laser[12] serves as pump source for the pulse generation by TPI-ASE, TPI-SPA, and TPI-AMP. The dyes rhodamine B in hexafluoroisopropanol and methanol, rhodamine 6G in HFIP, and PYC (1,3,1',3 -tetramethyl-2,2'-dioxopyrimido-6,6'-carbocyanine hydrogen sulfate)[13] in HFIP have been investigated. Frequency tunable light pulses in the wavelength region between 565 nm and 630 nm have been generated. Energy conversion efficiencies up to 3.5 percent have been obtained in a two-photon pumped generator-amplifier system. The divergence of the generated light is as small as $\Delta\theta \simeq 7\times10^{-4}$ rad.

2. Fundamentals

The dynamics of single-photon induced and two-photon induced ASE, SPA, and AMP are illustrated in the dye configuration coordinate diagrams of Fig.1a and 1b, respectively. The schematic experimental arrangements of amplified spontaneous emission (dye laser generator), seeding pulse amplification, and signal amplification (dye laser amplifier) are depicted in Figs.2a-2c.

The single-photon pumped ASE, SPA, and AMP are described roughly by the equations 1-3. A more detailed equation system is given in Ref.1.

$$\frac{\partial N_{S1}}{\partial t} \simeq \frac{1}{h\nu_L} \sigma_L (N_0 - N_{S1}) I_L \tag{1}$$

$$\frac{\partial I_L}{\partial z} \simeq -\sigma_L (N_0 - N_{S1}) I_L - \sigma_{ex}^L N_{S1} I_L \tag{2}$$

$$\frac{\partial I_F}{\partial z} \simeq h\nu_F \frac{N_{S1}}{\tau_{rad}} \frac{\Delta\Omega}{4\pi} + (\sigma_F - \sigma_F^{ex}) N_{S1} I_F \tag{3}$$

N_{S1} is the number density of dye molecules in the S_1-state. N_0 is the total number density of dye molecules. Eq.1 describes the S_1-state population. The absorption of the pump pulse is given by Eq.2. The first term is due to ground-state absorption and the second term is due
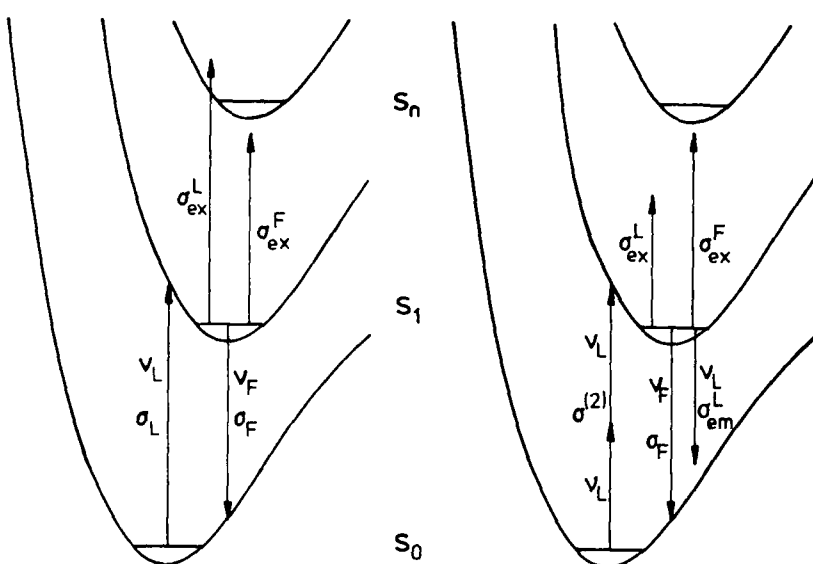
Fig.1: Single-photon induced (a) and two-photon induced (b) dynamics in configuration coordinate systems of dyes.

(a)

(b)
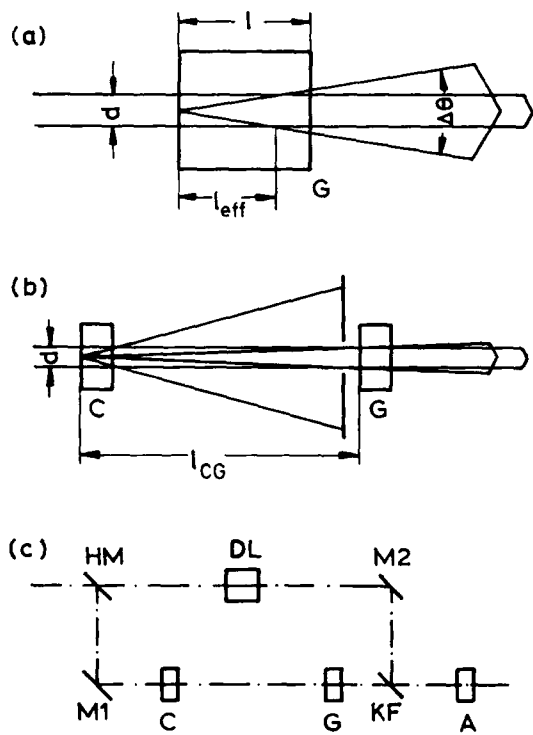
Fig.2: Schematic experimental layouts for (a) two-photon pumped amplified spontaneous emission (TPI-ASE) in generator cell G, (b) two-photon pumped seeding pulse amplification (TPI-ASE), and (c) two-photon pumped generator-amplifier system. C, cell for generation of ps light continuum. G, dye generator cell. A, dye amplifier cell. HM, 50 %-mirror, M1, and M2, 100 %-mirrors. KF, short-pass edge filter. DL, delay block.

to excited state absorption. Eq.3 handles the light emission. The first term gives the spontaneous emission. τ_{rad} is the radiative lifetime of the S_1-state and $\Delta\Theta$ is the solid angle of efficient amplified spontaneous emission [$\Delta\Omega = \pi(\Delta\Theta)^2/4$, $\Delta\Theta$ beam divergence of generated light]. The second term of Eq.3 is due to stimulated emission and describes the amplification of spontaneous emission (no input signal), the seeding pulse amplification (input of light continuum), and the signal amplification (input of ASE or SPA-signal).

Solution of Eq.3 gives an amplification factor (gain) $G = I_{F,out}/I_{F,in}$ of

$$G = \exp[(\sigma_F - \sigma_F^{ex})N_{S1}\ell_{eff}] \tag{4}$$

The dye concentrations in single-photon pumping are low and the pump pulses bleach the ground-state absorption at the cell entrance. The pump pulse penetration length ℓ_{eff} is derived from the relation (solution of Eq.2) $T \simeq \exp\{-[\sigma_L(N_0 - N_{S1}) + \sigma_{ex}^L N_{S1}]\ell_{eff}\} \leq \exp\{-\sigma_{ex}^L N_0 \ell_{eff}\} = \exp(-1)$ to be

$$\ell_{eff} \leq (N_0 \sigma_{ex}^L)^{-1} \tag{5}$$

The amplification factor is limited to (insertion of Eq.5 into Eq.4 with $N_{S1} \to N_0$)

$$G \lesssim \exp\left(\frac{\sigma_F - \sigma_{ex}^F}{\sigma_{ex}^L}\right) \tag{6}$$

For optimum signal output the dye cell length ℓ should be approximately equal to ℓ_{eff} in order to avoid reabsorption of generated light at frequency ν_F due to reabsorption in unexcited dye regions.

The two-photon pumped ASE, SPA, and AMP are described roughly by the Eqs.7-9. A detailed description is given in Ref.10.

$$\frac{\partial N_{S1}}{\partial t} \simeq \frac{1}{2(h\nu_L)^2}\sigma^{(2)}N_0 I_L^2 - \frac{1}{h\nu_L}\sigma_{em}^L N_{S1}I_L \tag{7}$$

$$\frac{\partial I_L}{\partial z} \simeq -\frac{1}{h\nu_L}\sigma^{(2)}N_0 I_L^2 + \sigma_{em}^L N_{S1}I_L - \sigma_{ex}^L N_{S1}I_L \tag{8}$$

$$\frac{\partial I_F}{\partial z} \simeq h\nu_F \frac{N_{S1}}{\tau_{rad}}\frac{\Delta\Omega}{4\pi} + (\sigma_F - \sigma_F^{ex})N_{S1}I_F \tag{9}$$

The first term of Eq.7 gives the S_1-state population by two-photon absorption. The second term is responsible for the S_1-level depopulation by stimulated emission. This term reduces the light amplification factor G at frequency ν_F since it reduces the S_1-level population. The stimulated emission at frequency ν_L does add to the pump pulse intensity (second term of Eq.8) but two pump pulse photons are absorbed (first term of Eq.7) and only one photon is returned. The equation of amplified spontaneous emission and stimulated emission (Eq.9) is identical to Eq.3. The amplification factor G is again given by Eq.4. High dye concentrations are needed in two-photon pumping to absorb the pump pulse effectively at reasonable pump pulse intensities (avoidance of dielectric breakdown or other nonlinear optical processes like stimulated Raman scattering) and sample lengths (order of confocal length of lenses). The pump pulse generally does not deplete remarkably the ground-state population and the S_1-state population at the cell entrance is approximately

$$N_{S1} \simeq \frac{1}{2(h\nu_L)^2}\sigma^{(2)}N_0 I_L^2 \Delta t_L \tag{10}$$

The effect of stimulated emission at the pump pulse frequency is neglected. Δt_L is the pump pulse duration. In most cases the excited state absorption of the pump laser determines the effective interaction length ℓ_{eff}. The two-photon transmission is $T \simeq \exp(-\sigma_{ex}^L N_{S1}\ell_{eff})/\{1+\sigma^{(2)}N_{S1}I_L[1-\exp(-\sigma_{ex}^L N_{S1}\ell_{eff})]/(\sigma_{ex}^L N_{S1})\} < \exp(-\sigma_{ex}^L N_{S1}\ell_{eff})$ and the condition $T \simeq \exp(-1)$ gives

$$\ell_{eff} < (\sigma_{ex}^L N_{S1})^{-1} \simeq \frac{2(h\nu_L)^2}{\sigma_{ex}^L \sigma^{(2)}N_0 I_L^2 \Delta t_L} \tag{11}$$

The maximum possible amplification factor is again given by Eq.6. The sample length should be approximately equal to ℓ_{eff}.

In the case of two-photon pumping, σ_{ex}^L may be smaller than in the case of single photon pumping (Fig.1) so that higher amplification factors may be obtainable. For the same dyes single photon pumping would require pumping with the second harmonic light of the pump laser which reduces the over-all efficiency.

For amplified spontaneous emission the generated pulse durations Δt_F ($\Delta t_F < \ln(2)\tau_F$, τ_F is lifetime of spontaneous emission) depend strongly on the amplification factor G (and bottle-neck effects[1,10,11]). The seeding pulse amplification of pump-pulse generated light continua gives pulse durations of approximately $\Delta t_F \simeq \Delta t_L/3$.

3. Results

3.1 Dyes. Spectroscopic parameters of the investigated dyes are listed in Table 1. Further informations are given in Ref.11. The absorption cross-section spectrum and stimulated emission cross-section spectrum[16] of rhodamine B in HFIP is depicted in Fig.3. The wavelength positions of two-photon excitation $\lambda_L/2$, excited state absorption λ_{ex}^L and λ_{ex}^F together with the region λ_F of amplified spontaneous emission (FWHM) are included.
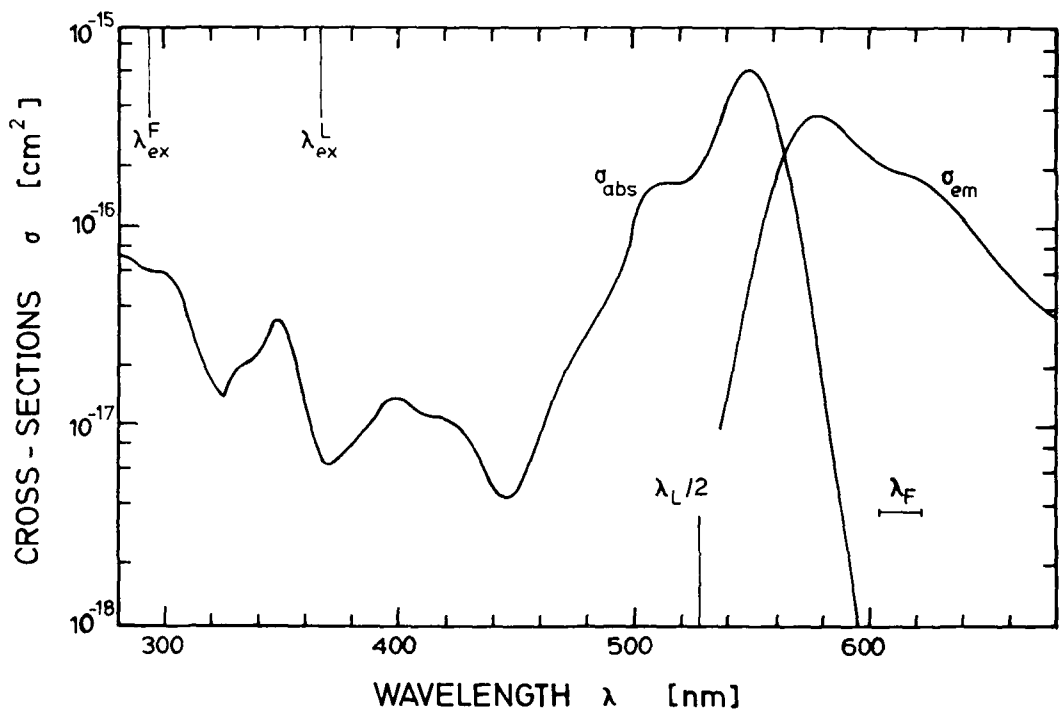
Fig.3: Absorption and emission cross-section spectrum of rhodamine B in hexafluoroisopropanol (HFIP).

3.2 Two-photon absorption. The measured energy transmissions of picosecond pump pulses ($\Delta t_L \simeq 5$ ps, $\lambda_L = 1.055$ μm) through 10^{-2} molar rhodamine B in HFIP are shown by the open circles of Fig.4. The solid curve is calculated by fitting the two-photon absorption cross-section $\sigma^{(2)}$ and the excited-state absorption cross-section σ_{ex}^L [10] (see Table 1). The solid circles and the dashed curve belong to the solvent HFIP. Above 1.5×10^{11} W/cm² the pump pulse transmission through the solvent reduces drastically by nonlinear optical effects. The solid energy transmission curve indicates optimum intensity conditions for amplified spontaneous emission around $I_{0L} \simeq 1.5 \times 10^{11}$ W/cm². The two-photon absorption parameters $\sigma^{(2)}$ and σ_{ex}^L of the investigated dyes are listed in Table 1.

3.3 Two-photon induced seeding pulse amplification (TPI-ASE). The displayed results belong to 0.01 molar rhodamine B in HFIP. In Table 1 results are summarized for the other dye solutions.

Fig.5a displays the ASE-energy conversion efficiency η_E versus pump pulse input intensity I_{0L}. The sample length is $\ell = 2$ cm. The circles are measured and the curve is calculated.[10,11] The energy conversion efficiency rises steeply and saturates above $I_{0L} \simeq 10^{11}$ W/cm² (see Eq.6). The energy conversion efficiency versus sample length is depicted in Fig.5b for $I_{0L} = 1.5 \cdot 10^{11}$ W/cm². Gain saturation is observed for sample lengths $\ell > 1$ cm.

The wavelength of maximum ASE emission, $\lambda_{F,max}$, (dash-dotted curve) and the spectral half-width of the ASE emission (width of hatched region) are shown versus pump pulse peak inten-

391
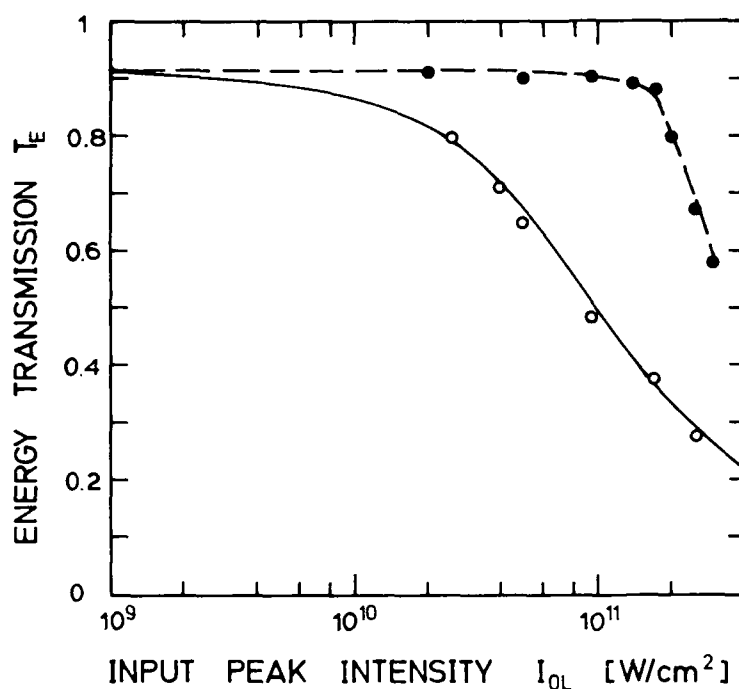
Fig.4: Energy transmission of pump pulses ($\lambda_L = 1.055$ μm, $\Delta t_L = 5$ ps) through 0.01 molar rhodamine B in HFIP (solid curve) and pure solvent HFIP (dashed curve). Sample length $\ell = 2$ cm.
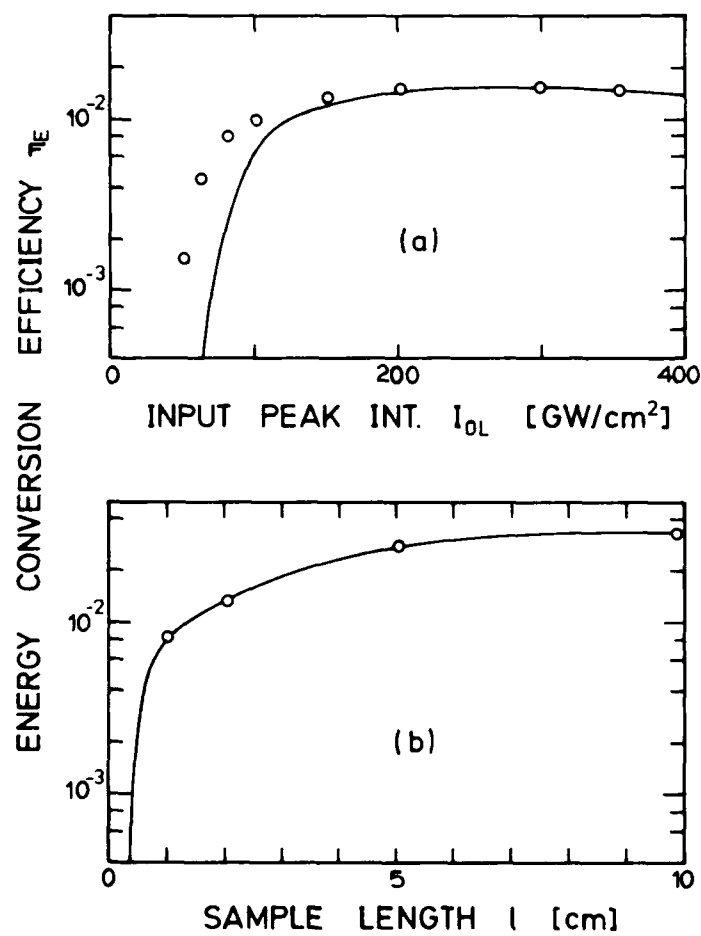
Fig.5: Energy conversion efficiency η_E of TPI-ASE versus (a) pump pulse peak intensity I_{0L} ($\ell = 2$ cm, solid curve calculated[11]) and (b) sample length ℓ ($I_{0L} = 1.5 \times 10^{11}$ W/cm²). Dye: 0.01 molar rhodamine B in HFIP.

392

sity in Fig.6a. The sample length is ℓ = 2 cm. $\lambda_{F,max}$ versus sample length is displayed in Fig.6b for I_L = $1.5 \cdot 10^{11}$ W/cm². The wavelength of maximum emission shifts to longer wavelengths with sample length because of fluorescence light reabsorption (see long-wavelength absorption tail of Fig.3). The spectral distribution of an ASE signal (ℓ = 2 cm, I_{OL} = $1.5 \cdot 10^{11}$ W/cm²) is reproduced in Fig.7a. The spectral distribution is rather flat (averaging over ASE-divergence angle).
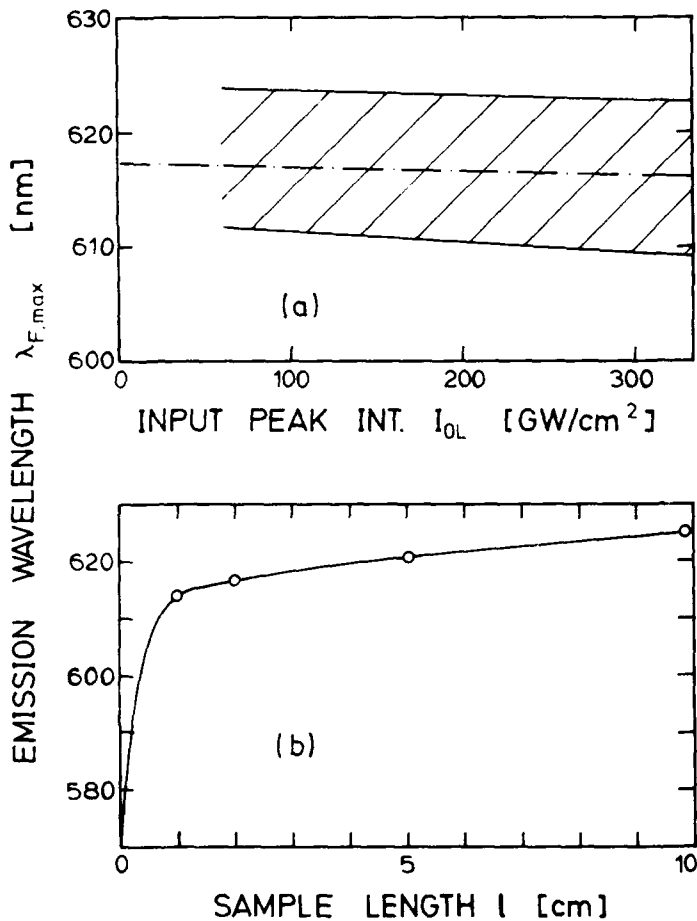
Fig.6: Wavelength of peak TPI-ASE emission versus (a) pump pulse peak intensity I_{OL} (ℓ = 2 cm) and (b) sample length ℓ (I_{OL} = 1.5×10^{11} W/cm²). Hatched region of (a) indicates spectral width (FWHM). Dye is 0.01 molar rhodamine B in HFIP.

The dependence of the ASE divergence $\Delta\theta$ on the input pump pulse peak intensity for ℓ = 2 cm and on the sample length for I_{OL} = 1.5×10^{11} W/cm² are depicted in Figs.8a and b, respectively. At low intensities the divergence increases drastically because of reduced gain, and at high intensities the divergence increases because of shorter effective interaction length ℓ_{eff} (Eq.11, $\Delta\theta$ = d/ℓ_{eff}, d beam diameter of pump pulse, see Fig.2a).

Calculated results of the ASE-pulse duration versus pump pulse peak intensity (ℓ = 2 cm) are presented in Fig.9[11]. The ASE pulse duration shortens strongly with increasing pump pulse intensity. Above I_{OL} = $8 \cdot 10^{10}$ W/cm² the ASE pulse duration Δt_F becomes shorter than the pump pulse duration Δt_L (dashed-dotted line). The inset of Fig.9 shows the temporal shape of the pump pulse (dashed curve) and of the ASE pulse at I_{OL} = 1.5×10^{11} W/cm² (solid curve).

3.4 Two-photon induced seeding pulse amplification (TPI-SPA). For the seeding pulse amplification experiments, the picosecond light continuum is generated in a 2 cm long D_2O cell[1] (Fig.2b). At I_L = 1.5×10^{11} W/cm² the energy conversion efficiency of the light continuum within a spectral width of $\Delta\lambda$ = 10 nm around 600 nm is approximately 5×10^{-5}. The seeding pulse amplification reduces drastically the divergence of the spectrally selective amplified light continuum ($\Delta\theta$ = d/ℓ_{CG}, ℓ_{CG} distance between D_2O cell and dye cell, see Fig.2b). A spectral distribution of the SPA signal generated by 0.01 molar rhodamine B in HFIP (ℓ = 2 cm, I_L = $1.5 \cdot 10^{11}$ W/cm²) is displayed in Fig.7b. The spectrum is strongly structured because the divergence angle $\Delta\theta$ becomes comparable to the coherence angle of the generated light[11]. The energy conversion efficiency of the SPA light is approximately the same as in the case of the ASE light, but the divergence is drastically reduced. Results of the energy conversion efficiency and of the beam divergence are listed in Table 1. The wavelengths of maximum spectral emission $\lambda_{F,max}$ and the spectral widths (FWHM) of emission are approximately
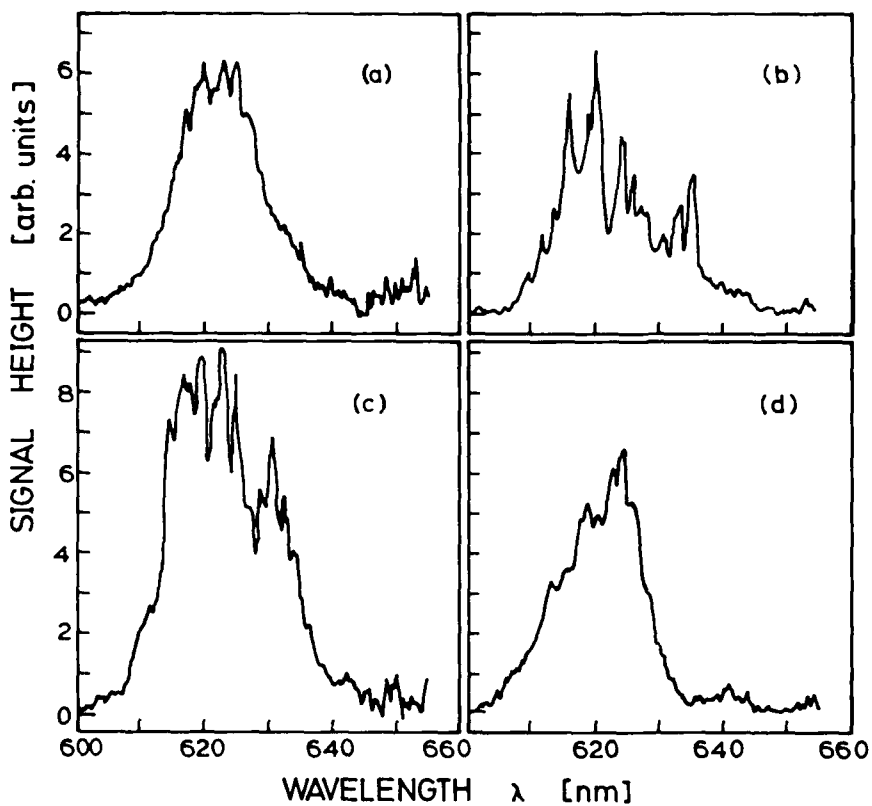
Fig.7: Spectral distributions of 0.01 molar rhodamine B in HFIP. Cell lengths ℓ = 2 cm. Pump pulse peak intensities $I_{0L} \simeq 1.5 \times 10^{11}$ W/cm². (a) TPI-ASE. (b) TPI-SPA. (c) amplified ASE signal. (d) amplified SPA-signal.

the same as in the case of amplified spontaneous emission.

3.5 Two-photon induced signal amplification (TPI-AMP). The TPI-ASE and the TPI-SPA signals may be further increased in energy, and the divergence may be further reduced in two-photon pumped dye laser amplifiers. Behind the dye generator cell spectral narrowing and spectral tuning is possible to generate narrow-band spectrally tunable light pulses.

With the experimental arrangement of Fig.2c, TPI-ASE and TPI-SPA signals have been amplified. In the generator cell and in the amplifier cell 0.01 molar rhodamine B in HFIP was applied in 2 cm long cells. The over-all energy conversion efficiency (signal behind amplifier to total input signal before beam splitter, Fig.2c) was a few percent (for TPI-ASE: $r_E \simeq 0.02$; for TPI-SPA: $r_E \simeq 0.035$). The beam divergence of the generated light behind the amplifier was $\Delta \simeq 7 \times 10^{-4}$ rad. Spectral distributions are shown in Fig.7c and d.

4. Conclusions

The two-photon pumped amplified spontaneous emission, seeding pulse amplification, and signal amplification allows to generate frequency tunable ultrashort light pulses at the anti-Stokes side of ultrashort fixed-frequency pump lasers. The over-all efficiency of two-photon pumped amplified spontaneous emission is very likely higher than the single-photon pumped amplified spontaneous emission which employs the second harmonic of the pump pulses. Very often the excited-state absorption of the second harmonic light is higher than the excited state-absorption of the fundamental light, which favours the two-photon pumped amplified spontaneous emission.

For the TPI-ASE and TPI-SPA experiments laser dyes and fast saturable absorbers may be employed. In TPI-ASE experiments the generated pulse duration is strongly gain dependent and fast picosecond saturable absorbers give shorter pulse durations than laser dyes with nanosecond fluorescence lifetime. The seeding pulse amplification of pump-pulse generated parametric light continua generates pulse durations of typically one third of the pump pulse duration.

Two-photon pumped generator-amplifier systems may be applied to other picosecond and femtosecond pump sources. They may be very fruitful for the generation of frequency tunable ultrashort light pulses in the near ultraviolet spectral region by employing visible pump pulses. Besides dyes other laser materials may be employed in two-photon pumped generator-amplifier systems (e.g. semiconductors[18]).

394
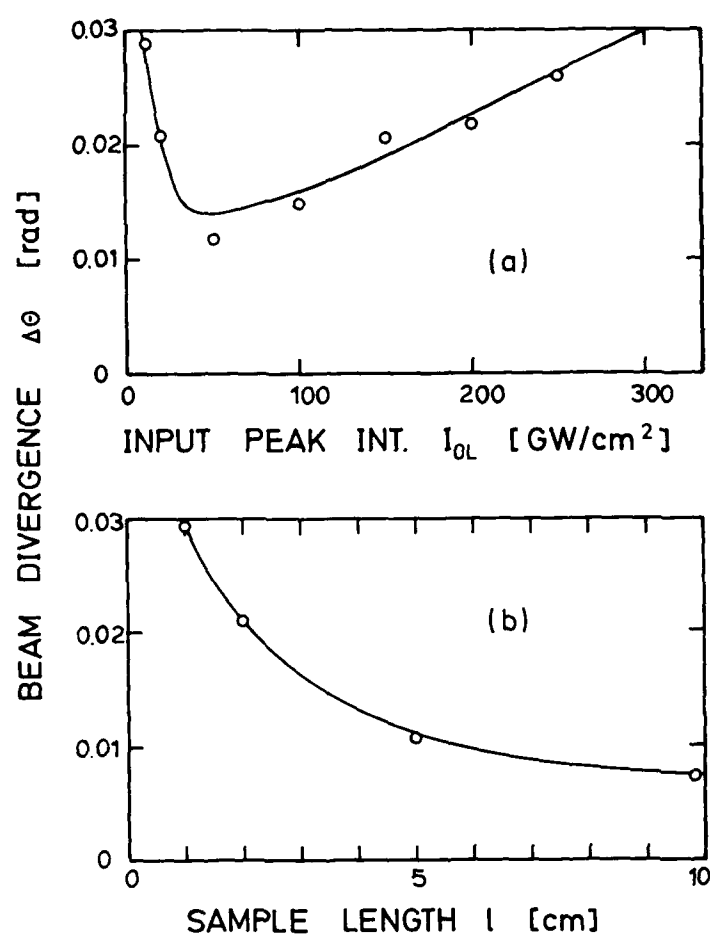
Fig.8: Beam divergence $\Delta\Theta$ of TPI-ASE signal versus (a) pump pulse peak intensity I_{0L} (ℓ = 2 cm) and (b) sample length ℓ ($I_{0L} \approx 1.5\times10^{11}$ W/cm²). Dye: 0.01 molar rhodamine B in *HFIP*.
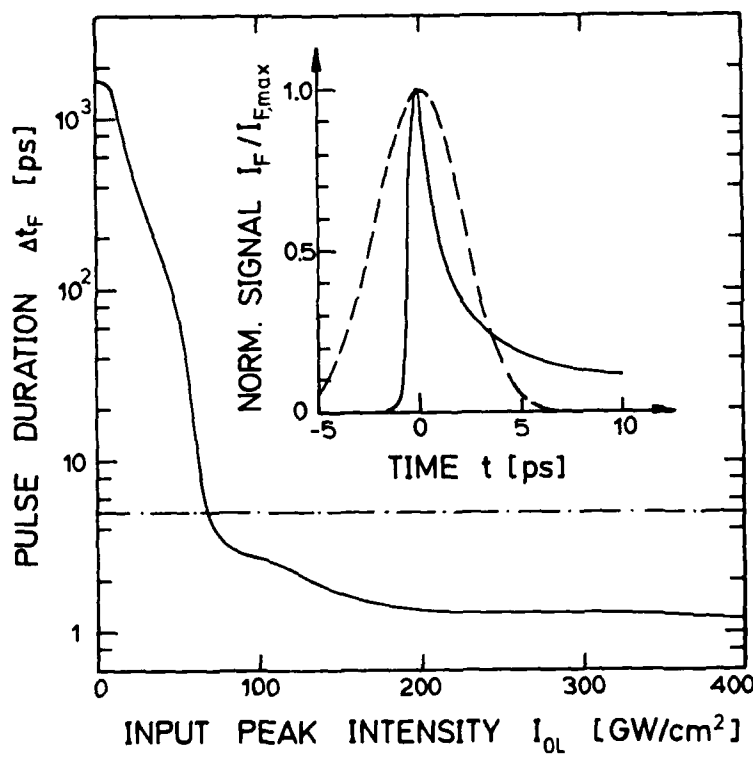
Fig.9: Calculated duration of TPI-ASE signal versus pump pulse peak intensity I_{0L} (sample length ℓ = 2 cm, dye concentration 0.01 mol/dm³). Dye parameters of rhodamine B in HFIP (Table 1) are used. Dashed-dotted line indicates pump pulse duration Δt_L. Inset gives temporal pulse shape of pump pulse (dashed curve) and of ASE-signal at I_{0L} = 1.5×10¹¹ W/cm².

Table 1: Dye parameters and dye performance data. ASE and SPA data belong to dye concentrations of $C = 10^{-2}$ mol/dm³ and pump pulses of $\lambda_L = 1.055$ µm, $\Delta t_L = 5$ ps, and $I_{0L} = 1.5 \times 10^{11}$ W/cm².

Parameter	Rhodamine B		Rhodamine 6G	PYC
Solvent	HFIP	Methanol	HFIP	HFIP
$\sigma^{(2)}$ [cm⁴s]	1.5×10^{-49}	1.5×10^{-49}	1×10^{-49}	1.8×10^{-49}
σ_{ex}^{L} [cm²]	1×10^{-17}	1.5×10^{-17}	5×10^{-18}	$\leq 2 \times 10^{-18}$
$\lambda_{F,max}$ [nm]	617	620	570	600
σ_F [cm²]	1.9×10^{-16}	1.5×10^{-16}	1.5×10^{-16}	1.85×10^{-16}
σ_{ex}^{F} [cm²]	3×10^{-17}	1×10^{-17}	9×10^{-17}	7.5×10^{-17}
τ_F [ns]	2.4	1.17	4.1	0.011
TPI-ASE				
r_E	1.3×10^{-2}	7×10^{-3}	5×10^{-4}	7×10^{-3}
$\Delta\Theta$ [rad]	2×10^{-2}	2×10^{-2}	2.5×10^{-2}	2×10^{-2}
$\Delta\lambda_F$ [nm]	13	20	8.5	12
Δt_F [ps]	1.7	4.5	10	0.35
TPI-SPA				
r_E	1×10^{-2}	7×10^{-3}	1×10^{-3}	3×10^{-3}
$\Delta\Theta$ [rad]	1.8×10^{-3}	2.5×10^{-3}	2×10^{-3}	3×10^{-3}

References

1. P. Sperber, W. Spangler, B. Meier, and A. Penzkofer, Opt. Quantum Electron. 20, 395 (1988).
2. P. Sperber, W. Spangler, B. Meier, and A. Penzkofer, in Proceedings, International Conference on Lasers'87, D.A. Duarte, Ed. (STS Press, McLean, VA, 1988) pp. 370-377.
3. C. Lin, T.K. Gustafson, and A. Dienes, Opt. Commun. 8, 210 (1973).
4. Zs. Bor and A. Müller, IEEE J. QE-22, 1524 (1986).
5. T. Elsaesser, H.J. Polland, A. Seilmeier, and W. Kaiser, IEEE J. QE-20, 191 (1984).
6. W. Lee, C. Ning, and Z. Huang, Appl. Phys. B40, 35 (1986).
7. A. Migus, I.L. Martin, R. Astier, A. Antonetti, and A. Orizag, in Picosecond Phenomena III, K.B. Eisenthal, R.M. Hochstrasser, W. Kaiser, and A. Laubereau, Eds. (Springer-Verlag, Heidelberg, 1982) pp.6-9.
8. P.C. Becker, H.L. Fragnito, R.L. Fork, F.A. Beisser, and C.V. Shank, in Ultrafast Phenomena VI, T. Yajima, K. Yoshihara, C.B. Harris, and S. Shionoya, Eds. (Springer-Verlag, Heidelberg, 1988) pp. 12-14.
9. V.I. Prokohorenko and E.A. Tikhonov, Sov. J. Quant. Electron. 16, 1214 (1986).
10. A. Penzkofer and W. Leupacher, Opt. Quantum Electron. 19, 327 (1987).
11. P. Qiu and A. Penzkofer, Appl. Phys. B, to be published.
12. A. Penzkofer and F. Graf, Opt. Quantum Electron. 17, 219 (1985).
13. A. Penzkofer, W. Leupacher, B. Meier, B. Runde, and K.H. Drexhage, Chem. Phys. 115, 143 (1987).
14. A. Penzkofer and W. Kaiser, Appl. Phys. Letters 21, 427 (1972).
15. A. Penzkofer and W. Kaiser, Opt. Quantum Electron. 9, 315 (1977).
16. A. Penzkofer and W. Leupacher, J. Luminesc. 37, 61 (1987).
17. L. Mandel and E. Wolf, Rev. Mod. Phys. 37, 231 (1965).
18. A. Penzkofer and A.A. Bugayev, Opt. Quantum Electron., to be published.

THERMAL EFFECTS IN AN EXCIMER-PUMPED DYE LASER

E. Berik, I. Berik and V. Davidenko
Institute of Physics, 202400 Tartu, USSR

Abstract

It is shown that the main reason for the efficiency reduction of the transverse-pumped pulsed dye laser is a short-focus negative cylindrical lens thermally formed in the active medium. This effect is well expressed under UV excimer pumping because of large Stokes losses in lasing molecules and fast nanosecond energy relaxation in the excited zone. Other consequences of thermo-optical aberrations - the dynamic shift of the lasing wavelength and the broadening of emission spectra - have been found and interpreted.

Introduction

The thermal processes, arising in the active medium of lasers under powerful pumping, often evoke disturbances in the laser cavity, thus influencing the characteristics of the output radiation. These processes proceeding in the millisecond time scale have been studied in solid-state lasers[1,2] and in flash-lamp-pumped dye lasers[3,4]. Later the presence of thermo-optical effects has been found in longitudinally-pumped pulsed dye lasers excited by Nd:YAG lasers[5,6]. For transversely-pumped dye lasers with the excitation by a nitrogen laser the saturation of the output energy on pumping with the power higher than 5 mJ has been noted[7]. However, this effect has neither been studied carefully nor interpreted.

In excimer-pumped pulsed dye lasers, the effects of the thermo-optical distortion of the excited zone should play a considerable role. It can be explained by the large Stokes losses in UV-excited dye molecules emitting in the visible or IR as well as by the considerable length of the excited zone and by the high energy of pumping available for excitation.

In this communication, we attempt to determine which of the thermal effects has time to influence the nanosecond lasing of the excimer-pumped dye laser and we try to calculate the results of this influence.

Theoretical approach

Let us consider the process of transverse excitation of the dye solution in the rectangular cell, performed by the output beam of an excimer laser (Fig. 1). The pumping beam spreading in z-direction has an intensity distribution in the cross-section near-Gaussian in Y-axis direction and rectangular in perpendicular direction, which is typical of transverse-discharge gas lasers.
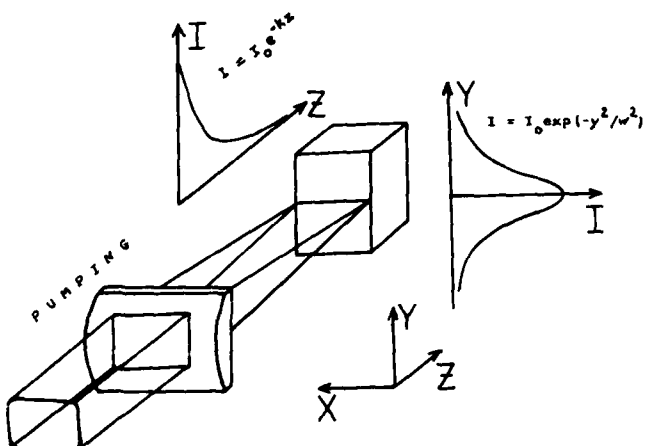
Fig. 1   The coordinates used and the distribution of the pumping intensity in the active medium.

Being focused by a cylindrical lens in YZ plane, the beam retains the Gaussian (or bell-shaped) profile of the intensity distribution

$$I(y) = I_o e^{-y^2/\omega^2} \tag{1}$$

with the halfwidth equal to $2\omega\sqrt{\ln 2}$.

On passing through the absorbing medium of the dye solution the pumping beam loses the intensity in accordance with the Bouger-Bear exponential law,

$$I(z) = I_o e^{-kz}, \tag{2}$$

where k is the absorption coefficient of the solution of the pumping wavelength. The law should be correct in our case of strong stimulated radiation reducing the concentration of the excited dye molecules and at moderate density of the pumping power.

Thus, the distribution of the energy accumulated by the solution, if the nonradiative losses of energy and reabsorption of lasing are negligible, can be written for YZ plane as follows:

$$Q(y,z) = AE_p \frac{\lambda_e - \lambda_p}{L\lambda_e} e^{-y^2/\omega^2 - kz}, \tag{3}$$

where λ_e and λ_p are the lasing and the pumping wavelengths, respectively, L is the length of the excited zone in X direction, E_p is the energy of the pumping pulse and A is a normalizing coefficient calculated from the equation

$$A \cdot \int_o^L \int_{-\infty}^{\infty} \int_o^{\infty} e^{-y^2/\omega^2 - kz} \, dx \, dy \, dz = 1, \tag{4}$$

A is equal to $k/\omega L\sqrt{\pi}$.

Typical concentrations of dye molecules in the solution for the excimer pump are of the order of $1 \div 3 \cdot 10^{-3}$ M/L, that corresponds to the distance between the molecules of $10 \div 15$ nm. The total number of dye molecules in the zone of excitation is about 10^{15} (the dimensions of the zone are determined by the laser cavity requirements). Thus, using a 5 mJ pumping pulse, we have to excite every molecule of the dye by about 5 times. The dye molecule, relaxed from the upper excited state within $10^{-13} \div 10^{-12}$ s, can be considered as a local (point) source of heat. It warms the homogeneous medium of the surrounding solvent in accordance with the equation

$$\partial T/\partial t - \gamma \Delta T/c\rho = \delta(r,t), \tag{5}$$

where $\int_o^{\infty} \int_o^{\infty} \delta(r,t) dr \, dt = Q$.

Here $T = T(r,t)$ is the local temperature, γ, c and ρ are respectively the coefficient of thermal conductivity, the heat capacity and the density of the solvent. Equation (5) has a solution of the form

$$T(r,t) = \frac{Q}{(2\sqrt{\gamma\pi t/\rho c})^3} e^{-\frac{|r|^2}{4\gamma t/c\rho}}. \tag{6}$$

In the case under consideration the time of the thermalization of the solution (a time required for reaching the thermal equilibrium in the space between the neighboring dye molecules) can be estimated from the formula

$$T(o,t_o) = 2T(1/2,o). \tag{7}$$

In the formula, 1 is the average distance between the dye molecules (in case of lower power density of excitation the value of 1 can exceed the intermolecular distance by several times).

This time is equal to

$$t_o = 1^2 c\rho/4\ln 2. \tag{8}$$

By using ethanol as a solvent (c = 0.59 cal·C^{-1}·g^{-1}, ρ = 0.78 g·cm^{-3}, γ = 4.3·10^{-4} cal·cm^{-1}·s^{-1}·C^{-1}) one can obtain t_o = 0.4 ns at 1 = 10 nm (dye concentration 2·10^{-3} M/l).

The obtained value of t_o shows a dynamic character of the formation of thermal non-uniformity in the dye solution, that allows one to consider it as a function of the pumped energy only.

Thus, we have

$$T(y,z,t) = \frac{kE_p(t)}{\omega L\sqrt{\pi}c\rho} \frac{\lambda_e - \lambda_p}{\lambda_e} e^{-y^2/\omega^2 - kz}. \tag{9}$$

398

The relaxation of the stimulated thermal macro-non-uniformity (i.e. the excited zone of dye solution) is described by the same equation (6) with $1 \sim 0.5$ mm (transverse size of the excited zone). In this case the calculation gives the relaxation time of the order of hundreds milliseconds.

The increment of the refraction index n in the excited zone, caused by the thermal distortion of the optical properties of the solution, can be written as

$$\Delta n(y,z,t) = \frac{\partial n}{\partial T} \cdot \Delta T(y,z,t), \tag{10}$$

where $\partial n/\partial T$ is the thermal dispersion of the refraction index of the solvent.

The thermal dispersion of n can be expressed as

$$\partial n/\partial T = (\partial n/\partial T)_\rho + (\partial n/\partial\rho) \cdot \partial\rho/\partial T. \tag{11}$$

In case of instantaneous subnanosecond heating of the solvent in the active zone at laser pumping there is no thermal expansion of the solution during the time of lasing. Thus we can neglect the second part in sum (11).

When the light beam passes through the medium with the gradient of the refraction index perpendicular to its axis, the beam will deviate in the direction of higher values of n. In accordance to[8] the radius of the curvature of the deviation can be expressed as

$$R = [\vec{j} \cdot grad(\ln n)]^{-1}. \tag{12}$$

By solving equation (10) for the independent coordinates Z and Y, we have

$$R_y^{-1} = 2 \frac{\partial n}{\partial T} \frac{kyE_p}{\omega^3\sqrt{\pi}c\rho n} \frac{\lambda_e - \lambda_p}{\lambda_e} e^{-y^2/\omega^2 - kz}, \tag{13}$$

$$R_z^{-1} = \frac{\partial n}{\partial T} \frac{k^2E_p}{\omega\sqrt{\pi}c\rho n} \frac{\lambda_e - \lambda_p}{\lambda_e} e^{-y^2/\omega^2 - kz}. \tag{14}$$

The solutions describe the formation of a negative cylindrical lens in the axis Y (in the center of the lasing beam ($Y = 0$) the refraction index has a minimum, as $(\partial n/\partial T)_\rho$ for the solvents used is negative). In the plane XZ, the beam deviates from the front wall of the dye sell. The deviation depends on the magnitude of z, i.e. the beam divergence increases as well.

The numerous factors influencing the spatial characteristics of the beam passing through the solution disturbed by the pumping pulse, make it difficult to obtain the exact expression for the variation of the laser output. Nevertheless, we can estimate this influence in the first approximation by studying the behavior of the rays passing through the key points with the co-ordinates in YZ plane ($\omega\sqrt{\ln2}$; k/2) and 0, k/2). The first of the points describes the beam deviation in Y-axis direction, the second, corresponding to the center of the beam, its deviation in z direction.

For Rhodamin 6G dye at $\lambda_e = 580$ nm, pumped by 10 mJ pulse of XeCl laser ($\lambda_p = 308$ nm), the calculation performed for these points with ethanol as a solvent (($\partial n/\partial T)_\rho = -0.24 \cdot 10^{-4}$, $n = 1.36$) gives when $k = 45$ cm^{-1} and $\omega = 0.017$ cm,

R_y (0.014 cm; 0.011 cm) = 11.7 cm,

R_z (0; 0.011 cm) = 12.2 cm.

The focal length of the thermally-formed negative lens, determined by the formula

$$f = R_y\omega\ln2/L, \tag{15}$$

is about 8 cm.

In the dye laser used, the dispersion plane of the Littrow-mounted diffraction grating coincides with the plane XZ and thus the deviation of the beam in Z-direction leads to the variation of the lasing wavelength in accordance with the expression

$$\Delta\lambda = \lambda\Delta\phi/Mtg\phi, \tag{16}$$

where $\Delta\phi$ is the full angle of deviation, ϕ is the grating angle and M is the magnification ratio of an intracavity beam expander.

Although the thermal deviations of rays in Y and Z directions are of the same order, they have different influence on the characteristics of the laser output. The beam deviation in the grating is compensated by the tuning of the lasing wavelength; Y-direction deviations

cause the cavity disadjustment and lead to the depression of lasing.

In general, the thermo-optical effects in the laser grow dynamically in accordance with the obtained pumping energy, $E(t) = \int_0^t P(\tau)d\tau$, and give the contribution in the output radiation which is proportional to the instantaneous power of dye laser.

Results and discussion

To detect the appearance of the thermally-induced effects in the pulsed dye laser one can record the spatial as well as spectral properties of the output radiation or its power.

The equipment used permits one to study any of these characteristics. The object of investigation was an excimer-pumped dye laser VL-10 developed in the Estonian SSR Acad. Sci.[9]. The laser has a modified Hänsch-type oscillator with a high-order ruled grating of 600 grooves/mm and a 40-fold multiprism achromatic beam expander. The laser is provided with one amplifier. The dye cell length L in the oscillator is equal to 20 mm; the circulation system guarantees the change of the dye solvent in the area of excitation in the time between the shots.

VL-10 has been excited by one or two XeCl excimer lasers of ELI-type, produced in Estonia[10]. The excimer lasers were synchronized with an accuracy better than ±3 ns. The temporal resolution of the recording system was of the order of 0.2 ns, the spectral properties of radiation were recorded by a diode-array-provided grating spectrometer with the resolution 2.2 pm[9].

The same multichannel recording system was used to determine the pumping power distribution in the dye. By translation the cylindrical lens in Z direction we have found its position where the bell-shaped profile of the intensity in Y direction has the required half-width (0.28 mm) (Fig. 2).
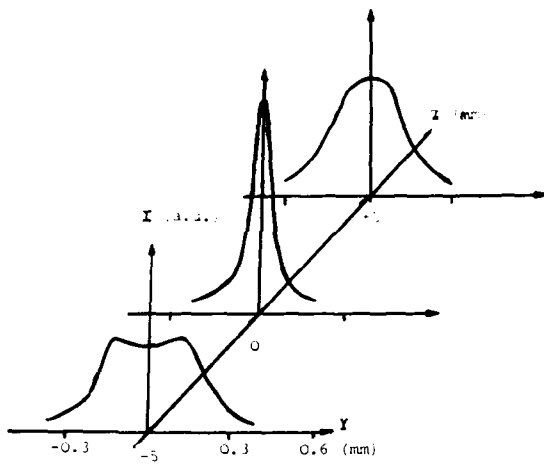
Fig. 2   Spatial distribution of the focused pumping beam near its waist. Lens focal length 76 nm.
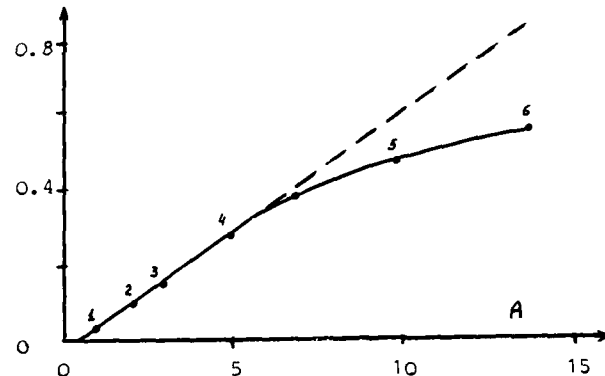
Fig. 3   Output energy of the dye laser oscillator as a function of the energy of the pumping pulse (A). Oscillograms of the dye laser output for some pumping energies (B). The points in Fig. 3A correspond to the profiles in Fig. 3B. Rhodamin 6G dye, lasing wavelength 585 nm.

400
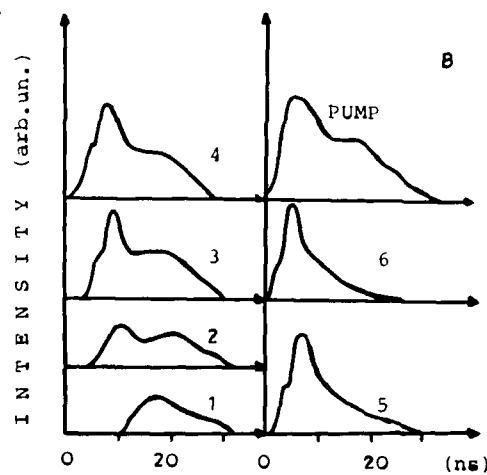
In the first stage of the experiment, we studied the effect of saturation of the output energy of the dye laser on a powerful pumping. The energy of radiation and the temporal form of the pulses were measured simultaneously (Fig. 3).

At very low pumping energy (near threshold) the dye lasing appears much later than the pumping pulse due to the necessity to make a few roundtrips in the cavity to reach the lasing. When the pumping power is increased, the evolution time becomes shorter and the dye laser pulse looks like a pumping one (point 4). This point corresponds to the maximum of the efficiency of the dye laser oscillator.

Further enhancement of E_p evokes only a small shift of the front part of the lasing pulse, the peak power remains proportional to the pumping energy. However, the tail of the pulse begins to disappear, that leads to the pulse shortening and to the efficiency degradation. At a very high power of excitation the dye laser pulse can be   many times shorter than the pumping pulse (point 6).

The measurements show that the depression of lasing studied grows in accordance with the absorbed pumping energy, i.e. it can be explained by the thermo-optical disturbance in the active zone.

For further verification of this version the two-pulse method of excitation has been used. The same volume of the dye solution has been excited by two successive pulses of excimer lasers (Fig. 4).
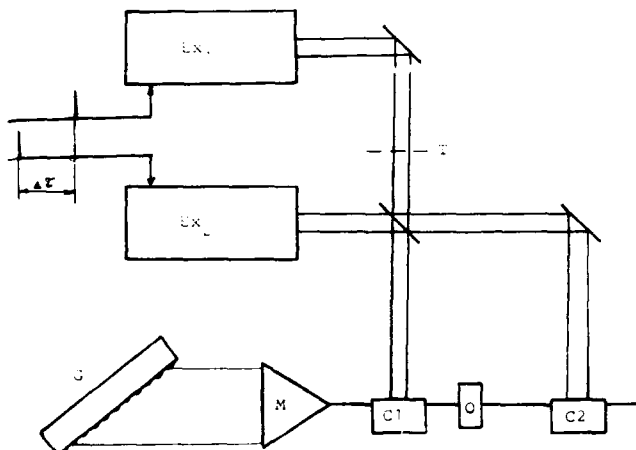
Fig. 4   The scheme of two-beam excitation of the dye laser. Ex1 and Ex2 - the excimer lasers; $\Delta\tau$ - variable delay; T - attenuator; C1 and C2 - oscillator and amplifier dye cells; M - 40-fold multiprism beam expander; G - diffraction grating; O - output coupler.

The first of them, a powerful pulse E_1 with a variable energy, forms the thermal disturbance in the dye solution. The second, probing pulse E_2, tests the lasing properties of the cavity with the thermal non-uniformity in the active medium. The energy of the probing pulse has been chosen weak enough to avoid its thermal self-action.

The oscillograms of the dye laser outputs (Fig. 5), obtained at a 50-ns delay between the pumping pulses, display the influence of the preliminary excitation on the lasing of the dye laser. By enhancing the energy of E_1 one can reach the absolute depression of the probing pulse. It shows that the effect of saturation under investigation has not been caused by two-photon non-linear processes. To exclude another possible version - the formation of the states or impurities in the excited zone, which can absorb the lasing radiation - the spatial and spectral measurements have been performed.

The increase of the energy of E_1 pulse is accompanied by a well-observable spatial broadening of the laser radiation in Y-direction. However, it is difficult to use this phenomenon

Fig. 5   Oscillograms of the dye laser oscillator output in the two-beam mode of excitation. Probing pulse energy E_2 = 2.5 mJ.

401
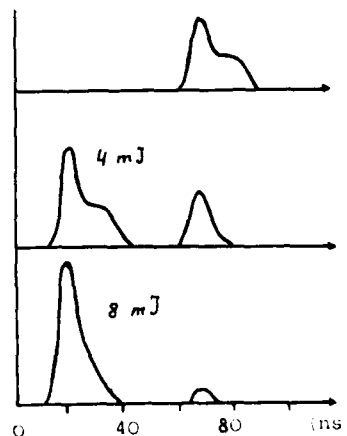
for quantitative measurements because of the strong reduction of lasing in the cavity with thermal disturbance.

The most reliable data were obtained by spectral measurements of the dye laser. The laser oscillator has also been excited by two delayed pulses of the excimer lasers, the second pulse pumping the amplifier as well. This permits one to record the lasing spectrum even of a very weak depressed probing pulse. By varying the energy of E_1 we have found a shift of the lasing wavelength of the probing pulse, which is linear with respect to the energy of the disturbing pulse. The dependence obtained in VL-10 dye laser, operating in the fifth order of grating at 585 nm, is shown in Fig. 6 (Rhodamin 6G dye of 0.79 g/l concentration).
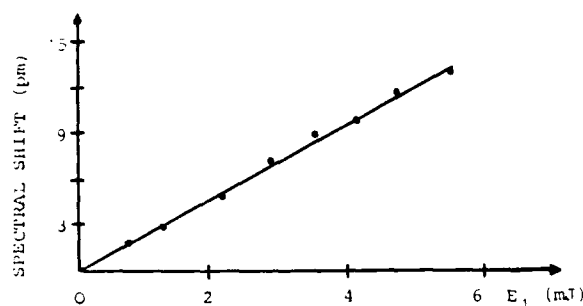
Fig. 6   Spectral position of the lasing line of the probing pulse vs the energy of the disturbing pulse E_1.

In each point of E_1 50 lasing pulses have been averaged, that permits one to determine the position of the line with the accuracy better that 0.5 nm. The shift of the lasing wavelength, measured at 4.5 mJ energy of the first pulse, is 13 nm. The calculations in accordance with (14,16) give under these conditions $\Delta\lambda = 10.5$ nm.

An asymmetrical broadening of the spectral profile of the probing pulse has been observed simultaneously with the spectral shift. The magnitude of the broadening in case of 4.5 mJ preexcitation energy is of the order of 50% of the initial linewidth of the laser line.

The situation, where the thermo-optical shift of spectral position of the line could be well observed, was specially inspired. In case of the single-shot excitation

$$I(\lambda) = \int_o^\infty G(\lambda,t)P_1(t)dt, \qquad (17)$$

where $G(\lambda,t)$ is a cavity transmission curve and $P_1(t)$ is an instant intracavity lasing power. As the thermal effects, shifting the lasing wavelength simultaneously, depress the lasing power due to the increase of the intracavity losses, the contribution of these effects to the line broadening is not so essential. One can say that the negative cylindrical lens serves as a preservative restricting the line broadening. However, the thermal lens reduces the duration of the laser pulse and decreases the line narrowing caused by the multipass evolution of lasing in the selective cavity.

It is difficult to depress the thermo-optical disturbance in the active medium, because the dimensions of the excited zone are defined by the spectral properties of the cavity. Besides, with the exception of water, ethanol has the minimum value of $(\partial n/\partial T)_\rho$.

Thus, on exciting the dye laser oscillator by an excimer laser, one has to restrict the energy of the pumping pulse to $5 \div 6$ mJ for blue and to $3 \div 4$ mJ for red dyes. This energy is sufficient in case of $15 \div 20$ ns duration of the pumping pulse. Problems may arise when the pulse duration exceeds 100 ns.

If the dispersion plane of the grating is turned by $90°$ in the XY plane, the thermo-optical cylindrical lens will lead to the symmetrical broadening of the spectral line of the laser, and the efficiency reduction will be the consequence of the shift of intracavity rays in Z-direction.

The same rules should be correct for the amplifier as well. However, owing to lower concentrations of dye molecules in the amplifier cell, the intermolecular relaxation of heat may take more time. As the thermo-optical gradients are inversely proportional to ω^2/k, the pumping energy saturating the first amplifier, where the dye concentration is three times lower and ω is three time larger, will be of the order of $50 \div 100$ mJ.

References

1. T. D. Foster, L. M. Osternik, J. Appl. Phys. 41, 3656 (1976).
2. В. Н. Быков, Н. Н. Горошкова, В. Р. Кушнир, Н. В. Шкунов, Электронная техника, 11, 64 (1978).
3. B. B. Snavely, F. P. Schäfer, Phys. Lett. 28A, 728 (1969).
4. C. M. Ferrar, IEEE J. Quant. Electron. QE-5, 550 (1969).
5. В. И. Безродный, В. И. Ващук, Е. А. Тихонов, ЖТФ, 48, 151 (1978).
6. Р. Б. Андреев, С. С. Гулидов, А. Г. Калицев, Д. И. Стаселько, В. Л. Стригун, Оптика и спектроскопия, 54, 350 (1983).
7. Molectron Corporation Applications Note, N 113 (1977).
8. М. Борн, Э. Вольф, Основы оптики, Изд. Наука, М. (1970).
9. E. Berik, V. Davidenko, Opt. Commun. 67, 129 (1988).
10. Е. Б. Берик, В. Т. Михкельсоо, Р. Э. Раамат, Э. А. Урбаник, Я. А. Эдула, Труды ИФ АН ЭССР, № 56, 93 (1984).

300 WATT DYE LASER FOR FIELD EXPERIMENTAL SITE

by

Patrick N. Everett

MIT Lincoln Laboratory
P.O. Box 73, Lexington, MA 02173

Abstract

A 6-beam flashlamp-pumped dye laser system is being installed at a field site. Each beam will produce 5 to 10 Joules in 2-μs pulses at 10 pps. Design, installation, and initial performance will be reviewed.

Introduction

MIT Lincoln Laboratory is currently installing a laser at a field experimental site. Six laser beams are required, each running at 10 pps, with 5 to 10 J per pulse, no more than 2 μs duration, and most of the energy within included angle 20λ/D. A bandwidth no more than 1 nm, centered at approximately 510 nm wavelength is required. The system must be able to run for 10 minutes at full power. Last year, at this conference[1,2], we gave a progress report on its engineering, and on the performance of a 1/3 scale model of the system. This year we will show photographs of the system partially complete at the site, and discuss progress and the initial operation of one laser beam.

Much of the equipment has now been installed on site, and is working. One of the six laser beams has been performing experiments for a number of months, and further beams are now being installed. We believe it will be the most powerful operating flashlamp pumped dye laser system.

The performance has not yet been optimized because some of the diagnostics are not installed and some components are improvised. However, we have delivered a total pulse energy of more than 5J.

The Optical Table and Lasers

One engineering challenge was how to support so much laser equipment on a firm base so the beams wouldn't wander, and yet bring in the fluid and electric services in a practical way, while allowing access for maintenance and alignment. Surrounding equipment must also be protected from the horrendous EMI. We decided to use a vertical optical table, 16' long and 9' high inside a screen room. The photograph in Figure 1 shows the table under construction. It is a steel shell, 18" thick, filled with concrete. The ends are buttressed, and it is bolted

down to a 3' thick concrete slab to further stiffen the table. The slab is in turn coated with steel plate to form the floor of the screen room which contains the immediate laser equipment. Experiments confirm that the angular motions under the normal vibrational environment of the site are certainly within 200 μrad, and probably much better. Figure 2 shows the front of the finished table with about 20% of the equipment mounted.
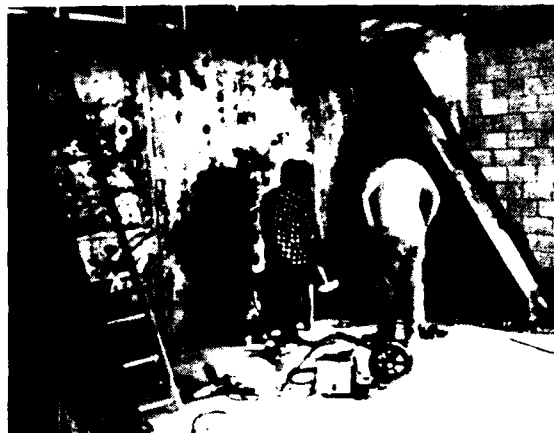
Fig. 1: Vertical Optical Table being built.

Fig. 2: Laser Side of Vertical Optical Table.

The laser heads shown are supplied by Candela Corp., developed from their normal commercial product. Each head has a pair of flashlamps two feet long, 7 mm bore, in a close-coupled pumping geometry. They pump a longitudinally flowing dye cell of the same

length and internal diameter 15 mm. Each lamp dissipates 500 J per pulse. Two heads are contained in each unstable confocal resonator, as shown in Figure 3. The resonator length is 2.5 m. There will be six such "double-dip" resonators, one for each beam, giving a total of 12 laser heads. This "double-dip" configuration is unusual but is simpler and easier to align than the alternative oscillator and amplifier configuration. Simple unstable resonators have a hole in the center of the output beam which causes some of the amplifier medium to not be used as shown in the lower part of Figure 3. This is wasteful and can lead to parasitics. All the medium is used in the "double-dip" configuration.
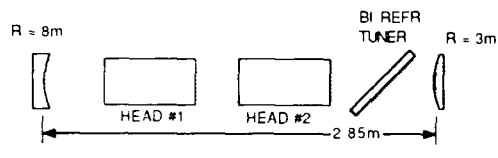
a) "DOUBLE-DIP" OSCILLATOR (USED)

b) OSCILLATOR + AMPLIFIER (CONSIDERED BUT NOT USED)

Fig. 3: Resonator has unstable confocal geometry.

The laser heads exhibit a positive lensing of tens of meters focal length as a result of flowing the dye solution at the 30 gallons per minute necessary for the rep-rate. This upsets the optics of the resonator. The performance is expected to improve when we compensate for this lensing by adjusting the curvatures and spacing of the resonator mirrors.

A birefringent filter is used for tuning. By setting it to 45° instead of the normal Brewster angle we reflect a small sampling of the intra-cavity energy distribution onto a TV monitor, as shown in Figure 4. This has confirmed there are no significant hot spots in the beam, and that some burning of optics was due to an inferior batch of coatings.
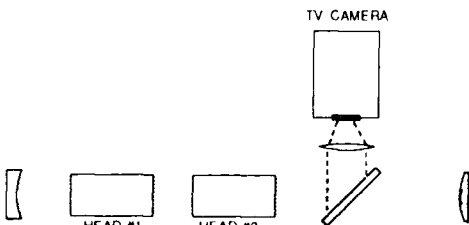
Fig. 4: Resonator Monitor.

Aligning and Diagnostics

Unstable resonators have been considered difficult to align. Our technique of injecting an oversized collimated beam back into the resonator, as shown in Figure 5, is working well. All six resonators are aligned with a single argon-ion laser running at 514 nm wavelength, a little longer than the operating wavelength of about 508 nm. This extra 6 nm takes us a little further from the trailing edge of the dye's pump band absorption and so gives higher transmission for the large number of tranversals needed. The six beam-splitters are used to inject a few percent of the beam into each of the laser resonators. Since the aligning beam is oversized and collimated, only the angle is important at each laser, and that is adjusted by the beam-splitter for that laser. The beam in each resonator collapses on successive passes to the diffractive core. It then expands again and finally re-emerges as an excellent simulation of the dye laser beam. The sample reflected off the birefringent filter, onto the TV monitor helps obtain a sensitive and quick alignment.
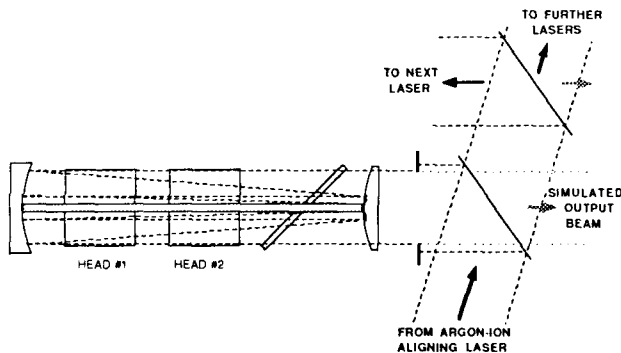
Fig. 5: Alignment with argon-ion laser.

The same beam splitters will direct a few percent of each outgoing laser beam into the common diagnostic path, as shown in Figure 6, for monitoring of energy, tuning, pulse-shape and timing, far-field, aiming, etc.

Each flash lamp is monitored by fiber-optic pick-offs which are multiplexed into a smaller number of diode sensors, with filtering to select the dye pump band. The approach is shown schematically in Figure 7. This shows how, for example, the fiber-optic pick-offs from the right hand lamps of a number of laser heads are multiplexed to one sensor. Since the different lasers are not fired simultaneously, the response is tied to the right lamp by its timing. This approach allows many more functions to be monitored without having an enormous number of sensors. The various diagnostics feed into a computerized monitoring system which displays and stores sampled information, with the intent of quickly catching any critical component performing below standard.
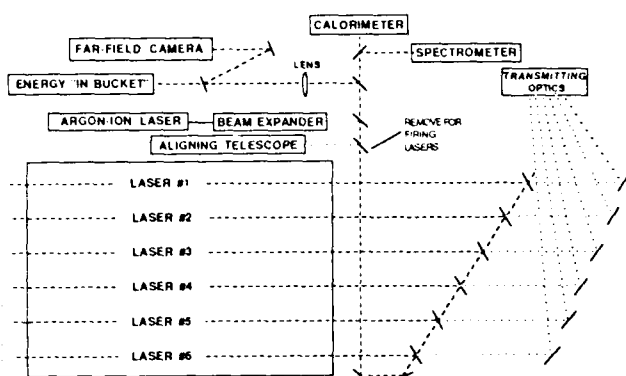
Fig. 6: Diagnostics and Alignment share the same path.

equalizing heat exchangers on the side-walls, and leave below the grating floor. The upper photograph shows the modulators removed and floor lifted to allow modifications to the piping.

Fig. 8: Manifolding to laser heads through waveguides to suppress EMI.
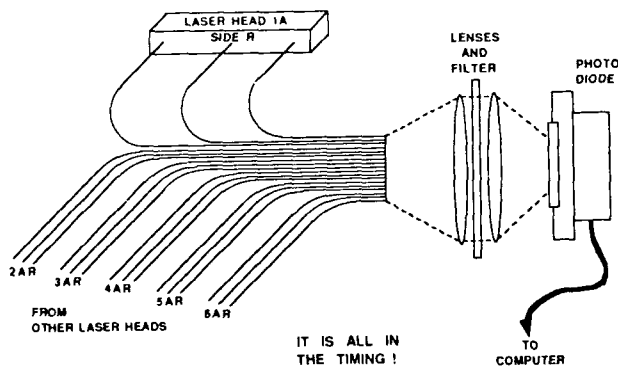
Fig. 7: Fiber optic multiplexing for monitoring flash-lamp performance.
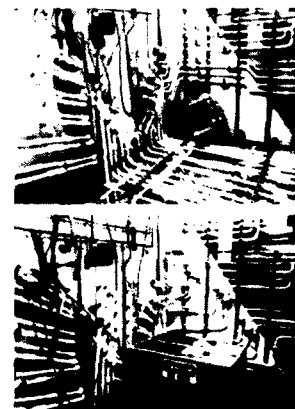
Fig. 9: Modulator side of bench.

Spatial filtering is done with lenses of a few meter focal length to avoid burning of apertures, which are typically about 2 mm diameter.

Services and EMI Suppression

The fluid pipes and lamp cables penetrate the 18" thick vertical optical bench through waveguide tubes, as shown in Figure 8. These prevent EMI transmission at frequencies below 2 GHz. An EMI box will cover the lasers to complete the enclosure, with the laser light also being emitted through similar waveguides. For maintenance, each laser head can be removed with its associated pipes after uncoupling behind the vertical bench. These pipes also provide the manifolding into the ten individual fluid ports of each laser.

We now move to the back side of the vertical optical table. Figure 9 shows the services penetrating through the wave guides. Remember that we are still within the screen room. In the lower photograph can be seen the modulators that store the flashlamp energy in capacitors. The charge is supplied to the capacitors at 40 kV, and then switched into the lamps with spark gap switches. The fluids come in, through temperature-

The manifolding for the fluids on the outside of the Screen Room wall is illustrated in Figure 10. Again the fluids traverse the Screen Room wall through waveguides to suppress EMI. Feedback systems maintain constant fluid pressure between the inlet and outlet manifolds for the fluids, using variable speed pumps. Thus the correct flow conditions in active heads are maintained independently of how many heads are actually flowing at any one time. With all lasers active there will be 360 gpm of dye solution, and 240 gpm of cooling water flowing.

Fig. 10: Manifolding and waveguides into Screen Room.

The Screen Room was constructed by Geiss Associates. The power supplies outside the screen room are shown in the upper part of Figure 11. They are manufactured by ALE Corporation. The pipes from the fluid handling room are in a trench under the grating. The lower photograph is looking the opposite direction in the same area and shows the controls. This whole area will be nearly filled with po. r supplies when the whole complement is installed.

Fig. 11: Screen Room, Supplies and Controls.

Fluid Handling

We now move into the dye and coolant handling room, shown in Figure 12. Stone and Webster Engineering Corporation designed this equipment for us, with consultation from SAIC Inc. It was fabricated and installed by the Fels Company. The design was developed for a flammable methanol/water dye solution, which complicated the engineering enormously. Recently we found we could use a non-flammable solution of acetamide in water.[3] As a consequence we now have an over-engineered system. With our new knowledge we could design a simpler system.
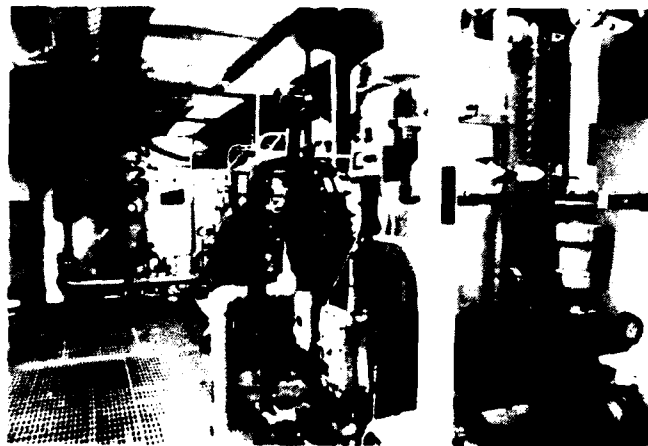
Fig 12: Fluid-Handling room.

The system will dissipate 1/4 MW when running at full power. The heat exchangers shown in Figure 13 will extract this heat from the dye and cooling water and reject it to water in a 10,000-gallon underground reservoir. From there it will be extracted with a chiller at a slower rate in between experiments. Alongside the heat exchangers we see the coolant system with its pump and surge tank.
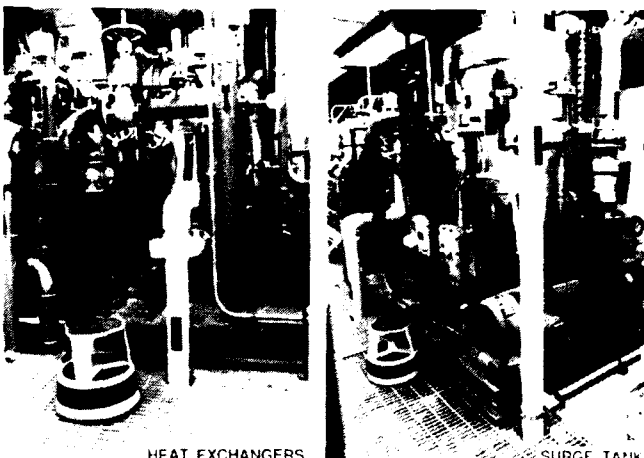
HEAT EXCHANGERS   SURGE TANK

Fig. 13: Cooling System.

The dye handling system is shown in Figure 14. It pumps 360 gpm, and will recycle the dye solution in real time. It uses activated carbon to take everything (dye and degradation products) out of a controlled portion of the returning dye solution, and then adds the requisite amount of fresh dye, all within the four-minute round-trip time of the system. Two variable-speed pumps in parallel circulate the dye to the lasers.

An essential part of the system is the pair of optical analyzers (top left) that measure the degradation and the dye content for control of the recycling system. The degradation shows up as increased absorption in the region of the lasing wavelength, and is measured by the one-meter analyzer. The measurement is centered at 550 nm. At this wavelength we are sufficiently far from the edge of the pump band that the absorption by the broad-band degradation products predominate. To obtain a meaningful reading the analyzer length needs to be approximately that of the lasers. The analyzer output is used to control a variable speed pump which diverts returning dye solution through the banks of carbon cleaning filters, shown top right in Figure 14.

The carbon cleaning system was immensely helpful in cleaning the initial contaminants out of the system and the solvent before any dye was added. With the analyzers we could watch it cleaning up from less than 10% transmission, for the one-meter path, to about 70% during the first few hours of flowing. It took a few weeks before the

solution stopped gradually degrading while
just standing unused. The transmission for
undegraded solution is about 70%, with or
without dye. As the solution degrades, 10%
further loss in transmission results in about
20% loss in laser output.   These are
preliminary figures. They will be firmed up
with more experiments.
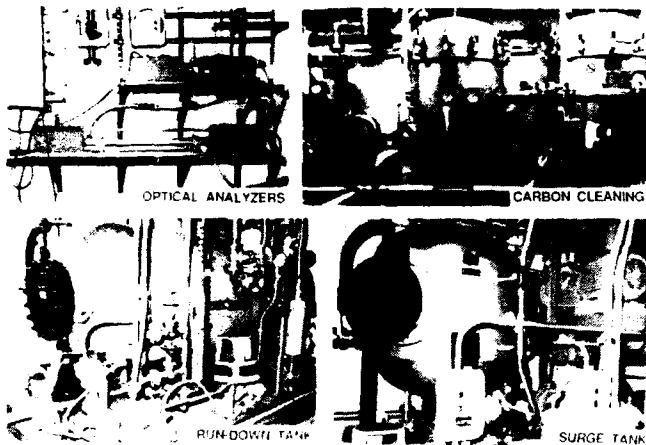
Fig. 14:   Dye Handling system

The original plan was to use 50% methanol
in the dye solution, and to add dye in the
form of a concentrated methanol solution.
The switch to acetamide presented a new
problem because the solubility of dye in
acetamide solution is too low to give a
practical concentrate. Our consultants led
us to the possibility of creating a finely
ground precipitate (of about 1 gm dye to 2 cc
water) to be injected as necessary. This
approach is still under development but
appears practical. The key is to have the
suspended dye powder fine enough that it
dissolves almost instantly when the
suspension disperses in the main flow.

Oxygen

The site is at elevated altitude and we
had to address the possible effect on the dye
solution. It is well known that the amount
of dissolved oxygen can be important.[4]
Dissolved oxygen is bad in that it encourages
dye degradation, but it is also known to be a
triplet quencher. In some dye lasers of this
type it is possible to completely suppress
lasing by removing the dissolved oxygen.
Accordingly the system was designed for
pressurization and for sparging of air or
oxygen. Recent tests have verified that
adding oxygen does increase the energy
output, as shown in Figure 15. The data is
not good enough to tell whether the curve
turns over at twice the sea-level
equilibriated level, but more oxygen is
certainly better up to that point.
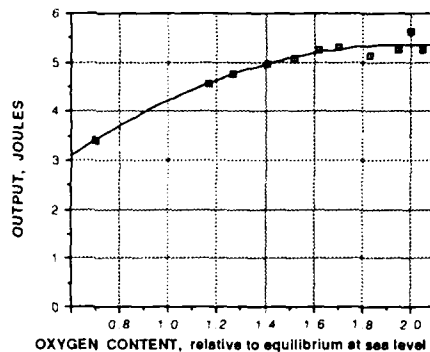
Fig. 15:   The importance of Oxygen control.

Materials

Throughout the system care has been taken
to use only wetted parts of materials known
to be compatible with the solvent and dye.
They include stainless steel, polyethylene,
polypropylene, and Buna-N for O-rings. The
plastic piping was used mostly in the screen
room to maintain flexibility around the laser
heads and to maintain EMI integrity when
passing through waveguides. The flexibility
around the laser heads makes alignment
practical, and is believed to suppress some
of the vibrations associated with the flow.

Conclusion

The system is now showing good promise of
meeting its goals, and is already serving a
limited role in supplying light for
experiments. We believe, when complete, it
will be the largest operating flashlamp
pumped dye laser.   It has been over-
engineered because of lack of some necessary
information, and we must have a working
system. With the information that we are
developing, a simpler system could be built
with the same performance. With retrofitting
of some of the techniques presented at this
conference (such as spectral transfer) the
sytem should provide more than 1 kW. The
system would have been simpler had it been
designed for a non-flammable solvent.

References

1. P. N. Everett, and B. G. Zollars, in Proceedings, International Conference on Lasers '87, F. J. Duarte, Ed. (STS Press, McLean, VA, 1987), pp. 291-296

2. B. G. Zollars, and P. N. Everett, in Proceedings, International Conference on Lasers '87, F. J. Duarte, Ed. (STS Press, McLean, VA, 1987), pp. 297-303

3. P. Crozet, and Y. Meyer, C. R. Acad. Sc. Paris, Electronique Serie B, t.271, pp. 718-721 (1970)

4. F. P. Schaffer, "Topics in Applied Physics, Vol. 1 Dye Lasers", (Springer-Verlag New York, 1977), pp. 58-60.

THE USE OF SPECTRAL CONVERSION TO INCREASE THE EFFICIENCY OF FLASHLAMP-PUMPED DYE LASERS

Dennis P. Pacheco, Henry R. Aldag, and Peter S. Rostler
Avco Research Laboratory/Textron
2385 Revere Beach Parkway
Everett, MA 02149

Abstract

This paper describes a simple, but very effective technique to increase the efficiency of flashlamp-pumped dye lasers. In this approach, a second dye solution is used to spectrally convert some of the lamp photons into the absorption band of the laser dye. With proper matching of the converter and laser dyes, we have observed a doubling of the laser output. Added benefits of this technique are extended laser dye life and a more uniform deposition of waste heat in the gain medium (which yields a better quality beam). The first part of the paper discusses the basic technical issues governing efficient dye laser operation and the regime in which the flashlamps are driven. Next, some early experimental results are described in which significant improvements in laser efficiency were observed in a laser device designed for high average power. In the third part, we discuss the effect of coupling geometry on converter photon usage. We describe a laser device which has been built utilizing an improved design and present some initial experimental results. We then present dye spectral data and computer modelling designed to determine efficient pairs of laser and converter dyes under our pump conditions. Finally, the modelling is used to compare medium quality with and without a converter dye.

Introduction and Background

Flashlamp-pumped dye lasers typically have energy efficiencies of 0.5-1.0%, depending on the dye and pumping conditions. This efficiency is usually calculated as laser output energy divided by the energy stored in the capacitor, and so is very nearly a wall-plug efficiency. One of the reasons for these low values is the relatively poor spectral match between the flashlamp emission spectrum and dye absorption profile. This can be understood from the following arguments. Saturation fluxes for laser dyes are typically on the order of 0.5 MW/cm^2. For efficient extraction, internal lasing fluxes must be several times this. To achieve these levels, pump fluxes need to be $\geq$ 0.1 MW/cm^2. This in turn requires high flashlamp blackbody temperatures (about 20,000 K) and efficient coupling into the gain medium. The peak of such a blackbody curve is below the quartz cutoff, and so the laser dye is being pumped out in the tail of the lamp emission spectrum (Figure 1). The major function of the converter dye is to absorb the plentiful UV photons and reemit them in the absorption band of the laser dye.

Figure 2 provides experimental verification of the fact that the lamps are black under dye-laser pumping conditions. This figure shows measured flashlamp spectra for a 7-mm bore commercial lamp at two different energy loadings (solid curves). These data were taken at ARL with a carefully calibrated optical multichannel analyzer (OMA). For purposes of comparison, blackbody spectra are superimposed for an 8 μsec pulse width (dashed curves). Note that as the energy input is increased from 140 to 440 J, there is a significant increase in the visible output, which would directly pump a laser dye. The increase in the output in the near UV, however, is disproportionately greater. In conventional designs, these UV photons are either unabsorbed by the dye because of gaps in the absorption spectrum, or else are absorbed and contribute to the photodegradation of the dye molecules and the deposition of waste heat in the gain medium.

Figure 2 also shows that at the lower energy loading, the lamp appears black down to about 4500 A. When the input is tripled, the fitting is good down to at least the quartz cutoff. Analysis of the kinetics of the plasma shows that this enhancement of the UV corresponds to a significant increase in the ionization level of the xenon. We know, however, that the flashlamp output cannot be completely black under these conditions, since this would correspond to more energy out of the lamp than was put in. The upper experimental curve corresponds to prototypical loading in our dye laser devices. Increasing the energy input beyond this level will increase the pump flux somewhat, but will largely cause the blackbody distribution to "fill in" well below the quartz cutoff, and therefore decrease overall efficiency. The regime of lamp operation for dye lasers can be contrasted with that for solid-state devices, in which the energy loading and effective temperature are much lower, and the plasma is partly transparent.

The selection of a spectral converter to match a given laser dye is relatively straightforward. The converter must of course have a high fluorescence quantum yield, but it need not be a laser dye or even an organic compound. It must be sufficiently soluble in the solvent of interest; this eliminates water in some cases, since relatively few dyes have a high enough solubility. Photochemical stability is a virtue, but it is not critical since a much higher concentration of photoproducts can be tolerated in the converter solution than in the laser solution. Perhaps the most important factor in making the selection is the proper matching of the spectra. This is shown in Figure 3, where we superimpose the absorption and emission spectra of Stilbene 420 (ST420) on those of Coumarin 504 (C504). In both cases, the solvent is 50% MeOH/50% H_2O. The hole in the absorption profile of C504 at 360 nm is filled by the primary absorption band of ST420. Furthermore, there is good overlap between the emission of the ST420 and the absorption of C504. Since the emission profiles of dyes have a tail on the long-wavelength side, it is preferable to choose a converter whose emission peaks to the blue of the absorption maximum for the laser dye.

The idea of spectrally converting some of the flashlamp emission is not new; a number of articles have dealt with this technique for dye lasers.[1-6] Some work has also been devoted to improving the performance of flashlamp-pumped solid-state lasers.[7,8] In this paper, we present work performed at ARL which is directed towards optimizing the effect. Furthermore, we point out several additional benefits in using this technique that have not been emphasized previously.

Early Experimental Results at ARL

Some of the first spectral-conversion experiments at ARL utilized a dye laser head containing a single dye channel and two linear lamps in elliptical reflectors. In this configuration, the pump light is imaged into the dye solution, although the quality of the image is not good due to the finite size of the emitting plasma. The only practical location for the converter solution in this head is in the flashlamp coolant. The sketch in Figure 4 indicates the geometry. Since the converter solution occupies a larger annulus than the lamp plasma, the imaging due to the reflectors is even poorer; the efficacy of the converter technique can still be tested however.

Representative results for the combination of ST420 and C504 are shown in Figure 5.[6] In both photographs, the upper trace shows the current pulse through the lamps. The lower trace records the temporal profile of the laser output. In (B), no converter dye was used, which means that only solvent was flowed through the water jackets. In (A), ST420 was added to the solvent. The energy enhancement was more than 75% in this case. The overall improvement in system efficiency is shown in Figure 6. With C504 as the laser dye and ST420 as the converter, efficiencies in excess of 1% were measured. At the highest energy input, the laser output was more than 7 J.[6]

Encouraged by the significant improvements in laser performance, we embarked on a program to optimize the effect. There were two major thrusts to the work: (1.) to explore various geometries for coupling the converted photons efficiently into the gain medium, and (2.) to obtain an extensive database on dye spectral properties to efficiently pair laser dyes with converters. The next two sections deal with these issues.

Effect of Geometry on Converted Photon Usage

As indicated earlier, the initial configuration of the experiments involved the converter solution in the flashlamp water jackets (depicted schematically in Figure 4). This is an inefficient coupling scheme, as is shown in Figure 7. The fluorescence from the converter dye is emitted isotropically, and the fate of each photon can be examined using geometrical optics. The rays labelled A correspond to converted light which escapes from the water jacket and is potentially collected and imaged into the gain medium. Ray B enters the black plasma and is lost. Rays C are trapped by total internal reflection (TIR) and are lost out the ends of the water jacket or are absorbed in the converter solution. Analysis shows that only about 45% of the converted photons are potentially useful. Even for these photons, absorption must occur in a single pass through the gain medium. Table 1 summarizes these results. A more efficient collection geometry is shown in Figure 8. In this scheme, a multichannel, slab sandwich is formed using four quartz plates. To a good approximation, this sandwich is index-matched throughout. The inner channel contains the laser dye solution, while the outer channels are reserved for the converter. In this view, the lasing direction is perpendicular to the figure.

Table 1. SUMMARY OF SPECTRAL CONVERTER PHOTON USAGE FOR TWO DIFFERENT CONFIGURATIONS

1. CONVERTER IN WATER JACKET (45% UTILIZATION)

    A) 45% ESCAPE (POTENTIALLY USEFUL, BUT MUST BE ABSORBED ON FIRST PASS)

    B) 13% RETURN TO FLASHLAMP (REABSORBED)

    C) 42% TRAPPED IN WATER JACKET BY TOTAL INTERNAL REFLECTION (EVENTUALLY LOST)

2. CONVERTER LOCATED IN CHANNEL ADJACENT TO LASER DYE (83% UTILIZATION)

    A) 17% ESCAPE THRU INCIDENT SURFACE (LOST)

    B) 17% COULD ESCAPE THRU REAR SURFACE (POTENTIALLY USEFUL, BUT MUST BE ABSORBED ON FIRST PASS)

    C) 66% TRAPPED IN MULTICHANNEL SLAB BY TOTAL INTERNAL REFLECTION (ALMOST ALWAYS ABSORBED IN LASING DYE)

With this geometry, converted pump light is collected very efficiently. About half of the fluorescence originating in the converter channel is emitted in the direction of the gain medium. Most of the photons that are unabsorbed in this first pass get additional chances to pump the laser dye, because they are trapped in the sandwich by TIR. The other half of the converter fluorescence is emitted in a direction opposite to the gain medium, but much of this is collected as well. There is a loss cone (based on the index mismatch) which corresponds to about 17% of the total converter emission in this case (Figure 8). The balance of the oppositely directed photons are again trapped by TIR and can make repeated passes through the gain medium. In total, about 83% of the converter fluorescence makes at least one such pass (Table 1).

There are other advantages associated with this slab scheme. High energy outputs are possible because of the large pumped volume together with spectral conversion. It is straightforward to scale the laser to even higher energies by simply extending the pump dimension (the left-right dimension in Figure 8). The laser actually becomes more efficient as this is done, because the end effects are proportionately smaller.

We have built a laser based on the above design principles; a photograph of the device is included as Figure 9. The view in the figure is roughly along the laser axis, and shows the three-channel, slab geometry. The sandwich is pumped by four linear lamps (the electrodes are visible in the figure); repetition rates of tens of Hz are achievable with proper system design including sizing of the pumps. This device is presently being characterized at ARL; some preliminary data are presented in the next section.

Spectral Data and Computer Modeling

A second emphasis in the development of our spectral-conversion capabilities was to establish a database on a wide variety of dyes, and develop computer simulations to predict the best dye pairings. A problem here is to acquire self-consistent datasets for the dyes and solvents of interest, and store them on disk for the simulation codes. Our approach was to build our own apparatus to characterize candidate dye solutions in terms of absorption spectra, emission spectra, and quantum efficiency as a function of wavelength. This has the twofold advantage that all the data are recorded on the same apparatus and any solvent can be used in the testing. The apparatus itself was described elsewhere;[9] a dataset for Rhodamine 590 in 50% MeOH/50% H_2O is given in Figure 10. Detailed spectra for a number of dye solutions have been recorded and stored on disk for the simulation codes.

One of the codes developed at ARL examines the various converter candidates for a given laser dye. The code assumes a slab geometry (as shown in Figure 8), and inputs measured lamp spectra (e.g., Figure 2) and dye properties (e.g., Figure 10). The outputs include the total fluorescence from the center channel with and without a converter dye. The results without a converter assume "solvent only" flowing in the outer channels. The code calculates the fluorescence of the laser dye, because an accurate prediction of the laser output requires knowledge of a number of cross sections and rates; these are not all known for most dyes. Calculation of the fluorescence enhancement, however, is relatively straightforward and provides a good semiquantitative measure of the expected improvement in laser performance.

Table 2 shows selected results for three commonly used dyes. Recall that our experimental results for the combination of ST420/C504 showed nearly a doubling of the laser output (Figure 5). This is better improvement than is predicted by the code. There are two possible reasons for this. First, the ST420/C504 data were taken with the imaging pump geometry described earlier. The more diffuse imaging of the converter light in that case brought some regions of the gain medium above threshold that did not lase without the converter dye. This was seen in the burn patterns taken at the output of the device. The computer code assumes a slab geometry in which the lasing aperture does not change when the converter is added. Secondly, the code looks only at fluorescence enhancements, and is therefore only a rough measure of the increase in laser output.

Table 2. PREDICTED FLUORESCENCE ENHANCEMENTS FOR SELECTED DYE PAIRINGS

THREE CELLS (0.5 cm WIDE) PUMPED FROM BOTH SIDES
MEASURED LAMP SPECTRUM NORMALIZED TO 1 JOULE/cm^2
PEAK ABSORPTION COEFFICIENT = 6 CM^{-1} FOR BOTH LASING AND CONVERTER DYES

LASER DYE	CONVERTER DYE	NO CONVERTER (J/cm^2)	WITH CONVERTER (J/cm^2)	ENHANCEMENT
C504	ST420	0.179	0.253	1.41
	LD423		0.268	1.50
	C445		0.262	1.46
RH590	LD473	0.128	0.243	1.90
	C480		0.271	2.12
SR640	C480	0.107	0.189	1.77
	C523		0.196	1.83

Laser data that we have taken in the slab device show a better correlation with the code. Figure 11 shows oscilloscope traces which demonstrate the energy increase obtained using LD473 to pump RH590. As before, the upper trace represents the current pulse through the flashlamps. Actually, there are two traces superimposed, indicating that the lamp loading was the same in both cases. The lower traces show the laser output with and without the converter dye. In this case, the increase in energy output is about 65%. The output coupling and dye concentrations were not optimized in this experiment, and so further improvement should be possible. In another experiment, we observed a doubling of the laser output when C480 was used to boost the output of RH590.

Additional Design Advantages with Spectral Conversion

So far, we have concentrated on the increase in pump flux when a converter is used. There are other significant benefits as well, such as longer laser dye life and better medium quality. It is well known that many laser dyes photodecompose more rapidly on exposure to the near UV of the flashlamps.[10] This is in fact why some systems employ a pyrex filter[10] or a caffeine solution[11] somewhere between the

lamp and dye solution. (The disadvantage of these "passive filters" is of course that the rich UV content of the lamps is simply thrown away.) With a converter dye, the near UV is utilized while protecting the laser dye from rapid photodegradation. As a result, laser dye life comparable to the "pyrex value" is achieved. In the converter solution, on the other hand, far higher concentrations of degradation products can be tolerated before the solution loses its functionality. That is, in a dye laser the output is a sensitive function of the distributed loss in the gain medium.[12,13] Consequently, relatively small concentrations of absorbers can materially affect the output energy. The function of the converter solution is simply to fluoresce into the neighboring gain medium. Since the optical path length involved is much shorter, the degradation of the solution is much less important.

Another benefit of using converters derives from considerations of waste heat management. Since flashlamp-pumped dye lasers are only on the order of 1-2% efficient, 98% of the input energy (much of which appears as heat) must be dealt with. In particular, it is important to keep it from the gain medium. The converter solution absorbs much of the near UV and emits photons that are a better spectral match for the laser dye. This significantly reduces the waste-heat deposition in the gain medium. The waste heat in the converter solution is carried away by the flow and dissipated in a heat exchanger. The resultant improvement in medium quality is shown graphically in Figure 12. In this figure, we have used our modeling to examine the differential heat deposition with and without converter. As before, we assume a slab geometry and input measured lamp and dye spectra. In the top curve, RH590 is used as the laser dye while the converter channels contain only solvent; the lower curve shows the results when a converter is used. The concentrations were adjusted to yield equal emission from the laser channel. Note that the concentration of the laser dye is several times lower when the converter dye is present. As seen in the figure, there is much less waste heat deposited in the gain medium with the converter; more importantly, the differential deposition is significantly reduced. The differences in heat deposition lead to refractive-index variations across the gain medium, and this degrades medium quality. During the pump pulse, the laser dye solution develops a thick, time-dependent lens which is hard to correct for in the resonator design. Minimizing this thermooptical distortion is important in applications where good beam quality or high spectral purity are required.

Analogous data for the converter channel are presented in Figure 13. The dye solutions are the same as for the lower curve in Figure 12. The dashed curves show the individual contributions from the lamps on the near and far side of a given converter channel. The light from the far side has of course been prefiltered by the other converter channel and, to a lesser extent, by the gain medium. In this case, the gradient in the waste-heat deposition is very large and unsymmetric, leading to poor medium quality during the pulse. Since the converter channels are intended to be nonlasing, this is not a problem. A major simplification in implementing a converter scheme is that flow quality, heat-deposition profiles and dye photostability are much less critical than for the laser-dye channel.

As a final note, we should emphasize that segregating the solutions is preferable to mixing the dyes together. Separating the dyes significantly reduces the waste heat deposited in the gain medium, and minimizes the possibility that excited states or degradation products of the converter dye will interfere with the lasing process. Our modeling has shown that under some conditions mixtures of dyes in the converter channel can lead to further improvements in laser performance. In such cases, it is especially important to provide a separate channel for the converters.

Acknowledgements

References

1. W.W. Wladimiroff, "Some Stable Fluorescent Converter Solutions Enhancing Optical Pumping in the Visible Region," Photochem. Photobiol. 6, 543 (1967).

2.   C.E. Moeller, C.M. Verber, and A.H. Adelman, "Laser Pumping by Excitation Transfer in Dye Mixtures," Appl. Phys. Lett. 18, 278 (1971).

3.   K. Nagashima and T. Asakura, "Tuning Properties of Flashlamp-Pumped Dye Lasers with Dye Mixtures," Opt. Commun. 19, 7 (1976).

4.   P. Burlamacchi and D. Cutter, "Energy Transfer in Flashlamp-Pumped Organic Dye Lasers," Opt. Commun. 22, 283 (1977).

5.   P. Mazzinghi, P. Burlamacchi, M. Matera, H.F. Ranea-Sandoval, R. Salimbeni, and U. Vanni, "A 200-W Average Power, Narrow Bandwidth, Tunable Waveguide Dye Laser," IEEE J. Quantum Electron. QE-17, 2245 (1981).

6.   Patrick N. Everett, Henry R. Aldag, John J. Ehrlich, G. Sargent Janes, Daniel E. Klimek, Franklin M. Landers, and Dennis P. Pacheco, "Efficient 7-J Flashlamp-Pumped Dye Laser at 500-nm Wavelength," Appl. Opt. 25, 2142 (1986).

7.   A.N. Fletcher, R.A. Hollins, R.F. Kubin, R.A. Henry, T.M. Atienza Moore, and M.E. Pietrak, "Luminescent Coolants for Solid-State Lasers," Appl. Phys. B30, 195 (1983).

8.   P. Lacovara, L. Esterowitz, and R. Allen, "Flashlamp-Pumped Ti:Al$_2$O$_3$ Laser Using Fluorescent Conversion," Opt. Lett. 10, 273 (1985).

9.   R.E. Schlier, "Quantum Efficiency Measurements and Fluorescence Predictions," Proceedings: Dye Laser/Laser Dye Technical Exchange Meeting, 1987, J.H. Bentley, Ed., MICOM Special Report RD-DE-87-1, pp. 67-107.

10.   See A.N. Fletcher, "Laser Dye Stability," Appl. Phys. B31, 19 (1983) and references therein.

11.   J. Calkins, E. Colley, and J. Hazle, "The Use of Caffeine as a Liquid Filter in Coaxial Flashlamp-Pumped Dye Lasers," Opt. Commun. 42, 275 (1982).

12.   W.W. Rigrod, "Homogeneously Broadened CW Lasers with Uniform Distributed Loss," IEEE J. Quantum Electron. QE-14, 377 (1978).

13.   D.P. Pacheco, H.R. Aldag, I. Itzkan and P.S. Rostler, "A Solid-State Flashlamp-Pumped Dye Laser Employing Polymer Hosts," in Proceedings of the Lasers '87 Conference (STS Press, McLean, VA, 1988), p. 330.
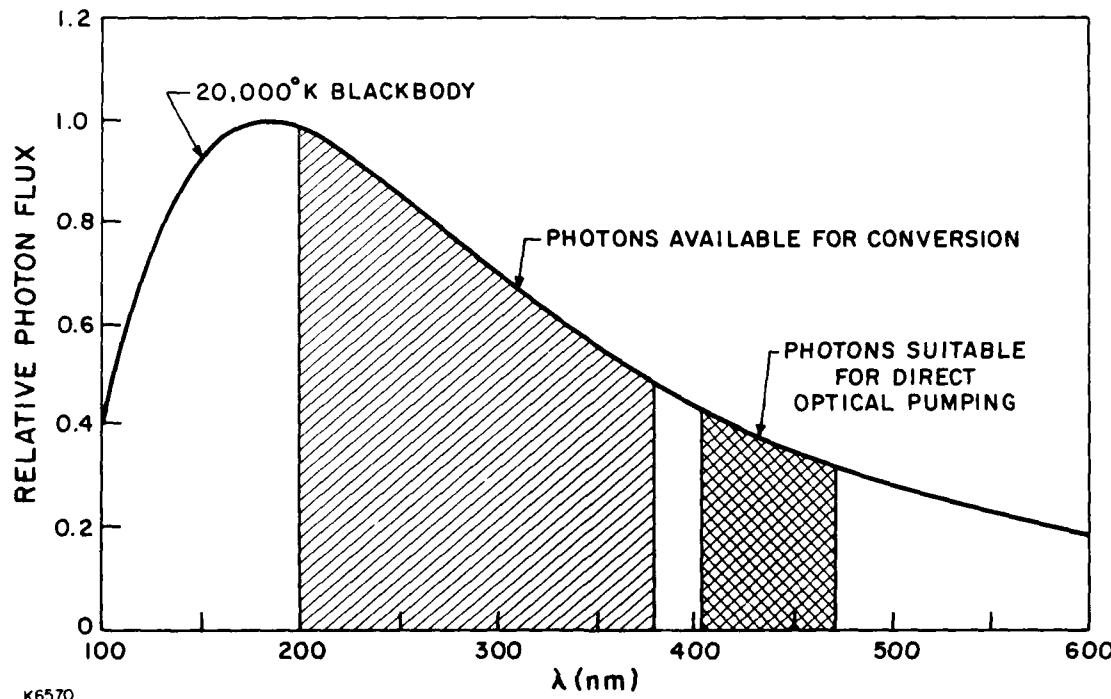
Fig. 1   Schematic Comparison of 20,000 K Blackbody Curve and Laser Dye Absorption Band
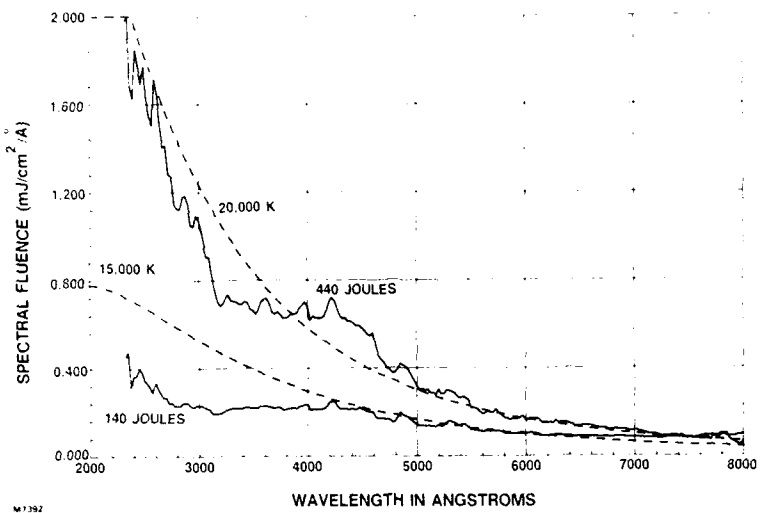
Fig. 2   Comparison of Measured Flashlamp Spectra with Blackbody Distributions
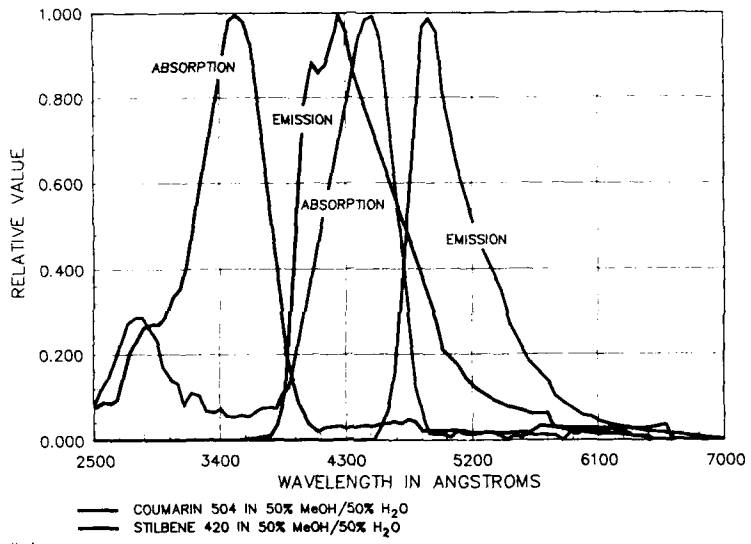
Fig. 3   Spectral Matching of Converter and Laser Dyes

K8286
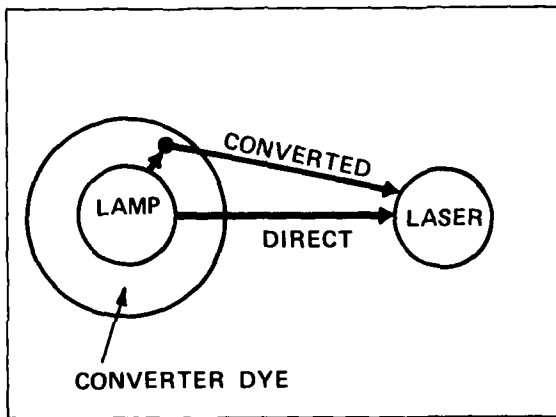
Fig. 4   Schematic Representation of Coupling Geometry with Converter Solution in Flashlamp Water Jacket

416

(A) WITH TRANSFER DYE (STILBENE 420)

(B) WITHOUT TRANSFER DYE

L3770
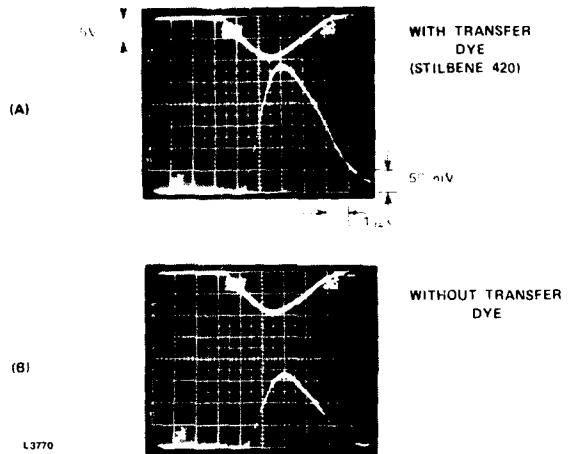
Fig. 5   Effect of Spectral Conversion on Laser Output of C504. The Upper Trace in Each Photograph Is the Lamp Current Pulse; The Lower Trace Is the Laser Output.
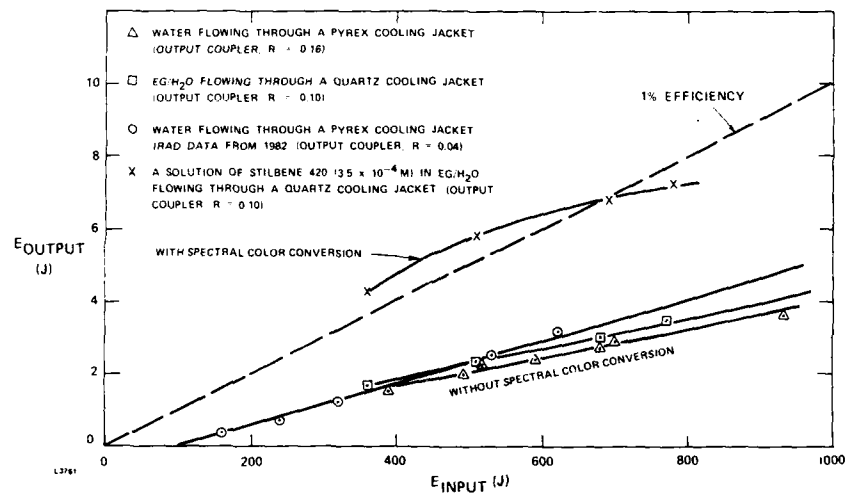
Fig. 6   Output of a Flashlamp Pumped Dye Laser Containing C504 with and without a Converter Dye (S1420).

ONLY 45% OF THE SECONDARY PHOTONS
ESCAPE TO BE POTENTIALLY USEFUL.
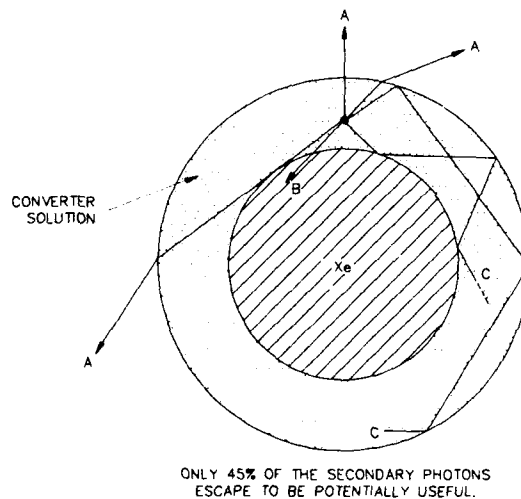
Fig. 7   Converted Photon Usage with Converter Solution in Flashlamp Water Jacket. See Table 1 for Explanation of Rays.

417

TOTAL INTERNAL REFLECTION IS A BONUS: ALMOST 83% OF
CONVERTED PHOTONS MAKE AT LEAST ONE PASS THROUGH LASER DYE
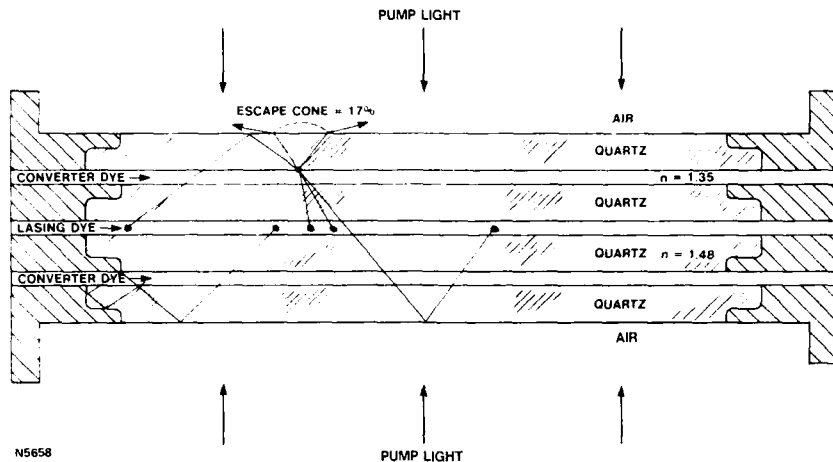
Fig. 8   Slab Configuration Showing Multiple Dye Channels
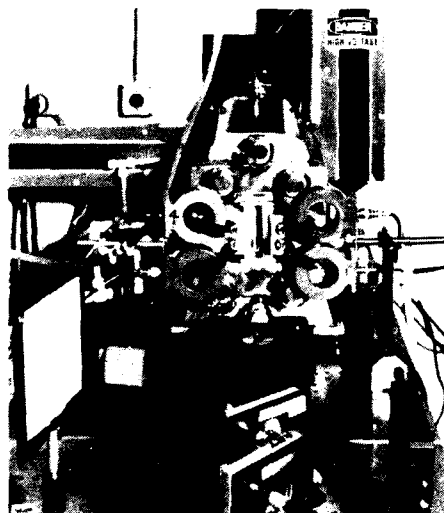
Fig. 9   Flashlamp Pumped Dye Laser Built at ARL Which Implements a Three-Channel Slab Design
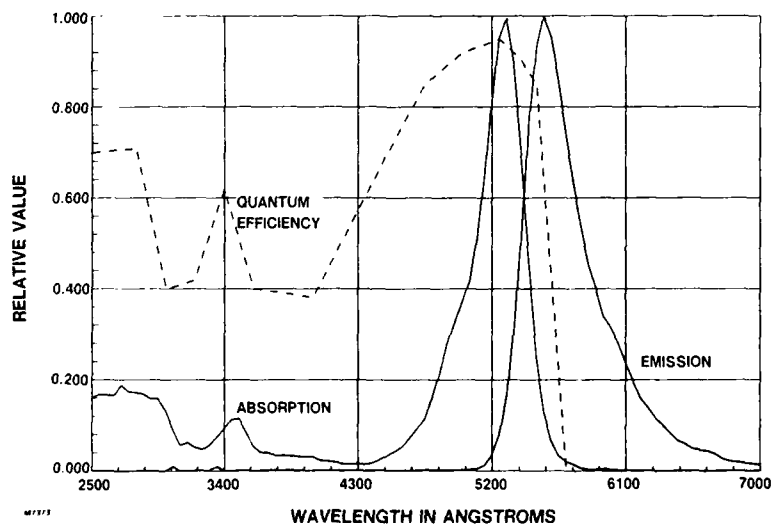
Fig. 10   Spectral Data for RH590 in 50% MeOH/50% H_2O. Detailed Spectra Are Stored on Disk for the
Computer Simulation Codes

418

LASER DYE: RHODAMINE 590 (5 X 10⁻⁵ M/ℓ)

CURRENT PULSES
(TWO SUPERIMPOSED)

WITH CONVERTER DYE
(LD473)

WITHOUT CONVERTER
DYE
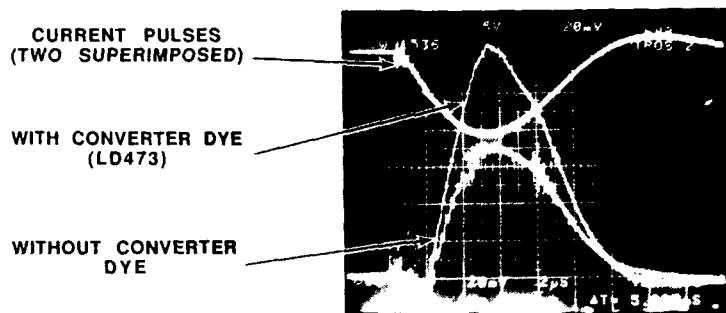
Fig. 11   Measured Laser Output for the Multichannel Slab Device with and without Converter Dye

TOTAL LAMP FLUENCE = 1 J/cm²
EQUAL EMISSION FROM LASER CHANNEL
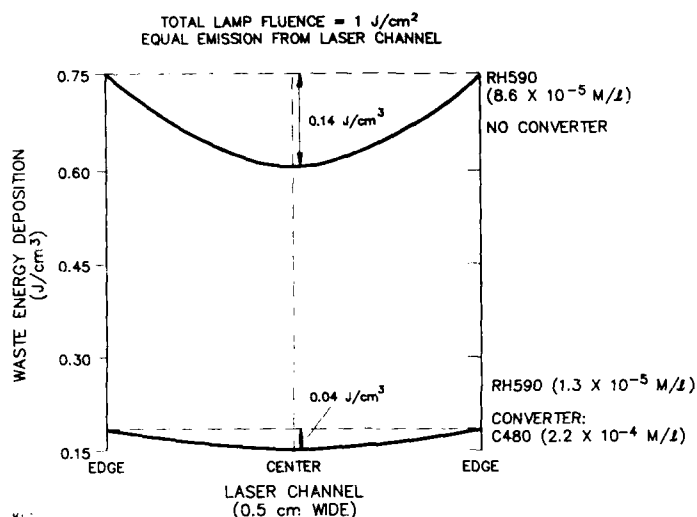
Fig. 12   Calculated Waste Heat Deposition across Laser Channel with and without Converter Dye. Dye Concentrations Have Been Adjusted for Equal Emission from the Laser Channel

TOTAL LAMP FLUENCE = 1 J/cm²
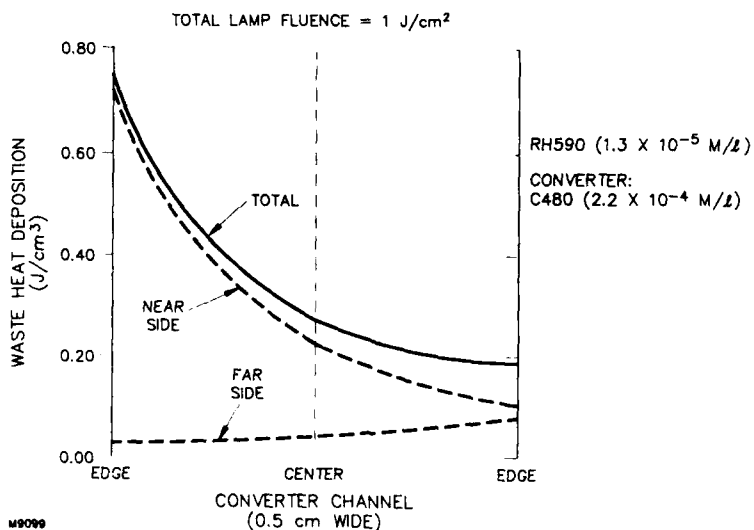
Fig. 13   Calculated Waste Heat Deposition across Converter Channel. Dye Concentrations Are Same as for Lower Curve of Figure 12

419

HIGH AVERAGE POWER EXCIMER LASER-PUMPED DYE OSCILLATORS

Roger A. Tennant, Michael C. Whitehead, Charles R. Tallman, and Richard W. Basinger

Chemical and Laser Sciences Division
CLS-5, MS E543
Los Alamos National Laboratory
Los Alamos, NM 87545

ABSTRACT

The design, construction, and testing of a high-average-power excimer laser-pumped dye oscillator is described. The system is designed to produce up to 75 W of average power in the near uv at a pulse repetition rate of 500 Hz.

Introduction

The wavelength tunability and high efficiency of excimer laser-pumped dye lasers makes them attractive for application in photochemical processes. A dye oscillator system designed to produce 150 mJ/pulse at 500 Hz and to be tunable through the 380- to 450-nm spectral region has been built and tested. The system is based on a single-stage power-oscillator dye laser currently pumped by two XeCl excimer lasers. The system is configured to operate at up to 250 Hz. To reach full power 500-Hz operation either two 500-Hz, 450-mJ/pulse excimer lasers, or four 250-Hz lasers would be required. The following paragraphs will summarize the system performance as well as system design and construction.

Performance Summary

First, the best performance to date will be summarized. The highest dye laser output yet attained is 170 mJ/pulse with a combined pump energy of 900 mJ/pulse from the two XeCl excimer lasers. The best optical conversion efficiency (based on energy actually delivered to the dye laser) is 27%. The highest pulse rate achieved to date is 240 Hz. A trigger problem on one of the excimer lasers prevented reliable operation at the full 250 Hz.

Typical performance of the excimer and dye lasers as a function of pulse rate is summarized in Figure 1. Note that the excimer laser output decreases slightly as pulse rate increases. Likewise, the output of the dye laser decreases slightly with increasing pulse rate. However, as shown in Figure 2, the dye laser efficiency is essentially a constant with increasing pulse rate. The dye laser efficiency plotted includes all beam transport losses and is essentially the ratio of dye oscillator output to excimer laser output.

System Design and Construction

Dye Laser Oscillator

The current dye laser oscillator was designed and constructed for use with dioxane as a solvent. Dioxane is highly volatile, flammable, toxic, and reactive. Unfortunately, it is also the best solvent for the Lambda Physik TBS dye that was used for this series of experiments. Construction materials were primarily aluminum and stainless steel. Seals used were ethylene propylene (EPDM) O-rings, Swagloks, and copper and aluminum gaskets with conflat flanges.

Two different configurations of dye oscillator were used. The first of the two concepts places the complexity in the fabrication and assembly of the quartz dye cell. The result was a fairly straightforward design for the dye cell holder, but a very expensive dye cell. Figure 3 shows the dye cell holder with an early version of the dye cell. Later versions of the dye cell were made up of four pieces of precisely cut and polished quartz glued together by an epoxy recommended by Master Bond, Inc. of Hackensack, New Jersey. Since, dioxane is very nearly a universal solvent, finding a glue that would not be dissolved was a very difficult task. Figure 4 shows a cross section of the dye cell holder and a schematic drawing of a dye cell. The flow direction is from top to bottom. After extensive testing of the internal flow geometry, it was discovered that the only flow straightener required was a 60 mesh screen just downstream of the conical section. Figure 5 shows what the final configuration of dye cell actually looked like. Also shown is one configuration of optical resonator used. The dye flow channel at the pump region was 4-mm wide, 70-mm long, and 19-mm thick. The excimer pump beam dimensions at the dye cell were typically 45-mm long and 2-mm high. The excimer beam length was limited to 45 mm due to the optical beam homogenizers used to shape and remove hot spots from the two pump beams.

After experiencing a great deal of difficulty in gluing the four pieces of optical-quality quartz together on a consistent, economical, and timely basis, we decided to design a dye laser cell that would use standard, round, flat optics. The prototype is shown in Figure 6. In this design, the complexity is placed in the metal components, not in those made of

quartz. The excimer laser pump windows in this instance are 2-in.-diam uncoated quartz substrates. The dye laser windows are 1-in.-diam quartz substrates and reflection coated on one side.

The flow direction is again from top to bottom. A 60 mesh screen is again used as a flow straightener between the top piece and the flow inlet section. The flow inlet section is a computer-designed contoured nozzle. The pump region flow cross section is 4-mm wide and 75-mm long. Downstream of the pump region is a constant angle diffuser section. A glue joint is still required on the 2-in. optics; however, the precision is now in the invar optic holders and not in the quartz. The most difficult part of the fabrication of this new concept is the welding of the four pieces of the nozzle assembly together. This was accomplished by use of electron beam welding. Figure 7 shows the final design version installed and operational.

Dye Laser Flow System

Several dye laser flow systems were built. A compact, portable system is shown in Figure 8. The essential components include a pump, a filter system, a surge tank/reservoir, a heat exchanger, and a fill system. The instrumentation on this system is fairly simple, consisting of mechanical pressure gauges, a mechanical flow meter, and thermocouples.

The most important component of the flow system is the flow pump. It is very important to match the pump to the pressure losses of the flow system. On the system in Figure 8, the pump is a March Model No. TE-5.5S-MD, which would pump a maximum of 15 gpm at a system pressure drop of 11 psig. This flow is adequate to give a clearing ratio of 3 at 500 Hz for the present dye oscillator. The motor is 1/3 hp. The seal is a barrier type with a magnetic coupling. The bearings are Rulon A. The shaft is alumina ceramic. The housing and impeller are stainless steel. The O-rings are EPDM.

The filter system has an aluminum housing with EPDM O-rings. The best filters used were four 0.1 μm Teflon filter cartridges manufactured by PALL Corporation. Millipore Corporation has a comparable product. Selection of the proper filters is very important as very small particles of dye and solvent reaction and decomposition products need to be removed in order to prevent optical damage of the dye cell due to the buildup of carbon deposits. Coarser filter cartridges are not as effective at removing these particles.

On this particular flow system, the surge tank/reservoir and the heat exchanger are combined in the stainless steel tank, which is only partly visible in Figure 8. The coolant used was a mixture of distilled water and antifreeze to eliminate corrosion problems.

The large tank shown on the right of Figure 8 is the dioxane loading and unloading tank. Quick disconnects were used to facilitate rapid hookup and disconnect. Due to a slight leakage through the quick disconnects, in-line ball valves were added later as a further safety feature. The dioxane-dye mixture was loaded into the transfer vessel in a fume hood. Then the liquid was transferred into and out of the flow system in a normal laboratory environment by use of argon gas pressure at the proper location. As an additional safety feature, the appropriate chemical face masks were used during transfer operations.

Excimer Lasers

The excimer lasers used were Lambda Physik Model EMG 203 MSC. The type of excimer was XeCl running at 308 nm. These lasers have produced 110 W at 250 Hz. At 125 Hz, an output of 0.5 J/pulse was typical on a fresh gas fill with clean optics. The pulse repetition rate was variable from 0 to 250 Hz. Pulse duration was about 35-ns FWHM. Power intensity and energy variations were typically about ±3%. Jitter from an internal trigger was about ±1.4 ns. The output fluence uniformity over the central 75% of the beam was within ±15%. The beam divergence was 1 mrad x 4 mrad. The missing pulse rate was <0.05%. These particular lasers were not equipped with cryogenic gas processors; hence, the run time to 80% output was only about 10^7 pulses. Other Lambda Physik lasers with cryogenic gas processors have demonstrated optics lifetimes in excess of 10^8 pulses.

Conclusions

Excimer-pumped dye lasers have been successfully run at high pulse rates and at high powers for hours at a time. Very rugged versions of dye lasers have been built and operated in ventilated enclosures in an environment not far removed from that found in a typical factory. Excimer laser technology is progressing very rapidly and optics lifetimes of greater than 10^8 pulses have been demonstrated. Hence, excimer-pumped dye lasers appear to be ready for industrial applications.
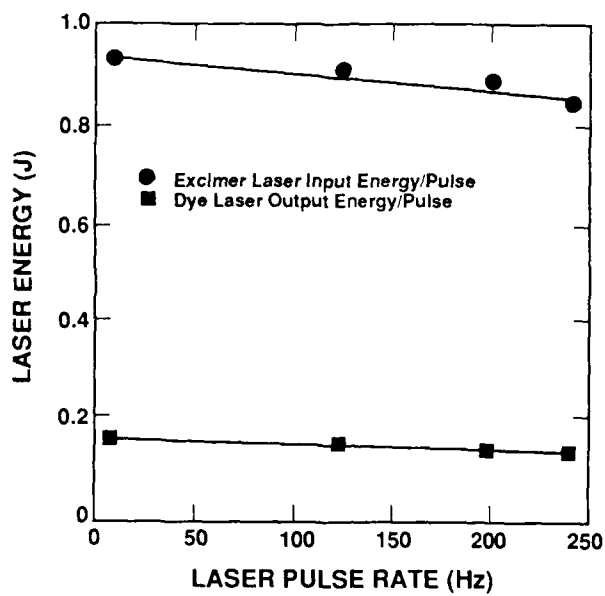
Fig. 1. Dye laser input and output.
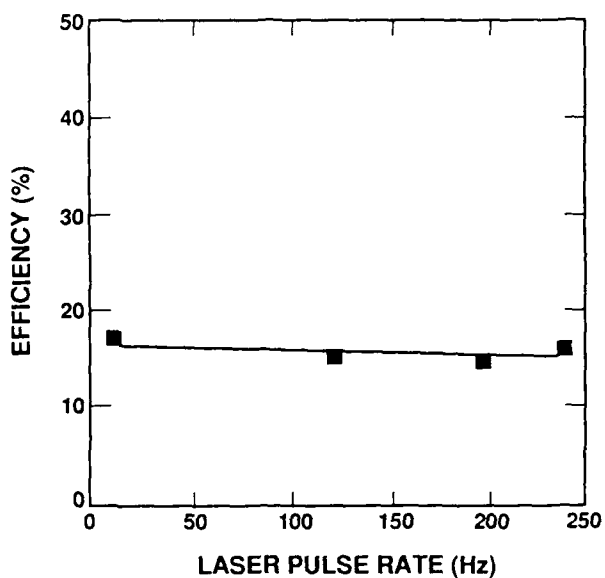
Fig. 2. Dye laser efficiency.
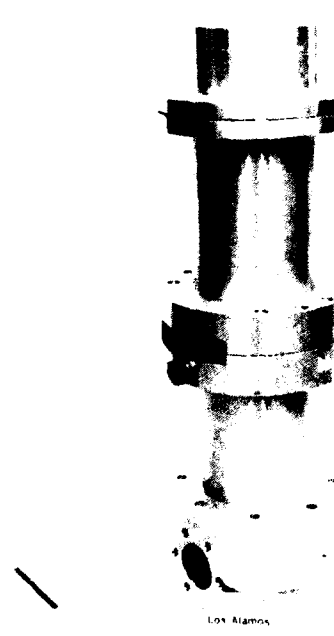
Fig. 3. Dye laser.
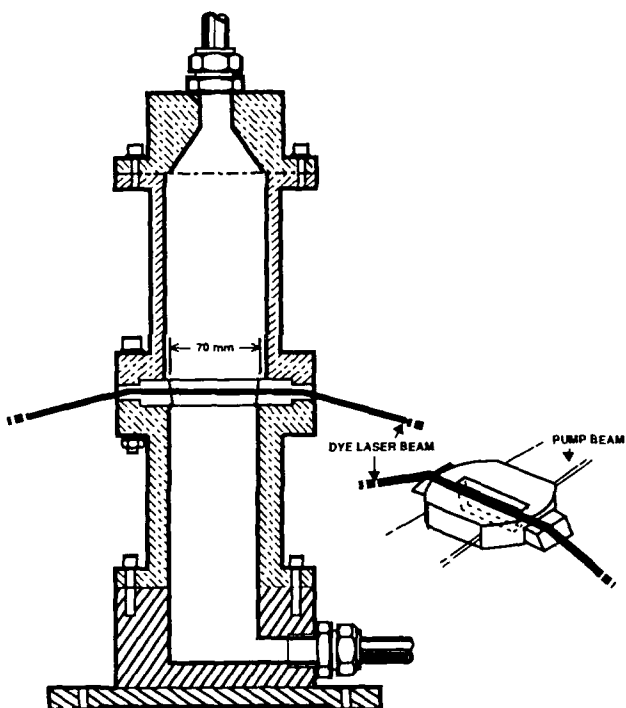
Fig. 4. Los Alamos dye amplifier cell.
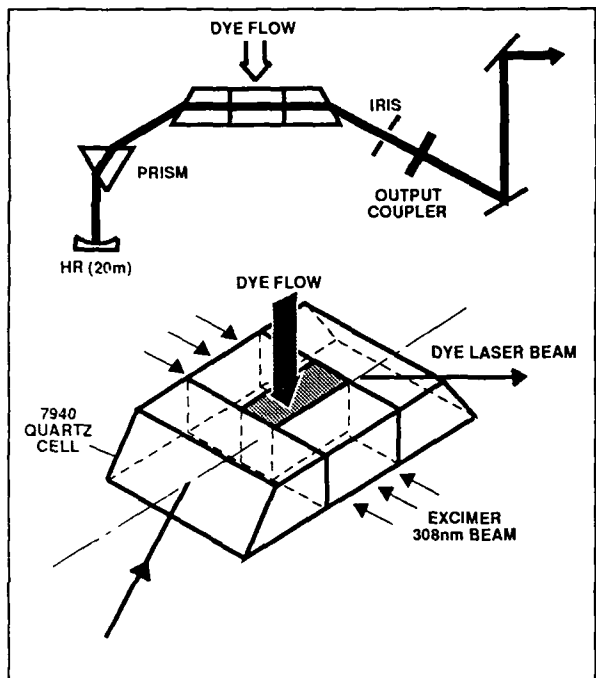
Fig. 5. Dye oscillator.

Fig. 6. Dye laser prototype.
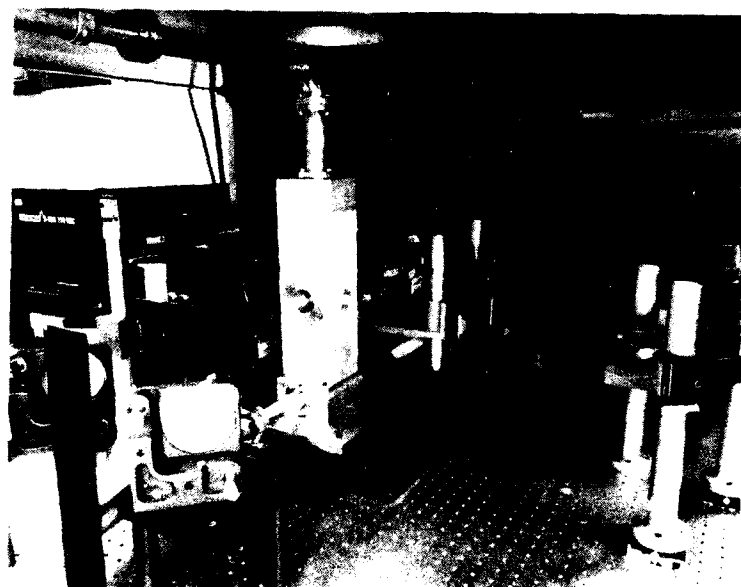
Fig. 7. Dye laser system.
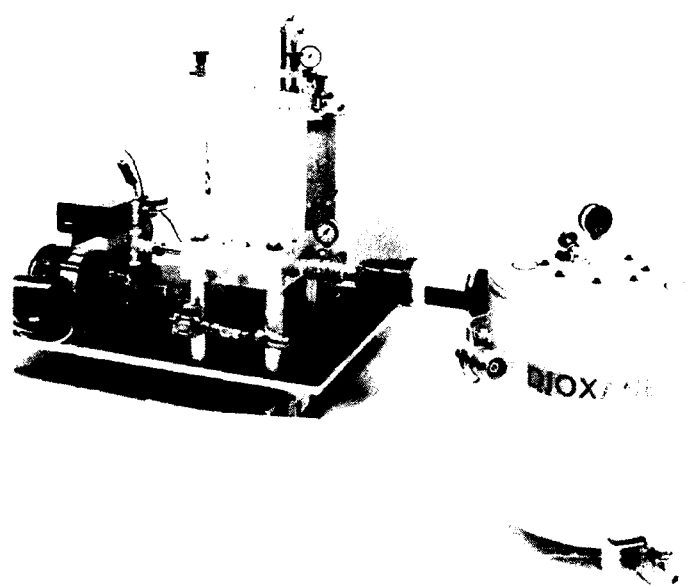
Fig. 8. Dye laser flow system.

TIME-RESOLVED PHASE AND INTENSITY MEASUREMENTS
OF A PULSED DYE LASER USING AN INTEGRATED-OPTICS WAVEFRONT SENSOR*

B. G. Zollars, R. H. Rediker, J. L. Swedberg, J. M. Mahan, and R. E. Hatch

Massachusetts Institute of Technology - Lincoln Laboratory
P. O. Box 73
Lexington, Massachusetts 02173

Abstract

An integrated-optics wavefront sensor has been used to measure the near-field phase and intensity distribution of a flashlamp-pumped, pulsed dye laser. The sensor's temporal resolution allows ten 200-ns snapshots of the wavefront to be taken during the laser's 2-µs, 4MW peak power pulse. The time-resolved wavefront measurements show large-scale temporal fluctuations of the phase during a single pulse, which explain the laser's previously measured poor beam quality.

At Lincoln Laboratory we are constructing a large, flashlamp-pumped, pulsed-dye laser system[1]. The system is made up of six independent laser beams, each operating at 10 pulses per second with an energy output of approximately 8 J per pulse. The average power output of the system, when complete, will be approximately 480 Watts, making it one of the largest flashlamp-pumped dye-laser systems in existence. Recently, we have been conducting experiments with a single laser beam of the six, with the main goal of characterizing the dye laser's energy and beam quality. This paper describes the results of some recent measurements made on the dye laser using a novel integrated-optics wavefront sensor. The integrated-optics sensor is unique in that it can make measurements of phase and intensity with 200-ns temporal resolution. Thus, it is an ideal tool for investigating the time-resolved behavior of the wavefront of lasers with pulse durations on the order of microseconds.

Figure 1 shows a photograph of the single laser and its associated diagnostic instrumentation mounted on the vertical optical bench in our test bed at the Laboratory. The laser is made up of two identical laser heads residing within the same unstable resonator. Dye solution flows longitudinally through each laser head, and is pumped by a pair of close-coupled linear flashlamps, each of which supports a 500-Joule electrical discharge. In the present experiments, most of the annular-shaped output beam is directed into a calorimeter for energy measurement. A portion of the beam is steered to a diagnostic area, where either the integrated-optics wavefront sensor or a far-field imaging camera is used to measure the laser beam characteristics.

A standard technique for measuring the beam quality of a laser is to determine the distribution of the laser's output energy in the far-field. Figure 2 shows a schematic of the arrangement we use to accomplish this measurement[2]. A small fraction of the laser's 14-mm diameter output is taken to the far-field by focusing it with a 2-m focal length lens. The resulting focal spot is imaged with a radiometrically calibrated 64 x 64 CCD (charge-coupled device) camera. The CCD camera is interfaced to a MicroVAX computer, allowing rapid read-out and analysis of the far-field image. Figure 3 shows the measured far-field distribution from a single pulse of the dye laser. The output energy for this particular laser pulse was 7 J. The camera array subtends a full angle of about 35 λ/D; this measurement indicates that the beam is about 15 times its diffraction limit.

The design goal for this laser calls for operation with better than 5 times diffraction-limited beam quality. The laser clearly does not meet this goal. This less than satisfactory beam quality could result from several different sources. Among the most plausible explanations for the large beam divergence are:

1) A static aberration in the resonator optics or dye cell windows.

2) Refractive index gradients in the dye medium resulting from vortices, cavitation, or shear heating due to the very high liquid flow rates through the dye cell.

3) Refractive index gradients resulting from inhomogenous heating of the dye fluid during the laser pulse, either from pump light or from absorption of the laser light itself.
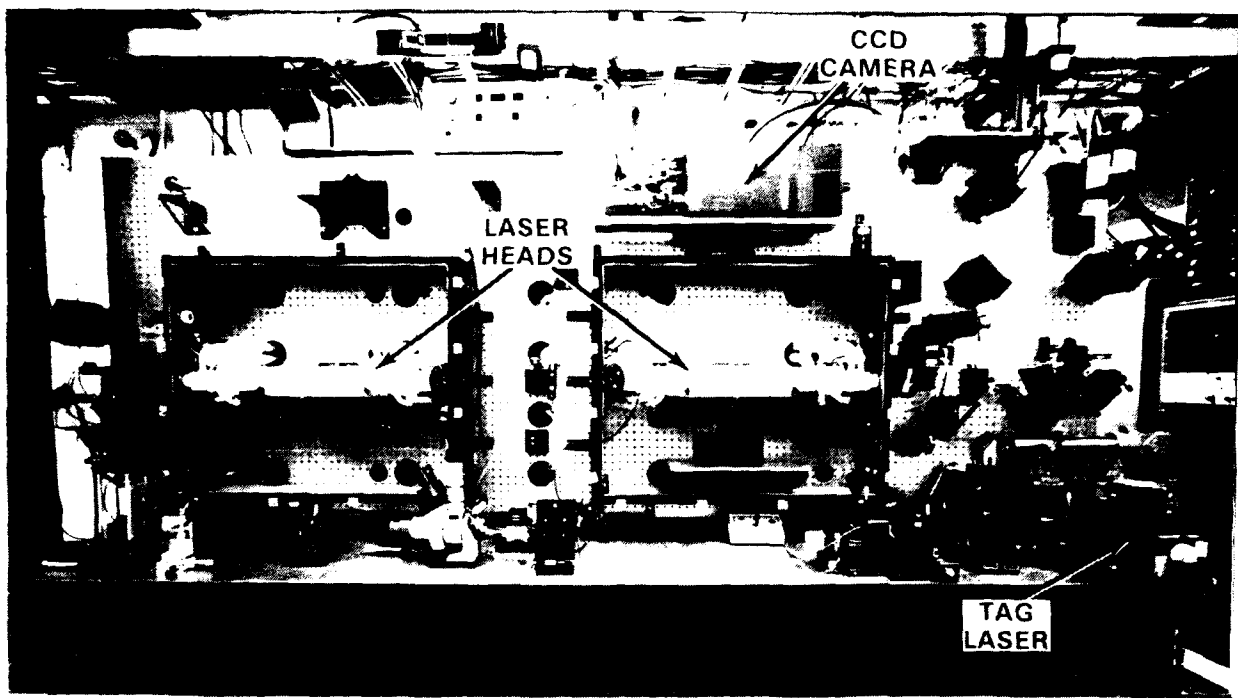
Figure 1. A single flashlamp-pumped, pulsed dye laser mounted on a vertical optical bench at Lincoln Laboratory. The CCD camera is used for measuring the far-field energy distribution of the laser The integrated-optics wavefront sensor is mounted on the horizontal portion of the optical bench.
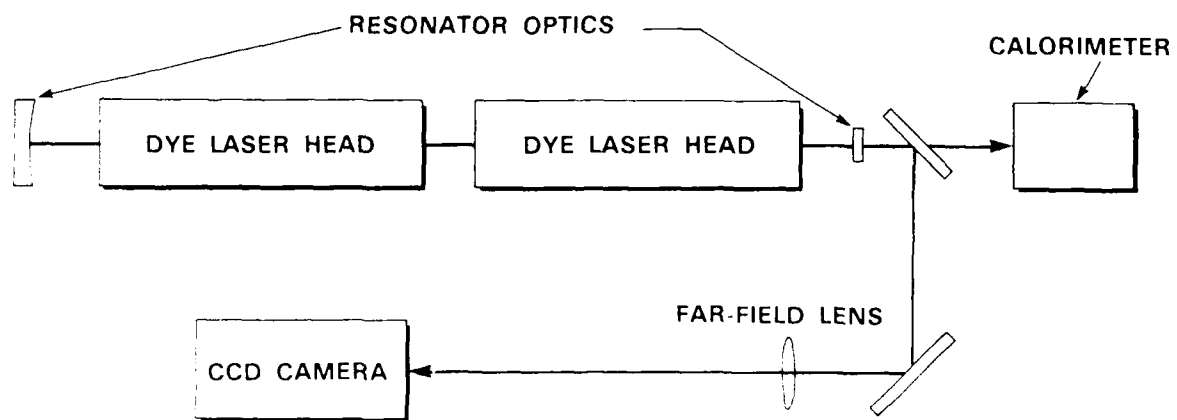
Figure 2. Schematic diagram of the arrangement used to measure the laser's far-field energy distribution.
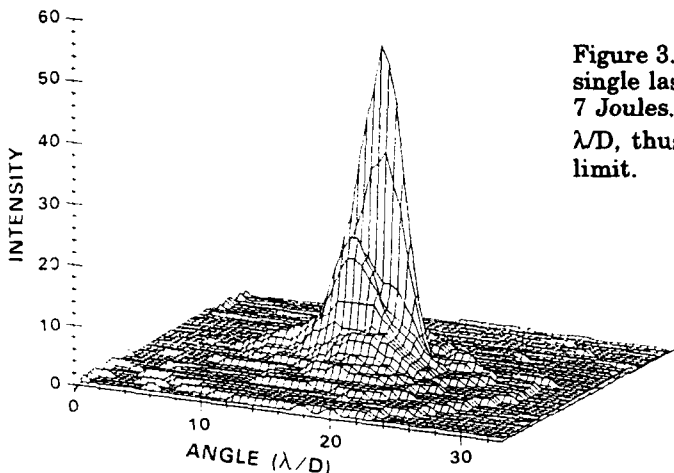
Figure 3. Measured far-field energy distribution for a single laser pulse. The total energy in this pulse was 7 Joules. The 64 x 64 CCD array subtends about 35 λ/D, thus the laser is about 15 times its diffraction limit.

Note that for case 3, the aberration would tend to vary during the envelope of the laser pulse, whereas for case 2, the aberration would be different for every individual laser pulse, but would be static for the duration of the pulse. We can thus distinguish between the possible reasons for the poor beam quality.

Earlier attempts to measure static aberrations such as would be produced by cases 1 and 2 above proved unsuccessful. These measurements involved shear interferometry of the dye laser output. It is clear that any evolution of the laser wavefront during the pulse would destroy the contrast of the interferogram, so we concluded that the degradation of the beam quality was due to dynamic refractive index gradients in the dye solution during the laser pulse. This provided the motivation for using a diagnostic instrument like the integrated optics wavefront sensor, which can resolve changes in the output phase of the dye laser during a single pulse.

Figure 4 shows a schematic view of the wavefront sensor[3]. It consists of several optical waveguides diffused into a one-dimensional array on a LiNbO$_3$ substrate. The waveguides are arranged in an alternating sequence of Mach-Zehnder interferometers (Y-junctions) and straight guides, with a total of 20 interferometers on the substrate. The local gradient of the input beam's wavefront is computed from the ratio of each interferometer's output to the outputs of its neighboring straight waveguides via the relationship,

$$\phi_n = 2 \cos^{-1} \left[\frac{\frac{2 P_{\phi n}}{B_n} - \left(\sqrt{P_n} - \sqrt{P_{n+1}} \right)^2}{4 \sqrt{P_n P_{n+1}}} \right]^{\frac{1}{2}} \tag{1}$$

where $P_{\phi n}$ is the power (or intensity) output from the n-th interferometer, P_n is the power output from the n-th straight waveguide, and ϕ_n is the phase gradient of the incoming wavefront in the locale of the n-th interferometer (along the direction of the array). The factors B_n take into account any losses in the Y-juctions of the interferometers, and are determined from pre-experiment calibration measurements with a planar wavefront.

To measure the intensity of the light exiting the waveguides, an array of CCD cells with on-chip buffer storage is used, as shown in figure 5. A single row of imaging CCDs integrates the output of the waveguides for times as short as 200 ns, after which the accumulated charge is shifted into the buffer storage via a row of transfer cells, the imaging row is cleared, and integration begins again. There is enough buffer storage in the array to make ten separate measurements. Typically, during experiments with the dye laser, each integration time is of 200-ns duration, giving a total observation time of 2 µs. At the end of the laser pulse, the ten measurements have been made, and the charge in each buffer storage cell is sequentially digitized and transferred to a computer for analysis. The wavefront gradients are computed from the waveguide intensities. The laser wavefront is obtained by integrating the calculated gradients.

Figure 4. Schematic diagram of the integrated-optics wavefront sensor. An alternating sequence of straight optical waveguides and Mach-Zehnder interferometers allows measurement of the wavefront phase gradients.
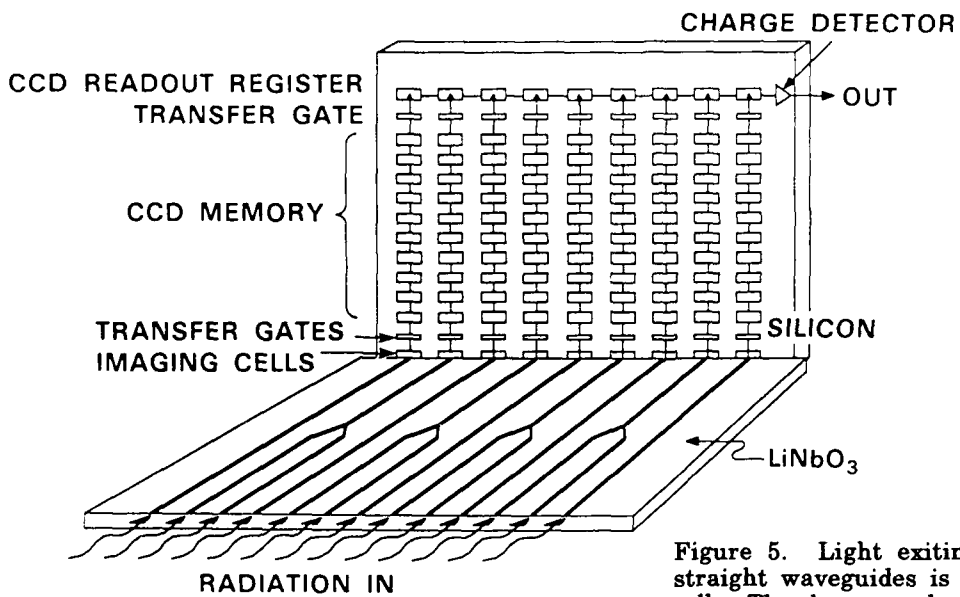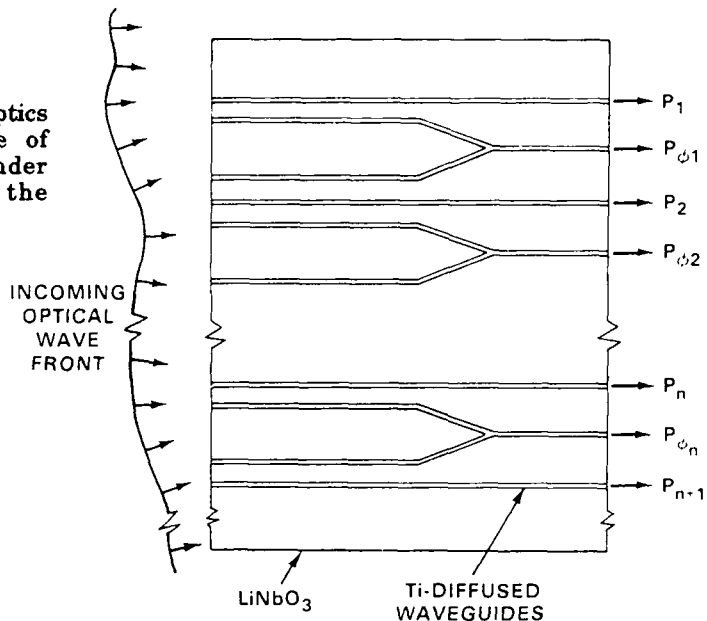
Figure 5. Light exiting the interferometers and straight waveguides is collected by a row of CCD cells. The charge produced is then shifted into buffer storage, to be read out and digitized after the laser pulse.
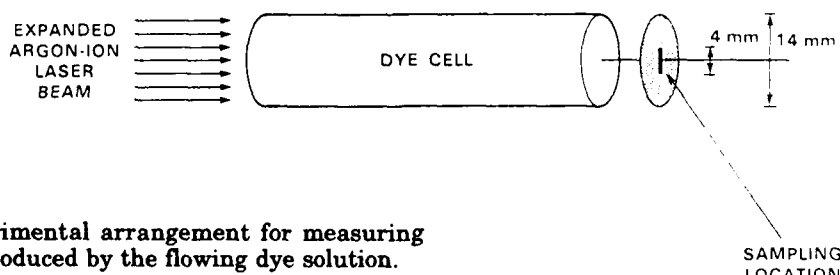
Figure 6. Experimental arrangement for measuring the aberration produced by the flowing dye solution.

The first series of wavefront sensor measurements were of aberrations induced solely by the flow of the dye solution through the dye cell. The measurements were made by passing an expanded, diffraction-limited argon-ion laser beam directly through a single dye cell and into the wavefront sensor. For these measurements, as shown in figure 6, the resonator optics were removed and the sensor measured the phase gradients along a 4-mm slice through the center of the 12-mm dye cell aperture. Figure 7 shows a surface plot of the flow-induced wavefront aberrations. Ten separate measurements of the phase were made, each with a 100-μs integration time. Note that the magnitude of the aberration is small, and there are no temporal fluctuations even on a millisecond time scale. Even though during operation the laser beam would sample this static aberration more than once, it is not large enough to cause the poor beam quality discussed earlier.

Figure 8 shows the experimental arrangement used for making the measurements of the time-resolved dye laser wavefront. A fraction of the laser output is sent through optics which image its near-field onto a mask which is of the same dimensions as the active input area of the interferometer array. The mask is then imaged onto the waveguide inputs. The light exiting the array of interferometer and straight waveguides is then imaged into the CCD array. The magnifications of the imaging optics are arranged so that the sensor measures the wavefront in a radial slice through the annular dye laser output beam. The results of ten 200-ns measurements during a single 2-μs long dye-laser pulse are shown in figure 9, and the total intensity seen by the straight waveguides as a function of time is shown in figure 10. The observed wavefront fluctuations are large in amplitude, and there is a great deal of temporal variation. One can see that early in the pulse, the overall tilt of the laser output is in one direction, during the middle of the pulse in the other direction, and then back in the original direction in the later part of the pulse. These large (on the order of 1 wave of tilt) changes in phase during the laser pulse are certainly consistent with poor beam quality.

With these time-resolved near-field phase and intensity measurements in hand, we wish to know whether they are consistent with the measured far-field intensity distribution. To make the comparison, we calculate the far-field energy distribution from the near-field phase and intensity provided by the wavefront sensor. Since the sensor is only capable of measurements along a radial slice of the beam, we must first assume that the intensity and phase fluctuations in the beam are cylindrically symmetric about the laser axis. Using this assumption, we can take the ten measured near-field phase and intensity time slices and convert each into an annular "near-field". By taking the Fourier transform of each time-slice, and then adding the resultant calculated intensities together, we produce the calculated far-field energy distribution. The results of this calculation appear in figure 11. One can see the good qualitative agreement between this calculated far-field and the measured far-field energy distribution of figure 3. These results confirm that to first order, the wavefront sensor measurements are consistent with a laser that is about 15 times its diffraction limit.

Figure 7. Surface plot of the flow-induced aberrations. Note that the aberration is static for times greater than 1 msec, and is insufficient to cause the poor beam quality.

429
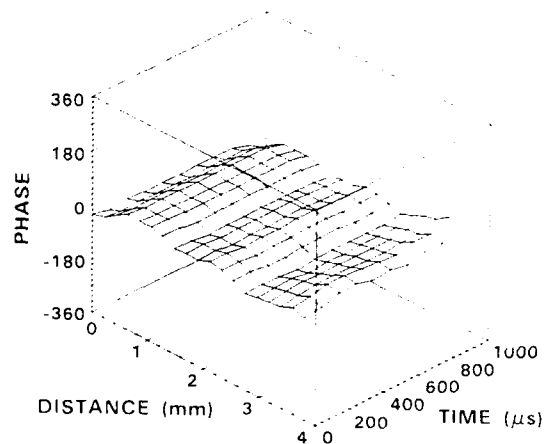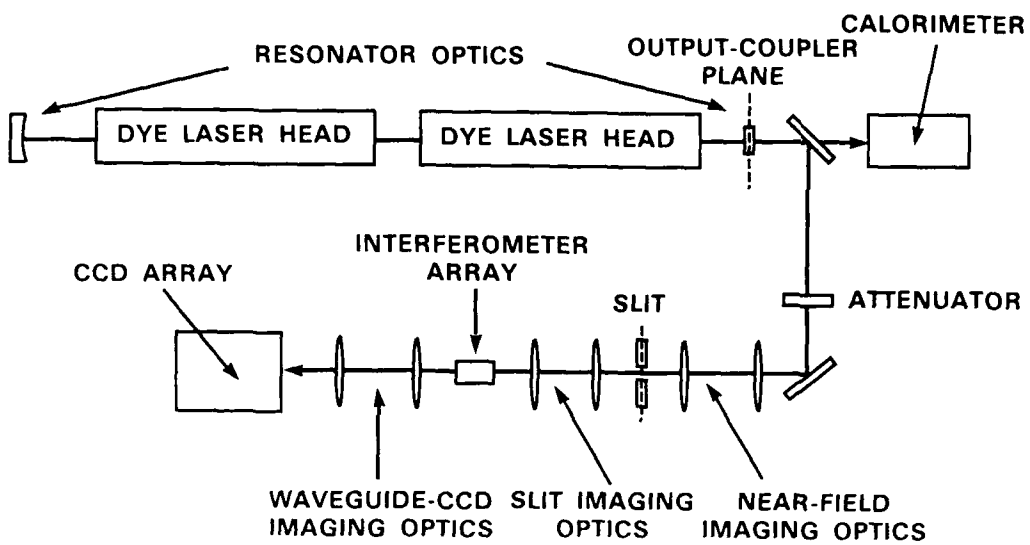
Figure 8. Experimental arrangement for measuring the time-resolved dye laser wavefront.
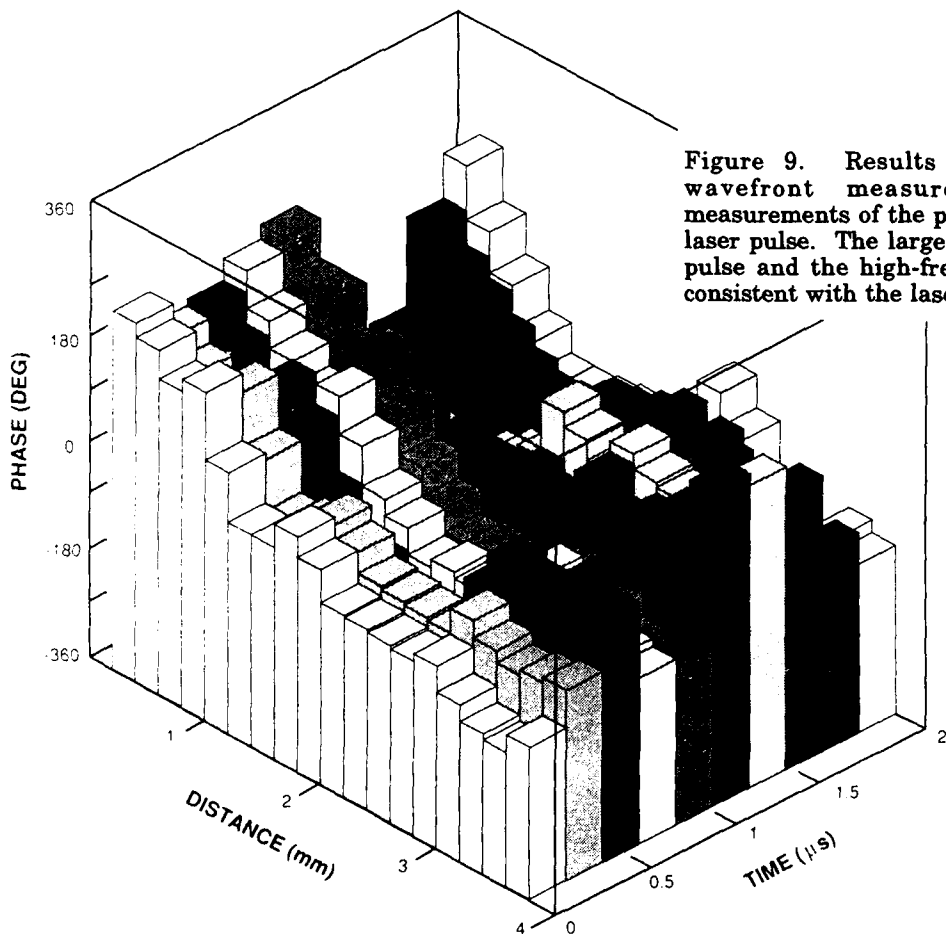
Figure 9. Results of the time-resolved laser wavefront measurements. Ten separate measurements of the phase are made during the 2-μs laser pulse. The large temporal variation during the pulse and the high-frequency spatial variations are consistent with the laser's poor beam quality.
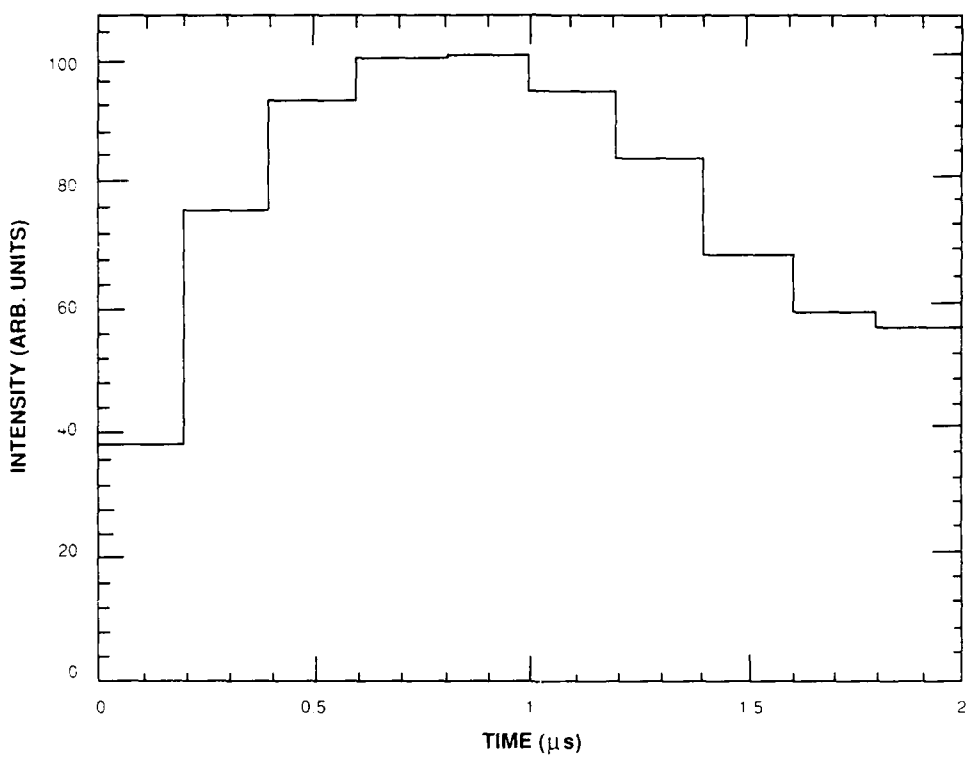
Figure 10. Total laser intensity as a function of time, as seen by the straight waveguides in the wavefront sensor array. These data are from the same laser pulse whose wavefront is shown in figure 9.
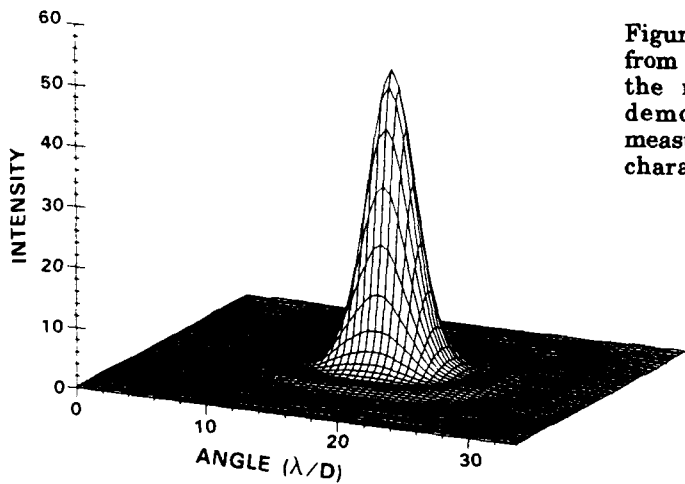
Figure 11. Far-field energy distribution calculated from the data of figure 9. The good agreement with the measured far-field distribution of figure 3 demonstrate that the wavefront sensor measurements are consistent with the observed laser characteristics.

The results of our measurements confirm that the poor beam quality of the dye laser is most probably due to rapidly varying aberrations in the dye medium during the dye-laser pulse. These aberrations could be due to inhomogeneities in the pumping light, or to self-heating by absorption of the laser light itself. Beam quality improvements could therefore be expected by reducing the heat load on the dye solution, minimizing solution absorption in areas away from the dye's pump absorption band, or converting "waste" light of wavelengths shorter than the dye pump band into useful light by other dyes or spectral transfer agents[4,5].

In summary, we have used a novel integrated optical wavefront sensor to measure the near-field phase and intensity fluctuations during the 2-µs pulse of a flashlamp-pumped dye laser. The sensor has a 200-ns temporal resolution, making it the fastest known device of its kind. The temporal resolution of the present device was limited only by the transfer speed of photoelectrons in the CCD. It is worth noting that CCDs have recently been produ.. d with charge transfer times on the order of 1-ns[6], making it possible to measure the dynamics of laser wavefronts with unprecedented nanosecond resolution. There can be no argument that such devices would help extract the physics inherent in the development and/or improvement of short-pulse lasers.

References:

1. P. N. Everett and B. G. Zollars, in Proceedings , International Conference on Lasers '87, F. J. Duarte, Ed. (STS Press, McLean, VA, 1988), pp. 291-296.

2. B. G. Zollars and P. N. Everett, in Proceedings , International Conference on Lasers '87, F. J. Duarte, Ed. (STS Press, McLean, VA, 1988), pp. 297-303.

3. R. H. Rediker, T. A. Lind, and B. E. Burke, J. Lightwave Technol. 6, 916 (1988).

4. C. E. Moeller, C. M. Verber, and A. H. Adelman, Appl. Phys. Lett. 18, 278 (1971).

5. D. P. Pacheco, P. S. Rostler, and H. R. Aldag, presented at the International Conference on Lasers '88, Lake Tahoe (1988), paper TF.4.

6. Y. T. Chan, in Proceedings, Conference on Charge-Coupled Device Technology and Applications, (NASA, Washington, DC, 1976), p. 89.

DIODE-LASER-PUMPED BLUE LIGHT SOURCES

W.P. Risk and W. Lenth

IBM Research Division, Almaden Research Center, 650 Harry Road, San Jose, California 95120-6099

Abstract

Miniature laser devices operating in the blue - green spectral region are interesting for a variety of applications including optical data storage, color displays and underwater optical communications. Nonlinear optical techniques can be combined with GaAlAs diode laser technology to yield compact sources of blue light. Most of the recent work on nonlinear laser designs has concentrated on frequency doubling of diode-laser-pumped 1064-nm Nd:YAG lasers to produce green light at 532 nm. Here, we report on two approaches for the generation of blue radiation using second-harmonic and sum-frequency generation of diode-laser- pumped Nd: YAG lasers. We have developed a very efficient diode-laser-pumped Nd:YAG laser operating at 946nm on the $^4F_{3/2} \rightarrow {}^4I_{9/2}$ transition. Using KNbO$_3$ as the nonlinear crystal, approximately 3 mW of output power at 473-nm was produced by intracavity second-harmonic generation. Investigations of nonlinear processes in KTiOPO$_4$ (KTP) showed that sum-frequency mixing of 1064-nm and 809-nm radiation is non-critically phasematched at room temperature. Since the 809nm mixing wavelength coincides with a strong absorption line of Nd:YAG, intracavity frequency mixing of a 1064-nm Nd:YAG laser and its 809-nm pump source can be employed for efficient generation of 459-nm radiation. The exceptionally large temperature and angle tolerances of this non-critically phasematched frequency-mixing process are advantageous for practical device applications. This intracavity sum-frequency mixing scheme permits high-speed modulation of the blue output by direct modulation of the 809-nm pump source. Short pulses of 5-ns duration were generated by direct modulation of the diode-laser injection current.

Introduction

The advent of high-power GaAlAs laser diodes has sparked interest in blue sources based on nonlinear frequency upconversion of the near-infrared laser-diode light. Direct nonlinear upconversion of GaAlAs laser diodes is possible[1], but the poor spectral and spatial mode properties of high-power laser diodes limits their suitability as sources for direct frequency upconversion. However, GaAlAs diode lasers are excellent pump sources for solid-state lasers, and the narrow spectral bandwidth and TEM$_{00}$ mode of diode-laser-pumped solid-state lasers are well-suited to frequency upconversion by second- harmonic generation or sum-frequency mixing. Two nonlinear mechanisms for frequency upconversion of diode-pumped solid-state lasers are discussed here. Both are based on $\chi^{(2)}$ processes in non-centrosymmetric crystals. Intracavity frequency doubling of a diode-laser-pumped 946-nm Nd: YAG laser produces blue light at 473 nm. Intracavity frequency mixing of the pump and laser fields of a diode-laser-pumped 1064-nm Nd: YAG laser was used to produce 459-nm light.

Intracavity Frequency Doubling of a 946-nm Diode-Laser-Pumped Nd: YAG Laser

Diode-laser-pumping of the $^4F_{3/2} \rightarrow {}^4I_{11/2}$ Nd:YAG transition at 1064-nm has been studied extensively and combined with intracavity frequency doubling to produce miniature green sources at 532 nm [2]. Diode-laser-pumping of the $^4F_{3/2} \rightarrow {}^4I_{9/2}$ transition at 946-nm is also of interest since frequency doubling of this wavelength would produce blue light at 473 nm. However, the gain cross-section of the 946-nm transition is roughly an order of magnitude lower than that for the 1064-nm transition, and the 946-nm transition terminates at the 857 cm^{-1} Stark component of the $^4I_{9/2}$ ground-state manifold, producing a reabsorption loss. As a result, diode-laser-pumped operation of a 946-nm laser is more difficult than diode-laser-pumping of the 1064-nm laser. Despite these problems, a 946-nm Nd: YAG laser can be efficiently pumped by high-power laser diodes[3]. Potassium niobate (KNbO$_3$) can be used for efficient frequency doubling of the 946-nm radiation. Non-critical phase-matching can be achieved if the KNbO$_3$ is heated to ~185°C, and this approach was used by Dixon, et al.[4], for frequency doubling of a 946-nm Nd: YAG laser pumped by a visible dye laser. Here, we use angle-tuned, type I phase-matching to achieve efficient frequency doubling at room temperature.

Figure 1 shows the experimental configuration used for diode-laser pumping of the 946-nm Nd: YAG laser. A near-hemispherical resonator was used. The flat front face of the Nd:YAG crystal served as the input mirror, which was coated for high reflectivity ($\geq$ 99.9%) at 946nm and high transmission (~92%) at the 809-nm pump wavelength. The flat exit face of the Nd:YAG crystal was antireflection-coated at 946nm. The 1-mm length of the Nd:YAG crystal was chosen as a compromise between making the crystal long to increase the pump absorption and making it short to reduce the reabsorption loss[5,6]. The curved (r = 5 cm) output mirror had a transmission of 0.16% at 946 nm. In addition, the mirror had sufficient transmission at 1064-nm to suppress oscillation of the $^4F_{3/2} \rightarrow {}^4I_{11/2}$ transition. The laser was pumped with a broad-area GaAlAs laser diode (Sony SLD-303-V). An anamorphic lens system was used to collimate and focus the diode-laser output in the laser crystal. The focused pump beam was nearly circular and had a waist (1/e^2) of approximately 40μm in the laser crystal. Temperature tuning of the laser diode was used to maximize the absorption (~ 40 %) of the pump light. Taking into account the transmission of the input coating, 37% of the pump light incident on the input mirror was absorbed in the 1-mm long Nd: YAG crystal. For efficient frequency doubling the 3.7-mm long KNbO$_3$ crystal was placed in close proximity to the Nd:YAG laser crystal near the cavity waist.

Figure 2 shows the 946-nm output power as a function of the diode-laser pump power. Without the $KNbO_3$ crystal in the cavity the lasing threshold was reached with 57.8 mW of incident pump power; the slope efficiency near threshold was 2.2%, and increased to 3.6% well above threshold. The increase in slope efficiency with pump power is generally present in any optically-pumped solid-state laser, but is more pronounced when the cavity loss is dominated by reabsorption losses which saturate at high laser powers[6] When the 3.7-mm long $KNbO_3$ crystal was inserted into the the cavity, the threshold increased to 85.6 mW and the slope efficiency decreased to 0.62% due to the additional loss introduced by the nonlinear crystal.

The loss of the $KNbO_3$ crystal can be estimated by comparing the threshold and slope efficiency of the 946-nm laser with and without the $KNbO_3$ crystal in the cavity. The round-trip loss of the cavity alone was determined to be 0.25%; the additional loss of the $KNbO_3$ crystal was 0.55%.[7]
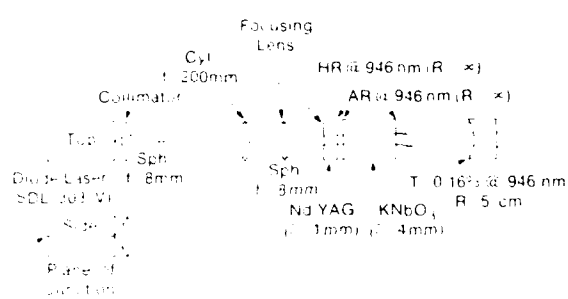
FIGURE 1: Experimental configuration for the diode-laser-pumped 946-nm Nd:YAG laser with intracavity frequency doubling.
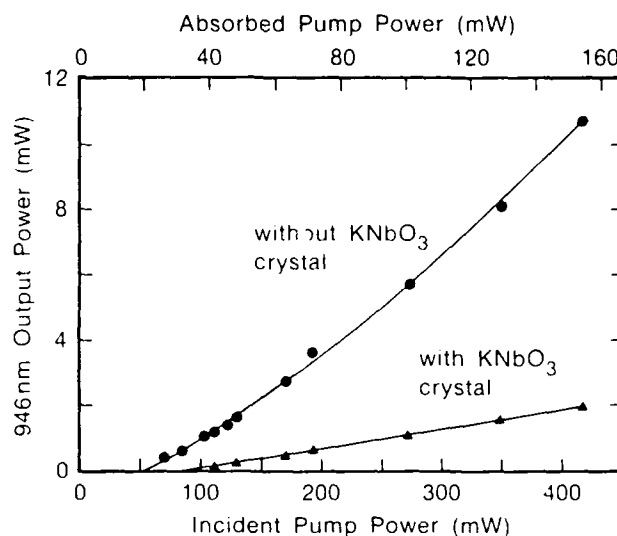
FIGURE 2: Output power at 946 nm versus diode-laser pump power with and without the $KNbO_3$ crystal present in the cavity.
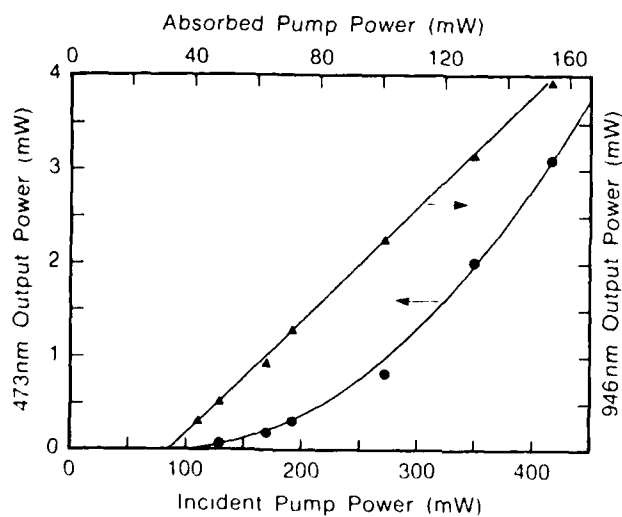
FIGURE 3: Blue 473-nm output power and corresponding 946-nm output power versus diode-laser pump power.

functions of the 809-nm source by using two 809-nm sources: one that is used only to pump the Nd:YAG laser and a second 809-nm source that has the correct polarization to participate in the sum-frequency mixing process (Figure 6). Figure 7 shows the 459-nm output power produced using an infrared dye laser, a narrow-stripe laser diode (Spectra Diode Labs SDL-1410-C), and a broad-area high-power laser diode (Sony SLD-302-V) as the second 809-nm source for intracavity frequency mixing as illustrated in Figure 6. The 809-nm input power was limited to ≤ 12 mW, the maximum power available from the narrow-stripe GaAlAs diode laser. The Nd:YAG laser was pumped with a 200-mW coherent laser array (SDL 2420) and the 1064-nm power circulating inside the resonator was ~ 6 W (unpolarized). The relatively low power of the second 809-nm source (≤ 12 mW) made no significant contribution to the pumping of the Nd:YAG laser. Consequently, the blue output power increased linearly with the 809-nm power of the mixing laser (see Figure 7). It is obvious from Figure 7 that the frequency mixing efficiency obtained with the narrow stripe diode laser is almost as large ($\sim 80\%$) as that obtained with the TEM_{00} infrared dye laser. The output of this diode laser, which operated in a single longitudinal mode, was collimated with a 0.6 N.A. lens and circularized with a 3X anamorphic prism pair. The broad-area laser diode was collimated with a 0.6 N.A. lens and circularized by a telescope composed of two cylindrical lenses. The blue power generated with this source is only $\sim 27\%$ of that obtained with the dye laser.

The decreased efficiency evident when diode lasers are used for mixing must be attributable to either the broader spectral bandwidth of the diode lasers or to the poor spatial mode characteristics of the diode lasers. The spectral bandwidth of the mixing process has been measured to be 3.3 nm (FWHM)[10], so that there should be little loss in efficiency due to spectral considerations, even in the case of high-power laser diodes whose multimode outputs typically have spectral widths of 2-3nm. In order to analyze the correlation between the spatial-mode quality of the mixing laser and the blue output power, the spot sizes of the focused 809-nm beams were measured using a television camera. The focused dye laser spot had a circular Gaussian intensity distribution with a $1/e^2$ waist of $\sim 11 \mu m$. The focused spot of the narrow-stripe diode laser was found to have an elliptical Gaussian distribution with waists of $\sim 28 \mu m$ and $\sim 21 \mu m$ along the major and minor axes of the ellipse. The intensity distribution of the focused broad-area GaAlAs diode laser is somewhat irregular but can be approximated by an elliptical Gaussian profile with minor- and major-axes waists of $\sim 47 \mu m$ and $\sim 120 \mu m$, respectively. The beam waist of the TEM_{00} 1064-nm intracavity radiation was calculated based on the cavity geometry to be $\sim 35 \mu m$. With these values for the beam waist, the relative frequency-mixing efficiencies for the narrow-stripe and the broad-area diode lasers are calculated to be 83% and 22%, respectively. The good agreement of these results with the experimental observations suggests that the different conversion efficiencies obtained for the three 809-nm lasers can be fully explained by the differences in the focused spot sizes. When the power of the broad-area diode laser was increased to 120mW, $50 \mu W$ of blue output was generated. In this case, the power of the 809-nm mixing laser was comparable to the pump power provided by the GaAlAs laser array and, consequently, lead to a substantial increase of the 1064-nm power compared to pumping with the diode-laser array alone. When the power of the mixing laser contributes significantly to pumping of the Nd:YAG laser the 459-nm output varies nonlinearly with the 809-nm mixing power and, in the high-power limit, will have a quadratic dependence on input power.

A number of straightforward improvements could be used to increase the blue output power over the present results. Polarizing the 1064-nm laser field would yield a factor of 2 increase in the blue output power. Increasing the power of the diode laser pumping the Nd: YAG laser from 200 mW to 1 W would yield a factor of 5 improvement. Recently, 150 mW output power from a narrow-stripe single-frequency GaAlAs diode laser was reported[14], and the use of such a device for frequency mixing would permit an increase in the blue output power by more than an order of magnitude compared to the present case. Scaling of the experimental results of Figure 7 to include these improvements predicts a 459-nm output power in the milliwatt range. An equivalent increase in output power might also be achieved using a high-power broad-area diode laser with better focusing optics.
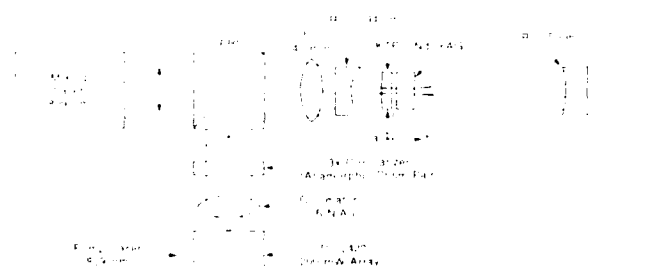
FIGURE 6: Experimental configuration used to separate the pumping and mixing functions of the 809-nm source.

Figure 3 shows the blue output power at 473 nm and the corresponding output power at 946 nm as a function of diode-laser pump power. The $KNbO_3$ crystal was placed approximately 0.5mm away from the Nd: YAG crystal. Since the output mirror had a transmission of only 50% at 473 nm, the blue power incident on the output mirror was approximately twice as large. Blue radiation is generated by the two counterpropagating components of the circulating 946-nm laser field. Approximately 28% of the blue power generated by the fundamental field passing through the $KNbO_3$ crystal in the direction of the input mirror is reflected back towards the output mirror. At 420 mW of diode-laser pump power, 3.1 mW of 473 nm radiation was emitted through the output mirror, indicating that 6.2 mW were impinging onto the mirror. Approximately 4.4 mW of 473-nm radiation were generated by the one-way passage of the 946-nm radiation through the crystal; an additional 1.8 mW of blue power were due to reflections from the input mirror. The 946-nm laser oscillated in a TEM_{00} mode with and without the $KNbO_3$ crystal present in the resonator. The blue output mode had a uniform intensity distribution which appeared to be essentially gaussian.

Sum-Frequency Generation of 459-nm Radiation in $KTiOPO_4$

The nonlinear material $KTiOPO_4$ (KTP) permits Type-II-phasematched frequency doubling of 1064nm radiation, and is frequently used in SHG experiments with Nd:YAG lasers.[2,8,9] Recent reexaminations of nonlinear processes in KTP have shown that sum-frequency mixing of 1064-nm and 809-nm radiation is non-critically phasematched at room temperature.[10] Additional studies of sum-frequency mixing in KTP including calculations based on Sellmeier's equations have recently also been reported in Ref. 11 and 12. In the non-critical phasematching configuration the beams propagate down the crystallographic b-axis with the 1064-nm light polarized parallel to the a-axis and the 809-nm light parallel to the c-axis. The generated sum-frequency radiation at 459nm is polarized along the a-axis. As shown in Figure 4, the wavelength that results in optimally phasematched frequency mixing with 1064-nm light coincides with the well-known 809-nm absorption peak of the $^4I_{9/2} \rightarrow {}^4F_{5/2}$ pump transition of Nd:YAG.[10] This coincidence can be utilized for the construction of a compact blue laser device based on frequency mixing of a Nd:YAG laser and its 809-nm pump source. The 3.3-nm (FWHM) phasematching bandwidth permits efficient sum-frequency mixing even with GaAlAs diode lasers that operate in several longitudinal modes. Detailed studies of this frequency-mixing process showed that phasematching occurs over an unusually wide temperature range of -50°C to 300°C.[10] The acceptance angles for rotation of the incident beams about the crystallographic c and a axes are 18° and 8° (FWHM), respectively. The wide temperature and angle tolerances of this nonlinear optical process are very advantageous for practical device applications.
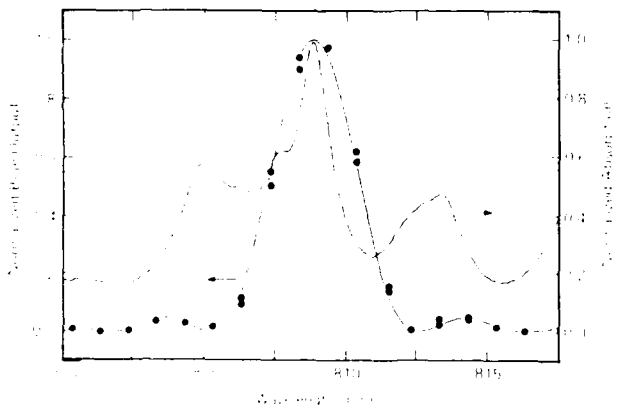
FIGURE 4: Blue output power (solid line) produced by mixing radiation in the 800-820 nm wavelength range with 1064nm radiation in KTP; absorption (dashed line) of Nd:YAG in same wavelength range.
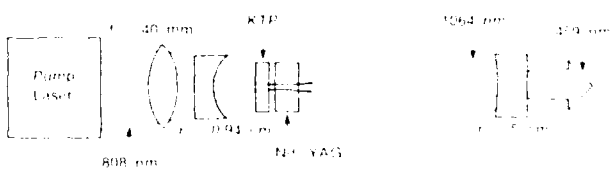
FIGURE 5: Experimental set-up for intracavity mixing of 1064 nm Nd:YAG laser radiation with 809nm pump radiation.

Figure 5 shows the experimental configuration used for efficient generation of 459-nm light. A KTP crystal is placed inside the cavity to mix the high-intensity 1064-nm intracavity laser field with the 809-nm pump field. In initial experiments using an infrared dye laser as the pump source in Figure 5, ~ 1 mW of blue output power at 459-nm was produced using 275 mW of 809-nm pump power. [13] Higher peak powers were obtained by gain-switching the Nd:YAG laser, and rapid modulation of the 459-nm light due to modulation of the 809-nm pump beam was demonstrated[13]. However, for a practical device, pumping with diode lasers is desirable. The 809-nm light performs two functions: pumping the Nd:YAG laser and mixing with the 1064-nm radiation. In order to investigate the use of diode lasers as sources of the 809-nm mixing radiation, it is desirable to separate the pumping and mixing

It is a particular advantage of intracavity sum-frequency generation that the blue output can be rapidly modulated by direct modulation of the 809-nm input without the speed limitations that exist for intracavity SHG due to the slow response times of the 1064-nm intracavity laser field. Even in the case of a single 809-nm pump laser, the 459-nm output follows fast modulation of the pump source while the time response of the 1064-nm radiation is limited by the cavity dynamics of the Nd:YAG laser.[3] Figure 8 shows a blue output pulse generated by direct modulation of the injection current of the 809-nm mixing laser using the two-laser pump configuration shown in Figure 6. The width (~ 5 ns) of the pulse shown in Figure 7 was limited only by the drive electronics and much faster modulation can be achieved.
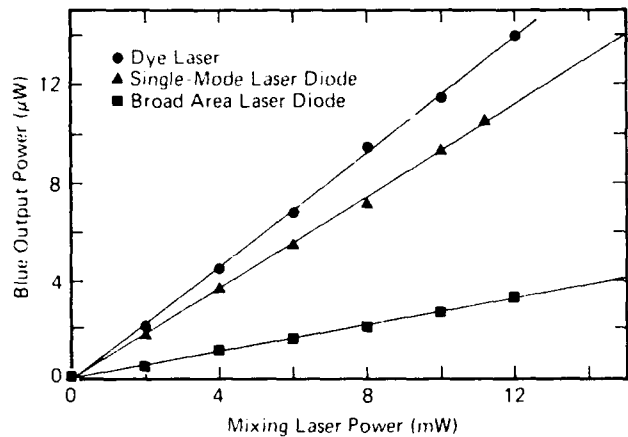
FIGURE 7: Blue output power at 459 nm as a function of 809nm mixing power provided by a dye laser, a single-mode laser diode and a broad area laser diode.

Blue Output Pulses @ 459 nm

Mixing Laser Pulses @ 809 nm
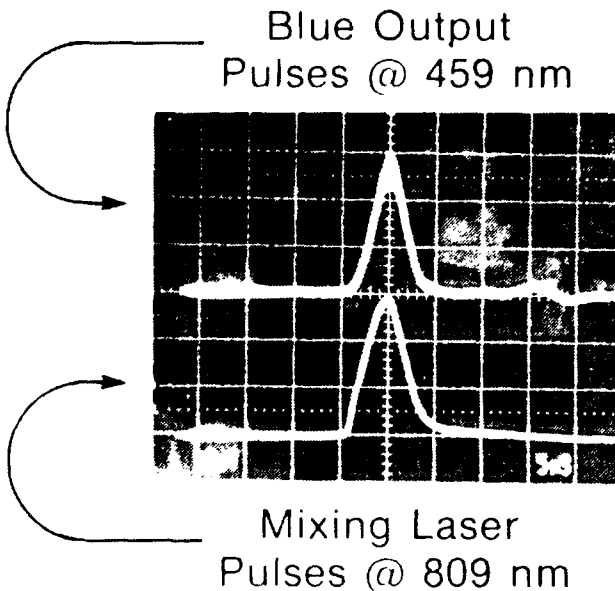
FIGURE 8: Generation of a short blue pulse by direct modulation of the laser diode (5 ns/div).

Conclusion

Nonlinear optical processes such as second-harmonic generation and sum-frequency mixing can be used for frequency upconversion of the infrared radiation produced by diode-pumped solid-state lasers. The use of diode-laser-pumped solid-state lasers permits the nonlinear process to be carried out inside the laser cavity where the intracavity intensity is high, leading to efficient upconversion. Furthermore, the poor spectral and spatial mode properties of the high-power diode laser are converted to the narrow spectrum and TEM_{00} mode of the solid-state laser. Miniature blue sources based on these techniques have been demonstrated with output powers of a few milliwatts, and scaling predicts the feasibility of powers of tens of milliwatts. Other features desirable for certain applications, such as rapid modulation, have been demonstrated.

References

1. J.-C. Baumert, P. Günter, and H. Melchior, Opt. Comm. 48, 215 (1983).
2. T. Baer, J. Opt. Soc. Am. B 3, 1175 (1986).
3. W. P. Risk and W. Lenth, Opt. Lett. 12, 993 (1987).
4. G.J. Dixon, Z.M. Zhang, R.S.F. Chang, and N. Djeu, Opt. Lett. 12, 137 (1987)
5. T.Y. Fan and R.L. Byer, Opt. Lett. 12, 809 (1987).
6. W.P. Risk, J. Opt. Soc. Am. B 5, 1412 (1988).
7. W.P. Risk, R. Pon, and W. Lenth, submitted to Applied Physics Letters.

8. F.C. Zumsteg, J.D. Bierlein, and T.E. Gier, J. Appl. Phys. 43, 4980 (1976). Vol. 898, (1988, in press).
9. Y.S. Liu, D. Dentz, and R. Belt, Opt. Lett. 9, 76 (1984).
10. J.-C. Baumert, F.M. Schellenberg, W. Lenth, W.P. Risk, and G.C. Bjorklund, Appl. Phys. Lett. 51, 2192 (1987).
11. K.Kato, IEEE J. Quantum Electron. QE-24, 3 (1988).
12. D.W. Anthon, G.J. Dixon, M.G. Reffl, and T.J. Pier, Proc. SPIE 898 (1988).
13. W.P. Risk, J.-C. Baumert, G.C. Bjorklund, F.M. Schellenberg, and W. Lenth, Appl. Phys. Lett. 52, 85 (1988).
14. D.F. Welch, W. Streifer, and D.R. Scifres, presented at Conference on Lasers and Electro-Optics, Los Angeles (1988), paper WB4.

NARROW-BAND, SOLID STATE, Ti:SAPPHIRE SOURCE OF 455 nm

D.D. Lowenthal, C.H. Muller, III,
J.J. Ewing, K. Kangas

Spectra Technology, Inc.
2755 Northup Way
Bellevue, Washington 98004-1495

Abstract

We have produced ~2.5 mW of narrow-band 455 nm radiation using a single longitudinal mode pulsed Ti:Sapphire oscillator operating at 911 nm followed by efficient frequency doubling. A Cs filter was used to demonstrate the narrow-band operation and frequency tuning capabilities.

Introduction

In this paper we report the first demonstration of narrow-band (~500 MHz) blue (455 nm) radiation using recently developed[1] single longitudinal mode (SLM) pulsed Ti:Sapphire laser technology. This narrow-band blue laser source generated 0.25 mJ/pulse at a 10 Hz repetition rate. Much higher energies will be possible by using this source to injection seed a power oscillator or as the master oscillator in a power amplifier chain.

Figure 1 illustrates two possible techniques for generating narrow-band blue radiation with Ti:Sapphire. In the first, a Ti:Sapphire (SLM), oscillator drives a power oscillator or amplifier at 911 nm. This beam is then frequency doubled to 455 nm. In the second case,
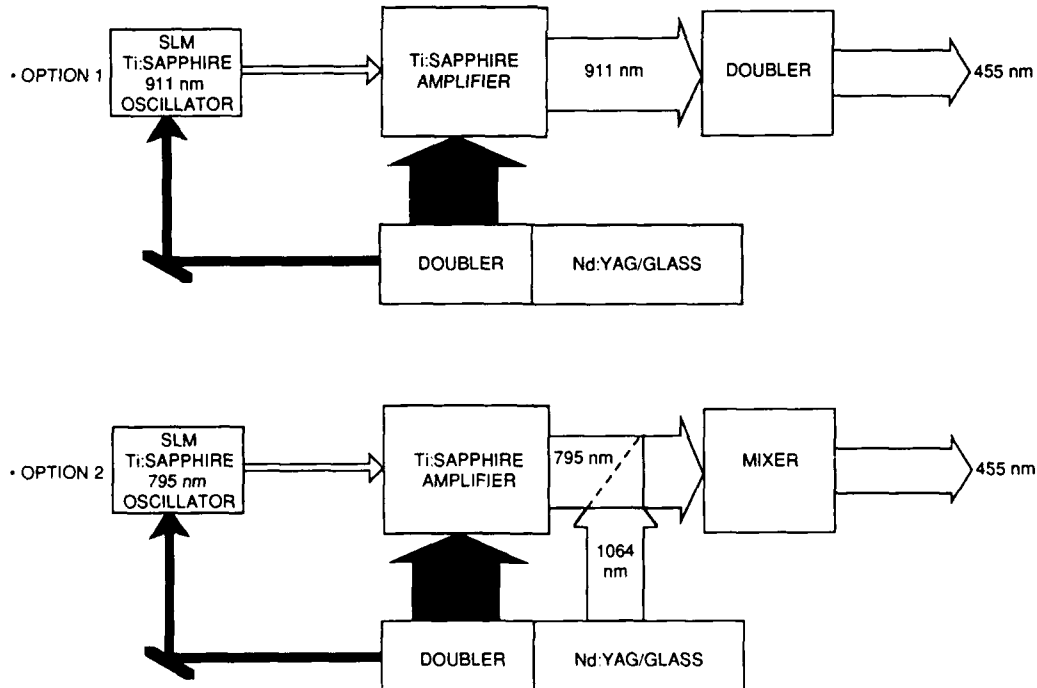
Figure 1. Two possible techniques for generating narrow-band blue radiation with Ti:Sapphire.

a SLM Ti:Sapphire oscillator drives a power oscillator or amplifier at 795 nm which is then frequency mixed with 1064 nm light to 455 nm. In this figure the pump laser is shown as a doubled Nd:YAG system; however, the Ti:Sapphire can be pumped directly using flashlamps and a fluorescent converter[2] which would result in a very compact, simple, laser device.

Consider the frequency doubling case (Option 1). The ratio E_{out} (455)/E_{pump} (1064) can be written as

$$\frac{E_{out}(455)}{E_{pump}(1064)} = \eta_{2\omega}(911) \; \eta_{TiS} \; \eta_{2\omega}(1064) \tag{1}$$

where $\eta_{2\omega}$ (911) is the frequency doubling efficiency for 911 nm → 455 nm, $\eta_{2\omega}$ (1064) is the frequency doubling efficiency for 1064 nm → 532 nm; and η_{TiS} is the intrinsic efficiency of Ti:Sapphire. For the frequency mixing case (Option 2) the expression is slightly more complicated because the unconverted 1064 nm light is available for mixing with 795 nm. Assuming the laser energy at 795 nm and 1064 nm is chosen to match the number of photons

$$\frac{E (795)}{E (1064)} = 1.34 \equiv \gamma \tag{2}$$

the efficiency ratio E_{out} (455)/E_{pump} (1064) becomes:

$$\frac{E_{out}(455)}{E_{pump}(1064)} = \eta_{2\omega}(1064) \; \eta_{TiS} \; \eta_{mix} \left(\frac{1+\gamma}{\gamma}\right) , \tag{3}$$

if

$$\eta_{2\omega} \leq \frac{\gamma}{\gamma + \eta_{TiS}} , \tag{4}$$

otherwise

$$\frac{E_{out}(455)}{E_{pump}(1064)} = \eta_{TiS} \; \eta_{mix} \left(\frac{1+\gamma}{\gamma + \eta_{TiS}}\right) \tag{5}$$

The two regimes of this second case result because as $\eta_{2\omega}$ (1064) increases one reaches a point where there is not enough 1064 nm radiation left over to mix equal photon numbers with the 795 nm beam.

Figure 2 presents these efficiency calculations in graphical form. Here, the ratio of output energy at 455 nm to the 1064 nm pump energy versus the frequency doubling efficiency is plotted. Several assumptions were made in order to develop these plots. First, the Ti:Sapphire intrinsic efficiency was chosen in the range 0.3 to 0.5. This accounts for the spread in the plots for each case. The left hand plot is constructed for a case where the frequency mixing efficiency is equal to the frequency doubling efficiency, i.e., $\eta_{2\omega}$ (1064) = $\eta_{2\omega}$ (911) = η_{mix}. He.e, the frequency mixing approach is almost always more efficient than the frequency doubling case. The knee in the plot occurs when Eq. (4) becomes an equality,

$$\eta_{2\omega} = \frac{\gamma}{\gamma + \eta_{TiS}} \tag{6}$$

In the second plot, the frequency mixing efficiency is held at 0.5 while the frequency doubling efficiency is varied; here, the frequency doubling case (Option 1) becomes more efficient when $\eta_{2\omega}$ is sufficiently high. In most practical cases $\eta_{2\omega} \leq 60\%$ and this implies
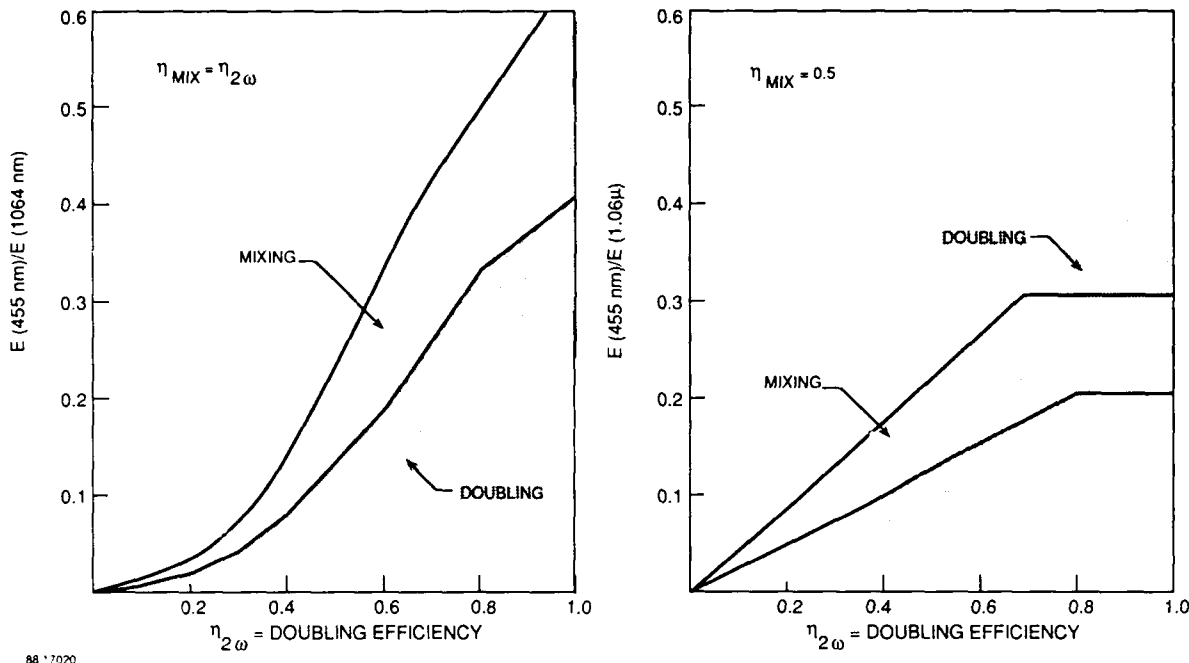
Figure 2. The frequency mixing approach (Option 2) can be more efficient than the frequency doubling approach (Option 1) but has higher complexity.

that the mixing approach will always be more efficient. However, this approach is also more complex because both the 1065 nm and 795 nm beams must be narrow-band, have good beam quality, and be properly aligned. As a result, for our first experiments we have chosen to study the frequency doubling approach (Option 1) using Ti:Sapphire.

EXPERIMENTAL MEASUREMENTS

Figure 3 is a schematic of the experimental arrangement. The SLM, pulsed, Ti:Sapphire grazing incidence oscillator provides the narrow-band tunable source. The Ti:Sapphire is a Brewster end cut piece about 1 cm in length and 6 mm in diameter. Its absorption length, at 532 nm, is ~ 2.5 cm^{-1}. The 532 nm pump beam was supplied by a Spectra Physics DCR-11 Nd:YAG laser delivering ~ 70 mJ/pulse in 5-10 ns at 10 Hz. The pump beam diameter in the Ti:Sapphire is about 0.1 cm giving a pump fluence of ~ 5-10 J/cm^2. Under these conditions, and with an 1800 line/mm grating, the oscillator provided ~ 1.0 mJ/pulse in 2-3 ns at 911 nm. The bandwidth was less than 1 GHz as determined with an etalon (10 GHz free spectral range). A photograph of this oscillator is presented in Figure 4.

The 2D intensity profile from this oscillator was measured using a frame grabber and TV camera. The result is shown in Figure 5, and indicates a smooth, Gaussian-like, profile. Further evidence for an output beam with a high quality phase front comes from the frequency doubling measurements that resulted in 25-30% frequency doubling efficiency in a KD*P crystal. Higher frequency doubling efficiencies could have been obtained with a higher energy per pulse beam; this is because less severe focusing would be used to achieve the required peak power densities.
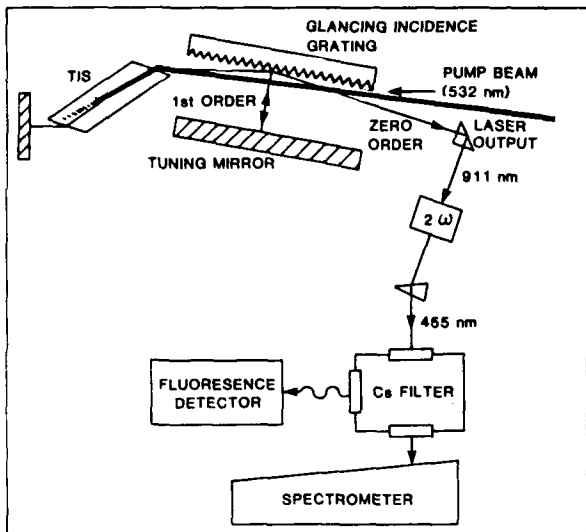
Figure 3. Schematic of experimental arrangement used to generate and monitor the narrow-band blue source.

Figure 4. Single-longitudinal-mode (SLM) pulsed Ti:Sapphire oscillator operating at 911 nm. The Brewster end cut Ti:Sapphire gain medium is seen near the photograph center, the grating is immediately to the left, and the tuning mirror directly behind the Ti:Sapphire rod.
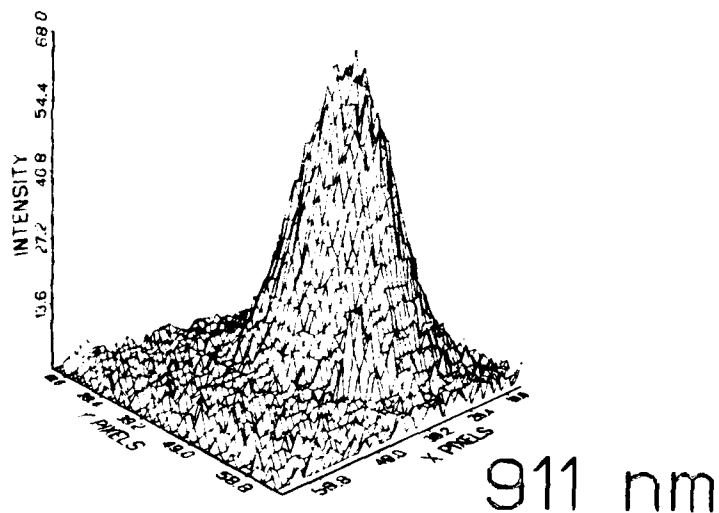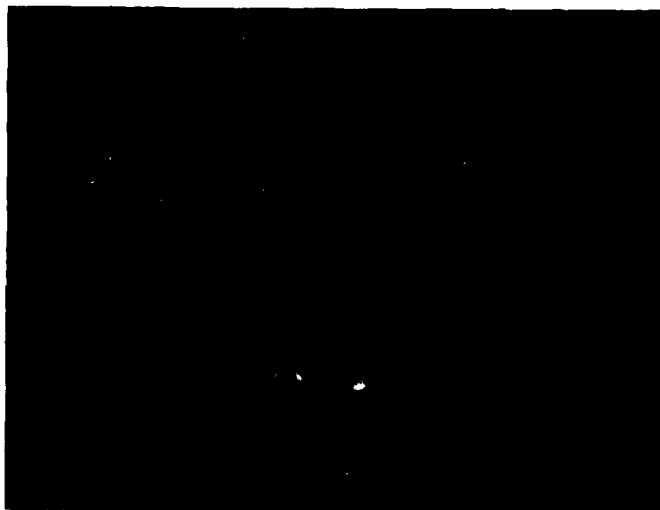
Figure 5. Near field 2D intensity profile of 911 nm beam from the single-longitudinal-mode Ti:Sapphire oscillator.

After doubling to 455 nm the blue beam was directed through a Cs cell which was heated to ~100°C to provide sufficient Cs atom density. When the oscillator is tuned to the Cs resonance a blue fluorescence track is observed through the cell as shown in Figure 6. An attempt was made to tune through the double absorption peaks (455.6608 nm and 455.6546 nm) of Cs by scanning the frequency of the oscillator and recording the NIR fluorescence signal. In our current oscillator configuration the output does not remain in a SLM condition while the output is tuned (the output mode-hops) so that a smooth scan through the Cs double absorption bands was not possible. Littman[3] has shown that this type of oscillator will tune over 10-100 cm^{-1}, without mode hops, if the tuning mirror rotation point is chosen correctly. In ongoing work, the oscillator will be reconfigured in the Littman geometry and smooth spectral scans will be possible.

Figure 6. Blue fluorescence track observed in Cs cell with Ti:Sapphire blue source tuned to 455 nm. Bright spots at end of track are caused by scattering from the Cs cell walls.

SUMMARY

In summary, we have generated narrow-band (<1 GHZ) blue (455 nm) laser radiation by doubling the output of a SLM, Ti:Sapphire, oscillator. This source of coherent blue laser radiation will become increasingly important and attractive as flashlamp pumped Ti:Sapphire and diode pumped Ti:Sapphire (through doubled Nd:YAG) technologies mature. This work was supported by Spectra Technology, Inc. IR&D funds.

References

1. K. Kangas, D. Lowenthal, C. Muller, Opt. Lett. 14, 21 (1989).

2. P. Lacovara, L. Esterowitz and R. Allen, Opt. Lett. 10, 273 (1985).

3. M. Littman, Appl. Opt. 23, 4465 (1984).

Single-Longitudinal-Mode, Tunable, Pulsed, Ti:Sapphire Laser Oscillator

K.W. Kangas, D.D. Lowenthal, C.H. Muller, III

Spectra Technology, Inc.
2755 Northup Way
Bellevue, Washington 98004-1495

Abstract

A 2.0 mJ per pulse, single-longitudinal-mode (SLM), Ti:Sapphire oscillator has been demonstrated using a grazing incidence grating cavity similar to a Littman/Shoshan arrangement. Experimental results, and modeling of the SLM behavior are presented.

Introduction

A single-longitudinal-mode (SLM), tunable, pulsed, Ti:Sapphire oscillator delivering up to 2.0 mJ has been demonstrated.[1] The oscillator cavity configuration is similar to that of Littman and Shoshan[2] with the dye cell replaced with a Brewster end cut solid state Ti:Sapphire rod measuring 6mm x 1.5 cm. Narrow band cw Ti:Sapphire oscillators have been demonstrated,[3] but to our knowledge, this is the first demonstration of pulsed, SLM, Ti:Sapphire operation. The oscillator's significance is its very compact geometry (cavity length $\simeq$6 cm), wide tunability, and simplicity (only four optical components including the active medium); plus, the oscillator provides two to three orders of magnitude more energy per pulse than a conventional Littman oscillator with a dye medium. This higher energy is due to the much higher saturation fluence level in Ti:Sapphire as compared to dyes.

Mode control is established with a 5 cm grating used at grazing incidence; the zero order reflection is used as the output while the 1st order reflection is fed back to provide oscillator action. The basic configuration is presented in Figure 1. In the work reported here, an 1800 line/mm grating was used and is oriented with a grazing angle α of a few degrees. The Ti:Sapphire was purchased from Union Carbide and has a pump absorption at 532 nm of 2.4 cm^{-1} and a figure of merit of 100. This corresponds to an absorption loss of ~0.024 cm^{-1}. Both the back cavity mirror and tuning mirrors are dielectric coated optics for maximum reflection in the NIR around 800 nm.

Tuning the oscillator over the Ti:Sapphire bandwidth is achieved by simply tilting the tuning mirror. Tuning has been obtained from 746-918 nm with currently available optics. The angular tilt needed to tune over a given bandwidth is obtained from the grating equation

$$\cos\alpha + \sin\theta_m = m\lambda/d \tag{1}$$

where α is the grazing angle, θ_m is the mth order reflection from the grating normal, λ the wavelength, d the grating period, and m the grating order. Tuning over the Ti:Sapphire bandwidth from 700-900 nm requires a total mirror rotation of 15 degrees. In these experiments the oscillator geometry has been configured to give synchronous tuning without mode-hop.[4] By choosing the correct pivot point for the tuning mirror, exact tracking of the cavity length and wavelength should be possible; continuous SLM operation over a limited bandwidth ($\leq$100 cm^{-1})has been achieved.

FLEXURE MOUNTS

TUNING MIRROR

Ti:SAPPHIRE

GRATING TILT CONTROL

GLANCING INCIDENCE GRATING

BACK MIRROR

HIGH RESOLUTION ROTATIONAL STAGE
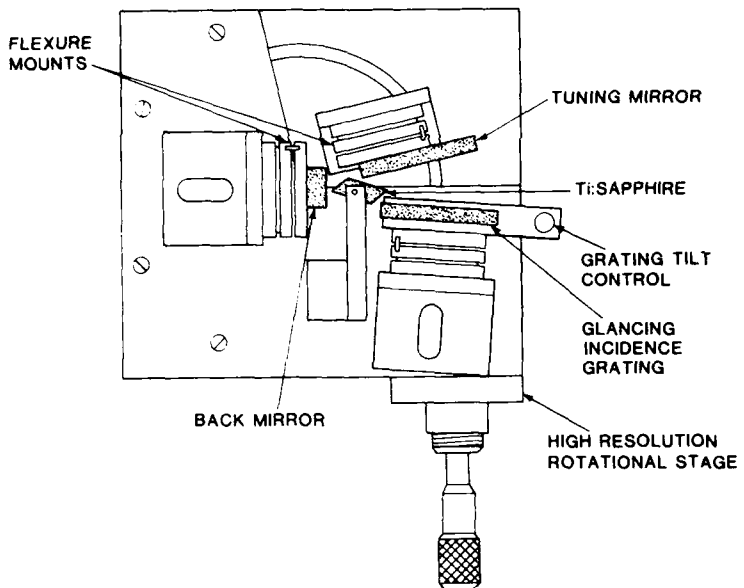
Figure 1. Single-longitudinal-mode (SLM), pulsed, Ti:Sapphire oscillator configuration.

Experimental Results

A Q-switched Spectra Physics DCR-11 is frequency doubled and used directly to pump the Ti:Sapphire, the pump pulse is ~5 ns in length. A 0.4 cm diameter 532 nm beam was focused using a 30 cm focal length lens; the pump beam focus occurs   the grating and then is allowed to expand slowly as it is absorbed in the Ti:Sapphire. This geometry was chosen to minimize the possibility of damage in the Ti:Sapphire crystal. For both types of pumping geometries the pump beam diameter in the Ti:Sapphire was ~1.0 mm giving a peak pump fluence of up to ~10 J/cm^2 with 70 mJ of pump energy.

When lasing occurs the oscillator provides a near Gaussian spatial profile and this was verified with a CID camera and frame grabber. Single longitudinal mode operation was verified by frequency doubling the Ti:Sapphire oscillator output and monitoring the presence of mode beating by recording the temporal output shape using a Tektronic 7401 oscilloscope and a Hamamatsu R1193U-02 SbCs biplanar photodiode. As a further diagnostic, the ring patterns from a 10 GHz Etalon with a finesse of 25 were analyzed and recorded with a commercial television camera/VCR combination.

Figure 2 presents the SLM output energy characteristics as a function of wavelength. In Figure 2a the multimode output energy is plotted versus wavelength for a 532 nm pump energy of 69 mJ. The pump beam diameter was ~1 mm resulting in a pump fluence of ~8 J/cm^2 (limited below this value by damage). Also, the threshold pump energy is shown versus wavelength. Note, under these pumping conditions the peak output energy per pulse is ~9 mJ at 800 nm and ~3 mJ at 900 nm. Larger output energies are possible with higher pump energies and larger pump beam diameters; however, the number of longitudinal modes will also increase. In Figure 2b the SLM output energy is plotted versus wavelength. Also included is a plot of the upper limit on pump energy that must not be exceeded if SLM operation is to be maintained. When SLM conditions are achieved both the output energy and ratio of gain to threshold gain remain constant over the tunable bandwidth. This property is easily understood in terms of the SLM startup properties of the grazing incidence oscillator and will be described in the following section.

SLM Ti:Sapphire Oscillator Modelling

For this laser oscillator configuration (regardless of the gain media) single longitudinal mode operation is limited to a narrow range of conditions. These conditions can be predicted using geometrical ray tracing and Gaussian beam propagation concepts. A summary of that approach is presented here. Assume that the oscillator is tuned to a wavelength λ so that oscillation occurs along the ray path shown in Figure 3. For any other wavelength,
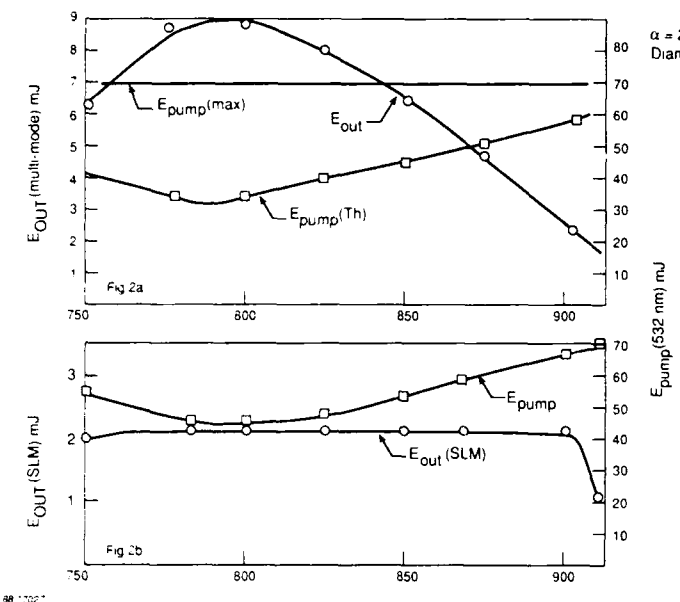
Figure 2. SLM, Ti:Sapphire, grazing
incidence tuning
characteristics. (a)
Multimode operation and
threshold conditions for
lasing. (b) Single-
longitudinal-mode
operation and upper limit
on pump fluence.

Figure 3. Illustration showing
components of the single-
longitudinal-mode,
tunable, pulsed,
Ti:Sapphire laser
oscillator. The cavity
length is $L_1 + L_2$ where L_1
is the distance from the
grating to the tuning
mirror and L_2 is the
distance from the grating
to the back mirror.
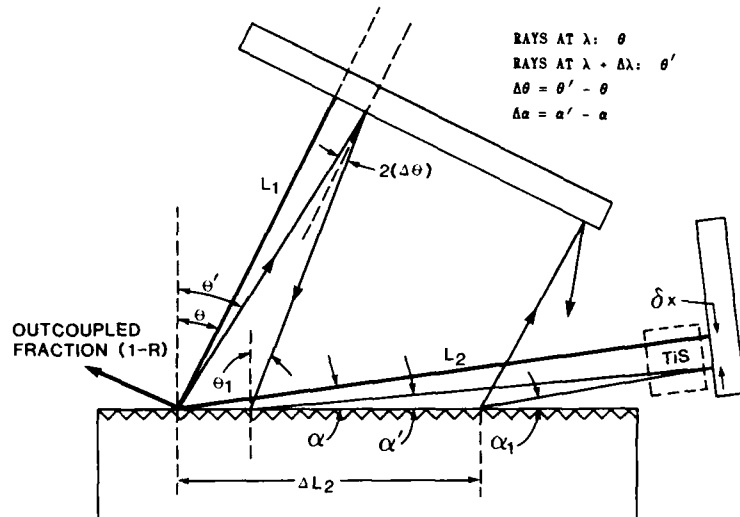
$\lambda' = \lambda + \Delta\lambda$, oscillation follows a different path by virtue of the grating dispersion; this different path leads to walk-off across the gain region (by an amount δx) on each round trip in the cavity. Consequently, rays at λ' will move across the gain region and experience lower total gain after N round trips as opposed to rays at λ. The cavity output intensity after N round trips is defined as I at λ, and as I' at λ'; both I and I' are initiated from spontaneous emission, defined as I_{start}, and are amplified with each round trip. The ratio (I'/I) is a measure of the mode fidelity when $\Delta\lambda$ is taken as the longitudinal mode spacing, $\lambda^2/2(L_1+L_2)$.

Values of (I'/I) were predicted by assuming a spatial gain distribution of width 2x and computing I' and I after each round trip in the cavity. When the intensity, I, reaches output flux levels (50 MW/cm^2) for the gain switched oscillator) the ratio (I'/I) is evaluated. Values of (I'/I) $\leq$ 0.05 are taken as sufficient to assure essentially single longitudinal mode operation. For a parabolic gain distribution, taken for convenience, the output intensity ratio after N round trips is approximately:

446

$$\log \left[\frac{I'}{I_{start}}\right] \simeq \left[N(1-\gamma) + \frac{\gamma}{3} N^2(N-1) \left(\frac{\delta x}{x}\right)^2\right] \log(R), \tag{2}$$

where I' becomes I when $\delta x=0$. Here, N is the number of cavity round trips, γ the ratio of gain to threshold gain, and R the output coupling reflectivity. It turns out that δx is different for each round trip and that the beam walks off both the gain region and the grating. However, for 5-10 round trips an average value of δx can be related to the cavity length, grazing angle of incidence, wavelength and grating period for cases where the tuning mirror and grating are approximately parallel.

$$\delta x(mm) = \frac{0.23 \lambda^2(\mu)}{\alpha(deg)d(\mu)} \left[\frac{L_2/L_1}{1 + L_2/L_1}\right] \tag{3}$$

Here α is the grazing angle in degrees, d is the grating period in microns and $L_1 + L_2$ the cavity length (see Figure 3). Clearly, δx must be as large as possible to reduce the ratio I'/I and to guarantee SLM operation. This requires that α and d are small, and the ratio of lengths (L_2/L_1) must be >1. In our current design $L_2/L_1 = 6$ with $L_1 = 1$ cm. Note that L_2 cannot be arbitrarily large due to diffraction effects.

Typical values ($\alpha=1.5°$, $\lambda = 0.8\mu$) lead to $\delta x = 0.1-0.15$ mm for gratings with 1200-1800 lines per mm, respectively. Figure 4 summarizes these results by plotting (I'/I) versus ($\delta x/x$). Each curve is for a different gain, γ, and number of cavity round trips to reach output intensities. The results are striking, and show a very limited range of gain and ($\delta x/x$) over which single longitudinal mode operation is possible. Increasing the gain requires large values of ($\delta x/x$) to maintain the same mode fidelity and lowering the gain below twice threshold leads to unstable operation.

Figure 4. Plot of calculated mode fidelity (I'/I) versus ($\delta x/x$) for various values of gain ($\delta x/x$) is the fractional gain region walk-off per cavity round trip - the gain region has a diameter of 2x.
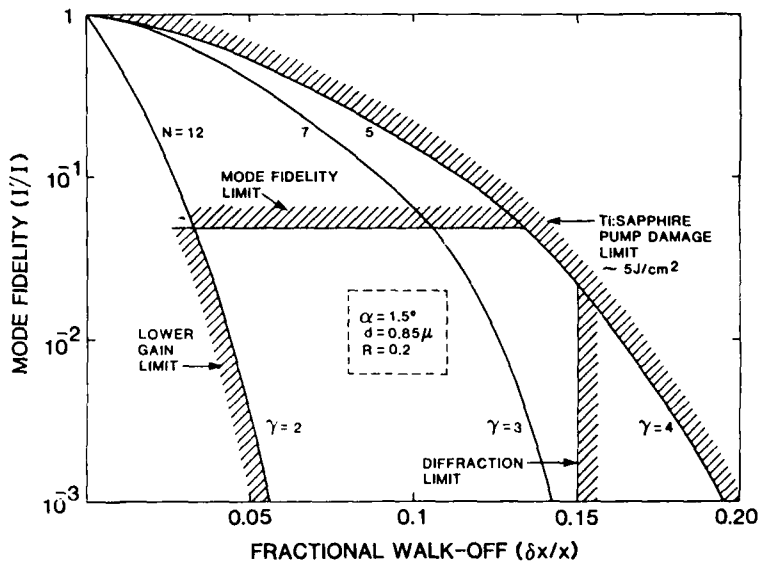
Further, diffraction limits the maximum value of L_2 and ($\delta x/x$). For example, we must require that the diffraction induced angular ray errors after N cavity round trips, β_N, be less than the angular shifts, $\Delta\alpha$, induced by the grating for adjacent longitudinal modes. The diffraction induced angular errors can be estimated using the Gaussian beam propagation equations. For a beam within its Rayleigh range one obtains:

$$\beta_N \simeq 2 (L_1 + L_2) \lambda^2 N/\pi^2 x^3. \tag{4}$$

From the cavity geometrical ray tracing one can show

$$\Delta\alpha \simeq \Delta\lambda/\alpha d = \lambda^2/2\alpha d(L_1 + L_2). \qquad (5)$$

setting $\beta_N \leq \Delta\alpha$ gives the upper limit on L_2 as

$$(L_1 + L_2) \leq \frac{\pi}{2} \frac{x^{3/2}}{(d\alpha N)^{1/2}} \qquad (6)$$

This result can be combined with Eq (3) to set an upper bound on $(\delta x/x)$.

$$\left(\frac{\delta x}{x}\right) \leq \frac{2.6 \ \lambda^2(\mu)}{N^{1/3}} \left\{ \frac{1}{[\alpha(\deg)d(\mu)]^4} \cdot \frac{L^3_2}{[L_1 + L_2]^5} \right\}^{1/3}. \qquad (7)$$

For our oscillator conditions $(\delta x/x)$ must be less than ~0.15 when $L_2 = 6$ cm. For larger values of L_2 the limit is even lower. This occurs because x must be increased as the cavity length grows in order to minimize diffraction spreading.

The combined effects of diffraction (forcing a larger beam size) and beam walkoff (forcing a smaller beam size $\delta x/x \geq .05$ to insure SLM operation) restricts the beam diameter, 2x, in the oscillator to ~ 1.0 mm with little flexibility for variation. This beam size restriction coupled with the ~ 1 J/cm^2 saturation fluence for Ti:Sapphire limit the SLM oscillator output to approximately 1-10 mJ. Other gain media (solids, dyes or gases) will have different limits. Additionally, the damage fluence for Ti:Sapphire, ~ 5-10 J/cm^2 for laser pumping, sets a limit on the gain as shown in Figure 4.

It is important to note that other gain media, such as Alexandrite and Nd:xxx, may also be used in this oscillator configuration. However, gain-length products ≥ 2 must be achievable in order to sustain oscillation with the high output coupling of the grazing incidence grating. Also, other pumping geometries are possible - for example, the oscillator also operates well with the pump beam incident through the back mirror.

In summary, a 2.0 mJ/pulse, SLM, Ti:Sapphire laser oscillator has been demonstrated and tuned from 746 nm to 918 nm. Its mode selection properties have been modeled, and limits set on its useful range of operation. Its advantages over dyes are many; including: high output energy per pulse, simplicity - no need to mix or change dye solutions and very wide tunability.

References

1. K. Kangas, D.D. Lowenthal, and C.H. Muller, III, Opt. Lett. 14, 21 (1989).

2. M.G. Littman, Opt. Lett. 3, 138 (1978); I. Shoshan, N. Danon and V. Oppenheim, J. Appl. Phys. 48, 4495 (1977).

3. P.A. Schultz, IEEE J. Quant. Electronics 24, 1039 (1988).

4. M.G. Littman, Appl. Opt. 23, 4465 (1984).

Injection Locking of Two-Dimensional, Monolithic, Surface Emitting Laser Diode Arrays

M. Jansen, J.J. Yang, L. Heflinger, S.S. Ou, M. Sergant,
J. Huang, J. Wilcox, E. Anderson, L. Eaton, and W. Simmons

TRW Space & Technology Group
Group Research Staff
One Space Park
Redondo Beach, Ca. 90278

Abstract

Two rows of surface-emitting (ten-element each), linear arrays were coherently locked to an external master oscillator. The free running array is spectrally coherent, and it is phase coherent under injection locking from an external master oscillator. A subset of the injection locked 2-D array is tuneable over a >60 angstroms spectral range. The monolithic array is robust, and maintains coherent lock, even when individual unit cells are turned off. Far-field fringe visibilities in excess of 60% were realized.

Summary

Injection locking of discrete edge emitting semiconductor diode lasers to an external master oscillator (MO) has been successfully demonstrated for single stripe devices[1], linear arrays[2, 3] and broad area lasers[4]. In this paper we report the coherent operation of an injection-locked two-dimensional (2-D) monolithic array of coupled resonators.

The coupled resonator concept features monolithic linear arrays (10 elements each), vertical and 45 degree outcoupling micromirrors for vertical emission[5], and interconnecting optical waveguides. Coherence across the device at a single wavelength is achieved by external injection locking.

Figure 1 shows a top view of the architecture, which consists of 10 surface emitting unit cells (each one comprising a ten element linear array), and one "driver" unit which couples the two rows of devices. The dimensions are illustrated in the lower insert.
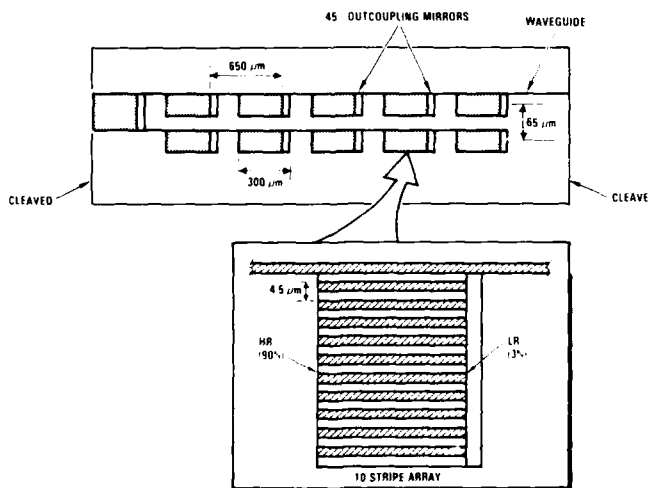
Figure 1- Top View of TRW Monolithic Surface Emitting Array Architecture

Each unit cell has 10 stripes, 300 microns long, with a threshold current of < 12mA per stripe. Evanescent coupling is used to couple the array elements in the lateral direction, as well as to provide coupling between the array and the interconnecting waveguides. 350 micron long waveguide sections couple the unit cells in the longitudinal direction.

A schematic diagram showing the transverse and lateral unit cell dimensions, and the device geometry (growth layers) are shown in Figure 2.

449
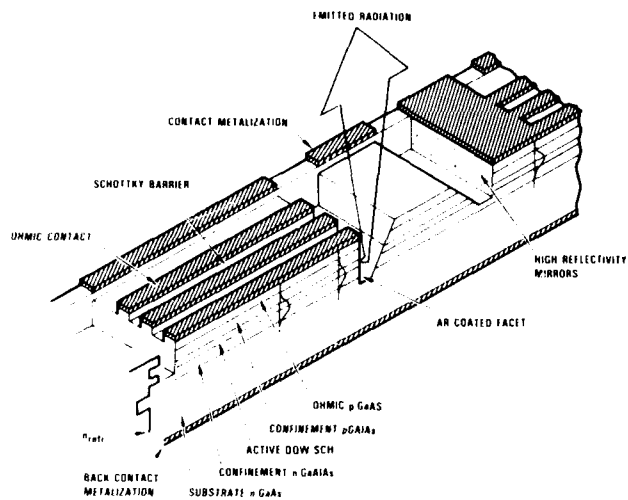
Figure 2- Transverse and Lateral Device Geometry

Each unit cell has 10 stripes, 3 um wide and 300 um long. The device transverse structure is a double quantum well-separate confinement heterostructure (DQW-SCH) grown by metal organic chemical vapor deposition (MOCVD). The 90^0 cavity mirrors of the unit cells are coated with a 3% low reflectivity (LR) facet, and a 90% high reflectivity (HR) coating. This choice provides an enhanced injection locking bandwidth (relative to uncoated mirrors) and single-ended emission, without a substantial efficiency penalty in operation. Figure 3 shows a schematic diagram of the unit cell crossection.
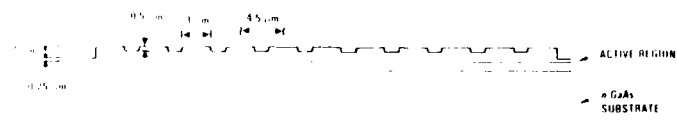
Figure 3- Unit Cell Crossection

The ten element array has 3 micron wide stripes, with a 4.5 micron center-to-center separation between the stripes. The coupling waveguide is etched to 0.25 microns from the active region to provide strong mode confinement.

The waveguide distribution network provides signal amplification to couple the unit cells coherently and efficiently. External injection locking forces strong phase coherence across the array, results in tuning over a significant wavelength band (> 60 A), and enhances the stability of the array.

The design is amenable to relatively simple aperture filling through the use of external optics. The planar wafer geometry provides efficient diode operation and output coupling, and simple heat removal through a back-plane submount. Finally, this array architecture is robust (light continues to propagate through degraded unit cells)

Device uniformity is achieved by using reproducibly uniform material growth, and fabrication techniques which are compatible with the monolithic integration on the wafer. We have developed MOCVD material growth techniques which result in very uniform material, as well as dry-etching technologies (reactive ion-etching and ion-milling), used for defining waveguide structures, and 45 degree outcoupling micromirrors and vertical laser facets with an optical quality comparable to that of cleaved devices.
Figure 4 shows a close-up view of the TRW packaged 2-D array, showing gold wire bonds to the unit cells, the driver which couples the two rows of unit cells, and the interconnecting waveguides. All the unit cells are turned-o.. and operational, and light comes out through the 45 degree mirrors, perpendicular to the page.

450
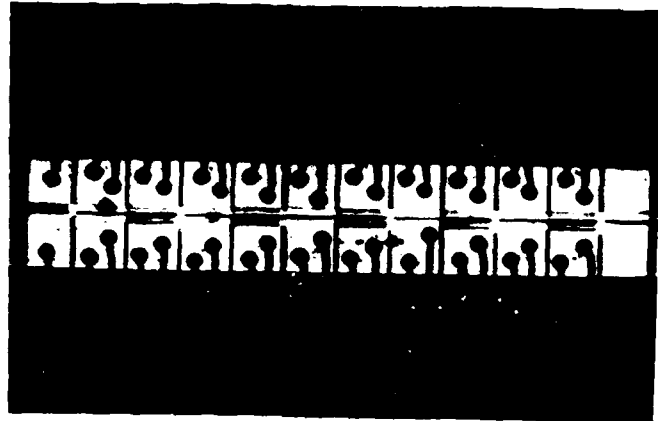
Figure 4- Close-Up View of 2-D Array in Operation (All Unit Cells Are Turned-On)

Figure 5 shows the characteristics of a typical unit cell device (10 element surface emitting array).
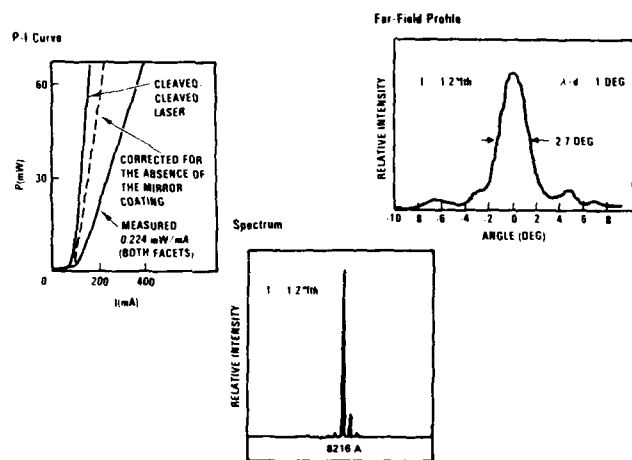
Figure 5 Unit Cell Caracteristics
a- P-I Curve
b- Free-Running Array Far-Field Profile
r- Spectrum

The P-I curve for an uncoated device shows that the device compares well with a cleaved device, both in threshold and efficiency. At 1.2 times threshold, the quantum well lasers have predominantly single mode spectra, and far-fields that are about twice the diffraction limit for typical devices.

Because of the nature of the coupling used in the device, (i.e. lack of isolation between unit cells), it behaves like a self-locked coupled oscillator. An external master oscillator (M.O.) is used to force it to lock at the M.O. wavelength, and also to provides coherence between rows of unit cells. Other advantages of injection locking include wide band tunability (> 50 angstroms), and added stability (this ties in to the M.O. stability).

In order to enhance the injection locking process (achieve wider locking bandwidth), one can lower the resonator Q, or increase the amount of injected power. A lower Q was achieved here by decreasing the facet reflectivity product to 0.027 from an uncoated value of 0.09. The injected power required to lock this array was of the order of 2 mW, resulting in injected ratios as large as 100:1.

Only 1x6 results were cleared for presentation at this time. The 1x6 array represents one row of unit cells and consists of the driver and five unit cell arrays. The experimental set-up for demonstrating coherent operation under injection locked conditions is illustrated in Figure 6.
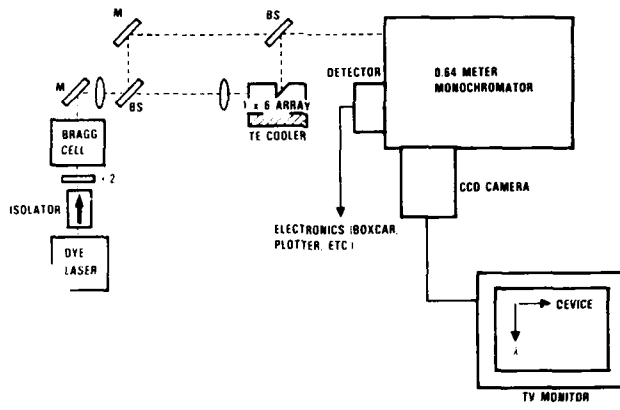
Figure 6 Experimental Arrangement for Injection Locking

1x6 arrays were injection locked from an external master oscillator (M.O.) under pulsed operation. The M.O. was a commercial dye laser. An isolator and half-wave plate were used to minimize reflections back into the M.O.. A Bragg modulator was used to synchronize the dye laser and slave laser pulses. The spectral output was monitored with the monochromator, while far-fields were measured directly with a CCD camera.

The 1x6 array exhibits spectral coherence under both free-running, and injection locked conditions, as illustrated by the free-running and injection locked array spectra of Figure 7.

Figure 7 a- Free-Running Spectrum of 1x6 Surface Emitting Array
          b- Injection Locked Spectrum of 1x6 Surface Emitting Array

The injection locked 1x6 array can be tuned over a greater than 60A spectral range, while maintaining phase lock. The high transparency of the quantum well material results in system robustness. Light continues to propagate through turned-off unit cells, and coherent lock is maintained under both free-running and injection locked conditions.

Fringe visibilities in excess of 60% have been achieved for single rows of unit cells, as illustrated in Figure 8. The fringe width is approximatley 1.6x the theoretical value predicted for a coherent array of light sources. Coherent output powers greater than 100 mW were obtained at this visibility level.

452

$\lambda/650\ \mu$
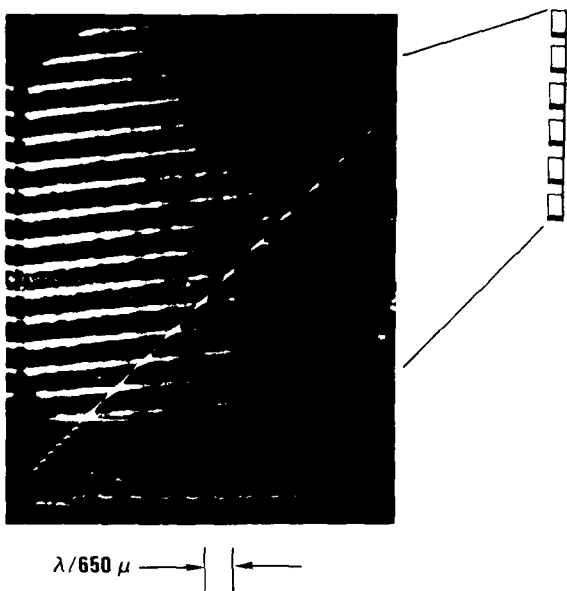
Figure 8-   Far-Field Interference Pattern for a 1x6 Row of Unit Cells

In conclusion , we have demonstrated a coherent, monolithic, robust, two-dimensional array of diode lasers. The free running array is spectrally coherent, and it is phase coherent under injection locking from an external master oscillator. An injection locked subset of the full 2-D array is tunable over a > 60 A spectral range. Far-field fringe visibilities in excess of 60% were achieved.

References
1.   S. Kobayashi and T. Kimura, IEEE J. Quantum Electron., **QE-17** (5) 681 (1981)
2.   J.P. Hohimer, A. Owyoung, and G.R. Hadley, Appl. Phys. Lett., **47** (12), 1244 (1985)
3.   L. Goldberg and J.F. Weller, Appl. Phys. Lett., **50** (24), 1713 (1987)
4.   G.L. Abbas, S. Yang, V.W.S. Chan and J.G. Fujimoto, IEEE J. Quantum Electron., **24** (4), 609 (1988)
5. J.J. Yang, M. Jansen and M. Sergant, Electronics Letters **22** (8) 438 (1986), and J.J. Yang, M. Sergant, M. Jansen, S.S. Ou, L. Eaton, and W. W. Simmons, Appl. Phys Lett. **49** (18), 1138 (1986)

THE DEVELOPMENT OF A COHERENT TWO-DIMENSIONAL LASER DIODE ARRAY

M.S. Zediker, H.R. Appelman, D.A. Bryan, T.E. Bonham,
B.G. Clay, J.A. Heidel, J.L. Levy, C.M. Harding,
D.J. Krebs, R.G. Podgornik, R.A. Williams, and R.R. Rice

McDonnell Douglas Electronic Systems Company
P.O. Box 516
St. Louis, Missouri 63166

Abstract

An integrated optics technology based on AlGaAs semiconductor material has been used to fabricate monolithic 10-emitter coherent-amplifier arrays. These arrays have demonstrated power outputs of 300 mW CW with only 2 mW injected power and greater than 0.8 coherence between any two amplifiers.

Introduction

An active waveguide medium is an essential feature for successful stacking of a two-dimensional array of laser diodes. Such an array can combine the highly divergent beams of many laser diodes into one narrow beam. The primary design challenge in a master oscillator power amplifier systems is the distribution of the signal to the power amplifiers. This design problem was solved by integrating a one-to-ten power distribution network with 10 power amplifiers on a 1.1 x 0.5 cm AlGaAs chip. This linear array is called a Unit Cell because it is the building block for a 100-emitter two-dimensional array of 10 such cells.

The high power capability of a one or two-dimensional array will be useful in laser communication systems, optical scanning systems, and laser radar systems. In addition, the integrated optics techniques used in the Unit Cell design represent a generic technology which would be useful in high-speed optical interconnects, high-speed optical computers, and multiplexers for optical switching networks.

Unit Cell Design

The Unit Cell is a one-to-ten distribution network and 10 power amplifiers integrated onto a single chip. The monolithic design is shown schematically in Figure 1 with the relative position and design of each component illustrated. The master oscillator signal (1-20 mW) is injected into the Unit Cell by an optical fiber at the input port. The signal propagates along the waveguide to the distribution network where it is amplified and divided into 10 signals of equal power. The 10 turning mirrors deflect the signals by 90° into the 10 phase modulators. Immediately following the phase modulators are the amplifiers, which boost the power level to 30 mW per amplifier.
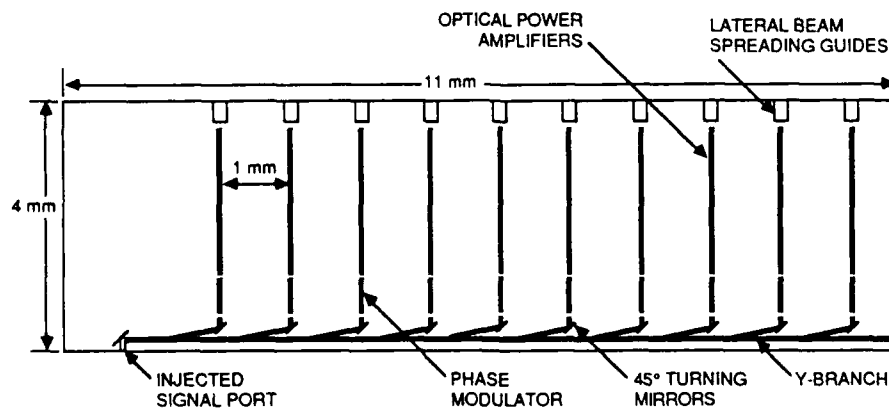
Figure 1. Schematic representation of the Unit Cell illustrates each of the components used to make the ten-amplifier linear array.

Waveguides using gain to overcome any losses are referred to as "active" integrated optics. An example is the Unit Cell distribution network, where the power in the waveguide is divided n times, with n branching waveguides, but the nth branch has the same power level as the first branch. This is accomplished by adding enough gain at each branch to compensate for the power split off at each prior branch in the distribution network along with any modal losses. The modal losses are power losses due to scattering or absorption in the material. This ability to add gain into an optical circuit, at the designer's discretion, creates new design capabilities that are not feasible with passive waveguides. We demonstrated this ability in the design of our Unit Cell.

The Unit Cell is a large-scale amplifier chain integrated on an AlGaAs wafer, with the gain supplied by a Graded Index Separate Confinement Heterostructure Single Quantum Well (GRIN-SCH-SQW) epitaxial structure. This material is suitable because it has very low passive modal losses ($10-20$ cm^{-1}) compared to Double Heterostructure material (120 cm^{-1}). We first observed this characteristic during tests on very long lasers (>1 mm) where the threshold of the device was observed to change only slightly as a function of laser length. These experiments indicated that the modal losses were $10-20$ cm^{-1}.

The waveguides used in the Unit Cell are forward-biased to overcome the modal losses of the material and any power losses due to the integrated components (e.g., scattering and transmission losses at the turning mirrors). The input branch becomes lossless at a current density between 150 and 300 A/cm^2, depending on the quality of the material. The distribution network, which has a periodic loss of 40% per power splitter (Y-Branch), must operate at a current density between 500 and 1000 A/cm^2 to achieve the same power levels at the first and tenth branches. The phase modulators operate at the same current density as an input branch, and the power amplifiers operate at a current density between 1500 and 2000 A/cm^2.

The waveguides used to build the Unit Cell are formed by a 5-micron-wide rib structure. The optical mode is confined laterally by the increased index in the GRIN-SCH-SQW layers below the rib. The magnitude of this perturbation is controlled by the depth of the etch that defines the rib. According to our initial calculations, a 5-micron-wide rib supports a single mode when the area outside of the rib is etched to within 0.5 micron of the quantum well. This produces a weak waveguide that is limited to straight runs or very large radius bends. The need for compact designs leads to the development of the integral turning mirrors shown in Figure 1.

The total internal reflection (TIR) mirror used in this design is formed by a Reactive Ion Beam Etching (RIBE) technique. The mirror is formed by etching through all of the epi-layers and relying on the index step between the AlGaAs guiding layers and air to reflect the laser mode. Figure 2 includes a picture of a typical mirror on a Unit Cell. The mirror is at the edge of the dark region (which is the deep etch) in the photograph.

BEAM EXPANDER   Y - BRANCH

TURNING MIRROR   RIB
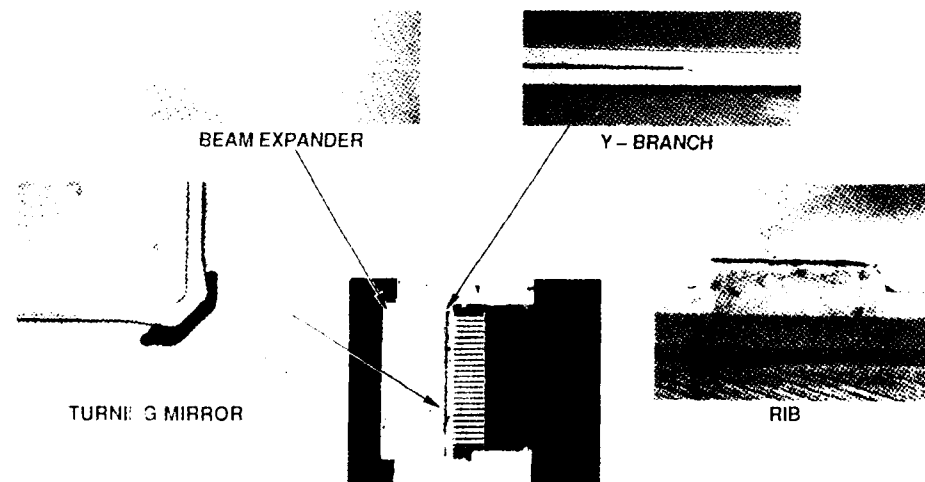
Figure 2. SEM photographs of the various components of the Unit Cell. The center photograph which is a top view, shows the Unit Cell on the left and the flexible electrical circuit on the right.

The phase modulators are sections of rib amplifiers that have been electrically isolated by a metal break from both the power amplifiers and the distribution network. The metal break, which is simply a gap in the metallization, provides a sufficiently high resistance to enable the forward bias on the phase modulators to be controlled independently of the other components on the chip. The phases of the optical modes are changed by the local heating of the guiding layers induced by the forward current. As the junction heats up, the refractive index increases, producing a longer optical path length and, consequently, a phase retardation at the output. Since this is a thermal effect, the bandwidth of the modulator is estimated to be only 500 kHz.

The final design for the Unit Cell was dictated by the constraints imposed on it by the two-dimensional array design (Figure 3). In particular, it was necessary to design the Unit Cell with all electrical and optical interfaces on one side of the cell. This configuration enabled the stacking of the Unit Cells into an array with minimal interference from the electrical and optical connections. As can be seen in Figures 1 and 2, the flexible electrical circuit and the optical fibers have easy access to one end of the Unit Cell.

100 EMITTER INJECTION LOCKED CONCEPT
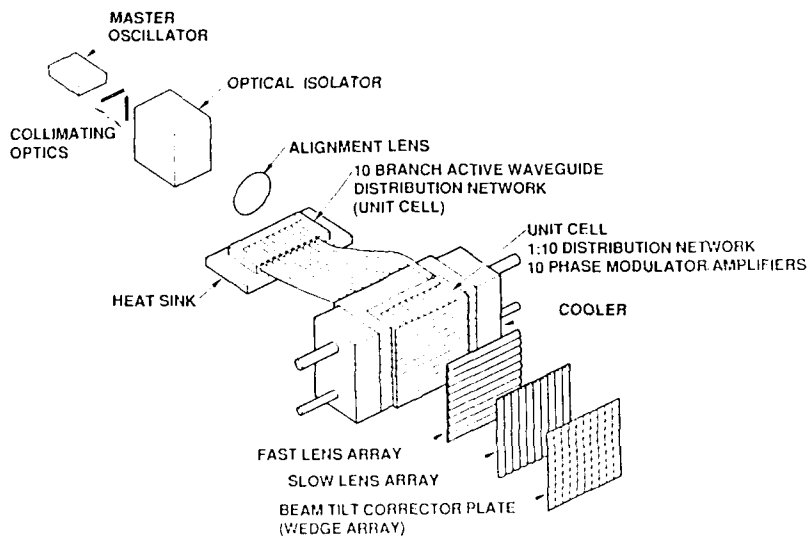
Figure 3. Ten Unit Cells are stacked to form the 100-emitter two-dimensional array. An eleventh cells serves as an active distribution network for the master oscillator.

Two-Dimensional Array Design

The 100-emitter, two-dimensional array design shown in Figure 3 is a stack of 10 Unit Cells injection locked by a single master oscillator. The master oscillator is free-space coupled to a Unit Cell through an optical isolator, which functions as the power splitter/amplifier. The use of an active splitter as a distribution network enables a relatively low-power master oscillator (10-30 mW) to injection lock the array.

The optical isolator is important to prevent optical feedback from disrupting the stability of the master oscillator. For example, any reflections or backward emissions from the input port could provide sufficient signal to disrupt the stability of the master oscillator. We are still experimenting with the amount of isolation required but at present we are using a Faraday rotator that is capable of attenuating a backward propagating signal by 30 dB. As a precaution against feedback and to ensure high optical transmission through each optical element of the system, all optical interfaces are coated with a high quality antireflection coating (R < 0.0025).

The distribution cell's 10 amplifier outputs are coupled to 10 optical fibers which transmit the injection locking signals to each of the Unit Cells in the array. These single-mode polarization-preserving optical fibers are butt coupled at each end with a 9-15% coupling efficiency for the signal. This should provide an injection locking signal of 1 to 4 mW at each Unit Cell in the array. Experiments have shown that this power level is sufficient to injection lock the Unit Cells (Figure 4).

MO POWER = 3 mW
OUT OF FIBER
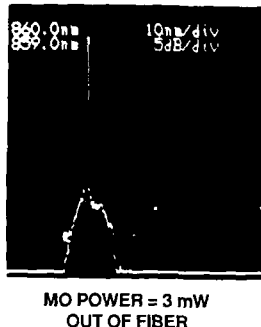
Figure 4. Injection-locking spectrum of a Unit Cell. The narrow peak is the amplified master oscillator signal and the broad spectrum is spontaneous emission. The vertical scale is 5 dB/div; the horizontal scale is 10 nm/div.

The array, when stacked, has a horizontal emitter spacing of 1.0 mm and a vertical spacing of 1.5 mm. Arrays of crossed cylindrical lenses, as shown in Figure 3, collimate the diverging beams. In the fast axis the lenses are approximately f/1; in the slow axis they are approximately f/5. Each lens produces a Strehl ratio of 0.9 at the best focus.

The mechanical components necessary in a stacked design make it difficult to align all 100 emitters to an absolute position. Consequently, the combination of tight alignment tolerances on the optics, realistic mechanical positioning errors for each emitter, and the use of crossed cylinder lenses for collimation, results in a small pointing error for each emitter. This pointing error is corrected by placing a small wedge plate in front of each emitter. This wedge plate is a microscope cover slip placed in a drop of cement, which is tilted to correct the pointing error. The small tilt on the wedge plate produces a wedge of optical cement under the plate, which is the actual correcting element. A more sophisticated technique using diffractive optics is currently being studied and appears promising.

Unit Cell Results

The GRIN-SCH-SQW material was grown and processed into Unit Cells by McDonnell Douglas. The ribs and mirrors were fabricated with the RIBE process. The metallizations and photolithography techniques are standard methods.

Characterization of each component's performance was determined by two methods. The first technique measures the threshold, slope efficiency, and modal characteristics of each component when it is operated as a laser. Using this technique, we have measured turning mirror losses as low as 0.10, Y-Branch splitting ratios of 60:40 (60% of power continues straight and 40% is split off), and beam expanders with a 5-micron-wide mode at one end of the device (1/e^2 points) and 14-micron-wide modes at the other end. These results were confirmed with injection-locking experiments. In addition, by using an injected signal, we confirmed the performance of the forward-biased phase modulators. A π - radian phase shift was observed for an 18 mA change in current. This phase shift corresponds to a 3 radian/C^o temperature coefficient. Finally, we characterized 5-micron rib lasers and laser amplifiers using these techniques. In general, the threshold current densities were higher for the lasers than expected (200-300 A/cm^2) while the slope efficiencies (0.5 W/A) were similar to the larger, 60-micron-wide, oxide-defined devices used to characterize each wafer.

The Unit Cells were tested by injecting a signal from a frequency-stablized laser diode while monitoring the optical spectrum and the fringe visibility. The power of this signal varied from 1 to 20 mW. Figure 4 is an optical spectrum of an injection-locked Unit Cell. The vertical axis is 5 dB/div and the horizontal is 10 nm/div. Calculation from this data shows that 0.8 of the power being detected by the spectrum analyzer is at the same frequency as the master oscillator. This result is in reasonable agreement with a measurement based on the visibility of the fringes in the far-field.

Since the emitters are equally spaced on the Unit Cell, the output is in the form of a classical Young's interference pattern. Figure 5 shows four sets of fringes for a working Unit Cell without collimating lenses. The fringes in Figure 5a are formed by interfering emitters 1 and 10, which are separated by 9 mm. The visibility of the fringes is calculated by taking the ratio of $(I_{max}-I_{min})/(I_{max}+I_{min})$ and is greater than 0.7. Figure 5b results when the phase front formed by all 10 emitters is flat. Figure 5c is the interference pattern for all ten emitters the phase front across the array is random. Figure 5d results when the phases of all emitters are equal. This interference pattern was obtained with the Unit Cell operating at 300 mW CW with only 0.6 mW (2 mW incident on the input port) injected by the master oscillator. The Unit Cell electrical-to-optical conversion efficiency was estimated to be 13%. The phase alignment was performed by adjusting the forward bias on each modulator by hand. The fringes were stable in position for time periods as great as one hour. The fringes shifted their position only when the master oscillator changed frequency.

EMITTER NUMBER ONE AND TEN   **FOUR ADJACENT EMITTERS**

TEN EMITTERS - PARTIALLY PHASED   **TEN EMITTERS - FULLY PHASED**
1/3 WATT
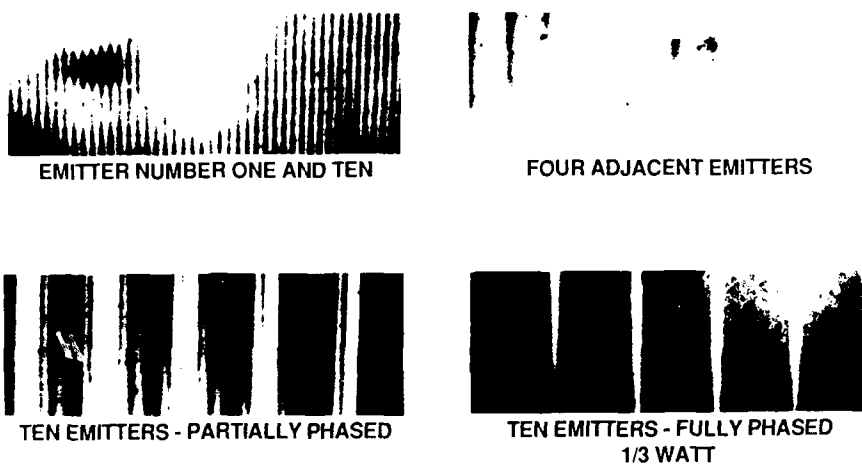
Figure 5. Interference fringes between emitters on a Unit Cell: a) emitters 1 and 10; b) emitters 1-4 phase aligned; c) emitters 1-10 randomly phased; and d) emitters 1-10 phase aligned.

Summary

An integrated optics technology has been described that was used to build a linear optical phased array. This Unit Cell consisted of several waveguide components that were integrated onto a single chip. With only a few milliwatts of injection power, the Unit Cells operated at 300 mW CW with greater than 0.80 coherence across the output aperture. This corresponded to a 13% electrical-to-optical power conversion efficiency.

The high power capability of these arrays suggests that laser communication systems, optical scanning systems, and laser radar systems based on laser diode arrays are feasible. In addition, the integrated optics techniques developed for the Unit Cell are sufficiently generic for application in high-speed optical interconnects for computers, high-speed optical computers, and multiplexers for optical switching networks.

EXPERIMENTAL VERIFICATION OF OPTICAL FEEDBACK REGIMES
FOR A 1.3 µm FP LASER DIODE

J. Käppel, W. Heinlein
Universität Kaiserslautern
Erwin-Schrödinger-Straße
D-6750 Kaiserslautern (FRG)

Abstract

Dominant mode linewidth and relative intensity noise of a ridge-waveguide diode laser were measured under variable optical feedback phase. Comparing the results to single-mode laser linewidth theory three feedback regimes are clearly identified and characterized.

Introduction

Fabry-Perot type diode lasers are widely used in fiber optic communication systems at 1.3 µm where chromatic dispersion of conventional fibers is minimal. These systems are deteriorated by small but inevitable amounts of parasitic feedback [1,2]. On the other hand controlled feedback can improve the laser's characteristics [3]. Therefore detailed information about the feedback behavior is needed. Theoretical and experimental work so far focussed mainly on single-mode lasers [4,5,6]. Our work concentrates on coherent feedback effects and correspondent experimental results.

Device under test

The laser under test was of metal-clad ridge-waveguide type[7]. Without feedback the sidemode suppression was more than 14 dB and the linewidth about 120 MHz for the chosen operating point.

Experimental set-up

To obtain exactly defined coherent feedback a short external cavity consisting of a collimating lens and a piezo-translatable plane mirror was assembled to the laser. Feedback phase could be adjusted using a special mirror position control scheme with a resolution of 10 nm. Feedback intensity was varied by tilted neutral density filters.

The experimental arrangement, sketched by Fig. 1, allows to use part of the emission for intensity noise evaluation while spectral analysis can be performed simultaneously. A grating spectrometer measures the longitudinal mode spectrum and selects a single mode for linewidth determination. Linewidth is measured either with high resolution using a self-heterodyne set-up[8] or by a confocal Fabry-Perot interferometer that is also used for monitoring the relative optical frequency deviation.
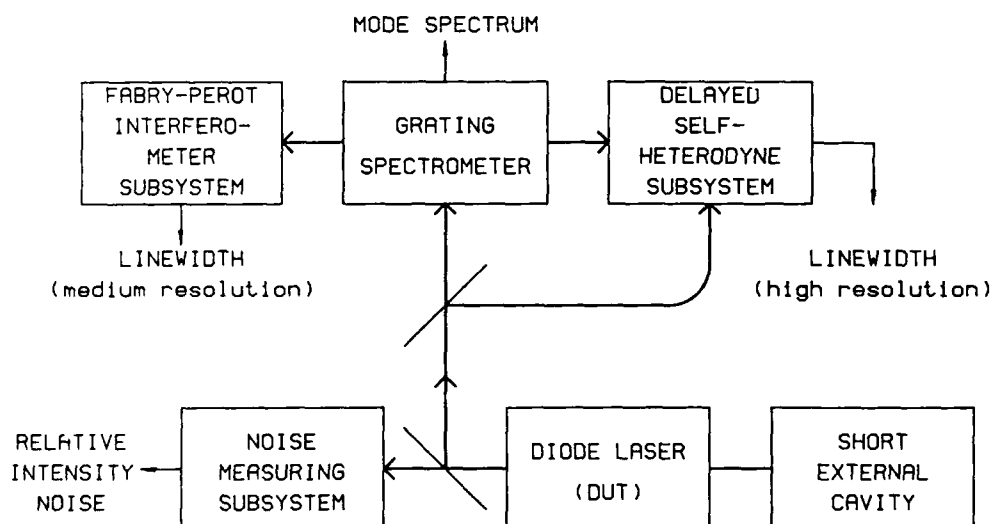
Fig. 1 *Scheme of experimental set-up*

Feedback strength

For characterization of the feedback strength we use the feedback parameter C given by[5]

$$C = a_x \cdot \frac{\tau_x}{\tau_0} \cdot \frac{1 - R}{\sqrt{R}} \cdot \sqrt{1 + \alpha^2} \qquad (1)$$

where a_x includes all field attenuation effects of the external cavity, τ_x is the external cavity roundtrip time, τ_0 the laser roundtrip time, R the power reflectivity of the laser facet and α Henry's linewidth enhancement factor.

Results

For s m a l l feedback intensity (C-0.15) Fig. 2 shows linewidth $\Delta\nu$ vs. feedback phase change $\Delta\varphi_x$. $\Delta\nu_0$ is the solitary laser linewidth. The dotted experimental values correspond well to the solid line that was calculated using single-mode laser theory [4] :

$$\Delta\nu = \Delta\nu_0 \cdot [1 + C \cdot \cos(\Delta\varphi_x)]^{-2}. \qquad (2)$$
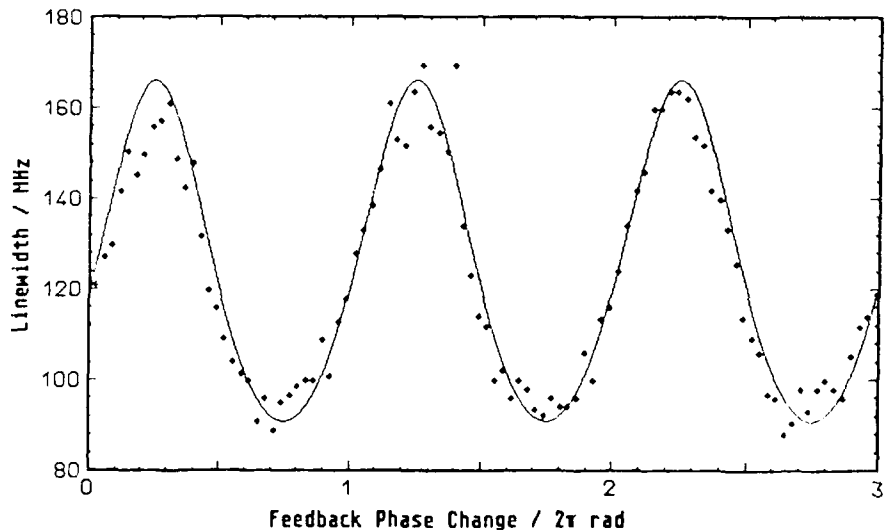
Fig. 2 *Linewidth vs. feedback phase change for small feedback (C - 0.15)*

Linewidth varies smoothly between 90 and 166 MHz. For the same amount of feedback the optical frequency deviation, plotted also against feedback phase change in Fig. 3, shows a sinusoidal
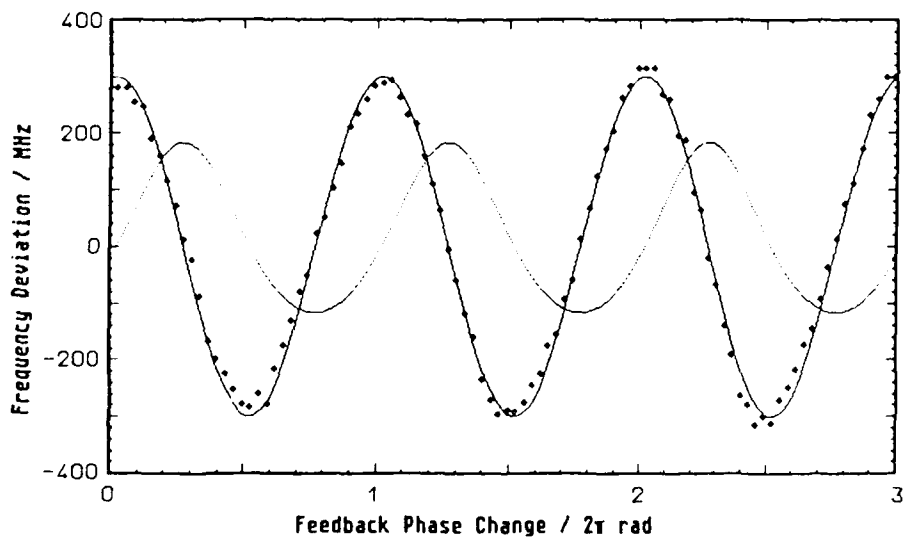
Fig. 3 *Optical frequency deviation vs. feedback phase change for small feedback (C - 0.15). Note: Positive frequency deviation means decreased optical frequency. Unscaled: linewidth.*

460

variation with an amplitude of 300 MHz. Linewidth is plotted unscaled for comparison. Note that low linewidth coincides with the rising slope of frequency deviation. (Such diagrams giving the relation between linewidth and optical frequency are important for the development of automatic linewidth control schemes.)

In the case of m e d i u m feedback intensity, exemplified by Fig. 4, the linewidth varies with feedback phase change from 50 MHz to very high values. We have fitted a theoretical curve (solid
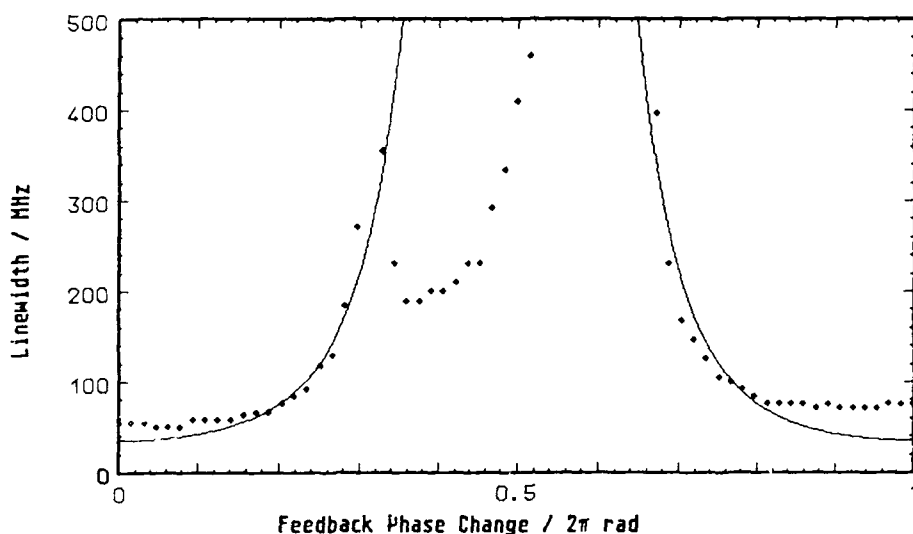
Fig. 4 *Linewidth vs. feedback phase for medium feedback (C - 0.85)*

line) using Eq. (2) with C-0.85. Linewidth does not reach its theoretical minimum due to poor sidemode suppression that results in enhanced mode partition noise. Between the rising slopes linewidth is lowered by external cavity mode (XCM)-hopping Though not totally resolved the effect becomes obvious in the time-averaged intensity spectrum, Fig. 5. The splitting of the emission line extends over a few GHz and varies with feedback phase[6].
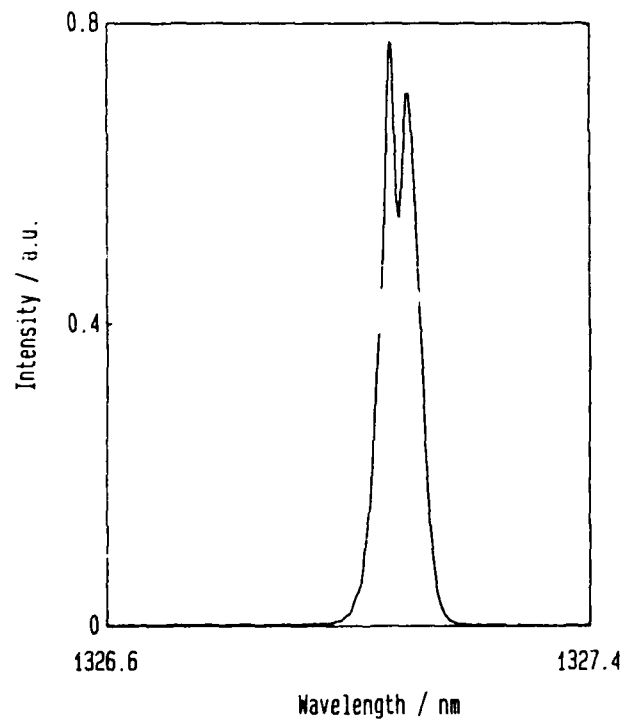
Fig. 5 *Intensity spectrum showing XCM-hopping for medium feedback (C - 0.85)*

461

For l a r g e feedback intensity the laser linewidth could be reduced to 2 MHz by varying the feedback phase. This is shown in the upper part of Fig. 6. The dots represent measurement data, the solid line calculated data using Eq. (2) with C=13. Again the lowest theoretical value is not reached because of mode competition. It is especially important to note that the measured data do not represent the same longitudinal mode. As feedback phase increases, mode switching occurs with a steep rise in linewidth. After a small amount of further phase increase, another mode becomes dominating, again with low linewidth. The measured relative intensity noise (RIN), see the lower part of Fig. 6, shows that this mode switching is accompanied by a sharp increase of mode partition noise. measured at 100 MHz within a bandwidth of 2 MHz. Note that the phase regions in which mode hopping occurs are of different extension.
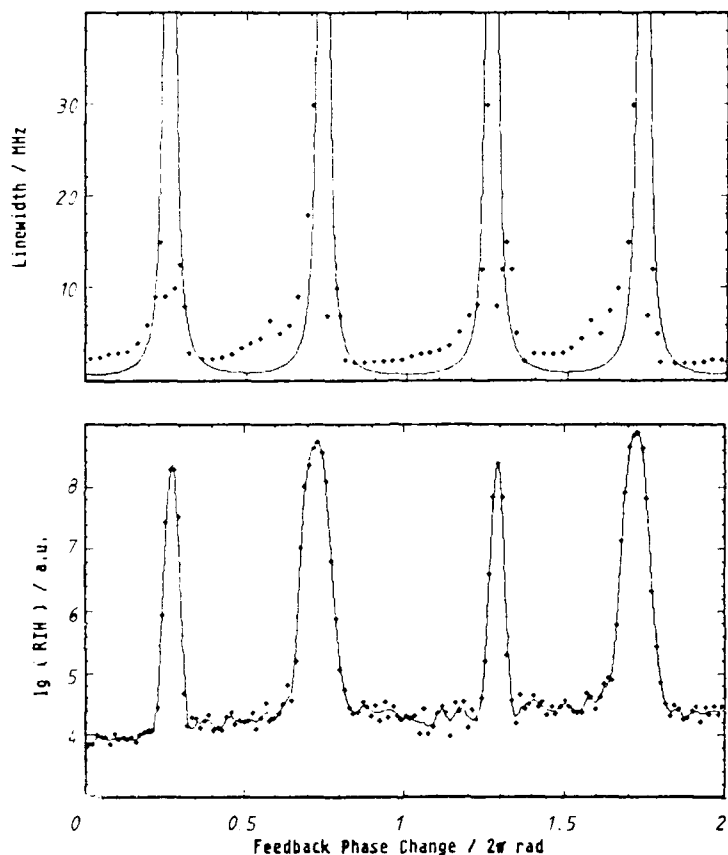
Fig 6 *Linewidth and Relative Intensity Noise (RIN) for large feedback (C = 13)*

Discussion

Plotting linewidth according to Eq. (2) as function of the feedback parameter C the diagram of Fig 7 results. Here the solid lines border the area in which a single-mode laser's linewidth lies, the exact value depending on the feedback phase. A multimode laser shows the same behavior only for sufficiently low feedback parameters C. In this case the laser is continuously tuned in frequency and linewidth, therefore the term "tuning region" seems appropriate. In the medium feedback regime line-splitting with values up to the XCM spacing occurs. However, our measurements suggest that mode hopping may occur already for C<1. For larger feedback parameters (C>1) longitudinal mode transitions took place and the laser was multimode within large feedback phase regions. These regions became smaller for increasing feedback intensity, so that sudden longitudinal mode jumps happened, if the feedback phase changed only slightly at critical values. For C around 10 the term "Fabry Perot mode (FPM) switching region" was chosen.

In conclusion the above exemplified cases characterize a typical FP diode laser's feedback behavior for a practical important range of feedback intensity, stressing especially the influence of the feedback phase that is of essential importance for both parasitic near reflections and short external cavities.
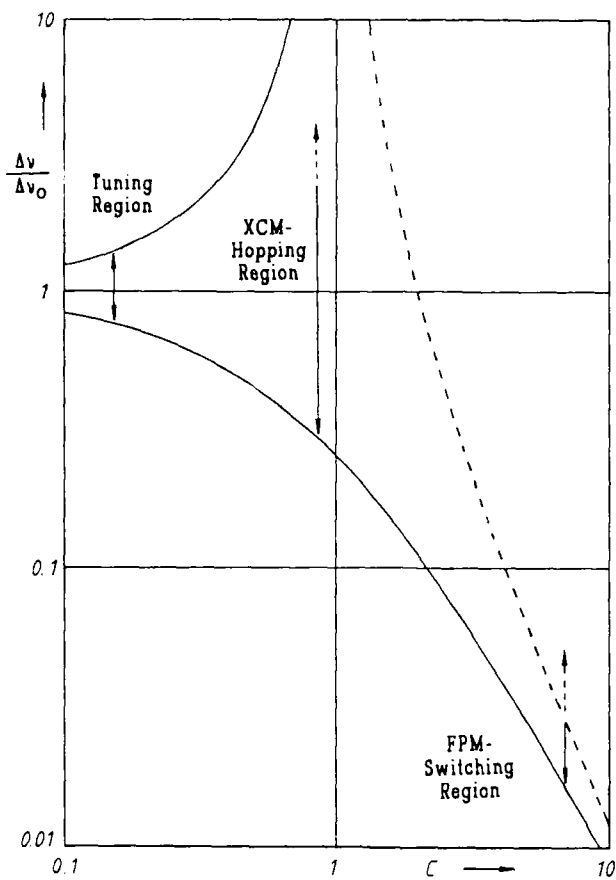
Fig. 7 *Normalized linewidth vs. feedback parameter.*
Solid lines: $cos\Delta\varphi_x = \pm 1$, dashed line: $cos\Delta\varphi_x = -1$.

Acknowledgements

References

1. K. Petermann, Laser diode modulation and noise (Kluwer, Dordrecht, 1988), pp. 250-285

2. R. S. Vodhanel, and J.-S. Ko, El. Lett. 20, 974 (1984)

3. G. Wenke, R. Gross, P. Meissner, and E. Patzak, J. Lightw. Tech. 5, 608 (1987)

4. G. P. Agrawal, J. Quant. El. 20, 468 (1984)

5. G. A. Acket, D. Lenstra, A. J. Den Boef, and B. H. Verbeek, J. Quant. El. 20, 1163 (1984)

6. R. W. Tkach, and A. R. Chraplyvy, J. Lightw. Tech. 4, 1655 (1986)

7. M.-C. Amann, B. Stegmüller, G. G. Baumann, and C. Hanke, presented at the European Conference on Optical Communication '86, Barcelona (1985), Tech. Dig. Vol. 1, pp. 85-88

8. T. Okoshi, K. Kikuchi, and A. Nakayama, El. Lett. 16, 631 (1980)
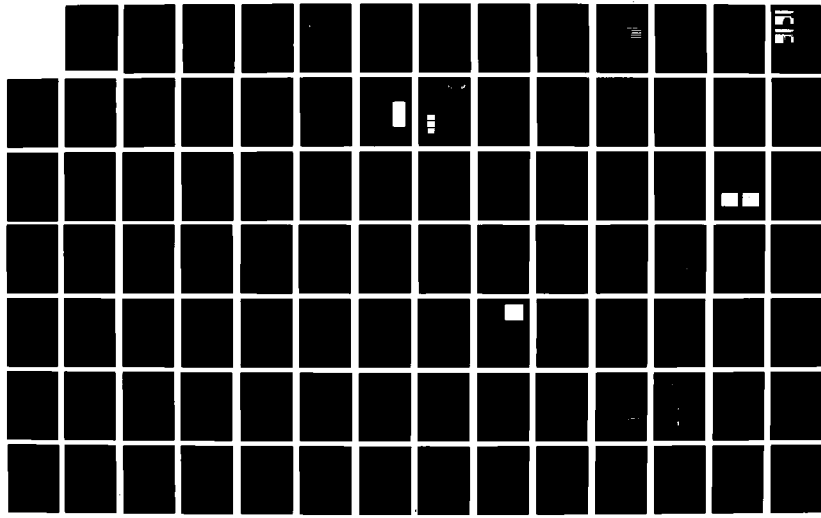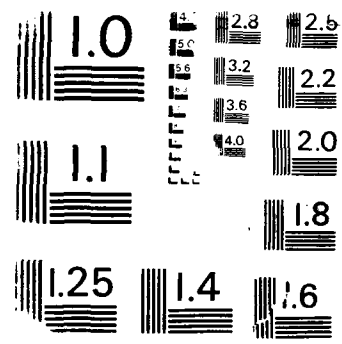
NEW METHOD FOR THE MINIMIZATION OF THE LINEWIDTH ENHANCEMENT FACTOR OF SEMICONDUCTOR LASERS

By J. Brachetti, W. Heinlein, University of Kaiserslautern,
Fachbereich Elektrotechnik
Postfach 3049
D-6750 Kaiserslautern
Fed.Rep. of Germany

Abstract

The linewidth enhancement factor α was numerically calculated using a new method based on the solution of the rate equations. Results show that α can be considerably reduced by increasing the volume of the cavity.

Introduction

In optical communication systems the spectral linewidth is desired to be very narrow. Due to the carrier dependence of the refractive index of the active layer in semiconductor lasers, however, there is an additional linewidth broadening. So a way to a reduction of the linewidth by reducing the linewidth enhancement factor is of great interest. The subject of this paper is to present a numerical method for the calculation and minimization of the linewidth enhancement factor α.

Linewidth Enhancement Factor

The linewidth enhancement factor is defined as the ratio of the change in the real and imaginary part of the complex refractive index due to fluctuations in carrier density[1]

$$\alpha = \frac{\Delta n'(n_e)}{\Delta n''(n_e)} \tag{1}$$

The basic idea of the method presented here is to calculate numerically the fluctuations of the carrier density represented by its maximum and minimum and hence to determine the change of the complex refractive index. Assuming a linear dependence of the real part on carrier density and expressing the imaginary part in terms of the gain the final equation for α is obtained:

$$\alpha = \frac{2\omega}{c} \frac{K(n_{emax} - n_{emin})}{g(n_{emax}) - g(n_{emin})} \tag{2}$$

For an explanation of the variables see Table I

Table I
meaning of symbols in Eq. 1-3

$n = n' + jn''$	complex refractive index of the active layer
n_e	carrier density or number of carriers (in Eq.3)
n_{emax}, n_{emin}	range of fluctuations of the carrier density
g	gain of the laser medium
S_ν	number of photons in the mode ν
F_e, F_ν	Langevin noise sources in the electron and photon equations
K	constant of proportionality (see Eq.3.1 of Ref.6)

Multimode Rate Equations

The maximum and the minimum of the carrier density is determined from the solution of the multimode rate equations including Langevin sources. The rate equations presented here follow the notation of Marcuse[2]:

$$\frac{dn_e}{dt} \;=\; \frac{I(t)}{e} \;-\; \frac{1}{\tau_{sp}}\, n_e \;-\; \frac{c}{n_g}\sum_\nu g_\nu(n_e)S_\nu + F_e(t)$$

$$\frac{dS_\nu}{dt} \;=\; E_{sp\nu}(n_e) \;-\; \frac{c}{n_g}(g_\nu(n_e)-\alpha_L)S_\nu + F_\nu(t)$$

(3)

Calculated Gain Function

The gain function is a very important parameter within the rate equations as well as for the evaluation of the α factor as given in Eq.(2). So special care was taken to determine the spectral gain under the assumption of a parabolic structure of the conduction and valence band. The analytic function approximating the numerical calculated gain is given in Eq. (4) and (5)[3]:

$$g_\nu \;=\; g\left(E = \frac{hc}{\lambda_\nu}\right) = \frac{n_g}{c}\frac{\gamma_\nu}{\tau_{sp}} D_\nu (a_2 n_e + b_2)\left\{1 - \exp\left(\frac{\xi_\nu - E_g - E_F - \tilde{a}\, n_a^{2/3}}{kT}\right)\right\}$$

(4)

$$D_\nu \;=\; \Delta\lambda_c / \left\{ \left(1 + \left(\frac{\lambda_\nu - \lambda_{sp} - a_1(n_e - b_1)}{\Delta\lambda_D}\right)^2\right) \pi\Delta\lambda_D \right\} h(\lambda)$$

(5)
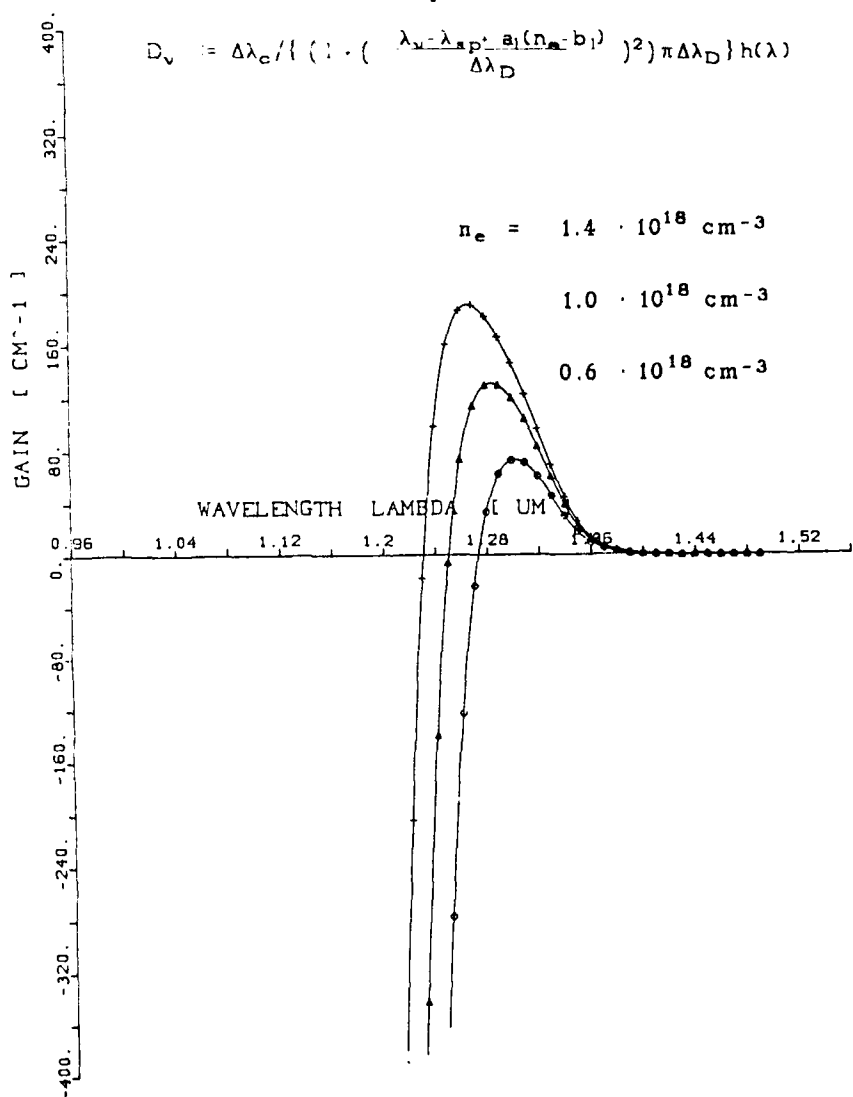
Fig 1 Gain function vs. wavelength calculated under the assumption of parabolic bands

465

In Fig. 1 the gain from Eq. (4) is plotted versus wavelength for carrier densities of 0.6, 1.0 and 1.4 10^{18} cm^{-3}. The main characteristics of this gain function are the spectral shift of the maximum, the nonlinear increase of the maximum with respect to carrier density and the spectral asymmetry of the gain.

Measured Gain Function

The modelling of the gain from Eq.(4) seems quite reasonable with regard to gain measurements[4] which are plotted in Fig. 2 for a mushroom type laser diode[5]. As can be seen from Fig. 2 the spectral shift of the gain maximum has to be taken into account.
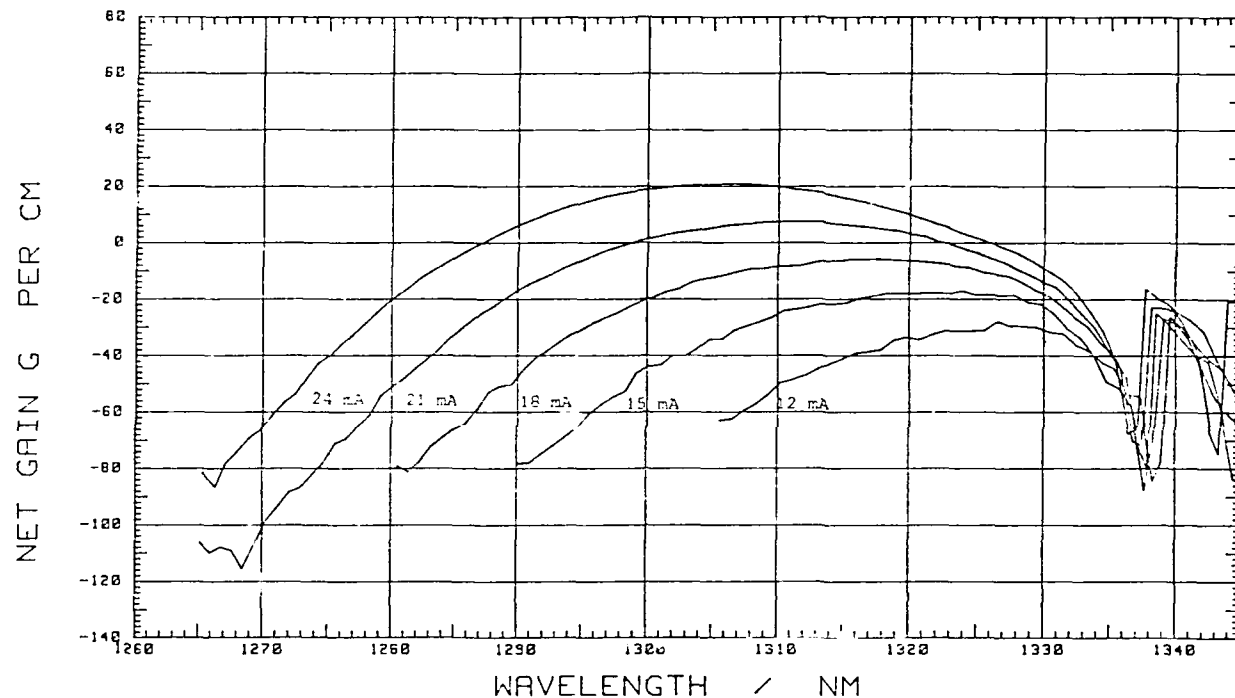
Fig. 2   Measured net gain versus wavelength for various injection currents (I_{th}=26mA)

With the parameters of the calculated gain function fitted to measurements simulations were carried out for varying geometrical structures of the cavity of the laser diode in order to determine the fluctuations of the carrier density. An example of these simulations with the parameters of Table II is shown in Fig 3.

Table II
values of parameters used in the simulation in Fig.3

y	= 0.62	w	= 2 μm	
T	= 293 K	d	= 0.2 μm	
E_g	= 0.945 eV (T=300K)	l	= 250 μm	
ΔE_g	= -18 meV	R_1	= R_2 = 0.3	
a_1	= 2.9546 $\cdot$ 10^{10} μm	x_0	= 25 cm^{-1}	
b_1	= 6 $\cdot$ 10^7	n_r	= 3.52	
a_2	= 0 584077	n_g	= 4	
b_2	= 2.49554 $\cdot$ 10^7	τ_{sp}	= 3 ns	
λ_{sp}	= 1.2331 μm	$1/T_{th}$	= 2	
$\Delta\lambda_D$	= 64 nm	f_m	= 100 MHz	
$i(t)$	= 1 + $i_m(t)$	i_m	= 11 mA	
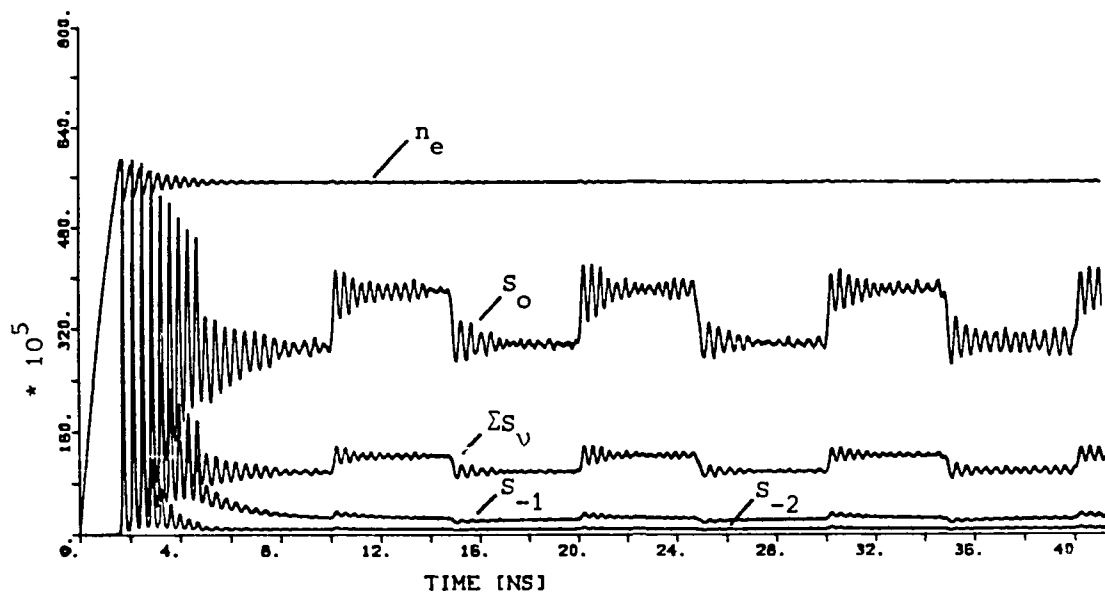
Fig. 3 Time dependence of the number of carriers and photons in the -2, -1 and main mode (total number of photons is plotted additionally).

The upper curve represents the number of carriers from which the maximum and minimum is determined.

Numerical Results

With these values of carrier density and the corresponding gain α factors were calculated from Eq. (2). In Fig. 4 results are plotted versus the volume of the cavity. Here the rectangular cross section was kept constant. The width was $w = 2$ μm, the thickness $d = 0.2$ μm. So the volume was increased by increasing the length.
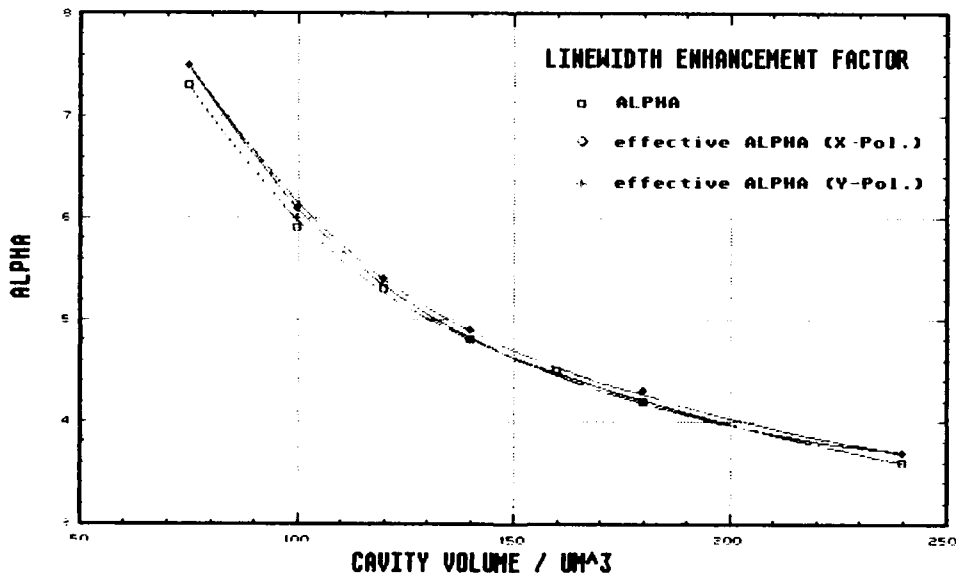
Fig. 4 Linewidth enhancement factors versus volume of the cavity. Intrinsic α factor (lower curve) and effective α factors (upper curves). (X-axis in lateral direction)

467

As can be seen by increasing the cavity length from L - 250 μm to L - 600 μm α can be reduced from 5.8 to 3.6. The upper curves represent effective α based on the calculation of effective refractive indices that were determined from the model of the active rectangular dielectric waveguide.[3]

In Fig. 5 the dependence of α on the width of the active stripe is plotted. For larger volumes of the cavity there is no significant dependence on the stripe width.
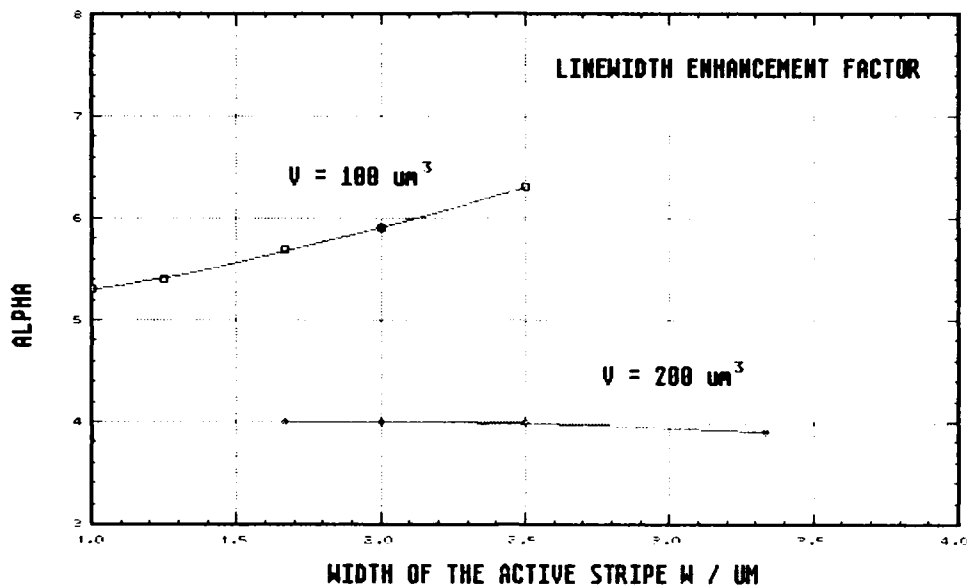
Fig. 5 Intrinsic linewidth enhancement factor α versus width of the cavity for a volume V - 100 μm³ and V - 200 μm³ respectively.

Also, no significant dependence of α on the injection current above threshold can be evaluated (Fig.6).
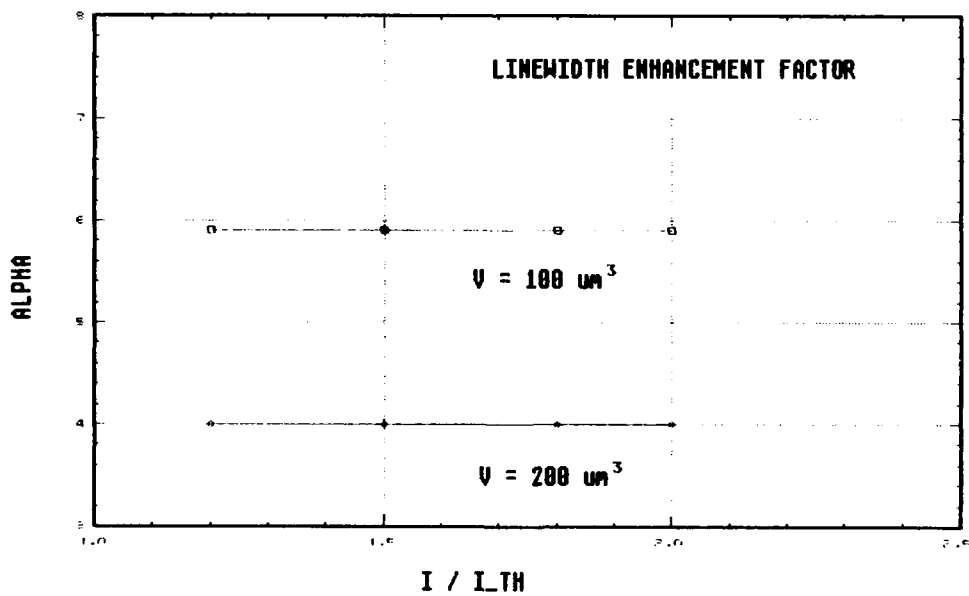
Fig. 6 Linewidth enhancement factor α versus the injection current (biased above threshold).

468

Conclusion

The method presented here permits the calculation of the linewidth enhancement factor α for a *specific* device and therefore the optimization (with regard to a reduction) by the variation of material, geometric and operational parameters. The result is that the α factor can be decreased by increasing the volume of the active cavity.

Acknowledgement

References

1. C. Henry, J. Quant. Electr., 18, 259 (1982)
2. D. Marcuse, J. Quant. Electr., 20, 1139 (1984)
3. J. Brachetti, W. Heinlein, submitted for publication
4. D. Cassidy, J. Appl. Phys., 56, 3096 (1984)
5. H. Burkhard, E. Kuphal, J. Quant. Electr., 21, 650 (1985)
6 F. Fiedler, A. Schlachetzki, Solid-State Electr., 30, 73 (1987)

LASER DIODE PHASE LOCKING USING PHOTOREFRACTIVE COUPLING

Paul D. Hillman and Michael Marciniak
Kirtland Air Force Base, NM 87117-6008

ABSTRACT

Several authors have reported strong frequency pulling while coupling laser diodes using phase conjugation. However, to our knowledge, no one has proven stable phase locking by interfering the laser outputs to show stable fringes. We have been successful in showing a stable lock, and compare our geometry with those proposed previously.

Contents

I. Introduction

Laser diodes show great promise because of their size, efficiency, and ruggedness, but are limited in their output power due to facet damage at high output densities. Use of larger facet areas yields lasers with uncontrollable transverse modes and poor wavefront quality. Many manufacturers offer arrays which add the power of "n" individual diodes incoherently, or coherently if the lasers are close enough on the chip so evanescent waves out of each gain section couple nearest neighbors. Unfortunately, in the latter case, although the nearest neighbors are phase locked (coherent with one another) they are very often $180°$ out of phase resulting in a two lobe far field pattern. Another disadvantage to this close pack arrangement is the problem of heat sinking the device. If "n" individual diodes could be made both coherent and in phase, higher brightness could be obtained when their outputs are combined into a single beam. Photorefractive coupling of individual lasers accomplishes this and several advantages will be discussed.

II. The Photorefractive Effect

To understand the relevant photorefractive phenomena that occur for laser coupling, five concepts must be brought forth. These include: index grating formation, degenerate four wave mixing, two wave mixing, beam fanning, and phase conjugate rings. In the following discussion all signs (charge, C-axis, etc.) relate to $BaTiO_3$. For other photorefractive materials they may be different, but this in no way changes the general concepts which are presented here.

If two coherent waves overlap, they will interfere to produce light and dark areas, or fringes. These fringes are not two dimensional as is usually thought since most observations are done on a screen, but they are three dimensional in space. If the waves are plane waves, the fringe intensity pattern is a layered stack of high intensity and low intensity planes. The normal to these planes (or the k vector) is normal to a vector which bisects the k vectors of the two original beams (k_1 and k_2)

and is parallel to k_1-k_2. The intensity of the interference pattern along the normal to these planes is shown in figure 1 and is proportional to $\sin^2(x)$. The light produces electron-hole pairs. The positive charges drift toward the low intensity regions producing planes of positive and negative electronic charges replicating the fringes. The charge distribution yields an electric field, according to Poisson's equation, which is shifted 1/4 period or $90°$ from the charge pattern. The electric field induces an index of refraction change through the Pockel effect. The net result is a volume index grating with repeating planes of high and low refractive index, parallel with the original fringe or intensity pattern, but shifted by $90°$. This shift is important in analyzing two beam coupling.
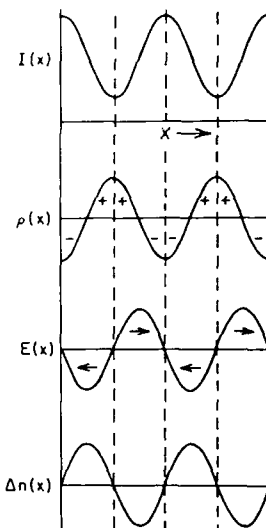
Fig. 1 Formation of a photorefractive index grating. (From ref. 1)

Degenerate four wave mixing is one means of producing a phase conjugate beam. In figure 2 there are 3 beams incident on an appropriate nonlinear medium, two pump beams, k_1 and k_2, and a signal beam k_s. The fourth beam is the exit beam k_s. The two pump beams are antiparallel and all incident beams should be of the same frequency. As depicted in figure 2 (top), if the first pump beam and the signal beam are coherent they will interfere and produce an index grating by the photorefractive effect. The second pump beam, antiparallel to the first, will Bragg reflect (scatter or diffract) from this index grating into the direction from which k_s came. A useful property of this interaction is that if the

two pump waves are phase conjugates of each other (their wave fronts are exactly opposite, for example one is converging the other diverging), the resultant index grating will not be flat planes but will have a shape due to the wavefronts of both the pump and the signal beam. When the second pump wave reflects from this grating, the aberrations of the pump waves cancel and the resultant beam, k_s^*, has a wavefront exactly opposite the signal's wavefront. This is known as phase conjugation. This property is important because the signal injected into a laser to phase lock it should have the same spatial mode profile as the laser itself to obtain good coupling. Another useful property of four wave mixing is that the pump beams can be of higher power than the signal beam. Under this condition, the beam returned antiparallel to the signal beam can be much stronger than the signal beam and it appears that the signal beam was reflected back onto itself with better than 100% reflectance!

beams interfere and produce an index grating in the photorefractive material. Due to the index grating being 90° phase shifted toward the +C axis from the interference fringes, and reflection from any grating causing a -90° phase shift, the beam propagating more towards the -C axis (beam 1) experiences no phase change upon reflecting from this grating. This beam combines with the transmitted beam (from beam 2) constructively. However, the beam propagating more towards the +C axis experiences a 180° phase shift and combines with the transmitted beam (from beam 1) destructively. The net effect is that it appears that the beam propagating more towards the +C axis (beam 2) is amplified and beam 1 is depleted. There is no crosstalk between the two beams' wavefronts. Beam 1's wavefront will be imprinted onto the formed grating. When beam 1 is reflected from the grating this wavefront shape is subtracted. This leaves beam 2' with just the wavefront of beam 2. The net useful result is that a weak diffraction limited beam may be amplified by a strong highly aberrated beam with very little detrimental effects to the wavefront.
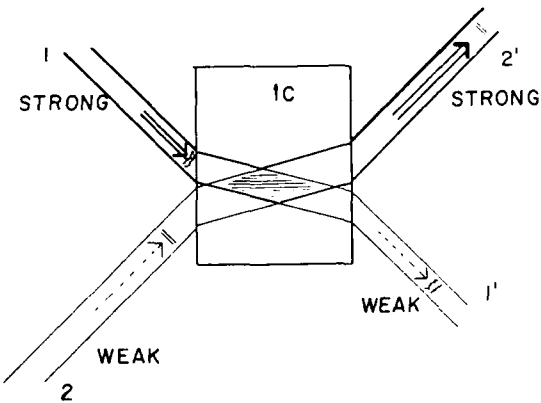
Fig. 3 Two beam coupling, aberrated beam 1 amplifies unaberrated beam 2.

Fig. 2 Degenerate four wave mixing, (top) k_1 interferes with k_s to form the grating, (bottom) k_2 interferes with k_s to form the grating.

Returning to figure 2 (bottom), the signal beam can also interfere with the second pump beam, and produce an index grating. In this case, the first pump beam reflects off the grating to produce the phase conjugate of the signal beam. Which case predominates can be determined a priori by having one of the pump beams incoherent (but of the same frequency) with the signal beam or rotating its polarization perpendicular to the signal's. When using a photorefractive crystal, the spacing of the fringes or the angle the grating vector makes with the crystal's C axis will help determine the dominant case. In the former case, either too wide (too long of a diffusion distance for the charges) or too narrow (too high of a spatial frequency) spacing of the fringes may render one case less prominent. In general, it should be remembered that the angle the signal beam makes with the pump beams is unimportant, the phase conjugate beam is always reflected back onto the signal beam!

Two beam coupling relies, as the name implies, on just two coherent input beams, figure 3. The two

Beam fanning, figure 4, was the initial photorefractive effect observed. It was initially thought to be laser damage to the crystal. By sending one beam into a photorefractive crystal, any scattered light that overlaps the original beam and is also propagating more towards the +C axis than the original beam is amplified by two wave mixing. In easily obtained geometries, this fanned light can comprise 20-30° and fully deplete the input beam. The beam will not fan beyond the C axis, thus the dotted beam, in figure 4, is not amplified.

The above phenomena and/or concepts can be combined to show how a self pumped phase conjugate ring works. It is quite useful since only a few milliwatts of input power are required, and because it is equal path, a source with a broad linewidth may be phase conjugated. As depicted in figure 5, the incoming beam is transmitted through the crystal, around the ring counter clockwise and reenters the crystal as beam 2. Beam fanning also occurs with some exactly antiparallel to beam 2. The fanned light transverses the ring clockwise and enters the crystal as beam 3. Beams 2 and 3 have travelled the same distance, they interfere and create an index grating by the photorefractive effect. This grating is initially very weak, but the incident beam Bragg

471
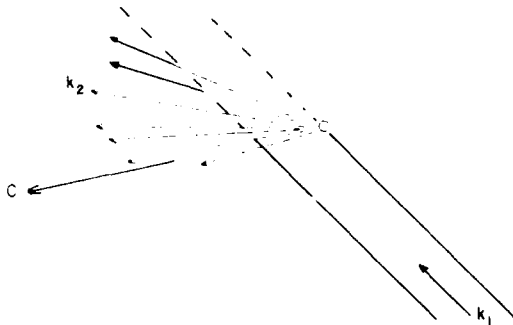
Fig. 4 Beam fanning, the crystal edges are beyond the edges of the figure.

reflects from this initial grating (with no phase change) causing beam 3 to now be much stronger. The process eventually stabilizes; the two counter propagating beams in the ring become nearly the same intensity. The resultant phase conjugate beam can be as much as 60% of the power of the incident beam.[2] The output beam is the coherent addition of the input that is divided into two beams, one that travels around the ring clockwise, the other counter clockwise, and recombined at the grating.
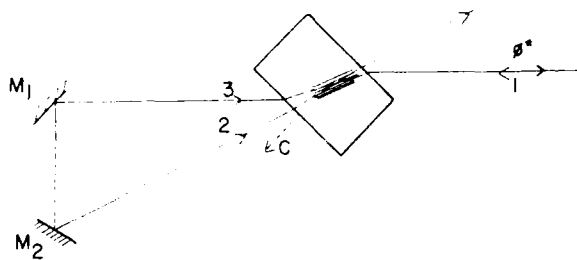
Fig. 5 The self-pumped phase conjugate ring.

The main use of such a ring, as far as this paper is concerned, is that inside the crystal, figure 5, there are two counter propagating beams that are phase conjugates of one another, exactly the re- quirement for the pump beams in degenerate four wave mixing! Sending a beam from a second laser into a photorefractive crystal with counter-propagating pump beams will yield a phase conjugate beam back into the second laser with its same mode structure, but the photons would be from the first laser. As discussed earlier, this beam must be coherent with at least one pump beam at first, i.e. the lasers must already be, at least partially, coherent (phase locked) for this to happen.

III. Previous Photorefractive Coupling Experiments

In the last three years several groups have sug- gested or reported use of photorefractive techniques to phase lock lasers: M. Cronin-Golomb et.al.[3], S. Segev et. al.[4], White et. al.[5], J. Feinberg[6], M. Kramer et. al.[7], S. Sternklar et. al.[8], A.M.C. Smout[9], and M. Ewbank[10]. Cronin-Golomb et.al. reported that they phase locked two GaAlAs lasers, Segev et. al. reported locking two GaAlAs laser arrays, references 5-7 reported phase locking other laser systems, dye and argon, while references 8-10 suggest other geometries. References 5-7 show both

that the frequencies of the two lasers were pulled to be the same and, at the same time, that the res- pective outputs show stable fringes when interfered. Unfortunately, the two groups (3 and 4) reporting diode laser phase locking only showed frequency pulling of the two sources (and only on a medium resolution monochromator, not a high resolution instrument) and not the interferometric data. The geometry and results from references 3 and 4 are summarized in figures 6 and 7. Because of the nonlinear nature of the semiconductor gain medium and the time delayed feedback (see section IV), questions about the locking phenomena with diode lasers remained.
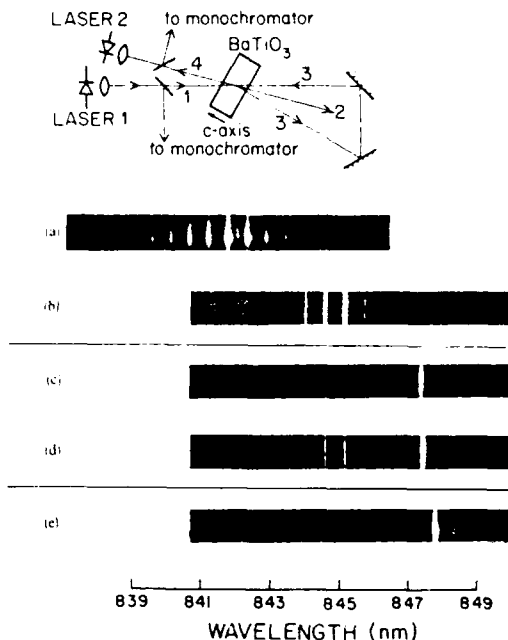
Fig. 6 (Top) Phase locking geometry, (bottom) a) uncoupled laser 1 without phase conjugate feedback, b) uncoupled laser 2 without phase conjugate feed- back, c) laser 1 coupled to laser 2, d) laser 2 coupled to laser 1, e) laser 1 with phase conjugate feedback, laser 2 off. (From ref. 3)

The early results of ref. 3 were very encouraging to many in the laser diode field as a possible way to phase lock several low power diode lasers which could then be combined into one beam with high brightness. Note that the arrangement in figure 6 is much like that suggested in the last section of this paper, and that the C axis in figure 6 was reported using a convention opposite than what is usually used. The authors of reference 3 concluded that laser 2 became coherent to laser 1 due, ini- tially, to fanned light from laser 1 injection locking laser 2 slightly. Thus, coherent four wave mixing could occur yielding stronger coupling.

We tried repeating this experiment, but with two major changes. To obtain the strongest fanned light from laser 1 onto laser 2, we placed laser 2 such that its beam was antiparallel to that shown (see fig. 9). Further, we used Sharp LT015 lasers which lase on a single transverse and single longitudinal mode when free running. Our initial results also showed the strong frequency pulling. The spectra of the lasers were almost identical, however, our

472
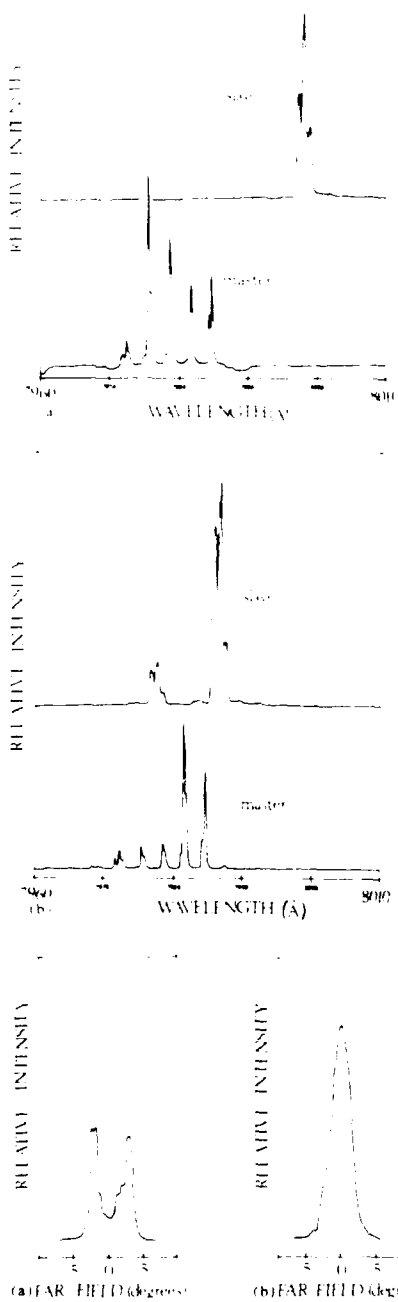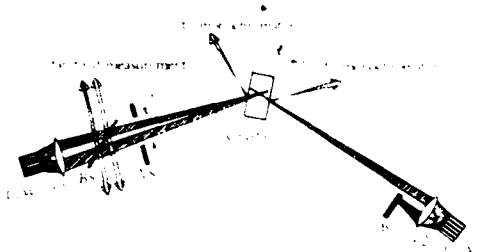
Fig. 7 (Top) Phase locking geometry, (middle) Spectra of the two arrays prior to locking and during locking, (bottom) far field of "slave" array before and after "phase locking". (From ref. 4)

single longitudinal lasers became multimode (other longitudinal modes began to lase). Often just two modes were observed. Under a variety of different path length conditions, we tried interfering the two laser outputs and did not find stable fringes (nor unstable ones as mentioned by Feinberg[6] due to the possibility of an approximate 1 Hz frequency difference between the two lasers). These negative results caused us to review the literature on conventional phase locking of diode lasers.

IV. External cavities, injection locking, and mutual coupling of diode lasers using conventional optics

External Cavities and injection locking properties of semiconductor lasers have been extensively studied over the last decade. We can't possibly review all this work but we can present results which define conditions that must be met for phase locking of laser diodes. In particular, laser diodes possess unique features (contrary to most gas, solid, and dye lasers) that are driven by the carrier dependent refractive index. This is known as the linewidth enhancement or antiguiding factor. As pointed out by Dente et. al.[11] and Tkach and Chraplyvy[12], diode lasers are very sensitive to even small amounts of feedback. At less than -80 db, some line broadening can occur. Larger amounts of feedback cause the power spectrum to become very wide and chaotic. A small change in the photon density in the semiconductor laser cavity will perturb the carrier recombination rate, the carrier density, the effective index of the gain medium, and therefore, the properties of the laser. In the model presented by Dente et. al.[11], which correlates well with experiments, reduction of the antiguiding factor reduces the feedback sensitivity and the model then predicts "normal" laser behavior.

Moeller et. al.[13] and Petitbon et. al.[14] describe theoretically and verify experimentally the injection locking properties of diode lasers. In these experiments, one laser, the master, is optically isolated from the other, the slave. The master injects a signal into the slave to phase lock it. A portion of each of the master and slave outputs were overlapped and the fringe visibility (V) measured to give a quantative description of the lock quality. This lock quality was measured as a function of the frequency difference (δ) between the slave (with no injection) and the master for several values of injected power or coupling (c). The region of δ and c space in which locking occurs is referred to as the lock band, the width of the lock band at constant coupling is referred to as $\Delta\delta$). As the injected power increased, two phenomena were prominent: the highest visibility occurred at larger detunings between the free running lasers (δ), and the width (or spread of permissible detunings, $\Delta\delta$) became wider. Representative values at weak coupling were δ = 0.2 GHz, $\Delta\delta$ = 0.8 GHz, V = 0.6, where at strong coupling δ = 15 GHz, $\Delta\delta$ = 5 GHz, V = 0.8. Such a plot is shown in figure 8. At all but the lowest coupling levels, the master laser must be at a lower frequency than the slave for a stable lock. It should be noted that the actual feedback and coupling levels are extremely difficult to measure experimentally since the level is predominately dependant on that fraction of the injected energy which couples into the lasing mode.

473
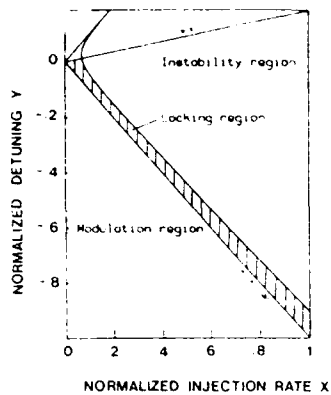
Fig. 8 Typical locking bandwidth for injection locking of diode lasers, the shaded region is where a lock occurs. (After ref. 14)

The above predicts a difficult scenario for mutual locking of lasers, which may also be looked at as concurrent injection locking. In this case, both lasers "see" each other. At perfect coupling and with low reflectance coatings on the front diode facets, the geometry may act as one long cavity but with two separate gain regions. The problem in this case occurs because locking will more than likely only occur under similar conditions (δ, c) described for injection locking. If laser 1 is considered the master, its frequency should be several GHz lower than laser 2 to obtain a good lock. But we can just as easily consider laser 2 the master, and if $\nu_1 < \nu_2$, the asymmetry results from the injection locking experiments show a poor lock. This paradox requires operating in the locking band space where δ can be both negative and positive simultaneously so either laser can be considered the master or slave. This only occurs for weak coupling (on the order of 10^{-4}) and where $\Delta\delta > \delta$ and $\delta \cong 0$.

Other requirements are necessary in the mutual coupling case. If laser 1 is to make laser 2 coherent with itself, the photons striking laser 2's facet should be coherent with those currently being emitted by laser 1 (and visa versa). Therefore, the two lasers should be no more than the longer of the two coherence lengths of the lasers apart. Further, the photons returning to laser 1 also need to be in phase with those being emitted by laser 1, so the two lasers also need to be an integer multiple of $\lambda/2$ apart. Moeller[15] has measured the locking bandwidth of two diodes that were mutually coupled using conventional optics. The coupling was found to be very critical. The lock quality increases at first then decreases as the coupling is increased. Moeller's results generally agree with the above discussion. With these points in mind, further photorefractive coupling experiments were undertaken.

VI. Photorefractive Coupling of Laser Diodes.

A schematic of our setup is shown in figure 9. Sharp LT015 GaAlAs lasers were chosen since they were single longitudinal and single transverse mode, high power (30 mW), and had the front facet antireflection coated. These lasers are index guided and have a V-channel substrate inner stripe structure. The measured coherence length was near 1/3 meter
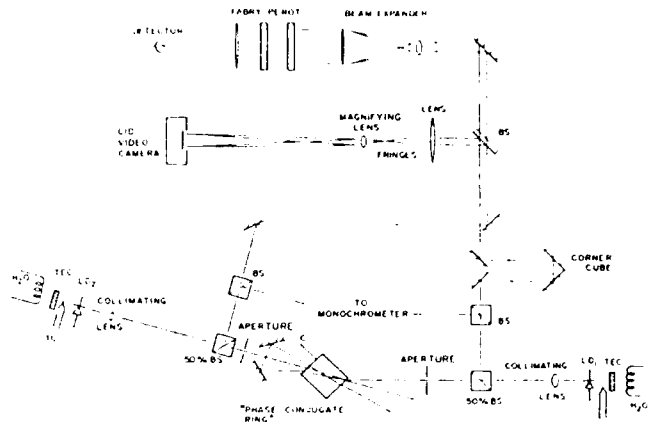
Fig. 9 Schematic of photorefractive coupling layout.

(0.9 GHz). Both lasers were operated near 60 mA (1.2 x threshold). The lasers were mounted on thermoelectric coolers which were mounted on water cooled brass blocks. Following the conclusions of the last section, each laser was each placed about 12 cm from the crystal, the total separation was about 24 cm, significantly less than the coherence length. The apertures in figure 9 were used to control the coupling strength. The path length from each laser to where the two output beams were interfered was made the same by adjusting the corner cube in the one arm. The interference fringes were magnified and projected onto a CID video camera. The Fabry-Perot was not used during this experiment. Note that this geometry is slightly different from that in figure 6 in that laser 2 is on the far side of the crystal from laser 1. This should, as explained before, make no difference. Laser 1 presumably produces the pump beams via the phase conjugate ring and laser 2 provides the signal in a four wave mixing geometry. The angle between the signal and pump beams is not critical. This location is better since the fanned light from laser 1 into laser 2 is stronger for initial injection locking of laser 2.

The procedure was as follows: after initial alignment and assurance of a phase conjugate return to laser 1 from the ring, laser 1 was blocked from the crystal. This allowed laser 2 to erase the gratings formed. The temperature and current of both lasers were tuned such that both were single mode and of the same frequency within 0.04 nm or 1.8 GHz, the resolution of the monochromator. Laser 1 was then unblocked from the crystal. Fringes were soon (< 2 seconds) seen on a TV monitor connected to the video camera. Slight current tuning (< 1 mA) of either laser maximized the fringe visibility. However, after about one minute the fringe visibility went to zero and no amount of tuning of either laser recovered the fringes. It was found that blocking the ring mirrors and repeating the procedure yielded fringes that did not lose visibility after 5 minutes. Thus, the lasers were definitely coherent or phase locked. Figure 10 shows the spectra of laser 1 (top), laser 2 (middle) and the image of the overlapped beams while the crystal was blocked from laser 1 (no coupling). Figure 11 shows the same when the crystal was unblocked from laser 1; the fringe visibility was about 0.4. The break up of the laser spectra vertically (parallel to the monochromator slits) is because the light from each
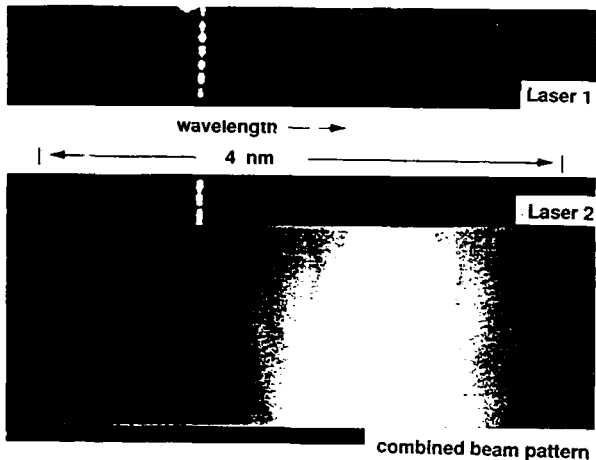
Fig. 10 Spectra of laser 1 (top), laser 2 (middle), and overlapped beams, no coupling case.
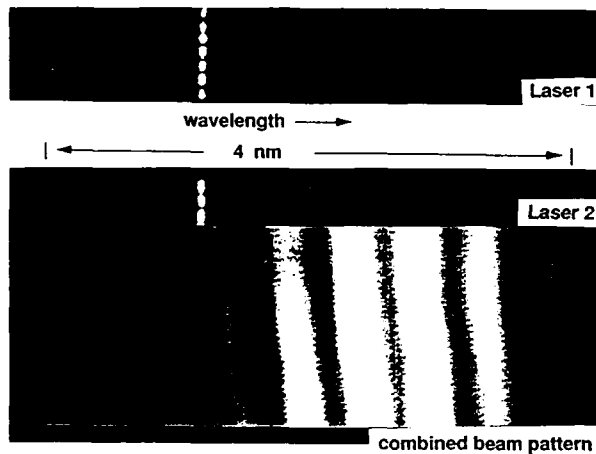
Fig. 11 Spectra of laser 1 (top), laser 2 (middle), and overlapped beams, photorefractive coupling allowed.

laser was brought to the monochromator via a fiber bundle; the bright spots are individual fiber ends imaged onto the entrance slit. Initially the crystal was cooled to 11° C as recommended by Cronin-Golomb et. al.[3], it was later found that cooling the crystal was unnecessary.

VII. Discussion

The above results are puzzling in two aspects: a) how do the two beams couple in the experiment without the ring, and b) in the first experiment, why did the visibility decrease to zero after one minute?

The coupling of two beams is depicted in figure 12. Both beams enter the crystal and fan toward the C axis. The fan is almost continuous. Each fan ray is related to a set of gratings due to interference between the scattered light and the original beam (see figure 4 and the discussion in section II). Each beam creates several sets of these gratings. There is only one pair, one from each beam, that has the same direction and spacing. This pair satisfies
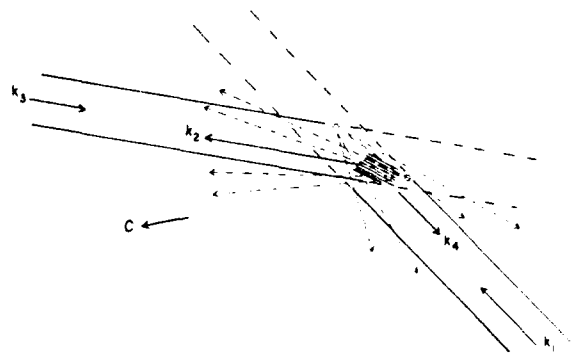
Fig. 12. Coupling of just two input beams, the crystal edges are beyond the edges of the figure.

the relation,

$$k_1 - k_2 = k_g = k_3 - k_4. \tag{1}$$

These two gratings reinforce each other and direct most of the beams' energy into their direction, causing them to build up and to deplete the other gratings. If k_1 and k_3 are nominally of the same wavelength the beams are directed toward each other by this grating. The beams do not have to be coherent for this phenomena to occur. In fact, if they are, two beam coupling may predominate. An advantage of this technique for laser coupling is the simplicity of alignment, the two output beams from the lasers just have to overlap within the crystal. This reduces the alignment constraints over conventional optical coupling by at least one dimension.

Note that the grating with its k vector in the same plane as k_1 and k_3 is not the only one to satisfy eq. 1. Since there is scattering of each beam out of this plane, there is also some fanning out of this plane. This allows k_2 (and k_4) to be a locus of rays that trace an ellipse. The ellipse is almost continuous going from antiparallel to k_3 (k_1) to the transmitted portion of k_1 (k_3) as its vertices (see D. Statman and B. Liby(16) or G. Salmo et. al.[17]). S. Sternklar and B. Fischer[18] state that slight focusing or spatial filtering the input beams prevents this out of plane diffraction.

It should also be noted that our final geometry is the same as that shown in figure 7 with one small exception, ref. 4 states the C axis is in the same direction as Z. Our experience and the above theory requires that the C axis lie between both input beams such that both beams can fan into each other. This arrangement has become known as the Double Phase Conjugate Mirror (DPCM). As presented, it is not a true four wave mixing interaction. At first glance, one might think the interaction regions in the mutually incoherent beam combiner[9] and the bird-wing conjugator[10] are the same type of coupling. However, Yeh et. al.[19] point out that in these geometries the coupling regions may be true four wave mixing interactions. On a final note, Sternklar and Fischer[18] demonstrate that this geometry phase conjugates the wavefront of each input beam with no cross talk but with the other beam's photons. Therefore, the beam injected into each laser should match that laser's mode. This may be the technique's biggest advantage over conventional coupling.

The other question posed at the beginning of this section was, "Why did the fringe visibility drop after one minute with the ring in place?" Figure 13 shows the spectra of laser 1 (laser 2 off) as the phase conjugate beam builds in intensity. Each trace is taken in 1/30 second and the vertical offset of each trace represents time (15 seconds per trace). The feedback causes the spectra to widen considerably. In the geometry with the ring, the DPCM builds very quickly (< 2 seconds) and the lasers phase lock. After a minute, the self-pumped ring phase conjugator builds to a point where the spectra becomes wide enough that the coherence length of the lasers becomes shorter than their separation and the phase lock is lost. Due to the DPCM still providing strong coupling between the lasers, they still emit the same spectrum or frequency. However, they are not phase locked. Closer examination of figure 6 shows that due to the two mirrors, laser 1 is essentially pumping the crystal from the lower right and this geometry therefore still contains a DPCM. This explains the observed coupling reported in ref. 3.
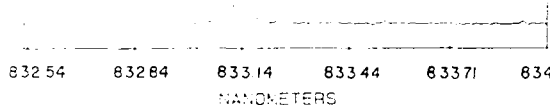
Fig. 13. Spectra of a diode laser with increasing phase conjugate feedback. The lowest (no feedback) spectra's width is probably due to instrument resolution.

The main advantages of photorefractive coupling are: a) injecting a matched mode into each laser; and b) reducing the alignment constraints over conventional coupling. Two other advantages not quite as apparent are: a) since the coupling depends on the fringe visibility in the crystal, which in turn depends on the laser linewidth, this may provide feedback to optimize, or at least stabilize critical coupling level; and b) a grating ion may spatially adjust itself to fulfill the $m\lambda/2$ requirement for the separation of the lasers. We are presently measuring the locking bandwidth (V, δ and c) using this technique to compare it with conventional coupling.

VIII. Conclusions

We have demonstrated coherent operation of two semiconductor lasers using photorefractive coupling. The lock was stable for over five minutes. Cooling the crystal was unnecessary. We believe we are the first to accomplish this. At the same time, we came to the conclusion that at the weak coupling levels required, the lasers need to be closer than their coherence length. We also conclude that for mutually coupling diode lasers, the locking band is very small.

Starting with lasers that, when free running, are much more than several linewidths apart, frequency pulling requires fairly strong injection to bring their frequencies together. This strong injection causes strong linewidth broadening which reduces the coherence length; and hence destroys the lock. Lasers integrated on the same chip should not have this problem.

Finally, it should be remembered that although two sources may have the same nominal wavelength, they are not necessarily coherent or phase locked, which is a necessary condition for beam combining to obtain maximum brightness.

Acknowledgements

References

1. Feinberg, J., "Optical Phase Conjugation in Photorefractive Materials", in "Optical Phase Conjugation", R. Fisher, Ed., p. 422, Academic Press, New York (1983).
2. Beckwith, P.H., "Self Pumped Phase Conjugation at 830 nm", submitted to Opt. Lett. (1988).
3. Cronin-Golomb, M., A. Yariv, and I. Ury, "Coherent coupling of diode lasers by phase conjugation", Appl. Phys. Lett. 48, 1240 (1986).
4. Segev, S., S. Weiss, B. Fischer, "Coupling of diode laser arrays with photorefractive passive phase conjugate mirrors", Appl. Phys. Lett. 50, 1397 (1987).
5. White, J. O., G.C. Valley, R. A. McFarlane, "Coherent coupling of pulsed dye oscillators using nonlinear phase conjugation", Appl Phys. Lett. 50, 880 (1987).
6. Feinberg, J., and G. D. Bacher, "Phase-Locking lasers with phase conjugation", Appl Phys. Lett. 48, 570 (1986).
7. Kramer, M., S. Sifuentes, C. Clayton, "Phase locking of ring dye lasers using incoherent beam coupling", Appl. Opt. 24, 1351 (1988).
8. Sternklar, S., S. Weiss, M. Segev, and B. Fischer, "Beam coupling and locking of lasers using photorefractive four-wave mixing", Opt. Lett. 11, 528 (1986).
9. Smout, A.M.C. and R. W. Eason, "Analysis of mutually incoherent beam coupling in BaTiO$_3$", Opt. Lett. 12, 498 (1987).
10. Ewbank, M. D., "Mechanism for Photorefractive Phase Conjugation using Incoherent Beams", Opt. Lett. 13, 47 (1988).
11. Dente, G. C., P. S. Durkin, K. A. Wilson, C. E. Moeller, "Chaos in the Coherence Collapse of

Semiconductor Lasers", IEEE J. Quantum
Electron., QE-24, 2441 (1988).

12. Tkach, R. W., and A. R. Chraplyvy, "Regimes of
Feedback Effects in 1.5-μm Distributed Feedback
Lasers", J. Lightwave Tech., LT-4, 1655 (1986).
Also see paper WF.2 this conference.

13. Moeller, C. E., P. S. Durkin, and G. C. Dente,
"Mapping the Injection-Lock Band of Semicon-
ductor Lasers", accepted to IEEE J. Quantum
Electron. January 4, 1989.

14. Petitbon, I. P. Gallion, G. Debarge, and C.
Chabran, "Locking Bandwidth and Relaxation
Oscillations of an Injection-Locked
Semiconductor Laser", IEEE J. Quantum Electron.,
QE-24, 148 (1988).

15. Moeller, C. E., private communication.

16. Statman, D. and B. Liby, submitted to JOSA B
(1988).

17. Salamo, M. J. Miller, W. W. Clark III, G. L.
Wood, E. J. Sharp, and R. Neurgaonkar, "Photo-
refractive rainbows", Appl. Opt. 27, 4356
(1988).

18. Fischer B. and S. Sternklar, "Self Bragg matched
beam steering using the double color pumped
photorefractive oscillator", Appl. Phys. Lett.
51, (1987) and Sternklar, S. and B. Fischer,
"Double-color-pumped photorefractive oscillator
and image color conversion", Opt. Lett., 51,
(1987).

19. Yeh, P., T. Y. Chang, and M. D. Ewbank, "Model
for mutually pumped phase conjugation", J. Opt.
Soc. Am. B, 5, 1743 (1988).

Fiber Lasers: Past, Present and Future
Elias Snitzer
Polaroid Corporation, 38 Henry Street, Cambridge, MA 02139

Abstract

With the development of low loss fibers and the availability of laser pump sources, there has been a renewed interest in rare earth doped glasses in fiber form which can be operated CW. Of particular interest have been neodymium emitting at 1.06μm and 1.33μm and erbium at 1.55μm. The latter two are in the wavelength windows that are currently used in fiber optics for telecommunications. The interest in neodymium emitting at 1.06μm is for the same motivation as large neodymium glass systems, mainly for its efficient conversion of pump to laser light output. After a review of the early work on fiber lasers, the current activity with various rare earth fibers will be described. The laser devices to be described are CW oscillators, amplifiers, mode locked outputs, and second harmonic generators.

Introduction

Continuous wave rare earth fiber lasers in low loss glass are the most recent development in glass lasers. In this paper a brief history is presented of the different "eras" of glass laser development. This is followed by a description of the early work on pulsed fiber lasers. Finally the results of selected experiments performed at Polaroid are presented.

The work on glass lasers is primarily work on neodymium lasers emitting at 1.06μm. While neodymium has been made to emit at 0.9 and 1.4μm and laser emission from other rare earths has been obtained, such as from ytterbium, holmium, erbium, praseodymium, samarium, and thulium, the high efficiency and ease of operation of neodymium at 1.06μm has made this glass laser continue to be the one of greatest interest. Erbium emitting at 1.54μm has received attention as an eye safe laser for range finding applications. More recently both erbium at 1.55μm and neodymium at 1.33μm have received attention because of their potential use as optical amplifiers in a communication system.

History

The earliest phase of rare earth glass lasers started with neodymium emission at 1.06μm.[1,2] In the early 60's the focus of attention was on scoping out the possible laser systems. Lasers were a new technology which received a great deal of attention from the scientific community, in part because of generous government funding. This work established the various lasing ions and their characteristic wavelengths of emission. Configurations and host compositions were explored that showed better thermal behavior, that is materials and configurations that showed minimal wave front distortion under high pumping conditions. There was also attention given to self Q-switching glasses which resulted from transient color centers that showed saturable absorption. In the first two references below the first one emphasizes the materials characteristics of glass lasers and the other emphasizes the device aspects.

The second phase of glass laser work was a device emphasis that resulted from the recognition that one could readily make high power pulsed lasers in the long pulse mode ($\sim$1ms), Q-switched, with or without mode locking, or in oscillator-amplifier combinations. For glass lasers the applications that emerged were in the three catagories of

1. range finders,
2. materials processing, such as welding and cutting,
3. high temperature plasma formation.

In the first two categories the different specifications required for different applications led to trade off choices between neodymium in glass vs. neodymium in YAG. In those situations in which low threshold and CW or high repetition rate applications were important, YAG with its considerably larger gain cross section per ion and better thermal conductivity often ended up being the preferred host. However, where larger pulse production was called for, where cost was an issue, or where mode locking could take advantage of the broader fluorescent light, the vitreous host was preferred. There were some areas where the choice was made based more on taste. For example, small Q-switch range finders for use in field military applications tended in the US to be YAG devices. Whereas in Western Europe the preference was for glass lasers in which the gain cross section per ion was made larger by the selection of special hosts, such as Al-Li-Mg silicates or phosphates. In materials working applications, the activity was divided between glass and YAG with more of it directed towards YAG in the US, but the converse was the case in Europe, including the Soviet Union.

The growing use of laser range finders and the concern for laser eye safety resulted in a search for eye safe laser range finders.[3] This lead to an erbium laser emitting at 1.54μm which could be readily Q-switched.[4] It was eye safe because of the water absorption in the eye preventing focusing of the energy on to the retina.

In the late 60's, range finders and materials working became established commercial activities, and the focus of research attention shifted to the generation of high temperature plasmas, particularly for controlled thermonuclear reactions (CTR). Although also promoted in Europe, soon Lawrence Livermore Labs was a dominant player in this activity, not only by the large amounts of money spent for glass laser development and procurement, but also by the technical leadership on rare earths in glass, device analysis and experimental work.[5,6] There was also a considerable activity in the Soviet Union on glass lasers for materials processing and in particular large oscillator amplifier combinations for CTR.[7]

The overwhelming materials concern for CTR was for a low non-linear index of refraction so as to get the highest possible light intensity without self-focusing and its consequent glass damage. This calls for low values of n_2 in the equation $n = n_0 + n_2 E^2$, where n_0 is the index of refraction for low intensity light and E is the electric field for the light wave. A second consideration for CTR applications related to high gain cross section glass. It is determined by the oscillator strength for the transition, which implies short life time for fluorescence, and narrow line width at 1.06μm. Although fluoride glasses looked promising, the difficulty in their fabrication in large sizes precluded a serious pursuit of these hosts. Of the oxides, alkali phosphates became the preferred host. Where the original potassium barium silicate had a gain cross section for neodymium at 1.06μm of 1.5×10^{-20} cm^2, a typical new phosphate host gives a cross section of 4×10^{-20} cm^2.

The next major development was the CW fiber laser, of which this report is an update. Fiber lasers had been investigated earlier, and more of these early experiments will be discussed presently. The initiation of this phase of glass laser work resulted from the recognition that with laser diodes to provide high brightness pumps at 0.8μm, where neodymium is strongly absorbing, and with the development of low loss glass fibers of predominately fused silica as the host, in small diameters there is not a

serious problem with heat loading and CW operation is readily obtained.[8] The era of the end pumped CW fiber laser was initiated by Stone & Barrus in 1973 and activities have since been undertaken in a number of laboratories, such as University of Southampton, British Telecom, Bell Labs, Stanford U., NTT, GTE and of course Polaroid. Of particular note is the extensive work at U. Southampton.[9]

Before describing in detail some of the results obtained with the CW fiber lasers, some of the general characteristics of these devices that distinguishes them from other lasers are noted. The most obvious feature that has already been alluded to is the ability to make a CW device. Another interesting characteristic is the ability to pump these devices well above threshold. For example, with reflectors that are 98% on a single mode fiber we have obtained thresholds for laser action as low as $75\mu W$. Yet the laser is capable of being operated with a pump of several hundred mW without saturation or degradation due to thermal effects. Another distinction of these lasers is that the host is a low loss glass, which leads to the situation that if microbends are avoided the losses are not dependent on absorption or scattering along the length of the fiber, but instead depend on the end reflectors. Both the values of their reflectivities and the perpendicularity of the end surface relative to the axis of the fiber are important.

Early Fiber Laser Work

The early fiber laser work utilized a flash lamp.[10] The first reported activity demonstrated single mode operation in fibers that were small enough to exhibit one or a few modes of operation in the device. Later there developed some specific interest in device applications for fibers. It is interesting that one of the applications was to use the fiber laser as a power amplifier. The idea was to start with a suitable coherent light source such as for example the HeNe laser emitting at $1.0621\mu m$. A neodymium fiber could be used to amplify this light and still preserve the coherence inherent to the HeNe laser. The experiment that was done used a single mode fiber with a $15\mu m$ diameter core and gave 40dB of gain to increase the HeNe output of $230\mu W$ up to 0.6W.[11] The output from the amplifier was demonstrated to have a coherence length in excess of 12.2 meters with a Michelson interferometer. In a second experiment, a $InAs_{0.17}P_{0.83}$ laser diode operating at $1.063\mu m$ had $4\mu W$ of its output focused into the same fiber amplifier for 47dB of gain to produce 0.2W of output.[12]

In another early experiment, the fiber laser was used as the preamplifier in a detection system. In such a device, the signal S is amplified by a gain G. In addition, the spontaneous emission due to the inversion associated with the laser constitutes an input noise N which experiences a net gain of G—1. The output is given by S G + N(G—1). It can be shown that the spontaneous emission noise N, when expressed as photons emitted per second, is given by the product of the optical bandwidth ($\Delta\nu$) multiplied by the number of propagating modes.[13] For low noise, the cross section can be reduced to single mode propagation. In addition to limiting propagation to a single mode, narrowing the optical bandwidth would further reduce the noise. An alternative strategy would be to use a post electronic detector which can discriminate against the DC spontaneous emission. Under the latter conditions, the noise is the fluctuations in the number of photons arriving in a given time period. The basic strategy of the use of a fiber laser preamplifier is to amplify the signal to the point where the noise of the input impedance in the post-electronic detector is not limiting, but instead the limitation is associated with the spontaneous emission noise. This in principal would allow one to detect only a few 10's of photons in a pulse with bit error rates of 10^{-9} or less. In 1969, such a detector was used to detect a Q-switch neodymium glass laser pulse with a line width of 10nm with a detectivity of 4×10^3 photons in the pulse. A value which is not very exciting today but in '69 was an achievement.

Current Fiber Laser Work

Although a number of glass lasers had been made to operate, the emphasis has been on neodymium at $1.06\mu m$ and $1.33\mu m$ and erbium at $1.55\mu m$. One of the wavelength bands for communications is in the region of $1.3\mu m$. While neodymium has a fluorescence in this region for the $^4F_{3/2}$-$^4I_{13/2}$ transition with its peak at $1.33\mu m$, the typical behavior in an MCVD prepared aluminosilicate host is laser emission at the longer wavelength of $1.4\mu m$. This results because in the $^4F_{3/2}$ state there is not only the downward transition to give gain but there is also the $^4G_{7/2}$ state at a higher energy value which provides more absorption than gain at $1.33\mu m$. The reverse is the case at $1.40\mu m$, because the excited state absorption is at the edge of the gain transition. There has been a recent interest in the heavy metal fluoride glasses as the host because the absorption lines are narrower and shift slightly such as to permit gain at $1.33\mu m$.[14]

Figure 1 shows the energy level diagram for the first three pump absorption bands and the transitions responsible for the observed laser emisssion of Nd in silicate glasses. Figure 2 gives the corresponding absorption specturm. The concentration of 1.1×10^{20} Nd ion/cc corresponds to approximately 1.5 wt % Nd_2O_3. The limit of solubility for Nd is SiO_2 alone is very low (of the order of a few hundred ppm). While low loss fibers can be made with this low concentration and still absorb essentially all of the pump light in end pumping, the advantage of the higher concentration is that it shortens the length of the device and also makes possible a substantial simplification in the pump by permitting the use of double clad, offset core configurations, which will be discussed later. It is customary to add small amounts of other constituents, such as GeO_2, P_2O_5, or Al_2O_3, which affect the index of refraction of the core and the thermal properties of the glass.

The fluorescent spectra for the aluminosilicate glass described is dependent on the pump wavelength. This is shown in Fig. 3. Other compositions have been made which exclude aluminum but have small concentrations of phosphorous which do not have a wavelength dependent pump characteristic. This points to a single site for Nd in a Si-P host but to multiple sites in Si-Al hosts.

Most of the work done in this laboratory has pumped with laser diodes operating in the region of $0.8\mu m$ or the krypton ion laser emitting at 0.752 and $0.799\mu m$. The core-cladding numerical aperture (NA), is defined by $(n_1^2-n_2^2)^{1/2}$, where n_1 and n_2 are the indices of refraction for core and cladding. Typical NA's were from 0.1 to 0.15. The cladding diameter could be of the order of $100\mu m$ up to 3mm. The large diameter cladding had a number of attractive features. The rod diameter was large enough so that it was not necessary to put a polymer buffer coating on the outside of the rod to avoid breakage. This made it possible to place the rods in a vacuum chamber for deposition of dichroic reflectors on the ends of the rods without concern for out gasing from the buffer coating. Also, with such a large area it was possible to grind and polish flats that were within 5 minutes of perpendicularity to the fiber axis. Lasers of this construction were operated with lengths between 5mm and 30cm. When pumped directly into the core, dichroic reflectors were used on the end of the rod. In Table 1 are given the values for the reflectivity used for laser emission in the three neodymium bands and the threshold values for laser action. In Fig. 4 are given the laser spectra at $1.06\mu m$ for three different values of the pump relative to threshold pump power P_{th}. Slopes above threshold for laser emission vs. absorbed pump power higher than 60% have been observed.

An important parameter is the value of gain in a single mode fiber per absorbed pump power. The gain is related to the parameters of the fiber and neodymium properties by: Gain (dB) = 4.3 P (A h ν)$^{-1}$ (σ τ) F, where A is the area of the core, h ν the

energy of the pump photon, σ is the gain cross section for neodymium in glass (about 2×10^{-20} cm^2), τ the fluorescent lifetime of neodymium (approximately 0.4 ms) and F is a factor that takes account of the field distributions for both the pump and laser emissions.[15] By pumping through a fiber of the same NA and diameter as the neodymium fiber, the measured value was 0.47dB/mW for a fiber with an NA of 0.15 and core diameter of 4μm.

Figure 5 shows a configuration in which a frequency selective element in the form of a thick film hologram grating is incorporated in the cavity to give stable laser emission at $1,083.41 \pm 0.01$nm for possible use in a magnetometer based on optical pumping of helium.

By use of an acousto-optic modulator within a cavity with end reflectors 150cm apart, for a single mode laser fiber length of 5cm and a lens used to collimate the divergent beam from the end of the rod, mode locked emission was obtained, whose characteristics are shown in Fig 6. The pulses are 0.1ns in duration, which is an order of magnitude shorter than previously reported mode locked fibers.[16] The shortening of the pulse width is due in part to less dispersion in the shorter fiber, which in turn is made possible by the higher concentration of Nd.

A major problem in the use of fiber lasers is end pumping. If the fiber is single mode, this requires a single mode pump source. Since there is always some loss in power conversion from pump to laser, the brightness of the laser output is less than the pump. To solve this problem, fibers were made which consisted of the neodymium containing core surrounded by a first cladding of lower refractive index, which in turn was surrounded by a second cladding of still lower index.[17] Pump light is focused onto the first cladding. The index of refraction scans on a preform from which this fiber was made are shown in Fig. 7. The area of the first cladding is one hundred times that of the core. The neodymium containing core of high index of refraction is offset from the center of the first cladding. If this was not done, the skew rays, which constitute the bulk of the light incident of the first cladding, would miss the core. From measurements on the preform it can be established how absorbing the core is. The best absorption of pump light would correspond to a uniform dispersion of the same amount of neodymium through the first cladding. As compared with this theoretical best value it was found that with the core in the center of the first cladding the absorption per unit length of pump light is reduced to less than 5% of theoretical best value. By offsetting the core as shown in Fig. 7, the absorption increased to 27%. This points up the very significant advantage of high concentration of neodymium. If only a few hundred parts per million concentrations are used, the fiber lengths for 10dB of pump power absorption would be many hundreds of meters. In comparison, with the higher concentration in the Al-Si glass, 8 meters of fiber were adequate to give a threshold of 7mW and an output of 49mW for 120mW of absorbed pump power for an overall efficiency of 41%.

A number of experiments were performed on erbium fibers to give laser amplification or oscillation in the region of 1.55μm.[18] Figure 8 gives the absorption and fluorescent spectra for 3×10^{19} erbium ions per cc in Al$_2$O$_3$ doped SiO$_2$ glass. By pumping in the region of 1.47-1.51μm inversion could be obtained in this 3 level system. The data obtained for various pump bands is shown in Fig. 9. A color center laser was used to generate the pump power and its output was focused onto the fiber core. The spread in the pump data is an indication of the experimental error associated with this end pumping experiment. The ability to pump at a wavelength so close to the laser emission at 1.55μm is due to the broadening of the upper and lower manifolds. In another set of experiments an MCVD fabricated fiber with 1.5×10^{19} Er ions/cc and 9.5×10^{20} Yb ions/cc gave laser action in erbium at 1.55μm by first pumping the ytterbium, which subsequently transfers its energy to erbium.

A very interesting observation has been made in second harmonic generation in fibers in which there has been "optical damage".[19] In order to produce second harmonic generation, it is necessary that the material lack a center of symmetry both microscopically and macroscopically. In addition, it is necessary to phase match the fundamental and second harmonic wavelengths. For large single crystals the latter implies that the indices of refraction at the two wavelengths be the same. This can be obtained in some non-cubic crystals by matching the extraordinary ray at one wavelength to the ordinary wave at the other wavelength. Glass lacks a center of symmetry microscopically but the random matter of glass makes it a centro-symmetric material on a macroscopic scale. The experiments were conducted with fibers whose cores were circular, single mode and low NA, and the core material was initially homogeneous and istropic. It was found that after illumination for several hours with high intensity Q-switched, mode locked light from a YAG laser, the fiber was capable of producing second harmonic when illuminated only at 1.06μm. The original observations were made on glasses which contained in the core GeO$_2$ and P$_2$O$_5$.[19] In Table 2 are shown the results of some experiments in which the constituents added to SiO$_2$ are listed in the first column. The NA for the fibers were all about 0.12. The peak power for 1.06μm light is given in the second column. The illumination was done with 5% of 0.53μm light added to the 1.06μm light to shorten the exposure times as described by Stolen and Tom.[20] The conversion to the second harmonic is shown in the third column. Other laboratories have obtained substantially higher values than shown in column 3; however, column 3 does indicate the relative importance of the additives in fused silica that are responsible for the self-organized, second harmonic generating fibers. Glasses were prepared which contained either only GeO$_2$ or only P$_2$O$_5$ or both with silica. The effect was even larger for GeO$_2$ alone than with both the germania and phosphorous present. With only phosphorous, there was no observed second harmonic light. An alumino-silicate was prepared which produced some 0.53μm light but considerably down from the germania containing glass. The biggest surprise was that by the addition of 1/2 wt % Yb$_2$O$_3$ to the alumino-silicate glass, there was produced a readily measurable amount of second harmonic emission. This suggests that the optical damage which makes the effect possible is not peculiar to germania but is generic to a family of possible defects in glass. The apparent lack of phase matching has been explained on the basis that the non-linear tensor which relates the fundamental to the second harmonic could have its sign reversed by the process of optical damage in step with the reversal in phase between the fundamental and second harmonic emissions.[20]

References

1. E. Snitzer, Appl. Opt. 5, 1487 (1966)
2. C.G. Young, Proc. IEEE, 57, 1267 (1967)
3. F.W. Quelle, SPIE Seminar on Laser Range Instrumentation, El Paso, TX (1967)
4. J.P. Segre, Proc. Electro-optics Cont, Montreux, Switzerland (1974)
5. "Laser Program Annual Report," Lawrence Livermore Laboratory, UCRL-50021-75 (1976), UCRL-50021-76 (1977) and UCRL-50021-77 (1978)
6. L.A. Riseberg, M.J. Weber, "Progress in Optics, Vol XIV" North-Holland, Amsterdam (1976)
7. V.N. Alekseev et.al. Sov. J. QE-16, 126 (1976)
8. J. Stone and C.A. Burrus, Appl. Phys. Lett 23, 388 (1973)
9. R.J. Mears, L. Reekie, S.B. Poole and D.N. Payne, Electron. Lett. 21, 738 (1985)
10. C.J. Koester and E. Snitzer, Appl. Opt. 3, 1182 (1964)
11. G.C. Holst, E. Snitzer, R. Wallace, IEEE QE-5, 342 (1969)
12. B. Ross and E. Snitzer, IEEE QE-6, 361 (1970)
13. E. Snitzer, Proc. of the First European Electro-optics Markets and Technology Conf., Geneva (Sept. 1972) 374 P.374
14. M.J. Miniscalo, L.J. Andrews, B.A. Thompson, R.S. Quimby, L.J.B. Vacha, M.G. Drexage, Electron. Lett. 24, 28 (1988)
15. M.J.F. Digonnet and C.J. Gaeta, Appl. Opt. 24, 333 (1985)
16. J.P. Akock, A.J. Ferguson, D.C. Hanna, A.C. Tropper, Electron. Lett. 22, 268 (1986)
17. E. Snitzer, H. Po, F. Hakimi, R. Tumminelli, B.C. McCollum, Optical Fiber Sensors Conf. New Orleans (1988) postdeadline paper PD 5.
18. E. Snitzer, H. Po, F. Hakimi, R. Tumminelli, B.C. McCollum, Optical Fiber Communications Conf. New Orleans (1988) postdeadline paper PD 2.
19. U. Osterberg and W. Margulis, Opt. Lett. 11, 516 (1986)
20. R.H. Stolen and A.W.K. Tom, Digest of Conf. on Lasers and Electro-Optics, Baltimore (1987), paper THL2.

REFLECTIVITY	LASER EMISSION AT		
	1.06µm	0.905µm	1.4µm
$R_{0.8µm}$	10%	15%	15%
$R_{1.06}$	>98%	20%	10%
$R_{0.905}$	—	94%	—
$R_{1.4}$	—	—	99%
THRESHOLD PUMP POWER	0.09mw	4.3mw	6mw

Table 1 Values for the end reflectors and threshold powers for cw fiber laser emission from Nd at 1.06, 0.9 and 1.4 µm.

CORE GLASS SiO_2 PLUS ADDITIVES IN WEIGHT PERCENT	PEAK POWER	2nd HARMONIC CONVERSION EFFICIENCY
4.2 GeO_2 3.4 P_2O_5	40 Kw	7×10^{-8}
4.3 GeO_2	40 Kw	4×10^{-4}
8.1 P_2O_5	40 Kw	$< 10^{-10}$
2.7 Al_2O_3	40 Kw	10^{-8}
3.6 Al_2O_3 0.5 Yb_2O_3	25 Kw	2×10^{-8}

Table 2 Self-organizing second harmonic generating single mode fibers.
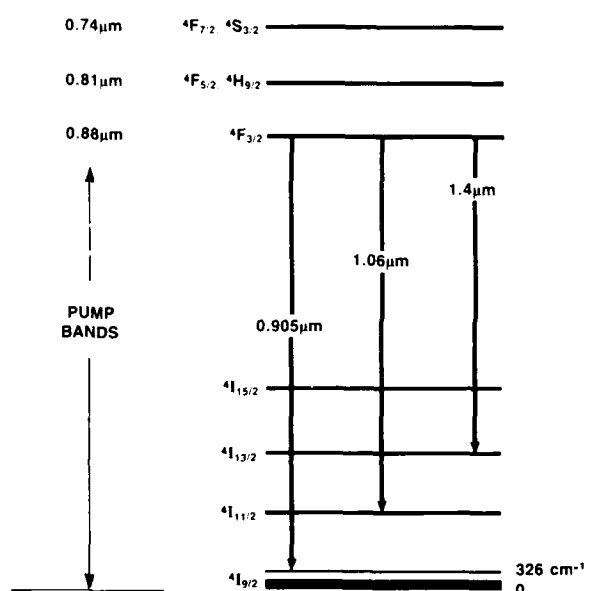
Fig. 1 Low lying energy levels of trivalent neodymium and the laser emissions in silicate glasses.
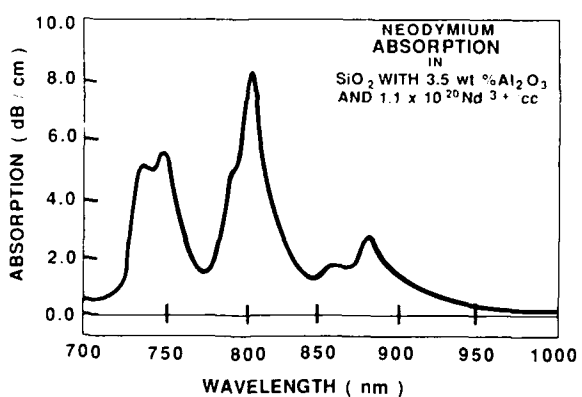
Fig. 2 Infrared absorption spectrum of 1.5 wt % Nd_2O_3 in SiO_2 with 3.5 wt % Al_2O_3
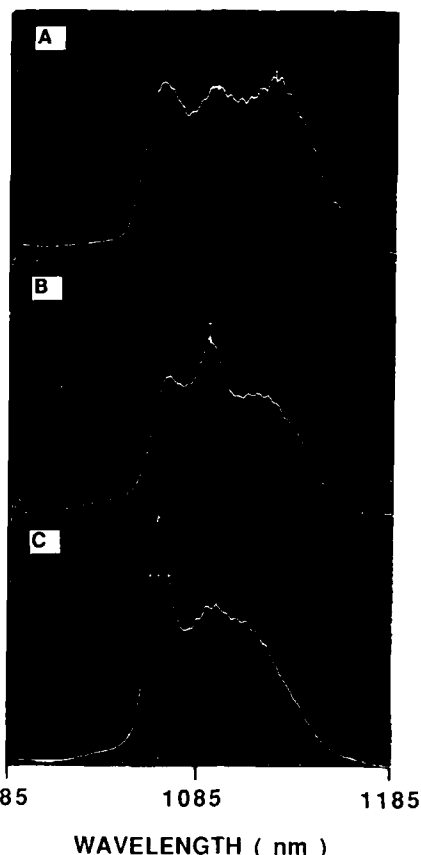
Fig. 3 The dependence of the fluorescent spectra in the $^4F_{3/2} - {}^4I_{11/2}$ transition on the pump wavelength for an MCVD prepared SiO_2 core with 1 wt % Nd_2O_3 and 3.6 wt % Al_2O_3. The pump wavelengths are 845, 826, 806 nm in frames A, B, and C, respectively
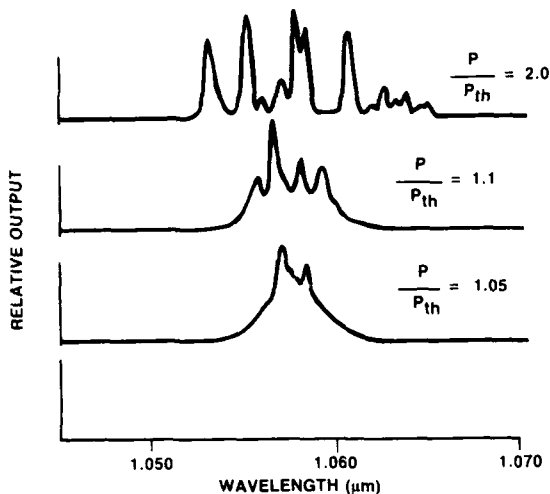
Fig. 4 The dependence of the laser spectrum on pump power above threshold P_{th} for 1 wt % Nd_2O_3 in SiO_2 with 3.6 wt % Al_2O_3.
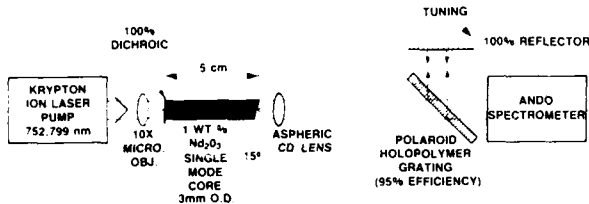
Fig. 5 Schematic for a tunable Nd fiber laser. Stable emission was obtained at 1083.41 ± 0.01 nm.
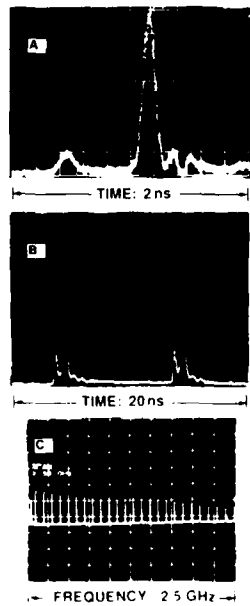
Fig. 6 The Q-switched output from a 5 cm long fiber in a 150 cm long cavity which contained an acousto-optic modulator. Frames A and B are time traces and C is the spectrum of the beat notes.
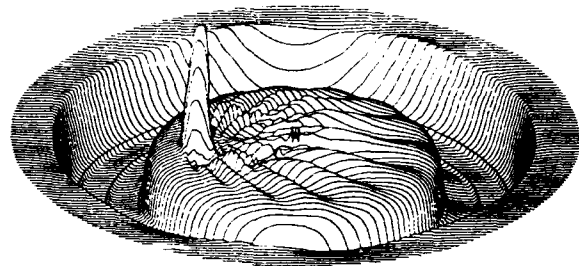
Fig. 7 Two dimensional index of refraction profile for the preform for the double clad, offset core, neodymium fiber laser.
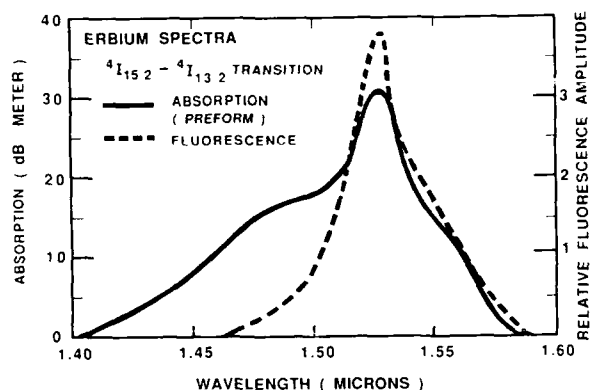
Fig. 8 Absorption and fluorescent spectra in the $^4I_{15/2} - {}^4I_{13/2}$ transition for erbium in SiO_2 with 3.6 wt % Al_2O_3
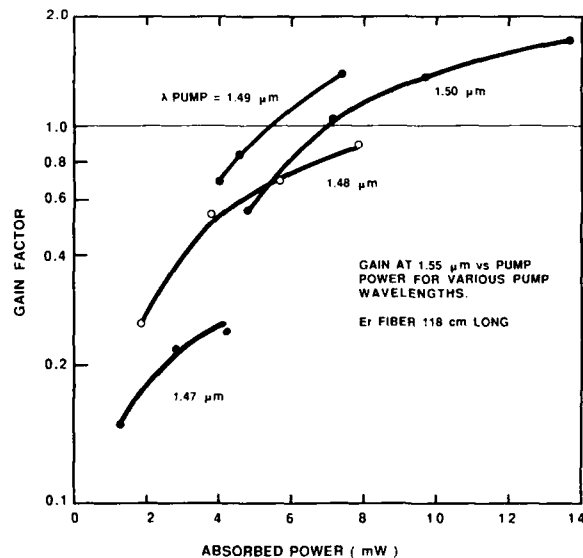
Fig. 9 Gain at 1.55 μm versus pump power at various wavelengths for 118 cm long Er fiber laser with $3x10^{19}$ ions/cc in SiO_2 with 3.7 wt % Al_2O_3.

483

PHYSICS OF FIBRE LASERS

D.C. Hanna
Department of Physics
University of Southampton
Highfield, Southampton SO9 5NH
U.K.

Abstract

Monomode fibres doped with rare-earth ions provide many attractive features as laser devices, including pumping by diode-lasers, wide tuning capability, Q-switched and mode-locked operation, and offer an effective route to new laser transitions. This paper highlights some of these features and provides illustrations taken from recent experimental results.

The glass fibre laser, invented by Elias Snitzer[1] in 1961, has been the subject of considerable recent interest since the demonstration by Mears et al[2] in 1985 of monomode fibre laser devices based on silica fibres. Monomode fibres doped with rare-earth impurities offer a number of features which make them attractive as lasers or amplifiers and the aim of this paper is to highlight some of these features and provide illustrations taken from recent experimental results. We also provide an extensive bibliography relating to fibre lasers.

Some of the features of interest are listed below:

* Simplicity of fabrication

* Excellent optical quality

* Freedom from thermal distortion

* Low threshold, allowing pumping by diode lasers, cw operation of 3-level lasers, and offering possibilities for new laser transitions

* High gain

* High efficiency

* Wide bandwidth, thus allowing significant tuning ranges, and short pulse operation via mode-locking

* Compatibility with monomode fibre devices such as couplers, modulators, integral grating devices etc.

* Low loss, thus allowing the use of long-fibre lengths, with consequences such as large nonlinear effects, large dispersion, ability to pump via weak absorption, etc.

For silica-based fibres, various fabrication techniques have been described (see Urqhart[3] for a recent review). These include a variation on the MCVD process in which the dopant is introduced as a vapour[4,5], and a more versatile solution-doping technique[6,7] which allows the dopant to be introduced from solution. The latter technique has allowed co-doping with different ions, at concentration levels sufficient to

achieve an efficient energy-transfer laser, as for example in the Yb:Er system[8]. For fibres based on fluorozirconate glass, quite different fabrication techniques are required, involving casting in a mould to make the preform[3], and techniques for fabricating monomode fibres are still at an early stage of development. Fluorozirconate glass fibres offer features which extend the capabilities of silica fibres, such as good IR transmission to longer wavelengths[9] and reduced rates of nonradiative decay as a result of the lower phonon energies. A consequence of the slower non-radiative decay is that laser emission has been observed in fluoride glass fibres from levels which in silica decay too fast to permit lasing. The table below lists those transitions reported to have lased to date (Dec. '88) in both silica and fluoride glass fibres.

Ion	Transition	Host	Wavelength (μm)	References
Nd^{3+}	$^4F_{3/2} - ^4F_{11/2}$	SiO_2	1.055 - 1.14	1,2,7,10-26
	$^4F_{3/2} - ^4I_{9/2}$	SiO_2	0.9 - 0.95	27-29
	$^4F_{3/2} - ^4I_{13/2}$	SiO_2	1.39	30
Er^{3+}	$^4I_{13/2} - ^4I_{15/2}$	SiO_2	1.53 - 1.60	33-41,8
Pr^{3+}	$^1D_2 - ^3F_4$	SiO_2	1.084	42,43
	$^1D_2 - ^3F_2$	SiO_2	0.886	43
Sm^{3+}	$^4G_{5/2} - ^6H_{9/2}$	SiO_2	0.651	44
Yb^{3+}	$^2F_{5/2} - ^2F_{7/2}$	SiO_2	1.01 - 1.162 ⎤ 0.974 ⎦	45,48,49
Tm^{3+}	$^3H_4 - ^3H_6$	SiO_2	1.88 - 1.96	50
Nd^{3+}	$^4F_{3/2} - ^4I_{11/2}$	Fluoride	1.05	55
	$^4F_{3/2} - ^4I_{13/2}$	Fluoride	1.35	31,32
Er^{3+}	$^4I_{13/2} - ^4I_{15/2}$	Fluoride	1.56	
	$^4I_{11/2} - ^4I_{13/2}$	Fluoride	2.7	53
Ho^{3+}	$^5I_7 - ^5I_8$	Fluoride	2.08	54
	$^5S_2, ^5F_4 - ^5I_5$	Fluoride	1.38	54
Tm^{3+}	$^3F_4 - ^3H_5$	Fluoride	2.3	52

Below we list some comments on the more noteworthy features of these transitions.

The Nd^{3+} $^4F_{3/2} - ^4I_{11/2}$ transition at around 1.06 μm is one of the most extensively studied transitions, having been implicated in each of the key developments of fibre lasers[1,7,10,2]. Operation on this transition has been demonstrated over a wide range of conditions. These include diode-pumped operation[11-14], Q-switched operation[15,11,16], mode-locked operation[17-19,14], tuned operation[20,21] and superfluorescent operation[22]. Operation with various resonator configurations has been demonstrated, including resonators with butted mirrors, with mirrors directly coated on the fibre ends[23], single

longitudinal mode operation in a fibre incorporating an integral grating[24,25], single longitudinal mode operation in a Fox-Smith resonator incorporating fibre loops as reflectors[25]. A summary of the performance characteristics reported to date include: thresholds of well below 1 mW, efficiencies of ~ 50%, single frequency operation with linewidth of ~ 1 MHz[25], mode-locked operation with bandwidth limited pulses of 20 psec[19], cw output power of 10 mw when diode-pumped[14], peak output power of ~ 100 w from a Q-switched diode-pumped laser[16], peak powers of ~ 1 kw in a mode-locked, Q-switched, diode-pumped laser[14], tuning over a range of 70-80 nm[20,21]. These results indicate some of the potential of fibre lasers.

For the Nd^{3+} $^4F_{3/2}$ – $^4I_{9/2}$ transition at ~ 0.9 μm, the lower laser levels lie in the ground manifold and therefore result in a 3-level character, due to the significant population in the lower laser level. Following the first observation of lasing on this transition in a fibre laser[27], tuned operation has been demonstrated[20,21], Q-switched and mode-locked operation[28], and diode pumped operation[29]. Generally performance levels are somewhat below those achievable on the $^4F_{3/2}$ – $^4I_{11/2}$ transition as a result of the 3-level character.

The Nd^{3+}, $^4F_{3/2}$ – $^4I_{13/2}$ transition, in the 1.3 μm region, suffers from excited state absorption[21] (ESA), a cause for some disappointment in view of the potential applications in optical communications for sources and amplifiers in this region. Lasing on this transition has been achieved in silica fibre[30], but the ESA forces operation at wavelengths too long (~ 1.4 μm) to be of interest for optical communications (this falls in a region of OH absorption). Fluoride glass fibres offer better prospects with reduced ESA problems, and shorter wavelength operation (1.33 -1.35 μm)[31,32].

The Er^{3+}, $^4I_{13/2}$ – $^4I_{15/2}$ transition at ~ 1.55 μm is of particular importance as it falls in the so called third transmission window of silica based communication fibres. Several different pump lasers have been used, the first operation being obtained with a 514 nm Argon laser pump[33]. An important breakthrough was made with the demonstration of pumping by a GaAlAs diode laser at 807 nm[34,35] since this offers the prospect of a very convenient package for in-line amplification in optical fibre communication systems operating at 1.55 μm. A problem that has been identified with pumping around 800 nm is that of ESA, of the pump radiation, which reduces the available gain[36]. Despite this the diode-pumped Er fibre amplifier may still prove to be a successful device, as the increased pump power requirements enforced by the ESA may be met using high brightness diode arrays which allow a significant fraction of their output to be coupled into a monomode fibre[37,14]. Meanwhile alternative approaches which reduce the ESA are being investigated. One of these[38] involves pumping with 980 nm radiation, for which ESA is absent, and has resulted in high gain, 24 dB for 11 mw of absorbed pump, i.e. 2.2 dB/mW. Another approach involves the use of fibre co-doped with Yb and Er, in which pumping takes place into the absorption band of Yb which then transfers its excitation to the Er[39]. The broad absorption band of Yb (~ 0.8 – 1.06 μm) allows pumping in regions away from the Er ESA. Results form this Yb:Er fibre include efificient pumping in the wavelength range of diode lasers (~ 0.8 μm)[40], NdYAG and NdYLF lasers[8,41] and demonstrate that the solution doping technique can achieve dopant concentrations sufficient to allow efficient energy transfer.

While the Nd^{3+} and Er^{3+} fibre lasers have so far received most attention there is a growing list of new fibre laser transitions, some of which have not previously been observed to lase in a glass host. An example of this is provided by the Pr^{3+} transitions $^1D_2 - {}^3F_4$ ($\sim$ 1.084 μm)[42] and $^1D_2 - {}^3F_2$ ($\sim$ 0.886 μm)[43], both of which have operated in a silica fibre, pumped by a cw Rhodamine 6G laser, but had not previously been reported in a glass host. Another example is provided by the Sm^{3+} doped fibre laser[44], operating on the $^4G_{5/2} - {}^6H_{9/2}$ transition at 0.65 μm, this being the first report on lasing on this transition in any host and the first example of visible fibre laser.

Other transitions recently observed to lase in fibres include the Yb^{3+}, $^2F_{5/2} - {}^2F_{7/2}$ transition[45], which in fact has two resolved transitions, a broad one centred at $\sim$ 1.064 μm (4-level laser) and a narrower one at 0.974 μm (3-level laser). The 4-level transition has previously been observed to lase in bulk glass[46,47], but not the three-level transition. Some interesting features of the Yb^{3+} fibre laser are the very wide tuning range achieved (1.01 - 1.16 μm)[48], in part due to the absence of any limitation due to ESA, and the observation of efficient superfluorescent emission on the 3-level (0.974 μm) and 4-level (1.04 μm) transition[49].

Tm^{3+} provides another interesting example. When pumped at 797 nm it has produced lasing[50] on the $^3H_4$ to $^3H_6$ transition at $\sim$ 1.85 μm. This (3-level) laser transition has previously been operated in pulsed fashion in bulk glass by Gandy et al[51]. The fluorescence emission in the fibre covers the range $\sim$ 1.7 μm to 2.2 μm, thus offering this as a potential tuning range and with the additional attractive possibility of diode pumping. It is interesting to note that fluorozirconate fibre doped with Tm^{3+} has instead operated[52] at 2.3 μm on the $^3F_4 - {}^3H_5$ transition (we have used the level notation of Gandy et al[51] rather than of Esterowitz et al[52]), since the $^3F_4$ level does not undergo rapid non-radiative decay as in silica glass.

Further examples of the additional laser transition made possible by reduced non-radiative decay rates in fluorozirconate glass fibres are found in Er^{3+}, on the $^4I_{11/2} - {}^4I_{13/2}$ transition at 2.7 μm[53], and Ho^{3+}, with transitions at [54] at 2.08 μm, $^5I_7 - {}^5I_8$ and at 1.38 μm, $^5S_2$, $^5F_4 - {}^5I_5$.

Summary

Developments in fibre lasers are taking place rapidly, with new laser transitions demonstrated and improved powers, efficiencies and gains. Fluuorozirconate fibres in particular offer the prospect of many more laser transitions with possibilities for energy transfer and up-conversion. Developments in diode lasers, enabling more pump power to be launched into monomode fibres[14] will play an important role in the future. New fibre geometries like the double-clad fibre[56] can also lead to efficient utilisation of pump power from high power diode arrays. With the increased power levels now being achieved in fibre lasers, particularly in Q-switched and/or mode-locked systems, nonlinear effects will become increasingly accessible and increasingly important.

References

1. E. Snitzer, Phys. Rev. Letters 7, 444 (1961).

2. R.J. Mears, L. Reekie, S.B. Poole and D.N. Payne, Electron. Lett. 17, 738 (1985).

3. P. Urquhart, IEE Proc., 135, PtJ, 385 (1988).

4. S.B. Poole, D.N. Payne and M.E. Fermann, Electron. Lett. 21, 737 (1985).

5. S.B. Poole, D.N. Payne, R.J. Mears, M.E. Fermann and R.I. Laming, J. Lightwave Technol. LT-4, 870 (1986).

6. J.E. Townsend, S.B. Poole and D.N. Payne, Electron. Lett., 23, 329 (1987).

7. J. Stone and C.A. Burrus, Appl. Phys. Lett. 23, 388 (1973).

8. M.E. Fermann, D.C. Hanna, D.P. Shepherd, P.J. Suni and J.E. Townsend, Electron. Lett., 24, 1135 (1988).

9. P.W. France, S.F. Carter, M.W. Moore and C.R. Day, Br. Telecom. Techn. J. 5, 28 (1987).

10. J. Stone and C.A. Burrus, Appl. Opt. 13, 1256 (1974).

11. I.M. Jauncey, J.T. Lin, L. Reekie and R.J. Mears, Electron. Lett. 22, 199 (1986).

12. M.W. Phillips, H. Gong, A.I. Ferguson and D.C. Hanna, Optics Commun. 61, 215 (1987).

13. K. Liu, M. Digonnet, K. Fesler, B.Y. Kim and H.J. Shaw, Electron. Lett. 24, 838 (1988).

14. I.N. Duling, L. Goldberg and J.F. Weller, Electron. Lett. 24, 1333 (1988).

15. I.P. Alcock, A.C. Tropper, A.I. Ferguson and D.C. Hanna, Electron. Lett. 22, 85 (1986).

16. W.L. Barnes, J.T. Lin, L. Reekie, D.B. Taylor, I.M. Jauncey, S.B. Poole and D.N. Payne, IEE Colloquium, Fibre Waveguide Devices, London, June 1988.

17. I.P. Alcock, A.I. Ferguson, D.C. Hanna and A.C. Tropper, Electron. Lett. 22, 269 (1986).

18. G. Geister and R. Ulrich, Optics Commun. 68, 187, 1988.

19. M.W. Phillips, A.I. Ferguson and D.C. Hanna, Optics Letts. (in press).

20. L. Reekie, R.J. Mears, S.B. Poole and D.N. Payne, J. Lightwave Technol, LT-4, 956 (1986).

21. I.P. Alcock, A.I. Ferguson, D.C. Hanna and A.C. Tropper, Optics Letts. 11, 709 (1986).

22. K. Liu, M. Digonnet, H.J. Shaw, B.J. Ainslie and S.P. Craig, Electron. Lett. 23, 1320 (1987).

23. M. Shimizu, H. Suda and M. Horiguchi, Electron. Lett. 23, 769 (1987).

24. I.M. Jauncey, L. Reekie, R.J. Mears and C.J. Rowe, Electron. Lett. 22, 987 (1986).

25. I.M. Jauncey, L. Reekie, J.E. Townsend and D.N. Payne, Electron. Lett. 24, 24 (1988).

26. P. Barnsley, P. Urquhart, C. Millar and M. Brierley, J.O.S.A., A, 5 1339 (1988).

27. I.P. Alcock, A.I. Ferguson, D.C. Hanna and A.C. Tropper, Optics Commun. 58, 405 (1986).

28. I.P. Alcock, A.C. Tropper, A.I. Ferguson and D.C. Hanna, IEE proc. J., 134, 183 (1987).

29. L. Reekie, I.M. Jauncey, S.B. Poole and D.N. Payne, Electron. Lett. 23, 884 (1987).

30. H. Po, F. Hakimi, R.J. Mansfield, R.P. Tumminelli, B.C. McCollum and E. Snitzer, Abstracts of Annual Meeting of Opt. Soc. Am. paper FD4, 103 (1986).

31. W.J. Miniscalco, L.J. Andrews, B.A. Thompson, R.S. Quimby, L.J.B. Vacha and M.G. Drexhage, Electron. Lett. 24, 28 (1988).

32. M.C. Brierley and C.A. Millar, Electron. Lett. 24, 438 (1988).

33. R.J. Mears, L. Reekie, S.B. Poole and D.N. Payne, Electron. Lett. 22, 159 (1986).

34. C.A. Millar, I.D. Miller, B.J. Ainslie, S.P. Craig and J.R. Armitage, Electron. Lett. 23, 865 (1987).

35. L. Reekie, I.M. Jauncey, S.B. Poole and D.N. Payne, Electron. Lett. 23, 1076 (1987).

36. R.I. Laming, S.B. Poole and E.J. Tarbox, Optics Letts. (in press).

37. R. Wyatt, B.J. Ainslie and S.P. Craig, Electron. Lett. 24, 1362 (1988).

38. R.I. Laming, M.C. Farries, P.R. Morkel, L. Reekie, D.N. Payne, P.L. Scrivener, F. Fontana and A. Righetti, Electron. Lett. (to be published January 1989).

39. E. Snitzer, H. Po, F. Hakimi, R. Tumminelli and B.C. McCollum, OFC New Orleans, PD2-1 (1988).

40. D.C. Hanna, R.M. Percival, I.R. Perry, R.G. Smart and A.C. Tropper, Electron. Lett. 24, 1068 (1988).

41. G.T. Maker and A.I. Ferguson, Electron. Lett. 24, 1160 (1988).

42. D.N. Payne, L. Reekie, R.J. Mears, S.B. Poole, I.M. Jauncey and J.T. Lin, Paper FNI CLEO '86, San Francisco (1986).

43. D.C. Hanna, R.M. Percival, M.W. Phillips, A.C. Tropper (in preparation).

44. M.C. Farries, P.R. Morkel and J.E. Townsend, Electron. Lett. 24, 709 (1988).

45. D.C. Hanna, R.M. Percival, I.R. Perry, R.G. Smart, P.J. Suni, J.E. Townsend and A.C. Tropper, Electron. Lett. 24, 1111 (1988).

46. H.W. Etzel, H.W. Gandy and R.J. Ginther, Appl. Opt. 1, 534 (1962).

47. E. Snitzer, IEEE J. Quantum Electron. QE-2, 562 (1966).

48. D.C. Hanna, I.R. Perry, R.G. Smart, P. Suni, A.C. Tropper (in preparation).

49. D.C. Hanna, I.R. Perry, R.G. Smart, P. Suni, A.C. Tropper (in preparation).

50. D.C. Hanna, I.M. Jauncey, R.M. Percival, I.R. Perry, R.G. Smart, P.J. Suni, J.E. Townsend and A.C. Tropper, Electron. Lett. 24, 1223 (1988).

51. H.W. Gandy, R.J. Ginther and J.F. Weller, J. Appl. Phys. 38, 3030 (1967).

52. L. Esterowitz, R. Allen and I. Aggarwal, Electron. Lett. 24, 1104 (1988).

53. M.C. Brierley and P.W. France, Electron. Lett. 24, 935 (1988).

54. M.C. Brierley, P.W. France and C.A. Millar, Electron. Lett. 24, 539 (1988).

55. M.C. Brierley, P.W. France, Electron. Lett. 23, 815 (1987).

56. E. Snitzer, H. Po, F. Hakimi, R. Tumminelli and B.C. McCollum, paper PD5-2, OFC '88, New Orleans (1988).

FLUORIDE FIBER LASERS

Leonard J. Andrews
GTE Laboratories, Incorporated
40 Sylvan Road
Waltham, MA 02254

Abstract

Silica telecommunications optical fibers show remarkable properties as lasers and traveling wave optical amplifiers when doped in the core with luminescent rare earth ions. Practical application of such fibers, especially in communications systems, is currently impeded by inefficiencies associated with excited state absorption (ESA). We show through Judd-Ofelt analysis that it is possible to mitigate the effects of ESA through the proper choice of glass matrix. This has led to the demonstration in fluoride fiber of the first neodymium glass laser to operate within the 1.3 micron telecommunications channel and to the substantial reduction of ESA at the 0.8 micron erbium pump band.

Introduction

In recent years, a great deal of progress has been made in developing optical fibers as host media for rare earth ion lasers and optical amplifiers. The particular advantages of these devices stems from the small core dimension found in single mode fiber which has a typical diameter of less than 10 microns. Such small active volumes permit not only high levels of optical excitation density and excellent coupling between pump and laser modes but also rapid thermal dissipation of excess heat that prevents catastrophic stress fracture of the glass. It has been possible to routinely demonstrate c.w. three level lasers[1], tunable lasing over linewidths broadened by ion-amorphous host interactions[2], and sub-milliwatt lasing thresholds[3], performance that is not feasible with bulk glass formats.

Considerable interest in these developments has arisen in the area of telecommunications because of the possibility of fabricating luminescent fiber amplifiers that can operate on optical signals directly without the need for photonic/electronic conversion. Impressive demonstrations have already been reported for erbium-doped silica fiber that show gain in excess of 30 dB[4], efficiency of 2 dB/milliwatt pump power[5], and very low noise[6] when such fiber is operated as a single pass, traveling wave optical amplifier. It is to be emphasized that this performance is achievable in a device that has no inherent polarization sensitivity and can be spliced into existing fiber networks with essentially negligible coupling loss. The two principal issues that remain to be overcome in order to make erbium fiber amplifiers of substantial practical interest are the low efficiency of the device when optically pumped at 0.8 micron, the nominal operating wavelength of AlGaAs laser diodes, and the small bandwidth of the 1.55 micron gain region which is only 3 nm for silica fiber amplifiers. We will show that the former characteristic can be improved by changing the erbium ion glass host from silica to certain non-conventional compositions such as fluorozirconate-based glasses, and, although it will not be described in this paper, we have also discovered that it is also possible to improve the bandwidth by at least a factor of three through similar changes in glass host.

The other rare earth ion of interest for telecommunications applications is neodymium because it has a luminescent transition centered near 1.3 micron, the "second" transmission window in optical fiber. The technology for neodymium fiber amplifiers is less developed than for erbium devices because in standard silica fiber the 1.3 micron luminescence has no optical gain within the communications window[7]. This situation is caused by a competing ESA which prevents gain at wavelengths other than at the red edge of the emission near 1.4 micron, a wavelength of no interest for communications. As is the case for erbium, this obstacle can be at least partially overcome by the judicious choice of non-conventional glass compositions.

Judd-Ofelt Analysis

The poor pumping efficiency of erbium ions at 0.8 micron and the lack of gain at 1.3 micron for neodymium ions are both manifestations of absorption between the metastable upper laser level populated by absorption of pump photons to still higher levels of these ions. These excited state transitions give rise to absorption bands that accidentally lie near 0.8 and 1.3 micron for Er^{3+} and Nd^{3+}, respectively. It is a characteristic of rare earth ion transition arising from f-electron configurations that the energies of the transitions are relatively insensitive to the ion host. This means that it is unlikely that the accidental degeneracies can be removed by differential shifting of the relevant ion states in various host materials, and this expectation was confirmed by us through a comparison of the ground state absorption of these ions in a variety of glasses. It was discovered that while small energy shifts could be induced by changing glass composition, the shifts among the various bands was very similar so that the relative spacings remain largely unchanged.

On the other hand, it is known that the linestrengths of f-electron transitions are somewhat sensitive to the ion surroundings, so that the possibility existed to lower the intensity of deleterious ESA transitions through the judicious choice of host materials. Fortunately, a very useful semi-empirical theory was developed in early 1960's independently photonic/electronic conversion. Impressive demonstrations have already been reported for erbium-doped silica fiber that show gain in excess of 30 dB[4], efficiency of 2 dB/milliwatt pump power[5], and very low noise[6] when such fiber is operated as a single pass, traveling wave optical amplifier. It is to be emphasized that this performance is achievable in a device that has no inherent polarization sensitivity and can be spliced into existing fiber networks with essentially negligible coupling loss. The two principal issues that remain to be overcome in order to make erbium fiber amplifiers of substantial practical interest are the low efficiency of the device when optically pumped at 0.8 micron, the nominal operating wavelength of AlGaAs laser diodes, and the small bandwidth of the 1.55 micron gain region which is only 3 nm for silica fiber amplifiers. We will show that the former characteristic can be improved by changing the erbium ion glass host from silica to certain non-conventional compositions such as fluorozirconate-based glasses, and, although it will not be described in this paper, we have also discovered that it is also possible to improve the bandwidth by at least a factor of three through similar changes in glass host.

The other rare earth ion of interest for telecommunications applications is neodymium because it has a luminescent transition centered near 1.3 micron, the "second" transmission window in optical fiber. The technology for neodymium fiber amplifiers is less developed than for erbium devices because in standard silica fiber the 1.3 micron luminescence has no optical gain within the communications window[7]. This situation is caused by a competing ESA which prevents gain at wavelengths other than at the red edge of the emission near 1.4 micron, a wavelength of no interest for communications. As is the case for erbium, this obstacle can be at least partially overcome by the judicious choice of non-conventional glass compositions.

Judd-Ofelt Analysis

The poor pumping efficiency of erbium ions at 0.8 micron and the lack of gain at 1.3 micron for neodymium ions are both manifestations of absorption between the metastable upper laser level populated by absorption of pump photons to still higher levels of these ions. These excited state transitions give rise to absorption bands that accidentally lie near 0.8 and 1.3 micron for Er^{3+} and Nd^{3+}, respectively. It is a characteristic of rare earth ion transition arising from f-electron configurations that the energies of the transitions are relatively insensitive to the ion host. This means that it is unlikely that the accidental degeneracies can be removed by differential shifting of the relevant ion states in various host materials, and this expectation was confirmed by us through a comparison of the ground state absorption of these ions in a variety of glasses. It was discovered that while small energy shifts could be induced by changing glass composition, the shifts among the various bands was very similar so that the relative spacings remain largely unchanged.

On the other hand, it is known that the linestrengths of f-electron transitions are somewhat sensitive to the ion surroundings, so that the possibility existed to lower the intensity of deleterious ESA transitions through the judicious choice of host materials. Fortunately, a very useful semi-empirical theory was developed in early 1960's independently by Judd[8] and Ofelt[9] that made it possible to calculate rather accurately the integrated intensity of induced electric dipole transitions between f-electron states of rare earth ions. This treatment provides a powerful tool for identifying glasses that have improved properties relative to silica in terms of reduced ESA intensity.

In the customary formulation of Judd-Ofelt theory, the electric dipole linestrength for transitions between rare earth f-electron levels is expressed in terms of a linestrength function S_m, which is given by the summation over the so-called Judd-Ofelt parameters and the doubly reduced matrix elements $U^{(i)}$ as shown in Equation 1.

$$S_m = \sum_{i=2,4,6} \Omega_i \; \| \, U^{(i)} \, \|^2 \qquad\qquad \text{Eq. (1)}$$

Essentially, the Ω_i contain atomic radial integrals and are determined empirically for each ion/host combination by fitting simple ground state absorption (GSA) spectra. Using the set of three Ω_i and the doubly reduced matrix elements, which are regarded to be host independent, the oscillator strength of the electric dipole transition between any two ion states can be calculated using Equation 2 in which ν is the frequency and J is the total angular momentum quantum number of the initial state.

$$f = \frac{8 \pi^2 \, m \, \nu}{3 \, h \, (2J + 1)} \; S_m \qquad\qquad \text{Eq.(2)}$$

Judd-Ofelt theory was used to calculate the ratio of ESA/GSA oscillator strengths in the 0.8 micron region for several Er[3+]containing glasses, and a partial summary of the results are contained in Table1.

Table 1. Judd-Ofelt Parameters (X e20 cm^2) and Calculated ESA/GSA Oscillator Strength Ratio for Er[3+] at 0.8 Micron.

glass	Ω_2	Ω_4	Ω_6	4I13/2 - 2H11/2 4I15/2 - 4I9/2
borosilicate[10]	2.9	0.4	0.2	1.75
phosphate[10]	3.7	0.8	0.8	1.19
fluorophosphate	3.4	1.8	1.2	0.99
fluorozirconate	2.5	1.4	1.0	0.98

It is evident from Table 1 that it is possible to improve the ESA/GSA ratio to the point of making the relevant transitions of equal strength by changing glass composition. The current results for pumping Er[3+] silica fiber at 0.8 micron show that amplifier operation is marginally efficient at this wavelength, so that it can be expected from the results of Judd-Ofelt analysis that a substantial improvement in amplifier efficiency can be realized in non-conventional glass fibers.

A similar analysis was performed for Nd[3+] in glass, only in this case the linestrength functions were compared for ESA and emission at 1.3 micron. Some of these results are listed in Table 2.

Table 2. Judd-Ofelt Parameters (X e20 cm^2)and Calculated ESA/Emission Linestrength Function Ratio for Nd[3+] at 1.3 Micron.

glass[11]	Ω_2	Ω_4	Ω_6	4F3/2 - 4G11/2 4F3/2 - 4I9/2
silica	6.0	4.7	4.1	1.08
phosphate	3.3	5.0	5.6	0.56
fluorozirconate	1.7	3.3	3.9	0.48
fluorophosphate	1.4	4.0	4.6	0.42
fluoroberyllate	0.2	3.9	4.6	0.28

As Table 2 suggests, silica is among the poorest choices for a 1.3 micron laser host because of the unfavorable intensity of the ESA. It fact, these results provide a satisfying rationale for the observed performance of Nd[3+]in silica,[1] and suggest that there are many glasses that should do better at 1.3 micron.

Erbium3+ ESA Spectra

To test the predictions of the Judd-Ofelt analysis for Er[3+] glasses, ESA difference spectra were measured for both a standard germania doped silica fiber and a fluorozirconate fiber of composition (in mol%) 53 ZrF_4 - 20 BaF_2 - 4 LaF_3 - 3 AlF_3 - 20 NaF (ZBLAN). The results are shown in Figure 1 where the difference spectra represent the change in fiber absorption constant $\Delta \alpha$ between fiber optically pumped at 514.5 nm by an argon ion laser and umpumped fiber. $\Delta \alpha$ is related to the difference in cross sections by Equation 3 and is positive for increased absorption and negative for bleaching.

$$\Delta \alpha = n_e l \ (\sigma_e - \sigma_g)$$
Eq. 3

Figure 1 shows the origin of the inefficiency for 0.8 micron pumping. In spite of the presence of a GSA band centered near 0.8 micron the, ESA difference spectrum shows only the presence of increased absorption when the silica fiber is optically pumped indicating that the ESA overwhelms GSA in this wavelength region. This result confirms earlier work at British Telecom[12] where the silica spectrum was first measured. Another ESA band also appears near 0.85 micron. By contrast, the ESA difference spectrum of the ZBLAN fiber only shows the 0.85 band. The region near 0.8 micron, although noisy, clearly demonstrates the absence of increased absorption indicating that the ESA and GSA intensities must be approximately the same. These results provide a clear qualitative confirmation of the Judd-Ofelt analysis, and strongly suggest that substantial improvements in Er[3+] amplifier pump efficiency at 0.8 micron will be realized in non-conventional fibers.

1.3 Micron Neodymium (3+) ZBLAN Fiber Laser

In the case of Nd^{3+}, the prediction of Judd-Ofelt theory was tested by conducting a laser experiment in a non-conventional fiber. For the test, it was convenient to fabricate a multimode fiber of fluorozirconate glass containing Nd^{3+} in the core. In ZBLAN glass, it was calculated that the integrated emission linestrength at 1.3 micron is about a factor of two greater than the ESA linestrength so that lasing should be feasible. Using the doped ZBLAN fiber, a simple broadband Fabry-Perot cavity was constructed with the fiber longitudinally pumped at 514.5 nm. Figure 2 shows the spectral output of the cavity, both below and above lasing threshold. Below threshold, the spontaneous emission spectrum is recorded, whereas above threshold the band collapses showing stimulated emission centered near 1.34 micron in the untuned cavity. Just above threshold the lasing is centered at 1.33 micron. This is the first demonstration of a glass laser which operates within the 1.3 micron telecommunications window[13].

It is noteworthy in Figure 2 that the peak of the fluorescence does not correspond to the free running laser wavelength. This mismatch is most likely caused by residual ESA which forces the peak gain region to lie to the red of the spontaneous fluorescence peak. Experiments are now in progress to accurately map out the gain region in these devices, although it now appears from a study of the 1.3 micron emission in a number of glasses that gain to the blue of 1.30 micron is unlikely.

Summary

Through the use of Judd-Ofelt theory as a predicative guide, it was shown possible to circumvent shortcomings of silica glass as a rare earth ion laser host for applications that are important for telecommunications. Fluorozirconate glass in particular was demonstrated to have properties superior to silica in terms of favorably perturbing rare earth ion radiative transition strengths to make possible improved luminescent optical amplifiers that operate at the 1.3 and 1.55 micron telecommunications windows.

References

1. R.J. Mears, L. Reekie, S.B. Poole, and D.N. Payne, Elect. Lett. **22**, 159 (1985)

2. I.P. Alcock, A.I. Ferguson, D.C. Hanna, and A.C. Tropper, Optics Comm. **58**, 405 (1986)

3. H. Po, F. Hakimi, R.J. Mansfield, R.P. Tumminelli, B.C. McCollum, E. Snitzer, presented at the 1986 Ann. Mtg. Optical Soc. Am., Seattle (1986), paper FD4

4. D.N. Payne and L. Reekie, presented at ECOC 88, Brighton (1988), p. 49

5. R.I. Laming, L.Reekie, D. Payne, P.L. Scrivener, F. Fontana, and A. Righetti, presented at ECOC 88, Brighton (1988), postdeadline paper

6. R.I. Laming, P.R. Morkel, D.N. Payne, and L. Reekie, presented at ECOC 88, Brighton (1988), postdeadline paper

7. P.R. Morkel, M.C. Ferries, and S.B. Poole, Optics Comm. **67**, 349 (1988)

8. B.R. Judd, Phys. Rev. **127**, 750 (1962)

9. G.S. Ofelt, J. Chem. Phys. **37**, 511 (1962)

10. F. Auzel, Ann. des Telecommunications **24**, 199 (1969)

11. S.E. Stokowski, R.A. Saroyan, and M.J. Weber, Nd-Doped Laser Glass - Spectroscopic and Physical Properties, Lawrence Livermore Laboratories, 1978, M-095

12. J.R. Armitage, C.G. Atkins, R. Wyatt, B.J. Ainslie, and S.P. Craig, presented at Opt. Soc. Am. Topical Mtg. On Tunable Solid State Lasers, Williamsburg (1987), paper WD3-1

13. W.J. Miniscalco, L.J. Andrews, B.A. Thompson, R.S. Quimby, L.J.B. Vacha, and M.G. Drexhage, Electronics Lett. **24**, 28 (1988)
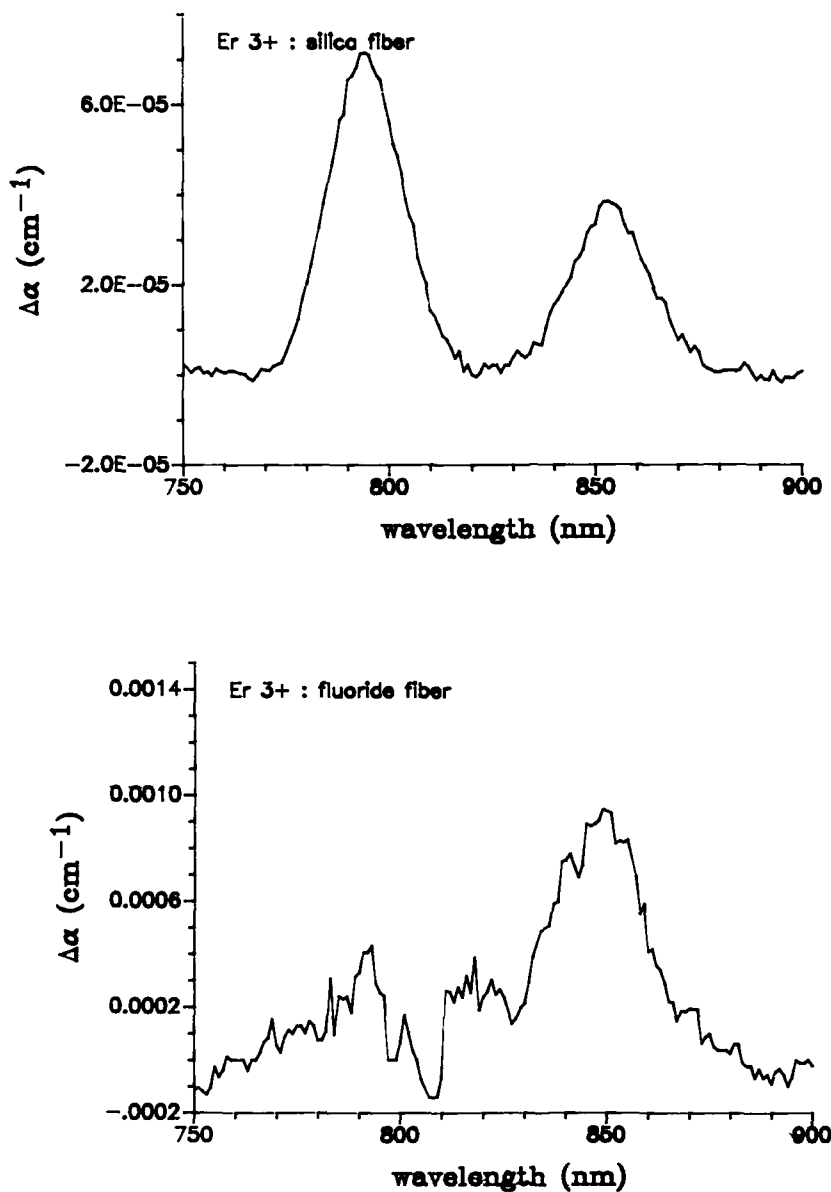
Figure 1. ESA difference spectra for Er^{3+} in germania doped silica fiber (upper) and ZBLAN fiber (lower). The absence of the 800 nm ESA band in ZBLAN fiber indicates closely similar GSA and ESA intensities in the fluoride glass.
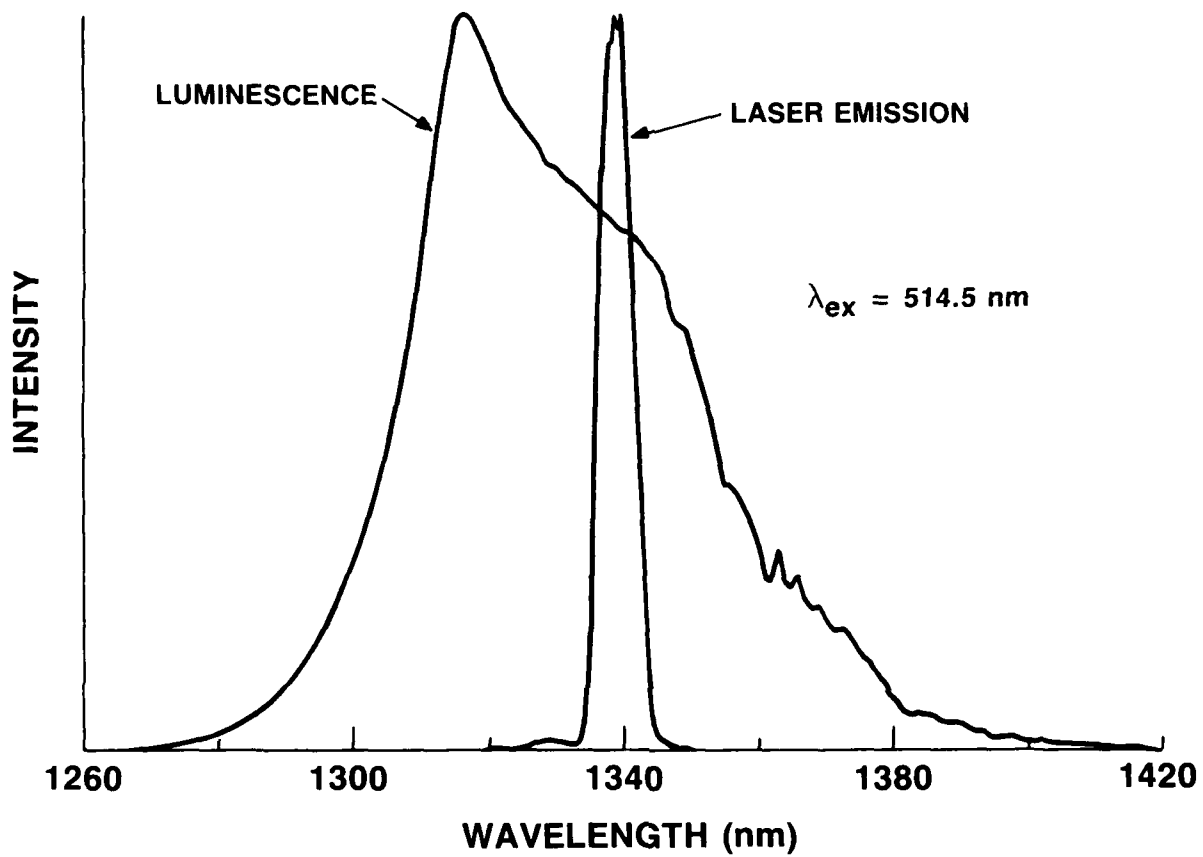
Figure 2. Spectral output of untuned Nd^{3+} ZBLAN fiber laser below threshold showing broad spontaneous emission and above threshold showing bimodal stimulated emission at 1.33 and 1.34 micron.

FIBER AMPLIFIERS FOR OPTICAL COMMUNICATIONS

E. Desurvire
AT&T Bell Laboratories
Crawford Hill Laboratory
Box 400 – Room HOH L-221
Holmdel, New Jersey 07733

Abstract

Properties of available fiber amplifiers and their relative advantages for optical fiber communications are reviewed. Emphasis is on erbium-doped fiber amplifiers operating in the second λ = 1.5 μm telecommunication window. The characteristics of this type of device as well as the main experimental results reported to date are summarized and put in perspective with the field of semiconductor amplifiers.

Optical amplifiers are of great importance in the field of fiber optics communications. They can be used for loss compensation in long haul fiber links[1], or as digital regenerative repeaters[2], or as preamplifiers for enhancing signal-to-noise ratio during detection[3]. A major advantage offered by direct optical amplification is the possibility of amplifying simultaneously several channels without the need of optoelectronic conversion and high-speed electronic interface. Semiconductor amplifier technology has matured considerably (see for instance refs. [4-5]) since the realization of the first GaAs laser diodes (1962). At about the same time, the first rare-earth glass lasers in 1961[6] started research on glass fiber amplifiers and laser sources[7-8]. With the availability of low-loss single-mode fibers (1970), fiber nonlinear optics using Raman, Brillouin and four-wave mixing effects[9] offered new possibilities for light generation and amplification. More recently (1985), modified vapor-phase techniques for fiber fabrication[10] have led to the realization of a large variety of rare-earth doped fiber sources and amplifiers (see for instance ref. [11]). With this perspective in mind, one may wonder what alternate solutions or possible advantages for fiber optic communications may now be offered by fiber amplifiers.

In this memorandum, the performance and capabilities of fiber amplifiers based on nonlinearities and rare-earth doping are reviewed. The main focus is on erbium-doped fiber devices operating in the λ = 1.5 μm telecommunication window, with a summary of various signal amplification experiments reported to date. Experimental results obtained on signal amplification are detailed. A low-noise, high-speed signal amplification experiment at 2 Gigabit/s is also reviewed. The main features of erbium-doped fiber amplifiers are then compared with semiconductor amplifiers.

The two main single-mode fiber amplifier types are (a) nonlinear fiber amplifiers and (b) doped-fiber amplifiers. Devices based on stimulated Raman and Brillouin scattering (SRS, SBS) and stimulated four wave mixing (SFWM)[9] belong to the first type. Neodymium (Nd) and erbium (Er) fiber devices (see for instance [7], [11], [12]) belong to the second type. Table 1 summarizes the main features of SRS, SBS, SFWM and Erbium-doped amplifiers. For the nonlinear types, the operating signal wavelengths are determined by the choice of the pump wavelength (SRS, SBS) or the phase-matching conditions (SFPM), and are therefore tunable over the two fiber telecommunication windows (λ = 1.3-1.5 μm). Since Nd-doped fibers operate outside the telecommunications windows near λ = 1.06 μm, the main effort is on Er-doped fiber amplifiers which operate near λ = 1.53 μm. A second criterion is the pump power requirement for achieving sizable signal gain (i.e. G > 10 dB). For SFPM, SRS and SBS, the pump powers are of the order of 100W, 1W and 10mW, respectively. For Er-doped devices, pump powers are less than 100 mW. Other important aspects are the required fiber lengths, the gain bandwidths and the gain sensitivity to signal polarization. For the four types of amplifiers, the fiber lengths range from 1m to 10 km, the gain bandwidths from 10 MHz to 12 THz, and only the Er type is intrinsically polarization insensitive (as discussed further below). For SRS, SBS and SFPM, as applied to nonpolarization-maintaining fibers, however, the effect of polarization scrambling results in a polarization insensitive (and reduced) gain. Figure 1 summarizes the main experimental results in terms of gains and related pump powers that have been reported over the past decade for nonlinear fiber amplifiers. The figure shows that SRS and SFPM can achieve gains in the 30-50 dB range with pump powers above 1W and 100W, respectively. These experiments required high-power CW or pulsed lasers and are not practical for communication applications. However, SRS can exhibit useful gains (∿5 dB) for fiber loss compensation with pump powers in the 100 mW range. SBS can provide 15 dB to 20 dB gains with pump powers in the 1 mW range. This indicates the possibility of practical laser diode pumped amplifiers.

Some qualitative and quantitative comparisons are made in Table 1. For instance, the advantage of SRS is its large gain bandwidth (12 THz), but its disadvantages are the long fiber lengths (km range) and relatively high pumping powers (Watt range). Practical applications of SRS to optical communications seem thus to be limited to signal boosting and possibly to compensation of fiber loss in long-haul links, through distributed gain. Laser-diode pumped SRS amplification of WDM optical channels using 60 mW pump power was reported[13], giving a 5 dB increase in output signal powers. Loss-compensating, distributed SRS gain is also amenable to soliton propagation[14], and has been recently demonstrated with 300 mW pump power for a 4000 km-long fiber distance[15]. On the other hand, SBS is characterized by a comparatively narrow gain bandwidth (typically 10-100 MHz), which can be broadened by pump modulation[16]. Thus, the use of SBS imposes a limitation in signal bit rate, and requires accurate pump and signal frequency control. The advantage of

SBS is its high gain for low pump power (10 mW), which is amenable to laser diode pumping. A SBS gain as high as 30 dB was reported for 250 Mbit/s FSK signal amplification with 12 mW AlGaAs laser diode pump power[17]. This experiment showed that the narrow SBS gain bandwidth can be adequately used as a means of selective amplification for frequency-division multiplexed signals. Loss compensation at 1.5 μm wavelength in a 37 km fiber length was also demonstrated with a 2 mW diode pump[18].

Figure 2 shows a graph similar to that of Figure 1, as applied to rare-earth-doped fiber amplifiers. The first Nd-doped fiber devices, operating at 1.06 μm wavelength, were reported in 1964 using for the signal source a Nd:glass laser rod[?] and in 1970 a InAsP laser diode[19]. The high-energy (200-350J) flashlamp pumping configuration used in these early experiments achieved gains in the 37-47 dB range. On the other hand, erbium-doped fiber amplifier experiments have been reported only since 1987, following a renewed surge of interest for rare-earth doped fibers[10,20] and the demonstration in 1986 of the first Er-doped fiber laser devices[21-22]. These lasers were optically pumped with an argon-ion laser (end-pumping configuration)[21], or with a gas discharge tube (the fiber being wound around it)[22]. As shown in Fig. 2, traveling-wave Er fiber amplifiers can be pumped at various wavelengths that correspond to the absorption bands of Er:glass 488 nm[23], 514-528 nm[24-26] [and this paper], 647-670 nm[27-31], 807 nm[32-33], 980 nm[?], and 1.49 nm[34]. The differences in gains for identical pump powers and pump wavelengths can be attributed to variations in fiber design (numerical aperture, core diameter), for which pump thresholds and modal overlaps differ. Further, the effect of pump excited-state absorption (ESA), observed in Er:glass[31,37,?], occurs at many of these pump wavelengths. The effect of ESA is an unwanted pump absorption that results in a reduced pumping efficiency. This point is illustrated in Figure 2. Gains of 35 dB were achieved using either 650 nm pump[31] or 514.5 nm pump[42], the launched pump power being about double (225 mW) in the second case. The lower pump power requirement at 670 nm for the same amplifier gain can be explained by the reduced effect of ESA at this wavelength[35,36].

Unfortunately, the effect of ESA is large around the wavelength of 800 nm, where high-power GaAlAs laser diodes are available for the pump. In spite of ESA, however, gains of 28 dB with 50 mW launched pump power (dye laser) were reported at this pump wavelength[33]; using a GaAlAs laser diode array, 6 dB gain with 35 mW launched pump power was also shown[33], the gain being limited by the amount of power that could be coupled into the fiber from this pump laser. With the development of single-transverse mode, high-power GaAlAs laser diodes, more efficient pump coupling should be achieved and high-gain (20 dB) operation of the fiber amplifier should be possible. In addition, the ESA effect can be reduced through a proper choice of glass co-dopants (e.g. GeO2, Al2O3) that are used as index-raising components. Further, other types of glass hosts, e.g. fluorozirconate glasses, for which the ESA effect is lesser than that of silica glass[23], may constitute alternative solutions. Finally, another possibility is offered by sensitization of Er:glass by ytterbium (Yb)[37]. The Yb3+ ions can then be pumped between 800 nm and 840 nm, far from the ESA bands of Er3+, and the Er3+ ions are excited through Yb – Er resonant energy transfer. Efficient Yb-sensitized Er fiber lasers pumped near 820 nm have been realized[38] and may be attractive for traveling-wave amplification.

The three remaining pumping wavelengths that are suitable to laser-diode pumping are 665 nm, 980 nm and 1490 nm. High-power (30 mW), room temperature operation of AlGaInP visible laser diodes with 667 nm wavelength have been reported recently[39], and may soon be suitable laser pump sources. The choice of near-infrared pump wavelengths (980 nm, 1490 nm) near the signal wavelength makes possible single transverse-mode pump operation, for which the gain is greater than in the multimoded case[40]. The 980 nm pump band, where no ESA exists, has given the best performance to date: a 24 dB gain was obtained for 11 mW launched pump, corresponding to a gain coefficient of 2.2 dB/mW[26]. In comparison, the gain coefficients reported at other pump wavelengths range from 0.13 to 0.23 dB/mW[26]. Finally, the 1.49 μm wavelength also represents a possibility for laser diode pumping. A gain of 1.7 dB with 14 mW absorbed pump power was recently demonstrated in an Er fiber amplifier using a color center laser tuned at 1.49 μm[34]. The cw powers in excess of 100 mW that have been achieved at 1.5 μm wavelength with so-called VIPS semiconductor lasers[41], could raise this gain result by an order of magnitude.

The typical signal input/output characteristic curve of an Er-doped fiber amplifier is shown in Figure 3. An unsaturated gain of 35 dB was obtained with 1m fiber length and 225 mW launched pump power at 514.5 nm[42], matching the best gain reported with λ = 670 nm[31]. The Er2O3 concentration in the fiber core was 1100 ppm, with Al2O3 used both as an index-raising co-dopant and a rare-earth glass solvent. The gain improvement from former results with 514.5 nm pump[24,25] can be attributed to optimized fiber geometric parameters, as well as to the reduced pump ESA observed in aluminosilicate Er:glass[36]. Further experimental results obtained with this type of fiber, as well as a comparison with theory will be presented elsewhere[42]. Theoretical fits to the experimental data, as shown by the solid lines in Fig. 3, could be obtained with a theoretical saturation power P_{sat} = 280 μW and the assumption of a homogeneous gain bandwidth of 35 nm. A homogeneous gain saturation behavior of the Er-doped fiber amplifier was indeed observed experimentally[42], and is consistent with the large Stark-splitting effect of the two energy levels participating in the 1.5 μm laser transition[43].

The gain/saturation output power characteristics of both 1.5 μm semiconductor amplifiers and Er-fiber amplifiers are shown in Figure 4. The open triangles correspond to results pertaining to Er-fiber amplifiers, and the other symbols represent results reported for traveling-wave or near traveling-wave semiconductor amplifiers. This figure shows that Er-fiber amplifiers have gain/saturation power characteristics that are comparable to traveling-wave or near traveling-wave semiconductor amplifiers. This is expected since index-matching cells or beveled fiber ends are always used in the Er-fiber amplifiers in order to prevent feedback. It is remarkable that these simple techniques for suppressing feedback are

equivalent to best anti-reflection coatings on semiconductor devices. The figure also shows that in the high saturation output power regime (i.e. +5 dBm to +10 dBm), the fiber gains are usually higher (i.e. +6 dB to 8 dB) than semiconductor gains.

The noise properties of Er-doped fiber amplifiers have been investigated by a few authors through measurements of signal-to-noise ratio and bit error rates (BER). Digital signal transmission experiments utilizing Er-fiber amplifiers were performed at rates of 140 Mbit/s[28,30,32] and up to 2 Gbit/s[25,42]. As a whole, these early experiments demonstrated the low-noise capability of Er-fiber amplifiers, as well as the possibility of their application as signal boosters or preamplifiers for improved signal detection in actual digital transmission systems. Figures 5 and 6 show results reported at 2 Gbit/s with a 11m-long Er-fiber amplifier pumped at 514.5 nm[25]. Comparison of the input and output bit sequences of the fiber amplifier (gain = +15 dB) in Fig. 5(a), as well as the corresponding output eye diagram (Fig. 5(b)), show the gain linearity and the immunity to intersymbol interference and patterning effects. Figure 6 shows a series of BER curves as a function of detected signal power, corresponding to different input signal powers. A BER of 10^{-9} was achieved with -27 dBm signal input (and with -30 dBm signal input with noise filtering), which represented a +3 dB (resp. +6 dB) improvement in receiver sensitivity[25]. Further experiments have yet to be done in order to assess whether fundamental differences in noise properties exist between Er-fiber amplifiers and semiconductor devices. Crosstalk effects in Er-fiber multichannel amplification are under investigation[42], and are expected to exhibit qualitative differences with semiconductor amplifiers, due to the nature of the laser systems involved. It is clear however, that the Er-fiber amplifier is well-suited for wavelength division multiplexed (WDM) communications, owing to its large (2500 GHz) gain bandwidth[25,28,42].

An important advantage for the fiber amplifier is its insensitivity to signal polarization. The gain in semiconductor amplifiers is known to be polarization-sensitive, due to a finite ratio of confinement factor of the TE and TM polarization modes[44]. However, there are alternative means to reduce this effect, for instance by increasing the active layer thickness[44], at the expense of the amplifier gain, or by using a Faraday rotator[52], which introduces some excess loss penalty. In the case of Er-fiber amplifiers, however, the gain was found to be intrinsically polarization-insensitive[25], even for fiber lengths as short as 1m[42]. This property can be attributed to both the cylindrical fiber geometry (for which the TE and TM transverse modes are degenerate), and to an intrinsically isotropic laser gain. This last property is observed at least in the highly multimoded pump regime. Linearly polarized pumping may result in some amount of polarization sensitivity, owing to possible cross-section anisotopy in the Er:glass, and this point is currently under investigation. Another advantage of fiber amplifiers is the low insertion loss penalty. The fiber-to-fiber insertion loss penalty is typically 10 dB for semiconductor amplifiers coupled with either microscope objectives or tapered fiber microlenses[48,50,53,54]. A lower bound of 6 dB for the fiber-to-semiconductor-to fiber coupling loss[50] seems to be a fundamental limit imposed by the differences in transverse mode geometries. In the case of the fiber amplifier, where the fiber mode size is 1.5 μm may differ somewhat from that of standard communication fibers, we evaluate this overall coupling loss to be of the order of 0.5 dB, owing to the good mode matching that can be achieved between standard fibers and the fiber amplifier types. Note that some additional excess loss (of similar magnitude) will be necessarity introduced by fiber splices and by the multiplexer coupler used to combine the pump with the signal.

In conclusion, we have shown that fiber amplifiers constitute an important and attractive alternative to semiconductor amplifiers. Indeed, keeping the focus on 1.5 μm erbium-doped fiber amplifiers, which seem at present to be the most amenable to practical laser diode pumping operation, their advantages reside in the simplified device manufacturing, in the possibility of low insertion loss in fiber systems and in intrinsic polarization insensitivity. A drawback is that rare-earth-doped fiber amplifiers are not available at present at the dispersion-free 1.3 μm wavelength, in use in most fiber communication systems. Further, their optical pumping requires the use of high-power laser diodes, whose long-term reliability is still uncertain. Both long-haul, point-to-point optical communications and fiber local area networks at 1.5 μm are potential applications for Er-doped fiber amplifiers.

REFERENCES

1. S. D. Personick, Bell Syst. Tech. J., vol. 52, no. 1, 117 (1973).
2. Y. Yamamoto, IEEE J. Quantum Electron., vol. QE-16, no. 10, p. 1073 (1980).
3. J. A. Arnaud, IEEE J. Quantum Electron., vol. QE-4, no. 11, 893 (1968).
4. J. C. Simon, J. Lightwave Technol., vol. LT-5, no. 9, 1286 (1987).
5. M. J. O'Mahony, J. Lightwave Technol., vol. LT-6, no. 4, 531 (1988).
6. E. Snitzer, Phys. Rev. Lett., vol. 7, no. 12, 44 (1961).
7. C. J. Koester and E. Snitzer, Applied Optics, vol. 3, no. 10, 1182 (1964).
8. J. Stone and C. A. Burrus, Appl. Phys. Lett., vol. 23, no. 7, 388 (1973).
9. R. H. Stolen, "Nonlinear properties of optical fibers", in Optical Fiber Telecommunications, S. E. Miller and A. G. Chynoweth Eds., New York: Academic, 1979.
10. S. B. Poole, D. N. Payne, R. J. Mears, M. E. Fermann and R. I. Laming, J. Lightwave Technol. vol. LT-4, no. 7, 870 (1986).
11. P. Urquhart, IEE proceedings, vol. 135, Pt. J., no. 6, 385 (1988).
12. D. N. Payne and L. Reekie, Proc. ECOC, Helsinki, Finland, 1987.
13. N. Edagawa, K. Mochizuki and Y. Iwamoto, Electron. Lett., vol. 23, no. 5, 197 (1987).
14. L. F. Mollenauer, J. P. Gordon and M. N. Islam, IEEE J. Quantum Electron., vol. QE-22, no. 1, 157 (1986).

15. L. F. Mollenauer and K. Smith, Optics Lett., vol. 13, no. 8, 675 (1968).

16. N. A. Olsson and J. P. Van Der Ziel, Electron. Lett., vol. 22, no. 9, 490 (1986).

17. R. W. Tkach, A. R. Chraplvyy, R. M. Derosier and H. T. Shang, Electron. Lett., vol. 24, no. 5, 261 (1988).

18. N. A. Olsson and J. P. Van Der Ziel, Appl. Phys. Lett., vol. 48, no. 20, 1329 (1986).

19. B. Ross and E. Snitzer, IEEE J. Quantum Electron., vol. QE-6, no. 6, 361 (1970).

20. L. Reekie, R. J. Mears, S. B. Poole and D. N. Payne, J. Lightwave Technol., vol. LT-4, no. 7, 956 (1986).

21. R. J. Mears, L. Reekie, S. B. Poole and D. N. Payne, Electron. Lett., vol. 22, no. 3, 160 (1986).

22. A. V. Astakhov, M. M. Butusov, S. L. Galkin, B. V. Ermakova and Yu. K. Fedorov, Opt. Spectrosc. (USSR), vol. 62, no. 1, 140 (1987).

23. C. A. Millar, M. C. Brierley, P. W. France, Proc. ECOC, Brighton, UK, 1988.

24. E. Desurvire, J. R. Simpson and P. C. Becker, Optics Lett., vol. 12, no. 11, 888 (1987).

25. C. R. Giles, E. Desurvire, J. R. Talman, J. R. Simpson and P. C. Becker, J. Lightwave Technol., vol. 7, no. 4, April 1989.

26. R. I. Laming, L. Reekie, D. N. Payne, P. L. Scrivener, F. Fontana and A. Righetti, Proc. ECOC, Brighton, UK, 1988.

27. R. J. Mears, L. Reekie, I. M. Jauncey and D. N. Payne, Proc. OFC, Reno, NV, 1987.

28. R. J. Mears, L. Reekie, I. M. Jauncey and D. N. Payne, Electron. Lett., vol. 23, no. 19, 1026 (1987).

29. J. R. Armitage, C. G. Atkins, R. Wyatt, in 8th National Quantum Electronics Conference, St. Andrews, Scotland, 1987.

30. R. I. Laming, P. R. Morkel, D. N. Payne and L. Reekie, Proc. ECOC, Brighton, UK, 1988.

31. D. N. Payne and L. Reekie, Proc. ECOC, Brighton, UK, 1988.

32. T. J. Whitley and T. J. Hodgkinson, Proc. ECOC, Brighton, UK, 1988.

33. T. J. Whitley and T. J. Hodgkinson, OPTCON, Santa Clara, CA, 1988.

34. E. Snitzer, H. Po, F. Hakimi, R. Tuminelli and B. C. McCollum, Proc. OFC, New Orleans, LA, 1988.

35. J. R. Armitage, C. G. Atkins, R. Wyatt, B. J. Ainslie and S. P. Craig, Proc. CLEO, Anaheim, CA, 1988.

36. R. I. Laming, S. B. Poole and E. J. Tarbox, Optics Lett., vol. 13, no. 12, 1084 (1988).

37. E. Snitzer and R. Woodcock, Applied Phys. Lett., vol. 6, no. 3, 45 (1965).

38. D. C. Hanna, R. M. Percival, I. R. Perry, R. G. Smart and A. C. Tropper, Electron. Lett., vol. 24, no. 17, 1069 (1988).

39. I. Suzuki, I. Hino, K. Kobayashi, A. Gomyo and S. Kawata, Proc. IQEC, Tokyo, Japan, 1988.

40. M. J. F. Digonnet and C. J. Gaeta, Applied Optics, vol. 24, no. 3, 3333 (1985).

41. H. Horikawa, S. Oshiba, A. Matoba and Y. Kawai, Appl. Phys. Lett., vol. 50, no. 7, 374 (1987).

42. E. Desurvire, C. R. Giles and J. R. Simpson, to be published.

43. J. N. Sandoe, P. H. Sarkies and S. Parke, J. Phys. D: Appl. Phys., vol. 5, 1788 (1972).

44. T. Saitoh and T. Mukai, J. Lightwave Technol., vol. 6, no. 11, 1656 (1988).

45. T. Saitoh and T. Mukai, Electron. Lett., vol. 23, no. 5, 218 (1987).

46. J. C. Simon, B. Landousies, Y. Bossis, P. Doussiere, B. Fernier and C. Padioleau, Electron. Lett., vol. 23, no. 7, 332 (1987).

47. G. Eisenstein, R. M. Jopson, R. A. Linke, C. A. Burrus, U. Koren, M. S. Whalen and K. L. Hall, Electron. Lett., vol. 21, no. 23, 1076 (1985).

48. N. A. Olsson, M. G. Oberg, L. D. Tzeng and T. Cella, Electron. Lett., vol. 24, no. 9, 569 (1988).

49. T. Mukai, T. Saitoh and O. Mikami, Electronics and Communications in Japan, Pt. 2, vol. 70, no. 2, 421 (1987).

50. M. J. O'Mahony, I. W. Marshall, W. J. Devlin and J. C. Regnault, Electron. Lett., vol. 21, no. 11, 501 (1985).

51. M. G. Oberg and N. A. Olsson, IEEE J. Quant. Electron., vol. QE-24, no. 1, 52 (1988).

52. N. A. Olsson, Electron. Lett., vol. 24, no. 17, 1075 (1988).

53. M. J. O'Mahony, I. W. Marshall, H. J. Westlake and W. G. Stallard, Electron. Lett., vol. 22, no. 23, 1238 (1986).

54. N. A. Olsson, M. G. Oberg, L. A. Koszi and G. Przybylek, Electron. Lett., vol. 24, no. 1, 36 (1988).

| EFFECT | SIGNAL WAVELENGTH | REQUIREMENTS | | | GAIN BANDWIDTH | POLARIZATION SENSITIVITY | POTENTIAL APPLICATION |
		PHASE MATCHING	PUMP POWER	FIBER LENGTH			
S RAMAN SCATTERING	TUNABLE	NO	1W	1 Km	12 THz	YES	LONG HAUL LINK LOSS COMPENSATION
S BRILLOUIN SCATTERING	TUNABLE	NO	< 10 mW	1-10 Km	10-100 MHz	YES	WAVELENGTH DIVISION DEMULTIPLEXING
S. FOUR PHOTON MIXING	TUNABLE	YES	100W	10m	2.5 THz	YES	—
RARE EARTH (Er^{3+}) DOPING	FIXED	NO	< 100 mW	1-10m	6.5 THz	NO	1.5 μm LOCAL AREA NETWORKS

Table 1 - Single-mode amplifiers features.
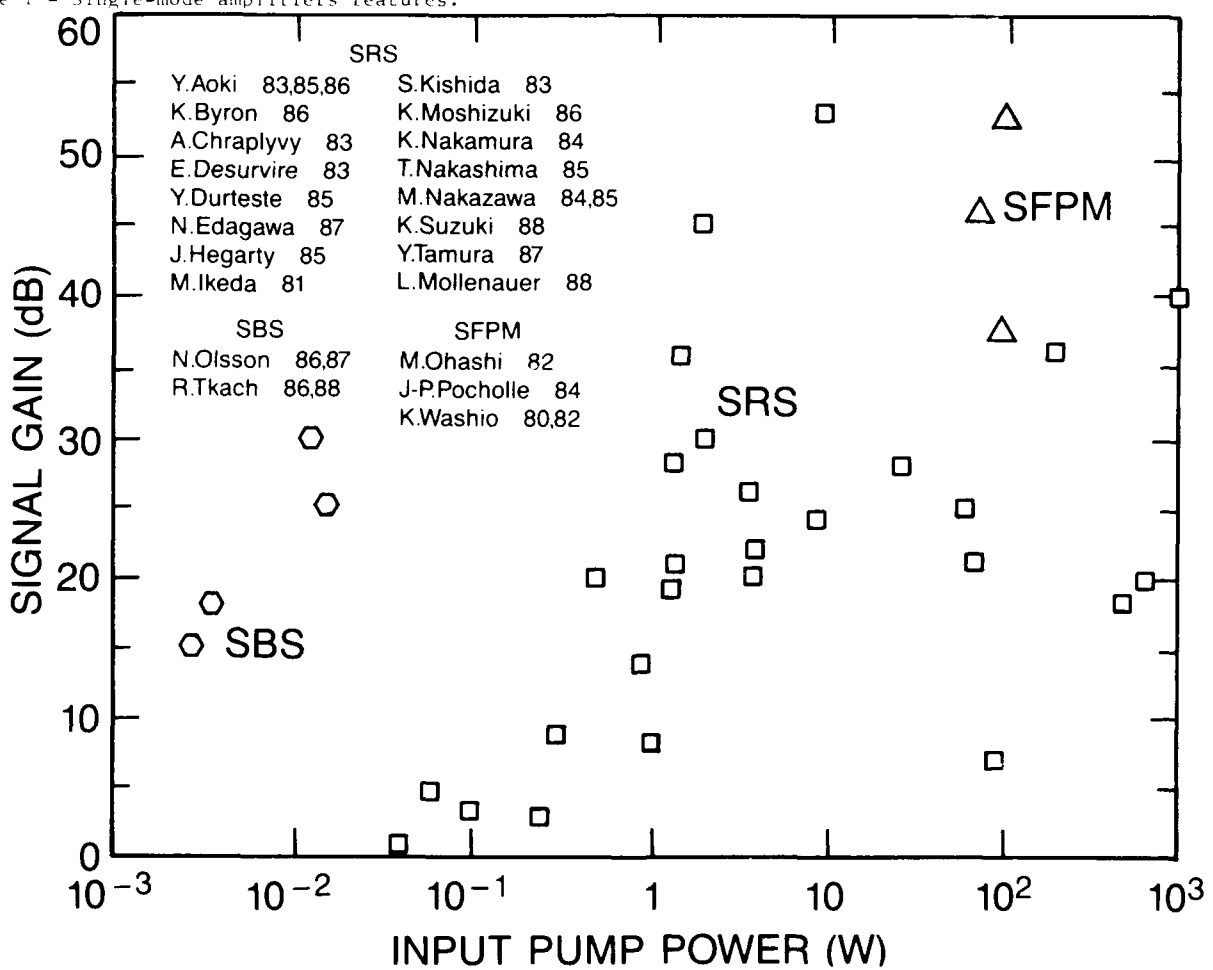
Figure 1 - Maximum gains vs. launched pump power reported for nonlinear fiber amplifiers. SFPM: stimulated four photon mixing, SRS: stimulated Raman scattering, SBS: stimulated Brillouin scattering.

500
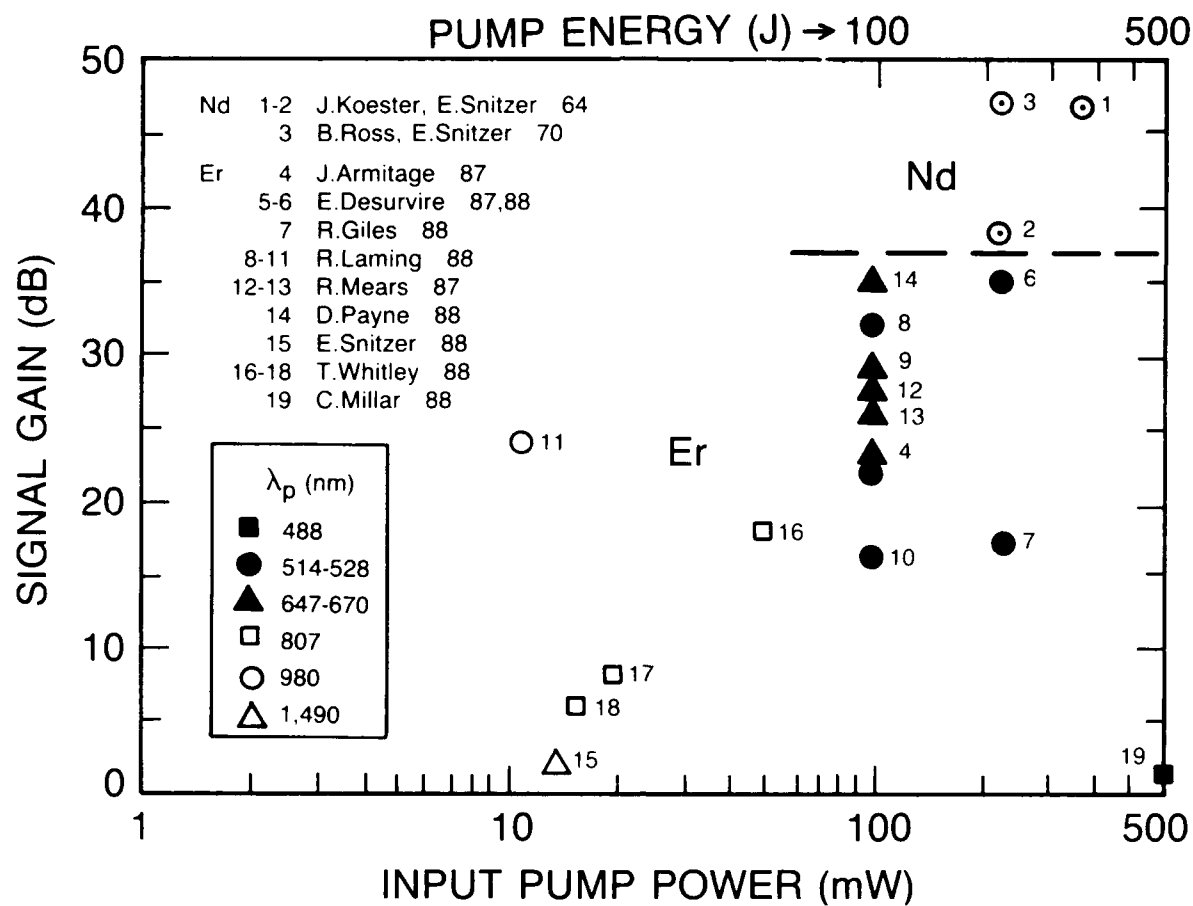
Figure 2 — Maximum gains vs. launched pump power; reported for rare-earth doped fiber amplifiers (Neodymium and erbium).
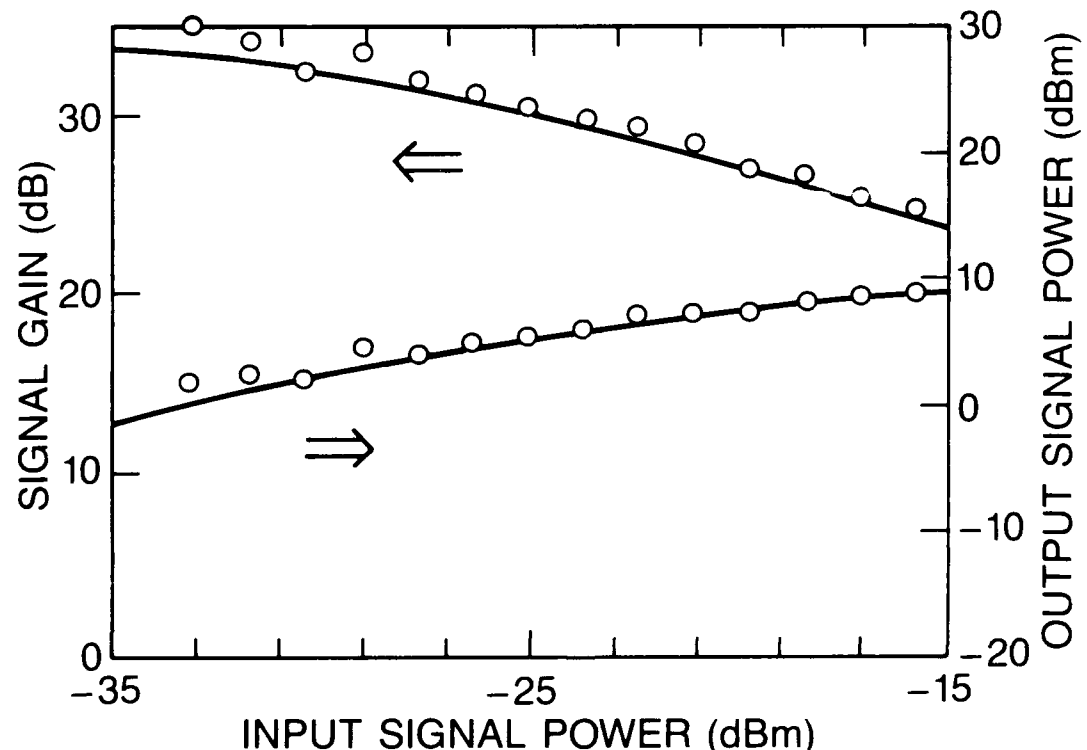
Figure 3 — Signal gain and output signal power at λ = 1.531 μm vs. input signal power, obtained with 225 mW pump at λ = 514.5 nm, in a 1m long erbium-doped fiber amplifier.
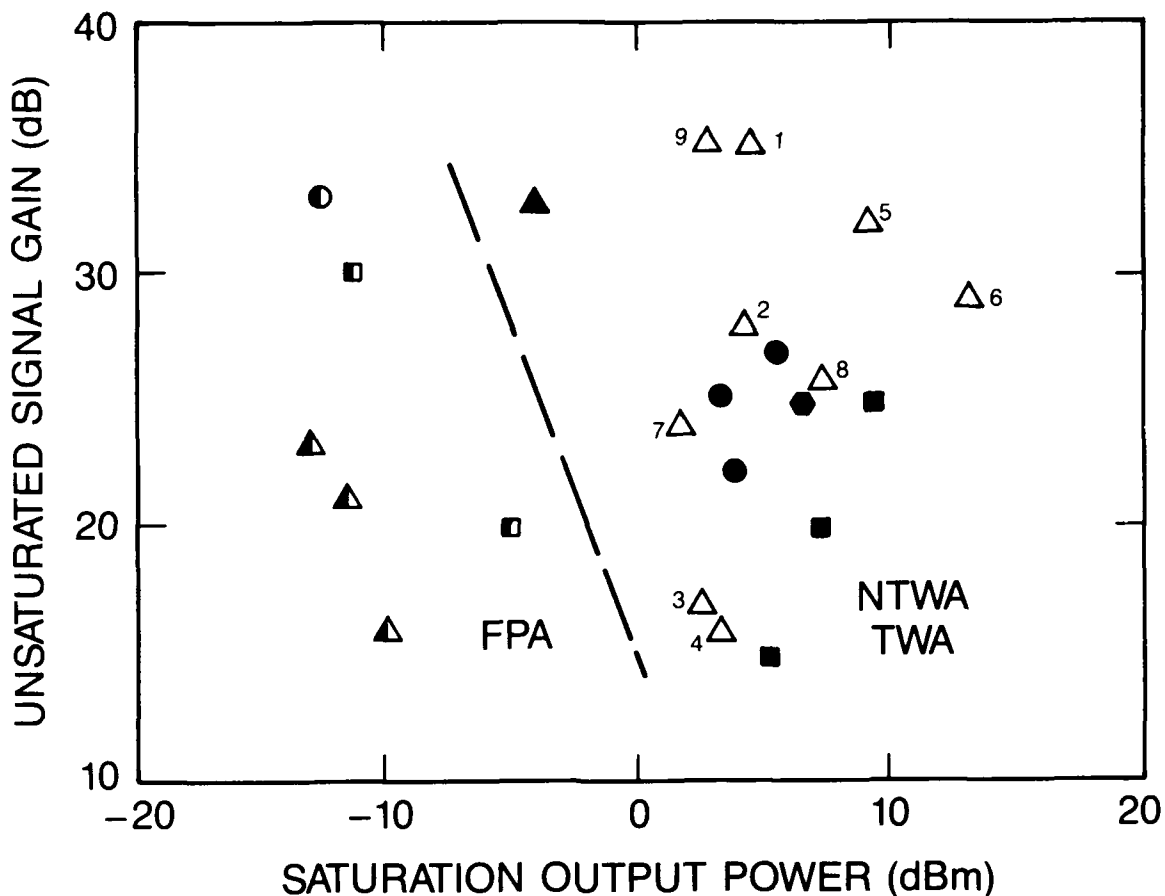
Figure 4 — Unsaturated signal gains vs. saturation output powers reported for Er-doped fiber and 1.5 µm semi-conductor amplifier devices. FPA: Fabry-Perot amplifiers, NTWA and TWA: near traveling-wave and traveling-wave amplifiers. Δ = erbium-doped fiber amplifiers: (1-2) Desurvire et al. [this paper and 42], (3) Giles et al.[25], (4-7) Laming et al.[26,30], (8) Mears et al.[28], (9) Payne et al.[31]; Near TW or TW semiconductor amplifiers: (■) Saitoh et al.[45], (●) Simon et al.[46], (▲) Eisenstein et al.[47], (◆) Olsson et al.[48]; Fabry-Perot semiconductor amplifiers: (□) Mukai et al.[49], (◐) O'Mahony et al.[50], (▲) Oberg et al.[51].

(a)

(b)
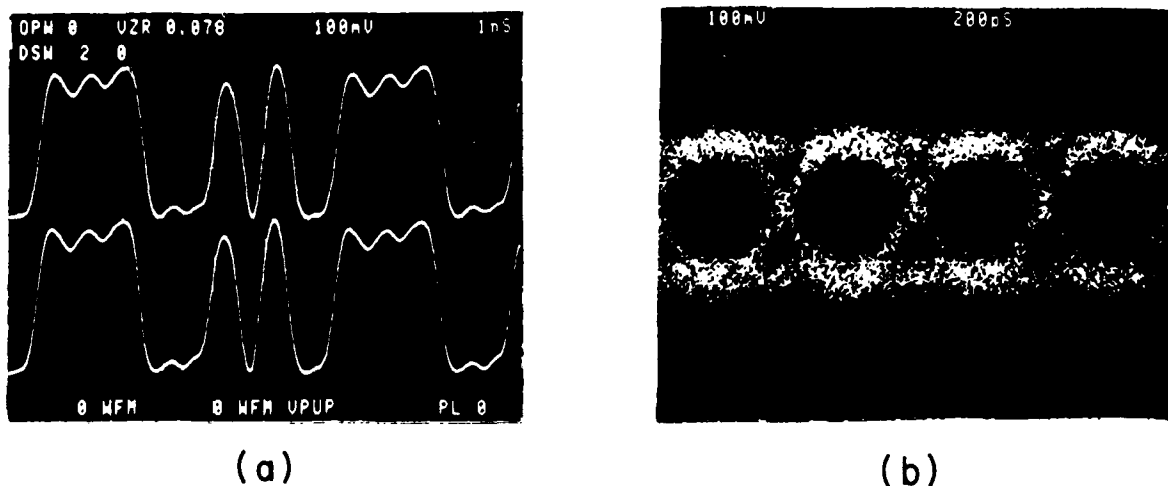
Figure 5 — Signal amplification experiment at 2 Gbit/s in an Er-doped fiber amplifier: (a) oscilloscope traces showing input and output ASK bit sequence (Hor. scale: 1ns/div); (b) eye diagram of output signal (Hor. scale 200 ps/div, arbitrary vertical scales). The pump wavelength was 514.5 nm and the gain +15 dB (after ref. [25]).
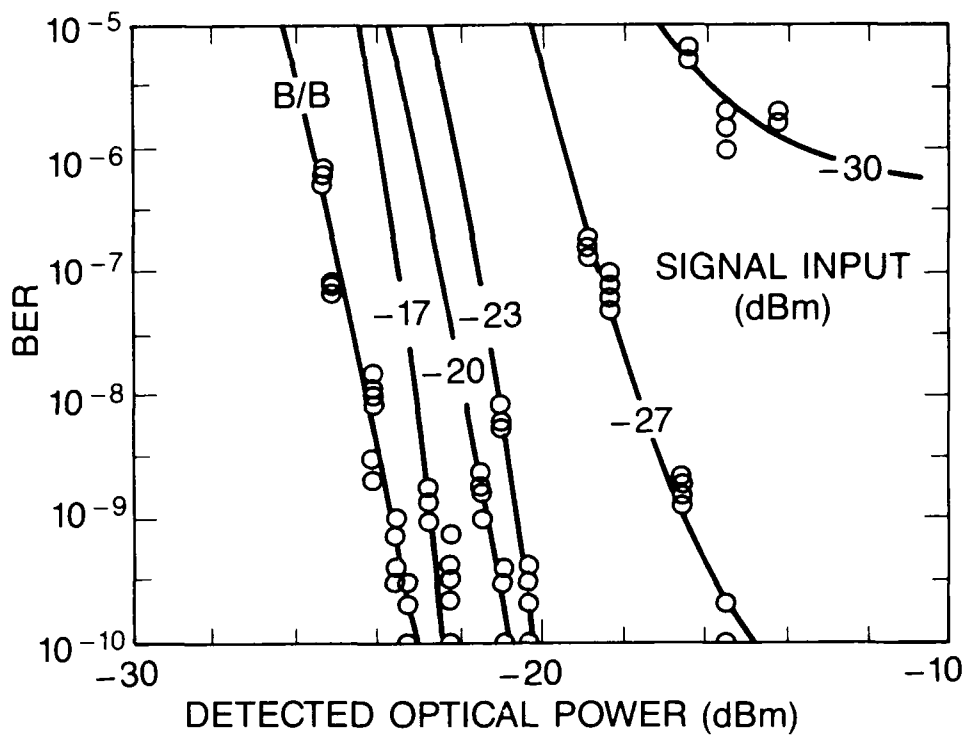
Figure 6 – Bit error rate curves obtained for different signal input powers ranging from -30 dBm to -17 dBm. B/B: back-to-back BER curve obtained without fiber amplifier. The amplifier gain is 15 dB (after ref. [25]).

ULTRAFAST NONLINEARITIES IN OPTICAL FIBRES

J.R. Taylor
Femtosecond Optics Group, Physics Department
Imperial College
Prince Consort Road
London SW7 2BZ
England

Abstract

Several schemes for the generation of ultrashort pulses using nonlinear processes in optical fibres are described. These include the pulse compression mechanism of high order solitons, essentially at a fixed wavelength and the generation of frequency tunable femtosecond pulses using soliton-Raman shaping mechanisms. Both single pass and oscillator arrangements are described, while in the normal dispersion regime a dispersion compensated fibre Raman ring laser was used which was capable of generating picosecond pulses for soliton studies.

Ultrashort pulse generation from high order solitons

In 1973 Hasegawa theoretically proposed [1] that the balance between self-phase modulation broadening and group velocity dispersion compression in the region of anomalous dispersion in a low-loss optical fibre led to the evolution of self-sustaining propagating pulses, the so-called solitons [2]-[4]. Higher order solitons than the fundamental are self-maintaining in the sense that their pulse shapes are periodic with fibre length on propagation, for a particular power, despite the fact that they undergo a series of narrowing and splitting on passage. In 1980 [5] the first experimental observations were made of the pulse compression and splitting nature of the soliton effects in a single-mode optical fibre. In that work, observations of solitons of $N \leqslant 4$ were reported. Pulse restoration at the soliton period was first demonstrated by Stolen et al [6] using the same colour centre laser source. Extreme picosecond pulse narrowing was subsequently reported by Mollenauer et al [7] through the generation of higher-order solitons (N>4), and results on splitting of the initial 7ps pulses from their colour centre laser were presented.

The availability of dispersion-shifted optical fibres [8] enables soliton generation and compression studies to be carried out in the $1.3 \mu m$ region as well as at the previously investigated $1.55 \mu m$ wavelength. Recently, in a scheme similar to that reported here [9], a compressed c.w. mode-locked Nd:YAG laser generating 2ps pulses was used to produce pulses as short as 90fs through a high-order soliton (N=7) effect at $1.32 \mu m$ in a single-mode optical fibre.

It has been shown that the minimum pulse duration achieved during the "breathing" of a multisoliton is approximately given by $\tau_{min} = \tau_0 (4.1N)^{-1}$ where τ_0 is the input pulse width and N the order of soliton. Clearly the lowest pulse durations are achieved with minimum input pulses and the highest soliton number and hence the highest powers possible.

The experimental scheme is shown in Figure 1. A c.w. mode-locked Nd:YAG laser was used as the initial source of 90ps pulses at 100MHz repetition rate with an average power of 1.8W, corresponding to a peak power of 200W. The pulses were optically compressed by means of an optical fibre-grating pair pulse compressor [10]. It is sufficient to mention here that for 800mW coupled into 200m of fibre (dispersion minimum around $1.5 \mu m$) and a 2.5m overall grating separation, pulses as short as 1.1ps (assuming sech^2 pulse shape) were derived. The compressed pulses had an average output power of 550mW, corresponding to a peak pulse power of 5kW. These pulses were then coupled into a piece of single mode fibre 40m long, with zero dispersion at $1.27 \mu m$, an effective core area of $96 \mu m^2$ and a dispersion value D=-5ps nm^{-1}km^{-1} at $1.32 \mu m$, while the loss was <0.5dB km^{-1} at $1.32 \mu m$. A maximum average power of up to 170mW was coupled into this second fibre, which corresponded to 1.6kW peak power. Temporal measurements were made by means of a second-order autocorrelation technique in the background-free configuration, using a <100 μm thick LiIO$_3$ angle-tuning crystal which gave a resolution of better than 10fs. A 0.25m scanning spectrograph in conjunction with a Ge photodetector was used to simultaneously record the pulse spectra.
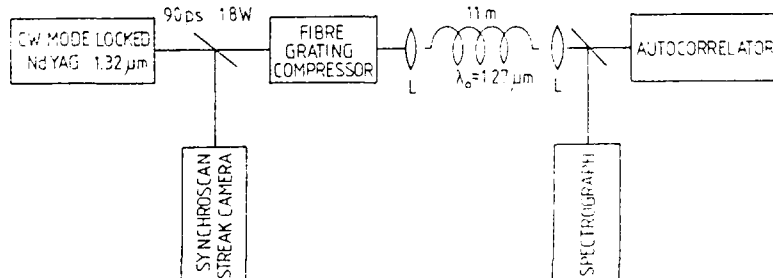
Figure 1.

The soliton period z_0 [2] for the fibre parameters and pulse-duration listed above was approximately 132m and the fundamental soliton power 8.2W. For peak powers up to 1.6kW coupled into the fibre, a soliton number N=14 is predicted, corresponding to a theoretically predicted [7] compression factor (τ/τ_0) of 57 at the point of first optimal narrowing.

As observed previously, the experimental compression ratio for a given soliton number agreed quite well with theoretically predicted results [11]. However, the position for the optimal narrowing length disagreed by a factor of 2.75 [11]. The optimal fibre length was determined empirically in a fibre-cut back process. Autocorrelations of the pulse profiles on exit from the second fibre were recorded as the fibre length Z was varied. The same rapid soliton-formation process in the initial few metres of the fibre was observed [11]. However, for the situation described above the optimum length was found to be 11m and pulses as short as 18fs (see Figure 2) were generated using this fibre length, corresponding to a measured compression factor of times sixty.
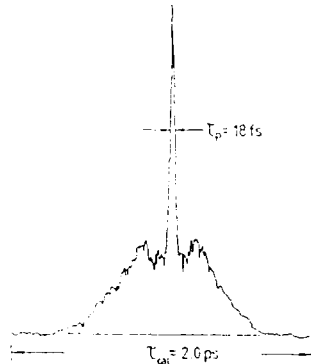
Figure 2:

As can be seen from Figure 2, the soliton pulses were situated on the top of a broad pedestal lasting 1.7ps and accounting for 69% of the total energy. This resulted in the peak powers of the 18fs soliton pulses being 29.3kW. At 1.32μm, a pulse of 18fs corresponds to four optical cycles. However, although ultrashort pulses even with reduced pedestals can be generated [12], the wavelength of the radiation is basically fixed to that of the input pulse. For many applications, frequency tunable sources of ultrashort pulses are preferable and methods of generating these are described below.

Single pass soliton-Raman generation

For relatively long picosecond pulses propagating in moderate lengths of single-mode optical fibre, stimulated Raman scattering is a dominant loss mechanism, with Stokes frequencies being generated with high conversion efficiencies. For silica-based fibres, the peak of the broad Raman-gain band is around 440cm^{-1} [12], but large Raman gain is possible for substantially smaller frequency shifts. The high Raman gain has led to the fabrication of fibre-Raman laser systems [13], which, owing to the relatively large gain bandwidth of the Raman process, were recently shown to generate subpicosecond pulses in a dispersion-compensated fibre-Raman oscillator operating in the region of positive group-velocity dispersion [14], and a similar system will be described below. For standard silica-based fibre, the dispersion minimum wavelength λ_0 is in the region of 1.32μm. Therefore, for a pump or incident laser wavelength in the region of the dispersion minimum, the generated Raman signal will be in a regime of negative or anomalous group-velocity dispersion. Vysloukh and Serkin [15] and Dianov et al [16] first indicated that this could give rise to self-compression of the amplified Raman component through a soliton-compression mechanism. This was subsequently demonstrated in the fibre-Raman amplification soliton laser by Islam et al [17]; the pump and Raman wavelengths, which were in the normal and anomalous dispersion regimes, respectively, straddled the dispersion minimum such that both components effectively propagated with nearly equal group velocities. The pump wavelength was provided from a tunable colour-centre laser, and, with proper cavity adjustment, the laser generated powers of approximately 1mW in pulses of 250fsec duration. Zysset et al [18] have shown, in a single-pass arrangement using 1psec pulses from a frequency-tunable dye laser, that Raman pulses as short as 160fsec can be generated. In a ring resonator they obtained peak powers of 2kW in 80fsec pulses.

However, obtaining frequency tunable, soliton pulses with durations in the regime of 100fs can be simplified, through the use of a single pass generation technique. The basic experimental arrangement consisted of a c.w. pumped actively mode locked Nd:YAG laser, operating at 1.32μm, generating 90ps pulses with an average power of ~1.8W, at a pulse repetition rate of 100MHz. The pump radiation was coupled in various lengths of single mode optical fibre, and the output was examined both spectrally and temporally with resolutions of 0.1nm and 20fsec respectively. Single mode optical fibres with various physical parameters were investigated. However, initial results were taken with a standard, single mode in the region of 1.31μm non polarization preserving fibre, with a 7μm core diameter and a <1dB/km loss at 1.32μm.

Streak camera records revealed that the transmitted pump pulse, at high average pump powers exhibited severe pulse depletion, to the base line level, and conversion efficiencies to the broad band Raman signal exceeded 60%. Figure 3 shows a typical spectrum recorded for an average pump power of 700mW at 1.32μm in 200m of single mode fibre.

505

1600 nm   1200 nm

Figure 3.

The Raman band extended from just above 1.32 μm to ~ 1.54 μm, centred around a broad maximum at 1.41 μm. On reduction of the pump power, the extent of the long wavelength component of the Raman signal decreased, with the maximum remaining around 1.41 μm. The feature at 1.32 μm corresponded to the fundamental signal, while that at 1.295 μm was associated with the short wavelength component of the modulation instability [19]. To the long wavelength side of the fundamental, the component of the modulation instability acts as a seed pulse for preferential Raman gain and is indistringuishable in the broad Raman band of Figure 3.

In the temporal domain, Figure 4 shows a typical background free autocorrelation trace of a 210fsec pulse spectrally selected from the broad Raman continuum.

TIME
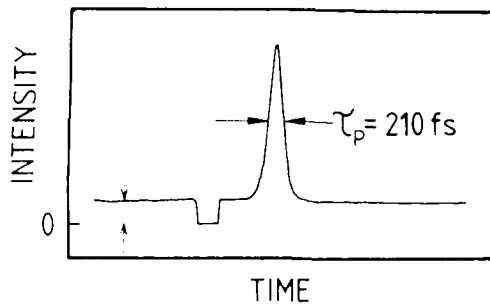
Figure 4.

In the region of 1.4 μm, a 200fs pulse requires ~ 35nm spectral bandwidth to support the pulse. The Raman continuum extended from 1.33 μm to beyond 1.5 μm, celarly well in excess of the required bandwidth. This is because the total spectrum is not solely associated with a single pulse. In fact, several single solitons exist in the generated band. This is clear from the fact that it is possible to generate tunable femtosecond pulses simply by using a spectral window to tune across the output spectrum, the corresponding pulses in the time domain are similar to that shown in Figure 4 [20,21].

For the experimental conditions described above, the soliton generation processes evolves from modulational instability [21,22]. The gain process providing amplification to the temporal modulations gives rise to compression and the formation of several solitons randomly spaced at various wavelengths. These solitons propagate with differing velocities giving rise to collisions and furtner spectral broadening.

However, modulational instability is not a prerequisite to initiate the process. It is possible to obtain similar single pass spectral and temporal behaviour by using a pump pulse in the normal dispersion regime. In this case it is pure Raman scattering which initiates the process [23], and under these circumstances the pump power levels to achieve threshold for continuum and ultrashort pulse generation are considerably high than for the modulation instability seeded case. In the latter, for a 3.3km fibre, 150fs fundamental solitons can be formed at an average pump power of only 20mW (100ps, pump pulses at 1.32 μm).

Fibre-Ring Soliton Raman Laser Systems

Following single pass soliton-Raman Generation, if the Raman signal emerging from the fibre is directed back to the fibre input in synchronism with a fundamental pump pulse, then where preferential amplification of the reinjected Raman signal is greater than the cavity losses, the establishment of laser oscillation is possible. Due to the very high gain of the SRS process, fibre Raman laser action can be obtained at relatively modest pump power levels.

The simplest cavity configuration is that shown in Figure 5. A beam splitter BS (100% at 1.32 μm, <5%R

506

at 1.4 μm) was used to direct the fundamental pump pulses via a X20 a.r. coated microscope objective L_1, into the Raman active fibre. Various lengths of fibre were used, with the similar parameters to those described above. At the fibre output, another X20 objective L_2 was used to collect and collimate the Raman radiation, which after reflection off two aluminium coated mirrors M, redirected the Raman signal via the beam splitter BS into the fibre input focussing microscope. Synchronism of the returning Raman signal with the input fundamental pump pulse was achieved by adjusting the fibre laser cavity length while observing the leakage transmitted and reflected returning fundamental radiation off BS. Cavity length adjustment was achieved by placing the fibre output end-lens assimbly L_2 on a translation stage with micron precision drive control. Coarse cavity adjustment was chieved by observing the temporal overlap of two componenets on the synchroscan streak camera. Final cavity adjustment was then obtained by precision control of the cavity length while monitoring the output power and soliton-Raman pulsewidth. Due to the long Raman interaction length, femtosecondsoliton-Raman laser action was possible over a wide range (cm) of cavity mismatch. However, the degree of the pedestal on the autocorrelation traces was more critically dependent on exact cavity match.

Figure 5.

The operation of the fibre laser systems was particularly dependent on the fibre length. for short lengths, modulational instability was the dominant single pass generation mechanism and on reinjection of the single pass signal in synchronism with a pump pulse, the modulational instability acted as a preferential seed for Raman gain, with resultant laser action taking place in a band separated by $150 cm^{-1}$ from the pump peak, instead of at the peak of the Raman gain around $440 cm^{-1}$ [24].

For substantially longer fibre lengths, laser operation on the band corresponding to the peak of the Raman gain was observed. This is illustrated in the spectra of Figure 6, which corresponds to a 300m fibre pumped in the single pass and resonator geometries, at an average pump power of 400mW. In single pass, under these conditions a single pulse with a pedestal of 5% of the autocorrelation intensity and duration of 100fs can evolve, as described in the first section. However, it is the modulational instability seeded Raman gain process which was responsible and operation was in a broadband around 1343nm (see Figure 6(a)). With feedback, true Raman amplification centred around the maxima of the gain (~ $440 cm^{-1}$) occurred with the lasing Raman band extending from 1384nm to 1420nm, with a half width of 25nm, capable of supporting 80fs pulses. Typically pulses of 150fs-180fs were generated, with pedestals of 5-7% appearing on the autocorrelation traces. The threshold for oscillation in the ring geometries was <20mW, and output pulses with peak powers in the kilowatt regimes were generated.

Figure 6.

Cascade Raman soliton fibre lasers

In the positive group velocity dispersion regime, the propagation of "long" picosecond pulses in single mode optical fibres can lead to substantial conversion efficiencies into the higher Stokes orders through the cascading process. However, in the negative group velocity dispersion regime the efficient generation of ultrashort Raman pulses through the soliton shaping mechanism prohibits the higher order generation

507

cascade process, since the interaction distance of the femtosecond pulses is prohibitively short for further efficient Raman generation. Consequently a fibre with a zero dispersion wavelength around 1.3 μm would not allow efficient 1.5 μm second Stokes generation from the soliton Raman pulses at 1.4 μm.

Optimization of fibre design and contruction [8] permits the manufacture of single mode optical fibres with specified zero dispersion wavelengths from 1.27 μm to 1.55 μm. Consequently cascade generation can take place in the positive group velocity dispersion regime and after generation of the Stokes order above the dispersion minimum, the cascade will cease. In this way broad tunability of the soliton-Raman operating band can be achieved.

To investigate the cascade-Raman soliton generation process the cavity configuration of Figure 5 was used, with the inclusion of a 5 μm thick pellicle which acted as a bandwidth limiting Fabry Perot device and also permitted with coupling of radiation from the cavity. A 600m length fibre was used, which was single mode at 1.32 μm with a 7 μm core diameter. In the spectral region 1.2 μm to 1.65 μm the loss was less than 0.6dB/km, except around 1.39 μm where the loss due to OH absorptionincreased to 2dB/km. The fibre had an optimized structure for dispersion minimum in the region of 1.46 μm, thus ensuring a positive group velocity dispersion of the first Stokes Raman band around 1.4 μm and negative dispersion for the cascaded second Stokes band at 1.5 μm. The dispersive values were 5ps/nm km and -2.5ps/nm km at 1.4 μm and 1.5 μm respectively. A typical average power coupling efficiency through the fibre lens coupling system of ~40% was achieved.

Figure 7 shows the output spectrum in the feedback ring geometry. In the single pass condition only the fundamental F and first Stokes bands S_1 were observed at the average pump power level of 500mW. Oscillation on the third Stokes band was only observed at the highest pump power level of 550-600mW.
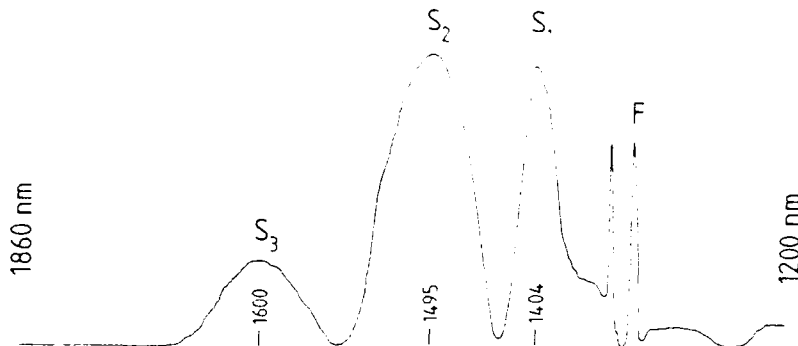
Figure 7.

Autocorrelation revealed that the second and third Stokes components had durations of 200fs and 230fs respectively. In addition, the pedestals of the autocorrelations were substantially reduced. From the relative heights of the soliton part of the pulse to the non soliton background pedestal, it was calculated that approximately 85% of the Raman energy was in the soliton pulse. The threshold for laser action on the S_2 band occurred for a fundamental pump power of about 150mW and for about 400mW average pump power, in an optimized system, up to 100mW average putput power in the second Stokes band was obtained. The average powers in the third Stokes bands were much lower being around 3-5mW.

Synchronously pumped, dispersion compensated fibre Raman ring lasers

In the normal dispersion regime, the combined effects of self phase modulation and group velocity dispersion give rise to temporal broadening of pulses. As was shown above with anomalous dispersion the fibre acts as a distributed compressor and a balance can be achieved between the dispersion and the non-linearity, giving rise to solitons and pulse compression. In order to overcome the problem of dispersion, for normally dispersive fibres it is possible to insert a negatively dispertive delay line which compensates for the combined effects of the self phase modulation and positive dispersion and permits the generation of subpicosecond pulses. This was originally demonstrated by Kafka et al [25] and recently by Dianov et al [26], for operation around 1.1 μm. We describe a similar system operating around 1.4 μm which is a simple and potential source of soliton pulses.

508
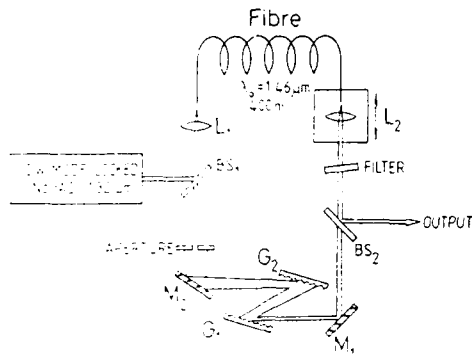
Figure 8.

The schematic of the synchronously pumped intracavity dispersion compensated fibre Raman ring laser is shown in Figure 8, the c.w. mode-locked Nd:YAG laser operated at 1.32 μm, generating 100ps pulses at a 100MHz repetition rate and with an average output power of $\sim$2.0W (200W peak) was used as the pump source. The pump radiation was directed towards the fibre input using beam splitter BS1, with reflectivity nominally 100% at 1.32 μm and 5% at 1.4 μm, for 45° angle of incidence. A x20 broad band anti-reflection coated microscope objective L1 was used to focus the pump radiation into the fibre. The fibre used was 400m long, non-polarisation preserving single mode at 1.32 μm, with a core diameter of 7 μm. In the spectral region 1.2 μm to 1.65 μm, the loss was less than 0.6dB/km, with an exception in the region of the water absorption 1.39 μm where the loss rose to $\sim$2dB/km. The fibre was tailored to have its dispersion minimum in the region of 1.46 μm which ensured efficient Raman generation and positive group velocity dispersion in the region of lasing operation around 1.4 μm.

On exiting the fibre, where typically an overall power coupling of 40% was achieved, the radiation was collected and collimated with an indentical microscope objective (L2) as used at the input, and directed via aluminium coated mirror M1 through a negatively dispersive delay line, comprising a pair of diffraction gratings in a single pass configuration. The gratings were of holographic type with 1200l/mm and approximately 70% diffraction efficiency at 1.4 μm at 75% angle of incidence. Mirror M2 directed the radiation from the dispersive delay line through an aperture (which selectively defined the wavelength on interest), and via beam splitter BS1, back into the input focusing microscope objective. A 2nm band pass dielectric filter central at 1.4 μmprovided output coupling from this fibre ring oscillator. By mounting the fibre end-lens L2 assembly on a translation stage which was driven with micron precision, synchronism of the fed back Raman signal with the input pump pulse was achieved to obtain the maximum output signal.

For a particular pump power, the grating separation and cavity length were adjusted for minimum duration output pulses. In the experimental situation described here the optimum grating separation was 18cm. For grating separation of 10% to 15% either longer or shorter than the optimum value, the fibre Raman ring laser produced pulses much longer than the optimum duration of 2.7ps. The pump power coupled into the dispersion shifted optical fibre was kept at an average power of 400mW, which is approximately the Raman threshold value for this fibre length. In the single pass arrangement no signal around 1.4 μm was observable.

Typically the average output power of the otimized laser system was 20mW, in pulses of 2.7ps, and the spectral bandwidth was 2nm, determined by the intracavity filter. Tuning could be achieved by moving the aperture across the intracavity dispersed spectrum. Figure 9 shows a typical autocorrelation of a generated pulse at 1.39 μm. It should be possible through system optimization and removal of the intra-cavity band-width limiting device to generate sub-pico-second pulses in this regime. However, the picosecond pulses generated with peak powers of 100W should find application in studies of soliton propagation and semi-conductor spectroscopy.
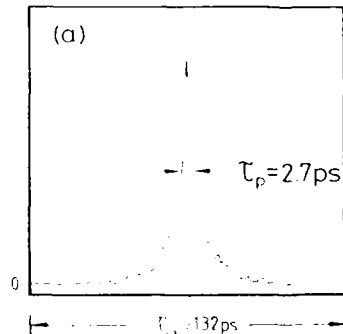
Figure 9.

Acknowledgements

References

[1]   A. Hasegawa & F. Tappert, Appl. Phys. Lett. 23, 142 (1973).
[2]   J. Satsuma & N. Yajima, Prog. Theor. Phys. Suppl. 55, 284 (1974).
[3]   A. Hasegawa & Y. Kodama, Proc. IEEE 69, 1145 (1981).
[4]   V.E. Zakarov & A.B. Shabat, Sov. Phys. JETP 34, 62 (1974).
[5]   L.F. Mollenauer, R.H. Stolen & J.P. Gordon, Phys. Rev. Lett. 45, 1095 (1980).
[6]   R.H. Stolen, L.F. Mollenauer & W.J. Tomlimson, Opt. Lett. 8, 186 (1983).
[7]   L.F. Mollenauer, R.H. Stolen, J.P. Goedon & W.J. Tomlinson, Opt. Lett. 8, 289 (1983).
[8]   B.J. Ainslie & C.R. Day, IEEE J. Lightwave Tech. LT4, 967 (1986).
[9]   K. Tai & A. Tomita, Appl. Phys. Lett. 48, 1033 (1986).
[10] A.S.Gouveia-Neto, A.S.L. Gomes & J.R. Taylor, Opt. Quantum Electron. 18, 423 (1987).
[11] A.S. Gouveia-Neto, A.S.L. Gomes & J.R. Taylor, Optics Lett. 12, 395 (1987).
[12] R.H. Stolen & E.P. Ippen, Appl, Phys. Lett. 22, 276 (1973).
[13] R.H. Stolen, Fibre Integr. Opt. 3, 21 (1980).
[14] J.D. Kafka, D.F. Head & T. Baer, in Ultrafast Phenomena V, Vol.46 of Springer Series in Chemical Physics G.R. Fleming and A.F. Siegman, eds. (Springer-Verlag, Berlin, 1986), p.51.
[15] V.A. Vysloukh & V.N. Serkin, Pis'ma Zh. Eksp. Teor. Fiz. 38, 170 (1983).
[16] E.M. Dianov, D. Ya Karasik, P.V. Mamyshev, A.m. Prokhorov, V.N. Serkin, M.F. Stelmakh and A.A. Fomichev, Piz'ma Zh Eksp. Teor. Fiz. 41, 42 (1985).
[17] M.N. Islam, L.F. Mollenauer adn R.H. Stolen, Ultrafast Phenomena V 46, 54 (1986).
[18] B. Zysset. P. Beard, W. Hodel and H.P. Weber, Ultrafast Phenomena V 46, 54 (1986).
[19] A. Hasegawa & W.F. Binkman, IEEE J. Quantum Electon. QE 16, 694 (1980).
[20] A.S. Gouveia-Neto, A.S.L. Gomes & J.R. Taylor. Invited paper MH1. Proceedings of Conference on Lasers and Electro Optics 1987, Baltimore.
[21] A.S. Gouveia-Neto, A.S.L. Gomes & J.R. Taylor, Optics Lett. 12, 1035 (1987).
[22] A.S. Gouveia-Neto, M.E. Faldon & J.R. Taylor, Optics Commun. 69, 325 (1989).
[23] A.S. Gouveia-Neto & J.R. Taylor, Electronics Lett. 24, 1544 (1988).
[24] A.S. Gouveia-Neto, A.S.L. Gomes & J.R. Taylor, IEEE J. Quantum Electron, QE 24, 332 (1988).
[25] J.D. Kafka, D.F. Head & T. Baer, Springer Series in Chemical Physics Ultrafast Phenomena, V 46, 51 (1986).
[26] E.M. Dianov, P.V. Mamyshev, A.M. Prokhorov & D.G. Fursa, Piz'ma Zh. Eksp. Teor. Fiz. 45, 469 (1987).

Picosecond Laserinduced Orientation of Nematic Liquid Crystals

H.J. Eichler, R. Macdonald
Optisches Institut, Technische Universität, D-1000 Berlin 12

Abstract

Laser-induced dynamic gratings in the nematic and isotropic phase of a liquid crystal 5CB using 532nm laser pulses are investigated. It is shown that optically induced molecular reorientation in the nematic phase as well as pretransitional orientation (optical Kerr effect) in the isotropic phase of a liquid crystal is possible in less than 100ps if sufficiently intense laser fields ($\approx$ 100mJ/cm²) are used. Experimental data obtained from self diffraction experiments agree well with calculations starting from a unified theory of molecular alignment.

Nonlinear optical processes in liquid crystals have attracted strong attention because of large nonlinear susceptibilities $\chi^{(3)}$ both in the nematic mesophase and the isotropic phase[1]. These nonlinearities are approximately independent of wavelength over the whole visible and near infrared region in contrast to other materials with large nonlinearities[2]. In nematics, unusually large optical effects based on optical-field induced molecular reorientation have been observed by using low power cw-laser beams[3] but reorientation will also occur if short laser pulses are used, as has been demonstrated with nanosecond pulses recently[4].

The dominant contribution to the optical nonlinearity in the isotropic phase comes from the optical-field induced alignment of the anisotropic molecules, known as pre-transitional behaviour or the optical Kerr effect[5]. This effect has also been investigated with nanosecond laser pulses, e.g. in degenerate four-wave mixing experiments[6]. The molecular orientation induced by stepwise optical excitation is built up to steady state with a time constant of some 10 ns for the optical Kerr effect and of some 100 ns for molecular reorientation processes in nematics (depending on optical field strength). So the 10 ns laser pulse duration in the previous short pulse experiments [4,6] is smaller or comparable to the molecular orientation build-up time.

In the present paper it is shown that molecular reorientation or field-induced alignment of molecules will also occur when much shorter laser pulses of about 80 ps are used. The optical field needed for picosecond orientation ($\approx$ GW/cm²) is somewhat higher compared to similar experiments with nanosecond lasers ($\approx$ MW/cm²). In our experiments we used a two-wave mixing arrangement and measured the self-diffraction efficiency of a laser induced dynamic grating corresponding to a transient, spatially periodic molecular orientation in a thin film of the cyanobiphenyl 5CB. Experiments have been done in both the nematic and the isotropic phase. The spatially inhomogeneous alignment under the influence of an optical field can be described by the unified theory for nonequilibrium phenomena in both the nematic an isotropic phase of a liquid crystal[7]. This theory leads to the well-known Erickson-Leslie approach for the nematic phase, where the dynamics of reorientation are described by a torque balance. On the other hand, one gets a similar equation for the alignment tensor in the isotropic phase, describing the dynamics of field-induced molecular alignment. Both effects, reorientation and alignment, lead to changes of the refractive index of the liquid. Considering two incident linearly polarized laser beams interfering in the sample, the resulting intensity fringes modulate the refractive index to form a phase-grating. The self-diffraction efficiency of such a thin phase-grating is given by[8]

$$\eta = (E_D/E_1)^2 = (\delta\Psi/2)^2 = (\pi \cdot d \cdot \delta n/\lambda)^2 \tag{1}$$

where δn denotes the amplitude of the index grating, d the sample thickness and the laser wavelength. E_D is the optical field diffracted into the first diffraction order from one of the input beams, e.g. E_1. For simplicity $E_1 = E_2$ is assumed. It should be noted that eq. 1 is valid only if the phase ampliutde of the grating $\delta\Psi \leq 0,1$ which is satisfied in our experiments. The amplitude of the laser-induced index-grating δn is calculated in the following for both phases.

a) nematic phase: Consider two laser beams incident on a homeotropic nematic film as shown in Fig.1. The dynamics of the molecular reorientation angle Θ following the Ericksen Leslie approach is given by [7,9]

$$\gamma_n \frac{\partial \Theta}{\partial t} - K\left(\frac{\partial^2 \Theta}{\partial y^2} + \frac{\partial^2 \Theta}{\partial z^2}\right) - \varepsilon_0 \varepsilon_a E^2 \left(\Theta \cos 2\beta + \frac{1}{2} \sin 2\beta\right) = 0 \qquad (2)$$

where flow and inertia effects have been neglected and we made the one-elastic-constant and the small angle approximation, $\sin \Theta \approx \Theta$ which is valid in the following wave-mixing experiments. K is the elastic constant, γ_n the effective viscosity coefficient and $\varepsilon_a = \varepsilon_\| - \varepsilon_\perp$ the optical dielectric anisotropy for perfectly aligned molecules. Θ is the reorientation angle of the director L measured from initial alignment and β denotes the anlge between optical axis and the initial alignment. Experimentally β is the angle of incidence (Fig.1). An approximate solution of eq.2 under hard boundary conditions ($\Theta(z=0) = \Theta(z=d) = 0$) is $\Theta = T_{(t)} \cos(gy) \sin(z\pi/d)$ where q $= |k_1-k_2|$ is the wavenumber of the interference pattern which is assumed to vary along the y-axis. The interference pattern consists of a contribution modulated with cos (gy) riding on a constant background level which is neglected here. Neglecting higher Fourier-components an equation for the time dependent amplitude $T_{(t)}$ is obtained (see ref.9 for details)

$$T_{(t)} = (\gamma_n)^{-1} \int_{-\infty}^{t} F_{(t)} \exp(-(t - t')/\tau) dt' \qquad (3)$$

where $F_{(t)} = \frac{1}{2}\varepsilon_0 \varepsilon_a E_{(t)}^2 \sin(2\beta)$ and $\tau = \gamma_n/\{\varepsilon_0 \varepsilon_a E^2 \cos 2\beta - K(q^2 + \pi^2/d^2)\}$. τ is a time constant characterizing the build up of the reorientation process in presence of an optical field. In our experiments $\varepsilon_0 \varepsilon_a E^2 \cos 2\beta \gg K(q^2 + \pi^2/d^2)$ so $\tau = \gamma_n/\varepsilon_0 \varepsilon_a E^2 \cos(2\beta)$, i.e. the elastic behaviour of a nematic does not affect the build-up time if sufficiently high fields are used. The reorientation decay time τ_D is also given by τ setting $E^2 = 0$ to give $\tau_D = \gamma_n/K(q^2 + \pi^2/d^2)$. The orientation decay is forced by the elastic torques. In our experiments e.g. $E = 10^8 V/m$, $d = \Lambda = q/2\pi = 30\mu m$, $K = 8 \times 10^{-12}$ N, $\gamma_n = 0,01$ kg/ms, $\varepsilon_a = 0,62$ result in $\tau = 200$ ns whereas $\tau_D = 100$ ms.

The build-up of the reorientation angle Θ described by eq.3 follows the incident energy $\int E_{(t)}^2 dt$ if the pulse duration $\tau_p \ll \tau$ which is the case in our experiments with picosecond optical fields $E_{(t)}$. The time constant τ plays no role in this case. The amplitude $T_{(t)}$ reaches a maximum at the end of the excitation pulse t $= \tau_p$ and decays exponentially with the relaxation time τ_D for t $> \tau_p$ if a square excitation pulse is assumed so that $E_{(t)} = E = const.$ during the pulse duration. For this case the amplitude Θ_{max} of the reorientation grating in the center of the sample at the end of the laserpulse is obtained by integrating eq. 3 to give

$$\Theta_{max} = \frac{1}{2} \gamma_n^{-1} \varepsilon_0 \varepsilon_a E^2 \tau_p \sin(2\beta) \qquad (4)$$

The change of the refractive index δn for a given small angle Θ is $\delta n = \sqrt{2} n_\perp n_\|^{-2} \varepsilon_a \Theta$ sin (2β) where $n_\perp = \sqrt{\varepsilon_\perp}$ and $n_\| = \sqrt{\varepsilon_\|}$ so that the amplitude of the index grating at the end of the incident laser pulse becomes

$$\delta n_{max} = (\sqrt{2}/\pi) \varepsilon_0 \varepsilon_a^2 n_\perp n_\|^{-2} \gamma_n^{-1} E^2 \tau_p \sin(2\beta) \qquad (5)$$

Substituting eq.5 into eq.1 gives the self-diffraction efficiency for the laser induced phase-grating as a function of laser intensity and the angle of incidence β. Some corrections have to be taken into account for comparisons with experiments, e.g. one has to integrate eq.1 over time if the diffracted energy is detected in a self-diffraction experiment (see ref.10 for details).

b) isotropic phase: Ordering in molecular orientation for the isotropic phase of nematics can be described[7] by an alignment tensor $a_{\mu\nu}$ which is a traceless symmetric tensor associated with the anisotropy of physical properties, e.g. with optical anisotropy

$$\varepsilon_{\mu\nu} - \delta_{\mu\nu}\bar{\varepsilon} = \varepsilon_a a_{\mu\nu} \qquad (6)$$

where $\bar{\varepsilon} = 1/3_\nu \Sigma \varepsilon_{\nu\nu}$ is the isotropic part of the dielectric tensor, $\varepsilon_a = \varepsilon_\| - \varepsilon_\perp$ the anisotropy for perfectly aligned molecules and $\delta_{\mu\nu}$ the Delta-Kronecker symbol. The birefrigence induced by ordering is $\delta n_{\mu\nu} = \frac{1}{2}(\varepsilon_{\mu\nu} - \delta_{\mu\nu}\bar{\varepsilon})/\bar{n} = \frac{1}{2}\varepsilon_a a_{\mu\nu}/\bar{n}$ where $\bar{n}$ is the refractive index of the isotropic liquid. The components of the alignment tensor $a_{\mu\nu}$ under the influence of an optical field are calculated from a differential equation similar to eq.2

$$\tau_a \frac{\partial a_{\mu\nu}}{\partial t} + A a_{\mu\nu} - l_a \Delta a_{\mu\nu} - \frac{1}{2} \epsilon_0 \epsilon_a (kTN)^{-1} (E_\mu E_\nu - \delta_{\mu\nu}\bar{E}) = 0 \qquad (7)$$

where τ_a is a "naked" relaxation time, l_a the correlation length, k the Boltzmann-constant, T the temperature, N the number density and $A = A_0(1-T^*/T)$ where A_0 and T^* are constants. The term with $\Delta a_{\mu\nu}$ can be neglected in our experiments, because typical grating-constants are in the magnitude of μm whereas the correlation length l_a is of molecular dimensions. So eq.7 reduces to

$$\frac{\partial a_{\mu\nu}}{\partial t} + \frac{1}{\tau} a_{\mu\nu} = \frac{F_{\mu\nu}(t)}{\gamma_i} \qquad (8)$$

where $\tau = \tau_a/A$ is the effective relaxation time, $\gamma_i = \tau_a NkT$ the effective viscosity and $F_{\mu\nu} = E_\mu E_\nu - \delta_{\mu\nu}\bar{E}$ the optical field tensor. The solution of eq.8 is a convolution integral similar to eq.3. In our experiments $\bar{E} = E \cdot \bar{e}_x$ and alignment occurs only in x-direction. So the amplitude of the induced birefrigence grating at the end of the laser pulse becomes

$$\delta n_{max} = \epsilon_0 \epsilon_a^2 \ (6\bar{n}\gamma_i)^{-1} \ E^2 \tau_p \qquad (9)$$

Eqs. (9) and (5) predict that in both phases of a liquid crystal optical nonlinearities will occur instantly with the optical field if picosecond pulses are used. The amplitude of the induced index grating as given in eq.(5) and eq.(9) is in the order of $\delta n = 10^{-5}$ using standard values like $n_\perp = 1.5$, $n_\parallel = 1.7$, $\bar{n} = 1.6$, $\gamma = 0,001$ kg/ms and $E = 10^8$V/m, $\tau_p = 100$ps. So self-diffraction effects should be observable in dynamic grating experiments with ultrashort laserpulses.

The experimental arrangement is schematically depicted in Fig.1. A mode-locked Nd:YAG laser with pulse selection emits a single linearly polarized pulse which is amplified and frequency doubled, so that green (532nm), 80ps FWHM laser pulses with energies up to 6mJ per pulse are obtained. Symmetrical splitting mirrors M produce two beams which are slightly focused onto the sample to form an intensity-grating. The angle between the two beams is 1 deg and the focused spot size is about 0.75mm (e^{-2}-diameter). Homeotropic alignment of the nematic 5CB is used in films of 30μm thickness, kept at constant temperatures of 25°C and 40°C for the isotropic phase. β is varied from 0 to 40 deg. The input energy and the first order diffracted energy are detected by calibrated Si-photodiodes. We first measured the diffraction efficiency depending on input energy. The results are shown in Fig.2 for the nematic and for the isotropic phase, exhibiting a nearly quadratic dependence as described by eq.1 combined with eq.5 or eq.9. Sample damage occurs at high energies W_{in} of about 5mJ. For the isotropic phase the input energy has to be limited further because of the appearance of additional defocusing effects at $W_{in} \geq 2$mJ leading to ring structures in every diffracted beam behind the sample as reported recently for similar experiments in silicon[11]. To compare theoretical values and measured values we fitted the effective viscosity coefficients to $\gamma_n = 0,015$ kg/ms for nematic 5CB which agrees well with measured comparable flow-viscosities in cyanobiphenyls[12] and $\gamma_i = 0,003$ kg/ms for isotropic 5CB which is 3 times smaller than measured viscosities for the optical Kerr effect with ns-laserpulses[6]. However this determination[6] of the viscosity γ_i is more indirect because γ_i is calculated from the measured parameters τ and A.

The evaluation of γ_i from eq.(1) and (9) is possible only if no additional nonlinear effects, e.g. deformation of the electronic cloud of the molecules, are present. Such effects are not considered in our model. Using nanosecond pulses, electronic nonlinearities play no significant role at least near the clearing point[5]. However, in our experiments, electronic nonlinearities may be more important than in experiments with nanosecond laserpulses because of higher optical fields using picosecond pulses. As a further proof of the molecular reorientation model describing the observed self-diffraction nonlinearity, the diffracted energy was measured in dependence of the angle of incidence β.

The diffraction efficiency depending on β is shown in Fig.3 for both phases. As predicted by eq.1 and eq.5 the nematic diffraction efficiency varies as $\sin^4(2\beta)$ whereas there is no dependence on β in the isotropic phase. It should be noted that even with $\beta = 0$ deg (normal incidence) we get a weak diffracted signal with the nematic sample in contrast to eq.5. This can be explained by fluctuations in the initial alignment or other grating effects. Beside of electronic nonlinearities finite absorption and temperature grating effects are also possible. However, it is well-known that cyanobiphenyls absorb very little in the green and observation of detectable temperature effects is only possible with additional dyes to enhance the absorption[13].

The agreement between the experimental and theoretical dependence of the diffraction efficiency on the angle of incidence for the nematic phase strongly supports our assumption that the observed self-diffraction effects are due to molecular orientation.

In conclusion, strong optical nonlinearities in a picosecond self-diffraction experiment associated with optically induced orientation processes in the nematic and the isotropic phase of a liquid crystal have been observed for the first time. It has been shown that the theoretical orientation build-up times of more than 10ns do not preclude molecular orientation by picosecond pulses. Comparing the induced nonlinearities for both phases, the main difference is given by a strong dependence on the angle between the optical field and the director in the nematic phase and in somewhat different effective viscosities. The measured self-diffraction efficiencies are in good agreement with theoretical expectations. Financial support from the Deutsche Forschungsgemeinschaft is gratefully acknowledged. The liquid crystals were kindly supplied by BdH Chemicals and Hoffmann LaRoche. We thank Prof. G. Heppke and Prof. S. Hess for helpful discussions and M. Glotz for build up the laser system.

References

/1/ I.C. Khoo, Y.R. Shen, Opt.Eng., Vol.24, p.579 (1985)

/2/ D.M. Pepper, Opt.Eng., Vol.21, p.156 (1982)

/3/ A.S. Zolot'ko et al., JETP Lett., Vol.32, p.158 (1980)

/4/ H. Hsiung, L.P. Shi, Y.R. Shen, Phys.Rev.A., Vol.30, p.1453 (1984)

/5/ G.K.L. Wong, Y.R. Shen, Phys.Rev.A, Vol.10, p.1277 (1974)

/6/ P.A. Madden, F.C. Saunders, A.M. Scott, IEEE J.Quant.Electron., Vol.QE-22, p.1287 (1986)

/7/ S. Hess, I. Pardowitz, Z.Naturforsch., Vol.36a, p.554 (1981)

/8/ H.J. Eichler, P. Günter, D.W. Pohl, "Laser-Induced Dynamic Gratings", Springer Series in Optical Sciences, Springer 1986

/9/ I.C. Khoo, J.Quant.Electron., Vol. QE-22, p.1268 (1986)

/10/ D. Langhans, J. Salk, N. Wiese, Physica 144C, p.411 (1987)

/11/ Chen Jun, H.J. Eichler, Appl.Phys.B, Vol.45, p.121 (1988)

/12/ J. Constant, E.P. Raynes, Mol.Cryst.Liq.Cryst., Vol.62, p.115 (1980)

/13/ I.C. Khoo, P. Normandin, Optics Letts., Vol.9, p.285 (1984)
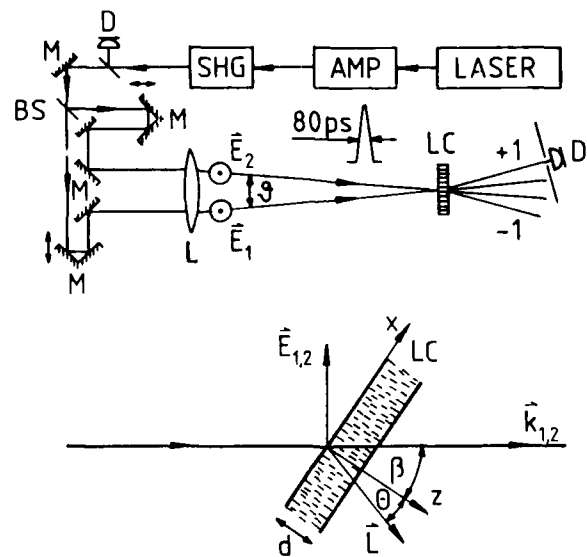
Fig.1: Selfdiffraction arrangement (M:Mirror, BS:Beamsplitter, LC:Liquid Crystal, D:PIN-10 Diode, L:Lens f = 1000 mm) and liquid crystal orientation ($\vec{L}$:director, $\vec{K}_{1,2}$:wave vectors of incident beams, $\vec{E}_{1,2}$:optical field strengths).
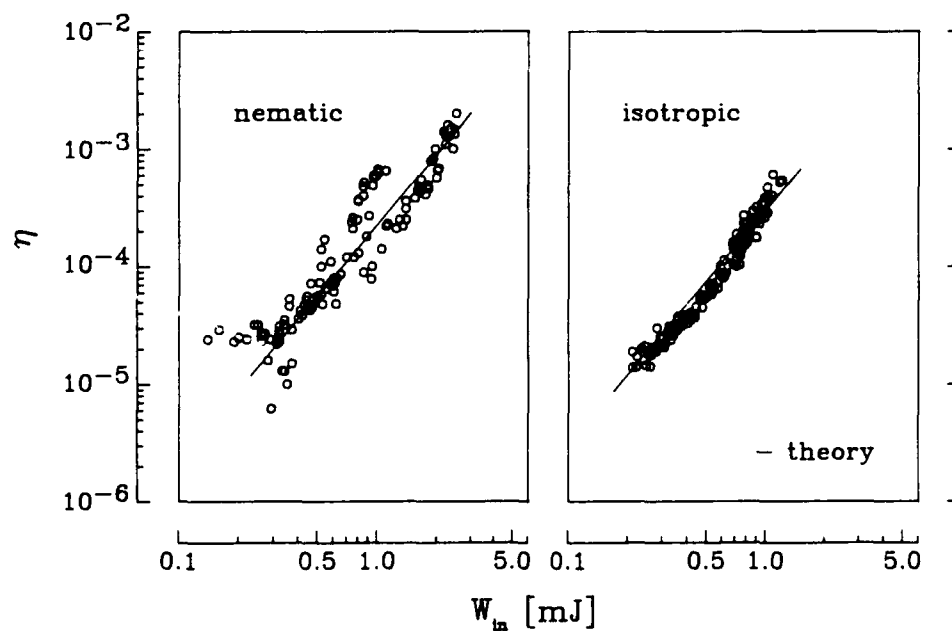
Fig.2: Diffraction efficiency vs. input energy W_{in} measured with nematic 5CB (T=25°C, β=22,5deg) and isotropic 5CB (T=40°C).
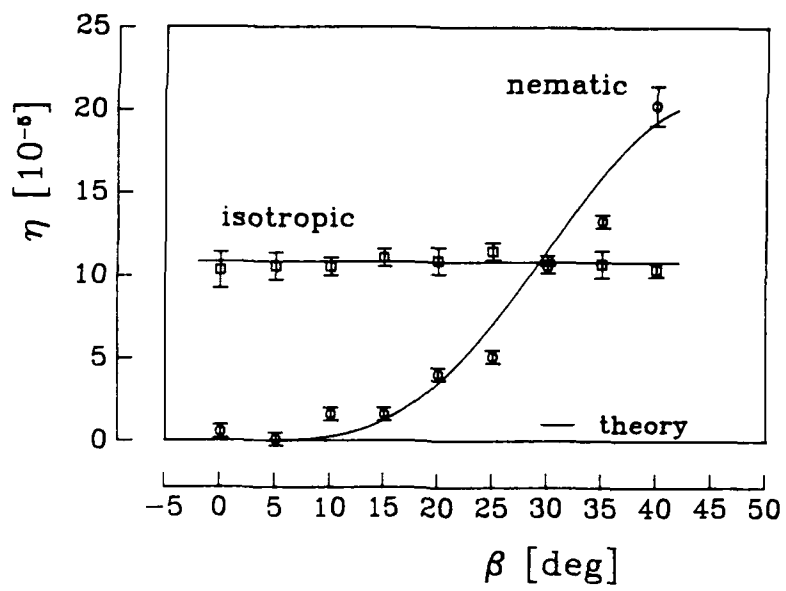
Fig.3: Diffraction efficiency vs. angle of incidence β measured with nematic and isotropic 5CB at W_{in}=0,54mJ.

POLARIZATION EFFECTS ON THE POPULATION AND ORIENTATIONAL GRATINGS

A.A. VILLAEYS

Groupe d'Optique Nonlinéaire et d'Optoélectronique
Institut de Physique et Chimie des Matériaux de Strasbourg
Unité Mixte 380046 CNRS - ULP - EHICS
5, rue de l'Université - 67084 STRASBOURG Cedex (France)

J.P. LAVOINE

Laboratoire des Systèmes Photoniques
Ecole Nationale Supérieure de Physique de Strasbourg
7, rue de l'Université - 67000 STRASBOURG (France)

A theoretical study of the nonlinear polarization in a molecular medium is presented. The medium is described by an ensemble of two-level systems and is subject to rotational diffusion. The model is valid far or near resonance, as well. It is only assumed that time variation of the field envelopes and rotational diffusion constant are much smaller than the transverse decay rate Γ_2. The nonlinear polarization is expressed as a function of the field polarizations. The results are applied to a four-wave mixing experiment to discuss the influence of the rotational diffusion. We evaluate the contribution of the population and orientational gratings. Their influence is discussed.

I. Introduction

Four-wave mixing has been used extensively these last few years. From the large number of physical processes attainable by this type of spectroscopy, generation of phase-conjugated signals has been successfully used in many works [1]. The particular case of transient four-wave mixing is of great interest for data processing [2] and spectroscopy [3]. The effects of field polarizations are relevant to select different types of processes. They are of particular interest to prevent the build-up of a thermally induced phase grating to measure resonant susceptibilities [4]. On the other hand, the physical picture frequently used to discuss four-wave mixing experiments introduces the concept of gratings ; that is, two beams create a grating of population and /or orientation, while the third beam interacts with the grating, giving rise to a diffracted beam. Of course, these gratings dependent on the field polarizations. For molecular media in liquid phase, orientational gratings can be affected by rotational diffusion. Theoretical descriptions of orientational gratings in picosecond excitation-probe experiments have been already made by different authors [5,6]. Recently Wherrett et al. [7] gave a theoretical description of transient four-wave mixing including rotational diffusion in molecular media. Later on, they applied their results to an excitation-probe experiment.

The main goal of the present work is to give a comprehensive and general description of the polarization effects in four-wave mixing. To this end, and taking advantage of the approach developed by Wherrett et al., we introduce a phenomenological diffusion term into the density matrix equations of the material system and fields. Next, we calculate the general expression of the third order term of the density matrix assuming that time variation of the pulse envelope and rotational diffusion constant are much smaller than the transverse decay rate Γ_2. All along, we do not introduce the rotating-wave approximation. Therefore, our results are valid for near and far-resonance cases, as well. Then, we consider the particular situation of a four-wave mixing experiment. Depending on the relative polarizations of the exciting beams, we define the different situations that can be supported by the population and/or orientational grating pictures and evaluate their corresponding contributions. It is shown that the rotational diffusion constant plays a fundamental role in elucidating typical physical situations.

II. Theory

The nonlinear medium is constituted by an ensemble of N two-level systems. Each of them is characterized by a dipole moment $\vec{\mu}$, longitudinal and transverse decay rates Γ_1 and Γ_2 respectively, and finally, transition energy $\hbar\omega_{21}$. This material system interacts with three pulsed beams. Therefore the total electromagnetic field $\vec{E}(\vec{r},t)$ can be written as :

$$\vec{E}(\vec{r},t) = \sum_\alpha \vec{E}_\alpha(\vec{r},t) \ , \ \alpha = 1,2,3 \tag{1}$$

with

$$\vec{E}_\alpha(\vec{r},t) = \frac{1}{2}\,\vec{\epsilon}_\alpha\,\mathcal{E}_\alpha(\vec{r},t)\,\exp\left[i\omega_\alpha t - i\vec{k}_\alpha\cdot\vec{r}\right] + c.c. \tag{2}$$

where c.c. stands for the complex conjugate part, $\vec{\epsilon}_\alpha$ for the unit polarization vector and $\mathcal{E}_\alpha(\vec{r},t)$ for the time dependent field amplitude. Moreover we assume that the perturbational approach is valid and calculate the third-order iterative solution for the density matrix. Rotational effects can be taken into account by introducing a phenomenological diffusion term into the density matrix equations. It is also assumed that orientational diffusion results from statistical processes which are independent of the applied fields. Therefore, the density matrix elements satisfy the equations, if $\rho \equiv \rho(\vec{r},t,\theta,\phi)$,

$$\frac{\partial}{\partial t}\rho_{11} = -\frac{i}{\hbar}\left(H_{12}\,\rho_{21} - \rho_{12}\,H_{21}\right) + \Gamma_1\,\rho_{22} + D_{11}\,\Delta_{\theta,\phi}\,\rho_{11} \tag{3}$$

$$\frac{\partial}{\partial t}\rho_{22} = -\frac{i}{\hbar}\left(H_{21}\,\rho_{12} - \rho_{21}\,H_{12}\right) - \Gamma_1\,\rho_{22} + D_{22}\,\Delta_{\theta,\phi}\,\rho_{22} \tag{4}$$

$$\frac{\partial}{\partial t}\rho_{12} = -\left[\Gamma_2 - i\omega_{21}\right]\rho_{12} + D_{12}\,\Delta_{\theta,\phi}\,\rho_{12} + \frac{i}{\hbar}H_{12}\left[\rho_{22} - \rho_{11}\right] \tag{5}$$

where θ and ϕ are the orientational coordinates of the dipole moment $\vec{\mu}$ defined with respect to the laboratory frame. D_{11}, D_{22} and D_{12} are the orientational diffusion constants and $\Delta_{\theta,\phi}$ is the Laplace operator in spherical coordinates. H_{12} represents the interaction matrix elements. In the dipole approximation it takes the form

$$H_{12}(\vec{r},t,\theta,\phi) = -\frac{1}{2}\mu_{12}\sum_\alpha\left\{\left[\vec{\epsilon}_\mu(\theta,\phi)\cdot\vec{\epsilon}_\alpha\right]\mathcal{E}_\alpha(\vec{r},t)\,\exp\left[i\omega_\alpha t - i\vec{k}_\alpha\cdot\vec{r}\right]\right.$$
$$\left. + \left[\vec{\epsilon}_\mu(\theta,\phi)\cdot\vec{\epsilon}_\alpha^*\right]\mathcal{E}_\alpha^*(\vec{r},t)\,\exp\left[-i\omega_\alpha t + i\vec{k}_\alpha\cdot\vec{r}\right]\right\}. \tag{6}$$

Here $\vec{\epsilon}_\mu(\theta,\phi)$ is the unit vector in the direction of the dipole moment $\vec{\mu}$ which can be written as $\vec{\mu} = \vec{\epsilon}_\mu(\theta,\phi)\mu$. It is assumed that μ has no diagonal elements. The diffusion constants D_{11}, D_{22} and D_{12} introduced in the relations (3-5) have been written in a general form accordingly to the Debye model [8]. We now assume that rotational diffusion is independent of the electronic state of the molecule, i.e., $D_{11} = D_{22} = D$ and that the decay rate of the polarization Γ_2 is large compared to D_{12} [9]. Then equations (3-5) can be expressed into the form

$$\frac{\partial}{\partial t}w(\vec{r},t,\theta,\phi) = 2i\left[\rho'_{21}(\vec{r},t,\theta,\phi)s(\vec{r},t,\theta,\phi) - \rho'_{12}(\vec{r},t,\theta,\phi)s^*(\vec{r},t,\theta,\phi)\right]$$
$$- \Gamma_1\left[w(\vec{r},t,\theta,\phi) - w_o\right] + D\,\Delta_{\theta,\phi}\,w(\vec{r},t,\theta,\phi) \tag{7}$$

$$\frac{\partial}{\partial t}\rho'_{12}(\vec{r},t,\theta,\phi) = -\Gamma_2\,\rho'_{12}(\vec{r},t,\theta,\phi) - iw(\vec{r},t,\theta,\phi)s(\vec{r},t,\theta,\phi). \tag{8}$$

The quantity $w(\vec{r},t,\theta,\phi)$ is the population difference between the excited state 2 and the ground state 1 for given values of θ and ϕ. In addition, $\rho'_{12}(\vec{r},t,\theta,\phi)$ corresponds to the coherence defined in the frame rotating at the transition frequency ω_{21}. Therefore, we have the relations

$$w(\vec{r},t,\theta,\phi) = \rho_{22}(\vec{r},t,\theta,\phi) - \rho_{11}(\vec{r},t,\theta,\phi) \tag{9}$$

$$\rho_{12}(\vec{r},t,\theta,\phi) = \rho'_{12}(\vec{r},t,\theta,\phi)\,\exp(i\omega_{21}t) \tag{10}$$

The expression of the function $s(\vec{r},t,\theta,\phi)$ is given by :

$$s(\vec{r},t,\theta,\phi) = -\frac{1}{2\hbar}\mu_{12}\sum_\alpha\left\{\left[\vec{\epsilon}_\mu(\theta,\phi)\cdot\vec{\epsilon}_\alpha\right]E_\alpha(\vec{r},t)\,\exp(-i\Delta_\alpha t)\right.$$
$$\left. + \left[\vec{\epsilon}_\mu(\theta,\phi)\cdot\vec{\epsilon}_\alpha^*\right]E_\alpha^*(\vec{r},t)\,\exp(-i\Omega_\alpha t)\right\} \tag{11}$$

where

$$\Delta_\alpha = \omega_{21} - \omega_\alpha, \qquad \Omega_\alpha = \omega_{21} + \omega_\alpha \tag{12}$$

$$E_\alpha(\vec{r},t) = \mathcal{E}_\alpha(\vec{r},t)\,\exp(-i\vec{k}_\alpha\cdot\vec{r}) \tag{13}$$

This description does not introduce the rotating-wave approximation. When introduced only equation (11) needs to be modified :

$$s(\vec{r},t,\theta,\phi)_{RWA} = -\frac{1}{2\hbar}\mu_{12}\sum_\alpha\left[\vec{\epsilon}_\mu(\theta,\phi)\cdot\vec{\epsilon}_\alpha\right]E_\alpha(\vec{r},t)\,\exp(-i\Delta_\alpha t).$$

Formal integration of Eqs. (7) and (8) is easily achieved to give :

$$w(\vec{r},t,\theta,\phi) = w_o + 2i\sum_{\ell}^{\infty}\sum_{m=-\ell}^{+\ell}\int_{-\infty}^{t}dt_1\int_{0}^{2\pi}d\phi_1\int_{0}^{\pi}d\theta_1\sin\theta_1$$

$$x \exp[-\Gamma_1(t-t_1)] \exp[-D\ell(\ell+1)(t-t_1)] Y_{\ell m}(\theta,\phi) Y_{\ell m}^*(\theta_1,\phi_1)$$

$$x [\rho'_{11}(\vec{r},t_1,\theta_1,\phi_1) s(\vec{r},t_1,\theta_1,\phi_1) - \rho'_{12}(\vec{r},t_1,\theta_1,\phi_1) s^*(\vec{r},t_1,\theta_1,\phi_1)] \tag{14}$$

and

$$\rho'_{12}(\vec{r},t,\theta,\phi) = -i \int_{-\infty}^{t} w(\vec{r},t_1,\theta,\phi) s(\vec{r},t_1,\theta,\phi) \exp[-\Gamma_2(t-t_1)] dt_1 \tag{15}$$

where $Y_{\ell m}(\theta,\phi)$ are the well-known spherical harmonics and w_0 is the initial value of the population difference. In the case of a uniform orientational distribution we get

$$w(\vec{r},-\infty,\theta,\phi) = w_0 = -1/4\Pi.$$

For the coherences we have $\rho_{12}(\vec{r},-\infty,\theta,\phi) = 0$. Using relations (14) and (15) and assuming Γ_2 large compared to the time variation of the fields amplitude, the perturbative solutions of Eqs. (7) and (8) up to the third order are readily obtained. To zero order, we get the initial population

$$w^{(0)}(\vec{r},t,\theta,\phi) = w_0.$$

To first order, we have a contribution to coherence only,

$$\rho_{12}^{(1)}(\vec{r},t,\theta,\phi) = \frac{iw_0}{2\hbar} \mu_{12} \sum_\alpha \{ \frac{\vec{\varepsilon}_\mu(\theta,\phi) \cdot \vec{\varepsilon}_\alpha}{\Gamma_2 - i\Delta_\alpha} \mathcal{E}_\alpha(\vec{r},t) \exp[-i(\Delta_\alpha t + \vec{k}_\alpha \cdot \vec{r})]$$

$$+ \frac{\vec{\varepsilon}_\mu(\theta,\phi) \cdot \vec{\varepsilon}_\alpha}{\Gamma_2 - i\Omega_\alpha} \mathcal{E}^*(\vec{r},t) \exp[-i(\Omega_\alpha t - \vec{k}_\alpha \cdot \vec{r})] \} \tag{16}$$

It must be noted that relation (16) giving the coherence to the first order is not dependent of the diffusion constant. With this result, we obtain the second order contribution,

$$w^{(2)}(\vec{r},t,\theta,\phi) = -\frac{w_0}{2\hbar^2} |\mu_{12}|^2 \sum_{\alpha\beta} \{ [(\vec{\varepsilon}_\mu(\theta,\phi)\cdot\vec{\varepsilon}_\alpha^*)(\vec{\varepsilon}_\mu(\theta,\phi)\cdot\vec{\varepsilon}_\beta) f_{1,\alpha\beta}(\vec{r},t) + \frac{1}{3}(\vec{\varepsilon}_\alpha^* \cdot \vec{\varepsilon}_\beta) f_{2,\alpha\beta}(\vec{r},t)]$$

$$x (F_\alpha + F_\beta^*) \exp[-i(\Delta_\beta - \Delta_\alpha)t] \exp[-i(\vec{k}_\beta - \vec{k}_\alpha)\cdot\vec{r}] + [(\vec{\varepsilon}_\mu(\theta,\phi)\cdot\vec{\varepsilon}_\alpha)(\vec{\varepsilon}_\mu(\theta,\phi)\cdot\vec{\varepsilon}_\beta) g_{1,\alpha\beta}(\vec{r},t)$$

$$+ \frac{1}{3}(\vec{\varepsilon}_\alpha \cdot \vec{\varepsilon}_\beta) g_{2,\alpha\beta}(\vec{r},t)] x F_\alpha^* \exp[-i(\Delta_\beta - \Delta_\alpha)t] \exp[-i(\vec{k}_\beta + \vec{k}_\alpha)\cdot\vec{r}]$$

$$+ [(\vec{\varepsilon}_\mu(\theta,\phi)\cdot\vec{\varepsilon}_\alpha)(\vec{\varepsilon}_\mu(\theta,\phi)\cdot\vec{\varepsilon}_\beta^*) g_{1,\alpha\beta}^*(\vec{r},t) + \frac{1}{3}(\vec{\varepsilon}_\alpha \cdot \vec{\varepsilon}_\beta^*) g_{2,\alpha\beta}^*(\vec{r},t)]$$

$$x F_\alpha \exp[i(\Delta_\beta - \Delta_\alpha)t] \exp[i(\vec{k}_\beta + \vec{k}_\alpha)\cdot\vec{r}] \tag{17}$$

where the various functions $f_{i,\alpha\beta}(\vec{r},t)$ and $g_{i,\alpha\beta}(\vec{r},t)$ are given by :

$$f_{i,\alpha\beta}(\vec{r},t) = \int_{-\infty}^{t} \mathcal{E}_\alpha^*(\vec{r},t_1) \mathcal{E}_\beta(\vec{r},t_1) \exp\{-[\Gamma_1 - i(\Delta_\beta - \Delta_\alpha)](t-t_1)\}$$

$$x [(1-\delta_{i1}) + (-1)^{1+i} \exp[-6D(t-t_1)]] dt_1 \tag{18}$$

$$g_{i,\alpha\beta}(\vec{r},t) = \int_{-\infty}^{t} \mathcal{E}_\alpha(\vec{r},t_1) \mathcal{E}_\beta(\vec{r},t_1) \exp\{-[\Gamma_1 - i(\Delta_\beta - \Delta_\alpha)](t-t_1)\}$$

$$x [(1-\delta_{i1}) + (-1)^{1+i} \exp[-6D(t-t_1)]] dt_1 \tag{19}$$

for $i = 1,2$. We have also defined the following quantities :

$$F_\lambda = \frac{i}{\Gamma_2 + i\Delta_\lambda} + \frac{i}{\Gamma_2 - i\Omega_\lambda} \quad , \quad \lambda = \alpha, \beta.$$

The functions $f_{i,\alpha\beta}(\vec{r},t)$ and $g_{i,\alpha\beta}(\vec{r},t)$ previously defined take into account the various overlapping of the pulsed fields. It is important to note that the terms involving $f_{1,\alpha\beta}(\vec{r},t)$ and $g_{1,\alpha\beta}(\vec{r},t)$ are predominant in the case where the orientational diffusion constant D is zero, i.e. for systems where no rotational diffusion takes place. On the other hand, $f_{2,\alpha\beta}(\vec{r},t)$ and $g_{2,\alpha\beta}(\vec{r},t)$ are predominant when D is important. At this stage of the calculation, the sole assumption which has been introduced on the field amplitudes is that their time variations are smaller than the transverse decay rate Γ_2. This assumption enables us to introduce mathematical simplifications due to the fact that $s(\vec{r},t,\theta,\phi)$ can be extracted from the time integration giving $\rho_{12}^{(1)}(\vec{r},t,\theta,\phi)$. We now assume that the time variation of the product $\mathcal{E}_\alpha(\vec{r},t)\mathcal{E}_\beta(\vec{r},t)$ is also much smaller than Γ_2. Therefore, as a consequence of the regularization properties of the convolution, the functions $f_{i,\alpha\beta}(\vec{r},t)$ and $g_{i,\alpha\beta}(\vec{r},t)$ will have a slowly varying time dependence with respect to the one due to Γ_2. It must be noted that this assumption which considers that the time variations of the field amplitudes are much smaller than Γ_2 is frequently encountered in many picosecond experiments performed with organic materials [10]. As a consequence, all effects due to the

dephasing time $T_2 = 1/\Gamma_2$ are neglected in our theoretical model. We are now able to calculate the third order term of the density matrix. Using relation (17), this last term takes the form :

$$\rho_{12}^{'(3)}(\vec{r},t,\theta,\phi) = -\frac{iw_o}{4h^3}|\mu_{12}|^2\mu_{12}\sum_{\alpha,\beta,\gamma}$$

$$\left[\frac{A_{\alpha\beta\gamma}(\vec{r},t,\theta,\phi)}{\Gamma_2-i(\Delta_\beta-\Delta_\alpha+\Delta_\gamma)}\exp[-i(\Delta_\beta-\Delta_\alpha+\Delta_\gamma)t]\exp[-i(\vec{k}_\beta-\vec{k}_\alpha+\vec{k}_\gamma).\vec{r}]\right.$$

$$+\frac{A^*_{\alpha\beta\gamma}(\vec{r},t,\theta,\phi)}{\Gamma_2+i(\Delta_\beta-\Delta_\alpha-\Omega_\gamma)}\exp[i(\Delta_\beta-\Delta_\alpha-\Omega_\gamma)t]\exp[i(\vec{k}_\beta-\vec{k}_\alpha+\vec{k}_\gamma).\vec{r}]$$

$$+\frac{B_{\alpha\beta\gamma}(\vec{r},t,\theta,\phi)}{\Gamma_2-i(\Delta_\beta-\Omega_\alpha+\Delta_\gamma)}\exp[-i(\Delta_\beta-\Omega_\alpha+\Delta_\gamma)t]\exp[-i(\vec{k}_\alpha+\vec{k}_\beta+\vec{k}_\gamma).\vec{r}]$$

$$+\left.\frac{B^*_{\alpha\beta\gamma}(\vec{r},t,\theta,\phi)}{\Gamma_2+i(\Delta_\beta-\Omega_\alpha-\Omega_\gamma)}\exp[i(\Delta_\beta-\Omega_\alpha-\Omega_\gamma)t]\exp[i(\vec{k}_\alpha+\vec{k}_\beta+\vec{k}_\gamma).\vec{r}]\right] \qquad (20)$$

with the definitions :

$$A_{\alpha\beta\gamma}(\vec{r},t,\theta,\phi) = \{[\vec{\epsilon}_L(\theta,\phi).\vec{\epsilon}_\alpha^*][\vec{\epsilon}_\mu(\theta,\phi).\vec{\epsilon}_\beta]f_{1,\alpha\beta}(\vec{r},t)$$

$$+\frac{1}{3}(\vec{\epsilon}_\alpha^*.\vec{\epsilon}_\beta)f_{2,\alpha\beta}(\vec{r},t)\}(F_\alpha+F_\beta^*)[\vec{\epsilon}_\mu(\theta,\phi).\vec{\epsilon}_\gamma]\mathcal{E}_\gamma(\vec{r},t)$$

$$+\{[\vec{\epsilon}_L(\theta,\phi).\vec{\epsilon}_\gamma][\vec{\epsilon}_\mu(\theta,\phi).\vec{\epsilon}_\beta]g_{1,\gamma\beta}(\vec{r},t)$$

$$+\frac{1}{3}(\vec{\epsilon}_\gamma.\vec{\epsilon}_\beta)g_{2,\gamma\beta}(\vec{r},t)\}F_\gamma^*[\vec{\epsilon}_\mu(\theta,\phi).\vec{\epsilon}_\alpha^*]\mathcal{E}_\alpha^*(\vec{r},t) \qquad (21)$$

and

$$B_{\alpha\beta\gamma}(\vec{r},t,\theta,\phi) = \{[\vec{\epsilon}_\mu(\theta,\phi).\vec{\epsilon}_\alpha][\vec{\epsilon}_\mu(\theta,\phi).\vec{\epsilon}_\beta]g_{1,\alpha\beta}(\vec{r},t)$$

$$+\frac{1}{3}(\vec{\epsilon}_\alpha.\vec{\epsilon}_\beta)g_{2,\alpha\beta}(\vec{r},t)\}F_\alpha^*[\vec{\epsilon}_\mu(\theta,\phi).\vec{\epsilon}_\gamma]\mathcal{E}_\gamma(\vec{r},t) \qquad (22)$$

From the expressions (16) and (20), we are now able to calculate the corresponding polarizations. At this end, we must average over all possible orientations of the dipole moments. This is accounted for by considering the ith-order averaged polarization terms.

$$\vec{P}^{(i)}(\vec{r},t) = \int_0^{2\Pi}d\phi\int_0^2 d\theta\sin\phi\left[\mu_{12}\rho_{21}^{(i)}(\vec{r},t,\theta,\phi)+\mu_{21}\rho_{12}^{(i)}(\vec{r},t,\theta,\phi)\right]$$

$$\times\vec{\epsilon}_L(\theta,\phi) \qquad,\quad i=1,3 \qquad (23)$$

The total averaged polarization is given by :

$$\vec{P}(\vec{r},t) = \vec{P}^{(1)}(\vec{r},t)+\vec{P}^{(3)}(\vec{r},t)$$

By introducing the expressions (16) and (20) into the relation (23), we obtain the final result.

$$\vec{P}^{(1)}(\vec{r},t) = \frac{i|\mu_{12}|^2}{6\hbar}\sum_\alpha\{[\frac{1}{\Gamma_2+i\Omega_\alpha}-\frac{1}{\Gamma_2-i\Delta_\alpha}]\vec{\epsilon}_\alpha\mathcal{E}_\alpha(\vec{r},t)\exp[i(\omega_\alpha t-\vec{k}_\alpha.\vec{r})]$$

$$+[\frac{1}{\Gamma_2+i\Delta_\alpha}-\frac{1}{\Gamma_2-i\Omega_\alpha}]\vec{\epsilon}_\alpha^*\mathcal{E}_\alpha(\vec{r},t)\exp[-i(\omega_\alpha t-\vec{k}_\alpha.\vec{r})]\} \qquad (24)$$

and

$$\vec{P}^{(3)}(\vec{r},t) = \frac{i|\mu_{12}|^4}{4\hbar^3}\sum_{\alpha,\beta,\gamma}$$

$$\vec{A}_{\alpha\beta\gamma}(\vec{r},t)[\frac{1}{\Gamma_2-i(\Delta_\beta-\Delta_\alpha+\Delta_\gamma)}-\frac{1}{\Gamma_2-i(\Delta_\beta-\Delta_\alpha+\Delta_\gamma)}]$$

$$\times\exp[i(\omega_\beta+\omega_\gamma-\omega_\alpha)t-i(\vec{k}_\beta-\vec{k}_\alpha+\vec{k}_\gamma).\vec{r}]$$

$$+A^*_{\alpha\beta\gamma}(\vec{r},t)[\frac{1}{\Gamma_2+i(\Delta_\beta-\Omega_\gamma-\Delta_\alpha)}-\frac{1}{\Gamma_2+i(\Delta_\beta-\Delta_\alpha+\Delta_\gamma)}]$$

$$x \exp[i(\omega_\beta+\omega_\gamma+\omega_\alpha)t-i(\vec{k}_\beta+\vec{k}_\alpha+\vec{k}_\gamma)\cdot\vec{r}]$$

$$+ \vec{B}_{\alpha\beta\gamma}(\vec{r},t)\left[\frac{1}{\Gamma_2-i(\Delta_\beta-\Omega_\alpha+\Delta_\gamma)} - \frac{1}{\Gamma_2-i(\Delta_\beta-\Omega_\alpha-\Omega_\gamma)}\right]$$

$$x \exp[i(\omega_\alpha+\omega_\beta+\omega_\gamma)t-i(\vec{k}_\alpha+\vec{k}_\beta+\vec{k}_\gamma)\cdot\vec{r}]$$

$$+ \vec{B}_{\alpha\beta\gamma}(\vec{r},t)\left[\frac{1}{\Gamma_2+i(\Delta_\beta-\Omega_\alpha-\Omega_\gamma)} - \frac{1}{\Gamma_2+i(\Delta_\beta-\Omega_\alpha+\Delta_\gamma)}\right]$$

$$x \exp[-i(\omega_\alpha+\omega_\beta+\omega_\gamma)t+i(\vec{k}_\alpha+\vec{k}_\beta+\vec{k}_\gamma)\cdot\vec{r}] \} \tag{25}$$

Here, the quantities $\vec{A}_{\alpha\beta\gamma}(\vec{r},t)$ and $\vec{B}_{\alpha\beta\gamma}(\vec{r},t)$ are vectors and are defined by the following expressions

$$
\vec{A}_{\alpha\beta\gamma}(\vec{r},t) = (\vec{\varepsilon}_\alpha^*\cdot\vec{\varepsilon}_\beta)\vec{\varepsilon}_\gamma \{\frac{1}{15}[(F_\alpha+F_\beta^*)\mathcal{E}_\gamma(\vec{r},t)f_{1,\alpha\beta}(\vec{r},t)+F_\gamma^*\mathcal{E}_\alpha^*(\vec{r},t)g_{1,\gamma\beta}(\vec{r},t)]
$$

$$
+ \frac{1}{9}(F_\alpha+F_\beta)\mathcal{E}_\gamma(\vec{r},t)f_{2,\alpha\beta}(\vec{r},t)\}
$$

$$
+ (\vec{\varepsilon}_\alpha^*\cdot\vec{\varepsilon}_\gamma)\vec{\varepsilon}_\beta \frac{1}{15}[(F_\alpha+F_\beta^*)\mathcal{E}_\gamma(\vec{r},t)f_{1,\alpha\beta}(\vec{r},t)+F_\gamma^*\mathcal{E}_\alpha^*(\vec{r},t)g_{1,\gamma\beta}(\vec{r},t)]
$$

$$
+ (\vec{\varepsilon}_\gamma\cdot\vec{\varepsilon}_\beta)\vec{\varepsilon}_\alpha \{\frac{1}{15}[(F_\alpha+F_\beta^*)\mathcal{E}_\gamma(\vec{r},t)f_{1,\alpha\beta}(\vec{r},t)+F_\gamma^*\mathcal{E}_\alpha^*(\vec{r},t)g_{1,\gamma\beta}(\vec{r},t)]
$$

$$
+ \frac{1}{9}F_\gamma\mathcal{E}_\alpha^*(\vec{r},t)g_{2,\gamma\beta}(\vec{r},t)\} \tag{26}
$$

and

$$
\vec{B}_{\alpha\beta\gamma}(\vec{r},t) = (\vec{\varepsilon}_\alpha\cdot\vec{\varepsilon}_\beta)\vec{\varepsilon}_\gamma [\frac{1}{15}g_{1,\alpha\beta}(\vec{r},t)+\frac{1}{9}g_{2,\alpha\beta}(\vec{r},t)]F_\alpha^*\mathcal{E}_\gamma(\vec{r},t)
$$

$$
+ (\vec{\varepsilon}_\alpha\cdot\vec{\varepsilon}_\gamma)\vec{\varepsilon}_\beta\frac{1}{15}g_{1,\alpha\beta}(\vec{r},t)F_\alpha^*\mathcal{E}_\gamma(\vec{r},t)
$$

$$
+ (\vec{\varepsilon}_\beta\cdot\vec{\varepsilon}_\gamma)\vec{\varepsilon}_\alpha\frac{1}{15}g_{1,\alpha\beta}(\vec{r},t)F_\alpha^*\mathcal{E}_\gamma(\vec{r},t) \tag{27}
$$

The relations (25), (26) and (27) give the general expression of the third-order nonlinear polarization for an isotropic medium subject to rotational diffusion.

III. Application to Degenerate Four-wave Mixing

Let us now apply our general result to degenerate four-wave mixing. We consider the well-known geometry where the medium is excited by two counterpropagating pump beams $\vec{E}_1(\vec{r},t)$, $\vec{E}_2(\vec{r},t)$ and by a probe beam $\vec{E}_3(\vec{r},t)$. Because of the phase-matching condition, only contributions associated to the terms $\vec{k}_1-\vec{k}_3+\vec{k}_2$ and $\vec{k}_2-\vec{k}_3+\vec{k}_1$ in relation (25) must be retained. $\vec{k}_1$, $\vec{k}_2$ and $\vec{k}_3$ are the wave vectors respectively associated to the pump beams and probe beam.

Therefore, the nonlinear polarization reduces now to the expression

$$
\vec{P}_{DFWM}(\vec{r},t) = \vec{C}(\vec{r},t)\left[\frac{1}{\Gamma_2-i\Delta} - \frac{1}{\Gamma_2+i\Omega}\right] \exp i[\omega t-(\vec{k}_1-\vec{k}_3+\vec{k}_2)\cdot\vec{r}] + c.c. \tag{28}
$$

where ω is the field frequency. Also we have $\Delta = \omega_{21}-\omega$ and $\Omega = \omega_{21}+\omega$. The vector $\vec{C}(\vec{r},t)$ is defined by the relation

$$
\vec{C}(\vec{r},t) = \frac{i|\mu_{12}|^4}{4\hbar^3}
$$

$$
\{(\vec{\varepsilon}_3^*\cdot\vec{\varepsilon}_1)\vec{\varepsilon}_2 \{\frac{1}{15}[(F+F^*)[\mathcal{E}_2(\vec{r},t)f_{1,31}(\vec{r},t)+\mathcal{E}_1(\vec{r},t)f_{1,32}(\vec{r},t)]+2F^*\mathcal{E}_3^*(\vec{r},t)g_{1,21}(\vec{r},t)]
$$

$$
+ \frac{1}{9}(F+F^*)\mathcal{E}_2(\vec{r},t)f_{2,31}(\vec{r},t)\}
$$

$$
+ (\vec{\varepsilon}_3^*\cdot\vec{\varepsilon}_2)\vec{\varepsilon}_1 \{\frac{1}{15}[(F+F^*)[\mathcal{E}_2(\vec{r},t)f_{1,31}(\vec{r},t)+\mathcal{E}_1(\vec{r},t)f_{1,32}(\vec{r},t)]+2F^*\mathcal{E}_3^*(\vec{r},t)g_{1,21}(\vec{r},t)]
$$

$$
+ \frac{1}{9}(F+F^*)\mathcal{E}_1(\vec{r},t)f_{2,32}(\vec{r},t)\}
$$

$$
+ (\vec{\varepsilon}_2\cdot\vec{\varepsilon}_1)\vec{\varepsilon}_3^* \{\frac{1}{15}[(F+F^*)[\mathcal{E}_2(\vec{r},t)f_{1,31}(\vec{r},t)+\mathcal{E}_1(\vec{r},t)f_{1,32}(\vec{r},t)]+2F^*\mathcal{E}_3^*(\vec{r},t)g_{1,21}(\vec{r},t)]
$$

$$
+ \frac{2}{9}F^*\mathcal{E}_3^*(\vec{r},t)g_{2,21}(\vec{r},t)\}\} \tag{29}
$$

where

$$
F = \frac{1}{\Gamma_2+i\Delta} + \frac{1}{\Gamma_2-i\Omega}
$$

The expression (28) combined with the relation (29) gives the general form of the nonlinear polarization for an isotropic medium subject to rotational diffusion. In order to discuss the physical meaning of this expression we first introduce the limit D=0 where no rotational diffusion takes place. Then the quantity $\vec{C}(\vec{r},t)$ reduces to :

$$\vec{C}(\vec{r},t) = \frac{i|\mu_{12}|^4}{4\hbar^3} \left[(\vec{\epsilon}_3^*\cdot\vec{\epsilon}_1)\vec{\epsilon}_2 + (\vec{\epsilon}_3\cdot\vec{\epsilon}_2)\vec{\epsilon}_1 + (\vec{\epsilon}_2\cdot\vec{\epsilon}_1)\vec{\epsilon}_3^*\right]$$

$$\times \left[\frac{1}{15} i(F+F^*)[\vec{\epsilon}_2(\vec{r},t)f_{1,31}(\vec{r},t)+\vec{\epsilon}_1(\vec{r},t)f_{1,32}(\vec{r},t)] + 2F^*\vec{\epsilon}_3(\vec{r},t)g_{1,21}(\vec{r},t)]\right] \tag{30}$$

Let us now consider the configuration of field polarizations defined by :

$$\vec{\epsilon}_3^*\cdot\vec{\epsilon}_1\neq0 \ , \ \vec{\epsilon}_3^*\cdot\vec{\epsilon}_2=0 \text{ and } \vec{\epsilon}_2\cdot\vec{\epsilon}_1=0$$

The term $\vec{\epsilon}_2(\vec{r},t)f_{1,31}(\vec{r},t)$ can be interpreted as the diffracted signal of the field $\vec{E}_2(\vec{r},t)$ by the population grating resulting from the interaction of the nonlinear medium with the superposition of fields $\vec{E}_3(\vec{r},t)$ and $\vec{E}_1(\vec{r},t)$. The term $\vec{\epsilon}_1(\vec{r},t)f_{1,32}(\vec{r},t)$ does not correspond to a population grating due to the fact that $\vec{E}_3(\vec{r},t)$ and $\vec{E}_2(\vec{r},t)$ have orthogonal polarizations. This is clearly demonstrated by taking an average over the dipole orientations in expression (17). Let us define the quantity :

$$\overline{w^{(2)}(\vec{r},t)} = \int_0^{2\pi} d\phi \int_0^\pi d\theta \sin\theta w^{(2)}(\vec{r},t,\theta,\phi) \tag{31}$$

where the overbar denotes the average over the angular orientation and $w^{(2)}(\vec{r},t,\theta,\phi)$ the second order contributions defined by the relation (17). By taking advantage of the relation

$$\overline{(\vec{\epsilon}_\mu(\theta,\phi)\cdot\vec{\epsilon}_\alpha)(\vec{\epsilon}_\mu(\theta,\phi)\cdot\vec{\epsilon}_\beta)} = \frac{1}{3}(\vec{\epsilon}_\alpha\cdot\vec{\epsilon}_\beta) \ ,$$

we get

$$\overline{w^{(2)}(\vec{r},t)} = -\frac{|\mu_{12}|^2}{2\hbar} \sum_{\alpha\beta}$$

$$\{\frac{1}{3}(\vec{\epsilon}_\alpha^*\cdot\vec{\epsilon}_\beta)[f_{1,\alpha\beta}(\vec{r},t)+f_{2,\alpha\beta}(\vec{r},t)](F_\alpha+F_\beta^*)\exp[-i(\vec{k}_\beta-\vec{k}_\alpha)\cdot\vec{r}]$$

$$+ \frac{1}{3}(\vec{\epsilon}_\alpha\cdot\vec{\epsilon}_\beta)[g_{1,\alpha\beta}(\vec{r},t)+g_{2,\alpha\beta}(\vec{r},t)]F_\alpha^*\exp(2i\omega t)\exp[-i(\vec{k}_\beta+\vec{k}_\alpha)\cdot\vec{r}]$$

$$+ \frac{1}{3}(\vec{\epsilon}_\alpha^*\cdot\vec{\epsilon}_\beta^*)[g_{1,\alpha\beta}^*(\vec{r},t)+g_{2,\alpha\beta}^*(\vec{r},t)]F_\alpha\exp(-2i\omega t)\exp[i(\vec{k}_\beta+\vec{k}_\alpha)\cdot\vec{r}]\} \tag{32}$$

This averaged quantity is non zero when the product $\vec{\epsilon}_\alpha\cdot\vec{\epsilon}_\beta$ is different from zero. The term containing the factor $\exp[-i(\vec{k}_\beta-\vec{k}_\alpha)\cdot\vec{r}]$ corresponds to a spatial modulation of the averaged population difference. The two other terms are different due to the oscillating factor $\exp(2i\omega t)$ or $\exp(-2i\omega t)$ and can be neglected in the case of near-resonant excitations. Therefore, we recover a spatial modulation of the population difference which is consistent with a population grating. It must be noted that the quantities $[f_{1,\alpha\beta}(\vec{r},t)+f_{2,\alpha\beta}(\vec{r},t)]$ and $[g_{1,\alpha\beta}(\vec{r},t)+g_{2,\alpha\beta}(\vec{r},t)]$ are independent of the diffusion constant as can be seen from relations (18) and (19).

Therefore, it is clearly shown that $\vec{\epsilon}_1(\vec{r},t)f_{1,32}(\vec{r},t)$ cannot be interpreted as resulting from a population grating because the condition $\vec{\epsilon}_3^*\cdot\vec{\epsilon}_2 = 0$ is satisfied. However, this cross-polarized field superposition induces an orientational grating [11] which diffracts $\vec{\epsilon}_1(\vec{r},t)$. At this point, we would like to emphasize, as a consequence of the different types of terms in the expression (30), the coexistence of population and orientational gratings. In fact, their contributions could be of the same importance. Finally, the third term $2F^*\vec{\epsilon}_3(\vec{r},t)g_{1,21}(\vec{r},t)$ of the relation (30) can be neglected in the case of resonant excitations. Both pump fields having orthogonal polarizations, their superposition can generate an orientational grating. Let us now consider the configuration of field polarizations corresponding to

$$\vec{\epsilon}_3^*\cdot\vec{\epsilon}_1 = 0 \ , \ \vec{\epsilon}_3^*\cdot\vec{\epsilon}_2 \neq 0 \text{ and } \vec{\epsilon}_1\cdot\vec{\epsilon}_2 = 0$$

This configuration can be described by similar considerations developed previously. The particular case with $\vec{\epsilon}_3^*\cdot\vec{\epsilon}_1 = 0$, $\vec{\epsilon}_3^*\cdot\vec{\epsilon}_2 = 0$ and $\vec{\epsilon}_2\cdot\vec{\epsilon}_1 \neq 0$ is quite different. The terms associated with $f_{1,31}(\vec{r},t)$ and $f_{2,32}(\vec{r},t)$ can be related to orientational gratings, but the quantity $2F^*\vec{\epsilon}_3(\vec{r},t)g_{1,21}(\vec{r},t)$ does not correspond to a static population grating. Instead, we have a moving grating oscillating with pulsation 2ω. This is clearly shown by considering relation (32), where for this particular configuration of field polarizations, only the factors $\exp(2i\omega t)$ and $\exp(-2i\omega t)$ give a contribution to the averaged population difference. This point, already mentioned by different authors [12] is rigorously established here.

Let us now consider the case where the orientational constant D is very large. Then $\vec{C}(\vec{r},t)$ can be written as

522

$$\vec{\varphi}(\vec{r},t) = \frac{i|\mu_{12}|^4}{4\hbar^3} \left\{ (\vec{\varepsilon}_3^*\cdot\vec{\varepsilon}_1)\vec{\varepsilon}_2 \ \frac{1}{9}(F+F^*)\boldsymbol{\mathcal{E}}_2(\vec{r},t)f_{2,31}(\vec{r},t) \right.$$

$$+ (\vec{\varepsilon}_3\cdot\vec{\varepsilon}_2)\vec{\varepsilon}_1 \ \frac{1}{9}(F+F^*)\boldsymbol{\mathcal{E}}_1(\vec{r},t)f_{2,32}(\vec{r},t)$$

$$\left. + (\vec{\varepsilon}_1\cdot\vec{\varepsilon}_2)\vec{\varepsilon}_3 \ \frac{2}{9}F^*\boldsymbol{\mathcal{E}}_3^*(\vec{r},t)g_{2,21}(\vec{r},t) \right\} \tag{33}$$

The first term corresponds to the diffraction of $\vec{E}_2(\vec{r},t)$ by the population grating resulting of the superposition of $\vec{E}_3(\vec{r},t)$ and $\vec{E}_1(\vec{r},t)$ interacting with the medium. The second term can be described in a similar fashion by exchanging $\vec{E}_1(\vec{r},t)$ and $\vec{E}_2(\vec{r},t)$ in the discussion above. Again we have a moving population grating described by the third term of the expression (33). It is interesting to note, that orientational gratings do not play a role in the case of high values of D. This is due to the fact that the spatial modulation of the field polarization resulting of the superposition of two cross-polarized fields is destroyed when orientational diffusion is important.

Relation (33) must be related to the one of the third-order nonlinear polarization which is used in many works. For an isotropic medium, and assuming a phenomenological description, the third-order nonlinear polarization is given by [13] :

$$\vec{P}^{(3)} = A[(\vec{E}_1\cdot\vec{E}_3^*)\vec{E}_2 + (\vec{E}_2\cdot\vec{E}_3^*)\vec{E}_1] + C(\vec{E}_1\cdot\vec{E}_2)\vec{E}_3^* \tag{34}$$

where unnecessary notations have been dropped. A and C are constants depending upon the particular mechanism of nonlinearity. In our case, A and C are time-dependent functions of the dynamics of the medium. If the time variation of the envelopes of the fields can be neglected with respect to the dynamical time scale, the coefficients of the terms $(\vec{\varepsilon}_3\cdot\vec{\varepsilon}_1)\cdot\vec{\varepsilon}_2$ and $(\vec{\varepsilon}_3\cdot\vec{\varepsilon}_2)\cdot\vec{\varepsilon}_1$ in relation (33) are equal. Consequently, in the case of rapid rotational diffusion, the structure of the third-order polarization (33) is identical to the one of the classical expression (34). Moreover, in both expressions, the contribution associated with a given polarization is a function of the overlapping of the sole fields which generate the grating. In the classical case, the overlapping is included in the scalar product of the fields, while in (33) it is a multiplicative factor. The situation is quite different when there is no rotational diffusion. While the general structure of Eq. (34) is still satisfied by $C(\vec{r},t)$ in Eq. (30), we do not have any longer the one-to-one correspondence between a particular grating and the overlapping of the fields which generate the grating. Here, for a given choice of the field polarizations, all the overlappings participate in the third-order polarization of the medium. It is of interest to note that this physical situation cannot be dealt with classicaly.

IV. Conclusion

We have presented a general expression of the third-order nonlinear polarization for an isotropic medium subject to rotational diffusion and interacting with three pulsed fields. This theoretical model can be used to study the influence of field polarizations and rotational diffusion constant on the conjugated field by solving propagation equations (14). The extreme cases of large- and zero-rotational-diffusion constant are attainable by this model. They correspond to liquids with rapid rotational diffusion and to dipole glasses with fixed dipole moments randomly oriented, respectively. From this unified treatment any physical sample experiencing four-wave mixing can be interpreted in terms of population and/or orientational gratings depending on the particular polarization configuration chosen in the experiment. Also their corresponding contributions have been evaluated.

V. References

[1]   R.A. Fischer, Optical Phase Conjugation (Academic, New-York, 1982)
[2]   T.R. O'Meara and A. Yariv, Opt. Eng. 21, 237 (1982)
[3]   Y.R. Shen, J. Quantum Electron. 22, 1196 (1986)
[4]   J.O. Tocho, W. Sibbett and D.J. Bradley, Opt. Commun. 37, 67 (1981)
[5]   A.B. Myers and R.M. Hochstrasser, IEEE J. Quantum Electron. 22, 1482 (1986)
[6]   D. Kühlke, Appl. Phys. B34, 129 (1984)
[7]   B.S. Wherrett, A.L. Smirl and T.F. Boggess, IEEE J. Quantum Electron. 19, 680 (1983)
[8]   T. Tao, Biopolymers 8, 609 (1969)
[9]   Y.B. Band and R. Bavli, Phys. Rev. A 36, 3203 (1987)
[10] C. Malonney and W. Blau, J. Opt. Soc. Am. B 4, 1035 (1987)
      (See, for example, the experimental values of T_2)
[11] R. Trebino, C.E. Barker and A.E. Siegmann, IEEE J. Quantum Electron. 22, 1413 (1986)
[12] Y.R. Shen, The Principles of Nonlinear Optics (Wiley, New-York, 1984)
[13] D.G. Steel, R.C. Lind, J.F. Lam and R.C. Giuliano, Appl. Phys. Lett. 35, 376 (1979)
[14] J.P. Lavoine and A.A. Villaeys, Phys. Rev. A, accepted for publication.

OPTICAL PARAMETRIC DIFFERENCE FREQUENCY GENERATION
IN A MNA SINGLE CRYSTAL FILM WAVEGUIDE

M.Ishida, T.Toda, T.Kinoshita, and K.Sasaki
Faculty of Science & Technology, Keio University
3-14-1, Hiyoshi, Yokohama 223, Japan

A.Yamada, H.Sasabe
Frontier Research Project, The Institute of Physical and Chemical Research
2-1, Hirosawa, Wako city, 351-01, Japan

Introduction

Recently, organic materials have been studied in spite of practical usefulness of inorganic materials such as lithium niobate(LiNbO$_3$) and potassium dideuterium phosphate (KDP) for frequency doubling.[1],[2],[3] Organic materials have several virtues in comparison with inorganic materials, such as nonlinear susceptibilities, a high speed optical response, and a high optical damage threshold. In this study, we tried to combine the virtues to waveguide structure. Waveguide structures have also advantages, such as to realize a high optical density, an integrated optical devices, and especially a phase matching by mode dispersion of the guided waves.[4] Actually this study is concerned with optical parametric interaction between different frequency guided waves. The paramrtric interaction substantially accompanies the sum or the difference frequency generation ; amplification of low level signal wave.[5],[6] In this paper, we report our experiments about the optical parametric difference frequency generation in a 2-methyl-4-nitroaniline (MNA) thin film waveguide.

Waveguide preparation and experimental setup

As well known, the largest element of SHG tensor of MNA crystal, d_{11}, is 2.5×10^{-10}(m/v) and the figure of merit is about 2000 times larger than that of LiNbO$_3$.[7]

A thin film of the MNA single crystal was prepared by a two step method. First, a polycarbonate stripe spacer was inserted between two pylex substrates to form a tapered capillary gap. The substrates were dipped into a molten MNA liquid. The molten MNA in a beaker was controlled at 130°C and filled into the gap by a capillary effect. After it was cooled, as the second stage mosaic like microcrystal film in the gap was recrystallized to make a large thin single crystal film. Typically we could get a tapered MNA single crystal film from 0.3μm to 1.0μm in thickness, and it is available structure for the phase matched optical parametric interaction by using a dispersion of effective index.

The experimental setup for optical parametric difference frequency generation is shown in figure 1. The pump source was a tunable pulsed dye-laser (Rh-6G) which was excited by a XeCl laser. The laser has a tunable range from 580nm to 600nm with power 12.5kW. The signal source was a cw He-Ne laser (1150nm). Both pump and signal waves were coupled into the tapered MNA waveguide by a traperoidal rutile prism. The wavelength of the generated idler wave (difference frequency wave) was measured by a monochromator with a photomultiplier and a boxcar integrator.
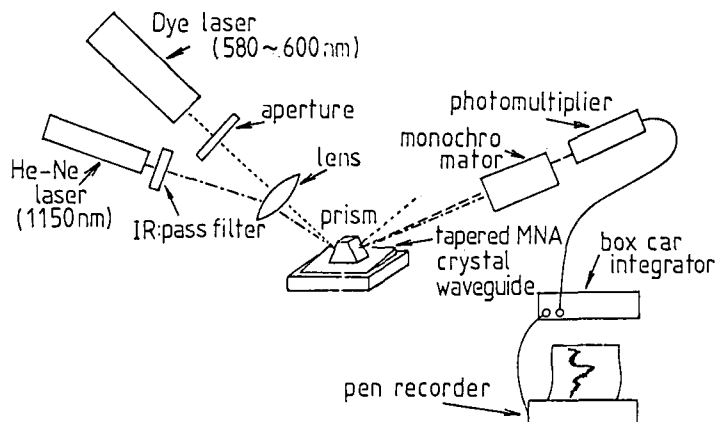
Fig.1 Experimental setup

Optical parametric interaction

When two waves, the pump wave of frequency ω_p and the signal wave of frequency ω_s are launched into a nonlinear optical materials, the signal wave can be parametrically amplified accompanying a new wave, so the called idler wave. The idler wave is the difference frequency wave ω_i. A relation is held among these waves as an energy conservation

$$\omega_p - \omega_s = \omega_i. \tag{1}$$

and phase matching condition (momentum conservation) to maximize the effect is given,

$$\Delta\beta = \beta_p - \beta_s - \beta_i = 0 \tag{2}$$

where β_p, β_s and β_i are the propergation constants of the pump, signal, and idler wave respectively.

Results and discussion

In our experiments phase matching among the three waves was observed by adjusting the thickness of the MNA waveguide. Figure 2 is mode dispersion curves of the propergation constants of three waves corresponding to the thickness of MNA waveguide. Actually the phase matching was realized by adjusting the tapered waveguide thickness as shown in figure 3. The dush line in figure 3 was given by parameter fittings such as the beam width of the light source, the fundamental Gaussian beam, the tapering inclination of the waveguide,and so on. Both lines show good agreement of the peak point and half widths of two curves. The peak was located at the thickness 0.489μm. It was a phase matched point in the dispersion curve of figure 2.
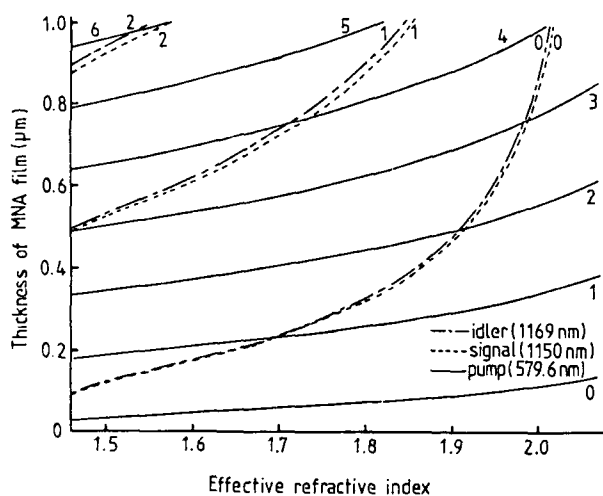
Fig.2 Mode dispersion curve
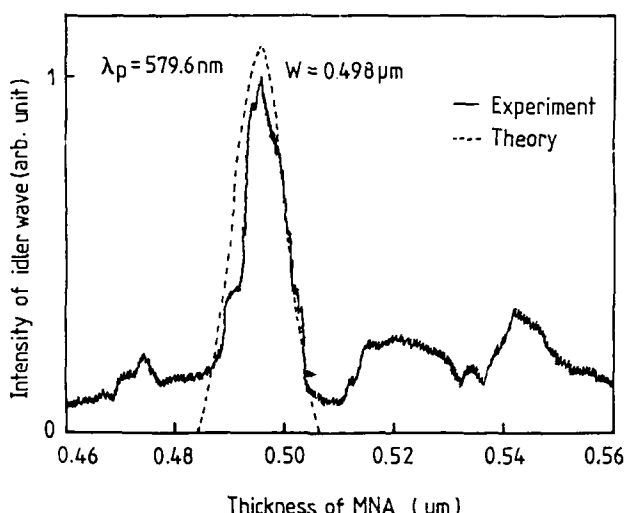
Fig.3 The characteristic of phase matching
Intensity of idler wave versus
the thickness of MNA film

Figure 4 shows the certification of the idler wave for the pump wavelength from 580nm to 595nm, and the wavelength region of idler wave was from 1173nm to 1233nm. The solid line is the theoretical curve by equation (1). Both lines give good agreement.

In our experiments the gain of idler wave was very small because of the insufficient coupling efficiency and the insufficient propergation length. To realize an efficient gain, it is necessary to refine the techniques of crystal growth and to use a more efficient coupler, for example, a grating coupler.

Recently, we newly established an efficient second harmonic generation using a grating coupler. Figure 5 shows the waveguiding mode lines of SHG. This pump source was Nd:YAG laser, its wavelength was 1064nm, and second harmonic generation was 532nm.
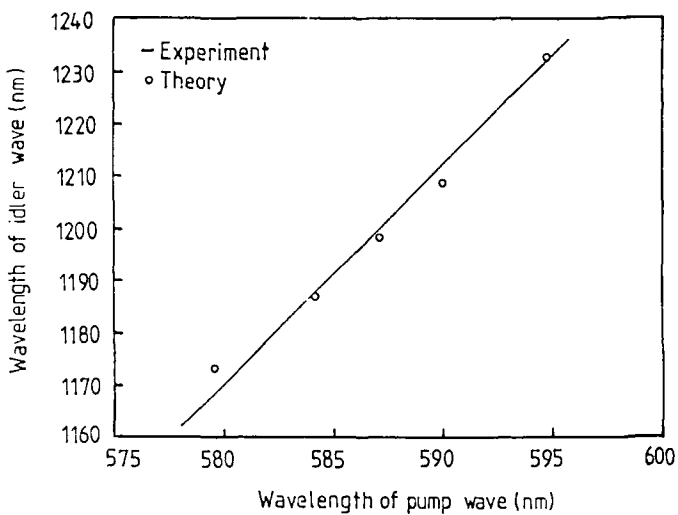
Fig.4 Tuning characteristic of idler wavelength

Fig.5 Mode lines of SHG

Conclution

We fabricated a thin film of MNA single crystal waveguide with taper from 0.3μm to 1.0μm, and observed the phase matched difference frequency generation in the tapered MNA single crystal waveguide with the tuning range from 1173nm to 1233nm.

References

1. K.Jain, G.H.Hewing, Y.Y.Cheng, and J.I.Crowley, IEEE J.Quantum Electron. QE17,1593(1981)
2. K.Jain, J.I.Crowley, G.h.Hewing, Y.Y.Cheng, and R.J.Twieg, Opt.Laser Tech.,13,297(1981)
3. J.Zyss, J.Non-Cryst.Solids 47,211(1982)
4. H.Itoh, K.Hotta, H.Takara, and K.Sasaki, Appl. Optics 25,1491(1980)
5. W.Sohler and H.Suche, Appl. Phys. Lett. 37,255(1980)
6. H.Suche, B.Hampel, H.Seibert, and W.Sohler, SPIE, Vol.578,156(1985)
7. B.F.Levine, C.G.Bethea, C.D.Turmond, R.T.Lynch, and J.L.Bernstein, J.Appl.Phys.,50,2523 (1979)

DEGENERATE FOUR-WAVE MIXING WITH THE USE OF INCOHERENT LIGHT

Takayoshi Kobayashi, Kazuhiko Misawa, and Toshiaki Hattori
Department of Physics, University of Tokyo
7-3-1 Hongo, Bunkyo-ku, Tokyo 113, Japan

Abstract

We study ultrafast relaxation dynamics by degenerate four-wave mixing with incoherent light. We apply the Kerr-shutter configuration, which has the advantage of easy alignment to obtain better signal to noise ratio (S/N) than ordinary forward degenerate four-wave mixing (DFWM). By means of this technique nonresonant optical Kerr relaxation time in CS_2 was resolved to be 1.7 ± 0.1 ps. We also applied this technique to dephasing measurements. The dephasing time of cresyl violet doped in a PMMA film obtained by this method was compared with the result from ordinary 2-beam DFWM. Finally the dephasing time in CdS microcrystallites was obtained to be 230 ± 20 fs.

1. Introduction

Ultrafast dynamical properties of optically excited states have attracted interest and they have been studied by many groups. In condensed matters relaxations are very fast because of the strong interaction between the like or different excitations and because of high density of energy levels. Therefore picosecond or sometimes even femtosecond time resolution is required for the studies. These ultrafast phenomena can only be resolved using optical nonlinear effects, because usual electronic instruments do not have such a ultrahigh time resolution. In ordinary time-resolved nonlinear spectroscopy, the time resolution is limited by the temporal width of pulses. Nowadays, the development of femtosecond lasers has realized ultrashort pulses as short as 6 fs [1]. However, such short pulses can be obtained only with a very sophisticated apparatus. The largest drawback of femtosecond lasers is the limited wavelength of the laser oscillation.

Recently incoherent light has been utilized for the ultrafast time-resolved spectroscopy by means of transient coherent optical effects [2-14]. Temporally incoherent light with a wide spectral width has a much shorter correlation time (τ_c) than its temporal duration, and incoherent light can be considered to generate macroscopic polarization in the similar manner to a train of coherent short pulses with pulse width equal to τ_c. The time resolution of the measurement using transient coherent phenomena is determined by τ_c. According to this principle, experiments with ultrahigh time resolution can be performed much more easily by using temporally incoherent light.

In the early stage the application of this technique was limited to dephasing time (T_2) measurements by degenerate four-wave mixing (DFWM). The first proposal was made by MORITA and YAJIMA [2]. They investigated theoretically electronic T_2 measurement under the assumptions that the envelope function of the electric fields of incoherent light is a complex Gaussian random process and that τ_c is much shorter than the relevant relaxation times. ASAKA et al. measured T_2 in Nd^{3+} doped glass by accumulated photon echoes according to the same principle [3]. Nowadays many studies on electronic dephasing are reported.

This technique has been applied to studies of not only electronic dephasing but also vibrational dephasing [4], electronic population relaxation [5], nonresonant optical Kerr relaxation [6], and luminescence lifetime [7]. As an incoherent light source, an incompletely mode-locked cw dye laser or a home-made dye laser pumped by a nanosecond-pulsed laser can be used. We have only to remove the tuning element from these lasers to obtain ultrahigh time resolution by extending the laser spectral width. In addition incoherent light source in the method is widely tunable. This is the main reason why we applied this method to the study on CdS microcrystallites which will be described in Chap. 5.

However, since the peak power of incoherent light is low, the intensity of the signal generated by incoherent light is much lower than that by ordinary femtosecond pulses. Thus we applied DFWM in the Kerr-shutter configuration, which has advantages of easy alignment and high signal selectivity. In the present paper we study DFWM using incoherent light in the Kerr-shutter configuration, especially its application to the dephasing time measurement [8]. We will describe a theoretical study in Chap. 2. We study optical Kerr effect in CS_2 in Chap. 3 and electronic dephasing in cresyl violet in Chap. 4. The application of the method studied in Chap. 4 to the measurement of dephasing time in CdS microcrystallites will be discussed in Chap. 5.

2. DFWM in the Kerr-shutter configuration

We apply DFWM in the Kerr-shutter configuration (Fig. 1) using incoherent light to measurements of various ultrafast relaxation times. A single beam of linearly polarized

light is divided into two. One of them (probe beam) is variably delaycd and focused onto the sample. The other (pump beam) is polarized $45°$ with respect to the probe beam and focused at the same point. The signal transmitted through a crossed analyzer is detected as a function of the delay between the two beams. Because the signal and the probe beams are collinear in the Kerr-shutter configuration, the direction of the signal can be easily identified, and the signal is detected selectively.
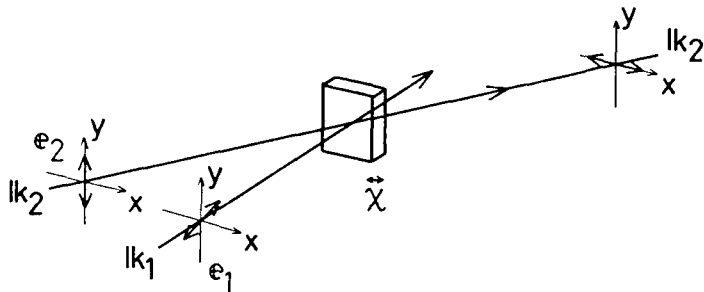
Fig. 1: DFWM in the Kerr-shutter configuration

The third-order polarization induced by total electric field $E(r,t)$ is written in the following equation.

$$P^{(3)}(r,t) \propto \int d(\Delta\omega)g(\Delta\omega)\int_{-\infty}^{t} dt' \int^{t'} dt'' \int^{t''} dt''' \exp[-(t'-t'')/T_1]\exp[-(t-t'+t''-t''')/T_2]$$

$$[\quad \overset{\leftrightarrow}{\chi} E(r,t')E(r,t'')E^*(r,t''')\exp[-i\Delta\omega(t-t'-t''+t''')]$$

$$+ \overset{\leftrightarrow}{\chi} E(r,t')E^*(r,t'')E(r,t''')\exp[-i\Delta\omega(t-t'+t''-t''')]\quad] \quad (1)$$

where $g(\Delta\omega)$ is the distribution function of the frequency difference between the transition frequency of the two-level systems and the laser frequency, with inhomogeneous width $\Delta\Omega$. T_1 and T_2 are the longitudinal and the transverse relaxation times of the relevant transition, respectively.

The electric field of the incoherent light is given as the sum of the pump and the probe fields

$$E(r,t) = e_1 E(t)\exp[i(k_1 r-\omega t)] + e_2 E(t-\tau)\exp[i(k_2 r-\omega(t-\tau))] \quad (2)$$

where e_i is the unit polarization vector of E_i, and in this configuration $e_{1x} = e_{1y} = 1/\sqrt{2}$ for the pump polarized $45°$ with respect to the probe; $e_{2x} = 0$; $e_{2y} = 1$ for the probe with vertical polarization. Since we detect the signal in the same direction as the probe beam in this configuration, we pick up the component with wavevector k_2. When the system to be studied has an extremely large inhomogeneous broadening, (1) is rewritten as

$$P^{(3)}(t) \propto \int_{-\infty}^{t} dt' \int^{t'} dt'' \exp[-(t'-t'')/T_1]\exp[-2(t-t')/T_2]$$

$$[\quad \overset{\leftrightarrow}{\chi} e_2 e_1 e_1 E(t'-\tau)E(t'')E^*(t''+t'-t)$$

$$+ \overset{\leftrightarrow}{\chi} e_1 e_2 e_1 E(t')E(t''-\tau)E^*(t''+t'-t)\quad] \quad (3)$$

Nonvanishing components of a fourth-rank optical nonlinear susceptibility tensor $\overset{\leftrightarrow}{\chi}$ are χ_{xxxx}, χ_{xxyy}, χ_{xyyx}, χ_{xyxy}, and those obtained by permutation among indices x,y, and z. Here we take the definition of χ_{ijkl} as the index l associates with the complex conjugate of the electric field E^*, which means that time ordering of three electric fields starts from the right-most index l and proceeds left to index j. We must be careful in specifying index ordering. These tensor components are considered to be independent of time development. Dynamic response in all tensor components is picked out as a common exponential factor, that is, a single set of T_1 and T_2 can describe the relaxations in isotropic media. This polarization has two terms. The first one is contribution of Kerr effect. The pump induces anisotropy in the sample resulting in the rotation cf the probe polarization. This contributes to constant background in accumulated photon echo. The second term is due to coherent coupling. The pump and the probe make a transient grating in the sample and the pump is diffracted into the probe direction. Since only the x-polarized light is detected, we take the x-component of the polarization. Therefore,

$$(\overset{\leftrightarrow}{\chi} e_2 e_1 e_1)_x = (\chi_{xyxy} + \chi_{xyyx})/2$$

$$(\overset{\leftrightarrow}{\chi} e_1 e_2 e_1)_x = (\chi_{xxyy} + \chi_{xyyx})/2 \quad (4)$$

528

And we define "polarization factor" g as,

$$g = (\chi_{xxyy} + \chi_{xyyx}) / (\chi_{xyxy} + \chi_{xyyx}) \tag{5}$$

In the following chapters we study two special cases; 1) non-resonant optical Kerr effect and 2) accumulated photon echo.

3. Nonresonant optical Kerr effect

3.1. Kerr study on simple molecular liquids

After the direct temporal measurement of the Kerr relaxation time in CS_2 was reported [15], molecular dynamics in various transparent liquids has been investigated using ultrashort pulse lasers [16]. Nowadays four relaxation times are reported. These are associated with 1) a picosecond relaxation by molecular orientational diffusive motion, 2) an intermediate relaxation of hundreds fs by intermolecular interaction, 3) an ultrafast relaxation around one hundred fs by libration, and 4) an instantaneous response of electronic nonlinear polarization. These time constants can be resolved also using incoherent light.

When the incident light is far off-resonant with the system, T_2 does not appear in the response function. Even in nonresonant case, induced polarization is written in the same form as Eq. (3) after T_2 is set to zero. Kerr relaxation is assumed to be a single exponential decay with a time constant T^{Kerr}. Thus T_1 is replaced with T^{Kerr} in Eq. (3).

$$P^{(3)}(t) \propto \int_{-\infty}^{t} dt' \exp[-(t-t')/T^{Kerr}] \, [E(t-\tau)E(t')E^*(t') + g \, E(t)E(t'-\tau)E^*(t')] \tag{6}$$

The signal intensity, which is proportional to the statistical average of $|[P^{(3)}]_x|^2$, is given as

$$I^{(3)}(\tau) \propto \int_{-\infty}^{t} dt' \int_{-\infty}^{t} ds' \exp[-2(2t-t'-s')/T^{Kerr}]$$

$$[\quad < E(t-\tau)E(t')E^*(t')E^\wedge(t-\tau)E^*(s')E(s') >$$

$$+ g < E(t)E(t'-\tau)E^*(t')E^*(t-\tau)E^*(s')E(s') >$$

$$+ g < E(t-\tau)E(t')E^*(t')E^*(t)E^*(s'-\tau)E(s') >$$

$$+ g^2 < E(t)E(t'-\tau)E^*(t')E^*(t)E^*(s'-\tau)E(s') > \,] \tag{7}$$

We assume that E(t) is a complex gaussian random process and τ_c is much shorter than T^{Kerr}. Using the factorization property of random gaussian process, we get signal intensity against τ using incoherent light as

$$I(\tau) = 1 + g(g+2)|G(\tau)|^2 + (2\tau_c^*/T^{Kerr})\exp[-\tau/T^{Kerr}] \qquad (\tau > 0) \tag{8}$$

where $G(u) = <E^*(t)E(t+u)>/<E^*(t)E(t)>$ and $\tau_c^* = \int_{-\infty}^{\infty} |G(u)|^2 du$. We take the definition of τ_c as a temporal width (FWHM) of $|G(\tau)|^2$. We can determine τ_c from the diffracted intensity proportional to $|G(\tau)|^2$ by the thermal grating in dye solution at room temperature. When we assume that $|G(\tau)|^2$ is a Gaussian function, $\tau_c^* = (\sqrt{\pi}/2\sqrt{\ln 2})\tau_c$.

The factor g is calculated to be 1/6 with the tensor components of nuclear origin [20].

3.2. Experimental

We measured Kerr relaxation times in liquid CS_2, which is one of the most famous Kerr media. Incoherent light around 590 nm was provided from a broad-band dye laser pumped by a nanosecond excimer laser. Its repetition rate was about 10 Hz. The dye laser had no tuning elements and τ_c was about 300 fs. Its end mirror was an aluminum mirror with high reflectivity and its output mirror was simply a glass plate. The laser beam which was linearly polarized by a Glan-Thompson prism was divided into two with equal intensity. One of them (probe beam) is focused on the sample through a polarizer. Then it is directed to a photomultiplier through an analyzer. The other (pump beam) is polarized 45° with respect to the probe beam using a Fresnel-rhomb pair, variably delayed with a translational stage and focused at the same point on the sample. A focusing lens and a pinhole were used to collect the signal efficiently and selectively. The signal was detected as a function of the delay. The electric signal from a photomultiplier was amplified with a home-made amplifier, and A/D converted data was stored and processed in a microcomputer. The system was automatically controlled by the computer. The experiment was performed at room temperature.

3.3. Results

Figure 2 shows the obtained data with the long tail coming from Kerr relaxation. Its time constant was 1.7±0.1 ps, which is very close to 1.50±0.05 ps reported in Ref. [17].

This picosecond relaxation is considered to be associated with molecular reorientation. The intensity ratio of the Kerr signal to the background is τ_c^*/T^{Kerr} according to Eq. (8). The better S/N is attained using incoherent light with the longer τ_c, on the other hand, the shorter resolution time with the shorter τ_c. We could resolve only the slowest relaxation time, because of disturbance due to a coherence spike near zero delay.

Delay τ (ps)
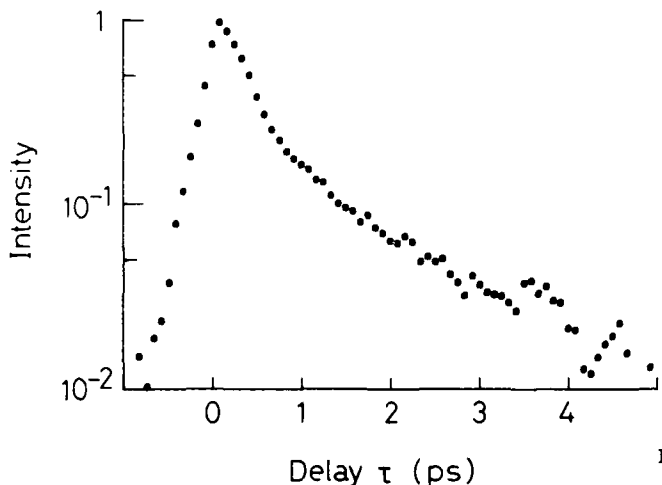
Fig. 2: Semi-logarithmic plots of the delay time dependence of signal intensity obtained from CS_2

3.4. Coherent coupling in Kerr effect

This coherence spike stands for the squared autocorrelation function of the incoherent light $|G(\tau)|^2$ and it is due to coherent coupling effect between pump and probe beams. Coherent coupling in optical Kerr effect in transparent media was pointed out where dephasing is instantaneous [18]. On the other hand in systems resonant with the incident light, dephasing is not instantaneous. This leads to phase-memory effect on the coherent coupling contribution to the signal intensity. When τ_c is much shorter than T_2, coherence spike has an asymmetric tail. This tail offers us a dynamical information about dephasing process.

4. Dephasing Measurement

4.1. Accumulated photon echo

For T_2 measurement, the elimination of excitation pulses by polarizers was suggested in forward three-pulse echo experiments [19]. The scheme of this method is similar to heterodyne-detected accumulated photon echo experiments. The signal intensity, which is proportional to the squared absolute value of the third-order polarization, is finite only when the pump beam is present. We calculated the signal intensity as a function of the delay time (τ) of the probe beam with respect to the pump beam for a two-level system and demonstrated that T_2 can be obtained from the trace.

Since temporally incoherent light can be regarded to be composed of pulses randomly distributed in time, this method is a type of accumulated photon echo experiments [10,11], of which signal can be heterodyne detected by the same equipment as a pump-probe experiment. The heterodyne detected signal is proportional to the nonlinear polarization induced in the material. It decays exponentially with a time constant $T_2/2$ when the system can be described by a simple two-level model with a broad inhomogeneous width. In the heterodyne method, phase-sensitive detection technique using a synchronously-pumped mode-locked dye laser with a high repetition rate and a lock-in amplifier are necessary to be applied to eliminate constant background. As a result S/N can be improved. On the other hand, when a nanosecond dye laser with a low repetition rate as 10Hz is used as an incoherent light source, scattered background noise makes it difficult to obtain high S/N.

Here, we make the following two assumptions for the system to be studied,

(i) $\quad \Delta\Omega \gg T_2^{-1}$

and

(ii) $\quad T_1 \gg \tau_c, T_2$

These assumptions satisfy the conditions necessary for accumulated photon echo. We implicitly assume constant populations of relevant levels in the material because of a long duration of incoherent light. Hence in case ultrashort pulses with low repetition rate are utilized, T_2 cannot be measured in the Kerr-shutter configuration.

Assumption (ii) allows us to rewrite (3) with the electric-field autocorrelation function $G(u) = \langle E^*(t)E(t+u)\rangle/\langle E^*(t)E(t)\rangle$ as,

$$[P^{(3)}(t)]_x \propto \int_{-\infty}^{t} dt' \exp[-2(t-t')/T_2] \, [E(t'-\tau)G(t-t') + g \, E(t')G(t-t'-\tau)] \tag{9}$$

We study dephasing in molecules doped in polymers and dephasing in semiconductors. In both cases $X_{xyxy} = X_{xxyy}$, hence g is equal to unity [20]. The signal intensity, which is proportional to the statistical average of $|[P^{(3)}]_x|^2$, is given as

$$I^{(3)}(t) \propto \int_{-\infty}^{t} dt' \int_{-\infty}^{t} ds' \exp[-2(2t-t'-s')/T_2]$$

$$\begin{aligned}
[\quad & G(s'-t')G(t-s')G(t'-t) \\
+ \; & G(s'-t'+\tau)G(t-s'-\tau)G(t'-t) \\
+ \; & G(s'-t'-\tau)G(t'-t+\tau)G(t-s') \\
+ \; & G(t'-t+\tau)G(t-s'-\tau)G(s'-t') \quad]
\end{aligned} \tag{10}$$

When τ_c is much shorter than T_2, $G(u)$ can be replaced with a delta function $\delta(u)$. After some calculations, we get the normalized signal intensity as follows.

$$I(\tau) = 1 \qquad\qquad\qquad (\tau < 0)$$
$$I(\tau) = [1 + 2\exp(-2\tau/T_2)]^2 \qquad (\tau > 0) \tag{11}$$

Usually we measure T_2 by ordinary 2-beam DFWM, detecting signals in the directions of $2k_1-k_2$ and $2k_2-k_1$. In ordinary 2-beam DFWM, intensity profile exhibits a single exponential decay with a time constant $T_2/4$. Even with the same T_2 the former have slower component of $\exp(-2\tau/T_2)$ due to cross terms between background and decay than the latter $\exp(-4\tau/T_2)$.

4.2. Two-component decay function

The response function in Eq. (1) is not always a single exponential. In this section we take an arbitrary response function $A(t-t'+t''-t''')$ in stead of $\exp[-(t-t'+t''-t''')/T_2]$. When the autocorrelation function $G(u)$ can be replaced with $\delta(u)$, Signal intensity $I(\tau)$ is expressed as

$$I(\tau) = [A(0)]^2 \qquad\qquad (\tau < 0)$$
$$I(\tau) = [A(0) + 2A(2\tau)]^2 \qquad (\tau > 0) \tag{12}$$

Later we discuss dephasing property with two decay components with $T_2^{(1)}$ and $T_2^{(2)}$ ($T_2^{(1)} < T_2^{(2)}$) as

$$A(2(t-t')) = f_1 \exp[-2(t-t')/T_2^{(1)}] + f_2 \exp[-2(t-t')/T_2^{(2)}] \tag{13}$$

where f_i is the amplitude of each exponential factor. The substitution of Eq. (13) into Eq. (12) yields

$$I(\tau) = [f_1 + f_2]^2 \qquad\qquad\qquad\qquad (\tau < 0)$$
$$I(\tau) = [f_1 + f_2 + 2f_1\exp[-2\tau/T_2^{(1)}] + 2f_2\exp[-2\tau/T_2^{(2)}]]^2 \qquad (\tau > 0) \tag{14}$$

These equations will be referred in Section 4.5.

4.3. Experimental procedure

In order to verify the applicability of the above method, we tried to measure T_2 in cresyl violet doped in a PMMA film at 2K. The dephasing of cresyl violet has been studied by photon echoes [14]. Cresyl violet has a bottleneck level with a long lifetime. Even if T_1 is short, accumulation of the transient grating occurs with the long lifetime of the bottleneck.

The experimental apparatus is the same as described in Chap. 3. An incoherent light source was a broad-band dye laser pumped by a nanosecond N_2 laser. The sample was immersed in superfluid liquid helium. A Babinet compensator was used to suppress the background due to the birefringence in the eight windows of the vessels.

4.4. Results

Figure 3(a) shows the result with two decay components. Signal intensity profile of photon echoes has two components. The slower and faster components are due to the zero-phonon line and the phonon-sideband, respectively. The saturation intensity of zero-phonon

line is lower than that of phonon side-band. Thus the excitation intensity should be low enough not to saturate the zero-phonon line. As the excitation intensity is increased, the relative intensity of the faster decay component becomes prominent. We compared the data obtained by the former configuration (Fig. 3(a)) and that by ordinary 2-beam forward DFWM (Fig. 3(b)) with the same sample. We should compare the decay time constants of long tails, because the faster decay property corresponding to phonon side-band depends on the excitation intensity. In addition, a sharp spike due to the light diffracted by a thermal grating, may overlap near zero delay. The dephasing time for the long tail was 57±1 ps by the Kerr-shutter configuration and 56±8 ps by the ordinary 2-beam forward DFWM. These two values agree with each other within experimental errors. This Kerr-shutter configuration enabled us to detect the signal with much lower excitation intensity or much lower repetition rate than the other DFWM configurations previously applied using incoherent light. The data obtained by 2-beam DFWM has poor S/N, even though the intensity of incident light in 2-beam DFWM was six times as that in the Kerr-shutter. As a result the relative intensity of the long tail is smaller in the 2-beam DFWM than in the Kerr-shutter. Actually we could obtain better S/N by the Kerr-shutter configuration than the other.
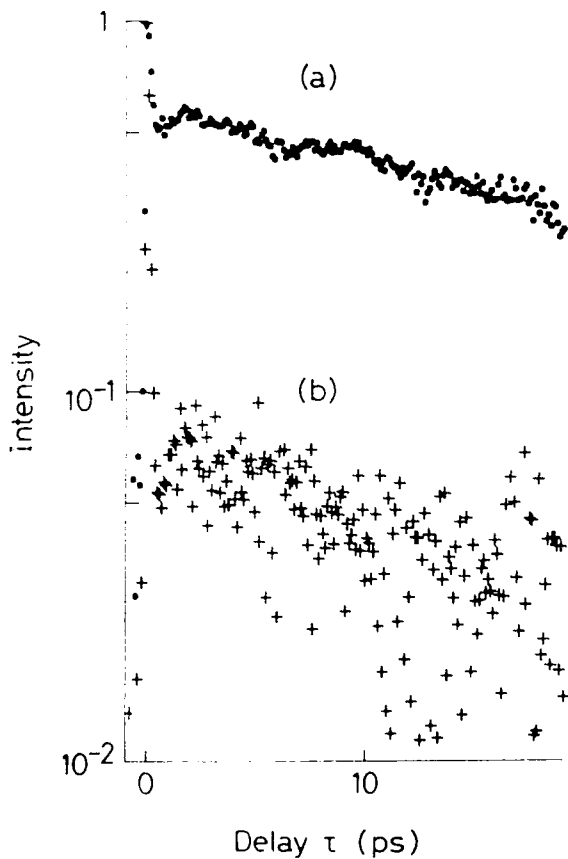
Fig. 3: Delay time dependence of signal intensity at 2K obtained from cresyl violet;
(a) by the Kerr-shutter configuration;
(b) by ordinary forward DFWM with two orthogonally polarized beams

4.5. Discussion

We cannot determine T_2 directly from the slope of a simple semi-logarithmic plot of signal intensity obtained by a Kerr-shutter experiment, since the signal is the squared sum of constant background and decay term. We estimate T_2 after some numerical data processing as follows. The obtained data contains other background noise such as scattering or leakage from the analyzer. The signal is normalized at zero delay after all background is subtracted. The normalized signal intensity corresponds to

$$I_{nor}(\tau) = (1/8)[\{1 + \frac{2}{1+f}\exp[-2\tau/T_2^{(1)}] + \frac{2f}{1+f}\exp[-2\tau/T_2^{(2)}]\}^2 - 1] \tag{15}$$

where $f = f_2/f_1$, $I_{nor}(0) = 1$, $I_{nor}(\infty) = 0$. When we fit a T_2 for slower component at large τ, the third term with $T_2^{(1)}$ can be neglected because $T_2^{(1)} < T_2^{(2)}$. Thus we can estimate a $T_2^{(2)}$ by means of the least-square method from the slope of the plot of the right-hand side of the following equation against τ, which is shown in Fig. 3(a).

$$-2\tau/T_2 = \ln[\sqrt{8I_{nor}(\tau)+1} - 1] - \ln[2f/(1+f)] \tag{16}$$

Here fitting parameters are T_2 and f.

In accumulated photon echo we always assume that T_1 is much longer than T_2 and τ_c. Under this assumption we consider the background term to be constant, so T_2 can be determined from the tail. Signals obtained by heterodyne detection depend on T_1 as well as T_2. Any fluctuation of the background affects the decay profile. In order to determine T_2 exactly, information about T_1 is necessary. We also assume extremely large inhomogeneous broadening. Finite inhomogeneous width was discussed in Ref. [12]. The same treatment is needed for the present study.

The obtained value 57±1 ps at 2K is shorter than 100 ps at 6K reported in Ref. [14]. There are two reasons for the disagreement. The first one is due to the difference in matrix, since dephasing takes place by interaction between excited electron in dye molecules and phonons in the matrix. The matrix is PVA in Ref. [14] while it is PMMA in the present study. Secondly the temperature of the sample may be higher than 2K. Laser light can heat up the sample immersed in superfluid liquid He. We did not measure the temperature change induced by the heating. This increase in temperature may induce faster dephasing.

5. CdS Microcrystallites

5.1 Introduction

Semiconductor microcrystallites are considered to be among promising materials used in nonlinear optical devices because of their large nonlinearity due to excitons confined in the particles. Many groups have been studying physical properties of microcrystallites using commercial semiconductor-doped glass filters . Phase decay in microcrystallites has also been studied. TOKIZAKI et al. investigated the dephasing process in a commercial filter [21]. These commercial filters can easily be afforded as samples containing microcrystallites of CdS_xSe_{1-x}. However, since excessive amount of zinc is used in the manufacturing process, microcrystallites with different stoichiometries such as ZnS and ZnSe are contained. Therefore commercial filters are not appropriate for the investigation of the basic properties of microcrystallites. In order to discuss physical properties of microcrystallites, it is necessary to study with a well-defined stoichiometry [22]. Thus we prepared pure CdS microcrystallites doped in a polymer film by "precipitation-in-gel" (PIG) method [23]. In the following chapters we report measurement of the dephasing time (T_2) in CdS microcrystallites using temporally incoherent light.

5.2. Experimental procedure

The absorption spectrum of the sample in Fig. 4 exhibits a shoulder around 420 nm which corresponds to the exciton absorption. The width of the shoulder is estimated as about 40 nm. If the particle size is uniform, exciton absorption should appear with a narrow peak. ALIVISATOS et al. reported homogeneous line width of CdSe microcrystallites to be 17meV (4nm) [24]. Hence the particles in this sample may have a broad distribution of diameters.

The experimental apparatus is the same as described in Chap. 3. An incoherent light source was a broad-band dye laser pumped by a nanosecond excimer laser. The laser dye was stilbene 420 selected to be nearly resonant on the exciton absorption. The correlation time τ_c was about 120 fs. Samples were immersed directly in superfluid liquid helium.
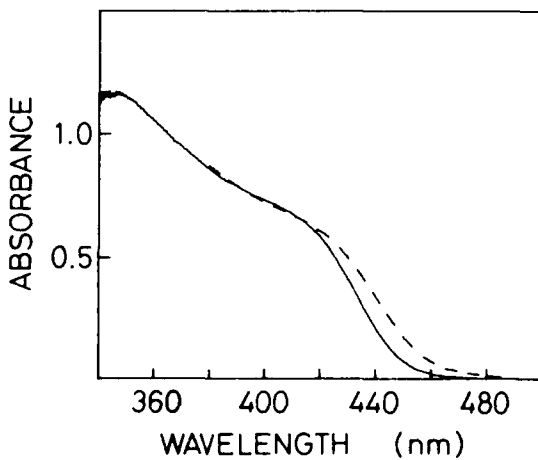
Fig. 4: Absorption spectra of CdS micro-crystallites doped in a polymer film; solid line: at 4K; dashed line; at room temperature

5.3. Result

We could successfully detect the signal of the DFWM by the new method using the Kerr-shutter configuration, while we failed in the ordinary 2-beam forward DFWM configuration. It is because quick and precise alignment can be done in the former method. That is why we called the new method "signal-selective". Two decay components can be seen in the obtained data from CdS microcrystallites with a mean diameter around 50 Å (Fig. 5). From this trace

we estimate the decay-time constant to be 230±20 fs for the faster component. This value is shorter than that of excitons confined in a GaAs quantum-well which is reported to be a few picoseconds by SCHULTHEIS et al. [25]. Since their sample contained a single quantum-well, they could tune the wavelength of the incident laser beam just resonant on the lowest level of the exciton absorption and dephasing becomes longer. However, the exciton absorption of our sample is inhomogeneously broadened. Thus we also excite higher levels of excitons and the dephasing of the higher levels may be faster. On the other hand, the homogeneous line width reported in Ref. [24] represents a dephasing time of 80 fs. Dephasing time obtained indirectly by hole-burning is shorter than that obtained by DFWM. Systematic errors tend to broaden hole width. This means underestimation of dephasing time.
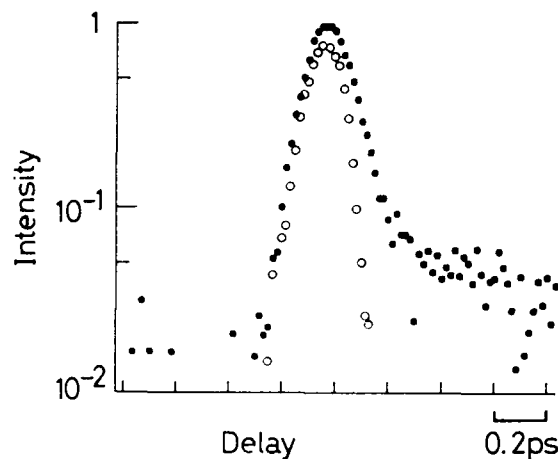
Fig. 5: Delay time dependence of signal intensity at 2K obtained from CdS microcrystallites

References

1. R.L. Fork, C.H. Brito Cruz, P.C. Becker, and C.V. Shank: Opt. Lett. 12, 483 (1987)
2. N. Morita and T. Yajima: Phys. Rev. A 30, 2525 (1984)
3. S. Asaka, H. Nakatsuka, N. Fujiwara, and M. Matsuoka: Phys. Rev. A 29, 2286 (1984)
4. T. Hattori, A. Terasaki, and T. Kobayashi: Phys. Rev. A 35, 715 (1987)
5. M. Tomita and M. Matsuoka: J. Opt. Soc. Am. B 3, 560 (1986)
6. K. Kurokawa, T. Hattori, and T. Kobayashi: Phys. Rev. A 36, 1298 (1987)
7. H. Nakatsuka, Y. Katashima, K. Inoue, and R. Yano: Opt. Comm. 69, 169 (1988)
8. K. Misawa, T. Hattori, and T. Kobayashi: submitted to Opt. Lett.
9. R. Beech and S.R. Hartmann: Phys. Rev. Lett. 53, 663 (1984)
10. S.R. Meech, A.J. Hoff and D.A. Wiersma: Chem. Phys. Lett. 121, 287 (1985)
11. S. Saikan, T. Nakabayashi, Y. Kanematsu, and a. Imaoka: J. Chem. Phys. 89, 4609 (1988)
12. T. Kobayashi, T. Hattori, A. Terasaki, and K. Kurokawa: Revue Phys. Appl. 22, 1773 (1987)
13. T. Kobayashi, A. Terasaki, T. Hattori, and K. Kurokawa: Appl. Phys. B 47, 107 (1988)
14. H. Nakatsuka, H. Sugiyama, and Y. Matsumoto: J. Lumin. 38, 31 (1987)
15. E.P. Ippen and C.V. Shank: Appl. Phys. Lett. 26, 92 (1975)
16. D. McMorrow, W.T. Lotshaw, and A. Kenney-Wallace: IEEE J. Quantum Electron. QE-24, 443 (1988)
17. J. Etchepare, G. Grillon, J.P. Chambaret, G. Hamoniaux, and A. Orszag: Opt. Comm. 63, 329 (1987)
18. J.L. Oudar: IEEE J. Quantum Electron. QE-19, 713 (1983)
19. M. Matsuoka, H. Nakatsuka, and M. Fujita: In Picosecond Phenomena II, ed. by R. Hochstrasser, W. Kaiser, and C.V. Shank (Springer, Berlin 1980) p.357
20. B.S. Wherrett, A.L. Smirl, and T.F. Boggess: IEEE J. Quantum Electron. QE-19, 680 (1983)
21. T. Tokizaki and T. Yajima: Ultrafast Phenomena VI, (Springer, Berlin), to be published.
22. Y. Wang and W. Mahler: Opt. Comm. 61, 233 (1987)
23. Y. Ohashi, H. Ito, T. Hayashi, A. Nitta, H. Matsuda, S. Okada, H. Nakanishi and K. Kato: Nonlinear Optics of Organics and Semiconductors ed. by T. Kobayashi (Springer, Berlin), to be published.
24. A.P. Alivisatos, A.L. Harris, N.J. Levinos, M.L. Steigerwald, and L.E. Brus: J. Chem. Phys. 89, 4001 (1988)
25. L. Schultheis, A. Honold, J. Kuhl, K. Kohler, and C.W. Tu: Phys. Rev. B 34, 9027 (1986)

REMOTE SENSING OF WINDS AND PARTICULATES
USING A CO$_2$ DOPPLER LIDAR

Madison J. Post
NOAA Wave Propagation Laboratory
Boulder, Colorado 80303

Introduction

The purpose of this paper is to summarize how we have applied the technology of pulsed, coherent, infrared Doppler lidar to making measurements of atmospheric winds and aerosols. In 1981 we built a hybrid lidar with components from the United Technologies Research Corporation.[1] In 1985 this system was upgraded with an injection-locked transmitter built by Spectra Technologies, Inc. to increase power output and to advance technology for possible application to space-borne systems.[2] Difficulties we encountered with the newer technology centered around frequency stability, both inter- and intra-pulse, due to mode purity and coupling between the power oscillator and the injection oscillator. These problems limit the accuracy of our wind measurements to about 2 m s^{-1} and prevent the expected increase in sensitivity to backscatter because signal processing bandwidth could not be reduced to match the transmitter pulse-shape bandwidth. However, the new system is still a significant improvement over the old, and we have gained valuable knowledge for designing space-based hardware.

A Doppler lidar works by transmitting a pulse of frequency-pure radiation that is scattered in all directions by particulates carried with the wind. A telescope collects the small fraction of the energy that is scattered directly backwards, and this energy is mixed with a highly stable, frequency-offset laser on the signal detector. Motion of the particulates along the beam will impart a Doppler frequency shift to the backscattered signal, so by measuring the beat frequency on the detector as a function of time delay, we measure the radial wind component as a function of range. A computer-controlled scanner, a real-time processor, and a color display[3] greatly enhance the utility of the system, permitting a scientist to survey the 3-D wind or aerosol field with breadth and flexibility, or to examine an interesting feature in greater detail. Real-time displays of intensity (aerosol scatter), mean radial velocity, or spectral width can be formatted as PPI, RHI, AZ-EL (raster), Range-Time, or VAD scans, and vertical wind profiles can be calculated within 2 minutes of data acquisition.

Field Work

We have used our Doppler lidar to observe many examples of previously unknown or undocumented atmospheric phenomena. Unfortunately, the color displays that depict the new data cannot be reproduced in this paper, but the references will give interested readers access to the data.

Between 1981 and 1984 we acquired over 600 vertical profiles of aerosol backscattering from the Boulder-Denver area.[4] These occurred during the interesting time that included the eruption of the El Chichon volcano. From this large data set we were able to glean information about diffusion and purging processes on a global scale, both in the stratosphere and in the troposphere, surmising that tropopause folding plays a significant role in these processes. Also, we observed that often the statistical distribution of backscatter at a given altitude was log-normal, indicating that mixing processes are multiplicative rather than additive in nature. We also discovered what appears to be a background signal intensity level--a floor below which the backscattering mixing ratio seldom falls.[5] Other aerosol-related field programs include a month-long observation of visible and sub-visible cirrus in central Wisconsin in 1987[6] (the FIRE parogram), and measuring many properties of aerosols and clouds at wavelengths of 10.59 and 9.25 microns from the volcanic mountain of Mauna Loa in Hawaii as part of 1988 MABIE (Mauna Loa Aerosol Backscatter Intercomparison Experiment).

In 1984 we participated in a multi-agency ASCOT (Atmospheric Studies in Complex Terrain) experiment in the Brush Creek basin in western Colorado, measuring the development, decay, and meanderings of the elevated nocturnal drainage flows that occur in such terrain.[7] Later that year we traveled to western Texas and observed the passage of a dry-line front that triggered the outbreak of severe weather to the north.[8] We have detected and analyzed several wind-shear related events, including clear-air downbursts,[9] and the collision of outflows from independent thunderstorms.[10] The development and decay of coastal breezes in complex terrain were studied in California.[11] In Colorado we captured the structure of a downslope windstorm, observing periodic coherent gusts and a leeward rotor for the first time.[12] Participation in a boundary layer experiment in Kansas (FIFE) showed our capability to measure momentum flux,[13] while our work in the 1987 Denver brown cloud pollution study helped us understand the nocturnal low-level reverse flows and the effects of high-rise buildings on mixing and transport.[14]

Certainly there are many more observations of this type to be made in the future to increase our understanding of micro- and meso-scale processes. However, the largest payoff would occur if such a system could be placed in Earth orbit to measure wind profiles globally. We first proposed this application in 1978,[15] and NASA has recently taken up the cause with its LAWS program.[16] Numerical weather forecasters have studied the implications of having good wind data on a global basis to input into prediction programs. They have concluded that winds are the most important single input to current numerical prediction models, and that with global wind profiles achievable from a LAWS instrument, the accuracy of weather predictions would increase significantly.[17]

References

1. Post, M.J., R.A. Richter, R.M. Hardesty, T.R. Lawrence, and F.F. Hall, Jr., NOAA's pulsed, coherent, infrared Doppler lidar-Characteristics and Data, Soc. Photo-Opt. Instr. Eng., 300, 60-65, 1981.

2. Hardesty, R.M., T.R. Lawrence, and R.E. Cupp, Performance of a 2-joule per pulse, injection-locked TEA laser for atmospheric wind measurements, Proc. Conf. on Lasers and Electro-optics, Apr. 26-May 1, 1987, Baltimore, 128, Opt. Soc. Am.

3. Hardesty, R.M., R.W. Lee, and D.L. Davis, Real-time processing and display of coherent lidar returns, Tech. Dig., Second Topical Meeting on Coherent Laser Radar, Aug. 1-4, 1983, Aspen, Opt. Soc. Am.

4. Post, M.J., "Atmospheric infrared backscattering profiles: Interpretation of statistical and temporal properties," NOAA Tech. Memo. ERL WPL-122, May 1985, 105 pp.

5. Rothermel, J., D.A. Bowdle, J.M. Vaughan, and M.J. Post, Evidence of a tropospheric aerosol backscatter background mode, accepted by Appl. Opt. Rapid Comm.

6. Hall, F.F., Jr., R.E. Cupp, and S.W. Troxel, Cirrus cloud transmittance and backscatter in the infrared measured with CO2 lidar, Appl. Opt., 27, 2510-2516, 1988.

7. Post, M.J., and W.D. Neff, Doppler lidar measurements of winds in a narrow mountain valley, Bull. Am. Met. Soc., 67, 274-281, 1986.

8. Parsons, D.B., R.M. Hardesty, and M.A. Shapiro, Mesoscale structure of the dryline and the formation of deep convection, Preprints, Int. Conf. on Monsoon and Mesoscale Met., Nov. 1986, Taipei, Am. Met. Soc.

9. Weber, B.F., F.F. Hall, Jr., and R.M. Hardesty, A positively bouyant downburst investigated in two dimensions with Doppler lidar, Proc. 15th Conf. on Severe Local Storms, 403-406, Baltimore, 1988, Am. Met. Soc.

10. Intrieri, J.M., A.J. Bedard, Jr., and R.M. Hardesty, Doppler lidar observations of colliding outflow boundaries, Proc. 15th Conf. on Severe Local Storms, 249-252, Baltimore, 1988, Am. Met. Soc.

11. Intrieri, J.M., Density currents in the atmosphere as observed by the NOAA Doppler lidar, Proc. LASE '89, Jan. 15-20, 1989, Los Angeles, Soc. Photo-Opt. Instr. Eng.

12. Neiman, P.J., R.M. Hardesty, M.A. Shapiro, and R.E. Cupp, Doppler lidar observations of a downslope windstorm, Mon. Weather Rev., 116, 2265-2275, 1988.

13. Eberhard, W.L., R.E. Cupp, and K.R. Healy, Doppler lidar measurement of profiles of turbulence and momentum flux, accepted for publication in J. Oceanic Atmos. Tech.

14. Eberhard, W.L., Wind fields and aerosol distributions in the Denver brown cloud observed by CO2 Doppler lidar, Proc. 6th Joint Conf. on Application of Air Pollution Met., Jan 30-Feb 3, 1989, Anaheim, Am. Met. Soc.

15. Huffaker, R.M. (Editor), Feasibility study of satellite-borne lidar global wind monitoring system, NOAA Tech. Memo. ERL WPL-37, Sept. 1978.

16. Butler, D.M., et. al., Earth observing system: Science and mission requirements, Working Group Report, Vol. 1, NASA Tech. Memo. 86129, 1984.

17. Atlas, R., E. Kalnay, W.E. Baker, J. Susskind, D. Reuter, and M. Halem, Simulation studies of the impact of future observing systems on weather prediction, Proc. 7th Conf. on Numerical Weather Prediction, 145, Montreal, June 17-20, 1985.

ATMOSPHERIC DEPOLARIZATION OF LIDAR BACKSCATTER SIGNALS

D. S. Kokkinos, M.T.S.
NYNEX Science and Technology
500 Westchester Ave.
White Plains, New York 10604

S.A. Ahmed, Prof.
City College of New York
138th St. & Convent Ave.
N.Y.C., New York 10031

ABSTRACT

Depolarization by atmospheric single and multi-step backscatter process is analyzed for its impact on a polarization discrimination DIAL lidar system designed for molecular air pollution monitoring. In this system polarizers are used instead of lossy narrow-band filters in the optical receiver. It is shown here that in this type of system undesirable depolarization effects are primarily caused by single step (180°) backscatter from non-symmetric small Mie particles, and from two step backscatter from particles of all sizes.

Single step backscatter depolarization is shown not to vary with receiver acceptance angle, for the small receiver angles required to encompass typical outgoing laser beam divergences. For multiple backscatter processes expected depolarization is proportional to the square of the acceptance angle for typical visibilities.

Backscatter models developed were confirmed by field tests over Km ranges using a flashlamp pumped dye laser lidar at 4500Å with a beam divergence of 0.5 mrad. Depolarization of less than 1% was obtained by limiting the acceptance angle to 1 mrad with no significant signal reduction. Depolarization was confirmed to vary with the square of the angle for larger angles.

The results demonstrate that a DIAL system using polarization discrimination to separate backscatter signals will not be significantly affected by depolarization effects as long as receiver acceptance angle is small enough to eliminate multiple backscatter.

I. INTRODUCTION

In existing Differential Absorption Lidar (DIAL)[1,2,3] systems used for molecular air pollution monitoring (Fig.1), laser pulses are emitted simultaneously or sequentially at two close-lying wavelengths. The output wavelengths correspond to a peak and a trough in the absorption spectrum of the pollutant being monitored. The concentration of the pollutant along a sample region is determined by measuring the relative attenuation of the lidar backscattered signals from the beginning and end of the sample lengths at each of the wavelengths. To discriminate between the two close-lying probe laser wavelengths, narrow-band filters are generally used in the lidar receiver. This approach prevents the DIAL technique from being readily used in a more versatile tunable wavelength mode. Furthermore the requirement for two narrow-band filters makes the technique impractical and difficult at near UV wavelengths where only relatively wideband filters are readily available. The wider bandwidth prevents use of both wavelengths simultaneously, which is the prefered mode of operation. Furthermore narrow-band and UV filters are lossy and their use results in additional penalties in system sensitivity.

To overcome these limitations and expand the versatility and applications of DIAL lidar systems, a polarization discrimination approach is used (Fig.2). In this approach, the lidar outputs at the two close-lying wavelengths are emitted simultaneously, but orthogonally polarized with respect to each other. The premise of the polarization discrimination scheme is that backscattered signals retain sufficiently the initial polarizations of the outgoing signals to permit polarization discrimination techniques to be used alone to separate the return signal at each of the two wavelengths. Thus the backscatter signals can be separated by using linear polarizers at the lidar receiver and a relatively large bandwidth filter which can accomodate the two probe wavelengths, to reduce daylight background noise to acceptable levels.

For a polarization discrimination DIAL scheme of this type, the depolarization inherent in atmospheric backscatter process is clearly of key importance as a potential source of error, and is the subject of this paper. An examination of atmospheric features is carried out in section II to determine the factors affecting polarization retention in elastic backscatter. The primary mechanisms expected to be responsible for depolarization of backscatter lidar signal received are identified and their combined effects are analyzed in the context of their impact on a polarization discrimination DIAL scheme. Based on that analysis a backscatter model is developed for the depolarization expected.

Section III describes the experimental demonstration of a polarization lidar system and the field tests on atmospheric depolarization carried out with the complete system

538

operating at a wavelength of 4500Å. Section IV presents the experimental results which confirm the backscatter model developed and shows values of depolarization under various scattering conditions.

II. ATMOSPHERIC DEPOLARIZATION PROCESSES

The physical processes that can cause depolarization in atmospheric elastic backscatter which are considered here include clear air turbulence, molecular (Rayleigh) scattering, particulate (Mie) scattering from symmetric and non-symmetric particles, scattering by large particles and multiple scattering.

For clear (molecular) air turbulence, expressions for the mean square polarization angle fluctuation have been obtained[4] showing a λ^2 dependance, and found to give less that 10^{-9} rad/Km rms change in polarization angle for optical wavelengths,λ. Therefore the cross-polarized components of backscatter produced will be 180dB below the backscatter of the original polarization and negligible as far as practical lidar considerations are concerned.

Rayleigh theory developed for the scattering of linearly polarized light by isotopic non-conductive particles with size small compared to the wavelength of the incident radiation predicts no depolarization from backscattering. However, due to the actual anisotropy of the atmospheric molecules , a contribution to the total depolarization should be expected from Rayleigh scattering. The amount of depolarization can be expressed by the linear depolarization ratio δ equal to I_c/I_p , where I_p is the intensity corresponding to the scattered field component which is parallel to the incident field, and I_c the intensity corresponding to the component of the scattered field which is perpendicular to the incident field (cross-polarized). The depolarization ratio can be calculated for scattering by single particle using Stoke's parameters (I_p,I_c,U,V) to express the polarization properties of each field i.e. incident and scattered, and a scattering matrix depending on the scattering geometry and the properties of scatterers. The matrix elements are functions of the polarizability tensor[5] of the individual molecule and their values as well as values of δ in the visible region 5000-6000Å have been reported[6] for molecules such as N_2,O_2,CO_2 , and H_2O.

Assuming as is reasonable with the small Rayleigh backscatter cross-section, that only singly scattered radiation is relevant to the lidar signal received, the weighted sum of δ's for the air molecules turns out to be $\delta_{RAY} \approx 0.015$ which is in agreement with the value 0.014 measured[6] for dry air. Condidering however that for typical 10Km visibility at 5000Å the Rayleigh backscatter coefficient is less than the Mie backscatter coefficient by a factor of 20, the affective contribution from Rayleigh backscatter to the total depolarization resulting from both Rayleigh and Mie backscatter will be $\delta_{RAY}/20$. This amount of depolarization is expencted to have negligible effect on the accuracy of a DIAL system measuring pollutant concentration.

The next scattering process considered is particulate (Mie) scattering. Mie theory developed for spherical, homogeneous, isotropic, dielectric particles with radius comparable to or larger than the wavelength of the incident radiation predicts no depolarization for single backscattering of linearly polarized light. In general, however, atmospheric scattering is not isotropic and particles are not spherical and dielectric. Therefore depolarization must be expected from Mie scattering which is more important due to the higher scattering cross-section associated with this process, compared to Rayleigh scattering. At this point it is interesting to consider two categories of Mie particles: symmetric and non-symmetric.

In both cases for a single particle a scattering matrix $\underset{\sim}{A}$ can be defined relating the incident field E to the scattered field E' by the relationship

$$\begin{bmatrix} E_p \\ \\ E_c \end{bmatrix} = \begin{bmatrix} A_{11} & A_{12} \\ \\ A_{21} & A_{22} \end{bmatrix} \begin{bmatrix} E_p \\ \\ E_c \end{bmatrix}$$

where p and c indicate components of the field parallel and perpendicular respectively to the plane of scattering. The plane of scattering is determined by the directions of propagation of the incident and scattered fields.

For Mie particles with reflectional symmetry about the scattering plane it can be shown that the scattering matrix[7] is a diagonal matrix. In that case incident radiation with electric vector parallel or perpendicular to the plane of scattering will not by depolarized. It is therefore clear that for forward scatter or backscatter there will be no depolarization by particles which have rotational symmetry with the axis of rotation oriented parallel to the direction of an incoming beam.

Thus water droplets which are spherical or spherical dust particles will cause no depolarization of backscatter at the direction of an axis of symmetry of the particle. However in the general case of non-symmetric particle(s) or groups of symmetric particles randomly oriented[8], the backscattered radiation will be depolarized.

For particles where the radius of curvature is much larger than the wavelength of the incident radiation (large particles) it is reasonable to consider the scattering from their surface in the context of scattering from a plane. In that case theoretical results[9] indicate no depolarization for 180° backscatter while scattering at other angles will in general be depolarized.

As a consequence of the above discussion, the two expected main sources of depolarization in signals backscattered to the lidar receiver can now be identified;

The first one , is the depolarization of single step backscatter radiation from non-symmetric particles, where the wavelength λ, is not much smaller than ρ , the radius of curvature of the particle reflecting surface; In that case the backscattered component would be, as discussed, depolarized.

The second source of depolarization is multiple scattering resulting from both symmetric and non-symmetric particles. Under these circumstances the light scattered more than once at angles other than 180° (backscatter), or 0° (forward scatter), will be depolarized; Again, it can be deduced, because of the random orientation of particles and scattering angles, that backscattered light scattered more than once reaching the lidar receiver will generally be unpolarized. Because the backscatter coefficients are all relatively small, for typical visibilities (5-20 Km), multiple scattering resulting from more than two interactions can be neglected.

Clearly detected depolarization resulting from multiple scattering, will be decreased if the acceptance angle of the receiver, is reduced from α , Fig.3 to ϑ ,since the multiple scattered component in the total backscatter received is reduced; Furthermore, since the amount of multiple scattering entering the receiver is approximately dependant on the area in the backscattering plane that is viewed by the receiver it can be expected to increase with the square of the receiver field of view α, at least for small receiver acceptance angles, until intensity along the scattering plane starts to be decreased more rapidly, by the inverse square law and hence reduce the rate of increase of the polarized backscatter with acceptance angle.

Thus the total depolarized backscatter is expected to be the sum of the single step 180° backscatter processes from non-symmetric particles, plus the component due to multiple (two-step) scattering from both symmetric and non – symmetric particles; If the field of view, α is larger than the outgoing beam divergence ϑ , the first component due to single step backscatter will be constant as the receiver acceptance angle α is further increased; Thus the total depolarized portion of the lidar return under these circumstances will have a component constant with increasing α , (beyond $\alpha = \vartheta$) due to single step 180° backscatter, plus a component that increases initially approximately with α^2 then more slowly due to multiple (two-step) backscatter process;

Without knowing the density distribution of non-symmetric particles, and the relative density of symmetric ones it is not possible to make an estimate of relative magnitude of the components;

III. THE EXPERIMENT

To demonstrate the viability of the polarization discrimination scheme, the lidar system was designed for the detection of NO_2 with the two close-lying wavelengths situated at 4478.5Å and 4500Å corresponding to an absorption peak and trough respectively in the NO_2 absorption spectrum. The polarization discrimination DIAL lidar system consisting of a flashlamp pumped dye laser transmitter and an optical receiver is illustrated in Fig.2. The main elements of the system are discussed briefly in this section, with consideration given to their features, which impact on the polarization discrimination scheme.

The Lidar transmitter shown in Fig.4 is a flashlamp-pumped organic dye laser system (model DL2100B made by Phase-R Co) capable of producing short laser pulses (250 nsec) at power levels of the order of 1 MWatt. Two diffraction gratings are used in the laser cavity as tuning elements for wavelength selection and for reduction of the dye laser output linewidth to desired level. The gratings are used in a Littrow configuration with the Blaze angle in the first order. With the organic dye 7-diethylamino -4- methyl coumarine dissolved in methanol at concentration 3×10^{-5} M/l maximum output energy was obtained consistent with less than 10Å linewidth in the wavelength region near 4500Å. The temperature of the flowing dye was kept at 15 °C where the dye was found to operate more efficiently. To obtain laser action at two orthogonally polarized wavelengths simultaneously, a dielectric coated polarizing beam-splitter was selected and used in the laser cavity. With the beam splitter each of the two wavelength lases along one of the polarizations and the two output beams are polarized at right angles to each other.

The two gratings were adjusted to have their groove profile perpendicular to the direction of polarization of the incident beam determined by the orientation of the intracavity polarizing element. That was found to give the best diffraction efficiency for the gratings used. Measurements of the laser output showed no detectable swing in wavelengths or change in peak output from shot to shot, while the polarization extinction ratio was found to be less than 10^{-5} for both polarizations. The output beam divergence was found less than 1 mrad. From the described transmitter design it is clear that the system can be adjusted to transmit two orthogonally polarized beams at the two wavelengths 4478.5Å and 4500Å suitable for NO_2 concentration measurements, or to transmit one polarized beam at

4500Å by using one grating for atmospheric depolarization measurements. To guide the laser beam from the laser output to emerge colinearly with the axis of the lidar receiver, front surface aluminum mirrors were used as shown in Fig.2. It was found that the minimum depolarization from reflection occured when the direction of polarization of the incident beam was parallel or perpendicular to the plane of incidence. The depolarization under these circumstances was found to be too small to be detected, in contrast to other relative inclinations of the plane of polarization and the plane of reflection where depolarizations as high as 2-3 percent were detected. Accordingly the orientations of the mirrors used to deflect the beams were arranged to comply with the above requirements for minimum depolarization by ensuring appropriate orientations of their planes of incidence to the polarizations of the two outgoing wavelengths.

In the optical receiver shown schematically in Fig.2 the backscattered light is collected by a telescope. The primary lens is an acrylic Fresnel lens with diameter 15 inches, thickness 1/8 inch and focal length 24 inches. To eliminate spurious light, an iris was placed in the plane containing the circle of least confusion of the Freshel lens. By varying the iris diameter, the receiver field of view can be narrowed or expanded. The backscattered light collected by the primary lens is collimated by a second lens 1.5 inch in diameter. The collimated light is then split according to polarization by means of a Glan-Taylor polarizing beam splitting crystal which has a principal transmittance ratio of approximately 10^6 . The angular orientation of the crystal was adjusted to give maximum transmittance for backscattered fields retaining the polarization directions of the outgoing beams. Each of the separated beams is directed to a separate photomultiplier (Amperex 56 AVP) with wideband filters at the imput. The photomultiplier signal is displayed on Tektronix type 549 storage scope and recorded photographically. Again from the receiver design it is clear that the receiver can be used to separate and measure the backscatter returns from orthogonally polarize ar outputs at 4478.5Å and 4500Å for DIAL applications, or separate the parallel ana e cross-polarized component from the backscatter of a single linearly polarized lidar output at 4500Å, for atmospheric depolarization measurements. Although the lidar transmitter and receiver systems achieve what is required of them for use in a polarization discrimination scheme it remains to determine in the experiment whether external factors related to atmospheric scattering properties permit practical implementation of the scheme.

Using the polarization discrimination DIAL system field tests were carried out from the CCNY Laboratory window to measure atmospheric depolarization. The lidar system was operated in a series of tests at a wavelenth of 4500Å. The transmitted signal was sent out at one polarization and the received signal detected at the same polarization (for reference) and the cross polarization, to observe the depolarization effects due to the atmospheric backscatter, as function of the field of view of the lidar receiver.

The field of view of the receiver was varied by means of the variable aperture iris at the focal point of the Fresnel lens collector. The aperture of the iris could be varied from 1 cm down to zero.

To determine the receiver field of view, as a function of iris diameter, a Helium-Neon laser was mounted in front of the telescope and its inclination varied and measured with respect to the lidar receiver axis to determine the maximum acceptance angle for different iris apertures. A typical lidar return obtained with receiver field of view of 1.5 mrad on a relatively clear spring day is shown in Fig.5. Returns at that time were very steady, giving less that 2 percent variation from shot to shot for the same aperture setting. The parallel and cross polarized returns were obtained simultaneously for both the parallel and cross polarized components.

IV. RESULTS AND DISCUSSION

The results of the series of tests at 4500A are shown in Fig.6, where the depolarization, δ , of a signal backscattered from a distance of approximately 1 Km is plotted as a function of the receiver field of view, α. Below 1 miliradian setting, the signal decreased rapidly as the receiver aperture decreased below the divergence of the outgoing beam.

To further analyze the results, they are shown in Fig.7 plotted on log-log coordinates. It can be seen that up to a field of view of 6 miliradians, the depolarized signal increases approximately as the square of the field of view (receiver acceptance angle). Beyond that, the depolarized signal ceases to increase as rapidly. These results are in conformity with the simple geometrical picture, explaining the depolarization as the sum of a single step (180°) backscatter process plus two step scattering from all other particles.

As can be seen from the results, by limiting the field of view to approximately 1 miliradian, or easily larger than the minimum necessary to encompass the transmitted beam divergence of 0.5 miliradians, the depolarization, δ , was less than 1% at no significant reduction of the polarized signal power.

The results demonstrate that a DIAL system using polarization discrimination to separate backscatter signals will not be significantly affected by depolarization effects as long as receiver acceptance angle is small enough to eliminate multiple backscatter.

REFERENCES

1. S. A. Ahmed, Appl. Opt. 12, 901 (1973)

2. R.L. Byer, Opt. and Quant. Elect. 7, 147 (1975)

3. S. A. Ahmed, J.S. Gergely and F. Barone, Remote Monitoring of Gaseous Pollutants by Differential Absorption Laser Techniques (EPA-600/2-80-049, New York, 1980)

4. J. Strohbehn and S. Clifford, IEEE Trans. Ant. Prop. 15, 416 (1967)

5. M. Davies, Some Electrical and Optical Aspects of Molecular Behavior (Pergamon, Oxford,1965) p. 133

6. V. E. Zuev, Laser Light Transmission Through the Atmosphere, E.D. Hinckley, Ed. (Springer-Verlag, New York, 1982)

7. P. Chylek, J. Opt. Soc. Amer. 67, 175 (1977)

8. S. R. Pal and A. I. Carswell, Appl. Opt. 17, 2321 (1978)

9. P. Beckman, The Depolarization of Electromagnetic Waves (Golem, Boulder, 1968) p.67
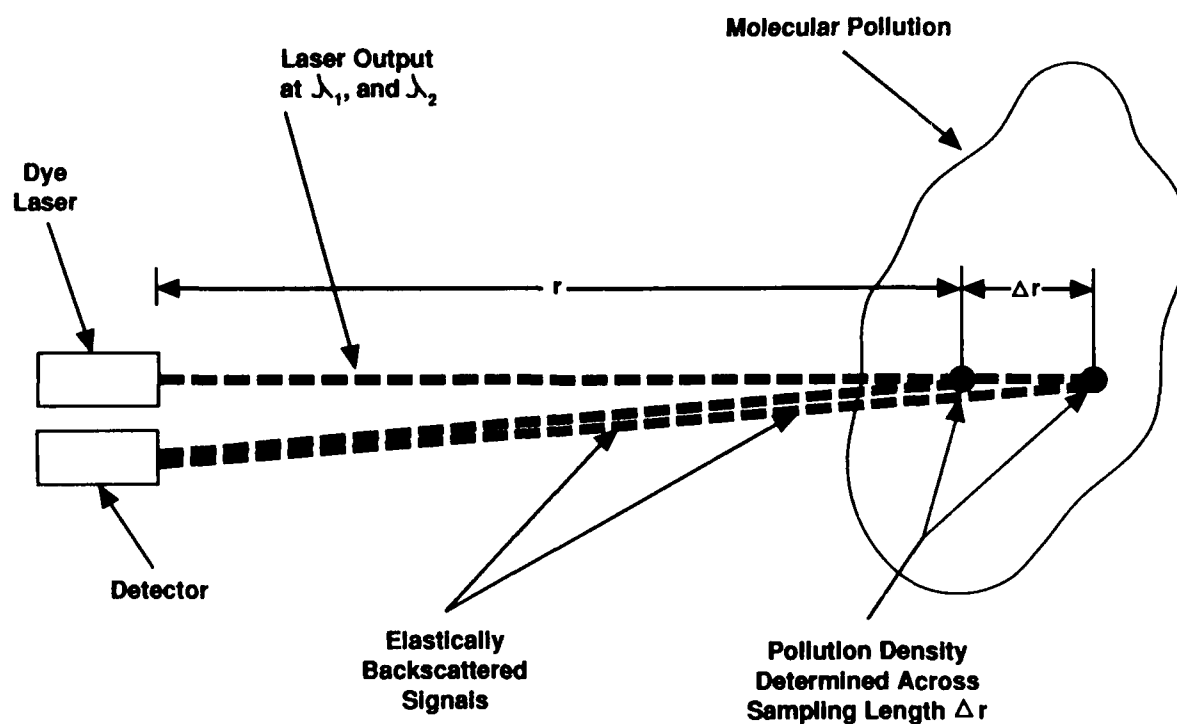
Fig.1. The Differential Absorption Lidar (DIAL) scheme.
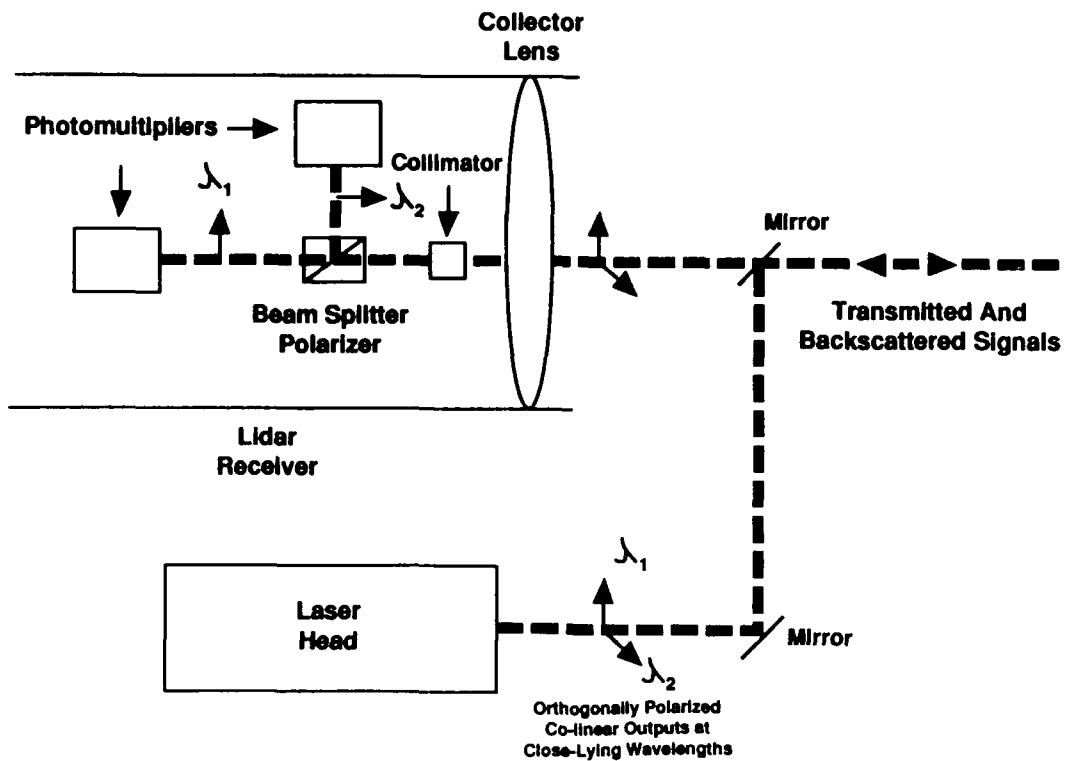
Fig.2. Schematic for DIAL lidar system utilizing polarization discrimination
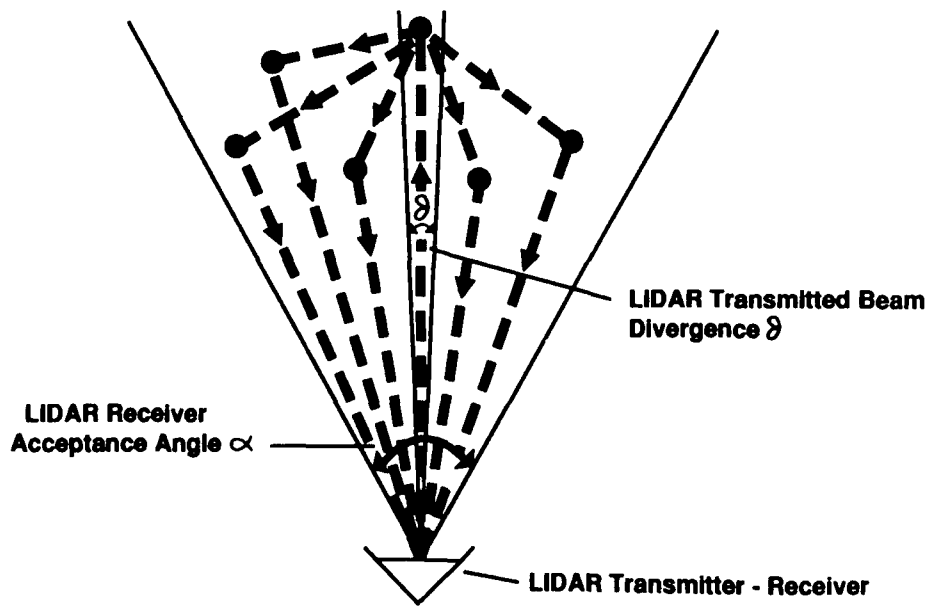
Fig.3. Reduction of received multiple backscatter by decreasing the receiver acceptance angle
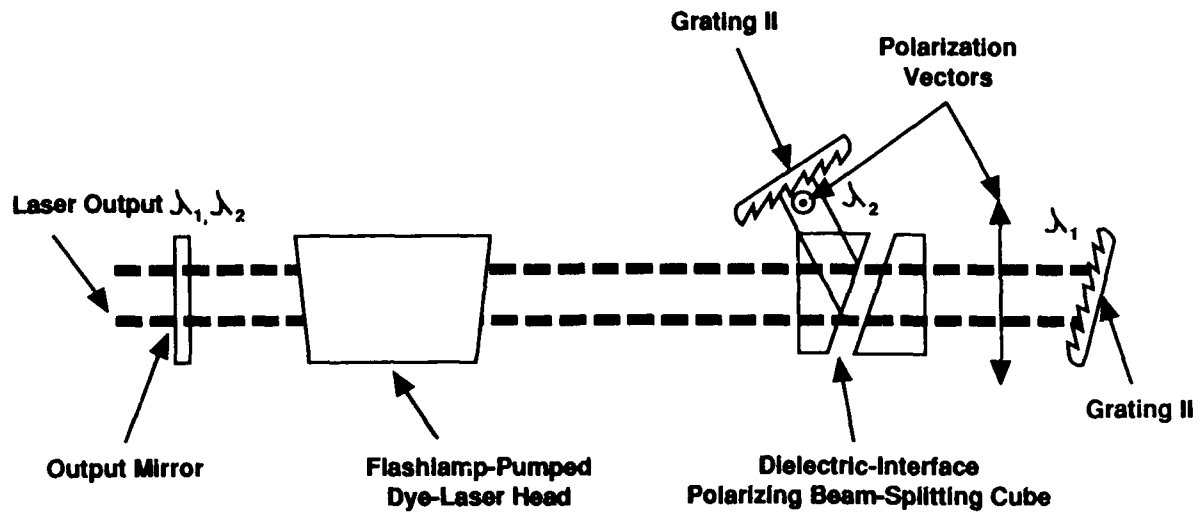
Fig.4. Optical arrangement for two simultaneous orthogonally polarized wavelength outputs
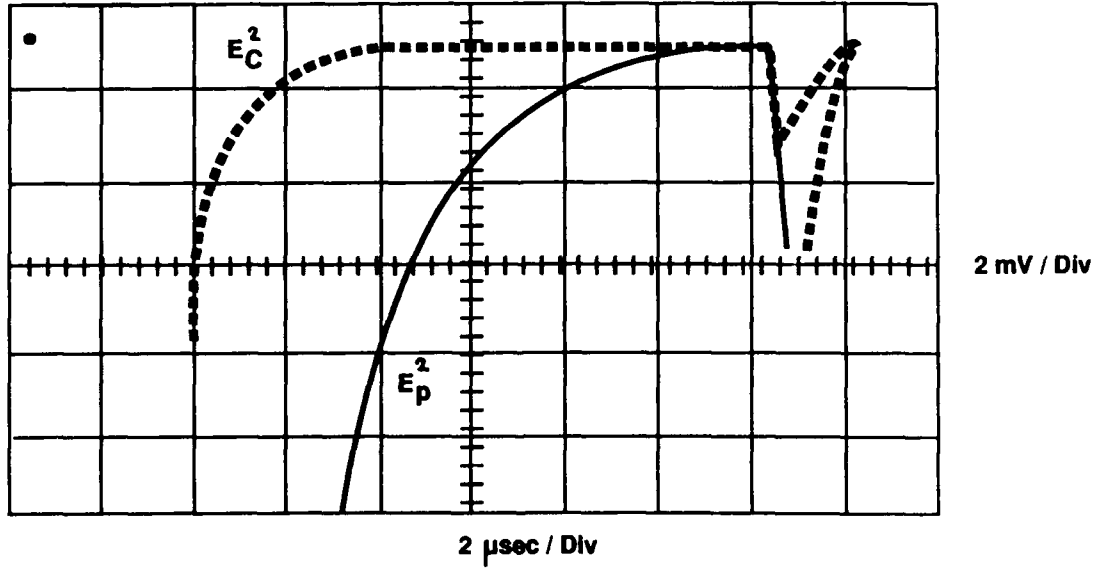
Wavelength $\lambda = 4500$ Å

Receiver Field of View $\Omega = 1.5$ mrad

Fig.5. Parallel and cross polarized LIDAR returns
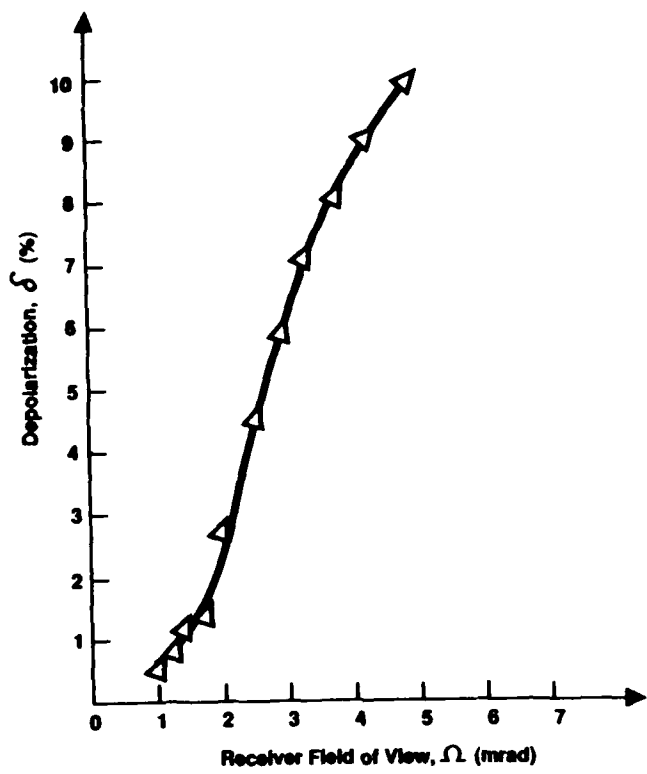
Fig.6. Depolarization of backscattered signal versus receiver field of view
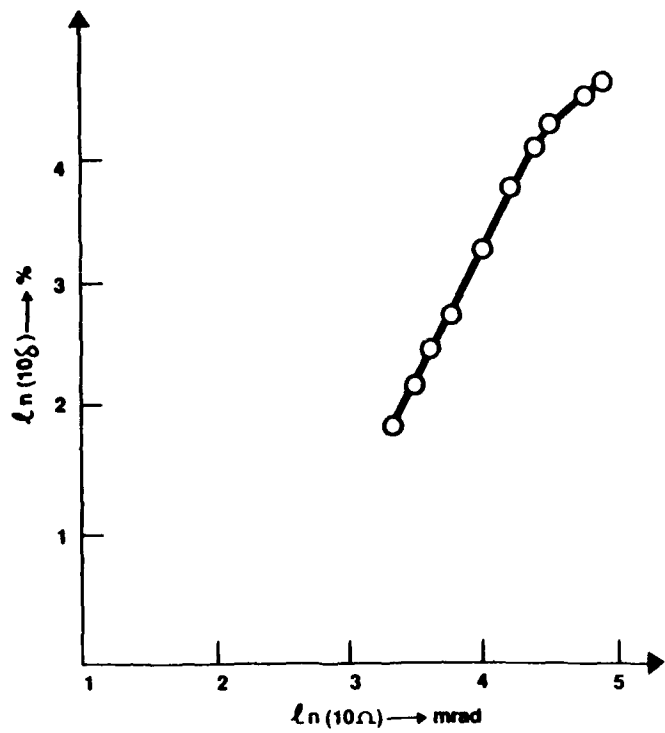
Fig.7. Logarithmic variation of depolarization with respect to the field of view

APPLICATIONS OF VISIBLE AND NEAR IR
DIODE LASERS IN ATOMIC PHYSICS

J. C. Camparo

Chemistry and Physics Laboratory
The Aerospace Corporation
P.O. Box 92957, Los Angeles CA 90009

Abstract

Over the past several years diode laser use has been expanding into both the basic and applied realms of atomic physics. To date near IR diode lasers have found application in the cooling of atomic beams to temperatures of only a few degrees Kelvin, and they are being incorporated into the development of next generation atomic clocks. In the present paper the diode laser characteristics that are of particular importance to the atomic physicist will be outlined, and two examples of the use of diode lasers in atomic physics will be reviewed.

I. Introduction

The credit for the first successful atomic physics experiment employing a semiconductor laser belongs to Bolger and Diels,[1] who in 1968 used a rapidly pulsed GaAs laser to generate photon echoes in a cesium vapor. More significant than any claim of primacy, however, was Bolger and Diels recognition that diode lasers had unique characteristics that could make them attractive for atomic physics research; in their specific case it was the unique characteristic of a very rapid dynamic response. Yet despite their impressive demonstration, the next twelve years saw relatively little application of these devices to problems in atomic physics research. This is not to say that diode lasers were completely ignored by the atomic physics community: Bykovskii and Velichanskii in the Soviet Union (and their colleagues), as well as Arditi and Picque in France performed a series of important investigations with diode lasers throughout the seventies.[2] Nontheless, when compared with the dye laser, the diode laser's influence on the course of atomic physics research was insignificant. Apparently, the diode lasers that were available during this period were just too difficult to work with,[3] and did not offer enough of an advantage over the dye laser to justify the extra experimental efforts that were required for their atomic physics applications. All of this changed in the early eighties with the introduction of commercial, room-temperature, single-mode AlGaAs diode lasers, and today a growing number of atomic physics research groups are taking advantage of the unique characteristics that these devices offer.

In the following sections of this paper I intend to discuss these room-temperature, single-mode diode lasers with regard to their application in atomic physics. In section II some characteristics of the diode laser that are particularly attractive for atomic physics research will be discussed. Though the specific items considered in this section will not exhaust the list of possibilities, they will nevertheless convey a sense of how the atomic physicist perceives the diode laser in relation to his investigations. To clarify this perception two examples of the diode laser's use in atomic physics will then be presented in section III. Finally, in section IV the diode laser's future in atomic physics will be assessed.

II. Some important diode laser characteristics

A. Narrow Linewidth

The linewidth of a single-mode diode laser $\Delta\nu_L$ is determined by quantum noise in the laser cavity, and is therefore described by the modified Schawlow-Townes relationship: the linewidth is proportional to the rate of flourescence into the lasing mode and inversely proportional to the number of laser photons in the cavity.[4] This simple relationship, however, is complicated slightly in the case of semiconductor lasers, due to the fact that the active region's index of refraction depends on carrier density. Specifically, though individual flourescent photons may add negligible random phase to the field, the fact that the carrier density undergoes relaxation oscillations after a flourescent event implies that the phase of the entire laser field is also modulated after a flourescent

event. This modulation significantly enhances the phase noise of the laser, and results in AlGaAs laser linewidths roughly an order of magnitude larger than what would be predicted by the modified Schawlow-Townes relationship alone: $\Delta\nu_L(observed) \simeq 10 - 100$ MHz.[5]

Diode laser linewidths narrower than this can be achieved, however, by employing simple optical feedback techniques. In essence, by reflecting laser light back into the active region a "normal" two-mirror diode laser cavity is turned into a three-mirror laser cavity, and this reduces the quantum noise limited linewidth in two ways.[6] First, since the third mirror is typically placed at macroscopic distances from the diode, the three-mirror cavity modes are more closely spaced than in the two-mirror case, which implies that the flourescent photons are distributed over more modes in the feedback situation. Consequently, the fraction of total spontaneous emission entering the single lasing mode is reduced. Additionally, since the longer three-mirror cavity stores more energy, the number of photons in the cavity is increased. As an example of the type of linewidth reductions that are possible, Dahmani et al.[7] were able to obtain estimated diode laser linewidths of approximately 20 KHz quite easily using an external etalon for optical feedback.

Laser linewidths of 10 MHz or less are more than adequate for many types of atomic physics experiment. For example, laser spectroscopy is an important aspect of modern atomic physics, and one can show that the natural linewidth $\Delta\nu_N$ of an electric dipole transition connected to an atomic ground state ($|1>$) has the form:

$$\Delta\nu_N \simeq \frac{4\pi r_0 c}{\lambda^2} \frac{g_1}{g_2} f,$$

where r_0 is the classical electron radius, f is the transition oscillator strength and g_i is the degeneracy of the ith state.[8] For strongly allowed transitions (f~1) in the AlGaAs wavelength range this expression yields $\Delta\nu_N$ ~ 15 MHz. Consequently, for atomic physicists interested in high resolution spectroscopy, the diode laser is an extremely attractive source of narrow-band optical radiation.[9]

In addition to spectroscopy, atomic physics experiments employing optical pumping can also require narrow linewidth lasers. As an example, consider optical pumping of cesium, illustrated in Fig. 1, which has application to atomic clocks. Primarily as a result of the hyperfine interaction between the magnetic moments of the cesium nucleus and the valence electron, both the ground ($6^2S_{1/2}$) and first excited states ($6^2P_{1/2}$ and $6^2P_{3/2}$) of cesium are split into various hyperfine levels which are labelled by a total atomic angular momentum quantum number F.[10] Since the energy level splitting between the two ground state hyperfine levels is only about 10^{-3} kT at typical experimental temperatures, atomic population is equally distributed among the various Zeeman sublevels of these hyperfine states in thermal equilibrium. (The Zeeman sublevels are labelled by the azimuthal quantum number m_F.) Consequently, the atomic system is incapable of absorbing microwave radiation corresponding to this atomic ground state hyperfine transition at 9193 MHz.
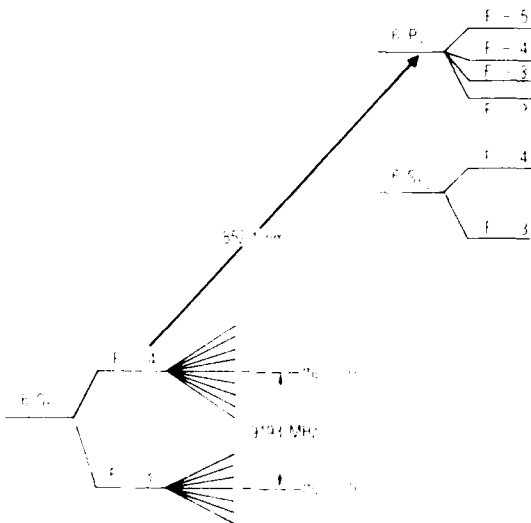
Figure 1. Energy level diagram for Cs133

If an AlGaAs diode laser (nominal ouput power ~ 10 mW) is tuned to the $6^2P_{3/2}(F=4)$ - $6^2S_{1/2}(F=4)$ transition at 852.1 nm, then after several absorption and emission cycles a significant population imbalance between the ground state F=4 and F=3 hyperfine manifolds will be created. This ground state optical pumping occurs because an atom in the excited state can decay into either of the ground state hyperfine manifolds, and because the narrow laser linewidth ensures that population in the F=3 hyperfine manifold will not be excited.[11] The depletion of the atomic ground state population in the F=4 hyperfine manifold can be experimentally monitored by observing the corresponding decrease in laser-induced-flouresence (LIF) from the optically pumped ensemble of cesium atoms. Now consider applying a microwave field to the optically pumped ensemble. If the microwave frequency is within ~ 10^{-7} of the ground state hyperfine transition frequency, then atomic population will return to the optically absorbing F=4 hyperfine manifold, and there will be an increase in the detected LIF. In an optically pumped atomic clock, the increased LIF signal can be used to stabilize the output of a quartz crystal oscillator to the atomic transition frequency, and the stabilized quartz crystal frequency can then be used to generate an ultra-stable atomic time scale.[12]

B. Tunability

In atomic physics applications wavelength tuning of the diode laser is typically accomplished by varying the diode's temperature. For the binary III-V semiconductor compounds an increase in the material's temperature results in a reduction of the bandgap energy,[13] which in turn results in a shift of the gain curve to longer wavelengths. Additionally, the material's index of refraction is temperature dependent,[14] so that an increase in temperature yields an increased optical length for the laser cavity, and hence a shift of the cavity mode wavelengths. For AlGaAs lasers the peak of the gain curve and the cavity modes shift at rates of approximately 0.25 nm/°C and 0.065 nm/°C, respectively.[2,15] Since the peak of the gain curve shifts to longer wavelengths faster than the cavity modes, diode laser tuning curves are characterized by mode hops, which occur when the peak of the gain curve shifts from the Mth cavity mode to the $(M+m)^{th}$ cavity mode. Though typically m = 1, values of m larger than unity as well as negative m values have been observed.[16] In general, however, the tuning curve takes on the "staircase" appearance illustrated in Fig. 2: i) mode hops have positive values of ~ 0.3 nm, ii) the continuous tuning ranges are on the order of 0.1 nm, and the full staircase may span a range as large as 10 nm. It is important to note that at AlGaAs diode laser wavelengths the continuous tuning ranges correspond to ~ 50 GHz optical frequency changes, which for many atomic physics experiments is a fairly broad continuous tuning interval.
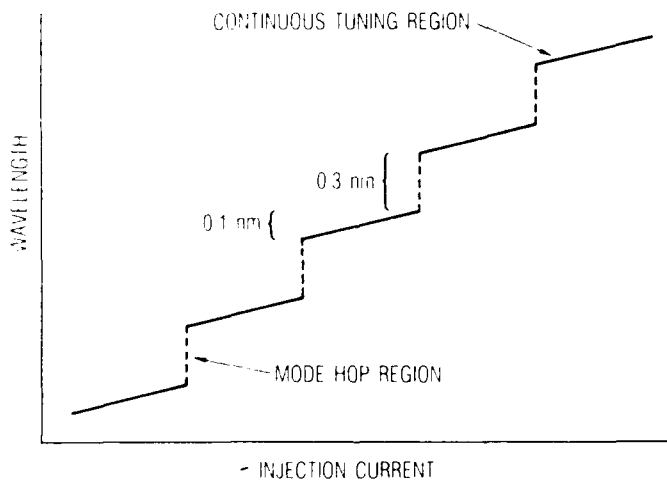
Figure 2. Illustrative diode laser tuning curve.

In diode lasers two major sources of heat are nonradiative recombination of carriers and photon reabsorption.[17] Since both of these heating processes are linear functions of the injection current, to first order there is a linear relationship between diode laser optical frequency and current. Consequently, in a typical spectroscopy experiment the signal from an atomic ensemble (e.g., LIF) is plotted as a function of injection current. To calibrate this spectrum it is standard practice to employ the laser's transmission through a high finesse Fabry-Perot etalon as a frequency marker: every time the laser scans a frequency interval equal to the free-spectral-range of the etalon, a mark is made on the atomic spectrum. It is with regard to this calibration procedure that diode lasers may have an additional advantage for laser spectroscopy.

In a recent series of experiments the continuous tuning region's degree of linearity was investigated for several TJS diode lasers (Transverse-Junction-Stripe). Specifically, a quadratic relationship between optical frequency and injection current was assumed, and the magnitude of the quadratic coefficient was estimated. The results showed that for an approximately one milliamp current change, the quadratic coefficient had a value less than 0.2% of the linear coefficient, which for these lasers is - -9 GHz/mA (the value of 0.2% was set by the experimental precision).[18] With regard to spectroscopy this result suggests that if one knows the value of the linear coefficient, perhaps by calibrating the diode laser with some known atomic energy level spacing, one can do away with the requirement for a high finesse etalon in many atomic spectroscopy experiments.

C. Rapid Dynamic Response

With regard to atomic physics the most important dynamic variable of the diode laser is its wavelength, and this can be either modulated or chirped rapidly by varying the laser's injection current. As illustrated in Fig. 3, the diode laser's modulation depth (d ν/di) as a function of modulation frequency f, is essentially described by three seperate regimes of operation.[19] For modulation frequencies below about 100 KHz, modulation of the injection current results primarily in a modulated heating of the diode laser (i.e., "thermal" regime), and modulation depths of approximately 3-10 GHz/mA for AlGaAs are not uncommon. However, for modulation frequencies much higher than this the thermal response of the laser is too slow to keep up with the modulated injection current, and a "second-order" effect becomes important: the dependence of the semiconductor's index of refraction on carrier density. In this "carrier" regime modulation depths of between 0.1 and 1 GHz/mA are obtained for AlGaAs. The modulation bandwidth of the diode laser is defined by the relaxation oscillation resonance of the laser, and is typically around a few gigahertz.[20] In addition to modulation, rapid sweeps (or chirps) of the laser's optical frequency can be induced by applying a single current pulse to the diode laser, and rates of 200 MHz/nsec have been reported in the literature.[21]
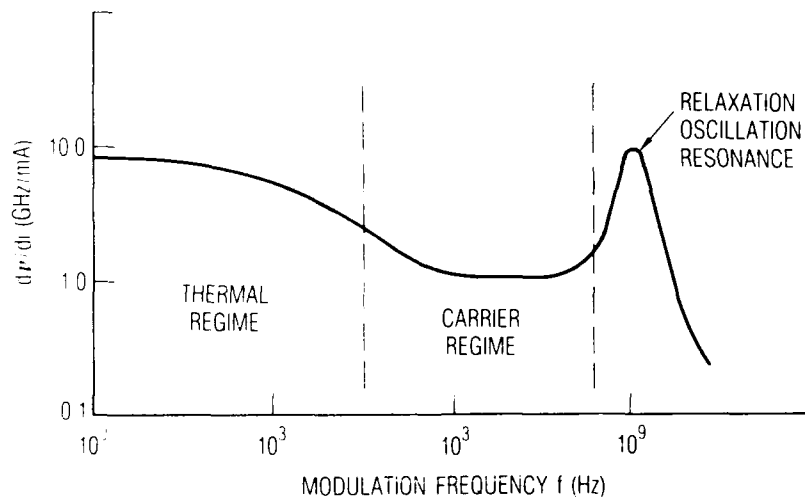
Figure 3. Typical AlGaAs modulation depth vs modulation frequency curve.

The intrinsic rapid dynamic reponse of the diode laser is a fairly n‌ ‌cteristic among light sources used in atomic physics. Lenth has shown that diode lasers can be emp‌‌‌‌ without any great effort for optical heterodyne spectroscopy, which is both a rapid and highly sensitive spectroscopic technique;[22] Camparo has discussed the possibility of optical adiabatic-rapid-passage using diode lasers, which results in a population inversion between the two levels coupled by the laser field;[2] and as demonstrated by Bolger and Diels the diode laser can be easily used to generate photon echoes in atomic systems.[1] Additionally, the ability of the diode laser wavelength to rapidly tune across an atomic transition could allow investigations of the transient behavior of atomic structure.[23] For example, consider an atomic system that experiences a perturbation starting at some time t_0, perhaps an electromagnetic perturbation.[24] Taking advantage of the diode laser's rapid chirping capability, an experimenter could tune across the atomic transition at time $t_1 > t_0$, and again a short time later at time t_2, and then again at time $t_3 > t_2$. I‌‌ this way it would be possible to obtain information regarding the evolution of atomic states following the perturbation. The diode laser's rapid dynamic response therefore has great

utility in atomic physics, and may prove to be one of this laser's most important characteristics for atomic physics applications.

III. Two Atomic Physics Applications of Diode Lasers

A. Cooling and Trapping of Neutral Atoms

Recently, there has been considerable interest in the ability of lasers to both produce and trap ultra-cold atomic ensembles,[25] and potential applications of these "laser cooled" samples range from manipulating antihydrogen to advanced atomic clocks.[26] As an example of laser cooling consider a beam of cesium atoms interacting with a counter-propogating laser beam, which is tuned to the cesium first resonance transition $(6^2P_{3/2} - 6^2S_{1/2})$ as illustrated in Fig. 4. In this particular example cooling is a consequence of the conservation of linear momentum during the photon absorption process: on absorbing a photon of momentum h/λ the cesium atom's velocity must be reduced in the direction of propogation by approximately 0.35 cm/sec. After a relatively short stay in the excited state (~ 30 nsec) the atom will emit a flourescent photon; and since this photon can be emitted into 4π steradians, the reduction of cesium velocity will on average persist. By scattering many photons in this way the beam of cesium atoms will be slowed.

$$p_i = h/\lambda \qquad p_a = mv$$
(a)

(b)

$$p_a = mv - h/\lambda$$
(c)
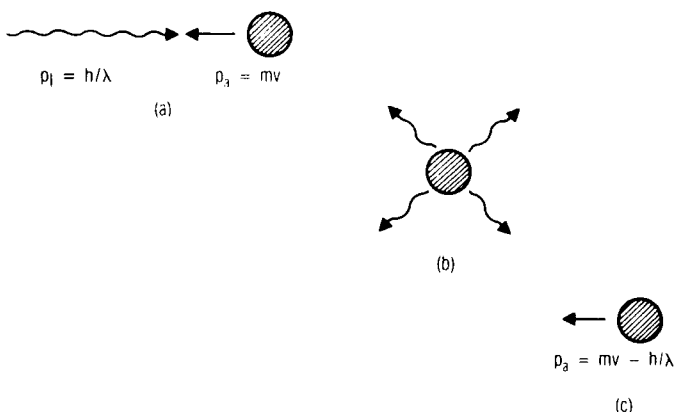
Figure 4. Laser cooling. (a) photon absorption, (b) photon emission,
(c) average velocity reduction.

Though the above description of the cooling process may seem simple enough, its practical realization often requires the laser to possess certain characteristics. In order to stop a thermal cesium atomic beam with a most-probable speed of 2.3×10^4 cm/sec (T = 150 °C) over a one meter path length, it is necessary for the laser to have an output intensity of between 10 to 100 mW/cm^2. Additionally, there is a Doppler shift of the atomic transition to the blue due to the fact that the atoms are moving towards the light source (~ 300 MHz for a thermal cesium beam), and as the atoms slow this Doppler shift will change. Consequently, in order to keep the laser tuned to the atomic resonance it is often necessary to chirp the laser frequency, and for the case considered here the required chirping rate amounts to ~ -30 MHz/msec. Thus, laser cooling can require an optical source with both a respectable output power and a relatively rapid dynamic response.

As previously mentioned diode lasers possess both of these characteristics, in addition to their low cost and ease of operation, and quite recently this laser's capability in the area of laser cooling was demonstrated. Using commercially available diode lasers Watts and Wieman[27] slowed and stopped a thermal beam of cesium atoms. Additionally, Wieman's group demonstrated that this slowed beam of cesium atoms could be loaded into an optical trap,[28] where three orthogonal beams from a second diode laser formed the confining potential well. Loading the trap several times, Wieman and his associates obtained a sample of 50 million trapped atoms, cooled to a temperature of ~ 100 μK. These results not only illustrate that diode lasers can cool and trap atomic species, they indicate that laser cooling can be done "easily" and inexpensively. This is important, since there are applications of laser cooling where the use of several expensive laser systems would be impractical.

B. Optical Pumping in Atomic Clocks

By international agreement the second is defined as the duration of 9,192,631,770 periods of the radiation corresponding to the Cs^{133} ground state hyperfine transition,[12] and this definition is realized in Cesium-Beam

atomic clocks similar to that shown schematically in Fig. 5. Here, an oven produces a thermal beam of cesium atoms with both hyperfine levels evenly populated. The beam passes through the inhomogeneous field of an "A-magnet," where atoms in the F=4 state are guided into a microwave cavity of the Ramsey design,[29] and atoms in the F=3 state are deflected into the wall of the vacuum chamber where they are gettered. (It should be noted that the guiding ability of the A-magnet is a function of the atomic velocities, and that these are approximately Maxwell-Boltzmann distributed.) If the microwave radiation in the cavity corresponds to the $m_F=0 - m_F=0$ ground state hyperfine transition, which to first order is insensitive to magnetic fields, then on exiting the microwave cavity there will be an increased density of atoms in the F=3 state. The beam then passes through the inhomogeneous field of a "B-magnet" which guides atoms in the F=3 state onto a detector. Consequently, the signal at the detector can be used to stabilize the source of microwave radiation to the Cs^{133} hyperfine transition frequency ν_{hfs}, and the stabilized microwave source can then be used to generate a precise time scale.
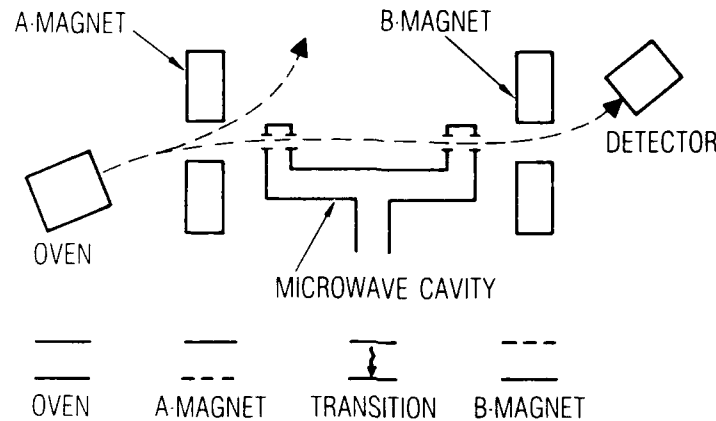
Figure 5. Conventional Cesium-Beam atomic clock.

The performance of the atomic clock is specified by its frequency stability and frequency accuracy.[30] Frequency stability refers to the variance of statistical fluctuations associated with a measurement of the cesium ground state hyperfine transition frequency, while accuracy refers to an uncertainty in the magnitude of systematic frequency offsets that exist in the device. With present technology, metrology laboratories typically achieve a frequency stability of ~ $10^{-14}\nu_{hfs}$ and a frequency accuracy of ~ $10^{-13}\nu_{hfs}$ for the Cesium-Beam clock.[30]
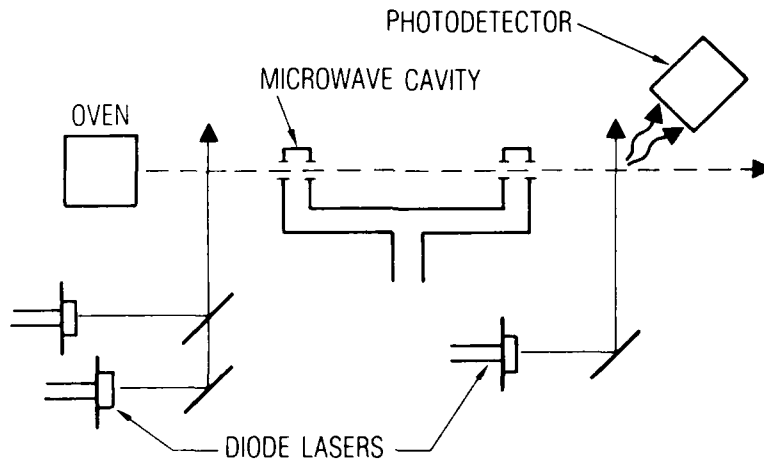
Figure 6. Diode Laser Cesium-Beam atomic clock.

In order to improve the realization of the second, several metrology laboratories throughout the world are building the next generation of Cesium-Beam clock, and as illustrated in Fig. 6 this atomic clock will use diode lasers both for state preparation and state detection.[31] As noted above the geometry of the present clock design only detects a small subclass of atomic speeds. Furthermore, only 1/16 of all atoms emitted from the oven can contribute to the clock signal (i.e., those in the $F=4$, $m_F=0$ state). Thus, at present there is an inefficient use of beam flux. However, by replacing the A magnet with diode lasers all atoms will be optically pumped into the ($F=4$, $m_F=0$) state, and the full velocity distribution from the oven will contribute to the clock signal. This will improve the signal-to-noise ratio of the device, and hence the frequency stability. Additionally, optical pumping and the elimination of the A and B magnets are expected to significantly reduce the magnitude of several important systematic frequency shifts in the Cesium-Beam clock, yielding an improved frequency accuracy.[32] Expectations are for an order of magnitude improvement in both stability and accuracy with these next generation Cesium-Beam atomic clocks employing diode lasers.[32]

IV. Present and Future Trends

As evidenced above, diode lasers are rapidly becoming an important tool for the atomic physicist. This trend is not only a result of the desirable characteristics of the laser, but is also driven by the fact that modern diode lasers are very inexpensive and fairly simple to operate. In this sense the impact of the diode laser on experimental physics can be likened to the impact of the personal computer on theoretical physics. With the advent of the personal computer, theorists found themselves in possession of an inexpensive yet powerful computing machine, and today a host of modestly funded physicists are conducting important theoretical investigations. Similarly, diode lasers are allowing "small-scale" researchers (i.e., experimentalists with modest financial resources) to make significant research contributions. However, even for well funded research facilities, the low cost and ease of operation of diode lasers can be of consequence. For example, a little more than a decade ago multi-laser experiments requiring the use of four or five single-mode lasers would have been considered as impractical, even ill conceived. Today, however, this need not be the case, as long as several of the lasers can be diode lasers. Thus, one can anticipate an ever widening role for the diode laser in both basic and applied atomic physics research, and as these devices push to higher powers and shorter wavelengths one can only expect this trend to be accelerated.

The future, however, is not without its darker aspects. Clearly, diode laser wavelengths are not driven by applications in atomic physics; yet as far as the atomic physicist is concerned the premier parameter describing the diode laser's operation is the nominal room temperature emission wavelength, about which he can only expect to tune by +/- 5 nm in order to reach his specific atomic transition. Consequently, even though the technology may exist to fabricate a diode laser with a specific nominal wavelength (e.g., by an appropriate choice of Al in the active region of an AlGaAs device), the laser may not be commerically available, and the atomic physicist may therefore be unable to perform his research. This is unfortunate not only for the physicist performing basic research, but also for the industrial scientist. For example, though theory indicates that diode lasers could yield several orders of magnitude improvement in the performance of commercial atomic clocks,[33] manufacturers are hesitant to commit R&D resources to this clock's development since there is a possibility that the required lasers will not be available in the future. Thus, though there is certainly a bright future for diode lasers in atomic physics, the question of whether this future includes a device employed to its full potential remains to be answered.

References

1. B. Bolger and J. C. Diels, Phys. Lett. 28A, 401 (1968).

2. J. C. Camparo, Contemp. Phys. 26, 443 (1985).

3. J. L. Picque, S. Roizen, H. H. Stroke, and O. Testard, Appl. Phys. 6, 373 (1975).

4. M. W. Fleming and A. Mooradian, Appl. Phys. Lett. 38, 511 (1981).

5. C. H. Henry, IEEE J. Quantum Electron. QE-18, 259 (1982).

6. G. P. Agrawal, in *Progress in Optics: Volume 26* (Elsevier Science Publishers, Amsterdam, 1988) pp. 163-225.

7. B. Dahmani, L. Hollberg, and R. Drullinger, Opt. Lett. 12, 876 (1987).

8. R. C. Hilborn, Am. J. Phys. 50, 982 (1982).

9. J. C. Camparo and C. M. Klimcak, Am. J. Phys. 51, 1077 (1983).

10. H. Kopfermann, *Nuclear Moments* (Academic Press, New York, 1958) pp. 4-41.

11. For a discussion of various optical pumping techniques see: W. Happer, Rev. Mod. Phys. 44, 169 (1972).

12. P. Kartaschoff, *Frequency and Time* (Academic Press, London, 1978).

13. H. C. Cascy and M. B. Panish, *Heterostructure Lasers Part B: Materials and Operating Characteristics* (Academic Press, New York, 1978) pp. 9-10.

14. M. Cardona, in *Proceedings of the International Conference on Semiconductor Physics Prague 1960* (Academic Press, New York, 1960) pp. 388-394.

15. D. Chambliss and M. Johnson, Opt. Commun. 48, 343 (1984).

16. J. C. Camparo and C. H. Volk, IEEE J. Quantum Electron. QE-18, 1990 (1982).

17. W. Nakwaski, IEE Proc. 131, 94 (1984).

18. J. C. Camparo, Y. C. Chan, B. Jaduszliwer and J. Malenfant, to be published.

19. S. Kobayashi, Y. Yamamoto, M. Ito, and T. Kimura, IEEE J. Quant. Electron. QE-18, 582 (1982).

20. K. Y. Lau and A. Yariv, in *Semiconductors and Semimetals Volume 22: Lightwave Communications Technology Part B*, W. T. Tsang, Ed. (Academic Press, Orlando, 1985), ch. 2.

21. G. L. Clark, L. O. Heflinger, and C. Roychoudhuri, IEEE J. Quantum Electron. QE-18, 199 (1982).

22. W. Lenth, Opt. Lett. 8, 575 (1983); IEEE J. Quantum Electron. QE-20, 1045 (1984).

23. P. Pokrowsky, W. Zapka, F. Chu, and G. C. Bjorklund, Opt. Commun. 44, 175 (1983).

24. K. I. Osman and S. Swain, Phys. Rev. A 25, 3187 (1982).

25. D. J. Wineland and W. M. Itano, Phys. Today 40, 34 (1987).

26. W. Ertmer and S. Penselin, Metrologia 22, 195 (1986).

27. R. N. Watts and C. E. Wieman, Opt. Lett. 11, 291 (1986).

28. D. Sesko, C. G. Fan, and C. E. Wieman, J. Opt. Soc. Am. B 5, 1225 (1988).

29. N. F. Ramsey, Phys. Today 33, 25 (1980).

30. C. Audoin and J. Vanier, J. Phys. E 9, 697 (1976).

31. See for example: S-I. Ohshima, Y. Nakadan, and Y. Koga IEEE Trans. Instrum. Meas. IM-37, 409 (1988), and references therein.

32. R. E. Drullinger, J. H. Shirley, D. J. Glaze and L. Hollberg, in *Proc. Fourth Symposium on Frequency Standards and Metrology, Ancona Italy* (Springer-Verlag), to be published.

33. J. C. Camparo and R. P. Frueholz, J. Appl. Phys. 59, 3313 (1986).

OPTICAL FEEDBACK EFFECTS ON SINGLE FREQUENCY SEMICONDUCTOR LASERS

R. W. Tkach and A. R. Chraplyvy
AT&T Bell Laboratories
Crawford Hill Laboratory
Holmdel, New Jersey 07733

Abstract

The effects of optical feedback on the spectra of single frequency semiconductor lasers are reviewed in terms of their impact on systems requiring spectral purity and stability. Effects are described, for feedback levels from -90 dB up to -8 dB.

Optical feedback effects on the spectra of single frequency semiconductor lasers[1] can severely degrade the performance of these lasers in applications such as coherent lightwave systems, or interferometric sensors, which rely on the spectral purity of the emitted light. It has been observed that feedback levels as small as -80 dB can significantly narrow or broaden the laser line 'dth. The rich variety of effects, arising from optical feedback can be categorized into five distinct regimes, depending on the feedback level and the distance to the reflection[2]. The five regimes of feedback effects are:

Regime I: at the lowest levels of feedback, narrowing or broadening of the emission line is observed, depending on the phase of the feedback. Effects are observable below -80 dB feedback level.

Regime II: at a feedback level which depends on the distance to the external reflector, the broadening, which is observed at the lowest levels for out-of-phase feedback, changes to an apparent splitting of the emission line arising from rapid mode hopping. The magnitude of the splitting depends on the strength of the feedback, and on the distance to the reflector.

Regime III: as the feedback is increased further, at a level which does not depend on the distance to the reflection (approximately -45 dB), the mode hopping is suppressed, and the laser is observed to operate on a single narrow line. Rayleigh backscatter from optical fibers falls in this regime, and causes dramatic frequency shifts in the laser output[3].

Regime IV: at a feedback level which does not depend on the distance to the reflection (approximately -40 dB), satellite modes, separated from the main mode by the relaxation oscillation frequency, appear. These grow as the feedback increases and the laser line eventually broadens to as much as 50 GHz. This has been termed "coherence collapse"[4].

Regime V: extended cavity operation with a narrow linewidth is observed at the highest levels of feedback, usually greater than -10 dB; typically it is necessary to antireflection coat the laser facet to reach this regime[5].

These five regimes of operation are experimentally very well defined and the transitions between them are easily identified. Figure 1 shows the feedback power ratios at which the transitions between regimes occur as a function of the distance to the reflection.

REFERENCES

1. R. Lang and K. Kobayashi: "External optical feedback effects on semiconductor injection laser properties," IEEE J. Quantum Electron., vol. QE-16, pp. 347-355, 1980.

2. R. W. Tkach and A. R. Chraplyvy: "Regimes of feedback effects in 1.5-μm distributed feedback lasers," J. Lightwave Tech., vol. LT-4, pp. 1655-1661, 1986.

3. A. R. Chraplyvy, D. M. Marcuse and R. W. Tkach: "Effect of Rayleigh backscattering from optical fibers on DFB laser wavelength," J. Lightwave Tech., vol. LT-4, pp. 555-559, 1986.

4. D. Lenstra, B. H. Verbeek and A. J. Den Boef: "Coherence collapse in single mode semiconductor lasers due to optical feedback," IEEE J. Quantum Electron., vol. QE-21, pp. 674-679, 1985.

5. M. W. Fleming and A. Mooradian: "Spectral characteristics of external-cavity controlled semiconductor lasers," IEEE J. Quantum Electron., vol. QE-17, 1981.
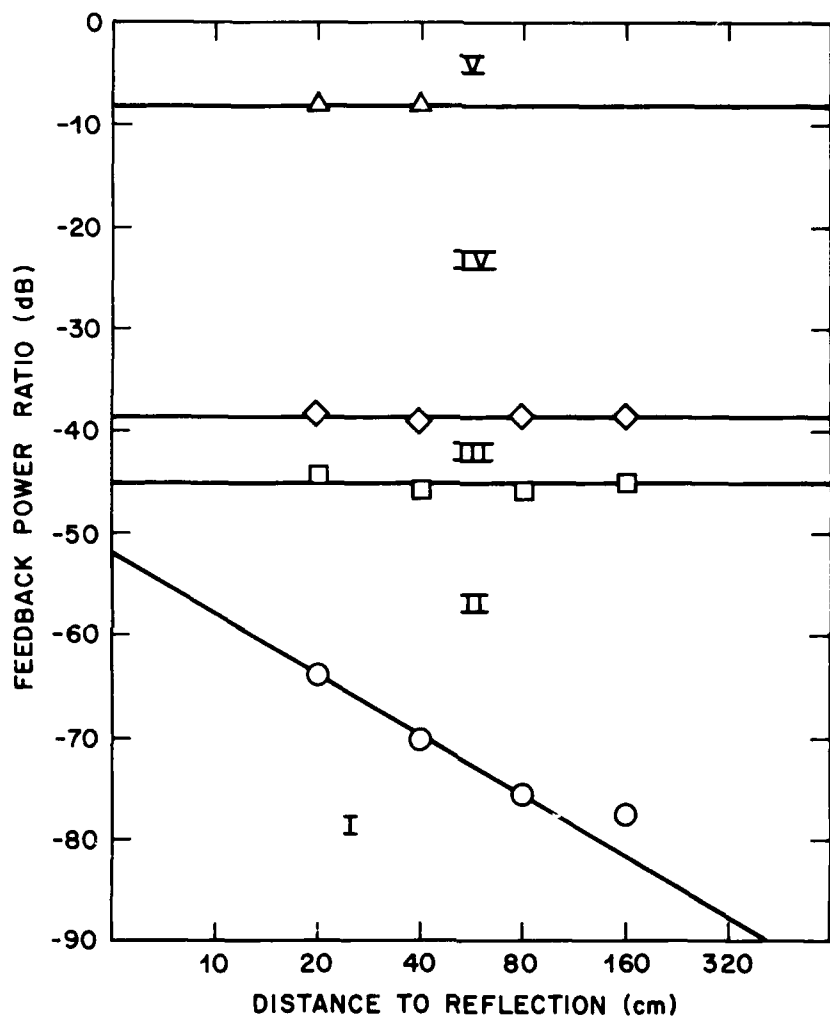
Figure 1: Plot of feedback power levels at which transitions between regimes occur, as a function of the distance to the reflection. Lines are drawn through the data points for clarity.

LIGHT SCATTERING BY AIR, HEATED FROM AN AEROSOL,

DUE TO PULSED IRRADIATION

George W. Sutton
Vice President
JAYCOR
P.O. Box 85154
San Diego, CA 92138-9259

Abstract

The problem of the scattering by air that has been locally heated by aerosols irradiated by a short pulse is addressed, through use of the heat conduction equation and scattering theory. The resulting air scattering cross-section increases as the square of the absorbed fluence. After a pulse, it increases to a maximum and then decays as the inverse of time. For absorbed fluences greater than $2j/cm^2$, the air scattering cross section can exceed that of the aerosol itself. For multiple irradiation pulses, the air scattering cross section increases logarithmically. For an aerosol cloud, the maximum air scattering cross section corresponds to the smallest size in the distribution, but the maximum occurs at a time corresponding to the largest size. The heated air scattering cross section then decays exponentially after the thermal wave from an aerosol reaches one third of the interparticle spacing.

Introduction

When a high energy radiation pulse propagates through aerosols in air, the heat absorbed by the aerosol heats the air surrounding it, changing its index of refraction, which can then cause subsequent scattering of light. In the following, the time-dependent light scattering cross section is calculated for the heated air surrounding an aerosol for pulsed irradiation whose pulse time is much smaller than an air diffusion time $\tau_D = a^2/K_a$ where a is the particle radius, and K_a is the thermal diffusivity of air. For example, for $K_a = 0.176$ cm^2/s and $a = 5 \times 10^{-4}$ cm, $\tau_D = 1.4$ μsec. It is initially assumed that the aerosol does not evaporate. (The effect of evaporation is discussed at the end of the paper.) The purpose of this work is to determine the dependence of the scattering cross-section on the irradiation fluence, its time dependence, the effect of the size of the aerosols and their heat capacity, and a typical distribution of aerosol sizes. Specifically, it is desired to understand the conditions under which the air scattering cross-section can exceed that of the aerosol. In addition, the heating of the air can cause collective refractive effects such as thermal blooming; thus, the rate at which a distribution of aerosols transfers its heat to the air is also of interest.

The heat transfer from the aerosol to the air is based on continuum physics, e.g., no temperature discontinuity from the aerosol to the air adjacent to the aerosol. The size distribution of aerosols used indicates a maximum number of density at a radius of 10^{-5} cm; the mean-free-path in air at sea level is smaller, 0.65×10^{-5} cm. However, at higher altitudes, this approximation should be replaced. The heat transfer rate to the air would be reduced, but its heat capacity is also reduced, as well as its index of refraction. These conditions can easily be analyzed within the framework of the present paper. The present paper uses the results of reference 1, in which the scattering of a monodisperse was considered.

Scattering Relations

For the scattering, Fresnel diffraction gives a relation between the near field electric field E_{nf} and the electric field in the far field E_{ff} as follows:[1]

$$E_{ff} = \frac{-i}{\lambda r} \int_{A_1} E_{nf}\, e^{ik_\lambda \, \vec{\theta} \cdot \vec{r}}\, dA \tag{1}$$

In Equation (1), it is assumed that light is propagated from or to an aperture of area A_1. This is an important consideration. For if the entire atmosphere within the aperture area were uniformly heated normal to the aperture area, the net phase shifts due to changes in the index of refraction would not result in any scattering. In Equation (1), r is the distance to the aperture's focal plane, $r > A_1/\lambda$, λ is the wavelength, $k_\lambda = 2\pi/\lambda$, $\vec{\theta} = \vec{j}\theta_x + \vec{j}\theta_y$, $\vec{r} = \vec{j}x + \vec{j}y$, $dA = dxdy$ and z is the direction of propagation. We are interested in the peak intensity in the far field; e.g., $\vec{\theta} = 0$; the decrease from its maximum value is attributed to the scattering cross section of the heated air. E_{nf} is evaluated in a plane just downbeam from the aerosol. The disturbed air causes a phase shift ϕ given by:

$$\phi = \frac{2\pi}{\lambda} \int_{-\infty}^{\infty} \Delta n \,(x, y, z) \, dz \qquad (2)$$

where Δn is the change in index of refraction of the air. The limits of integration are not actually $\pm \infty$; they extend over the length of the optical path. If the incident light electric field is E_0, then:

$$E_{nf} = E_0 \exp (i\phi) \qquad (3)$$

Substitution of Equations (2) and (3) into Equation (1) yields:

$$E_{ff} = \frac{-iE_0}{\lambda R} \int_{A_1} e^{ik_\lambda \int_z \Delta n \,(x,\,y,\,z)\,dz} \, dA \qquad (4)$$

In equation (4), it is assumed that the electric field E_0 is constant. Since the scattering is weak, the exponential is expanded as follows:

$$E_{ff} = \frac{-iE_0}{\lambda R} \int_{A_1} [1 + ik_\lambda \int_z \Delta n \, dz - \frac{1}{2} k_\lambda^2 (\int_z \Delta n \, dz)^2] \, dA \qquad (5)$$

The far field intensity I is given by $E_{ff} E_{ff}^*$, which from Equation (5) becomes:

$$I = \frac{E_0^2 A_1}{\lambda^2 R^2} \left[A_1 - k_\lambda^2 \int_{A_1} (\int_z \Delta n \, dz)^2 dA + k_\lambda^2 (\int_{A_1} \int_z \Delta n \, dz \, dA)^2 / A_1 \right] \qquad (6)$$

$E_0^2 A_1$ is the optical "power" through the aperture of the viewing optics. The second and third term thus represent the scattering cross section σ_s of the disturbed air surrounding the aerosol; e.g.,

$$\sigma_s = k_\lambda^2 \int_{A_1} \int_z (\Delta n \, dz)^2 \, dA - k_\lambda^2 (\int_{A_1} \int_z \Delta n \, dz \, dA)^2 / A_1 \qquad (7)$$

It is important to retain the second term on the right hand side of Equation (7). For example, if the optical path is uniformly heated, if only the first term on the right hand side is retained, the scattering cross-section would be finite. The second term caused the scattering cross-section to go to zero, as it should.

As a check on Equation (7) we evaluated the cross section of a sphere of radius a in which Δn is uniform. The result agrees with previous derivations[2].

$$\sigma_s = k_\lambda^2 \Delta n^2 \int_0^a 2 \pi \eta \, d\eta \, [\int_{-\sqrt{a^2 - \eta^2}}^{\sqrt{a^2 - \eta^2}} \Delta n(r) \, dz]^2 = 2\pi k_\lambda^2 a^4 \Delta n^2 \qquad (8)$$

Note that the second term in Equation (7) $\to 0$ for $A_1 \to \infty$, corresponding to a single particle.

The index of refraction change is caused by the heating of the air by the hot aerosol. The speed of an acoustic wave associated with this heat deposition is much faster than thermal diffusion, hence the heating is essentially isobaric, so that,

$$\frac{\Delta n}{(n-1)_a} \approx \frac{\Delta \rho_a}{\rho_a} \approx \frac{\Delta T}{T_a} \qquad (9)$$

557

for small temperature changes where T_a is the initial air temperature. Equation (7) then becomes:

$$\sigma_s = \frac{k^2(n-1)_a^2}{T_a^2} \int_{A_1} (\int_{-\infty}^{\infty} \Delta T(r)\, dz)^2\, dA - (\int_{A_1} \int_{-\infty}^{\infty} \Delta T(r)\, dz\, dA)^2/A_1 \qquad (10)$$

We next solve for the temperature field surrounding a single aerosol particle.

Air Heating by a Pulse-Heated Aerosol

To proceed, a model of the aerosol is chosen, as a homogeneous sphere of radius a. The initial temperature T_0 of the aerosol is given by:

$$\Delta T_0 = \frac{3\, JQ_a}{4\, \rho_p C_p a} \qquad (11)$$

where J is the irradiation fluence, Q_a is the absorption efficiency, and ρ_p, C_p are the aerosol mass density and temperature, respectively. The thermal conductivity of the aerosol is much larger than air, hence the aerosol is taken as isothermal. The solution for CW laser heating of a particle and the surrounding air has been given by Chan[3]; differentiation with respect to time of that result should then give the desired relation, as follows:

$$\Delta T(r, t) = \frac{2e^{-t/\tau}}{\sqrt{\pi}} \Delta T_0 \int_{\beta}^{\infty} e^{\frac{t\beta^2}{\tau u^2}}\, e^{-u^2}\, du \qquad (12a)$$

and

$$\Delta T(a, t) = \Delta T_0 e^{-t/\tau} \qquad (12b)$$

where $\tau = a^2 \rho_p C_p/3k_a$ and $\beta = (r-a)/\sqrt{4K_a t}$. However, Equations (12a) and (12b) do not satisfy exactly the following boundary conditions:

$$\frac{4}{3} \pi \rho_p C_p a^3 \frac{\partial T(a, t)}{\partial t} = 4\pi a^2\, k_a\, \frac{\partial T}{\partial r}(a, t) \qquad (13)$$

where k_a is the thermal conductivity of air. However, Carslaw and Jaeger[4] have also given the solution corresponding to both the case of CW heating and "pulse" heating in the form of a Laplace transform. For the latter, the inversion of the Laplace transform gives the aerosol temperature history as follows:

$$\Delta T(a, t) = \frac{2b\Delta T_0}{\pi} \int_0^{\infty} \frac{u\, e^{\frac{-K_a t u^2}{a^2}}\, du}{(u^2 - b)^2 + u^2 b^2} \qquad (14)$$

where $b = 3\rho_a C_a/\rho_p C_p$. The results of Equation (14) were compared to an exponential decay in Figure 1[1]. It is seen that they agree only for small ratios of heat capacity b. For $b \ll 1$, the integrand of Equation (14) becomes a Dirac delta function $-\delta(b^{1/2})$ and Equation (14) reduces to Equation (12b). Because aerosol heating corresponds to $b \ll 1$, Equation (12a) was used to determine the air temperature field. The integral of Equation (14) becomes[1,5]:

$$\frac{\sqrt{\pi}}{2} e^{t/\tau}\, e^{-\beta^2} \mathcal{R}w\, [(t/\tau)^{1/2} + i\beta] \qquad (15)$$

where $w(z)$ is tabulated in reference 6. However, for convenience, Equation (14) was evaluated numerically using Simpson's rule. Some temperature distributions are shown in Figure 2. The temperature field was then integrated along the propagation direction, squared, and integrated over the area normal to the distance of propagation. The result[1] is shown in Figure 3 as the integral $I(t) = \int (\int \Delta T (r) dz)^2 dA/\Delta T_0 a^4$ for aqueous and siliceous aerosols[1]. It can be seen that the scattering cross-section and time both scale as b^{-1}. These are therefore collapsed as shown in Figure 4. The ordinate spread corresponds to the curves of Figure 3. Also shown in Figure 4 is the curve corresponding to a point source of the same total heat capacity.

For a point source, the temperature distribution is given by:

$$\Delta T_a(r, t) = (\frac{\pi a^2 Q_a J}{\rho_a C_a})^2 \frac{e^{-r^2/4K_a t}}{(4 \pi K_a t)^{3/2}}$$

(16)

and the temperature integral becomes:

$$\int (\int \Delta T \, dz)^2 \, dA = (\frac{\pi a^2 Q_a J}{\rho_a C_a})^2 \cdot (\frac{1}{8\pi K_a t} - \frac{1}{A_1})$$

(17)

The actual curve is lower because heat is transferred to the air more slowly.
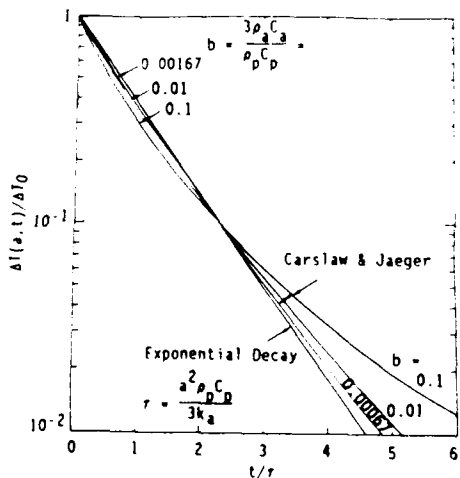
Figure 1.   For large ratios of heat capacity, aerosol temperature decays exponentially.
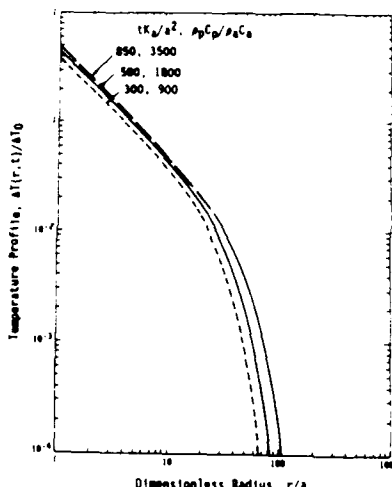
Figure 2.   Comparative temperature profiles at maximum air scattering cross section.
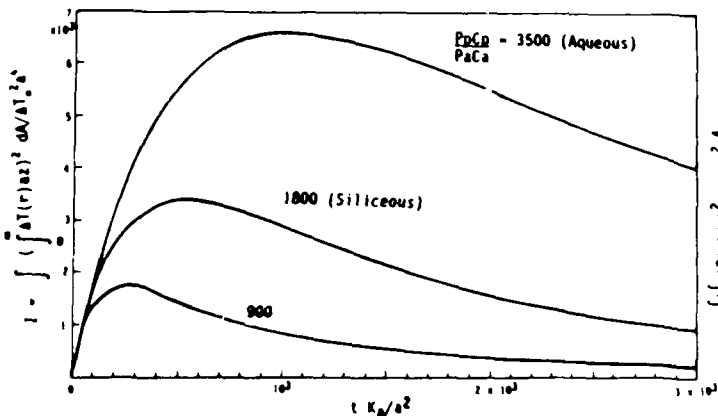
Figure 3.   Thermal contribution to scattering integral.
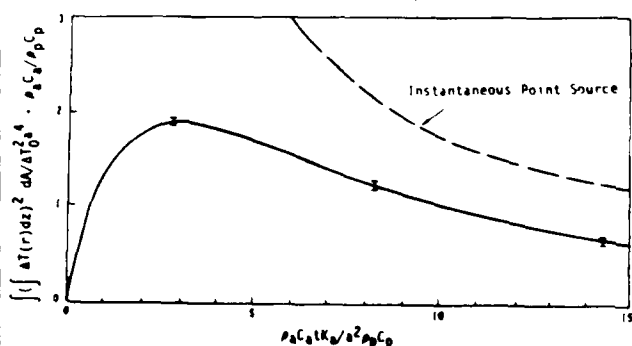
Figure 4.   Single aerosol-air scattering cross-section increases, then decreases as 1/time (initially).

559
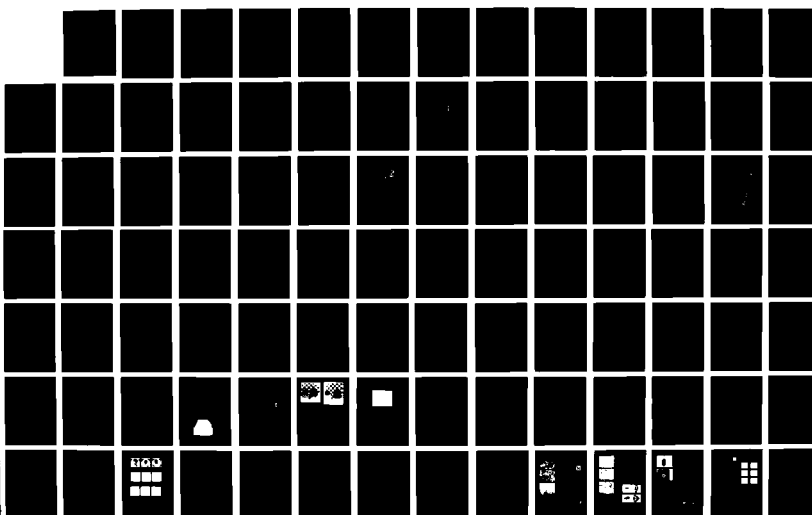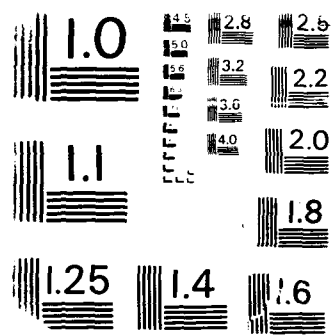
The ratio of the scattering cross section of air to the extinction cross section of the aerosol particle itself is then given by:

$$\frac{\sigma_s}{\pi a^2 Q_{ext}} = \frac{9 \pi (n - 1)_a^2 J^2 Q_a^2}{4 \lambda^2 T_a^2 \rho_p^2 C_p^2} I(t) \tag{18}$$

which is independent of a except for Q_a. Note the quadratic dependence on J. For the middle curve in Figure 3, for a siliceous aerosol, $I_{max} = 3400$, $\rho_p C_p = 2.6$, $(n - 1) = 2.7 \times 10^{-4}$, $T_a = 293°K$, $\lambda = 1.06 \times 10^{-4}$ cm, then

$$\frac{\sigma_s}{\pi a^2 Q_{ext}} = 0.388 \ (J \ Q_a)^2 \tag{19}$$

This is less than unity for $JQ_a < 1$ j/cm^2; but exceeds unity for $JQ_a \geq 2$ J/cm^2. The peak time $t_m = 500 \ a^2 K_a$, is 0.28 μs for $a = 10^{-5}$ cm (0.1 μm).

Aerosol Size Distribution

A typical aerosol distribution is shown in Figure 5, for the Southwestern part of the United States[7]. Of interest regarding thermal blooming is the rate of cooling of an aerosol distribution since this heat is transferred to the air causing not only scattering but also collective effects for coherent light. It was assumed that due to the pulse irradiation, the temperature increase of each aerosol was identical, corresponding to volumetric absorption. The results are shown in Figure 6. It is seen that the e-folding time is about 60 μsec. The corresponding scattering is shown in Figure 7. The long time to reach the maximum is governed by the largest size aerosols in the distribution, because they have the largest heat capacity and release their heat to the air slowly. The low peak scattering cross-section occurs because of the time distribution of peak scattering cross-section. The curve is dashed towards long times because of the decay is exponential for long times as is given later.
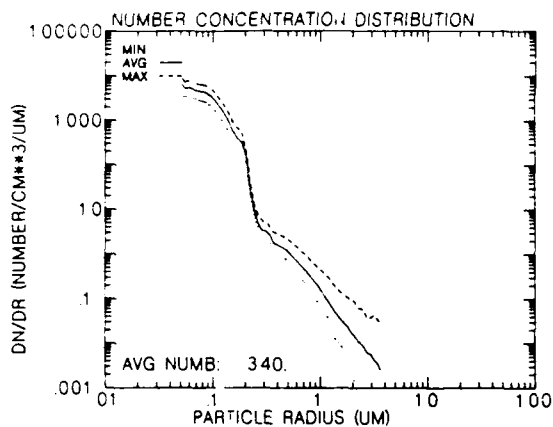
Figure 5.   Aerosol size distribution, Southwest U.S.
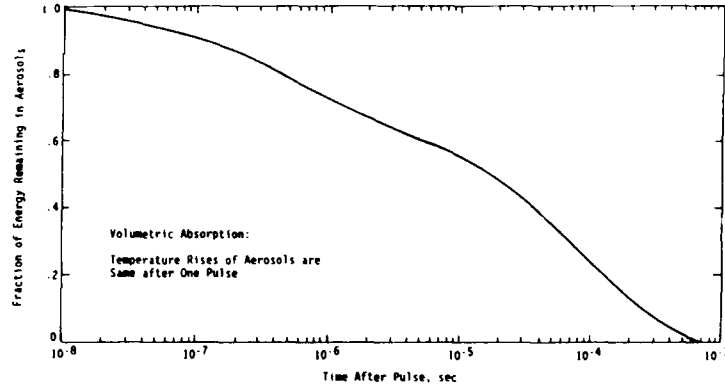
Figure 6.   Cooling of a measured aerosol size distribution - single size.
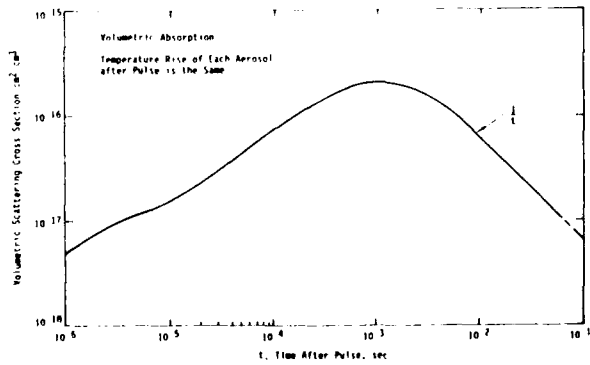
Figure 7.   Scattering cross-section for air for an aerosol size distribution - short times.

The scattering cross-section for the size distribution was also calculated for repetitive irradiations, equally spaced in time as characterized by a pulse repetition frequency, for a total time t. The scattering cross-section at time t is shown in Figure 8. For a single particle and an infinite number of pulses, an asymptotic limit was found[1]. However, an actual aerosol distribution will not have a homogeneous spatial distribution. Thus, as more pulses accumulate, some small volumes will become hotter than others. Then those volumes of air will scatter light. It is therefore believed that an asymptotic value for an infinite number of pulses will not exist for an actual aerosol distribution.
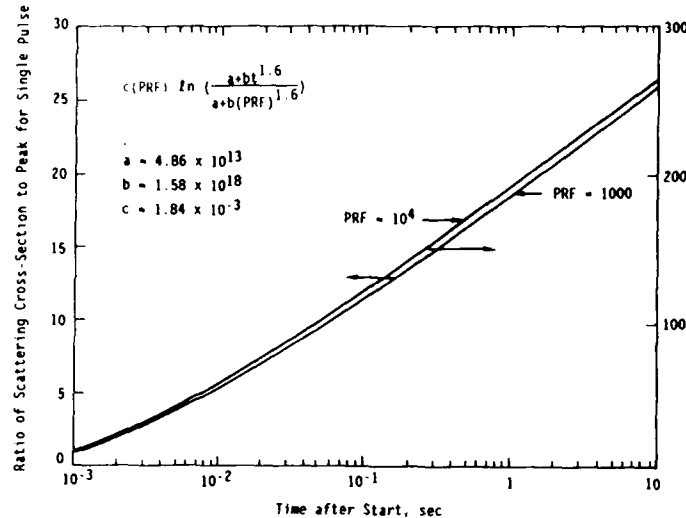
Figure 8. Effect of repetitive pulses on air scattering cross-section - measured aerosol size distribution.

Effect of an Aerosol Spatial Distribution

As indicated previously, for a single particle, the scattering cross-section will decrease inversely with time. However, after a time the air heated by one aerosol will be affected by neighboring particles. To gain some insight into this, a cubic infinite array of monodisperse aerosols were modelled. It was assumed that the distance between aerosols was 2b, and a cubic volume of initially heated air was 2a on a side. The temperature distribution was taken as:

$$\Delta T(x,y,x,t) = \sum_{k=0}^{\infty} \sum_{l=0}^{\infty} \sum_{m=0}^{\infty} A_{klm}(t)\cos(k\pi x/b)\cos(l\pi y/b)\cos(m\pi z/b). \tag{20}$$

The heat conduction equation was then solved with the result:

$$A_{klm}(t) = B_{klm} \exp[- K_a \pi^2 (k^2 + l^2 + m^2) t] \tag{21}$$

where:

$$B_{klm} \approx \frac{8\Delta T_0 \sin(k\pi a/b) \ \sin(l\pi a/b) \ \sin(m\pi a/b)}{\pi^3 klm \ [1 + \delta(k)] \ [1 + \delta(l)] \ [1 + \delta(m)]} \tag{22}$$

After maximum scattering, the scattering cross-section for a single aerosol decreases as:

$$\sigma_s = k_\lambda^2 (n - 1)^2 (\frac{aJQ_a}{T_a})^2 \{c + \frac{b^2}{\pi^2 a^2} c^2\} \tag{23}$$

where:

$$c = \sum_{k=1}^{\infty} \frac{\sin^2 (k\pi a/b)}{k^2} \exp (- 2K_a \pi^2 k^2 t/b^2) \tag{24}$$

561

For very large spacing b, equations 23 and 24 simplify to:

$$\sigma_s = k_\lambda^2 \ (n - 1)^2 \ (\frac{a^2 \pi J Q_a}{\rho_a C_a b T_a})^2 \ (c' + c'^2) \tag{25}$$

$$c' = \sum_{m=1}^{\infty} e^{-2_a m^2 K \pi t / b^2} \tag{26}$$

The results are shown in Figure 9. They clearly show the inverse time dependence until the thermal wave from one aerosol reaches about one-third of the distance to its nearest neighbor. Then, the scattering cross-section decays exponentially.
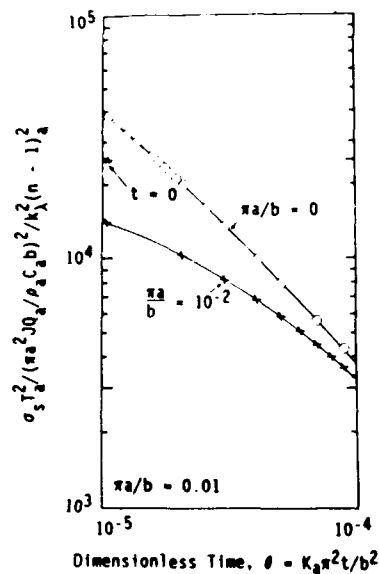
Figure 9(a). Temporal decay of scattering of a monodisperse cubic spatial distribution - short times.
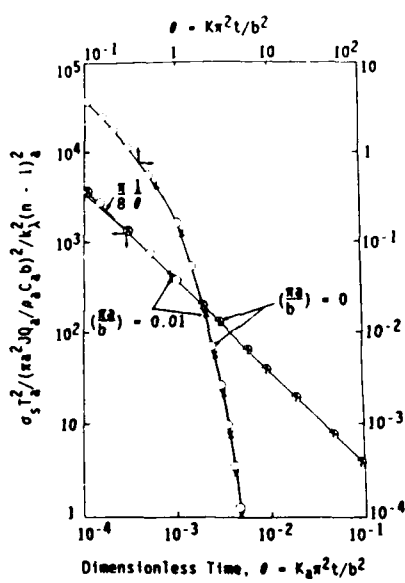
Figure 9(b). Temporal decay of scattering of a monodisperse cubic spatial distribution - intermediate times.
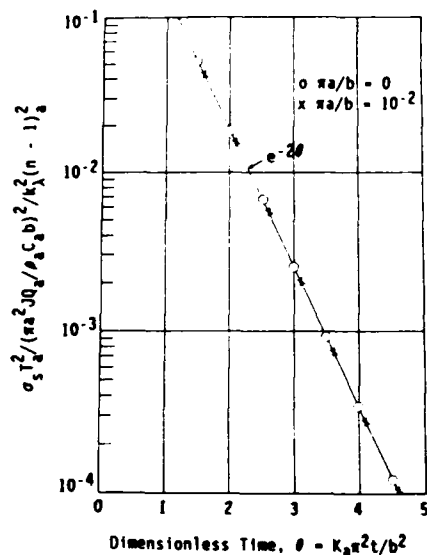
Figure 9(c). Temporal decay of scattering of a monodisperse cubic spatial distribution - long times.

Aqueous Aerosols

Thus far, only non-evaporating aerosols have been considered. However, the same techniques have been applied to an aqueous aerosol, which was completely evaporated by an irradiation pulse[8]. The model was that the droplet was evaporated into a sphere of heated water vapor, which then cooled by conduction to the surrounding air and diffusion. The scattering cross-section initially stayed constant but then decayed inversely with time. This result is now used to calculate the resulting temporal evolution of transmission. A typical result is shown in Figure 10. It can bee seen that evaporation greatly improves the diffraction-limited transmission, provided that recondensation does not occur in the time interval of interest.
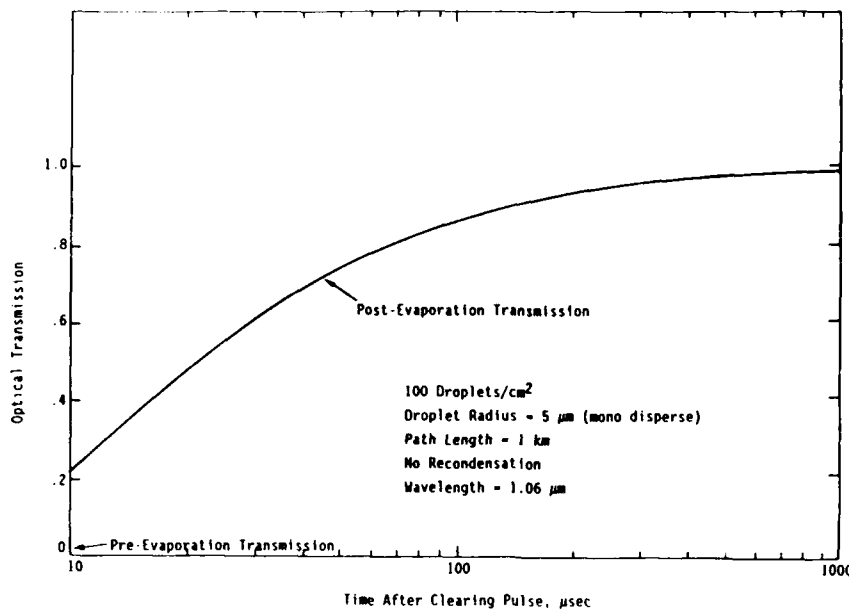
Figure 10. Optical transmission pre- and post-droplet evaporation.

Conclusions

The problem of light scattering by air which was heated by non-evaporating aerosols irradiated by short pulses has been modeled, and the model solved. The results predict that the air scattering cross section increases to a maximum value and then decays inversely with time. The maximum air scattering cross section can exceed the aerosol extinction coefficient for an absorbed fluence greater than 2 j/cm^2. These results were used for a typical aerosol size distribution. Multiple pulses can cause the effective cross section to become much greater than for single pulses. Finally, a spatial distribution of aerosols, the cross section will decay exponentially when the thermal wave from one particle reaches about 1/3 of an inter-particle spacing. For aqueous aerosols which are evaporated by the pulse, optical transmission of diffracted-limited light is improved considerably.

Acknowledgement

References

1. G. W. Sutton, Jour. App. Physics (March 1, 1988).
2. H. C. Van de Hulst, Light Scattering by Small Particles, Dover Publications, Inc., N.Y. 1981, p. 91
3. C. H. Chan, Appl. Phys. Letters, Vol. 26, No. 11, pp. 628-630 (June 1, 1975).
4. H. S. Carslaw, and J. C. Jaeger, Conduction of Heat in Solids, (Oxford 1959) pp. 349-350.
5. M. Abramowitz and I. A. Stegun, Handbook of Mathematical Function, (NBS No. 55, June 1964) No. 7.4.34, p. 304.
6. Ibid, p. 325.
7. D. Garvey, Helmet Conference, 28, 29 June 1988.
8. G. W. Sutton, Applied Optics, December 1, 1988.

PICOSECOND ULTRASONICS IN POLYTHIOPHENE AND POLYACETYLENE THIN FILMS.

G.S. Kanner and Z.V. Vardeny
Department of Physics, University of Utah
Salt Lake City, Utah 84112.

Abstract

We discuss an experimental method for picosecond ultrasonics measurements in the subterahertz frequency range in thin films. We have applied this technique to thin films of polythiophene and polyacetylene and obtained the longitudinal sound velocity at about 5 GHz. The spectral dependence for the detection of the photoinduced strain waves is demonstrated and explained.

Introduction

Ultrasonics has long been an important tool in both applied and fundamental science. The range of frequencies used in ultrasonic measurements is from 1 MHz to about 10 GHz[1]. Recently a method has been developed[2-4] to extend this frequency range to the terahertz region using picosecond techniques.

In this communication we describe the picosecond ultrasonic technique and its applications to thin films of conducting polymers, such as poly-thiophene (PT) and polyacetylene $(CH)_x$. In particular, we show the existence of periodic oscillations in the induced transmission $\Delta T(t)$. By measuring the polarization properties of the oscillations we prove they are due to a time-dependent strain in the thin films. We discuss the strain oscillations optical spectrum and the conditions under which the oscillations can be detected. In addition, the strain oscillations are used to measure the longitudinal sound velocity in thin films of two different conducting polymers at high phonon frequencies.

Phonon Generation and Detection by Picosecond Light Pulses

In our studies[2-4] we have used the polarized pump and probe technique with subpicosecond pulses. The generation and detection mechanisms of the strain waves are described schematically in Fig.1. The pump pulse is absorbed within the optical skin depth ζ $(= \alpha^{-1}$, where α is the absorption coefficient at the pump laser wavelength). Most of the energy absorbed is released very quickly to phonons due to hot carriers thermalization and fast
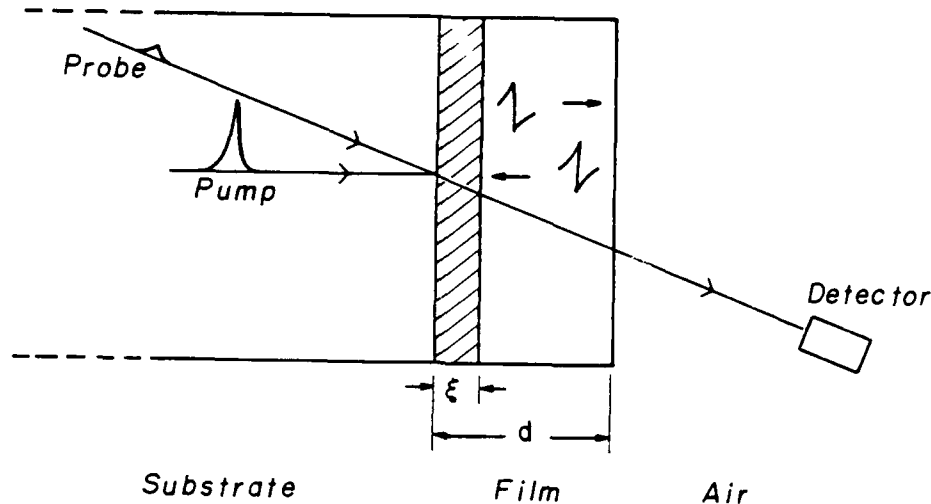
Fig.1: The experimental arrangement for measuring picosecond ultrasonics in thin films, using photoinduced changes in transmission. ξ is the optical skin depth. The N-shaped signal is a propagating strain pulse.

geminate recombination. This energy raises the layer temperature and sets up a stress as a result of thermal expansion. The stress produces a strain pulse propagating into the film, normal to the excited surface. The strain pulse bounces back and forth in the film by reflection off the interfaces. Its amplitude decreases in time due to acoustical attenuation and partial transmission into the substrate.

A second light pulse is passed through the film at a later time t. This (probe) pulse is produced by dividing off about 10% of the energy in the pump pulse and then introducing an additional optical path before the probe pulse reaches the sample. The transmission of the probe pulse through the film is measured as a function of the time delay introduced. The optical transmission T is sensitive to the motion of the acoustical pulse because the optical constants of the film, particularly the absorption coefficient α, depend on strain. The modulation $\Delta T(t)$ in T is caused by the modulation $\Delta \alpha$ in α as follows:

$$\Delta T(t) \sim \int \Delta \alpha(z,t)dz \sim \int \frac{d\alpha}{d\eta}\eta(z,t)dz \sim \frac{d\alpha}{d\eta}<\eta>(t)d \qquad (1)$$

where the integral is over the film thickness d, and $<\eta>$ is the average strain in the film at time t. While the strain pulse is propagating in the film, $<\eta>$ is essentially constant. However, when the pulse is reflected off the free surface, the propagating strain pulse becomes inverted, changing the sign of $<\eta>$.

565

If one surface of the film is free, the other rigidly attached to a substrate with a high acoustical impedance, the sign of $<\eta>$ changes once every round trip of the strain wave, and, as a result, there will be oscillations in $\Delta T(t)$ with a period

$$\tau = 4d/v \qquad (2)$$

where v is the longitudinal sound velocity.

Experiment

In our pump and probe experiment we have used a mode-locked Nd:YAG (Quantronix) laser which synchronously pumps a (Coherent) dye laser producing light pulses typically of 2 picosecond duration at a repetition rate of 76 MHz. The wavelength of the pump and probe beams can be tuned from 560 nm to about 670 nm. The intensity of the pump beam is modulated at 4 MHz using an acousto-optic modulator, and the in-phase $\Delta T(t)$ of the probe pulses is measured using a moderately fast Si photdiode, a frequency tuned preamplifier and a fast lock-in amplifier (5202 PAR). $\Delta T(t)$ has been measured with probe beam polarization either parallel to the polarization of the pump beam ($\parallel$),or perpendicular to it ($\perp$). The samples were transparent thin films (d $\leq$ 1000Å) of unoriented polythiophene $(C_2H_2S)_x$, electrochemically polymerized on conducting glass substrates. A film of cis-rich $(CH)_x$, polymerized on a sapphire substrate using the Shirakawa method, was also used in our measurements.

Results and Discussion

In Fig.2 we show the response $\Delta T(t)$ of a thin film of PT at 300K up to 450 picoseconds using a laser wavelength for both pump and probe beams of λ = 608 nm. $\Delta T(t)$ is induced very quickly at t=0, followed by a fast decay, but increasing again and producing a damped oscillation with period τ = 200±10 psec. Similar effects were also observed in thin films of of (80%) cis-rich $(CH)_x$ at 620 nm (Fig.3). The peak of $\Delta T(t)$ at t = 0 is of electronic origin[4,5] and its fast decay in both PT and $(CH)_x$ has been attributed to geminate recombination. This fast response is polarized -- $\Delta T = 2\Delta T\perp$ so that a photoinduced dichroism is generated at t=0[5]. This is not surprising in conducting polymers since they are in the form of long quasi-1-D chains grouped into single crystal fibrils which are isotropically distributed in the thin film planes. In Fig.4, on the other hand , we show that the photoinduced oscillations are unpolarized -- $\Delta T = \Delta T\perp$ (at about 150 psec), and they therefore cannot be of electronic origin. Moreover, the period τ increases linearly with the film thickness d,[2] in agreement with Eq.2.
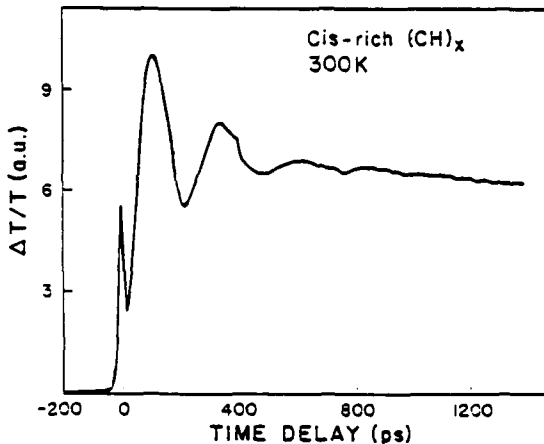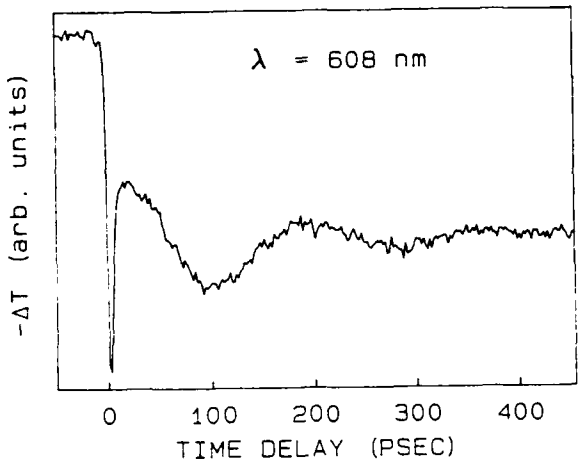
Fig.2: Transient ΔT/T in a thin film of polythiophene at λ ⁻ 608 nm with pump and probe polarizations perpendicular to each other.

Fig.3: Transient ΔT/T in a thin film of 80% cis/20% trans-$(CH)_x$ at λ ⁻ 620 nm with pump and probe polarizations perpendicular to each other.

We attribute the oscillatory response to strain pulse propagation, as discussed in the previous section. Using Eq.2, the measured τ and the film thickness, we can derive the longitudinal sound velocity for strain waves at frequency ν. We calculate v ⁻ 10±1 Å/psec in PT, and v ⁻ 15±5 Å/psec for $(CH)_x$ at ν ⁻ 5 GHz and 3.7 GHz, respectively. The uncertainties in v are due mainly to uncertainties in measurements of the film thickness.

The period of oscillation in the $(CH)_x$ film depends on the cis/trans percentage. τ decreases with the isomerization from cis to trans, as shown clearly in Fig.5. The measurements were repeated on the same film after 3 weeks (curve (b)) with τ ⁻ 160 psec, and after one year (curve (c)) with τ ⁻ 110 psec. Since the film thickness remains constant during isomerization, the only logical explanation for our findings is that the sound velocity increases with isomerization. At this point, the reason for this is not clear. We also found that the strain-induced ΔT(t) response decreases with the isomerization. This is clearly shown in Fig.5, where the various responses were normalized at t ⁻0.
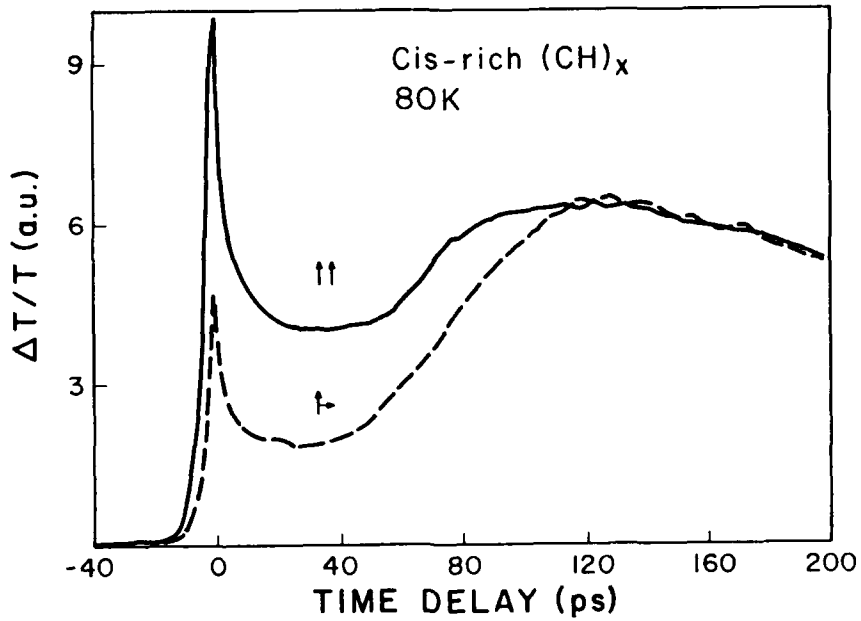
Fig.4: Transient $\Delta T/T$ in a film of 80% cis/20% trans-$(CH)_x$ with perpendicular ($\perp$) and parallel ($\parallel$) pump-probe polarizations at λ = 620 nm.
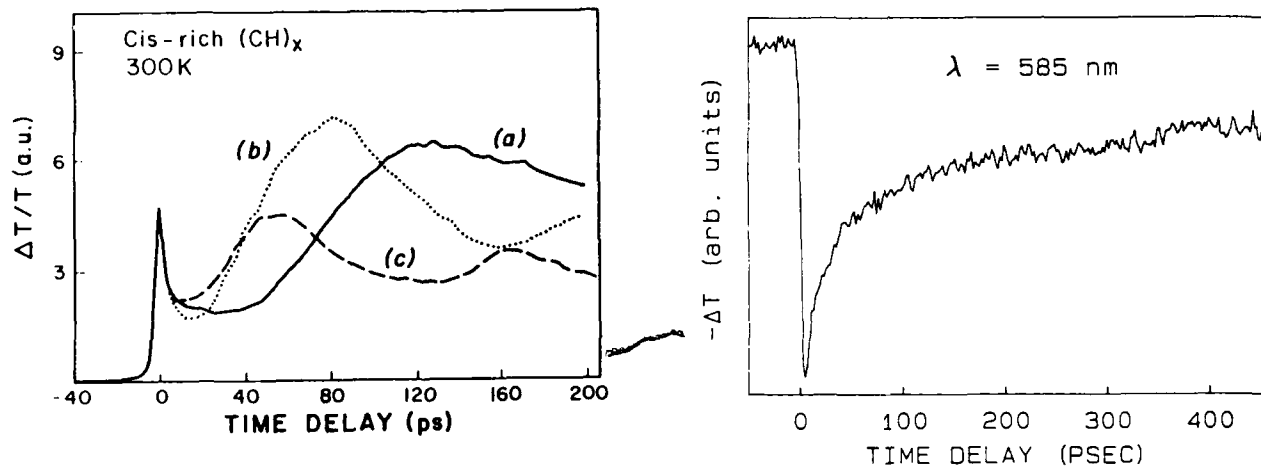
Fig.5: Normalized $\Delta T/T(t)$ of the same $(CH)_x$ film as in Fig.4: a) one day, b) three weeks, and c) one year after polymerization.

Fig.6: Same as Fig.2 for the PT film, but at λ = 585 nm.
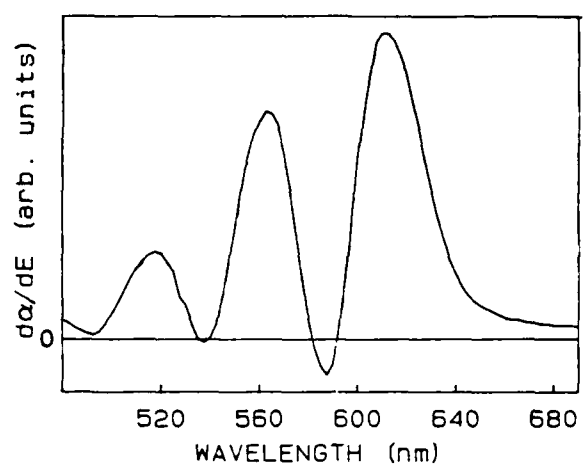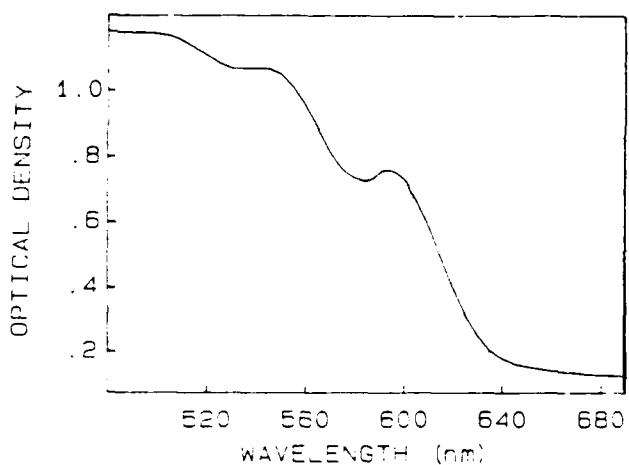
A more striking finding concerning the appearance of oscillations in $\Delta T(t)$ is shown in Fig.6. We measured $\Delta T(t)$ on the same film as in Fig.2, but with laser wavelength $\lambda = 585$ nm; there is no sign of any oscillatory response at this wavelength. This strange spectral dependence of the oscillatory response of ΔT ($= \Delta T_{osc}$) is related to the derivative of the of the film's absorption. From Eq.1 we get

$$\Delta T_{osc} \sim \frac{d\alpha}{d\eta} <\eta> \sim \frac{d\alpha}{dE} \frac{dE}{d\eta} <\eta> \qquad (3)$$

where $\frac{d\alpha}{dE}$ is the derivative of α at the probe wavelength and $\frac{dE}{d\eta}$ is the deformation potential of the film. From Eq.3 we see that the appearance of strain-related effects in $\Delta T(t)$ depends on $\frac{d\alpha}{dE}$; specifically, $\Delta T(t)$ will not contain any oscillatory response for probe wavelengths where $\frac{d\alpha}{dE} = 0$. The absorption spectrum $\alpha(\omega)$, and its derivative $\frac{d\alpha}{d\omega}$ were measured for the PT film using a Cary spectrometer and are shown in Fig.7. The oscillations in $\alpha(\omega)$ are probably due to phonon sidebands associated with the exciton transition at about 600 nm. These are not related to interference effects because the energy period does not depend on film thickness. The derivative clearly shows three such oscillations with an energy interval of almost 185 meV. From the spectrum of $\frac{d\alpha}{d\omega}$ we would expect ΔT_{osc} to be

maximum at about 610 nm, and to be nearly zero at about 585 nm. This is in agreement with our findings, such as $\Delta T(t)$ shown in Figs. 2 and 6. In fact, we were able to obtain a complete spectrum of $\Delta T(t)_{osc}$ over the range from 565 to 650 nm; the spectrum is in qualitative agreement with Fig.7 for $\frac{d\alpha}{d\omega}$.

References

1. D.O. Thomson and D.L. Chimenti, Review of Progress in Quantitative Nondestructive Evaluation, Plenum Press, N.Y., 1984
2. C. Thomsen, J. Strait, Z. Vardeny, H.J. Maris, J. Tauc, and J.J. Hauser, Phys. Rev. Lett. 53, 98ᶜ (1984)
3. C. Thomsen, H.T. Grahn, H.J. Maris, and J. Tauc, Phys. Rev. B 34, 412 (1986)
4. Z. Vardeny, Synth. Metals 28, D203 (1988)
5. Z. Vardeny, J. Strait, D. Moses, T.C. Chung, and A.J. Heeger, Phys. Rev. Lett. 44, 1657 (1982)

Analytical Solution for a Self-Phase Modulated and Self-Steepened Pulse in a $\chi^{(5)}$- Medium with Material Relaxation

Jamal T. Manassah and M.A. Mustafa
Photonics Engineering Center Department of Electrical Engineering
City College of New York, New York, New York 10031

Abstract

We derive the analytical solution for a self-phase-modulated and self-steepened pulse propagating in a nonlinear $\chi^{(5)}$- medium. The calculation is performed in the plane-wave approximation for dispersionless medium but with material relaxation present.

In this lecture, we consider the propagation of an ultrashort pulse in a $\chi^{(5)}$- medium (six-photon mixing). We perform this calculation in the plane wave approximation i.e transverse effects are neglected for a dispersionless medium, i.e sample is thin, but where self-steepening, i.e high intensity beam, and material relaxation, i.e characteristics material relaxation time of the order of pulse duration, are important. Physically, our calculation is applicable, for instance, in cases where the nonlinearity is due to two-quanta photogeneration of nonequilibrium carriers in certain semiconductors [1]. We will show that for large intensities, the pulse may self-steepen due to the lowering of the pulse peak group velocity caused by self-phase modulation, which qualitatively is similar to the same effect observed in $\chi^{(3)}$- medium as was shown in [2, 3, 4]. This amplitude self-steepening leads to an asymmetry in the spectrum [5, 6]. The incorporation of finite relaxation time in the expression of the Kerr index of refraction also contributes to the asymmetry of the spectrum and to its downshift (towards the Stokes side). Finally we use our derived expression for the amplitude and phase of the pulse to obtain the Young interferometer intensity distribution for this pulse [7].

In the phenemenological model that we consider, the nonlinear source term for Maxwell's equation is taken as:

$$ s = \frac{n\, n_4}{c^2} \frac{\partial^2}{\partial t^2} \left\{ |E|^4 E - c_1 E \frac{\partial}{\partial t} |E|^4 \right\} \tag{1} $$

i.e we are taking the first two terms of the noninstantaneous nonlinear polarization, where c_1 is the first moment of the delayed response kernel, it is essentially equal to the material response time. n_4 is the nonlinear Kerr coefficient, n is the linear index of refraction of the material and c is the speed of light in vacuum. This phenemenological model is valid for pulse duration longer than the material response time.

We will solve Maxwell's equation by the method of multiple scales [8]. We neglect diffraction effects and group velocity dispersion in our calculation. We introduce the normalized electric field Φ, such that $E = E_0 \Phi$ where E_0 is the amplitude of the incoming pulse, and the normalized coordinates $Z = z/v_g \tau$ and $T = t/\tau$ where τ is the incoming pulse width. Maxwell's equation, in the normalized coordinates is then given by:

$$ \left(\frac{\partial^2}{\partial Z^2} - \frac{\partial^2}{\partial T^2} \right) \Phi = \varepsilon' \frac{\partial^2}{\partial T^2} \left\{ |\Phi|^4 \Phi - \gamma' \Phi \frac{\partial}{\partial T} |\Phi|^4 \right\} \tag{2} $$

where the dimensional parameters ε' and γ' are given by:

$$ \varepsilon' = \frac{n_4 |E_0|^4}{n} \tag{3} $$

$$ \gamma' = \frac{c_1}{\tau} \tag{4} $$

The method of multiple scales introduce the scaled variables T_1, T_2, ... and Z_1, Z_2, ..., where $Z_n = (\varepsilon')^n Z$. A consistent expansion in powers of ε' to second order give the following differential equations:

$$\frac{\partial a}{\partial V_1} = 0 \qquad\qquad [5\text{-}a]$$

$$\frac{\partial \alpha}{\partial V_1} = \frac{K}{2} a^4 \qquad\qquad [5\text{-}b]$$

$$5 a^4 \frac{\partial a}{\partial U_1} = 2 \frac{\partial a}{\partial V_2} \qquad\qquad [6\text{-}a]$$

$$\frac{\partial \alpha}{\partial V_2} - \frac{a^4}{2} \frac{\partial \alpha}{\partial U_1} = -\frac{K}{8} a^8 + 2 K \gamma' a^3 \frac{\partial a}{\partial U_1} \qquad\qquad [6\text{-}b]$$

where $U_n = Z_n - T_n$, $V_n = Z_n$, $K = \omega_0 \tau$, ω_0 is the pulse center frequency and the normalized electric field is written as:

$$\Phi = A (U_1, V_1, U_2, V_2) \exp (i K U_0) \qquad\qquad [7]$$

$$A = a \exp (i \alpha) \qquad\qquad [8]$$

In the physical corrdinates U and V, the amplitude a and the phase α of A, then obey the following quasi-linearized partial differential equations:

$$\frac{\partial a}{\partial V} - \frac{5}{2} \varepsilon' a^4 \frac{\partial a}{\partial U} = 0 \qquad\qquad [9]$$

$$\frac{\partial \alpha}{\partial V} - \frac{\varepsilon'}{2} a^4 \frac{\partial \alpha}{\partial U} = \frac{K}{2} \varepsilon' a^4 - \frac{K}{8} \varepsilon'^2 a^8 + 2 K \gamma' \varepsilon' a^3 \frac{\partial a}{\partial U} \qquad\qquad [10]$$

The U-partial derivatives, appearing on the left hand side of eqs. [9] and [10], are responsible for self steepening and the term proportional to γ' expresses the finite relaxation time of the medium. We notice that, in this model, the finite relaxation time has no effect on the amplitude equation.

To discuss the impact of self-steepening and finite relaxation time, we shall index a and α by two dummy indices where the first index refer to self-steepening and the second to finite relaxation time. Each index takes the value (0, 1) for the effect being (absent, present). [It should be stressed that we can directly solve eqs. [9] and [10] in the most general case but we are going through these intermediate steps to clarify the role and meaning of the different terms in the equations]. We will now write the solutions in the four cases, for an initial sech pulse with zero phase:

(i) $\gamma' = 0$, $\varepsilon' V \ll 1$

$$[11\text{-}a]$$

$$a_{0,0} = \text{sech} (U)$$

$$\bar{\alpha}_{0,0} \equiv \frac{\alpha_{0,0}}{\kappa} = \frac{\varepsilon' V}{2} \text{sech}^4 (U) \qquad\qquad [11\text{-}b]$$

(ii) $\gamma' \neq 0$, $\varepsilon' V \ll 1$

$$[12\text{-}a]$$

$$a_{0,1} = \text{sech} (U) = a_{0,0}$$

$$\overline{\alpha}_{0,1} = \frac{\epsilon'V}{2} \operatorname{sech}^4 (U) - 2\gamma'\epsilon'V \operatorname{sech}^4 (U) \tanh (U) \qquad [12\text{-}b]$$

(iii) $\underline{\gamma' = 0}$

$$a_{1,0}^2 = \operatorname{sech}^2 \left(U + \frac{5}{2}\epsilon'V\, a_{1,0}^4 \right) \qquad\qquad [13\text{-}a]$$

$$\overline{\alpha}_{1,0} = -U - \frac{\epsilon'}{6} \int_0^v a_{1,0}^4(p,V)\,dp - \frac{5}{24}\epsilon'^2 \int_0^v a_{1,0}^8(0,q)\,dq$$

$$+ \tanh^{-1}\left[\sin g\,(U,V)\right] + \frac{\epsilon'}{6}\sin g\,(U,V) - \frac{\epsilon'}{18}\sin^3\left[g(\ U,V)\right] \qquad [13\text{-}b]$$

$$g(U,V) = \frac{\epsilon'}{2} \int_0^v a_{1,0}^5(U,q)\,dq + \sin^{-1}(\tanh U) \qquad [13\text{-}c]$$

(iv) <u>general case</u>

$$a_{1,1}^2 = a_{1,0}^2 = \operatorname{sech}^2\left(U + \frac{5}{2}\epsilon'V\, a_{1,1}^4 \right) \qquad\qquad [14\text{-}a]$$

$$\overline{\alpha}_{1,1} = \overline{\alpha}_{1,0} + \gamma' \ln (a_{1,1}) - \gamma' \ln\left[\operatorname{sech}\left[\tanh^{-1}(\sin g(u,v)) \right] \right] \qquad [14\text{-}b]$$

The above general solution for the amplitude, derived under the condition of no dispersion, is valid for all values of $V < V_{crit}$, where V_{crit} is the critical value of V at which the optical amplitude shock develops. Physically, the above solution is smoothed at the shock discontinuity by higher order derivatives in Maxwell's equation that are neglected in our present approximation. The value of V_{crit} is given by:

$$\epsilon'V = 5\frac{\sqrt{5}}{32} = 0.349 \qquad\qquad [15]$$

In fig 1, we plot the amplitude for different values of $\epsilon'V$. Self steepening increases with the value of $\epsilon'V$. The slope of the amplitude is given by:

$$\frac{\partial a_{1,1}}{\partial U} = \frac{-a_{1,1}^2\left(1 - a_{1,1}^2\right)^{1/2}}{10\,\epsilon'V\, a_{1,1}^4\left(1 - a_{1,1}^2\right)^{1/2} \pm 1} \qquad\qquad [16]$$

where (-, +) corresponds respectively to U (smaller, larger) than $-\frac{5}{2}\epsilon'V$.

In fig. 2, we plot $\overline{\alpha}_{0,1} - \overline{\alpha}_{0,0}$. This quantity, which represents the portion of the phase due to nonzero relaxation time for $\epsilon'V \ll 1$, is approximately linear in U and with a negative slope, which translates into a Stokes shift in the instantaneous frequency. This shift is similar to Gordon's self frequency shift [9], derived for χ^3 material. In fig. 3, we plot $\alpha_{0,1} - \alpha_{0,0}$ for different values of $\epsilon'V$ to qualitatively examine the effects of self-steepening on this Stokes shift.

In fig 4, we are plotting $\alpha_{1,1}$ the pulse total phase in the general case. (Henceforth, we will omit the subscripts to refer to the general case). We note that the presence of the γ'- term and the self-steepening term shifts the position of the phase maximum from the U = 0 axis. Furthermore, the maximum of the pulse amplitude and that of the phase are shifted with respect to each other, which as pointed out in [7] leads to a shift in the positions of the interference fringes of this pulse, for a Young set-up, from those of cw coherent light.

The normalized frequency sweep for this pulse, obtained by taking the U-partial derivative of $\bar{\alpha}$, is given, for the general case, by:

$$\frac{\partial \bar{\alpha}}{\partial U} = -1 - \frac{\varepsilon'}{6} a^4 + \frac{a}{\cos g} + \frac{\varepsilon'}{6} a (\cos g) - \frac{\varepsilon'}{6} a \left(\sin^2 g\right) (\cos g) + \gamma' \left[a (\tan g) + \frac{1}{a} \frac{\partial a}{\partial U} \right] \qquad [17]$$

In fig. 5, we are plotting this quantity. It should be remembered [5] that the maximum of this curve determines in each case the spectral frequency extent on the anti-Stokes side while its minimum determines the corresponding quantity on the Stokes side. As can be observed from the figure, the normalized frequency sweep is asymmetric with respect to the U = 0 axis. This results in an asymmetry of the spectral distribution between the Stokes and anti-Stokes portion of the spectrum. Furthermore, the absolute value of the maximum of $\frac{\partial \bar{\alpha}}{\partial U}$ is always bigger than that corresponding to its minimum value and therefore the anti-Stokes spectral extent is larger than the Stokes extent. In fig. 6, these extrema quantities are plotted as function of $\varepsilon'V$ for different γ's. These extrema were also shown in [7] to determine the domain of F(x), the Fourier transform of the visibility function of the Young intensity distribution with the general solution pulse as input. The function F(x) is given by [7]:

$$F(x) = \frac{1}{2} \frac{\displaystyle\int_{-\infty}^{\infty} dy \displaystyle\int_{-\infty}^{\infty} dU \, a^2(U) \cos\left[y\left(1 + \frac{\partial \bar{\alpha}}{\partial U} \right) \right] \exp(i x y)}{\displaystyle\int_{-\infty}^{\infty} dU \, a^2(U)} \qquad [18]$$

Where $y = K\Delta/\tau$ and Δ is the time delay between the interferometer two paths. The domain of F(x) lies between the lower bound $\left(1 + \left(\frac{\partial \bar{\alpha}}{\partial U} \right)_{min} \right)$ and the upper bound $\left(1 + \left(\frac{\partial \bar{\alpha}}{\partial U} \right)_{max} \right)$. In fig. 7, we plot the envelopes of F(x) for different cases. The domain for each case, as computed in fig. 7, agrees with the results of fig. 6.

The pulse spectral distribution is obtained by taking the absolute magnitude square of the Fourier transform of the pulse electric field. In fig 8, the spectrum is shown for selected values of the parameters. The important features found in our calculations are that:

1. As $\varepsilon'V$ increases, the spectrum is more asymmetric, and near the Stokes maximum extent the spectrum falls off rapidly;

2. As γ' increases, the spectrum is further shifted to the Stokes side and the maximum frequency extents are consistent with the results of fig. 6.

To understand the role of the non-zero relaxation time in the Stokes shift, let us calculate the mean frequency of the pulse normalized to the original center frequency. The normalized first moment of the frequency can be written in the time domain representation as:

$$\frac{\bar{K}'}{K} = \frac{\displaystyle\int_{-\infty}^{\infty} \left(1 + \frac{\partial \bar{\alpha}}{\partial U} \right) a^2 \, dU}{\displaystyle\int_{-\infty}^{\infty} a^2(U) \, dU} \qquad [19]$$

for small $\epsilon'V$, this quantity, for the $\chi^{(5)}$ medium, is given by:

$$\lim_{\epsilon'V \ll 1} \frac{\overline{K'}}{K} \approx 1 - 0.3\,\gamma'(\epsilon'V) \qquad [20]$$

the second term on the right hand side corresponds to the numerically computed Stokes shift. It should be noted that this shift is linear in the thickness of the material, and in the relaxation time and is quadratic in the intensity.

In conclusion, we presented in this lecture, the analytical solution for a pulse propagating in a $\chi^{(5)}$ - material with nonzero relaxation time in the regime where both self-modulation and self-steepening are present . As noted earlier, this theory can be tested in certain semiconductors with two-quanta photogeneration of nonequilibrium carriers.

REFERENCES

1. A. Borshch, M. Brodin, V. Volkov, N. Kurhtarev and V. Starkov, J. Opt. Soc. Am. A - 1 40 (1984).
2. F. De Martini, C.H. Townes, T.K. Gustafson and P.L. Kelley, Phys. Rev. 164 312 (1967) .
3. D. Anderson and M. Lisak, Phys. Rev. A 27 1393 (1983).
4. J.T. Manassah, M.A. Mustafa, R.R. Alfano and P.P. Ho, IEEE J. of Quantum Electronics QE-22 197 (1986).
5. J.T. Manassah and M.A. Mustafa "The Phase ,Spectral Shape and Frequency Shift of a Self-Phase Modulated Pulse" Phys. Lett A (to be published).
6. J.T. Manassah and M.A. Mustafa, Opt. Lett. 13 862 (1988) .
7. J.T. Manassah and M.A. Mustafa, Opt. Lett 13 752 (1988).
8. A. H. Nayfeh, Introduction to Perturbation Techniques (Wiley, New York: 1981).
9. J.P. Gordon, Opt. Lett. 11 662 (1986).

* * * * * *
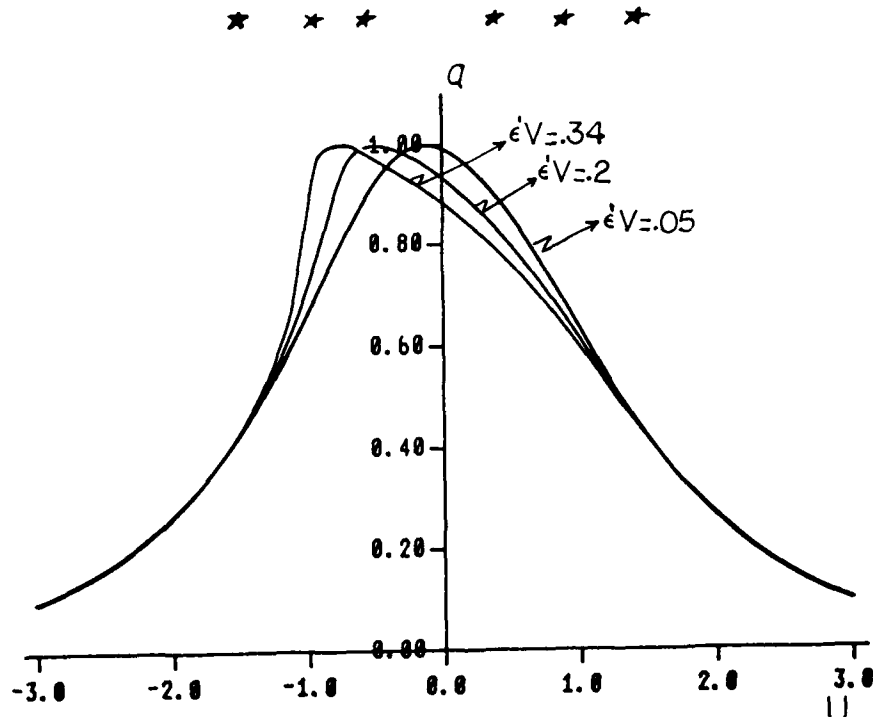
Fig. 1 The amplitude of the normalized electric field as function of U.
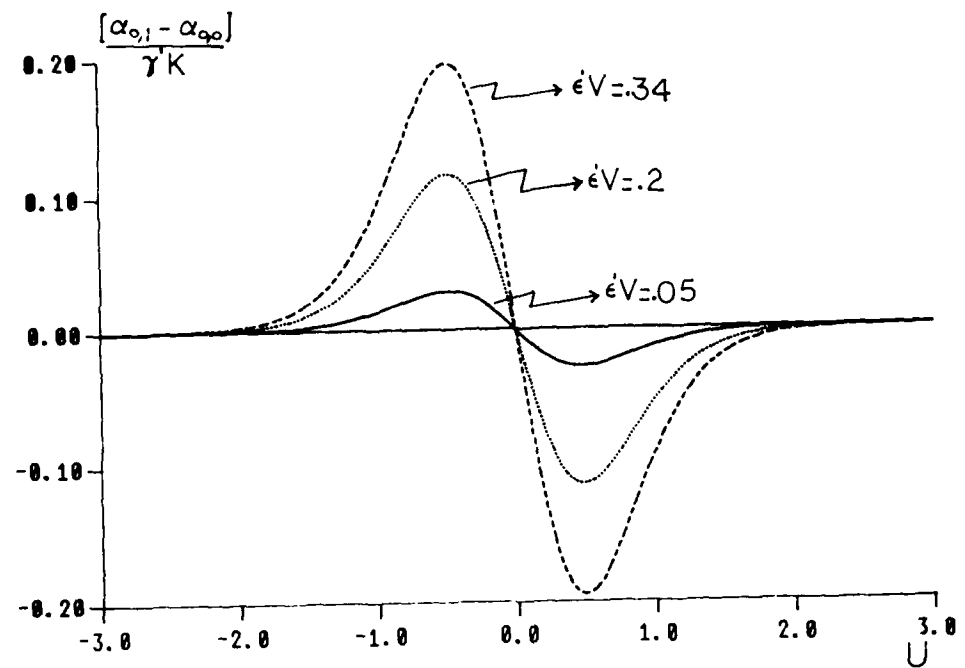
Fig. 2   The phase portion due to nonzero relaxation time, in the absence of self steepening, as function of U.
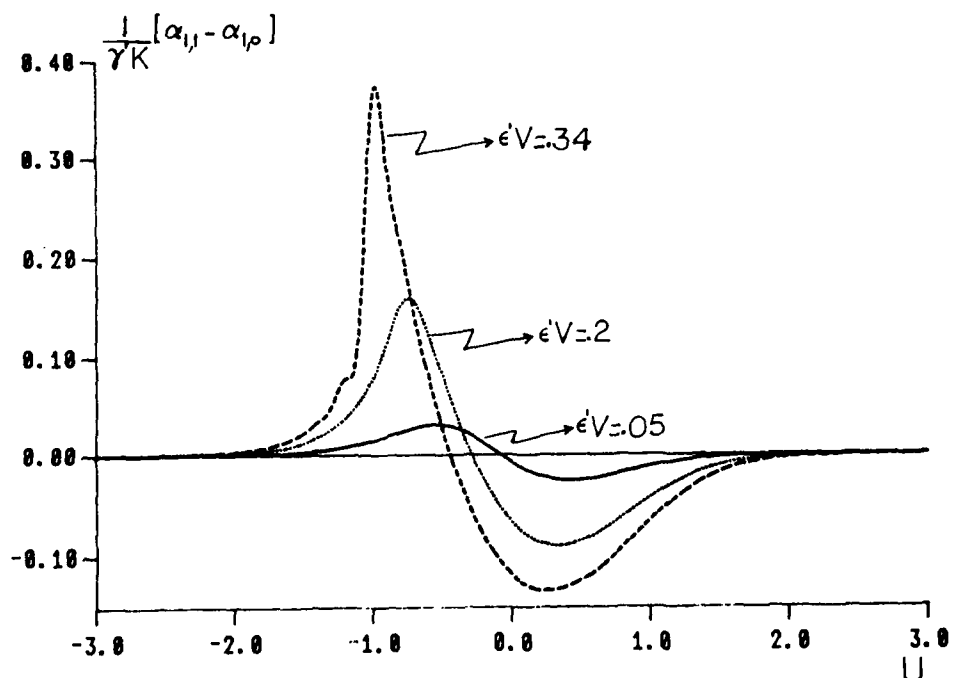
Fig. 3   The phase portion due to nonzero relaxation time, in the presence of self steepening, as function of U.
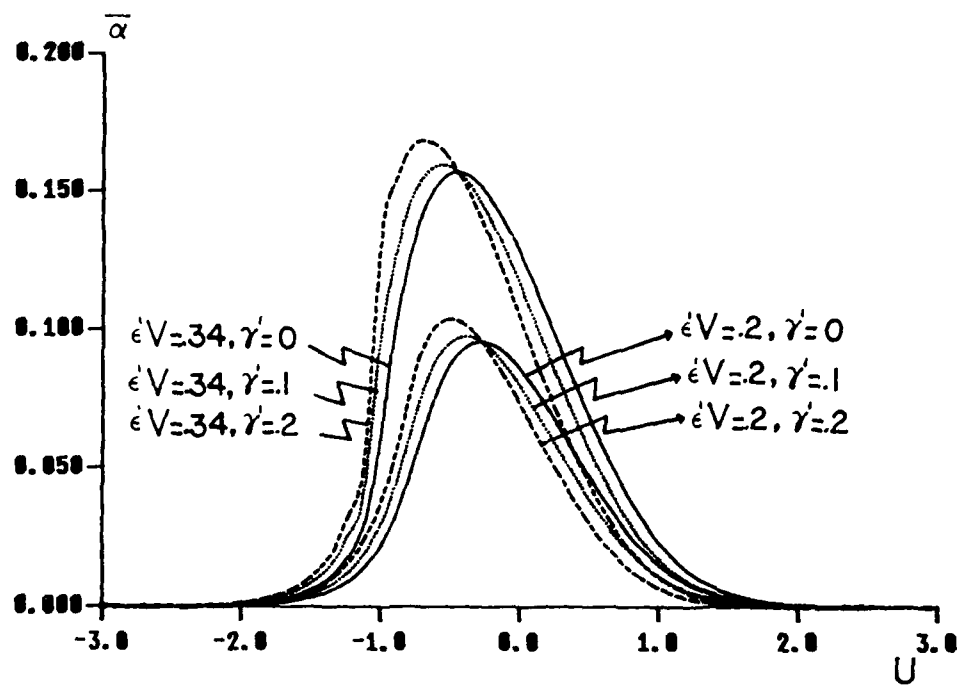
Fig. 4 The pulse normalized total phase as function of U.
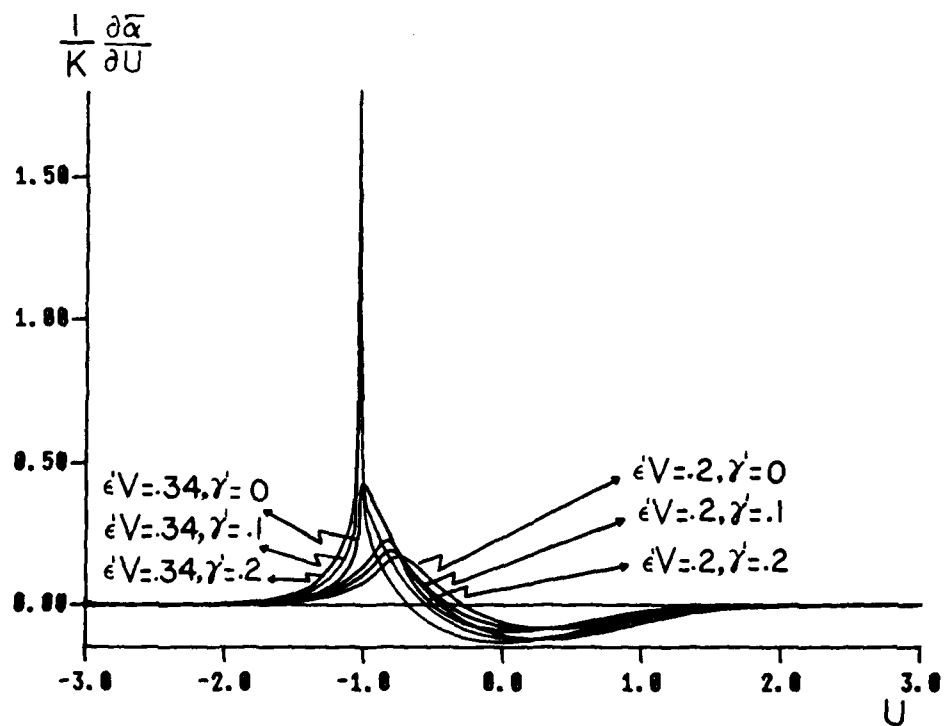
Fig. 5 The pulse normalized instantaneous frequency sweep as function of U.
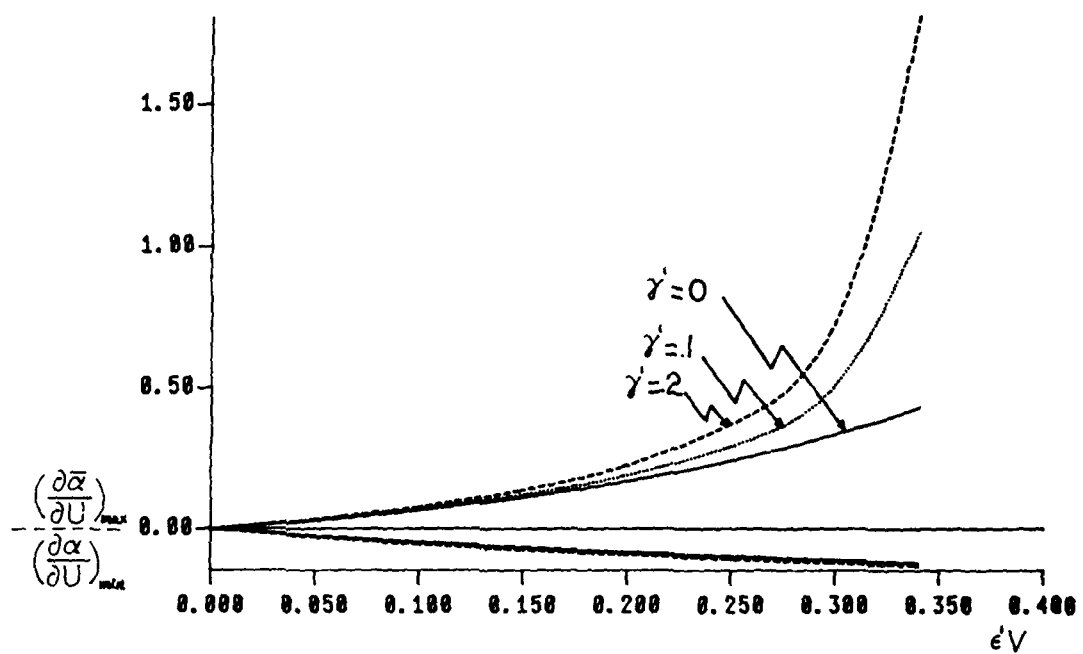
Fig. 6 The Stokes and anti-Stokes spectral distribution extents as a function of $\varepsilon'V$.
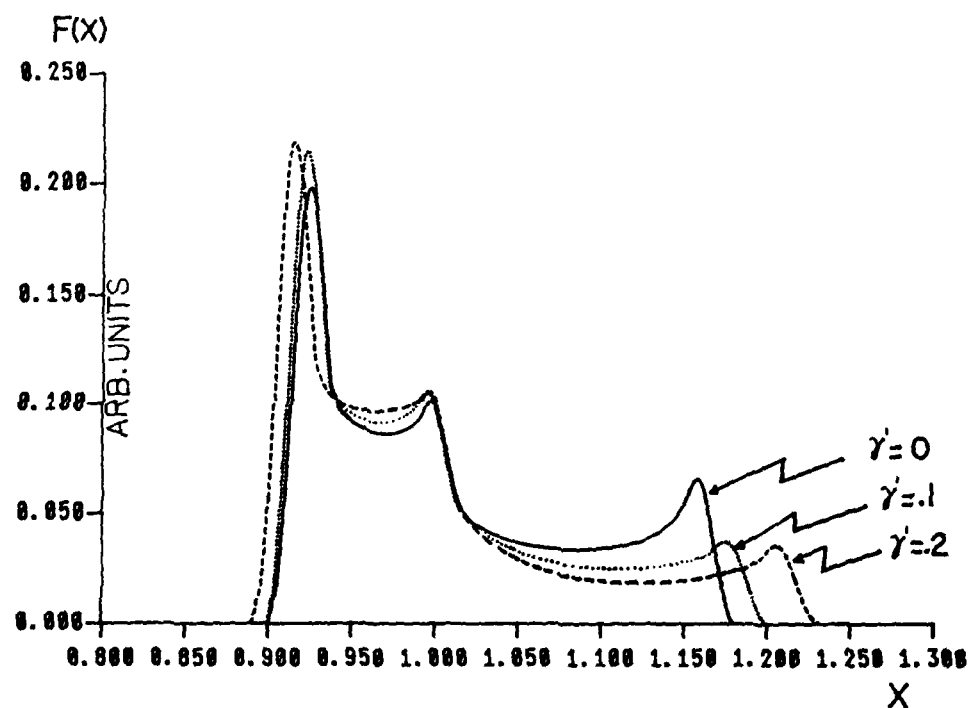
Fig. 7 The envelope of the Fourier transform of the Young visibility function.
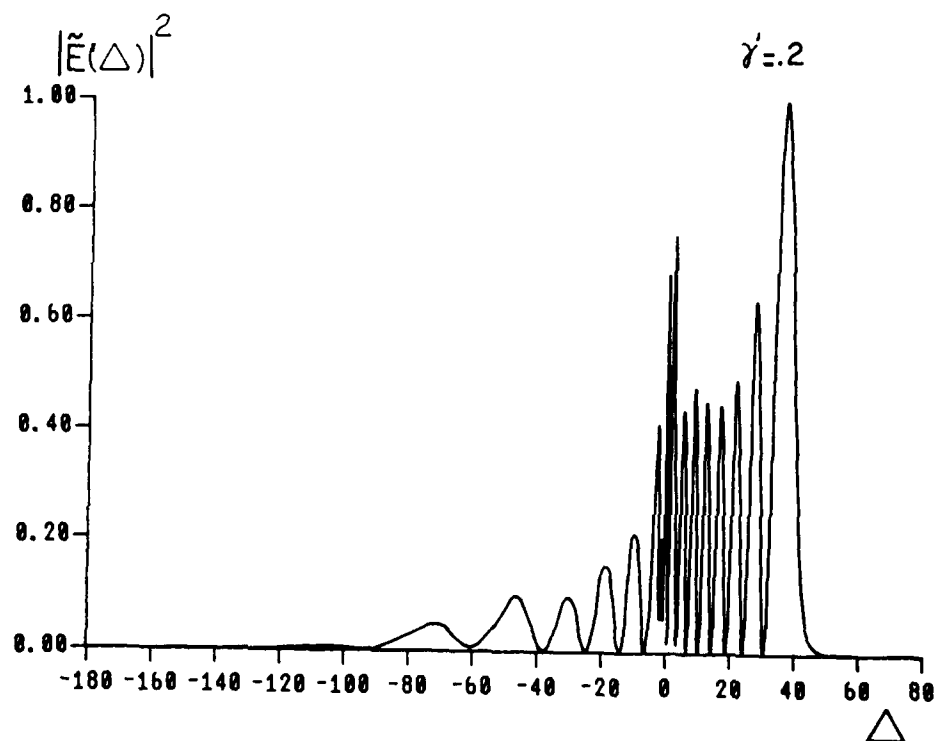
Fig. 8 The pulse spectral distribution as function of the normalized frequency difference multiplied by the pulse duration. Left is the anti-Stokes side.
Normalized center frequency   K = 300.   ε'V = 0.2.

TIME-RESOLVED FLUORIMETRY OF BENZO(a)PYRENE IN LIPOSOMES AND MICROSOMES
Kuang-pang Li
Department of Chemistry, University of Lowell
Lowell, MA   01854
M.R. Glick, R. Indralingam, and J.D. Winefordner
Department of Chemistry, University of Florida
Gainesville, FL   32611

Abstract

Both fluorescence emission spectra and fluorescence lifetimes are measured for benzo(a)pyrene in aqueous, methanolic, liposome and microsome environments and are used to differentiate the orientation and site position within the bilayer membranes of liposomes and microsomes. This study lends credence to the characterization of carcinogenic active sites within the membranes of cellular macromolecules.

Benzo(a)pyrene (BP) and many other potent polynuclear aromatic hydrocarbons generated by incomplete combustion of carbonaceous materials have been considered as major air pollutants in the United States and have been widely implicated in occupational and cigarette smoke-induced lung cancer[1-5]. BP is not carcinogenic per se. It is normally metabolized to non-toxic electrophilic products by a mixed function enzyme system consisting of the membrane bound cytochrome P-450 and a NADPH dependent cytochrome reductase[6,7]. Through some unknown mechanisms, however, BP can also be oxidized to proximate intermediates by the same enzyme system. These intermediates are believed to be epoxides or free radicals which readily react with cellular macromolecules, thus initiating the development of tumerigenic lesions[6-10]. Chemically speaking, this route of activation should be a very minor side reaction of the normal detoxification, otherwise smokers would be certainly doomed to have lung cancers. The proximate carcinogens thus formed should be very scarce. This makes their in vivo characterization extremely difficult.

The active site in the P-450 is known to be spacious enough to accomodate limited reorientation of the substrate molecules to yield positional isomeric products, but it is also restrictive enough to permit stereoselectivity[11]. In other words, the conformation of the BP molecule in the activated complex determines the route of oxidation. Apparently, most of the conformations led to non-toxic metabolites, but a few specific conformations with very remote chance of existence may give rise to proximate intermediates. Information about possible orientations of BP in the activated complex may be ultimately essential for mechanism elucidation of its activation and detoxification. Unfortunately, conformation study of the short-lived activated complex requires very sophisticated instrumentation such as picosecond time-resolved spectroscopy or low temperature site differentiation techniques. Details about the activated complex topology in the membrane would be required for data interpretation. However, if the BP molecule is transferred directly from the membrane to the P 450 active site, and if its orientation prior to binding to the active site is preserved in the activated complex, then the BP conformation in the activated complex may be predicted from the BP orientation in the residence site in the membrane. This hypothesis, of course, will depend upon whether BP in different residence sites is differentiable and whether the P-450 binding of BP is distinguishable. This preliminary report is to investigate the differentiability of the reactive BP in terms of spectral and temporal characteristics.

Materials and Methods

Benzo(a)pyrene (BP) and L-α-phosphatidyl choline (PC) were purchased from Aldrich and Sigma, respectively, and were used without further purification. Because of its potent carcinogenicity, BP was handled with great caution and used solutions were collected and stored in a labelled waste bottle for further treatment. Liver microsomes from maternal rats were donated by Dr. Wong, Pharmacology Department, University of Florida, Gainesville. The protein contents were estimated to be 25 mg/mL. No further purification was performed. Preparation of BP solutions and suspensions were described elsewhere[12]. Phosphate-buffered saline (PBS, pH 7.4) was used as the buffer for all measurements.

A Spex Fluorolog Fluorimeter was used for steady state fluorescence measurements. The fluorimeter was not equipped with a stirring device. Solutions were stirred manually for 30 s after mixing or before each spectral scanning. An excitation wavelength of 378 nm was used.

Time-resolved measurements were carried out with a laboratory-constructed fluorimeter (Fig. 1). A pulsed nitrogen laser (PRA) with a nominal pulse width of 0.2 ns was employed for excitation. The temporal BP emission was detected with a streak camera (Hamamatsu, Tokyo, Japan) and the streak signal was displayed on the monitor and later processed with

an IBM-PC using a Stanford SR245 interface module and a new version of the incorporated software (Stanford Research Systems, Inc., Palo Alto, CA). The software provided multiple exponential fitting for each fluorescence decay curve.

Results and Discussion

Before investigating the temporal characteristics of BP emissions, it is perhaps appropriate to review a few steady state spectra. Curve B in Fig. 2 is the emission spectra of BP in an aqueous suspension. The region 400-450 nm corresponds to emission of soluble BP molecules which can tumble relatively freely. In aqueous suspensions, BP molecules are scarce because of the high hydrophobicity of the hydrocarbon. Most of the BP molecules are gathered in the form of microcrystallites. The closeness of these BP molecules results in the formation of excimers upon irradiation. The excimers emit a relatively intense broad band with a maximum at 490 nm and a shoulder at 520 nm. Emission of BP in liposomes is given as curve C; the soluble BP emission is greatly enhanced, indicating a much higher number of freely tumbling BP molecules in the system. This is possible only when most BP molecules are "dissolved" in the midplane of the lipid bilayer. The excimer emission is seen to be unaffected. Since excimers can be formed only when there are ground state BP molecules very close to the excited BP molecules and since all BP microcrystallites are believed to be dissolved under the experimental conditions, the most appropriate interpretation of the excimer emission would be that it originated from those BP molecules trapped near the glycerol backbone of the bilayer. The lateral movement of these BP molecules is limited and their reorientation is restricted. The appearance of two spectral bands indicates distinguishable differences in the residence sites of these excimers or their molecular conformations.

The microsome solutions have some residual emission (curve A of Fig. 3) probably due to the intrinsic fluorescence of the proteins, but it is not significant as compared with BP emission either in the aqueous phase or in liposomes. This background emission is corrected in all time-dependent spectra, a few of which are reproduced in Fig. 3. This set of spectra were recorded at various times after a 10 μL aliquot of a BP suspension was introduced into a 2.00 mL buffer solution containing 40 μL of the original microsome solution. Prior to each scan, the solution was stirred for about 30 s. The 520 nm excimer band decreased as metabolism proceeded, whereas the 490 nm band increased slightly with time and eventually reached a constant value. This indicates that all BP excimers do not interact in identical ways toward the P-450-reductase complex and that those excimers emitting around 520 nm are most likely the reactive species. Recently, Nelson et al., studied the membrane topology of 34 different vertebrate cytochrome P-450 proteins and proposed a three dimensional model in which the P-450 may be envisioned as a thick triangle lying flat on the membrane surface with the heme group situated in the plane of the triangle facing the membrane surface. Lipid soluble substrate molecules approach the heme from the membrane[13], and, therefore, the active site and the possible access channel should be below the heme and facing the membrane. The P-450 is anchored to the membrane by two NH_2-terminal transmembrane helices. This model is agreeable with our experimental results which indicate that the reactive BP molecules most likely reside near the membrane surface and also have the most probable orientation.

Molecules in different environments normally exhibit different spectral characteristics. Their excited states may also have different lifetimes. To differentiate the BP excimers in the membrane, it is essential to study their relaxation behaviors. The following results may not be conclusive enough to provide positive site assignment of the excimers but to give some interesting information.

Fig. 4 shows the fluorescence decay of BP in methanol solution. An exponential function with three terms is used to fit the curve. Only a single lifetime of 6.7 ns is observed, indicating one BP species or one environment for BP in the solution. Since the time-resovled fluorimeter has not been precisely calibrated, lifetimes are expressed in terms of bin numbers in all the figures. Based on the company calibration of the streak camera, a bin approximately corresponds to 0.1 ns.

When there are two or more residence sites for BP in the system, particularly when BP in these sites are kinetically interchangeable, the fluorescence decay curve will be the result of overall relaxation of all involved BP species. The lifetimes obtained from fitting the decay curve are, therefore, the combined results of the individual relaxation constants. More information will be required to deconvolute these relaxation constants from the measured lifetimes. For simplicity, it is assumed here that the interchange of BP among sites is relatively slow compared to the fluorescence decay of excited BP molecules. That is, the residence sites of BP are independent, and the overall decay curve is simply the sum of individual relaxation of BP in different sites.

Curve-fitting of BP relaxation in aqueous suspension (Fig. 5) shows three distinct lifetimes of 23.4, 11.1 and 8.6 nm, respectively. The 23.4 ns is probably due to

background fluorescence which has a decay time of 22.5 ns, when pure buffer solution is used. The 8.6 ns, comparable to the 6.7 nm in methanol solution, could be assigned to the soluble BP and the 11.1 ns to BP in microcrystallites. When a large amount of PC liposome was mixed with BP suspension in the PBS solution (Fig. 6), two lifetimes of 11.0 and 12.2 ns, respectively, were observed. However, when the amount of PC was reduced, a lifetime of 5.0 ns rather than the 12.2 ns was obtained. Our previous report[12] showed that the BP excimer emission (both the 490 nm and 520 nm bands) decreased as the BP suspension was mixed with liposomes. As the ratio of lipid-to-BP increased, the excimer emission increased, passed through a maximum, and decreased again. If the short lifetime could be assigned to the water-soluble BP, the long lifetimes of 11.0 and 12.2 ns might be assigned to BP associated with the bilayer.

When microsomes were mixed with BP suspensions, the relaxation lifetimes were kinetically dependent. At about 1.5 min after mixing, a short lifetime corresponding to the water-soluble BP, a long lifetime corresponding to background drifting, and an inter-mediate lifetime of 10.0 ns were observed (Fig. 7l). At around 8.5 min, the lifetimes became 8.0, 10.1, and 12.7 ns, respectively (Fig. 7b). These three lifetimes converged to a single lifetime of 10.4 ns after 13.5 min of reaction had elapsed (Fig. 7c). Three different lifetimes of 10.7, 11.4, and 12.4 ns, respectively, reappeared as reaction was allowed to proceed over twenty minutes. The kinetic measurements (Fig. 3) showed that the BP excimers emitting a 520 nm were almost totally consumed in 18 min of reaction. The disappearance of the 12 ns lifetime' seemed to support its assignment to these excimers. Its reappearance at longer reactions times could be attributed to the redistribution of BP in the membrane.

The above preliminary assignment is only speculative; its consistency with other evidence is encouraging and justifies further investigation. Polarization measurements and fluorescence line narrowing studies are now being considered. We hope more accurate site differentiation and molecular orientation may be obtained.

References

1. National Academy of Sciences (1972): "Biological Effects of Atmospheric Pollutants, Particulate Polycyclic Organic Matter", Washington, D.C.

2. Colen, C.M. and Moore, B.P. (1978): in "Carcinogenesis, A Comprehensive Survey", (Jones, P.W. and Freudenthal, R.I. ed) Vol. 3, pp325-339, Raven Press, New York.

3. Epstein, S.S., Small, J., Sawicki, E., and Falk, H.L. (1965), J. Air Poll. Control Assoc., 14(4), 174-176.

4. Nelson, N. (1970), in "Inhalation Carcinogenesis" (Hanna, M.G., Nettasheim, P., and Gilbert, J. ed) pp3-12, USAEC, Division of Technical Information CONF-69001.

5. Heidelberger, C. (1976), in "Carcinogenesis, A Comprehensive Survey" (Freudenthal, R.I., Jones, P.W., ed) Vol. 1 pp1-8, Raven Press, New York.

6. Heidelberger, C. (1975), Annul. Rev. Biochemistry, 44, 79-121.

7. Pexuto, J.M., Lea, M.A., and Yang, C.S., (1976), Cancer Res., 36, 3647-3653.

8. Jerina, D.M. and Daly, J.W., (1974), Science, 185, 583-592.

9. Miller, E.C. and Miller, J.A., (1974), in "The Molecular Biology of Cancer", (Busch, H., ed) pp377-402, Academic Press, New York.

10. Sims, P. and Grover, P.L., (1974), Adv. Cancer Res., 20, 165-274.

11. Miwa, G.T. and Lu, A.Y.H., (1986), in "Cytochrome P-450, Structure, Mechanism, and Biochemistry", (Ortiz de Montellano, P. ed), Ch 3, pp77-87, Plenum Press, New York.

12. Li, K.P., Glick, M.R., Indralingam, R., and Winefordner, J.D., (1988), Spectrochim. Acta, Part B, (in press).

13. Nelson, D.R. and Strobel, H.W., (1988), J. Biolog. Chem., 263, 6038-6050.
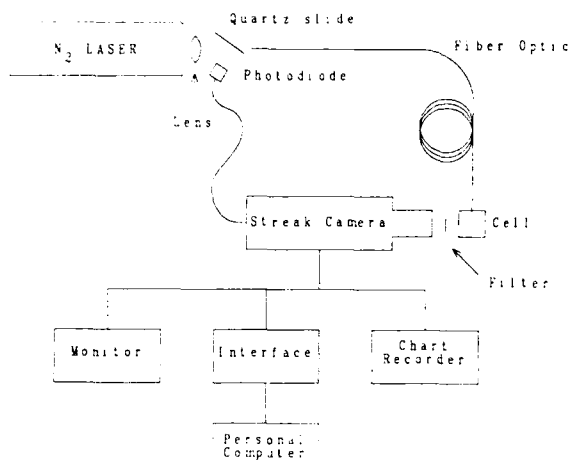
Figure 1. Schematic diagram of the time-resolved fluorimeter.
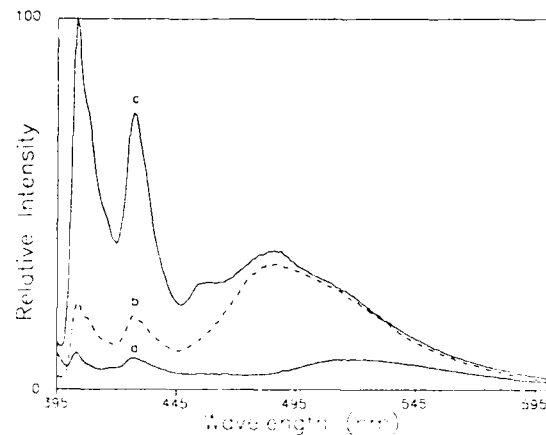
Figure 2. Emission spectra of BP.
(a) residual emission of 40 uL microsome in 2 mL PBS, (b) 50 uL of BP dispersed in 2 mL PBS, (c) 40 uL of microsome added to (b).
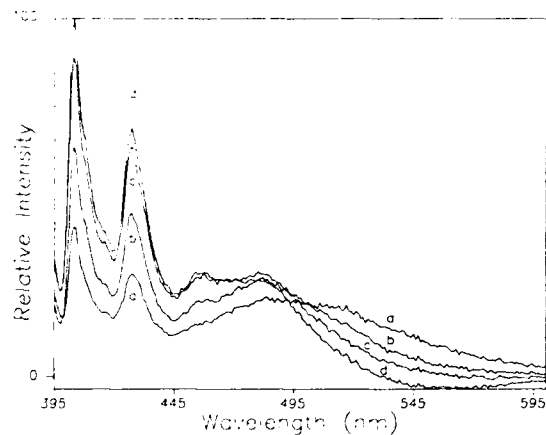
Figure 3. Time scan emission spectra of BP, corrected for microsomal residual emission.
(a) 10 uL of BP dispersion mixed with 40 uL of microsome in 2 mL PBS, 30 s after mixing, (b) 10 min after mixing, (c) 20 min after mixing, (d) 30 min after mixing.

$$y = A_1 \exp^{-(t/T_1)}$$

$A_1 = 0.205$ $T_1 = 6.67$
$A_2 = 0.205$ $T_2 = 6.67$
$A_3 = 0.205$ $T_3 = 6.67$
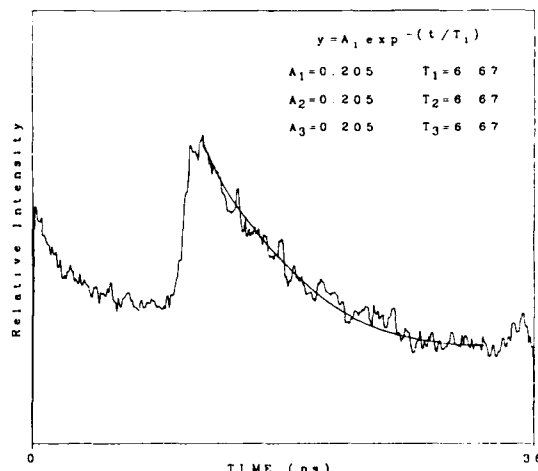
Figure 4. Relaxation decay curve of BP in methanol solution.
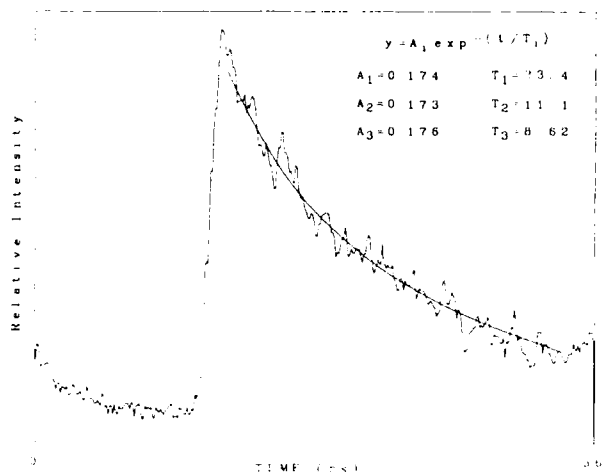
Figure 5. Relaxation decay curve of BP in methanol solution.
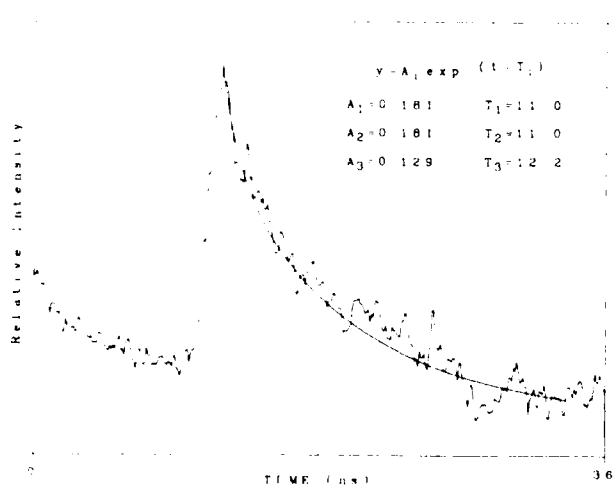
Figure 6a. Relaxation decay curve of BP in liposomes, high lipid/BP ratio.
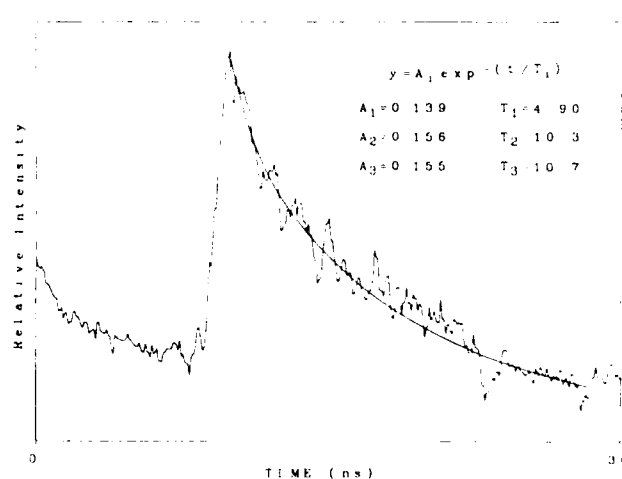
Figure 6b. Relaxation decay curve of BP in liposomes, low lipid/BP ratio.
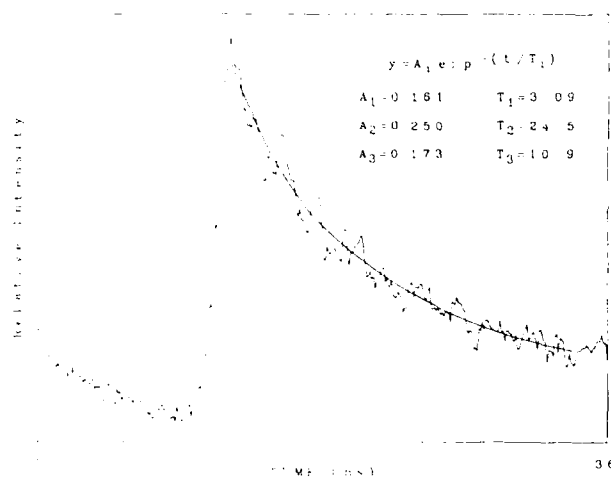
Figure 7a. Relaxation decay curve of BP in
microsomes, 1.5 min after mixing.

$y = A_1 exp^{-(t/T_1)}$

$A_1 = 0.161$ $T_1 = 3.09$

$A_2 = 0.250$ $T_2 = 24.5$

$A_3 = 0.173$ $T_3 = 10.9$
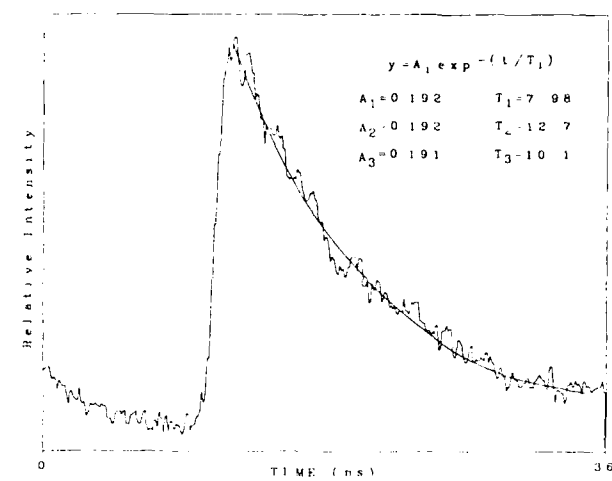
Figure 7b. Relaxation decay curve of BP in
microsomes, 8.5 min after mixing.

$y = A_1 exp^{-(t/T_1)}$

$A_1 = 0.192$ $T_1 = 7.98$

$A_2 = 0.192$ $T_2 = 12.7$

$A_3 = 0.191$ $T_3 = 10.1$
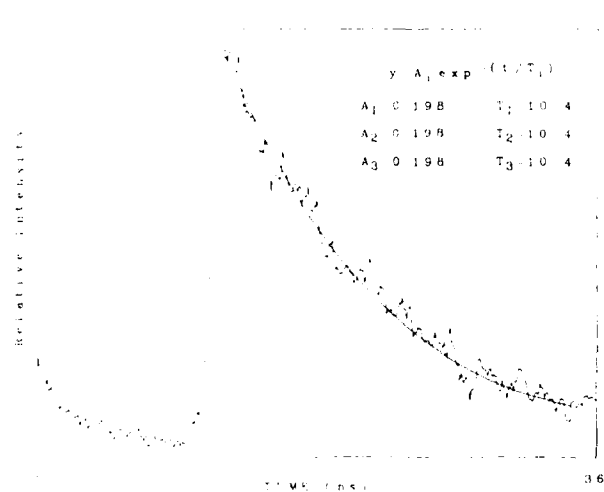
Figure 7c. Relaxation decay curve of BP in
microsomes, 13.5 min after mixing.

$y = A_1 exp^{-(t/T_1)}$

$A_1 = 0.198$ $T_1 = 10.4$

$A_2 = 0.198$ $T_2 = 10.4$

$A_3 = 0.198$ $T_3 = 10.4$
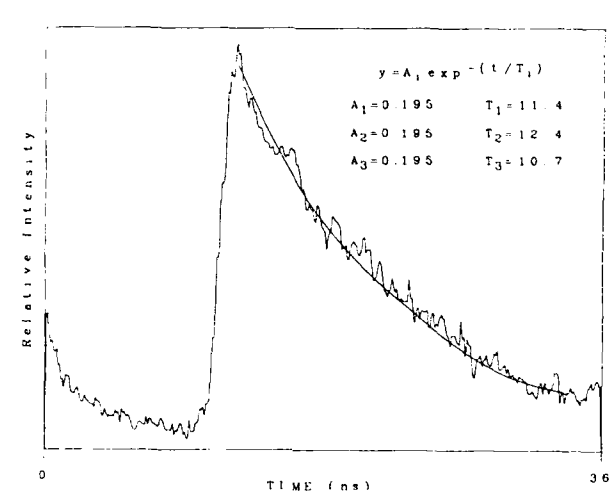
Figure 7d. Relaxation decay curve of BP in
microsomes, 22 min after mixing.

$y = A_1 exp^{-(t/T_1)}$

$A_1 = 0.195$ $T_1 = 11.4$

$A_2 = 0.195$ $T_2 = 12.4$

$A_3 = 0.195$ $T_3 = 10.7$

LASER VAPORIZATION FOR SAMPLE INTRODUCTION IN ATOMIC AND MASS SPECTROSCOPY

Joseph Sneddon

**Department of Chemistry
University of Lowell
Lowell, Massachusetts 01854**

Abstract

The use of a laser to ablate or vaporize a solid sample for subsequent introduction to an atomic or mass spectrometer for metal determination will be discussed. The advantages, disadvantages, instrumentation, possible mechanism of vaporization, analytical performance characteristics, and selected applications will be further presented.

Introduction

Despite the widespread use and acceptance of atomic and mass spectroscopy for metal determination, a major limiting factor for direct determination is the introduction of the sample, particularly a solid sample. A potentially useful technique for sample introduction of solid samples is laser ablation or vaporization. The versatility of laser ablation for sample introduction is summarized in Figure 1 and the advantages and disadvantages are summarized in Table 1.
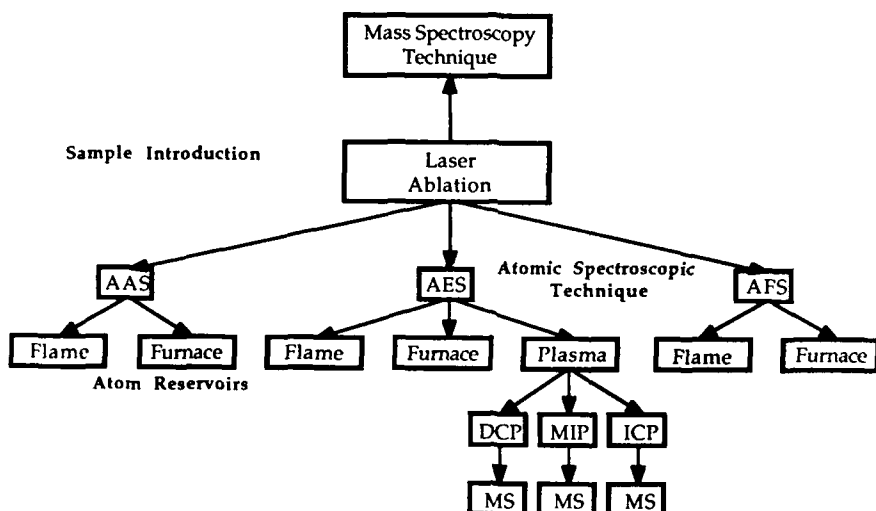
Figure 1. Atomic and mass spectroscopic techniques used with laser vaporization for sample introduction.

Table 1

Advantages and Disadvantages of Laser Vaporization for Sample Introduction to Atomic and Mass Spectroscopic Techniques.

Advantages	Disadvantages
1. Directly applied to solid samples with little or no sample preparation.	1. Standardization is difficult to achieve particularly if the sample to be analysed has an unknown and complex matrix.
2. Can use conducting and non-conducting samples.	2. Laser is expensive and leads to more complex instrumentation.
3. Can investigate surface heterogeneites in solid samples.	3. Detection limits are, generally not as low as established solution techniques (one to three orders of magnitude).
4. Mass of a few microgram or less required.	
5. High irradiance of laser will produce an efficient vaporization stage.	4. Precision typically 2-10 %, if hetergeneites do not exist (compared to < 1 % for established solution techniques).
6. Separation of vaporization and atomization-excitation stage may allow these separate experimental stages to be optimized for improved signal and accuracy.	5. Accuracy typically ± 5 % compared to < 1% for established solution techniques.
7. Hard, polymeric and high molecular weight compounds are vaporized.	6. Small portion of sample may not be representative of bulk

Instrumentation

The most frequently used lasers in atomic and mass spectroscopy when combined with sample introduction by laser vaporization are summarized in Table 2. Laser vaporization hasbeen coupled with the direct current plasma (DCP)[1], inductively

Table 2

Most Frequently Used Lasers in Atomic and Mass Spectroscopy.

1. Nd : YAG (1.064 μm)
2. CO_2 (10.6 μm)
3. Ruby (0.694 μm)
4. Nd : Glass (1.064 μm)
5. Nitrogen (0.337 μm)
6. Rare Gas / Halogen Excimer (Argon Fluoride : 0.193 μm)
(Krypton Fluoride : 0.248 μm)
(Xenon Chloride : 0.308 μm)
(Xenon Fluoride : 0.351 μm)

7. Dye (0.220-0.740 μm)

coupled plasma (ICP)[2], microwave induced plasma (MIP)[3], flame[4] and electrothermal atomizer (furnace)[5]. Atomic emission (AES) and atomic absorption spectroscopy (AAS) are widely used but atomic fluorescence spectroscopy(AFS) has found limited used with laser vaporization. The laser parameters which can effect the vaporization parameters are summarized in Table 3. The type of sample

Table 3.

Laser Parameters which can Effect the Vaporization Process

1. Wavelength : mass ablation rate, m (kg / s cm^2) = 110 (ϕa /10^{14}) $^{1/3}$ (λ) $^{-4/3}$
ϕa is absorbed flux, W/cm2. m would increase at shorter wavelengths and subsequently give higher sensitivity (more sample vaporized).

2. Pulse Rate : The higher the pulse rate, the greater the amount of material removed and subsequently the greater the sensitivity.

3. Irradiance : The greater the irradiance the greater the amount of material removed from the surface, and subsequently the higher the sensitivity.

in particular, the hardness can effect the signal[1].

Mechanism of Vaporization

Despite the potential, attraction and use of laser vaporization for sample introduction in atomic and mass spectroscopy, the exact mechanism is unknown at present. A schematic diagram of the proposed steps is shown in Figure 2[6].

Analytical Performance Characteristics and Selected Applications

The detection limits for various metals using laser vaporization for sample introduction to atomic spectroscopic techniques is shown in Table 4. In general, detection limits are in the low μg/g levels. Precision is typically under 10 %, accuracy at low levels of

Conclusion

Laser vaporization for sample introduction in atomic and mass spectroscopy will continue to attract attention of analytical chemists. Improvents in instrumentation and an understanding of the exact mechanism of the process will lead to more widespread use and acceptance.

References

1. P.G. Mitchell, L.J. Radziemski, and J. Sneddon, Appl. Spectros., 1987, 41, 141.
2. M. Thompson, J.E. Goulter, and F. Sieper, Analyst, 1981,106, 32.
3. F. Leis and K. Laqua, Spectrochim. Acta, 1979, 34B, 307.
4. R. Wennrich and K. Dittrich, Spectrochim. Acta, 1982, 37B, 913.
5. T. Kantor, L. Polos, P. Fodor and E. Pungor, Talanta, 1976, 23, 585.
6. S.J. Hein and E.H. Piepmeir, Trends in Anal. Chem., 1988, 7(4), 137.
7. J. Sneddon, P.G. Mitchell and N.S. Nogar, Chapter 9, Applications of Laser Plasmas, ed., L.J. Radziemski and D. A. Cremers,pub., Marcel Dekker, New York, 1989.
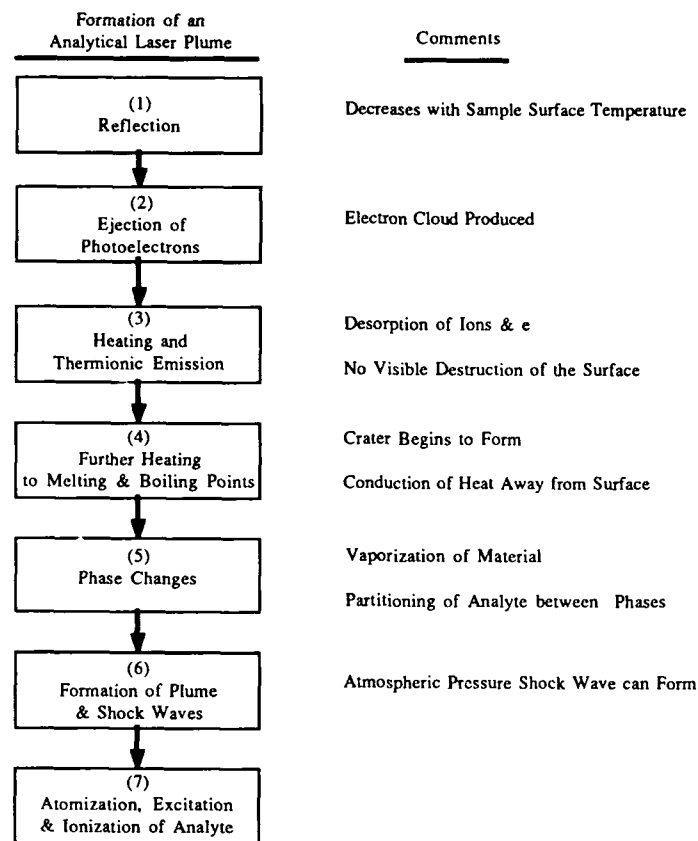
Figure 2. Schematic diagram of steps which can occur in the laser vaporization of a solid sample[6].

Table 4

Detection Limits for Various Metals Using Laser Vaporization - Atomic Spectroscopy

Metal	Analysis Method (µg/g [ppm])						
	ICP[1]	ICP[2]	DCP	MIP	ET	FLAME	ICP-MS
Al	20	2	-	9.3	11	-	-
Ag	-	-	-	-	-	-	0.3
As	-	-	-	-	-	-	2
Bi	-	-	-	-	-	-	0.2
Cd	8	0.6	48	-	-	-	-
Cr	10	1	31	-	20	-	-
Cu	9	0.3	21	2.4	7.2	10	-
Mg	-	-	-	-	1	-	-
Mn	3	0.3	18	-	37	20	-
Mo	20	2	30	-	10	-	-
Ni	20	1	32	12	24	-	-
Te	-	-	-	-	-	-	0.3
V	20	1	-	-	-	-	-
Zn	-	-	-	-	22	50	-
Zr	-	-	50	-	-	-	0.3

1. Q-switched.
2. Normal

Detection limits were taken from literature. Due to differences in instrumentation / operating conditions they should not be directly compared to each other.

± 5 %, and linearity over several orders of magnitude above the detection limit. The application of laser ablation in atomic and mass spectroscopy has been in major, minor, and trace metal determination in solid samples, organic and biomolecular analysis, and in photophysical and kinetic studies[7].

588

LASER IGNITION OF ENERGETIC MATERIALS
WITH A
PULSED ND:YAG LASER

L. R. Dosser, S. A. Siwecki, T. M. Beckman, and T. C. Girmann
EG&G Mound Applied Technologies[*]
P. O. Box 3000
Miamisburg, Ohio 45343-0987

Abstract

The laser is an ideal ignition source for energetic materials. It permits precise control of the ignition energy, and parameters such as the ignition threshold and the time to ignition can be determined. Optical fibers are used to deliver the ignition pulse and to monitor the time required to complete the burn of the energetic material. The light emission from the interaction of the Q-switched pulse from the Nd:YAG laser with two secondary explosives, pentaerythritol tetranitrate (PETN) and 1,3,5-triaminotrinitrobenzene (TATB), has been spectrally resolved using a 0.25 m monochromator with an optical multichannel analyzer detector. These spectra show definite band structure, which indicates that these experiments may lead to an understanding of the ignition chemistry.

Introduction

The properties of energetic materials, such as their ignition threshold, the time required for ignition to begin, and the burn rate of the material, are of primary importance to understanding these materials and how the devices that contain them function. The laser is an excellent ignition source for these materials. The laser energy can be very carefully measured and precisely controlled. By carefully adjusting the laser energy, the ignition threshold for the material can be determined. An optical fiber delivery system is used to direct the laser pulse to the material. By using this fiber and a second fiber to monitor the burn of the material, details of the ignition and burn can be obtained with each shot. Several energetic materials have been ignited in this manner using the un-Q-switched pulse from the Nd:YAG laser. The light flash produced in the ignition should contain information on the chemistry of the ignition as well as provide timing information. This ignition light was investigated by spectrally resolving the emission created when a Q-switched pulse from the laser impacted the surface of a pellet of a secondary explosive. The preliminary spectra taken from two different secondary explosives have indicated that considerable information may be obtained when the light emission is recorded under high resolution.

Experimental Results

The ignition of the energetic materials with the un-Q-switched pulse of the Nd:YAG laser was performed in the apparatus shown in Figure 1. The pulse from the Nd:YAG laser was reflected from the high reflector(HR) for the 1.064 micron wavelength, and coupled into the optical fiber with the appropriate lens. About 10 % of the laser pulse was split off and sent to a photodiode (not shown) to monitor the pulse and mark the initial time. The ignition light from the energetic material came back out of the fiber, was recollimated by the lens, was sent through the HR for 1.064 microns, and was sent to a second photodiode to record the ignition time. As the material burned to completion, an optical fiber at the end of the component transmitted the light to a third photodiode to record the function time of the device.
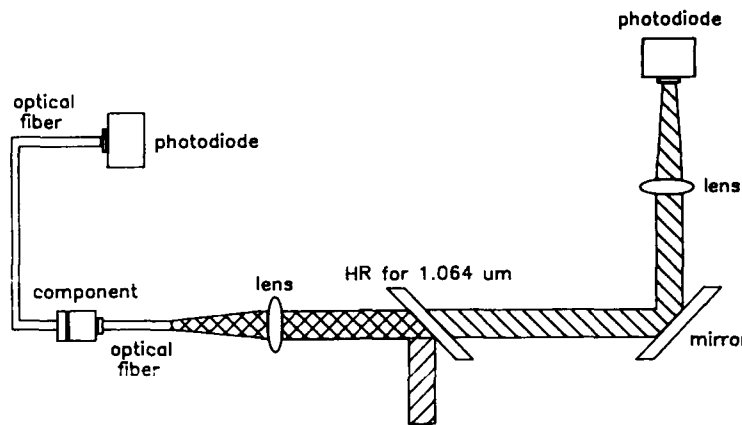
Figure 1 - Laser ignition apparatus.

An example of the type of data that is recorded is shown in Figure 2 a-d. The figure shows data from a small test device containing the pyrotechnic titanium potassium perchlorate. The first three sets of Figures (2 a-c) show only the laser pulse which was delivered through a 600 micron optical fiber, and the ignition light that was transmitted back out through this fiber. The three traces represent laser energies of 53, 72, and 100 millijoules, respectively. The laser pulse in Figure 4d was delivered through a 300 micron optical fiber and had an energy of 26 millijoules. The "breakout" light is superimposed on the laser pulse record, but the timing mark for the completion of the burn can still easily be measured. This system is currently being used to evaluate several pyrotechnic materials.

In addition to providing a timing mark indicating the start of ignition, the ignition light may contain information about the ignition chemistry. The chemical species produced during the interaction of a laser pulse with an energetic materials is being investigated using emission spectroscopy. By spectrally resolving the ignition light, it may be possible to identify specific chemical species, leading to an understanding of the laser initiation process. Comparison of energetic materials (secondary explosives and pyrotechnics) is possible, including the effects of various additives.

This technique was evaluated by spectrally resolving the light emission produced when a laser pulse impacted a pellet of a secondary explosive. A schematic of the apparatus used to perform these experiments is shown in Figure 3. A 10-ns Q-switched pulse from a Nd:YAG laser operating at 1064 nm was focused onto the surface of an explosive pellet in such a manner that it would not detonate. An evacuated chamber houses the pellet to prevent any interaction with the air. A quartz window allows the laser pulse to enter and the emission light to exit. The emission light is focused onto the end of a fiberoptic bundle, which transmits it to a 0.25 m monochromator. An optical multichannel analyzer (OMA) serves as the detector of the resultant spectrum. The OMA allows the simultaneous acquisition of approximately 300 nm of the spectrum, thus providing an efficient technique to study such fast events.

Figures 4 and 5 show the laser interaction emission spectra of pentaerythritol tetranitrate (PETN) and 1,3,5-triaminotrinitrobenzene (TATB), respectively. Both spectra cover the wavelength range from 360 nm to 660 nm. There is a definite band structure in each of these two spectra that needs to be investigated under higher resolution to make an identification of chemical species. The band structure of the two spectra is also quite different, which would be expected since two explosives are very different in chemical structure.
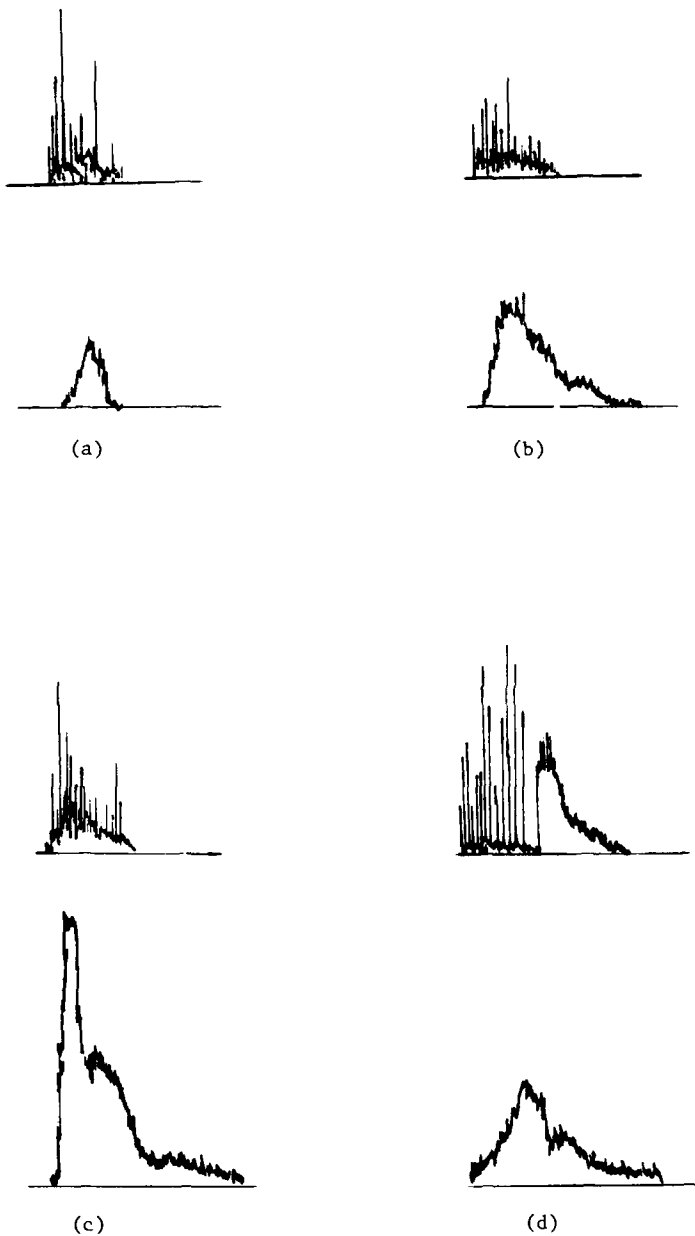
Figure 2 - Laser ignition data records.
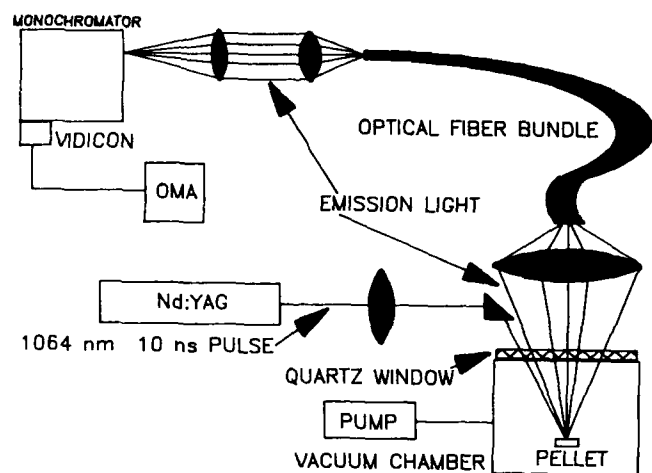
Figure 3 - Laser interaction emission spectroscopy apparatus.
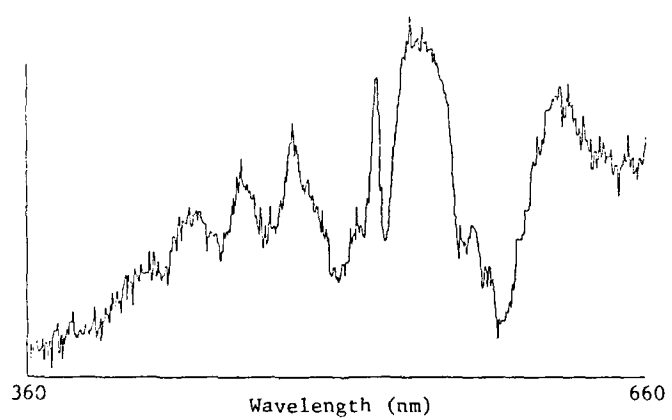
Figure 4 - Laser interaction emission spectrum of PETN.

360   Wavelength (nm)   660
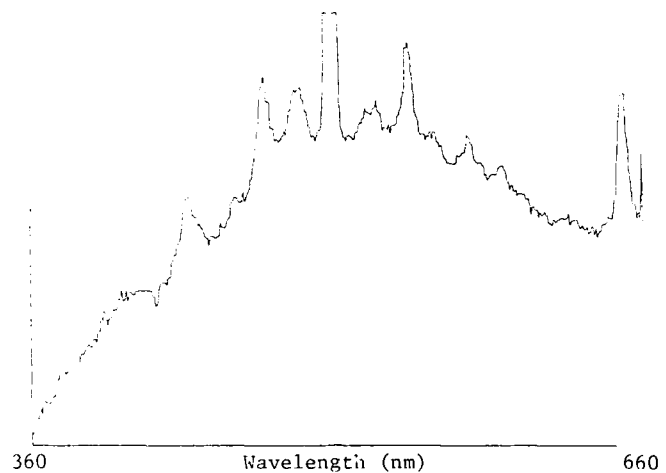
Figure 5 - Laser interaction emission spectrum of TATB.

Conclusions

Two different, but complementary, experiments have been established to evaluate the laser initiation of energetic materials. In one experiment, ignition thresholds and timing information on the interaction of the laser pulse with the energetic material can be obtained. In the other experiment, the ignition light is spectrally resolved to evaluate the ignition chemistry. Excellent spectra can be obtained, and future work should permit the identification of chemical species produced in the ignition. Experiments that temporally resolve the light produced in the ignition are also planned to further evaluate the ignition chemistry.

DIRECT VIBRATIONAL SPECTROSCOPY OF TRANSITION STATES

JACK A. SYAGE

Aerophysics Laboratory
P. O. Box 92957
The Aerospace Corporation
Los Angeles, CA 90009

Abstract

A technique for optically exciting and detecting vibrational resonances in transition state (TS) configurations of chemical reactions is described. By dressing the TS with intense infrared (IR) picosecond pulses ($>GW/cm^2$), for well-defined reactant initial conditions, resonant TS interactions such as absorption and stimulated emission can become manifested by measurable changes in the reaction rate and the product rovibrational distributions. In order that all TS configurations evolve during this pulse duration, a conventional pump-t-probe sequence using ultrashort pulses is used to initiate the reaction and to detect a product energy state after some time t that is short relative to the IR pulse duration. The transition states, therefore, evolve in an intense, but effectively continuous wave IR radiation field. The essential features illustrating the TS spectral lineshapes and experimental conditions were modeled by adopting a radiation-dressed potential surface and evaluating the vibrational transition probability by an exact density-matrix solution. Results are presented to describe, (1) the conditions under which significant TS transition probability occurs, and (2) how a frequency-resolved vibrational spectrum can be interpreted in terms of the detailed shape and dynamics of the reactive surface.

Introduction

During the course of a chemical reaction, a transformation of molecular bonds occurs which leads to structural configurations that are intermediate between reactants and products. These exceedingly short-lived structures have come to be known at "transition states". While it is true that the region known as the transition state can be rather diffuse and span a large configuration (or phase) space, the potential surface is believed to show ripples and shallow minima which can enhance the transient lifetimes of certain structures. The direct detection of transition states (or "reaction complexes") is considered one of the most important goals in chemistry and physics today.

One of the most fruitful approaches for obtaining transition state information has been to use crossed molecular beam systems to study the product angle-velocity distributions following monoenergetic collisional excitation.[1,2] State-to-state studies of reactant and product energy levels has also provided information that could be interpreted in terms of unique transition state properties.[2] The crossed beam and state-to-state experiments, however, do not directly observe the transition state, but rather derive detailed understanding via information obtained about the products.

Frequency-Domain Techniques: Brooks[3,4] and Polanyi[5,6] and their coworkers, using frequency-domain techniques, were the first to report evidence for spectroscopic detection of a transition state. The most compelling evidence by Brooks, et al.,[4] for TS absorption is an experiment based on the reaction K + NaCl + $h\nu$ → KCl + Na*. They observed emission from the Na D line for $h\nu$ excitation wavelengths that were off resonance from either reactant or product and concluded that the reaction com-

plex $[NaKCl]^\ddagger$ must be the absorbing species. These wing absorptions in the reactive complex have the same physical basis as collisional line broadening. Polanyi focussed on a complementary approach, searching instead for wing emission eminating from the $[FNaNa]^\ddagger$ reactive complex. These early studies were marked by exceptionally weak signals that rendered analysis rather tenuous. Only since 1987 have major advances been made in the endeavor to detect transition states. Polanyi, et al.[6] have provided a convincing demonstration of detection, by multiphoton ionization, of a transient $[HDD]^\ddagger$ configuration in the exchange reaction $H+D_2$ → $HD+D$. However, the technique only probes for TS geometries that have Franck-Condon overlap with the excited and ionic bound states of HDD. This experiment has yet to resolve any resonances of $[HDD]^\ddagger$ from which to obtain structural and dynamical information. Valentini and Nieh[7] have recently reported the remarkable observation of collisional resonances in the $H+H_2$ reaction that correlate with enhanced production of $H_2(v=1)$ averaged over all scattering angles. Although, not a direct observation, this result is, nonetheless, the most convincing measurement of vibrational structure in a TS. In another clever application, Neumark, et al.[8] formed stable anions of $ClHCl^-$ and then recorded photoelectron spectra to the unstable neutral complex $ClHCl$. The broad, but resolved spectrum is argued to represent vibrational information on the transition state region of the reaction $Cl+HCl$. The inevitable question regarding methods that rely on bound-unbound transitions, however, is to what extent the detected unbound geometry represents simply a Franck-Condon projections of the bound state.

Time-Domain Techniques: With continuing advances in ultrafast laser techniques, it is only natural that interest in time-domain techniques would ensue in the hunt for transition state detection. Zewail and coworkers have surged to the forefront in this endeavor with a number of important developments in 1987 and 1988.[9-11] Principal among these are results for the unimolecular

dissociation of ICN[9] and CH$_3$I[10] using a pump-t-probe scheme in which the probe frequency is tuned off-resonance of a reaction product. In so doing they observed signals that rise and fall with delay time t representing a transition state geometry that "passes through" a resonance with the probe frequency. The detection scheme is a variant of Brook's technique of using product emission to detect wing absorptions attributable to a collision complex. Instead, the reaction is unimolecular and initiated by a subpicosecond pulse. This has the advantage of providing very high instantaneous densities of transition state structures and the unquestioned benefits of time-resolved information. Using this same technique for the dissociation of NaI, Zewail and coworkers[11] have observed a periodicity in the formation of product Na due to a small nonadiabatic transition probability for reaction that occurs each time the vibrational motion of the excited NaI encounters a surface crossing transition region.

Transient Vibrational Spectroscopy

The optical detection of transition state configurations reported thus far have generated enormous excitement. However, there are still certain limitations to be overcome before they provide uniquely descriptive pictures of the transition state region. For instance, electronic transitions measure the energy difference between two different potential energy surfaces (PES); yet neither PES is likely to be known in the region of the transition state. Likewise, the use of bound-unbound transitions faces Franck-Condon restrictions that can severely limit the range of TS geometries that are actually detected.
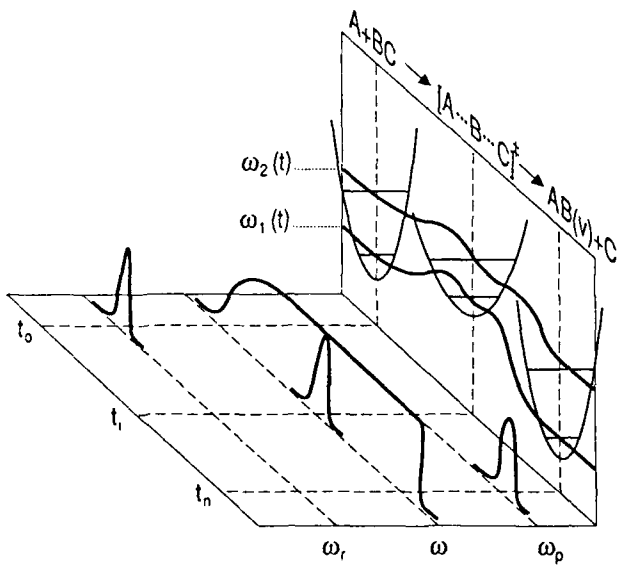
Fig. 1. Schematic of 3-pulse sequence for detecting vibrational resonances in transition states and reactive intermediate complexes. The pulses ω_r and ω_p refer to excitation of reactant and product, respectively. Idealized vibrationally adiabatic surfaces ($\omega_1(t)$ and $\omega_2(t)$) for the $[A \cdots B \cdots C]^\ddagger$ asymmetric stretch are drawn to correlate with reactant and product vibrations.

Concept of Experiment

We describe a technique that can provide vibrational spectra of transition states. The central idea here is that excitation of short-lived TS vibrations can become "imprinted" onto long-lived properties of the products (i.e., action spectroscopy) that can be routinely detected as a change in reaction probability or rate, and/or product rovibrational distribution. It has been recognized theoretically[12-14] that intense laser fields can interact with transition states and influence the course of a chemical reaction. The reactive-complex absorption wings, observed by Brooks[4] and Zewail[9-11] for electronic states, are an example of this phenomenon, in the sense that these absorptions produce electronically excited product. Work in this laboratory has shown that the conditions of a CW radiation dressed TS can be realized experimentally, in a manner that is sensitive to the detection of *vibrational resonances* in the TS.[15] The requirement of intense IR radiation ($>$GW/cm^2), during the course of the reaction, is satisfied by using short (e.g., picosecond) pulses. In order that all TS configurations evolve during this pulse duration, a conventional pump-t-probe sequence using ultrashort pulses is used to initiate the reaction and to detect a product energy state after some time t that is short relative to IR pulse duration. As represented schematically in Fig. 1, the presence of the ω long-pulse across the ω_r-τ-ω_p short-pulse interval describes a reaction that evolves in the presence of an intense CW radiation field.

Several modes of detecting TS vibrational resonances as a function of ω and τ can be envisioned to resolve the resonance frequencies, each providing unique details of the TS reactive PES and the coupling of vibrational energy to the reactive coordinate:

(1) Enhancement of reaction probability $P(\omega,\tau)$ or rate $k(\omega)$, due to TS absorption: This mode is particular sensitive if the excitation energy ω_r is below the reaction threshold.

(2) De-enhancement of $P(\omega,\tau)$ or $k(\omega)$, due to stimulated emission from collisionally excited TS vibrations: This variant would permit direct detection of the collisional resonances observed in molecular beam scattering experiments.[1,7]

(3) Excitation or de-excitation of product rovibrational energy corresponding to TS absorption or stimulated emission, respectively: The induced changes in the product state distributions can be correlated to the actual vibrational coordinates, amplitudes of motions, and angular momenta corresponding to the particular TS resonance.

(4) Ultrashort ω pulse that may be positioned within the reactive t period to probe early and late TS configurations. Exceptional time resolution ($\leq$ 100 fs) will be required, because the TS vibrational spectrum will be dominated by the most stable configuration.

The vibrational TS spectra are further enhanced by limiting the distribution of reactive trajectories so as to probe specific regions of transitional configuration space. This can be achieved by studying unimolecular reactions, or oriented bimolecular reactions initiated by dissociating a molecule in a suitably chosen van der Waals mixed dimer[16] (e.g., $XA \cdot BC \xrightarrow{-X} [A \cdots B \cdots C]^\ddagger \rightarrow AB + C$). A quantitative model for establishing the necessary experimental conditions, as well as interpreting the TS vibrational lineshapes, is presented later.

OPG

λ/4 POL λ/4 POL

ROD

AMP

KDP KDP

ROD

AMP

1064 nm
25 ps
50 mJ

LiNbO₃

IR 1-2 mJ
15 ps

Pockels
Cell

ML

ROD

OSC

532 nm
20 ps
10 mJ

DYE
LASER

VIS 2 mJ

UV 5 ps

OPG

355 nm
15 ps
10 mJ

KDP

VIS .5 mJ

near IR 10 ps
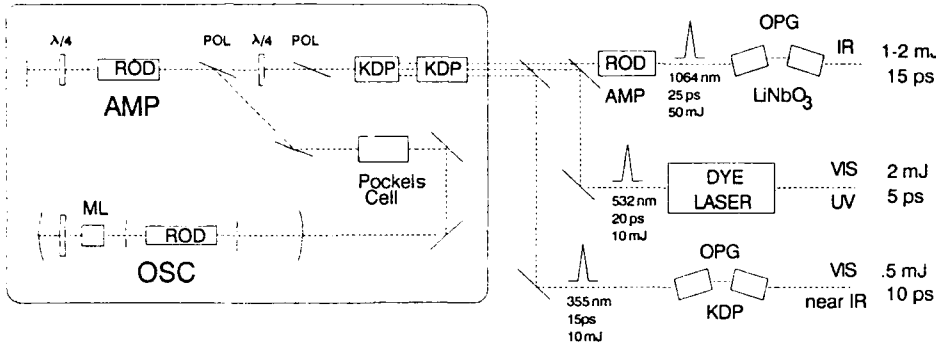
Fig. 2. Schematic for generating 3-pulse sequence, using a pulsed mode-locked (ML) Nd:YAG laser, short-cavity dye laser, and optical parametric generation (OPG) devices. Typical pulse energies and durations are indicated.

Experimental Arrangement

The three-pulse sequence diagrammed in Fig. 1 will be generated by a picosecond Nd:YAG laser pumping a combination of tunable optical parametric devices and a tunable ps dye laser. An arrangement, which makes use of the Nd:YAG fundamental (1064 nm) and the second (532 nm) and third harmonics (355 nm) is given in Fig. 2. Our approach takes maximum advantage of the high pulse energies provided by our pulsed and amplified mode-locked laser. Typical pulse energies and pulsewidths in the standard configuration are included in Fig. 2 for each stage leading to the three pulses, ω_r, ω, and ω_p.

The source of vibrational excitation in the transition state will take the form of 15-20 ps tunable IR pulses of about 1-2 mJ/pulse. This is generated by a standard nonlinear parametric method[17] which uses the intense 1064 nm Nd:YAG pulse to generate two sum frequencies in the IR with a tuning range of 1.5-5 μm. Modest focussing to beam diameters less than 1 mm gives the necessary > 10 GW/cm² pulse energies to vibrationally excite TS configurations. The pump (ω_r) and probe (ω) pulses require a large visible (VIS) and ultraviolet (UV) tuning range. This is provided by a short-cavity dye laser, pumped by the 532 nm Nd:YAG output. A second source of tunable visible frequencies is available by pumping an optical parametric arrangement with the 355 nm Nd:YAG harmonic.

Theoretical Description

In this section, we provide the beginnings of a quantitative basis for interpreting the TS spectra. The model calculations to follow not only demonstrate the soundness of the experimental approach, but make the physical connection between observed spectra and the detailed dynamics of a collision complex on a reactive potential surface.

The Photon-Dressed Potential Energy Surface

The essential features illustrating vibrational correlation, TS spectral lineshapes, and experimental conditions can be viewed by adopting a simple model for a radiatively dressed PES and evaluating the transition probability by an exact density matrix solution. This is an appropriate representation because the intense IR pulse ω appears as a constant radiation field over the short detected reaction period t, as illustrated in Fig. 1. For vibrational excitation on the same electronic surface, the Hamil-

tonian (in frequency units) may be written as

$$\mathcal{H} = \mathcal{H}_o(t) + \mathcal{H}_{int}(t)$$
$$\mathcal{H}_o = T_q + \omega a^+ a^-$$ (1)
$$\mathcal{H}_{int} = \mu(t) \cdot \epsilon_o(a^+ + a^-)$$

$\mathcal{H}_o$ consists of the nuclear kinetic energy operator T_q and the field-free radiation Hamiltonian where a^+ and a^- are the photon creation and annihilation operators. The interaction Hamiltonian $\mathcal{H}_{int}$ contain the dipole operator μ and laser electric field strength ϵ_o (we assume a single mode and polarization). Operation of $\mathcal{H}$ on the matter-radiation basis states gives the diagonal energy matrix elements,

$$\langle n, \chi_1 | \mathcal{H}_o(t) | \chi_1, n \rangle = \omega_1(t) + \omega$$
$$\langle n-1, \chi_2 | \mathcal{H}_o(t) | \chi_2, n-1 \rangle = \omega_2(t)$$ (2a)

where $|n\rangle$ and $|n-1\rangle$ are the photon states in an n-photon field (where we consider only one-photon transitions). The interaction of the dipole moment with the incident radiation field has only the off-diagonal elements

$$\langle n, \chi_1 | \mathcal{H}_{int}(t) | \chi_2, n-1 \rangle = \langle n-1, \chi_2 | \mathcal{H}_{int}(t) | \chi_1, n \rangle = \frac{\mu(t)\epsilon_o}{2}$$ (2b)

The time dependence arises from the effect of the reactive trajectory velocity vector $v(r,t)$ on the coordinate dependent Hamiltonian. The radiation-dressed lower surface is shifted from the uncoupled surface (given by $T_q|\chi_1\rangle = \omega_1|\chi_1\rangle$) by the radiation frequency ω. If the dressed lower surface approaches or crosses the upper surface then, depending on the interaction strength $\mu\epsilon_o$, a mixing of states occurs which makes possible a transition.

The mixing of the basis states gives the correct shape of the PES in the vicinity of the crossing. The true eigenfunctions $|\chi'\rangle$ and energies η' can be solved for the time-dependent Hamiltonian elements above, and are given by

$$|\chi_1'\rangle = |\chi_1\rangle \cos\theta + |\chi_2\rangle \sin\theta$$
$$|\chi_2'\rangle = -|\chi_1\rangle \sin\theta + |\chi_2\rangle \cos\theta$$ (3)

where

$$\tan 2\theta = \frac{\mu(t)\epsilon_o}{\Omega(t)}$$
$$\eta_{1,2}' = \pm[\mu(t)^2\epsilon_o^2 + \Omega(t)^2]^{1/2}$$
$$\Omega = (\omega_2 - \omega_1) - \omega$$

596

Rotation Matrix Solution

We find it advantageous to use the density matrix formalism for evaluating population probabilities or densities. The time-dependent probability of populating the upper level can be evaluated by solving the density matrix equation $\dot{\rho} = i[\rho, H]$ for the element ρ_{22}. This formalism has the advantage of leading to a solution that is completely general for all models of the PES surface and interaction strengths. Without presenting the full details[15] here, we solve for the four elements of ρ by casting them as a column vector and applying an appropriate transformation[18] to help decouple the equations. One obtains,

$$\dot{\rho}(t_n) = \mathcal{R}(t_n, t_o)\dot{\rho}(t_o)$$

$$\mathcal{R}(t_n, t_o) = \exp\left\{ i \int_{t_o}^{t_n} \mathcal{L}(t)dt \right\} \qquad (4)$$

where $\dot{\rho}$ is the column vector $\{\rho_{11} - \rho_{22}; i(\rho_{12} - \rho_{21}); \rho_{12} + \rho_{21}\}$ and $\mathcal{L}$ follows from the transformed equations $\frac{d}{dt}\dot{\rho} = i\mathcal{L}\dot{\rho}$. The evaluation of the evolution operator $\mathcal{R}(t_n, t_o)$ is essentially intractable except for the simplest Hamiltonian time dependences. However, in the appropriate representation,[18] $\mathcal{R}(t_n, t_o)$ takes the form of a rotation matrix that can be expressed conveniently by a piecewise product of rotation matrices

$$\mathcal{R}(t_n, t_o) = \mathcal{R}(t_n, t_{n-1}) \cdots \mathcal{R}(t_1, t_o) \qquad (5)$$

over incremental time intervals during which $\mathcal{H}$ is approximately constant. The coherence properties and their intermediate role in the time-evolved transition probability are fully preserved by this treatment.

The vibrational transition probability at the end of a reactive trajectory is evaluated by solving for the population difference $\rho_{11} - \rho_{22}$. For the initial condition $\rho_{12}(t_o) = \rho_{21}(t_o) = 0$, the r_{11} element of the product matrix $\mathcal{R}(t_n, t_o)$ must be evaluated. The product of matrices in Eq. (5) can be reduced to a product of 2x2 matrices $\mathcal{Q}(t_n, t_o) = \prod_{i=1}^{n} \mathcal{Q}(t_i, t_{i-1})$ consisting of the elements

$$q_{11}(\tau_i) = q_{22}^*(\tau_i) = \cos\frac{1}{2}\bar{b}_i\tau_i - i\cos\theta_i\sin\frac{1}{2}\bar{b}_i\tau_i$$

$$q_{12}(\tau_i) = q_{21}(\tau_i) = i\sin\theta_i\sin\frac{1}{2}\bar{b}_i\tau_i \qquad (6)$$

with terms defined as

$$\tan\theta_i = \frac{\Omega_i}{\mu_i \epsilon_o}$$

$$\Omega(t) = \omega_2(t) - \omega_1(t) - \omega$$

$$b(t) = \left[\mu(t)^2\epsilon_o^2 + \Omega(t)^2\right]^{1/2}$$

where $\tau_i = t_i - t_{i-1}$ and the bar represents the average value over the τ_i interval. The general solution for $\Delta\rho = \rho_{11} - \rho_{22}$ is then given by

$$\Delta\rho(t_n) = r_{11}(t_n, t_o)\Delta\rho(t_o) \qquad (7)$$
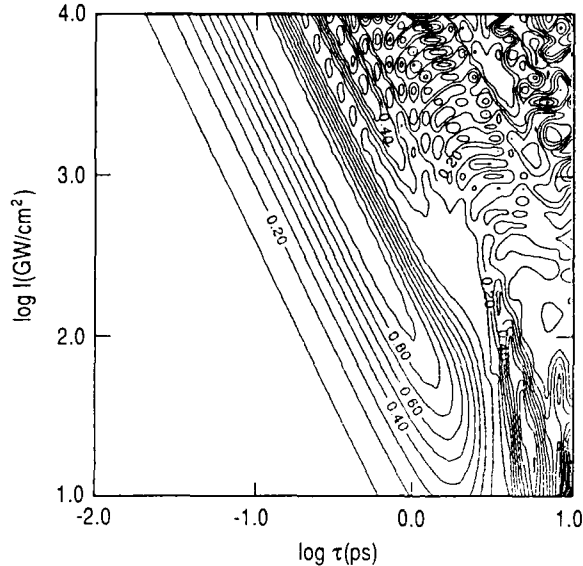
Fig. 3. Transition probability $P(v, v+1)$ for absorption ($\Delta\rho(t_o) = 1$) or stimulated emission ($\Delta\rho(t_o) = -1$) as a function of laser power density and quasibound lifetime τ. Parameters used in the contour plot were $\mu(t) = 0.2$ D, $\omega = 2020$ cm^{-1}, and $\omega_k(t) = a_k[(2t/\tau) - 1]^2 + b_k$ where $a_1 = 80$ cm^{-1}, $b_1 = 1000$ cm^{-1}, and $a_2 = 160$ cm^{-1}, $b_2 = 3000$ cm^{-1}.

where $r_{11}(t_n, t_o)$ is obtained from the elements of the product matrix $\mathcal{Q}(t_n, t_o)$ by the expression

$$r_{11} = \frac{1}{2}\left[(q_{11}^2 + q_{22}^2) - (q_{12}^2 + q_{21}^2)\right] \qquad (8)$$

Model Calculations

The above model will serve to demonstrate the experimental technique represented in Fig. 1 by addressing two important questions; (1) under what conditions will a significant TS transition probability occur, and (2) can a frequency-resolved vibrational spectrum be interpreted in terms of the detailed shape and dynamics of the reactive PES? These points are examined in Figs. 3-5. Although, we shall use a general strong-field, coherent density matrix solution, we adopt a simple model for the reactive trajectory in that we assume localized trajectories, no decay or relaxation processes other than reaction, and simple functional forms for the potential surfaces.

The calculated results are based on a shallow potential well in the TS region for a particular vibrational coordinate on the ground electronic surface. We assume parabolic well depths of 0.01 eV and 0.02 eV for the vibrational levels v and $v + 1$, and a dipole moment of 0.2 D. These values are consistent with [FHF][1] in the F+HF reaction. Transition probabilities $P(v, v + 1)$ are calculated as a function of IR laser power density I ($\epsilon_o \times I^{1/2}$), and trajectory time through this region (i.e., quasibound lifetime τ). We assume that regions outside of the well are vanishingly short-lived.

The results in Fig. 3 indicate that significant values of $P(v, v + 1)$ occur over a range of modest experimental conditions. For instance, $P(v, v + 1) > 0.25$ for $I = 100$ GW/cm^2 and $\tau > 300$ fs. The oscillations that are observed along τ (shown

bunched up due to the log scale) are analogous to Rabi cycling, which for resonance conditions occurs at frequency $\mu\epsilon_o$. For dynamic trajectories, the resonance condition is rapidly detuned by the changing potentials, however, phase accumulation can still lead to off-resonance oscillations provided that $\mu\epsilon_o \geq \Omega$. In realistic systems, the coherences will dampen rapidly either by (i) T_2 mechanisms, in which case the oscillation region reduces to the saturation condition $P = 0.5$, or by (ii) very different v and $v + 1$ quasibound lifetimes, in which case the shorter-lived state will behave irreversibly, making possible situations approaching $P = 1$.

The bandshape for the TS vibrational transition $v \rightarrow v + 1$ is calculated for excitation over the entire quasibound lifetime in Fig. 4. The spectrum reveals a distinct lineshape that does not change form as a function of laser field. The spectra are therefore interpretable in terms of the shape and dynamics of the transient vibrational potential; power broadening, at the high fields shown, does not contribute to the lineshape.

Fig. 4 represents the experiment in which the the IR pulse duration is long compared to the reaction time so that all TS configurations evolve in an intense, but effectively CW laser field. An exceptionally more powerful (and more challenging) adaptation can be conceived based on the use of ultrashort pulses (e.g., ≤ 200 fs) that are narrower than the quasibound lifetimes. The ω pulse can then be positioned at discrete intermediate time intervals along the reactive trajectory and in principle probe for different TS configurations. The recorded vibrational spectra will vary depending on where along the reactive PES the excitation takes place. This concept is similar to the 2-pulse sequence introduced by Zewail and coworkers[9-11] for electronic transitions in product absorption wings. The calculated time-dependent vibrational spectrum in Fig. 5 demonstrates the considerable detail and unique information that can be obtained regarding the dynamics and shape of the potential surfaces. The two-dimensional (ω, t) vibrational spectrum in Fig. 5 represents the direct change in vibrational frequency that occurs during a reactive trajectory.

Vibrational Correlation

The transition-state vibrational absorption technique described here is, in a sense, a state-to-state measurement, with the important difference that we consider state excitation of the TS. The correlation of TS vibrational excitation to measurable rovibrational excitation in the products is a "half collision" process that is physically not unlike that which occurs in unimolecular dissociations. Using this as an analogy, we can put forth a framework for the state-to-state half-collision reaction probabilities for vibrationally-excited TS reactions $[ABC(v')]^\ddagger \rightarrow AB(v)+C$. In order to present expressions that convey physical insight, we simplify the problem by invoking the collinear and quasi-diatomic approximations. The former assumption is realistic in so far as the minimum reactive PES is usually along the collinear coordinate in the complete reactive hypersurface. The latter approximation assumes that the bond that breaks is a normal vibrational coordinate. The state-to-state reaction probability $T_{v'v}$ is then given by the integral overlap of the initial and final wavefunctions

$$T_{v'v} = \iint dRdr \; \chi_{v'}(R,r)\chi_v(R,r) \qquad (9)$$

where we have defined the coordinates R and r as the internuclear distances A-B and B-C, respectively. The wavefunctions χ describe vibrational and translational motion and can be rigorously solved by Schrodinger's equations using a Hamiltonian contain-
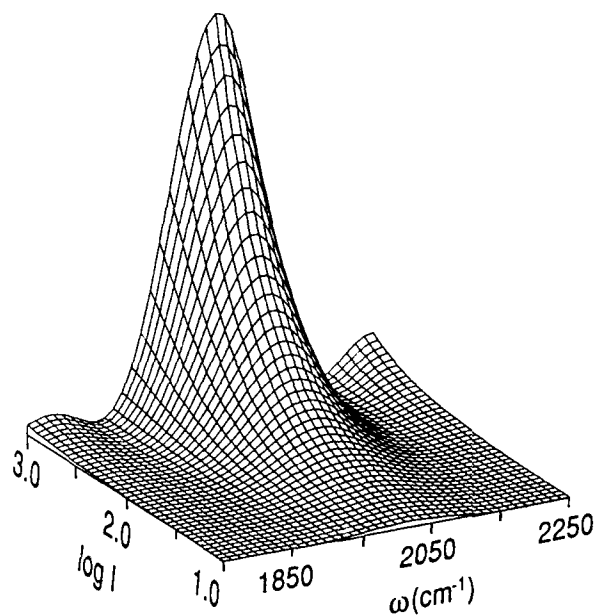
Fig. 4. Calculated transition state vibrational lineshapes. Continuous excitation over a trajectory liftime of 250 fs. Peak transition probability was $P = 0.89$ Other conditions were $I = 100$ GW/cm^2 and those in the caption to Fig. 3.
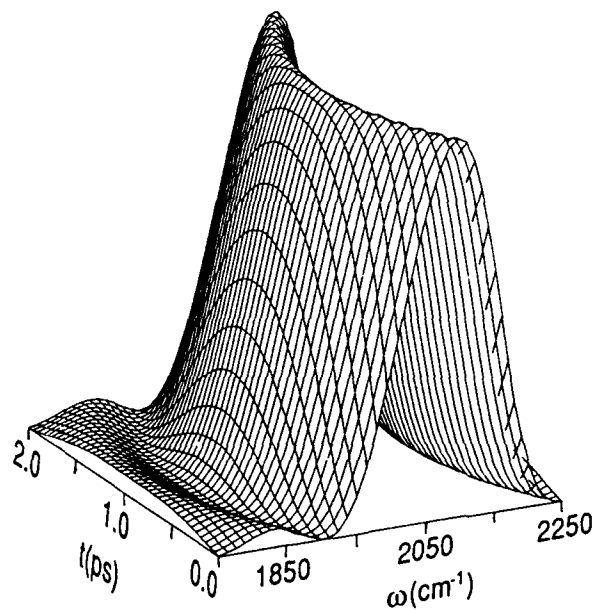

Fig. 5. Calculated transition state vibrational lineshapes. Discrete excitation over 200 fs intervals as a function of time during a reactive trajectory of lifetime 2 ps. Peak probability was $P = 0.10$. Other conditions were $I = 100$ GW/cm^2 and those in the caption to Fig. 3.

ing the relative nuclear kinetic energy operators evaluated at the critical TS coordinate. The Hamiltonian may also be modified by including a dressed photon field in the manner described above. The product wavefunctions are expanded in terms of a basis of vibrational functions $\phi_{v,j}(R,r)$ with an r-dependent equilibrium position R_0.

$$\chi_v(R,r) = \sum_j \phi_{v,j}(R,r)\alpha_j(r) \tag{10}$$

The coefficients $\alpha_j(r)$ are related to the relative product translational energy. Inserting Eq. (10) into Eq. (9) gives the final result

$$T_{v'v} = \sum_j S_{v',j}F_{j,v} \tag{11}$$

where

$$F_{j,v} = \iint dRdr \; \chi_{v'}(R,r)\phi_{v,j}(R,r) \tag{12a}$$

$$S_{v',j} = \int dr \; \chi_{v'}(R,r)\alpha_j(r) \tag{12b}$$

The half-collision state-to-state reaction probability given by Eqs. (11) and (12) reveals two possible mechanisms for final-state distributions; the $F_{j,v}$ terms [Eq. (12a)] describe the Franck-Condon contributions, while the $S_{v',j}$ terms [Eq. (12b)] represent the half-collision analog of the S matrix in scattering theory. The $S_{v',j}$ matrix elements describe the so-called final-state interactions, which considers product vibrational excitation due to the dynamics of the repulsive surface in the exit channel. Although, final-state interactions play an important role, experimental[2,19] and theoretical[20,21] evidence indicates that the product state distributions are most strongly affected by the multi-dimensional Franck-Condon factors. These results support the strong role that vibrational correlation can play in the interpretation of product rovibrational excitation in terms of the actual vibrational coordinates, amplitudes of motion, and angular momenta corresponding to a particular TS resonance.

References

1. D. M. Neumark, A. M. Wodtke, G. N. Robinson, C. C. Hayden and Y. T. Lee, *J. Chem. Phys.*, **82**, 3045 (1985); D. M. Neumark, A. M. Wodtke, G. N. Robinson, C. C. Hayden and Y. T. Lee, Phys. Rev. Lett., **53**, 226 (1984).

2. R. B. Bernstein, *Chemical Dynamics via Molecular Beam and Laser Techniques* (Oxford University Press, New York, 1982).

3. P. Hering, P. R. Brooks, R. F. Curl, R. S. Judson and R. S. Lowe, *Phys. Rev. Lett.*, **44**, 687 (1980); P. R. Brooks, R. F. Curl and T. C. Maguire, *Ber. Bunsenges. Phys. Chem.*, **86**, 101 (1982).

4. T. C. Maguire, P. R. Brooks, R. F. Curl, J. H. Spence, and S. J. Ulvick, *J. Chem. Phys.* **85**, 844 (1986).

5. P. Arrowsmith, S. H. P. Bly, P. E. Charters and J. C. Polanyi, *J. Chem. Phys.*, **79**, 283 (1983); J. C. Polanyi and R. J. Wolf. *J. Chem. Phys.*, **75**, 5951 (1981).

6. B. A. Collings, J. C. Polanyi, M. A. Smith, A. Stolow, and A. W. Tarr, *Phys. Rev. Lett.* **59**, 2551 (1987).

7. J-C. Nieh and J. J. Valentini, *Phys. Rev. Lett.* **60**, 519 (1988).

8. R. B. Metz, T. Kitsopoulos, A. Weaver, and D. M. Neumark. *J. Chem. Phys.* **88**, 1463 (1988).

9. M. Dantus, M. J. Rosker, and A. H. Zewail, *J. Chem. Phys.* **87**, 2395 (1987).

10. L. R. Khundkar and A. H. Zewail. *Chem. Phys. Lett.* **142**, 426 (1987).

11. T. S. Rose, M. J. Rosker, and A. H. Zewail, *J. Chem. Phys.* **88**, 6672 (1988).

12. J-M. Yuan and T. F. George, *J. Chem. Phys.* **68**, 3040 (1978); K-S. Lam and T. F. George, *J. Chem. Phys.* **76**, 3396 (1982).

13. A. M. F. Lau, *Phys. Rev. A* **16**, 1535 (1977); A. M. F. Lau and C. K. Rhodes, *Phys. Rev. A* **15**, 1570 (1977); J. Jiang and J. S. Hutchinson, *J. Chem. Phys.* **87**, 6973 (1987); J. C. Light, *J. Chem. Phys.* **66**, 5241 (1977).

14. A. E. Orel and W. H. Miller, *J. Chem. Phys.*, **70**, 4393 (1979); *ibid*, **72**, 5139 (1979); *ibid*, **73**, 241 (1980).

15. J. A. Syage, *Chem. Phys. Lett.* submitted.

16. S. Buelow, M. Noble, G. Radhakrishnan, H. Reisler, C. Wittig, and G. Hancock, *J. Phys. Chem.* **90**, 1015 (1986); G. Radhakrishnan, S. Buelow, and C. Wittig, *J. Chem. Phys.* **84**, 727 (1986).

17. A. Laubereau and W. Kaiser, *Rev. Mod. Phys.* **50**, 607 (1978); A. Seilmeier, K. Spanner, A. Laubereau, and W. Kaiser, *Optics Commun.* **24**, 237 (1978)

18. R. P. Feynman, F. L. Vernon, and R. W. Hellwarth, *J. Appl. Phys.* **28**, 49 (1957).

19. J. C. Polanyi, *Science* **236**, 680 (1987).

20. R. H. Bisseling, P. L. Gertitschke, R. Kosloff, J. Manz, *J. Chem. Phys.* **88**, 6193 (1988); R. H. Bisseling, R. Kosloff, J. Manz, *J. Chem. Phys.* **83**, 993 (1985).

21. K. F. Freed and Y. B. Band, in *Excited States, Vol. 3*, edited by E. C. Lim, (Academic, New York, 1977) p. 109; V. Halavee and M. Shapiro, *Chem. Phys.* **21**, 105 (1977); G. C. Schatz and J. Ross, *J. Chem. Phys* **66**, 1021, 1037 (1977).

PHOTOTHERMAL SPECTROSCOPY OF LASER MATERIALS

J.P. Roger, F. Charbonnier, D. Fournier and A.C. Boccara
Laboratoire d'Optique Physique - ER 5 CNRS
ESPCI, 10, rue Vauquelin
75231 Paris Cedex 05 - France

P. Robert
SFENA
B.P. 128
86101 Chatellerault - France

Abstract

The determination of optical absorption of mirrors and other low absorbing materials used in laser optics requires an highly sensitive method. Among the photothermal techniques used for spectroscopic investigation, the photothermal deflection (mirage) seems to be the most convenient one for such a characterization. We first recall the principle and the main detection schemes of mirage spectroscopy. We then describe the two experimental set up we have developed to perform reliable low absorption measurements in coatings and bulky materials at two different laser wavelengths (633 nm and 1.06 µm). The high signal to noise ratio achieved allows for instance the detection of absorption losses as low as 10^{-6} in dielectric coatings deposited on silica with a 30 mW incident power.

1 - INTRODUCTION

During the last decade photothermal methods have been applied to a large number of physical problems and materials characterization, such as : spectroscopic investigation, thermal parameters determination and also non destructive evaluation [1].

We would like to present here the results we have recently obtained in laser materials inspection especially for the determination of absorption losses in these materials.

Let us recall the principle and the sensitivity of a classical optical method for determining the *absorption* of low absorbing samples : the absorption value is deduced from the comparison of three measurements : measurement of the incident, transmitted and reflected powers. Thus, the accuracy becomes very low for absorption of the order or smaller than 10^{-3} time the incident power and can be strongly affected by diffusion losses. In the case of laser mirrors, the techniques based on cavity decay time measurements [2, 3] are highly sensitive. However these measurements integrate all the optical losses (absorption + diffusion + transmission) and the absorption component cannot be separately reached.

In a photothermal experiment, a part of the whole absorbed power being converted into heat, the resulting temperature variations, which are proportional to the absorbed power, are detected. Thus the photothermal signal is directly created by the power absorbed in the sample and the sensitivity of the method only depends on the incident power value and the noise of the detection. The diffusion process does not affect this kind of measurement.

For absorption losses measurement of laser materials, we have used the mirage detection [4] which has been proved to be a very sensitive, non contact, photothermal technique for the low absorbing materials spectroscopy [5]. The aim of this work was first to study multilayered coatings deposited on silica such as mirrors and antireflective coatings ; these coatings being made of stacks of low and high refractive index dielectric layers. We have also checked bulky materials used in laser optics such as silica and non linear optics materials.

2 - PHOTOTHERMAL SPECTROSCOPY BY MIRAGE DETECTION

Both modulated and pulsed excitations have been used in this work. We first consider the case in which the absorbing sample is illuminated by a modulated light source.

2.1. Thermal waves detection.

In order to understand the photothermal detection in the frequency domain, we have to introduce the concept of thermal wave. For a space region periodically heated (frequency f) by a planar source, the temperature variations behave like a damped wave (Fig. 1) :

$$T(x,t) = T_0 \exp(-x/\mu) \cos(2\pi ft - x/\mu) \quad (1)$$

Both the exponential damping and the propagation of this wave are monitored by a

$$T = T_0 \, e^{-\frac{x}{\mu}} \cos\left(2\pi f t - \frac{x}{\mu}\right)$$
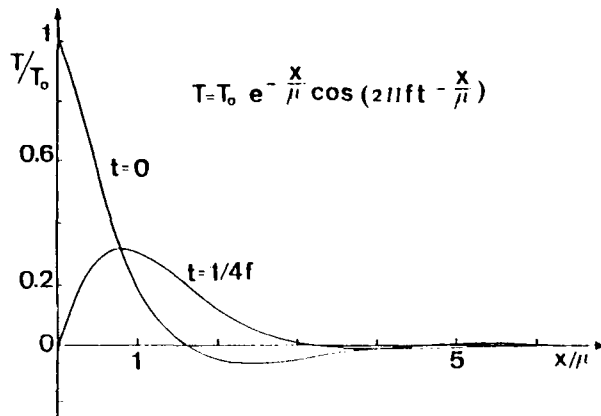
Fig. 1 - Thermal wave : spatial distribution of the periodic temperature at two different times, for a planar heat source $T_0 \cos 2\pi f t$ located at $x = 0$.

characteristic length μ called the thermal diffusion length and defined by :

$$\mu = (D/\pi f)^{1/2} \qquad (2)$$

D is the thermal diffusivity of the medium where the wave propagates. The thermal diffusion length roughly corresponds to the thickness of the layer which is periodically heated.

Some examples of μ values are given in the table 1 for three media : gas, liquid and solid at two frequencies.

	f = 10 Hz	f = 100 Hz
Air	0.8 mm	0.25 mm
CCl$_4$	0.06	0.02
SiO$_2$	0.16	0.05

Table 1. Values of the thermal diffusion lengths in various media, at two frequencies.

Among the various ways to detect the sample heating the mirage detection probes the thermal gradient associated to the thermal wave [4]. A laser beam (probe beam) which propagates through this gradient is deflected because the thermal gradient induces a refractive index gradient. The beam deflection is then measured by a position sensor and a lock in amplifier. The sensitivity of mirage detection is usually limited by the noise of the optical bench which is used to perform this measurement. In our laboratory we have built a mirage cell, described in ref. [6], which leads to the ultimate sensitivity which can be expected for such a detection. The noise corresponds to the shot noise of the position sensor illuminated by the probe beam.

2.2. Experimental schemes.

For spectroscopic characterizations using mirage detection, two experimental schemes can be considered [7] (Fig. 2).

2.2.a. Transverse detection.

In the first one (Fig. 2a) called transverse detection, the beam propagates in front of the heated sample surface and probes the gradient in the fluid adjacent to the absorbing sample. This scheme is usually used when the light source is a classical incoherent one, such as a monochromator or a Fourier transform spectrometer, or when the sample is opaque for the probe beam or has a bad optical quality. For one dimensional heat diffusion, the beam deflection Θ is given by :

$$\Theta = -\frac{L}{n} \frac{\partial n}{\partial T} \frac{\partial T}{\partial x} \qquad (3)$$

where L is the interaction length between the probe beam and the thermal gradient.

From the $\partial n/\partial T$ values reported in table 2, we notice that for transverse detection the use of a liquid, e.g. CCl$_4$, rather than air as deflecting medium leads to a large enhancement of the sensitivity.
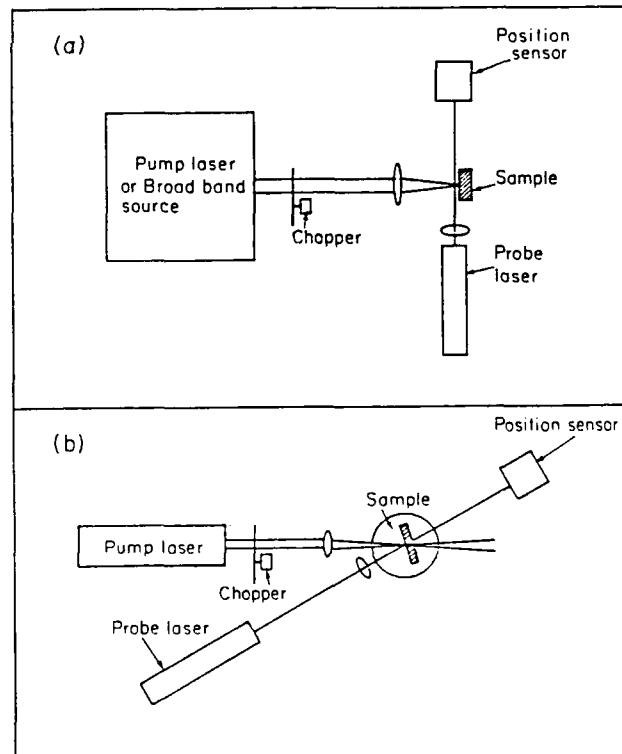
Fig. 2 - Experimental schemes of photothermal deflection spectroscopy : a) transverse detection, b) collinear detection.

	$\partial n/\partial T$ (K^{-1})
Air	-10^{-6}
CCl_4	$-5 \ 10^{-4}$
SiO_2	10^{-5}

Table 2. Temperature coefficient of index of refraction for various media.

A very important application of this scheme is the amorphous semiconductor films spectroscopy [8, 9]. As an example, Fig. 3 shows the photothermal spectrum of a 500 Å thick film of amorphous silicon deposited on silica. This data well illustrates both the sensitivity, better than an absorbance of 10^{-5}, and the large dynamic of the photothermal deflection spectroscopy.

A large number of laboratories working in the field of semiconductor thin films are now using transverse mirage detection for subbandgap absorption measurements.
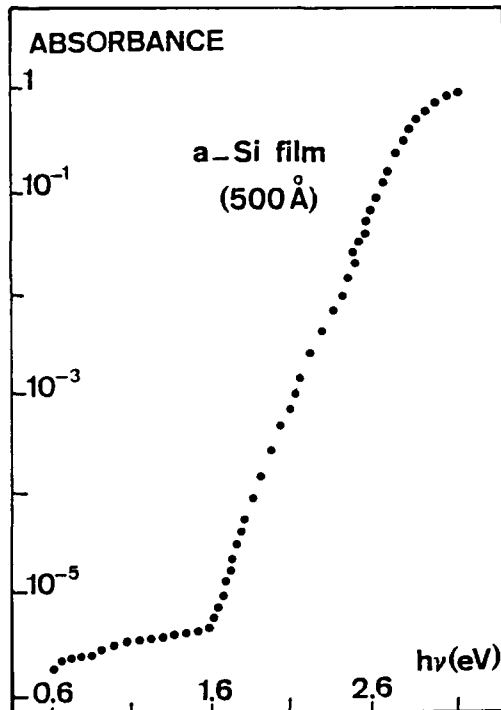
Fig. 3 - Photothermal spectrum of a 500 Å thick amorphous silicon film deposited on silica. The exciting source is a Fourier transform spectrometer and the film is immersed in CCl_4.

2.2.b. Collinear detection.

The figure 2b shows the collinear detection in which the probe beam propagates through the sample and probes the thermal gradient in the sample itself. This scheme leads to a better sensitivity than the previous one when the pump beam can be strongly focused, e.g. laser beam in

the TM_{00} mode. The gradient is created both by the gaussian spatial profile of the excitation and by the radial heat diffusion from this heated region.

We have used such a collinear scheme for laser materials characterization. This detection is suitable for experiments carried out with modulated as well as pulsed excitations. For the simple case of a bulky low absorbing sample and the two kinds of excitations, the theoretical expressions of the beam deflection have been previously given [5, 10] :

- With a modulated source, at high frequency, when the thermal diffusion length of the probed medium is much smaller than the gaussian pump beam radius, the deflection amplitude Θ is given by [5] :

$$\Theta = \frac{L}{n} \frac{\partial n}{\partial T} \frac{\alpha P_0}{n^3 f \rho C a^2} \left[-4 \frac{x_0}{a^2} \exp(-2x_0^2/a^2) \right] \quad (4)$$

where L is the sample thickness, P_0 is the incident laser power, α is the optical absorption coefficient, ρC the heat capacity per unit volume, a is the pump beam radius at $1/e^2$ intensity, x_0 is the separation between the intensity maxima of the pump and probe beams which are assumed to be parallel.

Θ exhibits a maximum for $x_0 = a/2$ which is the position of the maximum gradient of the pump beam profile. Indeed, at high frequency the radial temperature amplitude distribution is well described by the pump beam intensity one.

- With a pulsed source, the energy deposited in the sample during the pulse creates a gaussian temperature distribution which spreads when the heat diffusion occurs. The time dependence of the deflection is given by [10] :

$$\Theta(t) = \frac{L}{n} \frac{\partial n}{\partial T} \frac{4\alpha E_0}{n \rho C} \frac{2x_0}{(a^2+8Dt)^2} \exp \left[-2x_0^2/(a^2+8Dt) \right] \quad (5)$$

where E_0 is the pulse energy.

Figure 4 shows the signal behavior as a function of the time, calculated from this equation, for two probe beam-pump beam distances. If the probe beam is located at the maximum slope of the pump beam profile, the curve a is obtained. From the pulse, the thermal gradient continuously decreases while the heat diffuses. When the probe beam is removed (curve b) a maximum appears in the time dependence. The amplitude of this maximum decreases when the distance x_0 is increased.

If the sample is an absorbing coating deposited on substrate, Eq. (4) and (5) are more complicated, but the behaviors of the deflection signals are governed by the same parameters (the absorbed power (or energy) must be put in place of αP_0 (or αE_0)) and exhibit qualitatively the same features.
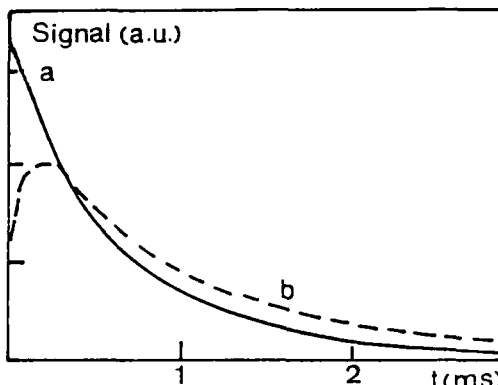
Fig. 4 - Theoretical time dependence of the collinear detection signal in a low absorbing thick sample with a pulsed excitation at t = 0 and for two pump-probe beams distances :

a) $x_0 = a/2$; b) $x_0 = a$.

3 - EXPERIMENTAL SET UP AND RESULTS

We had to determine absorption losses in laser materials at the working wavelength for two kinds of lasers : laser-gyro which uses a He-Ne laser (633 nm) and Nd^{3+}YAG laser (1.06 μm).

3.1. Laser-gyro mirrors characterization.

The aim of the first study was to build a set up which enables us to measure optical absorption losses in laser-gyro mirrors smaller than ten part per million. Since such losses strongly affect the performances of laser-gyro, it was of great interest for SFENA Company, which builds this device, to get close to a production line a fast, sensitive and accurate way of characterizing the absorption losses.

The collinear detection set up is shown in Fig. 5. The main component part is the previously mentioned low noise compact mirage cell [6]. Since the multidielectric mirrors under test are highly reflective at He-Ne laser wavelength, a laser diode (780 nm) for which reflection level is rather small is used as probe laser. The pump beam comes from a 30 mW He-Ne laser
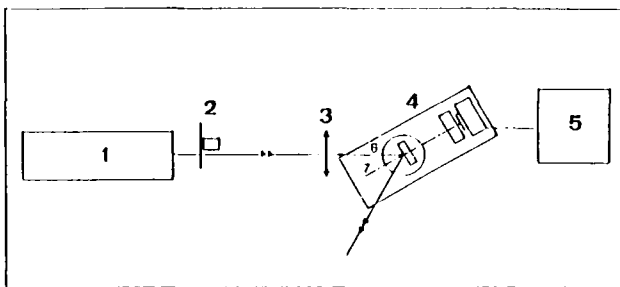
Fig. 5 - Experimental set up for absorption measurements of laser-gyro mirrors : 1) He-Ne pump laser, 2) chopper, 3) lens, 4) compact mirage cell, 5) lock-in amplifier, 6) focused He-Ne pump beam, 7) laser diode probe beam.

and is modulated by a chopper at 200 Hz. The lens which focusses the pump beam can be moved with an accuracy better than 1 μm in order to reach the maximum signal amplitude. This amplitude being proportional to the absorbed power constitutes the measured quantity for a given coating.

At 200 Hz, the thermal diffusion length μ is much larger than the coating thickness. A substrate thickness of the order of μ is then periodically heated and the radial temperature gradient is mainly probed within the transparent SiO_2 substrate. Thus the signal depends on the thermo-optical properties $(\partial n/\partial T, D, \Gamma C)$ of the substrate alone.

The measured quantity is proportional to the absorbed power in the coating but also depends on a lot of thermal, optical and geometrical parameters for which an accurate determination is critical. The simplest way to deduce the absolute value of the absorption from the measurement is then to calibrate the set up. For such a calibration, the photothermal signal given by a strongly absorbing coating deposited on the same substrate is measured. On the other hand, this coating absorption can be easily determine by a classical reflection transmission measurement. For instance, the coating used in this work absorbs ten percent of the incident power.

Finally, the sensitivity reached by using this set up corresponds to absorption level as low as one part per million and the measurements are reproducible within a few percents. Let us point out that the set up is now setting in an industrial environment where the same satisfactory performances are obtained.

3.2. Nd^{3+} YAG laser materials characterization.

The second part of this work was done in the framework of the EUREKA project and was devoted to the absorption losses determination of new YAG laser materials : mirrors, antireflective coatings and "transparent" materials used in laser optics. Such measurements are made necessary because these various components belong to the part of the future multikilowatt YAG laser and that a high level of absorption losses may induce severe irreversible damages.

For this characterization, we have used a set up design similar to the previous one (Fig. 5). However in this case the pump beam comes from a pulsed YAG laser. This laser usually gives a few nanosecond pulses. In order to avoid optical damages of the samples due to high peak power, the Q-switch in the cavity has been suppressed. Thus the laser works in the relaxed mode with a pulse duration of about 100 μs. The pulse energy is 30 mJ and the pump beam radius 60 μm. The signal of the position sensor is amplified by a broad band amplifier and stored by a digital oscilloscope. Then, the signal is averaged

signal (a.u.)

0.5   1   **t(ms)**
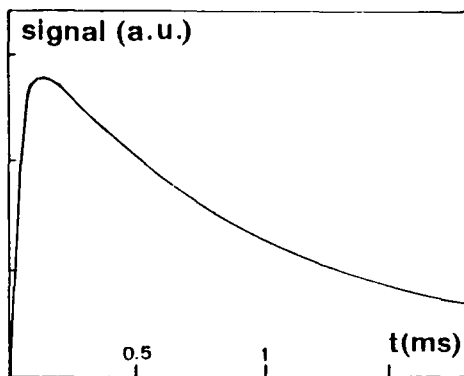
Fig. 6 - Photothermal signal vs time, after 100 scans, for a mirror of 20 ppm absorption level.

for a number of pulses in order to get a suitable signal to noise ratio.

Figure 6 shows the signal as a function of the time, after 100 scans, for a mirror which absorbs 20 ppm of the incident energy. The maximum amplitude is reached after 100 µs which is about the pulse duration. During the pulse the heat diffuses in the media over a distance of about 10 µm. Since the coating thicknesses are of the order of or smaller than 1 µm, the main component of the deflection signal comes from the substrate. The measured quantity for a given coating is the maximum signal amplitude and as previously the set up is calibrated by measuring a strongly absorbing sample. For a coating deposited on silica, the lowest absorption level which can be detected by the set up is of the order of 10^{-7}.

We have checked a lot of coatings : monolayers, mirrors and antireflective coatings made of various materials. Some typical results are reported in table 3.

Coating	Material	Absorption (ppm)
Mono-layers	MgF_2	4.7
	ZrO_2	6.6
	CeO_2	340
	Y_2O_3	9.5
	Al_2O_3	22
	Ta_2O_3	5
	SiO_2	1
Mirrors	TiO_2/SiO_2	19
	TiO_2/SiO_2	120
	ZrO_2/SiO_2	10.3
	Ta_2O_5/SiO_2	14.3
	Ta_2O_5/SiO_2	7.5
Antire-flective coating	Ta_2O_5/SiO_2	8

Table 3 - Composition and absorption values for various kinds of coatings deposited on silica.

At last, let us point out that with this set up we have been able to measure the absorption coefficient of several millimeters thick samples of silica and of non linear optics materials. In this case, pump and probe beams intersect in the bulk of the sample and calibration is performed by using water which gives a very strong signal at 1.06 µm. The signal equivalent to noise corresponds to an absorption coefficient of a few 10^{-6} cm^{-1} for a sample which has the thermal properties of silica.

4 - CONCLUSION

The reported results shows that collinear mirage detection is a very sensitive and quantitative method to determine very low absorption losses in coatings and also in bulky materials. The two described set up enables us to measure, for a coating deposited on silica, absorption level as low as 10^{-6} by using a 30 mW modulated laser as pump beam and 10^{-7} with a 30 mJ pulsed laser.

REFERENCES

1. "Photoacoustic and Photothermal Phenomena". Springer Series in Optical Sciences. Vol. 58, edited by P. Hess and J. Pelzl (Springer Verlag, Berlin, 1988).

2. J.M. Herbelin, J.A. McKay, M.A. Kwork, R.H. Ueunten, D.S. Urevig, D.J. Spencer and D.J. Benard. Appl. Opt. 19, 144(1980).

3. P. Elleaume, M. Velghe, M. Billardon and J.M. Ortega. Appl. Opt. 24, 2762 (1985).

4. A.C. Boccara, D. Fournier and J. Badoz, Appl. Phys. Lett. 36, 130 (1980).

5. A.C. Boccara, D. Fournier, W. Jackson and N.M. Amer. Opt. Lett. 5, 377 (1980).

6. F. Charbonnier and D. Fournier, Rev. Sci. Instrum. 57, 1126 (1986).

7. W.B. Jackson, N.M. Amer, A.C. Boccara and D. Fournier. Appl. Opt. 20, 1333 (1981).

8. N.M. Amer and W. Jackson, in Semiconductors and Semimetals, Vol. 21B, ed. J.I. Pankove (Academic Press, New York, 1984) p. 83.

9. K. Driss-Khodja, A. Gheorghiu and M.L. Theye, Opt. Comm. 55, 169 (1985).

10. O. Benchikh, D. Fournier, A.C. Boccara and J. Teixeira. J. Physique 46, 727 (1985).

PHOTOTHERMAL SPECTROSCOPY: THE PHASE-SHIFT, DEFLECTION, AND LENSING TECHNIQUES

R. Gupta
Department of Physics
University of Arkansas
Fayetteville, AR 72701

Abstract

A unified description of the photothermal phase-shift, deflection, and lensing spectroscopies is given. Both cw and pulsed cases are considered.

There is presently an extensive interest [1,2,3] in the techniques of photothermal spectroscopies, as many applications of these techniques have recently been found. Photothermal spectroscopies consist of three separate but related techniques: photothermal phase-shift spectroscopy, photothermal deflection spectroscopy, and photothermal lensing spectroscopy.

The basic idea underlying these techniques is simple: A laser beam (pump beam) passes through the medium of interest. The laser is tuned to an absorption line of the medium, and the optical energy is absorbed by the medium. If the collisional quenching rate in the medium is much higher than the radiative rate, most of this energy appears in the rotational-translational modes (heating) of the molecules. The heating of the medium modifies the refractive index of the laser irradiated region. The change in the refractive index of the medium is detected by a second (generally a HeNe) laser beam (probe beam). Three distinct methods of monitoring the refractive index change of the pump-beam-irradiated region are considered. In photothermal phase-shift spectroscopy (PTPS), the refractive index change is measured directly by placing the sample inside a Fabry-Perot cavity or in one arm of a Michelson interferometer. The refractive index change produces a change in the optical pathlength which is detected as a fringe-shift. The probe beam produces the interference fringes while the pump beam causes the refractive index change. In photothermal deflection spectroscopy (PTDS), a deflection of the probe beam is observed. The pump beam has a spatial profile (generally assumed to be a Gaussian), therefore, the refractive index of the pump-beam-irradiated region also acquires a similar spatial profile. This non-uniform refractive index causes a deflection of the probe beam, which can easily be detected by a position-sensitive optical detector. The signal is proportional to the gradient of the refractive index. The non-uniform refractive index also produces a lensing effect in the medium. A probe beam passing through the medium changes shape, resulting in a change in the intensity of the probe beam passing through a pin-hole. In this technique, the signal is proportional to the second derivative of the refractive index. This technique is called the photothermal lensing spectroscopy (PTLS). Historically, the three photothermal techniques have been discovered and developed separately. PTPS was discovered by Stone[4] and by Davis[5], and has found applications primarily in analytical chemistry. PTDS was discovered by Amer, Boccara, Fournier and collaborators [6,7,8,9] and has been found to be a very useful diagnostic tool. PTLS is the oldest[10,11] and has found applications, among other things, in analytical chemistry and in the measurement of collisional relaxation rates of molecules[12].

We have recently developed a rigorous theoretical model of this subject[13-17]. A unified treatment of all three detection schemes (PTPS, PTDS, PTLS) is given. No approximations are made, except that the medium is weakly absorbing. The theory is valid under the most general conditions, i.e., for both stationary and flowing media, and both pulsed (any pulse length) and cw (modulated as well as unmodulated) excitation. The theory predicts many interesting effects. In this paper we give a brief outline of the theory and describe some of the important results.

Central to the photothermal techniques is the creation of a temperature distribution by the absorption of the pump beam, and its subsequent evolution due to thermal diffusion and forced convection (flow). This temperature distribution is given by the solution of the differential equation[17]

$$\frac{\partial T(\vec{r},t)}{\partial t} = D\nabla^2 T(\vec{r},t) - v_x \frac{\partial T(\vec{r},t)}{\partial x} + \frac{1}{\rho C_p} Q(\vec{r},t) \,, \tag{1}$$

where $T(\vec{r},t)$ is the temperature above the ambient, v_x is the flow velocity of the medium which is assumed to be in the x-direction, D is the diffusivity, ρ is the density, and C_p is the specific heat at constant pressure of the medium. The first, second, and the third terms on the right in Eq. (1) represent, respectively, the effects of the thermal diffusion, flow, and the heating due to the pump beam absorption.

We assume that the pump beam propagates through the medium in the z-direction and it is centered at the origin of the coordinate system. We further assume that the medium is weakly absorbing. If the pump laser is a pulsed one, the heat produced per unit volume per unit time by the absorption of laser energy is given by

$$Q(x,y,t) = \alpha I(x,y,t)$$

$$= \begin{cases} \dfrac{2\alpha E_0}{\pi a^2 t_0}\, e^{-2(x^2+y^2)/a^2} & \text{for } 0 \le t \le t_0 \\[2em] 0 & \text{for } t > 0 \ , \end{cases} \tag{2}$$

where α is the absorption coefficient of the medium and $I(x,y,t)$ is the intensity of the laser beam. Implicit in Eq. (2) is the assumption that all of the absorbed laser energy is converted to heat and only a negligible portion is radiated as fluorescence. It is further assumed that this conversion of optical energy into heat takes place in a time scale much shorter than the typical thermal diffusion time in that medium. The total energy in each laser pulse is assumed to be E_0. The spatial profile is assumed to be a Gaussian with $1/e^2$-radius a. It is further assumed that the laser pulse turns on sharply at t=0 and turns off sharply at $t=t_0$. The assumption of a rectangular temporal profile is a good one, if the rise and fall times of the laser pulse are very short compared to the thermal diffusion and convection times. Solution of Eq. (1), with the source-term Q given by Eq.(2) is found[13,17] to be

$$T(x,y,t) = \frac{2\alpha E_0}{\pi t_0 \rho C_p} \int_0^{t_0} \frac{1}{[a^2 + 8D(t-\tau)]}$$

$$\times \exp\left[-2\{[x-v_x(t-\tau)]^2 + y^2\} / \{a^2 + 8D(t-\tau)\} \right] d\tau$$

$$\text{for } t > t_0 \tag{3}$$

For a short laser pulse ($t_0 < 10 \mu s$), Eq.(3) can be written in a closed form[13]. However, for longer pulses Eq. (3) must be integrated numerically. This integration may be conveniently performed using one of the commonly available subroutines in IMSL (International Mathematics and Statistics Library). Equation (3) predicts that the heat pulse has a nearly-Gaussian spatial profile, it moves downstream with the medium, and as it does so, it broadens due to thermal diffusion[13].

In many situations it is more desirable to use a cw laser source for the pump beam. Photothermal signals can be measured conveniently if the cw laser is amplitude modulated at some frequency ω, because then a phase-sensitive detection can be used. In this case, the source term may be written as

$$Q(x,y,t) = \frac{2\alpha P_{av}}{\pi a^2}\left[e^{-2(x^2+y^2)/a^2} \right] (1 + \cos \omega t), \tag{4}$$

where P_{av} is the average power of the pump beam in the presence of the modulation. The spatial profile is again assumed to be Gaussian with $1/e^2$-radius a, and the degree of modulation is assumed to 100%. Solution of Eq. (1), with the source term given by Eq. (4), is found[14,17] to be

$$T(x,y,t) = \frac{2\alpha P_{av}}{\pi \rho C_p} \int_0^{t} \frac{(1 + \cos \omega \tau)}{[a^2 + 8D(t-\tau)]}$$

$$\times \exp\left[-2\{[x- v_x(t-\tau)]^2 + y^2\} / \{ a^2 + 8D(t-\tau)\} \right] d\tau. \tag{5}$$

The integration over τ may be performed using the 64-point Gaussian quadrature[14].

606

(a)

(b)
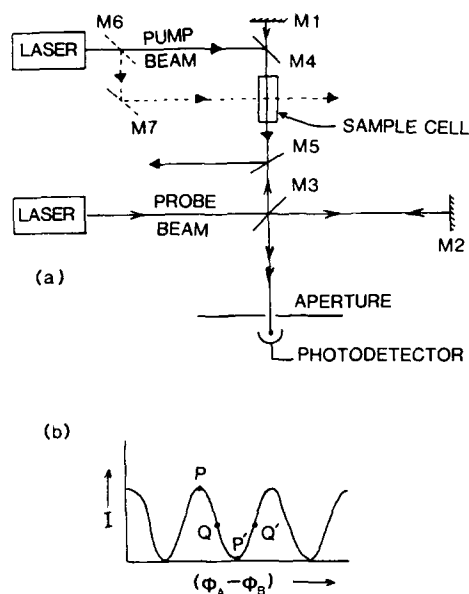
Fig. 1: Schematic illustration of
photothermal phase shift
spectroscopy (PTPS) experiment.
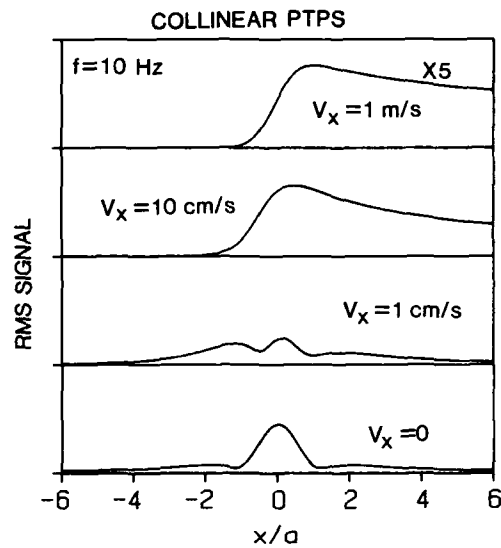
Fig. 3: Computed values of the RMS PTPS
signal for cw excitation and for flow
velocities as labeled.
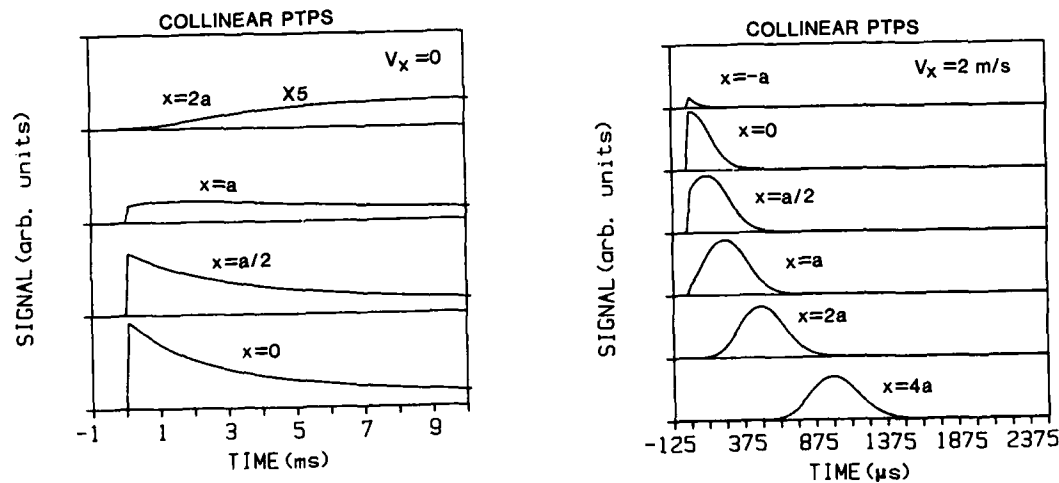
Fig. 2: Computed PTPS signals with pulsed excitation for a (a) stationary
medium, and (b) for a medium flowing with a velocity of 2 m/s.

(i) Photothermal Phase-Shift Spectroscopy (PTPS)

A typical experimental arrangement for PTPS is shown in Fig.1. The sample cell is placed in one arm of a Michelson interferometer. A change in the refractive index of the medium, caused by the absorption of the pump beam, is detected as an intensity change at the detector. M4 and M5 are dielectric mirrors which totally transmit the probe beam and totally reflect the pump beam. Broken lines show transverse PTPS while the solid lines show the collinear PTPS. The intensity change at the detector is given by[15,17]

$$\delta V(x,y,t) = V \cos[(\theta_A - \theta_B) - \gamma(x,y,t)] \tag{6}$$

where V is a constant that depends on the intensity of the probe beam and $\gamma(x,y,t)$ is the phase difference introduced by the pump beam. $(\phi_A - \phi_B)$ is the phase difference between the two interfering waves in the absence of the pump beam, and it determines the "operating point" on the intensity curve (Fig. 1(b)). If $(\phi_A - \phi_B) = m\pi$, the operating point is either p or p', and the intensity is quite insensitive to small changes in γ. On the other hand, if $(\phi_A - \phi_B) = (m+1/2)\pi$, the operating point is either Q or Q', and the intensity is quite sensitive to small changes in γ. The phase difference $\gamma(x,y,t)$ is given by

$$\gamma(x,y,t) = \frac{4\pi}{\lambda} \int_{path} \Delta n(x,y,t)ds \tag{7}$$

where the integration is carried out over the path of the probe beam. The change in the refractive index $\Delta n(x,y,t)$ is given by

$$\Delta n(x,y,t) = (n_0 - 1)\frac{T(x,y,t)}{T_A} \tag{8}$$

where T_A is the ambient temperature. Therefore the PTPS signal is given by (assuming $(\phi_A - \phi_B) = (m+1/2)\pi$)

$$\delta V = V \sin\left(\frac{4\pi}{\lambda}\frac{(n_0-1)}{T_A} \int_{path} T(x,y,t)ds\right) \tag{9}$$

where $T(x,y,t)$ is given either by Eq.(3) or by Eq.(5). For the collinear case the pump and the probe beams are both in the z-direction (ds=dz), and for the transverse case the pump beam propagates in the z-direction while the probe beam propagates in the y-direction (ds=dy). The integration over ds in Eq. (9) is straightforward.

Figure 2(a) shows the pulsed PTPS signals for the collinear case calculated using Eq.(9) for a stationary medium ($v_x=0$). Four curves are shown, for x=0,a/2,a, and 2a. The signal has the largest amplitude for x=0, since the change in the refractive index is the maximum at this position. The intensity of light at the detector suffers a transient change when the pump laser is fired and returns to its original value as the heat diffuses out of the region. As the distance between the pump and the probe beams is increased, the signal becomes smaller and broader. When the probe beam is outside the pump beam (x=2a), the heat arrives at the probe beam position via thermal diffusion, and therefore the peak signal occurs later in time and it is weak and broad. Signal shapes for a flowing medium (collinear case) are shown in Fig. 2(b). The flow velocity of the medium is assumed to be $v_x=2m/s$. A positive value of x corresponds to the probe being downstream from the pump beam. Signal shape is essentially the spatial profile of the pump beam broadened by thermal diffusion.

Some of the predictions of cw collinear PTPS are shown in Fig. 3. RMS values of the PTPS signals have been plotted against the distance between the pump and the probe beams, x, for a modulation frequency of 10 Hz. This distance has been expressed in units of the $1/e^2$-radius of the pump beam. The distance x is taken to be positive downstream. Four curves are shown, for $v_x=0$, 1 cm/sec, 10 cm/sec, and 1 m/sec. As the velocity increases, these curves become more and more asymmetric with the signal extending far to the right side (downstream). Low and zero velocity curves show interesting undulations. These undulations are a direct consequence of the change in temperature distribution as the pump beam intensity oscillates[15].
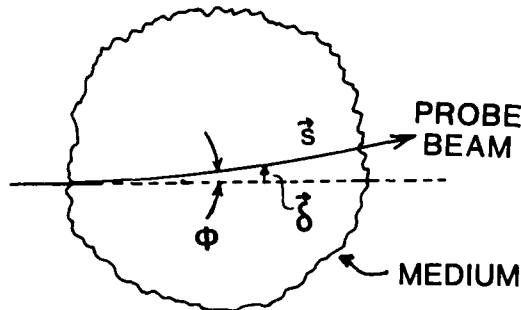
Fig. 4: Deflection of a probe beam propagating in an inhomogeneous medium.

COLLINEAR PTDS

Fig. 6: RMS values of the computed cw PTDS signals for flow velocities as labeled.

Fig. 5: Computed PTDS signals for pulsed excitation in a (a) medium moving with a velocity 2 m/s, and (b) in a stationary medium.
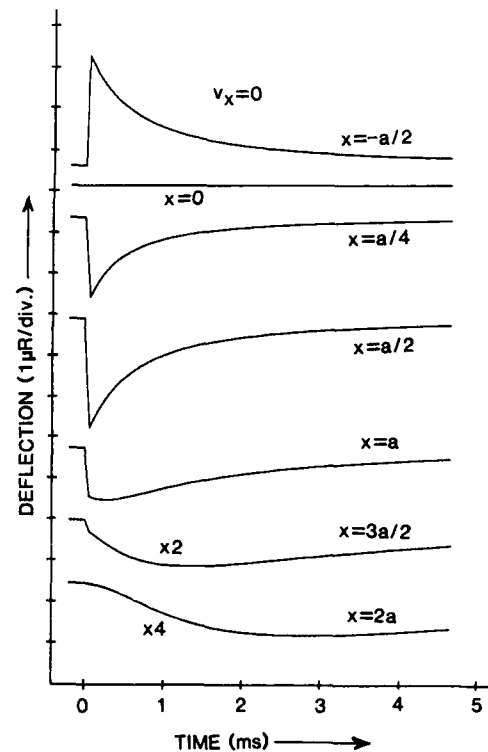
(ii) Photothermal Deflection Spectroscopy (PTDS)

The propagation of an optical beam in a medium of inhomogeneous refractive index is governed by the equation[13,17]

$$\frac{d}{ds}\left(n\frac{d\vec{\delta}}{ds}\right) = \vec{\nabla}_\perp n ,$$

(10)

where $\vec{\delta}$ is the perpendicular displacement of the beam (see Fig. 4) and $\vec{\nabla} n$ is gradient of the refractive index perpendicular to the beam path s. The refractive index $n(x,y,t)$ is related to the unperturbed refractive index n_0 (in the absence of the pump beam) by

$$n(x,y,t) = n_0 + \frac{\partial n}{\partial T}\Big|_{T_A} T(x,y,t) .$$

(11)

Therefore, for small deflection, the deflection angle ϕ in the x-direction may be written as

$$\phi(x,y,t) = \frac{1}{n_0}\frac{\partial n}{\partial T}\int_{path}\frac{\partial T(x,y,t)}{\partial x} ds ,$$

(12)

where $T(x,y,t)$ is given either by Eq. (3) or by Eq. (5). The differentiation with respect to x can be performed inside the τ-integral, the integration over ds is straightforward (ds=dz for collinear and ds=dy for transverse) and the τ-integration is performed numerically.

Fig. 5(a) shows some of the results predicted by Eq. (12) for the pulsed excitation. The transverse photothermal deflection has been plotted as a function of time for different positions of the probe beam. A positive value of x corresponds to the probe beam being downstream from the pump beam. We note that as the probe beam is moved upstream, the signal becomes smaller and narrower quickly because the heat has to diffuse against the gas flow. As the probe beam is moved downstream, the signal gets stronger at first and then acquires a shape which is essentially the derivative of the spatial profile of the pump beam (which is assumed to be a Gaussian here). As x is increased further, the signal becomes broader and smaller due to thermal diffusion. Fig. 5(b) shows results similar to those of Fig. 5(a) but in a stationary medium ($v_x=0$ in Eq. 12)). In this case, the signal is zero for x=0 because $\partial T/\partial x$ is zero at this point, and reverses sign as x changes sign, as expected. For small values of x($0<x<a$) the signal consists of a sharp deflection of the probe beam shortly after the pump laser firing, followed by a gradual return of the probe beam to its original position on the time scale of the diffusion time of the heat out of the probe region. The signal attains its maximum value for x=a/2 where the gradient of $T(x,y,t)$ is a maximum. For larger values of x, the peak of the signal occurs later in time, and the signal is broader and weaker, as expected.

Figure 6 shows the cw PTDS signals for the collinear case. RMS values of the deflection have been plotted as a function of the distance x between the pump and the probe beams for four velocities $v_x=0$, $v_x=1$ cm/sec, $v_x=10$ cm/sec, and $v_x= 1m/sec$. Solid lines are for modulation frequency of 10 Hz while the dotted lines are for 100 Hz modulation frequency. As the flow velocity of the medium increases, the curves become more and more asymmetric, as expected. Note that for large velocities, the signal downstream becomes very small even though a significant temperature distribution (above ambient) exists. This is because the gradient of the temperature in this region is very small. In order to understand the dip in the signal at x=a($v_x=1m/s$), one must examine the change in the temperature gradient as the pump laser intensity oscillates[14]. We also note that as the modulation frequency increases, the signal amplitude in general decreases, and for $v_x=0$, the signal peaks occur closer to x=a/2 because the heat is able to diffuse only a shorter distance during the modulation cycle.

(iii) Photothermal Lensing Spectroscopy (PTLS)

Figure (7) shows a typical scheme for the detection of a thermal lens. A thermal lens (sample with the pump beam passing through it) is placed a distance z_1 in front of the probe beam waist. A screen with a pin-hole is placed a distance z_2 in front of the thermal lens. Intensity of the probe beam passing through the pin-hole is observed by a photodetector. If the focal length of the thermal lens $f>>z_2$ (which is generally the case), and $z_2>>z_1$ (which can generally be arranged), then the signal s(t), defined as the fractional change of the probe beam power at the photodetector is[16,17]
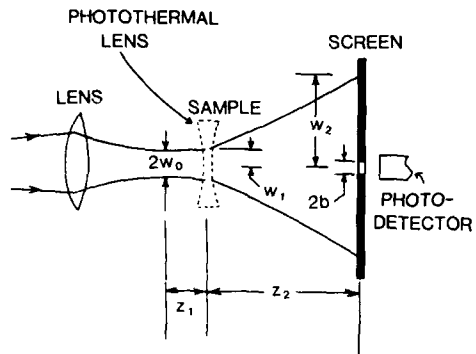
Fig. 7: Schematic illustration of a photo-thermal lensing experiment.
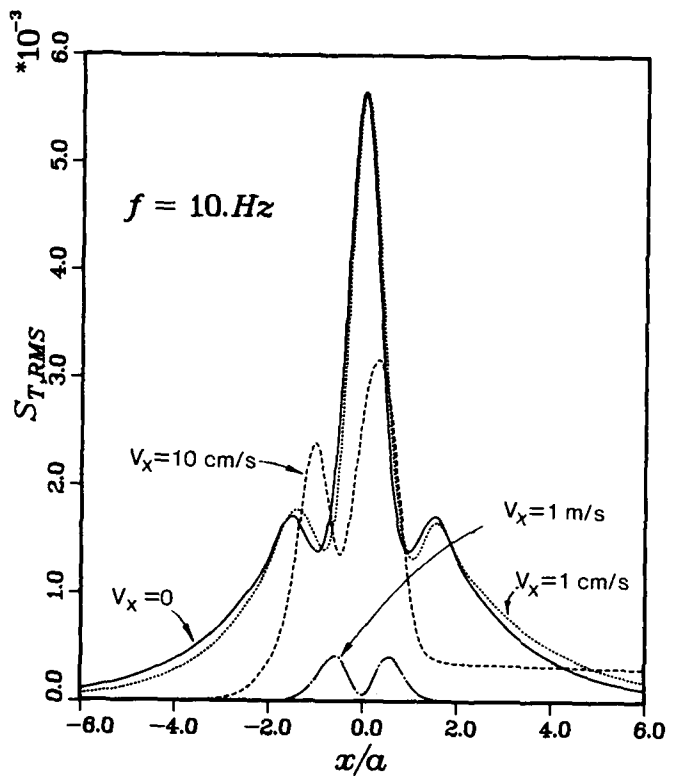
Fig. 9: Computed PTLS signals for cw excitation and for flow velocities as labeled.
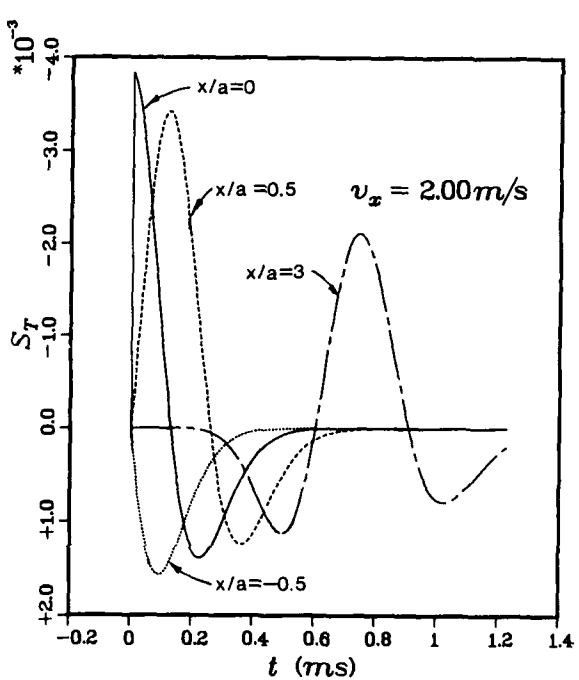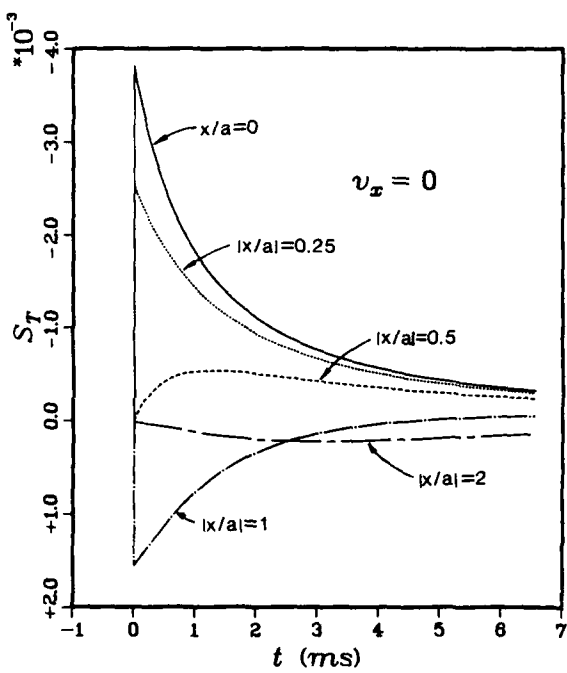
Fig. 8: Computed PTLS signals for pulsed excitation in a (a) stationary medium, and (b) in a flowing medium.

$$s(t) = z_1 \left(\frac{1}{f_x(t)} + \frac{1}{f_y(t)} \right) \qquad . \tag{13}$$

where f_x and f_y are the focal lengths of the (astigmatic) thermal lens in the x- and the y-directions. They are given by[16,17]

$$\frac{1}{f_x} = -\frac{\partial n}{\partial T} \int_{path} \frac{\partial^2 T(x,y,t)}{\partial x^2} \, ds \tag{14}$$

and

$$\frac{1}{f_y} = -\frac{\partial n}{\partial T} \int_{path} \frac{\partial^2 T(x,y,t)}{\partial y^2} \, ds. \tag{15}$$

The PTLS signal is then given by Eq. (13), with Eqs. (14) and (15), and T(x,y,t) given by either Eq. (3) or by Eq. (5). Again, the differentiations with respect to x and y can be performed inside the τ-integral, the integration over ds is straightforward, and the τ-integral is evaluated numerically.

Figure 8(a) shows a few typical pulsed PTLS signals in a stationary medium for the transverse case. The fractional change in the power at the detector has been plotted against time. A negative value of the signal corresponds to a diverging lens, while a positive value corresponds to a converging lens. For $|x| < 0.5a$, the photothermal lens behaves like a diverging lens. For $|x|=0.5a$ the signal vanishes at t=0 (because the second derivative of temperature is zero at this place). However, for t>0 some signal gets generated by the heat diffusing out from the inside of the pump beam. For $|x|>0.5a$, the photothermal lens behaves like a converging lens. Figure 8(b) shows pulsed PTLS signals in a flowing medium for the transverse case. In this case, the thermal lens travels downstream with the flow of the medium. The signal at x=3a shows the shape of the signal due to the entire lens. The thermal lens is a diverging lens in the center while it is a converging lens in the wings.

Figure 9 shows the cw PTLS signals for the transverse case. The RMS value of the signal is plotted against the pump-probe distance for modulation frequency of 10Hz. A stationary medium, and flow velocities of 1 cm/s, 10 cm/s, and 1 m/s are considered. The signal is symmetric about x=0 for $v_x=0$, and this symmetry is lost as v_x is increased, as expected. The apparent symmetry of the signal for $v_x=1$ m/s is fortuitous. For $v_x=0$, the signal consists of three peaks; the central peak corresponds to a diverging lens while the side peaks correspond to a converging lens. For higher velocities ($v_x>10cm/s$), the peaks on the left correspond to converging lenses, while those on the right correspond to diverging lenses.

References

1. R. Gupta, in Proceedings of the International Conference on Lasers '86, R.W. McMillan, Editor (STS Press, McLean, VA, 1987).

2. A.C. Tam, Rev. Mod. Phys. 58, 381 (1986).

3. S.E. Bialkowski, Spectroscopy 1, 26 (1986).

4. J. Stone, J. Opt. Soc. Am. 62, 327 (1972); Appl. Opt. 12, 1828 (1973).

5. C.C. Davis, Appl. Phys. Lett. 36, 515 (1980).

6. A.C. Boccara, D. Fournier, W.B. Jackson, and N.M. Amer, Opt. Lett. 5, 377 (1980).

7. A.C. Boccara, D. Fournier, and J. Badoz, Appl. Phys. Lett. 36, 130 (1980).

8. D. Fournier, A.C. Boccara, N.M. Amer, and R. Gerlach, Appl. Phys. Lett. 37, 519 (1980).

9. W.B. Jackson, N.M. Amer, A.C. Boccara, and D. Fournier, Appl. Opt. 20, 1333 (1981).

10. J.P. Gordon, R.C.C. Leite, R.S. Moore, S.P.S. Porto, and J.R. Whinnery, J. Appl. Phys. 36, 3 (1965).

11. C. Hu and J.R. Whinnery, Appl. Opt. 12, 72 (1973).

12. H.L. Fang and R.L. Swofford, in Ultrasensitive Laser Spectroscopy, David S. Kliger, Editor (Academic, NY, 1983).

13. A. Rose, Reeta Vyas, and R. Gupta, Appl. Opt. 25, 4626 (1986).

14. Reeta Vyas, B. Monson, Y.-X. Nie, and R. Gupta, Appl. Opt. 27, 3914 (1988).

15. B. Monson, Reeta Vyas, and R. Gupta, Appl. Opt. (submitted for publication, 1988).

16. Reeta Vyas and R. Gupta, Appl. Opt. 27, 4701 (1988).

17. R. Gupta, to be published in Photothermal Investigations of Solids and Fluids, Jeffrey A. Sell, Editor (Academic, NY, 1988).

Radiative Collisions in the Strong Field Regime

T. F. Gallagher[+], P. Pillet[†],

[+]Department of Physics
University of Virginia
Charlottesville, VA 22901, USA

[†] Laboratoire Aime Cotton
CNRS II, Bat 505 Campus d'Orsay
91405 Orsay Cedex, FRANCE

Abstract

Using Rydberg atoms in strong microwave fields we have studied radiatively assisted collisions in which the field is too strong to be treated perturbatively. Collisions in which the stimulated emission of up to four photons are absorbed have been observed, and a theory based on resonant collisional energy transfer between dressed atomic states has been developed to fit the data.

I. Introduction

A Radiatively Assisted Collision is one in which two atoms absorb or are stimulated to emit a photon during the collision. This process was first discussed under this name by Gudzenko and Yakovlenko.[1] Since typical atomic collisions do not last very long, $\sim 10^{-12}$s, an intense laser is needed to drive the process, and after the development of intense tunable dye lasers it was studied experimentally by several research groups, beginning with the work of Falcone et al.[2-5] There is, however, an alternative approach to studying this process, line broadening, in which, instead of having few atoms and many photons, there are many atoms and not few photons. In the perturbative limit the two approaches lead to the same result as has been shown by Gallagher and Holstein.[6]
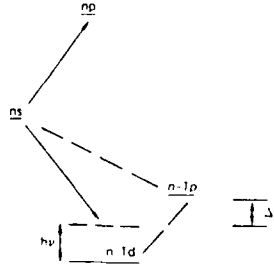
Figure 1 - Energy level diagram for two ns atoms to collide while emitting a photon. This leaves the atoms in the np and (n-1)d states

If we return to the radiative collision point of view, it is apparent that a major problem is the fact that the short duration of atomic collisions requires enormous optical powers to drive a radiatively assisted collision. Let us consider doing analogous experiments with Rydberg atoms. For a start we consider a resonant dipole-dipole collision process. The dipole-dipole interaction matrix element is approximately given by

$$H_I = \frac{\mu_1 \mu_2}{r} \qquad (1)$$

where μ_1 and μ_2 are the transition matrix elements of the two colliding atoms and r is the internuclear separation of the two atoms. We may derive a cross section by finding the impact parameter b

for which $H_I \cdot T = 1$ where T is the duration of the collision. Approximating T by b/v, v being the collision velocity, and using $r \sim b$ in H_I leads to the requirement

$$\frac{\mu_1 \mu_2}{b^3} \cdot \frac{b}{v} = 1 \qquad (2)$$

This yields immediately $b^2 = \mu_1 \mu_2 / v$. For Rydberg atoms $\mu \sim n_2$, so $b^2 = n^4/v$. The collision time T is obtained using this value of b,

$$T = \frac{n^2}{v^{3/2}} \qquad (3)$$

The cross section σ_0 is given by b^2,

$$\sigma_0 = \frac{n^4}{v} \qquad (4)$$

For typical thermal velocities, which are $10^{-4} - 10^{-3}$ atomic units, and n ~ 20, we find cross sections of 10^9Å^2 and collision times in excess of 1ns. Such collision times are several orders of magnitude longer than typical atomic collision times, making Rydberg atoms excellent candidates for the study of radiative collisions. In fact collision times in excess of 0.1 us have been observed.[7] A radiative collision, in which the energy resonance is produced with a microwave photons is shown in Figure 1. The dipole-dipole interaction of Eq. 1 is replaced by

$$H_I = \frac{\mu_1 \mu_2}{r} \frac{\mu_3 E}{\Delta} \qquad (5)$$

Here μ_1 is the ns-np transition matrix element of one atom, and μ_2 and μ_3 are the ns-(n-1)p and (n-1)p-(n-1)d transition matrix elements of the second atom, E is the microwave field amplitude and Δ is the detuning of the virtual intermediate level. For this collision to be as probable as a ns + ns → np + (n-1)p resonant collision the factor $\mu_3 E/\Delta$ must be of order one. This requirement gives us a requirement on the microwave electric field

$$E = \frac{\Delta}{\mu_3} \qquad (6)$$

The field required may be estimated, using $\Delta = 1 \text{ cm}^{-1}$ and $\mu_3 \sim 400 \text{ ea}_0$, to be ~ 50 V/cm which is a power level of ~ 6 W/cm². many orders of magnitude below the powers used in the optical experiments. We note that the estimate of Eq. (6) is to produce a radiatively assisted collision as strong as a resonant dipole dipole collision, a distinctly nonperturbative situation. The power levels mentioned, 6 W/cm² are modest, so it is not unreasonable to consider exploring the regime in which the microwave field has a strong effect on the collision.

614

II. Experimental Approach and Observations

In Figure 2 we show Na energy levels in an electric field. In a field the 18p and 17p levels both shift to higher energies, and at a field of ~400V cm the 18s state is midway between the two p states. Allowing resonant collisional energy transfer in the collision of two 18s atoms. At slightly lower fields collisions which become resonant upon the stimulated emission of one, two, or three microwave photons can be observed.[8] The experiments are carried out by exciting atoms to the 18s state and detecting those atoms which have been collisionally transferred to the 18p state.
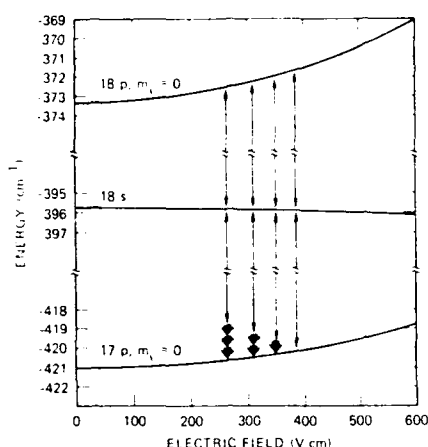
Figure 2 - Energy level diagram for Na as a function of electric field. The four sets arrows indicate the resonant collisional energy transfer processes. The short bold arrows indicate how many microwave photons are emitted, zero to three

The experiments are carried out using the apparatus shown in Fig. 3, which is described in detail elsewhere.[9] An effusive beam of Na atoms passes through a microwave cavity where the atoms are excited by two counterpropagating pulsed dye laser beams tuned to the 3s-3p and 3p-ns transitions. A pencil shaped volume of excited ns atoms is excited. The excitation takes place in combined microwave and static fields, and collisions between excited atoms are allowed to occur for 1μs, at which point the microwave field is switched off, and a high voltage pulse is applied to the septum in the cavity to field ionize only those atoms which have made the transition to the np state. There is a 1mm diameter hole in the top of the cavity allowing ions formed at a microwave field antinode to reach the detector. A static field, applied by putting a voltage on the septum, is slowly scanned to tune through the collisional resonances. The microwave cavity is a piece of WR90 waveguide 20 cm long closed at the ends. It is operated on TE$_{10n}$ modes, where n is odd, to produce an antinode of the microwave field at the center of the cavity. At 15.4 GHz the cavity has a Q of 2300 allowing microwave fields ~1kV/cm to be produced. This corresponds to intensities slightly in excess of 1kW cm².
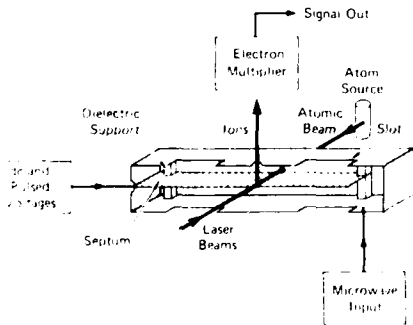
Figure 3 - Schematic diagram of the apparatus

One of the first results obtained with the apparatus is shown in Fig. 4, recordings of the 22s +22s → 21s + 22p collisional resonances with and without microwave power incident on the cavity.[10] The trace without microwaves has four collisional resonances corresponding to the fact that the electric field lifts the degeneracy of the |m| = 0 and 1 levels of the p states.[10] The two central resonances and overlapped in Fig. 4. The most interesting aspect of Fig. 4 is the fact that the one photon radiatively assisted collision signal is nearly as large as the resonant collision signal with < 1mW of incident microwave power.
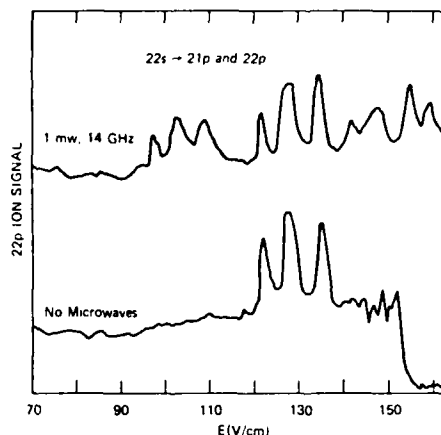
Figure 4 The 22s+22s → 22p+21p resonant collision signals with and without 1mW of microwave power. With 1mW of microwave power the radiatively emitted collisions are nearly as probable as the resonant collision process.

In Figure 5 we show a series of recordings for the 18s + 18s → 18p + 17p resonances.[10] It is convenient to label the four collisional resonances as $(m_\ell, m_\mu)^k$ where m_ℓ and m_μ are the |m| values of the upper and lower p states and k is the number of microwave photons emitted. In Fig. 5 the $(0,0)^k$ resonances are marked by an arrow and the number k, which is in the range zero to three. Examining Fig. 5 we note that the collisions involving more microwave photons become generally more probable as the power is increased. However on closer inspection we see that the k = 0 resonances disappear, at E$_{mw}$ ~ 150V/cm and reappear at E$_{mw}$ = 150V/cm. Similarly the k = 1 resonances disappear at 150V/cm. We can also see that all resonances shift to lower static fields with higher microwave power. Finally we can see that in many cases the resonances become more symmetric and narrower at higher microwave power. In Fig. 6 we plot the magnitudes of the $(0,0)^k$ signals as a function of the microwave power to show in a more systematic way the variation of the observed radiatively assisted collision cross section with microwave power. The observations shown in Fig. 5 are not unique but are similar to those obtain for other states.

615
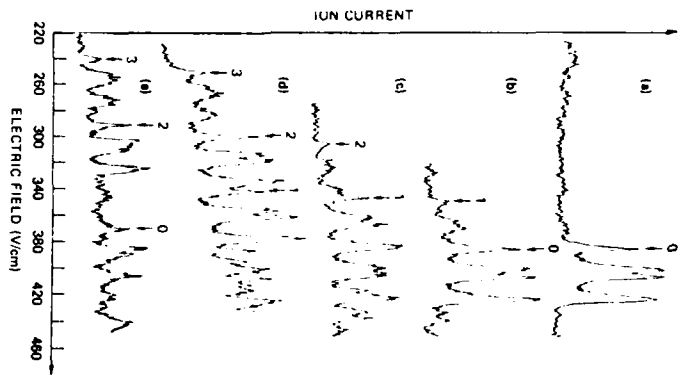
Figure 5 The 18s+18s → 18p+17p resonant collision signals for several 15.4GHz microwave field strengths (a) 0,(b) 13.5V/cm, (c) 50V cm, (d) 105V/cm and (3) 160V/cm. The arrows, numbered by k, point to the $(0,0)^k$ resonances, the lowest field members of each set of four resonances corresponding to the four possible combination of m values of the p states.

III. Theoretical Description

The observations Fig. 5 show that the radiative collision cross sections equal or exceed the resonant collision cross sections. In such a case the microwave field can not be treated as a small perturbation. To account for the strong effect of the microwave field we have treated the radiative collisions as resonant collisions between microwave dressed atoms. We here outline the theory.[10] Our treatment starts with the observation that, in the static field, the s states have nearly no energy shift while the p states exhibit large Stark shifts, which are to a first approximation linear as shown by Fig. 6. When a microwave field is added to the static field the energy of a p state oscillates synchronously with the microwave field. Stated another way, the energy of a p state is modulated by the microwave field. To a good approximation the wave function of atom A in a p state in a microwave field E sinωt is given by [12]

$$\chi_{mw} = \chi_s e^{-iW_A t} \sum_m J_m \left(\frac{\partial W_A}{\partial F} \Big|_{F_s} \right) \frac{F}{\omega}) e^{im\omega t} \qquad (7)$$

where $dW_A/dF|_{F_s}$ is the field derivative of the energy of Atom A at the static field F_s, and W_A is the energy at the static field F_s. A similar expression is found for Atom B.
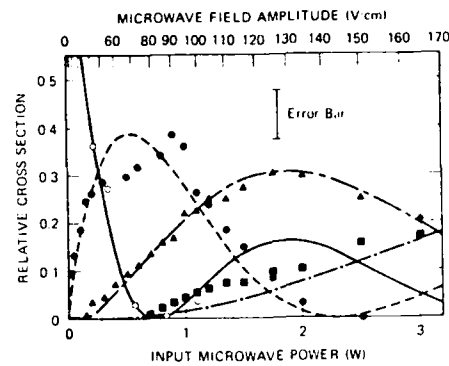
Figure 6 - Observed and calculated values of the cross section for zero photon (resonant) collisions (O,———) one photon assisted collisions (● — — —,), two photon assisted collisions (△.— —) and three photon assisted collisions (■ , ——·).

If we insert the wavefunctions of Eq. (7) into Eq. (1) we have a description for resonant collisions of dressed atoms. If we consider the resonance in which k photons are emitted. the resonant contributions to the matrix element are

$$H_I = \frac{\mu_1 \mu_2}{r^3} \sum_m J_m \left(\frac{\partial W_A}{\partial F} \Big|_{F_s} \frac{F}{\omega} \right). \qquad (8)$$

The k photon resonance thus corresponds to the coherent sum of all process in which a net of k photons are emitted, and the collisions between many sets of sidebands contribute, as shown by Fig. 7. Eq. (8) may be simplified to

$$H_I = \frac{\mu_1 \mu_2}{r^3} J_k \left[\left(\frac{dW_A}{\partial F} \Big|_{F_s} + \frac{\partial W_B}{\partial F} \Big|_{F_s} \right) \frac{F}{\omega} \right] \qquad (9)$$

Following the reasoning leading to Eq. 4 we conclude that the radiative collision cross section σ_k is given by

$$\sigma_k = \sigma_0 \mid J_k \left(\frac{dW_A}{\partial F} \Big|_{F_s} + \frac{dW_B}{\partial F} \Big|_{F_s} \right) \frac{F}{\omega} \qquad (10)$$

i.e. the radiative collision cross section is related to the resonant collision cross section by a Bessel function. Using a sightly more sophisticated theory the solid lines of Fig. 6 have been calculated to show the dependence of σ_k on microwave power. As shown by Fig. 6 the calculations are in excellent agreement with the experimental results.

We turn now to consider two other aspects of Fig. 5. First, the shift of the resonances to lower static fields is an AC Stark shift which is well accounted for by a more exact theoretical treatment than given here. Second the counter intuitive fact that the resonances become sharper and less symmetric at higher microwave powers can be understood by referring to Eq. (5). In a radiative collision there are two parts to the interaction a dipole dipole part and a radiative part. At low microwave powers the radiative part is small requiring a large dipole dipole part, or the close approach of the two atoms. The close approach increases the probability of collisions in the region where the interatomic potentials are not flat, leading to asymmetric resonances. It also means collisions of shorter duration, or wider collisional resonances.

IV. Conclusion

In sum it seems that Rydberg atoms and microwaves provide an excellent system in which the study radiative collision processes in a systematic fashion. While date only a few experiments have been done, they have stimulated the development of a Floquet theory along much the same lines as those used to treat other higher field phenomena.

References

1. L.I. Gudzenko and S.S. Yakovlenko, Zh. Eksp. Teor. Fig. 62, 1686 (1972) [Sov. Phys. JETP 35, 877 (1972)].

2. R.W. Falcone, W.R. Green, J.C. White, J.F. Young, and S.E. Harris, Phys. Rev. A 15, 1333 (1977).

3. P.H.Cahuzac and P.E. Toschek, Phys. Rev. Lett. 40, 1087 (1978).

4. A.V. Hellfeld, J. Caddick, and J. Weiner, Phys. Rev. Lett. 40, 1369 (1978).

5. W.R. Green, M.D. Wright, J. Lukasik, J.F. Young, and S.E. Harris, Opt. Lett. 4, 265 (1979).

6. A. Gallagher and T. Holstein, Phys. Rev. A. 16, 2413 (1977).

7. R.C. Stoneman, M.D. Adams and T.F. Gallagher, Phys. Rev. Lett. 58, 1324 (1987).

8. R. Kachru, N.H. Tran, and T.F. Gallagher, Phys. Rev. Let. 49, 191 (1982).

9. P. Pillet, H.B. van Linden van den Heuvell, W.W. Smith, R. Kachru, N.H. Tran and T.F. Gallagher, Phys. Rev. A 30, 280 (1984).

10. P. Pillet,R. Kachru, N.H. Tran, W.W. Smith and T.F. Gallagher, Phys. Rev. A. 36, 1132 (1987).

11. T.F. Gallagher, K.A. Safinya, F. Gounand, J.F. Delpech, W. Sander, and R. Kachru, Phys. Rev. A 5 1905 (1982).

12. S.H. Autler and C.H. Townes, Phys. Rev. 100 703 (1955).

STEPWISE SOLVATION OF REACTIVE ANILINE CATIONS

Jack A. Syage

Aerophysics Laboratory
The Aerospace Corporation
P.O. Box 92957
Los Angeles, CA 90009

Abstract

Single molecules of aniline were stepwise solvated with solvent shells M_n consisting of either NH_3, N_2H_4, CH_3OH, or H_2O and studied by mass-resolved one- and two-color resonance-enhanced multiphoton ionization (REMPI) and electron impact (EI) ionization. The influence of microsolvation was investigated for the processes of unimolecular dissociation and intracluster dissociative proton transfer. Dissociative proton transfer from aniline to M_n to form H^+M_n was strongly dependent on M_n proton affinity, which for a particular solvent generally increased with n. Consequently, a solvent size threshold for formation of H^+M_n was observed for NH_3 ($n \geq 3$), N_2H_4 ($n \geq 2$), CH_3OH (not seen, $n > 4$), and H_2O (not seen, $n > 4$). Calculated enthalpies of these reactions, using a model that accounts for the energetics of stepwise solvation, displayed excellent correlation with the observed results. In a second experiment, the solvation of the well-known $C_6H_5NH_2^+ \rightarrow C_5H_6^+ + HNC$ dissociation revealed a striking electron transfer mechanism whereby solvation with N_2H_4 led to extensive formation of $HNC \cdot M_n^+$. Although all the solvents studied have ionization potentials above that of aniline, only N_2H_4 has a value less than that of the fragment C_5H_6.

Introduction

One of the fundamental issues in reaction dynamics is understanding how solvent molecules influence the properties of a chemical reaction. This has traditionally been investigated by comparing the kinetics of gas phase reactions to that in solvents of varying viscosity.[1] In a recent study, we have refined a technique to sequentially solvate single reactive molecules with one or more solvent molecules.[2] The technique relies on the ability to form molecular clusters in a supersonic expansion. Clusters of solvent molecules, seeded with a single reactive solute molecule, can be formed under the appropriate expansion conditions and sample mixtures.

We present results for an investigation of the reactivity of a single aniline cation seeded within a solvent shell M_n of varying size (typically $n = 1$-10) consisting of either NH_3, N_2H_4, CH_3OH, or H_2O.[2] The reactivity of cations was chosen because the microsolvated reactant cation and the subsequent formation of charged products could be monitored by time-of-flight (TOF) mass spectrometry in the molecular beam apparatus. The cations were formed with specific initial energies by resonance enhanced multiphoton ionization (REMPI). We also compared these results to the chemistry of microsolvated aniline formed by electron impact (EI) ionization.

There are only a handful of studies in the literature that focus on the reactivity of large aromatic molecules in microsolvent shells. Most of these tend to deal with so called "soft" chemistry (e.g., charge transfer and intermolecular vdW bond dissociation. However, a few notable studies of hydrogen bond dissociation,[3] proton transfer reactions,[4,5] and microcluster crystallization[6] deserve citing. In the present investigation, emphasis was placed on how sequential solvation promotes or quenches "hard" chemistry (e.g., fragmentation and rearrangement). Aniline was chosen for this work because its unimolecular ion fragmentation properties have been extensively studied.[7,8] The molecule also permits a study of intracluster acid-base type chemistry such as dissociative hydrogen transfer from solvent to form protonated aniline cation and dissociative proton transfer from aniline cation to solvent to form protonated solvent. Our success in stepwise solvation provides us with the opportunity to systematically observe a gas phase reaction evolve toward solution phase behavior (i.e., "dissolve") on a molecule-by-molecule basis.

Experimental

The supersonic molecular beam time-of-flight (TOF) mass spectrometer has been described before[2,9] and is illustrated with a few recent modifications in Fig. 1. The vacuum system consists of differentially pumped source and ionization chambers. A temperature-controlled magnetic solenoid pulsed nozzle in the source chamber is used for the supersonic expansion which enters the ionization chamber through a 1-mm-diam skimmer. The extent of clustering is very sensitive to the relative delay between the excitation source (laser or e⁻ beam) and the pulsed valve firing is illustrated in Fig. 2. By exciting at the extremities of the gas pulse, it is possible to suppress larger clusters and still form a high yield of the singly solvated dimer. This should prove important in photodissociation experiments by helping to remove interferences from dissociation of larger clusters.

The acceleration grids for the TOF mass spectrometer consist of the standard three-grid configuration. We use 1-cm grid spacings, a 1-m drift tube, and typical extraction and acceleration fields of 100-200 V/cm and 1500-2000 V/cm, respectively. Deflector plates are used near the ion source to compensate for the forward velocity of the molecular beam. Ion signals are collected by measuring current versus ion TOF using a microchannel plate detector. Mass spectra are recorded using a 125-MHz bandwidth transient digitizer interfaced to an IBM AT computer.

Fig. 2. 1-C REMPI TOF mass spectra (MS) of aniline-$(NH_3)_n$ clusters as a function of the overlap of the laser pulse with the temporal profile of the pulsed valve (PV) output. Conditions were $\omega_1 = 294$ nm, 0.05 mJ/pulse, 50 psi He.

The laser pulses were mildly focused by using a 30-cm focal length spherical lens positioned to bring the light to a focus about 3-5 cm before crossing the molecular beam. For the 2-color (2-C) REMPI experiments, the ω_2 pulse was typically delayed (optically) by 3 ns from the ω_1 pulse. The laser pulse widths are about 4-6 ns. A pulsed EI ion source with scanning electron energy capabilities[10] was also employed for these studies.

Chemistry in Microsolvents

We investigated two reactions involving microsolvated aniline cation; the proton or acid dissociation reaction

$$C_6H_5NH_2^+ \longrightarrow C_6H_5NH + H^+ \qquad (1)$$
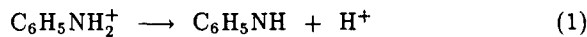
which is energetically unfavorable in the gas-phase, and the dissociation

$$C_6H_5NH_2^+ \longrightarrow C_5H_6^+ + HNC \qquad (2)$$
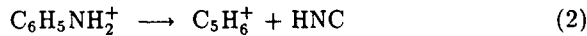
which is a well-known gas-phase reaction.[7,8]

Dissociative Proton Transfer

The first reaction is particularly interesting because it can become favorable in the presence of solvent molecules of sufficient basicity. The interesting question is how large a solvent shell is required to observe an acid-base reaction.

Fig 1. Schematic of the experimental apparatus. In the present work, 2-C excitation was achieved using a single dye laser and the 2nd, 3rd, or 4th harmonic of the Nd:YAG laser. Symbols are defined as follows: MCP = microchannel plate detector; PMT = photomultiplier tube; TMP = turbomolecular pump; DP = diffusion pump; BS = beamsplitter; λ EXT = wavelength extension components. Free jet fluorescence detection was not used in the present study.

A thermodynamic cycle appropriate to reaction (1) can be written that gives the gas phase reaction enthalpy

$$\Delta H_g = I_p(H) - I_p(A) + D_H(A\{-H\}) - D_{H^+}(M) \quad (3)$$

The I_p values are ionization potentials, and the D values are bond energies which are written to be interpreted as a hydrogen affinity (D_H) and a proton affinity (D_{H^+}). The addition of terms to include the energetics of stepwise solvation has been derived previously[2], and is given by

$$\Delta H_{s,n} = \Delta H_g + \sum_{i=1}^{n} \Delta E_{i,i-1}(A^+ M_i) - \sum_{i=2}^{n} \Delta E_{i,i-1}(H^+ M_i) \quad (4)$$

Here, the ΔE terms are solvation energies for successive addition of M to A^+ or H^+, respectively.

The appearance of the product $H^+ M_n$ in the REMPI mass spectra for M=NH$_3$, N$_2$H$_4$, and CH$_3$OH is presented in Fig. 3. From these and other spectra, the following observations are reached; (i) $H^+ M_n$ formed from $A^+ \cdot M_n$ precursor was observed for NH$_3$ and N$_2$H$_4$ with a solvent size threshold of $n \geq 3$; (ii) no protonated solvent $H^+ M_n$ was observed for CH$_3$OH or H$_2$O up to values of $n = 5$, representing the limit to acceptable signal-to-noise for these solvents.

As expected, proton transfer from aniline to M_n to form $H^+ M_n$ was strongly dependent on M_n proton affinity, which for a particular solvent generally increased with n. A small solvent threshold size for formation of $H^+ M_n$ was observed for the more basic solvents NH$_3$ ($n = 3$) and N$_2$H$_4$ ($n = 2$). The less basic solvents CH$_3$OH and H$_2$O, however, did not induce an acid-base reaction for solvent shell sizes up to $n = 4$. Qualitatively, it was found that as the solvent basicity increased, the number of solvent molecules required to initiate an acid-base reaction decreased.

Brutschy et al.[5] recently reported evidence for a threshold solvent size effect in the dissociative proton transfer involving toluene and p-xylene solvated with NH$_3$, CH$_3$OH, and H$_2$O. The relative ordering of the n threshold values for the various solvents was consistent with that observed in the present work, although the absolute values in the former work were shifted to smaller n. These results are in accord with the model for stepwise solvations developed above. Calculated microsolvation enthalpies $\Delta H_{s,n}$ are represented in Fig. 4.

A notable feature of the calculated results is the predicted increase in enthalpy at the first level of solvation $n = 1$ due to stabilization of the reactant side of reaction (9) without an offseting stabilization of the products. Subsequent solvation, however, stabilizes the products to a greater extent than the reactants so that the overall influence of solvation is to increase K_{eq} relative to the gas phase. A second feature is that the ordering of exothermicities, NH$_3$ > CH$_3$OH > H$_2$O, is in agreement with the present results and those of Brutschy et al.[5] This trend is most strongly correlated with the proton affinity $D_{H^+}(M)$.
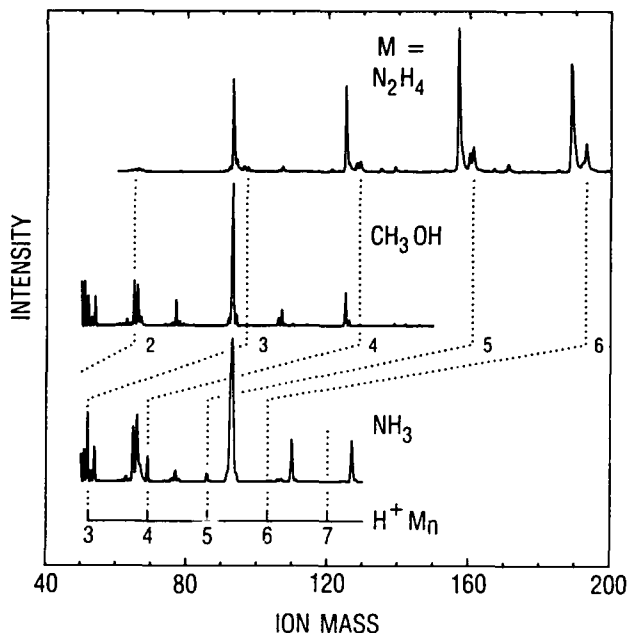
Fig. 3. 1-C REMPI/MS of $A^+ M_n$ clusters showing evidence for a critical solvent size in various solvents for dissociative proton transfer to form $H^+ M_n$. Pulse energies were about 1.0 mJ (295 nm) for $M = $ NH$_3$ and CH$_3$OH, and 0.40 mJ (233 nm) for N$_2$H$_4$.
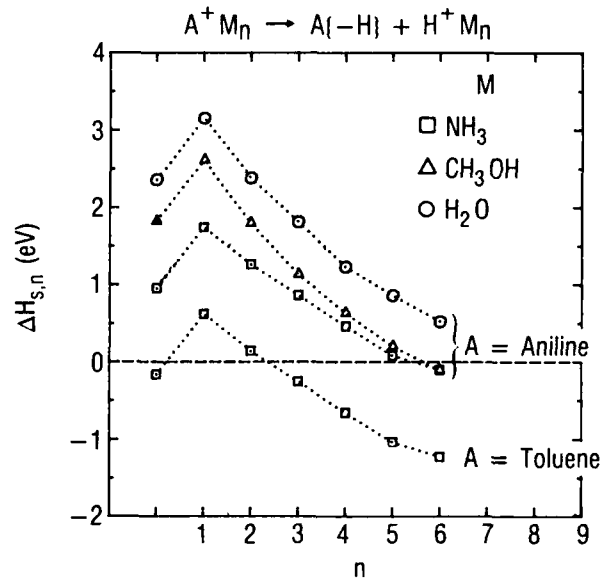
Fig. 4. Calculated stepwise solvation enthalpies as a function of solvent and shell size n for dissociative proton transfer. Calculated results are compared for A = aniline and toluene. The lefthand most data are for the gas phase reactions.

A third feature is that the calculated solvation enthalpies $\Delta H_{s,n}$ are more exothermic for A=toluene, thus explaining the smaller threshold values of n reported by Brutschy *et al.* for that system. The calculated curve for the reaction involving toluene-$(NH_3)_n$ is plotted in Fig. 4, although the calculated curves for all solvents are shifted in energy from the aniline-$(NH_3)_n$ data by essentially a constant representing the differences in the I_p and hydrogen bond dissociation energy $D_H(A\{-H\})$ of the aromatic cations.

Dissociation Induced Electron Transfer

The second reaction was studied with the original intent of examining solvent quenching of known gas-phase dissociation. In the course of this work, we observed a striking electron transfer mechanism that was strongly dependent on the properties of the solvent. This is diagrammed schematically in Fig. 5. The aniline cation is represented by AB^+ which dissociates as indicated above to $C_5H_6^+$ and HNC, represented by A^+ and B, respectively. Two different product pathways were observed, depending on the solvent molecule M. When solvated by NH_3, CH_3OH, or H_2O, AB^+ was observed to dissociate to the usual uncomplexed gas-phase products $A^+ = C_5H_6^+$ and higher threshold energy ions. When solvated by N_2H_4, the positive charge was observed to jump to a solvent molecule in the course of the dissociation. The dissociation-induced electron transfer can be very efficient as shown by the mass spectra in Fig. 6. For REMPI excitation at 233 nm, the electron transfer occurs with near unit probability, as evidenced by the strong HNC·N_2H_4 signal at mass to charge ratio m/q = 59 and the near absence of the $C_5H_6^+$ signal at m/q=65. These results occur because the aniline cation suddenly dissociates into two fragments that have larger ionization potentials (I_p). The solvent molecule N_2H_4 has a lower I_p than C_5H_6 and is in effect ionized by the product $C_5H_6^+$. The NH_3, CH_3OH, and H_2O solvent molecules, on the other hand, have higher values of I_p and hence electron transfer to these solvents is not energetically favorable. An interesting sidelight is that these results demonstrate that the bonding site for the first few solvent molecules is the amine group and not the aromatic ring of aniline.[2]

Summary and Conclusions

The influence of microsolvation was investigated for unimolecular dissociation and intracluster bimolecular hydrogen transfer and proton transfer. The solvation of unimolecular dissociation revealed a striking mechanism for electron transfer from fragment to solvent that depended strongly on the properties of the solvent molecules. For acid-base type reactions, distinct evidence for critical solvent size effects was obtained that correlated well with characteristic properties of the solvent (e.g., ionization potential, proton affinity, bond energies, etc.). These results systematically illustrate how a gas-phase reaction evolves toward solution-phase behavior (i.e., "dissolve") on a molecule-by-molecule basis.
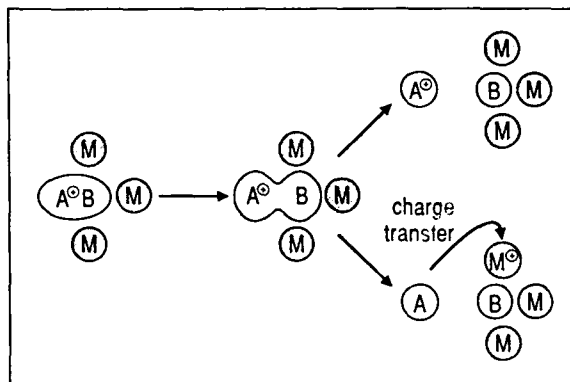
Fig. 5. Pictorial view of the process of dissociation and electron (or charge) transfer in microsolvated molecular clusters. AB^+ represents the aniline cation dissociating to C_5H_6 (A) and HNC (B). The solvent molecules M are shown preferentially bonded to B as determined experimentally.
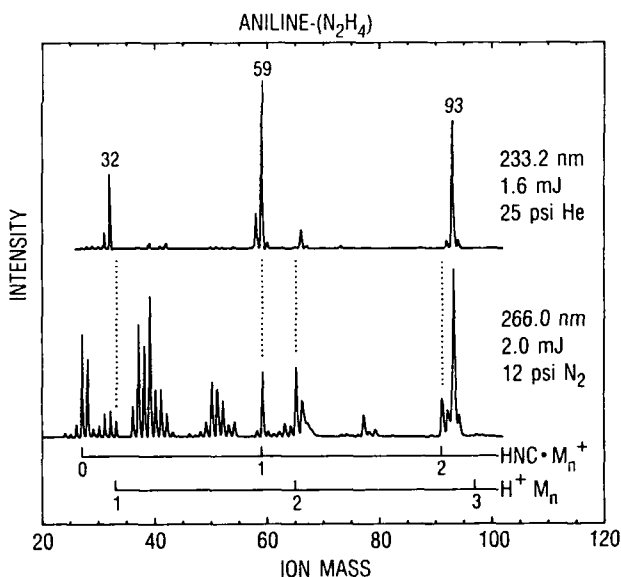
Fig. 6. 1-C REMPI/MS of A-$(N_2H_4)_n$ clusters for different excitation conditions. The appearance of the fragment clusters HNC·$(N_2H_4)_n^+$ is evidence for a dissociation-induced charge transfer mechanism. Numbers over peaks denote amu.

References

1. J. A. Syage, P. M. Felker, and A. H. Zewail, *J. Chem. Phys.* **81,** 4706 (1984).

2. J. A. Syage, *J. Phys. Chem.* **93,** in press (1989).

3. Felker, P. M.; Zewail, A. H. *Chem. Phys. Lett.* **94,** 448, 454 (1983).

4. (a) Cheshnovsky, O.; Leutwyler, S. *J. Chem. Phys.* **88,** 4127 (1988); (b) Cheshnovsky, O.; Leutwyler, S. *Chem. Phys. Lett.* **121,** 1 (1985).

5. Brutschy, B.; Janes, C.; Eggert, J. *Ber. Bunsenges, Phys. Chem.* **92,** 74 (1988).

6. Syage, J. A.; Wessel, J. E. *J. Chem. Phys.* **89,** 5962 (1988); (b) Wessel, J. E.; Syage, J. A. *J. Chem. Phys.* submitted.

7. (a) Kühlewind, H.; Neusser, H. J.; Schlag, E. W. *J. Chem. Phys.* **82,** 5452 (1985); (b) Proch, D.; Rider, D. M.; Zare, R. N. *Chem. Phys. Lett.* **81,** 430 (1981).

8. Baer, T.; Carney, T. E. *J. Chem. Phys.* **76,** 1304 (1982).

9. Syage, J. A.; Pollard, J. E.; Cohen, R. B. *Appl. Opt.* **26,** 3516 (1987).

10. Syage, J. A. *Chem. Phys. Lett.* **143,** 19 (1988).

NEW COUMARIN LASER DYES

T.-I Lin[+], M.V. Jovanovic[*], and R.M. Dowben[+**]

[+]Baylor Research Foundation, Baylor University Medical Center
P.O. Box 710699
Dallas, Texas 75226
[*]Department of Chemistry, Southern Methodist University
Dallas, Texas 75275
[**]Department of Neurology, University of Texas Southwestern Medical School
5323 Harry Hines Blvd., Dallas, Texas 75235

Abstract

Five new 7-julolidinocoumarins were prepared. All compounds also had substitutions in the 3-position where a carbonyl group adjacent to the ring was required for significant spectral red shift, effective fluorescence, and effective lasing. 4-Methyl-7-julolidinocoumarin-3-carboxylic acid showed an absorbance maximum at 425 nm and lased in the 502-538 nm range with a quantum efficiency of 0.27 at 524 nm. 7-Julolidinocoumarin-3-carboxylate methyl ester showed very similar properties.

Introduction

There is a need for efficient, stable, bleach-resistant laser dyes in the green-yellow portion of the spectrum for biophysical experiments. We synthesized five new 7-julolidinocoumarins and determined their spectral properties and lasing characteristics. The compounds were synthesized with several goals in mind, namely, to obtain longer wavelength lasing dyes with high extinction coefficients, longer fluorescence lifetimes, and high quantum yields, with better solubility in a variety of solvents.

Materials and Methods

The chemical structures of the five new 7-julolidinocoumarins are shown in Fig. 1. The detailed synthetic procedures will be published elsewhere. The compounds were purified by combinations of recrystallization from organic solvents and preparative thin layer chromatography. Chemical structure was confirmed by combinations of elemental analyses, mass spectrometry, NMR, and IR analyses.

7-Julolidinocoumarin Derivatives

Dye	R_3	R_4
1	CO_2H	CH_3
2	$CO_2\text{-}CH_3$	H
3	CH_2CO_2H	CH_3
4	$C_2H_4CO_2H$	CH_3
5	SO_3H	CH_3
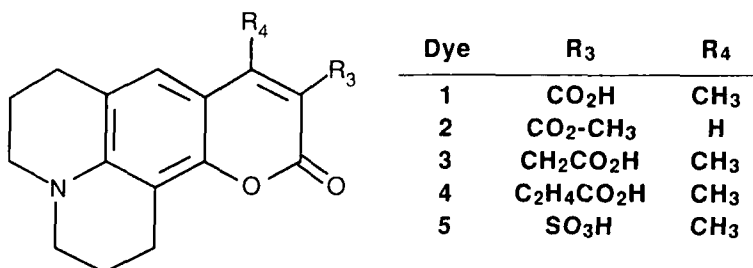
Fig. 1. Chemical structure.

Absorption spectra were determined on dye solutions in spectral grade dimethylformamide or dimethylsulfoxide using a Perkin-Elmer Model 552 spectrophotometer to better than 1 nm resolution. Fluorescence spectra were determined in a SLM-Aminco Model 500C spectrofluorimeter at room temperature. Lasing was induced by a flash lamp or argon laser, or particularly by a compact 2 mW pulsed nitrogen laser (Laser Science Model VSL-337) used in conjunction with a compact dye module (Laser Science Model DLM-120). This configuration offered versatility and interchangeability with easy access for changing dye solutions and optimizing lasing output.

The nitrogen laser was internally triggered at 20 pps giving 3 nsec pulses, 20 µJ. The dye laser module was tuned by a micrometer-driven grating using Littrow configuration optics. A beam expander/collimator was used to minimize stray light and direct the laser beam onto a side-on Hammamatsu R282 photomultiplier. Lasing intensity was measured in terms of photon counts versus wavelength in 2 nm increments. The results were not corrected for the spectral response of the photomultiplier nor for wavelength-dependent differences in grating efficiency.

Lasing efficiency was determined by using a radiometer (United Detector Technology Model 81 optometer) and comparing the outputs of the nitrogen and the dye lasers. The wavelength-dependent response of the detector was corrected with a calibration curve supplied by the manufacturer.

Results and Discussion

The absorbance spectra of the five new dyes yielded excitation and emission maxima listed in Table 1 along with those of five related 7-julolidinocoumarin dyes previously studied.[1,2] A carbonyl substitution at position 3 results in a significant red shift of the dye in the absorption spectra. Introduction of a methylene or ethylene bridge between the 3-position of the ring and the carbonyl group vitiates these effects.

Table 1. Some Spectral Characteristics of 7-Julolidinocoumarin Dyes

Dye	Longest Absorbance Peak (nm)	Fluorescence Emmission Maximum (nm)	Extinction Coefficient $10^4 M^{-1} Cm^{-1}$
1	425	487	24.4
2	440	503	14.9
3	282	360	9.8
4	278	361	8.1
5	285	307	10.0
Coumarin 102	390	468	2.2
Coumarin 314	437	478	4.5
Coumarin 334	452	491	4.1
Coumarin 343	440	482	4.3
Coumarin 338	433	473	4.3

The lasing characteristics of dyes 1 and 2 are shown in Figs. 2 and 3, respectively. Both dyes lase in the range 502 to 538 nm although the 3-carboxylate methyl ester has a somewhat broader lasing range (FWHM 26 nm). The quantum efficiencies of the two dyes also are similar at 27% measured with a power meter. Thus these dyes are very efficient and can be pumped with a low power pulsed nitrogen laser or low power flash lamp.
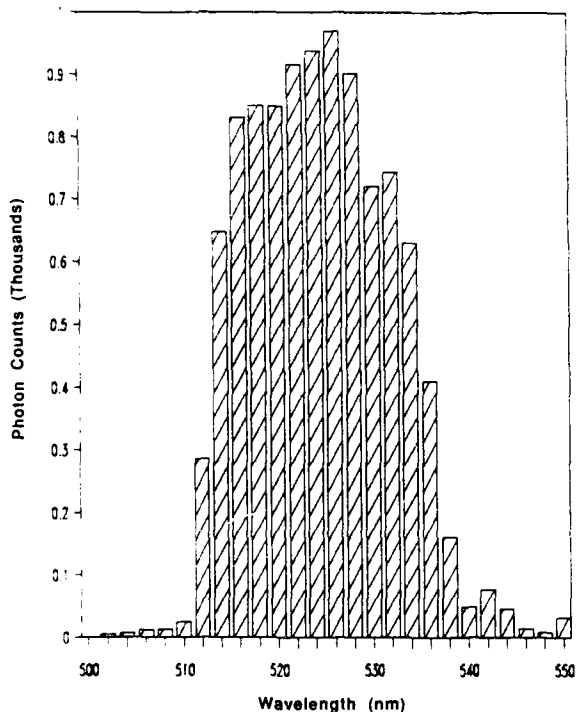
Fig. 2. Lasing characteristics of 5.6 mM dye 1 in dimethylformamide.
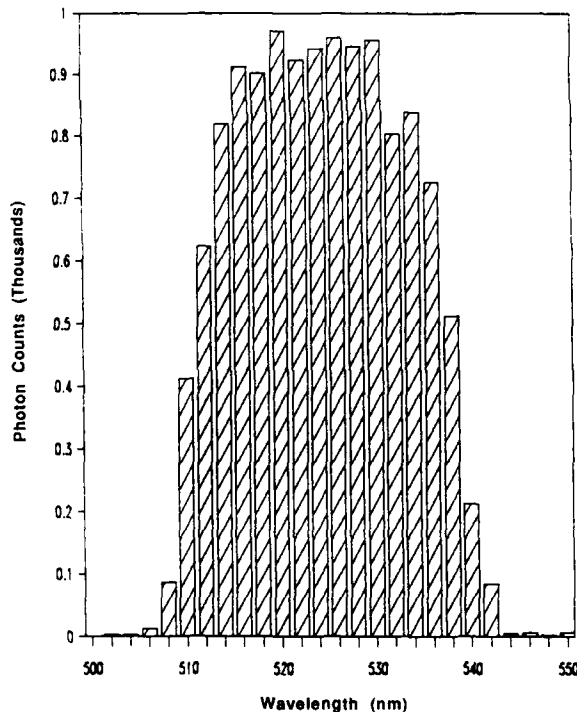
Fig. 3. Lasing characteristics of 8.4 mM dye 2 in dimethylformamide.

References

1. Kodak Laser Dyes, Kodak Publication JJ-169 (1987). Eastman Kodak Company, Rochester, NY 14650.
2. Kodak Laboratory & Research Products, Catalog No. 53 (1987-1988). Eastman Kodak Company, Rochester, NY 14650.

ANIONIC AND ZWITTERIONIC STRUCTURAL EFFECTS IN SOME PYRIDINIUM OXAZOLE LASER DYES

R. F. Kubin, R. A. Henry, M. E. Pietrak, and D. E. Bliss
Chemistry Division, Research Department, Naval Weapons Center, China Lake, CA 93555

ABSTRACT

We have looked at changing the anion of several cationic pyridinium oxazole laser dyes as well as at a zwitterionic form of these same dyes. These modifications might greatly improve dye lasing output. Our initial studies had shown that some of the pyridinium oxazole dyes had very long lifetimes but only a moderate output. Additionally, in the past, we had found a little effect upon changing anion but had noted dramatic improvement in output using detergents with some dyes. Results of the lasing tests showed that for one dye the zwitterionic dye form had an exceptional output of over 100 mJ for a 60 J input in our system. This is the first dye to actually exceed the output and to have a longer lifetime than rhodamine 6G. This was not a general result. Other zwitterions tested showed no exceptional output. Additionally,we noted essentially no change in output with change in anion. These results reinforce our earlier conclusion that only by affecting the electronic environment of the actual chromofluor does one change its lasing parameters.

INTRODUCTION

This laboratory has recently made a study of 25 pyridinium oxazole dyes.[1] Several of these dyes had extremely long lifetimes as measured in our dye laser. In each case of a long lifetime, the dye was in either ethanol or methanol with argon as the cover gas. Lifetimes were not always determined with air as the cover gas; however, in most cases with air the observed lifetimes were much less. Cover gas effects are somewhat subtle, running the range from no effect to a factor of ten plus in improved output when argon is the cover gas.[2] Additionally substituent effects have been noted for several auxofluors attached to the oxazole ring.[1] Because the pyridinium oxazole dyes are salts, solvent plays an important part in the ability of the dyes to lase. The possibility exists that different anions could change the photophysical properties of the dyes. We do not observe the anionic effects noted by Kauffman and Bentley with respect to the mesylate anion or the propanesulfone zwitterion over the tosylate anion.[3] We have observed that unless the electronic environment of the dye is changed appreciably the dye photophysical properties are stable.[1] Only small, although measurable, changes have been found between the tosylate and perchlorate salts of these dyes.[1]

EXPERIMENTAL

Our dye laser system is a Phase-R DL10Y laser head in a triaxial configuration. The cavity has a 100% reflector wide band rear mirror and we use output couplers with 20 to 90% reflectivity. For most of the dyes we have tested a 50% output coupler produces the highest output. Occasionally, as in this study, an 80% output coupler gave the highest output with some dyes. Temperature of coolant and dye solution can be controlled separately to 0.01°C.[4] Quantum yield measurements were made using a Spex F222 fluorimeter with quinine sulfate as the comparison standard. For the latter measurements, the dye concentrations were in the 10^{-7} M range with peak absorbances of ≤0.014. For the laser tests ,dye concentrations were 2×10^{-4} M, unless otherwise noted.

RESULTS

The basic dye molecule is shown in Figure 1 with the substitutions germane to this work. Based on the results of Kauffman and Bentley,[3] Kauffman[5] suggested that we try a zwitterionic dye form for

Structure
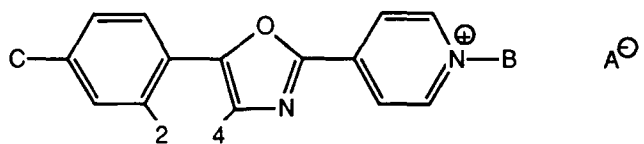
Group Location

A	B	C	2	4
Tosylate	Methyl	Methoxy	...	...
Mesylate	Methyl	Methoxy	...	...
Zwitterion		Methoxy	...	...
Tosylate	Methyl	Methoxy	Ethylene	bridge
Tosylate	Methyl	F	...	...
Perchlorate	Methyl	F	Ethylene	bridge
Tosylate	Methyl	F	...	Methyl
Zwitterion		F	...	Methyl
Zwitterion		F	Ethylene	bridge
Mesylate	Methyl	n-Butoxy	...	...
Zwitterion		n-Butoxy	...	...

Figure 1. The Basic Pyridinium Oxazole Dye.

for Ox 2.   (The short form nomenclature follows Reference 1, see Figure 2).   Also suggested was the mesylate anion (methanesulfonate).   Figure 3 shows the variants of the basic dye investigated in this
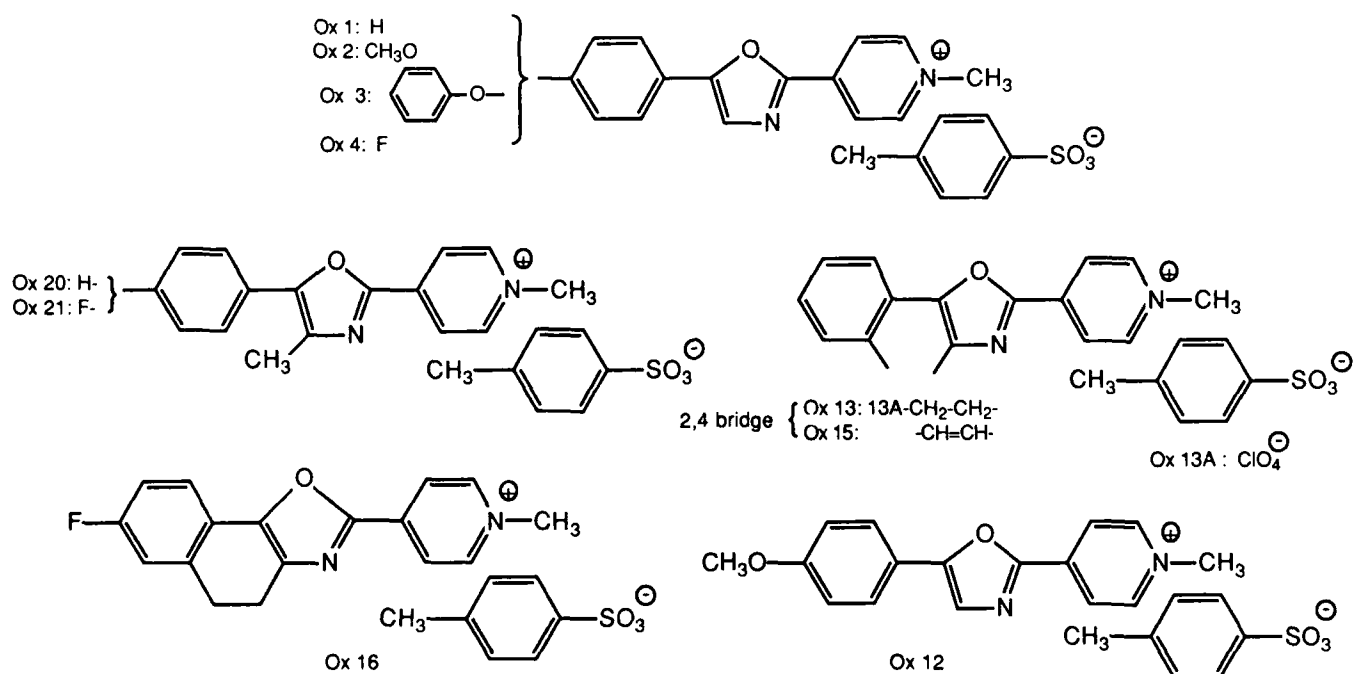
Figure 2. Comparison Dye Structures.[1]

626
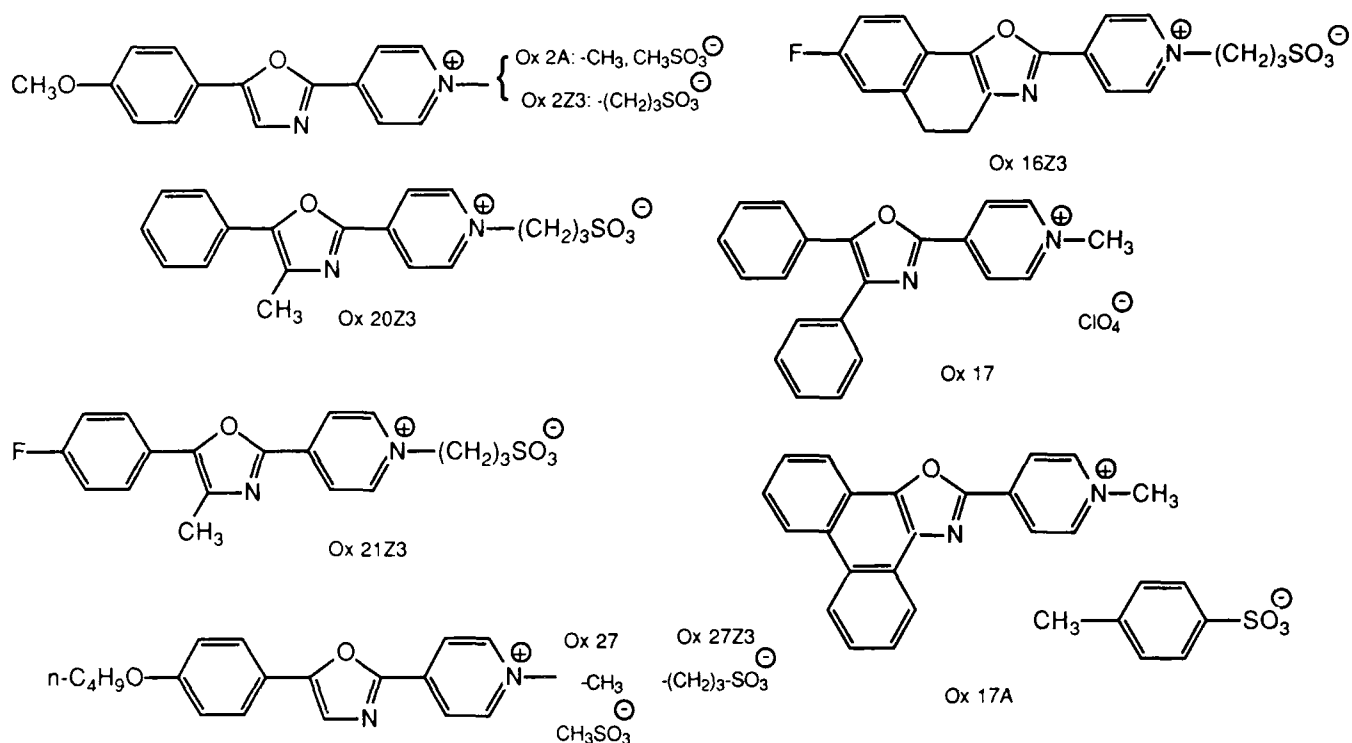
Figure 3. Dye Structures for this study.

work. For all of the data reported here, argon is the cover gas. We have found in the past,[1,6,7] that the use of argon as the cover gas can improve energy output by from 50% to a factor of 10 and improve fluorescence quantum yields by as much as 75% depending on the dye and the solvent. Some dyes have been unaffected by the use of argon to exclude oxygen. Table 1 gives the actual energy output observed for the dyes in this study as well as the comparison data from earlier studies. Except for Ox 2Z3 all

TABLE 1. Energy Output of Laser Dyes Related to the Basic Pyridinium Oxazole Dye.
The cover gas is argon.

Dye	Solvent	Energy In, J	Energy out, mJ	Dye	Solvent	Energy In, J	Energy Out, mJ
Ox 2	EtOH/H$_2$O	40	36.4	Ox 17A[a]	EtOH/H$_2$O	60	33.1
Ox 2A[a]	EtOH/H$_2$O	60	76.9	Ox 20	EtOH	55	37.4
Ox 2Z3[a]	EtOH/H$_2$O	60	106.3	Ox 20Z3[a]	EtOH	60	24.7
Ox 12	EtOH	35	41.0		EtOH/H$_2$O	60	37.8
Ox 13	EtOH	45	37.5	Ox 21	EtOH	55	42.2
Ox 13A	EtOH	45	44.9	Ox 21Z3[a]	EtOH	60	40.3
Ox 16	EtOH	60	30.7	Ox 27[a]	EtOH	60	76.9
Ox 17	EtOH	60	19.1	Ox I27Z3[a]	EtOH	60	58.3

[a] Present work.

the zwitterions have essentially the same or somewhat less output than the tosylate salts. (Except for Ox 13A, the perchlorate salt, all earlier work in Table 1 is for the tosylate salt). In the case of the Ox 2 series, the tosylate at the same energy input would have a somewhat larger output than the mesylate. The zwitterion, Ox 2Z3, had the highest output of any dye we have observed. Under the same conditions, rhodamine 6G put out 100.2 mJ. Actually Ox 12 has the largest slope efficiency of any of the pyridinium oxazole dyes tested, but Ox 12 has a small lifetime and was not tested previously at 60 J input. Table 2 lists the lasing parameters for the dyes in this work along with three comparison dyes.

627

TABLE 2. Lasing Parameters for Dyes in This Study. Solvent is ethanol unless otherwise indicated, cover gas is argon

Dye		1000 K[a]	t, J	1/c MJ/l	FOM kJ/l
Ox 2	EtOH/H$_2$O	2.63	26.2	438	1,152
Ox 2A	EtOH/H$_2$O	2.29	26.7	>>10,000[a]	...
Ox 2Z3	EtOH/H$_2$O	2.57	18.7	>>10,000[a]	...
Ox 20Z3		0.71	23.9	>>10,000[a]	...
Ox 21Z3		1.13	22.0	1,493	1,672
Ox 16Z3		1.77	22.2	25.2	44.6
Ox 17[b]	EtOH/H$_2$O	0.64	29.1	18.0	12.0
OX 17A	EtOH/H$_2$O	0.89	21.4	0.005	0.004
Rho 6G TFB[c]		3.35	15.9	345	1,200

[a] K is the slope efficiency, t is the threshold, 1/C is the lifetime, FOM is the figure of merit.

[b] From Reference 1.

[c] From Reference 8.

The fluorescence quantum yields of the dye variations are summarized in Table 3. With one exception, all the zwitterions have quantum yields >0.9. In the Ox 2 series, the tosylate and the mesylate have essentially the same quantum yield.

TABLE 3. Absorption and Emission Wave Length Maxima and Fluorescence Quantum Yields (FQY) for Selected Pyridinium Oxazole Dyes in Ethanol Under Air.

Dye	Absolute Peak, nm	Emission Peak, nm	FQY
Ox 2	410	567	0.73
Ox 2A	411.2	565	0.76
Ox 2Z3	409.7	563	0.92
Ox 16Z3	417.7	520	0.86
Ox 20Z3	389.7	491	1.03
Ox 21Z3	387.0	495	1.01
Ox 27	411.2	571	0.83
Ox 27Z3	411.8	567	0.91
Ox 17A	410.6	534	0.99
Ox 12	452.2	584	0.65

DISCUSSION

In our previous work[1] (Figure 1), A was generally the tosylate anion and the pyridyl nitrogen was quaterized with a methyl group in the B position. We found that substitution of a fluorine atom, methoxy or phenoxy groups for hydrogen in position C improved output and lifetime over the unsubstituted dye in a given solvent. Aliphatic substitution at the 4 position on the oxazole ring increased both output and lifetime. At the same time, substitution of F at position C reduced the output and lifetime; however, these parameters were both still greater than the basic dye, Ox 1. Bridging the 2 and 4 positions between the phenyl and oxazole rings produced results dependent upon the degree of saturation of the bridge. Compared to Ox 2, an ethylene link (Ox 12) greatly improved the slope efficiency while reducing lifetime significantly. Also compare Ox 13 and 13A with Ox 1. A vinylene link, Ox 15, showed an improved slope efficiency and was one of the dyes with a superior lifetime. On these dyes simultaneous substitution of a fluorine atom in position C considerably reduced both output and lifetime, though the resulting dyes are still better than the basic dye. Table 4 gives the lasing parameters taken from Reference 1 for comparison purposes. All the changes discussed affected the basic chromophore and influenced the lasing parameters strongly.

In sharp contrast to these results, changing from the tosylate salt to the perchlorate produced only small changes in the lasing parameters (compare Ox 13 and 13A in Table 4 and 1). Also see the

TABLE 4. Lasing Parameters for Comparison Dyes Used in This Work.
The solvent is ethanol and the cover gas is argon unless otherwise
noted. Taken from Reference 1.

Dye	1000 K	t, J	1/C MJ/l	FOM kJ/l
Ox 1	0.56	31.4	35	19.6
Ox 2	1.53	22.1	10,000	15,300
Ox 2 Methanol	1.0	15.6	10,000	10,000
Ox 3	2.1	23.8	485	1,018
Ox 4	1.12	25.3	32.8	36.7
Ox12	3.00	21.8	188	564
Ox 13[a]	1.64	22.5	3.2	5.2
Ox 13A[a]	1.84	22.1	1.7	3.1
Ox 15	1.29	25.8	10,000	12,900
Ox 16	0.85	26.8	61	52
Ox 20	1.57	26.8	704	1106
Ox 21	1.63	26.0	10,000	16,300

[a] Ox 13 and 13A not properly distinguished in Reference 1. Also note errors in parameters for Ox 13 in Reference 1.

differences between the tosylate and mesylate salts, Ox 2 and Ox 2A (Table 2)   Though the thresholds are similar, the slope efficiency of the mesylate is actually somewhat less than the tosylate.   The big improvement is observed in the lifetime.   It is noted that the lifetimes of Ox 2A, Ox 2Z3, and Ox 20Z3 are >>10,000.   What this number means is that over the test period no decay was observed in the dye. These dyes were tested from 1.5 to 4.5 million shots at 10 J input at 25 Hz with no loss in output. Thus only with Ox 2Z3, the propanesulfone zwitterion, do we observe enhanced output and that of only about 20%, not the 2.5 times observed by Kauffman and Bentley.[3]   The other zwitterionic dyes actually had slightly reduced outputs compared to tosylate or mesylate salts, even for Ox 27 where an n-butoxy was substituted for methoxy to try to improve solubility.

These findings reinforce our conclusion that only by changing the electronic environment do we affect the lasing parameters.   Changing anions has little affect on the lasing parameters.   Using a zwitterion only in one case, the only dye tested by Kauffman and Bentley, lead to improved performance. To see if more understanding of the complex effect of the zwitterion on the electronic environment can be gained, these dyes will be submitted to calculation of molecular orbital parameters

REFERENCES

1.   A. N. Fletcher, R. A. Henry, M. E. Pietrak, D. E. Bliss, and J. H. Hall, Appl. Phys. B43, 155 (1987).
2.   R. F. Kubin, A. N. Fletcher, M. E. Pietrak, and D. E. Bliss, in proceedings, International Conference on Lasers '87, F. Duarte, Ed. (STS Press, McLean, VA, 1987), pp. 1005-1009.
3.   J. M. Kauffman and J. H. Bentley, Laser Chem. 8, 49 (1988).
4.   A. N. Fletcher, D. E. Bliss, M. E. Pietrak, and G. E. McManis III, in proceedings, International Conference on Lasers '85, C. P. Wang, Ed. (STS Press, McLean, VA, 1986), pp. 797-804.
5.   J. M. Kauffman, private communication.
6.   A. N. Fletcher, R. A. Henry, R. F. Kubin, and R. A. Hollins, Optics Comm. 48, 352 (1984).
7.   R. F. Kubin and A. N. Fletcher, Chem. Phys. Lett. 99, 49 (1983).
8.   A. N. Fletcher, Appl. Phys. B31, 19 (1983).

FROM COMPUTERS TO HOLOGRAMS: 3-D IMAGING OF 3-D COMPUTER GRAPHICS

John R. Andrews
Webster Research Center
Xerox Corporation
800 Phillips Rd MS0114-20D
Webster, NY 14580

Abstract

Holography offers the opportunity for hardcopy and mass producible autostereoscopic 3-D viewing of images created with computer graphics. This talk will cover recent advances in holography for displaying 3-D computer graphics: wide viewing angle planar format holograms, geometric accuracy, and automated production using liquid crystal spatial light modulators.

I. Introduction

Three-dimensional computer graphics is of growing importance in a wide range of fields for both technical and non-technical applications. Some of these areas include computer aided design/engineering/manufacturing (CAD/CAE/CAM), architecture and facilities management, cartography, medical imaging, advertising and entertainment, and science (crystallography, pharmacology, etc.). Most large manufacturing companies rely heavily on 3-D computer graphics tools: CAD, CAE, and CAM to speed the process of bringing products into the marketplace. Visualization of the 3-D designs with the retention of the depth information could speed all of these processes. Other technical and non-technical business activities and even education can benefit from 3-D visualization. Each of these potential applications areas will require different things from holograms made from computer graphics imagery. However, the extent to which holography and in particular holographic stereograms can aid the visualization of depth will depend on how effective the display is and how quickly it can be created. The subjects for this paper, wide viewing angle and geometric accuracy, address the effectiveness of the display, and spatial light modulator writing of holographic stereograms addresses the issue of rapid creation.

II. Holographic Stereograms

The key depth que, absent from normal photography, that holography can provide is the small differences in the views for the left and right eyes, parallax. Normal holography requires a real 3-D object to record full parallax. An object created in a computer may not exist in the real world, making normal holography impossible. Holographic stereograms synthesize three-dimensional views by incorporating parallax, at least in the lateral plane, as a series of 2-D projections from different viewing locations.[1] The role of holography in this instance is to record the numerous views and the optics to enable restriction of observation to the view that would be seen by each eye at its location if the object were really in front of the viewer. The 2-D projections used to make holographic stereograms can be the result of photography of a real object or scene or the computed projections of an object in a 3-D computer graphics system. There are several commonly used processes for accomplishing this task. The one discussed here is a two-step process.[2] In the first step the film strip that contains the sequence of perspective views is projected onto a diffusing screen with coherent light. A movable slit placed over the holographic recording plate restricts the exposure by both the scattered light from the diffusing screen and the reference beam to a narrow band. The sequence of perspective images is recorded on neighboring segments of the master hologram. The perspective change between images, image magnification, and slit width are adjusted so that when the master hologram is reilluminated with the reference beam, a virtual image of the subject having normal horizontal parallax is seen. The second step converts the laser viewable hologram to an image plane hologram that is viewable in white light. To accomplish this the master hologram is illuminated with the conjugate reference beam to form a real image of the diffusing screen that is composed of a superposition of the entire sequence of views. This real image is holographically recorded with the holographic plate at the location of the image of the diffuser. This image plane hologram is viewable in white light when it is illuminated with the conjugate beam.

III. Wide Viewing Angle

The viewing zone for second generation holograms is the size of the viewing window formed by the master hologram. The angular range of viewing the master hologram is determined by the relative size of the master and image plane holograms and the distance between them. The required illumination of the master and image plane holograms without either reference beams overlapping the other hologram limits how close the holograms can be placed to one another. Figure 1 illustrates this geometric constraint. One can show that the maximum viewing half-angle ϕ is related to the reference beam angle θ by the following relationship:

$$\tan\phi = \frac{(m-w)}{(m+w)}\tan\theta \qquad (1)$$

where m is the master hologram width and w is the final hologram width. From Eq. (1) it is evident that the relative widths of the master and final holograms is the major determining factor in the final viewing angle. For a reference

beam angle of 45° and $m/w = 2$, $\phi = 18.4°$ and for $m/w = 4$, $\phi = 31°$. A second consideration that limits the quality of the holograms over wide viewing angles is related to the angular dependence of the light scattered by the diffuser. This is illustrated in Fig. 2 for three different types of diffuser.[3] For a Lambert's Law diffuser the intensity falls by half at an angle of 60°. The wide scattering angle means that the peak scattered intensity in the forward direction is relatively low leading to long exposure times for the holographic recording. Also these diffusers tend to have low spatial resolution due to multiple scattering. By using less diffusing material both of the negative effects can be reduced at the expense of a sharper fall-off in the scattering pattern and consequently a narrower effective viewing range. Fig. 3 shows a holographic stereogram having a viewing angle >60°. In this hologram the image is created by computed projections of a 3-D object in a computer. The edges of surfaces are represented by the visible lines and all of the hidden lines have been removed. In this example, where a flashed opal glass diffuser was used, the effect of the decrease in the scattered light intensity at large angles is minimal.
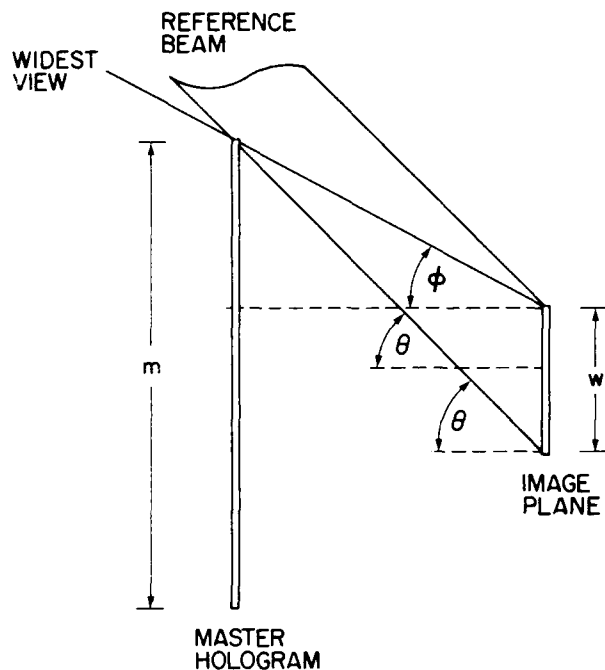

Figure 1   The disposition of the master and image plane holograms to determine the viewing angle.

SCATTERING BY VARIOUS DIFFUSERS

— LAMBERT'S LAW
$I(\theta) = I(O)\cos\theta$

--- FLASHED OPAL GLASS

—·— SAND BLASTED GLASS
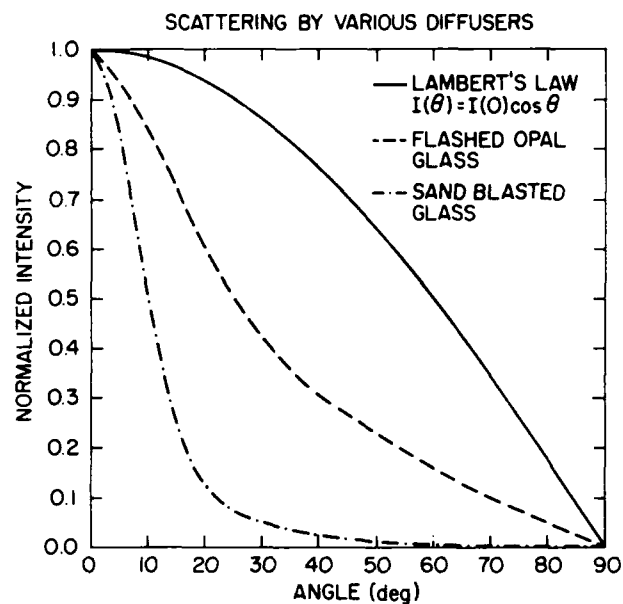
Figure 2   Scattering distribution for various diffusers (after Ref. 3).
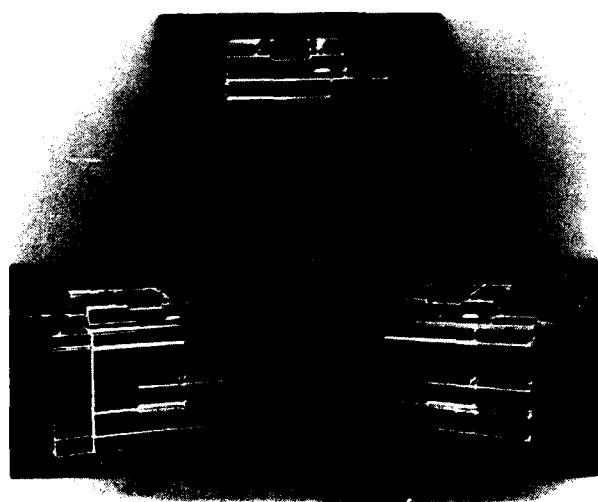

Figure 3   Photographs of a hologram from three viewing locations.

631

IV. Geometric Accuracy

Holographic stereograms that are created from projections of the 3-D object appropriate to photographic or visual imaging provide accurate representations if the viewer's eyes are located in the plane of the master hologram. At other locations the image is made up of a composite of portions of images from different viewing locations. The composite images result in distortion in the geometry that increases with the distance of the subject from the image plane. The push for a wide viewing angle in the final hologram leads to a situation where the viewing location is far from the master hologram, thus causing large distortion of the image from its original geometry. This situation is depicted in Fig. 4.

In most cases it is desirable to be able to accurately reproduce the geometry of the object that was created in the computer. This can be done by developing an imaging model that incorporates the horizontal parallax of the holographic stereogram.[5] A model for imaging by holographic stereograms can be understood by examining Fig. 5.
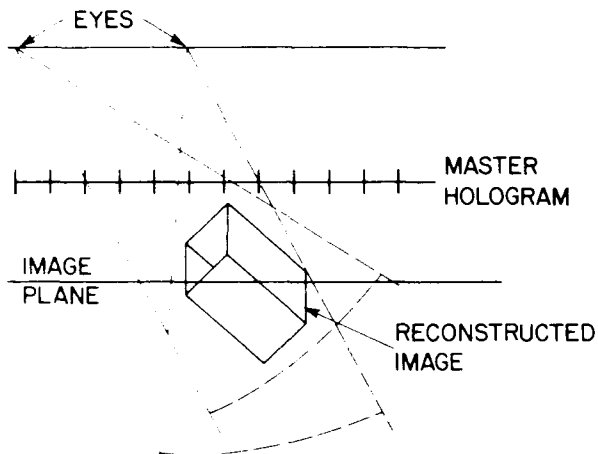

Figure 4   The viewing of an image through several slit holograms in the master.
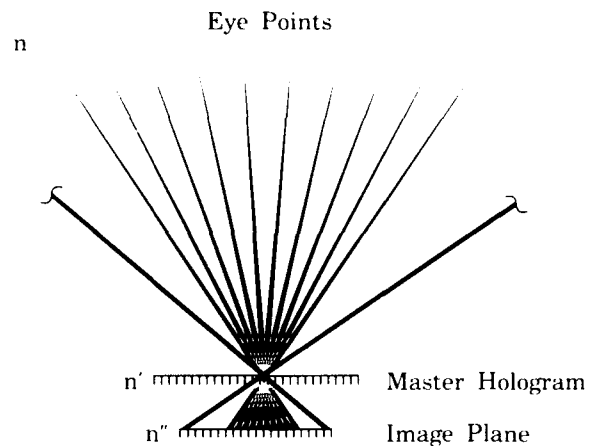

Figure 5   An appropriate imaging model for holographic stereograms has the image plane for any slit hologram contain segments from various eye points.

The image stored in any segment, n', of the master hologram consists of segments, n'', that are obtained from a range of eyepoints, n. The correct image plane film strip is obtained by segmenting the normal photographic perspective images and rearranging them into a secondary set of images that each have components from the range of eye points. This new film strip can then be holographically exposed in the usual way. In Fig. 6a a photograph of a holographic stereogram made using the normal photographic perspective views is shown. Note the shrinking of the dimensions for portions of the subject that come out of the plane and expansion of portions of the subject behind the plane. In Fig. 6b a photograph of a holographic stereogram is shown where the normal perspective images have been processed to form the film strip of secondary images as described above. The hologram made using the image processing algorithm gives   accurate geometric depiction of the subject.

V. Holographic Stereograms made Using Spatial Light Modulators

The use of photographic methods to accomplish the conversion of an incoherent CRT image to a coherent image offers resolution that exceeds any available computer display and has very high contrast (>100) and continuous gray scale. However, the time lag because of the film processing, the cost of film and processing, and the need for human involvement to load and unload film at both the photographic and holographic stations reduces the convenience of obtaining hard copy 3-D images of the 3-D computer graphics. We have been examining the use of spatial light modulators (SMLs) as a direct interface between the computer graphics and the holographic exposures in making holographic stereograms.[6,7] The use of SMLs could enable rapid, inexpensive, and automatable conversion of computer graphics into holograms.

Spatial light modulator technology is progressing rapidly from low resolution and low contrast to levels of performance that show promise for use in holography and coherent optical processing applications. For instance the currently available generation of SMLs are 2-D matrix addressed liquid crystal displays (LCDs). For instance the Kodak Data Show contains a Japanese-made LCD and contains the necessary interface for computer graphics. Some of its characteristics are: enhanced graphics adapter (EGA) data, 640X480 pixel resolution, 20.3X15.2 cm area, measured contrast of 16, and 8 gray levels. The EGA format is a standard for IBM PC® and compatibles and seems adequate for many computer graphics applications. Interface for Apple® PC's are also available. The contrast of 16 measured at 514.5 nm is still much lower than available with photography, but can prove adequate in some holographic applications.

The experimental arrangement that we use to make holographic stereograms using the LCD is shown in Fig. 7. An IBM PC compatible is used to drive the LCD. The computer calculations that provide the perspective images are typically performed on a mainframe computer or stand alone workstation and transferred to the PC for the
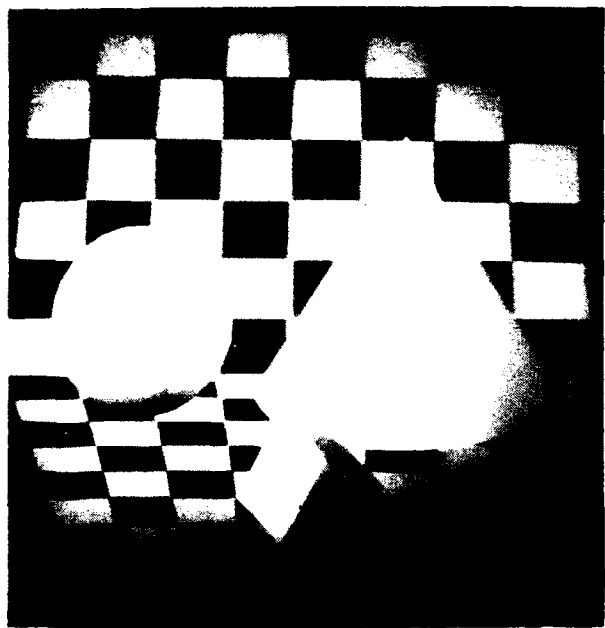
632
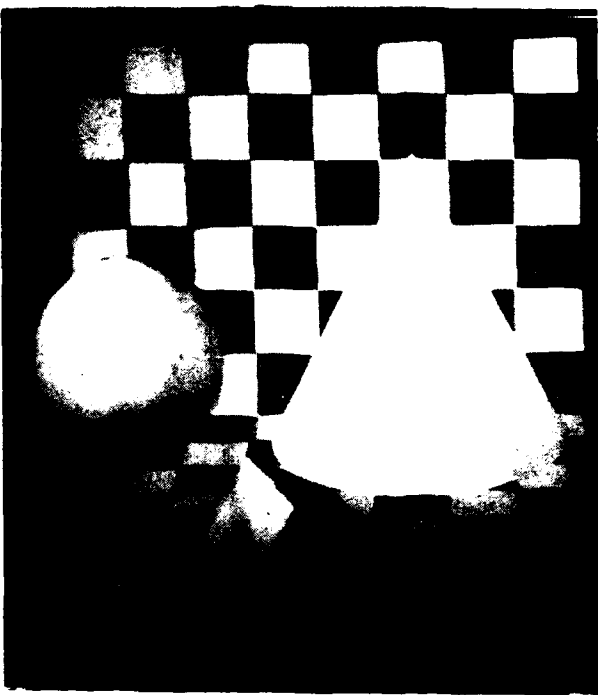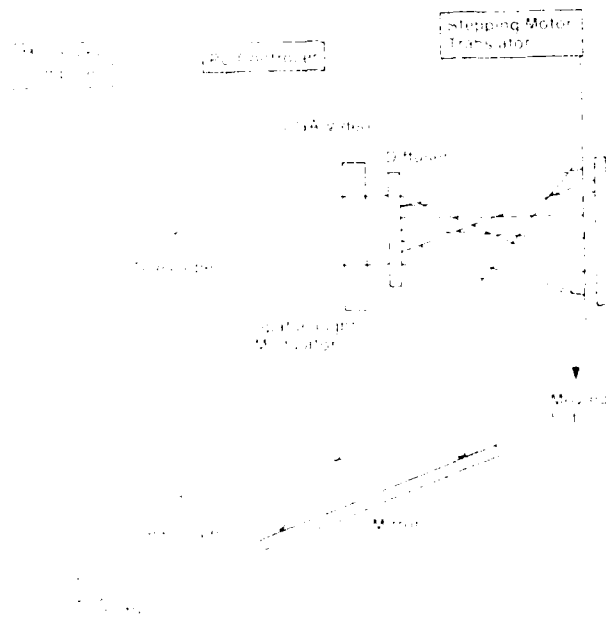
holographic steps. The PC controls the holographic exposures and slit motion as well as providing the graphics driver. The projector optics are modified from the 35 mm film projection optics. For the large format LCD, a telescope provides a plane wave at the input side and a diffuser at the output side provides a holographic image plane that is the same size as the LCD. A photograph of a hologram made using this technique is shown in Fig. 8. For simplicity this image is a single view of the chess game from a single viewing location. Note the reasonable visibility of the image, and the smoothness of the diagonal lines. The contrast is still substantially smaller than that available from the holographic process and provides the most significant limitation to the use of this technology. It is anticipated that further developments will provide commercial SMLs with both higher resolution and increased contrast.
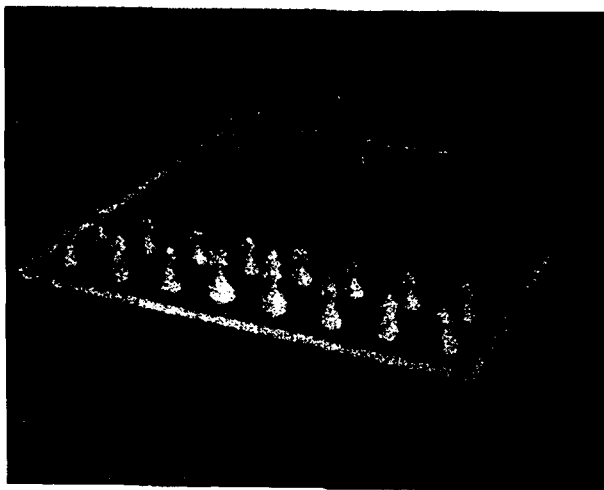
Figure 8   A picture of a hologram made using a
spatial light modulator.

VI. Conclusions

High viewability of holograms is an important factor in increasing their potential use in the work environment. This paper has discussed two aspects of viewability, limits on the viewing angle for planar format holographic stereograms, and obtaining geometrically accurate images from computer graphics. The ease of making holographic stereograms will place a limitation on the availability of holographic imagery in the workplace. The demonstration that currently available spatial light modulators can be used to make reasonable holographic images indicates that SLM technology is close to having a substantial impact on holography.

VII. Acknowledgements

The author would like to thank Mike Rainsdon for the computer graphics and especially for his contributions to the image processing algorithm. The fine photography of Floyd Johnson is also appreciated.

VIII. References

1. J. T. McCrickert and N. George, Appl. Phys. Lett. 12, 10 (1968).
2. M. C. King, A. M. Noll and D. H. Berry, Appl. Opt. 9, 471 (1970).
3. L. Levi, Applied Optics, Vol. 1, John Wiley and Sons, New York, 1968, pp336-339.
4. I. Glaser, Opt. Commun. 7, 323 (1973).
5. L. Huff and R. L. Fusek, Proc. SPIE 367, 84 (1982)
6. M. A. Teitel, S. A. Benton, J. Opt Soc. Amer. A 3, 53 (1986).
7. M. D. Rainsdon and J. R. Andrews, Proceedings of the SPSE 41st Annual Meeting, Washington D. C., May, 1988, pg 251.
8. J. R. Andrews and R. Damm, J. Opt. Soc. Am. A 4, P76 (1987).
9. J. R. Andrews, B. Tuttle, M. Rainsdon, R. Damm, K. Thomas, and W. E. Haas, Proc. SPIE 902, 92, (1988).

REAL-TIME HOLOGRAPHY USING SeGe FILMS

R.A. Lessard, L. Song, P. Galarneau, A. Singh
LROL-Physics Department, Université Laval
Ste-Foy, Qc, Canada G1K 7P4

Abstract

Real-time holography has been performed in SeGe thin films. Particular attention has been paid on recording based on crystallization. The main mechanisms involved in the process are discussed: the laser-induced temperature profile, the kinetics of crystallization of Se, the laser-induced crystallization and the diffraction efficiency of thin mixed gratings. The holographic recording properties of SeGe thin films will also be presented.

Introduction

In the perspective of the work, real-time holography is taken in its less restrictive sense which is development-free holography. It has its main applications in non-destructive testing and in optical mass data storage, its main advantages being cost effectiveness, time effectiveness and the simplicity of the process. Of course, the process describded by the more recent and more restrictive definition which involved dynamical gratings has a lot of advantages and applications such as real-time signal processing, phase conjugation and optical dynamic interconnection, nevertheless we will restrict ourself to the former sense.

The optical recording media that will be used efficiently in real-time holography have to fulfill a number of requirements. Amoung them, one may noticed a good chemical stability, a good thermal stability, a low energy consumption, a high generated optical contrast, a fast recording process and a low cost. The erasability may be required in some applications and has a strong importance in optical data storage. For erasable media, a fast recording process is needed and no mechanical deformation should occur during writing or erasing.

First demonstrated by Ovshinsky and his group[1], the laser induced reversible phase transition is an interesting means to store information, since it has the possibility of being erasable. The standard reversible amorphous to crystalline phase transition is schematized in Fig. 1. An intense short laser pulse is used to melt the recording media in a very short time with the minimum energy possible. The fast cooling that follow freeze the media which end up in the amorphous phase. The crystalline phase is obtained by the illumination of the media with a somewhat longer but less intense laser pulse. The intensity of the laser should be at a level such that the temperature of the media is just above the glass temperature transition for the time, governed by the pulsewidth, required to allow crystallization to occur. This process has the advantages of being erasable, all optical and often faster than other erasable scheme.
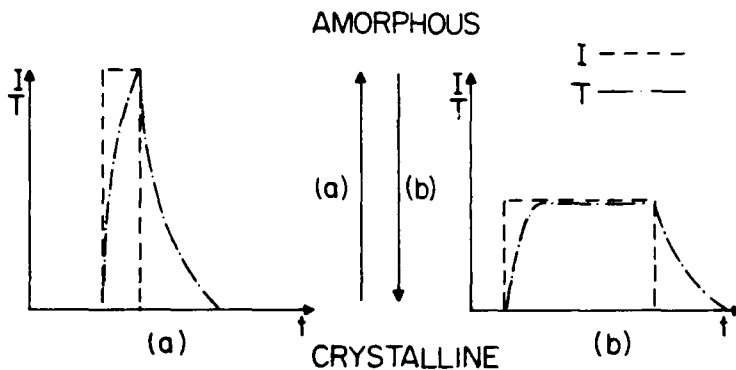
Figure 1. Reversible laser-induced phase transition.

The purpose of the work presented here was double. First, we wish to investigate the optical recording properties of SeGe thin films and second, we wish to understand more deeply all the aspects of the recording process. The choice of the material was dicted by the fact that Se has been found to be a good recording media[2-3], but the lifetime of the stored information is too short[4] due to the low crystallization activation energy (Ea) of Se. The use of Ge to form SeGe alloys is investigated as a means to overcome this problem.

The other aspects of our work was dedicted to the identification of the mechanisms involved and the relative importance of the relevant parameters. The evaluation of the

optical recording properties along with the modelling of the recording process were also part of that work. Although holographic recording based on amorphisation were realized in SeGe thin films[5], this paper will focus its attention on the crystallization process.

Physical mechanisms involved

Laser-induced temperature profile

The photo-induced phase transition is more a thermally induced phase transition where the laser is used as a heat source, than a truely optical induced process. Thus, the evolution of the laser-induced temperature profile is an important process to understand. The problem is schematised in Fig. 2, it is assumed to be an unidimentional problem since holographic recording were performed in SeGe thin films with spatial frequency up to 600 1/mm without degradation of the diffraction efficiency[2] and the absorption in the thin film is governed by the Beer-Lambert's law.
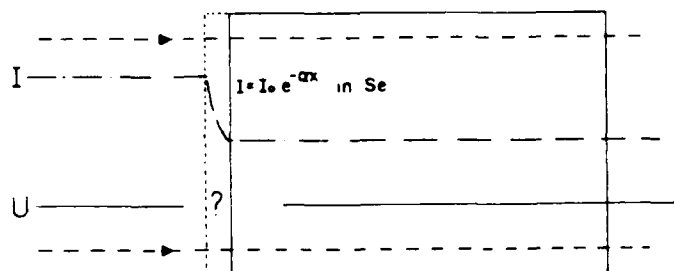
Figure 2. Laser-induced temperature profile.

The resolution of the heat diffusion differential equation with Newton's law of continuity at the interfaces (see equations 1) has been acheived using the Green's functions method[6].

The resulting equations have been used to simulated the temperature field in Se thin films deposited on glass substrate. A typical results is shown in Fig. 3. From those calculations it is clear that the holographic recording using a cw laser is an isothermal process. It is also evident that for pulsed illumination the interfaces conditions affect mainly the cooling behaviour.

Figure 3. Temperature profile in 200 nm thick Se film.
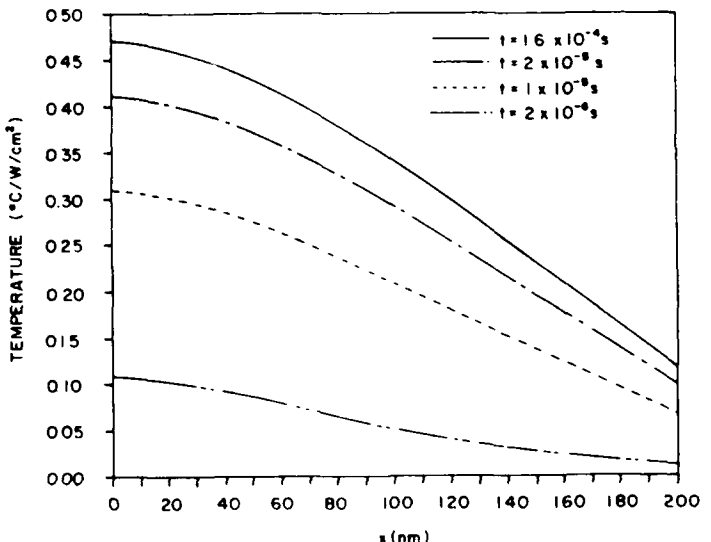
$$\frac{\partial U(x,t)}{\partial t} - a^2 \frac{\partial^2 U(x,t)}{\partial x^2} = i(x,t)_{abs}. \tag{1.a}$$

$$U(x,t)\big|_{t=0} = 0. \tag{1.b}$$

$$-\frac{\partial U(x,t)}{\partial x}\bigg|_{x=0} + H_1 U(x,t)\big|_{x=0} = 0. \tag{1.c}$$

and

$$+\frac{\partial U(x,t)}{\partial x}\bigg|_{x=1} + H_2 U(x,t)\big|_{x=1} = 0. \tag{1.d}$$

636

Kinetics of crystallization of Se

The kinetics of crystallization may be successfully described by the empirical equation of Avrami (equation 2.a) combined with the Arrhenius law (equation 2.b).

$$r = 1 - \exp(Kt^{n_A}) \quad , \tag{2.a}$$

$$K = K_O \exp(-Ea/RT) \quad , \tag{2.b}$$

where r is the crystalline fraction, K is the reaction rate, n_A is the Avrami exponent, K_O is the rate constant, Ea is the crystallization activation energy, R is the universal gaz constant and T is the temperature in Kelvin. For an isothermal process, the logarithmic expression of that equation (equation 3) leads to the determination of the Avrami exponent n_A and the crystallization activation energy Ea.

$$\ln(-\ln(1-r)) = \ln(K_O)-(Ea/RT)+n_A\ln(t) \quad , \tag{3}$$

Standard differential scanning calorimeter (DSC) experiments have been performed on the selenium powder used in our work and it was found[4] that Ea = 55.1 KJ/mol and n_A = 3.24.

The Fig. 4 shows the x-rays diffraction pattern for the as-deposited (a) and after annealing in an oven (b) Se thin film, from that figure it is easy to conclude that the as-deposited film were amorphous while the annealed one were crystalline showing prefered growth along the (100) and (101) direction of the hexagonal structure.
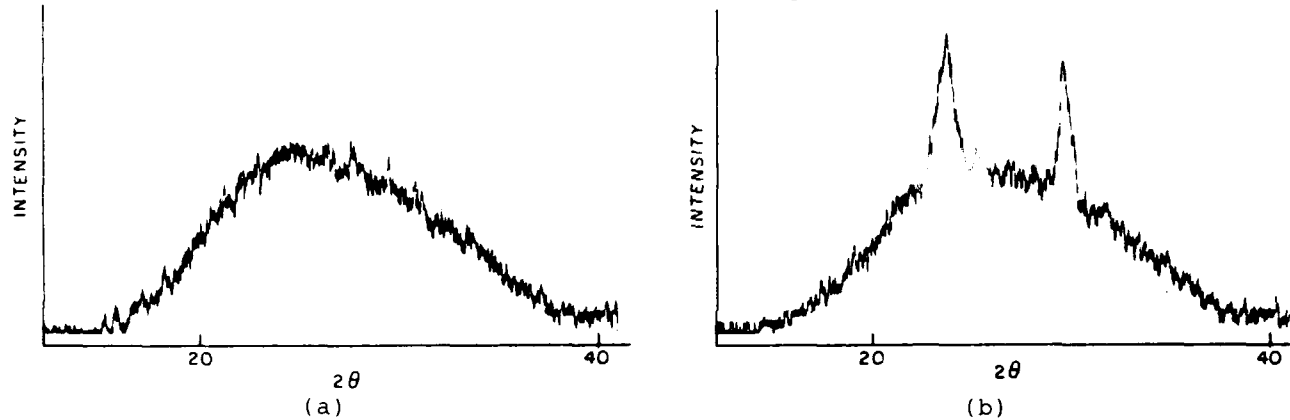
Figure 4. X-rays diffraction pattern of (a) as-deposited thin films and (b) after annealing at constant temperature in an oven.

The DSC experiments were inappropriated for kinetics study of thin films. Based on the approximations that the optical constants n and k vary linearly with r and that the optical transmittance vary linearly with r, a very low intensity optical transmittance technique was developped to investigate the kinetics of crystallization of thin films[7]. Both approximations were found to be valid on the investigated range of parameters using the Maxwell-Garnett theory and the standard thin films interference calculations.
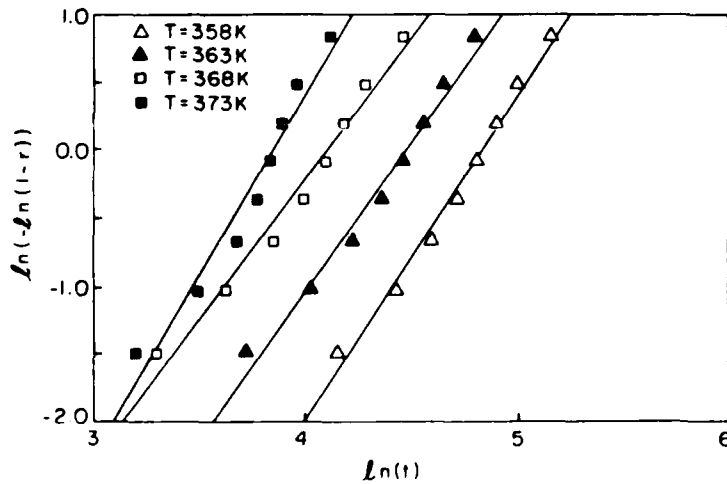
Figure 5. ln(-ln(1-r)) vs ln(t) for Se thin film held at 10°C during the deposition and annealed in an oven at constant temperature T.

637

It has been found that properties of Se thin films (such as oxydation speed) depend strongly on deposition conditions (such as substrate temperature). Thus a detailed study of the kinetics of crystallization in Se thin films that were deposited under different substrate temperature condition was realised. Typical results are shown in Fig. 5 and a summary of these results is presented in table 1. One may notice the increase of Ea with the temperature at which were held the substrate during the deposition.

Substrate temperature	10 °C	20 °C	35 °C	50 °C
Average value of n_A for annealing at 80, 90, and 95 °C	2.2	2.3	2.2	2.4
Value of n_A for annealing at 100 °C	2.7	3.7	3.8	3.8
Activation energy $(kJmol^{-1})$	157	167	191	245

Table 1. Kinetics properties of Se thin films vs substrate temperature during the deposition.

Laser-induced crystallization

(a)

(b)

(c)

(d)
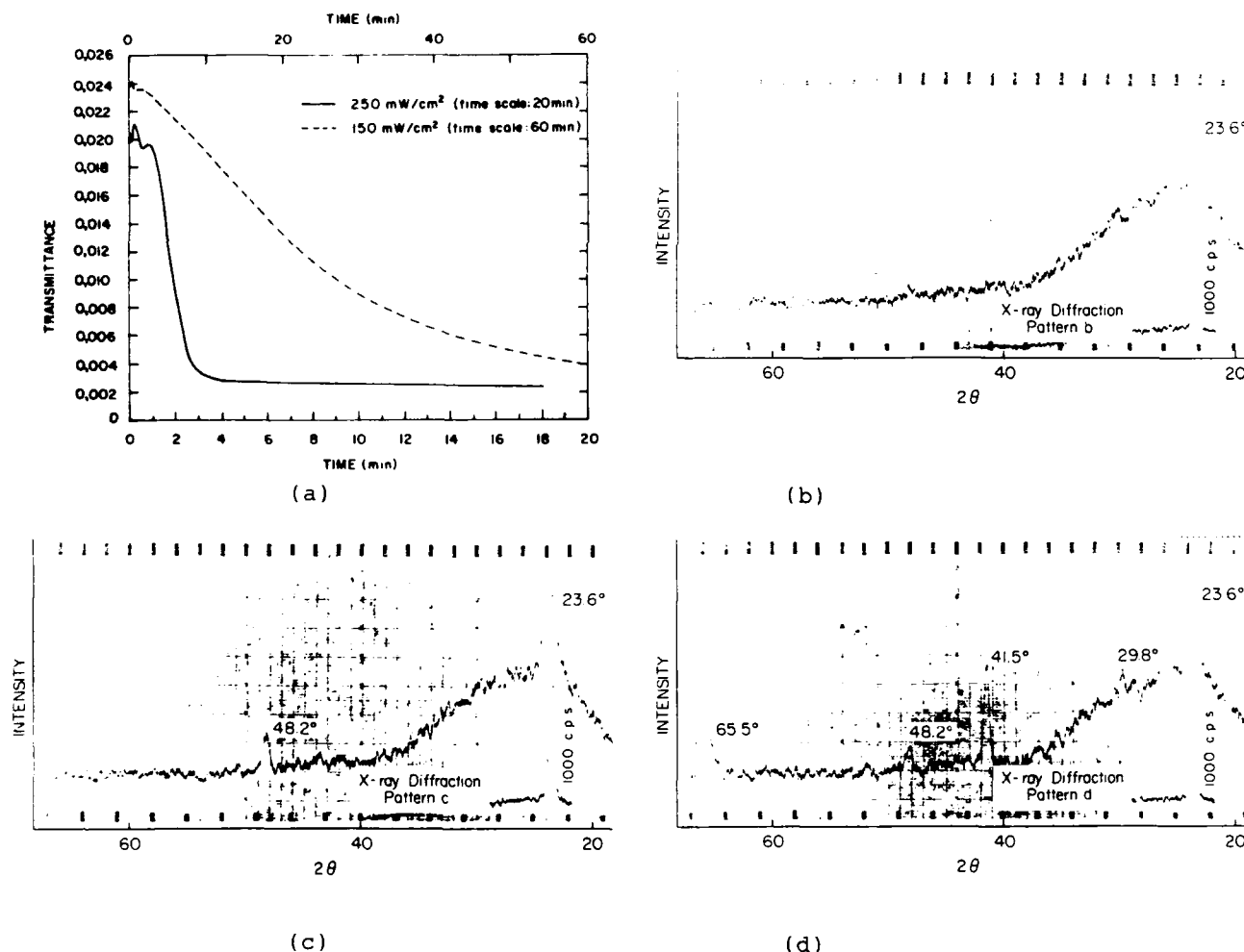
Figure 6. (a) Variation of optical transmittance of Se thin films for X-ray diffraction analysis experiment; (b)-(d) Patterns of X-ray diffraction analysis of Se thin films; (b) I = 250 mW/cm², t = 1.5 min; (c) I = 250 mW/cm², t = 4 min; (d) I = 250 mW/cm², t = 24 min.

Laser annealing was also performed on Se thin films[8]. At an intensity of 250 mW/cm^2 at 488 nm, the transmittance of the laser beam decreases for a period of 4 minutes and then remains fairly constant (see Fig. 6.a). X-ray diffraction patterns were taken at different steps during the laser annealing, it was found that laser-induced crystallization was the mechanism responsible for the variation of the optical transmittance. It was also noticed that until the transmittance reaches it final value, the crystallization occurs along the hexagonal (100) direction. After that, several peaks, corresponding to different crystalline orientation, appear on the x-ray diffraction pattern (see Fig. 6 b-d). The same experiment has been performed on $Se_{.91}Ge_{.9}$, the crystallization was also identified as a (100) hexagonal Se. Opposite to Se, no other crystalline orientation were seen for long laser exposure time.

Diffraction efficiency of thin mixed gratings

Generally, the diffraction efficiency of thin gratings is developped in two specific situations: the phase grating and the amplitude grating. In SeGe thin films a much more realistic description will involved both phase and amplitude modulation of the wavefront. The transmission Tr through the thin grating is described by equations 4.

$$ \left\{ T_{ro} - T_{r1} \cos(2\pi y/\Lambda) \right\} \exp(i[\varphi_o + \varphi_1 \cos(2\pi y/\Lambda)]), \tag{4} $$

where y is the coordinate parallel to the grating vector, Tr_i are constants related to the real part of the transmission, Φ_i are constants describing the phase content of the transmission and Λ is the step of the grating. Since Fraunhofer diffraction may be described by Fourier transform, one may use the convolution theorem to obtain the the diffraction efficiency of the grating[9] (see equation 5).

$$ \left[J_1(\varphi_1) - J_2(\varphi_1) \right]^2 + \left[T_{ro} J_1(\varphi_1) \right]^2 \tag{5} $$

where J_i are Bessel function of the ith order. A plot of the diffraction effiency in function of the phase modulation is shown in Fig. 7. In the even more realistic description of the transmission (see equation 6), the first order diffraction efficiency is thus given in equation 7, where I_i are modified Bessel functions of the ith order.

$$ \left[\cos(2\pi y/\Lambda) \right] \exp(i[\varphi_o + \varphi_1 \cos(2\pi y/\Lambda)]), \tag{6} $$

$$ \left\{ \left[I_1 \left[I_o(\varphi_1) - I_2(\varphi_1) \right] \right]^2 + \left[I_o(\beta_1) I_1(\varphi_1) \right]^2 \right\} \tag{7} $$
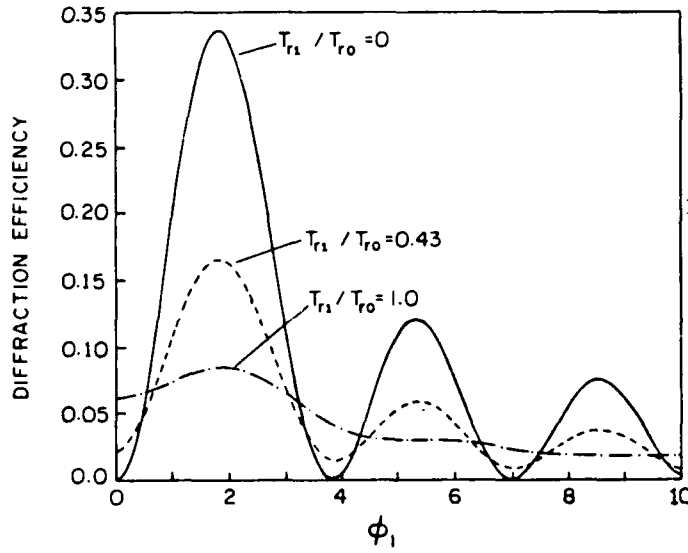
Figure 7. Diffraction efficiency of thin mixed gratings vs phase modulation, for different amplitude modulation.

The optical recording properties

Holographic recording with a cw laser

Holographic recording were performed in SeGe thin films using a cw Ar$^+$ laser at 488 nm[8]. The recording angle was 14° and the reading was performed at Bragg angle with a HeNe laser beam (632.8 nm). The diffraction efficiencies vs exposure time for different writing beams intensities in Se thin films are plotted in Fig. 8. As expected, a higher writing beams intensity results in a faster recording process. One may also notice the presence of an

639

optimum intensity for the writing beams, revealing the importance of the crystallization within the interfringes spacing. The measurement of the MTF of Se thin films was also been performed and is shown in Fig. 9. The bandwidth of that media is thus estimated to 800 l/mm. Fig. 10 to 12 show the diffraction efficiencies vs exposure time for different writing beams intensities in different alloys of SeGe. As the Ge concentration increase, the maximum diffraction efficiency decrease. Nevertheless, it is still desirable to add a small amount of Ge to allow crosslinking of Se which increase the stability of its amorphous phase.

Figure 8.   Diffraction efficiency vs time, in Se thin films for various writing beams intensities.

Figure 9.   Diffraction efficiency vs spatial frequency.
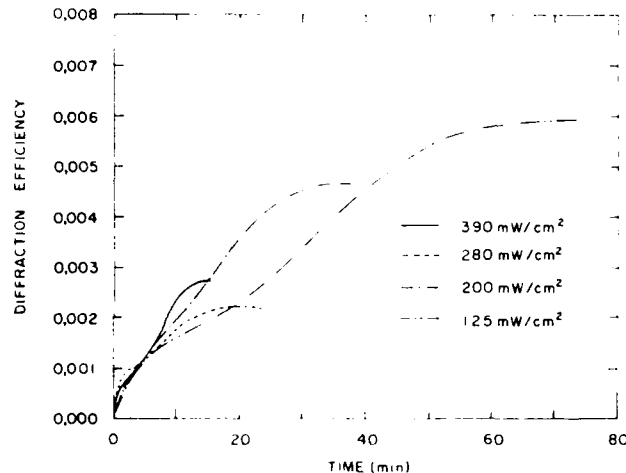
Figure 10. Diffraction efficiency vs time, in $Se_{91}Ge_9$ thin films for various writing beams intensities.
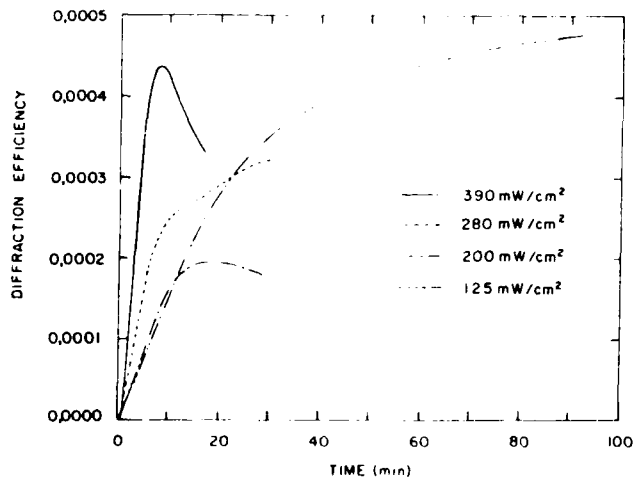
Figure 11. As Fig. 10 for $Se_{86}Ge_{14}$ thin films.
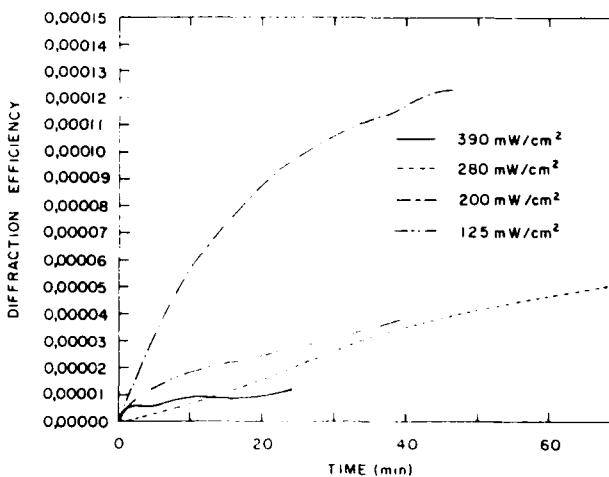
Figure 12. As Fig. 10 for $Se_{80}Ge_{20}$ thin films.

Holographic recording based on amorphisation

Holographic as well as bit-by-bit recording has been realised in SeGe thin films using amorphisation induced by a short laser pulse[5]. Fig. 13 shows the experimental setup for holographic recording and Fig. 14 gives a typical dependence of the diffraction efficiency vs energy density of the writing beams. The low efficiency approximation of the diffraction efficiency ($\eta = I_1/I_o$, where I_i is the ith order of diffraction) has been used to determine η. Erasing time shorter than 50 ns has been demonstrated in those media using the bit-by-bit recording scheme.
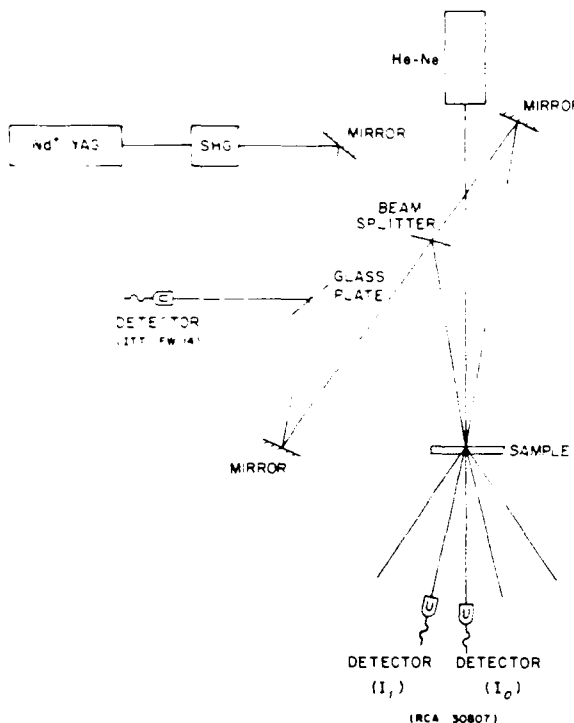
Figure 13. Experimental setup.
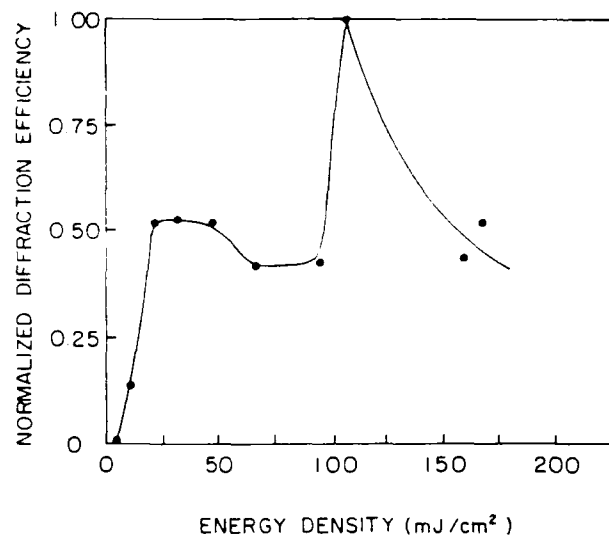
Figure 14. Diffraction efficiency vs incident energy density, in $Se_{50}Ge_{50}$ thin films.

The influence of the substrate temperature during the deposition

As it has been mentionned previously, the properties of the thin films were found to be very dependent on the deposition conditions such as substrate temperature. The optical
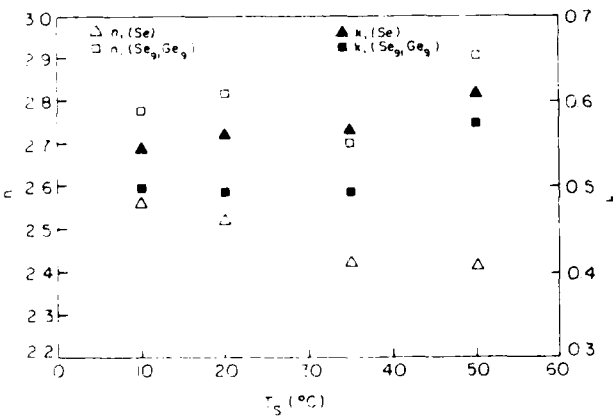
Figure 15. Optical constant vs substrate temperature during the deposition.
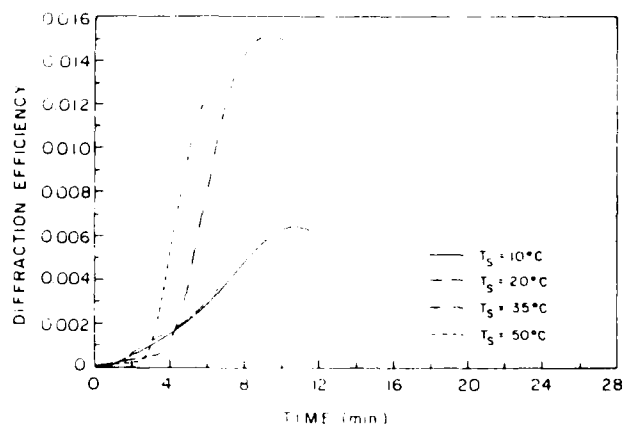
Figure 16. Diffraction efficiency vs time, for Se thin films deposited on substrates held at different temperature.

641

constant for example vary considerably with the temperature at which were held the substrate during the deposition $(T_s)^{10}$. That variation is presented in Fig. 15. Fig. 16 shows the evolution of the diffraction efficiency with exposure time for Se thin films deposited at different T_s. T_s values between 35°C and 50°C seem to be the optimal deposition condition. For $T_s \geq 60$°C, sublayer of crystalline Se are formed.

Conclusion

Holographic recording were realised in as-deposited amorphous SeGe thin films by means of laser induced crystallization. Deposition conditions has been identified as very critical parameters. T_s was an example of that dependence. The use of Ge to increase the stability of the amorphous phase of Se thin films has the effect of lowering the maximum value of the diffraction efficiency.

Acknowledgment

REFERENCES

1. S.R. Ovshinsky, **Reversible electrical switching phenomena in disordered structures**, Phys. Rev. Letters, 21, 1450 (1968); J. Feinleib, J. de Neufville, S.C. Moss, and S.R. Ovshinsky, **Rapid reversible light-induced crystallization of amorphous semiconductors**, Appl. Phys. Lett., 18, 254 (1971).
2. A. Singh, L. Song and R.A. Lessard, **Structural, morphological and optical recording characterization of selenium films**, Opt. Eng., 26, 944 (1987).
3. A. Singh, L. Song, R.A. Lessard, **Real-time hologram recording in SeGe films**, Appl. Opt., 26, 2474 (1987).
4. L. Song, P. Galarneau, R.A. Lessard, **Kinetic study of selenium used as optical data storage and holographic recording materials**, J. Mater. Sci. (To be published in January 1989).
5. P. Galarneau, C. Malouin, A. Singh, R.A. Lessard, **Hydrogen-implanted SeGe alloys as optical recording media**, Appl. Opt., 27, 4591-4594, (1988).
6. L. Song, P. Galarneau, R.A. Lessard, **Temperature distribution in an absorbing medium under laser illumination**, in preparation.
7. L. Song, P. Galarneau, R.A. Lessard, **Kinetics of crystallization of selenium thin films deposited on glass substrate**, submitted to Thin Solid Films.
8. L. Song, P. Galarneau, R.A. Lessard, **Optical recording characteristics of SeGe thin films at 488 nm**, Opt. Eng. (to be published in March 1989).
9. L. Song, P. Galarneau, R.A. Lessard, **Diffraction efficiency of thin mixed gratings: a convolution approach**, in preparation.
10. L. Song, P. Galarneau, M. Côté, R.A. Lessard, **Influence of the substrate temperature on the holographic recording properties of Se and SeGe thin films**, submitted to Applied Optics.

REAL-TIME PATTERN RECOGNITION USING PHOTON-LIMITED IMAGES

G. Michael Morris
The Institute of Optics
University of Rochester
Rochester, New York 14627

Abstract

The spatial coordinates of detected photoevents in a given area convey information about the classical irradiance of the input scene. In this paper the effectiveness of photon-counting techniques for image recognition is discussed. A correlation signal is obtained by cross correlating a photon-limited input scene with a classical intensity reference function stored in computer memory. Laboratory experiments involving matched filtering, rotation-invariant image recognition, and image classification are reported. For many images it is found that only a sparse sampling of the input is required to obtain accurate recognition decisions, and the digital processing of the data is extremely efficient. Using available photon-counting detection systems, the total time required to detect, process, and make a recognition decision is typically on the order of tens of milliseconds. This work has obvious application in night vision, but it is also relevant to areas such as robot vision, vehicle guidance, radiological and nuclear imaging, and recognition of spectral signatures.

Often input scenes contain a vast amount of information, which tends to make pattern-recognition decisions laborious and time consuming. In traditional digital pattern recognition methods, one digitizes the input scene using a two-dimensional detector, e.g. a solid-state photodiode array and a frame store. If the detector consists of, say, a 1000 x 1000 array of detection elements, then one has to process a million points of data. This is too much information for even very large computers to process in real time, so one generally transforms the input information into some sort of feature-space representation, e.g. through the use of edge-enhanced images, and makes the recognition decision based on this reduced data set.

We are investigating an alternative approach to the pattern recognition problem in which low-light-level (photon-limited) images are processed using photon-correlation methods[1-3]. In this scheme photoevents are detected at the maximum rate the detection/computer system can handle. One collects photoevents until there is enough information about the input scene to achieve an acceptable error rate for the given recognition task. Our studies indicate that in many cases only a sparse sampling (a small number of detected photoevents) of the input image is needed for accurate image recognition; hence, the time needed to detect, process, and make a recognition decision can be quite short, typically a few tens of milliseconds. In effect, this approach to pattern recognition lets nature randomly sample (compress) the image data from the input scene. The computer collects enough information (photoevents) to achieve the required error rate for the task, then makes the recognition decision. Key features of the method include: efficient data compression and processing; minimal hardware requirements; and operation with either laser or natural illumination.

A schematic of the two-dimensional, photon-counting detection system used in our experiments is shown in Fig. 1. An incident photon ejects an electron from the photocathode via the photoelectric effect. The ejected electron, e, impinges on a stack of microchannel plates, which produces an output charge packet, G e. The electron gain G is approximately ten million. The resulting charge packet is distributed to four electrodes located at the corners of a resistive anode, then amplified using a charge-sensitive preamplifier. Position-computing electronics (operational amplifiers) are used to calculate the location of the centroid of the charge packet. The x and y coordinates of the centroid are sent to the computer for subsequent processing and/or display.
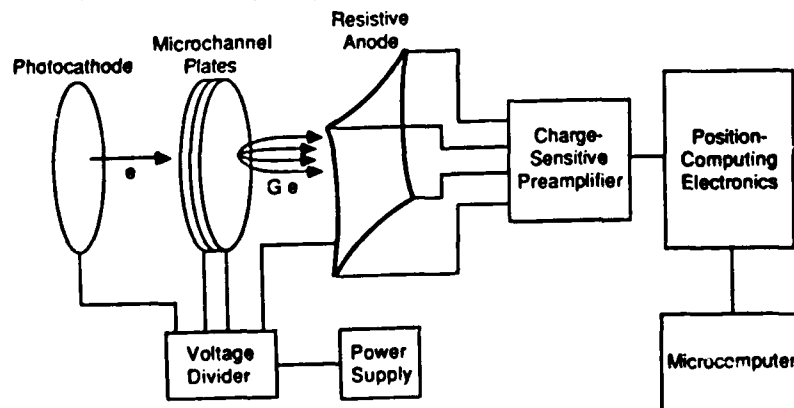
Fig. 1. Schematic diagram of a resistive-anode, photon-counting detection system.

N=4K
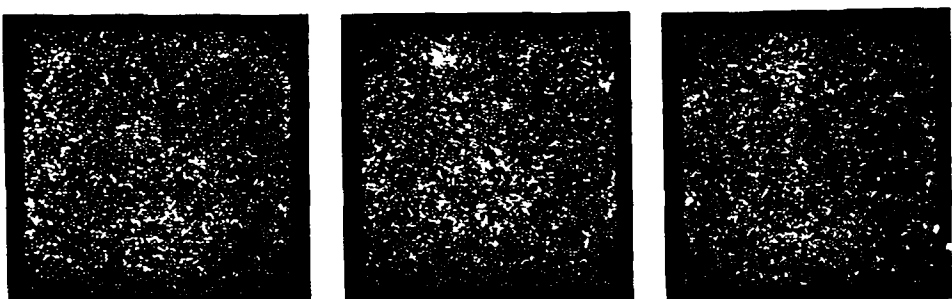
N=1K
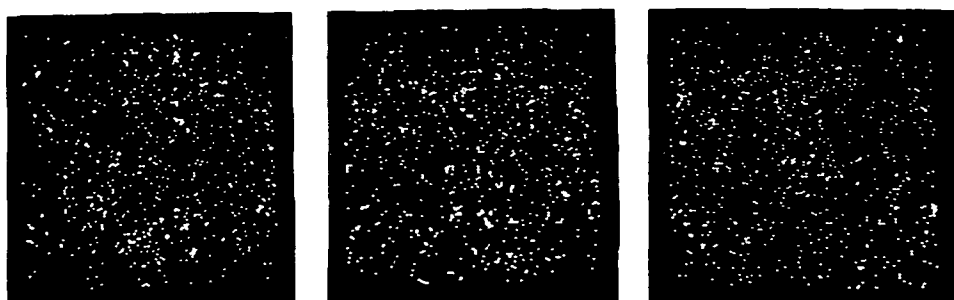
Fig. 2. Images of engraved portraits obtained using a two-dimensional, photon-counting detection system: first column, portrait of George Washington; second column, Abraham Lincoln; third column, Andrew Jackson. N is the number of detected photoevents over the entire image: top row, N = 20 million; middle row, N = 4,000; bottom row, N = 1,000. The spatial coordinates of each detected photoevent are digitized to 8-bit accuracy.

Images obtained using the photon-counting detection system of Fig. 1 are shown in Fig. 2. The total number of detected photoevents in each image is indicated. In each image there are 256 x 256 resolution cells.

A correlation signal is formed by cross correlating a photon-limited input scene with a classical intensity reference function stored in computer memory. Laboratory experiments involving template matching, rotation- and scale-invariant image recognition, and image classification have been performed. The performance that can be obtained in template matching experiments is illustrated by ROC curves in Fig. 3. The curves in Fig. 3 are based on experimental values of the mean value and variance of the correlation signal that was formed using the image of Washington (N=20 million photoevents) as the reference function and photon-limited input images. In Fig. 3, N indicates the total number of photoevents detected in the input image. Notice that when N = 1000 (see bottom row of Fig. 2), the probability of error in recognizing Washington is only 1 in 100,000. If the detector is operating at a rate of 100,000 counts per second, the total time to collect and process the data is 10 milliseconds.
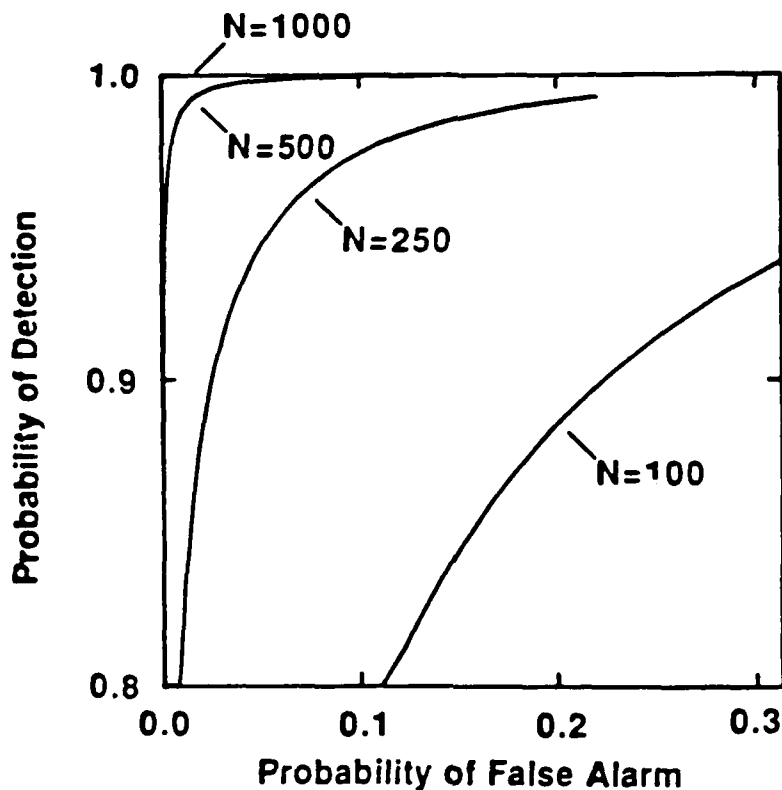
Fig. 3. ROC curves for the portraits of Washington and Lincoln for different values of N.

It is desirable, of course, to have a recognition system that can tolerate variations in input images, which are not important as far as a recognition decision is concerned. These variations can be divided into two basic categories: geometrical distortions of the image (e.g., rotation, scale, and position) and intrinsic variations of the image (e.g., changes in illumination, image clutter, and object occlusions). One could approach this problem by using multiplexed filters in which a separate reference function (filter) is used for each variation of the input object, but this leads to a computationally intense system design that is difficult to implement.

A more elegant approach to the problem of image distortion is to choose a reference function (filter) that produces a correlation signal that is invariant to the distortion of the input image. The theoretical and experimental results of our studies of invariant filtering are well documented in the literature. We have been quite successful in designing such filters for operation in the low-light-level correlation system. Rotation-invariant filtering using circular-harmonic filters[4], rotation and scale invariance using Fourier-Mellin descriptors[5], and image classification[6] have all been demonstrated.

Recently, we have also demonstrated a two-stage, template-matching procedure using photon-limited images[7]. In this scheme an input scene is searched using a small window (reference) function that is moved to various offsets within the input scene. The cross-correlation between the reference function and the input scene at a given offset is estimated by sampling the input using a small number of detected photoevents. The photon-limited correlation signal is used as a similarity criterion for comparing the input with the reference function. In the first stage, a small number of detected photoevents is used to find probable locations for the reference function. The threshold of the first stage is set to achieve the desired probability of detection. In the second stage, the locations identified in stage one are examined using a threshold and number of photoevents needed to obtain the required probabilities of false alarm and detection. Laboratory experiments have been conducted using a variety of images: simple objects, satellite images, and objects (trucks and tanks) contained in a cluttered background; this technique appears to be a promising method for correlation tracking in vehicle guidance.

In summary, we have found that a sparse statistical sampling of an input image is, in many cas~ ᵗicient to achieve accurate results for automatic target recognition. The principle is similar to that of statistical ᶜ ᵗ ᵢor quality control of manufacturing processes or for election polls, i.e., accurate measures of a process can bᵥ ᵤᵤᵢ ᵢᵥed using a small number of statistical samples. As a result of the sparse sampling and simplicity of the processing (table lookup and addition), the time needed to detect, process, and make recognition decisions can be quite short, typically, in tens of milliseconds or less. The hardware requirements are minimal (the processing power of an IBM PC-AT is quite adequate). Finally, the system is intensity based, therefore scene illumination can be provided by either laser or natural light sources.

645

References

1.   G. M. Morris, "Scene matching using photon-limited images," J. Opt. Soc. Am. A **1**, 482-488 (1984).

2.   G. M. Morris, "Image correlation at low light levels: a computer simulation," Appl. Opt. **23**, 3152-3159 (1984).

3.   G. M. Morris, "Pattern Recognition using Photon-Limited Images," in *Optical Computing and Processing*, H. H. Arsenault and T. Szoplik, eds., Academic, New York (1989).

4.   T. A. Isberg and G. M. Morris, "Rotation-invariant image recognition at low light levels," J. Opt. Soc. Am. A **3**, 954-63 (1986).

5.   T. A. Isberg and G. M. Morris, "Real-time estimation of moment invariants for pattern recognition," Proc. SPIE **938**, 1988).

6.   M. N. Wernick and G. M. Morris, "Image classification at low light levels,: J. Opt. Soc. A **3**, 2179-2187 (1986).

7.   T. A. Isberg and G. M. Morris, "Two-stage template matching using quantum-limited Images," Proc. SPIE **976**, (1988).

LASER-BASED AND IMAGING TECHNIQUES FOR THE CHARACTERIZATION OF INDUSTRIAL MATERIALS

P. Cielo
National Research Council Canada
Industrial Materials Research Institute
75 De Mortagne Blvd.
Boucherville, Québec J4B 6Y4 Canada

Abstract

A number of optical techniques for the characterization of industrial materials, such as polymers, composites and ceramics, will be discussed, including light scattering, thermoelastic and thermographic methods.

Introduction

Laser-based imaging techniques[1] are receiving an increasing amount of attention for the in-situ characterization of industrial materials because of their noncontact and noninvasive nature. Such characteristics make the laser-based approach convenient for continuous quality and process control because of their direct applicability to products which may be at high temperature, of difficult access or continuously moving along the production line. This paper reviews recent developments at the Industrial Materials Research Institute on laser-based characterization techniques including laser-ultrasound surface-acoustic-wave (SAW) velocimetry, photo-thermal methods and light-scattering analysis.

Polyblend analysis by light-scattering techniques

The great majority of polymer blends are immiscible from the thermodynamic standpoint and may be conceptualized in terms of relatively large deformable domains (usually in the order of microns) in a sea or matrix. The morphology of a blend may be changed dramatically depending on the processing conditions or material composition employed. Such changes are significant since the size and shape of the minor component is very important to the final performance of the product[2]. It is evident therefore that it is important to develop instruments which can rapidly analyze a polymer blend with respect to particle size and shape.

In this study polycarbonate/polypropylene blends were prepared to yield three different levels of domain size. The shape of the dispersed phase was maintained spherical. The three preparations may be denoted as blend 1, blend 2 and blend 3 in order of decreasing domain size, as shown in Fig. 1.

A number of optical techniques can be used to characterize polymer blends[3]. The noncontact nature and in-situ applicability of the optical techniques make them quite attractive for in-plant quality and process control applications. A substantial amount of work has been done in the field of small-angle light scattering which is essentially based on angularly scanning the Mie-diffraction pattern under polarized-light conditions (see Fig. 2). The applicability of such an approach is, however, limited to relatively thin films or very low second-phase concentrations in order to avoid multiple scattering effects which would smoothen the single-particle angular pattern to a cosine-distributed Lambertian angular pattern. Multiple scattering becomes significant at extinction values (i.e. attenuation of the undeviated light beam) of the order of 20%[4]. At such relatively low attenuation levels, small-angle scattering due to surface roughness is normally a major source of angular pattern perturbation. Such a noise source is usually eliminated by placing the sample between flat glass plates using a matching-index liquid to avoid reflections at the glass-sample interfaces. This is obviously not convenient for on-line industrial applications.

A more powerful approach for particle diameter evaluation in polydisperse blends is based on spectral analysis. If the light wavelength is varied, the spectral attenuation will be large for wavelengths much smaller than the particle diameter and small for wavelengths much larger than the particle diameter, as shown in Fig. 3. By measuring the relative spectral distribution of the light transmitted through a polymer-blend film one can thus obtain particle size information irrespectively of the film thickness or of the relative amount of the two separated phases.

When the spectra of these polyblend films are considered, Fig. 4, a much stronger attenuation is observed at low wavelengths because of scattering by the dispersed polycarbonate particles (the refractive indices at standard conditions of polycarbonate, 1.59, and polypropylene, 1.49, are sufficiently different to produce significant reflections at

the particle-to-matrix interfaces). As we can see, the attenuation range is gradually displaced toward longer wavelengths as the average particle diameter increases, corresponding to a displacement of the cutting edge of the extinction-ratio curve, Fig. 3. Such spectra can thus be used to obtain particle size information.

Further information can be obtained by light scattering on the average aspect ratio of the second-phase particles present on the blend. Molten flow during extrusion or molding often results in a certain degree of directionality for the minor phase depending on the hot stretch ratio (HSR) during forming (see Fig. 5). In this case, three sheets of 10% polycarbonate/90% polypropylene material were obtained with an HSR of 1, 5 and 10.4 respectively for the three ribbons of nearly 200, 100 and 70 μm in thickness. Electron micrographs (longitudinal sections) of ribbons extruded at the three hot stretch ratios are shown in Figure 5. In the absence of stretching (HSR 1), there is a combination of spheres, ellipsoids, and fibers near the edge of the film. At HSR 5 the polycarbonate is highly extended at the edge. When highly stretched at an HSR of 10.4, the minor phase was in a highly extended fibrous form.

A single-side approach was developed for the analysis of sheets of any thickness and with little dependence on the surface finish conditions. The depth of the material below the surface which can be probed by this method is of the order of a few mm, depending on the optical penetration depth of the light beam in the polyblend material. The basic principle is illustrated in Fig. 6 in the case of a polyblend containing fiber-like particles parallel to the sheet surface and oriented in a direction (a) perpendicular and (b) parallel to the plane of incidence of the laser beam. It can be understood from such a diagram that the incident beam is preferentially scattered in the plane ϑ perpendicular to the fiber direction. Moreover, light scattered by the fibers in the plane φ parallel to the fiber direction will hardly be intercepted by the camera aperture. A directional pattern elongated in the ϑ plane is thus expected when the illuminated volume is imaged by the camera.

Fig. 7 shows some examples of the pictures seen by the camera in the case of the above mentioned PP/PC ribbons of HSR=5 (Figs. 7a and 7b) and HSR=1 (Figs. 7c and 7d). In all cases the laser beam was incident from the left, at 45° from the normal, and the fiber-like particles were oriented in a vertical (a and c) or in a horizontal direction (b and d) in the plane of Fig. 7. In other terms, the plane of incidence of the laser beam was perpendicular to the fiber orientation (direction of incident beam $\vartheta = 45°$, $\varphi = 0$) for Figs. 7(a) and 7(c), while corresponding to the φ plane containing the fiber direction (laser beam at $\vartheta = 0$, $\varphi = 45°$) for Figs. 7(b) and 7(d). The elongation of the scattered-light pattern in a plane perpendicular to the fiber orientation, as discussed with reference to Fig. 6, is evident in these images.

The elongation and the direction of orientation of the particles in a polyblend material can clearly be inferred by an analysis of pictures of the kind shown in Fig. 7. It should be stressed that pictures such as (a) and (b) in this figure should be identical if the material were isotropic. By comparing Figs. 7 a and b with c and d we can see that the directionality of the patterns tends to disappear as the HSR, and thus the aspect ratio of the fiber-like particles, is reduced.

Thermographic characterization of composite materials

When nontranslucent materials are to be inspected, such as graphite-fiber filled composite materials, light scattering methods can no longer be used. In these cases, spot-heating thermographic methods can be resorted to for fiber directionality analysis. A typical configuration is shown in Fig. 8. The inspected part is spot-heated by a narrow laser beam or other point heat source, and the heat-propagation pattern is analyzed by an IR camera. If the material is oriented, such as a unidirectional graphite-epoxy sheet, an elliptical thermal pattern will be observed, with the ratio between the two principal axes (b/a) being related to the square root of the thermal diffusivities in the longitudinal and transverse directions. This may be used to evaluate the orientation of extruded or molded parts, or the relative thermal conductivities of the filler and the matrix in a composite.

Such an approach was investigated in the case of steel-fiber-filled polypropylene sheets with different steel concentration and orientation. Steel fibers nearly 1 mm long are incorporated in the polymer matrix to obtain good thermal and electrical conductivities for specific applications. Strong anisotropy may affect the conductivity properties if the fibers are not randomly oriented.

Some typical results obtained with black painted steel-polypropylene sheets spot-heated with a 0.5 W focused laser beam for 30 s and observed with an IR camera are shown in Fig. 9. In Fig. 9a the filler is preferentially oriented in the vertical direction; Fig. 9b corresponds to nominally random-orientation samples. The filler orientation can be clearly evaluated from the ellipticity of the thermal pattern, particularly in the case of

high steel concentration where fiber-to-fiber near-contacts are relatively frequent. Such patterns could be used to evaluate fiber concentration uniformity and local anisotropy by scanning the heating beam over the inspected part. This technique can be extended to a three-dimensional fiber-orientation evaluation at different depths below the surface[5].

The basic principle of our approach is the following. If a laser beam is focused on the surface of a composite sheet, the ellipticity of the thermal pattern which is observable by an IR camera around the heated spot will be determined by the anisotropy of the material situated in the immediate vicinity of the heated spot. As the thermal front propagates deeper and deeper within the material, the appearance of the pattern will be affected by successive layers situated deeper and deeper within the sample. This makes it possible to obtain three-dimensional filler orientation information on the inspected sheet.

The capabilities of such an approach are illustrated in Fig. 10. A double sheet composed of two layers, each 2 mm-thick and containing $(0°, 90°)$ mutually perpendicular fibers, is assumed to be surface heated by a focused, step-heating source. After a short heating time period, $t \approx \ell^2 / \alpha_T$, where ℓ is the sheet thickness and α_T its transverse thermal diffusivity, only the first layer interacts with the heat flow, so that the eccentricity tends to the square root of the assumed value 2 of the ratio between the longitudinal and the transverse (i.e., in the plane normal to the fiber direction) thermal conductivities in the composite material. The eccentricity which is referred to is the ratio b/a between the principal axes of the isotherms. The lower eccentricity value observed at shorter distances from the heated spot (along the longitudinal axis) is related to the presence in the model of an isotropic surface film, nearly 200 μm-thick on each layer, representing the average thickness of polymeric material which is normally encountered above the fibers. At longer heating periods a strong eccentricity is still visible at a distance from the heated spot smaller than the sheet thickness. At larger distances, however, the eccentricity tends toward the unity value which is expected for the average pseudo-isotropic properties of the $(0°, 90°)$ sheet. Consequently, a plot of the eccentricity vs. radial distance at the surface of an unknown sample makes it possible to evaluate the directional properties of the material at different depths below the surface.

The viability of this basic concept was verified on a number of samples comprising two sheets of nominally unidirectional, 2 mm-thick, steel-polypropylene samples with respectively 10% and 15% steel concentration bonded in a $(0°, 90°)$ configuration. The samples were held in a horizontal plane in order to avoid thermal-pattern distortions related to air-convection effects above the nearly 0.5 mm-diameter area of the black-painted sheet surface heated by the 0.1 W Argon laser beam. Moreover, time-domain image-subtraction methods before and after heating were used to compensate for reflectivity and camera-response nonuniformities across the imaged field.

A typical plot of the thermal-pattern eccentricity vs. radial distance, as obtained under stationary spot-heating conditions, is shown in Fig. 11. The eccentricity observed with the unidirectional (single-sheet) sample assumes a relatively constant value of the order of 1.2 typical of the 10% steel concentration. The lower values of the eccentricity at distances closer to the heating spot may be explained in part by the existence of a thin isotropic layer on top of the fibers, and in part by the finite diameter of the heating beam, whose effect was evaluated to an error of 4% at a distance equal to three times the heating source radius.

When a second sheet of perpendicular orientation is bonded on the bottom of the inspected sheet, the eccentricity values recorded near the heated spot are hardly affected, while the values far from the center gradually drop in agreement with the theoretical model. Such an approach thus appears to provide a rough evaluation of the average degree of fiber orientation at different depths from the surface, in spite of the strong dispersion of the data which is mainly related to the statistical fluctuations of the fiber distribution within the material.

Laser-ultrasonic characterization of materials

Figure 12 shows a typical setup for the generation and detection of ultrasonic waves. Elastic waves are generated in a laser-irradiated opaque material both because of thermoelastic-stress mechanisms. The transient stress field produced near the surface by the heating beam generates longitudinal, transverse and surface acoustic waves, each with characteristic directivity patterns.

Surface-acoustic-waves (SAW's) are particularly convenient for the detection of open-surface cracks or near-surface defects, as well as for materials characterization by acoustic-wave velocity and attenuation measurement with one-side access to the workpiece. Such waves may be focused by suitably shaping the laser-irradiated area to obtain a convenient directivity pattern.

649

A particularly simple apparatus for laser generation and detection of focused SAW's is shown in figure 13. A multimode Nd:YAG laser, giving typically 15 ns, 0.1 J pulses, is expanded by a Galilean telescope and focused through a negative axicon on the surface of the sample, where it produces typically a 15 mm diameter, 0.2 mm wide annulus. The diameter of the annulus can be varied by displacing the axicon longitudinally. The telescope decreases the beam divergence by an amount equal to its magnification. This results in a sharp annulus even with a multimode laser source.

The ultrasonic pulse can be detected on the center of convergence of the ring-shaped wave by a noncontact optical probe. A number of optical techniques can be used to probe acoustic waves, including knife-edge, diffraction, as well as position-sensing and velocity-sensing interferometers. In our experiments, a position-sensing Michelson interferometer was used with a sensitivity of 0.02 nm in a 30 MHz bandwidth when precisely focused on the surface.

Laser-generated ultrasound can be applied to a variety of industrial metrology tasks, such as surface crack detection or the detection of subsurface delaminations[6]. An application to coating thickness evaluation by ultrasonic velocimetry will now be described.

It is well known that materials coated with layers of different acoustic properties are frequency-dispersive when the acoustic wavelength is of the same order of magnitude as the coating thickness. The thickness or the acoustic properties of the coating layer can thus be evaluated by measuring the surface wave velocity at different frequencies. Noncontact, single-shot probing of laser-generated surface waves for such an application is an attractive possibility.

Some typical waveforms obtained at the centre of the laser-generated converging wave on electroplated copper samples with different coating thicknesses are shown in Fig. 14. The dispersive effect of the coating becomes increasingly evident as the coating thickness is increased. The temporal delay of the high-frequency components with respect to the low-frequency main pulse in the Ag-plated sample is apparent in Fig. 14c while in he thick Cr-plated sample, Fig. 14f, the high frequencies precede the main pulse. This was expected because the short wavelengths tend to propagate mainly within the coating which has an acoustic velocity lower than the substrate in the case of the Ag-plated sample, and higher than the substrate in the case of the Cr-plated samples. Coating-thickness evaluation can be performed from such waveforms by flight-time measurements, but better sensitivity can be obtained by time-resolved spectroscopic techniques.

Conclusion

Laser-based techniques are an attractive approach for the characterization of industrial materials. A few laser-based techniques coupled to either light-scattering, thermographic or ultrasonic methodologies have been described in this paper. The main interest of these techniques is their noncontact nature, making them a potential candidate for on-line inspection tasks.

References

1. P. Cielo, Optical Techniques for Industrial Inspection, (Academic Press, Boston, 1988).

2. P. Cielo, K. Cole and B.D. Favis, in Proceedings, Instrumentation and Automation in the Paper, Rubber, Plastics and Polymerization Industries, 1986, A. Kaya and T.J. Williams, Eds. (Pergamon Press, Oxford, 1987), pp. 161-170.

3. R.S. Stein, in Polymer Blends, D.R. Paul and S. Newmann, Eds. (Academic Press, New York, 1978) pp. 393-443.

4. J. Schroeder and J.H. Rosolowski, Proc. SPIE, 297, 156 (1981).

5. J.C. Krapez, P. Cielo, X. Maldague and L.A. Utracki, Polym. Comp., 8, 396 (1987).

6. P. Cielo and C.K. Jen, in Ultrasonics Symposium (IEEE, 1986) pp. 515-526.
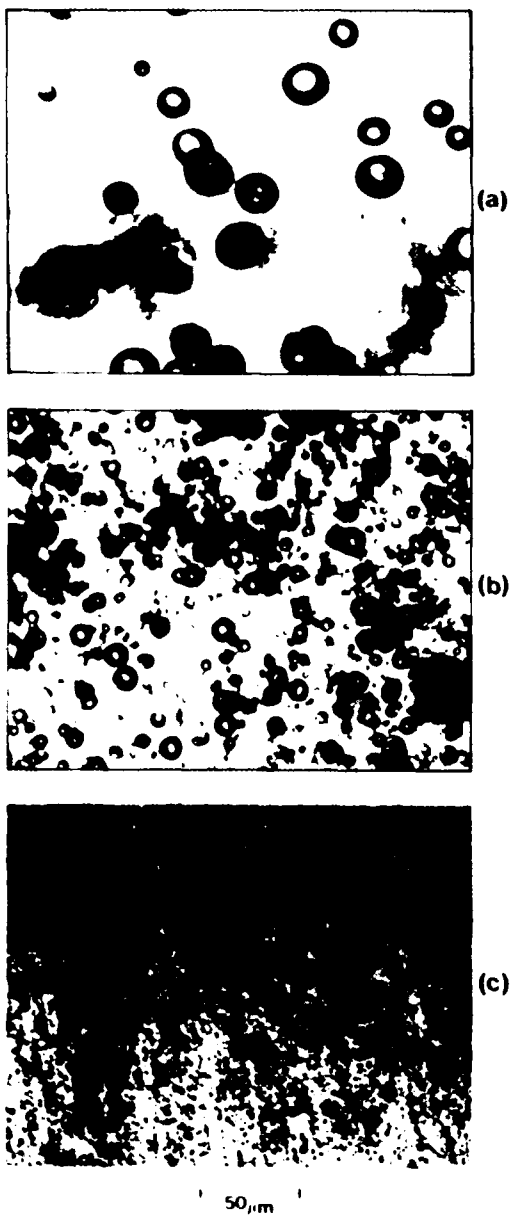
Fig. 1: Micrographs illustrating blends:
a) blend 1,
b) blend 2,
c) blend 3.
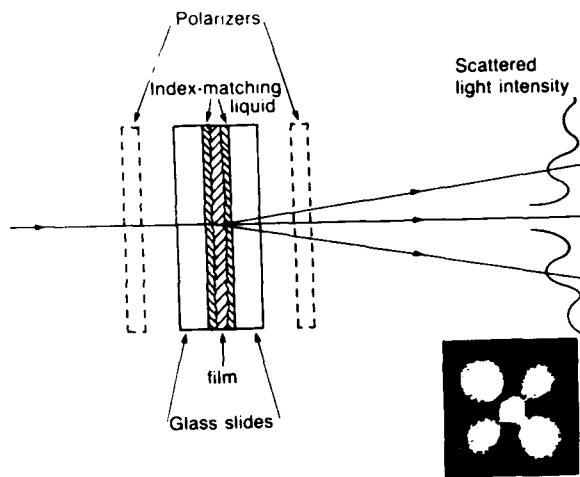
Fig. 2: A Mie-scattering setup for the optical characterization of a thin polymeric sheet.

$$\frac{4\pi d}{\lambda}\ (m\text{-}1)$$
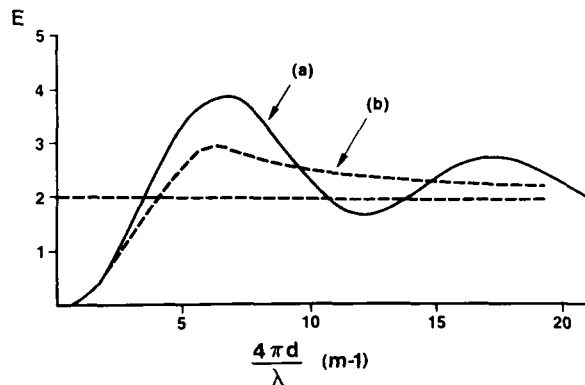
Fig. 3: Variation of the light-extinction coefficient E in a transparent medium containing dispersed spherical particles as a function of the particle mean diameter d and relative refractive index m for (a) a monodisperse and (b) a polydisperse distribution.
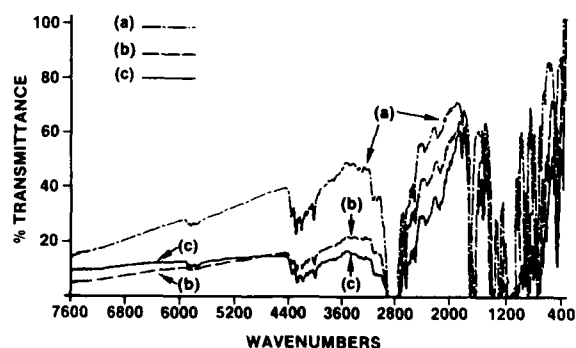
Fig. 4: Comparative transmission spectra for 90% polypropylene, 10% polycarbonate polymer blends with disperse spherical particles of typical diameters (a) 1-2 μm (b) 4-10 μm and (c) 10-20 μm.

651
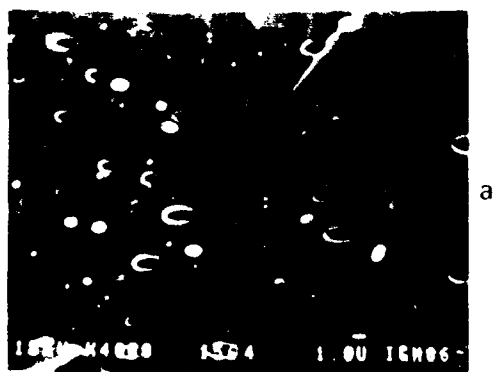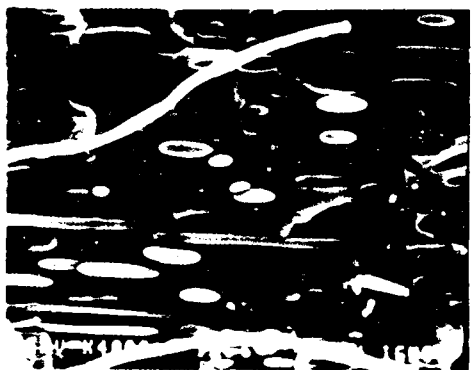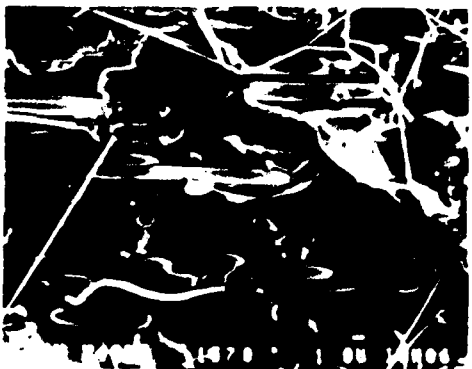
Fig. 5: Electron micrographs obtained in the center of a longitudinal section of 93% PP/7% PC (by volume) extruded ribbons with HSR values of (a) 1,(b) 5, and (c) 10.4.
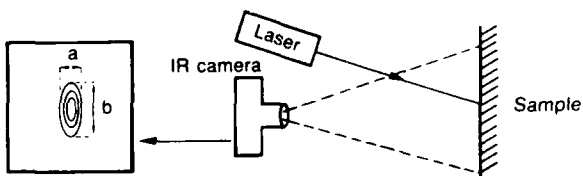
Fig. 8: Schematic setup for the thermographic analysis of phase orientation in composite materials.
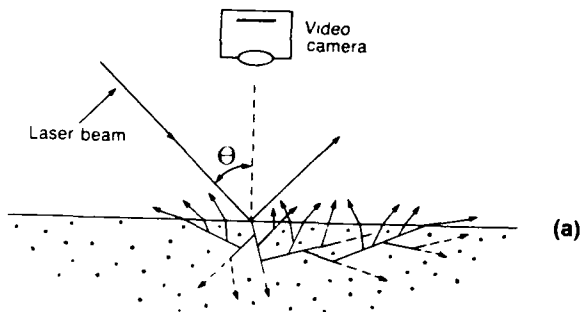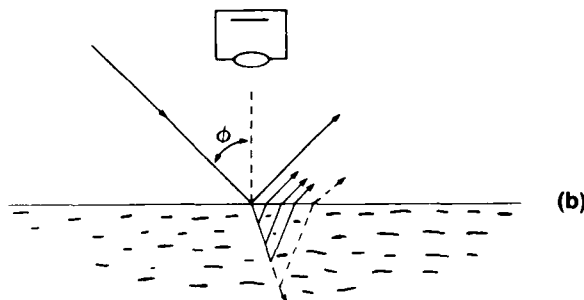
Fig. 6: Schematic diagram of light beam scattering within an oriented material for a beam incident (a) in the plane perpendicular to the fiber orientation, or (b) in a plane parallel to the fiber orientation.
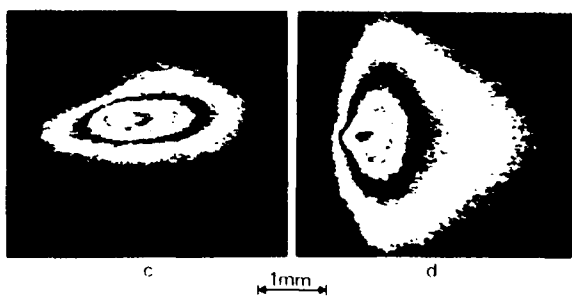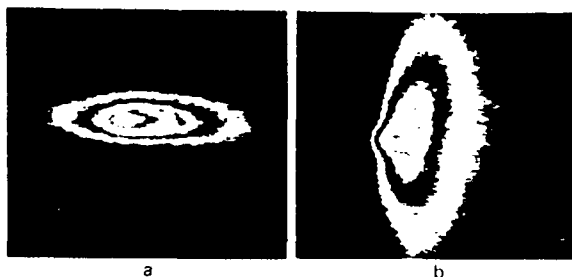
Fig. 7: Image obtained with an apparatus of the kind shown in Fig. 6 for PP/PC ribbons drawn with an HSR equal to 5 (pictures a and b) and 1 (c and d). The He-Ne laser beam was incident from the left at 45° from the normal, and the fibrillar particles in the ribbons were oriented either in the vertical (a and c) or in the horizontal (b and d) directions.

652

(a)

(b)
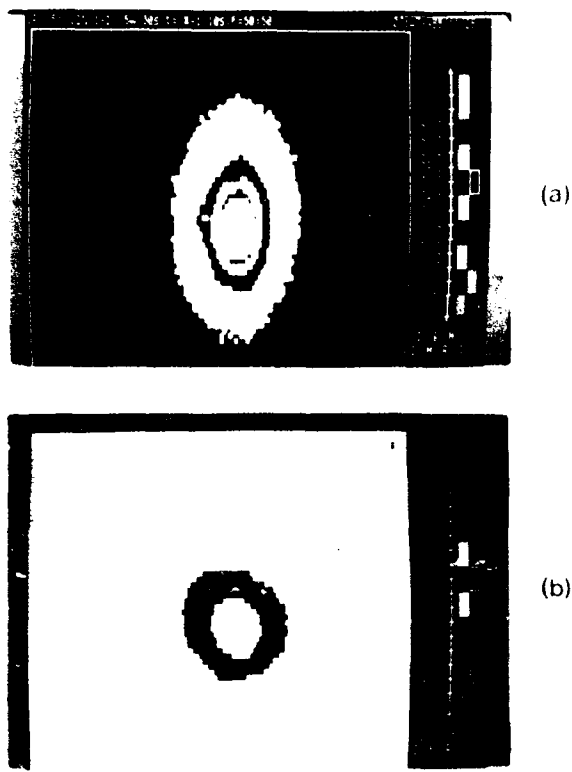
Fig. 9: Thermal patterns obtained with steel-polypropylene sheets with fiber concentration in weight of 12 percent, either linearly oriented (a) or randomly oriented (b). The image areas are typically 5 by 5 cm.

Distance from heated spot (mm)

Figure 10: Finite-difference simulation of the surface-pattern ellipticity in a double sheet containing mutually perpendicular fibers, as a function of the radial distance from the heated spot.

Distance from heated spot (mm)

Fig. 11: Experimental plots of thermal-pattern eccentricity vs. radial distance as obtained on a unidirectional single-sheet and on a (0°, 90°) double-sheet steel-polypropylene sample.
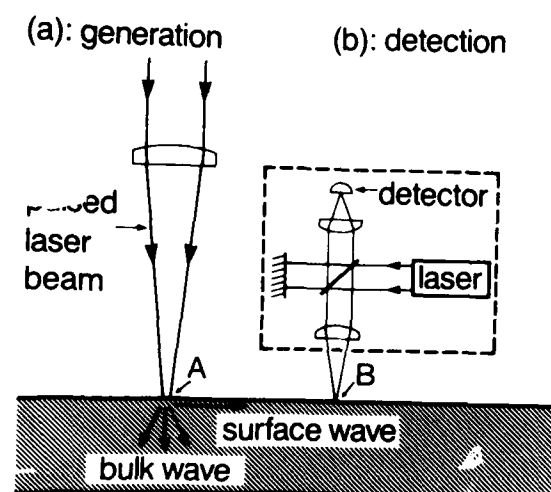
Fig. 12: Laser generation and detection of ultrasonic waves.

653
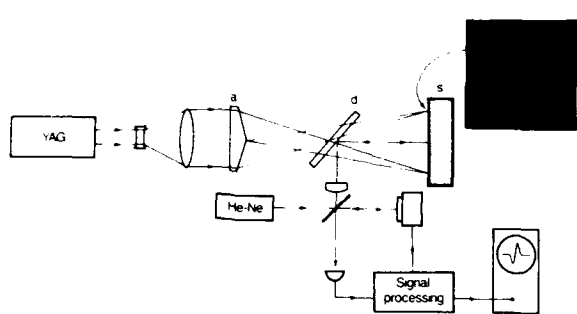
Fig. 13: Apparatus for laser generation and detection of convergent SAW's with a negative axicon. a: axicon, d: dichroic mirror.
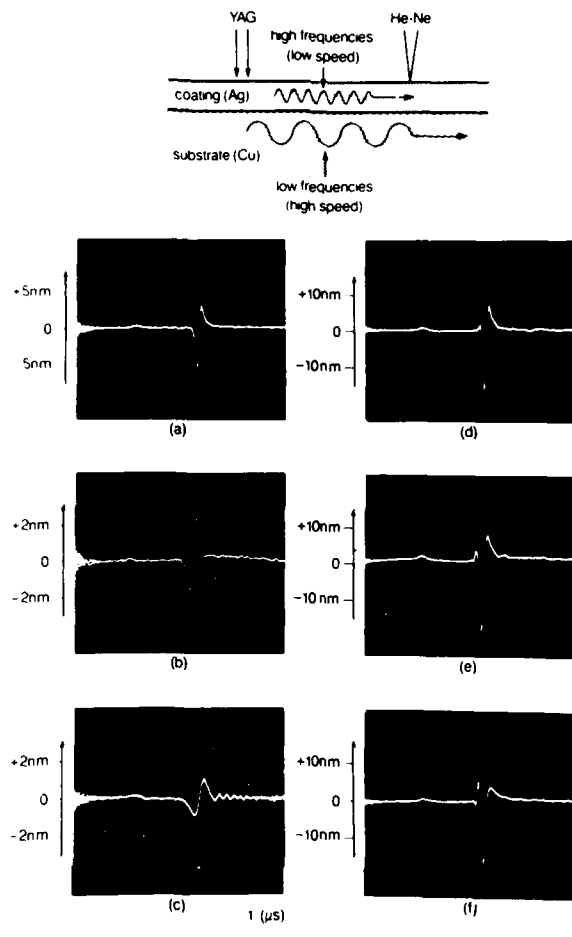
Fig. 14: Waveforms obtained on an electroplated copper sample:
(a) bare sample;
(b) 20 μm-thick Ag coating;
(c) 60 μm Ag coating;
(d) 7.5 μm Cr coating;
(e) 15 μm Cr coating and
(f) 40 μm Cr coating.

LASER ILLUMINATED HIGH SPEED PHOTOGRAPHY OF ENERGETIC MATERIALS
AND COMPONENTS WITH A COPPER VAPOR LASER

Larry R. Dosser, John W. Reed, and Margaret A. Stark

EG&G Mound Applied Technologies[*]
P. O. Box 3000
Miamisburg, Ohio 45343-0987

Abstract

Because components containing energetic materials function in a rapid and often violent manner, specialized diagnostics are required to study these events. Laser illuminated high speed photography has recently been used to record the functioning of these devices. A copper vapor laser capable of producing pulse rates of up to 10,000 pulses per second has been synchronized with a high speed film camera to record multiple laser illuminated images of the functioning component. This type of photography allows us to distinguish between hot particles and cold particles, measure burn rates, detect the effect of composition changes on performance, and observe the effect of design changes. Recent examples of the application of this technique are discussed.

Introduction

The evaluation of the functioning of devices containing energetic materials is of primary importance in determining the effect of design or composition changes. Laser illuminated high speed photography using a copper vapor laser has recently been applied to this type of evaluation. The laser is capable of operating at 10,000 Hz, but is operated at 6,000 Hz for most applications. At this pulse rate the laser has an average power of 30 W. Because the 30 ns pulse width of the laser essentially freezes all motion of the functioning component, it provides detailed images that were never before possible. The peak power of each laser pulse is approximately 170,000 W which provides ample illumination for the photography. Recent examples of the application of this technique to two types of igniters will be presented.

Experimental

The optical arrangement used to film the igniters is shown in Figure 1. The laser beam is
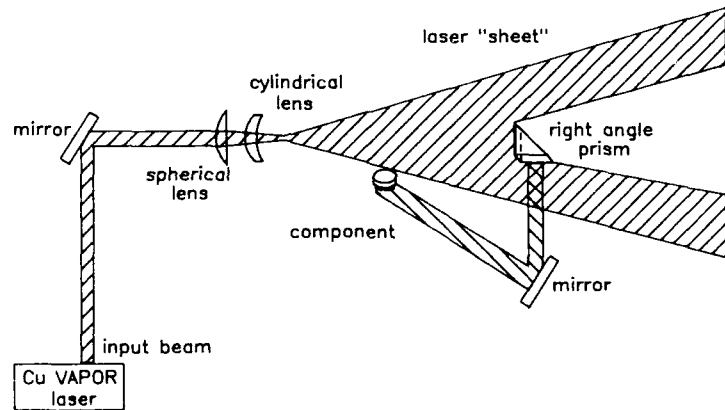
Figure 1 - Optics for high speed filming of components.
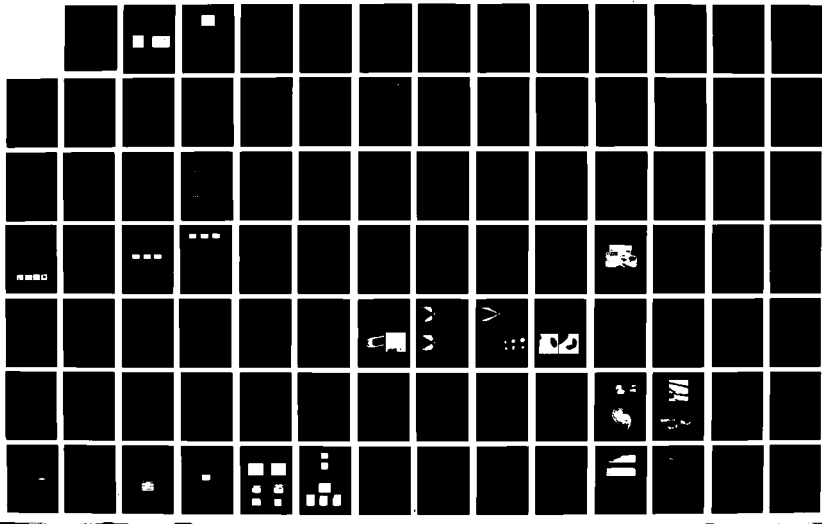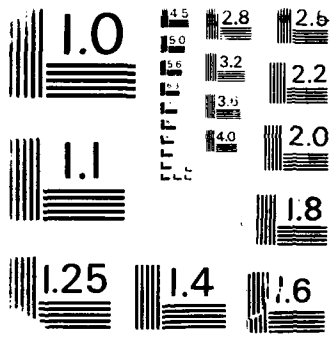
formed into a thin sheet using a spherical-cylindrical lens combination to illuminate the space above the center of the component. After the sheet passes across the component, a portion of it is captured with a right angle prism and reflected back around to illuminate the body of the component. This particular type of illumination is particularly useful in filming such components. In an orientation perpendicular to the laser sheet, the camera records the component and a field of view of approximately 15 cm above it. The light scattering (Mie scattering) from the smoke and particulates illuminated by the laser sheet provides a unique view of the internal structure (a cross-sectional view) of the igniter output.

During an experiment, the camera drives the laser with an appropriate delay that is set to a predetermined value depending on the camera speed. This ensures that when the laser pulse is at the experimental point, the camera shutter is open and the laser illuminated image is recorded. The shutter is open only for a few microseconds, requiring that the timing be quite precise. The camera is a rotating prism type that provides one trigger pulse to the laser per frame of high speed film. When an eight-sided prism is used in this camera, full frame images are recorded. For this work a 16-sided prism was used, and two images were recorded per frame. Since only one trigger pulse is provided per frame, one image per frame is laser illuminated, the other image is not. This provides a direct comparison between laser- and nonlaser-illuminated images. Such a comparison is extremely useful in distinguishing between hot and cold particles and for observing condensed phases versus gaseous species.

Results

The results from several different types of experiments on igniters were presented at the conference on a videotape that was made by transferring images from the high speed films to video by a special process. Examples of two different igniters taken from the films are shown in Figures 2 and 3.

Figure 2 - Igniter with glass-ceramic closure disk. Image is laser illuminated. No self illuminated image could be recorded.

Figure 3 - Igniter with metal closure disk. Right image is laser illuminated. Left image is from self illumination.

These two figures show the igniters fired on the bench top at ambient pressure. The powder loads in the two igniters were similar, but they had different closure disk assemblies. The igniter in Figure 2 had a glass-ceramic closure disk, whereas the igniter in Figure 3 had a scored metal closure disk. The figures clearly show the effect of changing the closure disk assembly. The metal closure provided greater confinement for the burning of the energetic materials, and as a consequence the device produced a higher pressure and flame temperature and functioned approximately three times more rapidly.

These two igniters were also fired under confinement in a plastic block. An example of this is shown in Figure 4.
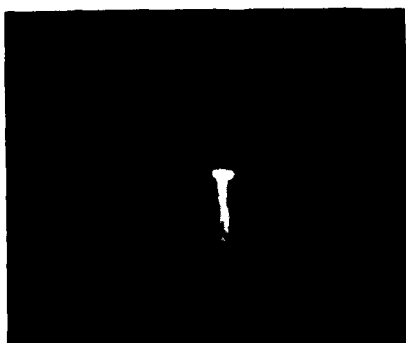
Figure 4 - Igniter from Figure 2 fired under confinement. Image is a combination of laser and self illumination.

The igniter used for this experiment was the same igniter shown in Figure 2. As would be expected, the igniter functioned much more rapidly when it was confined. When the igniter shown in Figure 3 was fired under similar confinement, there was considerable self-illumination that tended to obscure the photographic record. Recent filming of this igniter using a very narrow band (1 nm) interference filter shows promise for examining the igniter flames when they are fired under confinement.

Conclusion

The value of the copper vapor laser to illuminate and photograph the functioning of components that contain energetic materials has clearly been demonstrated. The dramatic effect of changing the closure assembly on an igniter could readily be observed. The function time for the two igniters could be determined directly from the film. The structure of the flames from the components is clearly visible and should be helpful in modeling these reactions. By comparing the laser-illuminated image to the image that is self-illuminated, information on the character of the flame can be determined. The difference between hot and cold particles, for example, was clearly visible.

657

THE INTENSITY DISTRIBUTION OF LIGHT SCATTERED FROM A RANDOM SOLID MEDIUM WITH STATIC SPATIAL FLUCTUATIONS IN THE SCATTERER DENSITY

by M. Kazmierczak and T. Keyes

Department of Chemistry, Boston University, Boston, MA 02215

Laser light propagation in a random solid medium of a finite size gives rise to scattering speckle patterns. Their statistical properties are well known. However, little attention has been paid to the statistical description of the angularly resolved laser speckles. It has recently been shown that the angular speckle obtained from a finite size random system can be analyzed within the framework of existing statistical theories but only in a specific range of scattering angles. It is thus our task to investigate the scattering intensity distribution beyond this range. The scattering volume is partitioned into constant phase slabs occupied by scatterers at a density which changes from slab to slab. These static spatial fluctuations are assumed to be Poissonian. This model enables us to derive the distribution of the scattered electric field which is represented by the Edgeworth series with skewed Gaussian leading term. Next, we obtain the cumulative distribution of the intensity as a function of scattering angle. The theoretical results are discussed in conjunction with data obtained from numerical simulations.

Light scattering from solid, optically transparent materials has recently become a subject of a great interest. Some materials of this type (e.g. glasses, glass-ceramics), due to their inherent structural randomness, uniquely scatter light, giving rise to patterns represented by random fluctuations of scattered intensity. These patterns, known as laser-speckle, are generated as a consequence of scattering of a light beam travelling through the medium by scatterers placed more or less randomly in it. Thus, the structure of the speckle pattern reflects the type of the spatial distribution of scatterers as well as their optical properties. The speckle pattern has been shown to be extremely sensitive to any kind of order which may occur in a sample.[1-7]

Speckle patterns can be obtained at fixed detector position by moving a sample perpendicularly with respect to the propagation direction of an incident light and measuring scattered intensity at each sample location. Plotting the intensities versus sample position will result in a typical speckle pattern with characteristic rapid intensity fluctuations. Similar pattern can also be produced by plotting the intensities measured at various scattering angles.

In spite of the vast literature concerning aspects of laser speckle, little attention has been paid to angularly resolved speckle patterns or the dependence of speckle properties on scattering angle. The latter has been shown to have a considerable impact on the quantities that are applied in an analysis of speckle patterns.[8,9] Also, the scattered intensity distribution has been shown to vary with a scattering angle. For large scattering angles this distribution obeys negative exponential statistics, provided that only single scattering is present. At small angles, the intensity distribution will decay non-exponentially.

Conditions that lead to a non-exponential distribution of intensity have been discussed by many authors[2,5,6,8] who have emphasized the role of a nonuniform distribution of phases associated with elementary scattered waves. We have recently analyzed the problem of the phase distribution in the context of its dependence on the scattering angle.[8] We were able to derive exact formulas which allowed us to keep track of the transition of phase distribution from its (nearly) uniform to nonuniform regime with scattering angle. The transition angle, named the critical angle θ_c, appeared to be dependent on the linear dimensions of the scattering volume, the number of particles active in the scattering process, and an incident wavelength. Only those intensities which have been scanned at angles $\theta > \theta_c$ obey exponential statistics.

In the following we attempt to analyze the form of a joint distribution function for the real and imaginary components of the scattered electric field which is expected to be obtained for $\theta < \theta_c$. Let us assume that the scattering volume is divided into slabs and write real, E_1^N, and imaginary, E_2^N, components of the field that is due to scattering from a single slab containing N scatterers, each of a size smaller than the incident wavelength

$$E_1^N = \sum_i E_{oi} f_1(\varphi_i) \tag{1a}$$

$$E_2^N = \sum_i E_{oi} f_2(\varphi_i) \tag{1b}$$

where E_{0i} is the amplitude of an elementary electric field scattered by ith scatterer, and $f_1(\varphi)$, $f_2(\varphi)$ are real and imaginary components of the phase function, respectively.

The characteristic function can be expressed for a single slab in the following form

$$F^{(N)}(K_1,K_2) = \int d\varphi dE_0 p(\varphi) p(E_0) \exp\left[i(K_1 E_1^N + K_2 E_2^N)\right] \tag{2}$$

where $p(E_0)$ and $p(\varphi)$ are distribution densities of field amplitude and phase, respectively.

It is possible to determine the characteristic function for the total electric field that emerges from the scattering volume provided that the nature of fluctuations in $F^{(N)}(K_1,K_2)$ over the slabs is known. These fluctuations are caused by spatial distributions of scatterers (which introduce different optical paths in different slabs) as well as by the number of scatterers which vary from slab to slab. We assume that this number is governed by a Poisson distribution. Then the total characteristic function is given by the series

$$F(K_1,K_2) = \sum_N \langle N \rangle^N / N! \, e^{-\langle N \rangle} F^{(N)}(K_1,K_2) \tag{3}$$

where $\langle N \rangle$ stands for the average number of scatterers in a slab. Inserting Eq.(2) into Eq.(3), and using Eqs(1a,b) we obtain

$$F(K_1,K_2) = \sum_N \langle N \rangle^N / N! \, e^{-\langle N \rangle} \left\{ \int d\varphi dE_0 p(E_0) p(\varphi) \exp\left[i E_0(K_1 f_1 + K_2 f_2)\right] \right\}^N \tag{4a}$$

In the derivation of Eq.(4a) we have assumed the complete statistical independence (incoherence) of elementary fields. These add to produce the fields E_1 and E_2. It is easy to observe that if the number of scatterers is large then the right-hand side of Eq.(4a) can be approximated by an exponential function

$$F(K_1,K_2) = \exp\left\{ -\langle N \rangle + \langle N \rangle \int d\varphi dE_0 p(E_0) p(\varphi) \exp\left[i E_0(K_1 f_1(\varphi) + K_2 f_2(\varphi)\right] \right\} \tag{4b}$$

The joint probability density for the total fields E_1 and E_2 can be calculated by taking the Fourier transform of the function (4b)

$$P(E_1,E_2) = (4\pi^2)^{-1} \int dK_1 dK_2 \exp\left[-i(K_1 E_1 + K_2 E_2)\right] F(K_1,K_2) \tag{5}$$

Let us expand the exponential function in the integrand of Eq.(4b)

$$\exp\left[i E_0(K_1 f_1(\varphi) + K_2 f_2(\varphi))\right] = \sum_{m_1 m_2} (i E_0 K_1)^{m_1}/m_1! \, (i E_0 K_2)^{m_2}/m_2! \, f_1^{m_1} f_2^{m_2} \tag{6}$$

Then the integral in Eq(4b) reads

$$\int d\varphi dE_0 p(E_0) p(\varphi) \exp\left[i E_0(K_1 f_1 + K_2 f_2)\right]$$
$$= \langle N \rangle^{-1} \sum_{m_1 m_2} (i K_1)^{m_1}/m_1! \, (i K_2)^{m_2}/m_2! \, M_{m_1 m_2} \tag{7}$$

where the joint amplitude-phase average is defined as follows

$$M_{m_1 m_2} = \langle N \rangle \int d\varphi dE_0 p(E_0) p(\varphi) E_0^{m_1 + m_2} f_1^{m_1}(\varphi) f_2^{m_2}(\varphi) \tag{8}$$

It is worthwhile to note that according to the above definition we have

$$M_{00} = \langle N \rangle; \quad M_{10} = \langle E_1 \rangle; \quad M_{01} = \langle E_2 \rangle \tag{9}$$

Using Eqs(6)-(9) in Eq.(5) results in the expression

$$P(E_1,E_2) = (4\pi^2)^{-1} \int dK_1 dK_2 \exp\left[-i(K_1 \Delta E_1 + K_2 \Delta E_2)\right]$$
$$\cdot \exp\left\{ -\tfrac{1}{2}K_1^2 M_{20} - \tfrac{1}{2}K_2^2 M_{02} - K_1 K_2 M_{11} \right\} \exp(S) \tag{10}$$

where

$$\Delta E_1 = E_1 - \langle E_1 \rangle$$
$$\Delta E_2 = E_2 - \langle E_2 \rangle \tag{11}$$

denote the fluctuation in the fields E_1 and E_2, and

$$\exp(S) = 1 + \sum_{m_1=3} (iK_1)^{m_1}/m_1! M_{m_1 0} + \sum_{m_2=3} (iK_2)^{m_2}/m_2! M_{0 m_2}$$
$$+ \sum_{m_1=1, m_2=1} (iK_1)^{m_1}/m_1! (iK_2)^{m_2}/m_2! M_{m_1 m_2} + R \tag{12}$$

Thus, Eqs(9) and (12) produce five independent integrals with an extremely complicated structure. The calculation of the joint probability is straightforward but tedious and yields the result

$$P(E_1, E_2) = (2\pi M^{1/2})^{-1} \exp\left\{ -(\Delta E_1^2 M_{02} - 2\Delta E_1 \Delta E_2 M_{11} + \Delta E_2^2 M_{20})/2M \right\}$$
$$\cdot \left\{ 1 + A + B + C + \tilde{R} \right\} \tag{13}$$

where

$$M = M_{20} M_{02} - M_{11} \tag{14}$$

The parameters A, B and C can be expressed by the following series, involving powers of the scattered field fluctuations and the averages given by Eq.(8)

$$A = \sum_{m=3} (-1)^m U^m \sum_{s=0}^{E(\frac{1}{2}m)} \left[(m-2s)! s! 2^s \right]^{-1} \tilde{U}^s M_{02}^s \tag{15a}$$

$$C = \sum_{m_1 m_2} \sum_{s_1}^{E(\frac{1}{2}m_1)} \sum_{1} \sum_{s_2}^{E(\frac{1}{2}(m_2+1))} (-1)^{m_2+s_1+s_2} \binom{m_2 + 1}{m_2} / 2^{s_1+s_2} (m_1-1-2s_1)! (m_2+1-2s_2)! s_1! s_2!$$

$$M_{m_1 m_2} \Delta E_1^{m_1-1-2s_1} M_{20}^{s_1+s_2-m_1} M_{11}^1 L^{m_2+1} \tilde{L}^{s_2} \tag{15b}$$

where

$$U = (\Delta E_2 M_{11} - \Delta E_1 M_{02})/M; \quad \tilde{U} = \left[U(\Delta E_2 M_{11} - \Delta E_1 M_{02}) \right]^{-1} \tag{16a}$$

$$L = (\Delta E_1 M_{11} - \Delta E_2 M_{20})/M; \quad \tilde{L} = \left[L(\Delta E_1 M_{11} - \Delta E_2 M_{20}) \right]^{-1} \tag{16b}$$

The parameter B can be obtained by replacing U and $\tilde{U}$ in Eq(15a) by L and $\tilde{L}$, respectively. The contribution of A, B and C to $P(E_1, E_2)$ can be analyzed with respect to their dependence on $\langle N \rangle$. Since $U \sim \langle N \rangle^{-1}$ and $L \sim \langle N \rangle^{-1}$ while $\tilde{U}$ and $\tilde{L}$ have a very weak dependence on $\langle N \rangle$, then the terms in the series A and B vary as $\langle N \rangle^{s-m}$. Analogously, the series C contains $\langle N \rangle$ in power $(1+s_1-m_1+s_2-m_2)$. Hence, the powers of $\langle N \rangle$ appearing in all three series indicate that the contribution they make to $P(E_1, E_2)$ decreases as $\langle N \rangle$ increases. The series remainder $\tilde{R}$ (which corresponds to the term R in Eq.(12)) decays much faster with $\langle N \rangle$ than A, B or C. If we assume, as we did before, that the number $\langle N \rangle$ is large then all the series can be completely ignored. The probability density $P(E_1, E_2)$ becomes the bivariate normal distribution

$$P(E_1, E_2) = (2\pi M^{1/2})^{-1} \exp\left\{ -(\Delta E_1^2 M_{02} - 2\Delta E_1 \Delta E_2 M_{11} + \Delta E_2^2 M_{20})/2M \right\} \tag{17}$$

In order to proceed with the analysis we must specify the parameter M as well as the mean fields $\langle E_1 \rangle$ and $\langle E_2 \rangle$. The latter are negligible at angles $\theta > \theta_c$, i.e. in the case of a fully developed laser speckle. However, if the scattering experiment is carried out at $\theta < \theta_c$ then both $\langle E_1 \rangle$ and $\langle E_2 \rangle$ differ from zero due to some phase coherence in the scattered light. Thus, one is able to observe at θ_c the transition of $P(E_1, E_2)$ from a Gaussian to a normal distribution provided that number of scatterers is large enough.

Since below θ_c both $\langle E_1 \rangle$ and $\langle E_2 \rangle$ depend on the scattering angle θ then their determination by Eqs(8) and (9) requires the knowledge of the relevant phase probability density $p(\varphi) = p(\varphi(\theta))$. We have recently derived such a distribution for a cylindrical scattering volume of base radius r and height l illuminated by a laser beam if wavelength λ.[8]. We were thus able to calculate $\langle E_1 \rangle$ and $\langle E_2 \rangle$ for arbitrary angle

$$\langle E_1 \rangle = 2\langle N \rangle \langle E_0 \rangle j_0(\Delta \varphi) J_1(\varphi_1) \varphi_1^{-1} \tag{18a}$$

$$\langle E_2 \rangle = \langle N \rangle \langle E_0 \rangle \Delta \varphi j_0(\tfrac{1}{2}\Delta \varphi) J_1(\varphi_1) \varphi_1^{-1} \tag{18b}$$

where $j_o(x)$ and $J_1(x)$ are Bessel functions, and

$$\varphi_1 = (2\pi/\lambda) r \sin\theta$$
$$\Delta\varphi = (4\pi/\lambda) l \sin^2(\theta/2)$$

(19)

We have also analyzed numerically the parameter M which appeared to be independent of M_{11} because $M_{11} \ll M_{10} = M_{02}$. Hence, $M = \langle I \rangle / 2$ where $\langle I \rangle$ stands for the mean scattered intensity.

Having derived the joint probability density for E_1 and E_2, Eq.(17), it is straightforward to calculate the probability density for the scattered intensity. We replace E_1 and E_2 in Eq.(17) by $\sqrt{I} \cos\Phi$ and $\sqrt{I} \sin\Phi$, respectively, where Φ denotes the overall phase of the scattered electric field. Integration over Φ results in the intensity probability density expressed by the Rice distribution that is the function of the scattering angle

$$P(I) = \langle I \rangle^{-1} \exp\{-(I + \langle N \rangle^2 \alpha^2)/\langle I \rangle\} I_o(2\alpha I^{1/2})$$

(20)

where $I_o(x)$ is the modified Bessel function, and α is given by the formula

$$\alpha = 2 j_o(\Delta\varphi/2) J_1(\varphi_1)/\varphi_1$$

(21)

Eq.(20) also provides an insight into the role of the proper choice of the angle in scattering experiments. Thus, an experiment at a certain angle with a given scattering volume may bring intensities that are distributed in some particular manner. If the next experiment is carried out under the same conditions and with an identical material but the scattering volume is of different linear dimensions then the intensities obtained may obey a new distribution. The change in scattering volume results in a change in the critical angle θ_c; decreasing this volume increases θ_c. Therefore, one has to change the observation angle in order to get the intensity distribution matching that of the first experiment.

Cumulative intensity distribution can be calculated using Eq.(20) in the following formula

$$P(I \geqslant I_o) = \int_{I_o}^{\infty} dI P(I)$$

(22)

which yields

$$P(I \geqslant I_o) = \exp\{-(I_o + \langle N \rangle^2 \alpha^2)/\langle I \rangle\}$$

$$\sum_{n}{}' (n!)^{-1} (\langle N \rangle^2 \alpha^2/\langle I \rangle)^n \sum_{k}^{n} (k!)^{-1} (I_o/\langle I \rangle)^k .$$

(23)

This function has been tested against simulation data obtained for cylindrical scattering volumes populated by randomly distributed point scatterers. Simulated volume (40 cubic microns) contained 20,000 scatterers and the incident wavelength was $0.1\mu m$. These parameters correspond to $\theta_c \cong 6°$. Fig.1 presents a comparison of the negative exponential statistics and the distribution of Eq.(23) with the actual intensity distribution obtained from the simulation at a scattering angle $\theta = 5°$. As expected, the exponential statistics strongly deviated from the simulated intensity distribution. Eq.(23) provides a much better approximation to that distribution. However the approximation is not satisfactory over the entire range of intensities studied. A remarkable divergence from the simulation curve is observed for intensities $I > \langle I \rangle$. The possible reason could reside in the approximation of Eq.(4a) by Eq.(4b) which is based on the assumption that the number of scatterers is very large. This was certainly not the case in our simulation. Another conceivable cause could be the choice of Poisson distribution for the scatterer number fluctuation in slabs. We have no pertinent experimental data available to test further the applicability of our theory. We believe that it would work better in the case of real multi-scatterer systems, for which Eq.(23) was derived.

In conclusion we have shown that in the case of single scattering from volumes containing a large number of randomly placed scatterers the intensity distribution turns out to diverge from the negative exponential distribution for scattering angles smaller than θ_c. Our analysis also shows that the discussion of experimental intensity distributions must recognize the role of observation angle. Inappropriate choice of the latter may result in bizarre behavior of the intensity distribution. The presence of a critical angle is a common feature of any real (finite) scattering system. Since the critical angle is in range of angles easily accessible to most spectrometers $(30° - 40°)$[8,9] the design of an experiment has to be performed with a great care in order to avoid statistics deterioration be coherence effects. These effects were also shown to disturb the intensity statistics in the multiple scattering.[10] The above analysis was intended to describe the intensity distribution that would be oberved at $\theta < \theta_c$. Applying simple arguments we were able to show that this distribution

differs remarkably from negative exponential statistics. Our intensity distribution partially matched the distribution obtained from simulation. The lack of a complete agreement was presumably a consequence of finite size effects in the simulation.
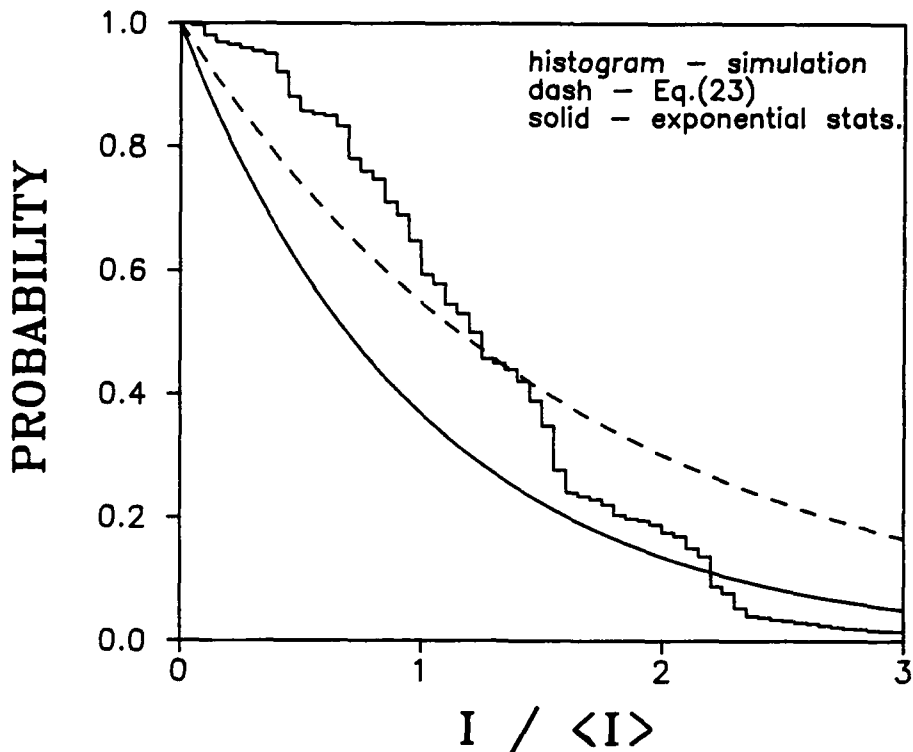
FIG.1. Comparison of intensity statistics(simulation) with Eq.(23) and negative exponential.

References

[1] A. Ishimaru, Wave Propagation and Scattering in Random Media,
          (Academic Press, New York, 1978), vols I and II.

[2] J.W. Goodman, in Laser Speckle and Related Phenomena, edited by J.C. Dainty,
          (Springer-Verlag, Berlin, 1964).

[3] H.M. Pedersen, Optics Commun., 16 63 (1976).

[4] B. Shapiro, Phys. Rev. Lett., 57 2168 (1986).

[5] E. Jakeman and R.J.A. Tough, J. Opt. Soc. Am., A4 1764 (1987).

[6] R. Barakat, Opt. Acta, 21 903 (1974); J. Opt. Soc. Am., 71 86 (1981).

[7] R. Gillies, M. Kazmierczak, T. Keyes, A.J. Wojtowicz and A. Lempicki,
          Phys. Rev., B36 9413 (1987).

[8] M. Kazmierczak, T. Keyes and T. Ohtsuki, Phys. Rev., B39 (1989) (in press)

[9] J.J. Chen, M. Kazmierczak, T. Keyes and A. Lempicki, Phys. Rev.,B (to be published)

[10] M. Kazmierczak, A. Lempicki and T. Keyes (in prepation)

ESTABLISHING A STANDARD FOR POLARIZED LASER LIGHT SCATTERING FROM MICROBIAL SYSTEMS

Willem P. Van De Merwe, Ph.D.
Laser Biophysics Center
Uniformed Services University of the Health Sciences
4301 Jones Bridge Road, Bethesda, Maryland 20814-4799

Donald R. Huffman, Ph.D.
Department of Physics
University of Arizona
Tucson, Arizona 85721

Burt V. Bronk, Ph.D.
US Army Chemical Research Development and
Engineering Center, Bldg. E5951
Aberdeen Proving Ground
Edgewood, Maryland 21010

Summary

In this paper we describe our efforts to establish a biological "standard" for polarized light scattering from microorganisms, which could serve as a "calibration" for the experimental setup, much like polystyrene spheres are used for similar purposes in physical experiments. We measured the S_{34} element of the Mueller scattering matrix for a lysogenic **E.coli** K12 bacterium and established the conditions under which the signal is reproducible between different laboratories. By varying biological parameters which influence the cells, we have begun to achieve some insight into what determines the signal. Specifically, we varied the size distribution of the bacteria by changing the growth conditions. Small changes in growth conditions gave rise to easily measurable changes in the signal which had not previously been predicted.

Introduction

Since the mid-seventies several investigators have reported "organism-unique" polarized light scattering signals as a function of scattering angle[1,2]. It was suggested that one could identify (fingerprint) micro-organisms by the signal. However, after these many years of investigation, no-one has yet published a unique scattering signal that was reproduced in other laboratories. Nor has anyone reported the effects of various parameters on the signal so that one might understand the sensitivity of the signal to slight variations, such as; size distribution, DNA content, growth conditions, etc. In this report we give examples in which relatively small changes in growth conditions (i.e. the stage of growth and growth medium) produces changes in the scattering signal which are larger than changes which others have indicated can distinguish between similar organisms. The signal evaluated is the angular-dependent Mueller matrix S_{34} element. The 16-element Mueller matrix completely characterizes the elastic light scattering properties of any object, being defined as the matrix which transforms the 4-element Stokes vector which, in turn, completely characterizes the intensity and polarization state of light[3].

To obtain reliable signals one has to understand the experimental set-up very well and recognize the various artifacts that could impact the final signal. In addition, one has to understand the biological parameters very well and recognize the effects of different preparation procedures. In other words, in order to establish whether or not one can "uniquely" identify a micro-organism by measuring a Mueller matrix element one needs expertise in experimental physics as well as in microbiology. If it turns out that the signal does not uniquely identify the organism, one must establish what the limitations are. In that case, it would be useful to identify groups of organisms that produce similar scattering signals.

Experimental Set-Up

At the University of Arizona we used the experimental apparatus set up several years ago by Huffman which is described in detail elsewhere[4,5]. A similar apparatus was set up recently at the Uniformed University of the Health Sciences (USUHS). In it, a HeNe laser beam is modulated by a time-varying retarder that converts the linearly polarized beam into

a beam that alternates between left and right circular-polarized light at a frequency of 50 kHz. The scattered light passes through a linear polarizer at 45 degrees to the scattering plane, and is detected by a photomultiplier tube (PMT). With a lock-in amplifier the 50 kHz component is measured. By electronically keeping the dc component of the PMT-signal (proportional to S_{11}) constant in the particular configuration, one measures the following combination of matrix elements:

$$(S_{14} + S_{34})/(S_{11} + S_{31})$$

Since for our system S_{14} and S_{31} are negligible, this may be approximated by:

$$S_{34}/S_{11}$$

The signal is expressed as a percent of the maximum value obtained after placing a quarter wave plate in the forward direction between the sample and phototube for calibration.

Biological Preparations

For our standard scattering organism we chose **Escherichia coli** K12 with heat-inducible lambda virus incorporated in the main chromosome. This **E.coli** was obtained from Dr. A. Maurelli at USUHS and is identified as χ 2712ts. Some of the advantages of this bacterium are that one can easily induce the expression of the virus, thus ensuring (with a large probability) that indeed one has the correct bacterium and not a look-alike contaminant that was grown instead. Upon induction the lambda virus genes are transcribed and within a known time (about 30-50 minutes, depending the temperature) 100 to 200 viruses have been formed in the bacterium and burst open the cell. This last step is easy to "eyeball" since it gives rise to a sharp change from a cloudy suspension to a clear one.

It is well-known that the volume and contents of an **E.coli** cell can be modified greatly by simply changing the medium in which it is grown[6]. Some other simple modifications giving rise to measurable changes in the cell include the stage of growth, the growth medium, the growth temperature, etc.

In general when one starts growing bacteria the cells are in a "lag" phase, that is they are not directly dividing. After this initial phase the bacteria enter into the "log" phase where the bacteria are actively dividing with the number of bacteria growing exponentially (the rate of growth is characterized by the "doubling time"). After the concentration of bacteria reaches a certain value, the bacteria start to interact and the rate of growth decreases, until the bacteria stop dividing and the bacteria are said to have entered the "stationary" phase. Figure 1 represents a typical growth curve, with the effect of induction also portrayed.

The **E.coli** K12 was grown at 30 degrees C, in LB broth with vigorous shaking. Stationary phase bacteria were generally harvested after growing the culture overnight. The log phase cells were harvested when the optical density (OD) of the sample was 0.05. The cells were centrifuged at about 3000g and the pellet resuspended in 0.9% NaCl (pH=5.7) at an OD of 0.05. The **E.coli** B/r was grown in an enriched medium and in a minimal glucose medium ("rich" and "poor" media) at 37 C.
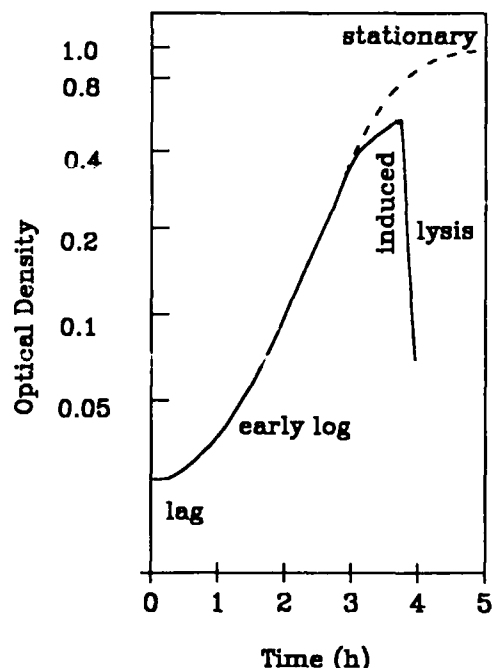
FIGURE 1. TYPICAL BACTERIAL GROWTH CURVE.
Lag phase, the bacteria are not yet actively dividing. Log phase, the number of bacteria increases exponentially. Stationary phase, the bacteria stop dividing. Induced/lysis, the lambda virus replicates and bursts open the cell.

The **E.coli** K12 and B/r were used as described above, at the USUHS and the University of Arizona.

Figure 2 shows the results of a reproducible signal between the two laboratories.

Figure 3 shows the effect of "stage of growth" on the signal.

Figure 4 shows the effect of different growth media on the signal.

Figure 5 shows the S_{34} signal obtained at wavelength 633nm (HeNe) and at 442nm (HeCd).
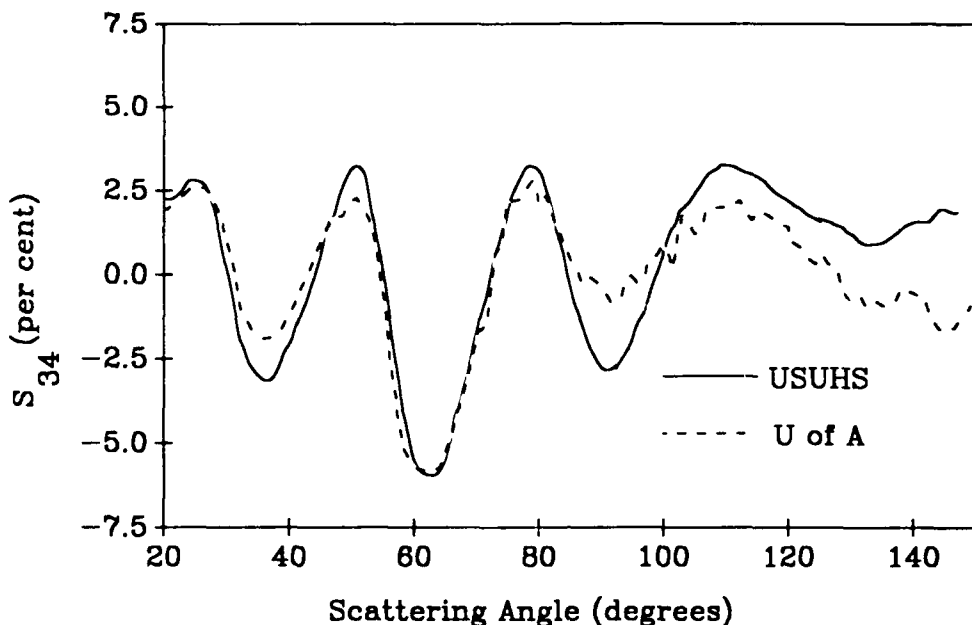
FIGURE 2. REPRODUCIBILITY OF S_{34} OF E.coli K12 BETWEEN LABORATORIES. The solid line represents data obtained at the USUHS and the dotted line data obtained at the U of A. The bacteria were in early log phase (see text).
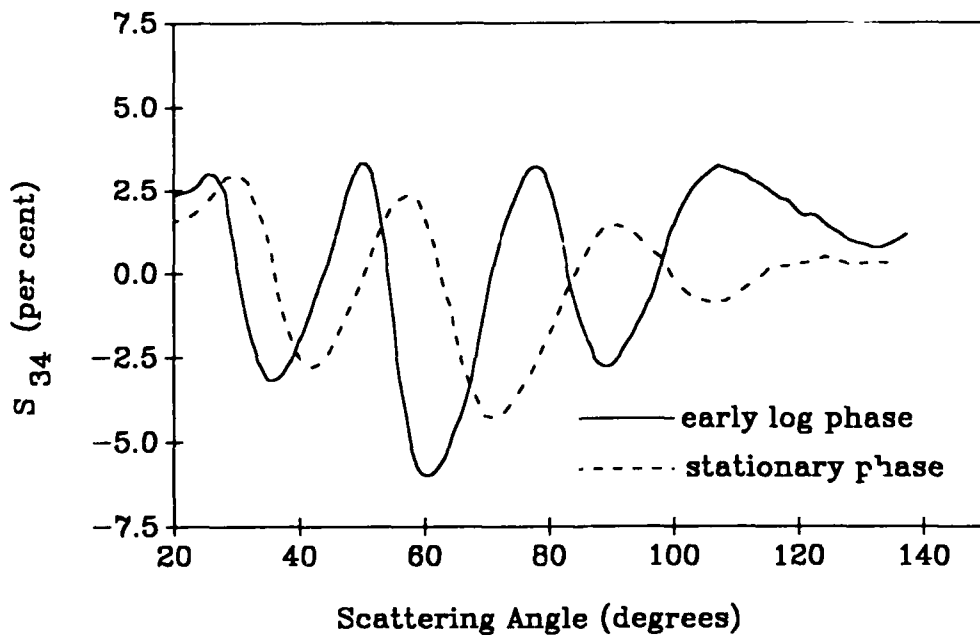
FIGURE 3. EARLY-LOG AND STATIONARY PHASE E.coli K12 S_{34} AS A FUNCTION OF SCATTERING ANGLE. The solid line represents the early-log phase and the dotted line the stationary phase.
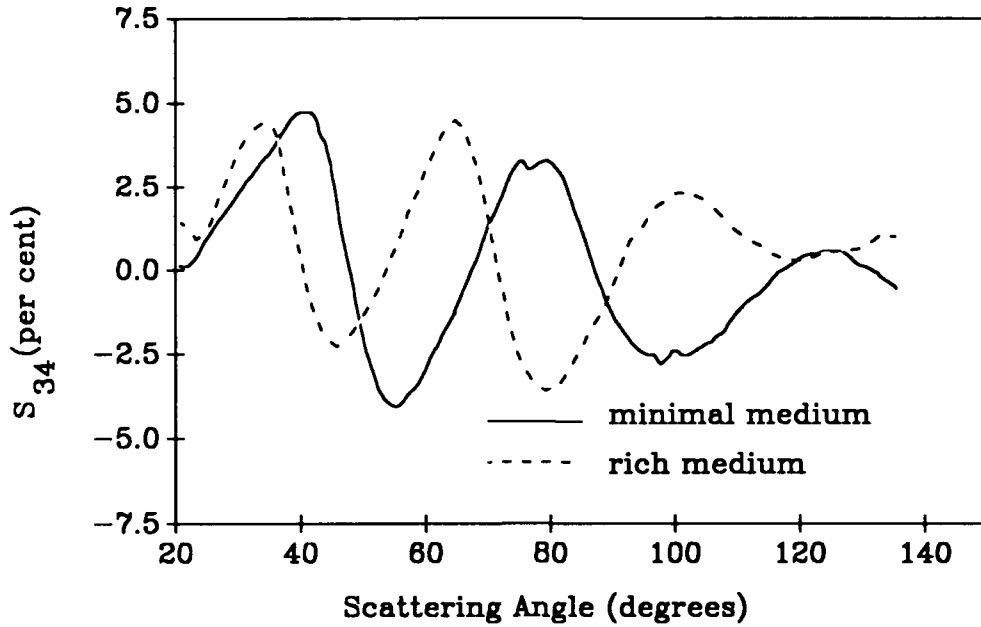
FIGURE 4. EFFECT OF GROWTH MEDIUM ON S_{34} OF E.coli B/r. The solid line was obtained growing the bacteria in a minimal glucose medium and the dotted line growing the bacteria in an enriched medium.
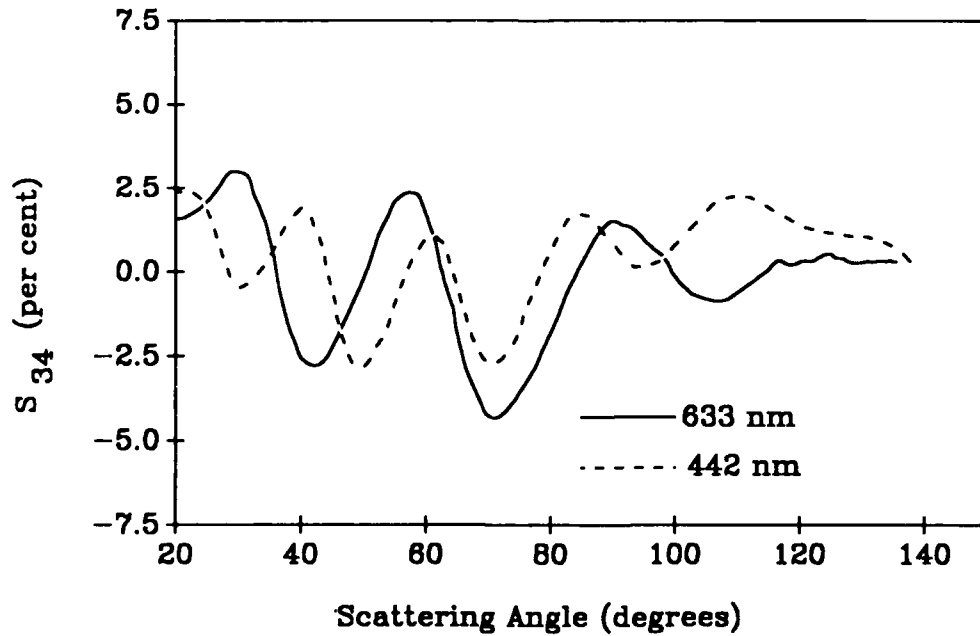
FIGURE 5. EFFECT OF LASER WAVELENGTH OF S_{34} OF E.coli K12. The solid line was obtained using HeNe red and the dotted line HeCd blue.

Discussion

The results of this paper indicate that a "standard" for S_{34} scattering can be established. For the standard we chose the lysogenic **E.coli** K12, because the purity of the sample can easily be verified by inducing the lambda virus expression. The S_{34} signal, as a function of scattering angle, within the same laboratory as well as between the USUHS and the U of A can be reproduced with the peak locations within 1 degree for angles less than 90 degrees, and the peak heights within 1 percent.

The reproducibility is very sensitive to the growth conditions of the bacterium. The best reproducibility could be established when the **E.coli** was actively growing in "log-phase" with an optical density of less than 0.05 (about 10 million bacteria per ml). Furthermore, the temperature, the growth medium, the aeration, the dilution factor and dilution medium influence the final scattering signal.

From the data collected thus far it appears that the S_{34} signal is strongly dependent on the average size of the bacteria. Size distributions for **E.coli** B/r, grown in different media, are well documented. In "rich" media the cells may be 1.6 times larger (volume) than in "minimal" media. The scattering signals show a substantial shift, with the "larger" bacteria yielding more peaks and each shifted towards smaller scattering angles relative to the peak position for the "smaller" bacteria. Similar shifts could be accomplished by changing the laser wavelength.

When the signal was taken with bacteria grown to the "stationary" phase the peaks were shifted substantially towards larger angles relative to the peak position established with "log-phase" growing bacteria. This also is consistent with size variations as verified by microscopic examination.

To further our understanding of the S_{34} signal we are pursuing modeling and study of different shapes of bacteria and other cells. In addition we are changing the contents of the bacteria in order to establish the sensitivity of the signal to the inward structure. First indications show that the internal structure does not significantly effect the signal at visible wavelengths. However, a shape or size change, accompanying a change of contents, will significantly effect the overall signal.

References

(1) W.S. Bickel and M.E. Stafford, Polarized Light Scattering from Biological Systems: A Technique for Cell Differentiation, J. Biol. Phys. 9, 53, 1981

(2) R. J. Fraatz, G. Prakash and F.S. Allen, A Polarization Sensitive Light Scattering System for the Characterization of Bacteria, Am. Biotech. Lab 6, 24, 1988

(3) C.F. Bohren, D.R. Huffman, Absorption and Scattering of Light by Small Particles (Wiley Interscience, 1983) pp 57-81

(4) A.J. Hunt, D.R. Huffman, A New Polarization-modulated Light Scattering Instrument, Rev. Sci. Instrum., 44, 1753, (1973)

(5) W.S. Bickel, et al., Application of Polarization Effects in Scattering: A New Biophysical Tool, PNAS, 73, 486, (1976)

(6) B.V. Bronk, D. Walbridge, Sensitivity to UV radiation as a function of DNA content in E-Coli B/r, Bioph.J. 31, 381, (1980)

OPTICAL METHODS FOR MEASURING ROTATIONS

Erik STIJNS

Vrije Universiteit Brussel, ALNA-TW,
Pleinlaan 2, B-1050 Brussel, Belgium.

Abstract.

An overview is given of different optical methods used to measure rotations. Both "classical" and "modern" techniques are described ; the physical principles are outlined, but the emphasis lays on the applications ; performances and limitations are compared.

Classical methods.

The measurements of angles and the measurements of rotations are old mechanical problems. The simplest way to do it is to take a rotating drum, on which an index is engraved; the reading of it can be improved with the help of vernier scale. The angles can be further devided by using the so-called small_angle_devider. Resolutions down to 0.1 second of arc are claimed (ref. 1). Such small angles can also be measured with an autocollimator; one speakes of an electronic_autocollinator if the position of the reflected beam is measured a slit and/or an array of detectors (fig. 1). Resolutions go from 0.1 to 0.001 arc sec (ref. 2). In order to automate those measurements different methods are used ; we will describe some of the optical ones. Let's mention for instance the optical_shaft_encoder, in which a slotted wheel, fixed to the rotating object, chops a light beam into pulses. By counting the number of pulses one can calculate, after a calibration, the angle of rotation or the number of revolutions.
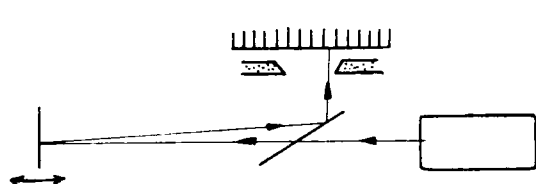
Schematic electronic autocollimator.

Figure 1

volts

5

100 arc sec

output vs angle
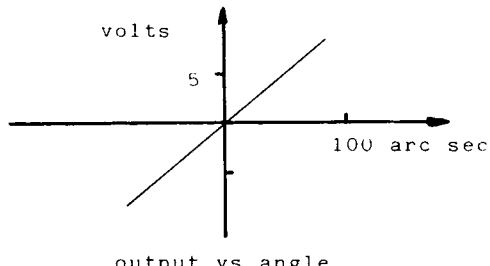
Another way of measuring rotations is the Moiré technique. A grating, fixed to the rotating object, passes by a fixed grating of the same period. Moving one grating with respect to the other gives light pulses, as one can easily check.

In order to measure fast rotations, one often makes use of the so-called optical_derotator, of which the stroboscope is the best known example. Flashes of light are sent towards the rotating object ; the period of those flashes is adapted so that one observes a seemingly stationary object, in which case the rotation rate of the rotating object can be calculated.

It seems there are no problems for measuring fast rotations or large angles. The problems real comes when one wants to measure small angles or slow rotations. This brings us to the main section of this paper : indeed optical methods are the only methods which allows the measurement of very small angles.
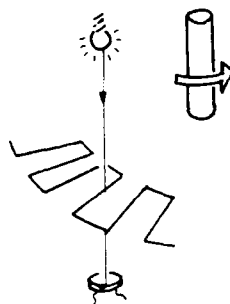
optical shaft encoder
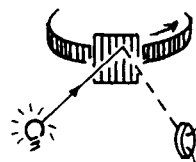
Figure 2

Moiré technique
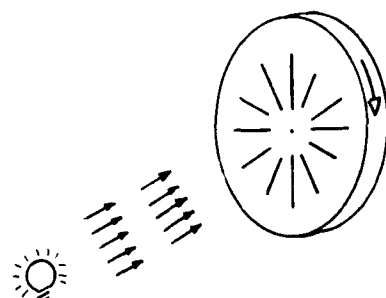
Figure 3

Optical derotation
(stroboscope)

Figure 4

Interferometric methods.

Those optical measurements are based on interferometry ; this implies that one invariantly uses a laser as a light source. Indeed, one needs a light source which gives a well-defined optical beam with a good longitudinal (and sometimes also transverse) coherence. The high brightness of the beam is moreover an additional convenience.
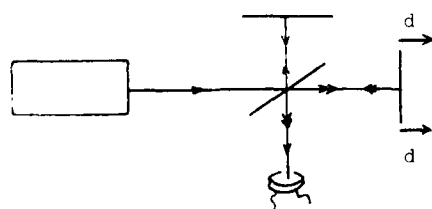
a : schematic
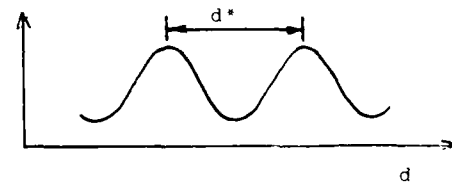
b : output at detector vs distance

Figure 5 : Michelson interferometer

The basic set-up of the Michelson interferometer is shown in figure 5a. When the last mirror is displaced over a distance d, the irradiance at the detector changes as a sine square function. The distance d* between two successive maxima corresponds to half a wavelength, which implies that the sensitivity of a simple Michelson interferometer for measuring linear displacements goes down to about 1/4 um. By usig simple geometrical tricks, it is possible to increase the sensitivity by powers of two ; and by electronically interpolating between fringes (ref. 3) the resolution goes down to a small part of a fringe. In this paper however we are not interested in translations, but we want to measure rotations, so we have to transform the translation into a rotation. That can be done in various ways; we can only give a few of them.
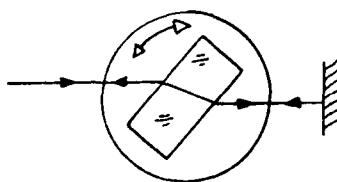
Figure 6
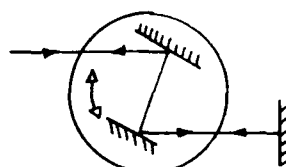
Figure 7

The most direct way is to insert, into one of the arms of the interferometer, a device, the optical path of which depends on the angle of rotation : figures 6 and 7 show two possible set-ups. The resolution of the set-up of figure 7 is 0.02 secarc (ref. 4). These schemes, however, have the inconvenience that you have to put something in the arms of the interferometer ; this is easily done in a lab, but it makes the method not interesting for applications in an industrial environment. For those applications it is better to separate the rotating device from the rest of the interferometer. A possible set-up is shown in figure 8 (ref. 5). Two retroprisms are mounted on the rotating object, while the rest of the interferometer forms a fixed unit. When used in conjunction with an up-down counter, the set-up is insensitive to vibrations ; a typical instrument gives 10000 fringes per degree of rotation. A more sensitive set-up, but also more difficult to align, is the so-called Optical Sine Bar, shown in figure 9 (ref. 6). Its resolution goes down to 60 msec of arc per fringe, and that's a very small angle : it is the angle giving a displacement of 1 mm at a distance of about 3 km !
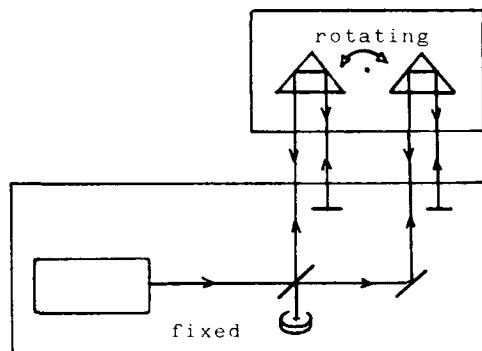
Figure 8
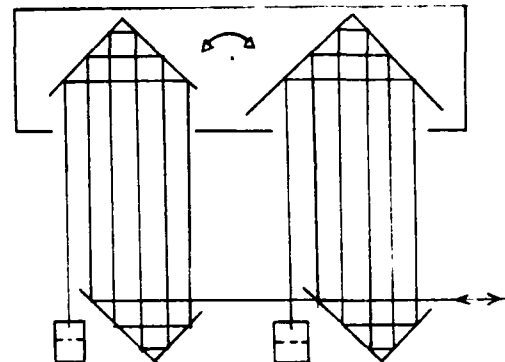
Figure 9

Closely related to the interferometric methods are the doppler methods. A linear movement of velocity v gives a (up or down) shift in frequency df according to $df/f = v/c$. Because df cann't be measured directly, one mixes the shifted frequency with the original one, in order to create a beat note. The mixing is usually done in a Michelson-type device (fig. 10) and so we are back to the interferometer.

The transformation of the translation into a rotation can be done in different ways ; we describe here only one of them (ref. 7). The laser is put in a magnetic field, which splits the laserline in two frequencies f1 and f2, each of them having another state of polarization ; a Wollaston prism send each of the two frequencies to a perpendicular mirror (fig. 11), mounted on the rotating device. If this device translates, the two frequencies undergo the same dopplershift df1 = df2. If, on the other hand, the device rotates, df1 ≠ df2 ; a new beat note (df1 - df2) is created, by which the rotation can be calculated. The sensitivity goes down to 0.1 sec of arc (ref. 7).
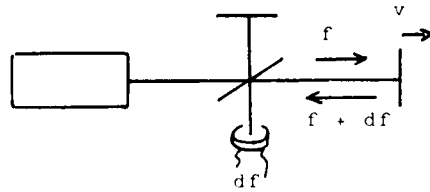
Figure 10
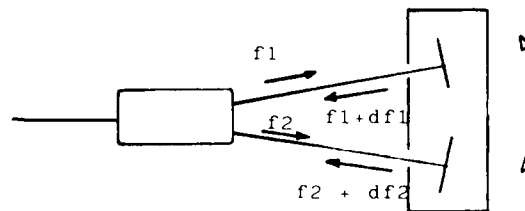
Figure 11

Inertial rotation sensors.

Up to now we have been concentrating on relative rotations, by which we mean that the rotations are measured with respect to a given reference frame. The rotating set-up is linked to the fixed reference frame by means of light beams (fig. 12). In inertial rotation sensors (IRS), on the other hand, absolute rotations are measured, i.e. rotations with respect to "fixed" stars of the universe (whatever that may be). The basic principle is the Sagnac effect. We will explain this in a classical way ; it can be shown that the classical formula is indeed a first-order approximation of the correct formula derived from the general theory of relativity (ref. 8).
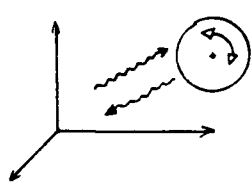
Figure 12
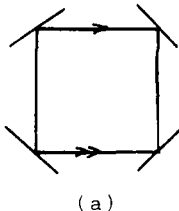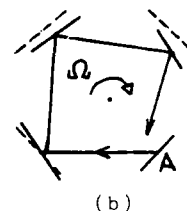
(a)   (b)

Figure 13

Consider a closed optical loop or ring, with perimeter P as shown in figure 13. Light can go around the loop in a cw or a ccw direction. Suppose now that the ring rotates with a rotation rate Ω , and look at the cw wave starting from point A. By the time the light arrives at the next mirror, this mirror moved a little bit. So for the cw wave the perimeter P seems to be increased by an amount dP. For the ccw wave on the other hand, the perimeter is decreased by the same amount. It is easy to show that dP : $4A\,\Omega/c$ with A the area of the loop and c the velocity of light. This is now exploited in the Sagnac interferometer (fig. 14a) ; two counterpropagating beams are sent in the interferometer. By measuring the phase shift between them at the output, the rotation rate can be calculated. This interferometer is not at all sensitive : A = 1 m2 and Ω = 270°/sec gives only a dP of about one tenth of the wavelength. The sensitivity can be increased either by putting the laser in the interferometer itself (the lasergyro) or by using a multiturn loop (fibre-optic rotation sensor). In a lasergyro (fig. 14b) the change in length is transformed into a change in frequency by virtue of the formula dP/P = df/f. So the cw and ccw waves now have a different frequency ; mixing them at the output gives a beat note with frequency f = $4A\,\Omega/p\,\lambda$. With the same numerical values as in the previous example, one finds a beat note of about 7 MHz. It should be clear now that such a device allows very small rotation rates to be measured ; as an example it is used to monitor the rotation of the earth. A real lasergyro has a number of errors, among which the so-called lock-in. Indeed, due to the nonlinearity of the laser gain cell, the two counterpropagating waves are coupled. When the beat frequency becomes too small, the two waves lock together, and the gyro is useless. By a number of clever tricks this mode-lockin region can be displaced : the lasergyro has now become a reliable instrument, with a sensitivity greater than 10-3 °/h, and it is used on different types of airplanes (ref. 9).

(b)

(a)
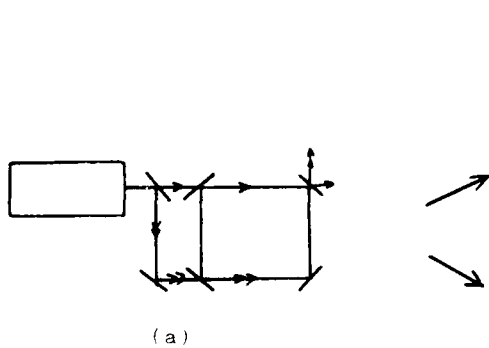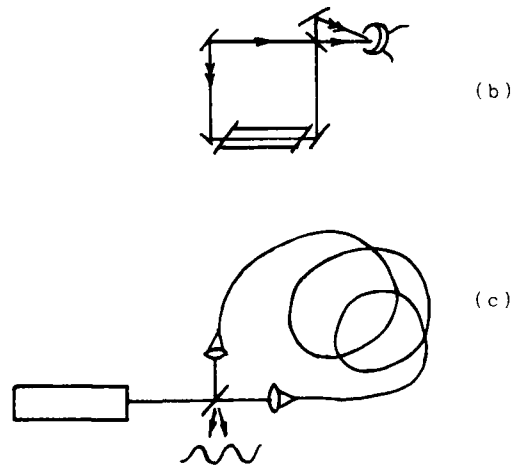
(c)

Figure 14

Another way to increase the sensitivity of the original Sagnac interferometer is to use a multi-turn optical fibre (fig. 14c). A set-up with, e.g., 1000 turns and an area A of 100 cm2 gives, for a rotation rate of 15 °/h (= rotation of the earth), a phase shift of 10-4 rad, a measurable value. The fibre rotation sensor shows no lock-in, because the light source is outside the ring ; so it is easier to build. On the other hand, a shift of an interference pattern is more difficult to measure than a frequency and the overall sensitivity of a fibre gyro is less than the sensitivity of a lasergyro.

Conclusion.

We can conclude that the mariage of optics, basic physics, and clever electronics has lead to new reliable instruments, with sensitivities which were unbelievable before the advent of the laser. However there still is a long way towards the ultimate sensitivity needed for some very exciting experiments in basic physics (ref. 10).

References.

1. MOORE Precision Tools product information on the "Moore 1440 Small-Angle Divider", 1985
2. MICRO-RADIAN product information on the "Electronic autocollimators MR'-150 series" (1983).
3. M. MITTELSTAEDT, Photonics Spectra, Vol. 20, N° 6, 73 (june 1986).
4. M. VAN DE MEULEBROECKE, presented at the Optical Meeting of the DGAO '74, Brugge, Belgium (1974), paper 26.
5. P. SHI, E. STIJNS, Appl. Opt. 27, 4342 (1988).
6. G.D. CHAPMAN, Appl. Opt. 13, 1646 (1974).
7. HEWLETT-PACKARD product information on the "55288S Dimensional Metrology Analysis System" (1984).
8. F. ARONOWITZ, in Laser Applications, Vol. 1, M. Ross Ed. (Academic Press, 1971) pp. 134-199.
9. F. ARONOWITZ, Photonics Spectra, Vol. 22, N° 9, 135 (sept. 1988).
10. M.O. SCULLY, in Proceedings of the Interational Conference on Lasers '87, F. Duarte, Ed. (STS Press, McLean, VA, 1988), pp. 1-3.

DEVELOPMENT AND APPLICATION OF A THREE-DIMENSIONAL
LASER DOPPLER VELOCIMETER SYSTEM TO
INTERNAL AND EXTERNAL FLOWS

Joseph A. Nouri
Mechanical Systems Manager
SCI Technology, Inc.
P.O. Box 1000, Huntsville, Alabama 35807

Abstract

A three-dimensional, tri-orthogonal, two-color, and Bragg-diffracted laser Doppler velocimeter system has been developed to measure simultaneously the three components of local mean velocity (u, v, w) and the associated turbulent quantities. The system is designed to measure flow parameters in very complex and highly three-dimensional, in both the mean-flow and the turbulent structure, internal and external flows. The developed system has successfully used to study the secondary motions by both the Reynolds-stress gradients and pressure gradients, corner flows, and turbulent boundary layer flow cases.

Introduction

Many important and practical engineering problems in industry involve very complex and three-dimensional turbulent flows. For example, most aircraft or general industrial installations have flow passages wherein hot gas passes through cascaded vanes geometries for extracting power and for flow turning purposes. The heat and/or mass transfer from the vanes is a critical feature of the installation which directly determines the durability and survivability of the cascade system. Moreover, the efficiency of the blade system to extract power, in the case of a turbine blade configuration, or to turn flow depends strongly on the degree and intensity of secondary and corner flows passing through the blades [1, 2]. This type of flow may represent stalled boundary layer flow and so the lift of the blades can be seriously degraded. It is clear that the evaluation of such complex fluid flows require physically perceptive analytical tools, generally as computer codes based on the flow field data of high quality for 3-D flow predictions, in order that engineers and designers can optimize blade configuration, staging, blade clearances, and inlet and outlet flow passage geometry [3, 4, 5].

The quality of three-dimensional laser Doppler velocimeter (LDV) measurements depends on several parameters determined by the transmitting and receiving optical configurations and the principle of signal processing. In applying the 3-D LDV technique for accurate and successful measurements in internal and external flow problems, conditions under which the measurements are carried out need to be fully considered. Also, it is of vital importance to know whether the system will satisfy the measurement requirements and what the optimum system concern should be focused on the flow measurement region and its accessibility for laser beams either through optical windows or through transparent sections [6].

This paper will describe a newly developed 3-D LDV system which is capable of simultaneously measuring the three components of velocity and providing the corresponding quantities of the turbulent fluid motion.

System Description

A schematic diagram of the newly developed 3-D LDV system is shown in Figure 1. A commercially available Argon-ion laser is used as a light source for the system. The laser produces a high power visible output at six simultaneous wavelengths from 514.5 nm to 457.9 nm in the portion of the full visible spectrum. The two strongest wavelengths, namely the 514.5 nm green line and the 488.0 nm blue line, are chosen by using an internal prism wavelength selector. The approximate output power is 43% in the green line and 20% in the blue line at full rated laser power.

In general, the optical system that can be used for the LDV measurements varies considerably based on different flow situations. In the present system in order to control the divergence of the laser output in the transmitting optics, a beam collimator is mounted
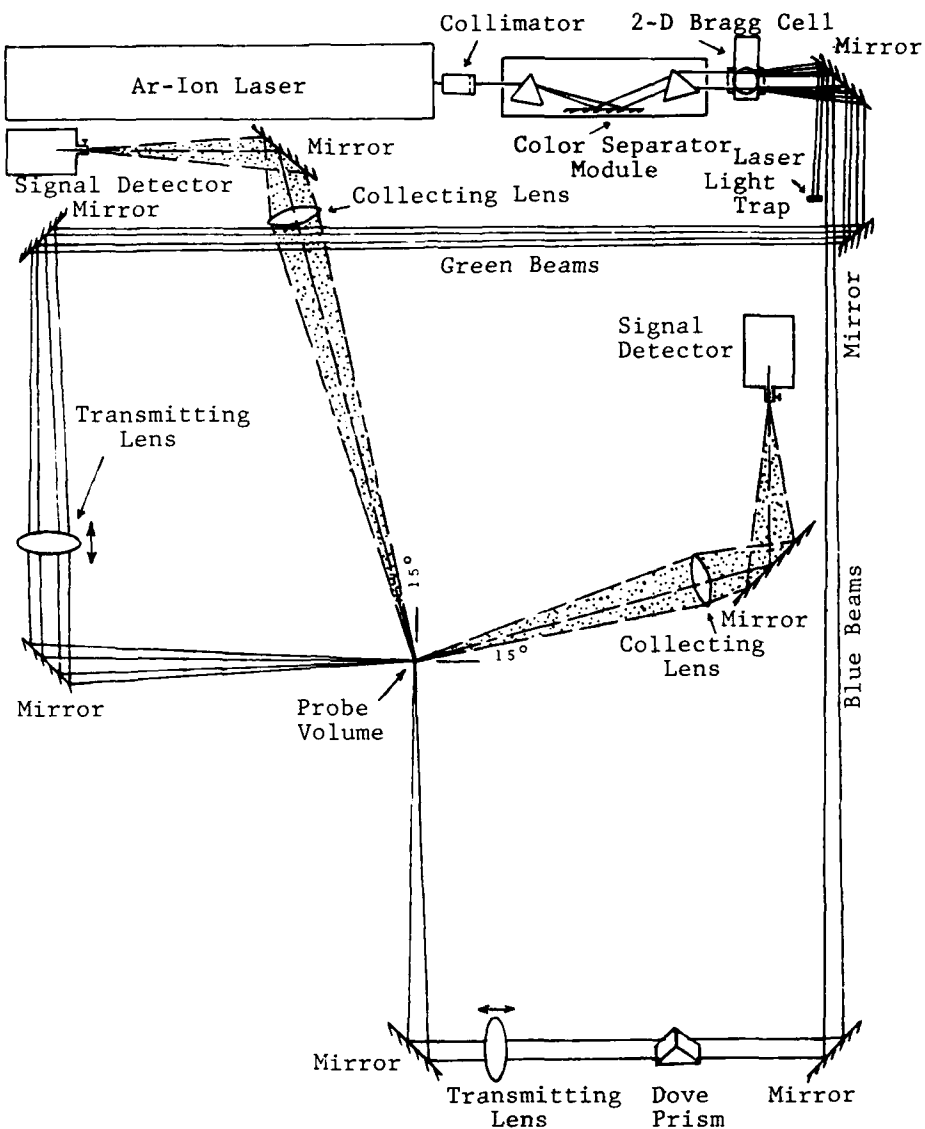
Figure 1: Three-Dimensional Laser Doppler Velocimeter System.

to the output aperture of the laser. The single collimated beam is separated into a green beam and a blue beam in an enclosed color separator module. Inside the module, as shown in Figure 1, the incident beam first is passed through a Brewster 60-degree angle dispersion prism and the dispersed colors are then reflected off a front surface beam-director mirror into a second 60-degree prism which is used to make the incident and transmitted beams coaxial. The output beams are parallel which can be adjusted in terms of spatial separation and position relative to the input beam.

To measure simultaneously the three orthogonal components of velocity in the same probe volume, it is necessary to generate three superimposed sets of interference fringes. This can be accomplished by applying the dual-beam optical frequency shifting technique where a single 2-D ultrasonic Bragg cell modulator is used [7]. The Bragg cell functions as both the beam splitter and the frequency shifter. Each crystal of the Bragg cell is made to oscillate in an odd overtone by a power amplifier referenced to a Phase Locked Loop (PLL) oscillator. The quartz transducers are cut for 5 MHz. fundamental frequencies and are operated in third and fifth overtones to produce frequency shifts in the beams of 15 and 25 MHz..

As shown in Figure 1, the two-color separated beams produced by the color separator module are passed into the Bragg cell's optical quality window and four equally intense

674

beams for each color beam are produced. The two green pairs of beams operating at a single wavelength are frequency shifted by the Bragg cell driver with carrier frequencies of 25 and 15 MHz. representing the x- and z- components of velocity, respectively. The third orthogonal component, representing the y-component of velocity, is formed using one of the blue pairs of beams at 488.0 nm with a frequency shift of 15 MHz.. Thus, frequency differences in orthogonal beam pairs are 15 and 25 MHz.. Non-orthogonal beam pairs have frequency differences of 10 and 40 MHz. and signal currents generated at these frequencies are removed by electronic filters after photo-detection. The four parallel green beams are then focused to a common point by an achromatic transmitting lens while the two parallel blue beams are brought to the same point by another achromatic transmitting lens after being rotated by a dove prism.

The probe volume in the present 3-D LDV system is composed of three superimposed sets of interference fringes. As shown in Figure 2, these interference fringes are produced by the
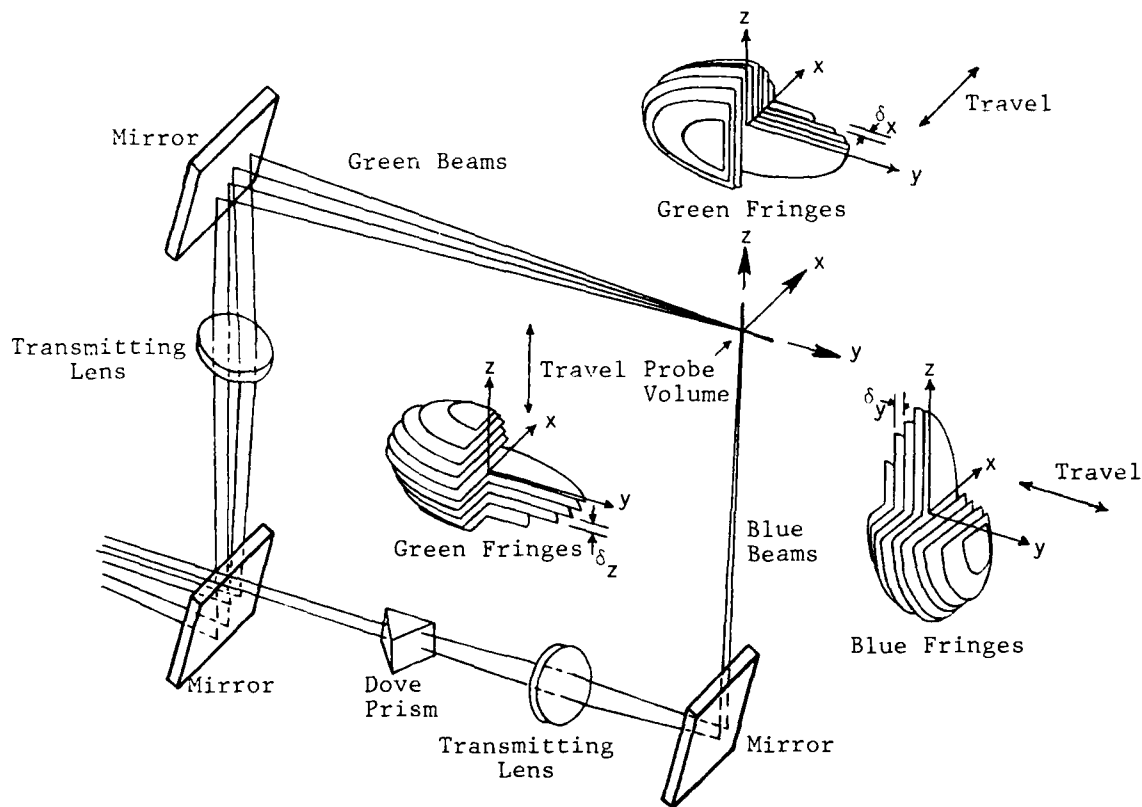
Figure 2: Formation of Three Supreimposed Sets of Interference Fringes in the Three-Dimensional Laser Doppler Velocimeter System.

intersection of six laser beams whose region of intersection is the measurement volume. The fringe pattern at the beam crossing point can be defined as a set of planes that slice the probe volume into a set of bright and dark areas. Each plane is normal to the plane defined by a set of crossed beams and parallel to the axis of the beam bisector. The intensity distribution for each pair of beams in the fringes is a sinusoidally modulated Gaussian. When a particle of size comparable to the laser wavelength light passes through these areas, it scatters light whose intensity varies within the Gaussian envelope [8].

For the collecting optics of the 3-D LDV system, two receiving lenses with a set of coated plane mirrors are positioned at an off-axis angle of 15-degree to collect. in the forward direction, the light scattered by particles traversing the probe volume in three different directions orthogonal to each other. Two photo-multiplier tubes are used as photo-detectors to convert the collected scattered light into an electrical signal. Narrow band interference filters of 1 nm bandpass are placed between the limiting aperture and the

675

photo-tube of each detectors to reject all light except the desired colors. One signal detector is used to receive both the x and z frequency shifted component signals while the other one is used to receive only the y component signal.

In order to scan a desired flow field, the laser, the transmitting optics, and the receiving optics of the 3-D LDV system can be mounted on an optical platform. A typical platform is shown in Figure 3. The optical table is usually placed on a milling machine
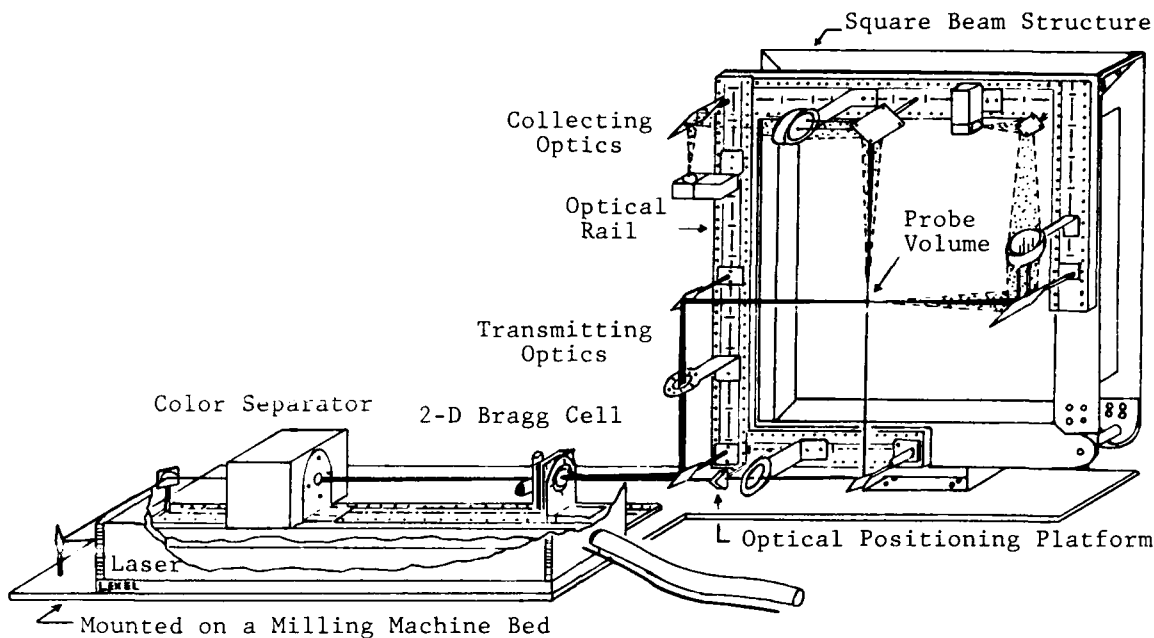
Figure 3: Typical Engineering Layout of the Three-Dimensional Laser Doppler Velocimeter System Optical Platform.

automated by three stepping motors, three linear magnetic scales, and computer controllers to provide three orthogonal directions of motion. A computer software is developed to control the drive system of the 3-D optical positioning table and a three-axis digital positioning readout system is used and programmed to display the position of the probe volume in the test section. The acquisition and the spatial positioning of the LDV probe volume are completely automated to minimize operator errors and the time required for data acquisition.

In the application of the present 3-D LDV system for measuring the fluid flow components, the existance of particles moving with the medium is essential because they are the source of Doppler shifted scattered light. The quality of the LDV data can be substantially improved by carefully controlling size, composition, and concentration of the particles in the fluid. The amount of light scattered from particles traversing an optical probe volume depends on the geometric diameter of the particle and its refractive index. It should be emphasized that the particle lag effects are significant when the fluid motion is transient, such as in the turbulent motion, accelerating and decelerating flows [3]. Also, the LDV results can be adversely influenced if the particle concentration is higher in one region of flow than in others. This phenomenon is more significant in viscous flows and may occur independently of particle lags. To eliminate this effect, the seed particles need to be well mixed with the flow medium and this can be achieved by uniform distribution of the particles upstream of the test section.

The velocity data for the 3-D LDV system are acquired by three standard high-speed Burst counters. Each counter is actually a combination of two time period counters each of which performs a signal period measurement. These time period counters are designed to start simultaneously but one counter, called the short fringe counter, stops after fewer fringe crossings that the second counter, called the long fringe counter. For simultaneous signal detection of the blue and green probe volumes, the signal time period measurement process is performed on each of the three velocity channels. As shown in Figure 4, the active pulses

676
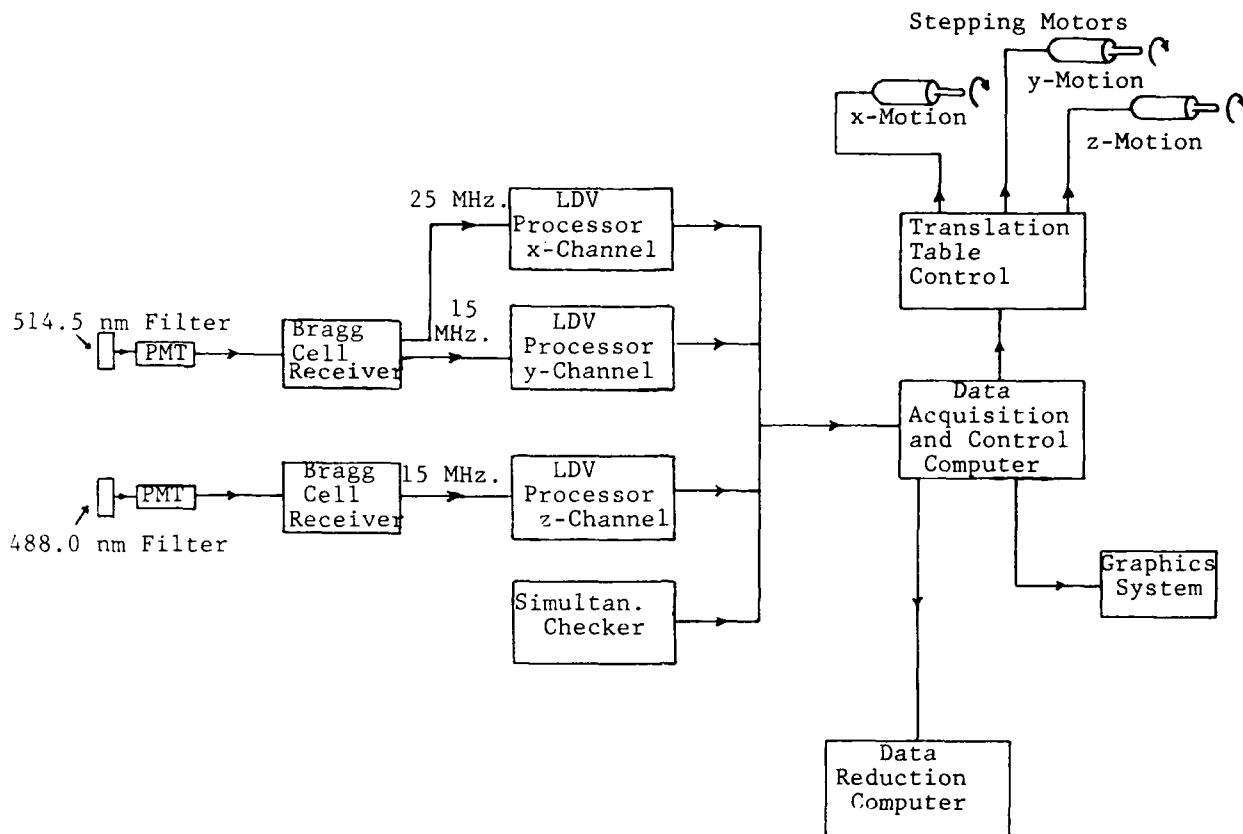
Figure 4: Block Diagram of the Three-Dimensional Laser Doppler Velocimeter Signal and Data Processing Systems.

from the three burst counters are passed to the "Simultaneity Checker." The computer is programmed in advance to record only those velocity data for which the three active pulses are coincident for at least one instant in time and for which an aperiodicity fail pulse is not produced by any of the burst counters [2].

In order to obtain the mean value of a velocity component, the turbulence intensity and other related parameters from the counter signal processor of the 3-D LDV system, it is necessary to apply a statistical analysis of the data. If N measurements of independent events is representative of the fluid flow velocity distribution function and if u_i (i = 1, 2, 3, ..., N) are the individual velocity measurements, then the time-averaged mean and mean-square velocity of the x-component of the velocity V = (u, v, w) are given by:

$$\bar{u} = [\sum_{i=1}^{N} (u_i \Delta t_i)] / \sum_{i=1}^{N} (\Delta t_i) \tag{1}$$

$$\overline{u'^2} = \sigma^2 = [\sum_{i=1}^{N} (u_i - \bar{u})^2 \Delta t_i] / \sum_{i=1}^{N} (\Delta t_i) \tag{2}$$

where the sums are taken over all measurements, the result u_i being associated with time Delta (t_i). In addition, the root-mean-square value and turbulence intensity can be written as,

$$(\overline{u'^2})^{1/2} = u' = \{ [\sum_{i=1}^{N} (u_i - \bar{u})^2 \Delta t_i] / \sum_{i=1}^{N} (\Delta t_i)] \}^{1/2} \tag{3}$$

$$(\overline{u'^2})^{1/2}/\bar{u} = \sigma / \{ [\sum_{i=1}^{N} (u_i \Delta t_i)] / \sum_{i=1}^{N} (\Delta t_i) \} \tag{4}$$

Similarly, the above quantities can be written for the y- and z-components of fluid velocity. Other statistical quantities of importance in the turbulent field, such as the average kinetic energy of turbulence, can be derived directly from the above equations [3].

677

Conclusions

An advanced dual-beam Bragg-diffracted two-color laser Doppler velocimeter system has been designed and developed to take simultaneous, three-component orthogonal velocity measurements and the corresponding turbulent quantities in complex three-dimensional internal and external viscous fluid flows.

Acknowledgment

References

[1] Bailey, D.A., "Study of Mean- and Turbulent-Velocity Fields in a Large-Scale Turbine-Vane," NAS3-19752, NASA-CR-3067, 1979.

[2] Nouri, J.A., et al., "Mean Velocity and Turbulence Measurements in a 90-degree Curved Duct With Thin Inlet Boundary Layer," NAS3-23278, NASA Contractor Report - 174811, NASA Lewis Research Center, 1985.

[3] Nouri, J.A., "Three-Dimensional Laser Doppler Velocimeter Studies of Flow in a 90-degree Curved Duct Having a Square Cross Section," Ph.D. Thesis, University of Tennessee Space Institute, Tullahoma, TN, 1987.

[4] Johnston, J.P. and Bradshaw, P., "Turbulence," Topics in Applied Physics, Volume 12, 1978.

[5] Kline, S.J., "Fluid Mechanics of Internal Flow," G. Sovran Edition, Elsevier, 1977.

[6] Durst, F., Melling, A. and Whitelaw, J.H., "Principles and Practices of Laser Doppler Anemometry," Academic Press, 1976.

[7] Nouri, J.A., "Two-Dimensional Laser Doppler Velocimeter Studies of a Subsonic Jet Impinging on a Flat Plate," Technical Report, University of Tennessee Space Institute, 1982.

[8] Hulst, H.C., "Light Scattering by Small Particles," Wiley, New York, 1987.

Ultrahigh–resolution, wide–field–of–view Cs optical
filter for the detection of frequency–doubled Nd lasers

T. M. Shay

New Mexico State University
Department of Electrical and Computer Engineering
Las Cruces, New Mexico 88003
(505) 646–4817

ABSTRACT

We report a simple theoretical model for the calculation of the dependence of filter quantum efficiency versus laser pump power in an atomic Cs vapor laser–excited optical filter. We present the calculations for a Cs filter transitions that can be used to detect the practial and important frequency–doubled Nd lasers. The results of these calculations show the filter's quantum efficiency versus the laser pump power. The laser pump powers required range from .7 to 15 mW per square centimeter of filter aperture.

I. INTRODUCTION

Quantum–limited, wide–field–of–view, narrow–bandwidth atomic resonance optical filters with fast temporal responses are needed as receivers for optical communications,[1] remote sensing, and laser radar.[1,2] The atomic Cs vapor laser–excited optical filters (LEOFs) are, in principle, narrow–bandwidth (0.001–nm), wide–field–of–view (2π sr), and high–quantum–efficiency filters. LEOFs offer simultaneously the resolution of a Fabry–Perot interferometer and an ideal field of view. Thus these devices are ideally suited for extracting weak narrow–bandwidth signals buried in strong nonresonant background radiation.

Narrow–bandwidth operation of an atomic vapor LEOF was demonstrated first by Gelbwachs et al.[3] and more recently by Chung and Shay.[4] LEOFs are atomic resonance optical filters that use photon absorption from the first excited state of an atom to a higher level as the signal transition. To achieve efficient and selective excitation of the Cs(6p) atoms, a narrow–bandwidth laser is used as the pump source. Fortunately, LEOFs do not require a high–power pump laser; on the contrary, reliable, efficient, low–power semiconductor lasers have been used to pump LEOFs.[4] The ability of LEOFs to be pumped by diode lasers demonstrates the practicality of these optical filters. In this paper we describe a theoretical model for the calculation of the dependence of filter quantum efficiency versus laser pump power in an atomic Cs vapor LEOF. The model is applied to Cs transition into that can be used as filters for doubled Nd in the following hosts: LNA and BEL.

II. BASIC PHYSICS

The physics of the narrow–bandwidth frequency upshifting process in the Cs LEOF is best illustrated by considering a single filter transition in Fig. 1. Ground state Cs atoms are excited to the Cs(6p) state by the absorption of diode–laser photons. The frequency upshifting occurs when the signal photons are absorbed on the (Cs $^6p^2P_{3/2}$ to $11d^2D_{3/2}$) transition at 534.2 nm. When the Cs(11d) atoms are produced, they will, in the absence of significant collisional deactivation, radiatively decay to the np levels (where $7 \le n \le 11$) by emitting infrared photons. The Cs(np) atoms, in turn, decay subsequently to the ground state and emit frequency–translated (violet) photons on the Cs(np to 6s) transitions. These violet photons are proportional to the number of signal photons absorbed and are typically wavelength shifted to the blue by more than 100 nm. Because of this large spectral shift, simple colored glass filters can effectively discriminate between upshifted signal photons and unshifted noise photons. The response time of this 534.2–nm filter is determined predominantly by the radiative lifetime of the Cs(11d) level, which has been calculated[5] to be 561 ns.

The Cs(7p – 6s) transition is one component of the upshifted (violet) photons. However, Cs(7p) atoms are produced in copious amounts via the following sequence of reactions. (We have recently measured the analogous process in Rb.[6]) First, the steady state population of Cs(6p) is high enough[7] so that a significant number of Cs(6d) atoms are produced via the reaction 1.

Reaction 1

$$Cs(6p) + Cs(6p) \longrightarrow Cs(6s) + Cs(6d).$$
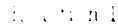
About 15%[5] of the Cs(6d) atoms decay radiatively to the Cs(7p) level. As a result this is a steady state production of photons on the Cs(7p $\longrightarrow$ 6s) 404–nm transition. If 404–nm photons are collected for our signal, this would constitute a significant steady state background noise. Therefore, the Cs(7p – 6s) radiation is not included as upshifted signal photons. By excluding this process, the noise of the LEOF can be limited by the background radiation that is within the signal bandwidth.

Table I summarizes the available filter transitions for a Cs LEOF, compatible doubled Nd lasers and the ideal cell quantum efficiencies for those transitions. Cs LEOF receivers can be designed for doubled Nd: BEL, LNA and Cr:GSGG. I have only investigated 3 of the 6 potential filter transitions because the necessary data is available only for the 3 of the transitions in Table I.

III. THEORETICAL MODEL

Again as an example, consider the 534.2 nm Cs transition. The intrinsic quantum efficiency is defined as the number of violet photons emitted per blue–green photon absorbed. In the absence of collisional deactivation of the Cs levels of interest, the intrinsic quantum efficiency for each of the violet np to 6s transitions can be calculated simply from the products of the branching ratios of the Cs(11d to np) and the respective Cs(np to 6s) transitions for ($8 \le n \le 11$).[5] The total filter quantum efficiency (5.3%) is obtained by adding the quantum efficiency of these transitions. However the Cs(11d to 6p) transition is the strongest transition out of the Cs(11d) level. In fact, there is a 55% probability that the radiative decay of the Cs(11d) atoms will occur through 534–nm photon emission. Therefore, the quantum efficiency for a green cell design can be increased by a factor of 2 if we trap the 534–nm photons inside our LEOF cell.

With clever optical and geometrical designs, the reemitted 534–nm photons can be effectively trapped inside the cell and can, for all practical purposes, be assumed to be completely converted into violet photons.

The ideal cell quantum efficiency (IQE), which includes the effects of the trapping of 534–nm photons, is given as

680

$$IQE = \frac{Total\ Quantum\ Efficiency}{1 - BR(534\ nm)} = 0.12,\tag{1}$$

where BR(534 nm) represents the branching ratio for the 534-nm transition.

Table I lists the Cs transitions and their wavelengths, identifies the doubled Nd laser that can be turned to a particular transition, and finally gives the ideal cell quantum efficiency (IQE) for each transition. The ideal cell quantum efficiencies range from 12% to 19%.

The IQE can be achieved only when (1) every signal photon incident upon the Cs cell is absorbed and (2) the violet photon emitted by a Cs atom escapes from the cell. In a practical system, neither of these conditions is strictly valid. Therefore we define a realizable quantum efficiency (RQE) that accounts for those absorption effects as

$$RQE = [1 - P(\lambda_s)] \sum_{j=1}^{5} IQE_j P(\lambda_j),\tag{2}$$

where λ_s is the incident signal wavelength, λ_j is the wavelength of violet (upshifted signal) photons that must exit the Cs cell to be detected, and $P(\lambda_s)$ and $P(\lambda_j)$ are the transmission probabilities for signal photons and violet photons, respectively. The first factor in Eq. (2) represents the probability that an incident signal photon will be absorbed in the cell, and the second term represents the probability that a violet photon escapes from the Cs cell.

Assuming that the signal photon bandwidth is much less than the absorption linewidth, Beer's law [Eq. (3)] can be used to calculate an accurate transmission probability, $P(\lambda_s)$, for the signal photons, as in

$$P(\lambda_s) = exp[-n_{6p}\,\sigma(\lambda_s)d],\tag{3}$$

where n_{6p} is the density of Cs(6p) atoms, $\sigma(\lambda_s)$ is the absorption cross section for the signal photons, and d is the average distance traveled by the signal photons in the Cs cell. Because all the Cs cell walls, except of course the entrance window, are highly reflecting at the signal wavelength, the shortest distance that a signal photon can travel and escape from the cell is twice the cell length, namely, 2L. Because the Cs(6p) level is created by the absorption of pump-laser radiation, the required laser pump power is set by defining the fixed value of the transmission probability $P(\lambda_s)$ for signal photons through the Cs cell. Thus $P(\lambda_s)$ is a design parameter for the Cs LEOF.

The probability $P(\lambda_j)$ that the violet photons, emitted on Doppler-broadened resonance lines, will escape from the Cs cell has been solved by Kopferman and Tietze.[3] Substituting their series solution for the absorption and Eq. (3) into Eq. (2), we obtain for the RQE

$$RQE = [1 - P(\lambda_s)] \sum_{j=1}^{5} IQE_j \left\{ 1 - \frac{\displaystyle\sum_{k=1}^{x} a_k (-1)^{k+1}[\sigma(\lambda_j)n_{6s}r]^k}{\displaystyle\sum_{m=0}^{x} b_m(-1)^m[\sigma(\lambda_j)n_{6s}r]^m} \right\},\tag{4}$$

$$a_k = \frac{2^{k+1} - 2}{(k+1)!(k+1)^{1/2}},\tag{5}$$

$$b_m = \frac{1}{(m+1)!(m+1)^{1/2}},\ and\tag{6}$$

where n_{6s} is the population density of ground-state Cs atoms, $\sigma(\lambda_j)$ is the absorption cross section for violet photons, and r is the radius of the Cs cell.

Finally, we need to evaluate the laser pump power required for our Cs LEOF. In our simplified model for the Cs LEOF, we make the following assumptions: (1) radiative loss processes are the dominant decay modes for excited Cs atoms, (2) the Cs cell walls have a fixed reflectivity R_p at the pump-laser wavelength, and (3) the Cs(6p) population is uniformly excited in the cell. Under those conditions, all of which are valid at the microtorr gas pressures of a Cs LEOF, we need to replace only the Cs pump photons that escape from the cell volume. Then the minimum laser pump power required for a LEOF is

$$P_L = (1 - R_p)n_{6p} L\pi r^2 hv_p A_{eff},\tag{7}$$

where $L\pi r^2$ is the cell volume, hv_p is the energy of the pump-laser photons, and A_{eff} is the effective spontaneous emission coefficient for the resonance-trapped pumped photons in the Cs cell. For a

Doppler—broadened atomic transition and a long cylindrical cell, by substituting the equation of Holstein[9,10] and Bieberman[11] and Eq. (3) into Eq. (7), we obtain the equation for the laser pump power required per unit area:

$$\frac{P_L}{\pi r^2} = \frac{(1 - R_p)h\nu_p A_{rad} \times 1.6\{-\ln[P(\lambda_0)]\}}{2\{\sigma(\lambda_p)n_{6s}r\{\pi \ln[\sigma(\lambda_p)n_{6s}r]\}^{1/2}\}\sigma(\lambda_0)},$$
(8)

where A_{rad} is the Einstein A coefficient for λ_p photons.

IV. DISCUSSION

Both Eqs. (4) and (8) depend on the $n_{6s}r$ product and are transcendental. The plot of RQE versus laser power per square centimeter of cell aperture for the Cs 534.2—nm transition is typical. Figure 2 was obtained by evaluating Eqs. (4) and (8) as $n_{6s}r$ was varied. Figures 3 and 4 are similar plots for the other transitions. The ground—state Cs atom density and cell radius product $n_{6s} \times r$ varies from 10^{10} atoms/cc to an upper limit of 10^{13}/cc. The upper limit is not set by collisions[12,13] but instead I have arbitrarily cut off the calculations at a ground state atom density, where the realizable quantum efficiency (RQE) is too low to be interesting. For a 12—in cell diameter, this corresponds to operating temperatures of between 19 and 69°C, respectively. The results of these calculations are shown in Fig. 2 through 4, where the lower vapor densities are on the left—hand side and higher vapor densities are on the right—hand side.

As we move to the left on the curve in Fig. 2 through Fig. 4, there is relatively little change in the RQE, but there is a significant reduction in the required laser pump power. The relatively slow decrease of RQE as the ground—state atom density is increased occurs because the absorption cross sections for upshifted signal photons, $\sigma(\lambda_j)$, are low enough that the escape probability for λ_j photons varies only slightly as $n_{6s}r$ is varied. However, the rapid reduction of the required pump power as $n_{6s}r$ is increased is a direct consequence of the much higher absorption cross section for pump photons. The fact that $\sigma(\lambda_p)$ is 285 times greater than the largest $\sigma(\lambda_j)$ cross section causes resonance trapping of pump photons to become significant long before there is significant self—absorption for the upshifted signal photons. A general characteristic of allowed radiative transitions is that the longer wavelength resonance transitions are stronger than the shorter wavelength resonance transitions. Therefore, for any LEOF using resonance pumping for excitation, the required pump power can be significantly reduced through resonance trapping.[14]

Table II lists the transition, the ideal cell quantum efficiency (IQE) and the 90% and 50% maximum realizable quantum efficiency (RQE) operating points. The table is presented to illustrate two potential operating conditions for a Cs LEOF. Note that at the 90% maximum RQE points the pump power required is roughly 6 mW/cm² at the 50% operating point it is roughly .8 mW/cm² for the 534 and 526—nm transitions. The 540—nm transition has its 90% and 50% maximum RQE points at 15 and 1.9 mW/cm², respectively. The higher pump power for the 540—nm transition is a direct consequence of the lower Einstein A coefficient for the 540—nm transition. This again points out explicitly the dramatic trade off of RQE versus laser pump power possible with the Cs LEOF.

In this case, a sufficient increase in $n_{6s}r$ can cause a factor—of—2 reduction in the RQE, and this simultaneously results in reducing the required laser pump power by a factor of 6. This is more than 2—orders—of—magnitude reduction of required pump power for the Cs LEOF without using resonance trapping to recycle the resonant pump radiation. Because simple, reliable, single—frequency laser diodes are commercially available from several vendors at the tens—of—milliwatt output levels, they can be used to pump high—quantum—efficiency Cs LEOFs. In fact, the use of a diode laser as a pump source will make these filters practical outside the laboratory environment. The Cs passive atomic resonance filter has a signal bandwidth of 1.5 pm, full width—at—half maximum (FWHM), however, because of the hyperfine structure of the Cs ground state there are several doppler resolved transitions. Only one of these transitions will transmit the signal but they will all transmit noise photons. Therefore, the noise bandwidth is roughly 12 pm for the passive Cs receiver. Thus for the Cs passive receiver the transmitter must be tuned to within 1.5 pm, while noise is transmitted over about 12 pm. In contrast, for the alkali LEOFs the noise and signal bandwidths are both .6 pm, because the hyperfine structure of the Cs(6p), Rb(5p), and K(4p) levels are much less than the doppler width of these transitions. Thus a Cs LEOF can offer six filter transitions for doubled Nd:lasers and has a noise bandwidth factor of 20 less than the noise bandwidth for a passive Cs filter. The ultimate sensitivity of these devices can, in principle, be as sensitive as the Cs passive atomic resonance filter.[1]

REFERENCES

1. J. A. Gelbwachs, IEEE J. Quantum Electronics, QE—24, 1266, July 1988.

2. H. Shimizu, S. A. Lee, and C. Y. She, Appl. Opt., 22, 1373, 1983.

3. J. A. Gelbwachs, C. F. Klein, and J. E. Wessel, IEEE J. Quantum Electron, QE–14, 77(1978).

4. Y. C. Chung and T. M. Shay, IEEE Journal of Quantum Electronics, QE–24, 709, May 1988.

5. A. Lingard and S. E. Nielsen, At. Data Nucl. Data Tables, 19, 533 (1977).

6. M. Allegrini, C. Gabbanini, and L. Moi, Journal Dephysique, 46, Page C1 (1985).

7. E. C. Apel, T. R. Gosnell, R. Samadani, and T. M. Shay, in the Digest of the Conference on Lasers and Electro–Optics. (Optical Society of America, Anaheim, CA, April 1988) p. 142.

8. H. Kopferman and W. Tietze, Z. Phys., 56, 604 (1929).

9. T. Holstein, Phys. Rev., 72, 1212 (1947).

10. T. Holstein, Phys. Rev., 83, 1159 (1951).

11. L. M. Bieberman, J. Exp. Theor. Phys. (USSR), 17, 416 (1947).

12. J. S. Deech, R. Luypaert, L. R. Pendill, and G. W. Series J. Phys. B, 10, L137, (1977).

13. A. C. Tam, T. Yabuzaki, S. M. Curry, M. Hou, and W. Happer, Phys. Rev., A17, The collisional deactivation rates for the Cs(11d,12d) atoms have not yet been measured but the rates in the following reference were used to estimate, 1862, (1978).

14. In spite of the strong resonance trapping, the cell can easily be uniformly excited by detuning the pump laser from line center.

TABLE I

Cs Transition	Wavelength(nm)	Compatible doubled Nd Laser	Ideal Cell Quantum Efficiency
$(6p^2P_{1/2} - 11d^2D_{3/2})$	534.2	Nd:BEL	.12
$(6p^2P_{1/2} - 12d^2D_{3/2})$	525.8	Nd:LNA	.13
$(6p^2P_{1/2} - 12s^2S_{1/2})$	540.4	Nd:LNA	.19
$(6p^2P_{3/2} - 12d^2D_{5/2,3/2})$	541.6	Nd:LNA	—
$(6p^2P_{3/2} - 13d^2D_{5/2,3/2})$	535.2	Nd:BEL	—
$(6p^2P_{1/2} - 13s^2S_{1/2})$	530.3	Nd:Cr:GSGG	—

1) Table I identifies the doubled Nd lasers that are compatible with specific Cs transitions and the ideal cell quantum efficiency for those transitions.

TABLE II

Wavelength(nm)	Ideal Cell QE	90% RQE max		50% RQE max	
		RQE	$P/\pi r^2 (mW/cm^2)$	RQE	$P/\pi r^2 (mW/cm^2)$
525.8	.13	.11	6.5	.06	0.9
540.4	.19	.15	15	.08	1.9
534.2	.12	.12	5.2	.05	0.7

2) Table II lists the transition wavelength, the ideal cell quantum efficiency (IQE) and the 90% and 50% maximum realizable quantum efficiency (RQE) operating points.

684
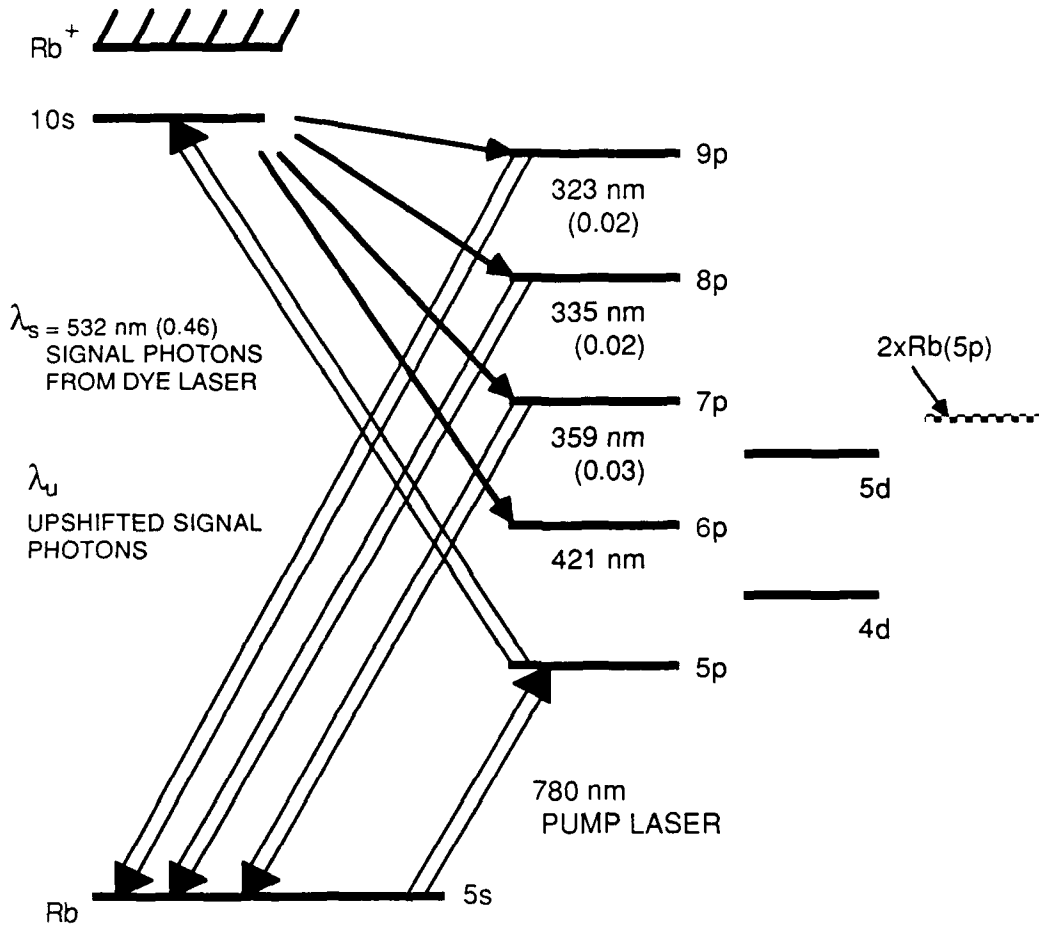
Figure 1. Partial energy diagram of Cs indicating the two dominant processes when 534—nm photons are absorbed in an actively pumped Cs. The numbers in parentheses are the quantum efficiency for generation of the associated violet photons following the absorption of a blue—green photon.
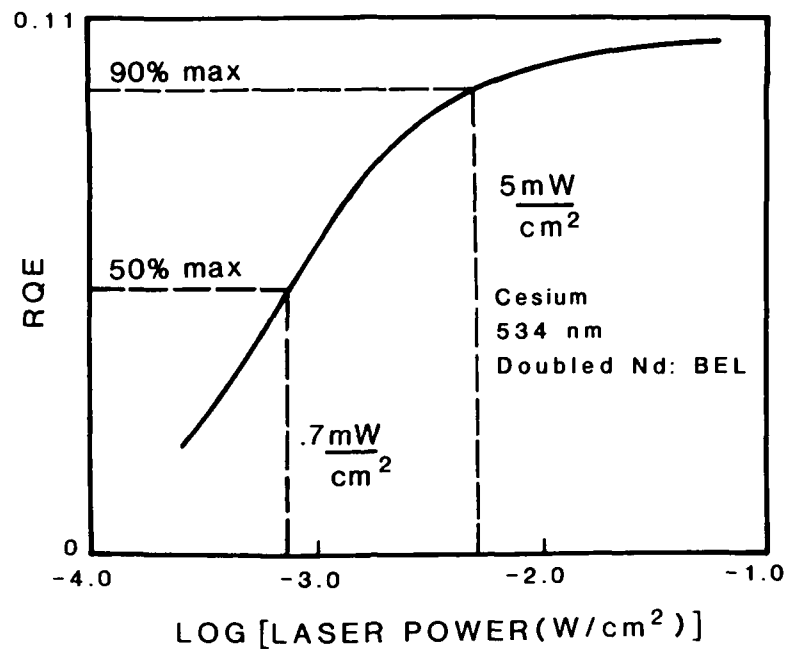
Figure 2. RQE versus laser pump power for the 534—nm transition when the cell signal transmission probability, $P(\lambda_0)$, is 0.1 and the reflectivity of the cell walls at the pump wavelength, R, is 0.98.
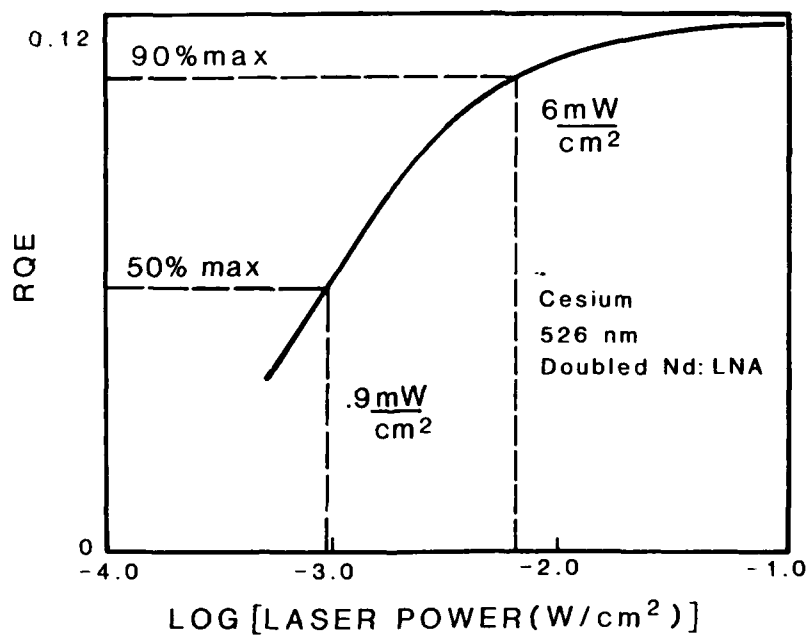
Figure 3. RQE versus laser pump power for the 526—nm transition when the cell signal transmission probability, $P(\lambda_0)$, is 0.1 and the reflectivity of the cell walls at the pump wavelength, R, is 0.98.
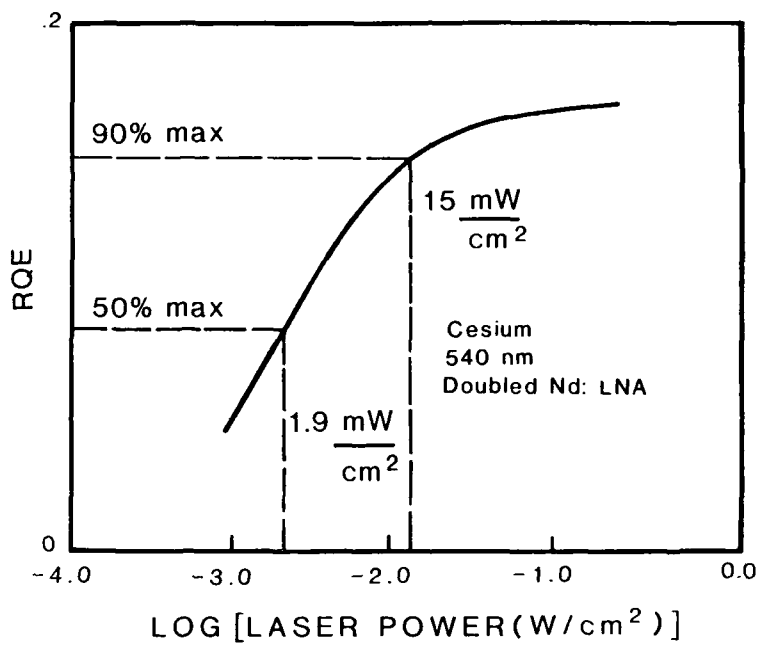
Figure 4. RQE versus laser pump power for the 540–nm transition when the cell signal transmission probability, $P(\lambda_0)$, is 0.1 and the reflectivity of the cell walls at the pump wavelength, R, is 0.98.

ELECTRICAL FEEDBACK TECHNIQUES
FOR STABILIZING HIGH POWER HeNe LASERS

Dr. Vincent P. McGinn
Associate Professor
University of Tulsa
Electrical Engineering Dept.
600 S. College Avenue
Tulsa, Oklahoma 74104-3189

Mr. Brian C. Smith
Graduate Student
University of Tulsa
Electrical Engineering Dept.
600 S. College Avenue
Tulsa, Oklahoma 74104-3189

Abstract

A light emitting diode (LED) monitors the current of a high power HeNe laser. This LED in combination with a second LED, photodiodes and operational amplifiers form a tracking loop which stabilizes the laser.

Key Terms

Feedback, Helium/Neon, Laser, Stabilization, Tracking Loop.

I. Introduction

Much interest has recently been shown in stabilizing gas discharge lasers [1,2]. The impetus for this pursuit stems from a wide variety of new and heretofore difficult scientific applications: gravity wave detection via multiple pass interferometers, high performance strap down gyroscopes, high capacity communication systems and emerging optical data processing techniques represent but a small cross section of the field. Such systems specify stringent requirements for the light source with regard to coherence (spatial and temporal), phase stability and narrowness of spectral width. Commercial manufacturers of gas discharge lasers have already demonstrated considerable effort in stabilizing their products. This is noted in the inherent mechanical integrity provided by the tube envelopes, permanent magnets distributed adjacent to the tube's longitudinal axis for unwanted (Infrared) wavelength suppression and proportional electronic feedback control for surrounding case temperature. This last method does much to thwart cavity length induced variations from ambient changes. As expected, thermal time constants are on the order of seconds. This is a consequence of the involved masses (case, heater, thermistors and laser tube) along with the thermal resistance linking components. Thus, slow variations in laser output power attributable to temperature changes may be actively minimized. A technique exhibiting faster response times has recently been reported which utilizes a servo controlled end mirror [2]. This method invokes a thermally compensated photodetector to sample the actual optical output of the laser.

With cavity, case and thermal designs addressed the remaining concern rests with the characteristics of the supporting electrical power source for the plasma. The theme of this proposal suggests that the electrical model of the laser and its power supply must be treated as an integrated electrical system. Electrical noise will manifest itself as optical noise. The D.C. power source may be modelled as a Thevenin equivalent circuit. An electrically quiet power source is mandatory. However, noise originating in the plasma may be minimized by exercising control over the Thevenin resistance of the power supply. This is achieved by electrical feedback. A novel method for monitoring the plasma current directly is offered along with the associated tracking controller. The approach can be effective over an electrical bandwidth extending from D.C. to beyond 20.0 Megahertz if the outlined precautions are addressed. Specifically, the frequency response characteristics of all components comprising the electrical feedback loop must be significantly better than the bandwidth to be controlled. Furthermore, electrical connections to the laser tube and the laser tube itself must be treated with regard to high frequency electrical performance. A high voltage vacuum tube (triode or tetrode) is located physically close to the laser tube and provides the required electrical current control as a shunt element to a high impedance power source. Proper design rules out unshielded high voltage power wire loops of any significant (2.0 cm or more) length. At frequencies of several Megahertz the inductive reactance of such "flying leads" renders the feedback ineffective.

II. Background

The subject laser for this study is the Spectra Physics Model 907. Intended for commercial applications it is similar to the more popular model 107-B2. Two units available for testing exhibited TEM_{oo} optical power outputs of 38.0 and 40.0 milliwatts when operated at rated current (11.5 milliamperes). These lasers utilize tubes which are approximately 1.0 meter in length. The surrounding case is equipped with a resistive heater. Case temperature may be accurately maintained at any temperature from 60.0 to 140.0 degrees centigrade via a second order proportional controller. Infrared suppression magnets are provided along the length of the case. Established study goals include: 1) Maintain the highest optical output power at 632.8 nanometers consistent with tube longevity, 2) Establish a beam amplitude ripple of less than 0.5 percent over the range of 40.0 Hz to 1.0 KHz, and 3) Provide a beam amplitude noise of less than 0.5 percent over the range of 10.0 Hz to 20.0 MHz. These two final specifications represent a 6.0 dB improvement over previously demonstrated performance.

III. Theory

Low frequency optical power variations and certain contributions to the finite spectral width may be regarded as "sidebands" to a mean dominant wavelength (i.e. a "carrier"). The nonlinear

electrical nature of the plasma then provides a convenient vehicle for heterodyning. Minimizing electrical current variations therefore results in a higher level of optical purity. Random current variations result in random power variations (i.e. amplitude modulation). "Pushing" refers to wavelength excursions induced by the same current fluctuations (i.e. frequency modulation). Common laboratory lasers exhibit pushing coefficients of approximately 2.6 kHz/microampere [1]. Wideband feedback techniques for the plasma address reduction of electrical current fluctuations. Once an electrical disturbance occurs, its attendant optical effects are unavoidable. Therefore, the feedback method must be envisioned as a dynamic (active) impedance control directed at minimizing current variations. These variations may originate in the power source or the laser tube itself.
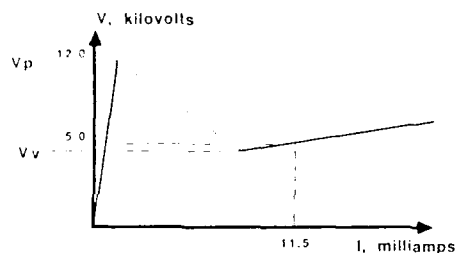
V, kilovolts

Fig. 1. Laser Characteristic.

A voltage vs. current plot of the laser tube is depicted in Fig. 1. V_p represents the striking or initial potential (typically 12.0 kilovolts). Once established, the plasma behaves approximately as a constant voltage generator. The fact that it is not an ideal voltage generator is revealed by a non-zero positive slope at and around the quiescent point (5.0 kilovolts, 11.5 milliamperes). Variations about the quiescent point on the operating curve are the undesirable noise components to be suppressed. This plot suggests an electrical model for the operating tube. Fig. 2. shows V_v as an ideal noiseless voltage generator. The positive slope is accounted for with a noiseless resistor, R. All noise components are lumped into an ideal voltage noise generator, V_N.
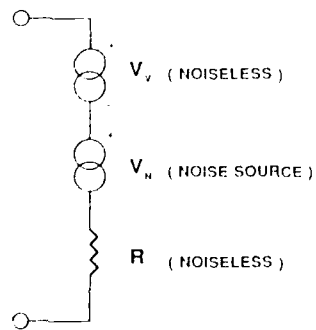
Fig. 2. Laser Input Electrical Model.

IV. Monitoring Methods

Certainly, optical power variations may be sampled with the aid of a photodetector. However, these devices provide integration over wide optical bandwidths. Therefore, bandwidth reduction from this monitor is not possible. Alternately, an optical spectrum analyzer may be configured based upon an interferometer invoking mechanically imparted doppler shifts. This is depicted in Fig. 3. The following legend is applicable: PET is a piezo electric transducer driven by function generator V_D. The transducer displaces mirror M. A second mirror M and beam splitters (B.S.) permit combining a doppler shifted beam with a sample of the main beam at photodetector (P.D.). The electrical output of this detector is a spectral representation of the optical output of the laser. It may be displayed directly on an oscilloscope with the aid of synchronization extending from V_D. These two monitoring methods are indirect (or secondary) techniques. If electrical control is to be exercised over the plasma current, a direct (or primary) parameter variations monitor is more suitable. If a light emitting diode (LED) is placed in electrical series with the laser tube (Fig. 4.), its brilliancy is a measure of the plasma current. Illumination from this LED may be optically coupled to a photodetector. Thus, the electrical signal from the photodetector is a measure of the plasma current. High intensity light emitting diodes and photodetectors are available [4] with frequency responses extending beyond 100.0 MHz. This approach to measuring plasma current inherently provides electrical isolation between the high voltage (5.0 kilovolts) power source and low level monitoring circuits.
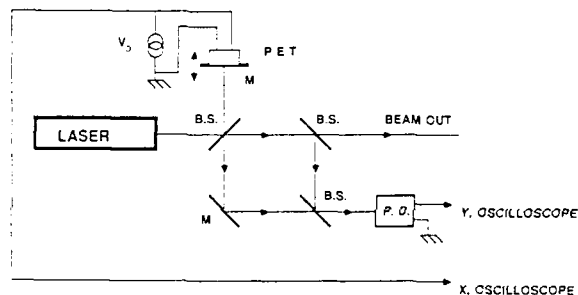
Fig. 3. Optical Spectrum Analyzer.

* SERIES LED AT LASER.
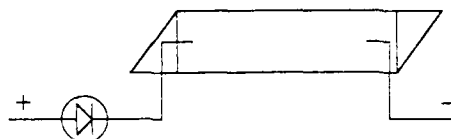
Fig. 4. Plasma Current Monitoring Method.

V. Power Sources

Commercial power supplies for gas discharge lasers include two basic designs: 1) Brute force and, 2) Switching. The brute force configuration consists of a step up transformer (for operation from the 50.0-60.0 Hz power mains), a rectifier, and a filter. Laser operating current is established with either a series ballast resistor or a current limiting impedance within the transformer itself. The switching system rectifies and filters power supplied by the mains immediately to yield low ripple direct current (D.C.). The available D.C. is used to power a high frequency (several to tens of kilohertz) oscillator. This in turn drives a high frequency step up transformer followed by a second rectifier and filter. High frequency components are made physically small and highly efficient. Both designs (brute force and switchers) require a starting circuit which initially produces a voltage impulse above the striking potential for the laser tube. Once established, the plasma is maintained at the quiescent point and the "starter" has no further function. Voltage multiplying rectifier sections are incorporated into many designs to provide the necessary high potentials.

Current regulation is usually applied on the low potential (primary) side of the step up transformer. Ferroresonance is common for stabilizing the input voltage to a brute force supply. Regulation adjustment applied to a switching power supply is a form of duty cycle control: For example, pulse width modulation (PWM, constant frequency).
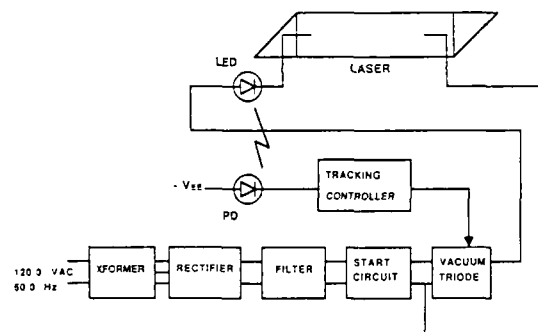
Fig. 5. Power Supply with Wideband Regulation.

The disadvantage associated with both of these low level regulation schemes manifests itself with slow (milliseconds to seconds) speed of response. Voltage step up transformers, low pass filters and current limiting devices all have extremely limited frequency responses. Thus, a high level wideband current regulation scheme is proposed (Fig. 5.). This system presumes that a voltage higher than the required laser operating potential is available and that the plasma has already been established. The output impedance of the high voltage power supply is made deliberately high with the addition of a series resistance. A vacuum tube shunting the laser thus exercises control over the plasma current. The tracking controller shown in Fig.6. provides the required interface between the aforementioned LED/photodetector combination and the high voltage vacuum tube regulator. The tracking controller actually supports two negative feedback loops. The external loop obviously adjusts plasma current. The internal loop, however, consists of a second LED/photodetector combination and transimpedance amplifier identical to the LED/photodetector and amplifier used to monitor the plasma current. The output signals of both amplifiers is compared in a third difference amplifier. The difference signal supplies current to subsequent transistor amplifier stages which control the vacuum tube grid voltage **and** the current to the second LED. Thus, the brilliancy of the second LED "follows" the brilliancy of the first LED. The known nonlinear effects of the optoelectronic components are thus minimized by this tracking and comparison action.

It must be stated that all optoelectronic devices and amplifiers must support a frequency bandwidth in excess of 100.0MHz. Many commercially available high frequency solid state amplifiers are suitable. External frequency compensation is required. With regard to high voltage vacuum tubes the situation is also encouraging. A popular Varian tetrode (4CX250B) has been tested as a suitable candidate. This device will operate up to 500.0 MHz.
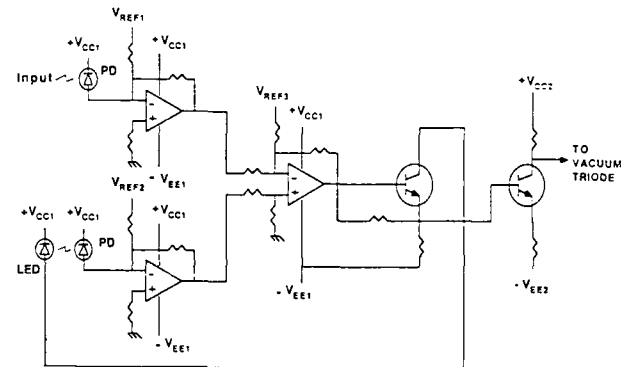
Fig. 6. Tracking Controller.

VI. High Frequency Considerations

System implementation is supported by the availability of optoelectronic devices responding to high modulation frequencies and the availability of wideband amplifiers. Therefore, overall success of performance depends on the proper interface of components. Adherence to high frequency fabrication techniques is mandatory. This includes ground plane establishment, physically short interconnections and proper placement of components. The complete system must be **colocated with the laser head itself.** Additionally, the laser tube must be electrically treated to support high frequency signals introduced on the high voltage power feed. The conductive length of the laser tube possesses considerable inductive reactance at high frequencies. This undesirable characteristic prevents efficient transmission of high frequency signals. A suggestion to remedy this effect employs a conductive sleeve around the laser tube. Such a sleeve may be formed with the external application of a chemical compound which is electrically conductive. Aquadag is a commercially available

product suitable for this purpose. The coaxial geometry established by the plasma and the sleeve constitutes an RLC transmission line. With proper termination, high frequency system performance is established.

VII. Summary

This report presents feedback control concepts and high frequency concerns as applied to stabilizing a gas discharge laser. Subsections supporting the system have been individually tested with expected results. Further study will attempt operation of the complete system. At that time overall performance will be noted, documented and reported. The authors wish to acknowledge with much appreciation support provided by Mr. Jim Nyikos. Discussions with many persons at Spectra Physics proved motivating and enlightening.

References

1.   Ch. Solomon, D. Hils and J. L. Hall, "Laser Stabilization at the Millihertz Level," JOSAB, Vol. 5, No. 8, Washington, D.C., August 1988.

2.   Bruce Peuse, "Active Stabilization of Ion Laser Resonators," Lasers and Optronics, Vol. 7, No. 11, Dover, N.J., November 1988.

3.   Ammon Yariv, Optical Electronics, 3rd Ed., Holt Rinehart and Winston, New York, N.Y., 1983.

4.   Gerd Keiser, Optical Fiber Communications, McGraw Hill, New York, N.Y., 1983.

COMBINED ELECTROOPTIC Q-SWITCH-FREQUENCY DOUBLER
FOR HIGH POWER LASERS[*]

Cs.Kuti,R.Sh.Alnayli[**],J.S.Bakos,P.Lásztity,I.Tóth,L.Vannay
Technical University of Budapest, Institute of Physics
1521 Budapest, XI.Budafoki u.8.F.I.10.

[**] on leave from Iraq for Ph.D. scholarship

Abstract

Combination of a Q-switch modulator and an optical second harmonic generator in the same crystal promises to be a useful way of laser operation with high efficiency second harmonic output. Basic e.o. problems in development of the combined Q-switched frequency doublers are presented.

1.Introduction

Optimum electrooptic cuts, i.e. crystal samples oriented to have minimum half-wave voltages, were theoretically analyzed earlier[1,2]. Recognizing that the optimum orientations of KDP (potassium dyhidrogen phosphate)-type single crystals are near to the I.type (ooe) phase-matching directions (Fig.1.) for optical second harmonic generation (SHG), the idea of combining a Q-switch modulator and an optical SHG has been emerged:

$$\varphi = 45^\circ \quad [1,2]$$
$$\vartheta_{opt} = 41.5^\circ \quad [1,2]$$
$$\vartheta_{pm} = 41.2^\circ \text{ at } 1.06 \quad [4]$$
$$V_{\frac{1}{2}} = 11.7\text{kV at } 0.63 \quad [1,2]$$
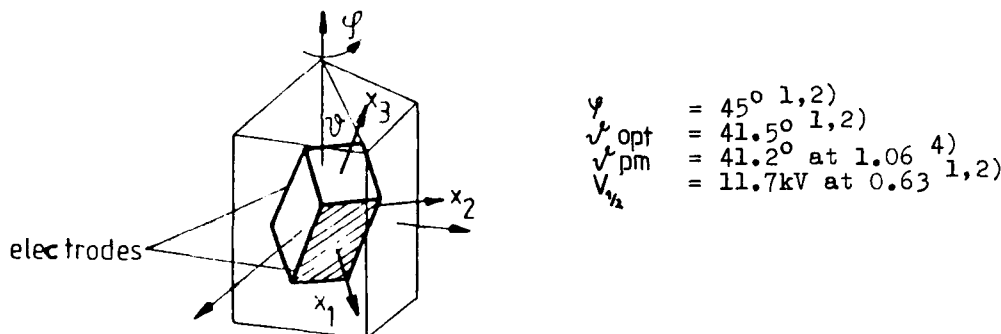
Fig.1. Orientation of optimum and SHG cuts and data for comparison.

The SHG crystal supplied with electrodes (Fig.1.) is placed in the laser cavity between a polariser and the rear mirror. The crystal is aligned for SHG direction. If a voltage of quarter-wave is applied on the crystal, the laser is closed. At desired level of population inversion the voltage is suddenly removed (switch-off operation) and development of the laser pulse starts with a simultaneous conversion of the fundamental into the SH wavelenght.

Inspite of simplicity in the principle of the combined Q-switch-SHG operation, several problems arise in practical performance of electrooptic operation and also in development, conversion and coupling out of laser pulses. Problems concerning Q-switch operation will be considered here, while the latters are to be discussed somewhere else.[3]

2.Influences of birefringence on the electrooptic operation

Unfortunately, birefringence of oblique cut KDP frequency doubler can significantly restrict the Q-switch operation. When light propagates obliquely to the optic-axis shortcomings, such as increased temperature sensitivity, decreased extinction and ray walk-off

caused by natural birefringence influence on the electrooptic operation. Since the benefit of combination of Q-switching and SHG in a single element would be conversion of laser radiation without increase of the number of the optical elements in the laser resonator it should be avoided to apply methods which use additional elements for birefringence compensation.

The following possible influences by birefringence on electrooptic operation has been considered and experimentally investigated:

- ray walk-off
- alignment of the crystal
- temporal and spatial variations of temperature
- parallelism of optical faces
- grown in birefringence nonuniformities.

3.Experiments and discussion

For considering the aspects of birefringence compensation one of our standard frequency doubling KDP cut used earlier to convert the near infrared output of a high-power Nd-glass laser to visible[4] has been examined. The experiments are performed in the common crossed polariser intensity arrangement. The incident He-Ne beam is polarised along the bisector of the X_1 and X_2 axes. The intensity of the transmitted light is measured by a photomultiplier.

Two, normalized modulator characteristics are depicted in Fig. 2. One of them is taken with the narrow, 1 mm diameter beam of a He-Ne laser. The second one (dotted line) is measured with an expanded, collimated beam filling the full aperture of the crystal. It is worth remarking the good agreement of the measured half-wave voltage with the calculated one.
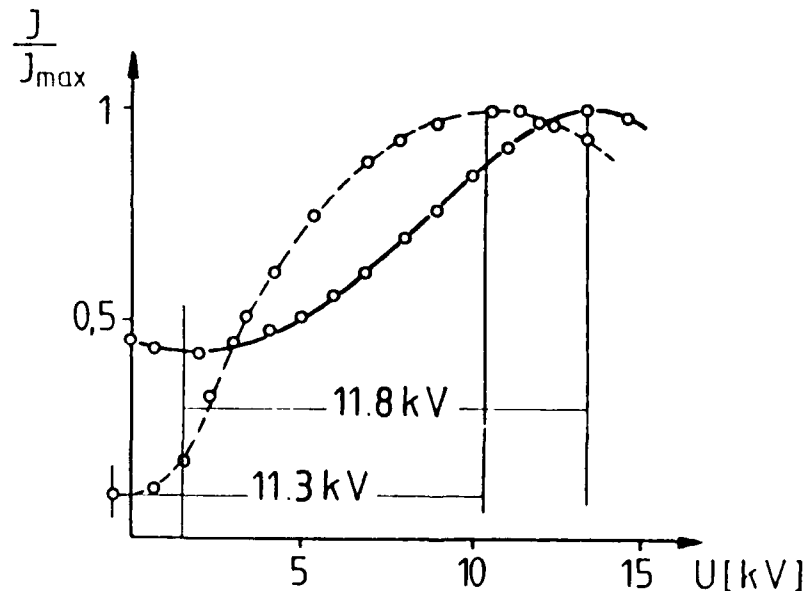
Fig.2.Normalized modulator characteristics

The influences on the electrooptic behaviour of the SHG crystal, as mentioned above, result from the fact that the light propagates along a birefringent direction.

3.1 Ray walk-off

The poor extinction with the narrow laser beam is partially due to the ray walk-off, i.e. separation of directions of the ordinary and extraordinary rays. This effect is decreased by beam expansion, when the rays can interfere because of their overlapping. This condition is usually fullfilled in modulator crystal with higher aspect ratio. Nevertheless, in the case of switch-off Q-switching operation, when the crystal is crossed twice by the light, the walk-off developed in the first pass will be automatically compensated after the refleciton on the rear mirror during the reversed crossing of the crystal.
However, it seems to be more complicated to avoid other influences of birefringence.

3.2 Alignment of crystals

The alignment of the Q-switch-frequency doubler crystal in the laser cavity is exclusively determined by the orientation condition of SHG, i.e. the light must be progagated along the phase matching direction.

3.3 Temperature and angle tuning of the electrooptic working point

Due to the birefringent SHG orientation the linearly polarised fundamental light arrives back at the polariser usually polarised elliptically, therefore the resonator will be only partially opened after switching off the closing voltage. To ensure the optimum condition for development of giant pulse we must tune the working point of the electrooptic modulator to total opening when no voltage is applied.
Retardation determining the ellipticity is expressed as

$$\Gamma = \frac{2\pi}{\lambda} \Delta n \left(\sqrt{\ell}, T \right) \cdot \ell \tag{1}$$

where ℓ and λ are the lenght of the crystal and the wavelength, respectively. The angle - and temperature -dependent effective birefringence in good approximation is given by fhe following expression where the temperature dependence is implied in the (n_e-n_o) birefringence:

$$\Delta n (\sqrt{\ell}, T) \approx (n_e-n_o) \sin^2 \sqrt{\ell} \tag{2}$$

Really, tuning the working point by slowly heating the crystal or changing the angle formed by the beam direction with the optic axis, a regular oscillation of the transmitted light intensity is observed. The period of the oscillation is estimated in the order of $1^{\circ}K$ and $0^{\circ}.1$ respectively. The observed values are in agreement with the "half-wave temperature"of $1.05^{\circ}K$ and "half-wave angle" of $0^{\circ}.032$ obtained from calculations based on temperature and angle dependence of the effective birefringence. The calculated values can be considered as upper limits under which the correct working point can be set by tuning the birefringence.

3.4 Influence of parallelism of optical faces

Inspite of expectations no significant improvement of extinction (I_{min}/I_{max}) by correct setting the working point is obtained. It is probable due to no satisfying parallelism of optical faces. In principle, from a rough estimation an extinction 1:25 requires for the dimensions of our sample a parallelism of about 10 seconds.

3.5 Effect of grown-in nonuniformities

In addition, grown-in nonuniformities of birefringence can result in further spoiling of extinction. Probably in good optical quality KDP crystals this effect can be neglected.

3.6 Temporal and spatial variation of temperature

Racalling the role of temperature the effect of stationary temperature distribution and that of the temperature fluctuations must be distinquished. Neither of them is observed in our experiments. According to the best 1:15 extinction, variations of temperature as high as $0.3^{\circ}K$ could be allowed.

4. Conclusions

Due to the oblique cut the Q-switch operation will be restricted by the natural birefringence as compared with the conventional, optic-axis cut modulators. Shortcomings by natural birefringence such as increased temperature sensitivity and spoiling of extinction could be improved by temperature stabilization, angle tuning and careful proc-

essing of the combined element.

On the other hand, explotation of the transversal driving configuration offers operation at lower voltages by elongation of the optical path.[5] However, the elongation results in increased temperature and angle sensitivity.

Referencies

1. G.E. Francois et al., Electr. Lett. 6, 778 (1970)
2. D. Kalymnios, ibid, 6, 804, (1970)
3. Kuti et al., to be published
4. A Yariv and P. Yeh, Optical Waves in Crystals, (John Wiley and Sons, New York, 1984)
5. Bakos et al., Acta Phys. Hungarica, 57, (3-4), pp.313-316, (1985)

ROLE OF PESO PROCESSES IN OPERATION OF ELECTROOPTIC DEVICES[*]

Cs. Kuti
Institute of Physics, Technical University of Budapest
1521 Budapest, Hungary

Abstract

Phenomena of Piezo-Electrically induces Strain-Optic (PESO) effects in linear electro-optic crystals are rewieved. Disturbance of PESO influences on the operation of electro-optic devices is discussed, and simple methods for suppressing these effects are demon-strated. Utilization of PESO phenomena for control of laser radiation is proposed.

1.Introduction

Piezo-Electrically induced Strain-Optic (PESO) effects can significantly influence the optical response of linear electrooptic crystals to electric fields. The way these proc-esses affect the optical response is determined by the electromechanical acoustical, and optical parameters of the crystal samples. In addition, the optical behaviour of the electrooptic devices depends sensitively on the orientation, shapes, and size of the electrooptic samples and temporal characteristics of driving signals.

Influences by the PESO-phenomena on operation of electrooptic devices may be inter-esting in two practical aspects. On the one hand, acoustic waves generated by the elec-trical driving signals can strongly disturb the electrooptic control of light via the strain-optic effect. At driving frequencies in the range of piezoelectric resonances, a regulated control is hardly possible without special preparation of the electrooptic samples[1]. Switching operation of electrooptic modulators is often limited by transient piezooptic influences[2]. On the other hand, by utilizing these effects, special low voltage modulator operating at piezoelectric resonances can be developed[3].

2.PESO influences on electrooptic operation

In the early 70's numerous reports concerning disturbing PESO influences on the opera-tion of electrooptic devices were published. Characteristic influences observed by our group in longitudinal Z-cut samples made of KDP (potassium dihydrogen phosphate) and isomorph crystals are shown in Figure 1. Figure 1.a.) shows the light transmission of a 0° Z KDP cell (dimensioned 15x15x25 mm^3 and supplied with end-plate electrodes with a 13 mm circular aperture opening) between crossed polarisers. The exposure light is from a Q-switched ruby laser with a delay of 2 microseconds after switching on the cell a driving pulse of 12 kV and 500 nsec (The photo is the 3rd frame of a "cine-film" on acoustic propagation taken in 1 microsecond steps on shot by shot basis[4]; Figure 1.b.) is the light transmission distribution along the diameter of the circular aperture detected by a linear array of silicon photodiodes[5]; Figure 1.c.)is the response

a.)   b.)   c.)   d.)
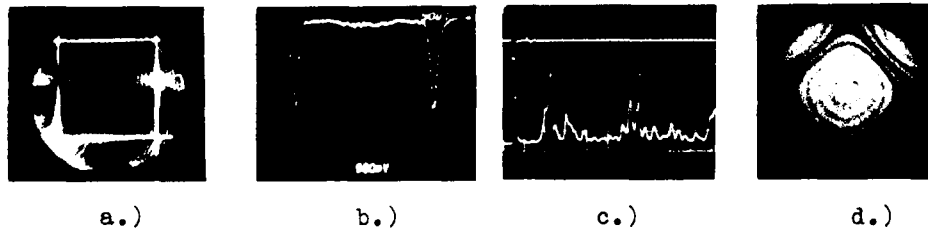
Figure 1. PESO influences in longitudinal KDP Z-samples

of a cylindrical ADP cell (diameter of 12 mm and length of 25 mm) with ring electrodes to the 12 kV, 500 nsec driving pulse. The light is a narrow (1 mm) He-Ne beam incident on the middle of the aperture[1]; Figure 1.d.) is the averaged transmission distribution due to the 1st overtone (3rd harmonics) of piezoelectric vibration of a 0° Z ADP sample[1]. (The photo was taken in an expanded He-Ne beam; it is worth to notice that the transmission of the sample of 15x15x25 mm^3 dimensions is 4-fold overdriven by the low voltage, 20 V amplitude RF signal at the 138,7 kHz resonance frequency.)

The piezoelectrically induced acoustic waves due to the strain-optic effect not only disturb, but in unfortunate situation can make impossible the normal way of electrooptic operation. Unfortunately, the best electrooptic materials, such as KDP-type crystals used to control of operation of high power solid-state lasers, $LiNbO_3$, a versatile material for electrooptic modulation in the visible and near-infrared, and CdTe, a perspectivic electrooptic material at CO_2 wavelength, are strongly piezoelectric.

The operation of electrooptic devices made of these electrooptic crystals is disturbed by the PESO effects in the time range of travelling time of acoustic waves across the crystals. The characteristic range is in the microsecond and submicrosecond order of magnitude depending on the dimensions of the modulator crystals. In frequency domain the PESO resonances are in the 0.1-10 MHz range.

3.Conventional methods for reduction of PESO influences

As a practical way to reduce the effect of acoustic waves, a mechanical clamping of the modulator crystals was very early applied[6,7]. Clamping by stiffening the crystal decreases the amplitude of acoustic generation and shifts the piezoelctric resonances to the higher frequency range. Shortcomings of induced mechanical stresses and contributed technological treatments make it inconvenient.

Other methods, such as embedding the modulator crystal in acoustically absorbing enviroment[8] or deposition of acoustically matched antireflective layers on the faces of the crystal[7] were also reported.

Instead of rectangular modulator crystals, cylindrical ones were used in longitudinal Z-cut KDP-type modulators[8]. Only moderated improvement was obtained. However, shaping the modulator crystal slightly conical and embedding it in silicon rubber bed, a fairly good suppression, in the range of lower frequencies, was achieved. Due to the cylindrical and conical shaping, excess technological treatments are required.

Trials are known, which treate the problem in the aspects of electronic driving. $LiNbO_3$ and DKDP Q-switches in voltage switch-off regime were switched to biased voltages to compensate optical bias by slowly releasing piezoelectric stresses[9]. Shaping of laser pulses with programmed driving to balance the PESO influences was also reported[10]

Limitations in time and place restrict further discussion of solutions reported so far. However, it is tought that problems on PESO influences just today often emerge. Disturbing resonances observed in the 1-10 MHz range in CdTe modulators devoted for intersatellite communication links were earlier reported[11]. According to our knowledge, a satisfactory suppression of these influences has not been solved yet[12]. Data on unsatisfactory PESO behaviour of electrooptic modulators can be found in the up to date catalogues of leading electrooptic firms as well.

Following up, methods, simple in principle and technology, will be demonstrated for reduction of PESO influences.

4.Reduction by orientation, shaping, and dimensioning

The prevention of intense acoustic generation by orientation of electrooptic samples is considered. Due to the fact that KDP longitudinal Z-cuts, independently of the orientation of their lateral faces, are electrooptically equivalent to each other, search for lateral face orientations with reduced acoustic wave generation was performed.[1] Considering that results only for 0^oZ and 45^oZ lateral face orientations are reported, the effect of the orientation of plane lateral faces on the acoustic generation has been analitically investigated.

Really, as the result of calculations shows in Figure 2., the efficiency of the acoustic generation exhibits a significant dependence on orientation. A couple of shear (T:transversal) and compression (L:longitudinal) waves is generated with displacement vectors in the XY-plane. The strain generated by unit driving voltage on a free, plane lateral face is illustrated as a function of φ, the angle formed by the X-axis and the normal of the lateral face. The direction dependence of the inverse phase velocity is also depicted.

A significant reduction is expected by change of the conventional 0° orientation of the lateral face to the 45° orientation. To demonstrate it, pulse response oscillograms are shown in Figure 3. For comparison the pulse response of the cylindrical ADP Z-cut is also depicted (To have better resolution ADP crystals of high piezoelectricity are

used: see that the PESO response of the 0° Z-cut, inspite of that amplitude of the driving pulse is under the dynamical half-wave voltage, is overdriven)
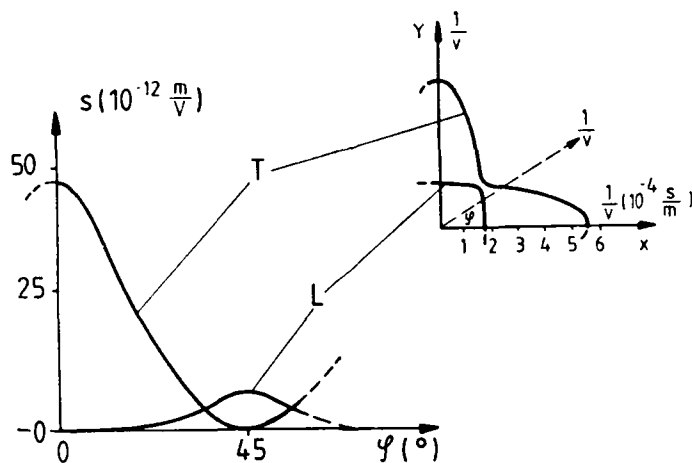
Figure 2. Orientation dependence of strain and inverse phase velocity
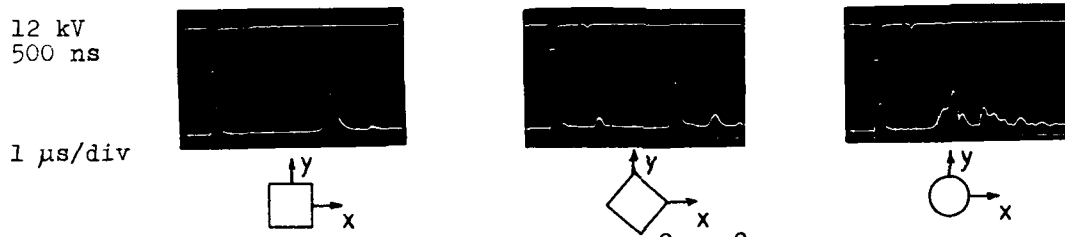
Figure 3. Pulse response of 0°, 45° and cylindrical Z-cut

At first, comparison of 2nd peaks of the 1st and the 2nd oscillograms is considered. They are PESO openings of the closed modulators due to the plane waves crossing each other in the middle of the aperture. The amplitude and delay of the PESO peaks determined from the oscillograms agree well with the analytical calculation. The physical interpretation of the lower amplitude and the earlier appearance of the PESO peak in the case of 45° orientation is reasonable: 45° compression waves are of lower amplitude and higher velocity than 0° ones owing to higher resistance of the crystal against compression. The 3rd oscillogram taken with the cylindrical crystal of Figure 1.c.) demonstrates a moderated reduction of amplitude and a broadening the PESO peak as it can be concluded from the orientation dependence.

The fairly high 3rd opening and the small amplitude 4th one of the 45° response have been experimentally identified as the effects of two-dimensional shear waves generated in the edge region of the lateral faces. The waves causing the 4th peak must be pure shear waves generated just on the edges, according to their travelling time. The high amplitude acoustic waves giving rise to the 3rd peak and rather spoiling the improvement expected, seem to be generated in narrow, near edge regions. The assumption is confirmed by the oscillograms shown in Figure 4. taken with a sample of 15mm x 25mm rectangular aperture instead of the 20 mm x 20mm square cross sections of the 0° and 45° samples. The effect of the near-edge waves is separated into two weaker peak.

Further improvement can be achieved by inclination of the laterral faces to the Z-axis when the length of overlapping of the acoustic waves along the optical path will decrease. In such a way distribution of the PESO effect of obliquely propagating acoustic waves can be ensured as it can be seen in the last photo of Figure 4.

Similar or higher degree of reduction is observed in the case of periodical driving. Only by orientation, shaping, and dimensioning, improvement more than two order of magnitude can be achieved.
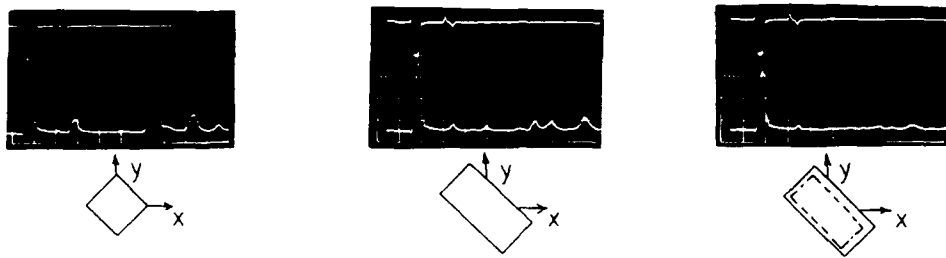
Figure 4. Separation of the effect of edge waves

5. Multi-element modulators with distributed PESO influences

An universal method for reduction of PESO influences on operation of modulators consisted of two or more electrooptical elements has been developed[13]. In contrary with conventional multi-element electrooptic modulator constructions, used often to decrease driving voltage or compensate birefringence, when identical electrooptic crystal samples are applied, the modulating elements must construct to be different in their PESO response.

Simplicity of the method can be easily demonstrated in the frequency domain. The modulator crystals are optically arranged seriesly, but electrically are connected parallel. The required driving voltage will be proportional inversely to the number of modulator crystals because of summation of the electrooptic effects, i.e. phase shift or retardation. Preserving the identical electrooptic behaviour of the modulator crystals, the dimensions determining the piezoelectric resonance vibrations are varied to detune gradually the piezoelectric resonances of the individual modulator crystals. Whereas, the direct electrooptic effect of the individual modulator crystals is summed up, the PESO contributions are distributed over a broad frequency range with amplitudes inversely proportional to the number of modulator cells owing to the decreased driving voltage.

Influence of PESO transients generated in electrooptic shutter operation similarly can be distributed over the aperture by proper dimensioning the transverse (aperture) sizes of the individual electrooptic elements. The more the number of the elements, the higher the reduction will be.

6. On possible role of PESO phenomena in control of laser radiation

The possibility of low voltage light modulation with PESO modulators working at piezoelectric resonances was very early recognized. Since the beginning of systematic search for laser radiation control devices, a respectable number of reports on different PESO devices has been published.[3]

Inspite of the benefit of low voltage modulation and simple construction, PESO devices are hardly applied in laser technique. Pobable it is due to modulation of narrow bandwith at discrete frequencies, nonuniform transmission owing to the resonance patterns of standing wave vibrations and also the moderated efficiency of generation of higher frequency vibrations.

However, it is believed that there are regimes of laser control where PESO devices could be applied. A comprehensive survey of earlier experiences and recent attempts to exploit the benefits of PESO phenomena in control of laser radiation are to be published.

References

1. Cs.Kuti, Thesis, Hung.Ac.Sci., Budapest, 1984
2. J.S.Bakos, Zs.Sörlei, Cs.Kuti, S.Szikora, Appl.Phys., 19, 59, 1979
3. V.B.Baglikov, V.H.Parigin, Vest.Mosc.Univ., 1967(5), 118, 1967
   R.Weil, D.Halido, J.Appl.Phys., 45, 2258, 1974
   H.Ben-Yosef and G.Sirat, Optica Acta, 29, 419, 1982
   P.Kálmán and A.Tóth, Ferroelectrics, 75, 169, 1987
4. J.S.Bakos et al, Acta Phys.Hung., 46, 203, 1979
5. J.S.Bakos et al, SPIE, 236, 404, 1980

6. E.A.Ohm, US Patent 3,354,325, 1969
7. J.Bousky, US Patent 3,572,897. 1971
8. T.A.Kuzovkova et al, Opt.Mech.Prom. 44,57, 1977
9. R.P.Hilberg, W.R.Hook, Appl.Opt., 9, 1939, 1970
10. E.R.Koecher, R.P.Novak, J.Phys.E 13,542, 1980
11. A.Bonek at el, Proc.LASERS,81 p144, 1981
12. private comm. by one of the authors of ref.11
13. Cs.Huti et al, US Patent, 4,735,490, 1988

NEAR OPTIMUM RECEIVER DESIGN FOR ASK-COHERENT COMMUNICATION SYSTEMS

I.F.K. AL-RAMLI
CIMARRON LIMITED
P.O. BOX 268
LONDON
SW15 3SX

ABSTRACT

Optimum filter, decision threshold and local oscillator power for binary ASK-coherent optical receiver have been obtained using calculus of variation. The optimisation is to minimise the probability of error (Pe) in the presence of laser phase noise (LPN), shot noise, ISI, dark current and coloured Gaussian thermal noise.

1 - INTRODUCTION

Generally coherent optical communication systems are very sensitive to the laser phase noise of the transmitting and local lasers. It has been experimentally demonstrated that an optical heterodyne ASK system can tolerate a relatively large phase noise varaince within the transmitter and local oscillator [1]. However, as the optical source power is very small (of order of a mW), the received power available for detection purpose will be quite small. The detection process is accompanied by various types of impairments, this fact necessitates a very careful design of the receiver for ASK-optical heterodyne communication system.

To accomplish the receiver optimisation, the laser phase noise has been assumed to have a zero-mean Gaussain probability density function of variance V_O^2 .

This paper gives a systematic approach for the design of a near optimum digital receiver for optical heterodyne ASK signalling scheme. This receiver is near optimum in the sense that it provides a performance of lowest Pe.

2 - RECEIVER ANALYSIS AND THE PROBABILITY OF ERROR

We assume a receiver model of the form in figure (1).
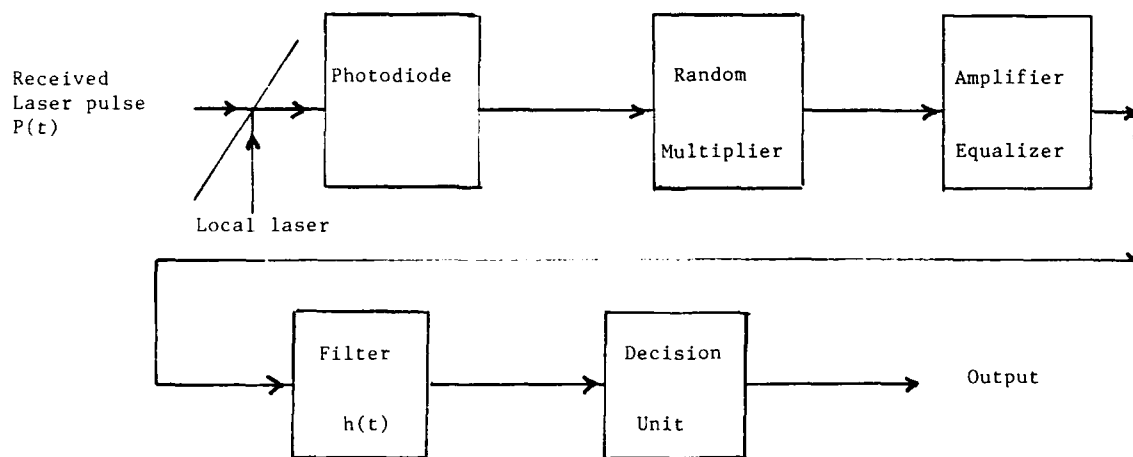
Figure 1. Laser receiver model

The optical pulses are detected and the decision unit samples the filter's output every T second to determine the a_is values, deciding upon a_i "1" or "0" in accordance with the sampled value being above or below the threshold F. The signal processing involves some errors caused by: (1) laser phase noise; (2) shot noise; (3) photodiode multiplication noise; (4) ISI and (5) thermal noise. In the model of figure (1), the input to the decision device is due to the sum of independent contributions from the signal optical power and various noise components in such optical receiver. At the receiver end the rate of signal photon

arrival is

$$Y_t(t) = (P_s/h\upsilon) \sum_{-\infty}^{+\infty} a_i P(t-iT) \quad \dots\dots\dots\dots\dots\dots\dots\dots \quad (1)$$

where a_i is the received pulse amplitude, which has one of the binary values (1,0). $P(t)$ is the received optical pulse shape. $h\upsilon$ is the photon energy. T is the pulse duration.

When the local laser is cw running and fairly stable in its output power P_L, the rate of photoelectron generation from the photodiode (with wide bandwidth) is given by:

$$Y_r(t) = (nG/h\upsilon_{1F}) \ (2P_S P_L)^{\frac{1}{2}} \cos\varrho \sum_{-\infty}^{+\infty} a_1 P(t-iT) \quad \dots\dots\dots\dots\dots \quad (2)$$

G is the average avalanche gain (in case of PIN-photodiode G=1), n is the detector quantum efficiency and

$$\varrho = w_{1F} \ t + \alpha \quad \dots\dots\dots\dots\dots\dots\dots\dots \quad (3)$$

w_{1F} is the frequency difference between the local laser (LO) output and the received signal photon frequency. α accounts for any phase mismatch due to the phase noise at the mixing surface between the LO and the coming optical signal. P_s is the received optical power.

The wanted signal component $Y_s(t)$ at the input of the decision unit is given as follows:

$$Y_S(t) = (nG/h\upsilon) \ (2P_S P_L)^{\frac{1}{2}} \cos\varrho \sum_{-\infty}^{+\infty} a_i P(t-iT)*h(t) \quad \dots\dots\dots\dots \quad (4)$$

* stands for convolution and $h(t)$ is the filter impulse response. The total noise variance of both states (ON (1) and OFF (0) are [2]

$$V^2_o = V^2_{os} + V^2_L + V^2_d + V^2_{th} \quad \dots\dots\dots\dots\text{for OFF-state}$$

$$\dots\dots\dots\dots\dots \quad (5)$$

$$V^2_1 = V^2_{1s} + V^2_L + V^2_d + V^2_{th} \quad \dots\dots\dots\dots\text{for ON-state}$$

where V^2_{1s} is the signal shot noise variance and given as:

$$V^2_{Is} = 2DP_S \ G^{2+x} B \int Y_t(t) \ h^2(t-\tau) \ dt \quad \dots\dots\dots\dots\dots\dots \quad (6)$$

(all integration signs are understood to have $-\infty$ to $+\infty$ limits) where $D=(n/h\upsilon)$ and $B=1/T$.

The local laser shot noise variance is:

$$V^2_L = 2DP_L \ G^{2+x} B \int h^2(t) \ dt \quad \dots\dots\dots\dots\dots\dots \quad (7)$$

The shot noise due to the multiplied dark current is given by following:

$$V^2_d = 2DP_d \ G^{2+x} B \int h^2(t) \ dt \quad \dots\dots\dots\dots\dots\dots \quad (8)$$

where P_d is the equivalent power due to the dark current.

The coloured zero-mean Gaussian thermal noise has a variance

$$V^2_{th} = N_o B \int (h^2(t) + (h^2(t) / W^2_o)) \ dt \quad \dots\dots\dots\dots\dots \quad (9)$$

where N_o and W^2_o are some parameters related to the type of preamplifier.

When the laser phase noise is considered as an independent source of noise and has a zero-mean Gaussian pdf [3] then the average Pe will be:

$$Pe = (P_1/2) \ \text{erfc} \ [(Y_1 - F)/(2(V_1^2 + V_\varphi^2 \ Y_1^2))^{1/2}]$$

$$+ (P_0/2) \ \text{erfc} \ [(F - Y_0)/(2(V_0^2 + V_\varphi^2 \ Y_0^2))^{1/2} \ ] \ \dots\dots\dots\dots \ (10)$$

where P_j is the probability of sending $j=(1,0)$. In the above equation obviously there is no possiblity to eliminate completely the effect of LPN by increasing the optical power. However, it would be possible to mitigate this effect by the proper choice of the extinction ratio.

3 - RECEIVER OPTIMISATION

According to equation (10) Pe is a function of the decision threshold F_0 local laser power P_L and a functional of the filter impulse response h(t). The optimum receiver will now be defined by minimising Pe relative to these parameters.

3-1 Optimum Threshold

The optimum threshold F_0 will minimise Pe such that:

$$- \frac{(Y_1 - F_0)^2}{(V_1^2 + V_\varphi^2 \ Y_1^2)} + \frac{(F_0 - Y_0)^2}{(V_0^2 + V_\varphi^2 Y_0^2)} = \ln \left[\frac{(V_1^2 + V_\varphi^2 \ Y_1^2)^{1/2} \ P_0}{(V_0^2 + V_\varphi^2 \ Y_0^2)^{1/2} \ P_1} \right] \ \dots\dots\dots\dots \ (11)$$

When best sensitivity to be achieved the shot noise due to the local laser illumination should dominate over all other source of noise. This implies

$$V_1 \approx V_0 \approx V_L \quad \text{and} \quad V_L \gg V_\varphi \ Y_1 \ , \ V_\varphi \ Y_0$$

then,

$$F_0 = (Y_1 + Y_0) \ / \ 2 \quad \text{if } P_0 = P_1 \qquad \dots\dots\dots\dots\dots\dots\dots\dots\dots\dots\dots\dots \ (12)$$

In a similar way we can deduce the condition for optimum local laser power:

$$Y_1 - \frac{(V_L^2 + V_\varphi^2 \ Y_1^2)}{(V_1^2 + V_\varphi^2 \ Y_1^2)} \ (Y_1 - F) \ \ P_0 = Y_0 - \frac{(V_L^2 + V_\varphi^2 \ Y_0^2)}{(V_0^2 + V_\varphi^2 \ Y_0^2)} \ (F - Y_0) \ \ P_1 \quad (12)a$$

3-2 Optimum Filter

If an optimum threshold and optimum P_L are chosen the Pe depends only on h(t). Pe is then a functional of h(t) and variational calculus technique can be used to find optimum filter. We obtain the differential equations:

$$[((a_1 + a_o)V_\omega^2 - (a_1 - a_o)/ \ rR/\overline{2} \ ) P(t) - 2V_\omega^2 I] \ G \ (2P_sP_L)^{1/2}$$

$$+ ((a_1 + a_o) \ P_sP(t) + 2P_s I + 2P_L + 2P_d + (N_o/DG^{x+2}))SG^{x+2} h(t)$$

$$= 2(N_o/D \ W_o^2) \ h''(t) \quad \dots\dots\dots\dots\dots\dots\dots\dots\dots\dots\dots\dots\dots \quad (13)$$

where $I = \sum\limits_{-\infty}^{+\infty} a_i \ P(t-iT)$

The numerical solution of equation (13) $h_o(t)$ represents the near optimum filter impulse response $h_o(t)$ is the function that minimises the Pe in (10). In order to find such a solution we need a prior knowledge of $(Y_1 - F)/(V_1^2 + V_\omega^2 \ Y_1^2)^{1/2}$, $(F - Y_o)/(V_o^2 + V_\omega^2 \ Y_o^2)^{1/2}$, $V_1/(V_1^2 + V_\omega^2 Y_1^2)^{1/2}$ and $V_o/(V_o^2 + V_\omega^2 \ Y_o^2)^{1/2}$.

However, the first pair of parameters can be considered as the degree of performance and could be setted to equal R. While the second pair of parameters represents the degree of laser phase noise contribution and could be setted to equal to some other contrast r.

Equation (13) includes all the important factors that effect the performance of optical ASK-coherent receiver system, namely: laser phase noise, quantum noise, multiplication noise, dark current, coloured Gaussian thermal and itersymbol interference. Since P(t) represents the received optical pulse shape, so the effect of the propagation channel (optical fiber or air) may be included by convolving the transmitted laser pulse shape with the impulse response of the propagation channel.

4 - PRELIMINARY RESULTS

When we consider a relatively practical case in which (1) $W_o^2 \longrightarrow \infty$ i.e. when the Gaussian thermal noise is a white noise and (2) there is a local laser shot noise domination. Thus, $h_o(t)$ can be obtained analytically as follows:

$$h_o(t) = \frac{((\ (a_1 - a_o)/ \ /\overline{2} \ Rr - (a_1 + a_o) \ V_\varphi^2) P(t) - 2V_\varphi^2 I)}{((a_1 + a_o) \ P_sP(t) + 2P_sI + 2P_L + 2P_d + N_o/DG^{+x2})} \ \frac{(2P_sP_L)^{1/2}}{(DG^{x+2})} \quad (14)$$

This includes all impairments mentioned above.

5 - CONCLUDING REMARKS

The Pe minimisation has been applied to optical receiver optimisation, accomodating all important noise sources encountered in optical ASK-coherent communication system. A general filter-design differential equation has been derived, its solution corresponds to the near optimum receiver filter. The technique has been applied to receiver for paractical case, for which an analytical solution has been deduced.

6 - REFERENCES

[1] J. Franz, and U. Helnerus, "Calculation of Bit Error Rate in ASK Heterodyne Systems With Envelope detection influenced by Laser Phase Noise", Elect. Letters, Vol.22, No.20, (1986), pp1072-1073.

[2] T/ Okoshi, K. Emura, K. Kikuchi and R. Th. Kersten, "Computation of Bit Error Rate of Various Heterodyne and Coherent Type Optical Communication Scheme", J. Opt. Commun. 2(1981)3, pp89-96.

[3] J. Franz, "Evaluation of the Prabability Density Function and Bit Error Rate in Coherent Optical Transmission Systems Including Laser Phase Noise and Additive Gaussian Noise", J. Opt. Commun., 6 (1985) 2, pp51-57.

LASER SAFETY SCHEMES - A USERS VIEWPOINT

J.A. FOLKES, J. TYRER, A.M. BANDLE*
Department of Mechanical Engineering
Loughborough University of Technology
Loughborough,
Leicestershire,
England, LE113TU.
* Health and Safety Executive, Liverpool, England.

Abstract

Advances in Practical Laser Safety have not kept up with advances in laser technology. This paper studies some of these areas such as degradation products, reflected or scattered radiation, radiation measurement and formal risk assessment (including the determination of nominal hazard distances/zones, NHD/NHZ's) in order to establish laser safety schemes.

Introduction

The expansion of lasers into industry is usually accompanied by grave concern regarding the safety aspects of such systems. In fact, a potential customer is often detered from using laser technology because of the complications and difficulties such new technology may bring. Laser safety standards[1-3] form a sound basis from which the relevant precautions may be taken. However, they are not readily understandable or "user friendly". They also do not fully cover the areas that may be of interest to the potential customer or laser user. The purpose of this work is to look, from a user's viewpoint, into some of these areas with a view to compiling practical laser safety schemes. Particular reference is made to the problems associated with the two common high power industrial lasers, the Neodymium YAG (Nd:YAG) and Carbon Dioxide (CO_2) lasers.

Laser Safety

The primary problem the laser user is faced with once the installation, operation and production aspects are overcome is how to ensure continued safety in normal use, day to day maintenance and, as appropriate, any on site servicing of the laser product. In order to satisfy the requirements stated in the national safety standard[1-3] the user will need to become familiar with:

a.   How the standard applies to the specific laser chosen.
b.   How the standard applies to the system being used.
c.   How the standard affects the environment the laser system is placed in.

The laser manufacturer usually supplies support information detailing laser classification and hazard assessment. Laser safety is not particularly well supported in journals, Suitable references for practical aspects include[4-6], with text books on the subject[7-9]. Several organisations now operate laser safety courses[10-12] and there is at least one commercial laser safety computer programme in existance[13]. However, some of the practical problems a potential laser user faces may not be addressed. For example:

Question:

    What are the requirement measurements?
    What is required to make the measurements?
    What measurements must be made to fully evaluate the hazard
    potential?
    Are there any by-products or degradation products which need
    assessing?
    What auxillary protection or housings are necessary?
    What material should be used for a protective housing?
    What is the nominal hazard zone/distance?

Five separate topics are addressed in an attempt to answer some of these queries.

1. Measurement

Instrumentation is necessary to measure laser power or energy if comparison to the laser safety standards is required. To the scientific community such instrumentation is commonplace and selection of instrumentation with the prefered or desirable requirements is not a problem. However, the newcomer or industrial laser user, is overwhelmed, firstly by the range of instrumentation (Figure 1) and secondly by the actual method of measurement to be in accordance with the laser safety standards.[1-3] To assist the choice, the user commonly needs to know what laser power or energy is emitted and occasionally requires details such as the mode structure of the beam or its alignment (particularly with high power CO_2 material processing lasers). The user must select the instrumentation which measures the right wavelength, power and/or energy, can withstand the required maximum power density and is of a suitable ergonomic design.[14,15,16] Having made this choice the meter must then be used to measure the laser radiation. The American Standard[1] explains that measurements should only be attempted by trained or experienced personnel and puts the onus on the laser classification scheme to minimise the need for laser measurements and calculations by the user. However, if measurement is necessary (for example, to calculate

Figure 1   Illustration of some of the wide range of instrumentation available for measuring laser power or energy

hazard distances or zones for a system) the laser should be "adjusted to the maximum output for the intended use". This means that in no circumstances will the output exceed this maximum level even if any mirrors are knocked or switches altered. A differentiation is also made between "intrabeam" viewing (where the eye is exposed to all or part of a laser beam) and "extended source" viewing (radiation that can be resolved by the eye into a geometrical image) in the 0.4 to 1.4 µm wavelength region, in most cases the "irradiance" is measured (in W/cm^2). Complication is introduced because a "limiting aperture" is required. This is the circular area over which irradiance (or radiant exposure) measurements should be made. The measurement is then made with instruments that average over circular areas defined by the "effective limiting aperture". This diameter is usually a 1 mm aperture for CO_2 lasers when viewed by the eye directly. This is a small enough aperture to detect "hot spots" in the beam. The beam at this wavelength is not focusable onto the retina (sensitive part of the eye). Similarly a 7 mm diameter aperture for visible and near infra red lasers (0.4 to 1.4 µm) is used. There is an increase in irradiance from the cornea (outer part of the eye) to the retina. This corresponds approximately to the ratio of the pupil area to that of the retinal image. This increase arises because at these wavelengths radiation which enters the pupil is focussed to a "point" image on the retina. The pupil is a variable aperture, however a 7mm diameter pupil is usually considered as a "limiting aperture" as this is a worst case condition. 7mm is derived from figures obtained from young eyes where diameters of this order have

706

been measured. Larger apertures must be used if the output is intended to be viewed with optical instruments, excluding eye glass lenses. Smaller diameter apertures may also be used provided correction factors are applied to ensure the required accuracy of measurement. If the entire beam enters the aperture no correction for beam size or "homogeneity" is necessary. For large beams the cross section should be sampled to obtain the maximum reading. Figure 2 shows the arrangement used for measurement for the purpose of laser classification. For extended sources in the 0.4 to 1.4 μm region the radiance may be measured. Care must be taken to ensure that the appropriate aperture and "solid angle of acceptance" (or conical field of view) is used.
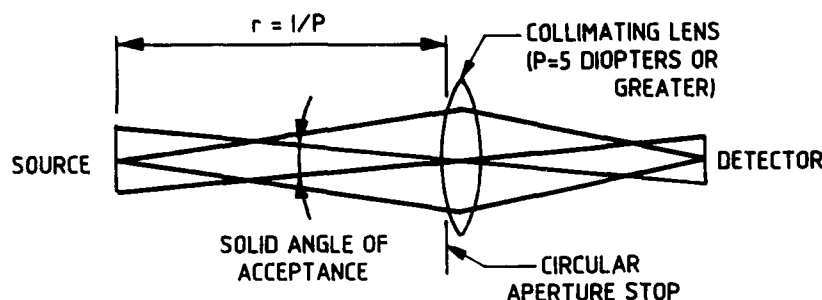
Fig. 2. Arrangement used for measurement for laser classification purposes.

From this information the user can identify the requisite measurements and methods necessary. However, it is not difficult to appreciate that the newcomer may be overwhelmed by the technicalities and phrases used. It is also difficult to know how these measurements apply in the particular installation or application. If the correct measurement procedure is followed then the laser power or irradiance will be measured in accordance with the relevant laser safety standard. This value may not be the same as specified by the laser manufacturer, but it will be the value required for any hazard calculations (section 3).

To summarise the user needs to:

1. Check the laser is at maximum output for the intended use.
2. Verify if the condition is intrabeam viewing or extended source viewing (1,5) if the laser emits in the 0.4 to 1.4 μm wavelength region.
3. Use the appropriate limiting aperture (Table 1).
4. Check that the instrument averages the measurement over the area of this aperture.
5. Check that the whole beam enters the aperture, if not, then the area of the beam that gives the maximum reading must be measured.

Other factors need to be checked about the instrumentation:

1. The instrumentation must be calibrated sufficiently well, ideally to permit overall measurement accuracies of ±20% wherever possible.
2. The instrumentation must be suitable for, and calibrated to the right wavelength.
3. The detector must be perpendicular to the beam when measuring.
4. The instrument must average the measurement over the whole of the circular area defined by the appropriate aperture used.

Maximum Aperture Diameters (Limiting Aperture) for Measurement Averaging					
		Wavelength Range			
Measurement	Exposure Duration, t (s)	Ultraviolet (0.2 to 0.4μm)	Visible and Near Infrared (0.4 to 1.4μm)	Medium and Far Infrared (1.4 to 10^1μm)	Submillimeter (0.1 to 1 mm)
Eye MPE	10^2 to 3×10^4	1 mm	7 mm	1 mm	11 mm
Skin MPE	10^2 to 3×10^4	1 mm	1 mm	1 mm	11 mm
Laser Classification	10^2 to 3×10^4	50 mm	50 mm	50 mm	50 mm

Table. 1. Selecting the appropriate limiting aperture

APPLICABLE TO THE AMERICAN NATIONAL STANDARD (1.)

2. Reflected/Scattered Radiation

There are many situations where reflected or scattered radiation presents a serious hazard. The design of protective enclosures for material processing applications using

either Nd:YAG or CO_2 lasers is of paramount importance. In 1983, Rockwell R J and Moss C E (17) reported that during Nd:YAG laser welding (after the welding event was initiated) the radiation levels measured were a function of the base material, direction of travel, distance and angle of detection, and laser power. Rockwell et al did not measure the peak levels produced during the laser welding event. These values would be higher and would be produced just on the onset of laser welding (Figure 3). The levels of the radiation measured were dependant upon the direction of the weld. The radiation levels were 25% higher when the metal was moving towards the worker. The highest irradiance level measured at 1m in the work was 10.6 mW/cm^2. Rockwell demonstrated that for typical Nd:YAG welding values (the reflectivity, p = 0.8, Power = 300W and a viewing angle of 45°) the scatter at a 'istance of 1m is approximately 3.2 mW/cm^2 (both experimentally and theoretically). The skin Maximum Permissible Exposure (M.P.E.) is 10^3 mW/cm^2 for long term exposure at a wavelength of 1.06 .m. The hazard distance may then be calculated to be 5.7 cm. For the eye the M.P.E. is 0.22 mW/cm^2 which gives a much larger hazard distance of 3.8m. The work therefore concludes that whilst radiation emissions from the plasma and molten metal does not warrant major concern, workers must use the appropriate safety protective eyewear.(1,8,17,18) The skin hazard is usually much lower. This is aided by the user often being sited at the operating console which is commonly over 1m away from the machinery area. However, there have been occasions when the operator has been exposed to significant levels of radiation, despite Rockwells findings. In welding the levels are dependant upon the weld geometry and configuration. Burns have also been caused by metal shapes falling through the defocussed beam after the shapes have been cut, and also from materials with irregular surface geometry.(19) The concept of a Nominal Hazard Zone (NHZ), or distance (NHD) helps with the visualisation of the extent of the hazard with respect to a laser. However, some materials are more reflective at a given wavelength, than other materials. The surface finish or coating of a material also has an effect on this reflectivity. The degree of risk is therefore dependant upon the material used. Figure 4(a) shows the theoretical reflectivity of different metals to a CO_2 laser (wavelength 10.6 .m).(20) Figure 4(b) shows the materials in order of highest to lowest risk, based on experimental data.
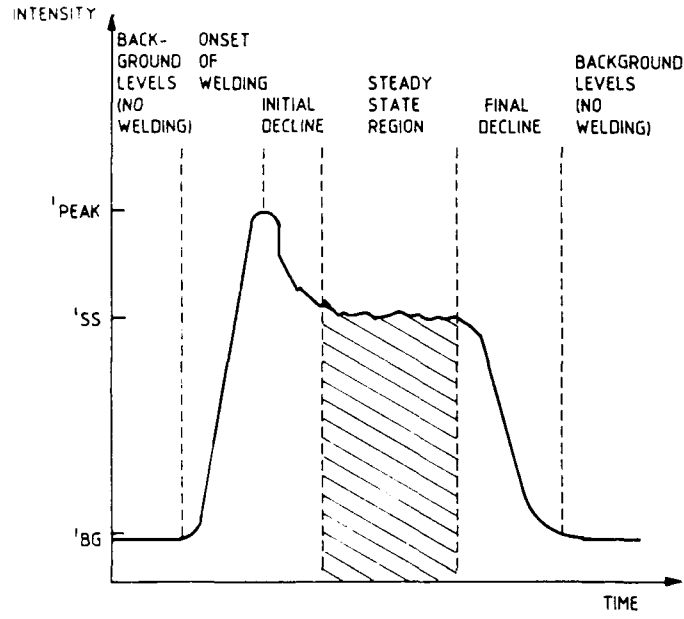
Fig. 3. Distribution of optical radiation (variation of intensity with time) produced from a typical laser welding event (17).

As the temperature increases the reflectivity of the material generally decreases, so once a cut or process is initiated then the hazard decreases. This is until the cut material drops away from the workpiece. Then there is the possibility of the material passing through the beam to give a stray reflection, if the laser is still switched on, as the piece falls.

Since an enclosure is usually necessary for material processing lasers to protect against stray reflections the enclosure material must be resistant enough to withstand the laser beam. For CO_2 lasers, polycarbonate is recommended as a clear enclosure material.(6) Polycarbonate has its limitations but is generally more resistant than materials such as acrylic for this purpose. For Nd:YAG lasers expensive plastic or glass materials which often incorporate filter or doping materials may be purchased (e.g. the Schott Glass KG3 or KG5) to serve as window materials usually in a metal housing. The selection of appropriate eyewear is also important to the user, however, there is adequate documentation elsewhere, regarding the suitable choice(1,7,8,18,21,22) and explanation of such terms as "optical density".

708

Material	*Reflectivity(%)	
	CO_2	Nd:YAG
1% Carbon Steel	95%	63%
(Polished) Stainless Steel	63%	53%
(Black Oxide) Stainless Steel	25%	10%
Iron	94%	65%
Nickel	96%	74%
Titanium	84%	60%
Brushed Aluminium	92%	75%
Gold	98%	98%
Copper	98%	98%

*Reflectivity decreases with heat

For CO_2 Laser

Aluminium Stainless Steel — Highly Reflective
Low Carbon Steel (oxidised black surface)
Brass Cast Iron
Low Carbon Steel
Carbon Fibre
Ceramic — Less Reflective

For Nd YAG (based on Rockwell's work (17))

Platinium — Highly Reflective
Stainless Steel
Mild Steel
Aluminium — Less Reflective

Fig 4(a) Theoretical Reflectivity of different metals at room temperature (20)
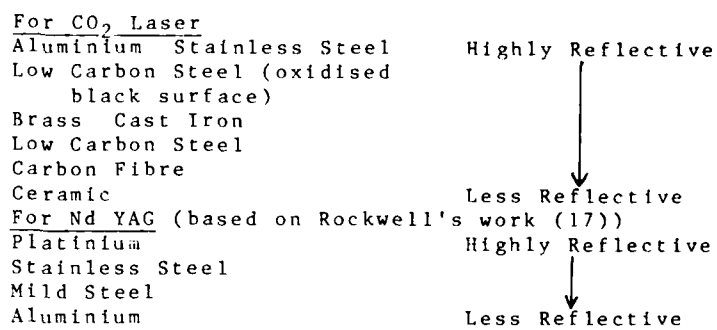
Fig 4(b) Reflectivity of different metals to a Nd:YAG and CO_2 laser radiation based on Experimental Data

3. Nominal Hazard Distance/Zone

The concept of Nominal Hazard Distance (NHD) or Zone (NHZ) or has recently been accepted as a way of conveying the hazard distance or envelope around a laser. Rockwell[4] discussed the Lens Expansion Numerical Simulation (LENS) equation:

$$R = F/b \, (4P/\pi \, MPE)^{1/2} \qquad (1)$$

where R is the safe range beyond the focal point (cm), F is the focal length of the lens (cm), b is the beam diameter of the incident of focusing lens (cm), P is the power in the laser beam at the focusing lens (W) and MPE is the Maximum Permissible Exposure level (in W/cm^2).

This is also in the American Standard[1]

$$NOHD = 1/\emptyset \sqrt{\frac{1.27 \, \Phi}{MPE}} \; (cm) \quad or \quad f/a \sqrt{\frac{1.27 \, \Phi}{MPE}} \; (cm) \qquad (2)$$

where the MPE is the Maximum Permissible Exposure limit (irradiance), Φ is the total power in the beam (W), $\emptyset$ is the emergent beam divergence, f = focal length of the lens, NOHD is the nominal ocular hazard distance[4] and a is the laser beam diameter (atmospheric attenuation is not taken into account[1]).

Whilst the concept of Laser Power and Beam Diameter are understood by most users, what these actually mean in terms of the safety standard may not necessarily be the same. This is of particular significance when trying to calculate the Nominal Hazard Distance or Zone from the equations above. Examples of these calculations are also given in the American Standard.[1] The user would automatically assume that the power of a laser was 5kW if it was stated by the manufacturer as such. Similarly, if the beam diameter was 45 mm this would then be assumed as correct. Using these two values, an Maximum Permissible Exposure (for both the eye and the skin) of 0.1 W/cm^2 and a focal length lens of 11cm, a nominal hazard distance (NHD) of 6.17 m may be obtained. If the energy distribution across a beam were uniform then this value would be acceptable. However, the energy distribution across a beam from a laser operating in the fundamental transmission mode (TEM_{00}) is not uniform. The TEM_{00} mode is a common mode for many industrial material processing lasers (except at high powers $\geq$ 3kW). The energy distribution usually has a Gaussian profile described by the expression.

$$I = I_0 exp - 2(r/w)^2 \qquad (3)$$

where I_0 is the irradiance on axis, I the irradiance at a radial distance r from the axis and w is a measure of the beam radius. Most manufacturers define the beam in terms of its total power (or energy) and its diameter as measured at the $1/e^2$ points (points where the beam irradiance has dropped to $1/e^2$ of its peak value, $I/I_0 = 0.14$) so the area defined contains 86.5% of the total power in the beam. If the average power is then calculated simply by dividing the total power by the beam area (at the $1/e^2$ point) then the peak irradiance will actually exceed the average value (by a factor of two). For safety reasons, therefore, the beam diameter in the standards is defined by the 1/e point ($I/I_0 =$

0.37, the area so defined contains 63.2% of the total power). If average power is defined in this way, then it is exactly equal to the peak value, hence it provides a safer upper limit for maximum irradiance[13].

For lasers where the beam profile is not a single mode then careful radiometric measurements to determine the effective beam diameter divergence and maximum value of irradiance or radiant intensity (energy per unit area) is necessary.

The $1/e$ beam diameter may be calculated from the $1/e^2$ beam diameter by a straight division of $\sqrt{2}$, provided the beam profile is a Gaussian form. For example where the manufacturers quote a beam diameter of 45mm then the $1/e$ beam diameter is more likely to be 32mm. This would give a Nominal Hazard Distance Zone of 8.73m which is considerably greater than 6.17m, the value calculated using $1/e^2$ beam diameter. Since it is very difficult to calculate the $1/e$ beam diameter for a non Gaussian beam, even if the $1/e^2$ beam diameter is known, accurate measurements must be made to determine the effective $1/e$ value. Hazard assessment based on calculations from equation (1) is, therefore, not as straight forward as it first appears for non Gaussian beam profiles. Beams with complex mode structures can represent a hazard well beyond any nominal hazard distance/zone calculated on the conservative Gaussian beam model due to the existence of local "hot spots" in the beam cross section. Similarly, the value of power used in the equation may not be the correct value to use. For example a 5 kW laser from a manufacturer may not be 5 kW as measured (see Section 1 Measurement) with a 1mm aperture and appropriate instrument at the point in the beam which gives the maximum reading.

Secondly, manufacturers tend to quote a lower power than the laser initially gives (to ensure it will actually give at least 5 kW if it is a 5 kW laser). In both cases if a higher power reading is measured the Nominal Hazard Distance or Zone will increase. It must be noted, however, that on safety labels for laser classification the maximum power stated on these is **not** the output power of the laser and is usually well in excess of what a laser will give. Perhaps, therefore, it should be suggested that this value is used, even though it may give a more restrictive Nominal Hazard Distance or Zone than necessary. The determination of the Nominal Hazard Distance/Zone can form part of a more formal risk analysis to be applied where the laser is integrated into a semi or fully automated plant and/or is interfaced with programmable electronic systems. This is explained more fully elsewhere.[23,24]

4.   Degradation Products

When cutting, welding or any other laser-target interaction process is occurring, potentially hazardous fumes and vapour may be produced. Very little information is available regarding the nature of these fumes. Generally the fumes have been compared with those arising from normal welding or thermal cutting processes. The standards recommend the use of adequate local exhaust ventilation. The levels of the fume should be below the "threshold limit values" (TLV) (levels above which the fumes would be harmful). Some work has been reported on fumes from plastics namely Acrylic and PVC. Doyle and Kokosa (25) report that 98% methyl methacrylate, with small quantities of benzene and toluene was detected during laser cutting of polymethylmethacrylate (acrylic). The remaining 2% of the vapour consisted of particulate aerosol matter, comprising of a complex mixture of polycylic aromatic hydrocarbons (of size < 2.5 µm). Doyle and Kokosa also analysed the by-products from laser cutting of polyvinylchloride (PVC) and detected Hydrogen Chloride (a very corrosive gas which forms hydrochloric acid when dissolved in water), benzene, vinylchloride (both known carcinogens), propene and toluene. These gases were combined with a 12% fraction of particulate polycyclic hydrocarbons and 14% shortchain polymeric materials. Powell et al[26] report some of these findings and conclude that the by products of all polymer cutting will contain a percentage of carcinogenic hydrocarbons. Work done on synthetic leather with a polyvinylchloride base[27] detected a wide range of products ranging from aromatic hydrocarbons to metal particulates (e.g. lead and titanium which are components of stabilisers and colouring pigments of the synthetic leather). The same workers detected metals ranging from chromium, nickel, cobalt and iron to aluminium, molydenum, copper, and tungsten on laser processing of several different metal alloys.

For the user it is important to consider that "adequate" fume extraction must be used. Factors that need to be considered include:

1.   the quantity and nature (particulate or vapour) of the by-product.
2.   the interface between the extraction system and any shielding or assist gas.

Both factors influence the design of the local exhaust ventilation and therefore must both be assessed to ensure adequate fume extraction is present.

Materials such as stainless steel, zinc coated steel, nickel alloys, marine plywood, ABS (a plastic), melamine (Phenylfuraldehyde coated), PVC and fibreglass have been monitored in

typical industrial locations with the fume extraction turned both on and off.

Preliminary results indicate that with the fume extraction off chromium, nickel and cobalt are present in quantity during Nd:YAG cutting of Nickel alloys. Similarly, for mild stainless and zinc coated steel high amounts (close to the threshold limit values, TLV) of iron were detected during CO_2 laser cutting. For stainless steel high values of nickel and chromium were also found. This implies that fume extraction is necessary even for materials such as steel (since the level of iron fumes is very high). Similarly, for some of the "exotic" metals, fume extraction is necessary since low quantities of toxic metals (e.g. cadmium) may be emitted. Some metals in particular present more of an occupational health hazard if they are present in higher valancy states than the normal ground state of the material. The threshold limit values of these metals are therefore much lower than other metals which do not have these potentially toxic higher valancy states. Particular care must also be taken when laser processing PVC since hydrochloric acid may be formed. Suitable filtering systems must be used in most cases to prevent potential emissions to the outside environment.

5. Laser Safety Schemes

To summarise all this information is only of use if it is collated in some easily accessible, workable form. The problems dealt with have generally been applicable to Nd:YAG or CO_2 material processing lasers. Similar practical difficulties exist with lasers used for other processes (e.g. medicine, printing, recording). The need for fume extraction may be required or, perhaps another aspect, such as measurement may be also necessary. In medical applications of laser beams it is imperative that the measuring equipment is accurate as well as being used in the proper way otherwise harm to the patient may be the result. For helium neon, argon and other visible light lasers reflected or scattered radiation may be important particularly in determining whether a system may be used in applications such as non destructive testing or process control.

The topics covered have given the potential user an insight into some of the problems or queries that may arise. There are, however, many other areas that lack practical advice and understanding. Questions may arise such as:

    What sort of interlock is necessary?
    Where may interlocks be brought from?
    What protective clothing is needed?
    Who supplies this protective clothing?

In an attempt to cater for these aspects as well, laser safety schemes are being compiled with a view to incorporating all such data. These will be both written and computer based. One element well progressed is an attempt to compile the standards into a database which can be interrogated using a personal computer. The information will be accessed by a user who has an application and wants to know what lasers and what safety precautions are necessary, or by a user who has a laser or material, and wants to know what application, or laser, and safety precautions to use. Details of this work will be published in the coming year.

Conclusions

This paper is presented to put across some of the practical problems associated with laser safety. The consideration of measurement, reflected and scattered radiation are imperative when formulating laser hazard zones. Degradation or by-products from laser processing are becoming increasingly more important as environmental considerations are becoming stricter. The potential laser user is confronted with a wealth of standards, references and information on laser safety. This is, however, not only overwhelming but often not readily understandable or accessible. This has therefore lead to the development of laser safety schemes which, will it is hoped, be of practical use to the laser user in the future.

Acknowledgements

References

1. American National Standard for the Safe Use of Lasers ANSI Z136.1 (Laser Institute of America, 1986.)

2. International Electrotechnical Commission. Standard Radiation Safety of Laser Products, Equipment Classification, Requirements and Users Guide (IEC Publication 825 Geneva, Switzerland 1984.)

3. British Standards Institute "Radiation Safety of Laser Products and Systems" BS4803; (1983).

4. R.J. Jr. Rockwell, Lasers and Applications 3 (11), (Nov. 1984) pp 65-69

5. R.J. Jr. Rockwell, Lasers and Applications, (Nov. 1986) pp 97-103

6. B.A. Ward, D.P.D. Brown, C.I. Walker, Case Study, "Safety Aspects of a High Power CO_2 Laser System for Class 1 Operation", UKAEA Culham Laboratory, Abingdon, Oxfordshire, UK, (1982). CLM-P664

7. D.H. Sliney, M.L. Wolbarsht, "Safety with Lasers and other Optical Sources", (Plenum Publishing Co, New York, 1980)

8. D.C. Winburn, "Practical Laser Safety" Occupational Safety and Health Series, Vol.11, (Marcel Dekker Inc., New York and Basel, 1985).

9. World Health Organisation Environmental Health Criteria 23 "Lasers and Optical Radiation", Geneva (1982).

10. Rockwell Associates Inc., Cincinnati, Ohio, U.S.A.

11. SIRA, London, England.

12. Centre for Extension Studies, Loughborough University, England.

13. A.R. Henderson, Proc. 1st Int. Conf. Lasers in Manufacturing (LIM 1) (Nov. 1983), pp 142-149.

14. "Choosing a Laser Power Meter" Lasers and Applications, (Nov. 1984).

15. J.E. Dennis, R.G. Bostrom, Laser and Optronics, (March, 1988) pp. 95-102.

16. J.A. Folkes, J. Tyrer, A.M. Bandle, "A Practical Guide to Selecting Laser Power and Energy Meters". Optics and Laser Technology. To be published.

17. R.J. Rockwell, C.E. Moss, J. Am. Ind. Hyg. Assn, (August 1983) pp 572-579.

18. Guide for the Selection of Laser Eye Protection. (Laser Institute of America, Toledo, OH, May 1984).

19. B. Holyoak, A.M. Bandle, - Laser Incidents, Cpt. 6, pp 47-57, Medical Laser Safety Report No.48, Institute of Physical Sciences in Medicine (1987).

20. T.L. Vanderwert, "Prospects brighter for Laser Welding", Machine Design, (1984).

21. Draft European Standard En 207E Personal Eye-Protection - Filters and Eye Protectors against Laser Radiation, (Sept. 1988).

22. Draft European Standard En 208E Personal Eye-Protection - Protectors for adjustment work on lasers and laser systems (Laser adjustment eye-protectors) (Sept. 1988).

23. A.M. Bandle, 1st Int. Symp. Effects Biologiques des Faisceaux Lasers et Normes de Protection, (Paris, Nov.1986) pp 33-37.

24. S.A. Edwards, A.M. Bandle, Proc. 4th Int. Conf. Lasers in Manufacturing (LIM4), (May 1987) pp 139-152.

25. Doyle D.J., Kokosa J.M., "Hazardous Byproducts of Plastics Processing with CO_2 Lasers". Int. Congress on Applications of Lasers and Electro Optics (ICALEO '85) (Nov 11-14 1985 San Francisco, USA).

26. Powell J., Menzies I.A., Scheyvaerts P.F., "CO_2 Laser Cutting of Non Metallic Materials" Lasers in Manufacturing 4 (LIM 4) (May 12-14 1987 Birmingham, UK).

27. VCSPS Ed Morozova V.M., "Guide to the Evaluation of Harmful Industrial Factors in the Laser Processing of some Polyvinylchlorides and Metals" All-Union Central Scientific Research Institute for Labour Protection Moscow (1984).

FIBER PROBE FOR LASER ANGIOPLASTY
RADIATING A COROLLA SHAPED BEAM

Vera RUSSO
Facoltà di Ingegneria, Università di Salerno
84100 Salerno
Stefano SOTTINI, Giancarlo MARGHERI, Paolo GUIDOTTI
I.R.O.E.-C.N.R.
Via Panciatichi 64, 50127 Firenze
Filippo CREA
Facoltà di medicina, II Università di Roma
Torvergata, Roma

Abstract
The experimental research on laser angioplasty is limited, at present, by the risk of mechanical or laser induced perforations, particularly in the case of coronary arteries. To get rid of this dr wback here a new fiber optic probe is described, characterized by a corolla shaped output beam and by no axial radiation. The probe consists of a conical fiber tip inserted in a particular quartz microcapsule. Its optical behaviour has been studied both experimentally and theoretically, using a ray tracing method. The results of some tests carried out on aorta wall from a cadaver seem to confirm that the new probe minimize the risk of vessel perforation, while its diameter is suitable even for coronary applications. An improved version of this new probe is also under test utilizing a multiple fiber. This device should allow the treatment even of a limited portion of the vessel wall.

Introduction
The recanalization of arteriosclerotic vessels by laser angioplasty is very promising ([1]) although many questions have not exhaustive answers yet; for example a lot of experiments must be done to investigate the ablation of arteriosomatic plaques by laser pulses ([2]) and the possibility of selective light absorption by the application of specific stains ([3]).

At present this investigation, particularly in the case of coronary arteries, are limited by some technical problems. Among them, the risk of mechanical or laser induced perforations is likely the most serious ([1,4,5,6]). A number of modified fiber optic delivery systems are under study, however the safety problem is still open.

In the following a new fiber optic probe is described which is expected to minimize the risk of vessel perforation, while its diameter is suitable even for coronary applications.

The new probe and its optical behaviour
The laser induced perforations are likely due to the high power radiated on axis by the bare fibers. Indeed, referring to Fig. 1a, even if the output beam is coaxial to the vessel, however it can pass beyond the arteriosclerotic area and perforate the vessel wall, expecially in the case of bends and bifurcations. This risk could be avoided if the fiber radiated a corolla shaped beam without any axial beam, as sketched in Fig. 1b.

Actually a class of fiber tips radiating light mainly along a cone coaxial to the fiber itself is well known ([7]). These tips, consisting of cone or truncated cone terminations, have been tested in the past e.g. in gastroentherology to remove occluding cancers ([8]). They have been also suggested to treat obstructions in blood vessels or bronchos. Unfortunately their shape enhances the risk of mechanical perforation and of tip breaking. Moreover the conical terminations still radiate on axis a non negligible part of the light, specially in the case of truncated cones.

To get rid of these drawbacks, the new probe still has a conical tip but inserted in a quartz microcapsule. This capsule is obtained from a small capillary tube which is suitably sealed on the top to get a toroidal lens, Fig. 2. This lens structure prevents the on axis radiation , generally increases the off-axis angle and tends to collimate the output. As a consequence, the new probe gives rise to a sharp corolla shaped beam. If this beam impinges on a screen, a crown light pattern is obtained, as shown in Fig. 3 , where the screen was about 5 cm far from the probe.

A typicall overall radiation diagram shows a dark axial cone with half aperture in the range 30-60 degrees depending on the angle of the conical termination and the shape of the

toroidal lens on the top of the microcapsule. This dark cone is surrounded by a bright crown whose angular thickness is only 5-6 degrees at 3 dB , thanks to the collimating effect of the toroidal lens.

In the new probe the laser power is spreaded over a relatively large solid angle in comparison with the case of bare fibers. It should be a further advantage of this probe, reducing the risk of perforation due to power fluctuations or wrong firing while the investigation about the suitable power densities for the angioplasty treatment should be made easier.

A theoretical model of the new probe was carried out where the propagation was obtained by ray tracing, while the intensity distributions were derived by associating a weight to each ray according to the following procedure: every ray incoming into the conical tip is assumed to carry the power intensity proportional to the gaussian factor $p = \exp-(\Theta /\Theta_0)^2$, where Θ is the angle of the ray with respect to the fiber axis, and Θ_0 is the standard deviation of the gaussian distribution representing the output from a bare fiber. If T is the transmittance of the whole system, cone plus capsule, the output intensity associated to the ray will be : $T \cdot p$. Then, taking the origin of the polar coordinates on the base of the cone, we sum all the contributions $T_i \cdot p_i$ of the rays travelling at an angle $(\Theta, \Theta + \Delta\Theta)$ where $\Delta\Theta$ is an angular step arbitrarily chosen and Θ is now an integer multiple of $\Delta\Theta$. Finally the power intensity $I = \Sigma_i T_i \cdot p_i$ is attributed to the angle Θ. A typical example of the obtained results is shown in Fig. 4. The aperture of the conical tip was 16 degrees. The profile of the microcapsule, that is the toroidal lensshape, was derived from a magnified picture of the sample which has been used subsequently for the experimental tests (Fig. 4a).

A meridional plane with the ray tracing is depicted in Fig. 4a, while in Fig. 4b the radiation intensity I, plotted versus Θ (continuous line), is compared with the experimental measurements (dots), carried out by feeding the probe with an argon laser. The agreement is pretty good despite the rough approximation of the theory. The darker zones in the ray tracing of Fig. 4a fit quite well with the 3 dB width of the two intensity peaks in Fig. 4b.

The behaviour of the new tip in aqueous environment has been investigated by the previous theoretical model. The results, summarized in Fig. 5 show that water, which is usually present in the vessels during the plaque treatments, is not expected to make the probe performance worse. On the contrary the intensity peaks (Fig. 5b) look sharper than in the previous case of Fig. 4b.

In order to make evident the key role of the toroidal lens in determining the output beam shaping, a bare fiber has been inserted in a microcapsule instead of a conical termination. Then the measured radiation pattern has been compared with the theoretical curve computed by the procedure above described. The results are summarized in Fig. 6. Even in this case a corolla shaped beam is obtnained but the half aperture of the dark cone is reduced: a typical value is about 20 degrees as shown in the figure.

Preliminary tests on aorta wall

Some preliminary tests have been carried out utilizing the new probe ([9]) characterized by a 0.2 mm core fiber and by a microcapsule of 1.2 mm diameter. A segment of aorta wall from a cadaver was opened longitudinally and fixed on a cork board with the lumen surface facing outward. This sample was irradiated in different points with argon laser light delivered by the fiber with the new probe and, for comparison, by a bare fiber (Fig. 7). Three different energy levels, 50, 75 and 100 J, have been used giving rise to different craters on the aorta wall (Fig. 8). As summarized in Fig. 9, in the case of the bare fiber the crater diameter is almost insensitive to the pulse energy, while its depth increases up to one millimeter with an evident risk of perforation. On the contrary in the case of the new tip, the crater enlarges with the energy (Fig. 9), while its depth, which is almost uniform at the periphery, increases slowly, therefore it can be kept under control.

An improved version of the probe

The probe considered up to now is characterized by a single fiber coaxial to the microcapsule. Moving this fiber off-axis the intensity distribution of the corolla beam becomes inhomogenous and eventually only a sector of the corolla is still bright. Therefore if a multiple fiber is inserted in the microcapsule in which the individual fiber are distributed in a ring arrangement, the output corolla beam is expected to consist of several sectors each illuminated essentially by a single fiber of this ring.

It is evident that on varying the coupling between the source and each fiber one should get only a partial illumination of the corolla beam. These effects have been seen experimentally

by inserting three Q-Q 100-140 μm fibers with flat tips into the microcapsule. The jacket was previously removed for about 3 cm length and the fibers have been tightened by a thermo-shrinked tube. Fig. 10 shows the spot obtained on a screen normal to the probe; a) when only one fiber is coupled to the source, b) when all fibers are feeded. The irregularities in the light pattern are due to the difficulties of perfect positioning the fibers in the capsule.In practice smaller fibers would be necessary. However this qualitative test confirm the possibility of side radiating only on a particular area corresponding to the arteriosclerotic plaque.

Conclusion

A new fiber probe has been designed and fabricated for the laser treatment of arterio-somatic plaques in coronary artheries. This new probe is able to side irradiate the vessel walls with good uniformity. Thanks to the lack of the axial beam, the risk of laser perforations should be minimized even in case of vessel bends or bifurcations. The risk of mechanical perforations and of fiber tip breaking should be also minimized by the rounded protective capsule.

The optical behaviour of the new probe has been investigated both experimentally and by ray tracing procedure. Although this theory is based on simple approximations, the results are in pretty good agreement with the experimental measurement.

Preliminary tests carried out on segments of aorta from a cadaver seem to confirm the expected advantages of the new corolla irradiating fiber probe.

An improved version of the probe could be fabricated by inserting a multifiber in the microcapsule instead of a single fiber. It should allow the operator to side radiate only a particular area of the vessel corresponding to the arteriosclerotic plaque.

References

1. S. C. Choy, I.E.E.E. Jour. of Quantum Electronics, QE-20, 12, 1420 (1980)
2. D. L. Singleton, G. Paraskevopoulos, R. S. Taylor, L. A. J. Higginson, I.E.E.E. Jour. of Quantum Electronics, QE-23, 10, 1772, (1987)
3. D. Murphy-Chutorian, J. Kosek, W. Mok, S. Quay, W. Huestis, J. Mehigan, O. Profitt and R. Ginsburg, Am. Jour. Cardiol., 55, 1293, (1987)
4. G. S. Abela, S. J. Normann, D. M. Cohen, et al., Circulation, 71, 403, (1985)
5. F. Crea, A. Fenech, W. Smith, C. R. Conti, G. S. Abela, Jour. Am. Coll. Cardiol., 61, i502, (1985)
6. F. Crea, G. S. Abela, A. Fenech, W. Smith, C. Pepine, C. R. Conti, Am. Jour. of Cardiol., 57, 171, (1986)
7. S. Sottini, in Proceeding, International Congress on Laser in Medicine and Surgery, Bologna, p. 133, (1985)
8. V. Russo, G. C. Righini, S. Sottini, S. Trigari, in Proceeding, SPIE, 522, 166, (1985)
9. F. Crea, G. Davies, B. Keogh, G. Margheri, V. Russo, S. Sottini, W. Mc Kenna, M. Pashazadeh, S. P. Allwork, A. Maseri, Laser in Medical Sciences (in press)
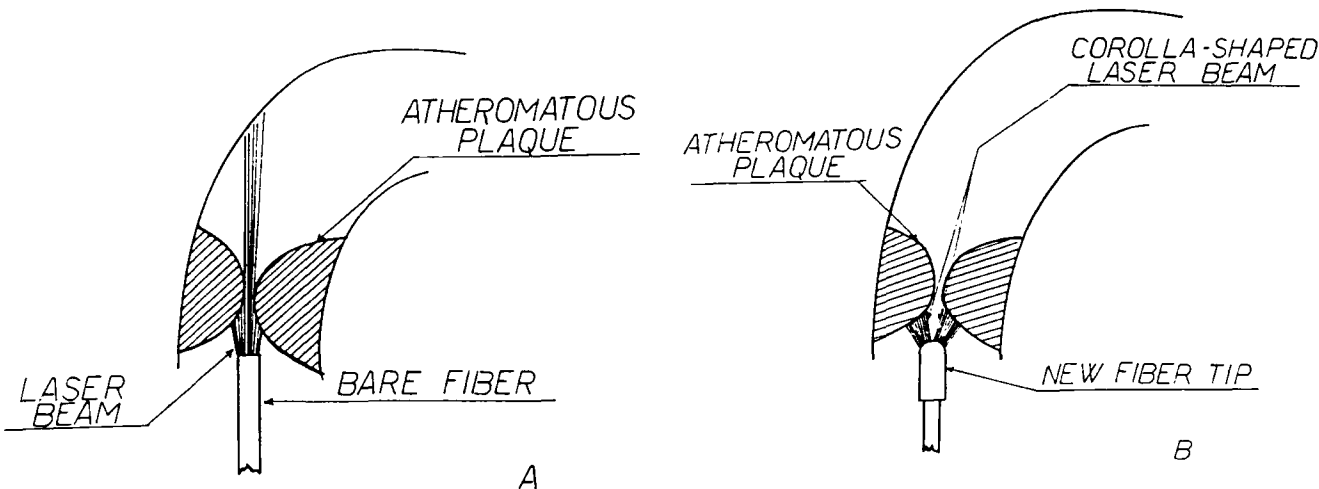
Fig. 1 - a) Bare fiber radiating mainly on axis. There is a serious risk of
            perforation of the forward healthy tissue.
         b) Special fiber tip radiating sideways a "corolla" shaped beam with
            no risk of perforation.

Fig. 2 - The new probe for laser angiopla-
         sty, consisting of a conical ended
         fiber inserted in quartz microca-
         psule. The PCS fiber has a core
         diameter of 200μm; the overall dia-
         meter of the capsule is 1.2mm. The
         "toroidal lens" on the top of the
         microcapsule is clearly visible.

Fig. 3 - Crown light pattern on a screen
         illuminated by the new probe. The
         screen was about 5cm far.
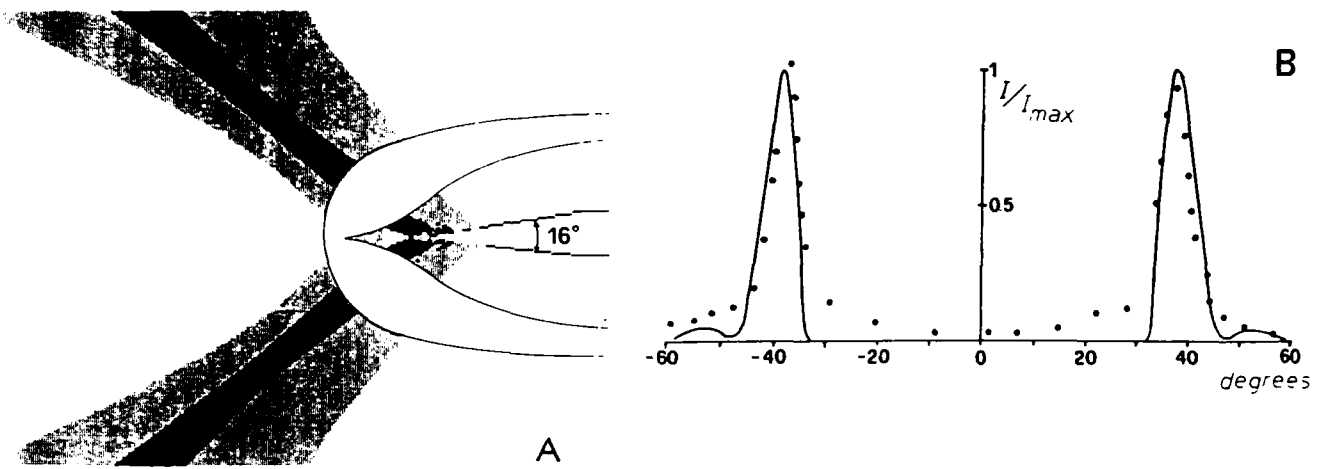
Fig. 4 - Optical behaviour of the new probe in air.
     a) Meridional plane with the ray tracing. the profile of the toroidal lens
        was derived from a magnified picture of the sample which has been used
        subsequently for the experiment.
     b) Experimental measurement (dots) and corresponding theoretical curve of
        the intensit, I versus the radiation angle θ.
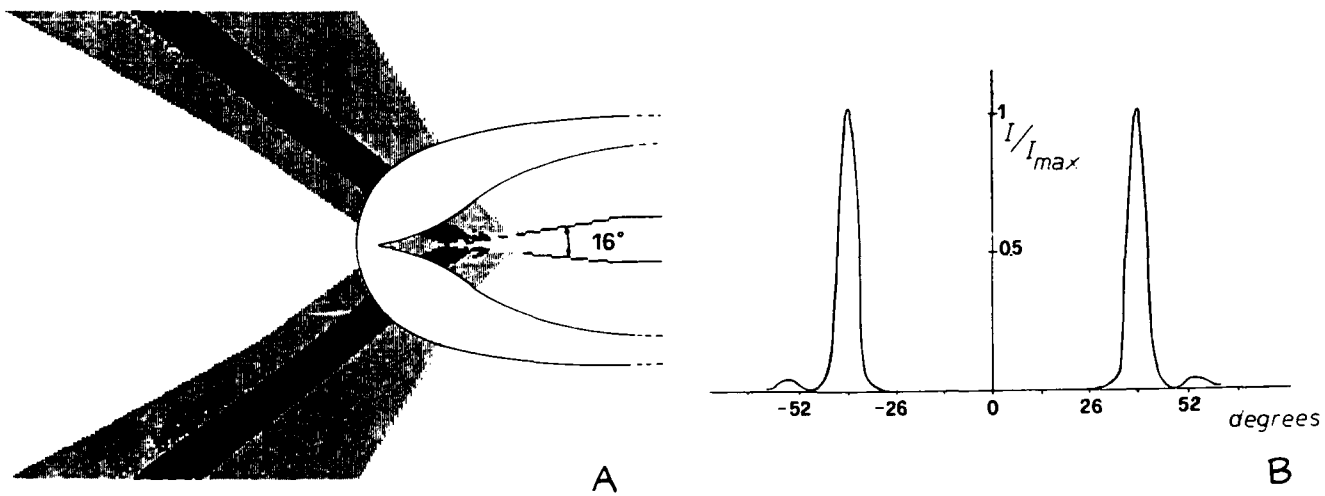
Fig. 5 - Behaviour of the new probe in aqueous environment.
     a) Meridional plane with the ray tracing.
     b) Theoretical curve of the ratiation pattern (I plotted versus θ).

717

A

B
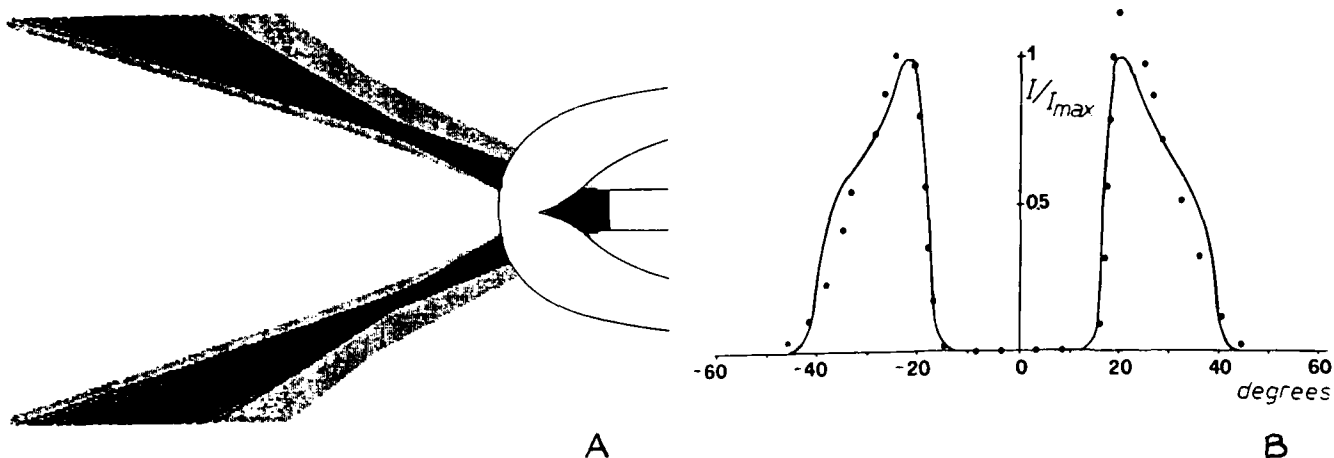
Fig. 6 - Optical behaviour of the new probe if a bare fiber is inserted in the
microcapsule instead of the conical tip.
a) Meridional plane with the ray tracing.
b) Experimental measurement (dots) and corresponding theoretical
curve of the radiation pattern (I plotted versus θ).
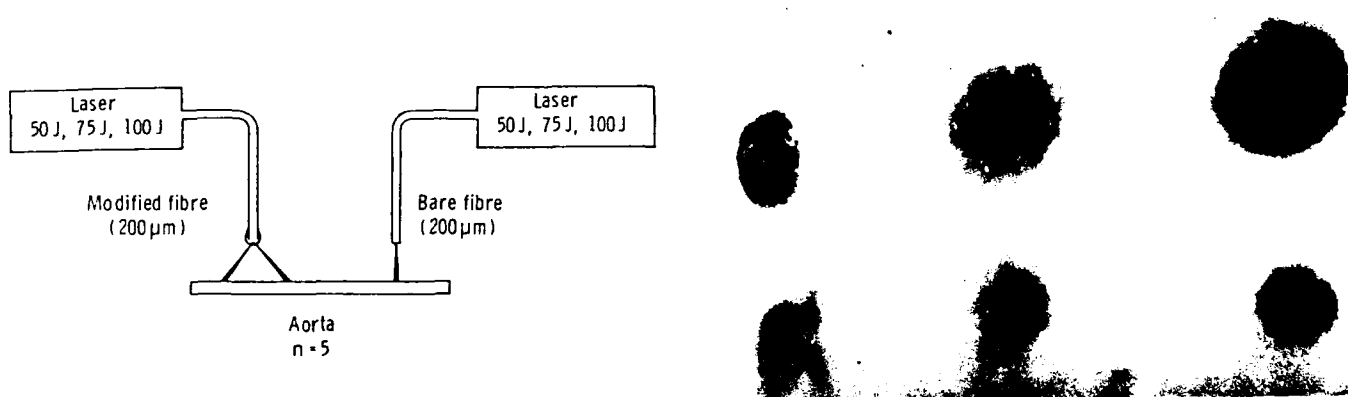
Fig. 7 - Sketch of the tests performed on a
post mortem aorta segment with a
bare fiber and a modified fiber.
The argon laser pulse of different
energy gave rise to the set of
craters shown in Fig. 8.

Fig. 8 - Set of craters obtained on a post
mortem aorta segment with the pro-
cedure outlined in Fig. 7.The new
probe was used to get the top row
craters while the bare fiber to
get the bottom row craters. The
energy of the pulses increased
from left to right (50,75 and
100 J respectively).

718
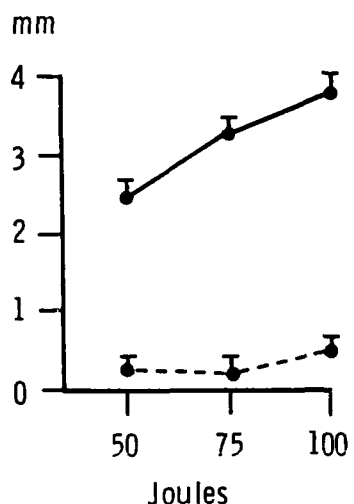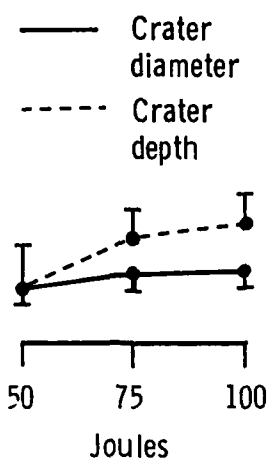
Fig. 9 - Diameter, size and depth of the craters shown in Fig. 8
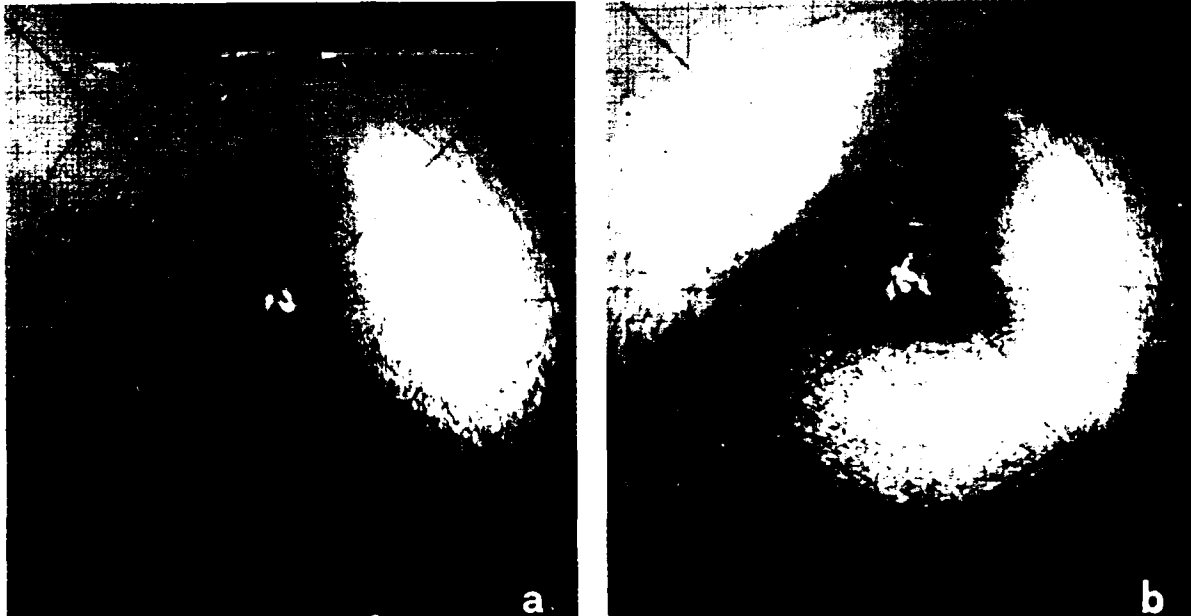
Fig. 10 - Spot obtained on a screen normal to the pr 'e (the squared hole at the
center of the screen corresponds to the axis of optical sistem).
a) When only one fiber is coupled to the source.
b) When all fibers are feeded.

PHOTOSTIMULATION OF BIOLOGICAL TISSUE WITH LASERS

Arthur D. Ericsson, M.D.
Associate Professor
Department of Neurology
Baylor College of Medicine
One Baylor Plaza
Houston, Texas 77030

Abstract

The world literature of biostimulation properties of coherent light has been summarized and our experience with the He-Ne laser [632.8 nm (nanometer)] at 2-15 mw/square centimeter (milliwatt) output has been described. In general, the clinical use of the He-Ne laser at lower 2-5 mw/square centimeter output has been found useful for stimulation of wound healing and collagen deposition in skin and subcutaneous tissues. On the other hand, at a higher output (5-15 mw/square centimeter) this laser is capable of penetrating tissue effectively and may be used for producing sensory nerve blockade and providing a surcease of pain in those patients with specific nerve or neuritic pain problem. Furthermore, other clinical uses of the He-Ne laser are under investigation.

A growing number of clinical reports claim beneficial effects due to Helium-Neon laser irradiation in pulses of 1 to 5 mW. Claims range from enhanced wound healing to regeneration of collagen in skin epidermis. Widely varying treatment cycles were used clinically and with different techniques, making correlation of results difficult, if not impossible.

The most relevant in vitro studies are available,[1-6] and there appears a correlative consistency under the following assum ns:

1. Coherence is essential for non-thermal collagen stimulation;

2. The collagen stimulation is correlated with mRNA, but not with mDNA or any of the enzymes studied;

3. The effects are frequency dependent; and

4. Collagen inhibition and/or destruction occurs at higher exposure levels when temperature increments occur.

However, Karu and Letokhov[6] confidently deny the specific relevance of coherence and proceed to show enhanced DNA responses in HeLa, E. coli, and Yeast for both coherent and incoherent light, but with important frequency variations in the visible range. They did not observe collagen and their organisms do not have collagen. Therefore, the Russian work does but directly contradict the three positive claims[2-4] for collagen stimulation by coherent light effects in normal eukarotic cells. Their exposure levels were in the range of 1 mJ/cm^2 to 10 mJ/cm^2. Curiously, results for the exposure of HeLa cells to a He-Ne laser at a fixed fluency of 10 mJ/cm^2 and varying intensity shows a threshold response at 1 mW/cm^2. The authors also claim considerable success in treating gastric ulcers with incoherent red light, but mostly with combined medical therapies.

Boulton and Marshal[2] found that the enhanced proliferation of human fibroblast cells due to pulsed red light occured only for the coherent laser irradiation. They applied 15 minute exposures of pulsed red light and observed the cell counts after 24 hours of incubation. The occurrence or non-occurrence of enhancement is statistically significant, although the reproducibility of the cell counts is somewhat debatable. Apparently, a growth factor is generated during the 15 minute irradiation period, while the 1 mW CW He-Ne laser was chopped into 3 ms (millisecond) pulses at 100 Hz (hertz) to give 90 mJ/cm^2 in 15 minutes at 0.1 mW/cm^2.

The Nd:YAG laser experiment[3] showed a marked decrease of both collagen production and DNA replication in human skin fibroblast cultures, whereas no such decreases were noted in cultures heated to the corresponding temperature by incoherent light. The 60 W CW-Nd:YAG laser outputs at 1064 nm. With an intensity of 389.6 W/cm^2, exposures of 3 to 12 seconds give 1.2 to 4.7 x 10^3 J/cm^2. This is roughly one thousand times more exposure than either the He-Ne or Ga-As experiments. It was surprising that the incoherent source had no effect at this level of exposure, but the coherent effects were confirmed.

The procollagen mRNA experiment[4] was based on biopsy specimens taken from wounded pigs. They compared mRNA levels found in unexposed controls, with the incoherent tungsten lamp, and the He-Ne laser. The incoherent exposure showed a slight enhancement, but the laser exposure demonstrated a marked effect for both type I and type III procollagen mRNA.

The In Vitro paper[5] gives additional results of the effect of the He-Ne laser on human lymphocyte response. The authors found inhibition of both lectin stimulation and spontaneous lymphocyte proliferation in vitro under low level exposure to Ga-As laser light. Similarly, the functional immune response to antigen stimulation was diminished as a result of laser irradiation.

Thomas Lam et al[1] tested four human fibroblast cell lines under two lasers:

1. A continuous wave He-Ne laser at 632.8 nm with average power of 1.56 mW. The cell lines were irradiated at 0.883 mW/cm^2 with total exposures of 0.053 to 1.589 J/cm^2; and

2. A pulsed Ga-As laser at 904.0 nm with 200 ns at 73 Hz and average power of 0.03 mW. The lines were irradiated at 0.222 mW/cm^2 with total exposures of 0.0133 to 0.40 J/cm^2, after correcting for a misunderstanding about the average power.

Both lasers caused enhanced procollagen formation without any observed effect on the specified enzyme assays. The cell temperature was not appreciably influenced by such low level radiation. The He-Ne laser showed a maximum enhancement at exposures of 0.15 J/cm^2, while the Ga-As laser showed DNA suppression at greater exposures.

The difference between the He-Ne and the Ga-As laser is most remarkable, and certainly deserves further exploration and verification. Cell line 1 had the highest initial collagen level and was more difficult to stimulate, whereas cell line 3 had the lowest initial collagen level and showed the greatest amount of stimulation (i.e., 36 times). Only cell line 2 was tested for DNA, and again the lasers showed differing results.

Table 1: Statistically Significant Results Versus Controls

Cell Line	He-Ne	Ga-As
1) (High Col.)	=Col.	2 x Col.
2)	Inc. Col., =DNA	Inc. Col, Dec. DNA
3) (Low Col.)	36 x Col.	=Col.
4)	No obs.	Inc. Col

List of Variables Occurring in the Experiments

Cell line: species, passage, clone, stability, etc.
Substrate/suspension
Trypsin procedure
Growth medium
Laser/incoherent source
Laser:frequency, intensity, exposure, spectral purity, amplitude stability, noise, single/multimode, CW/pulse, etc.
Dynamics of response: multiple exposures, incubations
Types of Observation: cell count, collagen, DNA, mRNA, enzymes, etc.
Use of Controls: statistical significance, reproducibility.

Why Coherent Light?

Three laboratories have found that coherent red light produces a biological effect that is not produced by incoherent light of the same frequency and intensity. The low intensity behavior rules out two photon absorption, and both one photon and two photon absorption occur without regard for coherence. Coherence means that the electric field can act as a classical force. The electric field due to a single photon is indeterminate; if the phase is known, then the amplitude is unknown, and vice-versa. A coherent state of many photons builds a classical representation of the electric vector; having definite phase and amplitude. Low frequency fields are usually coherent multi-photon states because the sources are driven by classical forces. The individual low frequency photons are below the energy threshold for easy detection. Laser coherence implies coherent optical photons with enough energy to act like photons and drive a classical force. The question is, "How does this force act to produce biostimulation?"

The induced dipole-dipole forces were discussed along with several other speculative ideas by H. Frolich.[11] At high frequency the induced forces are proportional to R^{-4} instead of being exponentially reduced by the static coulomb screening. It is very tempting to assume that these long range frequency dependent forces should play a role in the recognition processes before the stereographic effects can come into play. For example, a procollagen molecule needs to find the collagen fiber before thermal degradation occurs, and the resonant laser-induced forces should be helpful. Mitosis could be another example. The induced dipole forces might influence the assembly of mRNA or distort the superhelices enough to cause nicking. A caveat must be mentioned: There is no real evidence that this type of long range force is effective biologically. It is more likely that polyelectrolyte effects are hard at work.[12,13]

The various frequency ranges are listed in the table below. However, it is difficult to cope with all the phenomena occurring in a span of 14 orders of magnitude.

Table 2: Frequencies and Wave Lengths for Major Regions

Range	Frequency	Wave Number	Microns	Other
Visible	6×10^{14}	20000	$\frac{1}{2}$	500 nm
IR	3×10^{14}	10000	1	1000 nm
VIB	6×10^{13}	2000	5	
THERMAL	3×10^{13}	1000	10	
VIB	3×10^{12}	100	100	
MM	3×10^{11}	10	1000	1 nm
MW	3×10^{10}	1	10000	1 cm
ELF	30		10000 km	

The mechanism of biostimulation must have an energy path - i.e., causal connection. Somehow, the incoming optical energy must be converted to:

1. an electronic excitation;

2. a super-thermal vibration;

3. a sub-thermal breathing mode; or

4. molecular transport and assembly.

722

The red photons are rather low for electronic excitation. Furthermore, there are no known red chromophores, and electronic and sub-thermal vibration transitions do not depend on coherence.

Cases 3 and 4 are relevant. Ramon scattering with excitation of the degenerate sub-thermal breathing modes becomes a coherent process, and an increasing electric field will split the degeneracies and lead to a non-linear response. This type of Ramon scattering may include the effect of induced dipole-dipole forces in a polymer molecule, although this effect has not been established.

The mechanism of photostimulation must start somewhere. Frequently, we expect to initiate cell responses externally and then trigger a response in the cytoplasm; but a photoreaction in the DNA or the chromatin complex might be the trigger. It is also reasonable for laser light to interact directly in the cytoplasm and/or receptor proteins.

Direct photoreaction in the cytoplasm or membrane receptor protein is a logical candidate for the initial step, since it is suspected that both collagen mRNA and chymotrypsin (an enzyme) are structurally modified by red light. The evidence as regards mRNA[7] shows that He-Ne laser light (632.8 nm, 13.8 mW, 10 J/cm^2) on rat liver RNA causes increased UV absorption at 260 nm.

Possible Low Frequency Mechanism

Most lipid membranes and biopolymers are negatively charged and associated with a nearly equal number of positive counter ions. The cell membrane polarizes the adjacent layer of ionic media and generates a strong static electric field. A low frequency external field induces cyclic counter ion flow from pole to pole around the cell membrane. The coefficient of diffusion and the diameter of a typical cell imply a counter ion resonance frequency of roughly 20 cps. Water flow is induced along with the ions. The ions and the induced water move through a forest of transmembrane proteins and polysaccharides. The outreaching polymers are stressed and dragged towards the poles, where they accumulate, producing the capping phenomena seen in fluorescent studies. the oscillating flow liberates bound CA^{+2} and causes irreversible dispersal. Clearly, we have started a significant cell response without resorting to photonic transitions.

At 20 cps the induced counter ion flow tends to cancel the external field so that the applied electric field does not penetrate to the interior of the cell. However, a low frequency magnetic field, or a somewhat higher frequency electric field, will penetrate the cell membrane and induce effect on the several membranes and variously dispersed polyelectrolytes in the cytoplasm. A variable magnetic field will penetrate everything except a superconductor, or a large conductor with appreciable eddy currents. Hence, if variable magnetic fields are applied, we expect the Faraday-induced electric fields inside of the cell.

A Plausible Enzyme Mechanism for Low Frequency Biostimulation

Although an enhanced enzyme activation was not reported in the laser cell culture experiments, a key step may have been overlooked. Increased amounts of collagen mRNA were observed, and low frequency experiments found increased activity of ornithine decarboxylase (=ODC), enolase, and ATPase, along with increased amounts of cAMP, hyluranatic acid, and mRNA.

The first stage in the cascade of enzyme activity is activation of a cAMP-dependent protein kinase. A hormone or neurotransmitter binds to a specific receptor protein located on the outside of the plasma membrane. the first messenger never enters the target cell. The hormone-receptor complex diffuses to an adenylate cyclase in the plane of the bilayer. Adenylate cyclase contains at least two subunits. One possesses catalytic activity, and the other is a regulatory protein. The regulatory protein binds GPT. Only then does the catalytic protein become active, forming cAMP from ATP. The regulatory protein can hydrolyze GTP, and once GTP has been hydrolyzed, the catalytic subunit is no longer active. [One mechanism is through G protein activation by the frequency-dependent coherent light at 632.8 nm wavelength.] An enormous range of hormones also alter the activity of adenylate cyclase in higher organisms.

The second stage in the enzyme cascade is the activation of a protein kinase by cAMP. Cyclic AMP-dependent protein kinases are tetramers composed of two catalytic and two regulatory subunits. Cyclic AMP binds to the regulatory subunits, and the inactive protein dissociates into active catalytic subunits and regulatory subunits bound to cAMP. The newly phosphorylated protein thereby produces a physiological or metabolic response.

Clinical Considerations - He-Ne Laser

We have utilized the He-Ne laser (at 632.8 nm) 2-15 mW over 1-5 cm areas, from 10 seconds to 5 minutes over repeated areas in a variety of medical conditions. Absolute indications for the use of the He-Ne laser in medicine are:

Wound healing. In over 150 patients with severe decubiti deeply penetrating into musculofacial planes up to 10-15 cm deep and 3-8 cm in diameter have been treated with uniformly dramatic increases in granulation tissue and decubiti healing.

The following case is illustrative of the effects of the He-Ne laser upon wound healing:

The case is that of a 50-year-old male with adenocarcinoma of the kidney with metastasis to the spine and resultatnt paraplegia. The patient received irradiation to the spine and was concurrently treated with recombinant Interferon Alpha. He developed decubiti (bed sores) in 1987 on both buttocks that would not heal. In fact, they were grossly infected and the plastic surgeon had placed him on a medical treatment plan from January until the August 1988.

From January to August 1988 the decubiti simply grew larger and became even more grossly infected. On August 18, 1988, the left decubitus measured 4.5 inches deep and was 3.5 inches wide; the right decubitus measures 3.5 inches deep and was 3 inches wide. He was started on He-Ne laser treatment twice a week for 1-3 minutes per area at 5 mW output 632.8 nm. After the second treatment the pus and purulent material which filled both ulcers was no longer present and has never reappeared (although the medical management has not changed).

In the second week nodules of pink granulation tissue could be seen sprouting from each side and the base of the ulcer, and the following week spicules of granulation tissue were joining across the midline. Gradually, week by week, the granulation tissue filled in, along with the epithelium. By mid-October, the patient was able to resume work (sitting six hours a day). This is generally contraindicated in patients with routine decubiti management. Furthermore, by November 15, 1988, both decubiti were essentially healed.

Pain management. Early in the course of wound healing it was noted that patients noted a remarkable reduction of pain in the neurotomes treated with the He-Ne laser; this occurred without a loss of sensation. Therefore, In order to clarify pain pathway mechanism a normal ulnar nerve was stimulated via the He-Ne, and conduction velocities were recorded in the routine manner. The data are both biologically accurate and conform to the clinical observations. The following data is a summary of conduction velocity of the ulnar nerve irradiated with the He-Ne laser.

Ulnar Nerve Stimulation Effect of He-Ne Laser

STIMULUS IN $\frac{1}{2}$ SECONDS

LATENCY	AMPLITUDE	CONDUCTION VELOCITY	TIME EXPOSURE	DROP IN MS
5.3	20 uV	49.0 M/sec	0	0
5.6	20	46.4	30	-5%
5.8	20	44.8	60	-9%
5.9	20	44.1	120	-10%

Treatment of Pain Syndromes. Following the studies noted above, over 50 patients (450 patient treatments) have been irradiated with the He-Ne laser with an astounding 90% relief of pain. These patients were carefully screened prior to inclusion into the study, however, and only those cases of posttraumatic neuroma pain, post surgical neuroma, carpal tunnel syndromes, intercostal neuralgia, and specific bone metastasis (rib) pain were included as a part of an ongoing clinical research project.

Additional medical applications of the He-Ne laser are part of extensive clinical evaluation at Baylor College of Medicine.

This work has been generously supported by:

Baylor College of Medicine
The Institute of Rehabilitation and Research
Medcci Foundation.

The lasers utilized have been manufactured to specifications developed under FDA manufacturing codes by Bioquantum Technologies.

REFERENCES

1. T. S. Lam, R. P. Abergel, C. A. Meeker, J. C. Castel, R. M. Dwyer, and J. Uitto, Lasers in the Life Sciences 1, 61 (1987)

2. M. Boulton and J. Marshal, Lasers in the Life Sciences 1, 125 (1987)

3. R. P. Abergel, C. A. Meeker, R. M. Dwyer, M. A. Lesavoy, and J. Uitto, Lasers in Surgery and Medicine 3, 279 (1984)

4. D. Saperia, E. Glassberg, R. F. Lyons, R. P. Abergel, P. Baneaux, J. C. Castel, R. M. Dwyer, and J. Uitto, Biochemical and Biophysical Research Communications 138, 1123 (1986)

5. J. Uitto and G. P. Lansk, presented at the Sixth International Congress on Applications of Lasers and Electro-optics, San Diego (1987)

6. T.I. Karu and V.S. Letokhov, in Laser Photobiology and Photomedicine, S. Martellucci and A. N. Chester, Eds. (Plenum Press, 1985), pp 57

7. S. Passarella, E. Casamassima, E. Quagliariello, I.M. Catalano, and A. Cingolani, Ibid.

8. N. Kollias and W. R. Melander, Phys Let 57A, 102 (1976)

9. J. P. Biscar, Bull Math Bio 38, 29 (1976)

10. J. D. Rawn, Biochemistry (Harper and Row, 1983), pp 535-536

11. H. Frohlich, Adv in Electronics and Electron Physics 53, 85 (1980)

12. F. Oosawa, Polyelectrolytes (Marcel Dekker, Inc., 1971)

13. H. Eggerer and R. Huber, eds, Structural and Functional Aspects of Enzyme Catalysis. (Springer-Verlag, 1981)

14. M. Blank, ed, Mechanistic Approaches to Interaction of Electromagnetic Fields with Living Systems (Plenum Press, 1987)

LOW ENERGY LASER THERAPY

J. R. Basford, M.D., Ph.D.
Department of Physical Medicine
and Rehabilitation
Mayo Clinic and Foundation
Rochester, MN 55905

ABSTRACT

Low energy laser irradiation is promoted as a safe and effective treatment for a multitude of neurologi-cal, soft tissue and musculoskeletal conditions. Unfortunately, although a wide variety of laboratory and clinical effects have been reported, a mechanism of action is not established and therapeutic effec-tiveness is controversial. This paper briefly reviews the current clinical and experimental status of this interesting therapeutic approach.

INTRODUCTION

Early research with low energy lasers in the mid and late 1960s began in eastern Europe and Russia with initial efforts emphasizing wound healing, analgesia and cellular processes.[1,2] Over the years, this early activity has been supplemented further by research in that region, as well as, around the world. Nevertheless, despite a variety of interesting findings (Table 1), a mechanism of action is not established, treatment effectiveness remains arguable and Food and Drug Administration (FDA) approval for clinical use does not exist.

Currently however, low energy lasers (defined here as those with powers <50 mW) are used in many countries to accelerate wound healing, lessen pain and reduce inflammation in both animals and humans.[2,21-24] In the United States, "laser" treatment is less common and powers, for the most part, are restricted to powers of a milliwatt.[25]

TREATMENT RATIONALE AND MECHANISM OF ACTION

Two basic questions are appropriate when considering the potential effectiveness of low energy laser treatment: (1) does a significant amount of radiation reach the tissues being treated and, if it does, (2) how might a biological effect be produced? The first of these issues is addressed by considering the optical characteristics of tissue. The second, that of a mechanism of action, is more difficult.

The optical characteristics of tissues have been studied in detail. As a result, while light transmission, absorption and scattering are complex functions of tissue structure, pigmentation and wave-length, a number of general statements can be made. For example, a "window" of sorts exists for most soft tissues in the 0.60 to 1.3 um portion of the spectrum that includes most low energy lasers in clini-cal use. More specifically, the intensity of a beam in this region decreases by about 1/e (i.e., 37%) of its initial value at depths of 0.75 to 2.2 mm.[26] More graphically, about 1% of energy in a beam in the 0.605 to 0.850 um region penetrates the human chest wall[28] and a 1 mW HeNe laser (0.632 um) easily trans-illuminates a finger.

Thus, it is possible to accept that low energy laser radiation penetrates soft tissue well enough to deliver a reasonable amount of energy to superficial nerves, wounds and joints such as those in the hands and feet. Penetration to deeper depths is less and treatment effectiveness more problematical.

It is important to realize that, by definition, low energy laser treatment takes place at such low inten-sities that any effects that may take place result from the direct effects of the irradiation and not as the result of heating.[18,27-30] For example, if all the energy of a 50 mW laser beam (a power at the upper end of the low energy laser range) striking the surface of a two centimeter diameter area the skin for a minute is absorbed within a centimeter of the surface, the calculated tissue temperature elevation is less than 0.3° C. (Experimental measurements are in agreement with this expectation; minimal to 0.5° C temperature increases occur following irradiations at these energies.[13,31]) For the sake of com-parison, common physical therapy agents such as hot packs, ultrasound and shortwave diathermy may raise tissue temperatures by 5°C or more.[32]

It should be remembered that nonthermal photobiochemical processes occur throughout nature and are not uniquely associated with lasers. Ultraviolet light, for example, tans skin and kills germs with wave length specific reactions. Similarly other processes such as photosynthesis, vision and Vitamin D meta-bolism are more efficient at some wavelengths than others.

Although generalized heating does not occur, localized warming of subcellular structures is possible and may be capable of altering metabolic function. Restrictions, however, limit the magnitude of possible temperature inhomogenuit s.[33] For example, if the thermal relaxation time of an object is long compared with the treatment time warming occurs; if a relaxation time is short relative to the treatment time, little heating can occur. Specifically, small structures, such as mitochondria, which have large surface-to-volume ratios would be expected to have short relaxation times.

This expectation is correct. Relaxation times for objects of these sizes are known: nanoseconds for subcellular structures, microseconds for cells and milliseconds for 100 um tissue components.[33] Thus, for example, is it known that a XeF laser pulse of 0.05 to 0.4 J/cm^2 over 20 nsec can damage and kill melanocytes in the skin.[33] Exposure to similar energy levels occurs in low energy laser treatment, but requires seconds. Since seconds are many times longer than the relaxation times of these structures, selective heating during pulsed or continuous wave length low energy laser therapy is minimal.

Living cells maintain electrical gradients across their membranes and it is tempting to consider whether laser irradiation can disrupt these potentials. Focused high power laser beams can produce intensities of 10^{15} W/cm^2 [36] and have corresponding electric field strengths of 6×10^8 V/m. This is equivalent to a 4000-6000 V potential difference across the dimensions of a typical cell and is obviously large in comparison with the 50-70 mV potentials maintained by cells themselves. Beam intensities of low power lasers, on the other hand, are routinely less than 6 W/cm^2 and have corresponding electric fields of about 50 V/m. These fields are equivalent to 0.3-0.5 mV across a cell; a value that seems unlikely to perturb membrane potentials.

If low intensity laser irradiation does produce nonthermal reactions, the mechanism may involve either (1) properties of light in general, (2) the properties of laser radiation: collimation, coherency and monochromaticity or (3) the fact that lasers produce radiation that is more intense and/or more highly polarized than is normally available from other sources.

Information exists about these issues. For example, coherency and polarization may not be important as some studies report producing stimulative effects with noncoherent light.[1,2,10,37-39] In addition tissue scattering rapidly degrades beam coherency and low energy laser experiments are often done with fiber optic delivery systems which lessen both collimation and coherency. Given the number of studies which find stimulation of cellular processes following irradiation with very low energy noncoherent monochromatic sources, it may be that all that is needed is light at a specific intensity and wavelength.[10]

LABORATORY AND CLINICAL RESEARCH

As might be expected for a controversial technique, the research literature is fragmented and conflicting. Much work is poorly described and clinical evaluations, particularly in the earlier studies, are often neither controlled nor blinded. More recently research rigor and quality has improved. Nevertheless, as the following paragraphs illustrate, a multitude of scattered, and potentially inconsistent, results are reported.

Neuronal Function

Rochkind et al, for example, reported improved peripheral nerve regeneration in rats whose crush injured sciatic nerves were subsequently irradiated with a 17 mW HeNe laser.[40] Additional work by the same group, using the optic nerves of rabbits (as a model of CNS injury), also showed improved recovery and function following irradiation with a similar laser over a 8 to 15 day period.[41]

On a somewhat more applied level, some investigators find that low energy laser irradiation generates action potentials and suppresses clonus in humans.[40-44] Other studies, however, may not replicate these results.[45] In the same vein, some researchers report increased distal nerve latencies following irradiation,[42,44] while others find no change in either nerve conduction velocity, or action potential amplitude[27] following irradiation and no benefit in the treatment of median nerve compression neuropathy (carpal tunnel syndrome).[46]

Pain

Whether low energy laser irradiation produces analgesia also remains controversial. Thus, while some investgiations find no effect from low energy treatment, other describe pain reduction in animals as well as in a variety of human musculoskeletal, rheumatological and neurological conditions.

Musculoskeletal pain, in particular, has been an active area of study. Several studies,[47,48,49] for example, report 60-80% reductions in osteoarthritic pain following treatment with a variety of lasers (HeNe, Nd:YAG, and GaAlAs) and different techniques. Additional controlled studies of osteoarthritis and sports injuries[50,51] as well as uncontrolled studies with as many as 1600 subjects[24,52] also find treatment beneficial. However, not all investigators find low energy laser effective and investigations of epicondylitis,[29] as well as knee and thumb osteoarthritis may not detect benefit.[53,54,55]

Neck pain, headaches and back pain[23,48,49] have been studied in poorly controlled groups with 60-80% of the subjects reporting partial or total relief following treatment. Successful treatment of shoulder pain, tendonitis and periarthritis is also reported in uncontrolled trials[48,49,56] Other studies of tri-

geminal neuralgia, post herpetic neuralgia, radiculopathy and diabetic neuropathy also find 40 to 80% of those treated reporting some benefit.[28,47,48,49] While results such as these are intriguing, the studies are limited and can only be used to suggest further evaluation.

Rheumatoid Arthritis

Rheumatoid arthritis is another area of active investigation. One of the first controlled studies was a double blinded investigation of 30 patients reported in 1980.[68] At the conclusion of the experiment, the investigators reported a lessening in hand joint warmth, lessened pain, reduced erythema and improved function. With the exception of a decrease in platelet aggregation, laboratory and x-ray studies were unaltered.

It is significant that this study used a Q-switched laser at energies of 15-25 J. As such, it does not represent most low energy laser treatment since it involved higher energies than normal (15-25 J rather than 1-4 J) and extremely short pulse durations.

Other blinded studies of rheumatoid arthritis have been preferred with HeNe, GaAlAs and GaAs lasers at energies well within low energy range.[22,58,59,60] Most of the studies find treatment produces at least some lessening of pain, increase in function and/or reduction medication use. Some also report altered laboratory parameters such as the erythrocyte sedimentation rate (ESR), white count and C reactive protein (CRP) although a consistent pattern is not apparent. Whether or not these changes will prove to be clinically significant, remains to be seen.

Wound Healing

Acceleration of soft tissue wound healing (particularly within the first several days of wounding) is often reported in small animals such as rodents[4,38,39,61,62] as well as in humans (e.g., skin, mouth and cervix)[2,4,6,63] following low energy laser treatment. Unfortunately, the fact that many of the evaluations are poorly controlled and incompletely described makes interpretation difficult.

It may also be significant that the more successful studies are often done with animals such as rabbits, guinea pigs and rats whose skin is quite loose and heals in large part by contraction. Experiments with pigs, which have a more adherent skin and may serve as a better human model, tend to be less encouraging and may show little or no benefit.[28,64-67]

Safety

Since thermal damage and tissue destruction is not an issue with low energy laser therapy, safety issues center on protecting the eye (due to the sensitivity of the retina as well as the focusing ability of the cornea and lens) from direct exposure to the beam. For example, a brief glance at a 1 mW HeNe laser beam can produce a headache and protective lenses should be worn when using even the lowest powered lasers. Mutagenic and carcinogenic concerns are periodically raised but it should be remembered that lasers are prevalent in everyday life (bar code scanners, pointers, etc), industry and surgery, and that there has been a dearth of detrimental side effects.

REFERENCES

1.   N.F. Gamaleya, in Laser Applications in Medicine and Biology, M. L. Wolbarsht, Ed. (Plenum Press, New York, NY, (1977), p. 1

2.   E. Mester, A. F. Mester and A. Mester, Lasers Surg. Med. 5, 31 (1985)

3.   E. Glassberg, G. P. Lask and J. Uitto, American Society for Laser Medicine and Surgery Abstracts in Lasers Surg Med 8, 186 (1988)

4.   Z. Simunovic and A.D. Ivankovich, American Society for Laser Medicine and Surgery Abstracts in Lasers Surg Med 8, 175 (1988)

5.   K. Barabas, J. Bakos, D. L. Szabo, H. Sinay, G. Gaspardy, M. Bely, Zs. Balogh and G. Balint, American Society for Laser Medicine and Surgery Abstracts in Lasers Surg Med 8, 176 (1988)

6.   E. Mester, N. Toth, A. Mester, Laser Basic Biomed Res 22, 4 (1982)

7.   R. F. Lyons, R. P. Abergel, R. A. White, R. M. Dwyer, J. C. Castel, J. Uitto, Ann Plas Surg 18, 47 (1987)

8.   J. H. Herman and R. C. Khosla, Arthritis Rheum (abstract) 30 (Y Supplement), S128 (1987)

9.   L. B. Hardy, F. S. Hardy, S. Fine and J. Sokal, Abstract in Fed Proc 26, 668 (1967)

10. T. I. Karu, IEEE Journal of Quantum Electronics QE-23, 1703 (1987)

11. R. P. Abergel, R. M. Dwyer, C.A. Meeker, G. Lask, A. P. Kelly and J. Uitto, Lasers Surg Med 4, 291 (1984)

12. M. A. Trelles, E. Mayayo, L. Miro, J. Rigau and G. Baudin, American Society for Laser Medicine and Surgery Abstracts in Lasers Surg Med 8, 174 (1988)

13. H. Sato, M. Landthaler, D. Haina and W.B. Schill, Andrologia 16, 23 (1984)

14. S. Passsrella, E. Casamassima, S. Molinari, D. Pastore, E. Quagliariello, I. M. Catalano and A. Cingolani, FEBS Letters 175, 95 (1984)

15. S. Passarella, presented at the 1st Omega Low Power Laser Seminar, Guy's Hospital, London, (1988)

16. T. Kubasova, L. Kovacs, Z. Somosy, P. Unk and A. Kokai, Lasers Surg Med 4, 381 (1984)

17. S. Passarella, E. Casamassima, E. Quagliaraiello, G. Caretto and E. Jirillo, Biochem Biophys Res Comm 130, 546 (1985)

18. E.S. Vizi, E. Mester, S. Tizza, A. Mester, J Neural Transm 40, 305 (1977)

19. I. Itzkan, S. Tang, D. Bourgelais, American Society for Laser Medicine and Surgery Abstracts in Lasers Surg Med 8, 175 (1988)

20. D. T. Yew, S. L. L. L. Wong and Y. Chan, Acta Anat 112, 131 (1982)

21. Y. Oyamada, S. Izu, (abstract) In Proceedings of the 6th Congress of the International Society for Laser Surgery and Medicine, 80 1985)

22. H. C. Colov, N. Palmgren, G. F. Jensen, K. Kaa, M. Windelin, Submitted to Lasers in Medicine and Surgery (1987)

23. K. H. Caspers, (trans) Phys Med Rehabil 18, 426 (1977)

24. C. Shiroto, K. Ono and T. Ohshiro, Abstract in Lasers Surg Med 6, 172 (1986)

25. J. A. Kleinkort, R. A. Foley, physical therapy, Am J Acupunc 12, 51 (1984)

26. R. R. Anderson and J. A. Parrish 26. J Invest 77, 13 (1981)

27. D. G. Greathouse, D. P. Currier and R. L. Gilmore, Phys Ther 65, 1184 (1985)

28. R. Brunner, D. Haina, M. Landthaler, W. Waidelich and O. Braun Falco, Curr Probl Dermatol 15, 111 (1986)

29. T. Lundeberg, E. Haker and M. Thomas, Scand J Rehabil Med 19, 135 (1987)

30. R. L. Fork, Science 171, 907 (1971)

31. G. Boussignac, C. Vieilledent, H. Geschwind, (abstract) In Proceedings of the 6th Congress of the International Society for Laser Surgery and Medicine, 77 (1985)

32. J. F. Lehmann, B. J. De Lateur, in Krusen's Handbook of Physical Medicine and Rehabilitation, F. J. Kottke, G. K. Stillwell and J. F. Lehmann, Eds. (W. B. Saunders, Philadelphia, PA, (1982) 275

33. R. R. Anderson and J. A. Parrish, Science 220, 524 (1983)

34. A. L. McKenzie, J. A. S. Carruth, Phys Med Biol 29:619-641 (1984)

35. P. J. Kolari, Arch Dermatol Res 277, 342 (1985)

36. V. T. Tomberg, Nature 204, 868 (1964)

37. S. Young, W. Harvey, M. Dyso and C. Diamantopoulos, American Society for Laser Medicine and Surgery Abstracts in Lasers Surg Med 8, 186 (1988)

38. D. Haina, R. Brunner, M. Landthaler, O. Braun-Falco, W. Waidelich, Laser Basic Biomed Res 22, 1 (1982)

39. J. S. Kana, G. Hutschenreiter, D. Haina, W. Waidelich, Arch Surg 116, 293 (1981)

40. S. Rochkind, L. Barrnea, N. Razon, A. Bartal and M. Schwartz: Neurosurgery 20, 843 (1987)

41. M. Schwartz, A. Doron, M. Erlich, V. Lavie, S. Benbasat, M. Belkin, and S. Rochkind, Lasers Surg Med 7, 51 (1987)

42. J. B. Walker and L. K. Akhanjee, Brain Res 344, 281 (1985)

43. J. B. Walker, Brain Res 340, 109 (1985)

44. C. E. Bork and L. Snyder-Mackler, J Am Phys Ther Assoc 68, 223 (1988)

45. W. Wu, R. Ponnudurai, J. Katz, C. B. Pott, R. Chilcoat, A. Uncini, S. Rapport, P. Wade and A. Mauro, Brain Res 401, 407 (1987)

46. R. Ysla and R. McAuley, Arch Phys Med Rehabil 66, 577 (1985)

47. J. Walker, Neurosci Lett 43, 339 (1983)

48. M. Kroetlinger, Acupuncture Electrother Res 5:297-311 (1980)

49. G. Calderhead, T. Ohshiro, E. Itoh, T. Okada, Y. Kato, Laser Acupunct 21, 1 (1982)

50. G. Lonauer, Abstract in Lasers in Surgery and Medicine 6, 172 (1986)

51. O. Emmanouilidis and C. Diamantopoulos, Abstract in Lasers Surg Med 6, 173 (1986)

52. C. Bieglio and G. de Bisschop, Abstract in Lasers Surg Med 6, 173 (1986)

53. J. R. Basford, C. G. Sheffield, S. D. Mair and D. M. Ilstrup, Arch Phys Med Rehabil 68, 794 (1987)

54. R. Ysla and R. McAuley, Arch Phys Med Rehabil 66, 577 (1985)

55. R. McAuley and R. Ysla, Arch Phys Med Rehabil 66, 553 (1985)

56. J.A. Kleinkort and R. A. Foley, Clin Manag Phys Ther 2, 30 (1982)

57. M.A. Trelles and E. Mayayo, Lasers Surg Med 7, 36, (1987)

58. J.J.M. Soto and I. Moller, (Artritis Reumatoidea) Boletin Centro Documentacion Laser 14, 4, (1987)

59. H. Bliddal, C. Hellesen, P. Ditlevsen, J. Asselberghs and L. Lyager, Scand J Rheumatol 16, 225 (1987)

60. F.S. Mach, V.V. Tsurko, O. I. Lebedeva and A.P. Budreiniy, Rheumatologia 3, 36 (1983)

61. J. P. Cummings, Phys Ther 65, 737, (1985)

62. O. Ribari, Revue de Laryngolo 102, 11, (1981)

63. L. Kovacs, L. Varga, I. Palyi, S. Tisza, S. Gundy, E. Unger, P. Lapis, Laser Basic Biomed Res 22, 14 (1982)

64. J.R. Basford, H.O. Hallman, C.G. Sheffield, and G.L. Mackey, Arch Phys Med Rehabil 67, 151, (1986)

65. J.S. Surinchak, M.L. Alago, R.F. Bellamy, B.E. Stuck and M. Belkin, Lasers Surg Med 2, 267, (1983)

66. F.H.M. Jongsma, A.E.J.M. Bogaard, M.J.C. van Gemert and J.P. Hulsbergen Henning, Lasers Surg Med 3, 75 (1983)

67. J. Hunter, L. Leonard, R. Wilson, G. Snider and J. Dixon, Lasers Surg Med 3, 285, (1984)

68. J.A. Goldman, J. Chiapella, H. Casey, N.H. Bass, J. Graham, W. McClatchey, R.V. Dronavalli, R. Brown, W.J. Bennett, S.B. Miller, C.H. Wilson, B. Pearson, C. Haun, L. Persinski, H. Huey, M. Muckerheide, Lasers Surg Med 1, 93, (1980)

TABLE 1 -- CELLULAR EFFECTS OF LOW ENERGY LASER IRRADIATION

Phenomenon (References)	Change and Reported	Model	Laser
Collagen and protein synthesis (3-8)	Increase & Decrease	Human fibroblasts, rabbit skin, human synovium, Bovine cartilage	HeNe HeNe+GaAs Nd:PO$_4$ glass Nd:YAG
RNA Synthesis (3)	Increase	Mouse skin	HeNe
Cell Proliferation (9-11)	Increase & Decrease	Mouse fibroblasts, Human lymphocytes	Ruby HeNe GaAs
Cell Granule Release (12)	Increase	Mouse mast cells	HeNe
Cell Motility (13)	Increase	Human Sperm	Kr
Membrane Potential (14-16)	Increase	Rat liver mitochrondria, Human fibroblasts	HeNe
Cell Binding Affinities (16,17)	Increase	Human lymphocytes and fibroblasts	HeNe
Neurotransmitter Release (18)	Increase	Acetylcholine (guinea pigs)	Ruby
Oxyhemoglobin Dissociation (19)	Increase		
Phagocytosis (2)	Increase	Human leukocytes	Ruby
ATP Syntheses (14-15)	Increase	Rat liver mitochrondria	HeNe
Intercellular Matrix (20)	Increase	Mouse retina	HeNe
Prostaglandin Synthesis (6)	Increase	Rat skin	HeNe

SMALL ARTERY REPAIR WITH THE CO2 LASER

Eric A. Leefmans, M.D., John V. White, M.D., Mira L. Katz B.S., R.V.T.
and Anthony J. Comerota M.D., F.A.C.S.
Temple University School of Medicine, Philadelphia, PA 19140

ABSTRACT

Conventially sutured small arterial anastomoses have a high failure rate. Laser fusion arterial anastomoses of 1-2 mm. vessels have been successful and suggest a possible role of the laser in decreasing the high failure rate of small vessel anastomoses. We have, therefore, undertaken a study to examine if laser fused arterial anastomoses are feasible in 3-4 mm. vessels. Our short term data not only supports the feasibility of laser fused arterial anastomoses in the size range but also suggest that the healing process involves less inflammation and consequently less stricturing.

INTRODUCTION

Small vessel vascular repairs, though easy in principle, continue to vex even the best surgeons. There has been much improvement both in technique and materials since Alexis Carrel first introduced his triangulating technique in 1902. Nonetheless, early failures of distal small vessel bypasses are still common. It seems clear that we are a long way from the perfect anastomosis. Both systemic and local factors are involved in these early anastomotic failures. Hypercoagulable states and thrombocytosis enhance systemic thrombotic potential. Locally, the transmural passage of the needle induces multiple sites of injury to the arterial wall. The presence of suture material may incite inflammation, harbor infection, lead to granuloma formation, and alter or inhibit normal healing. In small vessels even apparently minor defects or trivial inflammation may result in anastomotic failure. Laser fusion of tissue eliminates the local injury induced by needle and suture. This has prompted us to investigate laser fusion as a possibly less traumatic method of performing vascular anastomoses.

THE LASER

Since the first report of laser vascular repair in 1979 (1) several investigators have studied laser vascular repair in search of the ideal technique for performing a vascular anastomosis (2,3). Amoung the currently available lasers, the CO2 laser has several merits which make it an excellent choice for vascular repair. With its 10.06 um. wavelength, the CO2 laser is primarily absorbed by water and its tissue interaction is not chromophore dependent. Consequently, the ubiquity of water in tissue results in the avid absorption of the laser beam near the vessel surface. This shallow depth of penetration permits very precise control of the tissue effect. Water absorption of the CO2 laser energy also results in the rapid dissipation of heat generated by the photothermal laser, thereby minimizing injury to adjacent tissue. Finally, the CO2 laser has milliwatt capability allowing the surgeon to fine tune the power output to 1/1000 of a watt (1 milliwatt).

POWER DENSITY

A standard Sharplan 1040 CO2 laser is attached to an operating microscope with a microslad containing a 300 mm. lens; with this set up, we have performed laser anastomoses of transected rabbit aortae. The laser power is set at 200 mW. Periodically the power delivered is checked with an external meter. The 300 mm. coupling lens of the microslad creates a 420 um. spot diameter which yields a power density of $145W/cm^2$.

Energy fluence, per se, is not an end point in the creation of an anastomosis. Instead, the visualization of light brown vessel edges melted together is used.

TECHNIQUE

The anastomosis is performed in four steps. First, the divided ends of the rabbit aorta are brought into tension-free approximation with the aid of an Acland clamp. Next, three 10.0 nylon mattress sutures are equidistantly placed as stay sutures. The placement of the mattress sutures everts and coapts the vessel edges. Eversion of the vessel edges increases the surface area to be fused together. The third step involves placing diverting tension on the stay sutures in a direction perpendicular to the long axis of the vessel. The final step is simply the directing of the laser beam to weld the vessel edges together. The laser power is continuously applied until a light brown color is seen along the vessel ends, which signifies fusion. Upon completion, an appropriately constructed laser fusion anastomosis should not appear charred or stenotic (Fig. 1).

RESULTS

In a series of twenty-one rabbit laser anastomoses constructed using this technique, there was a 100% success rate and a 100% patency rate, from 7 days to 6 months. Healing was assessed histologically from 7 days to 6 months postoperatively. A few additional anastomoses were performed to assess the acute histology at one hour.

Immediately after laser fusion, the flow surface in the area of the anastomosis is denuded of endothelial cells. The exposed collagen is dotted with only a few small platelet aggregates. Few viable cells remain in the media, and collagen in both the media and adventitia appears melted together. A "cap" of fused collagen bridges the adventitial surface of the vessel edges (fig. 2). The initial injury caused by the laser is therefore transmural, but there is no foreign material left behind to propagate further injury.

Histologically, at one week, there is minimal inflammation at the anastomotic site. The intima and media are only slightly thickened. A coagulum of collagen bridges the adventitial edges of the anastomosis. The only granulomas present are associated with stay sutures, not with the laser welded edges (fig. 4).

Scanning electron microscopy of the flow surface demonstrates smooth exposed acellular collagen acutely without significant platelet aggregations (fig. 3). By one month the intimal surface is covered with endothelium indistinquishable from that of distant sites. The only disruptions of the anastomotic site are the crevices dug by the stay sutures.

CONCLUSIONS

Using a power density of $145W/cm^2$ successful laser vascular anastomoses can be performed in 4mm rabbit aortae. Patency rates are excellent. The histology and electron micrographs are extremely promising in terms of the lack of inflammation, the lack of intimal and medial thickening, and the virtually flawless integrity of the flow surface after one month. Like sutured anastomoses, failure rates are technique dependent, emphasizing the need to critically evaluate and to define   chnical method of laser fusion if these anastomoses are to play a role in clinical surgery.

REFERENCES

(1). K.K. Jain, W. Gorisch, Repair of small blood vessel with the Neodymium-YAG laser: A preliminary report. Surgery 684-688, June, 1979.

(2). J.V. White, et al., Tissue fusion effect of the CO2 laser. Surgical Forum XXXVI: 455-457, 1985.

(3). C.R. Neblett, J.R. Morris, S. Thomsen, Laser-assisted microvascular anastomosis. Neurosurgery 19: 914-933, Nov., 1986

Fig. 1. Appearance of a laser fusion anastomosis immediately after completion.

Fig. 2. Histological appearance of a laser fusion anastomosis on day 1. Note the "cap" of collagen bridging the adventitial surface of the vessel edges. (Masson trichrome stain)

Fig. 3. Electron micrograph of the flow surface of the area at a newly formed anastomosis. Note collagen is intact. A few scattered aggregates of platelets cover the denuded subendothelium.

Fig. 4. Histological appearance of a laser fusion anastomosis at one week. Note the prominent fusion "cap" on the adventitial surface and the lack of inflammation. (H. and E. stain)

INDUSTRIAL LASER USE IN NAVY DEPOTS

Dr. Julius Alker
Industrial Engineer
Naval Air Systems Command
Naval Air Systems Command Headquarters
Washington, DC 20631-4300

Abstract

The United States Navy depots comprise the largest industrial complex on earth. They rework and repair ships, aircraft, engines, electronic instruments and components. Industrial lasers find increased use in these operations, such as, specialized, large scale measuring instruments used in dimensional verification, laser robotic vision controlled operations, scanners, and robotic depainters. A 3-D vision system combined with a seven axis inspection robot and a sophisticated computer system reduced propeller inspection time 90%. This combined with six axis robots shapes and balances ship propellers. 3-D vision systems provide increased welding capabilities at Naval shipyards. At the opposite end of the scale, laser scanners used in reverse engineering work to 0.002" tolerances and combined with CAD systems are programmed to provide shop level drawings. Naval air depots have under development computer controlled equipment with robotic laser vision systems. One system, a laser cutter and welder, will rework major aircraft engine components. Pairs of self propelled laser guided robotic depainter units are scheduled for operations in the mid 1990s. A robotic laser inspection and welding system reduces repair times several hundred hours an engine.

Discussion

Introduction

With six naval aviation depots, eight ship yards, an avionics center, numerous weapon and ordnance stations, ranges, laboratories and local repair and maintenance facilities the U.S. Navy commands the largest repair, research and maintenance complex on earth. An industrial complex of such magnitude routinely uses a number of laser cutting, welding, measuring and other such equipment, most of which are found in many industrial facilities. This presentation will deal with six specific types of equipment developed for the U.S. Navy; all use lasers vision systems in combination with robotics, sophisticated computation equipment, and often with machining centers.

Robotic laser depainting

The U.S. Navy has the largest depainting activity on earth. In the equipment rework or repair cycle paint is often removed from aircraft, ships and components. Current depainting methods use liquid chemicals, producing a large amount of hazardous liquid waste and also increase the total volatile organic compound levels in the air. This method must be eliminated in some areas of the country. The currently practiced alternate method to chemical depainting, abrasive blasting, produces a large amount of solid waste, which is easier to handle than the liquid and gaseous wastes derived from chemical depainting, but still constitutes waste elimination problems. The new method of aircraft laser depainting uses vehicles provided with a laser vision system able to determine the composition of the target area. The equipment is first flooded with xenon white light to standardize wave length, as the spectral analysis uses the reflected wave length emitted by the target area. The system can distinguish among paint, primer, and different substrates. Thus, it can be programmed to remove paint only, or paint and primer. When the composition of the target is determined, and plans call for its removal, the 4-6kW CO_2 pulsed laser fires to remove the paint of 1cm^2 area at a time. Operations are performed in a controlled environment constructed of five minute laser resistant walls, eliminating the release of organic compounds to the atmosphere, while protecting people from laser radiation. Current plans call for one robot on each side of the airplane (Figure 1). The operator positions the robots and then the automated system removes all the required material within the reach of the robot (generally a 2 FT strip). The operator will observe the operation and will be able to shut the cell down in case of malfunction. This method will reduce aircraft depainting costs 60%. The expected operational date for the equipment is January 1994.

Heat shield inspection/welding system

Inspection of engine heat shields is labor intensive, requiring 1,600 hours of preparation per engine for the P-3 aircraft. Defects in the heat shield lead to serious degradation of adjacent metal parts. To repair cracks the engine must be removed. If there are no defects in the heat shield, engine removal is a waste of time. The equipment under development will inspect and repair the heat shield of P-3 aircraft

without engine removal. The equipment is of a robot mounted on an aircraft stand, connected to a monitor and a microprocessor and supplied with a flexible multi-jointed arm fitted with five interchangeable end-effectors. The tail pipe is removed (1). The robot is mounted on the tail pipe mounting ring with the help of a keyway and key. With the cleaning end-effector the heat shield is cleaned with brushes and a solvent (2). Then the inspection end effector is mounted (3). Side looking charged couple devices and the light delivered from a strobe light by fiber optics provide for vision. The information is provided to the microprocessor and is stored in memory. The operator notes the defects, if any (4). The defective areas are cleaned to bare metal by the third end-effector (5). After cleaning, a stainless steel mash is placed over the defective areas and spot welded in place by a 1.5kW Nd:YAG laser through fiber optics, to prevent interference with the microprocessor (6). Finally, water soluble, high heat activated material is introduced into the mash (7). After the engines are fired the water evaporates from the sealant and the stainless steel mash fuses in place. The equipment is expected to be in operation by December 1990.

Cutting-welding work cell

A work cell has been developed primarily for the repair of jet engine combustion chambers. It will be able to handle work pieces up to 500 lbs, if within a 4 FT cube. The principle is the combination of a 3-D robotic vision system with robotic cutting and welding. All these are controlled by sophisticated computer systems. The work piece is placed on a two-shuttle system, so that while one work piece is worked, the other one can be loaded. The damaged areas are inspected and marked. The laser head is guided to the possible defective areas. The five watt argon ion laser beam delivered by fiber optics provides the light for the 3-D vision system. The vision system computer locates the defective areas with the help of the lateral effect silicon photodiod. It tracks the defect and determines whether it is a repairable or replaceable defect. Repairable cracks are welded, while damaged parts are removed by the 1.5kW CO_2 laser cutter. Pressurized nitrogen purges the beam delivery system, keeping particles away from the optics, while the weld is flushed by argon gas. The information on the cut is fed into the computer, which guides an other cutter to shape a replacement part. This part is fitted by the operator and welded in place. The entire system has unprecedented capabilities, not measurable at this time. It is estimated that productivity will be increased 100% with half the current staff. The system is expected to be in full operation by February 1989.

3-D Weld Seam Tracking System

The Naval Sea Systems Command is developing a welder combined with laser visual control for repairing small, irregular parts. The system provides a one pass laser tracking system in the presence of the arc. The computer with the 10 milliwatt infrared laser photodiod tracks the weld seam and identifies the weld type, measures the groove's angle, depth, and width approximately three inches ahead of the torch. It takes pictures at 1/30 second intervals, feeding this information into the computer, which then controls the six axis robot holding the torch. The operator can select the weld type and move the welding system rapidly between areas using a six-axis joystick. The equipment is expected to be in operation by 1992.

Reverse engineering

The program has two robotic vision and scanning systems, both to be combined with computer aided design (CAD) now under development.

The Naval Sea Systems Command's system will be used to plot ship layouts with the use of three strategically placed scanners using class I infrared photodiod lasers of 10 milliwatt power, developing a three dimensional image of the area. The image is then printed out, as is, or is transformed to working drawings by the CAD system. The tolerances are expected to be at the 0.1" level at 12 foot distance. This will help in the preparation for ship overhaul.

The Naval Supply Systems Command developed a similar system for the Rapid Acquisition of Manufactured Parts project. In this case four strategically placed scanners of one milliwatt capacity infrared laser photodiods develop the image of an object with 0.002" accuracy at four foot distance. This system combined with a CAD will be used in reverse engineering of parts not available on the market. Expected operational date of the integrated systems is January 1990.

Laser work station for propellers

It was always difficult to measure and shape propellers with conventional equipment. It was especially difficult to verify the specific complex curvatures. Furthermore, minor adjustments by grinding, chipping, welding, etc., could result in rough surfaces or deformations. The new automated propeller work station complex includes (1) a seven axis inspection robot using an infrared high pulse rate photodiod laser combined with a camera measuring system. It takes measurements every 0.1", or 2,000 times as many as used to be with conventional methods. This combined with a computer provides both a visual tracing of the passes and builds up a digital data base, creating an excess material map in the preprogrammed computer. The data can be printed out, for a permanent record. The computer provided with the "ideal" dimensions of the propeller in its data base controls the other stations of the system. Out of tolerance areas are then shaped (2) (3) by two six-axis robots by drilling, grinding, machining and welding. Finally, (4) balancing and checking of the finished product is performed by computer controlled equipment which indicates to the operator where to take off material. The final results are stored in memory and propellers are compared to this data base during overhauls or repairs. The equipment is partially operational. It will be expanded in the near future.
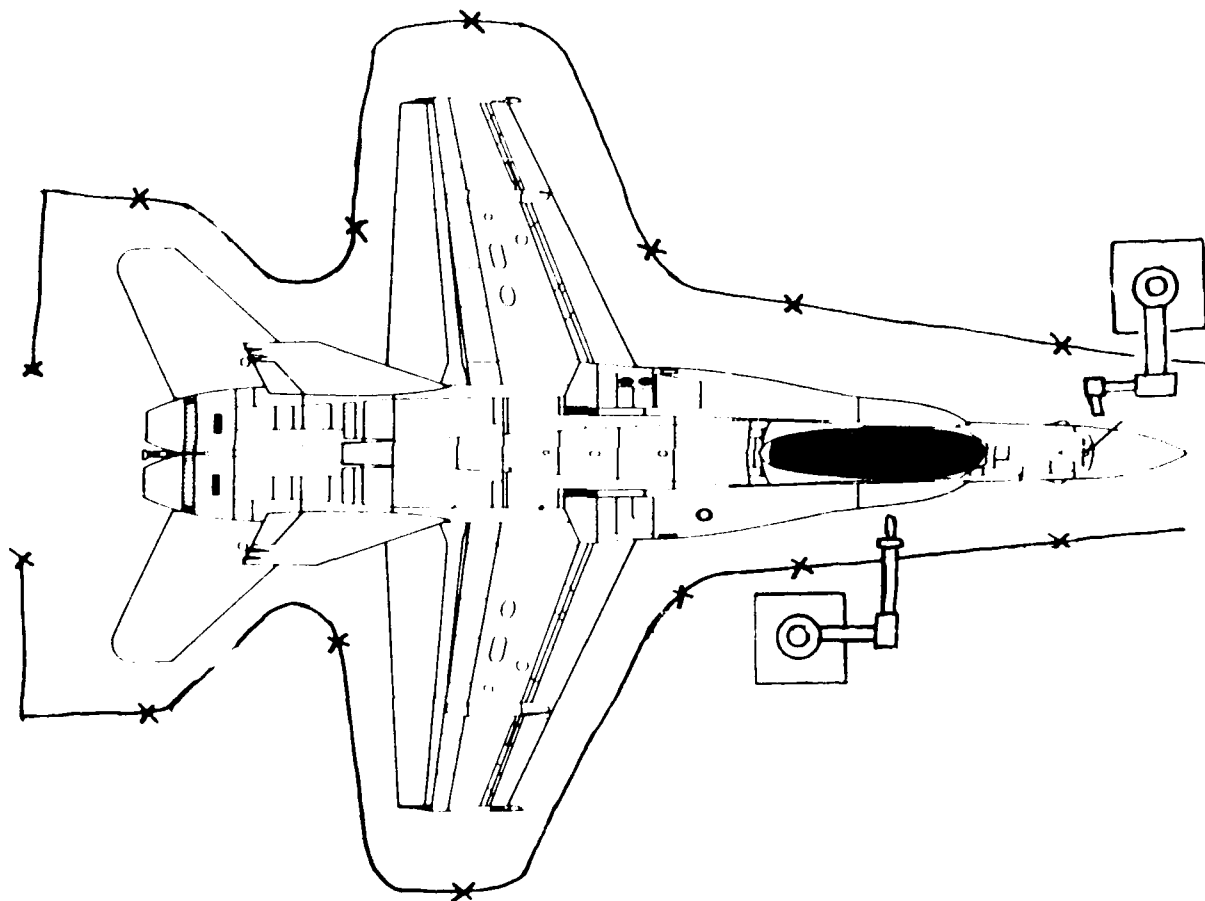
Figure 1.

ACOUSTIC SIGNALS FROM LASER BACK REFLECTIONS

W.M. Weerasinghe, J.N. Kamalu, W.M. Steen and R.D. Hibberd
Imperial College of Science, Technology and Medicine
Centre for Robotics and Automated Systems
Exhibition Road, London, SW7 2BX, England

Abstract

An acoustic technique is described to detect laser weld defects. The acoustic signal is compared with signals from a number of other sensors. The feasibility of using the acoustic signal in a real time knowledge based system for the control and monitoring of laser welding is shown.

Introduction

The implementation of real time knowledge based systems in manufacturing is increasingly becoming feasible with the advent of fourth generation fast computers. A good sensory signal to indicate the condition of the process is an important aspect of any control system. Acoustic signals emanating from beam handling mirrors have been shown to contain information relevant to both the condition of the laser and the process (1,2). The present paper describes the use of these acoustic signals in real time monitoring of laser welding and also a comparison is made with other available signals.

Experimental

Experiments were performed with a fast axial flow type 2 KW CO_2 laser, manufactured by Control Laser. The target material was mild steel. Argon was used as a shielding gas. Figure 1 illustrates the various sensory signals which were investigated. Refering to figure 1, S1 is a pyroelectric detector which looks at the CO_2 beam as emitted from the laser. It detects a small fraction reflected from the KCL flat. S2 is also a pyroelectric detector which looks at the CO_2 laser radiation reflected back from the workpiece. Again, a small fraction is reflected off the KCL flat. S3 is a ceramic piezo-electric acoustic transducer (Dunegan PAC WD) which responds to high frequency (>100KHz) acoustic stress waves in the water cooled copper mirror. S4 is also a similar acoustic transducer, which detects acoustic shock waves which are generated by laser induced plasmas and transmitted through air (3). S5 is a fast response silicon photo diode which looks at the visible plasma intensity during welding (4).

The pyroelectric detector system response was broad band (from 100 KHz up to 5MHz). A chopper was not necessary as the objective was to look at inherent temporal changes. The acoustic transducers were non-resonant with a broad band response between 100 KHz and 1.2 MHz. Unwanted lower frequency noise signals were not picked up, for example the noise from the flowing water in the mirror. All signals were time averaged using a fast r.m.s. device (bandwidth 2 MHz).
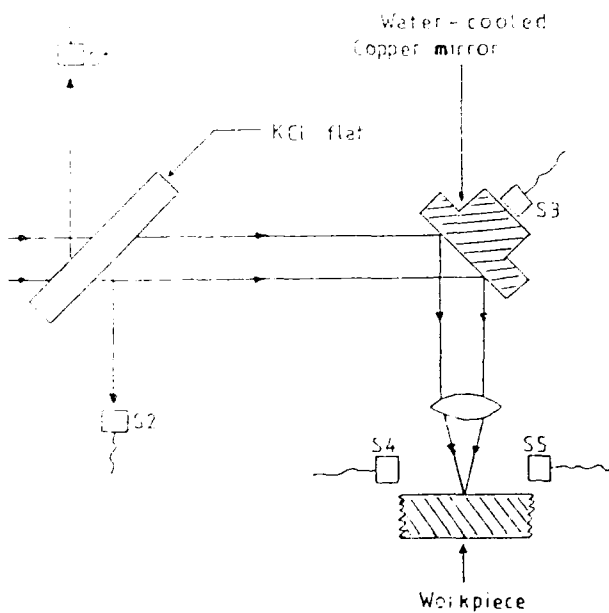

Figure 1: Experimental set-up for laser weld monitoring (gas shield nozzle not shown).

Signal Characteristics

The acoustic transducer S3, (Fig 1) responds to thermally induced stress waves in the copper mirror which are caused by high frequency intensity fluctuations in the beam. These intensity fluctuations are inherent in all lasers and are caused by, (5), superposition of axial and transverse modes (20 to 200 MHz), relaxation oscillations and, mode instabilities due to non-linear gain saturation (50 KHz to 5 MHz), variations in pumping power (for example, current ripples, mechanical and thermal instabilities of the laser structure, Hz to KHz). Of particular relevance to laser welding are relaxation oscillations which can be induced by optical feedback (6, 7). Back reflections from the workpiece enter the laser cavity and return as amplified damped oscillations. The frequency of the oscillations are given by (7, 8):

$$ \nu = \frac{1}{2\pi} \left[\frac{q \, g_0 - 1}{t_s \, t_c} \right]^{\frac{1}{2}} \quad Hz \tag{1} $$

and the decay time or the damping coefficient is given by:

$$ T_d = \frac{2 \, t_s}{(q \, g_0)} \quad sec. \tag{2} $$

where q is the unsaturated gain, g_0 is the gain at threshold, t_s is the lifetime of the upper excited laser level and t_c is the photon cavity lifetime. Equations (1) and (2) in effect describe the laser response to a step disturbance and such disturbances are caused by back reflections from the workpiece.

It can be shown that the frequency of the damped oscillations calculated by equation (1), lies within the bandwidth of the acoustic transducers, for values of $q \, g_0 = 1.8$ (9), $t_s = 0.4$msec. and $t_c = 0.4$nsec., relevant to the laser used. Further, if the time interval between back reflection disturbances are small compared to T_d in equation (2), the oscillations will be sustained and the beam intensity will be amplitude modulated according to weld plasma dynamics with a carrier frequency given by equation (1). This is illustrated in figure (2). Further, according to equation (1), the carrier frequency is independent of welding parameters. It only depends on laser parameters.
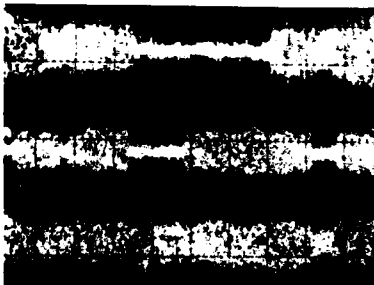

Figure 2: Total intensity modulation (bottom), due to relaxation oscillations which are sustained by frequent disturbances. The top two traces show partial modulation due to less frequent disturbances. Signals are not time averaged. 1 msec/div, 500 mv div.

There are also inherent disturbances in the laser which give rise to relaxation oscillations and, other instabilities may also lie within the response bandwidth of the detector. Acoustic signals generated by inherent fluctuations are generally weaker than those induced by weld back reflections and will be of different frequency if caused by phenomena other than relaxation oscillations.

The signals from the sensors S1, S2 and S3 are related to weld plasma stability. This is particularly so because the nature of the sensor elements is such that the sensors can only respond to changes in the measured physical quantities. The back reflector is in fact the weld plasma, the reflectivity of which depends on its density. Plasma 'stability' comprises the absolute changes in plasma density, the rate of change and the time interval between such changes. These three aspects of the plasma are closely related to the weld quality and each aspect introduces a particular characteristic to the time resolved strain signals from the sensors S1, S2 and S3.

Sensors S1 and S2 respond to plasma stability in addition to plasma 'volume' which does not necessarily relate to weld quality. Further, signals from S4 and S5 are direction sensitive and are orthogonal detection devices whereas S1, S2 and S3 detect co-axial with the beam.

Sensor S3 is truly 'non-contact'. A disadvantage is that weak characteristics of the laser are superimposed on the weld signal. Furthermore, damping characteristics of the mirror also affect the weld signal. These effects can be minimised by selecting a mirror with sufficient mass and, filtering the laser signals which are usually of a different frequency.

Detectors S1 and S2 require a beam sample but can be part of a feed-back lock system (10). They are susceptible to damage by unexpected power spikes. Further, because the pyro-electric sensor element area is small, only a small area of the weld pool will be viewed, whereas the copper mirror collects and integrates signals from the weld pool as a whole. Therefore, an array of pyro-electric sensors or focussing optics would be required to collect and analyse all the signals from the weld pool in the same manner as S3. An array of sensors would offset any error introduced by the variation in the transducing 'efficiency' across a single sensor element.

In summary, all detectors except S5 are a.c. driven, i.e. they respond to changes in the measured physical quantities and not to absolute constant values. For example, the pyro-electric detector generates a voltage proportional to the change in temperature of its sensing element caused by a change in intensity of radiation incident upon it. The sensitivity of the acoustic transducers drops sharply below 100 KHz and above 1.2 MHz. Unless otherwise stated, all signals presented are the time averaged r.m.s. envelope of a high frequency base signal.

Results and Discussion

Figure 3 shows the effect of back reflections on the laser output stability. The signals shown are from the optical signals S1 and S2. Initially, the beam was transmitted through the lens assembly and 'dumped'. The workpiece was then traversed under the beam for bead on plate welding.


Figure 3: The effect of back reflections on the laser output stability. 0.1sec./div., 0.1v div. S1 (bottom), S2 (top).

The signals shown in Figure 3, are the time averaged envelope of a high frequency (>100 KHz) base signal generated by the pyro-electric detectors. The signal S1 (bottom) increases during welding and remains low when the beam is 'dumped'. S2 (top), which looks at back reflections, responds only during welding. The increase in the signal S1 during welding represents an increase in beam intensity fluctuations and not an increase in laser power.

The observed frequency from sensors S1 to S4 was 200 - 290 KHz. The calculated frequency from equation 1 is 350 KHz. The observed frequency was independent of weld parameters. Frequencies up to 10 KHz were observed from the photo diode, S5.

Figures 4 (a,b), 5 (a,b) and 6 (a,b) are typical representative data acquired from a number of observations which show the signal S3 compared with S1, S4 and S5. The signals relate to bead on plate welding on a workpiece which was machined to reduce in thickness in steps of 0.25 mm along the welding direction. The objective was to look at the signals when the workpiece was brought in and out of focus during welding. With reference to figures 4, 5 and 6, the following observations were made
a) The sharp pulses at regular intervals correspond + steps in the workpiece. Therefore, a vertical distance of 0.25 mm is represented by the pulse interval. The lens focal length was 100 mm and the laser power density used was of the order 3×10^6 W/cm^2.
b) There is no correlation between S3 and S5 as shown in figure 4. The position where S3 is a minimum does not correspond to the position where S5 is a minimum. However, metallographic examination of the welds showed that the position of minimum S3 corresponds accurately to the position of deepest weld penetration.
c) There is no correlation between S3 and S4 as shown in figure 5. As was mentioned earlier, S4 and S5 respond to plasma 'volume' and 'intensity' in addition to 'stability'.
d) Good correlation was observed between S3 and S1 as shown in figure 6. Good correlation was also observed between S1 and S2 (see figure 7).
e) As was mentioned earlier, the signals from the sensors S1, S2 and S3 are only related to the weld plasma stability. The plasma density at a particular local area increases to a critical value and then reduces in a chaotic manner by rarefaction due to the corresponding changes in reflectivity and absorbed laser energy and, also due to melt pool dynamics. On either side of the focus, the plasma is highly unstable. For a condition of

higher laser power density, the absolute changes in plasma density will be smaller and the frequency or the rate of change will be higher, resulting in a more stable plasma. The corresponding effects on the laser back reflections are that the intensity fluctuations will be smaller and the frequency of disturbances entering the laser cavity will be higher. Therefore, for a condition of maximum plasma stability, the r.m.s. value of the signals S1, S2 and S3 will be a minimum due to the smaller fluctuations and the signal envelope will be less 'noisy' due to total modulation of the beam caused in a stochastic manner by the higher frequency of disturbances.

If the rate at which the plasma becomes stable (focus in) is lower than the rate at which it becomes unstable (focus out). Therefore, it is possible to infer which way the position of the focus has moved.

Figure 8 shows detection of a machine 1 mm wide 'V' groove. The welding speed was 100 mm/sec. In addition to the 'V' groove, spurious characteristics are shown on S1.
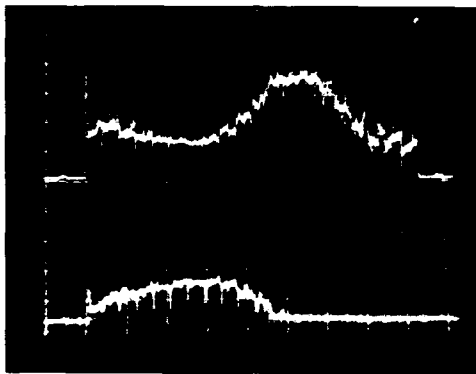
Figure 4(a): Bead on plate welding at 20 mm/sec. The workpiece was brought into focus from the left. S3 (top) is high on either side of the focus and reduces to a minimum near the focus. S5 (bottom) increases to a maximum near the focus.
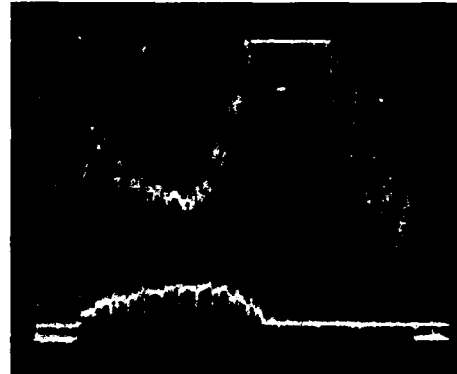
Figure 4(b): Magnification of the focus area in figure 4(a), showing no correlation between S3 and S5.
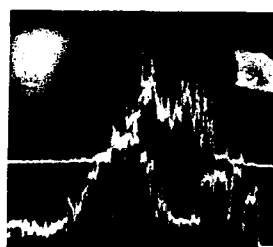
Figure 5(a): Same as 4(a). S3 (bottom) and S4 (top). Events outside intense plasma area are not recorded by S4.

Figure 5(b): Same as 5(a). S3 (bottom) and S4 (top). The general shape of S4 has changed.
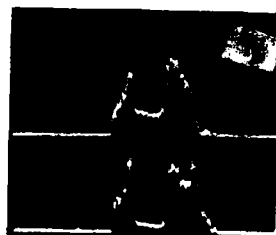

Figure 6(a): Same as 4(a). S3 (top) S1 (bottom). Shows good correlation.
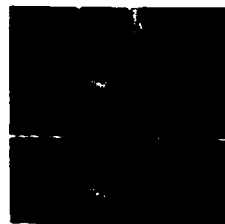
Figure 6(b): Magnification of the focus area in figure 6(a).

742
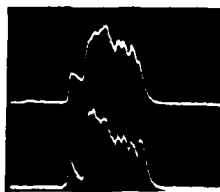
Figure 7: Weld pulse on a stationary target. S1 (top), S2 (bottom). Shows good correlation. 0.1 sec. div., 1.0 v/div.
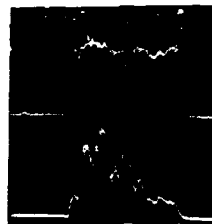

Figure 8: Detection of a machined 'V' groove. S3 (top), 0.2 v/div.; S1 (bottom), 0.5 v/div., 0.1 sec. div., groove width = 1 mm, welding speed = 100 mm/sec.

Figure 9 shows the effect of mistracking during a butt weld. The weld plasma will be less stable when the beam is on the butt and will become more stable as the beam 'wanders' off the butt, resulting in a corresponding gradual reduction of the signal as shown. However, the 'noise' in the r.m.s. envelope remains unaffected because it is related to the power density or a change in the focus position.

Figures 10 (a), 10 (b) and 10 (c), show weld pulses on a stationary target positioned on either side of the focus and at the focus. The initial 'peak', which represents keyhole initiating time, becomes a minimum at a condition of maximum power density. Usually, the focus is found in an arbitrary manner by finding the position where a 'blue plasma' is obtained. The weld pulses shown in figure 10 are within the 'blue plasma' region and the position of maximum power density was determined with a resolution of 0.5 mm. Mild steel targets with polished surfaces were used.

Figure 9: Effect of mistracking. S3 (top) and S4 (bottom).


a   b   c
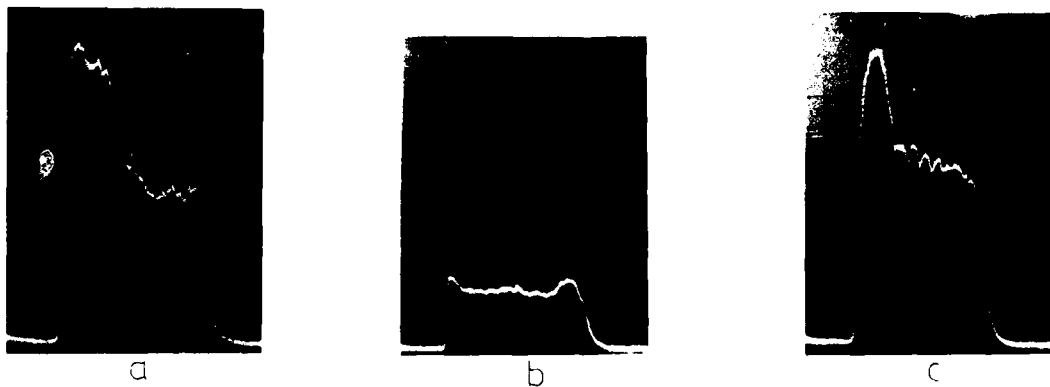
Figure 10: Weld pulses on a stationary target positioned on either side of the focus (a and c) and at the focus (b). Signal: 53, 50msec/div. The pulse starts from the left.

Acoustic signals were also detected from laser cavity mirrors. Good correlations were [...] between these signals and S4.

In drilling and cutting (oxygen assisted or otherwise), the signals S1, S2 and S3 [...] at the completion of drilling a through hole and when a through cut is made. [...] the plasma is confined in a blind hole or in a partially drilled through hole, or a [...] cut, a signal is recorded.

Signals were recorded on S1, S2 and S3 from a workpiece held at an angle (>45 degrees), which indicates that the plasma reflects the laser in a way which is insensitive to the [...] coordinates of the workpiece. This is an advantage for sensors which detect co-axial with the laser.

Conclusions

[...] plasma reflections during welding contain much information relating to the state of [...] weld. This information is contained in an amplitude modulated high frequency 'carrier' [...] can be analysed optically from a beam sample but a more versatile 'non-contact' [...] is to look at thermally induced acoustic stress waves in beam handling mirrors. [...] correlation was observed between the optical and the acoustic signals.

[...] main characteristics of the acoustic signal are the r.m.s. value, its fluctuations [...] A particular characteristic or a combination of characteristics [...] a particular weld defect. Therefore, the acoustic signal could be used as [...] in a weld real time knowledge based system to detect a particular weld defect in a [...] memory, using a shell structured inference technique. Such a system will be [...] in high volume welding where reject products can be identified and on [...] can be implemented.

Acknowledgements

References

1. J.M. Webster and W.M. Steen, In-Process monitoring of laser processes, in Proceedings, Conference ICALEO '87, Los Angeles, USA.

2. J.M. Webster, et al, Condition monitoring a CO_2 laser using acoustic signals, to be published.

3. [...], Acoustic emission monitoring of laser beam welding, Welding [...], Vol [...], No [...], September 1987.

4. [...] and G. Roth, Optical diagnostics of laser metal interaction during welding, in Proceedings, LIM3, June '86, Paris.

5. [...], D. Schuöcker, G. Herziger and P. Rahl, Diagnostic of high power CO_2 lasers, [...] Laser '85, Munich, Springer Verlag (1984).

6. [...], D. Schuöcker, L. Jocher and G. Herziger, Optical feedback during laser materials [...], in Proceedings, Laser '85, Munich, Springer Verlag (1984).

7. L. Wagner, et al, Modulation technique to control laser materials processing, IEEE [...] Quantum Electronics, Vol QE 10, No 2, (February 1974).

8. [...] and A. Yariv, The time behaviour and spectra of relaxation oscillations [...] lasers, IEEE J. of Quantum Electronics, Vol QE 8, No 2, (February 1972).

9. [...] and W.M. Steen, Laser oscillator amplifier systems, SPIE, Vol 668, Quantum [...].

10. [...], Private communication, V & S Scientific Ltd., Hertfordshire, UK.

PULSED CO$_2$ LASER PROCESSING OF THIN ION-IMPLANTED SILICON LAYERS

R. B. James
Theoretical Division
Sandia National Laboratories
Livermore, California 94550

and

W. H. Christie
Analytical Chemistry Division
Oak Ridge National Laboratory
Oak Ridge, Tennessee 37831

Abstract

We show that extremely shallow ($\leq$ 800 Å) melt depths can be easily obtained by irradiating a thin heavily doped silicon layer with a CO$_2$ laser pulse. Since the absorption of the CO$_2$ laser pulse is dominated by free-carrier transitions, the beam heating occurs primarily in the thin degenerately doped film. For CO$_2$ pulses with intensities exceeding a threshold value, surface melting occurs and the reflectivity of the incident laser pulse increases abruptly to about 90 %. This large increase in the reflectivity acts like a switch to deflect almost all of the energy in the remainder of the pulse, thereby greatly reducing the amount of energy available to drive the melt front to deeper depths in the material. Transmission electron microscopy shows no extended defects in the near-surface region after laser irradiation, and van der Pauw electrical measurements verify that 100% of the implanted arsenic dopant is electrically active.

Introduction

Pulsed laser processing of ion-implanted silicon has been applied extensively to the fabrication of high-efficiency solar cells.[1] It has been demonstrated that pulsed laser annealing is superior to thermal annealing for the removal of lattice damage caused by ion implantation, electrical activation of implanted dopants, and preservation of the minority carrier diffusion length in the base region of the solar cell.[2] Most of the advantages of laser annealing over conventional thermal processing result from the localization of thermal effects associated with the laser pulse and the increased control of several critical solar cell parameters (e.g., junction depth and free-carrier concentration).

There exists many reports on the use of pulsed lasers to melt ion-implanted silicon layers.[3] Almost all of these investigations have been conducted with a laser that has a photon energy greater than the bandgap, such as a ruby or excimer laser. Unfortunately, the energy deposited from a ruby or excimer laser always occurs within the absorbing layer at the surface, and one has little control over the penetration depth for a fixed photon energy. In order to melt extremely thin ($\leq$ 800 Å) layers with a ruby or excimer laser, one has to precisely control the pulse-energy density at a value close to the melt threshold, which is generally difficult due to beam reproducibility and spatial inhomogeneities. For low energy (< 10 keV) arsenic-implanted Si samples, we show in this paper that a pulsed CO$_2$ laser is particularly suitable for forming very shallow (< 800 Å) melt depths by controlled heating of only the thin degenerately doped surface layer. After laser irradiation the resultant profile of electrically active arsenic shows a region near the surface having a concentration exceeding the equilibrium solid solubility limit and an intermediate region in which the density falls rapidly toward the n-p electrical junction, both of which are important to the manufacturing of n$^+$pp$^+$ solar cells with high conversion efficiencies.

For CO$_2$ laser radiation ($\lambda \sim$ 10 μm), the absorption of the pulse energy in a shallow arsenic implanted Si layer is dominated by free-electron transitions within the conduction band. Since the free-electron concentration in the thin surface film can be several orders of magnitude greater than the underlying substrate, one can preferentially deposit the energy of the laser pulse in the thin film at the surface. If the duration of the pulse is short compared to the time required to conduct the heat out of the shallow surface layer, then the CO$_2$-laser-induced heating occurs only in the thin arsenic-implanted layer where the free-carrier density is large. Because molten silicon is metallic, the onset of surface melting causes the reflectivity of the sample to increase abruptly to about 90 %,[4] which is much larger than the reflectivity increase of a ruby or excimer laser pulse. This large increase of the reflectivity upon melting acts like a switch to reject most of the energy in the remainder of the CO$_2$ laser pulse, thereby reducing the amount of energy available to further heat the surface and drive the melt front to considerably deeper depths in the material. Furthermore, for applications where one has both heavily doped and undoped areas in the near surface region, one can spatially select the heavily doped regions for beam heating, without causing significant heating of the adjacent undoped material.[4-5] Thus, one can use a relatively large CO$_2$ laser pulse to simultaneously process many ion-implanted regions on the same or on different silicon wafers.

Experimental

A gain-switched, TEA CO$_2$ laser was used to generate the pulses at a wavelength of 10.6 μm. The laser

was operated with low nitrogen content in the gas mix, so that the amplitude of the long tail on the pulses could be greatly suppressed. About 80% of the energy in each pulse was contained in the form of a nearly Gaussian peak of 60-ns duration (FWHM). The remaining 20% of the pulse energy was in a second pulse that was delayed by about 300 ns from the first pulse and had a duration of 250 ns (FWHM). For the energy densities considered in this report, the second pulse makes a negligible contribution to the melt depths and durations of surface melting. As a result, the pulse-energy densities quoted in this paper are for the energy in the 60 ns primary pulse only.

The output pulse was diverged by a spherical convex mirror with a 1-m radius of curvature. The diverging beam was later collimated by a spherical concave mirror with 2-m radius of curvature. The collimated beam then impinged on a CO_2 laser beam integrator which spatially homogenized the beam to within $\pm 10\%$. The dimensions of the laser pulses were 12x12 mm in the target plane of the integrator. The energy density at the sample surface was adjusted by using additional lenses to change the spot size and linear attenuators to change the total energy in each pulse. A photon-drag detector and volume absorbing calorimeter were used to measure the intensity and energy of the laser pulses, respectively.

The samples used in the experiment were 340-μm thick, boron-doped silicon (100) wafers which, prior to implantation, had an electrical resistivity of 2-3 Ω-cm at room temperature. This resistivity corresponds to a free-hole concentration of approximately 6×10^{15} cm^{-3} and hole mobility of about 350 cm^2/V-s. The samples were implanted on one side with ^{75}As$^-$ ions at an energy of 5 keV to a dose of 2×10^{15} cm^{-2}, resulting in an arsenic profile that is peaked at about 70 Å from the surface with a standard deviation of about 25 Å. The samples were next thermally annealed at 873 K for twelve minutes to increase the fraction of electrically active arsenic and thereby increase the coupling of the CO_2 laser radiation to the near-surface region. The concentration of arsenic near the peak of the implanted profile exceeds the solid solubility limit, resulting in the formation of arsenic-rich precipitates in part of the implanted layer. Van der Pauw measurements on the thermally annealed samples showed a carrier density of 6.2×10^{14} cm^{-2}, carrier mobility of 30 cm^2 V-s, and sheet resistivity of 335 Ω/sq.

The free-electron concentration in the first 200 Å is greater than 10^{20} cm^{-3} so that the absorption coefficient (α) of the CO_2 laser radiation is large (> 2×10^4 cm^{-1}) near the surface. The lightly doped substrate is relatively transparent to 10.6-μm radiation and has a value of less than 10 cm^{-1} at room temperature. Thus, the laser-energy deposition is primarily in the thin film at the surface.

The samples were irradiated in air by CO_2 laser pulses at different energy densities. Van der Pauw measurements were used to determine the changes in the carrier concentration, carrier mobility, and sheet resistivity. A Fourier transform infrared spectrometer was utilized to study the laser-induced modification in the optical properties of the near-surface region. The microstructure of the near-surface region was investigated by cross-section transmission electron microscopy. Secondary ion mass spectrometry was utilized to measure the redistribution of the implanted arsenic and to investigate the possibility of controlling the dopant profiles by varying the energy density of the laser pulses.

Results and Discussion

Van der Pauw measurements were performed on the laser-irradiated samples, and the results showed that for pulse-energy densities (F_L) greater than about 5 J/cm^2, significant changes in the electrical properties of the ion-implanted layer occurred (see Table I). For values of E_L between 5.0 and 7.5 J/cm^2, there was an increase in the electron concentration (N_s) and a decrease in the sheet resistivity (ρ) with increasing E_L. The increase in N_s results from the partial melting of the arsenic-implanted layer and subsequent electrical activation of the arsenic upon solidification of the molten layer. At pulse-energy densities greater than about 7.5 J/cm^2, the melt front penetrated to a depth exceeding the implantation-damaged surface layer, and 100-% activation of the implanted arsenic was observed. At these higher values of E_L, the implanted arsenic redistributes to deeper depths, and the electron mobility begins to increase monotonically with E_L due to the reduced rate of carrier scattering by the ionized arsenic dopants.

The CO_2-laser-induced melting of the near-surface region also causes significant changes in the infrared optical properties of the silicon samples. A Fourier transform infrared spectrometer was used to obtai

Table I. Electrical properties of the arsenic-implanted silicon samples as a function of the incident pulse-energy density. Here, E_L is the energy density, N_s is the electron concentration, ρ is the sheet resistivity, and μ is the carrier mobility.

| E_L (J/cm^2)	N_s (10^{15} cm^{-2})	ρ (Ω/sq)	μ (cm^2/V-s)
0.0	0.62	335	30
4.4	0.65	318	30
5.3	0.96	233	28
6.1	1.62	135	29
6.8	1.81	104	33
7.5	2.00	92	34
8.4	2.01	76	41
9.2	2.00	51	59
9.9	1.99	48	65
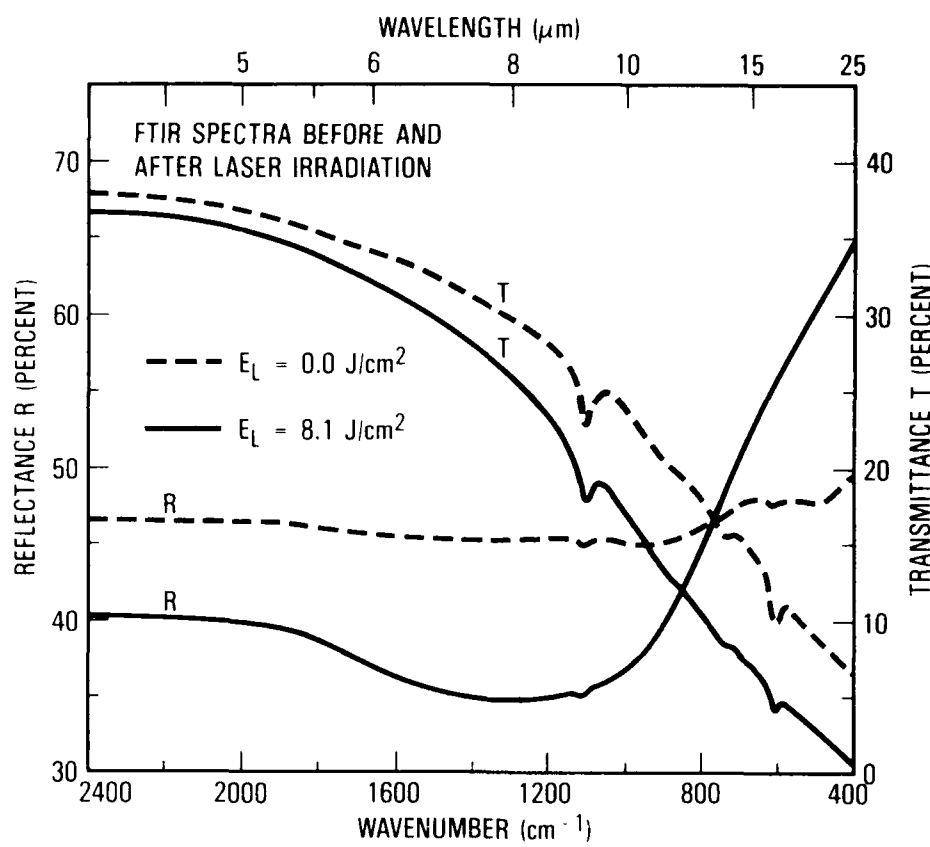
Fig. 1 Reflectance and transmittance spectra for an unirradiated sample and a sample after irradiation at $E_L = 8.1$ J/cm².

transmittance and reflectance spectra before and after laser irradiation. Figure 1 shows the total reflectance and transmittance spectra in the 400 to 2400 cm⁻¹ range for an unirradiated sample and a sample irradiated at $E_L = 8.1$ J/cm². After irradiation at $E_L = 8.1$ J/cm², the total reflectance was found to change from 45 % to 38 %, and the total transmittance changed from 22 % to 14 % for light having a wavelength of 10.6 μm. The increase in the free-carrier absorption is consistent with the measured increase (~ 223 %) in the electron concentration of the arsenic-implanted layer (see Table I).

We used cross-section transmission electron microscopy (TEM) to investigate the presence of extended defects in the ion-implantation-damaged layer. Figure 2(a) is a micrograph of a specimen that has been irradiated by a pulse having an energy density of 8.1 J/cm². At this pulse-energy density, the surface layer contained no extended defects with a size larger than 20 A, which is the smallest size that can be clearly resolved in the micrograph. In addition, the van der Pauw measurements on the sample showed that all of the implanted arsenic was electrically active. The TEM micrograph, together with the electrical measurements, indicates that the entire implantation-damaged layer was melted by the laser pulse and that liquid phase epitaxial regrowth of the molten layer occurred.

Another sample was also irradiated at 8.1 J/cm² and then heated in a furnace to 973 K for ten minutes to study the precipitation of the implanted arsenic. Fig. 2(b) shows a cross-section TEM micrograph of the specimen after furnace treatment. Arsenic-rich precipitates are observed to depths of about 250 A through out the near-surface region.

Secondary ion mass spectrometry (SIMS) was used to measure the arsenic profiles before and after laser irradiation. The results are shown in Fig. 3 for several different energy densities. For E_L less than 5 J/cm², no redistribution of the implanted arsenic was observed. For higher pulse energy densities, the arsenic was found to diffuse to deeper depths due to the penetration of the melt front and subsequent liquid phase diffusion in the near-surface region. The amount of redistribution was relatively small for pulse energy densities in the range of 5 to 8 J/cm². For $E_L > 8$ J/cm², the maximum depth of As diffusion begins to increase much more rapidly with increasing E_L and reaches depths of over 1000 A for pulse energy densities greater than 10 J/cm². No surface segregation behavior was observed in any of the laser irradiated arsenic implanted specimens.

Conclusions

We have shown that extremely shallow melt depths can be easily obtained by CO_2 laser annealing of low-
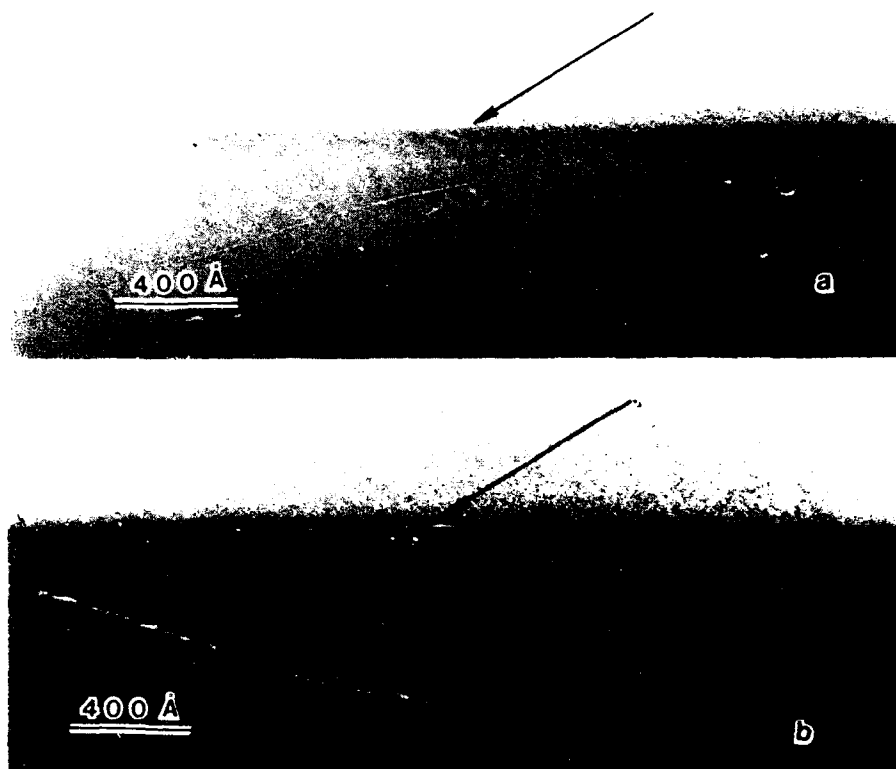
Fig. [...] photograph shows a cross-section TEM micrograph of a sample after irradiation by a CO_2 laser [...] energy density of 8.1 J/cm^2. The bottom photograph shows a different sample that was [...] F for ten minutes after being irradiated by a laser pulse at $E_L = 8.1$ J/cm^2. [...] surface is shown by an arrow in each photo.

energy ($\lesssim 5$ keV) arsenic-implanted silicon layers. Similar results are expected for other silicon samples having a thin degenerately doped surface layer and an underlying lightly doped substrate. The primary advantages of using a CO_2 laser to achieve very shallow melt depths, as compared to a ruby or excimer laser, are that the pulse energy is deposited only in the thin heavily doped layer at the surface and the CO_2-laser-induced melting of the surface layer causes the reflectivity to jump abruptly to a value of about 90 %. The large and sudden increase in the reflectivity upon melting acts like a switch to reflect most of the energy in the remainder of the laser pulse and thereby greatly reduce the amount of pulse energy available for driving the melt front to deeper depths. For a 60-ns pulse and pulse-energy densities (E_L) greater than about 7 J/cm^2, we find that all of the ion implanted arsenic is electrically active and the near-surface region is free of any extended defects.

Acknowledgments

References

1. [...] T. Young, G. A. van der Leeden, R. L. Sandstrom, R. F. Wood and R. D. Westbrook, Appl. [...] (1983).
2. [...] Young and R. F. Wood, Ann. Rev. Mater. Sci. 12, 323 (1982).
3. [...] Pulsed Laser Processing of Semiconductors, Vol. 23, edited by R. F. Wood, C. W. White and R. T. Young (Academic, New York, 1984).
4. R. B. James, G. A. Geist, R. T. Young, W. H. Christie and F. A. Greulich, J. Appl. Phys. 62, 2981 (1987).
5. R. B. James, J. Narayan, R. F. Wood, D. K. Ottesen and K. F. Siegfriedt, J. Appl. Phys. 57, 4727 (1985).
6. F. J. Trumbore, Bell Syst. Tech. J 39, 205 (1960).
7. W. G. Spitzer and H. Y. Fan, Phys. Rev. 106, 882 (1957).
8. W. G. Spitzer and H. Y. Fan, Phys. Rev. 108, 268 (1957).

ARSENIC ATOMS IN SILICON AFTER CO_2 LASER ANNEALING

E_L (J/cm^2)
▲ — 0.0
● — 7.6
■ — 9.1
X — 10.2
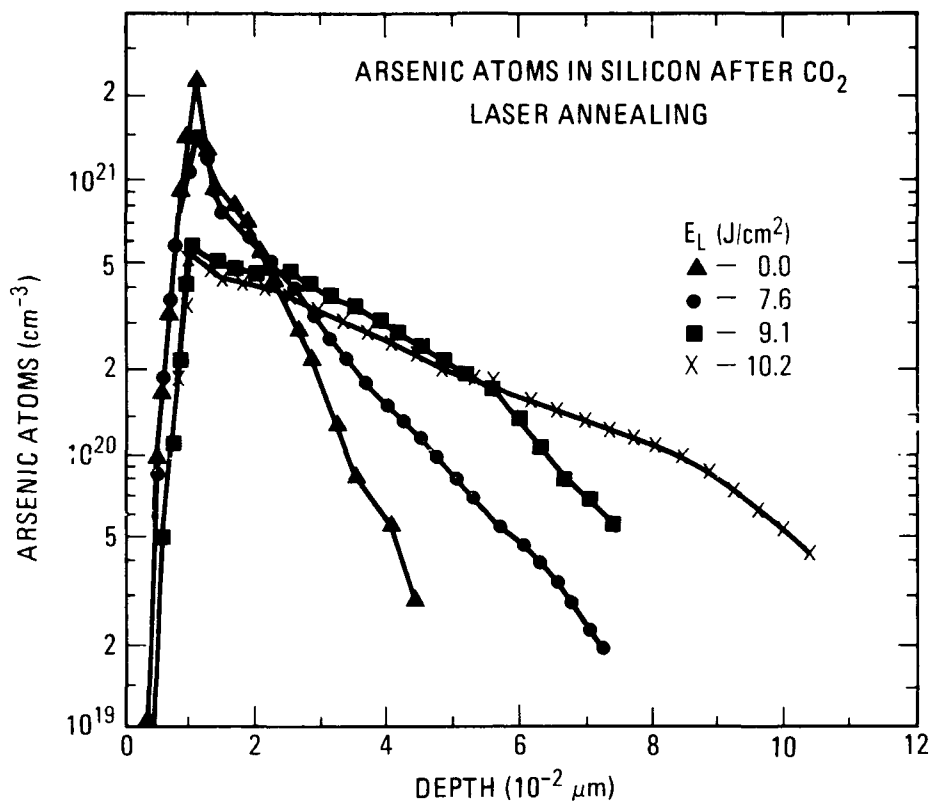
F . . . TIMS measure . . .ts of arsenic atoms as a function of depth for samples irradiated at different en-
. . . . .hm. . . . . The t . ur curves show the arsenic profiles for the following samples: ▲, an unirradiated
s. . . . . ●, a sample irradiated at E_L=7.6 J/cm^2; ■, a sample irradiated at E_L=9.1 J/cm^2; and X, a sample
irradiated at E_L=10.2 J cm^2.

LASER MACHINING DEVELOPMENTS AT MCDONNELL DOUGLAS

Peter L. R. Hoffman
Senior Engineer
Producibility and Standards Engineering

McDonnell Aircraft Company
Dept. 356, MC 1021310
P. O. Box 516
Saint Louis, Missouri 63166-0561

Abstract

Technological and economic pressures pushing laser technology into mainstream manufacturing are reviewed. Laser machining and welding projects from McDonnell Aircraft (MCAIR), McDonnell Douglas Astronautics - St. Louis (MDAC-STL), McDonnell Douglas Canada (MDCAN), and Douglas Aircraft Company (DAC) are detailed.

Introduction

McDonnell Douglas Corporation appreciates the unique material processing capabilities of lasers and in the past has applied them to solve specific manufacturing problems. Recently, the laser has taken on a new role. Lasers are no longer viewed as a highly specialized manufacturing technology which are economical only in special cases. Instead, with the advent of standard "off the shelf" Laser Machining Systems (LMS), lasers are taking their place on the shop floor along side Numerically Controlled (NC) Machining Centers and various general purpose computer controlled production equipment.

Key technological advances in combination with economic pressures have pushed laser machining out of the specialty market and into mainstream manufacturing. Laser Machining Systems available today are developed with ease of programming and dependability as a top priority. Machine tool builders have long since mastered the art of building rigid machines capable of high loading and accuracy. However, making these machines easy to program and capable of moving from 200 to 300 inches per minute on complex curvatures was an impossibility until recently. A new breed of multi-axis controllers are capable of handling the vast amount of data required to move a LMS through a complex path at high speeds. Look to the future to bring more sophisticated decoupled LMS control systems and the introduction of high performance composites in LMS frames for stiffness to weight capabilities well beyond metal based systems.

The economic pressures that have pushed laser machining into mainstream manufacturing are world market based. European and Japanese manufacturers have been aggres·ively exploiting laser machining technology. The world wide distribution of industrial lasers and the stiff international competition the United States faces is illustrated in Figure 1[1].

In addition to these international economic pressures, the defense industry is feeling the budget pinch out of Washington. Competition for the shrinking defense dollar is fierce. The sporadic allocation of money by congress for defense spending is demonstrated by the fluctuations in the Defense Budget Authority, Permission to Spend shown in Figure 2. Aviation Week and Space Technology 1988 Aerospace Forecast issue states: "Congressional defense analysts predict the downward trend in military spending will persist for at least several more years, intensifying the competition for dollars among new weapons, combat readiness, troop strength and research."[2] A flat or declining defense budget forces aerospace firms to push for productivity improvements to allow them to remain competitive. New technology, such as laser machining, is one way to improve productivity and survive the tight budget years.

McDonnell Douglas is concerned with developing superior products from both a performance and cost standpoint. For big ticket items such as advanced fighters, the total number produced is rarely over a thousand. The production quantities are even lower in the commercial aircraft, space systems, and some missile systems. Economy of scale can be applied on some standard parts produced in large quantities such as fasteners and clips. However, the majority of parts required to construct an advanced weapon system or commercial aircraft are highly specialized and require a great deal of "touch labor". A Laser Machining System, with its flexibility, repeatability, and accuracy has proven to be a valuable tool in today's highly competitive and volatile marketplace.

750

This paper will give an overview of four McDonnell Douglas components as they prepare to embrace laser machining as a standard production operation. Activities at McDonnell Aircraft, McDonnell Douglas Astronautics - St. Louis, McDonnell Douglas Canada, and Douglas Aircraft - Long Beach will be detailed.

McDonnell Aircraft Company (MCAIR) - St. Louis, Missouri

McDonnell Aircraft has been using a 1000 watt CO_2 laser trimming system since 1976 to cut boron epoxy composite prepreg for F-15 vertical and horizontal stabilizer skins (Figure 3). Also, MCAIR began laser scribing chem-mill maskant (a chemically resistant strippable coating) on flat aircraft parts in late 1985 (Figure 4). Both these systems represent sizable productivity improvements over their manual counterparts. In the case of boron/epoxy trimming, the difficult to cut boron fibers preclude the use of traditional ply cutting techniques (reciprocating saw). For chem-mill maskant scribing, the use of overlay templates and razors have been replaced with an automated 2-D Laser Scribing System.

A particularly troublesome Environmental Control System (ECS) duct (Figure 5) is shaped in two halves in a superplastic forming (SPF) process and subsequently welded. The titanium duct has an average wall thickness of .030". The difficult trim path required for this part combined with its thin gage has lead to unacceptable grind-to-fit time in preparing the two halves for welding.

For laser trimming of the duct, a single master trim line will be defined from MCAIR's Computer Aided Design Drafting (CADD) database (Figure 6). By using a master trim line for programming and cutting both halves of the ECS duct, an excellent fit up results. Argon will be used as an assist gas to reduce the creation of alpha case on the laser cut edge, allowing the two halves of the ECS duct to be welded without subsequent edge preparation. Figure 7 shows one half of the ECS duct being laser trimmed during recently performed feasibility studies. This part is currently undergoing the transformation from in-house manual trimming to out-of-house laser trimming.

MCAIR's Flame Cutting Process Specification has been updated to include laser cutting. Currently the laser cut edge and its associated Heat Affected Zone (HAZ) must be removed or subsequently welded to be structurally acceptable. However, all new sheet metal parts will be classified as primary, secondary or nonstructural. The nonstructural sheet metal parts will be laser cut without any subsequent edge treatment.

Unlike laser trimming, laser welding is not yet qualified as an official MCAIR Process. Laser welding is closely related to Electron Beam (EB) welding, a well established process at MCAIR. MCAIR's current EB welding equipment is shown in Figure 8. This equipment is limited to point-to-point straight line movement. Set-up and pump-down time of the vacuum chamber makes EB welding a slow and expensive process. Laser welding requires a fit-up similar to EB welding (.005" maximum gap). However, laser welding requires no vacuum chamber pump down. Both laser welding systems and EB welders are available with oscillating beams which effectively widen the weld path to accommodate for a less perfect fit up.

A final laser trimming application involves an F-15E Engine Access Door (Figure 9). The titanium door is made in a two-sheet superplastic forming/diffusion bonding (SPF/DB) process. After forming, the inner sheet between the stiffening ribs of the door is not structurally required. One option which has been successfully demonstrated is to allow the inner skin to form a 3/8" high raised pocket for subsequent laser trimming. Figure 10 shows three demonstration articles laser trimmed for proof of principle. The 6AL-4V titanium sheets are .100" thick at separations of .25", .50", and .75". In all three cases, the hole in the upper sheet was trimmed without the lower panel sustaining any damage. Figure 11 shows the laser trimming of an F-15E Engine Access Door modified to model the proposed raised pocket concept. Due to the cost involved in reworking the SPF/DB tool, we are evaluating the cost effectiveness of this approach. However, it demonstrates the applicability of the laser trimming process for future SPF/DB multi-sheet aircraft parts.

McDonnell Douglas Astronautics Company - St. Louis, Missouri (MDAC-STL)

McDonnell Douglas Astronautics Company - St. Louis has performed some interesting laser machining and welding studies in the development of a 29" long generic missile inlet duct (Figure 12). Two manufacturing approaches were considered for the inlet duct: cast titanium and a titanium sheet metal weldment. The main challenges faced in casting the structure are producing its complex geometry and thin wall requirements. As a titanium weldment, major challenges arise in the welding of titanium sheets varying in thickness from .050" to .200" from end to end. Secondly, gaining access to perform some of the welds is difficult. Laser trimming and welding is an ideal solution to these challenges since the laser power can be adjusted to compensate for the different thicknesses of the sheet metal components, and focal lengths can be selected to allow access to tight weld areas.
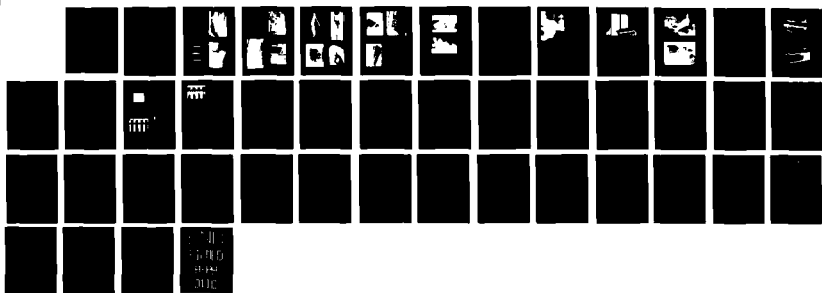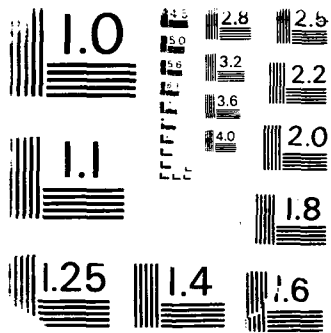
Figure 13 shows a feasibility test specimen produced out of .080" 6AL-4V titanium. The lower sheet was laser trimmed to an overall size of 20" x 10" and a series of slots were laser cut along its centerline. The other sheet was laser trimmed to an overall size of 20" x 6". A series of tabs that corresponded with the first sheet's slots were included along one edge. These two sheets were fit together and full penetration welds were made at the interface between the tabs and slots (Figure 14). This self-tooled tab and slot approach has the potential of producing substantial reductions in weld fixture tooling costs. Due to the favorable results achieved in these studies, plans are being made to extend this approach to an actual inlet structure.

Douglas Aircraft - Long Beach, California (DAC)

Douglas Aircraft is in the process of purchasing a 6-axis Laser Machining System for 3-D scribing of chem-mill maskant on 2024-T3 aluminum aircraft skins. A concept sketch of the laser scribing system is shown in Figure 15. A model of the system including its supporting loading and unloading equipment is shown in Figure 16. The laser scribing system is part of a new chem-mill facility being created to support production of the C-17 military transport. This project will result in a 3-D laser scribing system with a 44' x 11' x 5' work envelope. A 400 watt CO_2 laser will be used in place of a razor to vaporize a thin line of the chemically resistant chem-mill maskant without damaging the aluminum substrate. DAC has identified 33 C-17 aluminum skins up to 40' long for laser scribing. Beyond the high speed at which the laser can scribe in comparison to manual techniques, a significant tooling cost avoidance will result since scribing templates for these large aircraft parts do not have to be produced or maintained. **This system is currently up and running at DAC.**

McDonnell Douglas Canada - Toronto, Canada (MDCAN)

A laser trimming application being developed at MDCAN takes advantage of the unique attributes of laser machining. Figure 17 shows an assembled wing tip for the MD-80 commercial airliner. This .090" thick 6061-T6 aluminum wing tip requires rough routing and finish dressing of nine access panels and cut outs. One of many trim and drill fixtures used for this labor intensive operation is shown in Figure 18. The wing tip's 2024-T3 aluminum access doors currently require an additional forming operation plus routing and dressing. The approach under development at MDCAN is to trim the access doors and cut outs with a CO_2 LMS. The narrow cut produced by laser machining (typically .008"), allows an access door and cutout to be produced from the same formed part. Three times the heat affected zone .006" is manually removed from the laser cut edge while still remaining well under the .060" + -.030" gap tolerance. A doubler is used to form a sill for fastening the access doors to the wing tip. In addition, over 390 pilot holes will be laser cut on the same setup. Successful feasibility studies were recently completed on an actual MD-80 wing tip. The sizable cost savings projected for this application can be attributed to eliminating separate fabrication of the wing tip access doors.

Conclusion

The activities underway at McDonnell Aircraft, McDonnell Douglas Astronautics - St. Louis, McDonnell Douglas Canada, and Douglas Aircraft - Long Beach represent a good start toward the introduction of laser machining and welding into their manufacturing facilities. These examples are just a small sampling of numerous applications of laser technology. For laser trimming and welding to take the important position they are capable of in the future, a commitment must be made today to devote the time and money necessary to develop applications and justify equipment.
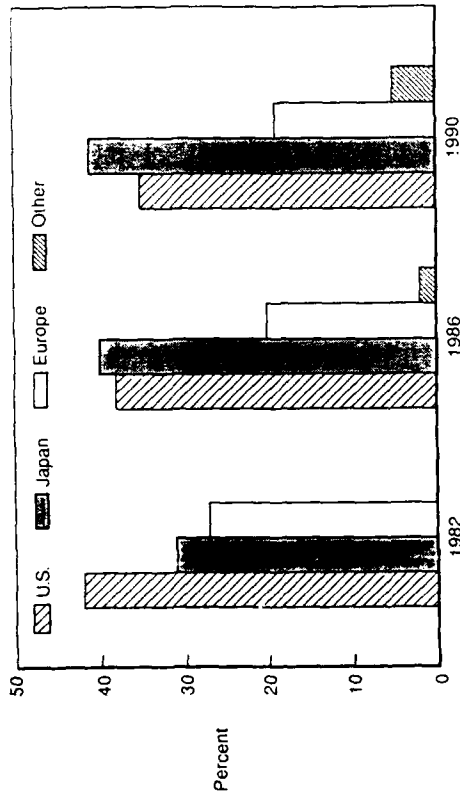
Figure 1 – Industrial Laser Distribution World Wide by Percentage of Total Installations.
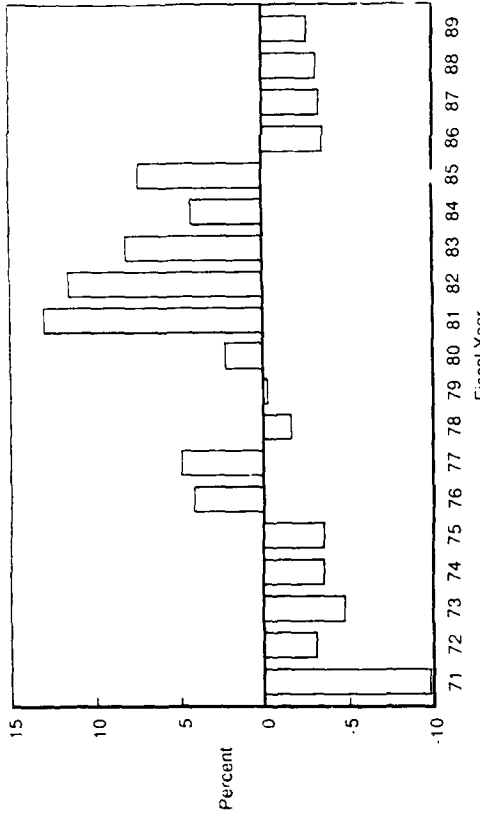
Figure 2 – The Shrinking Defense Budget for Aerospace.
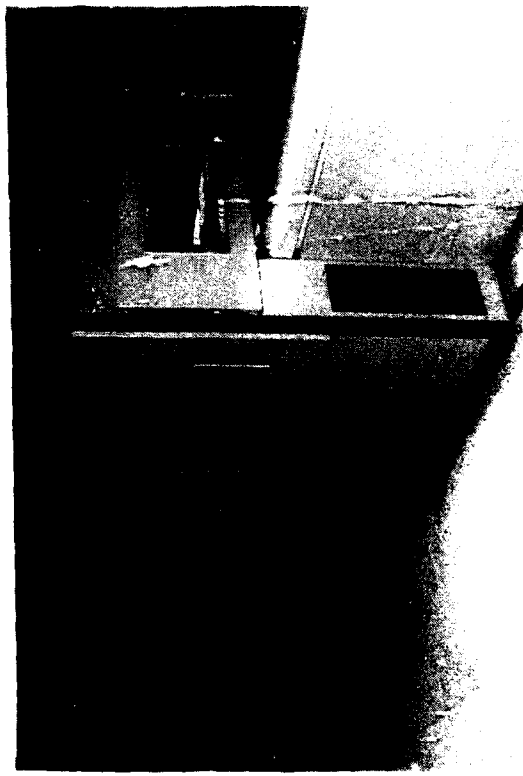
Figure 3 – Laser Trimming of Boron/epoxy Composite Prepreg at McDonnell Aircraft.


Figure 4 – 2-D Laser Scribing Equipment at McDonnell Aircraft.

Figure 6 - Master Trim Line for the F-15E Duct as Defined on MCAIR's Computer Aided Design Drafting (CADD) System.


Figure 8 - Electron Beam Welding Equipment at McDonnell Aircraft.
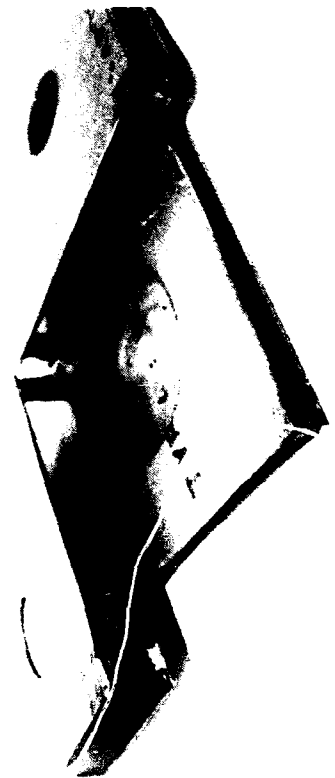
Figure 5 - F-15E 6AL-4V Titanium Environmental Control System (ECS) Duct.

Figure 7 - Laser Trimming of the F-15E ECS Duct.

Figure 12 — Reconstruction of Forging Apparatus Used to
Manufacture F-15 Door.

Figure 13 — Mcdonnell Douglas Aeronautics — St. Louis,
Inside Handle of a Forged Door.

Plate 9 — Two Sheet Superplastic Formed F-15
Engine Access Door.

Figure 14 — Laser Trimming of a Molded
F-15 Inside Access Door.

Figure 14 - Full penetration weld for the MDAC-STL Generic Inlet Duct Demonstration Article.
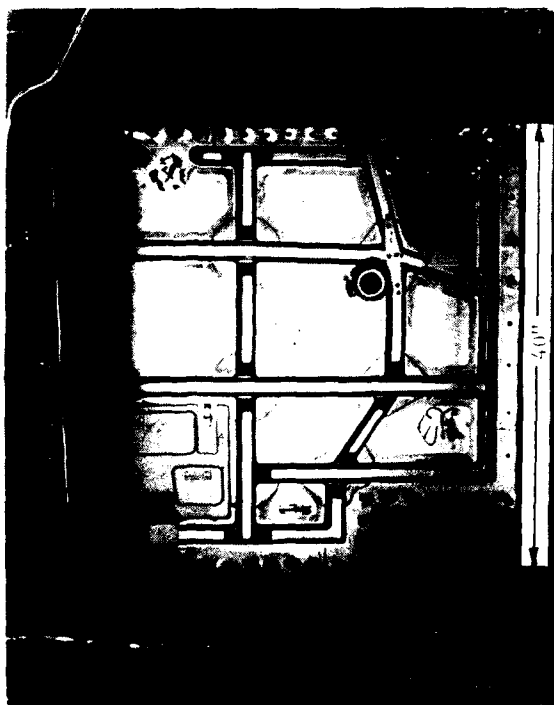
Figure 16 - Concept Model of the Laser Scribing Facility at Douglas Aircraft.

Figure 13 - Tab and Slot Laser Welded Demonstration Article for the MDAC-STL Generic Inlet Duct.

Figure 15 - Concept Sketch for Douglas Aircraft's Laser Scribing System.

756

Figure 17 - MD-80 Wing Tip at McDonnell Douglas Canada.

Figure 18 - Trim and Drill Fixture for the MD-80 Wing Tip.

1. Belforte Associates, P. O. Box 245, Sturbridge, MA 01566

2. Aviation Week and Space Technology - Aerospace Forecase and Inventory, March 1988

DEVELOPMENT OF LASERS AND LASER TECHNOLOGIES
AT VUMA, CZECHOSLOVAKIA

L. SENECKÝ, Dr.-Ing., et al.,
VUMA - The Research Institute for Mechanization and Automation,
915 28 NOVÉ MESTO NAD VÁHOM, CZECHOSLOVAKIA

A paper gives a survey of the most important results in the sphere of the laser technique and technology at VUMA. It comprises the results of the research and development of technological lasers and systems utilizing lasers in solving problems of production technologie. A non - fungible role of laser technologies, especially in the production of electronic elements is being stressed.

1. Introduction

In recent years there was a great swing in using lasers in industry, particularly in technology all over the world. It is linked with the successful development of the lasers being divided into two main types:the gas CO_2 lasers and solid-state lasers based on the Nd:YAG crystals.

The gas CO_2 lasers are used in various applications, mainly in mechanical engineering (sheet cutting, welding, thermal processing, film application etc.).

The solid-state lasers are utilized in the production of electronic elements but also in precision mechanics and in the fine-mechanical engineering.

There is a presuppose of using solid-state lasers of higher outputs also in the machinery.

Successful introduction of lasers into practice depends to a high degree on the appropriate positioning mechanisms (usually equipped with CNC) and working out of technology for individual applications.

At VUMA the development of laser-beam machining follows the development tendencies in the world. At present it is aimed at the utilization lasers in machinery and microelectronics.

2. Gassions CO_2 lasers

On the field of the gassious CO_2 lasers we have developed the 1kW unit, which is used for surface thermal processing, welding, cutting and for other technologies and research. It is an industrial laser operating at a continuous mode with an adjustable output of up to 1000 W at a wave length of 10.6 um. It belongs to the category of gas lasers excited directly by low-pressure electrical discharge with a high traversal gas flow rate through an optical resonator and convective cooling. Active medium is created by CO_2, nitrogen and He with a total pressure of 4.6 kPa. The optical resonator is unstable, confocal with an annular output beam with its 48 mm outer diameter.

The laser consists of these two essential units:
a laser unit (a low-pressure container with a fan, a vacuum pump, a cooler, a discharge chamber with the optical resonator)
- a power supply unit (a transformer, a thyristor regulator, a rectifier, a filter, regulating and control cirenits).
The laser must be equipped for parsicular application with the appropriate technological equipment. The technological accessories (a positioning mechanism with the focusing optics and a control system) are completed individually according to technological operation and the user's demands.

3. The solid - state lasers

At VUMA the development of the solid - state lasers came along with the needs of the electrical engineering industry.
It was directed at the utilization in the sphere of the ceramic and metal material cutting, trimming of film resistors, marking and lettering of details etc. The laser incorporates an active material (in a given case it is a Nd:YAG crystal), which is excited by optical pumping through a discharge tube being closed with it in a pumping cavity.

A power source is designed for the excitation of the discharge tube and supplies the energy. The continuous pulse width adjustment is used. The MU 1631 V pulse-laser parametres are as follows : pulse energy .... variable up to 9J
medium optical output .... up to 50 W
pulse repetition rate .... up to 130 Hz
pulse duration .... from 0.5 to 20 m s

Fig. 1 The MU 1631 V pulse laser operates with the Nd:YAG crystal at the wave length of 1.06 μm

The design of the afore - mentioned laser (Fig. 1) resulted in much new knowledge giving us the opportunity of thinking how to achieve higher parametres both medium output parametres and pulse energy ones. The application efficiency of this type of laser depends on the approach to an optical system fol laser beam transport and focusing and to positioning mechanism.

Another type of the laser developed at VUMA particularly for the pyrolytic graphite machining is a ELB 001 A continually pumped Q - switched Nd: YAG laser (Fig. 2). His power output at cw and in a multimode ranges up to 100 W.

The discharge tube is supplied by a converter thyristor source with the utmost output 2x6 kW. The laser water cooling system is used.

The laser operates at a wave length of 1.064 μm.

A modified type of a continually excited Nd:YAG laser was designed for the technological trimming systems of the monolithic and hybrid integrated circuits (the LTM 1 and the LTH.1 systems). A high-pressure krypton discharge tube through which the laser is excited is placed together with the active material in an elliptic cavity, while, at the same time, the cooling water is flowing through it. The pulse work which is necessary in the resistor film trimming can ben done by Q-switch. The advantage of this configuration is a convenient and fast control of time pulse sequence according to the controlsystem commands. The laser operates at TEMoo mode which is necessary for a quality cutting in the resistor film. Regarding this technological operation other laser parametres are optimalized as well. They are as follows:
- medium output at the pulse repetition rate
  1 kHz .... $P_s = 1$ W
- pulse length in the half
  pulse amplitude .... $t_{st} = 250$ us
- pulse repetition rate .... $1 \stackrel{st}{\div} 10$ kHz
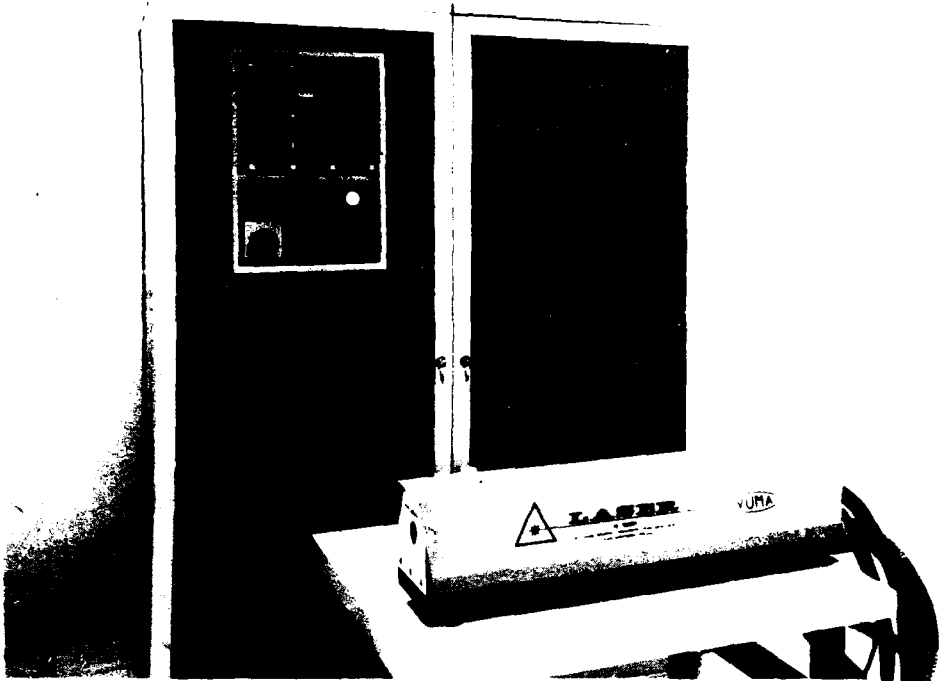
Fig. 2   ELB 001 A is the continuously pumped solid-state laser with the
Q-switching by the Nd: YAG crystal. The output power is up to 100 W.
The wave length is 1.06 um. The laser head is placed in the techno-
logical system for the machining of pyrographite. The head incorpora-
tes two holders with the mirrors of the resonator, the pumping cavity,
the accusto-optical modulator and a safety closing.
The output beam diameter is increased by an expander by means of the
mirror and the focusing lens is directed at a workpiece.

4. The laser systems for microelectronics

The precise adjustment of the resistance values in the resistor networks on the cera-
mic substrates is necessary in the electronic components production, particularly in the
hybrid integrated circuits (HIC) and the D/A converters. The values of the resistances are
adjusted by creating suitably placed slots in the resistor material. The laser beam is
successfully used for this operation. The laser technology offers high productivity and
quality trimming and together with the automatic measurement device the high precision of
the resistance adjustment as well.

The LTM-1 laser trimming system (Fig.3) for a 12-bit D/A converters was the first our
system. It incorporates a number of subsystems the functions of which are coordinated by
the computer control system. A positioning wafer system offers the controlled movement in
the X, Y, Z and φ axes. Two perpendicular optical systems of galvanometers fitted in a
block of the focusing and positioning optics locate the spot of the focussed laser beam in
the working area. The current in the galvanometers and thus, in fact, the deviation of the
beam is regulated by the control system. The measuring subsystem controls and evaluates
the values of the adjusted resistances and offers the data for processing in the control
computer. The adjusted chip is connected as a functional one and its output voltage or cu-
rent is evaluated after individual laser impacts with the help of the converter with a
very fast conversion. The measurement device is connected through the parallel adapters
with the computer system.

New principles of active trimming were used in designing the LTM-1 laser trimming
system for the thin-film resistors in the hybrid integrated circuits, thus the degree of
the automation process was increased.

Fig. 3　The LTM-1 laser trimming system for resistance adjustment
in the MDA 0565 and MDA 0566 12-bit D/A converters
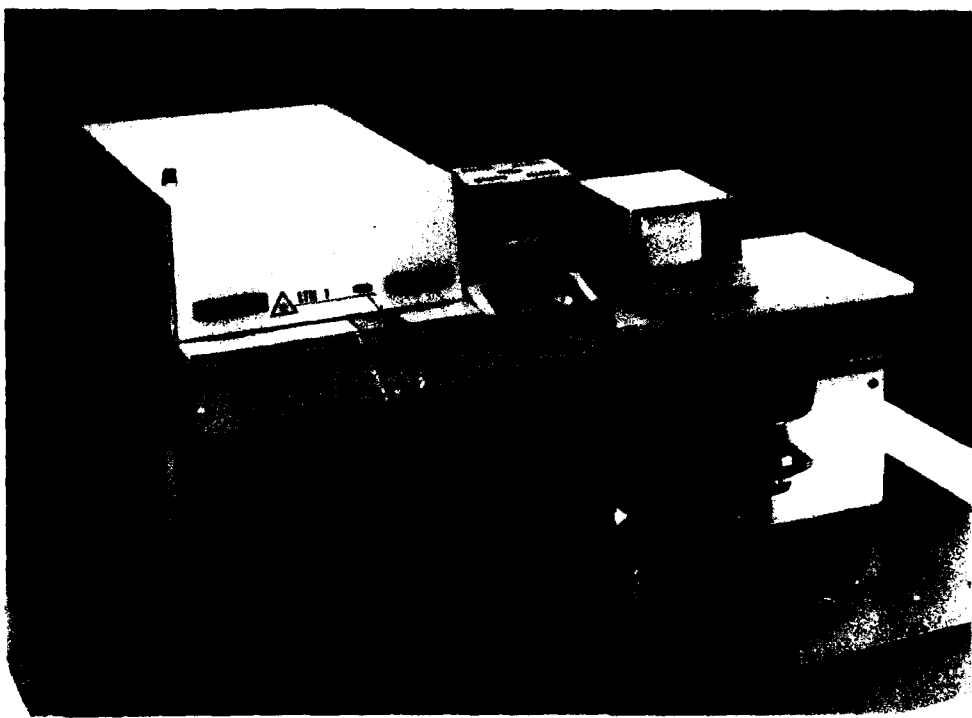
Fig. 4　A general view of the LTH-1 trimming system

The LTH-1 is a relatively complicated complex including the following items :
- a u, v - positioning table for the laser beam positioning with the control unit
- a video - system - a TV camera and a monitor for the substrate positioning control and monitoring the process
- the laser head fitted with the Nd:YAG solid-state laser operating with the Q - switch at the TEMoo - principal mode
- the substrate positioning table in the X,Y,Z, and φ axes controlled either manually by a joy-stick or automatically by the control system
- a probe card with the contacts and an appropriate holder connected with a measurement bridge
- and a control panel.

A SM 50/50 control computer operates as a central control system being connected through a IMS-II standard bus with separate functional blocks which are used for the lowest tech-nological level control. The measurement system is controlled by a dominant system. The transmitted data directly control the operation of the analoque circuits of an evaluating bridge and switching of the reed relays in the PIN electronics. The pins are connected through these relays from which measured values are read.

The percent deviation from the set resistance value is the back information.

The control panel is directly controlled in a similar way, the signals are transmitted to it for lighting up the LED signalling diodes and the values of the functional press buttons are read or the voltage values corresponding to the deviation of a joy-stick for speed and direction control of the servo-mechanisms.

The positioning modul of the laser beam consists of two microcomputer positioning regulators for the control in X,Y axes. These servo-systems are used for the movement of the focussed laser beam on a set contour. The control is autonomous and the central control system is required to set a desired position of speed and a so called control word. The control word is communicated to the servo-system for the mode operation. Here are the following mode operations:

1. Move to the desired position at max. speed without the control of technology.
2. Move to the desired position at the desired speed without the control of technology.
3. Move to the desired position at the desired speed with the control of technology.
4. The control on free coordinates by means of a control lever.
5. The difference member clearing.
6. Information calling on the momenta y position.

What do we understand by the conception of the control of technology? Because the laser used operates at the Q - switched mode requires from the control system generation of the switching pulses for the Q-switch. They are derived from the movement of the u,v - supports on which the rotary incremental sensors measure the position. Each information from the sensor can generate a starting pulse. (The minimum pulse distance is $2 \mu m$).
Because the average spot width of the laser beam is from 15 to 20 μm, it is necessary to control the spot overlap by individual laser "shoots". It enables the generation of the starting pulse after a n-pulse derived from the incremental sensor. The maximum value of n can be 15.

The substrate positioning is an important function block. It is the servo-system in X,Y,Z,φ axes by means of which the substrate can be positioned. On the substrate there is applied a contour under the laser head and the measurement points. The Y axis control coincides with the laser beam positioning control.
The (X,Y,φ) axes are used in step drives in an open loop. The control pulses are generated over the IMS-II bus by the central control computer. The position is read in a control computer register.
In the LTH-1 system the measuring bridge is used for resistances in the thin-film hybrid networks.
The percentual deviation of the resistor value according to setting of the nominal value can be measured.
The 12-bit A/D converter evaluates the final bridge misalignment. The process is based upon a Kelvin bridge principle (measuring throught four wires) where the effect of the leads resistance and the contact resistance of points is eliminated.

The accuracy of measurements for separate ranges is from 0.02 % to 1%.
For example in range from 100Ω +o100kΩ the highest accuracy is 0.05%.

The range of the accurcy can be selected. At higher accacies the offsets of opera-tion amplifiers and interference must be eliminated, thus the measurement is prolonged.
For the eliminating of the offsets it is necessary to measure at two polarities of the supply voltage. The interference can be eliminated by the sampling of the output bridge value or an active filter.

The work on the laser trimming systems of the resistors continues in the design of the systems for the thick-film hybrid integrated circuits with the automatic loading of the ceramic substrates with the maximum size of the substrate 6 inch in square.
The system LTH-2 is shown in Fig. 5.
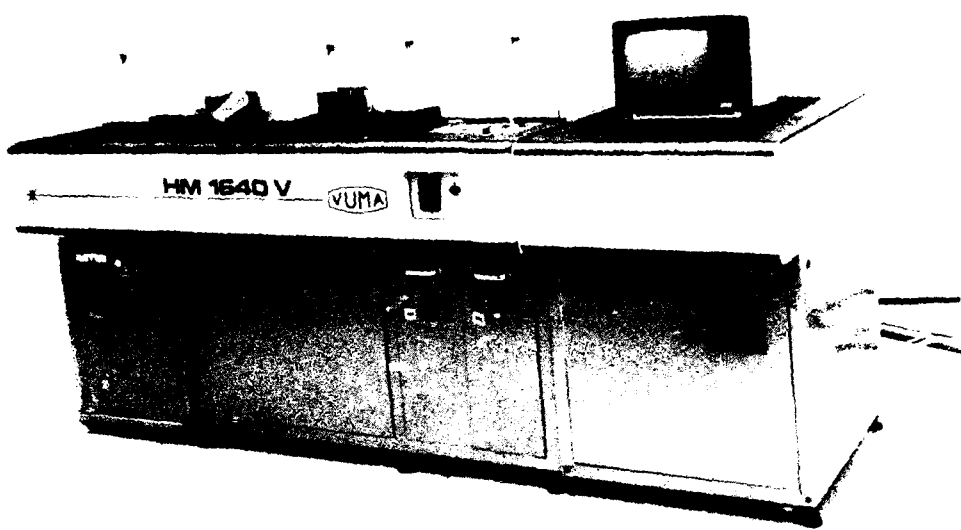
Fig. 5 A general view of he HM 1640 V laser trimming system with the automatic substrate insertion
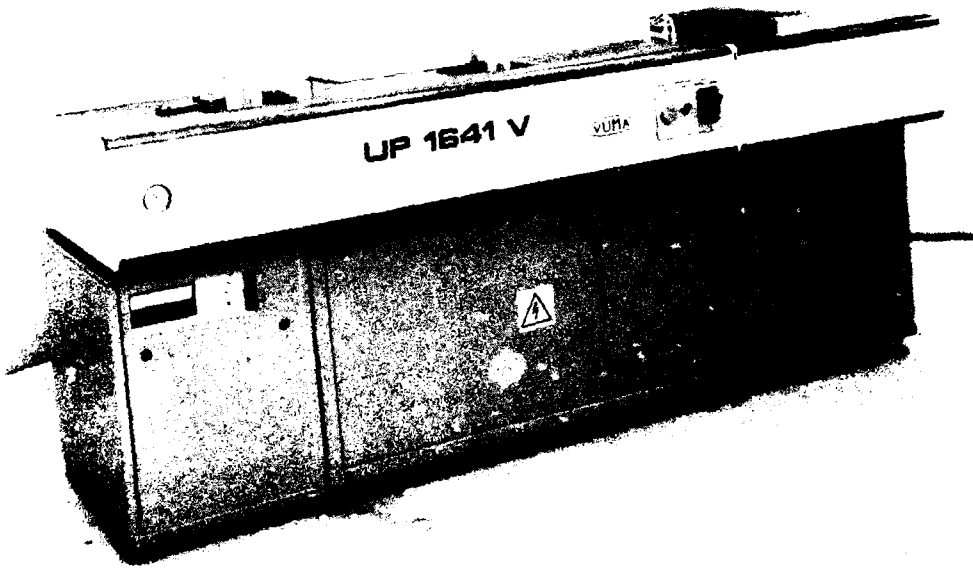
Fig. 6 A general view of the UP 1641 V laser silicon wafer marking system

5. The laser marking and lettering of details

This technology appears to be very effective and perspective.
Here are its advantages in comparison with the classical methods of marking :
- the material being marked is not affected by a mechanical tool therefore it is not subjected to wear and damage
- high marking speed
- the possibility of marking a wide range of metallic and nonmetallic materials
- quick change of the laser beam parameters by means of which the interaction radiation process with material can be effected in such a way that it may be either melted down or evaporated
- quick and comfortable change of the type, size and the way of marking from the control panel
- the long life of the mark
- the possibility of the process automation.

A UP 1641 V silicon wafer marking system (Fig.6) was designed for the application in the electronic components production.
The system operates with the Nd:YAG laser at the wave length of 1.064 um and is fitted with a manipulator for automatic wafer marking with the diameter of up to 6 inch by means of the system "from one cassette to another one". The mark is made according to a SEMI - OCR standard.

6. Conclusion

The development of laser technologies in the sphere of electronics has achieved important results. However, potential possibilities are not yet used.
The power CO_2 lasers which can assure higher quality and productivity of labour, and better utilization of material will be for the mechanical engineering of great importance.

LASER DAMBAR AND FLASH REMOVAL FOR PLASTIC MOLDED SURFACE MOUNT COMPONENTS WITH LEAD SPACING UNDER 20 MILS

AILBE MILLERICK, *Engineering Manager,*
High Density TAB Package Engineering
Equipment Development Group

NATIONAL SEMICONDUCTOR CORP. m/s 29-100

SANTA CLARA, CALIFORNIA 95052-58090.

ABSTRACT

High power Lasers are increasingly being used to replace conventional mechanical cutting methods in the removal of extremely fine features in electronics applications.

Current examples of this are in the area of photomask feature changing and metal trimming to effect changes in resistance values at the silicon level in order to vary the performance of analog circuits. Such applications deal with photolithographic features with 0.5 micron accuracy which do not necessitate the use of vision systems to find imperfect features.

National Semiconductor's Advanced Packaging Equipment Group set out to apply lasers to the problem of leadframe feature removal in fine pitch packages. The system developed is fully automated with high resolution parallel processing vision system, and magazine to magazine material handling.

INTRODUCTION

New silicon technology particularily in the field of Application Specific Integrated Circuits (ASIC's) create demands for more compact packaging of Integrated Circuits.

The requirement for higher numbers of connections to the outside world from 84 to 400 leads and short leads for faster signal processing has driven the footprint of molded surface mounted components to approach the same magnitude as that of the silicon. Silicon die sizes of 500 mils square are now becoming common place in ASIC's and as this happens; lead spacing becomes finer; and large die size has a more profound effect on the shrinkage variation of the plastic encapsulation material.

c.f. Figure 1. 180 lead TapePak®.

This leads to two areas of challenge:-

The pitch becomes too fine for conventional punch-die inter lead cutting;

The position of the features to be cut becomes unpredictable as the package sizes become larger.

Thus, the finest limits of mechanical punch die material cutting traditionally used for copper interconnect removal have been exceeded, and the package shrinkage variation exceeds required positioning tolerances.

The development of a laser material processing system has provided a flexible tooling solution which is capable of removing dambars between leads on 10 mil centerlines, and by integrating it with a vision system the dimensional variations caused by shrinkage can be

recognised. Programming of the process to accommodate new package designs, different die sizes (resulting in different shrink rates), and product changes can be accomplished in minutes, as opposed to weeks or months of characterization and development of hard tooling for this purpose.
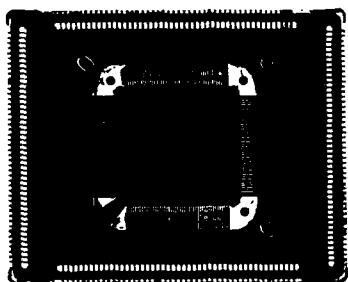
National Semiconductor 180 Lead

BACKGROUND

Dambars are a leadframe feature located just outside the area of the molded plastic IC body. For this application the dambars are located 10 to 20 mils from the body. Their function is to block (or dam) the flow of liquid molding compound between the leads during the molding process. Since dambars provide a direct electrical path between leads, they must be removed sometime after the molding process and before electrical testing of the component.

FIGURE 2: Leads on 15 mil centerlines joined by dambars. Molded body is above.

Figure 2 shows copper leads joined by the dambar. The dark area in the upper portion of the photo is the molded body encapsulating the die. The black squares bordered between two leads, the dambar, and the molded body is the flash that must be removed along with the dambar. The lead spacing is 15 mils, centerline to centerline.

For typical molded dual in line packages (DIPS), where lead spacing is 50 mils, the dambar removal process is accomplished with mechanical punch and die tooling. The punch removes the dambar and associated flash in one motion. In this case one may assume that each lead, and associated gap between each lead, is 25 mils wide. Then each punch is approximately 22 mils wide and must be absolutely positioned +/- one half mil. If the lead spacing is reduced to 15 mils, the punch width would be reduced to six and one half mils (.0065 inch), or about twice the width of a human hair ! The current carbide grinding limit is .008 inches. Obviously, for high leadcount, high density, encapsulated packaging to be practical, this mechanical method is not viable and non conventional solutions must be sought.

Mechanical Punch Configuration.
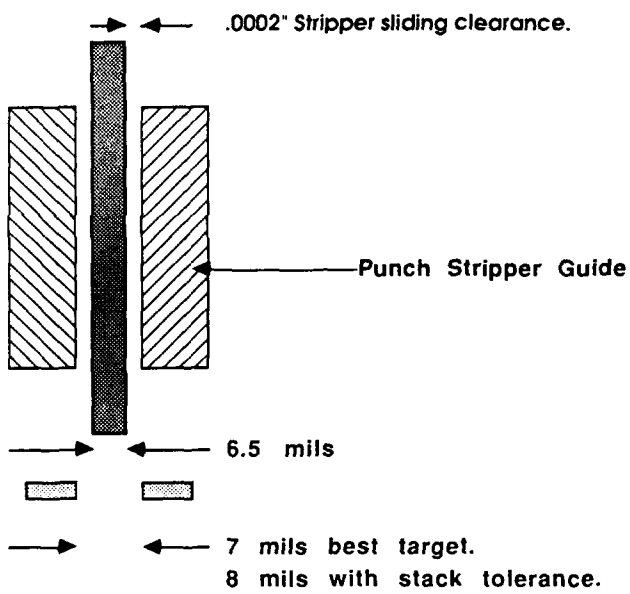
THE LASER PROCESS

To cut the one ounce cold rolled (2.8 mil thick) copper dambar a Q-switched YAG laser beam is used.
The Laser resolution is .0004 inches.

Figure 3 is an example of the dambar removal portion of the process. The focused laser creates a 1 mil kerf width separating the dambar at either end from the leads. The dambar removal tolerances are from flush with the lead to maximum .0005 inch protrusion.

766
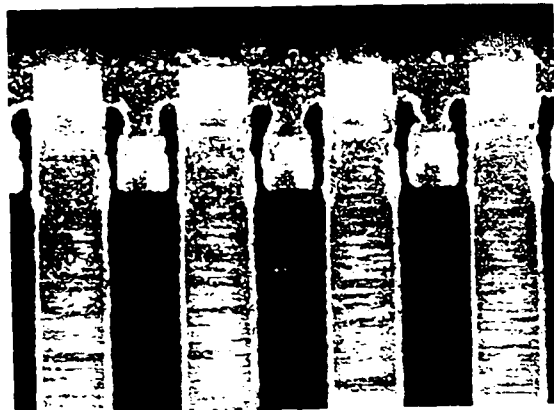
Figure 3: Dambars have been separated from leads with laser. Maximum permissible remaining dambar is .0005 inch.

Laser System Block Diagram
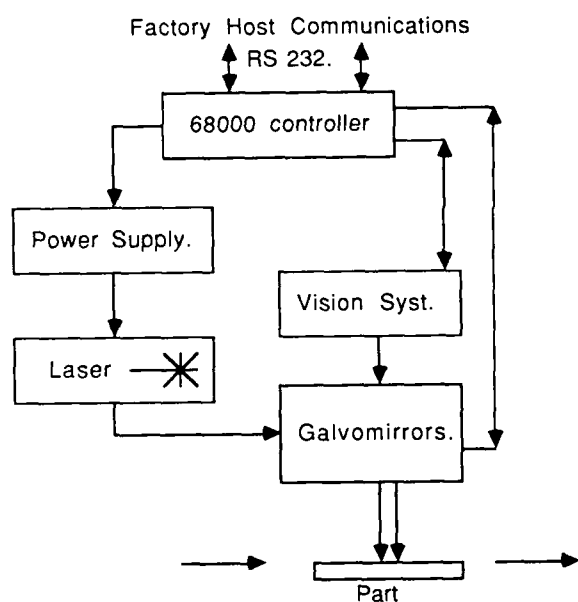
Figure 4. SYSTEM BLOCK DIAGRAM.

SYSTEM APPROACH.

Automatic magazine to magazine handling of the components in strip form is essential for hands off operation. Components are indexed one at a time into the lase site.

Galvo Mirrors.

For high response processing, the laser beam is directed by a galvo mirror assembly, while the part remains stationary.

Optimization of the cut path is important as it affects the rate at which parts are processed and process side effects.

The laser galvos scan more than 22 inches to process the 180 lead part with 64% laser cutting length efficiency. Vector co-ordinate execution in non-cutting mode are completed more rapidly (600X) improving time based laser efficiency to 99.97%.

This is 1200% faster than using servo X-Y moving of the part.

Vision.

Due to the required accuracy of the process, and the variation from part to part due to shrinkage, a vision system is incorporated to find selected reference points on the component. Because of the high resolution and speeds required camera movement is impractical.

The vision system is directed by another galvo mirror assembly. The field of view of the vision system is .050 inch square. The vision system has an array of 256 x 256 pixels, giving an edge detection accuracy of better than .0002 inch (2/10 of a mil).

The two galvo systems are calibrated to each other, but work asynchronously. The vision system finds reference points on the leadframe while the laser system cuts relative from these points. This "master calibration" need only be done once, however it is updated periodically to compensate for any drift of the two systems over time.

The complete processing station is contained in Class I housing to BRH standards, and operator assistance is required only for the loading and unloading of magazines of product.

OBSTACLES OVERCOME

Vaporized copper and molding compound waste generated by the process must be removed in such a fashion that they are not permitted to redeposit on the package. Remaining pieces of the dambar, as large as 8 mils square, must also be removed.

767

Changing incident light angles associated with galvo mirrors were found to provide inconsistent edge detection by the vision system. Therefore, top lighting, either pre- or post scanning, was unacceptable. Back lighting was found to provide a more stable image. The back lighting optics and debris removal chuck are incorporated together in a single design.

HIDDEN BENEFITS.

Fast prototyping of new packages is now possible using the Laser system to configure the leadframe and the package when molded oversize from existing package tooling. Tape feature change without production mask investment is simple and quickly done.

The flexibility of the system currently is capable of handling nine varieties of package with quick software change and minimal mechanical changeover.

Valuable engineering time and further capital funds are no longer tied up for every new design of package to be invented. Also, unused tooling, and spares, aren't sitting under-utilized while production time is slack for a particular product, as would be the case for hard tooling.

RESULTS & CONCLUSIONS.

The limits of laser accuracy are far from being exceeded. With one mil kerf width on high power Lasers the limitation will not be the laser but the system. Although it has never been tested, it is estimated that dambars associated with lead spacings of 2.0 mils could be removed by the method described in this paper.

The flexibility of the laser system has significantly reduced the prototype to product cycle time that is required for new package designs, and accordingly, the cost. One package was completed in 8 weeks using the Laser to prototype. The process of laser dambar and flash removal produces consistent and superior trimming quality compared to hard tooling.

It is a true non contact process.

Laser Processing as a production tool.

Advantages.

Process.

Non contact process for fine pitch thin foil interconnect.

Process is ***burrless.***

Plastic ***resin removal*** and cutting in the same process step.

Accuracy.
1.0 mil laser beam diameter.
0.2 mil resolution (image processor).

Flexibility
CAD addressable.
Process program parameters can be changed and stored in software.
Cutting programs can be changed easily.

Fast turn-around.

Packages can be prototyped quickly.
Oddball pitchs and leadcount can be run without retool.

Minimum Heat Affected Zone.

Tape can be cut from foil for planar and bump applications.

A LASER-APPLICATIONS LABORATORY COURSE FOR HIGH SCHOOLS

Gareth T. Williams
Professor of Physics
San Jose State University
One Washington Square, San Jose, CA 95192, USA.

Malcolm G. Cornwall
Principal Lecturer
Brighton Polytechnic
Lewes Road, Brighton BN2 4AT, England, Great Britain.

Abstract

The success of the low power HeNe laser as a teaching tool in higher education is well established. We have extended the laser's use to secondary education by developing a laboratory course having the form of a collection of laser-oriented electro-optic exercises which are described here in broad detail. The exercises are designed to lead to student research projects. The essence of this approach is to introduce the principles of optics by studying ways of modulating and manipulating laser beams. The course has been demonstrated in the form of hands-on workshops to groups of high school physics teachers who have enthusiastically endorsed it. The equipment used is a mixture of relatively expensive items such as a laser and an oscilloscope, and an assortment of inexpensive items such as small motors and polaroid sheets. Preparations are underway to "field test" this course with high school students in a classroom setting.

Introduction

The priority of optics in high school science education has been rejuvenated by the microelectronic and laser revolutions. Optoelectronics has become the leading edge technology for future generations of computers. Laser applications are proliferating; the one-time "solution-looking-for-a-problem" is now the basis for a host of new scientific and industrial devices and processes. Opto-electronics, fiber optics, laser technology, and the potential of optical computing have come together to create a "photonics" technology that promises to outstrip silicon in growth and importance before the 21st century. However, introductory physics courses in secondary and higher education reflect little of this trend, apart from the appearance of minor addenda to the traditional syllabus on "recent" developments such as lasers, fiber-optics and, perhaps, holography.

This article describes an innovative high-school-level optics laboratory course having laser applications as its main theme. Each laboratory exercise is centered around the use of the Helium-Neon laser as the key laboratory tool, and involves beam manipulation and modulation as the primary study areas. The student investigates basic optical principles using one of the key devices which has given rise to the new optics and applies these principles in simplified versions of photonic instrumentation and devices found in the "high-tech" world around them. With this approach we believe students will be inspired to explore further the world of optics, and the emphasis on applications can be coordinated with the introduction of other branches of science and technology. Indeed, it is intended that such further exploration be an integral part of the course by having each exercise lead to a student research project.

The course was designed and developed in 1988 by the authors, and has since been demonstrated to British and American high-school physics teachers in the form of hands-on workshops. Twelve student exercises were presented and a detailed description of one can be found in Ref. 1. The response to this technology-oriented approach to optics education has been very favorable.

The Laser-Based Course

The main "tools" of this course are a laser, an oscilloscope, a power supply, a function generator, and a camera. Secondary items are photodiodes, low voltage DC motors, small loudspeakers, a liquid crystal cell, lens and mirror holders, and an assortment of general-purpose holders. Burette clamps are particularly useful.

The class starts with a brief introduction to lasers and laser light and, perhaps more importantly, to laser safety. The CORD approach to laser safety[2] is appropriate here; students individually have to demonstrate their ability to operate a laser safely in performing a series of simple specific exercises.

The remainder of this paper describes in broad terms the fifteen areas of study covered by the course.

1. Using a laser for measuring large objects, and for studying beam divergence.

Initially the height of the laboratory and the length of a table at its other end can be measured using triangulation methods, and this idea can be extended to measuring the external dimensions of buildings. While doing this, the divergent nature of the beam will become obvious, and its angle of divergence can be measured and compared to manufacturer's "specs".

2. Using a laser to measure the optical properties of boundaries.

The directionality of a laser beam makes it a good approximation to a single ray. This property, together with its high irradiance, makes it an ideal probe for studying the bending of light at boundaries. A tank containing scattering particles in water to pick out the beam path as it bends works well. Cases that can be studied are refractions through a glass prism, a glass slab, and a hollow prism, and reflections from single plane mirrors and double mirrors. Total internal reflection is also a "natural" using this equipment.

3. Steering a laser beam with flat-surface devices.

The optical lever effect can be used effectively to reveal small movements of mirrors attached to thermally expanding bodies, or to building walls, and also to study movement of liquid surfaces. More interesting, however, are lightweight mirrors attached to motors or loudspeakers; beams can be swept at constant angular velocity, swept back and forth, or made to follow a circular path. If two units are used, then Lissajous figures can be formed, or interesting but complicated patterns produced if the input to one or both the loudspeakers are voice patterns or music. Rotating slabs and prisms are other interesting beam-sweeping devices.

4. Steering a laser beam using curved surfaces.

The focusing and expanding properties of lenses are discovered by studying the ways they "steer" or redirect narrow beams incident upon them (equivalent to rays). This leads to the concepts of focal point, focal length, conjugate points, and the function of lens systems. The key item for this project is the use of a loudspeaker scanner which effectively produces a fan of rays emanating from a point source. The lenses then focus or expand this fan in a strikingly visual manner, allowing calculations of focal lengths, etc.

5. Guiding beams with fibers.

The importance of fiber optics in today's technology dictates that a complete section be devoted to this topic. Large diameter plastic pipes and fibers can be used to demonstrate the basic principles. Numerical apertures can be measured, and the use of a series of fibers channeling into a common photodetector to measure the velocity of a body passing their free ends makes an interesting project. The activity shown at the workshops involved a tank containing three liquids which form layers having differing refractive indices, the middle one being the highest. The beam directed into this layer is trapped, the layers acting as a step-index fiber. What is fascinating about this arrangement is that in about 24 hours the layers diffuse partially into each other transforming the arrangement into a graded refractive index (GRIN) "fiber". In this case the beam follows a sinusoidal shaped path along the central layer. Measurement of the refractive indices of the liquids used and the selection of alternative liquids, plus the development of a schlieren system to visualize the boundaries between the liquids, all make for exciting extensions to these ideas.

6. Using a laser for spatial character reading.

The high directionality of a laser beam makes it ideal for studying fine detail when moving across an array of "characters". We have used stationary beams with moving patterns and moving beams with stationary patterns.

One of the loudspeaker scanners can be used to scan a stationary pattern in the form of a transparency, the transmitted beam then being collected by a positive lens and directed onto a small stationary photodetector placed at the point of focus. In this manner a spatial pattern is being translated into a series of electrical pulses. A stationary beam can also be passed through a spinning transparent disk on which is glued an opaque letter(s) before passing on to a photodetector connected to an oscilloscope. Rotating the disc at high speed while slowly traversing the beam radially along it gives a slowly changing oscilloscope pattern which, if studied carefully, reveals what letter is on the disc.

7. Studying the profile of a laser beam.

The essence of this experiment is to direct the beam onto a scanner and then onto a small photodetector. If the raw beam is to be studied, then it is necessary to allow a long run between the scanner and the detector in order for the natural divergence to produce a sufficiently large spot to be studied. If a lens is used, then the run does not have to be as great. In either case, a steady pattern can be obtained on the oscilloscope for analysis.

8.   Using a laser to study diffraction effects.
    Standard Fraunhofer diffraction patterns produced by the passage of a beam through sin-
gle, double, and multiple slits can be observed and analyzed by scanning them across a
fixed photodetector. Diffraction gratings can also be used.   One particularly interesting
"acousto-optic" experiment involves using a loudspeaker to generate ripples on a water sur-
face, and to study how laser light is scattered off this "diffraction grating".   The grat-
ing spacing can be varied by changing the frequency of the signal fed to the loudspeaker.
Fresnel diffraction also shows up well if the beam is allowed to shine onto a very distant
wall and objects are placed in the beam.

9.   Using a laser to study rotational and vibrational motion.
    Inexpensive DC motors capable of 500 rev/s can be bought at most hobby shops or surplus
stores.   Their angular velocities are voltage sensitive and they operate in the range 0-3V
which makes them very safe.   If a "floppy" disk of stiff paper with a slot cut out of it is
mounted onto the motor shaft, then the beam is broken into a series of pulses, which can be
used to "strobe" the motion of rotating or vibrating objects.   At the same time the chopped
beam can be sampled and displayed on an oscilloscope to determine the exact speed of the
chopper.   This is one experiment where the challenge of miniaturizing the system and the
possibility of using a conventional light source might be considered.

10.   Modulating a laser beam using polarizing sheets.
    If a polarizing sheet is spun at a constant angular velocity in a laser beam already
plane polarized, then the beam will have its irradiance modulated in a sinusoidal fashion
at twice the frequency of the rotating sheet.   The system hence acts as an optoelectronic
oscillator, the frequency of which can be varied by changing the DC voltage applied to the
spinner motor.   Some very interesting effects can occur when this beam is now directed onto
a glass plate at Brewster's angle.   For instance, if the stationary polarizing sheet has
its axis perpendicular to the plane of incidence, then upon reflection of the beam off the
plate and onto the photodetector, a signal at twice the frequency of the spinner will be
observed.   If the stationary sheet is turned through 90 degrees, then a frequency of four
times the spinner frequency will be seen.   It is this sort of thing that we want the stu-
dents to find for themselves, and to work at trying to understand what is happening.

11.   A study of the effect of passing a laser beam through a liquid crystal cell.
    Large liquid crystal display cells, either removed from some old equipment or purchased
new, provide a very interesting and inexpensive way of modulating a plane polarized laser
beam.   For transmission through the cell, the mirror glued to one surface must be peeled
off and replaced with an ordinary polarizing sheet.   The cell can be activated with a 7V
sinusoidal signal, maybe from the optoelectronic oscillator mentioned in Section 10!   It is
an interesting side exercise to find out which connector "pads" lead to which number seg-
ment.   Once a segment is found, then the beam can be passed through it to be modulated.   A
basic experiment here is to increase the excitation frequency, study the response of the
cell, and plot a response curve.

12.   Photodetector linearity.
    Four linearity-check methods suggest themselves and probably they should all be tried.
The first is to assume the law of Malus applies to the spinning polarizing sheet described
earlier and to search for and evaluate any deviations from the expected sinusoidal curve.
The second is to assume a Gaussian distribution of the beam irradiance in the "profile"
scanning experiment and again look for deviations.   The third is to assume an inverse
square relationship between irradiance and distance along the beam at large distances or
along a beam expanded by a lens.   The fourth is to stack neutral density filters in the
beam and note the corresponding transmissions as measured by the photodetector.
    In the last two of the above activities, the chopper could be used to allow one to work
with pulse heights rather than DC levels.

13.   Beam absorption in various materials.
    Measuring the incident and transmitted irradiances for various color filters, and vari-
ous numbers of the same color filter, gives good data for analysis.   The exponential nature
of absorption with distance traveled is clearly revealed, and the absorption of liquids
containing absorbing and scattering centers whose density might vary with time can be stud-
ied.   In addition, this is a good time to measure the reflectance of various surfaces such
as laser mirrors, aluminum mirrors, and so on.
    All studies of this kind can well be done using pulse height analysis after first chop-
ping the incident beam.

14.   Holography.
    Even though hologram making was not possible at the workshops due to time constraints,
it will certainly play a major role in the development of this course.   Holograms were
shown at both workshops and generated the usual excitement.   The authors have both had

experience at teaching holography classes and will probably concentrate in this course on small format Denisyuk holograms.

Conclusions

Laboratory exercises relating to each of the areas described in this paper have been developed and demonstrated before forty high school teachers. Following the demonstrations, the teachers had a chance to operate the assembled equipment themselves, and it was at this point, seeing their excitement, that we realized how valuable the laser could be as a teaching tool in science and technology education at the secondary school level. The laser is an exciting, impressive-to-be-seen-using instrument, a fact which is very important for the age group being considered; and the highly directional intense beam can be manipulated and modulated by a number of inexpensive devices to create a menu of exciting and scientifically important exercises. We are very satisfied with the results to date.

The next step is to enlarge upon the laboratory notes we have written so far, and to establish "laser labs" at a number of local high schools in order to evaluate their effectiveness in a classroom setting. Preparations are under way with a group of high school physics teachers to initiate a program in the Fall of 1989, and preliminary results should be available in the Spring of 1990.

References

[1] Williams, Gareth T. "The laser as a teaching tool in the high school science and technology curriculum". LASER TOPICS. Vol. 10, No. 3, Summer, 1988.

[2] The Center for Occupational Research and Development (CORD) publication entitled "Introduction to lasers".

PANEL DISCUSSION

HIGH POWER DYE LASER TECHNOLOGY
December 7 (1988), Harvey's Resort Hotel, Lake Tahoe, Nevada

MODERATOR:

F. J. Duarte
Eastman Kodak Company

PARTICIPANTS:

H. R. Aldag
AVCO Research Laboratory

R. W. Conrad
U. S. Army, MICOM

P. N. Everett
MIT Lincoln Laboratory

J. A. Paisner
Lawrence Livermore National Laboratory

T. G. Pavlopoulos
Naval Ocean Systems Center

C. R. Tallman
Los Alamos National Laboratory

Dr. Duarte:

In this introduction I would like to outline some very basic features of dye lasers which make these stimulated emission sources rather unique. First, it is well established that pulsed dye lasers can emit virtually at any wavelength from the near UV to the near IR. This is possible due to the availability of a large selection of dye molecular species. In addition, given the wide variety of pump sources, ranging from flashlamps and excimer lasers to Nd:YAG and copper lasers, there exists ample choice in laser output characteristics:

High peak powers
Large energy pulses (up to 400-800 J per pulse)
Short pulses (ns regime)
Long pulses (μs regime, flashlamp excitation)
Pulse repetition frequencies up to 20 kHz (copper laser excitation)
High average powers (in excess of several 100's of Watts)
Broadband emission
Narrow-linewidth emission

This flexibility is also reflected in the financial side where emission at a particular wavelength can be achieved through several different combinations and integrated systems offering significant contrast in capital and operational cost.

At this stage it is appropriate to indicate that the success of the dye laser is best underlined by its use in a wide range of applications:

Study of fundamental physical phenomena
Numerous types of spectroscopy techniques
Medicine
Industry
Laser Isotope Separation (LIS)
LIDAR
Military

It is in part due to this wide usage of dye lasers, and the proliferation of commercial manufacturers, that many people tend to dismiss the field of dye lasers as a mature technology needing little further development and research. Certainly, I tend to disagree with this perspective. Instead, I would like to advance the thesis that although much has been accomplished in the physics and technology of dye lasers still a lot remains to be done.

The latter point can be highlighted rather easily by focusing on a further example which will illustrate the strength and the assumed weakness of dye lasers. For several reasons, not explained here, in the past few years there has been considerable interest in blue-green lasers. Now, let us consider a few tunable blue-green lasers together with their transitions. It is clear that those lasers with atomic transitions can be tuned within a few GHz while the molecular lasers, such as HgBr, offer a much broader tuning range. However, in both cases the tuning ranges available are quite narrow when compared with the continuous wavelength coverage (from 430 to 550 nm) offered by coumarin dyes. Thus, the wide tunability advantage of dye lasers is made obvious. To this strength one should indicate the immediate assumed weakness: the short lifetime of the dye. This is certainly an area in need of fundamental research and more will be said later.

Now, I will focus on one aspect of dye lasers which has experienced significant advances in the last few years: linewidth narrowing. Since the introduction of the dye laser by Sorokin and Lankard in 1966[1] and until about 1972, dye lasers were known mainly as a source of tunable-broadband radiation. It was not until 1972 that a most fundamental laser characteristic, namely narrow-linewidth oscillation, was demonstrated by Hansch.[2] The development of the telescopic dye laser was followed by the introduction of the grazing-incidence grating technique and multiple-prism grating oscillators. In the Table we provide a summary of the performance of the different oscillators.

These dispersive techniques have been utilized to provide narrow-linewidth and single-longitudinal-mode oscillation at reasonable efficiencies and low ASE levels ($<10^{-5}$ to $<10^{-7}$). Moreover, in the case of high-prf copper-laser-pumped MPL and HMPGI oscillators extremely stable single-longitudinal-mode lasing has been reported and

Table

Cavity Type	Linewidth	% Eff.	Pump Source	Reference
Telescope	2.5 GHz 300 MHz[†]	20 2-4	N_2	T. W. Hansch, Appl. Opt. 11, 895 (1972)
MPL	1.6 GHz	14	N_2	F. J. Duarte and J. A. Piper, Opt. Commun. 35, 100 (1980)
Grazing- Incidence	1.25 GHz	4	Nd:YAG (2nd)	M. G. Littman and H. J. Metcalf Appl. Opt. 17, 2224 (1978)
	150 MHz	3	Nd:YAG (2nd)	M. G. Littman, Appl. Opt. 23, 4465 (1984)
HMPGI	1.15 GHz	7-10	N_2	F. J. Duarte and J. A. Piper, Appl. Opt. 20, 2113 (1981)
MPL	60 MHz[†]	5	Copper	A. F. Bernhardt and P. Rasmussen Appl. Phys. B 26, 141 (1981)
HMPGI	400 MHz	4-5	Copper	F. J. Duarte and J. A. Piper, Appl. Opt. 23, 1391 (1984)
MPL	375 MHz		Flashlamp	F. J. Duarte and R. W. Conrad Appl. Opt. 26, 2567 (1987)

[†]Incorporates intracavity etalon.

MPL (Multiple-Prism Littrow)

HMPGI (Hybrid Multiple-Prism Grazing Incidence)

documented utilizing interferograms resulting from the integration of several million laser pulses.

The success of these techniques has been demonstrated by their adoption to other laser systems such as TEA CO_2 lasers, excimer lasers, and solid state lasers. A parallel development has been the theory of beam divergence and intracavity dispersion. A particularly successful effort has been the understanding of multiple-prism dispersion.[3-7] This theory has been extended to other laser and electro-optic applications.

The development of linewidth narrowing techniques has been supported by the advance of wavelength tuning methods. Here, a comprehensive number of alternatives include piezoelectric displacement of gratings, etalons, and mirrors and pressure tuning. This field has seen the development of sophisticated electronic control systems and the implementation of ingenious physical schemes to achieve synchronous tuning.

In this area it should also be mentioned that several studies on thermal effects (see Refs. 8 and 9) have provided insight on design constraints for stable long term operation. Also, recent studies on linewidth instabilities in multimode lasers have been done by Westling and Raymer[10] and Berik and Davidenko.[11] Linewidth instabilities in double-longitudinal-mode flashlamp-pumped dye laser oscillators have been reported by Duarte and

Conrad[12] and Duarte et al.[13] These studies provide valuable information toward the physical understanding of this phenomena which may lead to its eventual neutralization.

Now, let me return to the question of dye lifetime. Undoubtedly, this is a difficult problem which, if solved, could provide a significant advance in dye lasers (Dr. Pavlopoulos will discuss this later). At present we have seen that there are some very effective alternatives in prolonging dye lifetime. First, we must ask the right question. Here, the appropriate selection of pump sources is important. For instance, direct excitation of the first singlet state not only improves efficiency but also makes the dye last longer. Our experience with high-prf copper-laser-pumped dye lasers indicates that the lifetime of rhodamine dyes is vastly superior for this type of excitation than for UV excitation involving higher singlet states. Next, it appears that the production of dyes with a higher degree of purity also helps as our recent experience at Eastman Kodak suggests. Here, I refer to coumarin 314 T which has been found to provide up to 50% more output than the parent compound under excimer-laser excitation and to offer a X 2 lifetime extension under flashlamp pumping. Also, recent work by Everett and Zollars[14] has demonstrated the effective use of dye purification systems that allow extended periods of operation under flashlamp-excitation.

A more fundamental question in need of attention is related to the excitation dynamics of pulsed dye lasers. Here we are in need of good workable and practical time dependent semi-classical and quantum models.

Let me conclude by reiterating that although dye lasers have proven to be a reliable and extremely versatile workhorse, a lot remains to be done. We should try to get this message across to government and industry so that an adequate level of dye laser research and development can be maintained in this country.

Dr. Aldag:

It is indeed a pleasure to be part of this distinguished panel, but I believe we also have a distinguished audience. I see a lot of familiar faces in the audience from the laser community. I will be concentrating on addressing some of the issues that Frank Duarte pointed out in his opening remarks in terms of the flashlamp-pumped dye lasers that we have been working on at the Avco Research Lab. We actually got into the dye laser business some 17 years ago with laser-pumped lasers using our Model C950 nitrogen laser pumping a small "Dial-A-Line" dye cassette. We still do some laser-pumped laser work, but we have become known for flashlamp-pumped dye laser work and it is this area on which I will concentrate.

The demonstrated advantages that we see, some very obvious, include wavelength agility; being able to tune to a particular wavelength either broadband or narrowband. Wavelength diversity, is met by a whole spectrum of dyes available from the near UV to the near IR. High energy, has been demonstrated at Avco with an output of 7 J per pulsed with 1% efficiency[15] and we're working on a system to yield 100 J per pulse. The Russians have published a paper yielding 400 J per pulse,[16] but I don't recall there being any rep rate involved in that particular situation. High Average Power was demonstrated at Avco at 1.2 J and 850 Hz - that gives us an average power in excess of 1 kilowatt. That, I think, would qualify as a high average power dye laser. There is no reason why higher energy pulsed devices cannot be operated at pulse rates from 10 to 100 Hz, so the opportunity in

very high average power dye lasers exist and will probably be demonstrated in the very near future. One of the real selling features of the flashlamp-pumped dye laser is the fact that for many applications you can demonstrate the performance that is required with a single laser head. Therefore without an amplifier, without frequency doubling, and without Raman shifting, you end up with a very compact system and very high system efficiency. Finally, there is a scheme for replenishing the dye system, a system that we devised at Avco which we call a filter and feed system on which I'll make some comments on near the end of my talk.

Flashlamp-pumped dye lasers were used in the laser isotope separation program at Avco that went on for about 10 years. Four of these flashlamp-pumped dye lasers were used and the beams were combined with a couple of dichroic mirrors and then sent to an adjacent room where we had the atomic uranium vapor separation apparatus. These units operated at 30 Hz for 12 hours a day, for periods of years, demonstrating the extreme reliability and ruggedness of the flashlamp-pumped dye laser. The flashlamp-pumped dye laser was actually the ring oscillator of a very narrow bandwidth system. We used a frequency doubled YAG laser pumping a dye cell and it is this low power dye cell which was tuned and narrowed with gratings and etalons and then fed into the flashlamp-pumped dye laser ring to give us the tuning capability needed. This type of injection locked tuning is certainly one way to get around having damage problems trying to build a tuned power oscillator at very high average powers. The flashlamp pumped dye laser that was used during this program, and for many other programs, is what we call a MK V. It's a transverse flow design. The flow comes-in and goes through some flow straighteners and then goes through a specially designed nozzle with cooling ports through the pump region, out through an exit nozzle and to an exit plenum and through a porous wall to isolate any downstream turbulence coming back into the pump region. Pumping is done with two elliptical reflectors. This type of configuration, where you're pumping a very small slug of dye, is ideal for applications requiring high rep rates in order to minimize the flow requirements. The pulse width of these devices were a nominal 1-2 microseconds. In one case we were using a blue green laser dye and some integrating optics to demonstrate a uniform field. It was in this device that we added a converter dye[15] (Stilbene 420) to the flashlamp cooling jacket in order to demonstrate 7 J output with 1% efficiency. For higher energy pulsed systems you have to design a device which has a larger volume of dye which is being pumped. For this we use a multi-lamp non-imaging system that we have developed at Avco. With this unit we have obtained much higher energies. As we outlined in our talk yesterday,[17] we use a slab geometry configuration with a multi-channel dye cell approach. The center channel being for the lasing dye, the outer two cells being for the converter dye. In this case we have a more efficient collection of the converter photons for pumping the laser dye. In addition, when we use the multi-lamp non-imaging configuration we improve our pump efficiency over the elliptical pump efficiency of the MK V by a factor of 1.6. So when we combine these two we expect to improve the dye laser efficiency from 1% that we've demonstrated to 1.5%.

We have also demonstrated that the solvent can be recovered from these systems. There are two methods that we commonly use in the laboratory for recycling our solvent. The batch method is to have a large enough system to contain enough dye and dye solvent to meet our experimental requirement. We have a built-in dye system in our laboratory and we have a number of 55 gallon drums that we use for our different dyes. A more economical approach is to use a dye replenishment system where we constantly take out some of the dye solution containing good dye, bad dye, photo degradation products; filter all of it out with a charcoal filter, put the clean solvent back into the system, but meter-in an

appropriate amount of dye concentrate to maintain the dye concentration of the dye laser device. In this type of system you do not operate at the optimum dye performance point. You have to select the 90% point or 80% point depending on how small you want to make everything. As an example of the sizes involved, I will give you a comparison of the batch and the filter and feed systems for a system that has a mission requirement of 10^4 pulses and a dye life of 10^5 J per liter to the 90% point. In this particular system 625 liters will be needed to maintain that performance with the batch method. In a filter and feed system the requirement is to have enough dye to meet your mission requirement, which in this case would be 30 grams of dye. Your volume is now dependent on the dye solubility in the particular solvent. In this case, the 30 grams required only 3 liters of solvent, together with the laser volume of 20 liters. Only 23 liters are needed compared to 625 liters. If we were to increase the mission requirement by a factor of 10, you see that the volume required with batch approach increases by a factor of 10. With the replenishment approach the 3 liters would become 30 liters and we have only 53 liters required for the program.

With this, I think I should close my remarks, but I will be glad to answer questions later.

Dr. Everett:

My recent experience is mostly the flashlamp pumped dye lasers. For these lasers "high power" means more than 100 W average. Such lasers are usually less than 1% efficient, meaning power inputs of at least 10 kW, and probably much more. I will describe one such system now being installed by MIT Lincoln Laboratory to conduct experiments. It will have 6 independent laser beams, each with over 5 J per pulse, 10 pps, in 2-μs pulses. Only two of the laser heads have as yet been installed, to make up one beam. There will be 12 heads, 2 per beam, to provide more than 300 W total. The new heads will be added above the existing ones, inside an emi box.

The laser heads are among the small items. We have the fluid piping, and the modulators, which consist mostly of capacitors that store the charge for dumping into the flashlamps. There will be 12 of these modulators.

The system was developed for a flammable dye solvent. Recently we found we could use a non-flammable solvent of acetamide in water. The engineering would have been simpler if we had dome so earlier. The lasers will dissipate 1/4 MW, running a 10-minute bursts. The cooling system pumps water through the laser heads, and extracts the heat to store temporarily in a 10,000-gallon underground tank. The dye handling system pumps 360 gpm, and will recycle the dye solution in real time. The degradation products and unfortunately the dye also, are taken out of the solution with carbon, as necessary, and fresh dye added, all within the 4-minute round-trip time of the system. The optical analyzers are essential for measuring the degradation and the dye content for control of the process.

The pictures shown give an idea of the scale involved in fielding such a laser using present-day technology. We are learning how to do it smaller and simpler if we had to do it again. The overall efficiency is only about 1/10 of 1%. Because of the time-table, we had to use brute-force engineering. There are ways available for increasing the efficiency, perhaps 10-fold, which could be retro-fitted if more energy is needed for the

experiments. I will mention these later. They would result in a much more powerful laser in the same space and with the same power consumption. I will now address some of the factors associated with such systems.

1. Spectral tuning for high power systems:

These systems typically work near the damage limit of the optics. Birefringent filters and uncoated etalons are generally good for frequency control, because they stand high power, have low loss, and can generally be inserted or removed without upsetting alignment. Prisms tend to detune as they warm up from absorbed power. Gratings tend to burn up. A single birefringent filter is useful for obtaining bandwidths between 0.1 and 1 nm. Narrower bandwidths are obtained by adding thicker birefringent filters or solid etalons. Both can be readily tuned by mechanical rotation. With multiple elements, gang tuning is required which adds complexity. Each successive element gives about another 7-fold narrowing, with perhaps 7% loss in energy. At very narrow bandwidths (MHz or less) the loss tends to increase more rapidly, probably due to incomplete spectral homogeneity of the dye.

Another approach is to control the bandwidth with a low-power oscillator and then amplify to reach high power. Then any frequency selective technique will do because its efficiency no longer matters. But the multiple stages make for a complex system. An "in-between" approach is to inject a large oscillator with a low-power signal of the desired bandwidth to force its oscillation. In general the feedback swamps any further injection after the initial tickler. The question then is how long does the spectrum stay locked to the injection? The locking can certainly last for microseconds after injection of a 50 ns pulse at the crucial time. However, it has been found that the locking is lost faster for very narrow injected bandwidths (MHz or less). A multi-pass amplifier can be formed from an unstable resonator with a small hole through the center of one of the mirrors. A low-power controlled-bandwidth signal is introduced through the hole and amplified by many passes as it expands in the so-called resonator. These devices have sometimes been called injection locked oscillators, but their performance is better understood as multi-pass amplifiers. The input must be sustained throughout the pulse unless the hole is very small. When the hole gets smaller than the diffraction-limited core it evolves into an injection-locked oscillator, and the analysis becomes complicated.

2. Beam quality:

Flashlamp-pumped dye lasers tend to have relatively poor beam quality, because of aberrations in the medium. This gets worse when high power is required. The medium needs to be flushed out between pulses. There is hope that phase conjugation will help. However, the typical distortions generally seem to contain quite high spatial frequencies, leading to the so-called "fried egg" nature of the far-field. This might have half the energy in a blob of about 15 lambda/D and the rest in a broad background. But even if the phase conjugation were to catch only half of the energy and put it into a tight beam, then this would be useful. The Raman approach may become useful for cleaning up a beam after it is generated.

3. Laser-pumping vs flashlamp pumping:

When pumping with a flashlamp, the size of the dye-cell must approximately match the lamp for good coupling. With lamp-pumping the power density is generally far below optimum. With a laser-pump a much small cell can be used, with greater efficiency because of the higher power density, which in turn reduces the heat budget. These factors also make for better beam quality. The laser-pump does not require good beam quality, and

multiple laser pumps can be multiplexed into a single dye cell. Laser-pumped lasers show a lot of further potential. For instance, at this conference last year, Avco Textron described a laser-pumped laser which achieved excellent beam quality by supersonically scanning the lasing beam through the medium during an extended pulse. Excimer and copper vapor lasers make very good pumps. I will not enlarge on them because there are others here much more expert than I.

4. Efficiency and scaling:

Given a good dye, the efficiency is usually limited by how hard it can be pumped. With flashlamp pumping the source is the limiting factor, and even 1% efficiency is hard to achieve. Spectral enhancement shifts unused light to the useful pumping spectrum and thus improves efficiency. There is still a lot of unrealized potential for this approach. With laser excitation, damage to the medium or to the optics is generally the limiting factor, and more than 30% efficiency can be achieved within these limits. But the efficiency of the laser pump should also be considered.

The dominating parts of typical flashlamp pumped dye lasers are the power supplies and fluid-handling systems. This is because the supplies must typically provide at least 100 times the output of the laser (1000 times in the case of the example). Nearly all this power becomes heat within the laser head, and must be carried away in the fluids. So scaling is dominated by the supplies and fluid handling systems.

5. Dye lifetime:

Dye lifetime has been considered important and much research has gone to improving it. However, cost of dye gets less as more is used, down to small numbers of dollars per gm. But the solvent remains expensive to buy, and often more to get rid of. Fortunately, very crude technology will get everything out of the solvent so new dye can be added for a fresh start. When dye degrades, it is typically from a very small fraction of the dye turning into a substance that absorbs at the lasing wavelength, thus destroying the laser output. We would like to take out only the contaminant and leave the good dye. As yet, there seems no practical process for doing this, but fortunately we can afford to throw away the dye. Real-time cleaning systems using carbon (as used in water processing) economically take everything out except the solvent. The equipment to renew the dye solution is a relatively small add-on to a typical high-power laser system. It pays for itself anyway in getting the initial crud out of the system and in allowing use of cheaper grades of solvent.

Once committed to dye solution recycling, the most efficient dye and solvent can be chosen regardless of dye life-time. This may for instance allow use of a non-flammable solvent. Safety Officers provide a strong inducement to use a non-flammable solvent for any big dye laser system, especially if the dye is pumped by flashlamps.

It is good practice to have an optical analyzer in the dye-loop to maintain a continuous check of the absorption near the lasing wavelength. It must have a path-length about as long as the laser to allow recognition of losses that can do significant harm (i.e. less than a few percent loss per pass of the laser). This can often save the worrisome question, "why isn't the laser lasing today?"

6. Ruggedness and reliability:

The lamps are usually considered the most fragile component of a flashlamp pumped dye laser system. Most breakage of lamps occurs in shipping, and in installation. Once

safely in place in a well-designed laser they tend not to break.

For specially demanding applications "end cap" seals are more rugged than other varieties, and some lateral support might have to be engineered if the lamps are long and skinny. However, the coolant usually gives some cushioning effect.

7.   Fragility of the technology to competing approaches:
       This is always a concern in any developing field. There is a strong desire to develop solid-state lasers, pumped with solid-state diodes. Present approaches work best in the near infrared, so for the near future the visible will be reached by frequency doubling or mixing. Dye lasers will probably have an economic advantage for some time, especially considering the exotic materials involved in the potential alternatives. There is something to be said for a medium which is self-healing and readily replaceable, with easy tuning.

8.   Dye laser research in the U. S.: Are we doing enough?
       The U. S. research seems very haphazard. Thank heavens for some small companies that have been willing to operate on shoe strings while hoping for a bright future. Fortunately some are now being rewarded in the medical field, but the medical field has no urge toward powerful systems. The bigger dye laser technology that I am most aware of was developed by industry with the mistaken notion that it would pay off in uranium enrichment. One might say that a lot of our dye laser technology has come about by mistake. This isotope effort is now being pursued in National Laboratories, and we hope their experience will be better.

Dr. Tallman:

My background is of 35 years of engineering, last 18 in laser development. I am a generalist, with depth in EE, material science, excimer lasers, etc. Specifically, I have been recently responsible for a large high power dye laser system. The following comments are concerns in the design, operation of this system.

We employ a XeCl Excimer (308 nm) transverse pumped dye laser using Lambda Physik EMG203 MSC pump lasers. The dye laser was designed by LANL and consisted of a MOPA configuration which initially was one oscillator and two dye amplifiers and as the system became optimized we were able to eliminate the second amplifier and finally, were successful in developing a single high power oscillator that met our requirement. We used Lambda Physik's TBS dye in Dioxane and successfully operated this system for over a year without major problems; however, there was considerable effort placed in the safety concerns in the handling of large quantities of these flammable and toxic materials.

Briefly, I would like to identify the topics of concern and areas of study and experience we had in this laser system:

I.   CONTAMINATION AND SYSTEM CHEMISTRY:

A.   Dye and solvent contamination

      1)   As received dye. Quality control in purity?

2)   As received solvent. What are the contaminants? What kinds of contaminants are sources of performance degradation? What do you do to remove materials such as particulates, cotton fibers from filters, water, other.

B.   Dye solubility

1)   How do you prevent undissolved dye particles from depositing on the windows, with resultant window damage?

C.   Pre-filtering, processing vs in-system filtering.

1)   What filers can you use? Cotton produces particulates, Teflon? How stable is the filter material with the solvent and dye and the products it's collecting?

D.   Reaction of the solvent with the plumbing, pumps, filters, seals, "O" rings. How clean is your plumbing o start with? What process should you use initially. How do you flush and clean this system after it's been down and opened?

E.   Effects of photochemistry in producing absorbers, chemical contaminants forming from the solvent and dye. Non-linear effects in the dye laser performance. Dye and solvent clean up systems. Metering in new dye to replace the chemically disabled dye, removal of absorbers. Dye stability considerations.

F.   Film deposits on the windows, reducing the transmission of laser pump and lasing beams. Lowering of the threshold of damage in window. Removal of film deposits.

G.   Dissolved air, in the solvent and its effect on the photochemistry of the solvent and dye stability under intense UV pumping.

II.   OPTICAL MATERIALS:

A.   Damage threshold for high grade quartz, and MgF_2, the effect of solvents on this threshold and surface photochemistry. Flow design effects, boundary layer thickness vs turbulence scrubbing (static vs flow damage threshold). Clearing ratio effects.

B.   Photoproducts chemically attacking the optical surfaces.

C.   Excimer laser beam uniformity considerations. Hot spots in the pump beam. Peak vs average fluence. The use of pump beam homogenizers.

III.   SAFETY CONSIDERATIONS:

A.   Fire

1)   We were handling as much as 90 liters of dioxane in the laser system. This included the reservoir and plumbing system. A small leak in this system operating at 60 psig with 60 gallons/min (4 liters/sec) presents a serious fire potential. Vapor leak detectors, alarms, pressure, flow sensing. Ventilation system.

2) What do you do when you must disassemble the dye cell? How do you vent the system safely? How do you fill and drain the system safely?

3) What if there is a leak and it flows on and into the large optical table with its 1/4-20 holes every inch. (We filled every hole with epoxy.)

4) Can a stray beam or beam stop provide sufficient energy to ignite the solvent vapors that might be at the cell?

5) At high flow rates dielectric fluids can generate very high voltages when flowing in dielectric materials. We had sparks jumping from Kynar plumbing and Kynar filter housings. Repeated sparking will produce a hole, and now you have the three necessary items for a fire; an ignition source, fuel and oxidizer if there is a leak to the room air. Threading a grounded wire down the plastic tubing is one solution, but be sure its grounded. We saw sparks flying all over a Kynar filter housing even though the tie bolts were all wired to ground.

B. Toxicity

1) Dioxane is carcinogenic. It enters the body by oral and dermal routes. Eye effects, lungs. Repeated exposure to low concentrations has resulted in human fatalities. Organ chiefly affected are the liver and kidneys. Death results from acute hemorrhagic nephritis. What protection do you use? Gloves, respirators, remote fill and drain.

2) Most dyes have not been fully analyzed for their health hazards. Should be treated as carcinogenic.

IV. EXCIMER LASER RELIABILITY:

A. Factors affecting the excimer laser run time at acceptable energy levels:

1) Gas Depletion of the halogen due to reaction with the metallic parts such as the discharge electrodes.

2) Buildup of absorbers, chemistry with organic internal components.

3) Deposits on the excimer laser windows. Products from reaction with the metal and organic internal components. The use of valves at the window for window removal without contamination of the rest of the laser with moisture. Window purging? How effective? How should it be done.

4) Gas clean up systems, electrostatic precipitators? External cryogenic traps. What contaminants can be trapped, what about the alternative of hot calcium chip furnace for removal of contaminants. How reliably can one inject the halogen.

B. Electrode wear. Pin preionizer electrode wear. Lifetime of electrodes, bearing, etc.

C.   Industrial laser performance specifications. What are reasonable expectations in
      continuous run times? What are the expected downtimes and operating costs in
      dollars/hour?

Dr. Paisner:

      Frank, I don't know if we have the largest average power dye laser system in the
world, and Henry's laser was very impressive, especially having been demonstrated many
years ago. However, it will certainly be true that in the near future the laser at
Livermore will be the largest dye laser system in the world. We have currently achieved
performance levels of 900 W average power in a multicolor beam and 600 W in a single color
beam at repetition rates in excess of 4 kHz. I'd like to describe the context of our dye
laser development program. In particular where we are going with our laser system and
what we have to demonstrate. The laser systems are being developed at the Lawrence
Livermore National Laboratory for the U. S. DOE in support of atomic vapor laser isotope
separation. We have two major industrial partners: Martin Marietta Energy Systems in Oak
Ridge, Tennessee, in our uranium isotope separation program for light water reactor fuel
and Westinghouse Idaho Nuclear Company, WINCO, in Idaho Falls in our specialized isotope
separation program. The latter involves enriching plutonium for defense applications.

      Uranium, like most of the heavy elements, the lanthanides and actinides, for example,
has an ionization potential of about six electron volts. Because of its large number of
optically active electrons, it has a plethora of energy levels in the visible. Therefore,
a three-step photoionization scheme which uses tunable dye light in the red is a viable
option. Additionally, a resonant multistep photoionization process requires short pulse
lasers because the energy levels in the excitation process have relatively short
lifetimes, perhaps 100 nanoseconds to several microseconds. So two of the requirements of
the laser system are that it provides short pulse radiation tunable to the electronic
transitions of interest. In order to guarantee isotopic selectivity, the process laser
system has to be spectrally narrow band. Inadequate spectral resolution simultaneously
wastes laser energy on the undesired isotope and results in lower enrichment performance.
Spectral control of the lasers is also of central importance to process design to maximize
the fraction photoionized; this includes addressing every magnetic sublevel of every
hyperfine level of every velocity class of the selected atoms in vapor flow. Of course,
very high average power is required for isotope separation at an industrial scale. The
reason for this is quite obvious. For example, a gaseous diffusion plant, operating at 10
million separative work units per year, processes 12-1/2 kg of feed and produces about 2
million kg of product. That's a lot of material. Over 40 kW of tunable power is required
to process this material. You can prove this to yourself by assuming a reasonable photon
utilization. That's a pretty awesome amount of laser power, until you realize that such a
laser isotope separation plant produces yearly enough fuel for 100, one gigawatt, nuclear
power plants. So there is a tremendous economic leverage in a laser isotope separation
plant.

      A critical design parameter for the process laser system is beam quality. To
efficiently utilize the process light, the laser beams must propagate through very long
columns of vapor. The typical beam qualities of 15-20 λ/D discussed in earlier
presentations, are unacceptable for our enrichment applications. Finally, the pulsed
tunable process light must be available at very high repetition rates to address all the
atoms flowing through the photozone. Typically, atoms travel at many hundreds of meters

784

per second. This translates into many tens of kilohertz pulse repetition rates for a several centimeter photozone. The requirements just outlined limit the search for a practical system for laser enrichment. The system we have been developing over the last fifteen years is a copper vapor laser pumped dye laser system. This system can meet all the laser requirements for isotope separation and can be scaled to plant performance levels. Basically, the system is arranged in a master oscillator power amplifier configuration. The master oscillator in the copper laser system is an injection locked small bore oscillator followed by three large bore amplifiers. The copper laser emits two wavelengths, one in the green and one in the yellow. Both colors are well-suited for pumping dyes. In our particular system each amplifier chain operates at approximately 4 kHz pulse repetition rate and a typical output power of 500 to 700 W. The copper light from many chains can be multiplexed, both spatially and temporally, to provide pump light to the dye system. In the Laser Demonstration Facility at Livermore we can accommodate ten corridors of copper laser chains. Each corridor contains six copper laser chains. Currently, two corridors are deployed, containing twelve small bore oscillators and 36 large bore amplifiers. When we deployed the second corridor, we actually transferred first corridor lasers to the second corridor and replaced them with new laser heads. The facility also has support systems to refurbish these copper lasers. This is a very important activity because the copper laser system operates 24 hours a day, seven days a week. Corridor one was first assembled in 1985 and ran for two years in full operation. Since each copper laser chain operates at 500 to 700 W, the copper corridors typically run at between 3,000 and 4,000 W each. It is very important to understand that system availability is essential in a uranium isotope separation plan. 40,000 W of tunable light is required at 100 percent availability. Less availability requires more laser hardware in the plant. The copper lasers have been designed for maximum availability. Each laser amplifier head requires 480 power, some buffer gas, some water and some signal cables from a supervisory computer system to operate. All other functions are contained within the laser enclosure. Each head is composed of several components called line replaceable units. A failed laser head is replaced on the wall. The failed component is replaced and sent to repair. The laser is then readied for service at an off-line test stand. Over the last several years the copper laser system has accumulated 500,000 hours of operating time. It's really a plant-like setting. I'll quickly go through the dye laser system in the next few minutes. There are a number of conventional facilities that support the dye laser system. A very large reservoir of dye is needed. Fortunately the dyes used are very stable under copper-laser excitation. As in the copper laser system, the dye system employs a master oscillator followed by several power amplifiers. The dye corridor shown in this viewgraph contains four dye laser chains. Although each dye laser chain layout is straightforward, the optical system is fairly complex as illustrated in this viewgraph. The amplifiers in this photograph are barely discernible. The web of mechanical and optical hardware handles the delivery of the copper laser pump power. In the optical system that we have deployed there are over 2,600 optical components. Optics and optical system design are key development areas in our program. We have mounted a major effort with qualified commercial vendors in the community to produce high quality, low loss coatings and substrates. I'll end by saying that unlike the dye laser system on Maui that is sent upwards to the heavens, the beam from our Laser Development Facility follows a more earthly route to other sites at Livermore. However, generating and sending spectrally tailored, temporal and spatially formatted high average power light over two kilometers to enrichment facilities at Livermore, as indicated in this aerial viewgraph, has been a challenge for our scientists and engineers. Over the next few years, the laser system at Livermore will be basically doubled in power with the deployment of the second copper corridor.

Dr. Pavlopoulos:

Since the first observation of laser action from organic dyes (about 20 years ago), intense activity has taken place. The main reason for this development is the unique dye-laser feature of being tunable over a wide range of wavelengths. In addition, dye lasers are suitable for high pulse repetition frequency (prf) operation (i.e., high average power output) because of the simplicity of cooling.

However, present flashlamp excited dye lasers, which employ commercially available laser dyes, have the following disadvantages. (1) Photodecomposition is more or less present in all presently available laser dyes. (2) Because most organic laser dyes can only be dissolved in organic solvents such as methyl alcohol, p-dioxane, dimethylformamide, etc., a fire and health hazard exists, especially for inexperienced personnel. Few laser dyes are water soluble. Unfortunately, most laser dyes are very unstable photochemically when water is employed as a solvent. (3) Another drawback is the requirement to use flashlamps with steep risetimes (in the 1-μsec range and less) to obtain laser action from the laser dye. Flashlamps meeting this stringent requirement are difficult to build for operation above 1000 J.

Efficiency limitations, low photostability, and the requirement to employ flashlamps with fast risetimes in present dye lasers using commercially available laser dyes is caused by excessive so-called triplet-state losses. If new laser dyes could be developed that exhibit reduced triplet-state losses, flashlamps for excitation could be employed that have slower pulse risetimes. Significantly, these flashlamps can be operated over much longer lifetimes, and are commercially available at several Joule ratings above 10,000.

The selection of organic dyes that show laser action is, at present, accomplished by trial and error. Thousands of organic dyes have been synthesized over the last hundred years and are commercially available. Thousands of them show strong fluorescence (i.e. high quantum fluorescence yield). However, only a few exhibit laser action under flashlamp excitation. The efficiency (0.2-1.5%) of presently available flashlamp excited laser dyes is closely related to the accumulation of dye molecules in their triplet state as the result of so-called intersystem crossing. These triplet-state molecules, generated during intense excitation, in turn absorb the laser light more or less efficiently, depending on the magnitude of their triplet absorption. In addition, most organic compounds (including laser dyes) undergo photodecomposition when present in their triplet state.

Although Rhodamine 6G has been known since 1967, it is still one of the most efficient laser dyes. It lases with about 1% efficiency when flashlamp pumped. The question is, then, why haven't more efficient laser dyes been synthesized since 1967? The answer appears to be that there is excessive triplet-triplet (T-T) absorption over the fluorescence (laser action) spectral region because of the presence of benzene (or its heterocyclic) derivatives in all presently available laser dyes.[18]

It is well known that the presence of benzene (and its heterocyclics) in organic compounds is responsible in most cases for carrying the spectroscopic property of fluorescence. Reviewing experimental data on T-T absorption of organic compounds published in the literature, it is apparent that all aromatic compounds possess strong (to

very strong) T-T absorption, stretching from their fluorescence spectral region to longer wavelengths.[19]

Should the search for new laser dyes concentrate on the few organic compounds (quasi-aromatic heterocyclic) that exhibit strong fluorescence but do not contain any homocyclic and/or heterocyclic aromatic groups? Some of these compounds seem to have low T-T absorption over their fluorescence spectral region. Laser dyes have been recently discovered in the quasi-aromatics of syn-9,10-dioxabimanes (syn-(R_2,R_1)bimanes) and pyrromethene-FB$_2$ complexes.[20]

Dr. Conrad:

When I was asked to sit on this panel, I thought it would be a very simple thing. I thought all I had to do was to sit down and make up a few charts, some of which said, what interesting things have been done in this technology area within the last two or three years, and make up a second set of charts that said, what do we do now? I didn't have any trouble with that first set of charts whatsoever. In fact, some of the things you've heard the other speakers say they are, in fact, on my charts. There are a few things that were not said, such as, for instance, some of the things that were shown here at the Lasers '87 conference; ~800 J achieved in an excimer laser-pumped dye laser.[21] Phase conjugation of a flashlamp-pumped laser,[22] ultra narrow-linewidth operation in flashlamp-pumped lasers.[12] Many of the people that you see here work on these things. In fact, that was an easy job. When I sat down and tried to think of what should we do next, I wound up writing a bunch of open-ended questions or open-ended items. I said we need more energy, we need shorter pulses, we need longer pulses, we need higher average power. And then I asked myself, who is actually going to fund open-ended questions like this? I decided I didn't know the answer, but as all of you are probably aware now, funding in this technology area has been going down sharply in the last couple of years. I am referring now specifically and only to DOD money. I am not talking SDI. I am not talking DOE. But certainly DOD funding for this technology has hit the skids and it looks like it is not going to be coming back up any time soon. In particular, the U. S. Army's program has lost most of its funding in the last couple of years and when I asked people why is this so, I get what I really couldn't call reasons. I would call them excuses. I get reasons like, dyes are very inefficient. Dyes are also toxic, carcinogens. They have very bad beam quality and this kind of thing. But those reasons don't make a whole lot of sense to me but they don't have to make sense to me. Somebody up there gives these as the reasons for essentially cutting our funding of the Army's dye laser program. So the real question is what do we do now in view of what I think is an inescapable fact that we are going to have very little DOD money to work with for the next couple of years. I mean, what could we do that would turn DOD and the Army's thinking around? In fact, is there any chance that we could ever turn it back? When I stop and think about what's happened in the DOD tactical laser programs in the last 20 years, which is about how long I have been working in it, I see things like in the early 70's millions and millions poured into continuous wave CO_2 lasers, very high power CO_2 lasers. Who do you know now that's working on very high power CO_2? And the answer is, probably not very many people. Shortly after that we got heavily involved and spent millions and millions on high energy pulsed CO_2 lasers. Well, at least in DOD you don't see very much more going on in that area either. Then came high power continuous DF lasers, HF-DF lasers, and it looked like that technology was also going to wind up on the shelf, and if it hadn't been for SDI it would probably be on the shelf still. Unfortunately, it looks to me as though this

technology area, dye laser technology, may very well wind up on DOD's shelf until something comes along that has a need for it. And that's really the bottom line and that's my perception of what the problem is at DOD and certainly the Army. What is the need? What is the application for this? I think that's really the root problem and frankly the Army does not know and what little work is being done in the area of tunable lasers now, at least in the Army, all of that money is going into the solid state laser area. So, the very bottom line question is, what do we do with the resources that we have? Well, clearly something like what some of the new dye chemistry has come up with, things that potentially promise increases in efficiency, perhaps factors of 2, 3 or even more, that seems like it would open someone's eyes. I mean, efficiency translates into size as far as the Army is concerned. If you make it three times more efficient, you can probably make it almost one third the size. And it seems that the Army has gotten an awful lot for its money out of the fundamental dye synthesis work that you've heard presented earlier here. My own personal feeling is that what little money the Army has is going to probably wind up in that area. Frankly, I don't think we have enough funds to afford to do anything else. An interesting example of that is, as you heard Henry mention earlier, the design and fabrication of a 100-J, 10-pulse a second pulsed dye laser that the Army has funded. Now, it looks like that laser or something very, very close to it, will be operational in some form in about April (1989). The really unfortunate thing is that at the present time the Army has no funding with which to do anything with it. I mean, at the present time, that laser will get built, will hopefully meet all of its specs and then will sit there. I don't know. I wish I did have the answers. All I'm saying is that we are going to have to get smart, not in the technical work that we do but in the technical work that we choose to do in order to get the very most out of the very small funding that I see coming down in the next several years. That's essentially it.

Dr. Duarte:

Thank you very much Ray. This was supposed to end up at 3:30 and then there will be a tea break and we'll come back for the second part. We have some time now for questions.

Prof. Benetti:

This is a question for Dr. Paisner, would you comment on the linewidth and ASE characteristics of your high prf dye laser?

Dr. Paisner:

The oscillator, which I didn't describe, is capable of single-mode operation. One of the design principles of our process is that we specify by design what the spectral linewidth is of the laser system. Since we spend so much money on the back end of the laser system, it pays to do the optical engineering, electro-optic engineering of the front end of the laser system. So we do it by a combination of smart oscillator design and electrooptics. We spectrally tailor the light out of what we call the wave form generator in our system. I don't know if that answers your question.

Dr. Duarte:

Jeff, can you add anything about the topic of ASE?

Dr. Paisner:

We try to keep it as low as we possibly can. A percent, less than a percent, something like that. In many cases we completely get rid of it. As you know, we need to use the copper laser as efficiently as possible so we run our amplifiers under heavy saturation conditions. You could easily get lots of ASE out of a system if you don't design the system right. But, if you design the system right, you can really minimize the amplified spontaneous emission.

Prof. Penzkofer:

Would you comment to what extent can the charcoal filter be used to remove the dye and dye degradation products.

Dr. Aldag:

I don't recall a number. We have made that measurement at AVCO and Pat was with us at the time, but these charcoal filters hold quite a bit. They remain in their filter cartridges for a long time before we have to change them, and there are ways of cleaning the charcoal, but it's not very economical so we just throw it out. Pat, you want to add anything to that?

Dr. Everett:

Yeah, I can add a little to that. My recollection from the numbers and these were done many years ago, conservatively, it was at last one gram of dye per hundred grams of carbon. And sometimes one got things as good as one gram per ten grams or maybe a little bit better. But in actual fact it's not a concern because activated carbon is such a cheap material and I think unless you had thousands of grams, and perhaps much more than that, absorbed in your carbon, you wouldn't even think of trying to reclaim it. You'd just put it in a landfill. We don't know of anybody who's been smart enough to figure out how to just take out the degraded product.

Question from the audience:

In your amplifier system, did you note a chirping in the laser, the single frequency, or the laser injected pulse?

Dr. Aldag:

The question relates to a chirping of the dye laser system. There was chirping and it was done in order to cover the particular linewidth of the uranium energy level.

Dr. Duarte:

Perhaps we ought to break and go to tea break and come back later on. Thank you.

References

1. P. P. Sorokin and J. R. Lankard, IBM J. Res. Dev. 10, 162 (1966)
2. T. W. Hansch, Appl. Opt. 11, 895 (1972)
3. F. J. Duarte and J. A. Piper, Opt. Commun. 43, 303 (1982)
4. F. J. Duarte and J. A. Piper, Opt. Acta 31, 331 (1984)
5. J. R. M. Barr, Opt. Commun. 51, 41 (1984)
6. F. J. Duarte, Opt. Commun. 53, 259 (1985)
7. R. Trebino, Appl. Opt. 24, 1130 (1985)
8. D. W. Peters and C. W. Mathews, Appl. Opt. 19, 4131 (1980)
9. F. J. Duarte, IEEE J. Quantum Electron. QE-19, 1345 (1983)
10. L. A. Westling and M. G. Raymer, JOSA B 3, 911 (1986)
11. E. Berik and V. Davidenko, Opt. Commun. 67, 129 (1988)
12. F. J. Duarte and R. W. Conrad, Appl. Opt. 26, 2567 (1987)
13. F. J. Duarte, J. J. Ehrlich, S. P. Patterson, S. D. Russell, and J. E. Adams, Appl. Opt. 27, 843 (1988)
14. P. N. Everett and B. G. Zollars, Proc. Int. Conf. Lasers '87, F. J. Duarte, Ed. (STS Press, McLean, VA, 1988), pp. 291-296
15. P. N. Everett, H. R. Aldag, J. J. Ehrlich, G. S. Janes, D. E. Klimek, F. M. Landers, and D. P. Pacheco, Appl. Opt. 25, 2142 (1986)
16. F. N. Baltakov, B. A. Barikhin, and L. V. Sukhanov, JETP Lett. 19, 174 (1974)
17. D. P. Pacheco, H. R. Aldag, and P. S. Rostler, presented at Lasers '88, paper TF.4
18. M. Maeda, Laser Dyes (Academic Press, New York, 1984)
19. I. Carmichael and G. L. Hug, J. Phys. and Chem. Ref. Data 15, 1 (1986)
20. T. G. Pavlopoulos, M. Shah, and J. H. Boyer, Appl. Opt. 27, 4998 (1988)
21. J. J. Ehrlich and S. P. Patterson, In Proc. Int. Conf. Lasers '87, F. J. Duarte, Ed. (STS Press, McLean, VA, 1988), pp. 304-307
22. S. D. Russell, J. J. Ehrlich, S. P. Patterson, R. W. Conrad, D. E. Klimek, and S. F. Folghum, ibid. pp. 680-684

Corrigenda

1. Page XV, line 29: the title quoted on this line was subsequently modified to that given on page V, line 6.
2. Page 4, line 2: "scource" should read "source".
3. The number on page "492" should read "486"
                       "491" should read "487"
                       "490" should read "488"
                       "488" should read "490"
                       "487" should read "491"
                       "486" should read "492"
4. Page 1153, line 29: "rule" should read "role".
5. Page 1154, line 30: "there not" should read "there are not".
                     38: "Maday" should read "Madey".
6. Page 1155, line 36: "are" should read "care".
7. Page 1159, line 41: "that" and "are being developed" should be deleted.
8. Page 1160, line 51: "And" should be deleted.
9. Page 1161, line 22: "very briefly review" should read "a very brief review".
10. Page 1162, line 5 : "ten" should be deleted.
                     25: "ten times difficult" should read "ten times as difficult".
                     35: "of things" should read "of the things".
11. Page 1166, line 55: "interfrerometry" should read "interferometry".
12. Page 1168, line 7 : "fr" should read "for".
                     19: "Standford" should read "Stanford".
                     36: "quesion" should read "question".
13. Page 1171, line 38: "safr" should read "safer".
14. Page 1171, line 63: "nuclear world" should read "nuclear free world".

END

FILMED

8-89

DTIC